Transactions of the ASME®

Transactions of the ASME, Journal of Heat Transfer (ISSN 0022-1481) is published quarterly (Feb., May, Aug., Nov.) for $165.00 per year by The American Society of Mechanical Engineers, 345 East 47th Street, New York, NY 10017. Second class postage paid at New York, NY and additional mailing offices. POSTMASTER: Send address changes to Transactions of the ASME, Journal of Heat Transfer, c/o THE AMERICAN SOCIETY OF MECHANICAL ENGINEERS, 22 Law Drive, Box 2300, Fairfield, NJ 07007-2300.
CHANGES OF ADDRESS must be received at Society headquarters seven weeks before they are to be effective. Please send old label and new address.
PRICES: To members, $40.00, annually: *to nonmembers, $165.00.*
Add $24.00 for postage to countries outside the United States and Canada.
STATEMENT from By-Laws. The Society shall not be responsible for statements or opinions advanced in papers or . . . printed in its publications (B7.1, para. 3).
 INDEXED by Applied Mechanics Reviews and Engineering Information, Inc.
Canadian Goods & Services Tax Registration #126148048.

Journal of Heat Transfer

Published Quarterly by The American Society of Mechanical Engineers

VOLUME 116 • NUMBER 1 • FEBRUARY 1994

TECHNICAL PAPERS

(Contents continued on page 7)

Contents (continued)

ANNOUNCEMENTS

Journal of Heat Transfer

Editorial

A Message From the Technical Editor

With this issue the ASME JOURNAL OF HEAT TRANSFER begins its 36th year of publication. Over the past 35 years, the journal not only increased in size from 329 pages in 1959 to about 1100 pages in 1993, but also solidified its position as one of the most respected technical journals in the field of heat transfer. The journal has maintained a tradition of excellence since its inception in 1959, and that tradition has been enhanced by numerous technical and associate technical editors through their enlightened editorial policies and guidance.

The JOURNAL OF HEAT TRANSFER continues to be interested in receiving outstanding technical articles of permanent interest to the heat transfer community. We plan to continue the policy of having a good mix of experimental, numerical, and theoretical articles dealing with all of the science and technology of heat transfer. We particularly encourage articles in areas of heat transfer that are the focus of new or renewed attention by researchers and practitioners, such as heat transfer on microscale, heat transfer in materials processing and manufacturing, multiphase heat transfer, and flow and heat transfer in porous media. However, with the exception of areas that are too new to do so, the Board of Editors expects the authors to validate and benchmark their numerical or theoretical predictions before the paper will be accepted for publication in the journal.

ASME does not consider symposia and conference proceedings papers as archival, and such papers are eligible for publication in all ASME *Transactions* journals. Authors of conference papers are therefore welcome to submit their papers to the journal at any time, if they feel that their work has reached the level of quality and completeness expected for an archival paper. However, a more reasonable approach is to submit a paper to the journal after it has been first reviewed for conference presentation. The editors do not actively solicit conference papers, but many authors submit their conference papers for consideration by the journal. Some of the most significant papers from the meetings are being published in the journal.

Our readers should know that the board of editors has been vigorously debating on how to make the material published in the journal more interesting and useful. Our mission is to communicate with our audience scientific research results of fundamental character, which have application in design. We, therefore, always urge authors to address not only their peer researchers, but the broader audience of practicing engineers. Specifically, in order to improve technology transfer between those who generate new research results and the practicing heat transfer engineers in industry who use them, the Board of Editors has decided to publish invited state-of-the-art design and research review articles. The objectives of the design review articles are to: (1) broaden coverage of heat transfer topics and applications; (2) improve presentation for use by practicing engineers; (3) increase participation of heat transfer engineers in industry; (4) increase academic/industry interaction; and (5) educate academic members of industrial needs, etc. The state-of-the-art design review articles should contain, but are not limited to, the following:

- Emphasis on topics of interest to, and recommended by, industry
- Broad scope—talk to the whole community
- Industrial application and the parameter space of interest to industry
- Comparison between theory/correlations/data
- Examples of how you use the information in the articles
- Assessment of the state-of-the-art
- Estimate of the uncertainties associated with this topic
- Recommendations: range of use, missing areas, research needs, etc.

To maintain the quality of an archival journal, the articles will be reviewed. The Board welcomes suggestions from readers for topics of the state-of-the-art design review articles. Topics and prospective authors from industry will be identified by the Board of Editors, and the technical editor will invite the author(s) to prepare the review articles.

The Board of Editors of the journal has had many discussions over the past two years of how to reduce the time from submission to publication. We are happy to report to our authors that we have managed to reduce somewhat the time from submission to completion of the review. For papers submitted in 1993, we were able to complete the review process in 8.5 months on the average. This includes first set of reviews, revisions, resubmission, re-review, and a final decision. Unfortunately, there are exceptions. The time from submission to publication has started to lengthen because of the increased backlog of unpublished papers. This has occurred in spite of tightened acceptance requirements. The number of papers submitted during 1993 increased to about 390 and represents an increase of about 50 articles over the previous year. Only about 40 percent of papers are finally published and, with very few exceptions, all require revision. On the average, the total time from submission to publication is now approaching 18 months, and efforts are being made to reduce this time. We continue to discourage authors from submitting overly long papers by returning them for revision prior to initiating the review process.

The JOURNAL OF HEAT TRANSFER benefits enormously from the efforts of a host of referees willing to provide evaluations of submitted work, all of them contributing their time on a voluntary basis. In order to recognize the exemplary service by the reviewers of the journal who combine expertise with a commitment to thoroughness, fairness, and adherence to rig-

orous standards for acceptance or rejection, the Board of Editors has established a special recognition award. The first group of individuals for the exemplary service award are:

Professor Theodore L. Bergman, The University of Texas at Austin

Professor James D. Felske, New York State University at Buffalo

Professor A. Haji-Sheikh, University of Texas at Arlington

Professor Adrienne Lavine, University of California at Los Angeles

Dr. Duane A. Nelson, Aerospace Corporation

The editors, authors, and readers of the journal owe a debt of gratitude not only to these few individuals but to all referees who provide reviews that are characterized by constructive feedback, objectivity, high standards, and promptness.

I also wish to ask readers to consider a personal subscription to the JOURNAL OF HEAT TRANSFER. A personal copy would enable you to have the latest research and technological developments in heat transfer at your fingertips. Subscriptions to the JOURNAL OF HEAT TRANSFER can be obtained by writing to the ASME Order Department, Fairfield, NJ 07007-2300. Subscription prices are $40.00 annually to ASME members and $165.00 annually to nonmembers or institutions. At the current annual subscription price to members, the cost is under 4 cents per page—a very low price by any standard of comparison.

In closing, the Board of Editors acknowledges, with deep appreciation, the strong support given to the journal by our authors and our readers. Comments, suggestions, and criticisms from our readers may be directed to any member of the Board of Editors and they, in turn, will see to it that such matters are discussed at the next editorial board meeting. We will continue to work with you. I am convinced that with your help, we will keep our journal as just about the most prestigious in our field, and I hope that together we can enhance that position and make it more valuable to our readers in the coming years. I personally welcome any comments and suggestions that will help us maintain and improve the quality of the journal.

Raymond Viskanta
Technical Editor
School of Mechanical Engineering
Purdue University
West Lafayette, IN 47907-1288

Invited Review Paper

Significant Questions in Thin Liquid Film Heat Transfer

S. G. Bankoff
Chemical Engineering Department,
Northwestern University,
Evanston, IL 60208-3120

Thin liquid films appear in many contexts, such as the cooling of gas turbine blade tips, rocket engines, microelectronics arrays, and hot fuel element surfaces in hypothetical nuclear reactor accidents. Apart from these direct cooling applications of thin liquid layers, thin films form a crucial element in determining the allowable heat flux limits in boiling. This is because the last stages of dryout almost invariably involve the rupture of a residual liquid film, either as a microlayer underneath the bubbles, or a thin annular layer in a high-quality burnout scenario. The destabilization of these thin films under the combined actions of shear stress, evaporation, and thermocapillary effects is quite complex. The later stages of actual rupture to form dry regions, which then expand, resulting in possible overheating, are even more complex and less well understood. However, significant progress has been made in understanding the behavior of these thin films, which are subject to competing instabilities prior to actual rupture. This will be reviewed briefly. Recent work on the advance, or recession, of contact lines will also be described briefly, and significant questions that still remain to be answered will be discussed.

Stability of Thin Continuous Films on a Heated Surface

The study of the stability of thin liquid layers draining down an inclined plane surface was initiated by Yih (1955) and Benjamin (1957) for the isothermal, linear stability case. Yih (1963) employed long-wave asymptotics, and thereby determined a critical Reynolds number. Benney (1966) derived a long-wave nonlinear evolution equation for the local thickness of a thin, isothermal liquid layer on a plane surface. Since that time a considerable number of extensions of the isothermal case have been made, such as those by Lin (1974), Gjevik (1970), and Pumir et al. (1983), to name only a few. The effects of heat transfer appear mainly in thermocapillary and vapor recoil effects. Since surface tension generally decreases with temperature, and for very thin layers on a heated surface, the troughs of waves are hotter than the crests (if the liquid is nonvolatile), liquid is convected away from the troughs, tending to destabilize the film. Similarly, for a volatile liquid, vapor recoil effects are destabilizing (Fig. 1). Bankoff (1971) added a vapor recoil term for the reactive pressure difference resulting from the faster evaporation from the wave troughs than from the crests on a heated surface. For very thin layers both effects may be present, since the heat transfer at the troughs may be so large that the liquid is no longer effectively in equilibrium with the vapor. Other instabilities may also be present. For layer thicknesses less than 100 nm, van der Waals forces come into play (Williams and Davis, 1982; Burelbach et al., 1988; Bankoff, 1959). Burelbach et al. (1988) considered wave growth on a thin liquid layer resting on a heated horizontal substrate, subject to evaporative, thermocapillary, and van der Waals instabilities, as well as mass loss. Figures 2 and 3 show film profiles at different dimensionless times for quasi-equilibrium evaporation when vapor recoil is important, and mass loss is more or less important, respectively. The thinning proceeds rapidly once the molecular dispersion forces come into play. A similar calculation by Tan et al. (1990), but with a nonisothermal substrate, predicted quite accurately the film thickness and temperature distribution measurements of Burelbach et al. (1990) (Fig. 4). This represented the first experimental confirmation of lubrication theory in the absence of any adjustable parameters. However, even here, significant questions arise. A continuous film of silicone oil on an Invar plate apparently dried out over the heated region of the substrate, leaving a continuous film over the unheated region. Orell and Bankoff (1971) similarly observed the breakup of a water film on a horizontal Bakelite plate in which an electrically heated stainless steel strip was flush-mounted. However, in the latter case the strip appeared to be quite dry, while with rupture and dryout of the nonvolatile, but well-wetting, oil, a very thin oil layer remained in the steady-state "dry" region. An interesting

II. FORMULATION

A. GEOMETRY

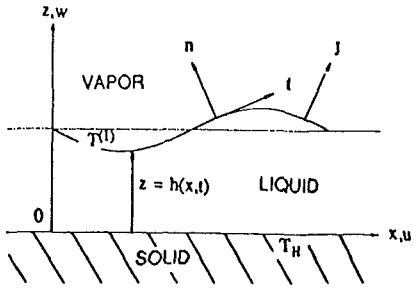

$h(x,t)$ = film thickness
$J(x,t)$ = mass flux due to evaporation
$T^{(I)}(x,t)$ = interface temperature
T_H = hot plate temperature (constant)
$\mathbf{n}$ = unit outward normal vector
$\mathbf{t}$ = unit tangent vector

Fig. 1 Diagram showing destabilization by vapor recoil

Contributed by the Heat Transfer Division and presented at the ASME Winter Annual Meeting, New Orleans, Louisiana, November 28–December 3, 1993. Manuscript received by the Heat Transfer Division August 1993; revision received November 1993. Keywords: Flow Instability, Reviews, Thin Film Flow. Associate Technical Editor: Y. Bayazitoglu.

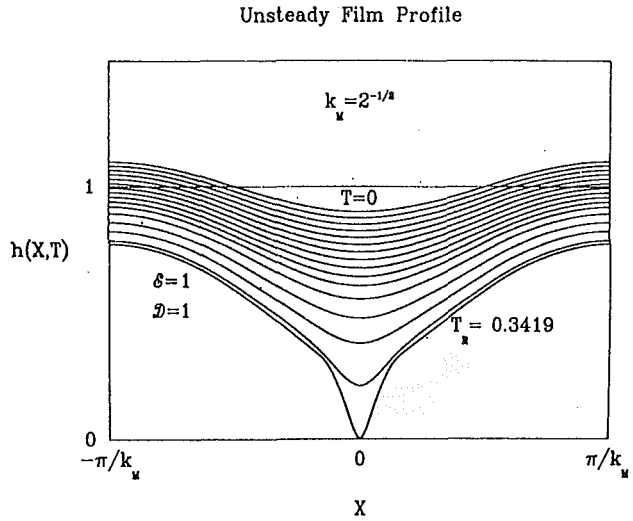

Fig. 2 Film profiles at different times with vapor recoil and mass loss from an evaporating liquid film (Burelbach et al., 1988)

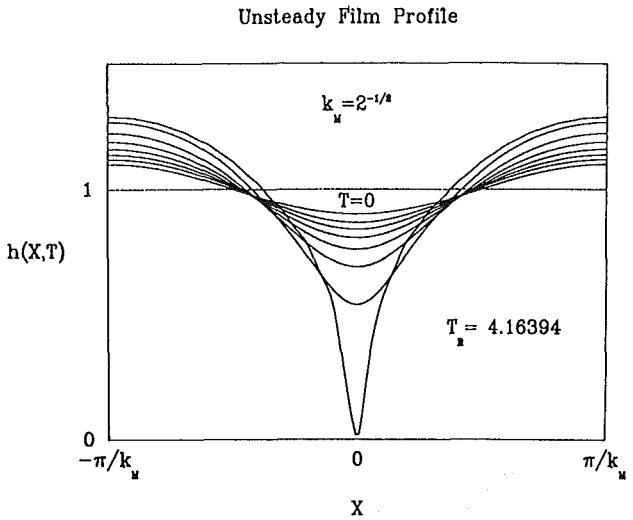

Fig. 3 Same as Fig. 2, except that mass loss is less rapid. k_M is the dimensionless wave number of the fastest-growing wave according to linear theory. T_R is the dimensionless estimated rupture time.

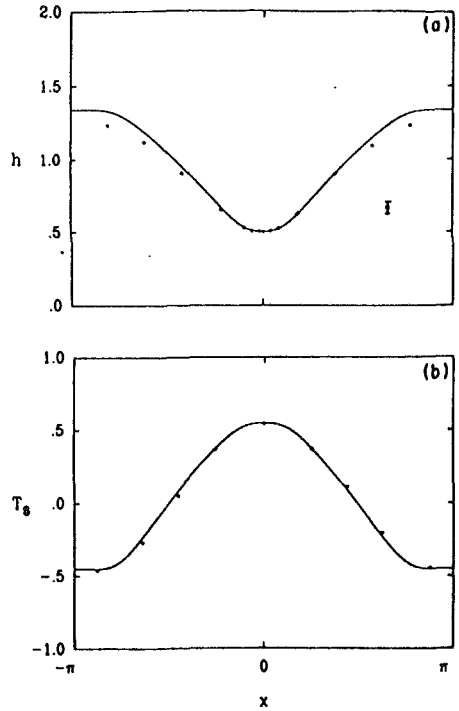

Fig. 4 (*a*) Film thickness data (Burelbach et al., 1988) compared to lubrication theory prediction for a nonisothermal Invar plate with silicone oil layer (Tan et al., 1990); (*b*) temperature profiles, predicted and measured

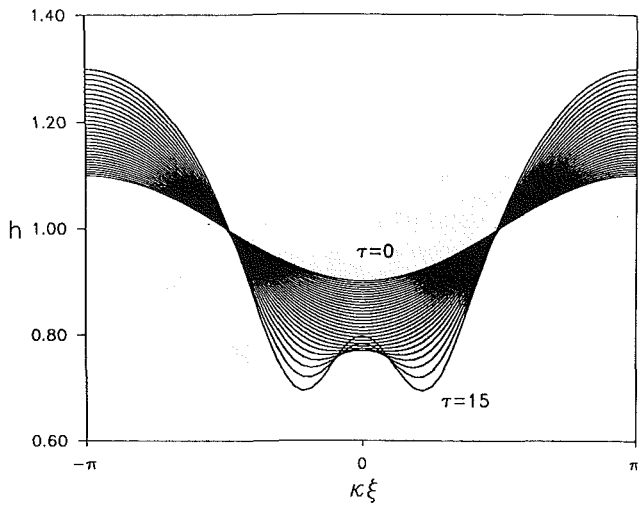

Fig. 5 Free-surface evolution for a thermocapillarity instability in the absence of gravity. $k = 0.7$ ($k_M = 2.03$), $KM/P = 1$, $K = 0.1$, $S = 0.1$: free-surface configurations with $\Delta\tau = 0.5$ up to $\tau = 15$; M is the Marangoni number; K is a surface thermal nonequilibrium parameter; and S is a surface tension parameter (Joo et al., 1991).

question is how the free surface "knows," in advance of actual rupture, whether or not the solid surface is well wetted.

Actual dryout involves the establishment of contact lines, with a corresponding apparent contact angle. Even for small contact angles, this is beyond the current capabilities of lubrication theory, which is a macroscopic theory. Details of this transition cannot be calculated at this time. Although the times involved are very short, the deformation of the downward-growing wave as it comes into close proximity to the solid surface determines the initial conditions for the subsequent expansion or contraction of a dry region by advance or recession of the contact lines. As shown by Joo et al. (1991) (Fig. 5), a single finger may develop downward upon heating a thin liquid layer, with specified values of the surface Biot number, Marangoni number, and surface tension number on a horizontal surface. The initial small disturbance is taken to be monochromatic, with dimensionless wavenumber $k = 0.7$ (the linearly fastest growing wavenumber, $k_m = 2.03$). At some point in time, depending on the parameters chosen, the downward growth slows because of the proximity of the bottom, and the tip flattens. The fundamental harmonic initially grows exponentially, but higher harmonics start to grow as the wave is distorted by the approach to the bottom. Because the two edges of the flattened region have large slope and positive curvature, they are rapidly drawn downward by capillary pressure. This creates both draining outward and a characteristic bulge in the center. The result is that the fingertip splits, producing two downward fingers. This eventually would be expected to produce two dry spots according to this two-dimensional lubrication calculation, but one cannot be sure. Wetting effects come into play that are not included in the evolution equation.

Three-dimensional effects can completely change the character of the response to heating. Joo and Davis (1992) and

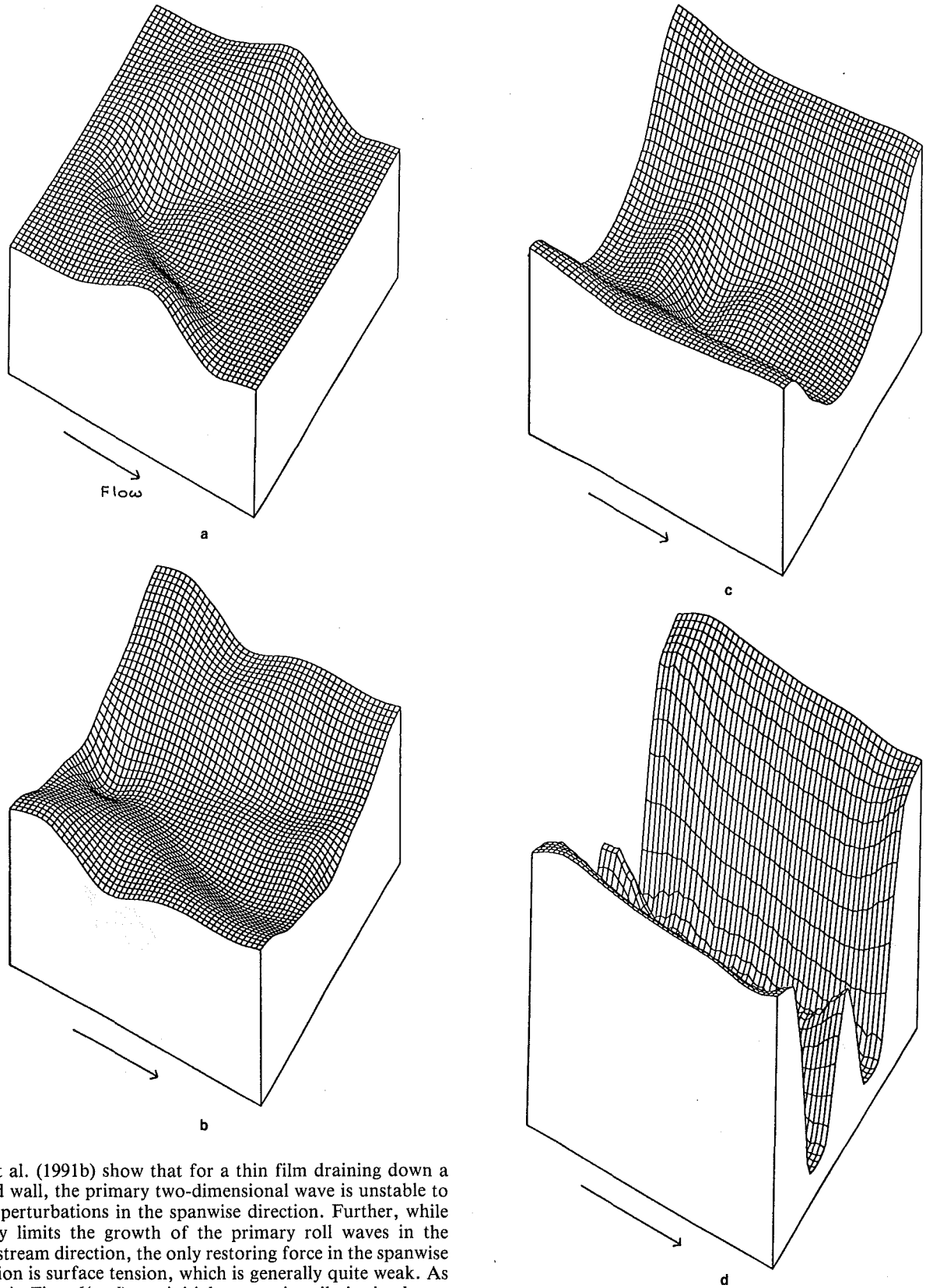

Fig. 6(*a, b, c, d*) **Successive stages in the evolution of a two-dimensional permanent wave with small spanwise disturbance on an inclined heated plate. The streamwise wave decays, and the spanwise one grows, eventually forming a prerivulet array.**

Joo et al. (1991b) show that for a thin film draining down a heated wall, the primary two-dimensional wave is unstable to small perturbations in the spanwise direction. Further, while gravity limits the growth of the primary roll waves in the downstream direction, the only restoring force in the spanwise direction is surface tension, which is generally quite weak. As shown in Figs. 6(*a–d*), an initial wave primarily in the downstream direction evolves in the cross-stream direction, and eventually becomes a single longitudinal roll. This breaks up into two rolls, in a manner reminiscent of the splitting of the tip of the two-dimensional finger. This represents a new mechanism for rivulet formation on a continuous, heated film. Generally, rivulets are formed by the diversion of liquid around a stable dry spot (Hartley and Murgatroyd, 1964; Murgatroyd, 1965; Chung and Bankoff, 1980), or by the unstable fingering of a contact line as it advances down an inclined, or vertical, dry surface (Troian et al., 1989; Hocking and Miksis, 1993).

There is still much to be learned about the behavior of unbroken thin liquid films on horizontal or inclined heated surfaces. The long-wave evolution equation is highly nonlinear, and depends on a number of parameters. A quite general evolution equation is given by Joo et al. (1991, 1993) for a film draining down an inclined plane surface:

$$h_\tau + \frac{E}{h+K} + Gh^2 h_\xi \sin\beta + \frac{2G^2}{15}(h^6 h_\xi)_\xi \sin^2\beta + \nabla\cdot\left(\left[\frac{KM}{P}\left(\frac{h}{h+K}\right)^2 + \frac{E^2}{D}\left(\frac{h}{h+K}\right)^3 - \frac{1}{3}Gh^3\cos\beta + \frac{A}{h}\right]\nabla h + Sh^3\nabla(\nabla^2 h)\right) + E\frac{5G}{24}\left(\frac{h^4}{h+K}\right)_\xi \sin\beta + EP\left(\frac{h}{h+K}\right)^3\left[\frac{E}{3(h+K)} + \frac{G}{120}(7h-15K)hh_\xi\sin\beta\right] = 0. \quad (1)$$

The parameters here are β, the angle of inclination; E, an evaporation number; G, a gravitational number, equivalent to a Reynolds number for a falling film; K, a surface thermal nonequilibrium number, or inverse Biot number; M, a Marangoni number, or dimensionless temperature coefficient of surface tension; P, the Prandtl number; S, a dimensionless surface tension number; and A, a dimensionless Hamaker constant for long-range molecular forces. The two-dimensional operator ∇ acts in the plane parallel to the solid surface, and h is the local film thickness. The small parameter, which is the ratio of the characteristic thickness of the film to a characteristic distance in the downstream direction, or wavelength, is incorporated into the scaling. τ and ξ are scaled dimensionless time and downstream distance, respectively. The terms proportional to E describe mass loss due to evaporation. The third term describes wave propagation and steepening. The fourth, fifth, and sixth terms generate instabilities due to mean shear flow, thermocapillarity, and vapor recoil, respectively. The next two terms represent the stabilizing effects of gravity and mean surface tension. This equation, in various limits of the parameters, reproduces the results of a number of previous investigations. Despite its apparent generality, there are a number of extensions still to be made. For one thing, a passive gas layer is assumed, which exerts no shear stress on the film. Thus, the phenomena involved in cocurrent annular flow, or countercurrent gas-liquid flow, including flooding, cannot be described with this equation. However, a uniform surface shear stress, based upon an empirical correlation for the interfacial friction factor, is readily incorporated. For a more precise description, a two-fluid evolution equation is required (Tilley et al., 1992, 1993a, b). Furthermore, binary liquid mixtures, which experience surface variations in composition and temperature due to differential distillation, may be subject to thermo-soluto-capillary instabilities, which would require a further modification of Eq. (1).

Kim et al. (1991, 1992, 1993) examined the interaction of an electrostatic field on a flowing liquid-metal film on a plane inclined surface, or inside a rotating cone. The application is the prevention of leaks due to micrometeorite impacts in a proposed class of space radiators. The electrostatic field exerts a tensile force on the liquid film, pulling it away from a puncture in the radiator shell. The interaction between the film and the field has been analyzed only to lowest order.

Reisfeld et al. (1991a, b) performed a long-wave analysis of a polymer solution flowing on a rotating horizontal disk. A new type of instability, called a transient instability, is found, in which the wave grows for some time and then decays. However, it may harden as the solvent evaporates, leaving a coating with weak spots after baking to remove the solvent completely. This is of concern for production of compact circuitry on computer chips, but has not been followed up.

Reisfeld and Bankoff (1992) consider the draining of a thin liquid film, originally of uniform thickness, around a horizontal cylinder, which may be heated or cooled, under the influence of gravity, thermocapillary, and van der Waals forces. The time evolution of this film (Fig. 7) can be a bit surprising, owing to the powerful effects of the latter forces on locally thin regions. Most cases show rather regular drainage, but rupture and establishment of a pendant cylindrical drop can also take place. This unsteady, two-dimensional flow, which can represent the slumping of a coating under gravity, represents the base state for three-dimensional surface perturbations that may be imposed. This represents a difficult nonlinear stability problem that has not been solved.

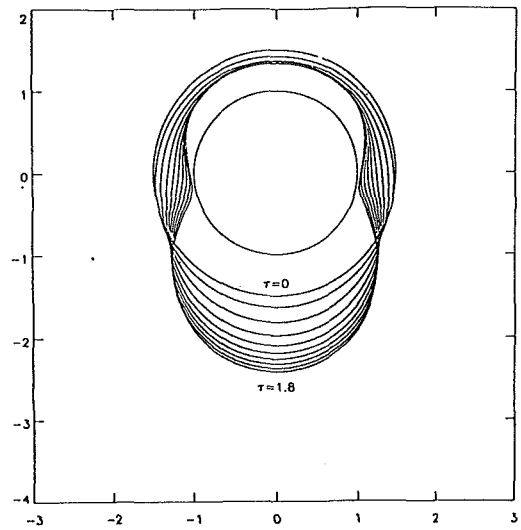

Fig. 7 Unsteady film flow and rupture of an initially uniform liquid film on a hot horizontal cylinder for $Bo^{-1}=0.1$ and $M=5$. Bo is the Bond number and M is a Marangoni number (Reisfeld and Bankoff, 1992).

The fact that a particular combination of parameters gives long-wave stability does not guarantee that short-wave instabilities, possibly due to viscosity and/or density stratification in a steady two-fluid system, will not be present (Tilley et al., 1992). Preziosi et al. (1989) and Hu and Joseph (1989) consider core-annular flows of oil and water in a pipeline. In lubricated pipelining viscous oil flows in the core, and a thin water layer is present along the wall. Under some conditions, owing to weak capillarity or to the magnitude of the viscosity ratio between the two fluids, small short-wave perturbations can grow. The full nonlinear stability problem has not been solved.

Finally, the extensions to rotating systems or to nonplanar solids, such as cylinders or spheres, are needed.

Mechanism of Subcooled, Forced-Convection Nucleate Boiling

An interesting application of thin-film evaporative heat transfer occurs in nucleate boiling under conditions of high heat flux, high liquid velocity, and high bulk liquid subcooling.

Gunther (1950) (see also Gunther and Kreith, 1950), in an early investigation connected with the cooling of liquid rocket nozzle throats, showed that heat fluxes of the order of 30 MW/m^2 were attainable in subcooled forced-convection boiling of water in small-diameter tubes at high velocities. Two major mechanisms were discussed at an early conference (Bankoff et al., 1956) aimed at understanding these results. The first mechanism, suggested by Gunther and Kreith (1950), is based on the additional turbulent mixing, or microconvection, that is achieved near the wall surface between the growing and collapsing bubbles. The second mechanism, discussed at the same conference by Snyder and also by Bankoff (see also Bankoff, 1959; Bankoff and Mikesell, 1959; Bankoff and Ma-

son, 1962; Snyder and Robin, 1969) focuses on latent heat transport through the bubble. When a vapor bubble grows on a solid surface, a thin liquid microlayer must be formed beneath the bubble in order to satisfy the no-slip boundary condition at the solid surface. The top of the bubble quickly grows beyond the wall thermal boundary layer into the cool liquid. Latent heat is transported through the bubble, with the microlayer evaporating simultaneously as condensation occurs over the cold polar cap.

This led to a considerable controversy in the literature, which is reviewed briefly by Tsung-Chang and Bankoff (1990). They also performed some calculations on the increased heat transfer rate because of sliding of the bubbles on the solid surface, thus continuously exposing new microlayer under the bubbles to evaporation. The net result was about a 50 percent increase over previous estimates of the evaporative contribution. However, these calculations, as well as those of Plesset and Prosperetti (1978) and Koffman and Plesset (1983), depend on the assumption that the liquid microlayer under the bubble remains continuous during its lifetime. Tsung-Chang and Bankoff (1990) note the probable existence of a moving contact line under the bubble in the case of water on stainless steel, as a result of instability and dryout of the microlayer under evaporation. For film thicknesses less than about 100 nm, a horizontal liquid film becomes unstable under the influence of van der Waals forces, and ruptures very rapidly, as shown by the analysis of Williams and Davis (1982), for an isothermal film, and Bankoff and Davis (1987) and Burelbach et al. (1988), for an evaporating film. According to the analysis of Cooper and Lloyd (1969), the local thickness of the microlayer is proportional to the square root of the time of its uncovering since the beginning of bubble growth. Hence the central region of the microlayer will rupture in items of order 1 μs (Burelbach et al., 1988), provided that the wall is only partially wetted (contact angle >0 deg). Engineering surfaces, such as stainless steel, commonly exhibit contact angles of 40 deg or more. The existence of a contact line in an evaporating system implies a temperature singularity. This is confirmed by the measurements of Cooper and Lloyd (1969) and Sharp (1964), who found large cooling effects shortly after the bubble boundary passes over thermocouples mounted just below the microlayer.

If there is indeed a moving contact line under the bubbles due to poor wetting in this high-flux application, it is easy to show that this corresponds to a logarithmic heat-flux singularity, which can be removed only by taking into account the heat flow in the solid.

Motions of Contact Lines on Heated Surfaces

The usual concept of a contact line, or common line, as the intersection of three mathematical surfaces immediately entails several paradoxes. A finite force per unit length is acting normal to the contact line at every point, so that an infinite stress is being exerted on the solid surface. However, the solid surface is not permanently deformed, or even measurably deformed. It is clear therefore that there is some structure in the immediate neighborhood of the apparent contact line. Furthermore, the motion of a mathematical contact line implies that fluid particles that are actually in contact with the solid surface move parallel to the surface. This violates the no-slip assumption, which has been tested and verified by numerous macroscopic experiments. The difficulties, however, exist only in a very small inner region in the neighborhood of the apparent contact. The velocity and stress singularity can be eliminated by postulating a slip length of molecular dimensions, where slip between the liquid and the solid is allowed to occur. Outside of this small region, the no-slip condition is applied. Furthermore, it is observed that the advancing and receding contact angles differ applied (contact angle hysteresis), and the difference increases with increasing contact line speed. This model allows matching conditions for the outer film region to be specified to within a single unknown slip length (Greenspan, 1978; Greenspan and McCay, 1981; Hocking, 1981, 1990; Silvi and Dussan, 1985; Haley and Miksis, 1991; Hocking and Miksis, 1993). However, the influence of the slip length is higher order if the surface is well wetted. Furthermore, on hot dry surfaces, the contact angle is large (Segev and Bankoff, 1980), owing to the near-absence of an adsorbed precursor layer. It is not known how to adjust the model for this circumstance.

There is a precursor film ahead of the macroscopic film front for unheated surfaces with small or zero contact angle (DeGennes, 1985; Cazabat, 1987). At the leading edge of the precursor film, which may be monomolecular in thickness, sideways motion of adsorbed fluid particles can occur by surface diffusion or by simultaneous evaporation and recondensation (Wayner and Schonberg, 1992). However, quasi-steady motion of the precursor film has been observed by electrical resistivity measurements only at very low contact line velocities (of the order of microns per second) (Cazabat, 1991). The shape of the interface then changes slowly from the adsorbed layer to the macroscopic film (DeGennes, 1985). For much faster contact line advance (Huppert, 1982) the dynamic contact angle, particularly on dry surfaces, may not be small, and there is a transition region of large curvature where van der Waals molecular dispersion forces and surface tension forces are comparable in magnitude. In this inner region the thickness varies rapidly, so that lubrication theory may not be applicable (Goodwin and Homsy, 1990). However, in this region of very large surface curvature close to the solid surface, the static stresses due to surface tension and van der Waals forces may dominate the viscous stresses. The details have not yet been worked out.

Troian et al. (1989) assumed the existence of a precursor film of constant unknown thickness, and matched an inner-region asymptotic solution to it, and to the film-front outer solution. This eliminated the need for a contact line, and hence for a contact angle. The advancing front is then very steep, with a bulge at the top, presumably because the bulk film can supply liquid faster than the transition region at the bottom can move forward. The linear stability of this front to spanwise perturbation is then analyzed, and shown to give a preferred wavelength for rivulet formation.

If contact angle hysteresis is ignored, and the contact angle is assumed to be small at all times, lubrication theory can be employed. Hocking and Miksis (1993) thus arrive at a dimensionless evolution equation for the film thickness in a two-dimensional ridge of fluid draining down an inclined plate in the x direction:

$$\frac{\partial h}{\partial t}+\frac{\partial}{\partial x}\left[h^2(h+\lambda)\left(\frac{\partial}{\partial x}\nabla^2 h+K\right)\right]+\frac{\partial}{\partial y}\left[h^2(h+\lambda)\frac{\partial}{\partial y}\nabla^2 h\right]=0 \quad (2)$$

where λ is an unknown slip length and K is here a dimensionless gravity component. This is examined for linear stability with respect to spanwise perturbations, in the special case of small capillary number. The characteristic speed is defined by the constant of proportionality in the empirical contact-angle/slip velocity relationship. At leading order the slip length does not appear, and a preferred wavelength can be deduced without recourse to any precursor film.

Both of these models have limitations. The former does not require the contact angle to be specified, and matches a precursor film of unknown thickness. The latter model requires a small dynamic contact angle as an empirical function of the contact line velocity, as well as an unknown slip length, which is, however, not very important.

The spreading of a liquid drop on a heated horizontal surface

has been treated, both without and with evaporation (Anderson and Davis, 1993), using the slip model. It is found that thermocapillary effects on the nonvolatile drop cause it to spread, while for the volatile drop, the mass loss results in a modified contact angle condition. For the nonvolatile drop good agreement is found with experiment (Ehrhard and Davis, 1991). The evaporating droplet has not yet been studied experimentally. The apparent contact angle increases as the evaporation rate increases, in agreement with an earlier observation by Chung and Bankoff (1980).

Nearly all the evaporation from the edge of a stationary, or slowly moving, film on a hot horizontal solid surface occurs close to this transition region (Wayner, 1978a, b; Truong and Wayner, 1987). In this region the film is thin enough that the temperature gradient in the liquid is high, but the van der Waals forces are weak, so that substantial evaporation can take place. However, if the curvature in the transition region is sufficiently large and positive, condensation can occur there, even though the wall is heated. In this fashion Wayner and Schonberg (1992) have recently proposed that contact line advances (recession) occur by condensation (evaporation) at the transition region between an adsorbed film and the bulk liquid. By assuming that the (condensing) evaporative mass flux in this region is independent of position in this short region for an isothermal system, the velocity of the receding (advancing) is also found to be constant. Upon integrating the force balance equation with dominant terms due to surface tension and long-range forces, over a region ranging from the thickness of the adsorbed precursor film to some multiple of this thickness where the bulk liquid properties exist, an expression is obtained for the departure of the contact angle from the equilibrium value. The method is also extended to nonisothermal systems. Qualitative agreement with isothermal low-velocity spreading data of several liquid-solid pairs was demonstrated for the contact line velocity as a function of the difference, $\Delta(\cos\theta) = (\cos\theta_d - \cos\theta_e)$, where θ_d and θ_e are the dynamic and equilibrium contact angles, respectively. For nonisothermal systems the contact line velocity is found also to depend on $\Delta T = T_{ev} - T_v$, where T_{ev} is temperature of the liquid at the liquid-vapor interface, and T_v is the temperature of the equilibrium vapor. This eliminates the need for an empirical expression for the departure of the dynamic contact angle from the static contact angle as a function of contact line speed. For moving contact lines this is a rich area for further research.

Spreading on Rough Surfaces

It is necessary to recognize that almost all solid surfaces have surface roughnesses that are at least of the order of a micron, which is an order of magnitude greater than the range of van der Waals forces. In an early paper, Shepard and Bartell (1953) reported the results of an interesting series of experiments on the wetting of rough paraffin surfaces. The surfaces were machined in two directions to give pyramidal asperities of known height and inclination to the horizontal. With liquids that wet the surface poorly, such as water, the hysteresis of the contact angle was almost exactly equal to the inclination of the asperities. With liquids of better wetting power, such as methanol, the situation became complicated by the fact that flow through the valleys, as well as over the tops of the asperities, was an important mode of advance and recession. They also observed that the degree of air entrapment depended primarily on the steepness of the asperities, and not on their height. Bankoff (1956) quantified these results by showing the surface of the film could be described in terms of a single parameter related to a Bond number, and that all possible configurations of the static film on a horizontal surface were segments of this curve. He then computed the free energy change of a liquid film of finite length in climbing an inclined barrier, and showed that for a long film this led to agreement with the data. Bankoff (1958) also computed wedge half-angles for surface grooves to entrap air under an advancing film. This calculation is related to the necessary conditions for a solid surface to initiate nucleation in boiling. This also suggests that on an unwetted surface there is no adsorbed precursor film (or effectively none), and that for rapidly advancing interfaces, air is trapped under the leading edge of the film. These effects have not yet been properly sorted out.

Another question that has not been addressed is the rapidly receding contact line, particularly on a hot, nonisothermal surface. This determined the rate of dryout after film rupture, and is hence quite important. Clearly, there is room for considerable further work.

Acknowledgments

This work was supported by the Department of Energy under Contract No. DE-FGO7-89ER12894. Discussions with my colleagues, S. H. Davis and S. W. Joo, have been very helpful.

References

Anderson, D. M., and Davis, S. H., 1993, "The Spreading of Volatile Liquid Droplets on Heated Surfaces," pending publication.

Bankoff, S. G., 1956, "The Contortional Energy Requirement in the Spreading of Large Drops," *J. Phys. Chem.*, Vol. 60, pp. 952–955.

Bankoff, S. G., Colahan, W. J., Jr., and Bartz, D. R., 1956, "Summary of Conference of Bubble Dynamics and Boiling Heat Transfer Held at the Jet Propulsion Laboratory," Memo No. 20-137, Jet Propulsion Laboratory, California Institute of Technology, Pasadena, CA.

Bankoff, S. G., 1958, "Entrapment of Gas in the Spreading of Liquid Over a Rough Surface," *AIChE J.*, Vol. 4, pp. 24–26.

Bankoff, S. G., 1959, "On the Mechanism of Subcooled Nucleate Boiling," Memo 30-38, Jet Propulsion Laboratory, California Institute of Technology, Pasadena, CA.

Bankoff, S. G., and Mikesell, R. D., 1959, "Bubble Growth Rates in Highly Subcooled Nucleate Boiling," *Chem. Eng. Progress Symposium Series*, Vol. 55, No. 29, pp. 95–102.

Bankoff, S. G., and Mason, J. P., 1962, "Heat Transfer From the Surface of a Steam Bubble in Turbulent Subcooled Liquid Stream," *AIChE J.*, Vol. 8, pp. 30–33.

Bankoff, S. G., 1971, "Stability of Liquid Flow Down a Heated Inclined Plane," *Int. J. Heat Mass Transfer*, Vol. 14, pp. 377–385.

Bankoff, S. G., and Davis, S. H., 1987, "Stability of Thin Liquid Films," *Physicochemical Hydrodynamics*, Vol. 9, pp. 5–8.

Benjamin, T. B., 1957, "Wave Formation in Laminar Flow Down an Inclined Plane," *J. Fluid Mech.*, Vol. 2, pp. 554–574.

Benney, D. J., 1966, "Long Waves on Liquid Films," *J. Math. Phys.*, Vol. 45, pp. 150–155.

Burelbach, J. P., Bankoff, S. G., and Davis, S. H., 1988, "Nonlinear Stability of Evaporating/Condensing Liquid Films," *J. Fluid Mech.*, Vol. 195, pp. 463–494.

Burelbach, J. P., Bankoff, S. G., and Davis, S. H., 1990, "Steady Thermocapillary Flows of Thin Liquid Layers. II. Experiment," *Phys. Fluids A*, Vol. 2, pp. 322–333.

Cazabat, A. M., 1987, "How Does a Droplet Spread?" *Contemp. Phys.*, Vol. 28, pp. 347–364.

Cazabat, A. M., 1991, "Wetting Films," *Adv. in Colloid and Interf. Sci.*, Vol. 34, pp. 73–88.

Chung, J. C., and Bankoff, S. G., 1980, "Initial Breakdown of a Heated Liquid Film in Cocurrent Two-Component Annular Flow. II: Rivulet and Drypatch Models," *Chem. Eng. Communications*, Vol. 4, pp. 433–453.

Cooper, M. G., and Lloyd, A. J. P., 1969, "The Microlayer in Nucleate Pool Boiling," *Int. J. Heat Mass Transfer*, Vol. 12, pp. 895–913.

De Gennes, P. G., 1985, "Wetting Statics and Dynamics," *Rev. Mod. Phys.*, Vol. 57, pp. 827–863.

Ehrhard, P., and Davis, S. H., 1991, "Nonisothermal Spreading of Liquid Drops on Horizontal Plates," *J. Fluid Mech.*, Vol. 229, pp. 365–378.

Gjevik, B., 1970, "Occurrence of Finite-Amplitude Surface Waves on Falling Liquid Films," *Phys. Fluids*, Vol. 13, pp. 1918–1925.

Goodwin, R., and Homsy, G. M., 1990, "Viscous Flow Down a Slope in the Vicinity of a Contact Line," *Phys. Fluids A*, Vol. 3, No. 4, pp. 515–528.

Greenspan, H. P., 1978, "On the Motion of a Small Viscous Droplet That Wets a Surface," *J. Fluid Mech.*, Vol. 84, pp. 125–143.

Greenspan, H. P., and McCay, B. M., 1981, "On the Wetting of a Surface by a Very Viscous Fluid," *Stud. Appl. Maths.*, Vol. 64, pp. 95–112.

Gunther, F. C., 1950, Progress Report No. 4-75, Jet Propulsion Laboratory, California Institute of Technology, Pasadena, CA.

Gunther, F. C., and Kreith, F., 1950, Progress Report No. 4–120, Jet Propulsion Laboratory, California Institute of Technology, Pasadena, CA.

Haley, P. J., and Miksis, M. J., 1991, "The Effect of the Contact Line on Droplet Spreading," *J. Fluid Mech.*, Vol. 223, pp. 57–81.

Hartley, D. E., and Murgatroyd, W., 1964, "Criteria for the Breakup of Thin Liquid Layers Flowing Isothermally Over Solid Surfaces," *Int. J. Heat Mass Transfer*, Vol. 7, p. 1003.

Hocking, L. M., 1981, "Sliding and Spreading of Thin Two-Dimensional Drops," *Quart. J. Mech. Appl. Math.*, Vol. 343, pp. 37–55.

Hocking, L. M., 1990, "Spreading and Instability of a Viscous Fluid Sheet," *J. Fluid Mech.*, Vol. 211, pp. 373–392.

Hocking, L. M., and Miksis, M. J., 1993, "Stability of a Ridge of Fluid," pending publication.

Hu, H., and Joseph, D. D., 1989, "Lubricated Pipeline: Stability of Core-Annular Flow," *J. Fluid Mech.*, Vol. 205, pp. 359–396.

Huppert, H. E., 1982, "Flow and Instability of Viscous Gravity Currents Down a Slope," *Nature*, Vol. 300, pp. 427–429.

Joo, S. W., Bankoff, S. G., and Davis, S. H., 1991, "Long-Wave Instabilities of Heated Falling Films: Two-Dimensional Theory of Uniform Layers," *J. Fluid Mech.*, Vol. 220, pp. 117–146.

Joo, S. W., Davis, S. H., and Bankoff, S. G., 1992, "A Mechanism for Rivulet Formation in Heated Falling Films," pending publication.

Joo, S. W., and Davis, S. H., 1992, "Instabilities of Three-Dimensional Viscous Falling Films," *J. Fluid Mech.*, Vol. 242, pp. 529–541.

Joo, S. W., Bankoff, S. G., and Davis, S. H., 1993, "Two- and Three-Dimensional Instabilities and Rupture of Thin Liquid Films Falling on Heated Inclined Plate," *Nucl. Eng. Design*, Vol. 141, pp. 225–238.

Kim, H., Miksis, M. J., and Bankoff, S. G., 1991, "Lightweight Space Radiator With Leakage Control by Internal Electrostatic Fields," *Proc. Eighth Symp. on Space Nuclear Power Systems*, Albuquerque, NM, CONF-910116, pp. 1280–1285.

Kim, H., Bankoff, S. G., and Miksis, M. J., 1992, "The Effect of an Electrostatic Field on Film Flow Down an Inclined Plane," *Phys. Fluids A*, Vol. 4, pp. 2117–2130.

Kim, H., Bankoff, S. G., and Miksis, M. J., 1993, "Electrostatic Field Effects on a Rotating Liquid Film Conical Space Radiator," *International Journal of Multiphase Flow*, Vol. 9, pp. 245–255.

Koffman, L. D., and Plesset, M. S., 1983, "Experimental Observations of the Microlayer in Vapor Bubble Growth on a Heated Solid," ASME JOURNAL OF HEAT TRANSFER, Vol. 105, pp. 625–632.

Lin, S.-P., 1974, "Finite Amplitude Side-Band Stability of a Viscous Film," *J. Fluid Mech.*, Vol. 63, pp. 417–429.

Orell, A., and Bankoff, S. G., 1971, "Formation of a Dry Spot in a Liquid Film Heated From Below," *Int. J. Heat Mass Transfer*, Vol. 14, pp. 1838–1842.

Murgatroyd, W., 1965, "The Role of Shear and Form Forces in the Stability of a Dry Patch in Two-Phase Film Flow," *Int. J. Heat Mass Transfer*, Vol. 8, pp. 297–304.

Plesset, M. S., and Prosperetti, A., 1978, "The Contribution of Latent Heat Transfer in Subcooled Nucleate Boiling," *Int. J. Heat Mass Transfer*, Vol. 21, pp. 725–734.

Preziosi, L., Chen, K., and Joseph, D. D., 1989, "Lubricated Pipelining: Stability of Core-Annular Flow," *J. Fluid Mech.*, Vol. 201, pp. 323–356.

Pumir, A., Manneville, P., and Pomeau, Y., 1983, "On Solitary Waves Running Down an Inclined Plane," *J. Fluid Mech.*, Vol. 135, pp. 27–50.

Reisfeld, B., Bankoff, S. G., and Davis, S. H., 1991a, "The Dynamics and Stability of Thin Liquid Films During Spin Coating. I. Films With Constant Rates of Evaporation or Absorption," *J. Appl. Phys.*, Vol. 70, pp. 5258–5266.

Reisfeld, B., Bankoff, S. G., and Davis, S. H., 1991b, "The Dynamics and Stability of Thin Liquid Films During Spin Coating. II. Films With Unit-Order and Large Peclet Numbers," *J. Appl. Phys.*, Vol. 70, pp. 5267–5277.

Reisfeld, B., and Bankoff, S. G., 1992, "Non-isothermal Flow of a Liquid Film on a Horizontal Cylinder," *J. Fluid Mechanics*, Vol. 236, pp. 489–520.

Robin, T. T., and Snyder, N. W., 1970, "Bubble Dynamics in Subcooled Nucleate Boiling Based on the Mass Transfer Mechanism," *Int. J. Heat Mass Transfer*, Vol. 13, pp. 305–318.

Segev, A., and Bankoff, S. G., 1980, "The Role of Adsorption in Determining the Minimum Film Boiling Temperature," *Int. J. Heat Mass Transfer*, Vol. 23, pp. 637–642.

Sharp, R. R., 1964, "The Nature of Liquid Film Evaporation During Nucleate Boiling," NASA TN D-1997.

Shepard, J. W., and Bartell, F. E., 1953, "Surface Roughness as Related to Hysteresis of Contact Angles. III. The Systems Paraffin-Ethylene, Glycerol-Air, Paraffin-Methyl, Cellosolve-Air and Paraffin-Methanol-Air," *J. Phys. Chem.*, Vol. 57, pp. 458–463.

Silvi, N., and Dussan, V. E., 1985, "On the Rewetting of an Inclined Solid Surface by a Liquid," *Phys. Fluids*, Vol. 28, pp. 5–7.

Snyder, N. W., and Robin, T. T., 1969, "Mass-Transfer Model in Subcooled Nucleate Boiling," ASME JOURNAL OF HEAT TRANSFER, Vol. 91, pp. 404–412.

Tan, M., Bankoff, S. G., and Davis, S. H., 1990, "Steady Thermocapillary Flows of Thin Liquid Layers: I. Theory," *Phys. Fluids A*, Vol. 2, pp. 313–321.

Tilley, B. S., Bankoff, S. G., and Davis, S. H., 1992, "Stability of Stratified Fluids in an Inclined Channel," presented at the Annual Meeting, Division of Fluid Dynamics, American Physical Society, Tallahassee, FL.

Tilley, B. S., Bankoff, S. G., and Davis, S. H., 1993a, "Stability of Stratified Fluids in an Inclined Channel," presented at the Session on Stability and Nonlinear Hydrodynamics, Annual Meeting, American Institute of Chemical Engineers, St. Louis, MO.

Tilley, B. S., Bankoff, S. G., and Davis, S. H., 1993b, "The Effect of Inlet Conditions on the Interfacial Behavior of Stratified Fluid Flow in an Inclined Channel," presented at the Annual Meeting, Division of Fluid Dynamics, American Physical Society, Albuquerque, NM.

Troian, S. M., Herbolzheimer, E., Safran, S. A., and Joanny, J. F., 1989, "Fingering Instabilities of Driven Spreading Films," *Europhys. Lett.*, Vol. 10, pp. 25–30.

Truong, J. G., and Wayner, P. C., Jr., 1987, "Effects of Capillary and van der Waals Dispersion Forces on the Equilibrium Profile of a Wetting Liquid," *J. Chem. Phys.*, Vol. 87, pp. 4180–4188.

Tsung-Chang, G., and Bankoff, S. G., 1990, "On the Mechanism of Forced-Convection Subcooled Nucleate Boiling," ASME JOURNAL OF HEAT TRANSFER, Vol. 112, pp. 213–218.

Wayner, P. C., Jr., 1978a, "A Constant Heat Flux Model of the Evaporating Interline Region," *Int. J. Heat Mass Transfer*, Vol. 21, pp. 362–364.

Wayner, P. C., Jr., 1978b, "The Effect of the London van der Waals Dispersion Force on Interline Heat Transfer," ASME JOURNAL OF HEAT TRANSFER, Vol. 100, pp. 155–159.

Wayner, P. C., Jr., and Schonberg, J., 1992, "Spreading of a Liquid Film on a Substrate by the Evaporation-Adsorption Process," *J. Colloid Interf. Science*, Vol. 152, pp. 507–520.

Williams, M. B., and Davis, S. H., 1982, "Nonlinear Theory of Film Rupture," *J. Colloid Interf. Sci.*, Vol. 90, pp. 220–228.

Yih, C.-S., 1955, "Stability of Parallel Laminar Flow With a Free Surface," *Quart. Appl. Math.*, Vol. 13, pp. 434–439.

Yih, C.-S., 1963, "Stability of Liquid Flow Down an Inclined Plane," *Phys. Fluids*, Vol. 6, pp. 321–334.

Y.-M. Lee
Department of Aeronautical Engineering,
Feng Chia University,
40724 Taichung, Taiwan

A. Haji-Sheikh
The University of Texas at Arlington,
Department of Mechanical
and Aerospace Engineering,
Arlington, TX 76019-0023

L. S. Fletcher

G. P. Peterson

Texas A&M University,
Department of Mechanical Engineering,
College Station, TX 77843-3123

Effective Thermal Conductivity in Multidimensional Bodies

The effective thermal conductivity in three-dimensional bodies is studied analytically. The three-dimensional model considers a spherical inclusion centrally located in a cubical body. Later, the spherical inclusion is replaced by an elliptical inclusion to study the biased effect or directionality of heat flux. Two different aspect ratios for the elliptical inclusion are considered. It is shown that the effective thermal conductivity is influenced by surface conductance in addition to geometric factors. Also, the effective thermal conductivity is measured for different samples. Spherical inclusions are placed inside cylindrical bodies for convenience of the experiments. The data show that cracks induced by applied pressure and thermal stress during the experiment reduce the thermal conductance. Using the measured effective thermal conductivity data, an analytical procedure is used to calculate the average values of the apparent contact conductance.

Introduction

Engineering systems often include heterogeneous materials such as composite parts, integrated electronics packages, and other solid bodies with inclusions of secondary materials. The secondary material can be a fiber, thermocouple, solder ball, or a layer of a different material. Composite materials are a class of heterogeneous materials widely used in aerospace, electronics, and automotive industries.

Zuzovski and Brenner (1977) compared the work of Rayleigh and Maxwell for computation of effective thermal conductivity in an infinite domain with periodically arranged spheres. Sangani and Acrivos (1983) modified the method of Zuzovski and Brenner (1977) to solve for effective thermal conductivity of a periodic array with inline and staggered arrangement of spheres also in an infinite domain. An accurate computation of temperature in a three-dimensional heterogeneous region is generally time consuming and cumbersome. For this reason, it is common practice to select average thermophysical properties to predict temperature and heat flux in heterogeneous bodies. Various properties of the medium are needed to determine the thermal conductivity of a heterogeneous medium; these include the statistical distribution of constituents, volume fraction, and the microstructure characteristics such as orientation, size, and connectivity of individual constituents (Ballah et al., 1988). Since it is difficult to take into account all available information, the common theoretical approach is to define lower and upper bounds for effective properties. Hatta and Taya (1985) adopted the equivalent inclusion method for an elastic field (Eshelby, 1957) to evaluate the effective thermal conductivity. Their results were within the bounds set by Nomura and Chou (1980) for short-fiber composites. An extensive survey related to average properties is given by Hashin (1983).

An experimental investigation of effective thermal conductivity was reported by Peterson and Fletcher (1989, 1990), Duncan et al. (1989), and Shonnard and Whitaker (1989). Most experimental studies consider perfect contact between different constituents. For heterogeneous materials, there is contact conductance between the phase boundaries due to poor mechanical and chemical adherence and the mismatch in the coefficient of thermal expansion (Hasselman and Johnson, 1987). Contact conductance produces a temperature jump at the phase boundary that results in the reduction of the effective thermal conductivity and degradation of the heat transfer capability of the materials (Benveniste, 1987; Hasselman and Johnson, 1987; Gu and Tao, 1988). There are many parameters that affect the contact conductance, such as the surface roughness, surface waviness, mean slope of individual asperities, mean temperature at the interface, interfacial contact pressure, loading history, and mechanical and thermophysical properties of heterogeneous materials (Peterson and Fletcher, 1990). A review of theoretical and experimental studies of contact conductance is given by Fletcher (1988).

Heterogeneous materials are encountered in various devices, e.g., microelectronic devices. These materials often have different thermophysical and mechanical properties. Even in the pure state, the thermal conductivity of heterogeneous materials may be directionally dependent. However, there are many situations when the assumption of isotropy in a single layer is used mainly to simplify the thermal analyses. For example, if there are many layers and all layers actively participate in the heat transfer process, an approximate computation of the temperature distribution may be based on average thermophysical properties. When there are marked differences in the value of thermal conductivity, the use of an average value is not a satisfactory approximation since the geometry of inclusions and layers will influence the temperature gradients and, consequently, the heat flux. Lee and Haji-Sheikh (1991) used heat-flux-conserving basis functions to solve for temperature distribution in a two-layer body with many ellipsoidal inclusions. They used nonorthogonal basis functions; however, their computed eigenfunctions were orthogonal. The Galerkin-based integral solution used by Lee and Haji-Sheikh (1991) maintains the continuity of heat flux and temperature across the contact surfaces (1) between layers and (2) between layers and inclusion.

The average or effective thermophysical properties are often used in the study of transient heat transfer in composite materials. Studies of transient heat conduction in layered materials are reported by Salt (1983), Horvay et al. (1973), Huang and Chang (1980), and Chester et al. (1984).

The computation and measurement of the effective thermal conductivity in finite domains are the subjects of this study.

Contributed by the Heat Transfer Division and presented at the ASME National Heat Transfer Conference, San Diego, California, August 9-12, 1992. Manuscript received by the Heat Transfer Division May 1992; revision received May 1993. Keywords: Conduction, Modeling and Scaling, Thermophysical Properties. Associate Technical Editor: C. E. Hickox, Jr.

The models selected for this study are multidimensional for which the numerical evaluation of the effective thermal conductivity is difficult. The effective thermal conductivity is calculated for the steady-state condition. The analytical calculations are for cubical bodies with spherical and spheroidal inclusions. Under the steady-state condition, the calculated effective thermal conductivity is influenced by the geometric shape of the inhomogeneities, and by the heat transfer coefficient at the surfaces. However, in the experimental evaluations, the phase separation and cracks have a profound effect on the apparent contact conductance between different materials. For improved accuracy of the measured data, the experimental setup requires cylindrical shaped specimens; therefore, spherical inclusions are placed inside cylindrical bodies. The measurements and subsequent computations show that the voids created by phase separation and delamination due to internal stress inhibit heat transfer. Voids created due to mechanical and thermal stress usually extend through the matrix phase, thus reducing the heat transfer across these materials and the effective thermal conductivity.

The goal of this study is to investigate the influence of different parameters on the effective thermal conductivity and to improve the data selection procedure. This work represents a parametric study of the effect of volume fraction, geometrical shapes, and surface conductance on the effective thermal conductivity. Later, the same computational method is used to analyze the experimental data of effective thermal conductivity and to resolve the value of contact conductance when there is inherent material separation.

The Galerkin-based integral method is used throughout these computations. The mathematical procedures are similar to the exact solution. Nonhomogeneous boundary conditions are dealt with by using a Green's function and the Green's function solution method reported by Haji-Sheikh and Beck (1990). A complete discussion of the technique is given by Beck et al. (1992). The alternative Green's function solution method (Beck et al., 1992) is used to improve the convergence of the numerical solutions. The advantage of this method is the higher accuracy and faster computation time in comparison with discretized numerical methods. Although the method of analysis is the same as the Galerkin finite element method, unlike the standard finite element method, it maintains the continuity of heat flux throughout the domain.

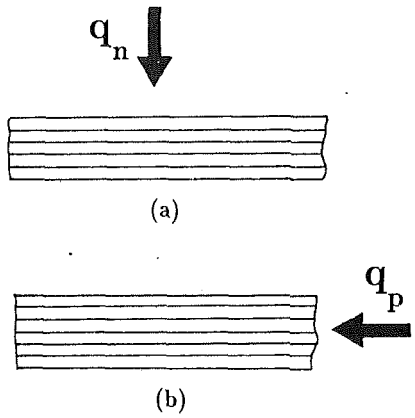

Fig. 1 Schematic of layered materials and the directions of one-dimensional heat flux

Effective Thermal Conductivity Model

The common practice is to define lower and upper bounds for thermal conductivity of heterogeneous materials. The lower bound of effective thermal conductivity is analogous to the thermal conductivity of a layered material in the direction perpendicular to the layers, Fig. 1(*a*). Assuming one-dimensional, steady-state conduction in the normal direction, Fig. 1(*a*), the average thermal conductivity, k_n, is derived as

$$1/k_n = \sum_i v_i/k_i \tag{1}$$

where v_i is the volume fraction of layer i. The upper bound is the average thermal conductivity in the planar direction of this layered material, Fig. 1(*b*), and it is defined by

$$k_p = \sum_i v_i k_i \tag{2}$$

Nomenclature

$\mathbf{A}$ = matrix
a, b, c = geometric dimensions, m
a_1, b_1, c_1 = half axes of an ellipse, m
a_{ij} = elements of matrix $\mathbf{A}$
$\mathbf{B}$ = matrix
b_{ij} = elements of matrix $\mathbf{B}$
C = contact conductance, $W/m^2 \cdot K$
c_p = specific heat, $J/kg \cdot K$
$\mathbf{D}$ = matrix with elements, d_{nj}
d = diameter of sample, cm
d_{nj} = coefficients
$\mathbf{d_n}$ = eigenvectors with elements d_{nj}
d_o = diameter of sphere, cm
f_j = basis functions
G = Green's function = $G(\mathbf{r}, t/\mathbf{r}', \tau)$
g^* = see Eq. (21)
H = auxiliary function
h = heat transfer coefficient, $W/m^2 \cdot K$
k = thermal conductivity, $W/m \cdot K$
k_i = thermal conductivity of ith layer, $W/m \cdot K$
k_n = thermal conductivity in normal direction, $W/m \cdot K$
k_p = thermal conductivity in planar direction, $W/m \cdot K$
m_i = mass fraction
N = number of eigenvalues
$\mathbf{P}$ = inverse of the transpose of $\mathbf{D} \cdot \mathbf{B}$ matrix
p_{ni} = elements of matrix $\mathbf{P}$
q = average heat flux, W/m^2
q^* = dimensionless average heat flux, $|q|c/[k_m(T_{\infty 1} - T_{\infty 2})]$
r = radial coordinate, m
r_o = radius of inclusion, m
$\mathbf{r}$ = position vector
$\mathbf{r}'$ = position vector, dummy variable
t = time, s
T = temperature, K
T^* = auxiliary or quasi-steady temperature, K
$T_{\infty 1}$ = ambient temperature for $z = 0$ surface, K
$T_{\infty 2}$ = ambient temperature for $z = c$ surface, K
U = conductance function
v_i = volume fraction of layer i
v_e = volume fraction of inclusion e, $V_e/(V_e + V_m)$
V = volume, m^3
x, y, z = coordinates, m
x_o, y_o, z_o = coordinates of the center of inclusion, m
γ_n = eigenvalue
ϵ = emittance
θ = dimensionless temperature = $(T - T_{\infty 1})/(T_{\infty 2} - T_{\infty 1})$
ρ = density, kg/m^3
τ = time, dummy variable, s
ϕ = boundary function

Subscripts

e = inclusion
eff = effective
i, j, n = indices
m = main domain
s = at surface

The average thermal conductivity, k_p, is obtained assuming boundary conditions of the first kind in addition to one-dimensional, steady-boundary conduction in the planar direction, Fig. 1(b). The average density and average specific heat are

$$\rho = \sum_i v_i \rho_i \tag{3}$$

and

$$c_{pa} = \sum_i m_i c_{pi} \tag{4}$$

where m_i is the mass fraction of layer i. The definition of average specific heat is valid if the condition of quasi-equilibrium can be approximated. These approximations are not always satisfactory, especially when conduction is multidimensional and transient (Ben-Amoz, 1970). The definitions for density, Eq. (3), and specific heat, Eq. (4), are used only for computation of transient temperature distribution and heat flux. However, the effective thermal conductivity is useful for the calculation of transient as well as steady-state temperature fields.

Preliminary to any calculation, it is essential to establish definition for the effective thermal conductivity in the presence of the surface heat transfer coefficient. Consideration is given to an equivalent homogeneous or orthotropic solid identical in shape to the original body and subject to identical boundary conditions. Under the steady-state condition, it is assumed that the exchange of heat with the surroundings is identical to that for the actual body. The thermal conductivity of this equivalent solid is equal to the effective thermal conductivity. Using the above definition, it is assumed that the total energy received by any surface of the equivalent solid is the same as the total energy received by the corresponding surface of the actual body. For example, if an equivalent solid is one-dimensional and the heat transfer coefficient, h, is the same on both sides, the following relation applies:

$$q_{in} = q_{out} = \frac{|\Delta T|}{c/k_{\text{eff}} + 2/h} \tag{5}$$

where $|\Delta T|$ is the difference in fluid temperature across the actual body and the equivalent solid. Similarly, q_{in} and q_{out} remain the same for both the actual body and equivalent solid and they are equal to average heat flux, $|q|$. This definition for the effective thermal conductivity, k_{eff}, will be used throughout this paper.

Mathematical Steps

The calculation of temperature and heat flux requires the solution of the diffusion equation

$$\nabla \cdot (k \nabla T) = \rho c_p \frac{\partial T}{\partial t} \tag{6}$$

over the entire domain of matrix and inclusion. The boundary conditions over the external surfaces can be of the first, second, or third kind. The thermophysical properties k, ρ, and c_p are position dependent but independent of temperature; see Fig. 2. An accurate closed-form solution of Eq. (1) is possible using the Galerkin method. A Galerkin solution that uses heat-flux-conserving basis functions (Haji-Sheikh, 1988) conserves the continuity of temperature and heat flux across the phase boundaries. Moreover, it can deal accurately with a temperature jump in the presence of an imperfect contact.

The procedure begins by selecting a set of basis functions that are usually nonorthogonal and are chosen to satisfy the boundary conditions. For a cubical body, $V = V_m \cup V_e$, each basis function for the main domain is a product of three one-dimensional basis functions. The product method is acceptable because the region shown in Fig. 2 is a regular body while its

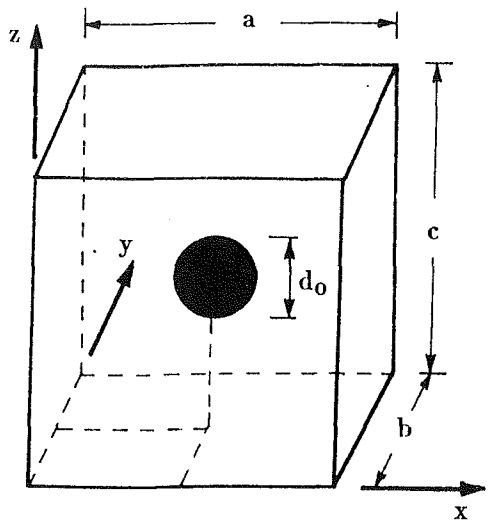

Fig. 2 A cubical body with spherical inclusion

outer surfaces are normal to the chosen coordinate system. For one-dimensional problems, the method of selecting the basis functions for the boundary conditions of first, second, and third kinds is described by Beck et al. (1992). These basis functions must be modified for the inclusion to describe the temperature and heat flux conditions at the phase boundary of the inclusion. Once the basis functions are in hand, the matrices **A** and **B** with elements (Beck et al., 1992),

$$a_{ij} = \int_V f_i \nabla \cdot (k \nabla f_j) dV \tag{7a}$$

and

$$b_{ij} = \int_V \rho c_p f_i f_j dV \tag{7b}$$

are calculated. The evaluation of the integrals in Eqs. (7a) and (7b) over the inclusion is, perhaps, a relatively difficult part of this computation. Once a_{ij} and b_{ij} are known, the matrices **A** and **B** are then used to calculate the eigenvalues and eigenfunctions. Standard subroutines that use the matrices **A** and **B** as their input perform all necessary matrix operations on equation,

$$(\mathbf{A} + \gamma \mathbf{B})\mathbf{d}_n = 0 \tag{8}$$

This equation is based on the Ritz–Galerkin variational principle (Kantorovich and Krylov, 1960). The outputs are the eigenvalues, γ_n, and eigenvectors, $\mathbf{d}_n$. The eigenvectors constitute the rows of matrix **D**. If **A** and **B** are $N \times N$ matrices, there will be N eigenvalues and N eigenvectors, each having N elements, then **D** is a $N \times N$ matrix. Details are available from Beck et al. (1992).

The basis functions for domains with inclusions are calculated through a two-step process. First, in the homogeneous domain bounded by the external surfaces, it is assumed that there is no inclusion and the basis functions are selected as discussed earlier. These functions are designated $f_{m,j}$, where the subscript m stands for the main domain. As long as one is within the main domain,

$$f_j = f_{m,j} \tag{9}$$

is the basis function. Next, the basis functions are modified within the inclusion bounded by the surfaces $\phi_e = 0$ using the relation

$$f_i = f_{e,j} = f_{m,j} + U_e + \phi_e H_e \tag{10}$$

The function $f_{e,j}$ is the modified basis function to be used within the inclusion and the subscript e stands for the inclusion. Notice that, if $U_e = 0$, the condition $f_{m,j} = f_{e,j}$ on the boundary of the inclusion is automatically satisfied. The continuity of heat flux on the $\phi_e = 0$ surface requires the following condition be satisfied,

$$k_m \frac{\partial f_{m,j}}{\partial n_e} = k_e \frac{\partial f_{e,j}}{\partial n_e} \tag{11}$$

When there is no contact conductance, $U_e = 0$ and the substitution of f_j from Eq. (10) into Eq. (11) yields the value of H_e (Haji-Sheikh, 1988),

$$(H_e)_{\phi_e=0} = -\frac{\left[\left(\frac{k_m}{k_e}-1\right)\frac{\partial f_{e,j}}{\partial n_e}\right]_{\phi_e=0}}{\left(\frac{\partial \phi_e}{\partial n_e}\right)_{\phi_e=0}}$$

$$= -\frac{\left[\left(\frac{k_m}{k_e}-1\right)\nabla f_{m,j}\cdot\nabla\phi_e\right]_{\phi_e=0}}{(\nabla\phi_e\cdot\nabla\phi_e)_{\phi_e=0}} \tag{12}$$

According to Eq. (10), any H_e function that yields Eq. (12) on the $\phi_e = 0$ surface is acceptable. It is suggested that either

$$H_e = (H_e)_{\phi_e=0} \tag{13a}$$

or

$$H_e = -\frac{\left(\frac{k_m}{k_e}-1\right)\nabla f_{m,j}\cdot\nabla\phi_e}{(\nabla\phi_e\cdot\nabla\phi_e)_{\phi_e=0}}, \tag{13b}$$

be used, whichever provides a simpler algebraic form. Equations (13a) and (13b) will be used whenever there is no contact conductance at the phase boundary. Equation (13a) produces satisfactory results for one-dimensional and some multidimensional problems. Equation (13b) yields basis functions with simpler mathematical forms. When an inclusion is spherical in a three-dimensional body or cylindrical in a two-dimensional region, the exact values $a_{i,j}$ and $b_{i,j}$ can be computed by symbolic algebra (Nomura and Haji-Sheikh, 1988).

In the derivation of Eq. (12), it is assumed that the thermal conductance between the main domain and the inclusion e is infinite. However, the effect of finite contact conductance can be included in the derivation. For instance, $f_j = f_{m,j}$ satisfies the external boundary conditions, then, within the inclusion e, Eq. (10) is satisfied (Haji-Sheikh and Beck, 1990) with U_e being an unknown. The interfacial jump condition for this problem is

$$k_m \frac{\partial f_{m,j}}{\partial n_e} = C_e\,(f_{m,j} - f_{e,j}) \tag{14}$$

Substituting $f_{m,j}$ from Eq. (9) and $f_{e,j}$ from Eq. (10) into Eq. (14) and recognizing that $\phi_e = 0$ at the contour of the inclusion e, the following relation for U_e is obtained:

$$U_e = -\frac{k_m}{C_e}\left(\frac{\partial f_{mj}}{\partial n_e}\right)_{\phi_e=0} \tag{15}$$

Next, the value of H_e is computed as described in the derivation of Eq. (12),

$$H_e = \frac{\left(\frac{k_m}{k_e}-1\right)\nabla f_{m,j}\cdot\nabla\phi - \nabla U_e\cdot\nabla\phi_e}{(\nabla\phi_e\cdot\nabla\phi_e)_{\phi_e=0}} \tag{16}$$

and then, reduced to assume the form of Eq. (13b).

When C_e is finite, Eq. (10) with U_e and H_e calculated from Eqs. (15) and (16), is used to define the basis functions inside the inclusions and subsequently calculate the temperature distribution. The spherical and elliptical inclusions are considered in this study. For elliptical inclusions, the denominator of Eq. (16) is coordinate dependent; however, for spherical inclusions it is a constant. The numerical computation of integrals for a_{ij} and b_{ij} using Eqs. (3) and (4) makes the CPU time relatively large. Generally, a three-dimensional numerical solution in complex-shaped bodies with small inclusions requires a large amount of CPU time. However, for special cases, one can use symbolic algebra to carry out these integrals analytically.

Following the computation of a_{ij} and b_{ij}, the remaining computational steps are universally applicable to homogeneous and heterogeneous bodies and they remain independent of the number of dimensions. All calculations following the computation of a_{ij} and b_{ij} are in a subroutine for general use. In the following calculations, it is assumed that the initial temperature and heat generation are zero. The temperature solution (Beck et al., 1992; Beck and Haji-Sheikh, 1990) can be reduced to the form

$$T(\mathbf{r}, t) = T^*(\mathbf{r}) + \frac{1}{\rho(\mathbf{r})c_p(\mathbf{r})}\left\{\int_{\tau=0}^{t} d\tau \int_V G(\mathbf{r}', -\tau|\mathbf{r}, -t)\,(k\nabla^2 T^*)\,dV' - \int_V \rho(\mathbf{r}')c_p(\mathbf{r}')G(\mathbf{r}', 0|\mathbf{r}, -t)\,T^*(\mathbf{r}')dV'\right\}, \tag{17a}$$

where G is the Green's function,

$$G(\mathbf{r}', -\tau|\mathbf{r}, -t) = \rho(\mathbf{r})c_p(\mathbf{r})\sum_{n=1}^{N} e^{-\gamma_n(t-\tau)} \times \left[\sum_{j=1}^{N} d_{nj}f_j(\mathbf{r})\right]\left[\sum_{i=1}^{N} p_{ni}f_i(\mathbf{r}')\right], \tag{17b}$$

p_{ni} is an element of matrix, $\mathbf{P}$,and $\mathbf{P}$ is the inverse of the transpose of the $\mathbf{D}\cdot\mathbf{B}$ matrix. The auxiliary function $T^*(\mathbf{r})$ is selected mainly to satisfy the nonhomogeneous boundary conditions. Its role is to accelerate the convergence; that is, to reduce the number of terms needed for an accurate solution. The closer $T^*(\mathbf{r})$ approximates the steady-state solution, the lesser will be the number of terms needed for an accurate steady-state solution. Notice that $T^*(\mathbf{r})$ must satisfy the nonhomogeneous boundary conditions in addition to the compatibility conditions at the interface of the inclusion. The parameter V_e represents the volume of the inclusion which can be spherical or elliptical, $V = V_m \cup V_e$ is the total volume, and V_m is the volume of the main domain. The specific shapes of theoretical and experimental models and the corresponding total volumes are given in the following sections.

Numerical Calculations

The preliminary model for this study is a cubical body that contains a spherical inclusion, Fig. 2. This approximates a periodic material domain that consists of an isotropic layer containing many spherical inclusions arranged, aligned, and equidistant from each other, and Fig. 2 represents one period. For one period, all surfaces normal to the x and y axes can be considered insulated and heat transfer occurs along the z axis in the negative direction. Clearly, the number of parameters that will influence the computation of temperature in this domain are numerous. For the sake of brevity, the effect of only a few parameters will be evaluated.

As stated earlier, the basis function in the main domain, f_{mj}, is a product of one-dimensional basis functions. The one-dimensional basis functions used in this study are tabulated by Beck et al. (1992). Once f_{mj} is known, the value of f_{ej} is known from Eq. (10). In the analytical computation of the effective thermal conductivity, the value of $C_e = \infty$ or $U_e = 0$ is selected mainly to reduce the number of parameters. Later,

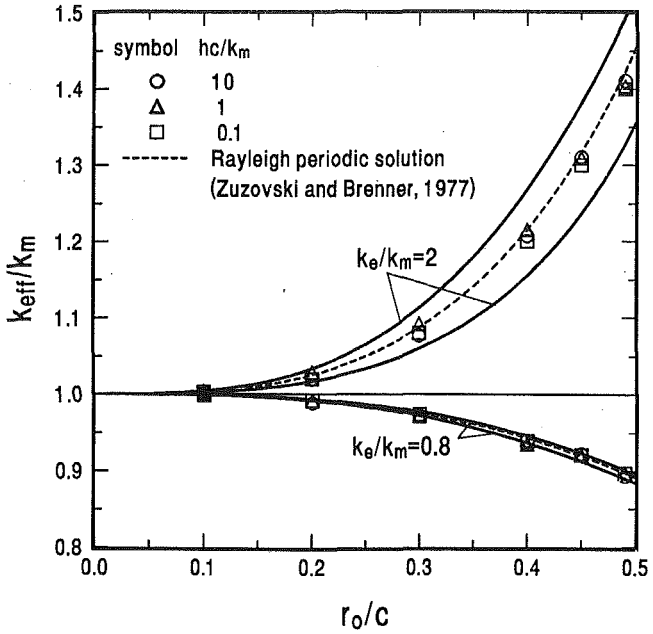

Fig. 3(a) Calculated effective thermal conductivity and comparison with layered materials, k_e/k_m = 2 and 0.8

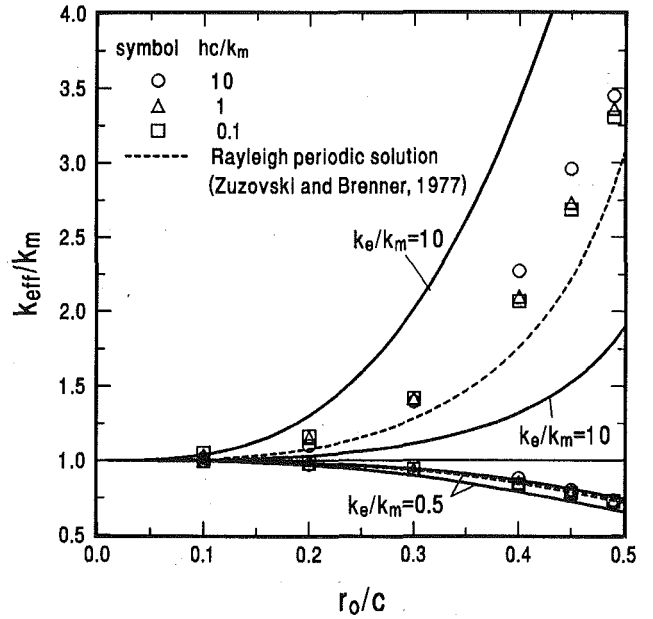

Fig. 3(b) Calculated effective thermal conductivity and comparison with layered materials, k_e/k_m = 10 and 0.5

a finite C_e is chosen and its value is computed by a trial and error procedure. The calculation of a_{ij} and b_{ij} includes analytical integration over the entire volume, V, and numerical integration over the inclusion volume, V_e. The subsequent analysis leading to the computation of the Green's function, G, Eq. (17a), is given by Beck et al. (1992). A generalized subroutine developed for this study is used to compute the eigenvalues, eigenvectors, and the remaining parameters in Eq. (17b).

Effective Thermal Conductivity

The dimensions of the main domain for spherical inclusions are chosen as $a = b = c$. The ratio of the radius of the inclusion to c serves as a parameter in the computations. Following the computation of temperature and total surface heat flux, the

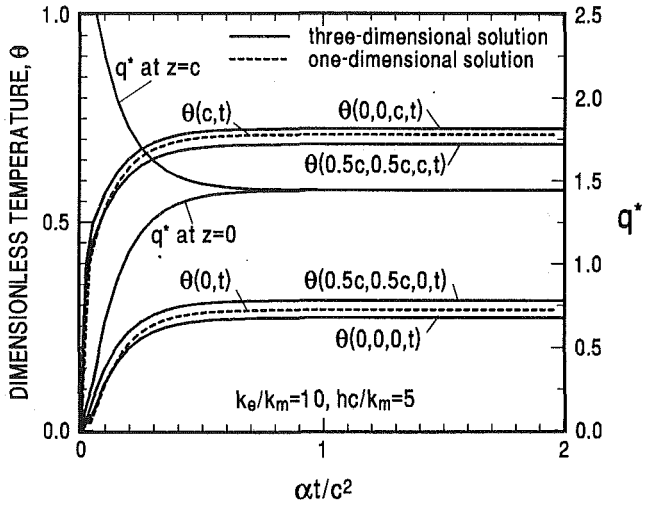

Fig. 4 Transient surface temperature and comparison with one-dimensional solution

effective thermal conductivity is computed using Eq. (5). The data are plotted in Figs. 3(a) and 3(b) as a function of r_o/c. One can obtain the volume fraction from the relation $v_e = 4\pi(r_o/c)^3/3$. The upper portion of Fig. 3(a) shows the effective thermal conductivity when $k_e/k_m = 2$. The data are for three Biot numbers, Bi = hc/k, of 0.1, 1, and 10. The lines in the figure are the so-called limiting values computed using Eqs. (1) and (2). The Biot number influences the value of the effective thermal conductivity; more details are given later. The bottom portion of Fig. 3(a) is for $k_e/k_m = 0.8$ and using Bi = hc/k, of 0.1, 1 and 10. The data show that the Biot number has a small influence on the effective thermal conductivity. Figure 3(b) is similar to Fig. 3(a) except the data are for $k_e/k_m = 10$ in the upper portion and for $k_e/k_m = 0.5$ in the lower portion. In both figures, it is assumed that there is infinite contact conductance between the inclusion and main domain. Clearly, neither limiting value, shown in Figs. 3(a) and 3(b), is a satisfactory approximation when the inclusion volume fraction is large. The dash lines in Figs. 3(a) and 3(b) are for a square arrangement of spheres periodically placed in an infinite medium; they represent a modified Rayleigh solution reported by Zuzovski and Brenner (1977). Except for $k_e/k_m = 10$, the agreement is satisfactory.

All data gathered to prepare Figs. 3(a) and 3(b) are for transient temperature and heat flux. The steady-state condition was approximated when time is large. Therefore, the transient temperature data are readily available and Fig. 4 was prepared to show the computed values of transient temperature at the corners and midpoints of $z = 0$ and $z = c$ surfaces. Also, in the same figure, the one-dimensional temperature is plotted at $z = 0$ and $z = c$ surfaces using the effective thermal conductivity. It is assumed that the value of ρc_p is the same for both matrix and inclusion. This figure shows that there is a noticeable temperature variation over the $z = 0$ surface and similarly over the $z = c$ surface. The one-dimensional equivalent temperature in Fig. 4 merely serves as an approximation. Also, the values of $q^* = |q|c/[k_m(T_{\infty 1} - T_{\infty 2})]$, at $z = 0$ and $z = c$ surfaces, are plotted in the same figure. Usually, at the steady-state condition, the two values of the surface heat flux approach each other within ±0.002 percent.

The effect of the variable surface temperature on the effective thermal conductivity can be quantified by examining Figs. 5(a) and 5(b). Figure 5(a) is for $r_o/c = 0.4$ and Fig. 5(b) is for $r_o/c = 0.49$. In each figure, the effective thermal conductivity is plotted as a function of k_m/h_c. Each curve in the figure is for a different value of k_e/k_m. When $k_e/k_m \geq 5$, the k_{eff}/k_m values drop rapidly by about 10 percent and then assume uni-

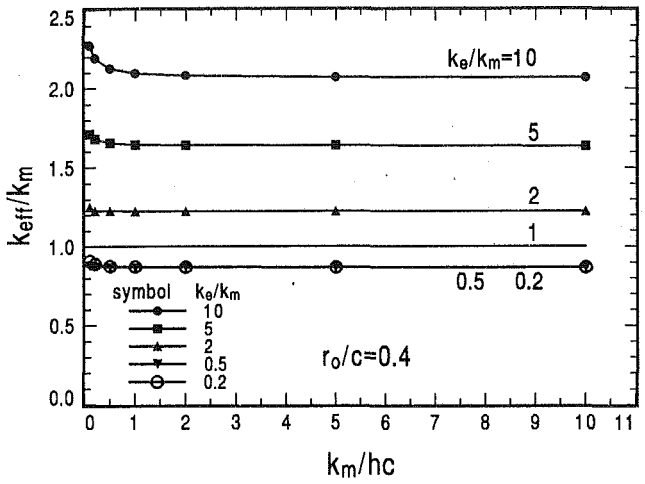

Fig. 5(a) Effect of surface heat transfer coefficient on the effective thermal conductivity, $r_o/c = 0.4$

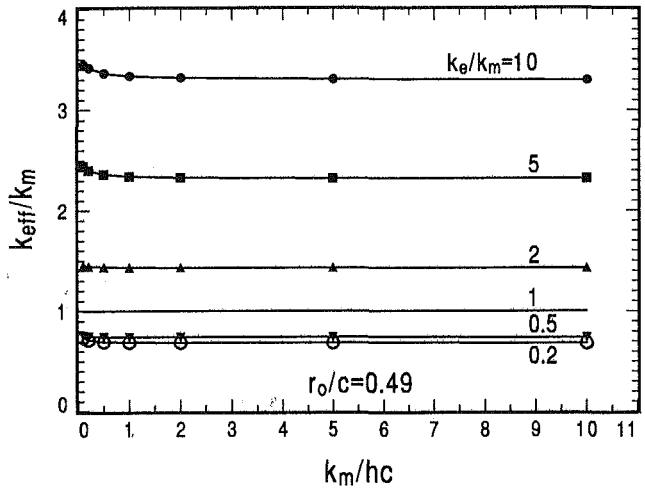

Fig. 5(b) Effect of surface heat transfer coefficient on the effective thermal conductivity, $r_o/c = 0.49$.

form values. For lower k_e/k_m, the k_{eff}/k_m values remain nearly unaffected by the changes in the surface heat transfer coefficient. As k_e/k_m becomes very small, the internal transfer of heat moves away from the central zone toward the outer region. This tends to move the k_{eff}/k_m values toward the upper limits.

The upper limit in Figs. 3(*a*) or 3(*b*) is the effective thermal conductivity for a two-layer body when the heat transfer is one dimensional and parallel to the layers. If one neglects the heat transfer between layers, the effect of surface heat transfer modifies Eq. (2) to the following form:

$$k_{eff}/k_m = \frac{v_e \mathrm{Bi}\,(k_e/k_m) + \mathrm{Bi}(1+v_e) + 2k_e/k_m}{\mathrm{Bi} + 2(1-v_e)\,(k_e/k_m) + 2v_e} \qquad (18)$$

Note that Eq. (18) also reaches an asymptotic value as Bi = $hc/k_m \to 0$ and will reduce to Eq. (1) when Bi = 0. For large or small values of k_e/k_m, the assumption of one-dimensional conduction in the derivation of Eq. (18) is no longer valid. Only when $k_e/k_m \sim 1$, the asymptotic values of Eq. (18) agree with the data in Figs. 5(*a*) and 5(*b*). For given values of k_e/k_m and v_e, Eq. (18) overestimates data when Bi is small and underestimates the data when Bi is large.

The measured heat flux data must have a high degree of accuracy in order to produce effective thermal conductivity data with reasonably accuracy. This problem becomes acute, especially when the Biot number is small. For instance, when $hc/k_m = 0.1$, the dimensionless average heat flux, q^*, for $k_e/k_m = 2$ is 0.04831, and Eq. (5) yields $k_{eff}/k_m = 1.426$. However, if q^* increased by 1.2 percent to 0.04894, Eq. (5) yields $k_{eff}/k_m = 2.318$, representing an increase of 60 percent. This latter k_{eff}/k_m value is for $hc/k_e = 0.1$ and $k_e/k_m = 5$. This underlines the need for highly accurate temperature and heat flux values to produce acceptable data for the effective thermal conductivity. The situation improves as the heat transfer coefficient increases. When $hc/k_e = 1$, a 1 percent error in the heat transfer value only produces a 12 percent error in the effective thermal conductivity; however, this magnification of error is greatly attenuated at $hc/k_e = 10$.

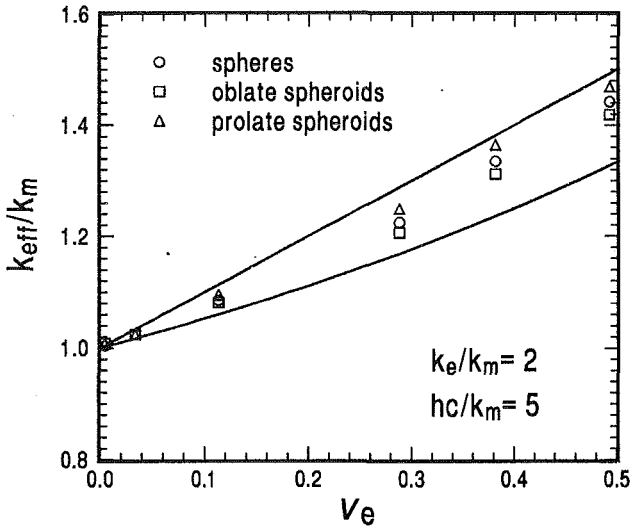

Fig. 6 The influence of geometric bias on the effective thermal conductivity

The effect of geometric bias on heat flow passages can be demonstrated by replacing spherical inclusions with elliptical inclusions. The equation for the surface of an elliptical inclusion is

$$\frac{(x-x_o)^2}{a_1^2} + \frac{(y-y_o)^2}{b_1^2} + \frac{(z-z_o)^2}{c_1^2} = 1 \qquad (19)$$

where x_o, y_o, and z_o are the coordinates at the center of the inclusion. An effective comparison requires an elliptical inclusion to occupy the same volume fraction as the corresponding spherical inclusion; Fig. 6 shows the effective thermal conductivity as a function of volume fraction. Three sets of data are presented: spherical inclusion, elliptical inclusion with $a_1 = b_1 = c_1/2$ (prolate spheroid), and elliptical inclusions with $a_1 = b_1 = 2c_1$ (oblate spheroid). The data are for $hc/k_m = 5$, and $k_e = 2$. The results show that an elongated inclusion in the direction of heat flux causes the effective thermal conductivity to approach the upper limit, whereas a flattened inclusion moves the effective thermal conductivity toward the lower limit.

Contact Conductance

The initial goal of this study was to set up an experimental procedure to verify the mathematical and numerical solutions described earlier. The measurement process resulted in delamination and cracks in the test samples due to mechanical and thermal stresses. The experimental procedure begins by measuring the effective thermal conductivity and comparing the results with analytically calculated data for the purpose of verifying the analytical results. The mathematical formulations and numerical procedures described earlier are used to analyze the experimental data. The analytical studies reveal the existence of phase separation and permit the computation of ap-

Table 1 Dimensions of the epoxy samples before and after tests

sample	inclusion type (dimensions in cm)	c (cm)		d (cm)	
		before	after	before	after
1	no inclusion	2.484	2.350	2.418	2.451
2	white glass sphere $d_o = 1.356 \pm 0.005$	2.553	2.388	2.426	2.520
3	black glass sphere $d_o = 1.712 \pm 0.012$	2.555	2.403	2.426	2.512
4	black glass sphere $d_o = 1.580 \pm 0.008$	2.502	2.393	2.438	2.487

Table 2 Measured thermal conductivity for resin-only sample (Sample 1)

T (K)	k ($W/m \cdot K$)		T (K)	k ($W/m \cdot K$)	
	before	after		before	after
308.708	0.521	0.487	381.302	0.851	0.796
317.694	0.583	0.545	387.111	0.887	0.829
326.063	0.599	0.560	395.562	0.935	0.875
334.608	0.650	0.608	401.086	0.983	0.919
343.236	0.682	0.638	409.000	1.068	0.999
351.509	0.730	0.683	414.318	1.109	1.038
359.536	0.755	0.706	420.739	1.176	1.100
366.985	0.786	0.735	426.960	1.225	1.146
373.861	0.822	0.769	444.351	0.917	0.857

parent contact conductance. For best accuracy and to achieve satisfactory experimental results, a value of $k_e/k_m < 5$ is desirable because Figs. 3(a, b) and 5(a-c) show that the effect of hc/k_m on k_{eff}/k_m is small. The materials chosen to satisfy this purpose are commercially available polyester resins, often called fiberglass resins, and spherical glass of different radii. In order to facilitate better conductance measurement, cylindrical samples with spherical inclusions were prepared. The final results are presented in three stages: (1) sample preparation, (2) conductance measurement, and (3) data analysis. Each of these three stages is discussed in a separate section.

Sample Preparation. Cylindrical samples were chosen to accommodate the measurement facility requirements for producing accurate experimental data. The samples were prepared by casting polyester resin in a cylindrical mold and allowing it to cure. The mold consists of two half-cylinders, which can be bolted together prior to casting. First, a small amount of resin mixed with hardener is poured into the mold and allowed to harden partially. A spherical ball was placed at its proper position and then additional polyester resin was supplied to the mold until it was full. A black dye was added to the resin in order to reduce the internal radiation exchange. Also, the spherical balls used were opaque white or black to minimize radiation exchange within the glass. After the resin was cured and fully hardened, each sample was polished and examined for trapped air bubbles. During the polishing of the samples it was noted that air bubbles were minimal or nonexistent. Four samples were chosen for testing. Sample 1 was a resin-only sample to measure the thermal conductivity of resin as a function of temperature. The dimensions of the four samples before the tests are in Table 1. Also, the diameters of the spherical inclusions (glass balls) used in Samples 2, 3, and 4 are given in Table 1. The chemical analysis of the glass balls was carried out by X-ray Photon Spectroscopy (XPS), also known as Elemental Spectroscopy for Chemical Analysis (ESCA). The chemical analyses of the atomic concentration after two minutes of sputtering the glass samples with ionized argon gas show the following concentrations are detected: silicon 31.2 percent, oxygen 56.9 percent, carbon 4.2 percent, aluminum 3.5 percent, sodium 1.3 percent, fluorine 1 percent, and calcium 1.4 percent (Lee, 1991). The glass can be classified as soft glass or soda lime glass but with lesser amounts of aluminum, sodium, and calcium than a typical soda lime glass. The thermal conductivity for various types of glass as a function of temperature is given by McLellan and Shand (1984).

Conductance Measurement. The overall conductance of each sample was measured at a preselected mean sample temperature. The apparatus that measures the effective thermal conductivity uses a vacuum chamber at a pressure of less than 10^{-3} Torr. The vacuum environment reduces the losses due to natural convection. A radiation shield was provided to assure one dimensionality of the heat flux. A known quantity of heat flux was applied and the temperature across each sample was measured. Heat flux meters were calibrated using a sample with known thermal conductivity (electrolytic iron from NIST/NBS). Because, the measurement procedure must take into account the interfacial contact conductance on both sides of the sample, contact grease was placed between the sample and the sample holder. Additionally, during the conductance measurement, a pressure of 6.08 MPa was applied to the sample to minimize the contact conductance. Thermocouples were embedded in the resin-only sample to verify the accuracy of the measurements and to quantify the contact conductance over the external surfaces of the sample. During the test, a finite temperature difference introduced across each sample and the heat flux were measured using calibrated heat flux gages. The one-dimensional conduction in the resin-only sample was used to calibrate the instruments and to account for the effect of the surface contact conductance between the sample holders. Notice that the temperature field in a sample with a spherical inclusion is not one dimensional and information external to the sample must be used to measure the contact conductance. For this reason, the test data for the resin-only samples were invaluable for use during the subsequent measurements. Once the heat flux and temperature difference across a sample were measured, the effective thermal conductivity was calculated from Fourier's law.

The effective thermal conductivity for each sample was measured at different mean sample temperatures. The mean sample temperature for the resin-only sample was increased from 308 K to 444 K. Since the isotherms within the samples with spherical inclusions are not parallel, the total heat flux was used to calculate the effective thermal conductivity. The measured data for polyester resins are given in Table 2. However, the three samples with inclusions were tested within a temperature range between 279 K and 408 K. The measured values of the effective thermal conductivity data for samples with inclusions are tabulated by Lee (1991) and graphically presented in Figs. 7, 8, and 9. The effective thermal conductivity was measured for different mean temperatures. The experimental uncertainty in the measurement of thermal conductivity is estimated to be ~3 percent at the lowest temperature and ~4.5 percent at the highest measured temperature. Since the material deformed during the test, each figure contains two sets of data. The dimensions for all four samples after the conclusion of the experiments are in Table 1. A change in the dimensions results in a change in the calculated temperature gradients and, consequently, alters the calculated effective thermal conductivities. The upper curves in the figures are obtained using the initial dimensions of the samples for each test. The lower curves in the figures are obtained using the same measured heat flux values; however, the sample dimensions after the conclusion of each test are used to calculate the effective thermal conductivity values. The abrupt change in the measured data in Fig. 8 during heating is caused by the separation of glass in the samples as the temperature increased. A casual examination of these data shows the thermal stress due to the temperature increase contributed to partial phase separation between the epoxy resins and glass. Notice that Sample

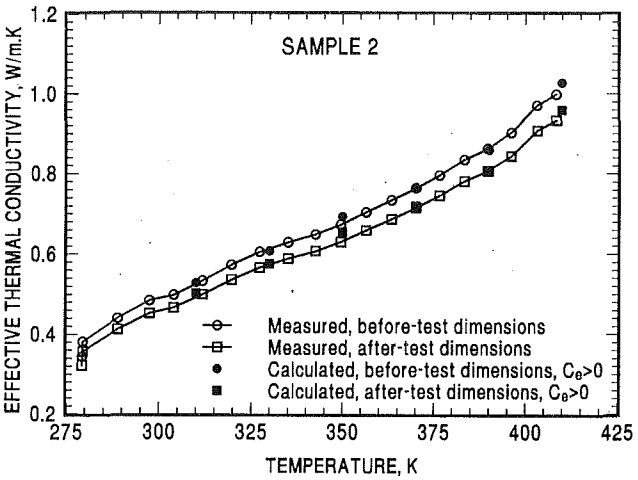

Fig. 7 Measured and calculated values of effective thermal conductivity for Sample 2

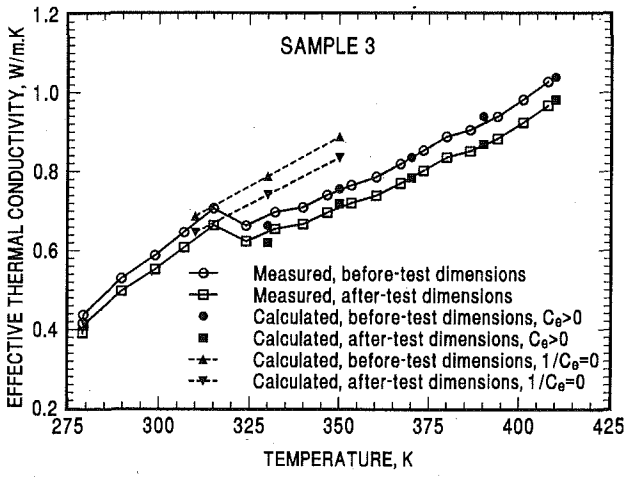

Fig. 8 Measured and calculated values of effective thermal conductivity for Sample 3

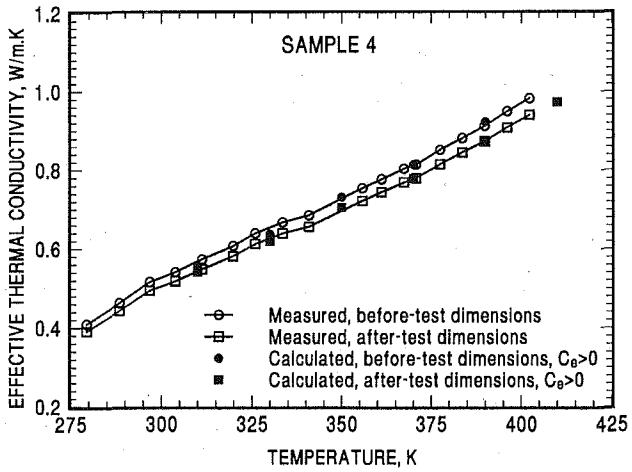

Fig. 9 Measured and calculated values of effective thermal conductivity for Sample 4

3 includes the largest sphere and that phase separation appeared during the test. Accordingly, Samples 2 and 4 with smaller spheres have suffered thermal-stress-induced phase separation and possibly cracked at the onset of the experiments.

Data Analysis and Results. In the following theoretical and experimental studies, the contact conductance, C_e, and its inverse, the contact resistance, $1/C_e$, are considered to be finite. Hence, the derivation leading to the computation of temperature and heat flux must include the contribution of the C_e parameter. An examination of the experimental data in Fig. 8 requires that the assumption of perfect contact between the epoxy resin and glass be discarded when the mean temperature is above 320 K. For example, although glass has a higher thermal conductivity than the epoxy resin, the measured effective thermal conductivity of samples with a glass inclusion is often lower than the thermal conductivity of the epoxy resin. This can be explained if we assume that, due to applied pressure and the disparity of thermal expansion coefficients, separation has occurred between the glass and the epoxy resins.

In order to quantify the extent of the separation, analytical steps described earlier are used to calculate C_e for the measured data. The basis functions for the matrix phase are obtained by the product method for cylindrical coordinates; r in the x-y plane and $z=z$. Dirichlet boundary conditions are used for the z direction while the cylindrical surface is insulated. The remaining numerical procedure is as described earlier in this paper with some modification. For simplicity of analysis, the calculations were performed for the steady-state condition. The solution reduces to the following form of the standard Galerkin method (Beck et al., 1992):

$$T = T^* - [\{\mathbf{A}^{-1}\cdot\{\mathbf{g}^*\}\}^T]\cdot\{f\} \tag{20}$$

where $\mathbf{A}$ is the same matrix described by Eq. (7*a*), $\{\mathbf{f}\}$ is a column vector with elements $f_1, f_2, \cdots, f_N$, and $\{\mathbf{g}^*\}$ is another column vector whose elements are

$$g_i^* = \int_V f_i(\mathbf{r})[k(\mathbf{r})\nabla^2 T^*(\mathbf{r})]dV \tag{21}$$

Computationally, Eq. (20) yields a faster solution because there is no need to calculate the elements of matrix $\mathbf{B}$; hence, the eigenvalues are not needed in Eq. (20).

Numerical results are obtained for two cases: (1) assuming perfect contact between the epoxy and the spherical glass and, (2) including the contact conductance, C_e, in the calculation. The thermal conductivities of the epoxy are taken from Table 2 using the temperature data at selected points between 310 K and 410 K; the thermal conductivities of glass are taken from McLellan and Shand (1984). At temperatures above 400°C, radiation affects the measured values of thermal conductivity; however, for these tests, the effective thermal conductivities measured are within the temperature range well below 400°C. The value of thermal conductivity for soda lime glass at 300 K is 1.4 W/m•K (Incropera and DeWitt, 1990). The thermal conductivity of fused silica and 96 percent silica (McLellan and Shand, 1984) is ~1.55 W/m·K at 300 K and ~1.65 W/m·K at 400 K. Depending on the chemical composition, the value of thermal conductivity for typical soda lime glass varies between 1.0 and 1.4 W/m·K. Because the glass spheres used here have a high degree of purity, it is assumed that k_e = 1.5 W/m·K at 300 K and increases by 0.001 W/m·K for every 1 K temperature rise.

The geometric dimensions used in the numerical calculations are obtained from Table 1. First, the effective thermal conductivity was computed assuming perfect contact between sphere and matrix. The computed effective thermal conductivity in the absence of contact conductance, for Samples 2 and 4, overestimate the experimental values, hence they are not plotted in Figs. 7 and 9. The experimental data of Sample 3, which has the largest sphere, are shown in Fig. 8. They are in good agreement with the numerical results and Rayleigh's solution for perfect contact at a lower temperature range, up to 320 K. Solid triangular symbols in Fig. 8 represent the calculated values assuming perfect contact, $1/C_e = 0$. The

Table 3 Calculated contact conductance, W/m^2·K, at different temperatures in samples with inclusions

T deg. K	Sample 2		Sample 3		Sample 4	
	before	after	before	after	before	after
310	0.087	0.087	—	—	0.119	0.142
330	0.087	0.087	0.152	0.164	0.119	0.142
350	0.087	0.087	0.152	0.164	0.119	0.142
370	0.087	0.087	0.152	0.164	0.119	0.142
390	0.087	0.087	0.152	0.164	0.119	0.142
410	0.087	0.087	0.135	0.152	0.119	0.142

experimental data show a sudden drop in the value of effective thermal conductivity at about 320 K; see Fig. 8. The jump in the measured values indicates possible separation at the interface between epoxy and glass. After this sudden drop in the experimental data, a finite C_e value was used in the analytical calculations to achieve agreement, as shown in Fig. 8. The value of C_e, for each sample, was obtained by a trial and error procedure and recorded in Table 3 for the specified conditions. As expected, for Samples 2 and 4, the separation occurred immediately upon loading and subsequent heating. For comparison, the experimental results (open symbols) and the calculated values using the average values of C_e (solid symbols) are plotted in Figs. 7, 8, and 9. Figures 7 and 9 show reasonably good agreement between analytical results and experimental data, assuming that there is finite contact conductance at the interface. Each set of numerically computed data, Figs. 7 and 9, is for an average contact conductance that produces the best agreement with the corresponding experimental data. Moreover, the reasonably good agreement between the calculated and measured data indicates that, over a small range of temperatures, the contact conductance is relatively independent of temperature.

The calculated values of contact conductance for each sample are listed in Table 3. There is a small difference in the calculated values of contact conductance using the before test and after test dimensions.The numbers reported in the table are small and well below expected values. Even under vacuum conditions, assuming heat transfer across the gap is by radiation alone, the value of the expected contact conductance is estimated from

$$C_e \simeq \frac{4\epsilon_e \epsilon_m \sigma \overline{T}^3}{\epsilon_e + \epsilon_m - \epsilon_e \epsilon_m} \tag{22}$$

where $\overline{T}$ is the mean temperature of the gap and $\sigma = 5.6 \times 10^{-8}$, Because of the black dye used in both glass and epoxy, the corresponding emittances ϵ_e and ϵ_m in Eq. (22) are large. For example, when $\epsilon_e = \epsilon_m = 0.9$ and $\overline{T} = 350$ K, Eq. (22) gives a value of $C_e \simeq 8$ W/m^2·K; this is significantly larger than the values reported in Table 3. A numerical study shows that a small decrease in the value of k_m can result in a very large change in the value of C_e. For this reason, it is important to examine the matrix for cracks and material damage that can inhibit the flow of heat.

The samples were examined to determine the extent of separation between the matrix phase and spheres. Sample 3 was broken apart for visual observation of damage. It showed a significant lateral separation of epoxy resin from the glass and existence of additional cracks in the matrix. Samples 2 and 4 were examined for internal cracks using an ultrasonic imaging system. Figures 10 and 11 show the computer-enhanced images produced from the upper, middle, and lower portions of each sample. The lightest images represent stronger echoes. The echoes in Figs. 10(*a*) and 11(*a*) are from the matrix phase in the upper portion of the sample; these echoes indicate existence of numerous cracks. Figures 10(*b*) and 11(*b*) show echoes from the sphere, separation gaps, and cracks in the matrix. Figures

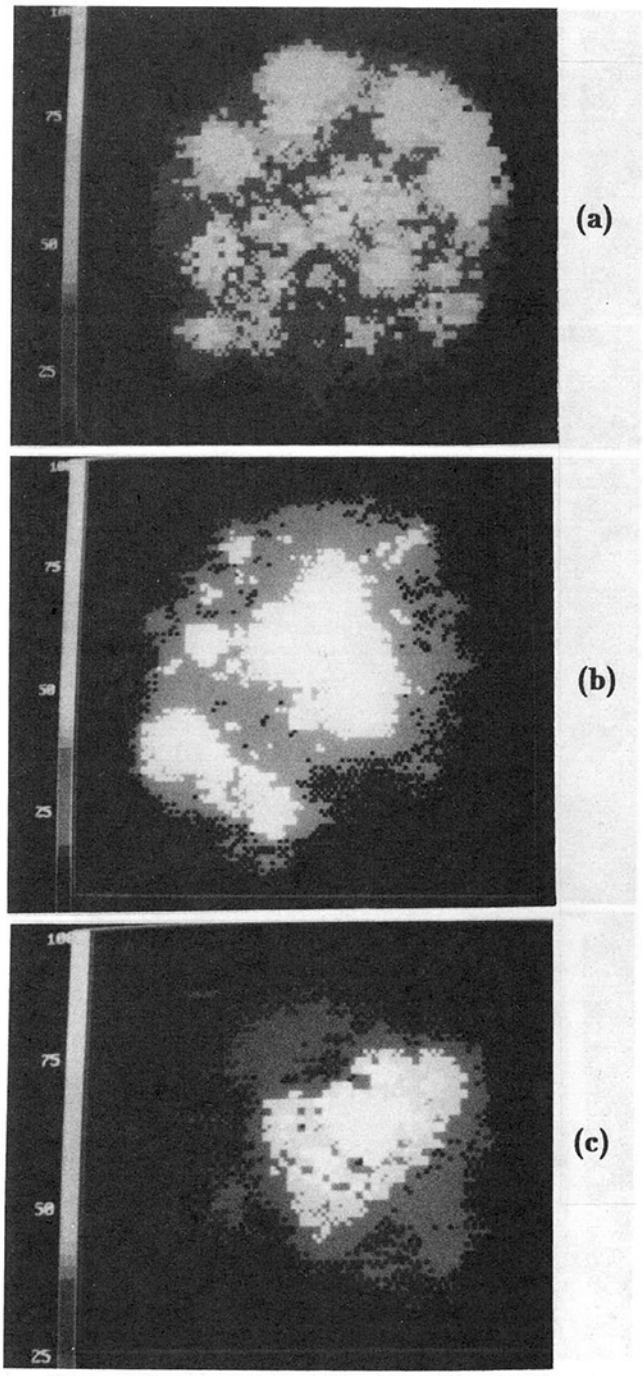

Fig. 10 Computer enhanced ultrasonic image of Sample 2: *(a)* hot side, *(b)* middle section, and *(c)* cold side

10(*c*) and 11(*c*) are for the lower third of Samples 2 and 4 and they show echoes mainly from the sphere. There are only a few low intensity echoes in the matrix phase in Figs. 10(*c*) and 11(*c*) indicating some separation and small voids. Apparently, thermal stress is a major contributor to the damage because the upper portion of each sample is at a higher temperature during the experiment.

An interesting byproduct of this study is the observation that the phase separation is accompanied by cracks in a brittle matrix phase and, in turn, cracks will further impede the ability of materials to transfer heat. The contact conductance reported in Table 3 also includes the contribution of the cracks to the matrix phase; therefore, it should be classified as the apparent contact conductance. It is remarkable that the calculated values

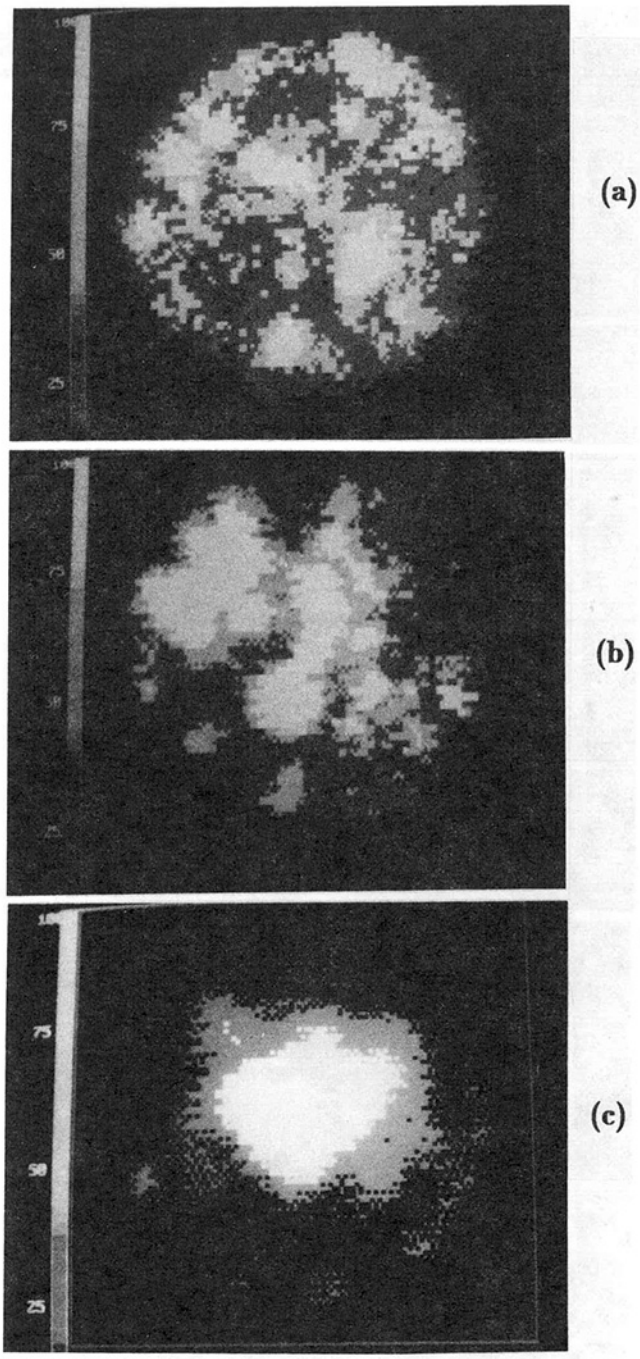

Fig. 11 Computer enhanced ultrasonic image of Sample 2: *(a)* hot side, *(b)* middle section, and *(c)* cold side

of the apparent contact conductance are in good agreement with each other and the experimental data. There is a small monotonic increase in the values of apparent contact conductance as the diameter of the spheres increases. This implies that a sample with a large sphere has less matrix material and less crack damage; hence, the effective contact conductance has a higher value. This can be shown by calculating, for example, the ratio C_e/r_o^2 for three samples using the data for "before" dimensions in Table 3. The result is $C_e/r_o^2 = \sim 490 \pm 18$ W/m^{4}K.

Conclusion and Remarks

The data presented in this paper show the capability of the Galerkin-based Green's function solution method to deal with multidimensional heat transfer problems. The numerical analyses are used to show the value of effective thermal conductivity for compact inclusion. The numerical data indicate that:

1 According to Figs. 3(*a*) and 3(*b*), the thermal effects of an inclusion can be ignored if $r_o/c < 0.1$ or $v_e < 0.004$.
2 For spherical or nearly spherical inclusions, the k_e values fall nearly midway between k_n and k_p values from Eqs. (1) and (2), Figs. 3(*a*) and 3(*b*).
3 Slightly elongated or slightly flattened inclusions yield nearly the same k_e as those for spherical inclusions; Fig. 6.
4 At higher k_e/k_m ratios, the surface heat transfer coefficient causes a sudden reduction in the values of k_{eff}/k_m with decreasing Biot number due to the temperature variations on the surfaces; Figs. 5(*a*) and 5(*b*).
5 The experimental study verifies that the mathematical formulations and numerical steps are equally valid for all finite bodies described in this paper.
6 The Rayleigh periodic solution is a satisfactory approximation when k_e/k_m is not very large.

The experimental data show that due to the mismatch of thermal expansion coefficients, the separation between the main phase and the inclusion is possible. The result is a low value of effective contact conductance or a high thermal resistance due to phase separation and crack formation. This can pose a serious problem, i.e., in high heat flux electronic devices. Also, the phase separation can produce voids containing gases at very low pressure. The transfer of heat across these voids is by radiation and molecular transport.

The calculation of C_e values were carried out on a mainframe computer; however, the remaining data were obtained on personal computers. The number of basis functions dictates the accuracy of the solution. When using polynomial-type basis functions (Beck et al., 1992), a high degree of accuracy was achieved using polynomials of degree 5 to 8. Polynomials of higher degree will not contribute to the accuracy of the solution. For spherical inclusions, it is possible to find the exact values for a_{ij} and b_{ij} using Eqs. (7*a*) and (7*b*). In this case, the computation time is extremely small; however, the integrations by numerical quadrature are relatively time consuming. The numerical integrations over an inclusion require approximately 15 min or less using a DOS-based Intel 486 processor. The remaining computation (CPU) time, including the computation of eigenvalues, is negligibly small (a few seconds).

Acknowledgments

The work of the first two authors is supported by the National Science Foundation, Grant No. CBT-8814934. The authors wish to thank Professor Joshi of the Department of Mechanical and Aerospace Engineering at the University of Texas at Arlington for providing the ultrasonic images.

References

Ballah, T. K., Middya, T. R., and Basu, A. N., 1988, "A Multiple Scattering Theoretical Approach to the Effective Thermal Conductivity of Disordered Solids and Its Dependence on Phase Geometry," *Journal of Physics, D: Applied Physics*, Vol. 21, pp. 567–573.

Beck, J. V., Cole, K., Haji-Sheikh, A., and Litkouhi, B., 1992, *Heat Conduction Using Green's Functions*, Hemisphere Publishing Corp., Washington, D.C.

Ben-Amoz, M., 1970, "The Effective Thermal Properties of Two Phase Solids," *Int. Journal of Engineering Science*, Vol. 8, pp. 39–47.

Benveniste, Y., 1987, "Effective Thermal Conductivity of Composites With a Thermal Contact Resistance Between the Constituents: Nondilute Case," *Journal of Applied Physics*, Vol. 61, pp. 2840–2843.

Chester, W., Bobone, R., and Brocher, E., 1984, "Transient Conduction Through a Two-Layer Medium," *Int. J. Heat Mass Transfer*, Vol. 27, pp. 2167–2170.

Duncan, A. B., Peterson, G. P., and Fletcher, L. S., 1989, "Effective Thermal Conductivity Within Packed Beds of Spherical Particles," ASME JOURNAL OF HEAT TRANSFER, Vol. 111, pp. 830–836.

Eshelby, J. D., 1957, "The Determination of the Elastic Field of an Ellipsoidal Inclusion and Related Problems," *Proc. Royal Soc.*, Vol. 241, A, pp. 376–396.

Fletcher, L. S., 1988, "Recent Developments in Contact Conductance Heat Transfer," ASME JOURNAL OF HEAT TRANSFER, Vol. 110, pp. 1059-1070.

Gu, G., and Tao, R., 1988, "Effective Thermal Conductivity of a Periodic Composite With Constant Resistant," *Journal of Applied Physics*, Vol. 64, pp. 2968-2972.

Haji-Sheikh, A., 1988, "Heat Transfer in Heterogeneous Bodies Using Heat-Flux-Conserving Basis Functions," ASME JOURNAL OF HEAT TRANSFER, Vol. 110, pp. 276-282.

Haji-Sheikh, A., and Beck, J. V., 1990; "Green's Function Partitioning in Galerkin-Based Solution of the Diffusion Equation," ASME JOURNAL OF HEAT TRANSFER, Vol. 112, pp. 28-34.

Hashin, Z., 1968, "Assessment of the Self Consistent Scheme Approximation: Conductivity of Particulate Composites," *Journal of Composite Materials*, Vol. 2, pp. 284-300.

Hashin, Z., 1983, "Analysis of Composite Materials—A Survey," *Journal of Applied Mechanics*, Vol. 50, pp. 481-505.

Hasselman, D. P. H., and Johnson, L. F., 1987, "Effective Thermal Conductivity of Composites With Interfacial Thermal Barrier Resistance," *Journal of Composite Materials*, Vol. 21, pp. 508-515.

Hatta, H., and Taya, M., 1985, "Effective Thermal Conductivity of a Misoriented Short Fiber Composite," *Journal of Applied Physics*, Vol. 58, pp. 2478-2486.

Horvay, G., Mani, R., Veluswami, M. A., and Zinsmeister, G. E., 1973, "Transient Heat Conduction in Laminated Composites," ASME JOURNAL OF HEAT TRANSFER, Vol. 95, pp. 309-316.

Huang, S. C., and Chang, Y. P., 1980, "Heat Conduction in Unsteady, Periodic, and Steady States in Laminated Composites," ASME JOURNAL OF HEAT TRANSFER, Vol. 102, pp. 742-748.

Incropera, F. P., and DeWitt, D. P., 1990, *Fundamentals of Heat and Mass Transfer*, Wiley, New York.

Kantorovich, L. V., and Krylov, V. I., 1960, *Approximate Methods of Higher Analysis*, Interscience Publishers, Inc., New York.

Lee, Y.-M., 1991, "Thermal Analysis of Heterogeneous Solid," Ph. D. Thesis, University of Texas at Arlington, Arlington, TX.

Lee, Y.-M., and Haji-Sheikh, A., 1991, "Temperature Field in Heterogeneous Bodies: a Non-orthogonal Solution," *Fundamental of Conduction*, ASME HTD-Vol. 173, pp. 1-9.

McLellan, G. W., and Shand, E. B., 1984, *Glass Engineering Handbook*, McGraw-Hill, New York.

Nomura, S., and Chou, T. S., 1980, "Bounds of Effective Thermal Conductivity of Short-Fiber Composites," *Journal of Composite Materials*, Vol. 14, pp. 120-129.

Nomura, S., and Haji-Sheikh, A., 1988, "Analysis of Transient Heat Conduction in Complex Shaped Composite Materials," ASME *Journal of Engineering Materials and Technology*, Vol. 110, No. 2, pp. 110-112.

Peterson, G. P., and Fletcher, L. S., 1989, "On the Thermal Conductivity of Dispersed Ceramics," ASME JOURNAL OF HEAT TRANSFER, Vol. 111, pp. 824-829.

Peterson, G. P., and Fletcher, L. S., 1990, "Measurement of the Thermal Conductance and Thermal Conductivity of Anodized Aluminum Coatings," ASME JOURNAL OF HEAT TRANSFER, Vol. 112, pp. 579-585.

Salt, H., 1983, "Transient Conduction in a Two-Dimensional Composite Slab—I. Theoretical Development of Temperature Mode," *Int. J. Heat Mass Transfer*, Vol. 26, pp. 1611-1616.

Sangani, A. S., and Acrivos, A., 1983, "The Effective Conductivity of a Periodic Array of Spheres," *Proc. Roy. Soc. London*, Series A, Vol. 386, pp. 263-275.

Shonnard, D. R., and Whitaker, S., 1989, "The Effective Thermal Conductivity for a Point-Contact Porous Medium: an Experimental Study," *Int. J. Heat Mass Transfer*, Vol. 32, No. 3, pp. 503-512.

Zuzovski, M., and Brenner, H., 1977, "Effective Conductivities of Composite Materials Composed of Cubic Arrangements of Spherical Particles Embedded in an Isotropic Matrix," *Zeitschrift für angewandte Mathematik und Physik*, Vol. 28, pp. 979-992.

Thermal Conductivity of Thin Metallic Films

Sunil Kumar

George C. Vradis

Department of Mechanical Engineering,
Polytechnic University,
333 Jay Street,
Brooklyn, NY 11201

This study examines the effect of transverse thickness on the in-plane thermal conductivity of single crystal, defect-free, thin metallic films. The imposed temperature gradient is along the film and the transport of thermal energy is predominantly due to free electron motion. The small size necessitates an evaluation of the Boltzmann equation of electron transport along with appropriate electron scattering boundary conditions. Simple expressions for the reduction of conductivity due to increased dominance of boundary scattering are presented and the results are compared with other simplified approaches and experimental data from the literature. Grain boundary scattering is also considered via simple arguments.

Introduction

In this study the effect of transverse thickness on thermal conductivity is investigated by considering free electron transport via the Boltzmann transport theory. The imposed temperature gradient is along the film, as is the direction of the heat flow. The effect of scattering of electrons at the boundaries of the film, which may be neglected for very thick films or bulk samples, becomes increasingly dominant as the thickness decreases. At thicknesses of the order of mean free paths the resistance due to the boundary scattering is expected to dominate the conduction process as compared to that of the bulk scattering processes. The additional boundary scattering-induced resistance to electron motion reduces the effective thermal conductivity of the film. The thermal conductivity of the film is thus not the intrinsic material property as it is for bulk samples since it now additionally depends on the film thickness, a geometric parameter. The present study examines reduction in thermal conductivity of metallic films where the primary heat carriers are the free electrons. Similar studies for dielectric films (Morelli et al., 1988; Lambropoulos et al., 1989; Majumdar, 1991) and other microscale heat transfer regimes can be found elsewhere (Flik et al., 1991).

The valid progress in micro- and nanoscale technologies has made it possible to utilize very thin films for a variety of applications. Examples are thin films in semiconductor and superconductor electronic devices and thin membranes and films in sensors and micro-actuators. Additionally, during the fabrication process of semiconductor and superconductor devices thin films are first deposited, usually at high temperatures, and then etched into specific shapes and patterns. Metallic films are deposited on the substrate to be used for the interconnects and superconductor films for creating Josephson junctions and film-based detectors. The study is prompted by the need to evaluate and predict the thermal transport characteristics of such films.

Previous Approaches

Previous examinations of the variations of thermal conductivity with thickness of thin films have primarily been confined to the electrical conductivity (e.g., Fuchs, 1938; Wilson, 1936; Tellier and Tosser, 1982). Thermal conductivity of thin metallic films was considered by some studies (Tien et al., 1969; Tellier and Tosser, 1982) where it was argued that since the thermal conductivity of pure bulk samples is proportional to the electrical conductivity of the same samples via the Wiedemann–Franz law, the reduced thermal conductivity of thin films must also have the same proportionality with the reduced electrical conductivity of the same films. This law is mathematically stated as (Wilson, 1936; White and Tanish, 1960; Kittel 1986)

$$\frac{\kappa}{\sigma T}=\Gamma=\frac{\pi^2}{3}\frac{k^2}{e^2}, \tag{1}$$

where κ and σ are the thermal and electrical conductivities, Γ is the Lorenz constant, k the Boltzmann constant, and e the electron charge. The above is theoretically and experimentally shown to be identically satisfied for pure bulk metals but has not been proved for thin films. Tien et al. (1969) assumed that the above was valid for thin films and assumed that

$$\frac{\kappa_{\text{film}}}{\kappa_{\text{bulk}}}=\frac{\sigma_{\text{film}}}{\sigma_{\text{bulk}}}, \tag{2}$$

where the ratio of film electrical conductivities was obtained from the Boltzmann analysis of Fuchs (1938).

Other studies (Tellier and Tosser, 1982) geometrically evaluated the reduction in the mean free path due to the termination of path lines at the boundaries. By assuming that the conductivity is proportional to the mean free path, it was argued that a reduction in the mean free path implies a proportional reduction of conductivity. A drawback of these approaches is that some assumptions are required for the distribution of the origination points of the path lines in a film since the actual statistical distribution of such is not available. The only two analytical assumptions available are that of uniform origination in the film and of boundary origination, both of which are not intuitively convincing. Two of these closed-form results based on geometric averaging are by Thompson (1906) (as reported by Fuchs, 1938) for boundary origination

$$\frac{\sigma_{\text{film}}}{\sigma_{\text{bulk}}}=\frac{l_{\text{film}}}{l_{\text{bulk}}}\approx\frac{1}{2}\,\delta\left[\ln\delta+\frac{3}{2}\right],\ \delta<1, \tag{3}$$

and by Flik and Tien (1990), who analyzed superconductor films, using boundary origination

$$\frac{\kappa_{\text{film}}}{\kappa_{\text{bulk}}}=\frac{l_{\text{film,longitudinal}}}{l_{\text{bulk}}}=1+\frac{4}{\pi}\,\delta\left(\ln\frac{1+\delta+S}{1+\delta-S}-\frac{1}{2}S\right)-\frac{2}{\pi}\cos^{-1}\delta,\ \delta<1, \tag{4}$$

Contributed by the Heat Transfer Division and presented at the ASME National Heat Transfer Conference, San Diego, California, August 9–12, 1992. Manuscript received by the Heat Transfer Division September 1992; revision received April 1993. Keywords: Conduction, Thin Film Flow. Technical Editor: R. Viskanta.

and uniform origination

$$\frac{\kappa_{film}}{\kappa_{bulk}} = \frac{l_{film,longitudinal}}{l_{bulk}} = 1 + \frac{2}{\pi}\,\delta \ln\frac{1+\delta+S}{1+\delta-S} - \frac{2}{\pi}\cos^{-1}\delta - \frac{2}{3\pi}\frac{1}{\delta}(1-S^3),\ \delta<1, \quad (5a)$$

$$= 1 - \frac{2}{3\pi}\frac{1}{\delta},\ \delta \geq 1. \quad (5b)$$

Here δ is the normalized film thickness ($=L/l$), L is the film thickness, l the mean free path, and $S=(1-\delta^2)^{1/2}$. Equation (3) computes the reduction in the mean free path whereas Eqs. (4) and (5) evaluate the reduction in the component of the mean free path along the longitudinal direction of the film by geometric assumptions. Equations (3) and (4) assume that all the path lines originate at the boundaries whereas Eq. (5) assumes that the path lines originate uniformly along the transverse direction.

The disadvantages of the geometric methods of the kind presented above are threefold (Fuchs, 1938; Tellier and Tosser, 1982). First, the statistical distribution of the mean free paths as functions of electron energy are neglected. Second, the true mean free path based on the average of free paths of all the electrons in the metal at a given moment is not computed and instead the mean of all free paths of a given electron is evaluated. Last, the effect of specularity of scattering cannot be accounted for at the boundaries since the boundary is always treated as a termination point for any path length, which is not the case for specular reflections. In contrast, the present study does not rely on geometric arguments and the complete Boltzmann equation with the Fermi-Dirac distribution of free electrons is solved to evaluate the reduction in thermal conductivity due to the increased dominance of interactions of electrons with boundaries.

Theory

The thermal conductivity is determined by the heat flow resulting from a temperature gradient in conditions such that there is no electric current. There is a redistribution of the conduction electrons to create an electric field **E** of the right amount to counteract the drift velocities of the electrons due to the temperature gradient so that the net electric current is zero. Assuming an isotropic material, the electric field is set up in the same direction as the temperature gradient, which is along the x direction (see Fig. 1).

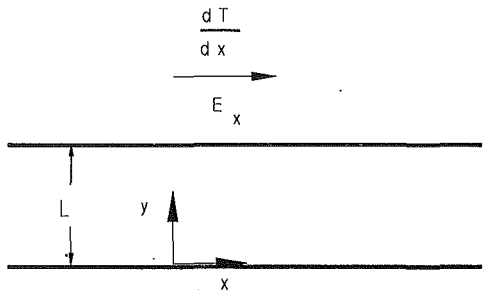

Fig. 1 The schematic of the system under consideration

At the outset, the assumptions that are tacitly implicit in the following derivations are enunciated. These assumptions are not very restrictive and are listed as follows:

1. The atoms occupy a very small volume of the metal.
2. Even though a temperature gradient exists, the variations of temperature are small over a distance of the order of the mean free path.
3. The collisions of the electrons with each other are neglected. Electron–electron scattering is very infrequent due to the Pauli exclusion principle and, coupled with effects of Coulomb interaction screening, is thus negligible (Kittel, 1986).
4. The metal is pure, homogeneous, and has a perfect lattice without grain boundaries, i.e., scattering from other sources such as impurities and grain boundaries are neglected. (Grain boundary scattering effects are considered briefly at the end of the paper.)
5. A relaxation time can be defined for the scattering processes within the metal film. This relaxation time, due to electron–phonon interactions, is at most a function of the electron energy and is not a function of the direction of travel.
6. The conduction of heat is by electrons only. At temperatures above Debye temperature θ this is always valid for pure metals as demonstrated by the Wiedemann–Franz law, which indicates that the ratio of thermal conductivity to the product of electrical conductivity (which is due to electron motion only) and temperature is a

Nomenclature

$\mathbf{a}$ = acceleration vector of magnitude a
A = constant defined in the text
B = ratio of film thickness to grain diameter
$\bar{c}$ = Euler's constant $=0.5772156649$
C = constant in the definition of relaxation time
d = average in-plane grain diameter
e = electron charge $=1.6\times10^{-19}$ Coulomb
$\mathbf{E}$ = electric field vector of magnitude E and components E_x, E_y, E_z
f = electron number density in the space–velocity space
f_0 = equilibrium distribution of f
g = probability density used in the definition of f
h = Planck's constant $=6.63\times10^{-34}$ J-s
$\mathbf{H}$ = magnetic field vector of magnitude H
I = integrals defined in the text
j = electric current
k = Boltzmann constant $=1.38\times10^{-23}$ J/K
$\mathbf{k}$ = wave vector with components k_x, k_y, k_z
l = mean free path
L = thickness of film
m = electron mass $=9.11\times10^{-31}$ kg
n = number of electrons per unit volume
p = fraction of electrons scattered specularly
q = heat flux
R = reflection coefficient at grain boundaries
t = time
T = temperature
T_0 = degeneracy temperature $=\zeta_0/k$
$\mathbf{v}$ = velocity vector of magnitude v and components v_x, v_y, v_z
x, y, z = Cartesian coordinates
α = function defined in Eq. (32)
β = function in Eq. (14)
γ = expression related to correction term
Γ = Lorenz number
δ = ratio of film thickness to mean free path $=L/l(\zeta)$
ϵ = kinetic energy
ζ = chemical potential or Fermi level
ζ_0 = Fermi energy, equal to ζ at 0 K
θ = Debye temperature
κ = thermal conductivity
σ = electrical conductivity
τ = relaxation time

constant, see Eq. (1). At very low temperatures, $T \ll \theta$, the above is also valid for pure metals, indicating that electrons are still dominant in the heat conduction process in pure metals at very low temperatures (White and Tanish, 1960). For intermediate temperatures the Wiedemann–Franz law does not hold. The constant of proportionality changes slightly at cryogenic temperatures where other effects may also begin to be important.

7 The thicknesses are large enough so that the classical Boltzmann equation remains valid.

Assumption 2 ensures that the dependence of the probability density function on temperature is weak so that a perturbation method analysis can be implemented. Assumptions 3 and 4 ensure that scattering effects other than the essential electron–phonon interactions are suppressed, thereby reducing the number of parameters and bringing into prominence the effects of the boundary scattering phenomenon. Whereas assumption 3 follows from the principles of solid state physics, scattering from grain boundaries and other lattice defects and impurities are functions of the specific geometric nature of the lattice and are functions of the process used for the thin film fabrication. It is seen that these scattering processes can be made reasonably negligible for bulk samples at room temperatures or higher if the metal is pure and thus assumption 4 seems reasonable. However, various experiments (Nath and Chopra, 1974; Kelemen, 1976) indicate that practical implementation of this assumption for thin films is not entirely trivial. Temperature ranges between the Debye temperature θ and the degeneracy temperature T_0 ($=\zeta_0/k$) of the metals will be specifically considered to facilitate the consideration of the electron–phonon scattering via a closed-form expression for the relaxation time τ. However, as seen later, this is not a significant limitation since the results show that the exact representation of the scattering time is not required except for very high temperatures. Values of τ, T_0, and other properties of selected metals are presented in Table 1.

The simplified form of the steady-state Boltzmann equation (Kittel, 1986; Bass et al., 1990; Kumar and Vradis, 1991) after eliminating the nonrelevant terms is

$$-\frac{eE_x}{m}\frac{\partial f}{\partial v_x}+v_x\frac{\partial f}{\partial T}\frac{dT}{dx}+v_y\frac{\partial f}{\partial y}=-\frac{f-f_0}{\tau}, \tag{6}$$

where $\mathbf{v}$ is the velocity vector with Cartesian components v_x, v_y, and v_z, and $f(\mathbf{v}, y)$ is the number of electrons in the unit volume around y that have their velocities lying in the unit range of velocities around $\mathbf{v}$. Here e is the electron charge, E_x is the electric field (assumed constant) set up in the x direction, m is the electron mass, T is the temperature, and $\tau(\mathbf{v})$ the effective relaxation time due to all scattering processes in the bulk. The coefficient of the first derivative on the left side of the above equation represents the acceleration of the electron which is assumed constant. If the effects of boundary scattering were neglected, f would not explicitly depend on the position. The scattering of the electrons within the medium, usually represented by the collision integral, has been replaced by an effective relaxation time τ. The expression of τ is the same as that used for classical Boltzmann analyses of the conductivity and specific values are available from the bulk conductivity measurements.

The equilibrium distribution function $f_0(\mathbf{v})$ is a function of the kinetic energy ϵ and is given by the Fermi–Dirac statistics as

$$f_0(\mathbf{v})=2\left(\frac{m}{h}\right)^3 g_0(\epsilon),\quad g_0(\epsilon)=\frac{1}{\exp[(\epsilon-\zeta)/kT]+1},$$
$$\epsilon=\frac{1}{2}m|\mathbf{v}|^2, \tag{7}$$

where k is the Boltzmann constant and ζ is a parameter called the Fermi level, which is the chemical potential of the electrons according to Gibbs thermodynamics and is determined by the electron number density present. The occurrence of the factor 2 is due to each translational state having 2 states of electronic spin. The equilibrium distribution is a function of the magnitude of the velocity only and not its vector direction. The distribution function g_0 gives the probability that an orbital at energy ϵ is occupied by an electron. The value of ζ can be easily obtained for metals as (Wilson, 1936)

$$\zeta=\zeta_0-\frac{\pi^2k^2T^2}{12\zeta_0}-\ldots,\quad \zeta_0=\frac{h^2}{8m}\left(\frac{3n}{\pi}\right)^{2/3}. \tag{8}$$

If the total number n of electrons per unit volume is assumed to be equal to the valence electrons of the metal the value of ζ_0/k (called the degeneracy temperature T_0) is high according to the above relation. Thus if T is less than this value then f_0 is almost constant between the range of energies between zero and the Fermi level and decreases rapidly to zero at larger values.

An electron moves freely through a perfect lattice without disturbance and the conductivity is rendered finite only due to scattering from imperfections such as displacements from perfect lattice configurations or lattice defects. Thus finite conductivity is introduced due to the quantized lattice vibrations or phonons and defects and imperfections, which include grain boundaries and impurities. The scattering from sources other than phonons is shown to be negligible at room temperatures and above for most carefully prepared pure metals. For the temperature range above Debye temperature the value of τ can be uniquely defined by electron–phonon interactions. This value of τ can be shown to be as follows (Wilson, 1936):

$$\tau=C\frac{\theta}{T}\epsilon^{3/2},\quad T>\theta, \tag{9}$$

where θ is the Debye temperature and C is a constant that is related to the properties of the material. The assumption used in the development of this relation is that the motions of the electrons and phonons are independent to the first order. This formulation indicates that the mean free paths of the electrons are not constant but a function of the electron energies, the magnitude of the mean free path being proportional to the square of the energy, i.e.,

$$l(\epsilon)=\tau v=C\sqrt{\frac{2}{m}}\frac{\theta}{T}\epsilon^2=l(\zeta)\left(\frac{\epsilon}{\zeta}\right)^2. \tag{10}$$

The constant C may be determined by comparing the thermal conductivity κ of the bulk material to that obtained by solving the Boltzmann equation as shown subsequently.

Another consideration in the definition of relaxation time is the equivalence between thermal and electrical relaxation times. In general, two different cases corresponding to imposed electric field and imposed temperature gradient are evaluated for obtaining the electrical and thermal conductivities, respectively. In order to relate the two conductivities as stated by the Wiedemann–Franz law, the corresponding relaxation

Table 1 Properties of some metals

Metal	Temperature Debye θ [K]	Temperature Degeneracy T_0 [K]	Fermi Energy ζ_0 [J]	Relaxation Time† $\tau(\zeta)$ [s]	Mean-Free Path† $l(\zeta)$ [m]
Li	430	5.6×10^4	7.5×10^{-19}	8.8×10^{-15}	1.14×10^{-8}
Na	160	3.7×10^4	5.0×10^{-19}	3.2×10^{-14}	3.36×10^{-8}
K	99	2.5×10^4	3.3×10^{-19}	4.1×10^{-14}	3.49×10^{-8}
Cu	310	8.2×10^4	1.1×10^{-18}	2.7×10^{-14}	4.24×10^{-8}
Ag	220	6.4×10^4	8.8×10^{-19}	4.0×10^{-14}	5.56×10^{-8}
Au	185	6.4×10^4	8.8×10^{-19}	3.0×10^{-14}	4.17×10^{-8}
Be	900	1.6×10^5	2.3×10^{-18}	5.1×10^{-15}	1.15×10^{-8}
Mg	330	6.5×10^4	1.1×10^{-18}	1.1×10^{-14}	1.74×10^{-8}
Al	410	1.4×10^5	1.9×10^{-18}	8.0×10^{-15}	1.60×10^{-8}
Bi	80	2.1×10^2	2.9×10^{-21}		

† Values are at room temperature for electrons at Fermi level (data from Wilson, 1936; Myers, 1990).

times must remain the same for the two different transport processes. Equilibrium of electrons can be reached by two mechanisms: scattering processes that change direction but do not change energy significantly, or that change energy but not direction (White and Tanish, 1960). The latter can be shown not to contribute to electrical resistance and hence the electrical and thermal conduction are strictly equal if the latter is absent. The scattering of electrons by phonons or lattice waves at temperatures greater than Debye temperatures is large-angle and elastic, and therefore corresponds to the former mechanism only. Thus the expression of τ presented above is valid for both the electrical and thermal cases (see White and Tanish, 1960, and the references cited within for details).

Whereas the scattering of electrons by phonons in the bulk is accounted for by the relaxation time τ, the boundary scattering is accounted for by the boundary conditions. The additional functional dependence of f on y is chosen to account for the variation in the transverse y direction due to reflection of the electrons at the boundaries.

The electric current density $j_x(y)$ and its average $\overline{j_x}$ are given by

$$j_x(y) = -e\int\int\int v_x f(\mathbf{v}, y)d\mathbf{v},\ \overline{j_x} = \frac{1}{L}\int_0^L j_x(y)dy. \quad (11a)$$

Similarly the local heat flux $q_x(y)$ and the average flux $\overline{q_x}$ are given by

$$q_x(y) = \int\int\int v_x \epsilon f(\mathbf{v}, y)d\mathbf{v},\ \overline{q_x} = \frac{1}{L}\int_0^L q_x(y)dy. \quad (11b)$$

In the above $d\mathbf{v}$ refers to $dv_x dv_y dv_z$.

The solution strategy is to evaluate the electric current, set it to zero thereby yielding the expression for E_x, and then substitute it in the expression for heat flux. The mathematical development presented subsequently in this paper is not discussed in detail for the sake of brevity. Most of the intervening steps and the integrations are algebraically tedious but are logically straightforward.

The difference between f and f_0 is taken to be f_1, i.e.,

$$f(\mathbf{v}, y) = f_0(\mathbf{v}) + f_1(\mathbf{v}, y), \quad (12)$$

and is substituted into the Boltzmann equation. Since f is expected to be of the order of the equilibrium value f_0, the terms containing f_1 are neglected compared to similar terms containing f_0. This simplifies the transport equation to

$$-\frac{eE_x}{m}\frac{\partial f_0}{\partial v_x} + v_x\frac{\partial f_0}{\partial T}\frac{dT}{dx} + v_y\frac{\partial f_1}{\partial y} = -\frac{f_1}{\tau}. \quad (13)$$

The solution to the above is

$$f_1(\mathbf{v}, y) = \left[\frac{eE_x}{m}\frac{\partial f_0}{\partial v_x} - v_x\frac{\partial f_0}{\partial T}\frac{dT}{dx}\right]\tau \times\left[1+\beta(\mathbf{v})\exp\left(\frac{-y}{\tau v_y}\right)\right], \quad (14)$$

where $\beta(\mathbf{v})$ is an arbitrary function of $\mathbf{v}$.

Assuming that a fraction p of the electrons are scattered specularly from the surface and the rest are scattered diffusely, the above can be written as (see Fuchs, 1938, for mathematical details)

$$f_1(\mathbf{v}, y) = \left[\frac{eE_x}{m}\frac{\partial f_0}{\partial v_x} - v_x\frac{\partial f_0}{\partial T}\frac{dT}{dx}\right]\tau \times\left[1-\frac{1-p}{1-p\,\exp(-L/\tau v_y)}\exp\left(\frac{-y}{\tau v_y}\right)\right],\ v_y>0, \times\left[1-\frac{1-p}{1-p\,\exp(L/\tau v_y)}\exp\left(\frac{L-y}{\tau v_y}\right)\right],\ v_y<0. \quad (15)$$

First the velocities are converted into polar coordinates with the polar angle measured from the y axis. After integration over the angles, an integration over the y direction is conducted to yield the average current and heat flux. After performing these integrations the current is given by

$$\overline{j_x} = \frac{-CAe\theta}{T}\left\{\left[eE_x + T\frac{\partial}{\partial T}\left(\frac{\zeta}{T}\right)\frac{dT}{dx}\right]I_{p3} + \frac{1}{T}\frac{dT}{dx}I_{p4}\right\}, \quad (16)$$

which yields, after setting the current to zero,

$$eE_x + T\frac{\partial}{\partial T}\left(\frac{\zeta}{T}\right)\frac{dT}{dx} = -\frac{1}{T}\frac{dT}{dx}\frac{I_{p4}}{I_{p3}}. \quad (17)$$

The following expression based on the mathematical form of the Fermi distribution f_0 has been used in the derivation of the above:

$$\frac{\partial f_0}{\partial T} = \frac{\partial f_0}{\partial \epsilon}T\frac{\partial}{\partial T}\left(\frac{\epsilon-\zeta}{T}\right). \quad (18)$$

After substituting the above expression into the evaluation of $\overline{q_x}$ the following is obtained:

$$\kappa_{\text{film}} = \frac{\overline{q_x}}{-dT/dx} = \frac{CA\theta}{T^2}\frac{I_{p3}I_{p5} - I_{p4}I_{p4}}{I_{p3}}. \quad (19)$$

where

$$A = \frac{16\sqrt{2}}{3}\pi\frac{\sqrt{m}}{h^3}. \quad (20)$$

A similar derivation as the above to evaluate the bulk thermal conductivity by letting $f_{\text{bulk}}(\mathbf{v}) = f_0(\mathbf{v}) + f_1(\mathbf{v})$ and following the same steps yields

$$\kappa_{\text{bulk}} = \frac{q_x}{-dT/dx} = \frac{CA\theta}{T^2}\frac{I_3I_5 - I_4^2}{I_3}. \quad (21)$$

Here the integrals I_{pn} and I_n are

$$I_{pn} = -\int_0^\infty \epsilon^n\frac{\partial g_0}{\partial \epsilon}\gamma_p(\epsilon)d\epsilon,\ I_n = -\int_0^\infty \epsilon^n\frac{\partial g_0}{\partial \epsilon}d\epsilon. \quad (22)$$

where

$$\gamma_0 = 1 - \frac{3}{8}\left(\frac{L}{\tau v}\right)^{-1} - \frac{3}{4}\left[\frac{L}{\tau v} - \frac{1}{12}\left(\frac{L}{\tau v}\right)^3\right]Ei\left(-\frac{L}{\tau v}\right) - \exp\left(-\frac{L}{\tau v}\right)\left[\frac{5}{8} + \frac{1}{16}\left(\frac{L}{\tau v}\right) - \frac{1}{16}\left(\frac{L}{\tau v}\right)^2 - \frac{3}{8}\left(\frac{L}{\tau v}\right)^{-1}\right], \quad (23a)$$

$$\gamma_p = 1 - \frac{3}{8}(1-p)\left(\frac{L}{\tau v}\right)^{-1} + \frac{3}{4}(1-p)^2\left(\frac{L}{\tau v}\right)^{-1} \times\sum_{n=1}^{\infty} p^{n-1}\left[-Ei\left(-\frac{Ln}{\tau v}\right)\left[\left(\frac{Ln}{\tau v}\right)^2 - \frac{1}{12}\left(\frac{Ln}{\tau v}\right)^4\right] + \exp\left(\frac{-Ln}{\tau v}\right)\left[\frac{1}{2} - \frac{5}{6}\left(\frac{Ln}{\tau v}\right) - \frac{1}{12}\left(\frac{Ln}{\tau v}\right)^2 + \frac{1}{12}\left(\frac{Ln}{\tau v}\right)^3\right]\right],\ p\neq 0 \quad (23b)$$

Here Ei is the exponential integral function (Gradshteyn and Ryzhik, 1980), and τv the mean free path $l(\epsilon)$ corresponding to the velocity $v\ (=(2\epsilon/m)^{1/2})$.

The resultant ratio of the film thermal conductivity to the bulk value is given by

$$\frac{\kappa_{\text{film}}}{\kappa_{\text{bulk}}} = \frac{I_{p3}I_{p5} - I_{p4}I_{p4}}{I_{p3}}\frac{I_3}{I_3I_5 - I_4I_4}. \quad (24)$$

The integrals I_{pn} and I_n may also be approximately evaluated via an asymptotic expansion of the form (Wilson, 1936)

$$I_{pn} \approx \zeta^n \gamma_p(\zeta) + \frac{\pi^2}{6}(kT)^2 \frac{d^2[\zeta^n \gamma_p(\zeta)]}{d\zeta^2} + \frac{7\pi^4}{360}(kT)^4 \frac{d^4[\zeta^n \gamma_p(\zeta)]}{d\zeta^4} + \frac{31\pi^6}{15120}(kT)^6 \frac{d^6[\zeta^n \gamma_p(\zeta)]}{d\zeta^6} + \ldots, \quad (25a)$$

$$I_n \approx \zeta^n + \frac{\pi^2}{6}(kT)^2 \frac{d^2\zeta^n}{d\zeta^2} + \frac{7\pi^4}{360}(kT)^4 \frac{d^4\zeta^n}{d\zeta^4} + \frac{31\pi^6}{15120}(kT)^6 \frac{d^6\zeta^n}{d\zeta^6} + \ldots. \quad (25b)$$

If the above asymptotic expansions are used and only the leading terms retained, the above conductivity ratio can be approximated by the following

$$\frac{\kappa_{film}}{\kappa_{bulk}} \approx \gamma_p(\delta(\zeta)) \quad (26a)$$

$$= 1 - \frac{3}{8}\frac{1}{\delta} - \frac{3}{4}\left[\delta - \frac{1}{12}\delta^3\right] Ei(-\delta) - \exp(-\delta)\left[\frac{5}{8} + \frac{1}{16}\delta - \frac{1}{16}\delta^2 - \frac{3}{8}\frac{1}{\delta}\right], \quad p = 0. \quad (26b)$$

$$= 1 - \frac{3}{8}(1-p)\frac{1}{\delta} + \frac{3}{4}(1-p)^2\frac{1}{\delta} \times \sum_{n=1}^{\infty} p^{n-1}\left[-Ei(-n\delta)\left[(n\delta)^2 - \frac{1}{12}(n\delta)^4\right] + \exp(-n\delta)\left[\frac{1}{2} - \frac{5}{6}(n\delta) - \frac{1}{12}(n\delta)^2 + \frac{1}{12}(n\delta)^3\right]\right], \quad p \neq 0, \quad (26c)$$

where the asymptotic expression of the bulk conductivity can be written as

$$\kappa_{bulk} \approx \frac{1}{3} CA\theta k^2 \pi^2 \zeta^3 \approx \frac{\pi^2 n k^2 T \tau(\zeta)}{3m}. \quad (27)$$

These approximate expressions for the ratio of film to bulk thermal conductivities are the same as the leading order terms obtained by Fuchs (1938) for electrical conductivity ratio, indicating that the leading order behavior of the ratios of film thermal and electrical conductivities to their respective bulk conductivities is identical, as postulated by Tien et al. (1969).

Results

The ratio of film to bulk thermal conductivities is a function of $L/l(\zeta)$, p, and ζ/kT, as seen from the mathematical development in the previous section. All of these parameters appear in the function γ_p, which accounts for the boundary scattering aspects within the integrals I_{pn}, and the latter also appears in the equilibrium distribution f_0. However, the leading order asymptotic expansion, Eq. (26), indicates that the parameters of greatest importance are $L/l(\zeta)$, the ratio of the film thickness to the mean free path of electrons occupying the energy at the Fermi level, and p, the fraction of electrons scattered specularly at the surface. As $L/l(\zeta)$ becomes larger the conductivity ratio aymptotes toward unity.

Figure 2 shows the conductivity ratio for different film thicknesses for completely diffuse boundaries ($p = 0$). As a comparison, the geometric results of Eqs. (3)–(5) are also plotted. The boundary origination solutions do not match the Boltzmann results and yield physically unrealistic values as the film thickness exceeds the mean free path $l(\zeta)$. This is to be expected since the assumption that all path lengths originate at the boundaries lengths presumes that the film is very thin. However, the uniform origination results exhibit the correct trends even though they overpredict the value of film thermal conductivity. Uniform origination takes into account the reduction in the path lengths of the electron that are within the distance of a mean free path from the boundaries and evaluates the average mean free path assuming that all path lengths originate with uniform probability along the thickness of the film. This approach is physically expected to yield a reduction in thermal conductivity with decreasing thickness, but will not yield correct conductivity ratios since the origination is not uniform along the film thickness. A uniform origination would imply a uniform termination of path lengths along the thickness, which would imply no size effects and is opposite of the expected results.

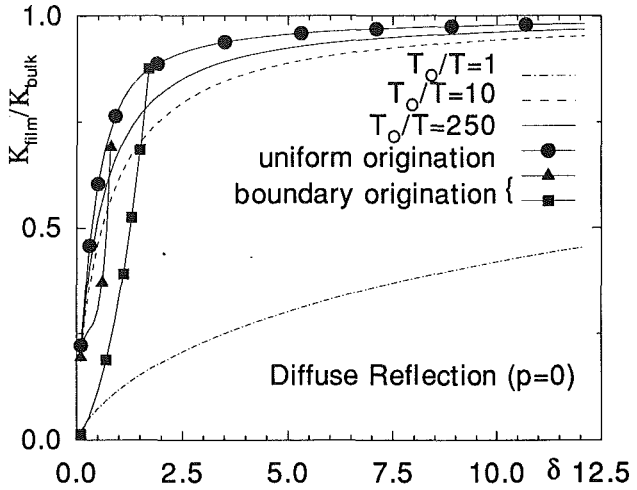

Fig. 2 The ratio of bulk to film conductivities for diffuse scattering at surfaces ($p = 0$). The geometric evaluations of reduction of path lengths via uniform and boundary origination (Fuchs, 1938; Flik and Tien, 1990) are also shown.

Figure 2 also shows that the asymptotic expression, Eq. (26), is adequate if the value of $\zeta/kT = T_0/T$ is greater than approximately 100 and is within 10 percent if T_0/T is greater than 10. Since the degeneracy temperature of most metals (with the exception of anomalous metals such as bismuth) is of the order of 10^4 K, the conductivity of metallic films at operating temperatures up to 1000 K may be evaluated by Eq. (26). In view of the above results, it is apparent that the exact mathematical form of the relaxation time τ is not essential to predicting the reduction in thermal conductivity via the asymptotic expression. The parameter of importance is the mean free path l of the electrons occupying the orbitals at Fermi level. This is a consequence of the rapid change in the Fermi-Dirac distribution at the Fermi level. As the temperatures decrease this change becomes increasingly sharp and the asymptotic expression thus becomes more accurate. Additionally, since the asymptotic expressions for the reduction in electrical conductivity and the reduction in thermal conductivity are identical, the thermal conductivity data can be easily obtained experimentally by measuring the electrical conductivity, which is easier to measure. Similar results are also observed for other values of the reflection parameter p, and can be found elsewhere (Kumar and Vradis, 1992). This result implies that only free electrons at the Fermi level contribute to the thermal conductivity at such temperature ranges and that it is adequate to consider only Fermi level electrons in the evaluation of reduction of thermal conductivity by other scattering mechanisms. Figure 3 shows the variation of the thermal conductivity ratio by considering different values of the specularity fraction p in the asymptotic closed form expression, Eq. (26). If all the electrons are scattered specularly ($p = 1$) then the film conductivity equals that of bulk conductivity. However, it is expected that diffuse reflection will dominate since the wavelength of the electrons is typically of the order of atomic dimensions ($\approx$ 5–10 angstroms) and the rms roughness of surfaces is usually much greater. Therefore the scattering will be diffuse unless the surface is atomically flat, which is rare.

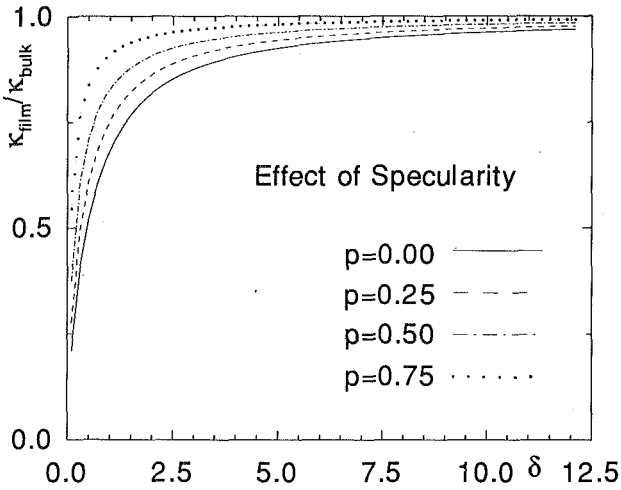

Fig. 3 The ratio of bulk to film conductivities for partially specularly scattering surfaces using the asymptotic expression, Eq. (26)

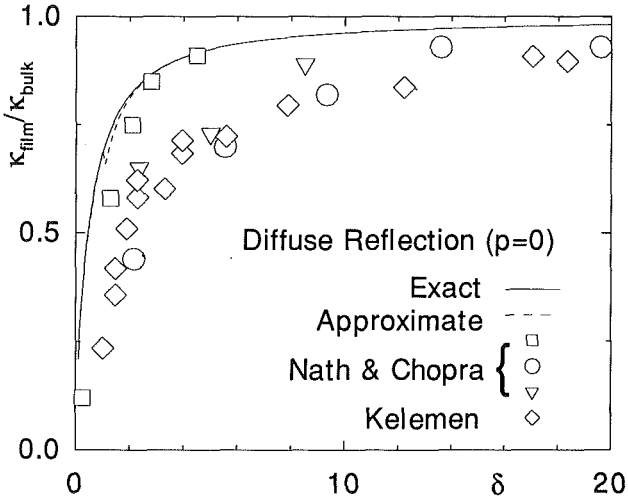

Fig. 4 The ratio of bulk to film conductivities for diffuse scattering at surfaces ($p=0$) showing exact and approximate asymptotic expressions, Eqs. (26) and (28). Experimental data for copper films are also shown from Nath and Chopra (1974): (squares) film deposited at room temperature but measured at 100 K, (circles) deposited at room temperature and measured at 325 K, (triangles) deposited at 500 K and measured at 325 K; and Kelemen (1976): (diamonds) evaluated at 300 K.

Thus, as indicated by the above discussion, Eq. (26) is important. Since it is not easy to evaluate, the following approximations are presented:

$$\frac{\kappa_{film}}{\kappa_{bulk}} \approx 1-(1-p)^2 \sum_{n=1}^{\infty} np^{n-1}\left[1-\frac{3}{4}n\delta(1-\bar{c}-\ln(n\delta)+n\delta/2)\right], \quad \delta \le 1, \quad (28a)$$

$$\approx 1-\frac{3}{8}(1-p)\frac{1}{\delta}, \quad \delta > 1 \quad (28b)$$

Here $\bar{c}$ is Euler's constant used in the expansion of the exponential integral function (Gradshteyn and Ryzhik, 1980). The above approximate expressions are compared with the detailed mathematical expression of Eq. (26) in Fig. 4 for diffuse reflection. It is seen that the approximate expressions are accurate for all practical considerations. The experimental data of Nath and Chopra (1974) and Kelemen (1976) for copper films are also shown in the figure.

The data of Nath and Chopra (1974) for copper films comprise three different sets. The first set (squares in the figures) is film deposited at room temperature but measured at 100 K. The second set (circles) is deposited at room temperature and measured at 325 K, and the third set (triangles) is deposited at 500 K and measured at 325 K. To convert the data to the present form the values of the mean free path $l(\zeta)$ are taken to be 1450 and 360 angstroms at 100 and 325 K, respectively, and the corresponding bulk conductivities are 1.18 and 0.97 cal/cm·s·K (Nath and Chopra, 1974). The data of Kelemen (1976) for copper films (diamonds) is evaluated at 300 K ($l=393$ angstroms, $\kappa_{bulk}=0.97$ cal/cm·s·K). The data for films at 100 K follows the theoretically predicted curve but the others are overpredicted by the curves. This suggests that other mechanisms such as scattering from grain boundaries or defects also plays an important role. Since the 100 K results do not indicate the presence of any other scattering mechanisms, it is conjectured that phonons also contribute as heat carriers in the films at the low temperature of 100 K. Thus this data set (squares) is eliminated from further analysis and only the data sets at 325 and 300 K are considered.

The other important scattering mechanism, in addition to boundary scattering, is grain boundary scattering. Nath and Chopra (1974) do not report measured values of grain sizes, nor does Kelemen (1976). Nath and Chopra (1974) indicate that they believe the grain diameters to be of the order of 100 angstroms for the film deposited at room temperature and 1000 angstroms for deposition at 500 K. If the grain boundary scattering is considered as modifying the relaxation time τ in the film, while the grain size increases with thickness, the analysis in the previous section can be modified as follows. By considering only electrons at the Fermi level, the relaxation time for the film can be obtained by Matthiessen's rule (Myers, 1990; Bass et al., 1990)

$$\frac{1}{\tau_{film}}=\frac{1}{\tau_{bulk}}+\frac{1}{\tau_{grain}}, \quad \tau_{grain}=\frac{d}{v_{Fermi}}. \quad (29)$$

Equations (26) and (28) can be modified for $p=0$ as

$$\frac{\kappa_{film}}{\kappa_{bulk}}=\frac{\tau_{film}}{\tau_{bulk}}\gamma_0(L(1/l+1/d)), \quad (30a)$$

$$\approx \frac{1}{1+B/\delta}\left[1-\frac{3}{8}\frac{1}{\delta+B}\right], \quad B=\frac{L}{d}, \quad \delta+B>1. \quad (30b)$$

Here d is the average in-plane grain diameter, which is considered to be proportional to the film thickness (De Vries, 1988) and B is the proportionality constant as shown. The value of B would depend on the deposition temperature and any subsequent heat treatment. At higher deposition temperatures B is expected to decrease, even though such a trend is not apparent from the conductivity data of Nath and Chopra (1974).

A few studies have considered scattering from grain boundaries only and have evaluated the following associated reduction in thermal conductivity (De Vries, 1988)

$$\frac{\kappa_{film}}{\kappa_{bulk}}=1-\frac{3}{2}\alpha+3\alpha^2-3\alpha^3\ln\left(1+\frac{1}{\alpha}\right), \quad (31)$$

where

$$\alpha=\frac{l}{d}\frac{R}{1-R}=\frac{B}{\delta}\frac{R}{1-R}. \quad (32)$$

Here R is the reflection coefficient of the conduction electrons striking the grain boundaries ($0\le R\le 1$). Using this formulation, and adding the resistances due to the two scattering mechanisms, the following approximation can be obtained (Qiu and Tien, 1992):

$$\frac{\kappa_{film}}{\kappa_{bulk}}=\left[1+\frac{3}{8}\frac{1}{\delta}+\frac{7}{5}\alpha\right]^{-1}, \quad \delta>1. \quad (33)$$

The results of Eqs. (30*b*) and (33) are plotted in Fig. 5 along with the experimental data. The value of B is reported to be approximately 5.0 by De Vries (1988) but other researchers

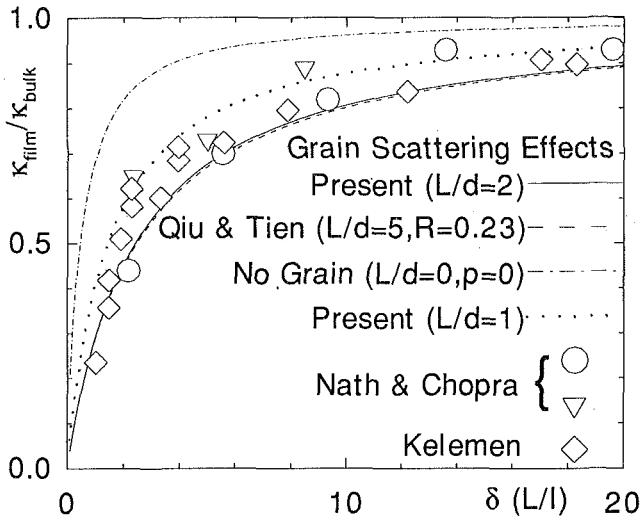

Fig. 5 The ratio of bulk to film conductivities for diffusely scattering surfaces considering grain boundary scattering by the present method, Eq. (30), and Qiu and Tien's method, Eq. (33)

have conjectured even smaller values. In the absence of specific grain diameter information the assumption that $d \approx L$ (i.e., $B = 1.0$) is a logical one. The values of R reported in the literature are compiled by Qiu and Tien (1992); R is chosen to be 0.23, along with $B = 5.0$, by them for matching the present set of data. For the equation developed in this study, the assumption $d = L$ ($B = 1$) matches the data quite well. However, a value of $d = L/2$ ($B = 2$) is shown since it agrees with the expression of Qiu and Tien (1992) and matches the experimental data equally well. The advantage of the equation developed in the present study, Eq. (30*b*), is that it requires the estimation of only one parameter B, and the parameter R is not required. It must be noted that the experimental data shown are obtained by reading the actual conductivity values from the graphs of the published papers and converted to the present form by selecting values of mean free path and bulk conductivity from the literature. This may lead to slight variations in the interpretation presented elsewhere of the same data.

Conclusions

A simple solution within the framework of the Boltzmann transport theory has been presented for single crystal thin films of pure metals that are free of defects and impurities. The resulting closed-form expressions predict the reduction in the thermal conductivity due to boundary scattering. The mathematical formulation also indicates that the reduction in electrical and thermal conductivities are identical for cases of practical importance in thin film technology. Grain boundary scattering is also considered via a simple model and simple closed-form expressions are obtained that match experimental data.

There are four conclusions to be drawn from this study. The first is that the asymptotic expression for boundary scattering limited conductivity ratio, which considers electrons only at the Fermi level, is within 10 percent of the full solution if ζ/kT is greater than 10. Since most operating and processing temperatures fall in this range, the asymptotic expression will suffice, except for anomalous metals such as Bi whose degeneracy temperatures are quite small. Secondly, the boundary scattering limited thermal and electrical conductivity ratios are identical if only electrons at Fermi level are considered. Thirdly, the geometric techniques for evaluating the reduction in mean free path due to boundary scattering do not match the Boltzmann solutions even though uniform origination solutions show the same qualitative trends. The last is that the reduction of conductivity due to size effects alone persists to thicknesses of the order of 15 times the mean free path of the electrons at the Fermi energy level at normal operating temperatures and to considerably higher thicknesses for much higher temperatures. If grain boundary scattering is also present, thicknesses on the order of 50 times mean free path are affected. The presence of micro-cracks and micro-grooves may also further influence the film thermal conductivity (Redondo and Beery, 1986), as will defects, impurities, and dislocations.

Acknowledgments

The authors thank the reviewers for their insightful comments and for suggesting many improvements to the paper. SK acknowledges partial support from the New York State Center for Advanced Telecommunications Technology and the National Science Foundation (CTS-9210727).

References

Bass, J., Pratt, W. P., and Schroeder, P. A., 1990, "The Temperature Dependent Electrical Resistivities of the Alkali Metals," *Reviews of Modern Physics*, Vol. 62, pp. 645–744.

De Vries, J. W. C., 1988, "Temperature and Thickness Dependence of the Resistivity of Thin Polycrystalline Aluminum, Cobalt, Nickel, Palladium, Silver and Gold Films," *Thin Solid Films*, Vol. 167, pp. 25–32.

Flik, M. I., and Tien, C. L., 1990, "Size Effect on the Thermal Conductivity of Thin Film Super-Conductors," ASME JOURNAL OF HEAT TRANSFER, Vol. 112, pp. 872–881.

Flik, M. I., Choi, B. I., and Goodson, K. E., 1991, "Heat Transfer Regimes in Microstructures," in: *Micromechanical Sensors, Actuators, and Systems*, ASME DSC-Vol. 32, pp. 31–47.

Fuchs, K., 1938, "The (Electrical) Conductivity of Thin Metallic Films According to the Electron Theory of Metals," *Proceedings of the Cambridge Philosophical Society*, Vol. 34, pp. 100–108.

Gradshteyn, I. S., and Ryzhik, I. M., 1980, *Table of Integrals, Series, and Products*, Corrected and enlarged edition, Academic Press, New York.

Kelemen, F., 1976, "Pulse Method for the Measurement of the Thermal Conductivity of Thin Films," *Thin Solid Films*, Vol. 36, pp. 199–203.

Kittel, C., 1986, *Introduction to Solid State Physics*, 6th ed., Wiley, New York.

Kumar, S., and Vradis, G. C., 1991, "Thermal Conduction by Electrons Along Thin Films: Effects of Thickness According to Boltzmann Transport Theory," in: *Micromechanical Sensors, Actuators, and Systems*, ASME DSC-Vol. 32, pp. 89–101.

Kumar, S., and Vradis, G. C., 1992, "Thermal Conductivity of Thin Metallic Films by Electron Transport," in: *Heat Transfer on the Microscale*, ASME HTD-Vol. 200, pp. 55–62.

Lambropoulos, J. C., Jolly, M. R., Amsden, C. A., Gilman, S. E., Sinicropi, M. J., Diakomihalis, D., and Jacobs, S. D., 1989, "Thermal Conductivity of Dielectric Thin Films," *Journal of Applied Physics*, Vol. 66, pp. 4230–4242.

Majumdar, A., 1991, "Microscale Heat Conduction in Dielectric Thin Films," *Thin Film Heat Transfer—Properties and Processing*, ASME HTD-Vol. 184, pp. 33–42.

Morelli, D. T., Beetz, C. P., and Perry, T. A., 1988, "Thermal Conductivity of Synthetic Diamond Films," *Journal of Applied Physics*, Vol. 64, pp. 3063–3071.

Myers, H. P., 1990, *Introductory Solid State Physics*, Taylor and Francis, New York.

Nath, P., and Chopra, K. L., 1974, "Thermal Conductivity of Copper Films," *Thin Solid Films*, Vol. 20, pp. 53–62.

Qiu, T. Q., and Tien, C. L., 1992, "Size Effect on Non-equilibrium Laser Heating of Metal Films," in: *Micromechanical Systems*, ASME DSC-Vol. 40, pp. 227–242.

Redondo, A., and Beery, J. G., 1986, "Thermal Conductivity of Optical Coatings," *Journal of Applied Physics*, Vol. 60, pp. 3882–3885.

Tellier, C. R., and Tosser, A. J., 1982, *Size Effects of Thin Films*, Elsevier Publishing, New York.

Tien, C. L., Armaly, B. F, and Jagannathan, P. S., 1969, "Thermal Conductivity of Thin Metallic Films and Wires at Cryogenic Temperatures," *Thermal Conductivity*, Plenum Press, pp. 13–19.

Wilson, A. H., 1936, *The Theory of Metals*, Cambridge University Press, New York.

White, G. K., and Tanish, R. J., 1960, "Lorenz Number for High-Purity Copper," *Physical Review*, Vol. 119, pp. 1869–1871.

Heat Transfer From a Very High Temperature Laminar Gas Flow With Swirl to a Cooled Circular Tube and Nozzle[1]

L. H. Back
Group Supervisor:
Fellow ASME

P. F. Massier
Staff Member.

Jet Propulsion Laboratory,
California Institute of Technology,
Pasadena, CA 91109

An experimental investigation was carried out to appraise the effect of swirl on heat transfer in the laminar boundary layer development region in a highly cooled tube and nozzle. The ratio of gas-side wall-temperature-to-stagnation-temperature ranged from 0.095 to 0.135. In the swirling flow of argon with ratio of peak-tangential-velocity-to-axial velocity of 3.6 at the injection port, the level of heat transfer to the tube wall was increased from 200 to 60 percent above the level without swirl. In the swirling flows, the wall heat flux level was significantly higher in the tube than in the nozzle downstream. Because of the relatively high heat transfer to the wall, there were appreciable reductions in stagnation enthalpy in the flows that spanned a range of Reynolds numbers from about 360 to 500.

Introduction

Interest in rotating flows spans a wide range of applications that involve spin-stabilized projectiles, fixed and rotary wing tip vortices, swirl atomizers, twisted-tape swirl generators, vortex tubes and energy separation, flame stabilization, etc. In a flow acceleration device such as a nozzle in a rocket engine, introduction of swirl in the flow is an attractive way of throttling the mass flow rate and thrust with a small penalty in the reduction of specific impulse (Mager, 1961; Massier, 1965a, b, c). In arc heaters and plasma electrical propulsion devices, gas is sometimes injected tangentially upstream of the electrodes to stabilize the flow. When the arc heater is aligned axially with a larger diameter tube and nozzle downstream, there is an abrupt circular channel expansion at the end of the electrode and flow separation occurs there. Flow reattachment occurs downstream along the larger diameter tube. In this situation, the highest heat transfer occurs in the reattachment region for both swirling and nonswirling flows as observed in the measurements by Back et al. (1972). Increases in heat transfer with swirl have been observed along the convergent portion of nozzles with axial alignment (Massier, 1963), but there was little change in heat transfer in the throat region where it is locally the highest along the nozzle. This same trend was predicted by laminar boundary layer analysis by Back (1969) who also gives some information on the velocity field in conical contraction regions in swirling flows.

In this experimental investigation we have oriented the arc heater normal to the axis of a tube and nozzle as depicted in Fig. 1 and introduced the flow tangentially as shown in the end view to appraise the effect of swirl directly. With this configuration, which has not been investigated previously, it was possible to deduce the magnitude of swirl as inferred from end wall pressure measurements. Experimental results and numerical calculations (Massier et al., 1969; Back, 1972, 1973; Back and Massier, 1972) obtained with negligible swirl in arc-heated flows through a tube-nozzle system with an upstream plenum chamber form the basis for comparison of swirling flow. Characteristic features of these flows at moderate pressures and large ratios of core-flow-to-cooled-wall-temperature are large property variations across the flow and relatively low Reynolds numbers so that the flow is laminar. For higher Reynolds number swirling turbulent flows through tubes the reader is referred to the investigations by Khalil (1982) and Dhir et al. (1989), which indicate enhancement in heat transfer with swirl.

Experimental Apparatus and Instrumentation

A diagram of the test apparatus is shown in Fig. 1. Arc-heated argon enters the circular tube through one tangential port near the end wall as shown in the end view. The gas then flows through the tube, supersonic nozzle, heat exchanger (not shown), and into a vacuum system. The tube diameter D was 4.95 cm and the injection port diameter was 1.91 cm, with the centerline located 3.96 cm from the end wall. In the nomenclature shown in Fig. 1, x is the axial distance along the tube from the end wall, and z is the axial distance along the tube measured from the center of the tangential port. The convergent-divergent nozzle had a conical half-angle of convergence of 27.5 deg and a conical half-angle of divergence of 5 deg. The throat diameter was 0.779 cm. The nozzle inlet section was a circular arc with radius of curvature of 2.48 cm and the

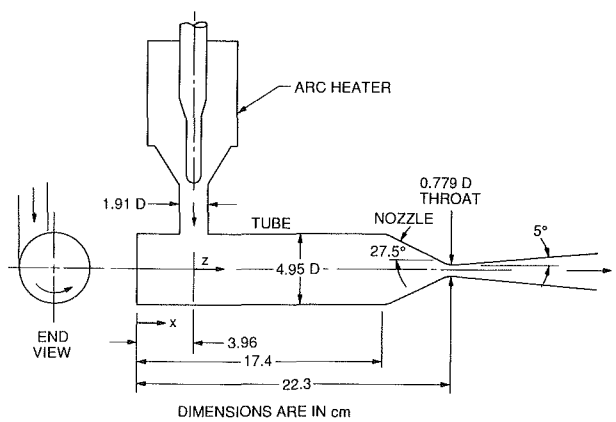

Fig. 1 Test apparatus

[1]The research described in this paper was carried out at the Jet Propulsion Laboratory, California Institute of Technology, under contract with the National Aeronautics and Space Administration.

Contributed by the Heat Transfer Division for publication in the JOURNAL OF HEAT TRANSFER. Manuscript received by the Heat Transfer Division January 1992; revision received April 1993. Keywords: Forced Convection, High-Temperature Phenomena, Rotating Flows. Associate Technical Editor: D. M. McEligot.

throat section was a circular arc with a radius of curvature of 1.52 cm. The rocket type of nozzle was operated in a choked mode.

Semilocal heat-flux distributions along the test apparatus were obtained by calorimetry in circumferential coolant passages with passage widths relatively small in the nozzle compared to the nozzle radius. In the tube upstream the coolant passage widths were about the same as the tube radius. The ratio of gas-side wall-temperature-to-stagnation-temperature ranged from 0.095 to 0.135 over the range of stagnation temperatures from 4030 to 2740 K. The total enthalpy or temperature in the gas was determined from an energy balance on the flow up to the end of each coolant passage along the tube and nozzle. The water flow rate for each passage was measured with a calibrated variable area flowmeter (near midscale readings) with an uncertainty of less than 1 percent of the actual value. Temperature rise of the water flowing through each passage was measured directly with calibrated differential thermocouples. These were constructed in a multiple arrangement for each passage such that there were at least three thermocouples in series thereby providing comparatively large voltage readings, which enhanced the accuracy to uncertainties of less than 1 percent in temperature differences. The typical temperature difference between the inlet and outlet temperature of the coolant water for each passage was about 7°C (13°F) for one test and 5°C (9°F) for the other test. The flow rates through the passages were adjusted to maintain nearly the same temperature rise in each passage to minimize axial conduction between the passages. Water essentially at room temperature entered the passages so that external heat loss to the surroundings was negligible. Water-side wall temperatures were obtained from the inlet water temperature and passage heat fluxes by using conventional heat transfer relations for channel flow. The gas-side wall temperatures were then calculated from the heat conduction equation. The wall was basically isothermal compared to the very high gas temperatures.

The longitudinal static pressure distribution along the constant-diameter duct and the radial static pressure distribution on the endwall were determined from numerous small sharp-edged taps without burrs with large hole depth-to-diameter ratios. At these locations pressures were measured with manometers containing silicone oil. Readings were obtained to within 0.5 mm on the linear scale with an uncertainty of about 0.0000680 atm (0.001 psi). Several manometer boards containing from 6 to 12 tubes each about 2 m high were used and these were referenced to each other in series. For example, with this arrangement six separate boards would provide an equivalent tube height of 12 m (39 ft). Pressures along the nozzle wall were measured with manometers containing mercury since those longitudinal differences were much larger than the ones along the upstream tube.

The applied power to the electric arc that heated the gas was measured with an ammeter and a voltmeter. The inlet temperature of argon was measured with a thermocouple, and the flow rate of argon was measured with a rotameter. All of this instrumentation was carefully calibrated.

Table 1 Experimental conditions for argon flow with swirl through a cooled tube (D = 4.95 cm) and nozzle

Test No.	$\bar{H}_{ti}$, J/g	$\bar{H}_w/\bar{H}_{ti}$	Re_{Di}	P_{ti}, atm	$\dot{m}$, g/s	$\bar{T}_{ti}$, K
57-23HB	2100	0.095	509	0.619	3.105	4030
57-20H	1430	0.135	363	0.264	1.657	2740

Most of the remaining thermal energy in the gas after it left the nozzle was removed by cooling to room temperature in a water heat exchanger before the gas entered the vacuum pump. The temperature rise of the water and its flow rate in this exchanger were also measured very carefully.

Verification of these accuracies was obtained by summing the individual heat loads to the coolant passages and heat exchanger, and comparing this result with the applied power to the arc heater upstream where argon at ambient temperature was injected radially through ports in the wall. The difference between these total heat transfer rates was less than 1 percent of the applied power. This indicates an exceptional check on the measurement technique. Individual uncertainties in the local Nusselt number, Q, reciprocal Graetz number, Ξ, and total enthalpy ratio, $\bar{H}_t/\bar{H}_{ti}$, are estimated to be 2.3, 1.4, and 1.4 percent, respectively, based on the method described by Kline and McClintock (1953).

Test Conditions and Results

Numerous tests were conducted some time ago, but in most of those tests the arc heater flow discharged centrally normal to the axis of the tube and nozzle. Only in the latter part of the test sequence was the flow introduced tangentially through an offset tee as shown in Fig. 1. For this configuration, argon was introduced radially into the arc heater chamber in order not to complicate the flow conditions at the tube inlet, i.e., the flow into the tube had only a tangential component. Table 1 lists the conditions for two tests conducted for comparison with tangential injection—one with a moderate inlet temperature and one with a "high" inlet temperature. Higher inlet temperatures were not feasible as we found in a subsequent test where the arc burned out, presumably because swirl was not introduced in the arc heater to stabilize the arc discharge.

This set of limited laminar flow experiments under very difficult experimental conditions are reported herein. They have not been reported in the literature previously, and may also be useful in appraising more recent numerical predictions of variable density swirling flows through pipes without the complexity of turbulence modeling (i.e., see Hogg and Leschziner, 1989, and Hirai and Takagi, 1991, although there are other computer codes as well).

The inlet condition for the swirling flow along the tube,

Nomenclature

A = cross-sectional area of tube
D = tube diameter
F = function defined in Eq. (4)
H = enthalpy
I = first ionization potential for argon
$\dot{m}$ = mass flow rate
P = pressure
Pr = Prandtl number
q = wall heat flux
Q = dimensionless wall heat flux, Eq. (2)
r = radial distance
r_w = wall radius
R = gas constant
Re_{Di} = Reynolds number $= \dfrac{\dot{m}}{A}\dfrac{D}{\mu_i}$
T = temperature
v = tangential velocity
w = axial velocity
x = axial distance from end wall
z = axial distance from centerline of tangential port
α = ionization fraction
μ = viscosity
Ξ = dimensionless axial coordinate, Eq. (3)
ρ = density
ω = exponent of viscosity–temperature relation

Subscripts

i = inlet condition
p = peak value
t = stagnation condition
w = wall condition

Superscript

$\bar{(\ )}$ = average value

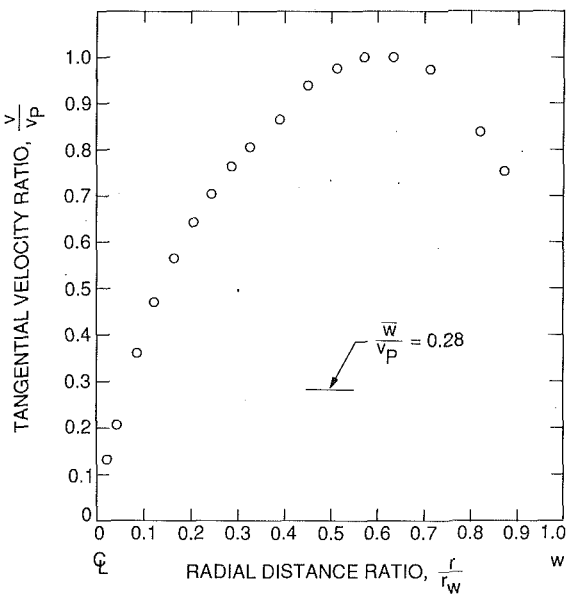

Fig. 2 Tangential velocity variation radially across the flow: Test 57-23HB

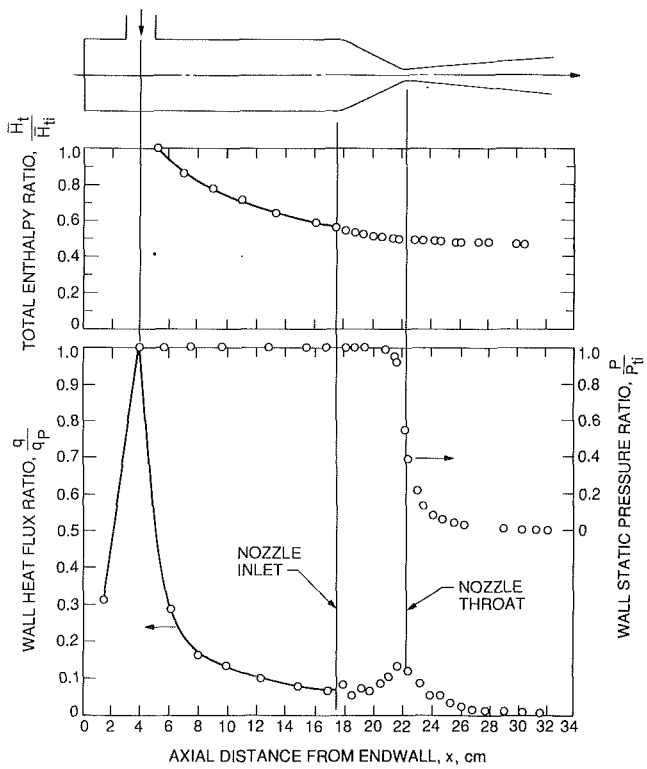

Fig. 3 Wall heat flux, total enthalpy, and wall pressure variation along the tube and nozzle: Test 57-23HB

denoted by the subscript i, was taken at the end of the coolant passage containing the tangential injection port section. From an overall energy balance on the gas flow from the inlet of the arc heater up to this location the total enthalpy $\overline{H}_{ti}$ for test 57-23HB was 2098 J/g (902 Btu/lb) and the stagnation temperature $\overline{T}_{ti}$ was 4030 K (7260 R). Even at this high temperature the degree of ionization or the ionization energy fraction for argon is negligible, e.g., see Massier et al. (1969). For this test the ratio of wall to stagnation enthalpy $\overline{H}_w/\overline{H}_{ti} = 0.095$, and the Reynolds number based on the average axial mass flux through the tube and tube diameter, $\mathrm{Re}_{Di} = \frac{\dot{m}}{A}\frac{D}{\mu_i}$, was about 500. The total pressure p_{ti} was about 0.62 atm and the mass flow rate about 3.1 g/s (0.00684 lb_m/s) for this test. For the other test, 57-20 H, the total pressure, mass flow rate, Reynolds number, and stagnation enthalpy were lower, as seen in Table 1.

Figure 2 shows the approximate tangential velocity variation radially across the flow that was estimated from the end wall pressure measurements for test 57-23HB by using the following form of the radial momentum equation in the tube:

$$\frac{\partial p}{\partial r} \simeq \frac{\rho v^2}{r} \tag{1}$$

that balances the radial pressure gradient and centripetal acceleration. In applying this relation to obtain the tangential velocity component v, the density ρ was calculated from the equation of state $p = \rho RT$, which is a good approximation for argon even at these high temperatures, and by assuming the gas temperature to be about 4500 K in the vicinity of the injection port. The measured static pressure increase radially across the flow amounted to 0.00769 atm (0.113 psi). The radial pressure gradient was obtained from a curve fit to the measured static pressures.

As seen in Fig. 2, the peak tangential velocity v_p occurred at about $r/r_w \simeq 0.6$ and amounted to $v_p \simeq 86$ m/s. This value is about one-half the value of the average velocity in the tangential port upstream; the decrease is presumably due to momentum exchange with the flow in the tube and losses associated with the injection process. The line in Fig. 2 shows the ratio of the average axial velocity in the tube to the peak tangential velocity $\overline{w}/v_p$, which is 0.28. Inverting this ratio gives a value of 3.6 for the relative magnitude of the swirl velocity compared to the axial velocity in the tube. The type of swirling flow evident in Fig. 2 indicated a nonlinear core flow region and an outer region that differs from a potential vortex due to the presence of the wall boundary layer. These differences in the vortex distribution may be due to the rather large injection port size, comparable to the tube radius (Fig. 1), and the approximate nature of the tangential velocity estimates, which probably have an uncertainty of the order of 10 percent. Although end wall pressure measurements were made only for the higher total enthalpy test, the relative magnitude of swirl was believed to be comparable for the lower total enthalpy test by inference from similar ratios of average velocity in the tangential port upstream to axial velocity in the tube.

Figure 3 shows the wall heat flux distribution and total enthalpy variation along the tube and nozzle for the higher temperature test 57-23HB. The peak heat flux q_p in the tube occurs at the tangential port location, being as high as 109 W/cm^2 (0.667 (Btu/sec-in^2)). The wall heat flux then decreases along the tube, more sharply initially and then more gradually, somewhat similar to boundary layer development regions in flows without swirl. In the convergent section of the nozzle the heat flux increases partly because of the increase in axial mass flux along the contraction region and reaches a local peak value just upstream of the throat, similar to nonswirling flows (e.g., Back and Massier, 1972). In the divergent section of the nozzle, the wall heat flux decreases again to relatively low levels primarily because of the decrease in axial mass flux in the supersonic flow region. Clearly, the results shown in Fig. 3 indicate the significantly high wall heat flux level in the swirling flow in the tube. At the end of the tube before the nozzle the average stagnation enthalpy shown in the upper part of Fig. 3 decreased to almost one-half of the inlet value. Subsequent decreases in stagnation enthalpy in the nozzle are relatively small due to the lower nozzle wall heat flux level and reduced surface area. Measured wall static pressures (normalized by the total pressure upstream) area also shown in Fig. 3 on the scale on the right side. There was negligible pressure variation in the tube, less than 0.0007 atm (0.01 psi) while in the nozzle

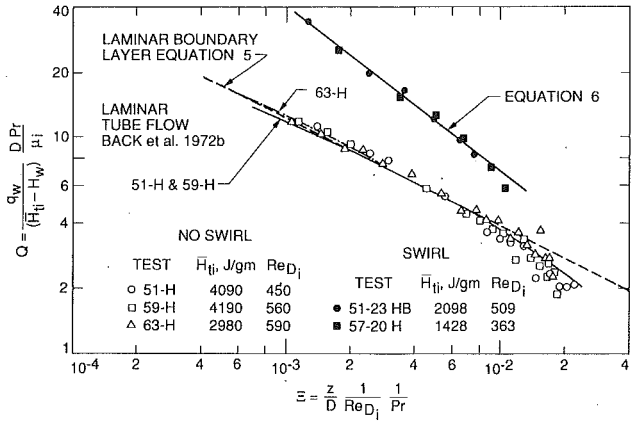

Fig. 4 Correlation of heat transfer results along the tube with and without swirl in the flow

the pressure decrease associated with flow acceleration to supersonic speeds was typical of rocket nozzle operation for the choked condition, (e.g., Back and Massier, 1972).

The wall heat flux distribution along the tube and nozzle for the lower temperature test 57-20H was similar in shape to test 57-23HB, but the heat fluxes were less at the lower stagnation enthalpy, mass flow rate, and Reynolds number. These data are shown subsequently in the representation of Fig. 4 in terms of usual heat transfer parameters.

To place the heat transfer data in the tube in perspective for swirling flow, Fig. 4 shows as a reference datum previously reported results by Back (1972) for very high-temperature laminar flow of argon without swirl in the entrance region of a cooled tube. In this situation three arc heaters were located upstream from which heated argon discharged radially into a plenum chamber. The mixed, high-temperature gas was then accelerated through a short, bell mouth contraction section with a contraction area ratio of 5.3 before entering the tube (Massier et al., 1969, Fig. 1). In the representation of Fig. 4 the dimensionless wall heat flux or Nusselt number is given by

$$Q = \frac{q}{(\bar{H}_{ti} - \bar{H}_w)} \frac{D\,\mathrm{Pr}}{\mu_i} \tag{2}$$

and the dimensionless axial coordinate or reciprocal of the Graetz number is

$$\Xi = \frac{z}{D} \frac{1}{\mathrm{Re}_{Di}} \frac{1}{\mathrm{Pr}} \tag{3}$$

where z is axial distance from the tube inlet, and the subscript i refers to the inlet condition. For the nonswirling entrance region flows shown by the open symbols in Fig. 4, the inlet stagnation enthalpies were even higher than the present values with swirl, and extended up to 4190 J/g (1800 Btu/lb), which corresponded to a stagnation temperature of 7890 K (14,200 R) for test 59-H in particular. Even at this very high temperature the ionization energy fraction $\alpha l/\bar{H}_{ti}$ was only 0.019. For these tests the ratio of wall-to-stagnation-enthalpy $\bar{H}_w/\bar{H}_{ti}$ ranged from 0.039 to 0.055, and the Reynolds number Re_{Di} ranged from 450 to 590.

Various predictions are shown in Fig. 4 for nonswirling flow through the tube. The dashed curve is from a variable-property, laminar boundary layer analysis by Back (1968) for low-speed flow, which is of the form

$$\frac{q}{(H_{ti} - H_w)\rho_i w_i} \left(\frac{\rho_i w_i z}{\mu_i}\right)^{1/2} \mathrm{Pr}^{2/3} = F\left(\omega, \mathrm{Pr}, \frac{H_w}{H_{ti}}\right) \tag{4}$$

Translation of this prediction to the representation of Fig. 4 gives

$$Q = \left(\frac{F}{\mathrm{Pr}^{1/6}}\right) (\Xi)^{-1/2} \tag{5}$$

Values of $F/\mathrm{Pr}^{1/6}$ for monatomic gases[2] (such as argon (Pr = 2/3) for which the exponent ω of the viscosity-temperature relation is 3/4, e.g., Amdur and Mason (1958)) increase slightly with the relative amount of wall cooling being equal to 0.389 at $H_w/H_{ti} = 0.04$ relative to a value of 0.352 at $H_w/H_{ti} \simeq 1.0$; see Back (1972). The nonswirling heat transfer data agree quite well with the laminar boundary layer prediction in the inlet region of the tube as seen in Fig. 4, but then are lower further downstream because the thermal penetration extends to the centerline of the tube and the driving potential for heat transfer is less than the difference $(H_{ti} - H_w)$ just downstream of the tube inlet. As a result, the boundary layer prediction overestimates the heat transfer rate, and agreement with the experimental data is afforded by the tube flow predictions shown in Fig. 4, which were described previously by Back (1972).

The heat transfer data in the tube obtained with swirl flow in this investigation are shown in Fig. 4 by the solid symbols. In this representation the axial distance z is measured from the centerline of the tangential port. These data appear to be correlated at the two different stagnation enthalpy and flow rate conditions of the tests. In the inlet region of the swirling flow there is a considerable increase in heat transfer above the nonswirling flow case, the increase amounting to about 200 percent. In progressing along the tube, the relative increase diminishes and amounts to about 60 percent, near the tube exit where the swirling flow data appear to decrease more as the nonswirling flow data do apparently due to the nonadiabatic core flow.

The swirling flow heat transfer data indicate significant increases in the level of heat transfer above the nonswirling case, and can be described by the following relation, shown in Fig. 4:

$$Q = c(\Xi)^{-3/4} \tag{6}$$

with the empirical constant $c = 0.23$. Because of the set of limited experiments, it is not possible to infer any generality for the empirical relation given by Eq. (6) that correlates the data as shown in Fig. 4. Lower or higher values of the ratio of peak-tangential-velocity-to-average-axial-velocity in the tube or different swirl strength are expected to influence the magnitude of the increase in heat transfer with swirl.

Detailed information on the flow and thermal structure and boundary layer development in these flows is very difficult to obtain experimentally because internal probes disturb the swirling flow field and also require cooling to maintain their integrity. Radial distributions of the stagnation enthalpy, however, were obtained with a 0.318-cm-dia calorimetric probe fabricated from three concentric tubes, being straight with the tip pointing in the radial direction. The probe was located in the tube downstream of the tangential port a distance of 12.2 cm from the end wall. The enthalpy of the gas was computed from measurements of the coolant flow rate and temperature rise, the gas flow rate through the inner tube of the probe, and the temperature of the cooled gas sample as it emerged from the probe. It was also necessary to obtain a measurement of the rate of heat transferred to the probe at each radial position for the condition of zero sampled flow rate. These results are not shown because the average enthalpy determined from the probe data was below the average value based on the external energy balance, presumably because the axial mass flux distribution ρw was not known, and some of the cool gas in the boundary layer near the tube wall probably flowed radially inward along the outer wall of the probe tube in the swirling flow and entered the tube during sampling. The integrated average enthalpy was based on $\int H_t\, dA$ instead of $\int \rho w\, H_t\, dA$ since the axial mass flux distribution was not known.

[2]See Back (1966, appendix) for the thermophysical properties of monatomic gases that were used herein.

Nevertheless, the enthalpy probe data did indicate a radially symmetric enthalpy distribution, and that the edge of the thermal boundary layer along the wall was about 15 percent of the tube radius at this axial location 3.3 tube radii downstream from the tangential port centerline.

Concluding Remarks

Significant increases in laminar heat transfer from 200 to 60 percent along the flow were found in the inlet region of a tube in a swirling flow compared to nonswirling flow. The type of swirling flow investigated herein involved single tangential port injection where the ratio of peak tangential velocity to average axial velocity was a factor of 3.6. The wall heat flux level was significantly higher in the tube than in the nozzle downstream in the swirling flows, and there were appreciable reductions in stagnation enthalpy in the flows because of the large rate of wall cooling.

Acknowledgments

The authors express their gratitude to Mr. M. Noel, Mr. S. Kikkert, and R. Duncan for operation of the system and acquisition and reduction of the experimental data.

References

Amdur, I., and Mason, E. A., 1958, "Properties of Gases at Very High Temperatures," *The Physics of Fluids*, Vol. 1, No. 5, pp. 370–383.

Back, L. H., 1966, "Laminar Boundary Layer Heat Transfer From a Partially-Ionized, Monatomic Gas by the Similarity Approach," Jet Propulsion Laboratory TR 32-867.

Back, L. H., 1968, "Effects of Severe Surface Cooling and Heating on the Structure of Low-Speed, Laminar Boundary Layer Gas Flows With Constant Free-Stream Velocity," Jet Propulsion Laboratory TR 32-1301.

Back, L. H., 1969, "Flow and Heat Transfer in Laminar Boundary Layers With Swirl," *American Institute of Aeronautics and Astronautics Journal*, Vol. 7, No. 9, pp. 1781–1789.

Back, L. H., Massier, P. F., and Roschke, E. J., 1972, "Partially Ionized Gas Flow and Heat Transfer in the Separation, Reattachment and Redevelopment Regions Downstream of an Abrupt Circular Channel Expansion," ASME JOURNAL OF HEAT TRANSFER, Vol. 94, No. 1, pp. 119–127.

Back, L. H., 1972, "Very High Temperature Laminar Flow of a Gas Through the Entrance Region of a Cooled Tube—Numerical Calculations and Experimental Results," *International Journal of Heat and Mass Transfer*, Vol. 15, No. 5, pp. 1001–1021.

Back, L. H., and Massier, P. F., 1972, "Viscous, Non-adiabatic Laminar Flow Through a Supersonic Nozzle—Experimental Results and Numerical Calculations," ASME JOURNAL OF HEAT TRANSFER, Vol. 94, No. 4, pp. 437–445.

Back, L. H., 1973, "Nonisothermal Laminar Flow of Gases Through Cooled Tubes," ASME JOURNAL OF HEAT TRANSFER, Vol. 95, No. 1, pp. 85–92.

Dhir, V. K., Tung, V. X., Chang, F., and Yu, J., 1989, "Enchancement of Forced Convection Heat Transfer Using Single and Multi-stage Tangential Injection," *Heat Transfer in High Energy/High Heat Flux Applications*, ASME HTD-Vol. 119, pp. 61–68.

Hirai, S., and Takagi, T., 1991, "Numerical Prediction of Turbulent Mixing in a Variable-Density Swirling Pipe Flow," *International Journal of Heat and Mass Transfer*, Vol. 34, No. 12, pp. 3143–3150.

Hogg, S., and Leschziner, M. A., 1989, "Second-Moment-Closure Calculation of Strongly Swirling Confined Flow With Large Density Gradients," *International Journal of Heat and Fluid Flow*, Vol. 10, No. 1, pp. 16–27.

Khalil, E. E., 1982, "Heat Transfer to Turbulent Pipe Flows With Swirl and Following a Sudden Enlargement," *Proceedings of the Seventh International Heat Transfer Conference*, Vol. 3, pp. 57–62.

Kline, S. J., and McClintock, F. A., 1953, "Describing Uncertainties in Single Sample Experiments," *Mechanical Engineering*, Jan., pp. 3–8.

Mager, A., 1961, "Approximate Solution of Isentropic Swirling Flow Through a Nozzle," *American Rocket Society Journal*, Vol. 31, No. 8, pp. 1140–1148.

Massier, P. F., 1963, "Heat Transfer to Convergent-Divergent Nozzles From Ionized Argon," Jet Propulsion Laboratory Space Programs Summary, No. 37-24, Vol. IV, pp. 105–108.

Massier, P. F., 1965a, "Axisymmetric Steady Flow of a Swirling Compressible Fluid Through a Convergent-Divergent Nozzle Without External Heat Transfer," Jet Propulsion Laboratory Space Programs Summary, No. 37-33, Vol. 4, pp. 133–141.

Massier, P. F., 1965b, "Swirling Flow of Argon Through an Axisymmetric Convergent-Divergent Nozzle," Jet Propulsion Space Programs Summary, No. 37-34, Vol. 4, pp. 149–157.

Massier, P. F., 1965c, "Thrust Comparisons of Swirling and Non-swirling Flows of Argon Through a Convergent-Divergent Nozzle as Determined From Wall Pressure Measurements," Jet Propulsion Laboratory Space Programs Summary, No. 37-35, Vol. 4, pp. 161–165.

Massier, P. F., Back, L. H., and Roschke, E. J., 1969, "Heat Transfer and Laminar Boundary Layer Distributions in an Internal Subsonic Gas Stream at Temperatures up to 13,900 R," ASME JOURNAL OF HEAT TRANSFER, Vol. 91, No. 1, pp. 83–90.

R. O. C. Guedes

M. N. Ozisik

Mechanical and Aerospace Engineering Department,
North Carolina State University,
Raleigh, NC 27695-7910

R. M. Cotta

Programa de Engenharia Mecanica,
COPPE/UFRJ,
Universidade Federal do Rio de Janeiro,
Rio de Janeiro, RJ 21945, Brazil

Conjugated Periodic Turbulent Forced Convection in a Parallel Plate Channel

The transient conjugated turbulent heat transfer with axial conduction in the wall and convection boundary conditions is solved with the generalized integral transform technique for the flow of a Newtonian fluid in a parallel-plate duct subjected to periodically varying inlet temperature. A lumped model that neglects transverse temperature gradients in the solid, but takes into account the axial heat conduction along the wall, is adopted. Accurate numerical results are presented for the fluid bulk temperature, wall temperature, and wall heat flux. The effects of the conjugation parameter, fluid-to-solid heat capacitance ratio, and Biot number on the behavior of the periodic responses are investigated.

Introduction

The study of the thermal response of the duct wall and the fluid temperatures to a periodic disturbance applied at the inlet in forced convection inside ducts is important in heat exchanger equipment theory and applications, such as start-up and shut-down processes, power surge, etc. Also of interest is the cyclic variation of temperature in regenerative heat exchangers where hot and cold fluids pass in succession. The main difficulty in the analysis of such problems is that the analysis usually leads to a complex eigenvalue problem for which no known solutions are available.

Only a limited amount of work is available in the literature on conjugate heat transfer problems with periodically varying inlet temperature. Sparrow and de Farias (1968) appear to be the first investigators who included the effect of wall conjugation in the problem of forced convection inside a parallel-plate channel for the case of slug flow. Cotta et al. (1987) utilized the solution methodology advanced by Cotta and Ozisik (1986) to solve the conjugated forced convection inside ducts for slug flow with periodically varying inlet temperature. Kakac et al. (1990), Li and Kakac (1991), and Guedes and Cotta (1991) also used the methodology described by Cotta and Ozisik (1986) to solve conjugated forced convection problems inside ducts for the case of convective boundary conditions. Kim and Ozisik (1990) solved such complex eigenvalue problems directly by using a shooting method along with the Runge-Kutta method in the complex domain.

In this work we examine the effects of wall conjugation including the axial conduction in the wall for turbulent flow inside ducts.

Mathematical Formulation

We consider turbulent forced convection of a Newtonian, constant property, hydrodynamically developed but thermally developing fluid flowing inside a parallel-plate channel. The inlet temperature is assumed to vary periodically in time. We seek the thermal response of the system to such periodic disturbances after initial transients have died out. The outer surface of the duct is subjected to convection with an environment at a constant temperature T_∞. Figure 1 illustrates the geometry and coordinate system. The axial heat conduction within the duct walls is considered in the analysis. Neglecting free convection, viscous dissipation, and axial conduction along the fluid, the mathematical formulation of this transient conjugated problem in dimensionless form is given by:

Solid Region:

$$\frac{\partial^2\Theta_s(R, Z, \tau)}{\partial R^2}+\frac{16}{(C\,\mathrm{Pe})^2}\frac{\partial^2\Theta_s(R, Z, \tau)}{\partial Z^2}=\alpha_{fs}\frac{\partial\Theta_s(R, Z, \tau)}{\partial\tau},$$

$$\text{in } 1<R<\delta,\ 0<Z<L,\ \tau>0 \qquad (1.a)$$

$$\frac{\partial\Theta_s(R, 0, \tau)}{\partial Z}=0,\quad 1\le R\le\delta,\ \tau>0 \qquad (1.b)$$

$$\frac{\partial\Theta_s(R, L, \tau)}{\partial Z}=0,\quad 1\le R\le\delta,\ \tau>0 \qquad (1.c)$$

$$\frac{\partial\Theta_s(\delta, Z, \tau)}{\partial R}+\overline{\mathrm{Bi}}\,\Theta_s(\delta, Z, \tau)=0,\quad 0<Z<L,\ \tau>0 \qquad (1.d)$$

Fluid Region:

$$\frac{\partial\Theta_f(R, Z, \tau)}{\partial\tau}+W(R)\frac{\partial\Theta_f(R, Z, \tau)}{\partial Z}=$$

$$\frac{\partial}{\partial R}\left(\epsilon(R)\frac{\partial\Theta_f(R, Z, \tau)}{\partial R}\right)\ \text{in } 0<R<1,\ Z>0,\ \tau>0 \qquad (2.a)$$

$$\Theta_f(R, 0, \tau)=\exp(i\Omega\tau),\quad 0\le R\le 1,\ \tau>0 \qquad (2.b)$$

$$\frac{\partial\Theta_f(0, Z, \tau)}{\partial R}=0,\quad Z>0,\ \tau>0 \qquad (2.c)$$

Solid–Liquid Interface:

$$\Theta_f(1, Z, \tau)=\Theta_s(1, Z, \tau) \qquad (3.a)$$

$$k_{fs}\frac{\partial\Theta_f(1, Z, \tau)}{\partial R}=\frac{\partial\Theta_s(1, Z, \tau)}{\partial R} \qquad (3.b)$$

where the various dimensionless quantities are defined in the nomenclature. Here, there is no need for an initial condition since we are interested in the periodic solution of the problem.

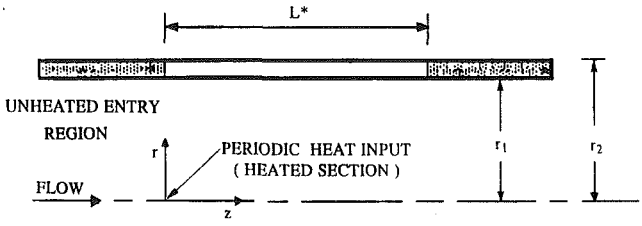

Fig. 1 Geometry and coordinate system

Contributed by the Heat Transfer Division and presented at the ASME National Heat Transfer Conference, San Diego, California, August 9–12, 1992. Manuscript received by the Heat Transfer Division May 1992; revision received May 1993. Keywords: Conjugate Heat Transfer, Heat Exchangers. Associate Technical Editor: R. J. Simoneau.

The models used for turbulent velocity distribution and eddy diffusivity are the same as those described by Kim and Ozisik (1990).

Since the analytical solution of the problem defined by Eqs. (1)-(3) is quite involved, we consider radial lumping of the wall Eq. (1.*a*), as follows: Equation (1.*a*) is operated on by the operator

$$\frac{1}{\delta-1}\int_1^{\delta} dR \tag{4}$$

to yield

$$\frac{1}{\delta-1}\left(\frac{\partial\Theta_s(\delta, Z, \tau)}{\partial R}-\frac{\partial\Theta_s(1, Z, \tau)}{\partial R}\right)+\frac{16}{(C\,\mathrm{Pe})^2}\frac{\partial^2\Theta_{sm}(Z, \tau)}{\partial Z^2}=\alpha_{fs}\frac{\partial\Theta_{sm}(Z, \tau)}{\partial\tau} \tag{5}$$

and the average wall temperature is defined as

$$\Theta_{sm}(Z, \tau)=\frac{1}{\partial-1}\int_1^{\delta}\Theta_s(R, Z, \tau)dR \tag{6}$$

The derivative terms appearing inside the bracket in Eq. (5) are eliminated by utilizing the boundary conditions (1.*d*) and (3.*b*) to yield:

$$\frac{1}{\delta-1}\left(-\overline{\mathrm{Bi}}\,\Theta_s(\delta, Z, \tau)-k_{fs}\frac{\partial\Theta_f(1, Z, \tau)}{\partial R}\right)+\frac{16}{(C\,\mathrm{Pe})^2}\frac{\partial^2\Theta_{sm}(Z, \tau)}{\partial Z^2}=\alpha_{fs}\frac{\partial\Theta_{sm}(Z, \tau)}{\partial\tau} \tag{7}$$

Assuming that temperature changes across the wall thickness are relatively small, we invoke the thin wall approximation:

$$\Theta_s(1, Z, \tau)\approx\Theta_s(\delta, Z, \tau)\approx\Theta_{sm}(Z, \tau) \tag{8}$$

then, introducing Eqs. (8) and (3.*a*) into Eq. (7) we obtain

$$\beta\frac{\partial^2\Theta_f(1, Z, \tau)}{\partial Z^2}=\frac{\partial\Theta_f(1, Z, \tau)}{\partial R}+\mathrm{Bi}\,\Theta_f(1, Z, \tau)+\frac{1}{a^*}\frac{\partial\Theta_f(1, Z, \tau)}{\partial\tau} \tag{9.*a*}$$

where

$$\mathrm{Bi}=\frac{\overline{\mathrm{Bi}}}{k_{fs}},\quad \beta=\frac{16(\delta-1)}{(C\,\mathrm{Pe})^2 k_{fs}} \tag{9.*b*,*c*}$$

$$a^*=\frac{k_{fs}}{\alpha_{fs}(\delta-1)}\equiv\frac{(\rho C_p)f}{(\rho C_p)_s(\delta-1)} \tag{9.*d*}$$

Thus, the original heat conduction Eq. (1.*a*) for the wall is transformed into a boundary condition given by Eq. (9.*a*) for the fluid energy Eq. (2.*a*) at $R=1$. Furthermore, the conjugation parameter, β, incorporates the effects of the three parameters that govern the complete conjugated problem, namely, aspect ratio δ, Peclet number Pe, and thermal conductivity ratio k_{fs}. The limiting case of $\beta\to 0$ represents negligible axial conduction in the wall, while the parameter a^* represents the fluid-to-solid thermal capacitance ratio.

Quasi-Steady-State Formulation

We assume a periodic solution in the form

$$\Theta_f(R, Z, \tau)=\tilde{\Theta}(R, Z)\exp(i\Omega\tau) \tag{10}$$

where the space-dependent function $\tilde{\theta}(R, Z)$ is yet to be determined. Since we are interested in the quasi-steady response (i.e., after the initial transients have passed), the problem for the determination of the function $\tilde{\theta}(R, Z)$ is obtained by introducing Eq.(10) into Eqs. (2), to yield

$$W(R)\frac{\partial\tilde{\Theta}(R, Z)}{\partial Z}=\frac{\partial}{\partial R}\left(\epsilon(R)\frac{\partial\tilde{\Theta}(R, Z)}{\partial R}\right)-i\Omega\tilde{\Theta}(R, Z),\quad \text{in } 0<R<1,\ Z>0 \tag{11.*a*}$$

$$\tilde{\Theta}(R, 0)=1,\quad 0\le R\le 1 \tag{11.*b*}$$

$$\frac{\partial\tilde{\Theta}(0, Z)}{\partial R}=0,\quad Z>0 \tag{11.*c*}$$

and the boundary condition at $R=1$ needed for this problem is obtained by introducing Eq. (10) into Eq. (9.*a*), to give

Nomenclature

a^* = thermal capacitance ratio $=(\rho C_p)_f/(\rho C_p)_s$
Bi = fluid Biot number $=h_\infty r_1/k_f$
$\overline{\mathrm{Bi}}$ = wall Biot number $=h_\infty r_1/k_s$
C = maximum to mean velocity ratio $=u_{\max}/\bar{u}$
C_p = specific heat
D_e = equivalent diameter $=4r_1$
h_∞ = ambient heat transfer coefficient
i = imaginary number $=\sqrt{-1}$
k_s, k_f = solid and fluid thermal conductivity
k_{fs} = thermal conductivity ratio $=k_f/k_s$
L^* = length, dimensional
L = length, dimensionless $=16L^*\alpha_f/C\bar{u}D_e^2$
Pe = Peclet number $=\bar{u}D_e/\alpha_f$
Pr = Prandtl number $=\nu/\alpha_f$
Re = Reynolds number $=\bar{u}D_e/\nu$
r = transverse coordinate, dimensional
r_1, r_2 = distance of the inner and outer surfaces of the wall from the centerline, respectively, dimensional
R = transverse coordinate $=r/r_1$
t = time variable
$T_s(r, z, t)$ = solid temperature
$T_f(r, z, t)$ = fluid temperature
T_∞ = ambient temperature
$\bar{u}$, $u_{\max}$ = average and maximum flow velocity
$u(r)$ = velocity distribution, dimensional
$W(R)$ = velocity distribution $=u(r)/u_{\max}$
z = axial coordinate, dimensional
Z = axial coordinate, dimensionless $=16z\alpha_f/C\bar{u}D_e^2$
α_f, α_s = fluid and solid thermal diffusivity
α_{fs} = thermal diffusivity ratio $=\alpha_f/\alpha_s$
β = conjugation parameter, Eq. (9.*c*)
δ = aspect ratio $=r_2/r_1$
ΔT_c = inlet temperature amplitude at centerline
$\epsilon(R)$ = dimensionless diffusivity $=1+\epsilon_h/\alpha_f$
ϵ_h = eddy diffusivity of heat
$\Theta(R, Z, \tau)$ = $(T(R, Z, \tau)-T_\infty)/\Delta T_c$
$\tilde{\Theta}(R, Z)$ = quasi-steady dimensionless temperature, Eq. (10)
μ_i = eigenvalues of problem (12)
ν = kinematic viscosity
τ = dimensionless time $=\alpha_f t/r_1^2$
$\Psi(\mu_i, R)$ = eigenfunctions of problem (12)
ω = inlet frequency, dimensional
Ω = inlet frequency, dimensionless $=\omega r_1^2/\alpha_f$

$$\frac{\partial\tilde{\Theta}(1, Z)}{\partial R}+\left(\mathrm{Bi}+\frac{i\Omega}{a^*}\right)\tilde{\Theta}(1, Z)=\beta\frac{\partial^2\tilde{\Theta}(1, Z)}{\partial Z^2} \quad (11.d)$$

Summarizing, the original problem defined by Eqs. (1), (2) and (3), is now transformed to the solution of a periodic problem defined by Eqs. (11.*a*, *b*, *c*, and *d*).

An attempt to solve the complex problem (11) analytically would lead to the solution of a complex eigenvalue problem. Thus, it would strongly depend on the evaluation of the complex eigenvalues and complex-valued eigenfunctions of the corresponding nonclassical. Strum–Liouville problem in the complex domain, for which no known solution is available. To alleviate such a difficulty, we follow the ideas in the generalized integral transform technique by considering the following auxiliary problem, which is related to the solution of the classical steady-state Graetz problem:

$$\frac{d}{dR}\left(\epsilon(R)\frac{d\Psi(\mu_i, R)}{dR}\right)+\mu_i^2W(R)\Psi(\mu_i, R)=0 \quad \text{in } 0<R<1 \quad (12.a)$$

$$\frac{d\Psi(\mu_i, R)}{dR}=0, \quad R=0 \quad (12.b)$$

$$\frac{d\Psi(\mu_i, R)}{dR}+\mathrm{Bi}\,\Psi(\mu_i, R)=0, \quad R=1 \quad (12.c)$$

Utilizing the eigenfunctions of this system, we define the following integral transform pair:

Inversion:

$$\tilde{\Theta}(R, Z)=\sum_{i=1}^{\infty}\frac{\Psi(\mu_i, R)}{N_i^{1/2}}\bar{\tilde{\Theta}}_i(Z) \quad (13.a)$$

Transform:

$$\bar{\tilde{\Theta}}_i(Z)=\int_0^1 W(R)\frac{\Psi(\mu_i, R)}{N_i^{1/2}}\tilde{\Theta}(R, Z)dR \quad (13.b)$$

where the normalization integral is given by:

$$N_i=\int_0^1 W(R)\Psi^2(\mu_i, R)dR \quad (13.c)$$

Equation (11.*a*) is now operated on by the operator $\int_0^1\frac{\Psi(\mu_i, R)}{N_i^{1/2}}dR$ to obtain

$$\frac{d\bar{\tilde{\Theta}}_i(Z)}{dZ}+\mu_i^2\bar{\tilde{\Theta}}_i(Z)+i\Omega\sum_{j=1}^{\infty}A_{ij}^*\bar{\tilde{\Theta}}_j(Z)=\frac{1}{N_i^{1/2}}\left(\Psi(\mu_i, 1)\frac{\partial\tilde{\Theta}(1, Z)}{\partial R}-\tilde{\Theta}(1, Z)\frac{d\Psi(\mu_i, 1)}{dR}\right) \quad (14)$$

where

$$A_{ij}^*=\frac{1}{N_i^{1/2}N_j^{1/2}}\int_0^1\Psi(\mu_i, R)\Psi(\mu_j, R)dR \quad (15)$$

The terms inside the bracket on the right-hand side of Eq. (14) are determined from manipulation of the boundary conditions, Eqs. (11.*d*) and (12.*c*), as

$$\Psi(\mu_i, 1)\frac{\partial\tilde{\Theta}(1, Z)}{\partial R}-\tilde{\Theta}(1, Z)\frac{d\Psi(\mu_i, 1)}{dR}=-\frac{i\Omega}{a^*}\Psi(\mu_i, 1)\tilde{\Theta}(1, Z)+\beta\Psi(\mu_i, 1)\frac{\partial^2\tilde{\Theta}(1, Z)}{\partial Z^2} \quad (16)$$

This result is introduced in Eq. (14) to give:

$$\frac{d\bar{\tilde{\Theta}}_i(Z)}{dZ}+\mu_i^2\bar{\tilde{\Theta}}_i(Z)+i\Omega\sum_{j=1}^{\infty}A_{ij}^*\bar{\tilde{\Theta}}_j(Z)\frac{\Psi(\mu_i, 1)}{N_i^{1/2}}\left(\beta\frac{\partial^2\tilde{\Theta}(1, Z)}{\partial Z^2}-\frac{i\Omega}{a^*}\tilde{\Theta}(1, Z)\right) \quad i=1, 2, \ldots \quad (17)$$

Equation (17) contains the two unknowns, $\bar{\tilde{\Theta}}_i(Z)$ and $\tilde{\Theta}(1, Z)$. An expression for the latter is developed by integrating Eq. (11.*a*) over the duct cross section to obtain:

$$\frac{d\Theta_{av}(Z)}{dZ}=C\frac{\partial\tilde{\Theta}(1, Z)}{\partial R}-Ci\Omega\int_0^1\tilde{\Theta}(R, Z)dR \quad (18)$$

where the fluid bulk temperature is defined as

$$\Theta_{av}(Z)=C\int_0^1 W(R)\tilde{\Theta}(R, Z)dR \quad (19)$$

Now, replacing $\tilde{\Theta}(R, Z)$ by its equivalent inversion formula (13.*a*), Eq. (19) becomes

$$\Theta_{av}(Z)=C\sum_{i=1}^{\infty}\bar{f}_i\bar{\tilde{\Theta}}_i(Z) \quad (20)$$

where we defined

$$\bar{f}_i=\int_0^1 W(R)\frac{\Psi(\mu_i, R)}{N_i^{1/2}}dR \quad (21)$$

Then, the term $\partial\tilde{\Theta}(1, Z)/\partial R$ in Eq. (18) is expressed as:

$$\frac{\partial\tilde{\Theta}(1, Z)}{\partial R}=\sum_{j=1}^{\infty}\bar{f}_j\frac{d\bar{\tilde{\Theta}}_j(Z)}{dZ}+i\Omega\sum_{j=1}^{\infty}\bar{h}_j\bar{\tilde{\Theta}}_j(Z) \quad (22)$$

where

$$\bar{h}_j=\frac{1}{N_j^{1/2}}\int_0^1\Psi(\mu_j, R)dR \quad (23)$$

By introducing Eq. (22) into (11.*d*) we obtain

$$\beta\frac{\partial^2\tilde{\Theta}_w(Z)}{\partial Z^2}=\left(\mathrm{Bi}+\frac{i\Omega}{a^*}\right)\tilde{\Theta}_w(Z)+\sum_{j=1}^{\infty}\bar{f}_j\frac{d\bar{\tilde{\Theta}}_j(Z)}{dZ}+i\Omega\sum_{j=1}^{\infty}\bar{h}_j\bar{\tilde{\Theta}}_j(Z) \quad (24)$$

where the notation $\tilde{\Theta}_w(Z)\equiv\tilde{\Theta}(1, Z)$ is introduced for simplicity.

The second derivative term in Eq. (17) is now eliminated by substituting Eq. (24) into Eq. (17), resulting in the following system of coupled differential equations:

$$\sum_{j=1}^{\infty}A_{ij}\frac{d\bar{\tilde{\Theta}}_j(Z)}{dZ}+\sum_{j=1}^{\infty}B_{ij}\bar{\tilde{\Theta}}_j(Z)=\frac{\Psi(\mu_i, 1)}{N_i^{1/2}}\mathrm{Bi}\tilde{\Theta}_w(Z) \quad (25)$$

After truncating the infinite sums to a sufficiently large order N, Eq. (25) is written in the matrix form as

$$\mathbf{A}\bar{\tilde{\Theta}}'(Z)+\mathbf{B}\bar{\tilde{\Theta}}(Z)=\mathbf{g}\tilde{\Theta}_w(Z) \quad (26.a)$$

where prime denotes derivative with respect to Z and various quantities are defined as

$$\mathbf{A}=\{A_{ij}\}, \quad A_{ij}=\delta_{ij}-\frac{\Psi(\mu_i, 1)}{N_i^{1/2}}\bar{f}_j \quad (26.b)$$

$$\mathbf{B}=\{B_{ij}\}, \quad B_{ij}=\delta_{ij}\mu_i^2+i\Omega\left(A_{ij}^*-\bar{h}_j\frac{\Psi(\mu_i, 1)}{N_i^{1/2}}\right) \quad (26.c)$$

$$\mathbf{g}=\{g_i\}^t, \quad g_i=\frac{\Psi(\mu_i, 1)}{N_i^{1/2}}\mathrm{Bi} \quad (26.d)$$

where δ_{ij} is the Kronecker delta and the superscript t denotes the transpose. The system (26.*a*) is now rearranged, in the form

$$\frac{d\bar{\tilde{\Theta}}_i(Z)}{dZ}+\sum_{j=1}^{N}E_{ij}\bar{\tilde{\Theta}}_j(Z)=S_i\tilde{\Theta}_w(Z) \quad (27.a)$$

where

$$\mathbf{E}=\{E_{ij}\}, \quad \mathbf{E}=\mathbf{A}^{-1}\mathbf{B} \quad (27.b)$$

$$\mathbf{S}\{S_i\}^t, \quad \mathbf{S}=\mathbf{A}^{-1}\mathbf{g} \quad (27.c)$$

Equation (27.*a*) is introduced into Eq. (24) in order to eliminate the first derivative $d\bar{\Theta}_i(Z)/dZ$, providing

$$\beta\frac{d^2\tilde{\Theta}_w(Z)}{dZ^2}-\left(\mathrm{Bi}+\sum_{k=1}^{N}\bar{f}_k S_k+\frac{i\Omega}{a^*}\right)\tilde{\Theta}_w(Z)= -\sum_{j=1}^{N}\left(\sum_{k=1}^{N}(\bar{f}_k E_{kj}-\delta_{jk}i\Omega\bar{h}_k)\right)\bar{\Theta}_j(Z) \quad (28)$$

Thus, Eqs. (27) and (28) are two coupled equations for the determination of the unknowns $\bar{\Theta}_i(Z)$ and $\tilde{\Theta}_w(Z)$. The boundary conditions for this coupled system of ordinary differential equations are given by:

$$\bar{\Theta}_i(0)=\bar{f}_i \quad i=1, 2, \ldots, N \quad (29.a)$$

$$\frac{d\bar{\Theta}_w(0)}{dZ}=0, \quad \frac{d\bar{\Theta}_w(L)}{dZ}=0 \quad (29.b,c)$$

Equations (27.*a*) and (28) are rewritten as a single first-order system as

$$\mathbf{y}'=\mathbf{P}\mathbf{y} \quad (30.a)$$

where prime denotes derivative with respect to Z, $\mathbf{P}$ is the coefficient matrix, and the vector $\mathbf{y}$ is defined as

$$\mathbf{y}=\{\bar{\Theta}_1(Z), \ldots, \tilde{\Theta}_N(Z), \bar{\Theta}_w(Z), \bar{\Theta}_w'(Z)\}' \quad (30.b)$$

The $(N+2)\times(N+2)$ elements p_{ij} of matrix $\mathbf{P}$ are given by:

Elements	Range of i	Range of j
$-E_{ij}Z$	$i\le N$	$j\le N$
S_i	$i\le N$	$j=N+1$
0	$i\le N$	$j=N+2$
$\delta_{j,N+2}$	$i=N+1$	$j\le N+2$
$-\frac{1}{\beta}\left(\sum_{k=1}^{N}(\bar{f}_k E_{kj}-\delta_{jk}i\Omega\bar{h}_k)\right)$	$i=N+2$	$j\le N$
$\frac{1}{\beta}\left(Bi+\sum_{k=1}^{N}\bar{f}_k S_k+\frac{i\Omega}{a^*}\right)$	$i=N+2$	$j=N+1$
0	$i=N+2$	$j=N+2$

Equation (30.*a*) provides a first-order system for the solution vector $\mathbf{y}(Z)$. The eigenvalues λ and eigenvectors ξ of matrix $\mathbf{P}$ are obtained from the following algebraic problem:

$$(\mathbf{P}-\lambda I)\xi=0 \quad (31)$$

The solution vector is then constructed as

$$\mathbf{y}(Z)=\sum_{j=1}^{N+2}D_j\xi^{(j)}\exp(\lambda_j Z) \quad (32)$$

where the constants D_j are determined by constraining the solution (32) to satisfy the boundary conditions (29.*a*, *b*, *c*) resulting in the following linear system of N complex algebraic equations:

$$\sum_{j=1}^{N+2}D_j\xi_i^{(j)}=\bar{f}_i \quad i=1, 2, \ldots, N \quad (33.a)$$

$$\sum_{j=1}^{N+2}D_j\lambda_j\xi_{N+1}^{(j)}=0 \quad (33.b)$$

$$\sum_{j=1}^{N+2}D_j\lambda_j\xi_{N+1}^{(j)}\exp(\lambda jL)=0 \quad (33.c)$$

Once the vector of transforms, $\mathbf{y}(Z)$, is determined, the inversion formula, Eq. (13.*a*), is applied to construct the solution for the original fluid temperature $\tilde{\Theta}(R, Z)$; the lumped wall temperature, $\tilde{\Theta}_w(Z)$, is obtained directly from the $(N+1)$th element of the solution vector, $\mathbf{y}(Z)$.

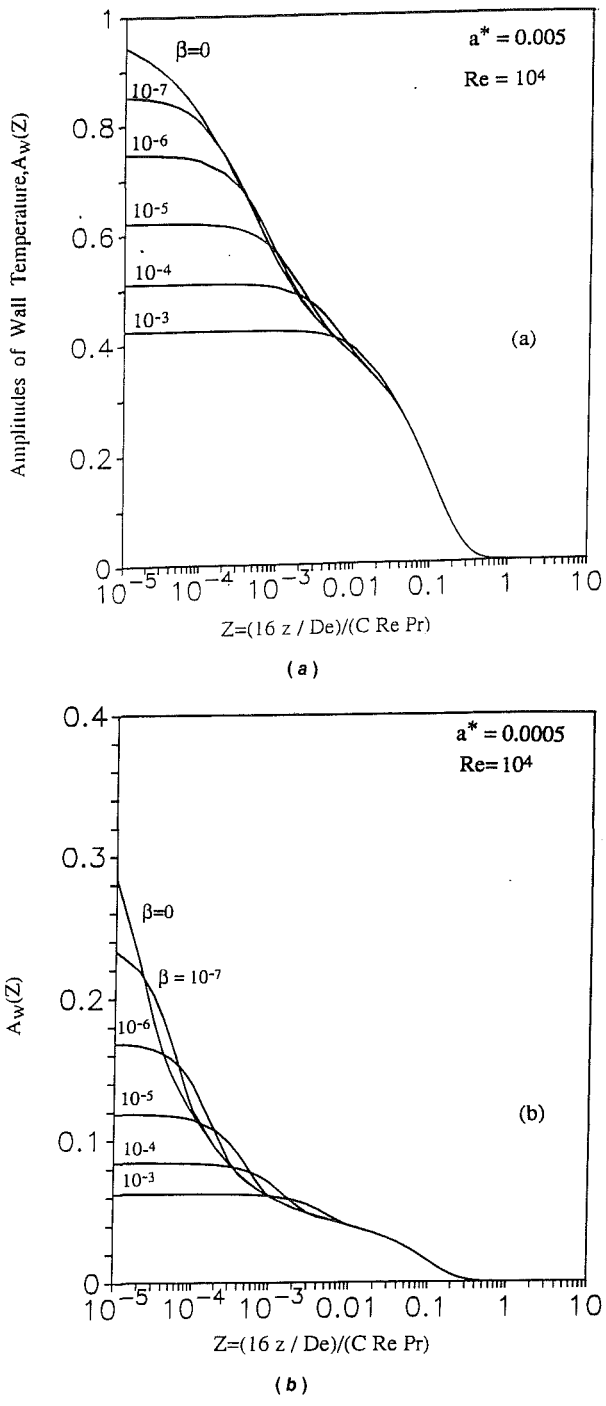

Fig. 2 Effects of the conjugation parameter, β, on the amplitude of wall temperature: (*a*) for $a^*=0.005$ and $\mathrm{Re}=1\times10^4$, (*v*) for $a^*=0.0005$ and $\mathrm{Re}=1\times10^4$

The wall and fluid bulk temperatures and wall heat flux are presented in polar form in terms of amplitudes and phase lags with respect to the inlet condition, in the form:

$$\Theta_w(Z)=A_w(Z)\exp(-i\phi_w(Z)) \quad (34)$$

where

$$A_w(Z)=\{[\mathrm{Re}(\Theta_w(Z))]^2+[Im(\Theta_w(Z))]^2\}^{1/2} \quad (35)$$

$$\phi_w(Z)=\tan^{-1}\left(\frac{Im(\Theta_w(Z))}{\mathrm{Re}(\Theta_w(Z))}\right) \quad (36)$$

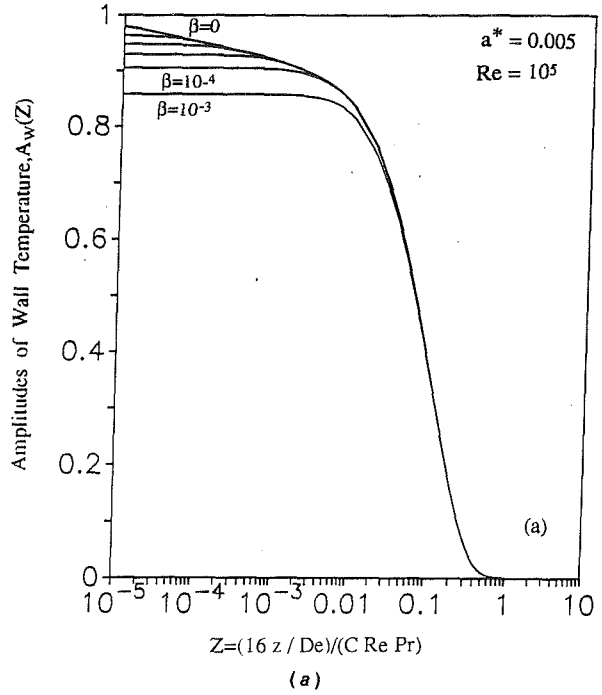

(a)

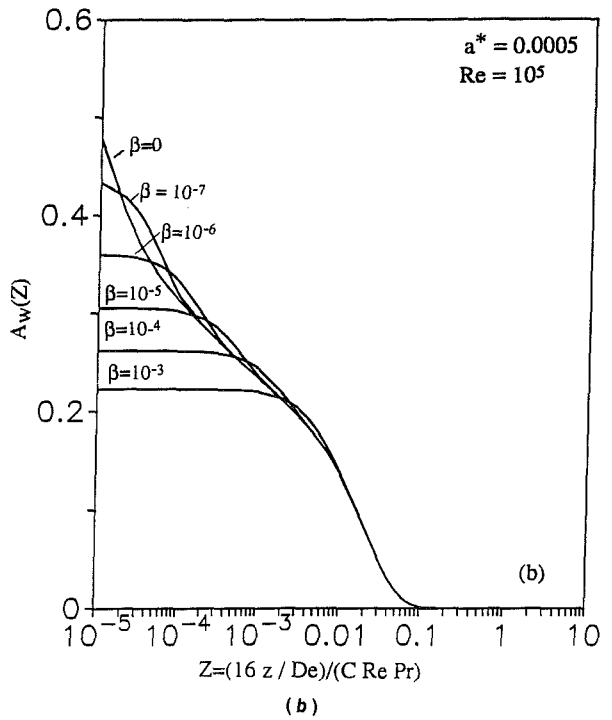

(b)

Fig. 3 Effects of the conjugation parameter, β, on the amplitude of wall temperature: (a) for $a^* = 0.005$ and $Re = 1 \times 10^5$, (b) for $a^* = 0.0005$ and $Re = 1 \times 10^5$

Results and Discussion

Based on the preceding analysis, we now present some typical results for the dimensionless wall temperature, bulk temperature, and wall heat flux. The complete solution is obtained from Eq. (32) by using the IMSL subroutines package (1987) to handle the complex matrix eigenvalue problem (31) and the complex linear system of algebraic Eqs. (33). The eigenvalues, eigenfunctions, and norms of the Strum–Liouville problem (12) are automatically and accurately computed by the sign-count method (Mikhailov and Ozisik, 1984).

The infinite system, truncated at 60 terms, proved to be more than sufficient to insure an accuracy of four significant digits everywhere in the region. For regions sufficiently away from the inlet only a few terms were necessary.

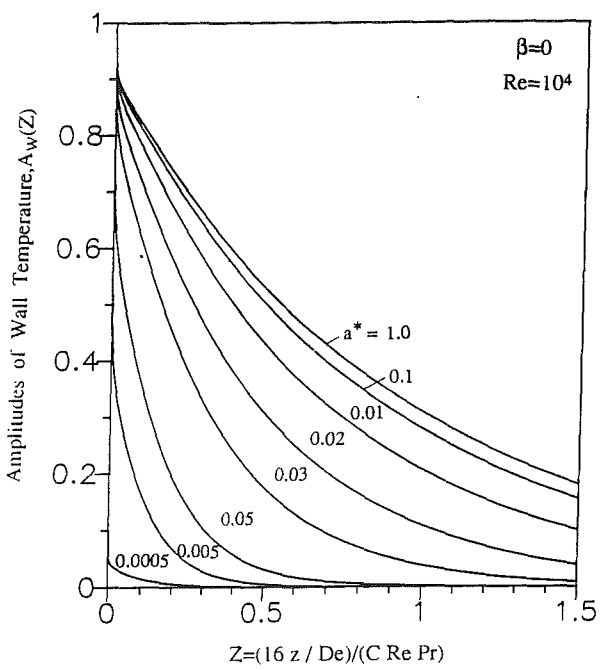

Fig. 4 Effects of fluid-to-wall thermal capacitance ratio, a^*, on the amplitude of wall temperature

For computational purposes, a set of Reynolds numbers $Re = 1 \times 10^4$, 5×10^4, and 1×10^5 is considered and calculations are performed for different values of the parameters a^*, β, and Bi for $Pr = 0.72$. To illustrate the effects of axial heat conduction in the wall on the amplitude and the phase lag for the fluid and wall temperatures, the value of the dimensionless frequency of inlet oscillations was fixed at $\Omega = 0.1$.

As pointed out by Sparrow and de Farias (1968), when the fluid is a gas and the wall is a metal, a^* is much less than unity, i.e., of the order of $10^{-3} \sim 10^{-4}$. For example, for regenerative heat exchangers with sheets of metal 0.018 in. thick and an extremely close spacing of 0.045 in. between the plates, a^* would be roughly 5×10^{-4} (Sparrow and de Farias, 1968; Gram and Kessler, 1966). Also, for such a situation, the values of the conjugation parameter β would range from $\beta = 0$ to $\beta = 10^{-3}$.

Figures 2(*a*) and 2(*b*) show the amplitudes of the wall temperature for $a^* = 5 \times 10^{-3}$ and $a^* = 5 \times 10^{-4}$ for different values of the conjugation parameter by fixing $Re = 1 \times 10^4$ and $Bi = 1$. For the smaller value of a^* (i.e., 5×10^{-4}), oscillations in fluid temperature are damped within a short distance from the duct inlet because of the larger thermal capacitances of the wall, thus markedly reducing the wall temperature oscillation. For the larger value of a^* (i.e., 5×10^{-3}), the thermal wave penetrates farther downstream due to the smaller thermal capacitance of the wall and, consequently, requires a longer length for the same amount of heat to be stored at the wall. The curves for different β represent the effects of the wall axial conduction. With increasing β, the amplitudes of the wall temperature are flattened due to the improved heat diffusion along the wall, especially in the region very close to the inlet where the thermal gradients are more accentuated.

Figures 3(*a*) and 3(*b*) show the same case as in Fig. 2 but for $Re = 1 \times 10^5$. As expected, the amplitude decays slower along the channel as the Reynolds number increases. Also, the horizontal portion of the curves for different values of β come close together as the Reynolds number is increased from 10^4 to 10^5.

Figure 4 presents the effects of the parameter a^* on the amplitude of the wall temperature for the case of negligible

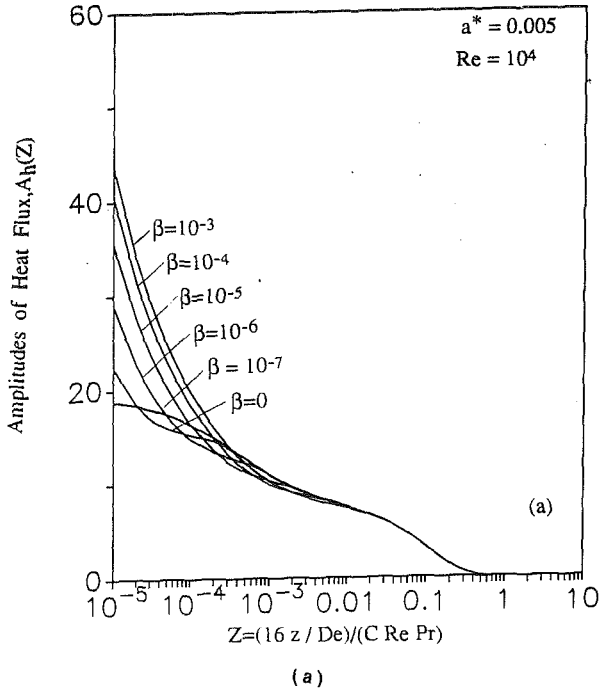

(a)

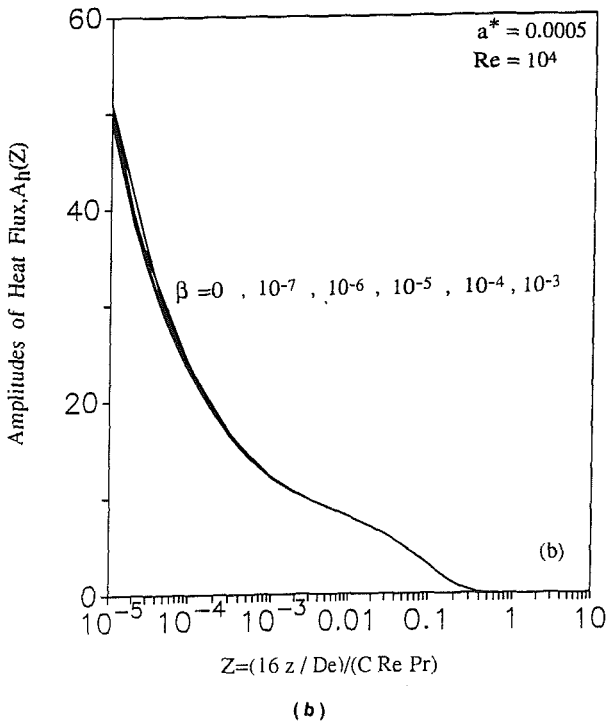

(b)

Fig. 5 Effects of the conjugation parameter, β, on the amplitude of heat flux: (*a*) for $a^* = 0.005$ and $Re = 1 \times 10^4$, (*b*) for $a^* = 0.0005$ and $Re = 1 \times 10^4$

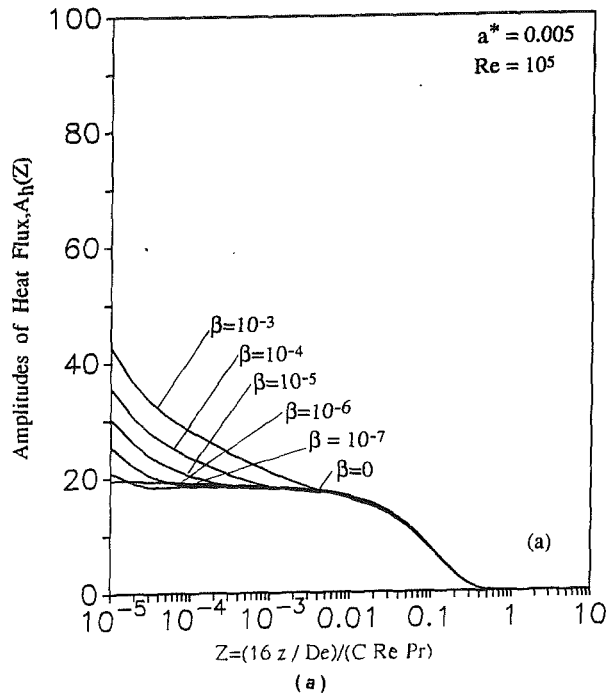

(a)

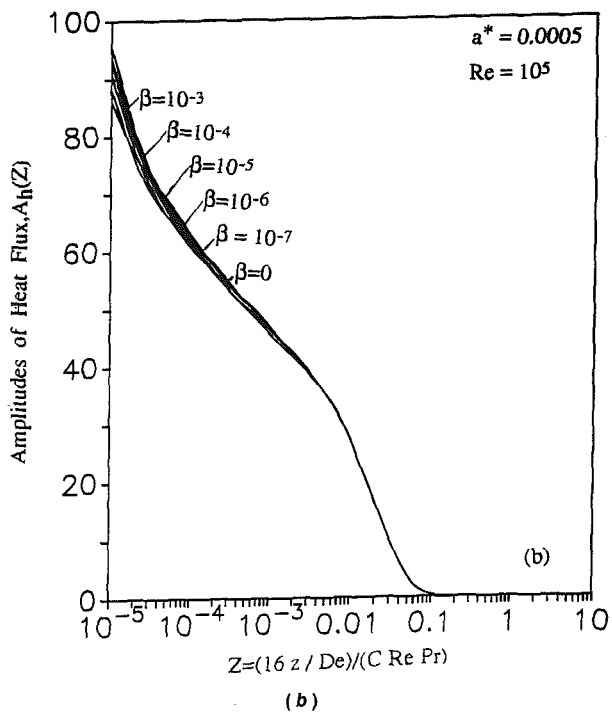

(b)

Fig. 6 Effects of the conjugation parameter, β, on the amplitude of heat flux: (*a*) for $a^* = 0.005$ and $Re = 1 \times 10^5$, (*b*) for $a^* = 0.0005$ and $Re = 1 \times 10^5$

wall axial conduction (i.e., $\beta = 0$). The wall amplitude decays faster as the value of a^* decreases. In the range of Reynolds number considered here, β has little effect on the amplitude of the fluid bulk temperature. The effect of a^* on the amplitude of fluid bulk temperature follows similar trends as of the wall temperature amplitude shown in Fig. 4, except the curves are much closer.

Similar trends are observed with higher Biot number ($Bi = 10$), but results are not presented here due to space limitations. Increasing the Biot number decreases the wall amplitude over the range of β considered here, since the external thermal resistance becomes smaller.

Figures 5(*a*) and 5(*b*) show the effects of the parameters a^* and β on the amplitudes of the dimensionless heat flux at the fluid-wall interface for $Re = 1 \times 10^4$. With the smaller value of a^* (Fig. 5*b*), the heat flux amplitudes are larger, since the radial temperature gradients are more pronounced, due to the significant attenuation in the wall temperature, especially for a short distance from the inlet. On the other hand, with the larger a^* (Fig. 5*a*), the axial conduction along the wall increases the heat flux amplitude, as shown by the curves for different β. The effects are more pronounced near the inlet and negligible for smaller values of a^* (Fig. 5*b*).

Figures 6(*a*) and 6(*b*) show the effect of a^* for the same cases shown in Figs. 4(*a*) and 4(*b*) except for $Re = 1 \times 10^5$. As expected, the amplitudes are larger for this case than for the

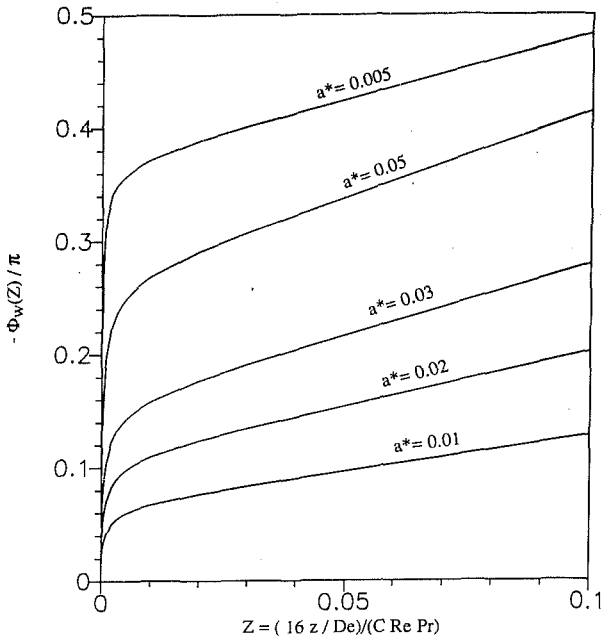

Fig. 7(*a*) Effects of fluid-to-wall thermal capacitance ratio, a^*, on the phase lags of wall temperature for Re = 1 x 10^4 and Bi = 1

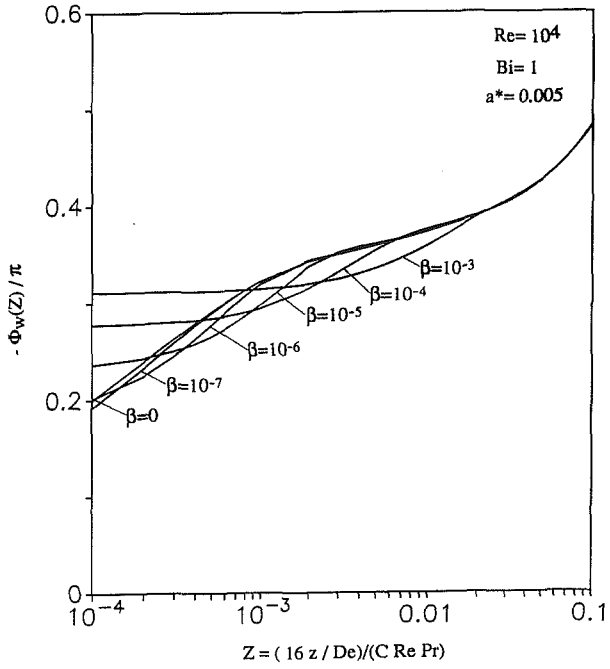

Fig. 7(*b*) Effects of the conjugation parameter, β, on the phase lags of wall temperature for Re = 1 x 10^4 and Bi = 1

previous one. The curves for different β are closer to each other and therefore the effect of wall axial conduction is less important.

Figures 7(*a*) and 7(*b*) show the effects of the parameters a^* and β on the phase lags of the dimensionless wall temperature distribution. As a^* decreases, the heat storage at the wall increases, delaying the information sensed at each axial location downstream with respect to the inlet disturbance, carried by the thermal wave. Consequently, the phase lag increases. For regions close to the inlet, the wall axial heat conduction effect predominates and tends to decrease the phase lag, advancing the information sensed by the downstream positions.

The present methodology can be used in the prediction of temperature and heat flux distributions inside the channel of a thin-walled heat exchanger equipment and to evaluate its unsteady performance, especially in the thermal entrance region.

Conclusions

A methodology is presented for solving conjugated turbulent forced convection inside a parallel-plate channel with periodically varying inlet temperature and convective boundary conditions including the effects of axial conduction in the wall. At a fixed frequency $\Omega = 0.1$ considered here, the effects of the wall axial conduction are more pronounced at lower Reynolds number. The effects of the heat capacitance ratio are more pronounced at small Biot number. The inlet temperature oscillation decays more slowly along the duct for the higher Reynolds number. For systems of gases flowing inside metal walls, the effects of conjugation cannot be neglected in regions close to the inlet.

Acknowledgments

The authors acknowledge the North Carolina Supercomputing Center for use of the Cray Y-MP computer. R. O. C. Guedes wishes to acknowledge the financial support provided by CNPq from Brazil.

References

Cotta, R. M., and Ozisik, M. N., 1986, "Laminar Forced Convection Inside Ducts With Periodic Variation of Inlet Temperature," *International Journal of Heat and Mass Transfer*, Vol. 29, pp. 1495–1501.

Cotta, R. M., Mikhailov, M. D., and Ozisik, M. N., 1987, "Transient Conjugated Forced Convection in Ducts With Periodically Varying Inlet Temperature," *International Journal of Heat and Mass Transfer*, Vol. 30, pp. 2073–2082.

Guedes, R. O. C., and Cotta, R. M., 1991, "Periodic Laminar Forced Convection Within Ducts Including Wall Heat Conduction Effects," *International Journal of Engineering Science*, Vol. 29, pp. 535–547.

Gram, A. J., and Kessler, G. W., 1966, "New Regenerative Air Heater," *Mechanical Engineering*, Vol. 88, pp. 45–47.

IMSL Library, 1987, *Edition 7*, GNB Building, 7500 Ballaire Blvd., Houston, TX.

Kakac, S., Li, W., and Cotta, R. M., 1990, "Unsteady Laminar Forced Convection in Ducts With Periodic Variation of Inlet Temperature," ASME JOURNAL OF HEAT TRANSFER, Vol. 112, pp. 913–920.

Kim, W. S., and Ozisik, M. N., 1989, "Turbulent Forced Convection Inside a Parallel-Plate Channel With Periodic Variation of Inlet Temperature," ASME JOURNAL OF HEAT TRANSFER, Vol. 111, pp. 882–888.

Kim, W. S., and Ozisik, M. N., 1990, "Conjugated Laminar Forced Convection in Ducts With Periodic Variation of Inlet Temperature," *International Journal of Heat and Fluid Flow*, Vol. 11, pp. 311–320.

Li, W., and Kakac, S., 1991, "Unsteady Thermal Entrance Heat Transfer in Laminar Flow With a Periodic Variation of Inlet Temperature," *International Journal of Heat and Mass Transfer*, Vol. 34, pp. 2581–2592.

Mikhailov, M. D., and Ozisik, M. N., 1984, *Unified Analysis and Solutions of Heat and Mass Diffusion*, Wiley, New York.

Sparrow, E. M., and de Farias, F. N., 1968, "Unsteady Heat Transfer in Ducts With Time Varying Inlet Temperature and Participating Walls," *International Journal of Heat and Mass Transfer*, Vol. 11, pp. 837–853.

A. Gopinath
Lecturer.

A. F. Mills
Professor.

Department of Mechanical, Aerospace, and Nuclear Engineering,
University of California at Los Angeles,
Los Angeles, CA 90024-1597

Convective Heat Transfer Due to Acoustic Streaming Across the Ends of a Kundt Tube

Convective heat transfer due to acoustic streaming across the ends of a tube supporting a standing sound wave is investigated. Analytical techniques are used along with the numerical solver PHOENICS for the solution of the complete elliptic form of the equations governing the steady transport due to the streaming motion. A parametric study of the effects of the controlling acoustic and geometric variables is conducted, and Nusselt number correlations are developed for air. The results obtained can be used in the thermal analysis of test cells for containerless processing of materials in space using acoustic levitation.

1 Introduction

The objective of this study is to investigate the steady momentum and heat transport rates due to acoustic streaming in an air-filled tube supporting an axial standing sound field. The work is motivated by a series of basic science experiments planned for a Space Shuttle flight, for which there is a need to design and control the thermal features of a suitable cell for the containerless processing of materials at near zero gravity. The objective of some of the experiments is to isolate and study, in the absence of buoyancy, the effects of thermocapillary-dominated phenomena on the structure and properties of metal alloys and glasses. The alloy samples (usually spheres) are acoustically levitated to avoid physical contact with the container walls and thereby reduce contamination and other related surface effects. The levitated samples are positioned in a furnace in order to obtain controlled heating/cooling conditions in an inert gas environment. The use of a sound field (versus a magnetic field) to levitate and position the samples is considered especially attractive, since it prevents directional effects from being introduced into the alloy properties. However, the required sound fields of the order of 150–175 dB at 1000–2000 Hz give rise to strong (steady) acoustic streaming flows around the samples and on the walls of the test cells. The associated convective heat transfer rates are instrumental in determining heating/cooling rates (as recognized, for example, by Rey et al., 1991), and hence the material structure and thermophysical properties of the alloys. A proper knowledge of the transport processes between the samples and the chamber walls is thus important to the successful design and execution of these experiments. An earlier paper by Gopinath and Mills (1993) dealt with the convective heat transfer rate from a levitated sample modeled as an isolated isothermal sphere. Here the focus will be on determining the steady heat convection due to streaming generated on the walls of the levitation chamber in the absence of any samples.

The acoustic levitation chamber is modeled as a Kundt tube carrying an axial plane standing sound wave and subject to a longitudinal temperature gradient. The end walls of the tube are treated as isothermal and the side wall is taken to be adiabatic. At first, the behavior of the steady streaming flow field in the Kundt tube is completely determined. This result is then used to examine the problem of convective heat transport across the isothermal ends of the Kundt tube. Only small temperature differences are considered, to allow the constant property assumption and thereby concentrate on obtaining a basic understanding of the physics of the transport processes involved. The solution technique used combines the method of matched asymptotic expansions and the numerical solution of nonlinear partial differential equations. The numerical fluid mechanics and heat transfer solver, PHOENICS, is employed for the purpose of conducting a parametric study of a wide range of acoustic and geometric parameters. Particular attention is given to the case (of interest) corresponding to large streaming Reynolds numbers, R_s, and the results for heat transfer in the air-filled tube are obtained in the form of correlations for the average Nusselt number, Nu.

2 The Kundt Tube Model and Governing Equations

A potential acoustic levitation chamber to the used in containerless processing has high-intensity acoustic drivers at one end and a high-temperature furnace at the other, and presents a difficult engineering system to simulate and understand. However, for the purposes of this study the levitation chamber can be quite simply and accurately modeled as an air-filled Kundt tube with noncompliant walls. The acoustic effects of the chamber are treated by considering the influence of a z axis longitudinal plane standing sound wave field in the tube, excited to near-resonant frequencies. Resonant effects and related shock formations are not dealt with here. Successful use of these simplifications has been made by Rudnick and Barmatz (1990) in a study of the oscillational instabilities of levitated samples. To model the thermal effects of the chamber, the observations of Trinh et al. (1986) are applied to treat the end walls of the Kundt tube as isothermal and the side wall as adiabatic. It must be emphasized that the interactions of the acoustic and thermal fields through the properties of the medium are neglected as a first approximation. The influence of a gravity field (if present) is initially ignored in an attempt to isolate and understand the heat transfer process due to streaming. The detailed reasons for the choice of such a model and its attendant limitations may be found elsewhere (Gopinath, 1992).

Fluid flows induced by sound fields are characterized by multiple length scales. For a tube supporting an axial plane standing sound wave with a velocity distribution of the form $U_\infty \cos(\omega\tau^*) \sin(2\pi z^*/\lambda)$, these length scales are the tube radius, r_0, the displacement amplitude of the fluid particle in the sound wave, $A = U_\infty/\omega$, the wavelength of the sound-wave, λ, the viscous diffusive thickness, $\delta \sim \sqrt{\nu/\omega}$, and the thermal diffusive thickness, $\delta_T \sim \sqrt{\alpha_T/\omega}$. Some important deductions can be made from a comparison of these primary length scales,

Contributed by the Heat Transfer Division for publication in the JOURNAL OF HEAT TRANSFER. Manuscript received by the Heat Transfer Division June 1992; revision received May 1993. Keywords: Enclosure Flows, Materials Processing and Manufacturing Processes, Microgravity Heat Transfer. Associate Technical Editor: R. J. Simoneau.

which in turn allow the governing equations to be presented in a considerably simplified form.

The most important condition is that the flow be treated as incompressible. This condition is based on the magnitude of the wave-slope parameter, $\alpha = Ak$ ($k = 2\pi/\lambda$ is the wave number). In this problem α is very small compared to unity, which ensures that the Mach number based on the velocity amplitude, U_∞/c, is small and allows compressibility effects (entering through relative density changes, which are conventionally related to high-speed effects) to be ignored. However, the above condition is sufficient to assume incompressibility only in steady flows. In unsteady flows, as present in this problem, an additional condition to be fulfilled is based on the assumption that the Kundt tube plays the role of a "narrow" acoustic wave-guide, this narrowness condition being $r_0 k \ll 1$ (Landau and Lifshitz, 1987, Section 80). This condition ensures that the extent of the flow region is small compared to the (radian) wavelength of the sound wave and hence allows the propagation of disturbances in the fluid to be treated as instantaneous. Actual values of this so-called wave aspect-ratio parameter, $r_0 k$, encountered in this study are of $O(1)$ and the implications of this discrepancy are discussed later in Section 3. For the tube length varied in integral multiples of half the wavelength ($L = n_z\lambda/2$) to satisfy the near-resonance condition required for levitation, the parameter $r_0 k$ is directly related to the aspect ratio (length/diameter), $\mathfrak{A}$, of the Kundt tube as,

$$\mathfrak{A} = \frac{\pi n_z}{2(r_0 k)} \tag{1}$$

where n_z is a positive integer representing the plane wave mode of the standing sound field, and is equal to the number of stable axial locations available for the positioning of the levitated sample.

The other parameter of importance is the frequency parameter, $N = r_0/\delta$, which is a measure of the extent of the penetration of the viscous diffusive effects of the oscillatory sound field on the scale of the tube radius. For small values of N, the retarding effects of the stationary walls spread across the tube cross section and yield the well-known parabolic velocity profile for the primary oscillatory flow. On the other hand, for the large values of N considered in this study, the fluid velocities change across sharp gradients in narrow Stokes boundary layers on the tube walls to attain the oscillatory values corresponding to the standing sound wave. When a temperature difference is present between the ends of the tube, addition of the thermal diffusive length scale, δ_T, introduces Pr as a corresponding dimensionless parameter.

The assumptions above establish the parameter range of interest, satisfy the conditions for solenoidality of the velocity field, and thereby render major simplifications to the governing equations. The equations are formulated in a rotationally symmetric cylindrical reference frame in (r, z) coordinates. The origin is chosen at the center of the cool (left) end of the tube containing the acoustic drivers. The equations of motion and energy are formulated in terms of the axisymmetric stream function and the fluid temperature in the tube. These equations are nondimensionalized by using the scales ω^{-1}, r_0, $\lambda/2\pi$ (the radian wavelength), U_∞, and $U_\infty r_0^2$ for the time, radial distance, axial distance, velocity, and stream function, respectively. With the temperature difference in the fluid, $T - T_C$, normalized with respect to the driving temperature difference, $T_H - T_C$, the governing equations are,

$$\frac{\partial}{\partial \tau}(E^2\psi) + \frac{\alpha}{r}\left[\frac{\partial(\psi, E^2\psi)}{\partial(r, z)} + \frac{2}{r}E^2\psi\frac{\partial\psi}{\partial z}\right] = \frac{1}{N^2}E^4\psi \tag{2}$$

$$\frac{\partial\phi}{\partial\tau} + \frac{\alpha}{r}\left[\frac{\partial(\psi, \phi)}{\partial(r, z)}\right] = \frac{1}{\mathrm{Pr}N^2}\Delta^2\phi \tag{3}$$

with boundary conditions

$$\phi = 0,\ \psi = 0,\ \frac{\partial\psi}{\partial z} = 0 \text{ at } z = 0 \tag{4}$$

$$\phi = 1,\ \psi = 0,\ \frac{\partial\psi}{\partial z} = 0 \text{ at } z = \pi n_z \tag{5}$$

$$\frac{\partial\phi}{\partial r} = 0,\ \psi = 0,\ \frac{\partial\psi}{\partial r} = 0 \text{ at } r = 1 \tag{6}$$

where the condition $\psi = 0$ has been used along the outer bound-

Nomenclature

A = displacement amplitude of the sound wave $= U_\infty/\omega$
$\mathfrak{A}$ = aspect ratio of Kundt tube $= L/2r_0$
c = speed of sound in the fluid $= \omega/k$
f = frequency of the sound field $= c/\lambda$
I_0 = reference sound intensity, $= 10^{-12}$ W/m^2
k = wave number $= 2\pi/\lambda$
L = length of the Kundt tube $= n_z\lambda/2$
n_z = plane wave mode of standing sound field
N = frequency parameter $= r_0/\delta$
Nu = average Nusselt number $= Q/Q_{\mathrm{ref}}$
Nu_0 = average Nusselt number for $r_0 k = 1$
Nu_r = reduced average Nusselt number $= (\mathrm{Nu} - 1)/(\mathrm{Nu}_0 - 1)$
Pr = Prandtl number
Q_C, Q_H = heat transfer rate through the cool and hot ends
Q = average heat transfer rate $= (Q_C + Q_H)/2$
Q_{ref} = reference conduction heat transfer rate
r = dimensionless radial coordinate $= r^*/r_0$
r_0 = radius of the Kundt tube
$\hat{r}_0$ = scaled radius of the Kundt tube $= r_0(r_0 k)$
R_s = *external* streaming Reynolds number $= U_\infty^2/\omega\nu$
$\mathfrak{R}_s$ = *internal* streaming Reynolds number $= R_s(r_0 k)^2$
SPL = sound pressure level (in decibels)
T = temperature of the fluid
T_C, T_H = temperature of the cool and hot ends of the Kundt tube
u_r, u_z = dimensionless radial and axial velocity components
U_∞ = velocity amplitude of the sound wave
z = dimensionless axial coordinate $= kz^*$
α = wave slope parameter $= Ak = U_\infty/c$
α_T = thermal diffusivity of the fluid
δ = Stokes layer thickness $= \sqrt{\nu/\omega}$
δ_T = thermal diffusive thickness $= \sqrt{\alpha_T/\omega}$
δ_Q, Δ_Q = numerical measures defined in Section 4
λ = wavelength of the sound field
ν = kinematic viscosity of the fluid
ρ = density of the fluid
τ = dimensionless time $= \omega\tau^*$
ϕ = dimensionless temperature difference $= (T - T_C)/(T_H - T_C)$
ψ = dimensionless stream function $= \psi^*/U_\infty r_0^2$
ω = angular frequency $= 2\pi f$
ω_0 = dimensionless angular frequency in Eq. (11)

Superscripts

* = dimensional quantities

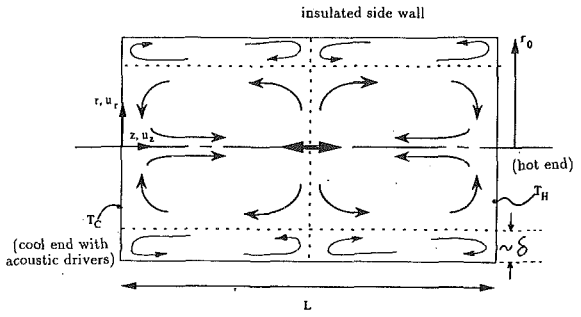

Fig. 1 The axisymmetric cylindrical coordinate system for the Kundt tube model. A schematic of the acoustic streaming motion in the inner and outer regions is shown for the fundamental mode ($n_z = 1$). The double arrow represents the direction of oscillation of the standing sound field. Proportions have been exaggerated for clarity.

ary together with the symmetry and finiteness conditions of the imposed standing sound wave along the centerline, $r = 0$. In the above equations $\phi = (T - T_C)/(T_H - T_C)$ and the operators are,

$$E^2 = E_r^2 + r_0^2 k^2 \frac{\partial^2}{\partial z^2} \text{ where } E_r^2 = r\frac{\partial}{\partial r}\left(\frac{1}{r}\frac{\partial}{\partial r}\right) \tag{7}$$

$$\nabla^2 = \nabla_r^2 + r_0^2 k^2 \frac{\partial^2}{\partial z^2} \text{ where } \nabla_r^2 = \frac{1}{r}\frac{\partial}{\partial r}\left(r\frac{\partial}{\partial r}\right) \tag{8}$$

The velocity components are defined as,

$$u_z = \frac{1}{r}\frac{\partial \psi}{\partial r} \text{ and } u_r = -\frac{r_0 k}{r}\frac{\partial \psi}{\partial z} \tag{9}$$

3 The Streaming Flow

It is appropriate at this stage to outline the solution technique and briefly examine the origin of the steady streaming terms. As mentioned earlier, this study is concerned with cases of $\alpha \ll 1$, $N \gg 1$ and $r_0 k \sim O(1)$. It is well known that for this parameter regime the governing equation of motion does not permit a uniformly valid solution in the entire domain, and thus the matched asymptotic technique must be used. This requires independent solutions to be developed in different regions of the domain in terms of variables appropriate to each region. These independent solutions are made to satisfy the boundary conditions pertinent to their respective domains and are also suitably matched in the zone of overlap. Similar methods are also used to determine the temperature distribution in the fluid. The focus here is on the steady transport due to acoustic streaming on the tube walls and a more detailed description of the origin and nature of this mechanism as relevant to this problem can be found in a recent study by Gopinath (1992). Here only the notable features are summarized to provide a proper perspective to the complete problem.

From Eq. (2) it is clear that in the limit of $\alpha \to 0$ the inertial terms become vanishingly small. The resulting linear equation can be solved to obtain an exact $O(1)$ solution, which satisfies all the boundary conditions including the $\sin z \cos \tau$ periodic variation of the impressed standing sound wave. However, the complete solution form involves an unwieldly representation in terms of integrals of modified Bessel functions, which has limited use in this study and hence is not dealt with here. It also follows that all subsequent corrections to this basic linear solution satisfy homogeneous boundary conditions. These corrections include contributions from the nonlinear inertial terms and result in the generation of higher, but weaker harmonics in the flow. In particular, when considering the $O(\alpha)$ correction to the stream function it becomes clear from Eq. (2) that the basic linear solution contributes to the forcing function via the nonlinear inertia terms. This gives rise to terms with a time dependence of the form $\sim \cos^2 \tau = (1/2)(1 + \cos 2\tau)$. Then, for this $O(\alpha)$ contribution to the stream function, a time-independent term is created in addition to the second harmonic. It is this dominant $O(\alpha)$ component of the steady flow, termed acoustic streaming, and its transport effects, which are of prime concern in this study. From the need to satisfy homogeneous boundary conditions, the steady streaming velocity grows from a value of zero on the tube walls, its distribution in the tube core being governed by the different flow parameters.

The source of this streaming motion can be traced to viscous Reynolds-like stresses in a narrow Stokes-layer region of dimensional thickness of $O(\delta)$ present on the walls. This narrow region is identified as the inner region in contrast to the outer region, which constitutes the remainder of the tube cross section. By a suitable transformation of variables it can be shown that Eqs. (2)–(9) can be applied to the inner region under the incompressible flow assumption, which is satisfied by the long-wavelength approximation condition, $\delta k = r_0 k/N \ll 1$, a condition that is independent of the dimensions of the Kundt tube. This assumption is a far less restrictive stipulation (than the one used for the outer region, namely $r_0 k \ll 1$) and is directly suited for the parameter range of interest in this study. The equation governing the steady motion in the inner region that arises in this process is very similar to the one solved by Stuart (1966, p. 675) for explaining the boundary layer structure of *external* steady streaming flows. The results of his analysis are applicable and after some minor modifications can be shown to predict a steady recirculatory flow pattern in the inner region, which is half-wavelength periodic (see Fig. 1). The details of the behavior are not included here, and it suffices to note that a dominant $O(\alpha)$ steady axial drift velocity component persists at the outer edge of this Stokes layer region. For the frequency parameter range of interest in this study ($N \sim O(10^3)$) the thickness of the inner Stokes layer region can be considered relatively negligible: Thus the steady drift velocity effectively plays the role of a slip velocity at the solid surface in driving the flow in the outer region, and is directed toward the velocity nodes of the impressed standing sound field (Lighthill, 1978, p. 416). A noteworthy feature of the steady drift velocity is that despite being generated by viscous Reynolds-like stresses, its magnitude of $\sim \alpha U_\infty = U_\infty^2/c$ is independent of the viscosity of the fluid. A Reynolds number defined on the basis of this velocity magnitude and a suitably scaled tube radius, $\hat{r}_0 = r_0(r_0 k)$ (scaled in anticipation of the outer flow formulation in Eq. (12)),

$$\Re_s = \alpha U_\infty \frac{\hat{r}_0}{\nu} = \frac{U_\infty^2}{\omega \nu}(r_0 k)^2 = \left[\frac{A}{\delta}(r_0 k)\right]^2 \tag{10}$$

is an *internal* streaming Reynolds number and plays a fundamental role in determining the nature of the steady transport in the outer region. This new measure, $\Re_s$, is not an independent parameter and can be written as $\Re_s = \alpha^2 N^2$. Having been expressed in this manner as the product of a large parameter (N^2) and a small parameter (α^2), the magnitude of $\Re_s$ is as yet undetermined. Also from the definition in Eq. (10) it follows that $\Re_s = R_s(r_0 k)^2$, where R_s is the well-known streaming Reynolds number, first identified by Stuart (1966) as the parameter that characterizes *external* steady streaming flows. Gopinath and Mills (1993) provide a relation for R_s in air in terms of the acoustic signal characteristics for a plane standing sound wave as,

$$\text{SPL (in dB)} = 10 \log_{10}(\omega_0 R_s) \text{ where } \omega_0 = \frac{\rho c \nu \omega}{2 I_0} \tag{11}$$

with I_0 being a reference intensity equal to 10^{-12} W/m^2. Typical values of the acoustic signal used in the levitation process range in SPL from 150 dB–175 dB with frequencies of 1 kHz–2 kHz from which the R_s values have been deduced to be of $O(10^2)$—$O(10^3)$.

For the associated heat transfer problem it can be shown

from Eq. (3) that the leading order temperature distribution is time independent, and that the transport of heat across the narrow inner layer is essentially diffusive for fluids with Prandtl number of $O(1)$. The resistance to heat transfer is negligible in this inner region and the fluid remains essentially isothermal *across* the inner Stokes layer. This does not provide any information on the driving temperature gradient in the bulk of the fluid and attention is now turned to the convective transport effects responsible for heat transfer in the outer region.

Based on the above deductions, it requires some manipulation (in a manner suggested by Riley, 1966) of the original form of the governing Eqs. (2)–(9) of *unsteady* transport, to arrive at the governing equations of *steady* transport in the outer region; details are omitted here for brevity and may be found from Gopinath (1992). It can be shown that the variations of the steady component of the $O(\alpha)$ contribution to the stream function, ψ_{1s}, and the $O(1)$ temperature, ϕ_0, are governed by,

$$\frac{1}{r}\left[\frac{\partial(\psi_{1s}, E^2\psi_{1s})}{\partial(r, z)}+\frac{2}{r}E^2\psi_{1s}\frac{\partial\psi_{1s}}{\partial z}\right]=\frac{1}{\mathcal{R}_s}E^4\psi_{1s} \tag{12}$$

$$\frac{1}{r}\left[\frac{\partial(\psi_{1s}, \phi_0)}{\partial(r, z)}\right]=\frac{1}{\mathrm{Pr}\mathcal{R}_s}\nabla^2\phi_0 \tag{13}$$

which can be recognized as the complete governing equations of motion and energy for steady viscous and laminar constant property flow in axisymmetric cylindrical geometry at a Reynolds number $\mathcal{R}_s$. The above equations must obey symmetry and finiteness conditions on the tube centerline, $r=0$, and should be made to satisfy matching conditions from the inner region (Landau and Lifshitz, 1987),

$$\left.\begin{aligned}\psi_{1s}&\rightarrow\frac{3}{8}(1-r)\sin(2z)\\ \partial\phi_0/\partial r&\rightarrow 0\end{aligned}\right\}\ \text{as}\ r\rightarrow 1 \tag{14}$$

along with the isothermal and no-slip velocity conditions on the end-walls. Due to their decoupled nature, once the flowfield is determined from Eq. (12), the temperature distribution can be ascertained from Eq. (13) for a given Prandtl number.

It should be noted that the validity of the governing equations in the above form is restricted to the narrow wave-guide limit, $r_0k\ll 1$, which makes it possible to incorporate the characteristics of the streaming flow in the outer region into a single controlling parameter, namely $\mathcal{R}_s$. However for values of $r_0k\sim O(1)$ as encountered in this study, the effects of r_0k and R_s need to be treated independently via a numerical solution of the complete elliptic form of the governing equations of motion and energy for the outer region, subject to the boundary conditions in Eq. (14) prescribed by matching with the inner region. Before pursuing the numerical solution some important deductions can be made (by making a comparison with the analysis of Eqs. (12)–(14) for the limiting parameter range $r_0k\ll 1$, $\mathcal{R}_s\ll 1$) regarding the symmetry and periodicity of the steady transport in the outer region. A comparison of this type is profitable, since by virtue of their confined nature, the underlying features of such internal flows remain essentially unchanged over a wide range of parameter values. The flow field that arises in this limiting case is well known as the reason for the formation of ridgelike dust deposits in simple Kundt tube experiments performed with a tuning fork, a classic example for which dates back to the study by Lord Rayleigh (1884). The flow is well known to have a cellular recirculatory pattern in the form of periodic pairs of counterrotating vortices lying between successive nodal planes. The steady drift is directed toward the nodal planes along the side wall and is balanced by a return flow toward the antinodes along the centerline. For the corresponding streaming flow pattern in plane-parallel wall geometry, reference may be made to a discussion by Landau and Lifshitz (1987, Section 80).

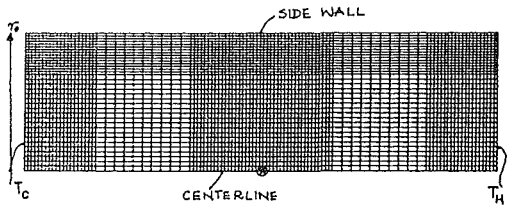

Fig. 2 The computational domain for the Kundt tube model used in PHOENICS

For the temperature field in the undisturbed state, the temperature profile is linear across the tube ends and the isotherms are simply circular planes normal to the tube axis. In the presence of the streaming motion, however, the fluid remains radially isothermal only at specific locations corresponding to the nodal/anti-nodal planes along which the flow is purely radial, whereas in the rest of the tube the conductions isotherms are "swept" in the direction of the steady flow as illustrated later in Section 5 (Fig. 6).

The features discussed above are essentially preserved for the parameter range of interest in this study too, although the magnitude of the velocity and the resulting gradients in the velocity and the temperature are larger for the stronger acoustic signals considered. It might be noted in passing that for the special case of $r_0k\ll 1$ and $\mathcal{R}_s\gg 1$, Eqs. (12)–(14) predict the presence of a second boundary layer structure on the side wall of the tube. However, this parameter regime is beyond the scope of this study and is left aside for future consideration. Treatment of the steady transport due to acoustic streaming of this kind (i.e., in enclosed geometries) has been restricted to the earlier studies of Haddon and Riley (1979, 1981) for a different class of problems: the two-dimensional fluid flow and heat transfer in the annulus between two concentric circular cylinders, when the inner cylinder performs small amplitude harmonic oscillations.

4 PHOENICS and the Numerical Method

PHOENICS is a general purpose computer program (developed by CHAM Ltd.) for the numerical analysis of fluid flow, heat transfer, and chemical reaction problems. PHOENICS can be used to solve coupled sets of partial differential equations for the conserved quantities and in its general form can account for temporal changes, inertial/convective effects, diffusive effects and also source terms, all in the presence of interacting material phases (Rosten and Spalding, 1987). The numerical algorithm is derived from the SIMPLE algorithm explained by Patankar (1980).

When applied to the Kundt tube model, the rotationally symmetric cylindrical domain is divided into finite volume ring elements and the symmetry about the centerline is utilized to consider only half the tube as shown in Fig. 2. For the boundary conditions, use is made of the default settings in PHOENICS, which treat the boundaries of the computational domain as impervious to mass, momentum, and energy. Such zero flux conditions are especially useful when the domain is divided along symmetry planes whereas the nonhomogeneous boundary conditions are implemented via source terms. All the boundaries of the computational domain are impervious to the mean flow of mass; the side wall is also impervious to the flow of heat and constant temperatures at the end walls are designated. The axially periodic slip velocity condition in Eq. (14) is specified at the outermost radial nodes, whereas the end walls are simply treated as no-slip boundaries.

PHOENICS provides the user with a large number of options to control the approach to the final solution. However, elaborate control procedures are not required in this study since the physical nature of the problem offers some simple inherent checks to ensure proper accuracy and convergence. From the

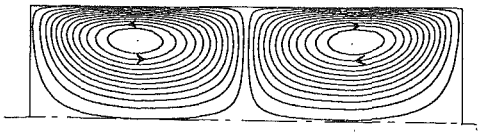

Fig. 3 Contour plots of the recirculatory streamlines of steady flow in the Kundt tube for $R_s = 150$, $n_z = 1$, $r_0k = 1$

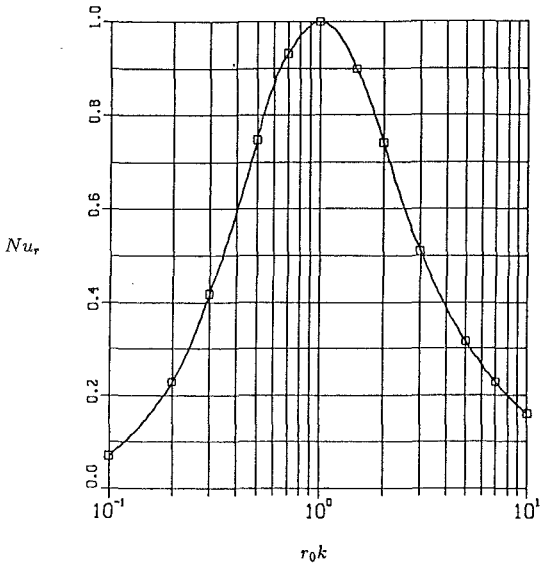

Fig. 4 Variation of Nu_r with r_0k for $R_s = 150$

Kundt tube model in Fig. 1 it is clear that with an insulated side wall all the heat is transferred from the hot end (Q_H) to the cool end (Q_C). This feature is used to monitor the solution process on the basis of:

1 The convergence rate of the mean value of the heat transfer rate

$$\delta_Q^{i,j} = \left| \frac{Q^i - Q^{i-j}}{Q^i} \right| \text{ where } j \text{ is the iteration-sweep interval} \quad (15)$$

2 The normalized fractional difference between the end heat transfer rates

$$\Delta_Q^i = \left| \frac{Q_H^i - Q_C^i}{Q^i} \right| \quad (16)$$

where $Q^i = (Q_H^i + Q_C^i)/2$ refers to the average heat transfer rate across the ends of the tube at the ith iterative sweep of the numerical solution. In this numerical study it was considered optimum to ensure that $\delta_Q^{i,j} \le 10^{-4}$ and $\Delta_Q^i \le 1$ percent. The former criterion was found to be more important in determining the number of iterations, whereas the latter criterion was critical in selecting a paper grid for the two end heat transfer rates to be sufficiently close. It was simultaneously ensured that the sum of the residuals for the temperature variable (provided by PHOENICS) was a small fraction (less than 1 percent) of the heat transfer rate, Q. Typical values of the convergence and accuracy data are displayed in Table 3.

5 Numerical Results

The numerical results obtained under the constant property assumption are discussed in this section. Air properties are chosen at $T_C = 20°C$, the temperature of the cool end. A temperature difference of 50°C is imposed across the ends (for calculation purposes) by maintaining the temperature of the hot end at $T_H = 70°C$. The average Nusselt number is defined as the ratio of the computed heat transfer rate to the reference conduction heat transfer rate,

Table 1 The average Nusselt number, Nu_r, as a function of the parameter r_0k for $R_s = 150$

r_0k	r_0 [cm]	$\mathcal{A}$	Q_{ref} [W]	Q [W]	Nu	Nu_r
0.1	0.55	15.71	7.11E-04	8.21E-04	1.155	0.070
0.2	1.09	7.85	0.0028	0.0043	1.516	0.229
0.3	1.64	5.24	0.0064	0.0123	1.924	0.418
0.5	2.73	3.14	0.0178	0.0472	2.652	0.748
0.7	3.82	2.24	0.0348	0.1065	3.056	0.931
1.0	5.46	1.57	0.0711	0.2281	3.208	1.0
2.0	10.92	0.79	0.2844	0.7498	2.636	0.741
3.0	16.38	0.52	0.6400	1.3610	2.127	0.510
5.0	27.30	0.31	1.7775	3.0176	1.698	0.316
7.0	38.21	0.22	3.4840	5.2354	1.503	0.228
10.0	54.59	0.16	7.1098	9.6314	1.355	0.161

$$\text{Nu} = \frac{Q}{Q_{\text{ref}}}, \text{ where } Q_{\text{ref}} = \frac{\kappa_f(\pi r_0^2)(T_H - T_C)}{L},$$

$$\text{with } L = n_z \frac{\lambda}{2} \quad (17)$$

Typical values of the operating parameters employed in the acoustic levitation experiments range in SPL values of 150 dB–175 dB, frequencies of 1 kHz–2 kHz, and wave-aspect ratio parameter values r_0k, of 0.3–5.0. The corresponding input parameters supplied to PHOENICS are:

1 The streaming Reynolds number, R_s
2 The wave aspect ratio parameter, r_0k
3 The plane wave mode of the standing sound wave, n_z
4 The frequency of the acoustic signal, $f = 1$ kHz

The relation in Eq. (11) is used to ensure that the SPL prescribed by these input parameters remains within the expected range. The resulting *dimensional* values required by PHOENICS are calculated from these input values as follows:

1 Wavelength of sound field, $\lambda = c/f$
2 Tube length, $L = n_z(\lambda/2)$
3 Tube radius, $r_0 = (r_0k)\lambda/2\pi$,
4 Magnitude of the $O(\alpha U_\infty)$ axial slip velocity component from Eq. (14),

$$|u_z^{*(s)}| = \frac{3}{8}\alpha U_\infty = \frac{3}{8}\frac{U_\infty^2}{c} = \frac{3}{8}R_s\frac{2\pi f\nu}{c} = \frac{3}{4}I_0\frac{10^{\text{SPL}/10}}{\rho c^2} \quad (18)$$

The choice of the computational grid was closely related to the physical parameters involved, with a finer grid being selected in regions of larger gradients. The auxiliary graphics program, PHOTON, was used to view the temperature and velocity fields to verify the symmetry expected from the discussion at the end of Section 3. The stream function distribution obtained from a suitable integration of the velocity field clearly illustrates the recirculatory nature of the streaming flow (see Fig. 3).

5.1 Effect of the Narrowness Condition. The effect of varying r_0k on the heat transfer rate was studied: The results for the fundamental mode ($n_z = 1$) with $R_s = 150$ (corresponding to SPL = 154.7 dB, $f = 1$ kHz) are presented in Table 1 in terms of a reduced Nusselt number, $\text{Nu}_r = (\text{Nu} - 1)/(\text{Nu}_0 - 1)$, where $\text{Nu}_0 = \text{Nu}$ for $r_0k = 1$. For small values of r_0k corresponding to the narrow waveguide limit, the heat transfer across the ends is mainly due to conduction, and the Nusselt number approaches the value predicted by the small $\mathcal{R}_s$ approximation. For large values of r_0k, the tube aspect ratio is small and in this stubby cylinder limit too, the heat transfer rate approaches the value for conduction heat transfer across the narrow gap between two large isothermal circular planes. The effect of the streaming motion is found to be a maximum only for intermediate radii corresponding to $r_0k = 1$. These results are illustrated in Fig. 4.

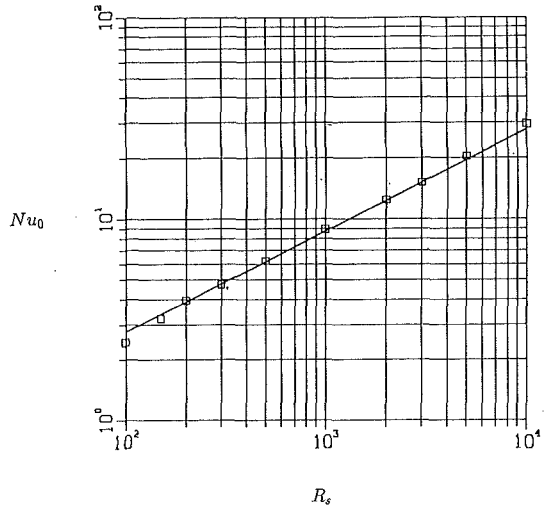

Fig. 5 Variation of Nu_0 with R_s for air

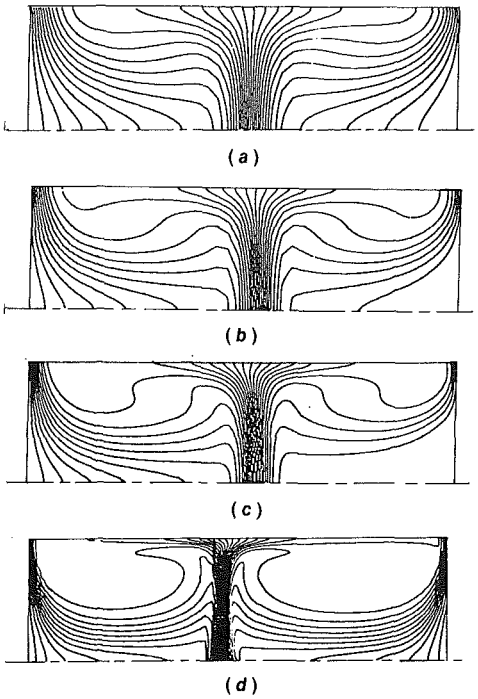

Fig. 6 Contour plots of the temperature showing the swept nature of the isotherms for $n_z = 1$, $r_0k = 1$: (a) $R_s = 150$; (b) $R_s = 300$; (c) $R_s = 500$; (d) $R_s = 2000$

5.2 Effect of Acoustic Signal Strength. This effect was studied by varying the SPL (at a fixed frequency of 1 kHz) and was implemented by varying the input value of R_s. Based on the results of Section 5.1, a value of $r_0k = 1$ was used to study the maximum effects of the streaming motion for each value of R_s. The results are presented in Table 2 for the smallest possible wave node ($n_z = 1$) required to levitate the sample. A plot of Nu_0 as a function of R_s in Fig. 5 shows a power law relationship, which can be fitted well with a $\sqrt{R_s}$ correlation as,

$$Nu_0 = 0.27\sqrt{R_s} \tag{19}$$

For the Prandtl number dependence of Nu_0, it is difficult at this stage to make a prediction based on conventional boundary layer analyses, although judging from the results of Gopinath and Mills (1993) for a similar problem, Nu_0 can be expected to have a power dependence on Pr with the exponent being between 0.5 and 1.0 in the Prandtl number range for gases.

Table 2 The average Nusselt number, Nu_0, as a function of R_s

R_s	SPL [dB]	$\lvert u_z^{*(s)}\rvert$ [cm/s]	Q [W]	Nu_0
100	153.0	1.08	0.1813	2.50
150	154.7	1.62	0.2281	3.21
200	156.1	2.16	0.2803	3.80
300	157.8	3.24	0.3363	4.72
500	160.8	5.39	0.4425	6.22
1000	163.0	10.79	0.6348	8.93
2000	166.1	21.57	0.8848	12.44
3000	167.8	32.35	1.0780	15.16
5000	170.8	53.93	1.4540	20.45
10000	173.0	107.85	2.1100	29.68

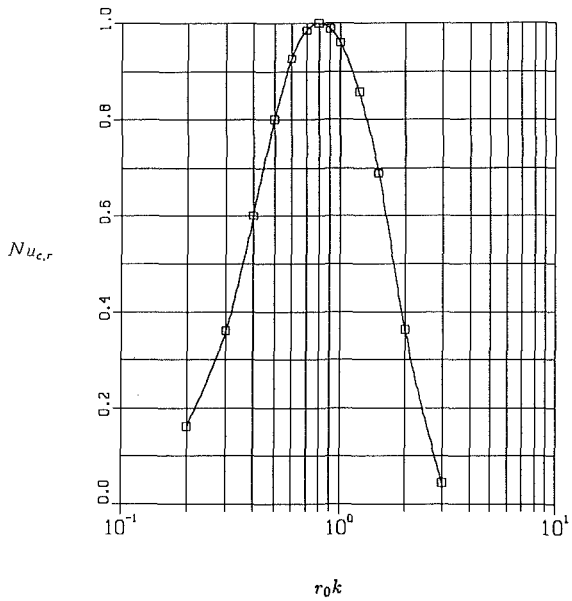

Fig. 7 Variation of $Nu_{c,r}$ with r_0k for $R_s = 150$ (see Eq. (21))

From the contour plots of the temperature in Fig. 6 it is clear that the isotherms exhibit a distinct "swept" nature as discussed at the end of Section 3. From the symmetry of the flow, the temperature along the centerplane ($z = \pi/2$) is a constant for $n_z = 1$ and is equal to the average ($\phi = 1/2$) of the values at the hot and cool ends. This feature can be extended to higher plane wave modes ($n_z \geq 1$) to infer that the nodal/antinodal planes are isothermal and have temperatures given by

$$\phi = \frac{n}{2n_z} \text{ at } \frac{z^*}{L} = \frac{n}{2n_z} \text{ for } 1 \leq n \leq 2n_z - 1 \tag{20}$$

5.3 The Local Temperature Field. One of the primary goals is to predict the local temperature field into which the sample is introduced when levitated into its stable position along the centerline of the test cell. Contour plots of the temperature in Fig. 6 indicates that such regions (marked ⊗ in Fig. 2) are characterized by negligible radial gradients and large axial gradients of the temperature. A limiting form of the governing energy equation can be used to show that this local axial temperature gradient is linear (a feature confirmed by the numerical results) and permits a correlation with the average Nusselt number, Nu, across the ends of the tube. The results from a parametric study of the effect of r_0k (as in Section 5.1) on this local axial temperature gradient, Nu_c, where

$$Nu_c = \left|\frac{\partial\phi}{\partial(z^*/L)}\right|_{r=0} \text{ at } \frac{z^*}{L} = \frac{2n-1}{2n_z} \text{ for } 1 \leq n \leq n_z \tag{21}$$

Table 3 Representative convergence and accuracy data for a typical run ($R_s = 150$, $r_0k = 1$, $n_z = 1$)

isweep	$\delta_Q^{i,100}$ [$\times 10^4$]	Δ_Q^i [%]	$\frac{\sum Q_{resid}^i}{Q^i}$ [%]	$Nu^{(i)}$
1000	23	13.47	26.80	3.1943
1100	15	8.93	17.75	3.1991
1200	10	5.93	11.81	3.2023
1300	6.6	3.95	7.93	3.2044
1400	4.7	2.64	5.43	3.2059
1500	2.8	1.77	3.82	3.2068
1600	1.9	1.20	2.83	3.2074
1700	1.2	0.82	2.28	3.2078
1800	0.94	0.56	1.90	3.2081
1900	0.62	0.40	1.69	3.2083
2000	0.31	0.29	1.54	3.2084

are shown in Fig. 7 for $R_s = 150$ in terms of a reduced local Nusselt number, $Nu_{c,r} = (Nu_c - 1)/(Nu_{c,max} - 1)$. On this plot the peak value, $Nu_{c,max} = 6.66$, and is found to occur at $r_0k \approx 0.80$. The behavior shown in Fig. 7 is similar to that in Fig. 4 although it was found from results not shown here that the value of r_0k at which Nu_c reaches a maximum varies with R_s in such a manner that the product, $R_s \times (r_0k)^2$, at which this maximum occurs is a constant for all R_s. This characteristic of the results was confirmed numerically for a range of values of R_s by verifying that, if for example $R_s = 200$, then $Nu_{c,max}$ would occur at $r_0k \approx 0.69$. In addition, this peak value $Nu_{c,max}$, was found to be consistently equal to about 2.05–2.15 times the value of Nu_0 for the corresponding value of R_s.

5.4 Other Effects. Among the input variables, a study of the influence of varying n_z (with all other factors fixed) amounts to a study of the effect of varying the tube length in integral multiples of half the wavelength. From the symmetry of the cellular flow pattern and the nature of the dependence on the z coordinate in the governing energy equation, a linear dependence of the heat transfer rate on the tube length is expected. Only a few runs were required to confirm this conjecture and Nu was found to be essentially unchanged with n_z. However, in levitation experiments it is more likely that a test cell of given dimensions is used, for which a change in n_z is bound to be accompanied by a change in the frequency used as a positioning tool for the levitated sample. As the resonant mode is increased, more stable sample positions become available, thereby allowing a more precise axial location of the sample. Such a change can be incorporated into the parameters that have already been considered in Sections 5.1 and 5.2 as shown below. If, for example, the frequency of the fundamental mode ($n_z = 1$) were to be doubled to correspond to the first overtone ($n_z = 2$), it follows from Eq. (1) that r_0k must also be doubled. In addition, if the signal strength were changed to a different SPL, Eq. (11) can be used to determine the new value of R_s at the current frequency. With the new operating conditions (R_s, r_0k) thus established, the results for the Nusselt number presented earlier in Sections 5.1 and 5.2 for $n_z = 1$ can be used by exploiting the independence of Nu on n_z.

5.5 Convergence Rate and Numerical Accuracy. The convergence criteria employed in this study (briefly outlined at the end of Section 4) are presented in Table 3 for a typical numerical run ($R_s = 150$, $r_0k = 1$, $n_z = 1$). The corresponding values of the sum of the temperature residuals are also provided for estimating the accuracy.

As noted earlier, finer grids were required to capture the large gradient effects for larger values of R_s. This also implied a larger number of iterative sweeps for a given accuracy. The mesh size for each R_s was selected by refining the grid until the improvement in the solution was within a certain tolerance, chosen to be of second decimal place accuracy in the Nusselt number.

6 Closure

Convective heat transfer rates due to acoustic streaming were determined for a temperature difference imposed across the ends of a Kundt tube supporting a standing sound wave. After a comparison of the length scales involved in the problem, important simplifying assumptions were made and the governing equations of motion and energy were stated in Section 2. Basic results for the streaming flow were given in Section 3 from which some deductions were made regarding the time-independent velocity and temperature fields. The need for a numerical solution was pointed out and the solver PHOENICS was adopted for this purpose, the workings of which were briefly described in Section 4. The numerical results have been presented in Section 5 for a range of the controlling parameters, along with Nusselt number correlations developed for air.

Acknowledgments

The authors gratefully acknowledge financial support for this work received from the National Science Foundation on Grant No. CTS-8918777. PHOENICS was available for use at the University of California at Los Angeles through an academic user group; the responsible group member is Professor A. F. Mills. PHOENICS was installed by Mr. A. DeBoer at the Office of Academic Computing, UCLA.

References

Gopinath, A., 1992, "Convective Heat Transfer in Acoustic Streaming Flows," Ph.D. Dissertation, School of Engineering and Applied Science, University of California at Los Angeles, Los Angeles, CA.

Gopinath, A., and Mills, A. F., 1993, "Convective Heat Transfer From a Sphere Due to Acoustic Streaming," ASME JOURNAL OF HEAT TRANSFER, Vol. 115, pp. 332–341.

Haddon, E. W., and Riley, N., 1979, "The Steady Streaming Induced Between Oscillating Circular Cylinders," *Quart. J. Mech. Appl. Math.*, Vol. 32, pp. 265–282.

Haddon, E. W., and Riley, N., 1981, "The Heat Transfer Between Concentric Vibrating Circular Cylinders," *Quart. J. Mech. Appl. Math.*, Vol. 34, pp. 345–359.

Landau, L. D., and Lifshitz, E. M., 1987, *Fluid Mechanics*, 2nd ed., Pergamon Press, Oxford, UK, pp. 305–308.

Lighthill, M. J., 1978, "Acoustic Streaming," *J. Sound Vib.*, Vol. 61, pp. 391–418.

Patankar, S. V., 1980, *Numerical Heat Transfer and Fluid Flow*, 1st ed., Hemisphere Publishing Corp., Washington, DC.

Rayleigh, Lord, 1884, "On the Circulation of Air Observed in Kundt's Tubes, and on Some Allied Acoustical Problems," *Phil. Trans. Roy. Soc.*, Vol. A175, pp. 1–21.

Rey, C. A., Merkley, D. R., Hampton, S., DeVos, J., Mapes-Riordan, D., and Zatarski, M., 1991, "Containerless Processing at High Temperatures Using Acoustic Levitation," *Advances in Space Research*, Vol. 11, pp. 769–777.

Riley, N., 1966, "On a Sphere Oscillating in a Viscous Fluid," *Quart. J. Mech. Appl. Math.*, Vol. 19, pp. 461–472.

Rosten, H. I., and Spalding, D. B., 1987, *The PHOENICS Reference Manual, Ver. 1.4, Rev. 06*, CHAM Ltd., Wimbledon, United Kingdom.

Rudnick, J., and Barmatz, M., 1990, "Oscillational Instabilities in Single-Mode Acoustic Levitators," *J. Acous. Soc. Am.*, Vol. 87, pp. 81–92.

Stuart, J. T., 1966, "Double Boundary Layers in Oscillatory Viscous Flows," *J. Fluid Mech.*, Vol. 24, pp. 673–687.

Trinh, E. H., Robey, J., Jacobi, N., and Wang, T., 1986, "Dual-Temperature Acoustic Levitation and Sample Transport Apparatus," *J. Acous. Soc. Am.*, Vol. 79, pp. 604–612.

Visualization of Flow Phenomena Near Enhanced Surfaces

T. S. Ravigururajan
Department of Mechanical Engineering,
The Wichita State University,
Wichita, KS 67260

A. E. Bergles
Department of Mechanical Engineering,
Aeronautical Engineering & Mechanics,
Rensselaer Polytechnic Institute,
Troy, NY 12180

Passive augmentation techniques such as surface disruptions are being increasingly used in heat exchangers. Although many working correlations have been suggested to predict their thermal-hydraulic characteristics, the physical phenomena governing the heat transfer enhancement have not been clearly understood. The paper describes a qualitative study on the flow phenomena near an enchanced surface. Water was used as the working fluid. Experiments were conducted for different coil wire diameters and for a Reynolds number of 150–2600. The results show the simultaneous existence of different flow patterns in enhanced flow. Also, the study confirmed that the developing length is very much smaller than that of a smooth tube, even for laminar flow.

Introduction

The heat exchanger industry is seeking ways to reduce the size and cost of heat exchangers. The enhancement of heat transfer has become an important factor in achieving these goals. Enhancement can be accomplished through two broad techniques: active and passive. Of the two, the passive technique (through surface roughness and displaced promoters) is more commonly employed. For instance, enhanced tubes are used in refrigeration industry and in power-plant condensers.

Surface disruptions promote augmentation through the disturbance of the viscous layer close to the surface. Several correlations have been proposed based on the Reynolds analogy to predict the thermal-hydraulic characteristic of flows over such surfaces. Recently, Ravigururajan and Bergles (1985) proposed comprehensive heat transfer and friction factor correlations for single-phase enhanced flow that are applicable for a wide range of roughness parameters. However, to employ enhanced surfaces in power plant condensers, engineers require information on fouling of such surfaces. In a recent study (Smith and Dirks, 1985), it was estimated that fouling of heat exchangers costs around $4.2 to $10 billion/year. Chenoweth (1990) lists energy losses, maintenance cost, and lost production as some of the reasons behind these expenses. While TEMA and HTRI have established standards for smooth tube fouling, no firm recommendations have yet been made regarding augmented tubes. Rabas et al. (1990) note that the fouling characteristics in enhanced tubes used in utility condensers appear to be similar to those of plain tubes. However, in a recent investigation, Watkinson (1990) suggests fouling factors of 0.6 to 1.2 times that of the plain tube fouling factors depending on the area increase. He also noted that the heat transfer increase is adversely affected by fouling.

Despite these attempts, no satisfactory explanation could be offered on the physical mechanism(s) that control heat transfer enhancement. Also, the impact of these enhanced flow fields on the fouling characteristics has yet to be clearly established. More fundamental studies are needed on the flow mechanism(s) of enhanced flows to establish the various characteristics of augmented surfaces, including the fouling characteristics. In the present study, simple flow visualization experiments were carried out to gain insight into the various flow patterns that occur in enhanced tube-side flows.

Background

Although the pressure drop and heat transfer in enhanced tubes have been widely studied, the physical nature of the flow that is responsible for the augmentation is not yet clearly understood. This has made flow-pattern analysis an important aspect of many investigations.

Reasonable evidence suggests that two basic types of flow can occur inside a ribbed tube enhanced with intermediate helix angles. The first is the rotational flow mainly caused by the helix angle of the ribs. The extent to which this is carried from the near-wall region into the core depends on the existing flow conditions. The other type of flow commonly encountered in ribbed tubes is crossover flow. The momentum in the axial direction is much larger than the angular momentum caused by the ribs; this results in the fluid crossing over the ribs. One of the characteristics of this flow is the reattachment of the fluid to the surface between the ribs. An important design factor that controls this reattachment length is the ratio of rib pitch to height. Further, the space downstream of the rib to the reattachment point is characterized by recirculation zone as noticed by Hishida et al. (1974). Another possible flow pattern is simple axial flow in enhanced tubes where the helix angle of the disruption is zero.

In an enhanced tube the type of flow depends, to a large extent, on the height, helix angle, and pitch of disruption, Reynolds number, and to a lesser extent, on the profile shape. In one of the earlier studies, Webb et al. (1971) indicated that the flow enhancement is brought on by the constant separation and reattachment of the flow caused by the repeated ribs. Li et al. (1982) report the existence of rotational flow for both laminar and turbulent flows. A more interesting observation was made by Nakayama et al. (1983), who noticed the change of flow from a rotational to a crossover pattern as the helix angle is increased, with the transition occurring between 45 and 60 deg. The present study is an attempt to establish the influence of the roughness parameters on the flow mechanism behind the enhanced flows.

Analysis of Existing Data

As part of a larger study, an extensive data base (Ravigururajan and Bergles, 1985) was developed based on the existing literature on enhanced tubes. These data were gathered from various sources, and care was taken to cover a wide range of tube and flow parameters. Tabulated data were used primarily. Wherever they were unavailable, enlarged plots were digitized using an HP-7470A Plotter. The data base was restricted to single-phase turbulent flows and only for Newtonian fluids. It is well known that the flow patterns for small p/e (<8) differ from those observed at larger p/e (Rabas, 1988). This is especially true for near-transverse ribs that have helix angles

Contributed by the Heat Transfer Division and presented at the ASME National Heat Transfer Conference, Minneapolis, Minnesota, July 28–31, 1991. Manuscript received by the Heat Transfer Division September, 1991; revision received June 1993. Keywords: Augmentation and Enhancement, Flow Visualization, Fouling. Associate Technical Editor: D. M. McEligot.

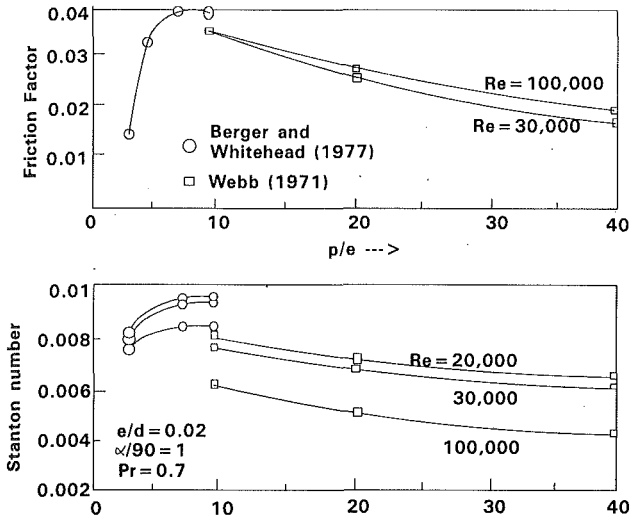

Fig. 1 Effect of *p/e* on friction factor and Stanton number at different Reynolds numbers

greater than 75 deg. When the flow is interrupted by a rib, the boundary layer close to the wall is separated, and reattaches to the wall downstream of the rib at a distance of 6 to 8 times the roughness height. The reattachment point vanishes when the pitch of roughness is reduced to less than about 6–8*e*, and the main flow is forced to "glide over" the ribs and a secondary flow is created between the ribs.

The effects of the flow patterns on the friction and heat transfer are clearly illustrated in Fig. 1. This plot is based on the data of Berger and Whitehead (1977) and Webb et al. (1971). These were the only studies that could be compared, because they involved similar types of roughness. No single study could be identified that investigated the disruption characteristic in the range p/e = 2–20. The augmented friction factor increases as the roughness pitch to height ratio decreases, reaching a maximum at p/e = 8. The heat transfer increase follows the same trend, reaching a peak value at p/e = 8. The friction factor drops dramatically, when the ribs are spaced any closer. However, the heat transfer coefficient also decreases, but at a much slower rate. For instance, when the p/e ratio is reduced from 8 to 3, the friction factor reduction is 75 percent, while the corresponding reduction in heat transfer is only about 20 percent. This trend confirms the results of a previous study on wire coil inserts by Sams (1957). Moreover, beyond a certain upper limit, the influence of Reynolds number on friction factor is marginal. This limit is determined by the disruption height and pitch.

This impact of roughness design on the augmented friction factor and heat-transfer performance can only be explained in terms of a change in the flow behavior. Webb (1969) suggests qualitatively that the flow may fail to reattach when the ribs are closely spaced (p/e less than 5). One possible explanation is the increase in rib surface area as a result of the closeness of the ribs.

Experimental Study

The experimental setup used an available constant-head reservoir that was supplied with water through an inlet at the bottom. The tank itself was divided into two halves by a wall

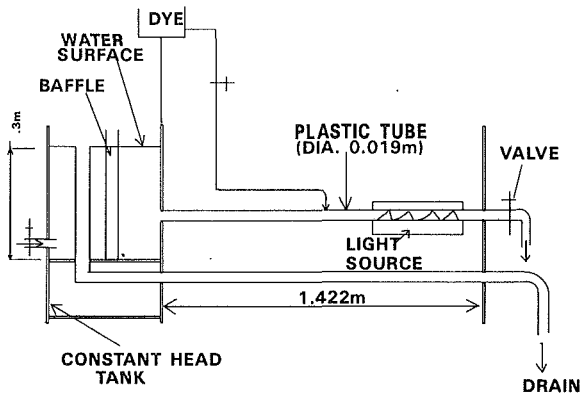

Fig. 2 Schematic diagram of flow visualization setup

Table 1 Wire coils used for flow visualization

No	Wire dia. [mm]	Pitch [mm]	angle [deg]	e/d	p/e
1	0.9525	19.05	72.3	0.05	20.0
2	1.575	19.05	72.3	0.08	12.1
3	2.28	19.05	72.3	0.12	8.36
4	1.575	88.9	34.0	0.08	56.4
5	0.9525	22.23	69.6	0.05	23.34

Outside diameter of coils d = 19.05 mm

of baffles. The entering water was calmed by the baffles before it entered the other half of the tank. An overflow drain maintained a constant head in the tank. The fluid outlet was on the side wall near the bottom. The water from the outlet passed through a transparent 19.05-mm-dia plexiglass, tube, where the actual experimentation was carried out. The flow in the tube, and therefore the Reynolds number, was controlled by a needle valve at the end of the tube. A schematic diagram of the experimental rig is shown in Fig. 2.

Wire coils were inserted into the transparent tube. The visualization of the flow patterns was aided by injection of colored dye into the tube. Dyes of different colors were introduced at different places such as at the surface, just above the surface (less than the disruption height), and in the core itself (greater than disruption height). This was done to identity the different types of flow that might exist near the wall and in the core. A red color dye was injected close to the wall and the blue color dye was injected just above the disruption height. Both the dyes were injected at 20 diameters upstream of the wire coil. The dyes facilitated observation of the behavior of different layers of fluid. The colored fluid particles flowed along or parallel to the surface of the tube, which indicated the absence of any noticeable buoyant forces.

Table 1 gives dimensions of the various wire coils that were used. A Reynolds number range of 100 to 2600 was considered in this study. Also, the disturbances that create the necessary conditions for an effective enhancement occur very close to the surface where the flow is viscous, even when the core flow is at a very high Re. The experiments were carried out several times to verify satisfactory repeatability of flow patterns. The lighting was provided by two 200-W floodlights. The still pictures were taken with an exposure time of 1/250 s with ISO400

Nomenclature

a = helix angle, deg
d = diameter, mm
e = rib height, mm
f = fanning friction factor
h = heat transfer coefficient, J/m^2-K-h
Nu = Nusselt number
p = pitch of ribs, mm
Pr = Prandtl number
Re = Reynolds number
St = Stanton number

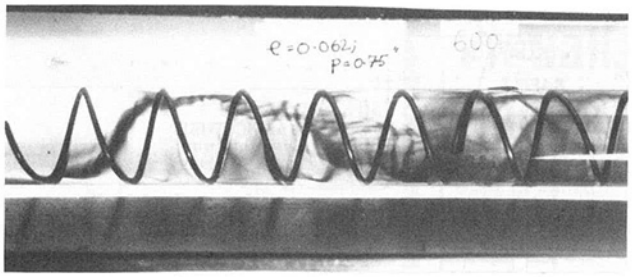

Fig. 3 Effect of rib height on augmented flow pattern for Coil 2 (Re = 600)

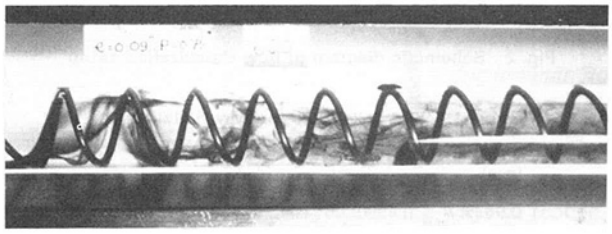

Fig. 4 Effect of rib height on augmented flow pattern for Coil 3 (Re = 600)

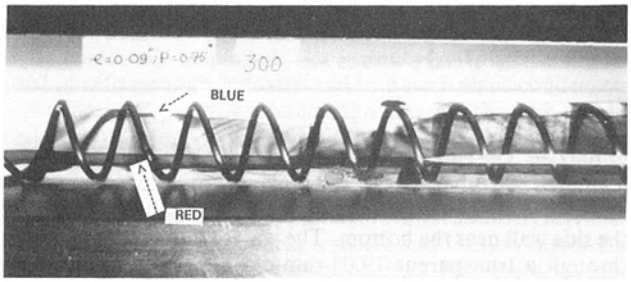

Fig. 5 Influence of rib on rotational layer at Re = 150 (Coil 3)

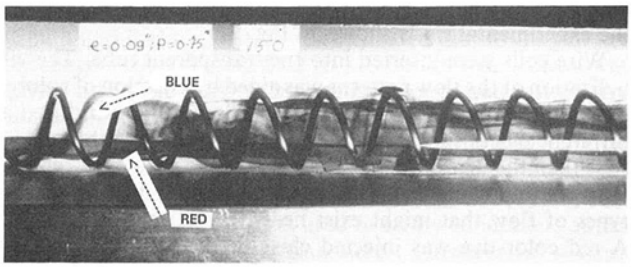

Fig. 6 Rib influence on rotational pattern at Re = 300 (Coil 3)

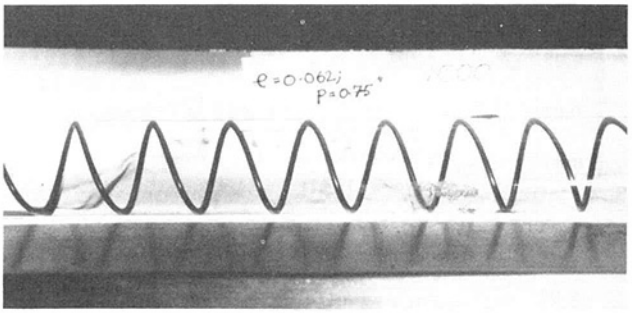

Fig. 7 Helix angle effect on onset of turbulent flow (Coil 2)

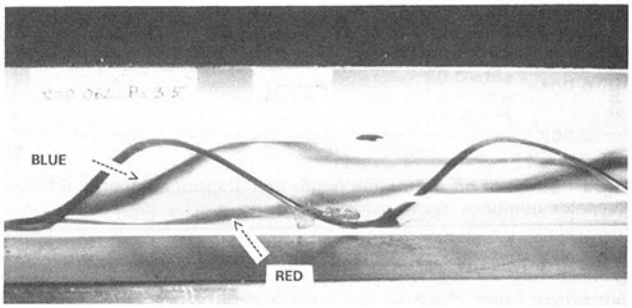

Fig. 8 Helix angle effect on onset of turbulent flow (Coil 4)

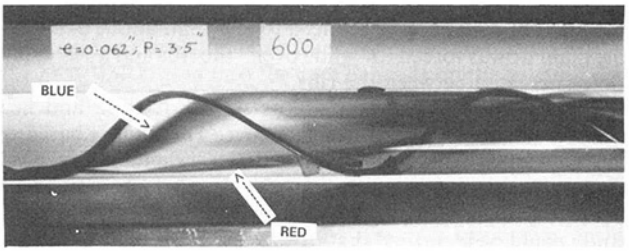

Fig. 9 Reynolds number effect on rotational layer thickness (Coil 4)

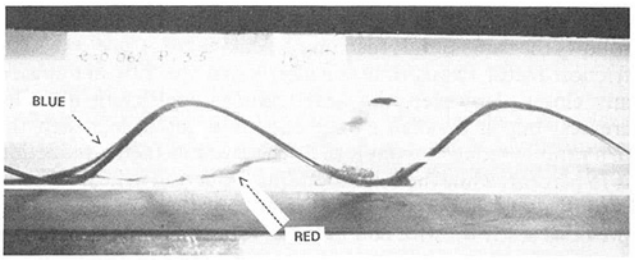

Fig. 10 Effect of Re on rotational angle (Coil 4)

35 mm color slide films. According to the manufacturers' specifications, the uncertainty in the mass flow rate was within ±1.653 kg/h with 20 to 1 odds (±4.5 percent).

The results are reproduced in Figs. 3–12.

Discussion and Inferences

The following inferences on the effects of the roughness height, helix angle, and Re can be drawn from these figures:

1 As the roughness height increases, the transition Re decreases (Figs. 3 and 4).
2 An increasing roughness height increases the angle of rotation (Fig. 5).
3 The hydrodynamic developing length seems to be insignificant even at a Reynolds number of 300 (Figs. 5 and 6). However, this should be viewed with caution. Detailed mean and rms velocity measurements will be needed before a statement could be made conclusively. Also, thermal developing length may be different from hydrodynamic developing length.
4 Decreasing the helix angle decreases turbulence. This delays the onset of turbulent flow to a higher Re, but still <2300 (Figs. 7 and 10).
5 The thickness of the rotational layer decreases with increasing Reynolds number. (Figs. 8, 9, and 10).
6 Rotational angle tends toward the rib helix angle as Re is decreased (Figs. 9 and 10).
7 Figures 11 and 12 indicate the early onset of turbulent flow (Re = 1600) and the presence of a rotating layer of fluid even in turbulent flow.

Much of the resistance to heat transfer occurs in the viscous sublayer, and any disturbance to it should contribute positively to heat transfer augmentation. This may be accomplished in several ways: a reduction in sublayer thickness (through higher Re), introduction of a rotational motion (through the introduction of helical rib), and an increase in turbulent intensity caused by the shear layer.

While the roughness height introduces rotation into the laminar flow, any excessive height will most likely compromise the heat transfer gain through a large increase in pressure drop.

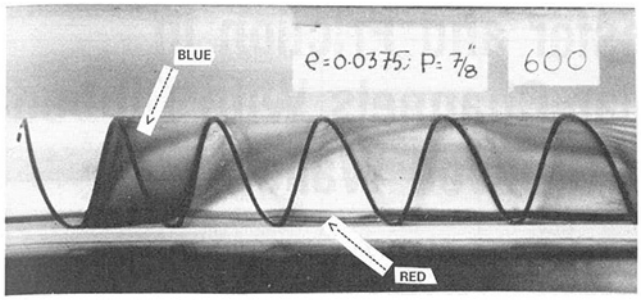

Fig. 11 Flow at Reynolds number = 600 (Coil 1)

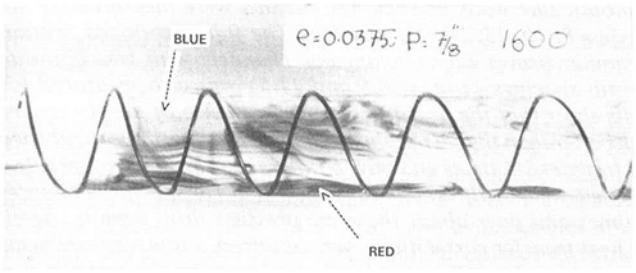

Fig. 12 Flow at Reynolds number = 1600 (Coil 1)

This is primarily because the crossover pattern of the already highly turbulent layers cause a drag on the disruption with little benefit to the heat transfer enhancement.

The flow visualization tests in the present study prompt some interesting inferences on the effects of ribs. Generally, a pipe flow remains laminar for $Re < 2000$ even in the presence of very strong disturbances (Schlichting, 1956). However, this pertains exclusively to smooth tube flows without any upstream disturbance. The disturbances encountered in enhanced tube flows are governed by theories of stabilities. Transition to turbulence could occur at lower Reynolds numbers when two or three-dimensional roughnesses are large enough. A discussion to this effect can be found in the same reference. Recent investigations by Obot et al. (1990) show clearly the existence of lower transition Reynolds numbers in enhanced flows. They suggest that the decrease in transition number in enhanced tube flows can be considered as an important correlating concept.

Although highly qualitative, the present study strongly suggests that both rotational and crossover patterns exist in flow over a ribbed surface even in turbulent flow for intermediate helix angle, which is also inferred by Yampolsky et al. (1984). Tests for $Re > 1600$ resulted in high enough turbulence that the dye was thoroughly mixed within a few diameters. Dye injection tests conducted in smooth tube (without any wire coils) showed the presence of laminar flow well up to a $Re = 2300$. This strongly suggests that the turbulence in enhanced flows is mainly caused by flow instabilities due to the wire coils.

The study is intended to raise more questions on the concept of enhanced flows. More detailed studies are needed to get quantitative information on the effects of the variables involved, and the flow patterns they form, to understand fully their influence on heat transfer enhancement. The observation made in this study may vary for higher Re flows normally encountered in heat transfer equipment. Nevertheless, the results from this investigation offer an initial viewpoint for any such future endeavors.

Conclusion

A study was conducted to determine the possible flow patterns associated with single-phase enhanced in-tube flows. An analysis of the existing experimental data base indicates that at an optimum p/e ratio of eight both the friction and heat transfer coefficient reach maximum values. The analysis suggests a different flow pattern for p/e less than six. The flow visualization tests indicate the presence of both a rotational layer close to the wall and a crossover layer at the core. The rotational pattern dominates when smaller rib helix angles (less than 30) are used whereas a crossover pattern appears to dominate when the helix angle is greater than 70 deg. The tests showed that a developing length is almost insignificant in augmented tube flows. Furthermore, the rib design drastically affects the flow pattern, and thereby, the friction factor, heat transfer coefficient, and fouling characteristics.

Acknowledgments

This study was supported by Argonne National Laboratory and the work was carried out at Iowa State University.

References

Berger, F. P., and Whitehead, A. W., 1977, "Fluid Flow and Heat Transfer in Tubes With Internal Square Rib Roughening," *J. Br. Nucl. Energy Soc.*, Vol. 2, pp. 153–160.

Chenoweth, J. H., 1990, "Final Reports of the HTRI/TEMA Joint Committee to Review the Fouling Section of the TEMA Standards," *Heat Transfer Engineering*, Vol. 11, No. 1.

Hishida, M., Okamoto, Y., Negoya, S., and Hanawa, J., 1974, "Experimental Observation on Flow Effects in Heat Transfer of Wired Turbulence Promoters," presented at the Second Symposium on Flow Visualization ISAS, University of Tokyo, July 15–16.

Li, H. M., Ye, K. S., Tan, Y. K., and Deng, S. J., 1982, "Investigation on Tube-Side Flow Visualization, Friction Factors and Heat Transfer Characteristics of Helical-Ridging Tubes," *Heat Transfer 1982*, Proceedings, Seventh International Heat Transfer Conference, U. Grigull et al., eds., Hemisphere Publishing Corp., Washington, D.C., Vol. 3, pp. 75–80.

Nakayama, M., Takashashi, K., and Daikoku, T., 1983, "Spiral Ribbing to Enhance Single-Phase Heat Transfer Inside Tubes," *Proceedings, ASME–JSME Thermal Engineering Joint Conference*, Honolulu, HI.

Obot, N. T., Esen, E. B., and Rabas, T. J., 1990, "The Role of Transition in Determining Friction and Heat Transfer in Smooth and Rough Passages," *International Journal of Heat and Mass Transfer*, Vol. 33, No. 10, pp. 2133–2143.

Rabas, T. J., 1988, "The Selection of Energy Efficient Enchancement Geometry of Single-Phase, Turbulent Flow Inside Channels: Part 1—Design Criteria, Benchmark Enchancement Types, and the Swirl and Reattachment Mechanism," Argonne National Laboratory, Energy Systems Div. Report, Contract W-31-1-9-Eng-38.

Rabas, T., Merring, R., Schaefer, R., Lopez-Gomez, R., and Thors, P., 1990, "Heat-Rate Improvements With the Use of Enhanced Tubes in Surface Condensers," EPRI Conference, Boston.

Ravigururajan, T. S., and Bergles, A. E., 1985, "General Correlations for Thermal-Hydraulic Correlations for Internally Enhanced Tube Flows," ASME HTD-Vol. 62.

Sams, E. W., 1957, "Heat Transfer and Pressure Drop Characteristics of Wire-Coil Type Turbulence Promoters," TID-7529, Pt. 1, Book 2, pp. 390–415.

Schlichting, H., 1968, *Boundary-Layer Theory*, 6th ed., McGraw-Hill, New York.

Smith, S. A., and Dirks, J. A., 1985, "Cost of Heat Exchanger Fouling in the U.S. Industrial Sector," *Proceedings, Symposium on Industrial Heat Exchanger Technology*, ASM.

Watkinson, A. P., 1990, "Fouling of Augmented Heat Transfer Tubes," *Heat Transfer Engineering*, Vol. 11, No. 3, pp. 57–65.

Webb, R. L., 1969, "Turbulent Heat Transfer in Tubes Having Two-Dimensional Roughness, Including the Effect of Prandtl Number," Ph. D. Thesis, University of Minnesota, Minneapolis, MN.

Webb, R. L., Eckert, E. R. G., and Goldstein, R. J., 1971, "Heat Transfer and Friction in Tubes With Repeated-Rib Roughness," *International Journal of Heat and Mass Transfer*, Vol. 14, pp. 601–618.

Wieland-Werke, A. G., 1978, "High Performance Tubes for Flooded Evaporators," Wieland Product Information SAW-15e-06.

Wither, J. G., and Young, E. H., 1971, "Steam Condensing on Vertical Rows of Horizontal Corrugated and Plain Tubes," *Industrial and Engineering Chemistry, Process Design and Development*, Vol. 10, pp. 19–30.

Yampolsky, J. S., Libby, P. A., Launder, B. E., and LaRue, J. C., 1984, "Fluid Mechanics and Heat Transfer in Spiral Fluted Tubing," Technical Report No. GA-A17833, Dec., General Atomic Company.

Heat Transfer and Friction in Rectangular Channels With Ribbed or Ribbed-Grooved Walls

Y. M. Zhang[1]

W. Z. Gu

Institute of Engineering Thermophysics,
Chinese Academy of Sciences,
Beijing, People's Republic of China 100080

J. C. Han

Turbine Heat Transfer Laboratory,
Department of Mechanical Engineering,
Texas A&M University,
College Station, TX 77843

The effect of compound turbulators on friction factors and heat transfer coefficients in rectangular channels with two opposite ribbed-grooved walls was determined for a Reynolds number range of 10,000 to 50,000. The channel width-to-height ratio was 10. The fully developed heat transfer coefficients and friction factors on the ribbed-grooved and smooth side walls of each test channel were measured for six rib-groove spacings ($p/e = 8$, 10, 15, 20, 25, and 30). The fully developed friction and heat transfer in similar aspect ratio rectangular channels with two opposite ribbed walls with two rib spacings (p/e = 8.5 and 11.5) was also measured for comparison. The results show that the heat transfer performance of the rib-groove roughened duct is much better than the rib roughened duct. The rib-groove roughened wall enhances the heat transfer 3.4 times and pays 6 times the pressure drop penalty, whereas the rib roughened wall, with similar rib height and rib spacing, enhances the heat transfer 2.4 times and pays about the same pressure drop penalty. Semi-empirical friction and heat transfer correlations were obtained. Flow measurements show that the roughened ducts have flatter velocity profiles than the smooth duct and rib-groove roughened duct produces higher turbulence intensity than the rib roughened duct. The flatter velocity profile and higher turbulence intensity are responsible for producing higher heat transfer.

Introduction

One well-known method of enhancing heat transfer on a surface is to roughen the surface by the use of repeated ribs. The ribs break the laminar sublayer and create local wall turbulence due to flow separation and reattachment between the ribs, which greatly enhances the heat transfer. Developing and fully developed turbulence heat transfer and friction in ducts with rib turbulators on two opposite walls of the channel have been extensively studied (Burggraf, 1970; Han, 1984; Boyle, 1984; Han and Park, 1988; Han, 1988; Han et al., 1989). The results show that angled ribs give a much higher heat transfer rate than transverse ribs, and narrow aspect ratio ducts perform better than wide aspect ratio ducts. The angled ribs provide better heat transfer performance than the transverse ribs because of the secondary flow induced by the rib angle, in addition to breaking the laminar sublayer and producing local wall turbulence. The rib angle effect decreases in the wide aspect ratio ducts because the ribs on two opposite walls are too close to each other, which retards the rib angle induced secondary flow. The effects of rib angle orientation on the local, regionally averaged heat transfer distributions and pressure drop in a square duct with two opposite ribbed walls were recently re-examined (Han et al., 1991; Han and Zhang, 1992). The results show that the "broken" V-shaped rib performs better than the V-shaped rib and, consequently, better than the angled rib. The effects of rib height and rib spacing on turbulent heat transfer and pressure drop in rectangular channels were reported by Zhang et al. (1984), Taslim and Spring (1987), Roeller et al. (1991), and Liou and Hwang (1992). The effects of rib profile (shape) on turbulent heat transfer and pressure drop in rectangular ducts also were reported (Taslim and Spring, 1991). Considerable data have been reported for rib roughened heat transfer and pressure drop in the flow passages of different cross-sectional areas: flow in ribbed circular tubes (Webb et al., 1971; Gee and Webb, 1980; Sethumadhavan and Raja Rao, 1983), between ribbed parallel plates (Han et al., 1978), in ribbed triangular ducts (Metzger and Vedula, 1987), and in ribbed annular ducts (Dalle Donne and Meyer, 1977; Meyer, 1982). This study focuses on enhanced heat transfer in ribbed or ribbed-grooved rectangular ducts.

The effects of rib height, rib spacing, rib shape, and rib angle orientation on heat transfer coefficients and friction factors over a wide range of Reynolds numbers have been well established for the square, rectangular, and other cross-sectional ducts. Semi-empirical friction and heat transfer correlations have been developed for heat transfer designers. However, heat transfer designers are continually seeking the high-performance enhanced surface. The concept of combined turbulence promoters was examined for this study. It is of interest whether the surface with compound rougheners (ribs plus grooves) can perform better than the surface with single rougheners (ribs only). It is well known that ribs break the laminar sublayer and create local wall turbulence, and also enhance heat transfer. The addition of grooves between any adjacent ribs may induce vortices in and around the grooves, which may greatly enhance the heat transfer on the flat wall portion between the ribs. Therefore, the combined ribbed and grooved turbulence promoters may produce even higher heat transfer than the ribbed promoters.

The objective of this study is to investigate the effect of compound roughness on heat transfer and pressure drop in rectangular channels for Reynolds numbers between 10,000 and 50,000. Eight rectangular channels were tested. Two of the channels are roughened by ribs on two opposite walls. The remaining six channels have rib and groove rougheners on two opposite walls of the channel. Each of the rectangular channels has a width to height ratio (W/H) of 10 and a length to hydraulic diameter ratio (L/D) of 20. In rib-groove roughened channels, the rib height (or groove depth) to hydraulic diameter ratio (e/D) is 0.028; the rib pitch (or groove pitch) to height ratio (p/e) equals 8, 10, 15, 20, 25, and 30, respectively. In

[1]Current address: Turbine Heat Transfer Laboratory, Department of Mechanical Engineering, Texas A&M University, College Station, TX 77843.

Contributed by the Heat Transfer Division for publication in the JOURNAL OF HEAT TRANSFER. Manuscript received by the Heat Transfer Division April 1992; revision received July 1993. Keywords: Finned Surfaces, Heat Exchangers, Turbines. Associate Technical Editor: T. W. Simon.

Table 1 Eight wall geometry studied

CASE NO.	WALL CONDITIONS	p/e	e/D
1	Ribs-Grooves	8.00	0.028
2	Ribs-Grooves	10.0	0.028
3	Ribs-Grooves	15.0	0.028
4	Ribs-Grooves	20.0	0.028
5	Ribs-Grooves	25.0	0.028
6	Ribs-Grooves	30.0	0.028
7	Ribs only	8.50	0.020
8	Ribs only	11.5	0.020

rib roughened channels, the rib height to hydraulic diameter ratio (e/D) is 0.020; the rib pitch to height ratios (p/e) are 8.5 and 11.5, respectively. Table 1 lists the six ribbed-grooved walls and two ribbed walls. The heat transfer coefficients and the heat transfer versus pressure drop performance for both the ribbed-grooved side (or ribbed side) and smooth side walls of the channel were obtained and compared for the eight enhanced surfaces. The semi-empirical friction and heat transfer correlations are provided. The velocity and turbulence distributions in the rib-roughened channel and the rib-groove roughened channel were measured for the case of Re = 55,000, $p/e = 10$, and $e/D = 0.028$ to understand the heat transfer augmentation mechanism better.

Experimental Program

Test Apparatus. The air from the compressor passes through the filter, orifice meter, and stabilizer, then enters the test channel, and finally flows out through the exhaust valve. Figures 1(*a*) and 2(*a*) are the typical test channels with ribbed walls and ribbed-grooved walls, respectively. The air flow rate through the test channel was measured by the orifice meter with a **U**-tube manometer. Figures 1(*b*) and 2(*b*) show the schematics of the cross section of the rib roughened rectangular channel and the rib-groove roughened rectangular channel, respectively. Each test duct consists of four parallel stainless steel plates, which are 40 cm long ($L = 40$ cm) and 0.2 cm thick ($\delta = 0.2$ cm).The aspect ratio of the test duct width to height ratio (W/H, $W = 10$ cm, $H = 1$ cm) is 10. The test duct orientation is such that the two opposite roughened walls of the rectangular cross section are vertical and the two opposite smooth walls are horizontal. These ribs (Fig. 1*c*) or ribs-grooves (Fig. 2*c*) were uniformly machined on the wide side of the plate surface in a required distribution (see Table 1). In this study, the rib height (e) equals the groove depth (g) for all six ribbed-grooved walls listed in Table 1. The foil heaters were cemented on the back surface of the test duct. The entire test duct was enclosed in fiberglass insulating material. The unheated smooth entrance duct (not shown) was made of plexiglass plates and has the same cross section and length as that of the test duct. The entrance duct serves to establish hydrodynamically fully developed flow at the entrance to the heated duct. The wall temperatures of the test section were measured by 18 copper-constantan thermocouples distributed along the length (at 40, 60, and 80 percent of the duct length) and across the perimeter of the test section (see Figs. 1*b* and 2*b*). Thermocouples also are used to measure the bulk mean air temperature entering and leaving the test section. Two pressure tapes are used for the static pressure drop measurement across the test section.

Nomenclature

A_c = cross-sectional area of rectangular channel
A_s = heat transfer surface area
C_p = specific heat of air
D = channel hydraulic diameter = $2WH/(W+H)$
e = rib height
e^+ = roughness Reynolds number
f = friction factor in a channel with two opposite ribbed walls or with two opposite ribbed-grooved walls
f_0 = friction factor in fully developed turbulent flow in smooth tubes
f_r = friction factor for four-sided ribbed channel or four-sided ribbed-grooved channel
G = mass flux ρu_∞
$G(e^+)$ = heat transfer roughness function
g = groove depth
g_c = conversion factor
h = heat transfer coefficient
H = height of rectangular channel = 1 cm
k = thermal conductivity of stainless steel
K = thermal conductivity of air
L = length of rectangular channel = 40 cm
Nu = Nusselt number = hD/K
p = rib or groove pitch
Pr = Prandtl number of air
Δp = pressure drop across the entire test channel
q = net heat transfer rate, Eq. (8)
R = friction roughness function
Re = Reynolds number = $\rho D u_\infty/\mu$
St = Stanton number = Nu/RePr, $h/\rho C_p u_\infty$
St_o = Stanton number in fully developed turbulent flow in smooth tubes
St_r = ribbed side wall or ribbed-grooved side wall Stanton number
St_s = smooth side wall Stanton number
T_b = local bulk mean temperature of air
T_i = inlet temperature of air
T_o = outlet temperature of air
T_r = air temperature of standard condition
T_u = local turbulence intensity, $\sqrt{\overline{u'^2}}/\overline{u}$, Eq. (3)
T_w = corrected local inner wall temperature
T'_w = measured local outer wall temperature
T_{wire} = hot-wire temperature
u = local velocity of air
$\overline{u}$ = local mean velocity of air
u' = local fluctuating velocity of air
u_∞ = bulk mean velocity of air, m/s
V_m = measured voltage when local velocity of air is u
V' = local voltage fluctuation
V_o = initial voltage when local velocity of air is zero
V = voltage of standard condition
W = width of rectangular channel = 10 cm
x = axial distance from air flow direction
y = vertical distance from wall
δ = stainless steel wall thickness
θ = temperature corrective factor
ρ = average density of air
μ = average dynamic viscosity of air

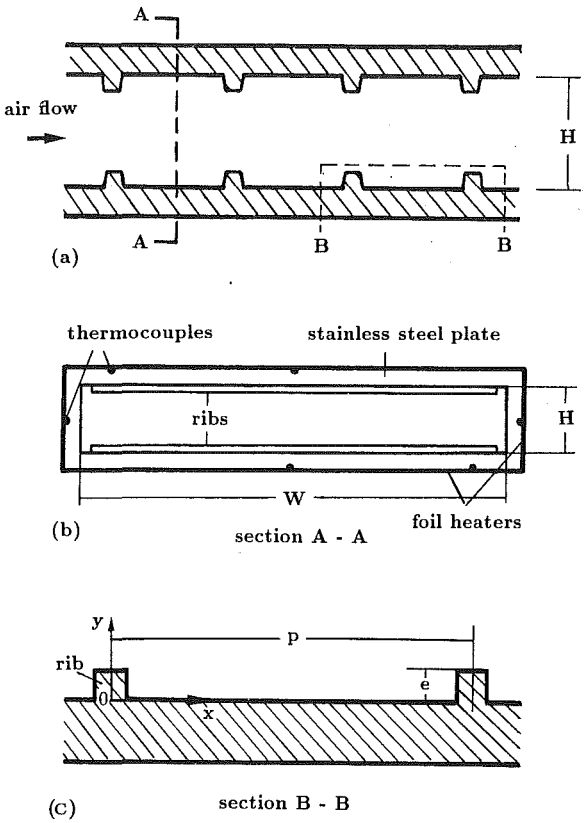

Fig. 1 Schematic of the test section for the ribbed wall

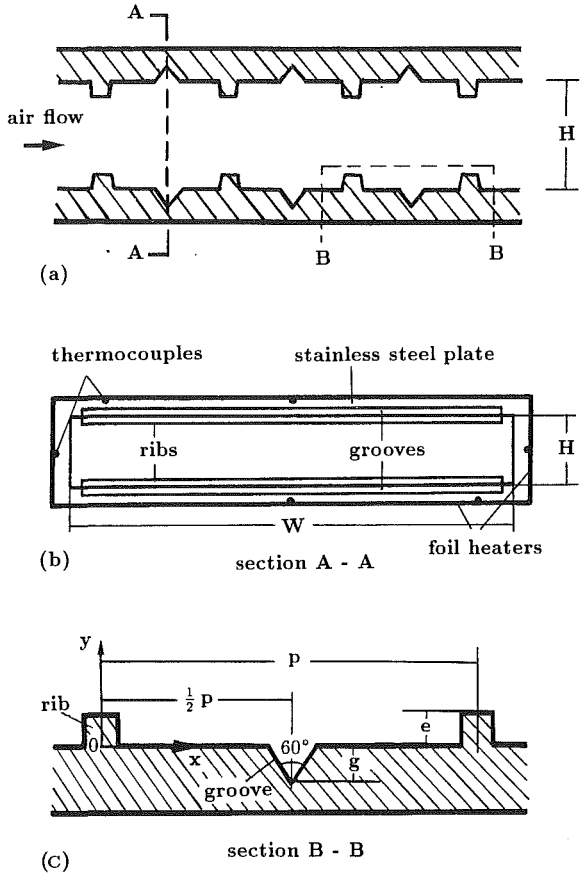

Fig. 2 Schematic of the test section for the ribbed-grooved wall

Three plexiglass rectangular ducts (one smooth, one ribbed, and one ribbed-grooved) were used to measure the distribution of the flow velocity and turbulence. The dimensions of these plexiglass ducts are five times those of the heat transfer ducts. For the rib roughened duct, the rib pitch to height ratio (p/e) is 10, and the rib height to hydraulic diameter ratio (e/D) is 0.028. For the ribbed-grooved roughened duct, the rib pitch (or groove pitch) to height (or groove depth) ratio p/e or p/g) is 10, and the height (or groove depth) to hydraulic diameter ratio (e/D or g/D) is 0.028. Figures 1(c) and 2(c) show the schematics of the rib geometry and rib-groove geometry, as well as the flow region to be used to measure the velocity and turbulence distributions. The air velocities were measured along the y direction (from wall to channel centerline) at $x/p=0.5$. The air turbulence also was measured along the y direction (from wall to channel centerline) at $x/p=0.5$ as well as in the x direction in a range of $0 < x/p < 1$ at several y locations from the wall.

Data Reduction. A hot-wire anemometer (DISA 55M, 55M10 and 55D35 RMS) was used to measure the distributions of velocity and turbulence intensity of air in plexiglass rectangular channels with two opposite ribbed walls or rib-grooved walls. The hot wire (5 μm diameter, 1 mm length) and measurement system were calibrated in a standard wind tunnel. A relationship of the standard condition measured voltage versus local air velocity (V versus u) was established. The air velocity can be read directly from (V versus u) with a measured voltage.

To obtain the root mean square value of the local velocity of air and local fluctuating velocity of air from the voltage, a correlation of the air velocity and voltage is necessary for analogy along the (V versus u) curve. It was found that the following correlation corresponded well with the (V versus u) curve:

$$V^2 = V_o^2 + B\bar{u}^n + C\bar{u} \tag{1}$$

The factors B, C, and n in Eq. (1) were obtained as: $B=2.783$, $C=-0.184$, and $n=0.583$. Equation (1) can also be expressed as:

$$2VdV = (nB\bar{u}^n + C\bar{u})(d\bar{u}/\bar{u}) \tag{2}$$

Therefore, the turbulence intensity of air can be calculated by:

$$Tu = \sqrt{\bar{u}'^2}/\bar{u} = 2V\left(\sqrt{\bar{V}'^2}\right)/(1.62\bar{u}^{-0.583} - 0.184\bar{u}) \tag{3}$$

The $\left(\sqrt{\bar{u}'^2}\right)$ used in Eq. (3) was obtained by $\left(\sqrt{\bar{V}'^2}\right)$, which can be determined from the voltage meter of the hot-wire anemometer over a period of 0.5 seconds. Note that Eq. (3) was obtained based on the assumption $dV \propto d\bar{u}$, which may be inaccurate when turbulence intensity is large or when on the nonlinear part of the V–u curve.

The working conditions of this study were slightly different from the standard condition. Therefore, a temperature corrective method was used in the present study for diminishing the effect of the different working conditions. The temperature corrective correlation for air can be expressed as:

$$V = \theta V_m \tag{4}$$

where:

$$\theta = [(T_{\text{wire}} - T_r)/(T_{\text{wire}} - T_b)]^{1/2} \tag{5}$$

Equation (4) shows that the voltage of the standard condition (V) is modified by the production of the temperature corrective factor θ and the measured voltage V_m. The local velocity of air then can be read directly from the V–u curve with the corresponding air bulk mean temperature (T_b). In this study, temperature corrective factor was small because the temperature differences between the standard and working conditions

were varied between 5–10°C, where thermal property effects are minimal.

A micromanometer measured the pressure drop across the test section. The friction factor in fully developed duct flow can be determined by measuring the pressure drop across the flow channel and the mass flow rate of the air. The friction factor can be calculated from:

$$f = \Delta p/[4(L/D)(G^2/2\rho g_c)] \quad (6)$$

The friction factor f is based on isothermal conditions (test without heating). The uncertainties for ΔP, L/D, and G were 5, 3 and 5 percent, respectively. By using the uncertainty estimation of Kline and McClintock (1953), the maximum uncertainty in the friction factor is estimated to be less than 9 percent for Reynolds numbers greater than 10,000. The friction factor f of the present study was normalized by the friction factor for fully developed turbulent flow in smooth circular tubes ($10^4 < \text{Re} < 10^6$) proposed by Blasius as:

$$f/f_o = f/[0.046\ Re^{-0.2}] \quad (7)$$

An averaged outlet temperature T_o of the air was used in Eq. (8) to obtain the exact net heat transfer rate. The averaged outlet temperature of the air was obtained by averaging 10 thermocouples located in the outlet cross section of the test channel and profiled in different locations. The net heat transfer rate can be calculated from:

$$q = C_p\ GA_c\ (T_o - T_i) \quad (8)$$

The local heat transfer coefficient was calculated from the net heat transfer rate per unit surface area to the cooling air, the corrected wall temperature (T_w) on each measured section, and local bulk mean air temperature as:

$$h = q/[A_s(T_w - T_b)] \quad (9)$$

The local outer wall temperature T_w' was read from each cross-sectional thermocouple output. The corrected local inner wall temperature T_w for Eq. (9) was calculated by the one-dimensional heat conduction equation as:

$$T_w = T_w' - (q\delta/kA_s) \quad (10)$$

where the axial and spanwise heat conductions were not considered in this study. Equation (9) was used for the rib side wall or ribbed-grooved side wall and the smooth side wall heat transfer coefficient calculations. The A_s was based on the smooth surface area, not including the area increases due to ribs or grooves.

The maximum heat loss from the roughened side wall and smooth side wall was estimated to be less than 5 and 6 percent, respectively, for Reynolds numbers greater than 10,000. The uncertainties of q, based on Eq. (8), was 6 percent. The local outer wall temperature T_w' was kept at 120–125°C for three axial locations in the fully developed region of the test channel. The inlet bulk mean air temperature was 26 to 30°C depending on the test conditions. The local bulk mean air temperature used in Eq. (9) was calculated assuming a linear air temperature rise along the flow channel. The uncertainty of $(T_w - T_b)$ was 5 percent. Therefore, the uncertainties of q, A_s, and $(T_w - T_b)$ were 6, 3, and 5 percent, respectively. By using the uncertainty method of Kline and McClintock (1953), the maximum uncertainty in the heat transfer coefficient was estimated to be less than 9 percent, while the maximum uncertainty in the Stanton number was estimated to be less than 10 percent for Reynolds numbers larger than 10,000.

The local Stanton number of the present study was normalized by the Stanton number for fully developed turbulent flow in smooth circular tubes correlated by McAdams as:

$$\text{St}/\text{St}_o = (h/\rho C_p\ u_\infty)/(0.023\ \text{Re}^{-0.2}\ \text{Pr}^{-0.6}) \quad (11)$$

Friction and Heat Transfer Correlations. Webb et al. (1971) applied the friction and heat transfer similarity laws, which were derived from the law of the wall for flow over rough surfaces, to correlate the friction factors and heat transfer coefficients for turbulent flow in circular tubes with periodic rib roughness elements. Han (1988) extended the friction and heat transfer similarity laws to correlate the friction factors (f_r) and heat transfer coefficients (St_r) for turbulent flow in rectangular channels (W/H given) with four-sided periodic rib turbulators (e/D given) as follows:

$$R = (f_r/2)^{-1/2} + 2.5\ln(2e/D) + 2.5\ln[2W/(W+H)] + 2.5 \quad (12)$$

$$G(e^+) = R + [f_r/(2\ St_r) - 1]/(f_r/2)^{1/2} \quad (13)$$

$$e^+ = (e/D)\ \text{Re}\ (f_r/2)^{1/2} \quad (14)$$

where the friction roughness function R is independent of roughness Reynolds number e^+ in the fully rough condition, but the heat transfer roughness function $G(e+)$ is increased with increasing e^+. Equations (12) and (13) imply that, for a given rectangular channel W/H, the friction factor f_r and the heat transfer coefficient St_r for any geometrically similar roughness family (i.e., any e/D ratio) may be correlated by the friction roughness function R and heat transfer roughness function $G(e^+)$, respectively. A family of periodic rib turbulators is defined as geometrically similar if the rib pitch and rib shape are not varied. In this study, Eqs. (12) and (13) were employed to correlate the friction factors and heat transfer coefficients for turbulent flow in rectangular channels with ribbed-grooved roughened walls. Since this study is for turbulent flow in rectangular channels with two opposite, instead of four-sided, ribbed-grooved walls. Therefore, the friction factors f_r in Eqs. (12) and (13) for four-sided rough walls were replaced by the friction factors f for two opposite rough walls suggested by Han (1988) as:

$$f_r = f + (H/W)(f - f_0) \quad (15)$$

where f_0 can be approximately calculated from the Blasius equation for turbulent flow in circular tubes with smooth wall as indicated in Eq. (7), $f_0 = 0.046\ \text{Re}^{-0.2}$.

In this study, Eqs. (12)–(15) were used to determine R and $G(e^+)$ by measuring f and St_r for turbulent flow in rectangular channels (given W/H) with a pair of opposite ribbed walls or ribbed-grooved walls (given e/D) and incorporating f_0 (given Re). The effect of nongeometrically similar factors such as rib pitch (i.e., P/e ratio) on the R and $G(e^+)$ correlations could be experimentally determined. For detailed derivations of the friction and heat transfer similarity laws for the ribbed channel, refer to Han (1988).

Experimental Results and Discussion

Velocity and Turbulence Distributions. Figure 3 shows velocity profiles in the y direction at the middle of two adjacent ribs for the smooth wall (no ribs), rib-roughened wall ($P/e = 10$, $e/D = 0.028$) and ribbed-grooved roughened wall ($P/e = 10$, $e/D = 0.028$) with $\text{Re} = 55{,}000$. The velocity profiles are different for the three different wall conditions. Due to the turbulence and mixing caused by the ribs and grooves, the velocity gradients near the wall for the ribbed and ribbed-grooved walls are larger than for the the smooth wall. The velocity profiles are relatively flat for the ribbed and ribbed-grooved walls compared to the smooth wall, and the ribbed-grooved wall is slightly flatter than the ribbed wall. The flatter profiles enhance the transfer of momentum and energy, and hence increase surface friction as well as convection transfer rates.

Figure 4 shows the turbulence intensity distributions in the y direction (vertical distance from the wall) at the midplane between two ribs for the smooth (no ribs), ribbed and ribbed-grooved wall ($P/e = 10$, $e/D = 0.028$) with $\text{Re} = 55{,}000$. The results show that the gradients of the turbulence are much larger in $0 < y/e < 1$ for the ribbed wall and ribbed-grooved

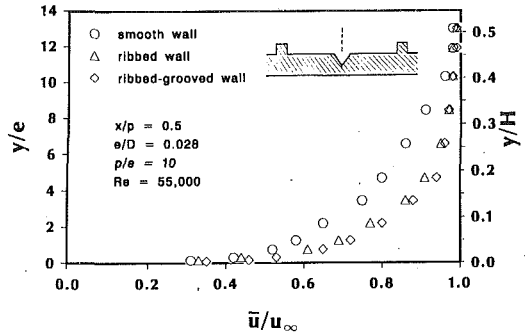

Fig. 3 Velocity profiles for smooth, ribbed, and ribbed-grooved ducts

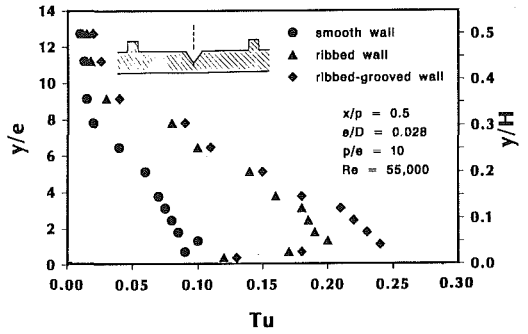

Fig. 4 Turbulence intensity profiles in the *y* direction for smooth, ribbed, and ribbed-grooved ducts

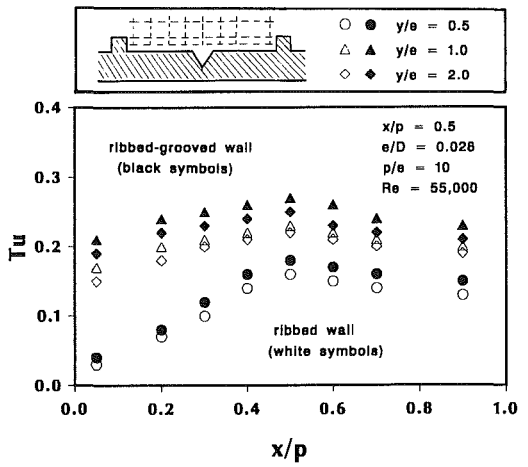

Fig. 5 Turbulence intensity profiles in the *x* direction for ribbed wall and ribbed-grooved wall at $y/e = 0.5$, 1.0, and 2.0

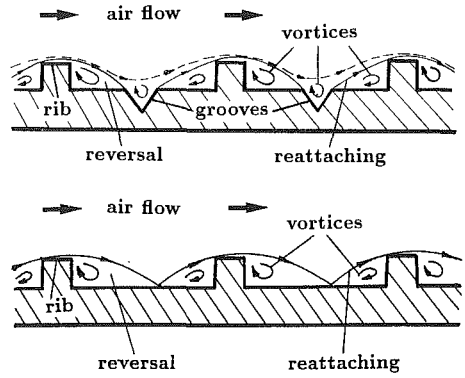

Fig. 6 Conceptual flow pattern in channel with ribbed-grooved wall or ribbed wall

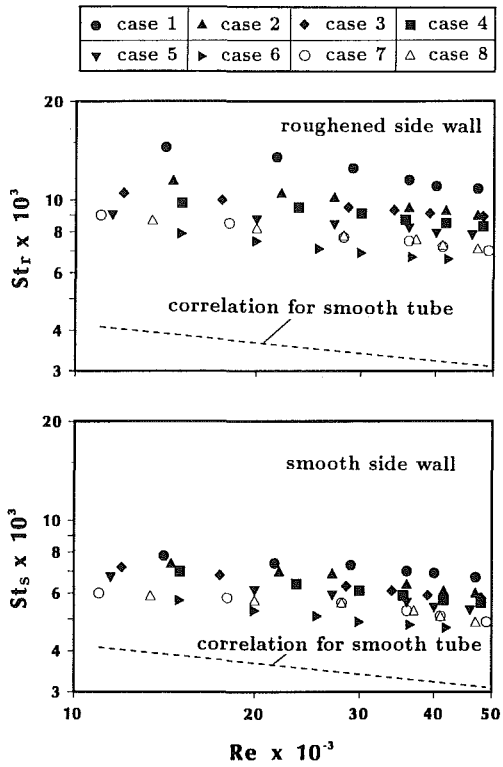

Fig. 7 Stanton number versus Reynolds number for six rib-groove and two rib configurations studied

wall than for the smooth wall. The strongest turbulence intensities were produced in the $y/e = 1$ region for the three different wall conditions. The turbulence intensity for the ribbed-grooved wall is higher than the ribbed wall and subsequently higher than the smooth wall. The turbulence intensities for the ribbed and ribbed-grooved walls in the $1 < y/e < 10$ region are much higher than the smooth wall. The effects of the rib and rib-groove disappear after $y/e > 10$ and the turbulence intensities are about the same for the three different wall conditions.

Figure 5 shows the turbulence intensity distributions in the flow direction for both ribbed and ribbed-grooved walls ($P/e = 10$, $e/D = 0.028$). The turbulence intensities were measured between two ribs ($0 < x/p < 1$) on three levels of $y/e = 0.5$, 1.0, and 2.0 with $\mathrm{Re} = 55{,}000$. The results show that the turbulence increases behind the rib and reaches the maximum value near the midplane between the ribs ($x/p \approx 0.5$) and then decreases slightly before approaching the next rib. The turbulence is larger for the ribbed-grooved wall than for the ribbed wall, with the strongest turbulences produced at $y/e = 1$. Figure 6 shows a conceptual view of flow separation from the rib, reattachment on the wall, and vortices generated from the rib and groove. The additional vortices created by the grooves are responsible for the higher turbulence in the ribbed-grooved wall. This rib-groove generated high turbulence will produce a higher surface heat transfer than the ribbed wall.

Heat Transfer and Pressure Drop. Figure 7 shows the Stanton number (roughened side walls or smooth side walls) versus Reynolds number for the ribbed (cases 7 and 8) and ribbed-grooved channels (cases 1 to 6). Please refer to Table 1 for the legend of case numbers. The roughened side wall Stanton numbers are the average value of the two opposite ribbed-grooved side wall (or ribbed side wall) Stanton numbers in the fully developed region (total of 12 thermocouples at 40, 60, and 80

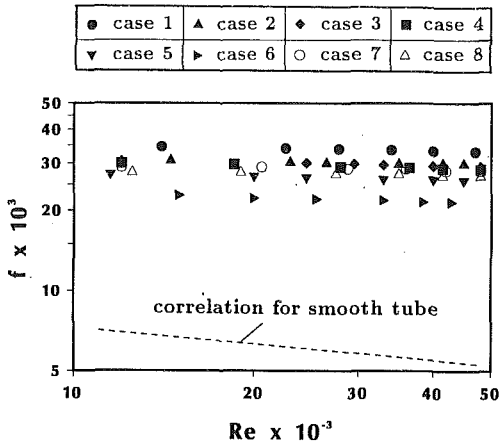

Fig. 8 Friction factor versus Reynolds number for six rib-groove and two rib configurations

percent of the duct length). Similarly, the smooth side wall Stanton numbers are the average value of the two opposite smooth side wall Stanton numbers in the fully developed region. The Stanton number correlation for fully developed turbulent flow in smooth circular tubes is also included for comparison. The results show that, as expected, the Stanton number decreases slightly with increasing Reynolds number. The ribbed-grooved wall provides higher Stanton numbers than the ribbed wall over the range of Reynolds numbers studied. The ribbed-grooved wall with $p/e = 8$ (case 1) provides the highest heat transfer coefficients. The Stanton numbers decrease with increasing p/e ratio ratio (see Table 1). The ribbed-grooved wall with $p/e = 30$ gives the lowest heat transfer coefficients (case 6). The corresponding smooth side wall Stanton numbers are higher for the ribbed-grooved ducts than those for the ribbed ducts. The smooth side wall Stanton numbers also decrease with increasing p/e ratio.

Figure 8 compares the friction factor for two ribbed ducts and six ribbed-grooved ducts (see Table 1 for the legend). The pressure drops across the test channel are measured at the unheated flow conditions. The friction factor correlation for fully developed turbulent flow in smooth circular tubes is also included for comparison. The results show that the friction factors stay almost at constant values with increasing Reynolds numbers. The ribbed-grooved duct with $p/e = 8$ (case 1) produces the highest friction factors over the range of Reynolds numbers studied. The friction factors decrease with increasing p/e ratio from 8 to 30. The friction factors for the ribbed-grooved ducts are compatible with the ribbed ducts.

Heat Transfer Performance Comparison. Figure 9 shows the Stanton number ratio of the roughened side wall or the smooth side wall versus the friction factor ratio for the ribbed and ribbed-grooved ducts over a range of Reynolds numbers between 12,000 and 48,000. The results show that, in general, the Stanton number ratio (heat transfer augmentation) increases with an increase in the friction factor ratio (pressure drop increment). The Stanton numbers for the ribbed-grooved walls (Cases 1 and 2) are higher than for the ribbed walls (Cases 7 and 8) at similar p/e values. The St/St_o ratios for the ribbed-grooved ducts decrease with an increase in the p/e ratio. The ribbed-grooved duct with $p/e = 8$ (Case 1) provides the highest heat transfer augmentation and a comparable pressure drop penalty. In the ribbed-grooved ducts, the St_r/St_o ratio is insensitive to Reynolds numbers but the f/f_o ratio increases with an increase in Reynolds numbers. The ribbed-grooved wall with $p/e = 8$ (Case 1) provides 3.4 times the heat transfer augmentation with 5.7 to 7.1 times the pressure drop penalty, whereas the rib roughened wall (Case 7), with similar rib height

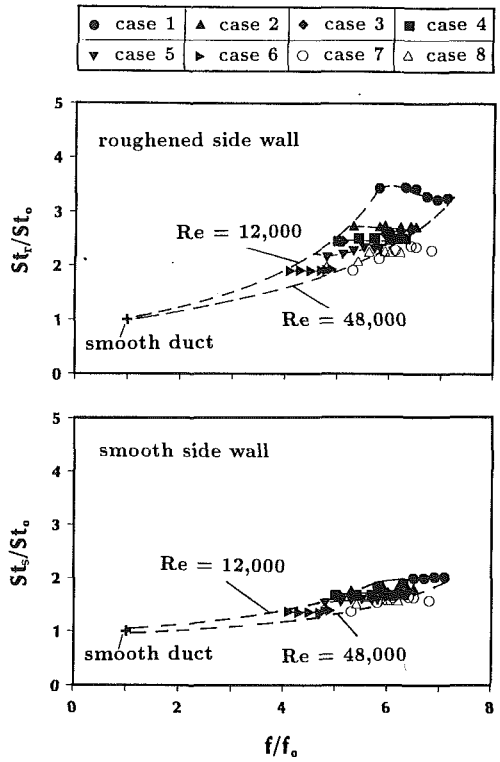

Fig. 9 Stanton number ratio versus friction factor ratio for six rib-groove and two rib configurations

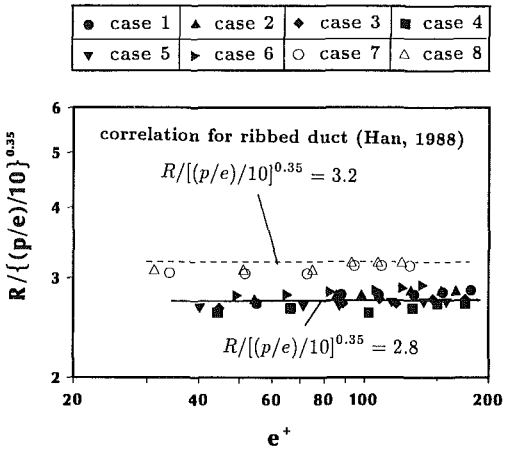

Fig. 10 Friction factor correlation

and rib spacing, enhances the heat transfer 2.4 times and pays about the same pressure drop penalty. The heat transfer enhancement is about 1.9 to 2.8 times with 4.1 to 6.4 times the pressure drop penalty for ribbed-grooved ducts with $p/e = 10$–30 (Cases 2–6). The smooth side wall heat transfer enhancements for the ribbed-grooved ducts are slightly higher than that for the ribbed ducts at similar p/e values.

Heat Transfer and Friction Correlations. Figure 10 shows the friction roughness function R, versus the roughness Reynolds number, e^+, for the ribbed-grooved and ribbed ducts for a range of studied Reynolds numbers (see Table 1 for legend). The wall similarities based on the roughened channel analysis discussed earlier were employed to correlate the friction and heat transfer data for fully developed turbulent flow in rectangular channels with two opposite ribbed-grooved or ribbed walls. According to the friction similarity law derived in Eqs. (12) and (15), the measured friction factor f, the channel aspect

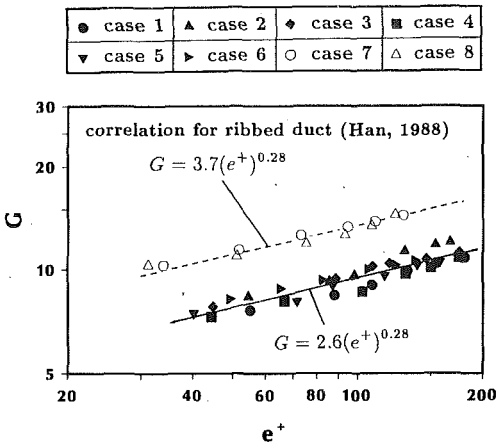

Fig. 11 Heat transfer correlation

ratio W/H, the rib height (or groove depth) to hydraulic diameter ratio e/D, and the Reynolds number could be correlated with the friction roughness function R. Figure 10 shows that the present friction results for the ribbed walls (ribs only, no grooves, Cases 7 and 8) compare well with the previous correlation by Han (1988) for the ribbed ducts (broken line in Fig. 10). This implies that the present friction factors for the ribbed ducts (ribs only, no grooves, cases 7 and 8) are reliable. Therefore, the data for the ribbed-grooved ducts (cases 1–6) should be reliable, too. The present friction results for the ribbed-grooved walls (Cases 1–6) were correlated using equations (12) and (15). The effect of P/e ratio on the friction roughness function R for the ribbed-grooved duct (solid line in Fig. 10) can be written as:

$$R = 2.8[(p/e)/10]^{0.35} \tag{16}$$

Equation (16) is valid for $e^+ \geq 40$, $8 \leq p/e \leq 30$, and $10{,}000 \leq \mathrm{Re} \leq 50{,}000$. The deviation of Eq. (16) is ± 5 percent. After R is experimentally correlated from Eq. (16), the ribbed-grooved duct friction factor f can be predicted by Eq. (12) and Eqs. (14) and (15) for a given e/D, p/e, W/H, and Re. Note that R in Eq. (16) is independent of e^+. This implies that the friction factor is almost independent of the Reynolds number (see Fig. 8, i.e., in the fully rough region with $e^+ \geq 40$).

Figure 11 shows the heat transfer roughness function $G(e^+)$ versus the roughness Reynolds number e^+ for the ribbed-grooved and ribbed ducts for the range of studied Reynolds numbers (see Table 1 for the legend). According to the heat transfer similarity law derived in Eqs. (12)–(15), the measured Stanton number on the ribbed-grooved wall St_r, the friction factor f, and the friction roughness function R could be correlated with the heat transfer roughness function $G(e^+)$. The heat transfer roughness function $G(e^+)$ for all studied rib and rib-groove configurations increases with an increase in the roughness Reynolds number e^+. The heat transfer roughness function for the present ribbed wall (ribs only, no grooves, cases 7 and 8) is about the same as the previous correlation developed by Han (1988) for the ribbed ducts (broken line in Fig. 11). Again, this implies that the present heat transfer coefficients for the ribbed ducts (ribs only, no grooves, cases 7 and 8) are reliable. So, the data for the ribbed-grooved ducts (cases 1–6) should also be reliable. The present heat transfer results for the ribbed-grooved walls (Cases 1–6) were correlated using Eqs. (12)–(15). The correlation of the heat transfer roughness function $G(e^+)$ for the ribbed-grooved duct (solid line in Fig. 11) for air ($\mathrm{Pr} = 0.71$) can be written as:

$$G(e^+) = 2.6(e^+)^{0.28} \tag{17}$$

Equation (17) is valid for $e^+ \geq 40$, $8 \leq p/e \leq 30$, and $10{,}000 \leq \mathrm{Re} \leq 50{,}000$. The deviation of Eq. (17) is ± 5 percent. After $G(e^+)$ is experimentally correlated from Eq. (17), the ribbed-grooved wall Stanton number St_r for a given e/D, p/e, W/H, and Re can be predicted by Eqs. (12)–(15). Note that Fig. 11 shows the G values for the ribbed-grooved ducts (cases 1–6) are lower than those for the ribbed only ducts (cases 7 and 8). According to Eq. (13), the lower G values have the higher heat transfer coefficients (St_r) for turbulent flow in rough channels. For example, the Stanton number St_r calculated from these correlations for the ribbed-grooved duct with $P/e = 10$, $e/D = 0.028$, and $\mathrm{Re} = 10{,}000$ is 36 percent higher than that for the ribbed only duct with the same P/e, e/D, and Re. This further verifies that the heat transfer coefficients for the ribbed-grooved ducts are higher than those for the ribbed only ducts at the same roughness height and pitch (P/e, e/D) and Reynolds number conditions.

Concluding Remarks

The effect of compound turbulators on friction factors and heat transfer coefficients in rectangular channels with two opposite ribbed-grooved or ribbed walls have been investigated. The measurements of the velocity and turbulence distributions also have been performed. The main findings of the study are:

1 The ribbed-grooved or ribbed duct with the same Reynolds number flow produce a much flatter velocity profile than the smooth duct. For the same Reynolds number flow and similar rib e/D and p/e ratio, the ribbed-grooved duct generates a relatively higher turbulence intensity than the ribbed duct. The turbulence intensity has the highest value at one rib height from the wall and at the midplane between two adjacent ribs. The flatter velocity profile and higher turbulence intensity are responsible for producing higher heat transfer enhancement and larger pressure drop penalty.

2 The heat transfer coefficient and friction factor values in the ribbed-grooved ducts are higher than those in the ribbed ducts for similar rib height and spacing. The Stanton number and friction factor values for ribbed-grooved ducts decrease with an increase in the value of the rib-groove pitch-to-rib height (p/e). The ribbed-grooved duct with $p/e = 8$ provides the highest heat transfer augmentation and largest pressure drop penalty compared to other larger p/e cases.

3 For similar rib height and spacing, the rough side of the ribbed-grooved duct enhances heat transfer 3.4 times while the rough side of the ribbed duct enhances heat transfer 2.4 times. The smooth side of the ribbed-grooved duct enhances heat transfer by 2 times and the smooth side of the ribbed duct enhances heat transfer 1.7 times. Both the ribbed-grooved and ribbed duct pay about the same 6 times the pressure drop penalty.

4 Based on the ribbed channel analysis, semi-empirical friction and heat transfer correlations have been obtained for the rectangular channel with two opposite ribbed-grooved walls. The correlations are valid for $e^+ > 40$ and $8 \leq p/e \leq 30$.

Acknowledgments

The project was sponsored by the China National Science Foundation and performed at the Institute of Engineering Thermophysics, Chinese Academy of Sciences, Beijing, People's Republic of China.

References

Boyle, R. J., 1984, "Heat Transfer in Serpentine Passages With Turbulence Promoters," ASME Paper No. 84-HT-24.

Burggraf, F., 1970, "Experimental Heat Transfer and Pressure Drop With Two-Dimensional Turbulence Promoter Applied to Two Opposite Walls of a Square Tube," *Augmentation of Convection Heat and Mass Transfer*, A. E. Bergles and R. L. Webb, eds., ASME, New York, pp. 70–79.

Dalle Donne M., and Meyer, L., 1977, "Turbulent Convective Heat Transfer From Rough Surfaces With Two-Dimensional Rectangular Ribs," *International Journal of Heat and Mass Transfer*, Vol. 20, pp. 582–620.

Gee, D. L., and Webb, R. L., 1980, "Forced Convective Heat Transfer in Helically Rib-Roughened Tubes," *International Journal of Heat and Mass Transfer*, Vol. 23, pp. 1127–1136.

Han, J. C., Glicksman, L. R., and Rohsenow, W. M., 1978, "An Investigation of Heat Transfer and Friction for Rib-Roughened Surfaces," *International Journal of Heat and Mass Transfer*, Vol. 21, pp. 1143–1156.

Han, J. C., 1984, "Heat Transfer and Friction in Channels With Two Opposite Rib-Roughened Walls," ASME JOURNAL OF HEAT TRANSFER, Vol. 106, pp. 774–781.

Han, J. C., and Park, J. S., 1988, "Developing Heat Transfer in Rectangular Channels With Rib Turbulators," *International Journal of Heat and Mass Transfer*, Vol. 31, pp. 183–195.

Han, J. C., 1988, "Heat Transfer and Friction Characteristics in Rectangular Channels With Rib Turbulators," ASME JOURNAL OF HEAT TRANSFER, Vol. 110, No. 2, pp. 321–328.

Han, J. C., Ou, S., Park, J. S., and Lei, C. K., 1989, "Augmented Heat Transfer in Rectangular Channels of Narrow Aspect Ratios With Rib Turbulators," *International Journal of Heat and Mass Transfer*, Vol. 32, No. 9, pp. 1619–1630.

Han, J. C., Zhang, Y. M., and Lee, C. P., 1991, "Augmented Heat Transfer in Square Channels With Parallel, Crossed and V-Shaped Angled Ribs," ASME JOURNAL OF HEAT TRANSFER, Vol. 113, pp. 590–596.

Han, J. C., and Zhang, Y. M., 1992, "High Performance Heat Transfer Ducts With Parallel Broken and V-Shaped Broken Ribs," *International Journal of Heat and Mass Transfer*, Vol. 35, pp. 513–523.

Kline, S. J., and McClintock, F. A., 1953, "Describing Uncertainties in Single-Sample Experiments," *Mechanical Engineering*, Vol. 75, Jan., pp. 3–8.

Liou, T. M. and Hwang, J. J., 1992, "Turbulent Heat Transfer Augmentation and Friction in Periodic Fully Developed Channel Flows," ASME JOURNAL OF HEAT TRANSFER, Vol. 114, pp. 56–64.

Metzger, D. E., and Vedula, R. P., 1987, "Heat Transfer in Triangular Channels With Angled Roughness Ribs on Two Walls," *Experimental Heat Transfer*, Vol. 1, pp. 31–44.

Meyer, L., 1982, "Thermohydraulic Characteristics of Single Rods With Three-Dimensional Roughness," *International Journal of Heat and Mass Transfer*, Vol. 25, pp. 1043–1058.

Roeller, P. T., Stevens, J., and Webb, B. W., 1991, "Heat Transfer and Turbulent Flow Characteristics of Isolated Three-Dimensional Protrusions in Channels," ASME JOURNAL OF HEAT TRANSFER, Vol. 113, pp. 597–603.

Sethumadhaven, R., and Raja Rao, M., 1983, "Turbulent Flow Heat Transfer and Fluid Friction in Helical-Wire-Coil-Inserted Tubes," *International Journal of Heat and Mass Transfer*, Vol. 26, pp. 1833–1844.

Taslim, M. E., and Spring, S. D., 1987, "Friction Factors and Heat Transfer Coefficients in Turbulated Cooling Passages of Different Aspect Ratios, Part I: Experimental Results," 23rd AIAA/ASME/SAE Conference, Paper No. AIAA-87-2009.

Taslim, M. E., and Spring, S. D., 1991, "An Experimental Investigation Into the Effects Turbulator Profile and Spacing Have on Heat Transfer Coefficients and Friction Factors in Small Cooled Turbine Airfoils," 27th AIAA/ASME/SAE Conference, Paper No. AIAA-91-2033.

Webb, R. L. Eckert, E. R. G., and Goldstein, R. J., 1971, "Heat Transfer and Friction in Tubes With Repeated-Rib Roughness," *International Journal of Heat and Mass Transfer*, Vol. 14, pp. 601–617.

Zhang, Y. M., Gu, W. Z., and Xu, H. Q., 1984, "Enhancement of Heat Transfer and Flow Characteristics in Rib Roughened Rectangular Channels," *Journal of Engineering Thermophysics*, Vol. 5, No. 3, pp. 275–280.

Local Heat Transfer in Enclosed Co-rotating Disks With Axial Throughflow

S. Y. Kim

J. C. Han

G. L. Morrison

Turbine Heat Tranfser Laboratory,
Department of Mechanical Engineering,
Texas A&M University,
College Station, TX 77843

E. Elovic

General Electric Company, GEAE,
Cincinnati, OH 45215

Local heat transfer in enclosed co-rotating disks with axial throughflow is investigated. The rotating cavity has two plane disks and a cylindrical rim (shroud). The ratio of the rim span to the disk outer radius is 0.4 and the ratio of the disk inner radius to outer radius is 0.25. The objectives of this study are to investigate the effects of axial coolant flow rate, rotation speed, and disk surface temperature on the local heat transfer coefficients inside the disk cavity. Both uniform disk surface heat flux and uniform disk surface temperatures are tested for axial flow Reynolds numbers between 2500 and 25,000 rotational Reynolds numbers between 0 and 5.11 $\times$ 10^5, and rotational Grashof numbers between 5 $\times$ 10^6 and 1.3 $\times$ 10^{10}. The results show that the local heat transfer coefficients for the nonrotating cavity increase with increasing axial flow Reynolds number. In general, the local Nusselt numbers at large radii of the disks and rim increase with increasing rotational Reynolds number. However, the local Nusselt numbers at small radii of the disks initially decrease and then increase with increasing rotational Reynolds number. The uniform heat flux condition provides slightly higher heat transfer coefficients than those for the uniform wall temperature condition.

Introduction

Advanced aero-engines operate at high compression ratios and high turbine entry gas temperatures, which provide high thermal efficiency and power density. The trend in compressor design is toward high pressure ratio (30–40) that results in high exit temperatures (550–650°C). The engine designer needs to predict accurately the transient temperature distribution of the compressor disk and casing in order to estimate the thermal growth and fatigue life of compressor disks, rotor and casing clearances for the whole flight cycle. Similarly, the trend in turbine design is toward high entry gas temperature (1400–1500°C), which is well above the allowable metal temperature. Therefore, highly sophisticated and efficient cooling technologies such as film, impingement, or rib/pin turbulator cooling are employed for vanes and blades of advanced gas turbines. Careful design of rotor-casing clearances is required to achieve the high efficiencies of modern turbines. A procedure similar to that of the compressor is necessary, i.e., detailed transient thermal analysis throughout the flight cycle for the turbine disk and casing.

In order to estimate the thermal growth and fatigue life of turbine and compressor disks, the gas turbine designer needs to calculate their temperatures. Thus an accurate knowledge of the distributions of the local heat transfer coefficient in rotating disks is particularly important. The ability to predict disk cavity temperatures accurately offers the cooling flow designer important benefits. The designer knows that too little flow results in hotter disk cavity temperatures and reduced component life while too much flow results in reduced engine performance. A balance can be achieved between component life and engine performance by accurately estimating disk cavity temperatures.

The rotating disk geometry in a real engine is complicated (see Fig. 1). The essential features of compressor disks and cavities with net zero radial flow can be modeled like those in Fig. 2. A rotating cylindrical cavity with axial throughflow

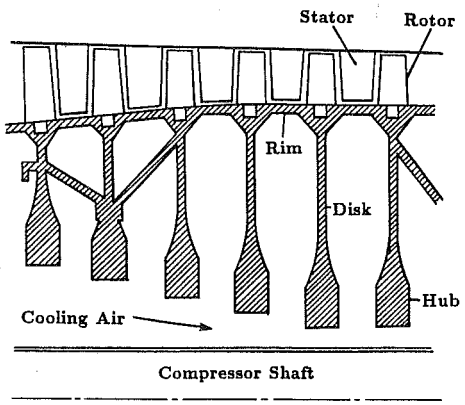

Fig. 1 Sketch of typical compressor disks and cavities with zero net radial flow

(Fig. 2) is a simplified representation of two co-rotating compressor disks where cooling air passes axially through a central hole (or annulus if a central shaft is used). The axial throughflow of cooling air induces secondary flow inside the cavity between adjacent disks and, under rotation conditions, this flow can be greatly affected by the temperature difference between the disks and coolant. The main parameters that affect the distributions of the local heat transfer coefficient are coolant flow rate, disk temperature, rotation speed, and cavity configuration.

Farthing et al. (1992a, 1992b) studied the local heat transfer and flow structure in rotating cavities with axial throughflow of cooling air. Flow visualization and laser-Doppler anemometry were used to study the flow structure inside isothermal and heated rotating cavities for a range of axial-gap ratios, axial Reynolds numbers, rotational Reynolds numbers, and cavity temperature distributions. Local heat transfer on the upstream and downstream disks were measured in two rotating cavity rigs in which cooling air passed axially through the center of the disks for a range of flows, rotational speeds, and temperature distributions. The distributions of local Nusselt num-

Contributed by the Heat Transfer Division for publication in the JOURNAL OF HEAT TRANSFER. Manuscript received by the Heat Transfer Division June 1992; revision received May 1993. Keywords: Compressors and Pumps, Enclosure Flows, Rotating Flows. Associate Technical Editor: R. J. Simoneau.

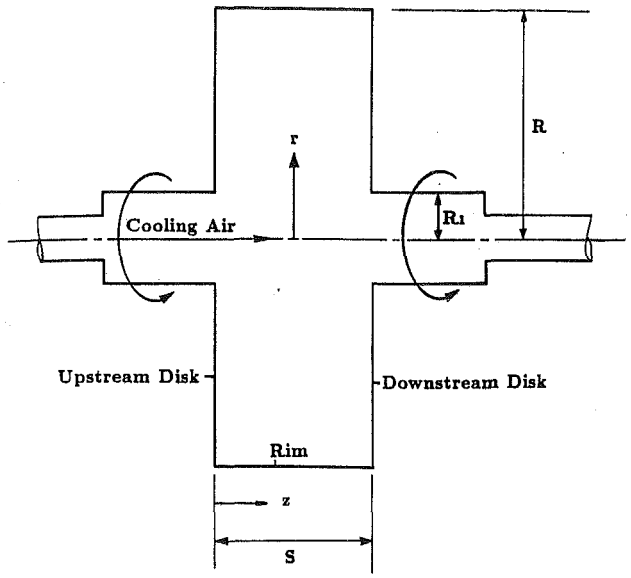

Fig. 2 Sketch of rotating cylindrical cavity

bers were similar for both the upstream and downstream disks for the case of a symmetrically heated cavity. For an asymmetrically heated cavity (one disk is hotter than the other), the local Nusselt numbers on the hotter disk were similar to those in the symmetrically heated cavity but greater in magnitude than those on the colder disk. The local Nusselt numbers increased radially for the case of radially increasing temperature distribution. However, there were no heat transfer measurements on the rim (shroud) of the rotating cavity because it was unheated and insulated during the heat transfer experiments.

Long and Tucker (1992) studied the rim heat transfer with heated or unheated disks. The heat transfer coefficients were determined based on the measured air temperature inside the cavity instead of at the inlet of the cavity as used by Farthing et al. (1992a). The results indicated that the heat transfer coefficient from the rim was slightly affected by the disk temperature. Heating the rim did not significantly affect the local heat transfer coefficient from the disks.

This study focuses on the effects of axial flow Reynolds numbers, rotational Reynolds numbers, and surface heating conditions on the distributions of the local heat transfer coefficient in enclosed co-rotating disks with axial throughflow. The disk geometry and operating conditions of the study are: (1) the ratio of inner radius to outer radius of disks, $R1/R$ = 0.25; (2) the ratio of axial distance between disks to outer radius of disks, $G = S/R = 0.4$; (3) axial Reynolds number, Re_z = 2500 ~ 25,000; (4) rotational (tangential) Reynolds number, $\mathrm{Re}_t = 0 \sim 5.11 \times 10^5$; (5) rotation number, Ro = 0.84 ~ 25.1; (6) rotational Grashof number, $\mathrm{Gr}_y = 1.8 \times 10^6 \sim 2.2 \times 10^{10}$; and (7) surface heating condition, uniform surface heat flux, and uniform surface temperature, respectively. It should be noted that the typical ranges of these parameters in gas turbine engines are: $0.2 < R1/R < 0.6$; $0.2 < G < 0.6$; $10^4 < \mathrm{Re}_z < 10^5$; $10^5 < \mathrm{Re}_t < 10^7$; $1.0 < Ro < 50$; and $10^{11} < \mathrm{Gr}_y < 10^{13}$.

This paper is part of the results from the research program "Local Heat Transfer in a Rotating Cavity With Axial Throughflow" (Kim, 1992). The results for uniform surface heat flux (case A) and uniform surface temperature (case B) are presented in this paper. Additional information related to this study may be found in Kim et al. (1993) for case 1—upstream and downstream disks with radially increasing temperature but lower than rim, and case 2—upstream and downstream disks at uniform temperature but lower than rim, and in Kim and Han (1993) for BC1—upstream disk colder than downstream disk and rim, and BC 2—downstream disk colder than upstream disk and rim.

Test Facility and Instrumentation

Rotating Rig. Figure 3 shows a schematic of the rotating rig. The hollow rotating shaft is driven by a 25-hp (18.6 kW) AC motor with a toothed belt drive pulley system through a frequency-controlled motor controller with a maximum rotating speed of 3400 rpm. The rotation speed is measured by a digital photo tachometer. The rotating speed for this study varies up to 1200 rpm. The rotating shaft and supporting bearing system are horizontally mounted on a rigid, heavy steel table. The rotating cavity is connected perpendicularly to the rotating shaft. The regulated compressor air is routed through an orifice meter to the entrance (upstream) of the hollow ro-

Nomenclature

A = copper ring or copper rim surface area
A_s = total surface area of the cavity rim = $2\pi RS$
D = disk bore diameter = $2R1$
G = gap ratio = S/R
Gr_L = rim Grashof number = $\beta\Delta T\Omega^2 RL^3/\nu^2$
Gr_y = modified disk Grashof number = $\Omega^2 r y^3 \beta\Delta T/\nu^2$
h = local heat transfer coefficient
$\bar{h}$ = area-averaged heat transfer coefficient
k = thermal conductivity of air
L = characteristic length of the rim = $A_s/P = S/2$
Nu = local Nusselt number = $q_s'' r/k(T_w - T_i) = hr/k$
Nu_L = modified rim Nusselt number = $q_s'' L/k(T_w - T_i) = hL/k$
Nu_y = modified local Nusselt number = $q_s'' y/k(T_w - T_i) = hy/k$
$\overline{\mathrm{Nu}}$ = area-averaged Nusselt number = $\bar{h}R/k$
P = perimeter of the rim = $2\pi D$
Pr = Prandtl number
q_{net} = local net heat transfer rate
q_s'' = local net heat flux = q_{net}/A
r = radial coordinate
R = outer radius of disk
$R1$ = inner radius of disk
Ro = rotation number = $\Omega R1/V_z$
Re_t = rotational (tangential) Reynolds number = $\Omega R^2/\nu$
Re_z = axial Reynolds number = $V_z D/\nu$
S = axial distance between disks
T_i = air inlet temperature
T_w = local disk or rim surface temperature
$T_{w,\max}$ = maximum disk or rim surface temperature
ΔT = local temperature difference between disk or rim surface and inlet air = $T_w - T_i$
V_z = axial flow velocity
Z = axial coordinate along the rim
y = radially inward distance measured from the rim (shroud)
β = coefficient of volumetric thermal expansion
θ = nondimensional surface temperature = $(T_w - T_i)/(T_{w,\max} - T_i)$
μ = dynamic viscosity
ν = kinematic viscosity
ρ = fluid mass density
Ω = angular speed of rotating disk

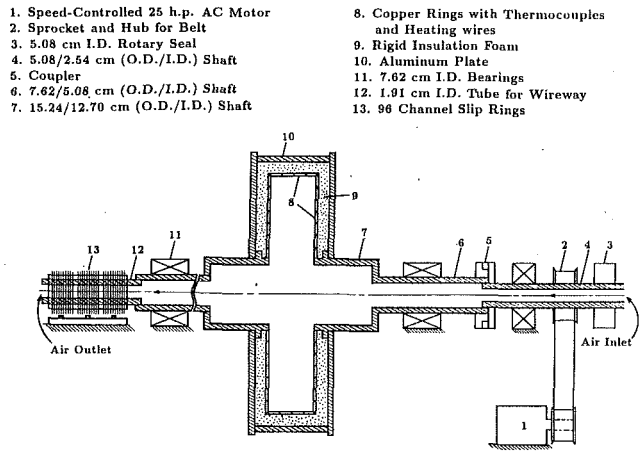

Fig. 3 Schematic of the rotating test rig

tating shaft through a rotary seal. The coolant flows through the rotating cavity and is exhausted into the atmosphere at the exit (downstream) of the hollow rotating shaft. The slip ring systems are attached to the exit portion of the hollow rotating shaft. A 96 contact slip ring transfers outputs to the stationary data acquisition systems from heaters and thermocouples attached to the rotating cavity.

Test Section Instrumentation. The rotating cavity consists of two plane disks and a cylindrical rim (shroud). The plane disk has a 5 in. (12.55 cm) inner diameter (bore) and a 20 in. (50.2 cm) outer diameter. The cylindrical rim has a 4 in. (10.04 cm) width between the two disks (i.e., the S/R ratio = 0.4 and the $R1/R$ ratio = 0.25). This study uses the stepped hollow shafts to drive the rotating cavity and simulate a larger disk bore-to-outer diameter ratio ($R1/R$ = 0.25) as shown in Fig. 3. To understand heat transfer behaviors for rotating cavity thermal design it is better to have a test section that can determine the local heat transfer coefficients on the upstream and downstream disks and the rim of the entire rotating cavity. Figure 4 shows the dimensions of the upstream (or downstream) disk and the stretched rim (shroud). The disks and rim are composed of copper rings, rigid urethane foam, and aluminum plate. The inner wall of each disk contains seven pieces of copper ring with a dimension of 1/8 in. (0.315 cm) thickness and 15/16 in. (2.36 cm) width. The rim is fabricated the same as the disks. The inner wall of the rim contains four pieces of copper ring that have a 1/8 in. (0.315 cm) thickness, 15/16 in. (2.36 cm) width and a 20 in. (50.4 cm) inner diameter. The total weight of the rotating cavity (test section) is about 150 pounds (68 kg). Note that the resistance heating wires are uniformly cemented between the copper ring (or copper rim) backface grooves and the urethane foam to ensure good contact. Each of the copper rings (or copper rim) has its own resistance wires with an independently controlled variac transformer to provide a controllable surface heat flux (or surface temperature). A 1/16 in. (0.158 cm) thick insulation material (model clay) is inserted between every two copper rings (or copper rims) to reduce heat conduction. The cylindrical rim is isolated from the plane disk by 1/16 in. (0.158 cm) thick, rigid urethane foam to reduce heat conduction. The entire heated test section is insulated by 1 in. (2.52 cm) thick, rigid urethane foam placed between the copper rings (or copper rims) and the outer aluminum casing.

The slip ring system has 96 channels (points) for heating and thermocouple wires. Thirty-six channels transfer the output from 18 thermocouples attached to the 18 rings/rims (i.e., each ring/rim with one thermocouple at the same angular position (see Fig. 4)) to a data logger interfaced to a 386 PC computer. Four channels measure the inlet and outlet coolant

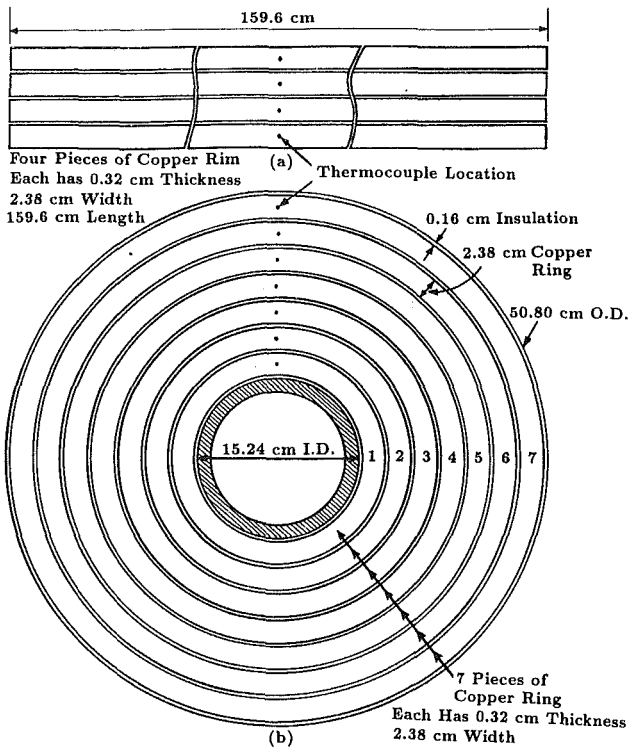

Fig. 4 Sketch of disk dimensions: (*a*) stretched rim, (*b*) upstream or downstream disk surface

temperature from the rotating cavity and an additional 36 channels transfer the output from heating wires individually attached to the 18 rings/rims (i.e., each ring/rim with two channels) to a 36 point variac transformer connected with digital multimeters. The local wall (or coolant) temperature and heating power (voltage drop and current) are measured through these slip ring assemblies and the associated meters. The temperature of the air inside the rotating cavity is not measured.

Data Analysis. The local heat transfer coefficient (h) is calculated from the local net heat transfer rate (q_{net}) per copper ring or rim surface area (A) to the cooling air, the local wall temperature (T_w) on each copper ring or rim, and the inlet cooling air temperature (T_i) as:

$$h = (q_{net})/[A(T_w - T_i)] \quad (1)$$

Equation (1) is used for the upstream and downstream disks and rim surface heat transfer coefficient calculations. The local net heat transfer rate is the electrical power generated from the heater minus the local heat loss from each copper ring or rim. The electrical power generated from the heater is determined from the measured heater resistance and voltage on each ring or rim of the cavity. The effect of the local wall temperature variation on the local heater resistance is estimated to be less than 2 percent but is included in the data reduction. The effect of radial wall conduction between copper rings on the local net heat transfer rate is less than 2 percent but is also included in the data analysis. Heat loss tests are performed to determine the total heat loss from each of the copper ring or rim walls for a no-flow condition (with rotation but without coolant flow). The heat loss calibration is performed by supplying power to each copper ring or rim for steady state. This is done for several different power inputs to obtain the relation between the total heat loss from each copper ring or rim surface and the corresponding surface temperature. The heat loss calibration is performed for two different thermal conditions (case A—uniform surface heat flux, and case B—uniform surface

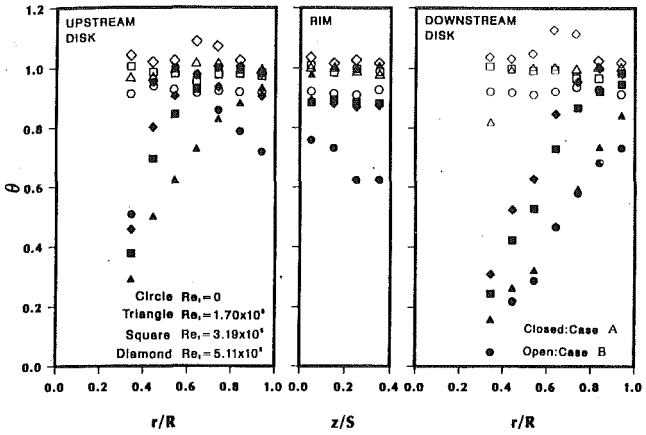

Fig. 5 Dimensionless temperature distribution in a rotating cavity for cases A and B at Re_z = 25,000

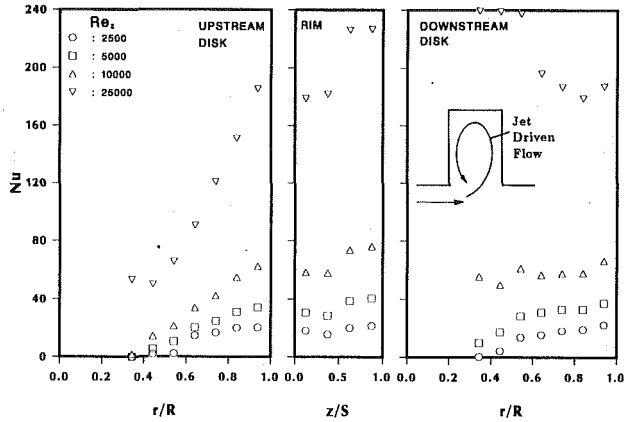

Fig. 6 Effect of axial Reynolds number on the local Nusselt number distribution for case A at Re_t = 0

temperature) and four rotation speeds (0, 400, 750, and 1200 rpm), respectively. It should be noted that experimentally determined heat loss for each copper ring or rim in case A—uniform surface heat flux condition (i.e., nonuniform surface temperature)—includes convection loss to the test section outer surface due to rotation, radiation loss to the test section outer surface, and radiation loss among the copper rings or rims inside the cavity. The amount of heat loss from the copper ring or rim varies from 100 W/m^2 to 900 W/m^2 depending on the rotating speed and surface temperature.

The local wall temperatures used in Eq. (1) are read from the thermocouple output of each copper ring and rim. The inlet cooling air temperature is measured by a single thermocouple (about 25°C). Figure 5 shows the dimensionless surface temperature distribution, $\theta = (T_w - T_i)/(T_{w,\max} - T_i)$, for case A and B conditions and four rotational Reynolds numbers at an axial Reynolds number of 25,000. The results show that the θ for case A varies from 0.2 at the disk inner radius to 0.9 near the disk outer radius for upstream and downstream disks but stays at about 1.0 for the rim. Case B is about 1.0 for θ at the upstream and downstream disks and rim.

The local heat transfer coefficient calculated from Eq. (1) is converted into the dimensionless local Nusselt number (Nu = hr/k for the disk, Nu = hR/k for the rim). The properties in the Nusselt and Reynolds numbers are evaluated at the average of the inlet and outlet coolant temperatures. The uncertainty of the local heat transfer coefficient is affected by the local wall-to-coolant temperature difference ($T_w - T_i$) and the net heat input to the coolant flow from each heated copper ring. The uncertainty of the local heat transfer coefficient increases when decreasing ($T_w - T_i$) and the net heat input. The uncertainty also increases for low heat inputs such as at low Reynolds numbers. Based on the method described by Kline and McClintock (1953), the typical uncertainty in the Nusselt number is estimated to be less than 8 percent for Reynolds numbers larger than 10,000. The maximum uncertainty, however, could be up to 20–25 percent for the lowest heat transfer coefficient near the upstream disk entrance of the cavity at the lowest Reynolds numbers tested.

Test Results and Discussions

Effect of Axial Reynolds Number

Nonrotating Cavity. The local heat transfer results (per copper ring) for the upstream and downstream disks are presented as the radial distributions of the Nusselt number (Nu versus r/R), whereas the results of the rim are presented as the axial distributions (Nu versus z/S). Figure 6 shows the effect of axial Reynolds numbers on the local Nusselt number distributions of the upstream disk (left figure), downstream disk (right figure), and rim or shroud (middle figure) for the uniform wall heat flux condition (case A) for the nonrotating cavity (Re_t = 0). Note that the Nusselt number is defined as Nu = hr/k where r varies from the first ring to the seventh ring for the upstream and downstream disks and equals R for the rim. The results show that (1) the local Nusselt number in the cavity increases with increasing axial Reynolds number; (2) the Nusselt number on the upstream disk increases with r/R ratio; (3) the Nusselt number on the downstream disk increases with r/R except for the higher axial Reynolds number; and (4) the Nusselt number reaches the high value near the downstream portion of the rim for a given axial Reynolds number. This may be because the cooling air moves into the cavity from the axial throughflow and causes flow circulation in the cavity. Because of the cavity configuration, the cooling air moves into the cavity from the entrance of the downstream disk toward the rim and then flows along the upstream disk back to the axial mainstream. Based on this cavity flow path, the Nusselt number has a high value at the downstream disk, the rim, and the upstream disk large radii, respectively. The strength of the cavity-induced flow recirculation (or jet driven flow) and the local Nusselt number of the cavity increases with increasing axial Reynolds number.

Rotating Cavity. Figures 7 and 8 show the effect of Reynolds numbers on the local Nusselt number distributions for the uniform wall heat flux condition (case A) on the rotating cavity ($Re_t = 1.7 \times 10^5$ and $Re_t = 5.11 \times 10^5$, respectively). Two general trends are observed: (1) the local Nusselt numbers with rotation are relatively lower than those without rotation, and (2) the local Nusselt numbers with rotation increase with increasing axial Reynolds number. This may be because the heated rotating cavity induces another secondary flow (buoyancy-driven flow) near the rim and the large disk radii. This rotation-induced secondary flow near the rim may reduce the size of the cavity-induced flow. The local Nusselt numbers with rotation are therefore lower than those without rotation. However, it is expected that the Nusselt numbers would be higher for further increasing rotation speed. Note that Farthing et al. (1992b) did flow visualization and identified the regimes of vortex breakdown in an isothermal rotating cavity. The present flow conditions are $Re_z/10^5 = 0.025 - 0.25$ and $Re_t/10^5 = 1.7 - 5.11$. According to Farthing et al., the present rotating flows are in nonaxisymmetric (mode Ib) and axisymmetric (modes IIa and IIb) vortex breakdown conditions.

Effect of Rotational Reynolds Number. To understand the effect of rotation on the cavity heat transfer, some of the above-mentioned test data were replotted as Nu versus Re_t. Figures 9–11 show Nu versus Re_t at three selected locations (the first,

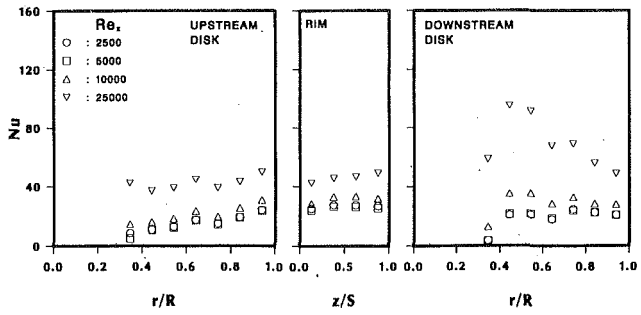

Fig. 7 Effect of axial Reynolds number on the local Nusselt number distribution for case A at $Re_t = 1.7 \times 10^5$

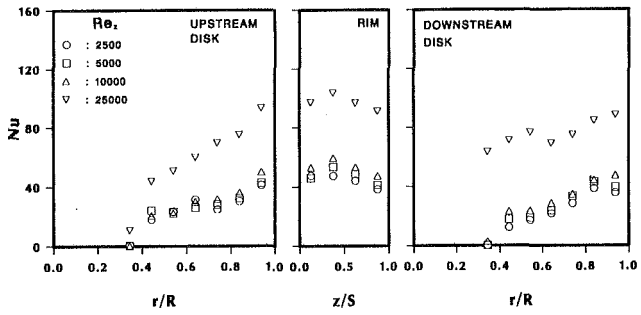

Fig. 8 Effect of axial Reynolds number on the local Nusselt number distribution for case A at $Re_t = 5.11 \times 10^5$

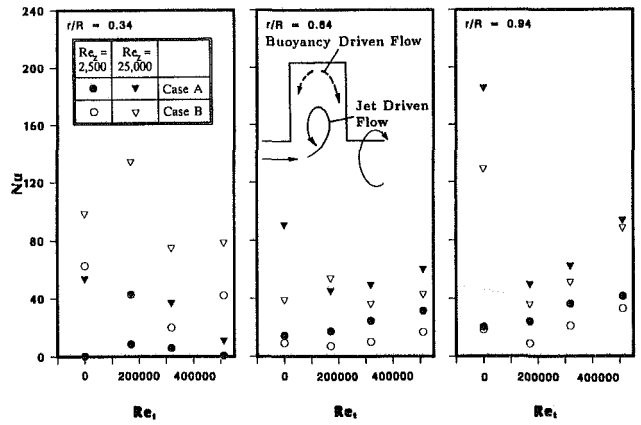

Fig. 9 Nusselt number versus rotational Reynolds number at three radial locations on the upstream disk

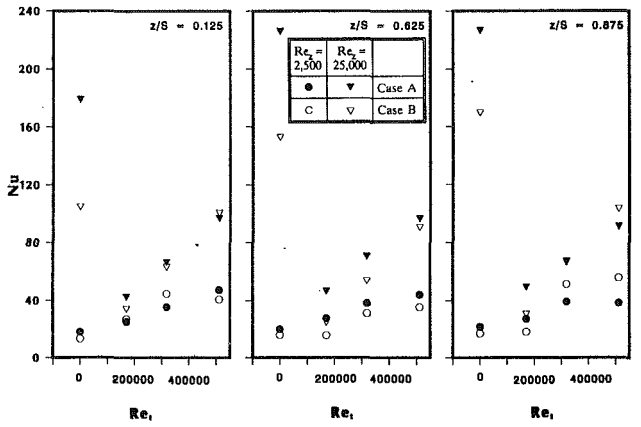

Fig. 10 Nusselt number versus rotational Reynolds number at three axial locations on the rim surface

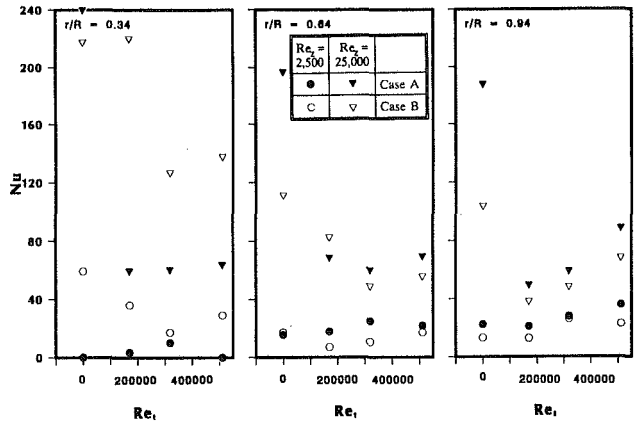

Fig. 11 Nusselt number versus rotational Reynolds number at three radial locations on the downstream disk

fourth, and seventh ring on the upstream and downstream disk, and the first, third, and fourth ring on the rim) for uniform wall heat flux (case A) and uniform wall temperature (case B) condition. The general trends of the results are: (1) The Nusselt numbers from the upstream (and downstream) disk entrance to the central (see Figs. 9 and 11) at $r/R = 0.34$ and 0.64 initially decrease and then increase with increasing rotational (tangential) Reynolds numbers, (2) the Nusselt numbers near the large disk radius (see Figs. 9 and 11) at $r/R = 0.94$ increase monotonically with increasing rotational Reynolds number; and (3) the Nusselt numbers on the rim (see Fig. 10 at three locations: $z/S = 0.125$, 0.625, and 0.875) increase monotonically with increasing rotational Reynolds number except those for high axial Reynolds number ($Re_z = 25{,}000$) at nonrotating conditions ($Re_t = 0$, triangular symbol).

As previously discussed, the cavity induces recirculation flow while the rotation induced buoyancy flow. The size and strength of the flow recirculation in the cavity increase with axial flow rate (axial Reynolds number) but decrease with rotation (rotational Reynolds number). Meanwhile, the strength of the buoyancy flow in the cavity increases with rotation and disk radius. This implies that the buoyancy-induced effect (or buoyancy-driven effect) on the Nusselt number is strongest at high rotation and large disk radius (and rim), while the cavity-induced effect (or jet-driven effect) on the Nusselt number is strongest at low rotation and small disk radius. Therefore, the local Nusselt numbers at large radius and rim (buoyancy-driven dominated) increase monotonically with increasing rotational Reynolds number while the local Nusselt numbers at small radius (jet-driven dominated) initially decrease and then increase with increasing rotational Reynolds number.

Effect of Disk Wall Temperature. Figures 9–11 also show the effect of disk wall temperature (cases A and B) on Nu versus Re_t plots at three selected locations for $Re_z = 2500$ and 25,000 respectively. The results show that the uniform wall temperature condition (case B) has higher Nusselt numbers at a small radius while the uniform heat flux condition (case A) has higher Nusselt numbers at a large radius and rim. This may be because the uniform heat flux case has a larger wall-to-coolant temperature difference that induces greater buoyancy-driven flow near the large radius and rim. The reverse is true at the small radius. It is worthwhile to mention the effect of other types of heating conditions on the cavity Nusselt number. Kim and Han (1993) studied the rotating cavity heat transfer for two heating conditions: BC1—upstream disk temperature lower than the downstream disk and rim, and BC2—downstream disk temperature lower than the upstream disk

and rim. They found that the Nusselt numbers on the higher temperature disk are greater than those on the lower temperature disk. Kim et al. (1993) investigated the rotating cavity heat transfer for two heating conditions: case 1—upstream and downstream disks with radially increasing temperature but lower than rim, and case 2—upstream and downstream disks at uniform temperature but lower than rim. They reported that the Nusselt numbers at small radii and rim for case 2 are higher than those for case 1. The reverse is true at large radii. These studies suggest that a higher disk temperature has a greater buoyancy effect near the disks and thus produces higher disk Nusselt numbers. The lower disk temperature has a greater buoyancy effect near the rim and creates higher rim Nusselt numbers.

Nusselt Number Versus Grashof Number—Comparison With Natural Convection Correlations and Previous Results. Figure 12, Nu_y versus Gr_y (and Gr_L), shows the comparisons between this study and the natural convection correlations, as well as the previous results (Farthing et al., 1992a) for three rotational Reynolds numbers, one axial Reynolds number, and two thermal boundary conditions. Note that $Nu_y = hy/k$ and $Gr_y = r\Omega^2\beta\Delta T y^3/\nu^2$, where y is measured from the inward rim for the upstream and downstream disks. Also shown are correlations for natural convection (Farthing et al., 1992a) in air for Pr = 0.72 from a heated vertical flat plate with a constant surface temperature given by:

$$Nu_y = 0.36\ Gr_y^{0.25} \quad \text{for laminar flow} \tag{2}$$

$$Nu_y = 0.022 Gr_y^{0.4} \quad \text{for turbulent flow} \tag{3}$$

where y is now the radial outward length from the disk inner radius and the centripetal acceleration ($r\Omega^2$) is replaced by the gravitational acceleration (g). The experimental results from Farthing et al. (1992a) for the case of a symmetrically heated cavity with a linearly increasing temperature distribution are also included for comparison. The Farthing et al. results (shaded region in Fig. 12) are based on the following conditions: $Re_z = 2 \times 10^4$, $Re_t = 2 \times 10^5$-5×10^6, $G = 0.138$, $R1/R = 0.106$, $Gr_y = 10^5$-10^{11}, and the rim (shroud) is unheated and insulated. The present results are based on: $Re_z = 2.5 \times 10^4$, $Re_t = 1.7 \times 10^5$-5.11×10^5, $G = 0.4$, $R1/R = 0.25$, $Gr_y = 10^6$-10^{10}, and the rim (shroud) is heated. Note that the rim results (middle figure) of this study are plotted as $\overline{Nu}_y$ versus Gr_L, where $Nu_y = \overline{Nu}_L = \bar{h}L/k$ and $Gr_L = R\Omega^2\beta\Delta\overline{T}L^3/\nu^2$ are the averaged Nusselt and Grashof numbers for the rim, respectively. Also shown in the rim results (middle figure) is the correlation for natural convection (Incropera and DeWitt, 1990) in air for Pr = 0.72 from the face down heated plate at constant surface temperature given by:

$$\overline{Nu}_L = 0.27 Gr_L^{0.25} \quad \text{for } Gr_L = 10^5\text{-}10^{10} \tag{4}$$

where $\overline{Nu}_L = \bar{h}L/k$, $Gr_L = g\beta\Delta\overline{T}L^3/\nu^2$, L (characteristic length) $= A_s/p = S/2$, A_s = surface area of the rim, and p = perimeter of the rim.

Figure 12 shows that the modified Nusselt numbers (Nu_y) on the upstream and downstream disks (left and right figures) of this study (cases A and B) and those of Farthing et al. (1992a) are mostly lower than the natural convection correlations for a vertical wall, except that the present results are higher at the downstream disk entrance (i.e., larger Gr_y values). The Nusselt numbers for $Re_z = 25{,}000$ agree fairly well with those of Farthing et al. ($Re_z = 2 \times 10^4$) except the present data are lower and higher, respectively, at large radii ($Gr_y = 10^7$) and small radii ($Gr_y = 10^{10}$). However, the Farthing et al. data are approximately parallel to the laminar natural convection correlation and the present data are parallel to the turbulent natural convection correlation. This may be because of the different cavity geometries and different wall heating conditions between the two studies: Farthing et al. has a smaller disk bore ($R1/R = 0.106$), narrower gap between disks ($G =$ 0.138), linearly increasing disk temperature with unheated rim; this study has a larger disk bore ($R1/R = 0.25$), wider gap between disks ($G = 0.4$), uniform wall temperature or heat flux with heated rim. The averaged Nusselt numbers on the rim (middle figure) increase with increasing rotational Grashof numbers. However, the present rim data are lower than the natural convection correlation from the face down heated plate.

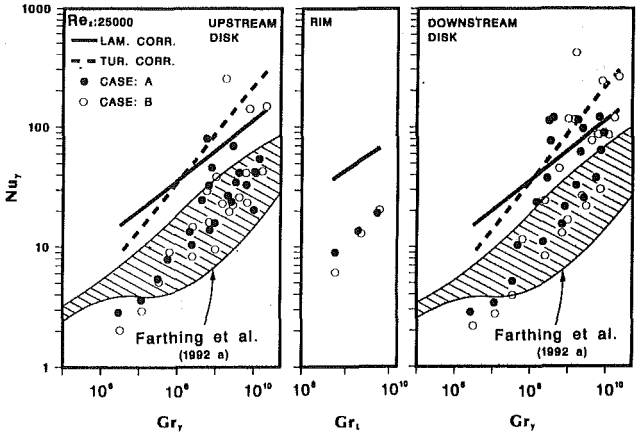

Fig. 12 Effect of rotational Grashof number on the local Nusselt number distribution for case A and case B at Re_z = 25,000 and comparison with previous results

Note that both this study and that of Farthing et al. (1992a) employ the inlet cooling air temperature as a reference for calculating local heat transfer coefficient distributions inside the rotating cavity (as shown in Eq. (1)). The local heat transfer coefficients of this study and those of Farthing et al. are therefore lower than the "real" values because the cooling air temperature inside the disk cavity should be higher than its inlet value. The present Nu_y values shown in Fig. 12 would be higher and closer to the natural convection correlations if the cavity air temperature instead of the inlet air temperature were used for the local heat transfer coefficient calculations. The effect is more severe at large disk radii and rim where the local air temperature is greater than its inlet value.

Long and Tucker (1992) determined the rim heat transfer coefficients by measuring cavity air temperature instead of inlet air temperature. They found that the rim Nusselt numbers are closer to the natural convection correlation for the horizontal plate.

Average Heat Transfer Results—Effect of Rotational Reynolds Number. The average Nusselt numbers on the upstream disk, rim, and downstream disk are the area-weighted average values of the local Nusselt numbers on the upstream disk, rim, and downstream disk, respectively. Figure 13 shows the average Nusselt number ($\overline{Nu}$) versus rotational Reynolds number (Re_t) for two axial Reynolds numbers (Re_z) for both thermal conditions (cases A and B). The results are: (1) The average Nusselt numbers on the upstream disk, rim, and downstream disk increase with increasing axial Reynolds numbers for both of the studied boundary conditions, (2) the average Nusselt numbers on the upstream and downstream disks and the rim increase with increasing rotational Reynolds numbers for lower axial Reynolds number, while the average Nusselt numbers initially decrease and then increase again with further increasing rotational Reynolds number for the higher axial Reynolds number, (3) rotation has more effect on the average Nusselt numbers for the higher axial Reynolds number case, and (4) the average Nusselt numbers on the downstream disk and rim are higher than on the upstream disk for the higher Reynolds numbers case.

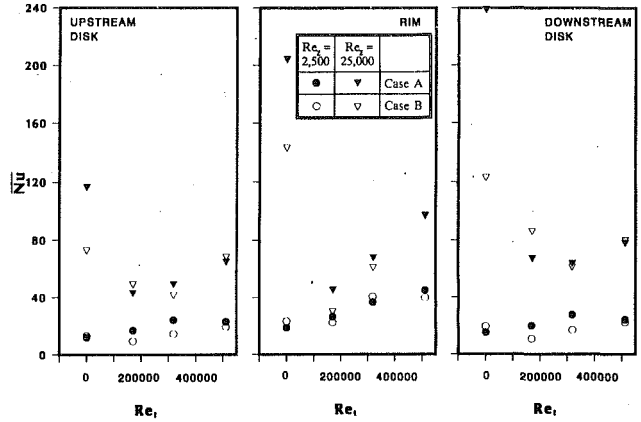

Fig. 13 Effect of rotational Reynolds number and axial Reynolds number on the averaged Nusselt number distribution for cases A and B

Concluding Remarks

The local heat transfer coefficients in a rotating cavity have been studied for four axial Reynolds numbers (Re_z = 2500, 5000, 10,000 and 25,000), for rotational Reynolds numbers (Re_t = 0, 1.7, 3.9, and 5.11 × 10^5), and two surface heating conditions (uniform wall heat flux and uniform wall temperature). The rotating cavity has two plane disks and a cylindrical rim with a constant value disk gap ratio (G = 0.4) and disk inner radius to outer radius ratio ($R1/R$ = 0.25).
The findings are:

1 For the case of a nonrotating cavity, the local Nusselt number decreases from the downstream disk inner radius to the outer radius (except for lower axial Reynolds numbers) and then reaches a high value near the downstream of the rim. It then decreases again from the upstream disk outer radius to the inner radius. The Nusselt numbers decrease with decreasing axial Reynolds number.

2 For the case of rotating cavity, the local Nusselt numbers at small radii initially decrease and then increase with increasing rotational Reynolds number, while the local Nusselt numbers at large radii and rim montonically increase with increasing rotational Reynolds number. The Nusselt numbers decrease with decreasing axial Reynolds number for a fixed rotational Reynolds number.

3 The Nusselt numbers at large disk radii and rim for the uniform heat flux case are higher than those for the uniform wall temperature case. The reverse is true at small disk radii. These suggest that a higher disk temperature creates higher disk Nusselt numbers; a lower disk temperature produces higher rim Nusselt numbers. The effect of the disk heating condition decreases with increasing rotational Reynolds number (less jet-driven flow) for a fixed axial Reynolds number, and increase with increasing axial Reynolds number (more jet driven flow) for a fixed rotational Reynolds number.

4 The modified local Nusselt numbers (Nu_y) of this study on the upstream and downstream disks agree fairly well with those of Farthing et al. (1992a) at Re_z = 25,000. However, both studied results are mostly lower than the natural convection correlations for the vertical flat wall. The Farthing et al. data are approximately parallel to the laminar natural convection correlation while the present data are parallel to turbulent natural convection. The Nusselt numbers on the rim are also lower than the natural convection correlation values for a face down heated plate.

5 The area-averaged Nusselt numbers on each surface of the cavity increase with increasing axial Reynolds number. The downstream disk and rim have higher average Nusselt numbers than the upstream disk for the higher axial Reynolds number. The average Nusselt numbers for the higher axial Reynolds number initially decrease and then increase with increasing rotational Reynolds number. However, the average Nusselt numbers for the lower axial Reynolds number increase monotonically with increasing rotational Reynolds number for both thermal conditions.

Acknowledgments

This project was sponsored by General Electric Company—Aircraft Engines and NASA Center for Space Power. Their support is greatly appreciated. Sincere appreciation goes to Ms. Pam Hoestenbach for her technical writing assistance.

References

Farthing, P. R., Long, C. A., Owen, J. M., and Pincombe, J. R., 1992a, "Rotating Cavity With Axial Throughflow of Cooling Air: Heat Transfer," ASME *Journal of Turbomachinery*, Vol. 114, pp. 229–236.

Farthing, P. R., Long, C. A., Owen, J. M., and Pincombe, J. R., 1992b, "Rotating Cavity With Axial Throughflow of Cooling Air: Flow Structure," ASME *Journal of Turbomachinery*, Vol. 114, pp. 237–246.

Incropera, F. P., and DeWitt, D. P., 1990, *Fundamentals of Heat and Mass Transfer*, 3rd ed., Wiley, New York, p. 548.

Kim, S. Y., 1992, "Local Heat Transfer in a Rotating Cavity With Axial Throughflow," Ph.D. Dissertation, Texas A&M University.

Kim, S. Y., Han, J. C., Morrison, G. L., and Elovic, E., 1993, "Influence of Surface Heating Condition on Local Heat Transfer in Enclosed Co-rotating Disks With Axial Throughflow," ASME Paper No. 93-GT-258.

Kim, S. Y., and Han, J. C., 1993, "Surface Heating Effect on Local Heat Transfer in an Enclosed Co-rotating Disk With Axial Throughflow," presented at the 6th International Symposium on Transport Phenomena in Thermal Engineering, Seoul, Korea, May 9–13.

Kline, S. J., and McClintock, F. A., 1953, "Describing Uncertainties in Single-Sample Experiments," *Mechanical Engineering*, Jan., pp. 3–8.

Long, C. A., and Tucker, P. G., 1992, "Shroud Heat Transfer Measurements From a Rotating Cavity With an Axial Throughflow of Air," ASME Paper No. 92-GT-69; ASME *Journal of Turbomachinery*, in press.

An Experimental Investigation on Forced Convection Heat Transfer From a Cylinder Embedded in a Packed Bed

K. Nasr

S. Ramadhyani

R. Viskanta

School of Mechanical Engineering,
Purdue University,
West Lafayette, IN 47907

Forced convection heat transfer from a cylinder embedded in a packed bed of spherical particles was studied experimentally. With air as the working fluid, the effects of particle diameter and particle thermal conductivity were examined for a wide range of thermal conductivities (from 200 W/m K for aluminum to 0.23 W/m K for nylon) and three nominal particle sizes (3 mm, 6 mm, and 13 mm). In the presence of particles, the measured convective heat transfer coefficient was up to seven times higher than that for a bare tube in crossflow. It was found that higher heat transfer coefficients were obtained with smaller particles and higher thermal conductivity packing materials. The experimental data were compared against the predictions of a theory based on Darcy's law and the boundary layer approximations. While the theoretical equation was moderately successful at predicting the data, improved correlating equations were developed by modifying the form of the theoretical equation to account better for particle diameter and conductivity variations.

Introduction

In the on-going search for techniques to augment convective heat transfer, attention has recently been directed at the possibility of embedding the heat transfer surface in a packed bed. Chrysler and Simons (1990) suggested the use of packed beds of spherical particles to enhance convective heat transfer from microelectronic chips while Kuo and Tien (1988a) suggested the use of a foam metal for the same application. Mohamad and Viskanta (1989) and Xiong and Viskanta (1992) examined the merits of using a packed bed of ceramic particles to enhance heat transfer from combustion products to coolant tubes embedded in a porous-matrix combustor-heater. These and other potential applications of the concept indicate the need for information on heat transfer coefficients associated with convection from surfaces embedded in porous media. The present paper reports the results of an experimental study of forced convective heat transfer from a heated cylinder in a packed bed of spherical particles. The physical situation is depicted schematically in Fig. 1. An air stream, at a temperature T_∞ and an approach velocity U_∞, enters the packed bed and flows around an embedded cylindrical surface. The flow velocity is high enough to render buoyancy effects negligible.

The heat transfer augmentation produced by the porous matrix is attributed to a combination of effects, including thinning of the hydrodynamic and thermal boundary layers around the cylinder, increased mixing (thermal dispersion), and direct conduction through the porous matrix. Previous theoretical studies (Cheng, 1982; Minkowycz et al., 1985) addressed the problem by employing the boundary layer approximation to the energy equation in conjunction with Darcy's law. The porous medium was treated as a continuum by volume-averaging the properties of the solid and fluid phases. As noted by Pop and Cheng (1992), this approach may be justified if the particles of the porous matrix are much smaller than the thickness of the thermal boundary layer. If the particle size is comparable to or exceeds the boundary layer thickness, the validity of the approach may be questionable. In addition, the use of Darcy's law implicitly neglects the no-slip condition at the solid surface, the effects of fluid inertia, and the variations of porosity near the surface.

Based on the aforementioned boundary layer analysis, Cheng (1982) provided an expression for the variation of the local Nusselt number over an isothermal cylinder under forced flow conditions:

$$\mathrm{Nu}_\theta = 0.5641\mathrm{Pe}_\theta^{0.5}\sqrt{2\theta}\,\sin\theta(1-\cos\theta)^{-0.5} \qquad (1)$$

Integration of the local Nusselt number over the cylinder surface yields an expression for the average Nusselt number:

$$\mathrm{Nu}_D = 1.0157\mathrm{Pe}_D^{1/2} \qquad (2)$$

In these expressions, the Nusselt and Peclet numbers are based on an effective (volume-averaged) thermal conductivity of the porous medium.

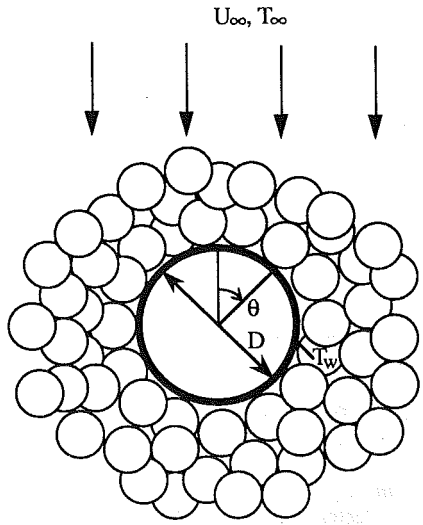

Fig. 1 The physical problem and coordinate system

Contributed by the Heat Transfer Division for publication in the JOURNAL OF HEAT TRANSFER. Manuscript received by the Heat Transfer Division October 1992; revision received June 1993. Keywords: Forced Convection, Porous Media. Associate Technical Editor: C. E. Hickox, Jr.

Other theoretical studies of the problem have been presented by Huang et al. (1986) and Badr and Pop (1988). The finite difference calculations of Badr and Pop, which involved the use of Darcy's law but did not require the boundary layer approximations, were in good agreement with the boundary layer solutions by Cheng (1982) and Minkowycz et al. (1985).

The only previous experimental data related to the present situation appear to be those of Fand and Phan (1987) who used a packed bed of 3 mm glass spheres with water as the fluid medium. They advanced several hypothetical arguments to develop an empirical correlation of their data in the form:

$$\mathrm{Nu}_D = 1.48(0.255 + 0.699\ \mathrm{Re}_D^{0.5})\mathrm{Pr}^{0.29}\mathrm{Re}_p^{0.179};\quad \mathrm{Re}_p > 100 \quad (3)$$

The stagnant effective thermal conductivity of the porous medium is to be used in both the Nusselt and the Prandtl numbers. No comparison with previous theoretical studies was presented.

The purpose of the present paper is to report the results of experimental studies of forced convection heat transfer from a circular cylinder embedded in a packed bed of spherical particles. Several packing materials, encompassing a wide range of thermal conductivities, have been employed with air as the working fluid. The experiments have been performed with spherical particles of various diameters in order to generate a large data base. The experimentally determined Nusselt numbers have been compared with the predictions of previously proposed correlations to assess the applicability of those correlations to the present range of parameters. In addition, the effects of relevant physical variables including particle diameter, particle thermal conductivity, and fluid velocity have been examined.

Experimental Apparatus and Procedures

The experimental arrangement, shown schematically in Fig. 2, consisted of a blower assembly, heat transfer test section, a venturi flow meter, and instrumentation to measure temperatures and electrical power inputs. The test section was a Lexan duct of 15.1 cm × 12.7 cm cross section and 17.8 cm length. In order to obtain uniform inlet air flow, a smooth bell-mouth entrance was attached to the test section. The Lexan duct contained a packed bed of spheres in which a 15.1-cm-long heated copper tube of 12.7 mm o.d. was embedded. The spheres were supported by a thin perforated plate located at the bottom of the duct, as shown.

The copper tube was heated internally by a 9.5 mm o.d. electrical cartridge heater powered by a DC power supply. The small air gap between the heater and the copper tube was filled by Omegatherm 201 (silicone paste), a high-temperature high-thermal conductivity paste (k = 2.38 W/m K) to minimize the contact resistance. The heater voltage and current were measured by digital multimeters, and the electric power input to the heater was calculated from the measured current and voltage settings. The power input was controlled so that a temperature difference of approximately 10°C was maintained between the tube and the inlet air. A higher temperature difference (>10°C) was intentionally avoided in order to minimize fluid property variations.

The tube was instrumented with five copper-constantan thermocouples at the locations shown in Fig. 3. Three thermocouples were attached to the outer tube surface midplane at 120 deg intervals from the top of the tube. Two more thermocouples were attached to the tube at a plane 5.1 cm away from the midplane and at different angular locations, to monitor any longitudinal and circumferential temperature changes. Thermocouple leads were brought out along longitudinal grooves toward the cylinder end, covered with conductive paste, and then smoothed. The end view of the instrumented tube shown in Fig. 3 indicates the surface grooves and their dimensions. The inlet air temperature was measured by a thermocouple located at the top of the bed entrance and approximately 7.5 cm above the heated cylinder. All ther-

Table 1 Physical and thermophysical properties of the packing materials at room temperature

Material	d_p (mm)	d_p/D	k_s (W/m K)	k_s/k_f	Porosity (%)
Aluminum	3.24	0.255			0.37
	6.33	0.498	200	7605	0.38
	12.23	0.963			0.39
Alumina	2.77	0.218			0.36
	6.64	0.523	40	1520	0.37
	9.79	0.771			0.38
Glass	2.85	0.224			0.37
	6.00	0.472	1.01	38	0.37
	13.53	1.065			0.39
Nylon	6.35	0.500	0.23	8.7	0.37
	12.7	1.000			0.39

Nomenclature

A = surface area of the cylinder
D = cylinder diameter
d_p = particle diameter
h = average heat transfer coefficient
k = thermal conductivity
Nu_D = cylinder-averaged Nusselt number = hD/k_m
Nu_θ = local Nusselt number on cylinder surface = $q_W D\theta/2k_m(T_W - T_\infty)$
Pe_D = average Peclet number = UD/α_m
Pe_p = particle Peclet number = Ud_p/α_f
Pe_θ = local Peclet number on the cylinder surface = $U_\infty D\theta/2\alpha_m$
Pr = Prandtl number used in Eq. (3) = ν/α_m
Q = power input to the electric heater
Q_{loss} = heat losses due to contact conduction from heated cylinder to the walls of the test section
q_w = local heat flux at the wall of the cylinder
Re = Reynolds number based on superficial velocity
T_b = bulk bed-air temperature away from the cylinder surface
T_w = cylinder wall temperature
T_∞ = temperature of the approaching fluid
U = superficial fluid velocity
U_∞ = velocity of the approaching fluid
α = thermal diffusivity
θ = angle measured from forward stagnation point
μ = dynamic viscosity of the fluid
ν = kinematic viscosity of the fluid
ρ = density of the fluid
ϕ = bulk porosity of the packed bed (porous medium)

Subscripts

D = based on cylinder diameter
d = dispersive
f = fluid
m = stagnant
p = based on particle diameter
s = solid

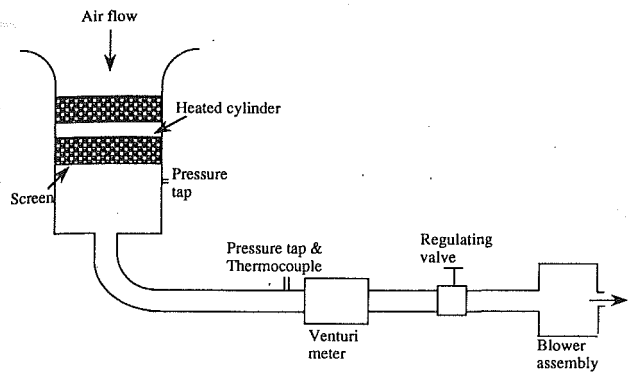

Fig. 2 Experimental apparatus

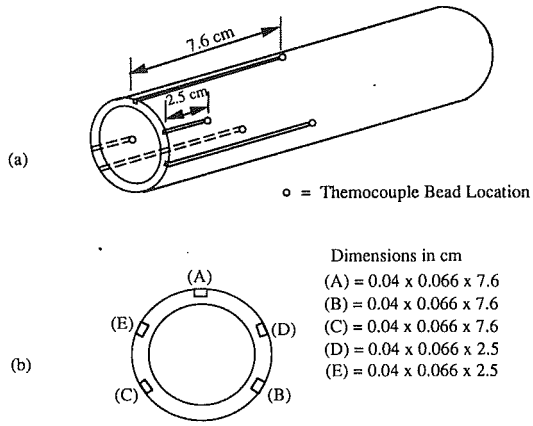

Fig. 3 Instrumented cylinder: (*a*) isometric view and (*b*) end view

mocouples were calibrated using a constant-temperature water bath.

An Omega (Model 2176 A) digital thermometer was employed for all the temperature measurements. The temperatures were monitored and recorded after steady-state conditions had been reached. The steady-state surface temperature, T_s, was taken as the average of the readings of the five thermocouples installed on the surface of the cylinder. This simple averaging procedure is valid since the surface of the copper cylinder was isothermal to within 0.2°C.

A stainless steel perforated plate held the spheres in place. To avoid any possible blockage of the air passages, a fine mesh stainless steel screen was placed on top of the perforated plate. The inlet and throat diameters of the venturi meter were 88.9 mm and 50.8 mm, respectively. The pressure drop across the venturi meter was measured using a **U**-tube manometer for high pressure drops and a Gilmont micromanometer (Model G-1500-A) at low values of pressure drop. To establish the temperature and pressure of the air stream for evaluation of thermophysical properties, a thermocouple and a pressure tap were installed downstream from the test section and 5 cm upstream from the inlet to the venturi meter. The measured temperature and pressure enabled determination of the values of the density and kinematic viscosity needed for mass flow rate calculations. The blower assembly contained three centrifugal blowers that induced atmospheric air through the test section. The flow direction was downward through the test section. A regulating valve in the line allowed the volume-averaged velocity in the test section to be varied from approximately 0.2 m/s to 4 m/s.

The porous media used in the experiments were packed beds of solid spheres made of aluminum, alumina, glass, and nylon covering a wide range of solid thermal conductivity (200 W/m K to 0.23 W/m K). The alumina "spheres" were, in fact, very short cylinders with hemispherical end caps for which an equivalent diameter was determined. Table 1 contains the physical characteristics of each packing material. The solid thermal conductivity data for all the packing materials, except nylon, were taken from Touloukian et al. (1970). The thermal conductivity of nylon was obtained from Kohan (1973).

For each set of experiments, the test section was filled with a packing material up to a height of 16 cm above the screen. The spheres were poured randomly into the channel and leveled. The choice of 16 cm for the bed height is based on a conservative estimate of the distance needed to eliminate undesirable boundary effects such as those resulting from the presence of the screen holding the beads. Indeed, separate runs were made for a bed height of 12 cm and no significant change in the heat transfer results were noticed.

The bulk porosity of the porous medium (packed bed) was computed for each run from the defining equation

$$\phi = \frac{V_t - V_p}{V_t} \tag{4}$$

where V_p is the ratio of the measured weight of the particles that occupy the test section to the density and V_t is the test section total volume minus the volume of the cylinder.

Data Reduction. All individual temperature measurements were first corrected using their corresponding calibration curves. The five temperature readings were averaged to give an average surface temperature for the cylinder. The power input to the heater was computed from measurements of the voltage and current. The heat losses from the cylinder to the Lexan supporting walls were estimated to be 0.9 and 3.8 percent of the heater power input at high and low flow rates, respectively. Knowledge of the power input, estimate of heat losses, and surface temperatures allowed for the computation of the average heat transfer coefficient from the defining equation:

$$h = \frac{Q - Q_{\text{loss}}}{A(T_w - T_b)} \tag{5}$$

With the exception of the density, all of the thermophysical fluid properties (specific heat, dynamic viscosity, and thermal conductivity) were based on the film temperature and calculated using regression curve fits (ASHRAE, 1976). The fluid density was computed employing the ideal gas law.

The results were reduced to dimensionless parameters, which take on different forms depending on the choice of the length scale and the thermal conductivity used in the nondimensionalization. One of the possible choices for the thermal conductivity is the volume-averaged (effective) conductivity of the bed. Several theoretical and empirical models for evaluation of this parameter have been reported (Wakao and Kaguei, 1982; Churchill, 1986; Tsotsas and Martin, 1987; Prasad et al., 1989). In their review, Tsotsas and Martin (1987) recommended the model of Zehner and Schlünder (1970) for the stagnant effective thermal conductivity:

$$k_m = k_f \left\{ 1 - \sqrt{(1-\phi)} + \frac{2\sqrt{(1-\phi)}}{1-\lambda B} \times \left[\frac{(1-\lambda)B}{(1-\lambda B)^2} \ln\left(\frac{1}{\lambda B}\right) - \frac{B+1}{2} - \frac{B-1}{1-\lambda B} \right] \right\} \tag{6}$$

where $B = 1.25[(1-\phi)/\phi]^{10/9}$ and $\lambda = k_f/k_s$.

Previous researchers (Yagi and Kunii, 1960; Yagi et al., 1961; Lerou and Forment, 1977; Wakao and Kaguei, 1982; Cheng and Vortmeyer, 1988) have noted that the thermal conductivity of a packed bed is enhanced by thermal dispersion. Various models of thermal dispersion, involving an additive contribution to the stagnant effective conductivity, have been proposed by these and other investigators (Hunt and Tien, 1988; Kuo and Tien, 1988b; Hsu and Cheng, 1990; Kaviany, 1991). In general, these models suggest that the additive (dispersion)

Table 2 Comparison between measured and predicted heat transfer coefficients using the Churchill and Bernstein (1977) correlation for a cylinder in a crossflow

Re_D	h (Exp.) (W/m^2 K)	h (Pred.) (W/m^2 K)	Error (%)
1087	34.5	35.6	3.1
1273	37.4	38.7	3.5
1738	43.9	45.1	2.7
2123	48.7	49.3	1.2
2485	52.8	52.3	-0.95

contribution to the effective thermal conductivity may be calculated by an expression of the form

$$\frac{k_d}{k_f} = C\mathrm{Pe}_p \tag{7}$$

The proportionality constant, C, is around 0.1 (Yagi et al., 1961). As will shortly be discussed, the results of the present study show that the stagnant effective thermal conductivity is much more suitable than the dispersion-enhanced conductivity in correlating the data.

An uncertainty analysis was performed to estimate uncertainties in the reported data. The relative uncertainty in mass flow rate was found to be ±1.8 percent at low flow rates and ±1.5 percent at high flow rates. The relative uncertainty in the temperature difference between the surface of the cylinder and the incoming air was estimated to be ±1.4 percent. Accounting for heat losses and following the procedure described by Moffat (1988), the relative uncertainty in the heat transfer coefficient was estimated to be ±1.8 percent under high air flow rates, and ±4.2 percent under low flow rates. The uncertainties in the Nusselt and Peclet numbers are greatly influenced by the uncertainty in the effective thermal conductivity model employed to scale these parameters. Based on an estimated uncertainty of ±20 percent in the effective thermal conductivity, the uncertainties in the Nusselt and Peclet numbers were estimated to be ±20.5 and ±20.1 percent, respectively.

Results and Discussion

Test Setup Evaluation. The experimental apparatus was evaluated by comparing the results obtained for the heat transfer coefficient of a cylinder in crossflow with well-established correlations for this configuration. In these tests, the particles were removed from the duct, and the cylinder was mounted in the empty duct. Electric current and voltage settings and steady-state temperatures were recorded for various air velocities. From the measured data, the average heat transfer coefficient was calculated from Eq. (5) for comparison with the correlation proposed by Churchill and Bernstein (1977). Table 2 shows this comparison for various Reynolds numbers. The good agreement between the experimental results and the correlation provides considerable confidence in the accuracy of the data subsequently obtained with the porous media in the duct.

The procedure of collecting experimental data was repeated and checked periodically for reproducibility. Separate test runs were occasionally repeated and the results were found to be reproducible. In addition, the sensitivity of the heat transfer results to the bed height surrounding the heated tube was checked by measuring the heat transfer coefficient for two different bed heights composed of 2.85 mm glass particles. It was concluded that a bed height of 8 cm about the heated cylinder would be sufficient for heat transfer measurements. A conservative bed height of 16 cm about the embedded cylinder was selected for the experiments.

Table 3 Heat transfer enhancement due to the presence of particles around the cylinder

Material & Size	Re_D	Nu_D-Embedded	Nu_D-Bare	Ratio
Glass (2.85mm)	2157	133	24	5.5
	560	51	12	4.3
Glass (13.5mm)	4000	137	33	4.2
	1100	61	17	3.6
Aluminum	2456	174	25	7.0
(3.24 mm)	660	80	13	6.2
Aluminum	4220	166	33	5.0
(12.23 mm)	613	60	12	5.0

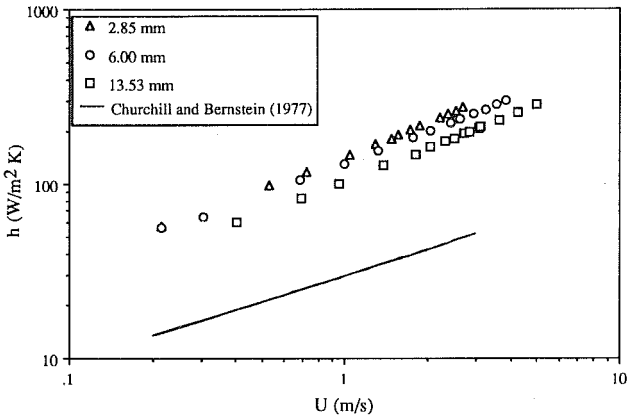

Fig. 4 Effect of particle diameter on the heat transfer coefficient for a bed of glass particles

Heat Transfer Enhancement Due to the Presence of Particles. To illustrate the effectiveness of the particles in enhancing heat transfer from the cylinder, a comparison of sample results for the bare cylinder to one embedded in a packed bed is presented in Table 3. The ratio of the Nusselt number for an embedded tube to that for a bare tube is presented in the last column of the table. It is observed that the packed bed increases the Nusselt number greatly (up to seven times for aluminum spheres), indicating that the particles serve as effective enhancers for forced convection heat transfer. In addition, the packing material with a high thermal conductivity (aluminum) has a higher ratio than material of approximately the same size but of low conductivity (glass).

Effect of Particle Diameter on Heat Transfer. For a given packing material, it was found that variations in the particle size influenced the heat transfer coefficient. The average heat transfer coefficient was found to increase with decreasing particle diameter. Figure 4 is a sample plot illustrating this feature for the cylinder embedded in a bed of glass spheres. The increase in heat transfer is partly attributed to the magnitude of contact conduction to particles touching the cylinder. With smaller particles, the cylinder has more contact points with the surrounding bed, and conduction into the bed is enhanced. In addition, the bed permeability near the embedded cylinder is smaller for small particles, giving rise to thinner velocity boundary layers and higher heat transfer (Pop and Cheng, 1992). It is noted that Eq. (2), which is based on Darcy's law and the boundary layer approximation, does not address the increase in heat transfer due to smaller size particles since its formulation does not take into account either of the foregoing physical effects. To illustrate graphically the heat transfer enhancement due to the particles, the prediction of the correlation by Churchill and Bernstein (1977) for a cylinder in crossflow

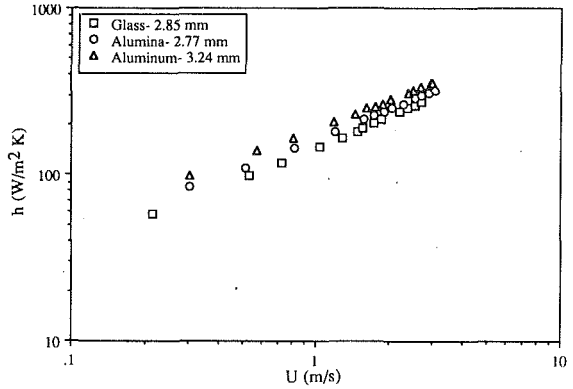

Fig. 5 Effect of particle conductivity on the heat transfer coefficient for the 3 mm nominal size particles

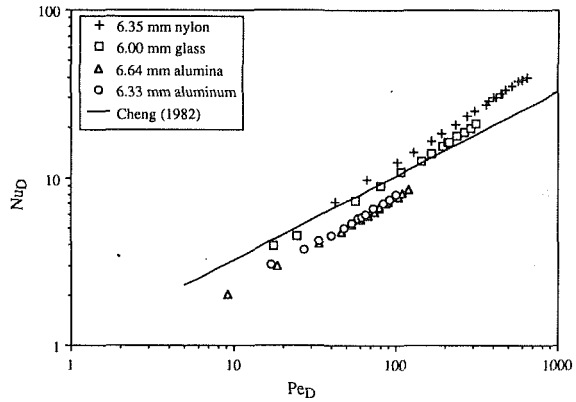

Fig. 7 Comparison of measurements with the predictions of the boundary layer solution for the 6 mm nominal size particles

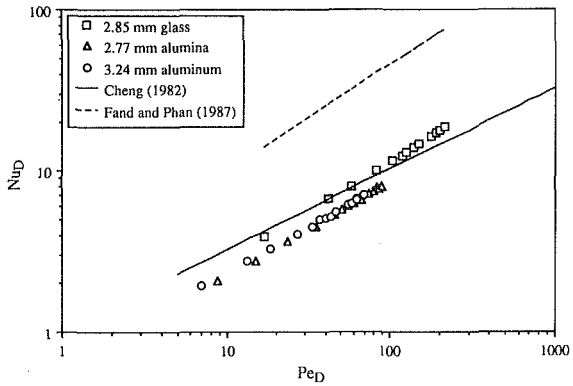

Fig. 6 Comparison of measurements with the predictions of the boundary layer solution for the 3 mm nominal size particles

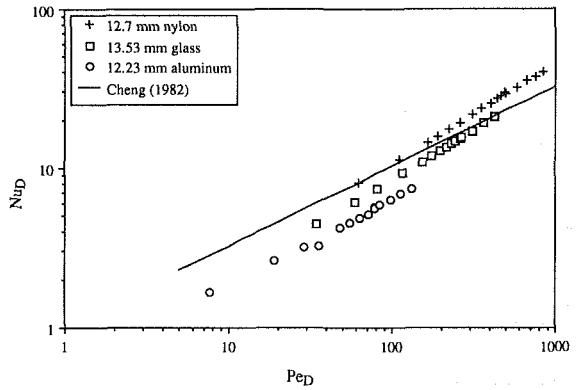

Fig. 8 Comparison of measurements with the predictions of the boundary layer solution for the 13 mm nominal size particles

is also displayed in Fig. 4. Clearly, very substantial enhancements are possible by embedding the cylinder in a packed bed.

Effect of Particle Conductivity on Heat Transfer. For convenience in identification, the spheres used in this study may be divided into three nominal particle sizes. The actual diameter of the nominally 3 mm particles are 2.85 mm for glass, 2.77 mm for alumina, and 3.24 mm for aluminum. The 6 mm nominal diameter corresponds to 6.35 mm for nylon, 6.00 mm for glass, 6.64 mm for alumina, and 6.33 mm for aluminum. The 13 mm average diameter particles include the 12.7 mm nylon, the 13.53 mm glass, and the 12.23 mm aluminum. Figure 5 shows that the highest heat transfer coefficient for the 3 mm particles is associated with the use of aluminum as the packing material. This is due to the high thermal conductivity of aluminum, which results in high contact conduction. The heat transfer coefficient in the aluminum bed is about one and a half times that corresponding to glass. Similar results are obtained (not shown here) for the 6 mm and 13 mm nominal sizes, respectively. Thus, it is concluded that for a constant particle size, an increase in particle conductivity yields an increase in the heat transfer coefficient.

Comparison of Experimental Data With the Predictions of the Boundary-Layer Model. The present experimental results will now be compared to the theoretical predictions based on the boundary-layer approximation and Darcy's flow model, Eq. (2). As suggested by Eq. (2), the Nusselt and Peclet numbers are computed based on the cylinder diameter and the stagnant effective thermal conductivity given by Eq. (6). Figures 6–8 compare the experimental results with the predictions of the boundary-layer approximation for the 3 mm, 6 mm, and 13 mm nominal size particles respectively. The solid line, corresponding to Eq. (2), is in reasonable agreement with the data, but the slopes of the data trends displayed by the different packing materials differ from the slope of the theoretical equation, because Eq. (2) does not fully account for variations in the thermal conductivity of the packing materials. For the two smaller diameters, the maximum deviation between the data and the theoretical equations is about 48 percent, while for the largest diameter particles, the difference is as high as 85 percent. In addition, thermal dispersion is present and plays a major role in the existing difference between the predictions of the theoretical equation and the experimental results. Typically, thermal dispersion is accounted for through a dispersive conductivity that is added on to the stagnant conductivity as given by Eq. (7). This dispersive conductivity exhibits an increase with an increase in the particle Peclet number. Under forced flow conditions, the dispersive conductivity overwhelms the stagnant conductivity. It was found that when a superposition of the dispersive and stagnant conductivities is used, the experimental data did not display the same linear behavior shown in Figs. 6–8. To examine whether the discrepancy between the predictions of the theoretical and the experimental results was due to the phenomenon of thermal dispersion, the data were also plotted in terms of a Nusselt number and a Peclet number based on the dispersion-enhanced effective conductivity. When plotted in this manner, it was found that the theoretical equation predicted Nusselt numbers several times higher than the measured values. In addition, the measured data no longer fell along straight lines in these plots but fell along curves that initially displayed an increase of Nusselt number with Peclet number followed by a decreasing trend for higher Peclet numbers. This suggests that the dispersion-enhanced effective conductivity is not a suitable parameter for correlating the data.

Table 4 Correlation constants a and b relating the Nusselt and Peclet numbers: $Nu_D = aPe_D^b$, $Nu_D = hD/k_m$, $Pe_D = UD/\alpha_m$

Packing Material	Particle Diameter (mm)	a	b	Pe_p Range	Standard Deviation (%)
Nylon	6.35	0.653	0.637	75 - 1175	0.26
	12.7	0.592	0.627	220 - 2930	0.23
Glass	2.85	0.602	0.638	25 - 340	0.6
	6.00	0.621	0.611	60 - 1030	0.7
	13.53	0.467	0.627	240 - 2980	0.3
Alumina	2.77	0.539	0.601	35 - 380	0.5
	6.64	0.549	0.569	90 - 1210	0.4
	9.79	0.523	0.553	150 - 2050	0.3
Aluminum	3.24	0.602	0.579	45 - 440	0.5
	6.33	0.568	0.569	190 - 1140	0.7
	12.23	0.489	0.557	165 - 2845	1.0

Figure 6 also displays the experimental correlation proposed by Fand and Phan (1987). Their correlation, Eq. (3), was recast in terms of the axis variables of Fig. 6 for the purpose of comparison. Clearly, the predictions of Eq. (3) lie appreciably higher than both the present experimental data and the predictions of Eq. (2). A likely explanation for the discrepancy between the present data and those of Fand and Phan is that Eq. (3) was obtained by correlating data for a 3 mm glass–water system for which the ratio of the thermal conductivity of the solid to the fluid thermal conductivity is close to unity. When applied to the glass–air system, the ratio is no longer one, but rather close to fifty.

The foregoing comparisons show that neither Eq. (2) nor Eq. (3) is entirely satisfactory in correlating the data obtained in the present study.

Correlations of the Heat Transfer Results. Figures 6–8 clearly show that while the predictions of Eq. (2) are in reasonable agreement with the data, systematic differences exist depending upon both the particle diameter and the particle thermal conductivity. In order to provide correlating equations of greater accuracy, least-squares fits were developed for each of the data sets in this study. As suggested by Eq. (2), the Nusselt numbers were correlated against the Peclet numbers by equations of the form

$$Nu_D = aPe_D^b \tag{8}$$

where a and b are empirical constants obtained from least-squares fitting of the experimental data.

Table 4 summarizes the correlation constants a and b for all of the packing materials. The standard deviation of the data from each corresponding correlation is provided in the last column of the table. In general, the exponent b tends to decrease with increasing thermal conductivity of the packing material, but is relatively independent of particle diameter. The factor a is dependent on the particle diameter and tends to decrease slightly with increasing particle diameter.

Each of the correlations in Table 4 applies to a specific packing material and a specific particle size. A more general correlation that accounts for the major parameters (d_p, D, k_s, k_f, ϕ, and U) was developed by expressing the Nusselt number as a function of the following dimensionless groups:

$$Nu = f(Pe, k_s/k_f, D/d_p) \tag{9}$$

The appearance of the Peclet number in the correlation is suggested by the form of the theoretical equation, Eq. (2), while the dimensionless ratios (k_s/k_f) and (D/d_p) are used to account for the different particle thermal conductivities and the effect of particle size relative to tube diameter, respectively.

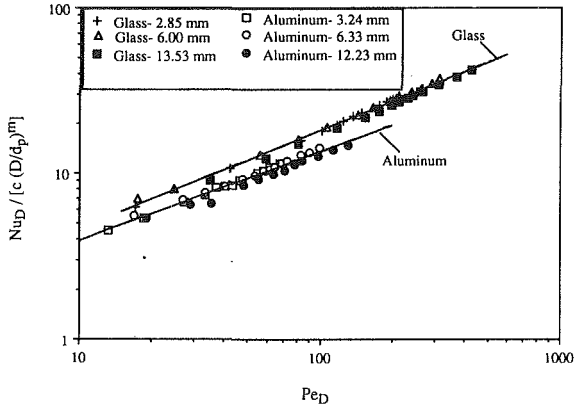

Fig. 9 Correlation of the data for glass and aluminum particles accounting for the diameter effect

Table 5 Constants c and m used to incorporate the diameter effect employing the stagnant effective thermal conductivity

Packing Material	Range of (d_p / D)	c	m
Nylon	0.5 - 1.0	0.592	0.141
Glass	0.2 - 1.07	0.503	0.150
Alumina	0.2 - 0.8	0.530	0.0158
Aluminum	0.2 - 0.96	0.496	0.151

The particle diameter to tube diameter ratio was explicitly incorporated into the correlating equation for the Nusselt number by expressing the parameter a in Eq. (8) in the form

$$a = c(D/d_p)^m \tag{10}$$

The outcome of this approach is shown in Fig. 9, in which the data for all the glass and aluminum particles are plotted. The three data sets for the three different sizes of glass spheres collapse closely onto a single line and the three data sets for aluminum collapse fairly well onto another line. Similar plots (not shown here) were obtained for the other packing materials. Values of c and m were obtained by a least-squares approach for each packing material and are presented in Table 5.

The particle-to-fluid thermal conductivity ratio was incorporated into the correlating equation for the Nusselt number by expressing the parameter b in the form

$$b = e(k_s/k_f)^n \tag{11}$$

Using a least-squares approach, suitable values for the parameters e and n were found to be 0.66 and -0.0174, respectively. This expression for the exponent b is suitable for all of the packing materials employed in this study. Thus, the generalized form of the correlating equation is:

$$Nu_D = c(D/d_p)^m [Pe_D^{0.66(k_s/k_f)^{-0.0174}}] \tag{12}$$

where the Nusselt and Peclet numbers are based on the cylinder diameter and stagnant effective thermal conductivity and the parameters c and m are tabulated in Table 5. Equation (12) may now be applied to each packing material using the corresponding values of c and m from Table 5. However, it would be desirable to develop a single correlation suitable for all the packing materials and particle diameters employed in this study, as can be found tabulated in Table 1. Average values of c and m were chosen to obtain such a correlation yielding the following empirical form:

$$Nu_D = 0.53(D/d_p)^{0.114} [Pe_D^{0.66(k_s/k_f)^{-0.0174}}], \quad \left\{ \begin{array}{c} 1 < (D/d_p) < 5 \\ 10 < (k_s/k_f) < 7600 \end{array} \right\} \tag{13}$$

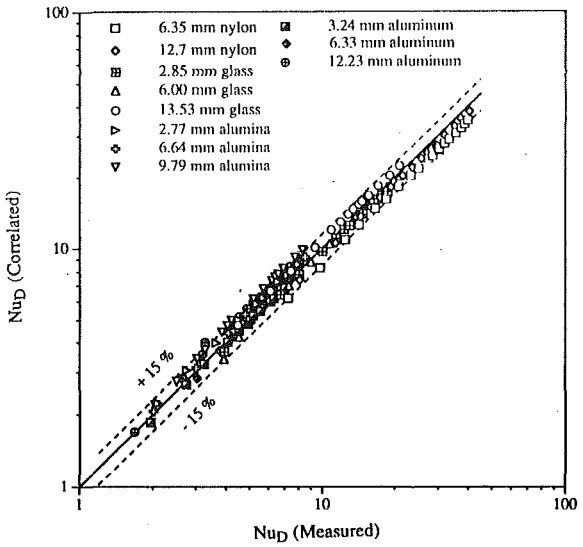

Fig. 10 Comparison of measured Nusselt numbers with those correlated by Eq. (13)

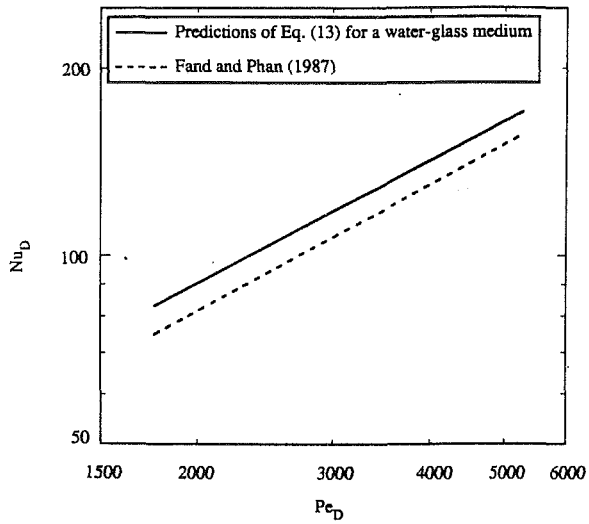

Fig. 11 Comparison between the predictions of Eq. (13) and Eq. (3) for a water-glass system

The predictions of Eq. (13) are compared to the measured values of Nusselt number in Fig. 10 for all packing materials. Of the 167 data points plotted on the figure, 95 percent lie within ±15 percent of the correlating equation. According to Haughey and Beveridge (1969), the packed beds investigated here are of the "poured random packing" mode having bulk porosities between 0.375 and 0.391. If the bed had been vibrated, the mode of packing is classified as "close random packing" with minimum porosities of 0.359 to 0.375. Therefore, as to the universality of the present results, Eq. (13) may still be used with reasonable confidence since the porosity ranges for the two modes of packing are close to each other.

In order to obtain an independent confirmation of the applicability of Eq. (13) over the ranges of the dimensionless groups employed in it, the equation was applied to the data obtained by Fand and Phan with water and 3 mm glass spheres. Their best fit equation [Eq. (3)] lies within 10 percent of the values predicted by Eq. (13). The comparison is shown in Fig. 11. Finally, it is worth noting that there are three regimes by which fluid flow through porous media is characterized (Fand et al., 1987): the Darcy regime, $Re_p < 1$; the Forchheimer regime, $5 < Re_p < 80$; and the turbulent regime, $Re_p > 120$. According to this classification, the present data for the 3 mm nominal size particles fall in the Forchheimer and turbulent regimes, while those for the 6 mm and 13 mm size particles cover the turbulent regime solely.

Conclusions

An experimental study of forced convection heat transfer from a cylinder embedded in a packed bed is reported. The presence of particles enhances heat transfer greatly when compared to the case of a bare tube in crossflow. The effects of particle diameter and particle conductivity on heat transfer were investigated. It was shown that the heat transfer coefficient increases with diminishing particle diameter and increasing thermal conductivity of the packing material.

The experimental results were compared to the predictions of the boundary layer solution based on Darcy's law. The experimentally determined Nusselt numbers were found to vary linearly with the Peclet number on a log-log scale, but the slopes depended on the packing materials and differed from the value of 0.5 predicted by the boundary layer analysis. The discrepancies between the experimental data and the analytical prediction arise from the fact that Darcy's law is not applicable for this physical problem. In addition, for the relatively large particle diameters used in this study, the assumptions embodied in the boundary layer analysis are no longer valid. It is clear that improvements to the theoretical model are needed to account for the pertinent physical phenomena. Since experimental data for this physical configuration are scarce, the present experimental results, showing the effects of particle diameter and material thermal conductivity, may serve as a data base for the verification of improved models. To facilitate the use of the data in future studies, as well as in practical applications, separate correlating equations for each of the packing materials, as well as a single correlation applicable to all the packings, have been developed.

Acknowledgments

This work was supported jointly by the Gas Research Institute, under contract No. 5090-260-1927, and Institute of Gas Technology's sustaining membership program.

References

ASHRAE, 1976, *ASHRAE Thermophysical Properties of Refrigerants*, New York.

Badr, H., and Pop, I., 1988, "Combined Convection From an Isothermal Cylinder Rod Buried in a Porous Medium," *International Journal of Heat Mass Transfer*, Vol. 31, pp. 2527-2541.

Cheng, P., 1982, "Mixed Convection About a Horizontal Cylinder and a Sphere in a Fluid-Saturated Porous Medium," *International Journal of Heat and Mass Transfer*, Vol. 25, pp. 1245-1247.

Cheng, P., and Vortmeyer, D., 1988, "Transverse Thermal Dispersion and Wall Channelling in a Porous Bed With Forced Convective Flow," *Chemical Engineering Science*, Vol. 9, pp. 2523-2532.

Chrysler, G. M., and Simons, R. E., 1990, "An Experimental Investigation of the Forced Convection Heat Transfer Characteristics of Fluorocarbon Liquid Flowing Through a Packed-Bed for Immersion Cooling of Microelectronic Heat Sources," in: *AIAA/ASME Thermophysics and Heat Transfer Conference, Cryogenic and Immersion Cooling of Optics and Electronic Equipment*, ASME HTD-Vol. 131, pp. 21-27.

Churchill, S. W., and Bernstein, M., 1977, "A Correlating Equation for Forced Convection From Gases and Liquids to a Circular Cylinder in Crossflow," ASME JOURNAL OF HEAT TRANSFER, Vol. 99, pp. 300-305.

Churchill, S., 1986, "The Thermal Conductivity of Dispersions and Packed Beds—An Illustration of the Unexploited Potential of Limiting Solutions for Correlations," in: *Advances in Transport Processes*, Vol. IV, A. S. Mujumdar and R. A. Mashelkhar, eds., Wiley Eastern Ltd., New Delhi, pp. 394-418.

Fand, R. M., Kim, B. Y. K., Lam, A. C. C., and Phan, R. T., 1987, "Resistance to the Flow of Fluids Through Simple and Complex Porous Media Whose Matrices Are Composed of Randomly Packed Spheres," ASME *Journal of Fluids Engineering*, Vol. 109, pp. 268-274.

Fand, R. M., and Phan, R. T., 1987, "Combined Forced and Natural Convection Heat Transfer From a Horizontal Cylinder Embedded in a Porous Medium," *International Journal of Heat and Mass Transfer*, Vol. 30, pp. 1351-1358.

Haughey, D. P., and Beveridge, G. S. G., 1969, "Structural Properties of Packed Beds—A Review," *The Canadian Journal of Chemical Engineering*, Vol. 47, pp. 130–140.

Hsu, C., and Cheng, P., 1990, "Thermal Dispersion in a Porous Medium," *International Journal of Heat and Mass Transfer*, Vol. 33, No. 8, pp. 1587–1597.

Huang, M., Yih, K., Chou, Y., and Chen, C., 1986, "Mixed Convection Flow Over a Horizontal Cylinder or a Sphere Embedded in a Saturated Porous Medium," ASME JOURNAL OF HEAT TRANSFER, Vol. 108, pp. 469–471.

Hunt, M. L., and Tien, C. L., 1988, "Non-Darcian Convection in Cylindrical Packed Beds," ASME JOURNAL OF HEAT TRANSFER, Vol. 110, pp. 378–384.

Kaviany, M., 1991, *Principles of Heat Transfer in Porous Media*, Springer-Verlag, New York.

Kohan, M. I., 1973, *Nylon Plastics*, Society of Plastics Engineers, SPE Monographs, Wiley, New York.

Kuo, S. M., and Tien, C. L., 1988a, "Heat Transfer Augmentation in a Foam-Material Filled Duct With Discrete Heat Sources," in: *Intersociety Conference on Thermal Phenomena in the Fabrication and Operation of Electronic Components*, IEEE, New York, pp. 87–91.

Kuo, S. M., and Tien, C. L., 1988b, "Transverse Dispersion in Packed-Spheres Beds," in: *Proceedings of the 1988 National Heat Transfer Conference*, ASME HTD-Vol. 96, pp. 629–634.

Lerou, J. L., and Forment, G. F., 1977, "Velocity, Temperature and Conversion Profiles in Fixed Bed Catalytic Reactors," *Chemical Engineering Science*, Vol. 32, pp. 853–861.

Minkowycz, W., Cheng, P., and Chang, C., 1985, "Mixed Convection About a Nonisothermal Cylinder and a Sphere in a Porous Medium," *Numerical Heat Transfer*, Vol. 8, pp. 349–359.

Moffat, R. J., 1988, "Describing Uncertainties in Experimental Results," *Experimental Thermal and Fluid Science*, Vol. 1, pp. 3–17.

Mohamad, A., and Viskanta, R., 1989, "Combined Convection-Radiation Heat Transfer in a Surface Combustor-Process Heater," in: *Simulation of Thermal Energy Systems*, R. F. Bohem and Y. M. El-Sayed, eds., ASME HTD-Vol. 124, pp. 1–8.

Pop, I., and Cheng, P., 1992, "Flow Past a Circular Cylinder Embedded in a Porous Medium Based on the Brinkman Model," *International Journal of Engineering Science*, Vol. 30, pp. 257–262.

Prasad, V., Kladias, N., Bandyopadhaya, A., and Tian, Q., 1989, "Evaluation of Correlations for Stagnant Thermal Conductivity of Liquid-Saturated Porous Beds of Spheres," *International Journal of Heat and Mass Transfer*, Vol. 32, pp. 1793–1796.

Touloukian, Y. S., Powell, R. W., Ho, C. Y., and Klemens, P. G., 1970, *Thermal Conductivity—Metallic Elements and Alloys*, Vols. 1 and 2, IFI/Plenum, New York.

Tsotsas, E., and Martin, H., 1987, "Thermal Conductivity in Packed Beds: A Review," *Chemical Engineering Process*, Vol. 22, pp. 19–38.

Wakao, N., and Kaguei, S., 1982, *Heat and Mass Transfer in Packed Beds*, Gordon & Breach, New York.

Xiong, T. Y., and Viskanta, R., 1992, "A Basic Study of a Porous-Matrix Combustor-Heater," in: *Fossil Fuel Combustion Symposium*, R. Ruiz, ed., ASME PD-Vol. 39, pp. 31–39.

Yagi, S., and Kunii, D., 1960, "Studies on Heat Transfer Near Wall Surface in Packed Beds," *American Institute of Chemical Engineers Journal*, Vol. 6, pp. 97–104.

Yagi, S., Kunii, D., and Wakao, N., 1961, "Radially Effective Thermal Conductivities in Packed Beds," in: *International Developments in Heat Transfer*, ASME, New York, Part IV, pp. 742–749.

Zehner, P., and Schlünder, E. U., 1970, "Thermal Conductivity of Granular Materials at Moderate Temperatures" [in German], *Chemie Ingenieur Technik*, Vol. 42, pp. 933–941.

Wall Roughness Effects on Stagnation-Point Heat Transfer Beneath an Impinging Liquid Jet

L. A. Gabour

J. H. Lienhard V

W. M. R. Heat and Mass Transfer Laboratory, Department of Mechanical Engineering, Massachusetts Institute of Technology, Cambridge, MA 02139

Jet impingement cooling applications often involve rough surfaces, yet few studies have examined the role of wall roughness. Surface protrusions can pierce the thermal sublayer in the stagnation region and increase the heat transfer. In this paper, the effect of surface roughness on the stagnation-point heat transfer of an impinging unsubmerged liquid jet is investigated. Experiments were performed in which a fully developed turbulent water jet struck a uniformly heated rough surface. Heat transfer measurements were made for jets of diameters 4.4–9.0 mm over a Reynolds number range of 20,000–84,000. The Prandtl number was held nearly constant at 8.2–9.1. Results are presented for nine well-characterized rough surfaces with root-mean-square average roughness heights ranging from 4.7 to 28.2 μm. Measured values of the local Nusselt number for the rough plates are compared with those for a smooth wall, and increases of as much as 50 percent are observed. Heat transfer in the stagnation zone is scaled with Reynolds number and a roughness parameter. For a given roughness height and jet diameter, the minimum Reynolds number required to increase heat transfer above that of a smooth plate is established. A correlation for smooth wall heat transfer is also given.

Introduction

Liquid jet impingement is an effective method for cooling surfaces owing to the high heat transfer coefficient produced. Among its industrial applications are the hardening and quenching of metals, tempering of glass, and cooling of turbine blades and electronic components. The surface roughness of these materials can play a significant role in the heat transfer, and thus should not be neglected. Hot rolled steel has an average roughness height of 12.5–25 μm (Kalpakjian, 1985) while gas turbine blades can have roughness protrusions ranging from 1.5 to 11 μm (Taylor, 1990). Wall roughness on the order of only a few microns in height, as for the cases mentioned, can significantly increase the heat transfer by disrupting the thin thermal boundary layer at the stagnation point. Relatively low levels of surface roughness may be expected to be influential, since, for example, this boundary layer can be on the order of 10 μm thick for a typical cold water jet. Although numerous investigations of the fluid flow and heat transfer beneath an impinging jet can be found in the literature, the effect of wall roughness has received little or no attention.

One of the few studies of impingement heat transfer to rough surfaces is that of Sullivan et al. (1992) who investigated the use of extended surfaces to augment heat transfer for the cooling of electronic chips. Submerged FC-77 jets of various diameters were used to cool one smooth and two roughened spreader plates attached to simulated electronic circuit chips. The two roughness types investigated were sawcut and dimpled patterns, with roughnesses of 0.30 mm and 0.10–0.30 mm, respectively. Their results cover the full range of smooth to fully rough flow, in which fully rough conditions were assumed to be achieved when the heat transfer reached the same rate of decrease with flow rate as for the smooth surface, following a sharp departure from smooth wall behavior at a lower flow rate. A unit thermal resistance, which accounted for conduction through the plate as well as convection at the surface, was shown to decrease by as much as 60 percent when the plates were roughened.

The present study concentrates on rough-wall stagnation-point heat transfer beneath an impinging turbulent liquid jet. Because the shear stress is zero at the stagnation point (Nakoryakov et al., 1978), standard rough wall theory cannot be applied directly: Typical roughness scaling depends on the friction velocity, $u^* = \sqrt{\tau_w/\rho}$, which vanishes at the stagnation point. Since the stagnation zone flow field is characterized by the strain rate or the radial velocity gradient, $B = 2\partial U/\partial r$ (White, 1974; Liu et al., 1992; Stevens et al., 1992), B becomes the dominant scaling parameter in place of the shear stress; near the wall, B produces a viscous length scale proportional to Reynolds number. Other deviations from rough wall turbulent boundary layer theory may result from the very highly accelerated flow near the stagnation point, which would tend to damp boundary layer turbulence originated by either roughness or free-stream turbulence (Moffat and Kays, 1984). Furthermore, the structure of this rough wall boundary layer is not clear. Roughness elements could pierce a sublayer and lower the thermal resistance, thus increasing the heat transfer. However, there is no guarantee of an intrinsically turbulent outer layer in this highly accelerated boundary layer; the role of free-stream turbulence may simply be to disturb the thin thermal boundary layer. If roughness destroys this layer, the fully rough flow condition may be solely dependent on the wall thermal conductivity and roughness size, shape, and spacing, as opposed to being limited by a substantial outer layer mixing process. In the absence of detailed flow measurements, these issues must remain ambiguous.

The present investigation is motivated by the fact that many surfaces that require impingement cooling are rough, while the existing impingement heat transfer correlations apply to smooth surfaces. Experiments were performed to characterize wall roughness effects on heat transfer beneath an unsubmerged turbulent liquid jet impinging normally against a flat, constant heat flux surface. Stagnation-point Nusselt numbers were measured for various Reynolds numbers, jet diameters, and wall roughnesses. As a baseline for comparison, smooth wall data were taken under the same conditions and the effect of nozzle-to-target separation on Nusselt number was briefly investigated. The results of this paper provide Nusselt number as a function of Reynolds number and a dimensionless wall

Contributed by the Heat Transfer Division and presented at the National Heat Transfer Conference, Atlanta, Georgia, August 8–11, 1993. Manuscript received by the Heat Transfer Division April 1993; revision received August 1993. Keywords: Forced Convection, Jets. Associate Technical Editor: A. Faghri.

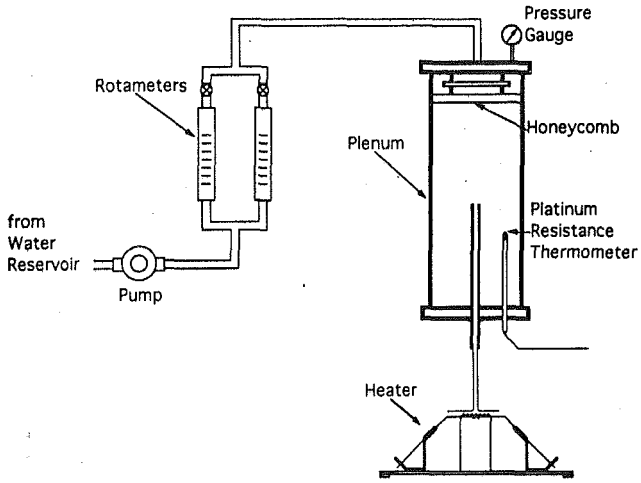

Fig. 1 Experimental arrangement

roughness. Suggestions are made for scaling to other Prandtl numbers.

Experimental Apparatus and Procedures

Experiments were performed to determine the local Nusselt number at the stagnation point of a turbulent liquid jet impinging on a rough wall. The experimental apparatus is illustrated schematically in Fig. 1 and consists of a flow loop and an electrically heated target plate. A fully developed, turbulent water jet impinges vertically downward and strikes a uniformly heated, flat, rough surface on which temperature measurements are made. The edges of the sheet are well beyond the stagnation region and do not affect the flow there. With the exception of a few experiments on the effect of nozzle-to-target spacing, the spacing was held constant at $l/d = 10.8$. Cold water at 12–16°C was used in order to raise the heat transfer and lower the experimental uncertainty in the Nusselt number, as well as to create a narrow Prandtl number range of 8.2–9.1.

The nozzles used to produce the liquid jets were made from tubes of inner diameters 4.4, 6.0, and 9.0 mm. The outlets of the tubes were carefully deburred to create smooth inner walls so that the highly disturbed surfaces of the jets can be attributed exclusively to turbulence. The tubes were 70–110 diameters long in order to ensure fully developed turbulent flow at the outlet. Contraction of these turbulent jets is less than 1.5 percent, so the mean jet diameters can be approximated by the nozzle diameters. The tube diameters were measured with precision calipers and have estimated uncertainties of ±0.2, ±0.7, and ±0.5 percent for the 4.4, 6.0, and 9.0 mm nozzles, respectively. (All uncertainties are at a 95 percent confidence level following the ASME Standard, PTC 19.1-1985.)

The liquid flow rate was varied from 0.098 to 0.637 l/s as determined from either of two rotameters connected in parallel in the flow loop. Primary calibration of the rotameters was performed by measuring the time required for a given volume of water to pass through the flow loop into a container. Performance of the rotameters was checked by calculating the jet's velocity, u_f, from the pressure reading of a Bourdon-type pressure gage at the top of the plenum. The flow rates were used to calculate the Reynolds number, which varied from 20,000 to 84,000. Uncertainty reached a maximum of ±3.2 percent for the volumetric flow rate and ±5 percent for the Reynolds number.

The jet impinges normally onto an electric heater, which consists of a 0.1016-mm-thick 1010 steel shim instrumented for temperature measurement and connected to a low voltage, high current generator (Fig. 2(*a*)). A slightly pressurized, hollow plexiglass box beneath the heater prevents water from flowing onto the underside of the shim and minimizes backlosses (which are negligible). The current supplied to the heater and the voltage drop across its length (between the bus bars) were measured. Knowledge of the electrical power dissipated by the heater, together with the heater area between the bus bars, was used to calculate the heat flux, which reached a maximum of 130 kW/m^2. As a check on the power measurements, the resistance of the sheets was also monitored while varying the current, giving an average resistance of 2.25 mΩ for all the sheets, with individual measurements differing from this value by less than ±0.5 percent. The change in effective shim thickness due to roughening the surfaces had a negligible net effect on the heat flux: While the shim thickness is slightly reduced in the area of the roughness, the current density increases by a proportional amount, offsetting the decrease in total thickness. Uncertainty in the heat flux was an average of ±4.2 percent.

The wall temperature was measured by three 0.076 mm iron-constantan (type J) thermocouples, all located on the back of the heater at the stagnation point, (Fig. 2(*b*)). The thermocouples were attached to the back of the steel shim and electrically isolated from it by 0.06-mm-thick Kapton tape. This attachment maintains good thermal contact of the thermocouple wires with the plate owing to the low resistance of the tape relative to natural convection resistance on the underside of the plate. Fin effects associated with the three thermocouples were estimated and are negligible.

During the experiments, ten voltage readings were taken for each thermocouple and averaged to reduce random error. The average of the voltages from the three thermocouples was used to calculate the wall temperature. The thermocouples were also calibrated with the heater power off before and after each run to reduce systematic errors. The incoming jet temperature ob-

Nomenclature

B = radial velocity gradient = $2(\partial U/\partial r)$
B^* = dimensionless radial velocity gradient = $2(d_j/u_f)(\partial U/\partial r)$
c_p = heat capacity of liquid
d = nozzle inner diameter
d_j = jet diameter $\approx d$
h = heat transfer coefficient
k = rms roughness element height
k^* = nondimensional roughness height = k/d_j
k_f = thermal conductivity of the impinging liquid
l = distance between nozzle outlet and target plate
Nu_d = Nusselt number based on jet diameter = $q_w d_j/k_f(T_w - T_f)$
Pr = Prandtl number = $\mu c_p/k_f$
Q = volumetric flow rate of jet
q_w = wall heat flux
Re_d = Reynolds number of jet = $u_f d_j/\nu$
r = radial distance from stagnation point
T_f = incoming jet temperature
T_{film} = film temperature = $(T_f + T_w)/2$
T_w = wall temperature on liquid side
t = heater sheet thickness
U = radial velocity just outside boundary layer
u^* = friction velocity = $\sqrt{\tau_w/\rho}$
u_f = bulk velocity of impinging jet = $4Q/\pi d_j^2$
δ_t = thermal boundary layer thickness
μ = dynamic viscosity of liquid
ν = kinematic viscosity of liquid = μ/ρ
ρ = liquid density
τ_w = shear stress at wall

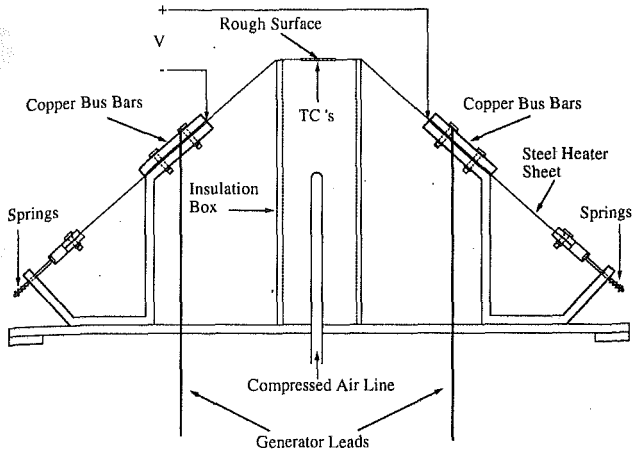

Fig. 2(*a*) Schematic diagram of heater arrangement

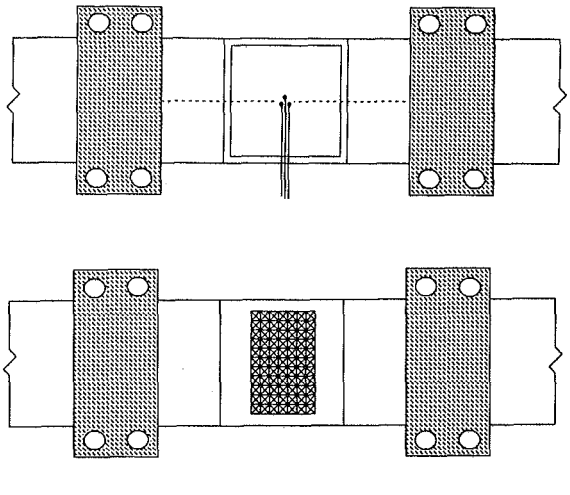

Fig. 2(*b*) Heated sheet as viewed from underside; (*c*) heated sheet as viewed from above

tained from the thermocouples under isothermal conditions was in agreement with that obtained from a platinum resistance thermometer located in the plenum to within the reading errors of the instruments, verifying that the bulk temperature change of the jet as it travels from the plenum to the target is negligible. A prior calibration of the thermocouples and the platinum resistance thermometer was performed by comparison to a mercury-in-glass thermometer. After calibration, the three devices agreed to within the reading errors of each instrument. The final uncertainty in the measured temperature was $\pm 0.05°C$.

The Nusselt number is based on the difference between the wall temperature, T_w, and the incoming jet temperature, T_f:

$$\mathrm{Nu}_d = \frac{q_w d_j}{k_f (T_w - T_f)} \tag{1}$$

where q_w is the wall heat flux and d_j is the jet diameter. Since the thermocouples were located on the back of the heater sheet, corrections amounting to no more than 10 percent were made to account for the vertical conductive temperature drop through the sheet (for details see Liu et al., 1991). The corrections were based on the smooth wall sheet thickness, and the reduction in thickness due to the roughness had a negligible effect on this result. Uncertainty in the mean Nusselt number ranged from ± 7.5 to ± 10 percent. Radial conduction in the sheet is negligible.

All liquid properties are evaluated at the film temperature, $T_{\text{film}} = (T_f + T_w)/2$, and were obtained from Touloukian (1970). Complete details of the flow loop, electric heater, calibration procedures, and uncertainty analysis are given by Gabour (1993).

Surface Characterization

The rough surfaces were produced by scoring a 3.4 cm^2 central portion of the steel shims in four directions in an attempt to simulate natural (homogeneous, isotropic) roughness (the pattern of scoring is as shown in Fig. 2(*c*)). This process results in ridges adjacent to the troughs. The ease of fabricating these surfaces contributed to the choice of this type of roughness. The distance between parallel roughness troughs ranged from 0.2 to 1.0 mm.

The nine rough surfaces were characterized by a root-mean-square average roughness as obtained from profiles of the surfaces. A DEKTAK 3030ST with a 2.5 μm radius stylus was used to make the measurements. The DEKTAK is a surface texture measuring system that makes measurements electromechanically by moving the sample in a straight line beneath a diamond-tipped stylus. The DEKTAK was carefully calibrated by scanning a standard 1 μm step and making the necessary adjustments to obtain the correct reading. A scan length of 10 mm and a stylus force of 0.3 N were used. Ten profiles were generated for each surface at intervals of 0.5 mm across the length of the sheet. An rms roughness height was calculated by the DEKTAK along the length of each profile, and the ten squared rms values were averaged. Due to the finite radius of the stylus, the path traced as it scans the surface is in principle smoother than the actual roughness of the surface. However, since the blade used to score the surfaces was triangular with a maximum width of 160 μm, we believe that the stylus was able to resolve the roughness contours accurately. Care was taken during the experiments to ensure that the jets were centered over the area that was used for the surface profiles. The roughness measurements were repeated after the experiments were completed to ensure that the steel shims had not rusted sufficiently to cause changes in any sheet's roughness. The rms roughness heights for the nine rough surfaces ranged from 4.7 to 28.2 μm while the smooth surface had an rms roughness of 0.3 μm. Some typical surface contours are given by Gabour (1993).

Experimental Results

The effect of nozzle-to-target spacing on the smooth wall stagnation-point Nusselt number was examined for the 4.4 mm nozzle over an l/d range of 0.9–19.8. The Nusselt number remained essentially constant over this range, with any slight deviations falling within the uncertainty of the experimental data; thus, a single nozzle-to-target spacing of $l/d = 10.8$ was employed for the remainder of the experiments.

The smooth wall Nusselt number data for the three nozzles are plotted in Fig. 3(*a*) and are represented by

$$\mathrm{Nu}_d = 0.278 \mathrm{Re}_d^{0.633} \mathrm{Pr}^{1/3} \tag{2}$$

to an accuracy of about ± 3 percent. Although the experimental Prandtl number was held nearly constant at 8.2–9.1, the standard high Prandtl number exponent of 1/3 is adopted in this correlation. The smooth wall correlations of Lienhard et al. (1992) and Pan et al. (1992) evaluated at a Prandtl number of 8.3 are included in Fig. 3(*a*) for comparison. Since the Reynolds number exponent is typically 0.5, Fig. 3(*b*) shows a comparison of the 0.5 and 0.633 Reynolds number exponent slopes on a log–log plot. Although an exponent of 0.5 may work for Reynolds numbers less than 35,000, 0.633 fits the data over the generally higher Reynolds number range investigated. This may account for some of the disagreement with the previous correlations, which assumed an exponent of 0.5. In addition, the Lienhard et al. (1992) result had an rms scatter of about ± 10

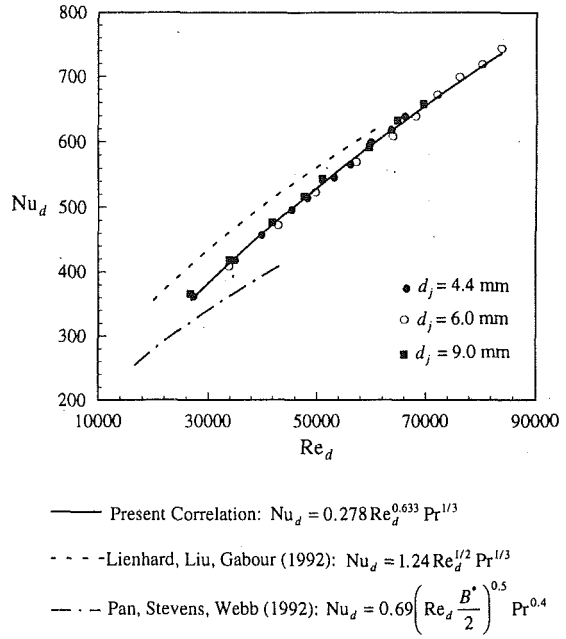

Fig. 3(a) Stagnation-point Nusselt number as a function of Reynolds number showing present data with present and past correlations

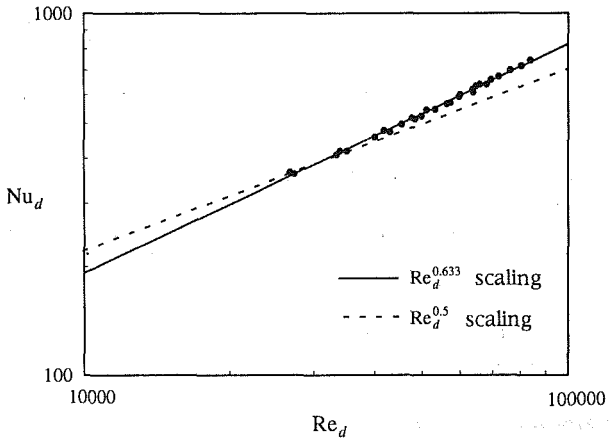

Fig. 3(b) Comparison of Reynolds number exponents for Nusselt number correlations

Fig. 3 Smooth wall results

percent, and the more precise results here do lie within the 95 percent confidence limits (2σ level) of the previous result.

The rms average roughness values for the ten surfaces are given in Table 1. The Nusselt numbers for each surface are shown in Figs. 4(*a–c*) as a function of jet Reynolds number for the 4.4, 6.0, and 9.0-mm jets, respectively. As expected, the Nusselt number increases with increasing wall roughness for each diameter, with the roughest surface (S10) producing the highest Nusselt number in all cases. The effect of roughness is clearly dependent on Reynolds number and jet diameter.

In general, the Nusselt number data for each surface tend to lie on distinct lines, with slope increasing as roughness increases. An exception occurs for surfaces S1, S2, and S3 in Fig. 4(*c*). The data from those surfaces lie on essentially the same line, implying that the roughnesses of S2 and S3 are ineffective for increasing heat transfer for the 9.0 mm nozzle. Apparently the roughness elements do not protrude substantially through the thermal sublayer, allowing the surfaces to behave as if they were smooth. At Reynolds numbers higher than examined for these surfaces, a transitionally rough regime may be reached, in which the roughness elements do disrupt the sublayer, thereby causing the data to rise from this line.

Table 1 Root-mean-square roughness heights for the ten heater surfaces. Uncertainties in the rms roughness heights range from ±4.5 to ±9 percent.

SURFACE	RMS ROUGHNESS (μm)
S1	0.3
S2	4.7
S3	6.3
S4	8.6
S5	13.1
S6	14.1
S7	20.1
S8	25.9
S9	26.5
S10	28.2

The effect of decreasing Reynolds number is to thicken the thermal boundary layer and thus to reduce the influence of roughness. With the exception of the roughest surfaces—S7 through S10 for the 4.4 mm nozzle and surfaces S9 and S10 for the 6.0 mm nozzle—the Nusselt number data tend to collapse to the smooth wall curve at the lower Reynolds numbers. Presumably these few exceptions also collapse at a lower Reynolds number, but owing to the limited Reynolds number range employed in this study, this presumption cannot be verified.

Differences between the smooth and rough wall data become more pronounced as jet diameter decreases, with results for the 4.4 mm nozzle in Fig. 4(*a*) showing the largest roughness effects. For example, at a Reynolds number of 40,000 there is a 32 percent increase in the Nusselt number for surface S10 over surface S1 for the 4.4 mm nozzle, while at the same Reynolds number the increase is 27 and 14 percent for the 6.0 and 9.0 mm nozzles, respectively. At a Reynolds number of 66,000, the increases rise to 47, 34, and 23 percent, respectively. This behavior can be explained by examining the effective thermal boundary layer thickness as determined from the smooth wall Nusselt number expression (Eq. (2)) with $Nu_d = d_j/\delta_t$:

$$\delta_t = \frac{3.60 d_j}{Re_d^{0.633} Pr^{1/3}} \tag{3}$$

As jet diameter decreases, boundary layer thickness decreases. Similarly, as Reynolds number increases, boundary layer thickness decreases. Roughness of a given height, k, is likely to have a greater impact on heat transfer under conditions for which δ_t is smaller, since its protrusion into (or through) the thermal boundary layer is greater.

The direct use of δ_t as a scaling parameter is problematical. When $k \ll \delta_t$, δ_t retains a reasonably clear physical meaning (a thermal boundary layer thickness) and we might expect, for example, that a threshold value of k/δ_t would characterize the onset of roughness effects. When k is near or greater than δ_t, δ_t lacks a direct physical significance. In this study, k/δ_t ranges from 0.19 to 4.11. In order to find a more appropriate scaling of the wall roughness, we may apply dimensional analysis.

For the fixed wall material and roughness geometry employed in this study, the dimensional functional equation for the heat transfer coefficient of the rough wall thermal boundary layer is $h = f(k_f, d_j, \rho, c_p, \mu, u_f, k)$. Dimensional analysis reveals that the corresponding Nusselt number is a function

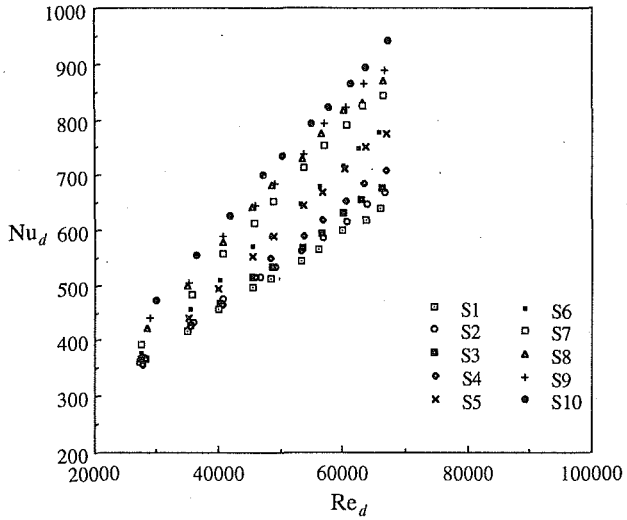

Fig. 4(*a*) 4.4 mm nozzle

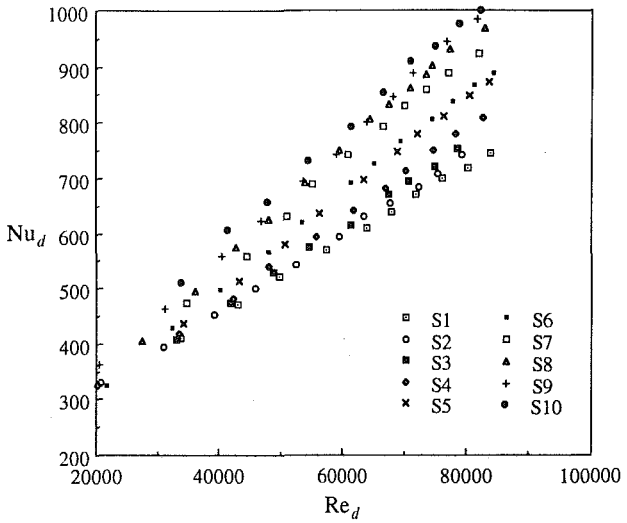

Fig. 4(*b*) 6.0 mm nozzle

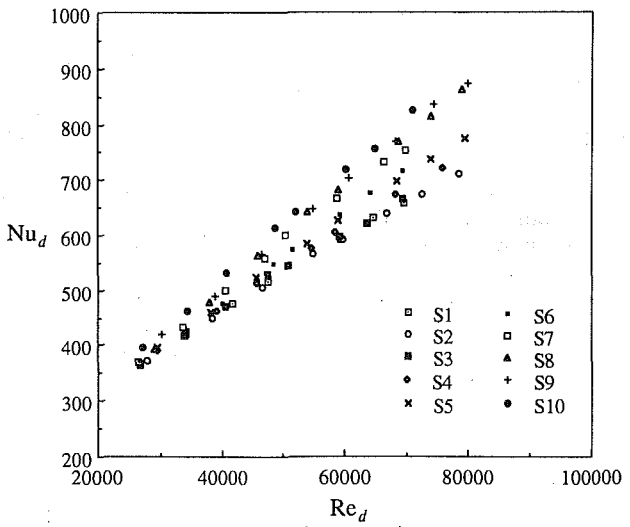

Fig. 4(*c*) 9.0 mm nozzle

Fig. 4 Stagnation-point Nusselt number for the ten surfaces as a function of Reynolds number

of Reynolds number, Prandtl number, and a roughness parameter, k/d_j, which we shall call k^* hereinafter. While the ratio of k to some sublayer-type length scale (δ_{sub}, say) would be a more standard descriptor of roughness effects than k/d_j, both ratios will express the same physics if $\delta_{sub}=f(\mathrm{Pr}, \mathrm{Re}_d, d_j)$. The better engineering parameter is k/d_j, which is clearly defined and accurately measurable. Since the Prandtl number was held essentially constant in this study, we can focus on the two remaining independent parameters, Re_d and k^*.

The Nusselt number is plotted as a function of Reynolds number in Figs. 5(*a*) and 5(*b*) for a few values of k^*. Each value of k^* represents and collapses data for different surfaces under different sized nozzles. At a given Reynolds number, the Nusselt number is the same for a given value of k^*, lending confidence that no other parameters are involved in the Nusselt number dependence. This also verifies that the ten surfaces are geometrically similar and only differ from one another by the rms height of roughness. Figure 5(*c*) compares the magnitude of the Nusselt number for the full range of k^* investigated, showing fitted curves with the individual data points left out for clarity. The Nusselt number increases with increasing values of k^* and approaches smooth wall behavior as Reynolds number decreases. An exception is curve 6, which crosses some other curves. We note that curve 6 is based on only one diameter and one surface, as opposed to an average of 2 to 4 diameter/surface combinations for the other fitted curves.

Figure 5(*c*) was compared to Fig. 3(*a*) to determine a criterion for transition from smooth wall to roughness influenced heat transfer. Departure from smooth wall behavior was taken to occur at the Reynolds number for which the rough wall Nusselt number became 10 percent larger than the corresponding smooth wall Nusselt number. Some of the larger k^* curves were extrapolated to lower Reynolds numbers to estimate this value, since those curves appeared to be in the roughness affected regime for the entire Reynolds number range investigated. Figure 6 shows this transition Reynolds number as a function of k^*. On the basis of this figure, we estimate that the heat transfer will remain in the smooth regime for

$$k^* < 5.95\mathrm{Re}_d^{-0.713}. \tag{4}$$

Above this value the flow may be considered rough walled.

Since the Prandtl number was held constant for the experiments, its role in the transition criterion is not clear from the data. However, under the rather broad assumption that Eq. (4) is in the form of a k/δ_t threshold with $\delta_t \propto \mathrm{Pr}^{-1/3}$, a calculation suggests that the heat transfer may remain in the smooth-wall region for:

$$k^* < 12.1\mathrm{Re}_d^{-0.173}\mathrm{Pr}^{-1/3} \tag{5}$$

As a result of the limited range of the data, an assessment of the possible appearance of "fully rough" behavior at high k^* or higher Re_d was not possible.

Conclusions

Stagnation-point heat transfer to an unsubmerged turbulent jet impinging on a rough surface was investigated. The effects of nozzle-to-target spacing, Reynolds number, and wall roughness were examined. Results from nine well-defined rough surfaces were compared to smooth wall data taken under the same conditions.

- The effect of nozzle-to-target separation on the stagnation-point Nusselt number for a smooth wall was found to be negligible over an l/d range of 0.9–19.8, with any variations falling within the experimental uncertainty of the data. The smooth wall Nusselt number is well represented by $\mathrm{Nu}_d = 0.278\mathrm{Re}_d^{0.633}\mathrm{Pr}^{1/3}$ to an accuracy of ±3 percent.
- Heat transfer at the stagnation point can be significantly increased by the presence of roughness elements, which can

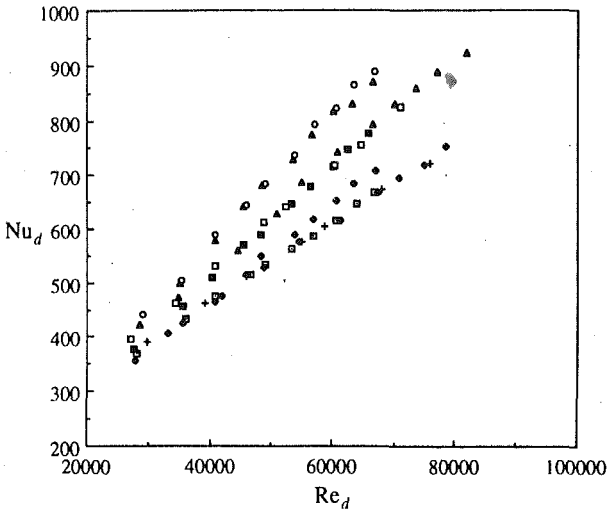

□ S2, $d_j = 4.4$mm, $k^* = 0.00107$
◆ S3, $d_j = 6.0$mm, $k^* = 0.00105$
+ S4, $d_j = 9.0$mm, $k^* = 0.00096$
■ S6, $d_j = 4.4$mm, $k^* = 0.00320$
▫ S10, $d_j = 9.0$mm, $k^* = 0.00313$
▲ S7, $d_j = 6.0$mm, $k^* = 0.00335$
• S4, $d_j = 4.4$mm, $k^* = 0.00195$
▲ S8, $d_j = 4.4$mm, $k^* = 0.00589$
○ S9, $d_j = 4.4$mm, $k^* = 0.00602$

Fig. 5(*a*) Stagnation-point Nusselt number as a function of Re_d and k^*

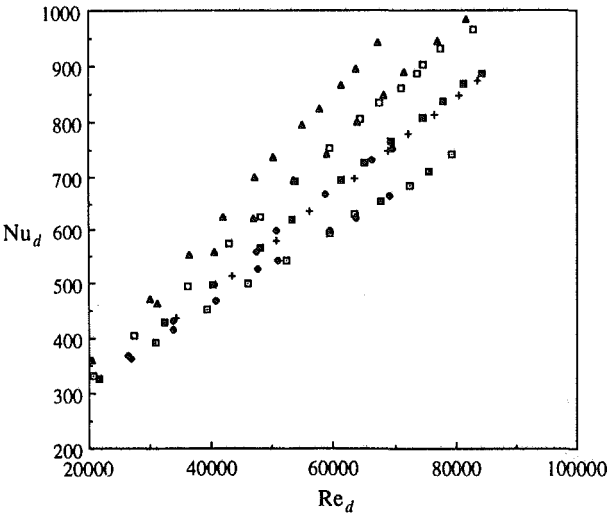

□ S2, $d_j = 6.0$mm, $k^* = 0.00078$
◆ S3, $d_j = 9.0$mm, $k^* = 0.00070$
+ S5, $d_j = 6.0$mm, $k^* = 0.00218$
• S7, $d_j = 9.0$mm, $k^* = 0.00235$
■ S6, $d_j = 6.0$mm, $k^* = 0.00235$
▫ S8, $d_j = 6.0$mm, $k^* = 0.00432$
▲ S9, $d_j = 6.0$mm, $k^* = 0.00442$
▲ S10, $d_j = 4.4$mm, $k^* = 0.00641$

Fig. 5(*b*) Stagnation-point Nusselt number as a function of Re_d and k^* (other values)

disrupt the thin thermal boundary layer. Heat transfer enhancement increases with increasing Reynolds number and decreasing jet diameter due to the corresponding thinning of the thermal boundary layer. Specifically, the Nusselt number was found to depend on k/d_j and Re_d. Increases in the Nusselt number over that of a smooth wall were as large as 50 percent.

• Departure from smooth wall behavior was defined by the Reynolds number at which the rough wall Nusselt number became 10 percent larger than the corresponding smooth wall

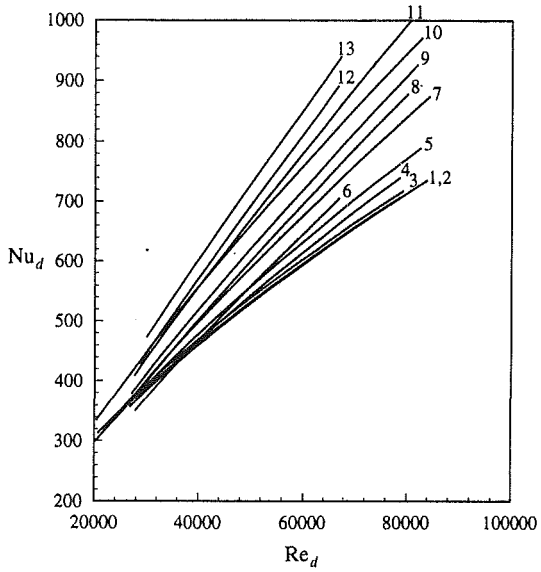

Fig. 5(*c*) Curve-fits for Nu_d as a function of Re_d and k^* for the full range of k^* investigated: $k^* = 0.00052$–0.00641

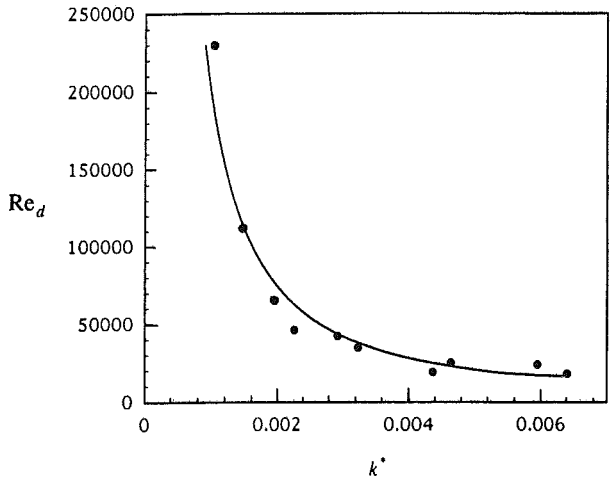

Fig. 6 Departure from smooth wall behavior based on a 10 percent increase in Nusselt number: present data and curve fit

Nusselt number. From this, the flow was found to remain in the smooth regime for $k^* < 5.95 Re_d^{-0.713}$; beyond this value the flow may be considered rough walled. More data are needed for Reynolds numbers less than 20,000 and greater than 80,000, as well as for k less than 5 μm and greater than 30 μm, to examine fully the transition to smooth behavior and the expected existence of a fully rough regime.

• Since the Prandtl was held essentially constant, its exact influence is not known. However, for high Prandtl number liquids, we believe that the wall will behave as if it were smooth for $k^* < 12.1 Re_d^{-0.713} Pr^{-1/3}$. Further investigations of Prandtl number effects, and also of wall thermal conductivity effects, are obviously needed.

Acknowledgments

This work was supported in part by the A. P. Sloan Foundation and the National Science Foundation under grant No. CBT-8858288. Laurette A. Gabour would like to acknowledge support from a National Science Foundation Graduate Research Fellowship.

References

Gabour, L. A., 1993, "The Effects of Surface Roughness on Stagnation-Point Heat Transfer During Impingement of Turbulent Liquid Jets," Master's Thesis in Mechanical Engineering, Massachusetts Institute of Technology, Cambridge, MA.

Kalpakjian, S., 1985, *Manufacturing Processes for Engineering Materials*, Addison-Wesley Publishing Company, Inc., Reading, MA, pp. 180–194.

Lienhard V, J. H., Liu, X., and Gabour, L. A., 1992, "Splattering and Heat Transfer During Impingement of a Turbulent Liquid Jet," ASME JOURNAL OF HEAT TRANSFER, Vol. 114, pp. 362–372.

Liu, X., Lienhard V, J. H., and Lombara, J. S., 1991, "Convective Heat Transfer by Impingement of Circular Liquid Jets," ASME JOURNAL OF HEAT TRANSFER, Vol. 113, pp. 571–582.

Liu, X., Gabour, L. A., and Lienhard V, J. H., 1992, "Stagnation Point Heat Transfer During Impingement of Laminar Liquid Jets: Analysis With Surface Tension Effects," *General Papers in Heat Transfer*, ASME HTD-Vol. 204, pp. 173–182.

Moffat, R. J., and Kays, W. M., 1984, "A Review of Turbulent-Boundary-Layer Heat Transfer Research at Stanford, 1958–1983," *Advances in Heat Transfer*, Vol. 16, pp. 241–365.

Nakoryakov, V. E., Pokusaev, B. G., and Troyan, E. N., 1978, "Impingement of an Axisymmetric Liquid Jet on a Barrier," *Int. J. Heat Mass Transfer*, Vol. 21, pp. 1175–1184.

Pan, Y., Stevens, J., and Webb, B. W., 1992, "Effect of Nozzle Configuration on Transport in the Stagnation Zone of Axisymmetric, Impinging Free-Surface Liquid Jets: Part 2—Local Heat Transfer," ASME JOURNAL OF HEAT TRANSFER, Vol. 114, pp. 880–886.

Stevens, J., and Webb, B. W., 1991, "Local Heat Transfer Coefficients Under an Axisymmetric, Single-Phase Liquid Jet," ASME JOURNAL OF HEAT TRANSFER, Vol. 113, pp. 71–78.

Stevens, J., Pan, Y., and Webb, B. W., 1992, "Effect of Nozzle Configuration on Transport in the Stagnation Zone of Axisymmetric, Impinging Free-Surface Liquid Jets: Part 1—Turbulent Flow Structure," ASME JOURNAL OF HEAT TRANSFER, Vol. 114, pp. 874–879.

Sullivan, P. F., Ramadhyani, S., and Incropera, F. P., 1992, "Use of Smooth and Roughened Spreader Plates to Enhance Impingement Cooling of Small Heat Sources With Single Circular Liquid Jets," Session on Direct and Indirect Cooling Techniques in Electronic Packaging, 28th ASME/AIChE National Heat Transfer Conference, San Diego, CA.

Taylor, R. P., 1990, "Surface Roughness Measurements on Gas Turbine Blades," ASME *Journal of Turbomachinery*, Vol. 112, pp. 175–180.

Touloukian, Y. S., 1970, *Thermophysical Properties of Matter*, Purdue University, West Lafayette, IN, Vol. 3, p. 120; Vol. 11, p. 94.

White, F. M., 1974, *Viscous Fluid Flow*, McGraw-Hill, New York.

Effects of Interactions Between Adjoining Rows of Circular, Free-Surface Jets on Local Heat Transfer From the Impingement Surface

S. J. Slayzak

R. Viskanta

F. P. Incropera

Heat Transfer Laboratory,
School of Mechanical Engineering,
Purdue University,
West Lafayette, IN 47907

Experiments have been conducted to obtain single-phase local heat transfer coefficient distributions associated with impingement of one or two rows of circular, free-surface water jets on a constant heat flux surface. The nozzle diameter, the centerline-to-centerline distance between nozzles in a row, and the nozzle-to-heater separation distance were fixed at 4.9, 6.3, and 89.7 mm, respectively. Two row-to-row separations (81 and 51 mm) were considered, and nozzle discharge Reynolds numbers were varied over the range from 16,800 to 30,400. The interaction zone created by opposing wall jets from adjacent rows is characterized by an upwelling of spent flow (an interaction fountain) for which local coefficients can approach those of the impingement zones. Interactions between wall jets associated with nozzles in one row can create sprays that impact the adjoining row with sufficient momentum to induce a dominant/subordinate row behavior. In this case the interaction zone is juxtaposed with the subordinate row, and local coefficients in the impingement and wall jet regions of the affected row may be significantly enhanced. This result contrasts with the deleterious effects of crossflow reported for submerged jets throughout the literature. Spray-induced enhancements, as well as interaction zone maxima, increase with decreasing row-to-row pitch and with increasing Reynolds number.

Introduction

Although jet impingement flow and heat transfer have long been active areas of research, the preponderance of existing literature deals with submerged jets, particularly for conditions corresponding to multiple jets in an array (Martin, 1977). For arrays, attention has focused on interactions between gaseous impinging jets and means by which spent fluid may be vented to prevent crossflow from hampering impingement heat transfer. Gases are not suitable for high heat flux applications, however, and liquid jets must be employed.

In recent years liquid jet impingement has received special consideration for electronic cooling (Incropera, 1989), as well as renewed attention for primary metal cooling (Tseng et al., 1991; Filopovic et al., 1992). Both applications can involve interactions between free surface, liquid jets. While boiling is inherent in the quenching of metals and may be used in electronic cooling schemes, examination of a single-phase system is an appropriate first step toward understanding flow and heat transfer phenomena associated with interacting free-surface jets.

Ishigai et al. (1977) were the first and, to date, only investigators to consider local heat transfer variations produced by two interacting free-surface, circular jets. Hydrodynamic conditions in the interaction zone between the two jets varied with proximity, ranging from weak disturbances at large separations to a forceful, fountainlike ejection of fluid at close separations. For this vigorous form of wall jet interaction, the interaction zone did not appreciably alter local heat transfer coefficients if the colliding flows had already undergone transition to turbulence. However, a substantial enhancement resulted if the collision occurred prior to transition. For submerged air jets, Gardon and Cabonpue (1962), Korger and Krizek (1966), and Gardon and Akfirat (1966) reported secondary maxima in transport coefficients for the interaction zone, which in some cases were comparable to the primary peaks for the impinging jets. Similar results were obtained in more recent studies (Koopman and Sparrow, 1976; Saad et al., 1980; Mikhail et al., 1982; Behbahani and Goldstein, 1983), which also revealed an increase in the magnitude of the secondary peaks with increasing Reynolds number and decreasing nozzle-to-nozzle spacing. This behavior indicates that enhancement is related to the amount of momentum retained by the interacting wall jets.

This study was motivated by the growing importance of free-surface liquid jets in materials processing and, in particular, by the application of arrays of such jets. The study focused on interactions between circular, free-surface jets aligned in a single row, as well as on interactions between an in-line array of two such rows. For an impingement surface at which a uniform heat flux was maintained, local convection coefficients were determined in the interaction zones. Experiments were performed for fixed values of the nozzle diameter (4.9 mm), the pitch between nozzles in a row (6.3 mm), and the nozzle-to-plate separation (89.7 mm). Jet impingement velocities were varied over the range $2.1 \leq \bar{V}_j \leq 4.5$ m/s, with equivalent velocities maintained for each of the nozzles in a row or an array. Two values of the row-to-row pitch (51 mm and 81 mm) were also considered.

Phenomena that can influence the hydrodynamics of impinging free surface circular jets include *splattering* and *hydraulic jump*. Splattering refers to droplet ejection from a

Contributed by the Heat Transfer Division for publication in the JOURNAL OF HEAT TRANSFER. Manuscript received by the Heat Transfer Division March 1993; revision received June 1993. Keywords: Flow Visualization, Forced Convection, Jets. Associate Technical Editor: A. Faghri.

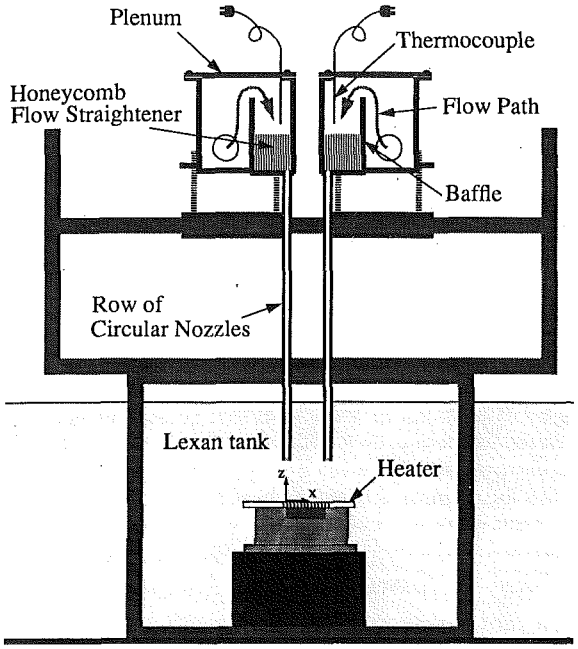

Fig. 1 Section view of the plena and nozzles positioned over the heater module

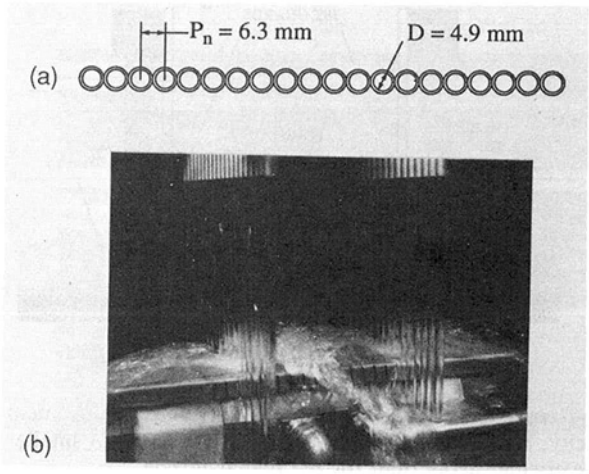

Fig. 2 Array of circular free-surface jets: (*a*) cross section of nozzles in a single row; (*b*) two rows of impinging jets and wall jet interaction zone

radially spreading wall jet, and according to Lienhard et al. (1992), it will occur when the parameter $\omega \equiv \mathrm{We}_D \exp[(0.971/\mathrm{We}_D^{1/2})(H/D)]$ exceeds 2120. For the conditions of this study, $190 \lesssim \mathrm{We}_D \lesssim 1230$ and $690 \lesssim \omega \lesssim 2040$. Hence, splattering was not expected, nor was it observed. Moreover, using the correlation developed by Stevens and Webb (1991) for onset of the hydraulic jump, the smallest radius at which the jump could occur for the conditions of this study is 76 mm ± 11 mm, which is outside the spatial domain of interest. Hence, hydraulic jumps should not occur, nor were they observed.

Experimental Procedures

The heater module of this study was identical to that used by Vader et al. (1991) and consisted of a 0.66-mm-thick Ni–Cr–W–Mo impingement plate ohmically heated by direct current to achieve a uniform heat flux. The 0.66-mm-thick plate was spring tensioned to compensate for thermal dilation while maintaining the desired flatness. To maintain the highest plate temperatures without inducing boiling, the heat flux was fixed at 0.5 MW/m^2. The plate was 260 mm long by 35.7 mm wide, and temperature measurements were made on its bottom surface by an array of 21 thermocouples. The thermocouples were spring-loaded against the surface, and a silicone paste (Omegatherm 201; thermal conductivity of 2.3 W/m°C, electrical resistivity of 10^{12} Ω-m) was applied to each thermocouple bead to provide electrical isolation with good thermal contact. The thermocouples were positioned at 5.08 mm intervals along the longitudinal midline of the heater plate, and spanwise (y) temperature variations were determined by repositioning the nozzles relative to the heater.

An existing plenum design (Zumbrunnen et al., 1990) was modified to allow two rows of jets to be positioned to within 25 mm of each other (Fig. 1). Jet temperatures were measured just upstream of hexagonal honeycomb flow straighteners and were maintained at 30 ± 0.1°C throughout the experiments. The flow rates used to calculate average jet velocities were measured upstream of the plena using turbine flowmeters, which were accurate to within 1/2 percent of full scale (0.08 l/s and 0.02 l/s). The flow rates were used to determine nozzle discharge velocities, from which impingement velocities were determined by correcting for gravitational acceleration of the descending jets.

The nozzles were constructed of 585 mm lengths of seamless, stainless steel tubing and were cold-soldered together to maintain colinearity (Fig. 2). The tubing had a nominal wall thickness of 0.7 mm, yielding an internal diameter of 4.9 mm and allowing six jets per row to impinge on the 35.7 mm wide heater. The tube length-to-diameter ratio exceeded 100, insuring fully developed turbulent flow for the conditions of the study. The center-to-center spacing of the tubes was 6.3 mm, providing a dimensionless pitch of 1.28. The 4.9 mm nozzle diameter was chosen to approximate the 5.1 mm width of planar nozzles used in another jet impingement study (Slayzak et al., 1994). Results from the two studies will be compared to assess the effect of geometric differences for planar nozzles

Nomenclature

D_n = diameter of a circular nozzle
h = local heat transfer coefficient
$\overline{h}$ = average heat transfer coefficient
H = height of a nozzle discharge above the impingement surface
L = prescribed distance along the impingement surface
P_r = distance between nozzle rows (row pitch)
P_n = nozzle-to-nozzle separation in a row (nozzle pitch)
q'' = local surface heat flux
r_i = radius of a circular jet at impingement
Re_{ri} = impingement Reynolds number = $\overline{V}_j r_i/\nu$
Re_D = Reynolds number = $\overline{V}_n D_n/\nu$
T_f = measured fluid temperature
T_w = calculated temperature of the impingement surface
$\overline{V}_j$ = average jet impingement velocity
$\overline{V}_{jl}$ = average impingement velocity of the jets on the left
$\overline{V}_{jr}$ = average impingement velocity of the jets on the right
$\overline{V}_n$ = mean velocity at nozzle discharge
We_D = Weber number = $\rho \overline{V}_n^2 D_n/\sigma$
W_n = width of a planar nozzle
x, y, z = longitudinal, spanwise, and vertical coordinate directions
ν = kinematic viscosity
ρ = mass density
σ = surface tension

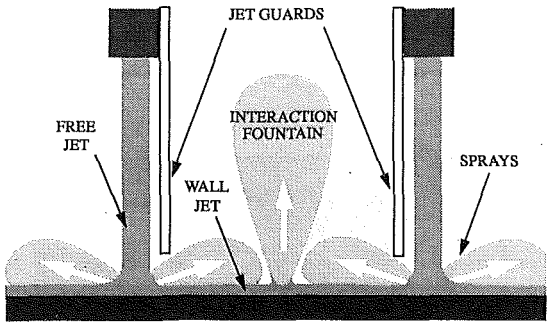

Fig. 3 Positioning of the jet guards

and arrays of circular nozzles. For the same impingement velocity, the requisite flow rate would be 43 percent smaller for the circular array than for the planar nozzle.

Once installed over the heater, the plenum/nozzle assemblies were carefully leveled/squared before being locked into place. Each nozzle remained vertical while being adjusted to the prescribed height above the plate. The rows were then positioned at the desired pitch, such that they were parallel to each other and perpendicular to the x axis of the heater. Finally, six jets per row were centered over the heater width by allowing low flow rates to pass through the nozzles. These resulting jets acted as plumb weights, allowing accurate determination of the impingement locations.

Impingement of the opposing wall jets formed by the two rows of circular nozzles produced an *interaction fountain*, which vigorously ejected water from the plate. However, for the row pitches considered in this study, water from the fountain impacted the free-surface jets prior to impingement. Related disturbances were of sufficient magnitude to affect momentum exchange in the wall jet interaction zone, causing the fountain to careen back and forth and to impact the jets with such force as to cause momentary loss of jet coherence. To stabilize the flow field, jet guards were constructed of 3.2-mm-thick acrylic, and securely positioned as shown in Fig. 3. The sprays labeled in the figure were formed by the post-impingement interaction of adjacent jets in a row, and the fountain was subsequently formed by interaction of the resultant wall jets. With the guards in place, the free-surface jets descended unimpeded to the plate and oscillations of the fountain were reduced to several millimeters. Moreover, the wall jets were less susceptible to disruption by spent flow reimpinging in the form of droplets. Because the impingement surface was only 35.7 mm wide and the interaction fountain was often many times that in height, much of the spent fluid fell clear of the plate. Only when the fountain was relatively weak (low impingement velocities) did most of the ejected fluid re-impinge on the wall jets, causing the oscillation of the interaction zone to increase in amplitude.

To facilitate flow visualization, the heater module was replaced by an acrylic plate, which permitted optical access from below. The plate was graduated at 10 mm intervals to aid in matching flow conditions with heat transfer measurements. A camera was positioned below the plate, and good contrast was typically obtained by using Kodak TMAX 400 film with aperture and shutter settings of f/4 and 1/500 s. With the flow field diffusely illuminated from the side and slightly above the plate, irregularities in the free surface turned the light toward the camera, which was centered below the interaction zone.

Temperatures measured at the bottom surface of the heated impingement plate were used with a solution of the two-dimensional heat equation to obtain the temperature field within the plate and the distribution of the convection heat transfer coefficient along the impingement surface. The solution domain included 150 nodal points in the flow direction, requiring use of a cubic spline, least-squares procedure to interpolate associated back surface temperatures from the 21 thermocouple measurements. Details of the data reduction procedure are provided by Vader et al. (1991). In this study each of the 21 temperature measurements comprising an experimental run corresponded to the arithmetic mean of 100 readings taken over the course of approximately 12 minutes. An experimental run was taken to represent a quasi-steady condition if the average variation in the difference between the wall and jet temperatures differed by less than ± 0.5°C from one run to the next. This criterion was typically met within the first three runs, regardless of the degree of unsteadiness in the flowfield. Due to the heater thickness, the thermocouples did not respond to thermal transients produced at the heater surface by movement of the interaction zone. Transient conduction in the plate attenuated temperature excursions induced at the wetted surface by oscillations of the interaction zone, and none of the measured temperatures varied by more than 1°C during a run, regardless of the oscillation amplitude or frequency.

With local temperatures and heat fluxes known for the impingement surface, local convection coefficients may be computed:

$$h(x) = q''/[T_w(x) - T_j] \tag{1}$$

and, in turn, may be used to determine an average heat transfer coefficient for the surface:

$$\bar{h} = \frac{\overline{q''}}{\overline{\Delta T}} = \frac{(1/L)\int_0^L [h(x)\cdot\Delta T(x)]dx}{(1/L)\int_0^L \Delta T(x)dx} = \frac{q''}{\int_0^L \Delta T(x)dx} \tag{2}$$

where $\overline{\Delta T} = \overline{(T_w - T_j)}$. Although it is not computationally convenient for design calculations, $\bar{h}$ provides a useful figure of merit for determining the relative heat transfer effectiveness of single and dual jet configurations. To facilitate a comparison between single and dual row configurations, L is equated to the row pitch, P_r, and $\bar{h}$ for a single row is calculated over the same region as that for the two-row system to which it is being compared. The product of the heat transfer coefficient and temperature difference in the integrand of the numerator (the local heat flux) is constant for the heater. An experimental uncertainty analysis based on accepted procedures (Moffat, 1988) yielded convection coefficient uncertainties of ± 18 percent.

Results and Discussion

Experiments were performed for a fixed heat flux ($q'' = 0.5$ MW/m^2), jet temperature ($T_j = 30$°C), nozzle-to-plate spacing ($H = 89.7$ mm), and nozzle diameter ($D_n = 4.9$ mm). The jet impingement velocity was varied over the range $2.1 \le \bar{V}_j \le 4.5$ m/s, and two values of the row-to-row spacing ($P_r = 51$, 81 mm) were considered, along with conditions for a single row ($P_r \to \infty$). In addition to delineating conditions associated with an array of circular, free-surface jets, results are compared with those obtained for planar jets in a prior study (Slayzak et al., 1994). Operating conditions of the two studies were virtually equivalent, with planar nozzles of width $W_n = 5.1$ mm replacing rows of circular nozzles with $D_n = 4.9$ mm.

Single Row Conditions. Figure 4 provides longitudinal heat transfer coefficient distributions for a single planar jet and a single row of circular jets. For the planar jet, Fig. 4(a), a local maximum at the stagnation line ($x = 0$) is followed by a sharp reduction due to laminar boundary layer growth. Transition to turbulence subsequently increases the heat transfer coefficient to a second maximum, beyond which the coefficient again decreases due to turbulent boundary layer development. Average heat transfer coefficients correspond to the region

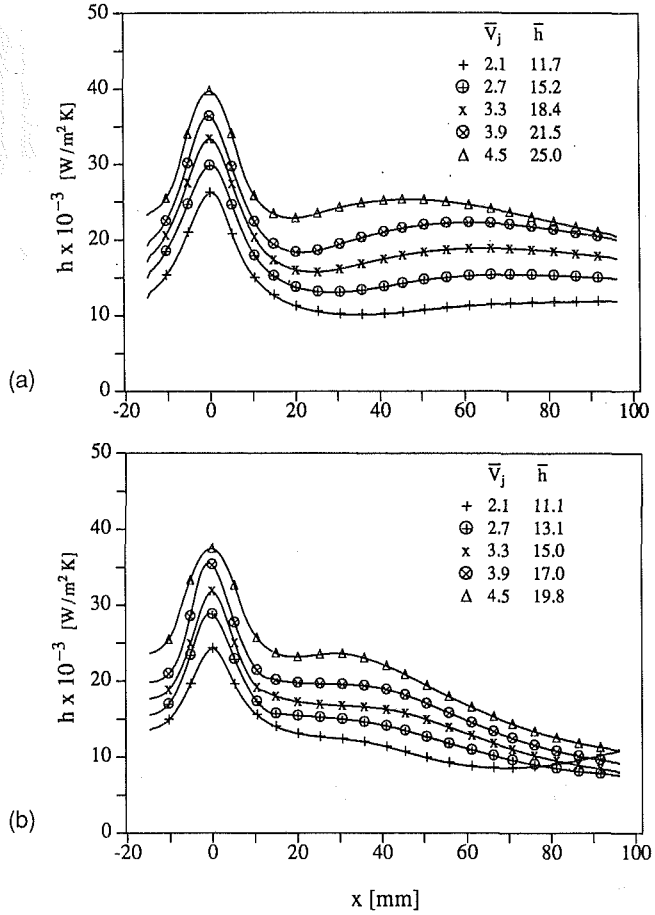

Fig. 4 Local heat transfer coefficient distributions for impingement of (*a*) single planar jet (W_n = 5.1 mm) and (*b*) a single row of circular jets (D_n = 4.9 mm)

$0 \leq x \leq 81$ mm, which encompasses the larger row pitch used in the multiple jet experiments.

For a single row of circular jets, Fig. 4(*b*), the longitudinal distribution of h more closely resembles results corresponding to the radial distribution of h for a single circular jet. While there is evidence of transition from laminar to turbulent flow in the region $20 \lesssim x \lesssim 30$ mm, the dominant trend is one of decreasing h with increasing x. Although these results were obtained with the heater midline positioned halfway between adjoining jets, the trend characterized all spanwise locations. Stevens and Webb (1991) measured radial heat transfer coefficient distributions for a single turbulent, axisymmetric water jet and found the distributions to be characterized by a sharp drop outside the stagnation region, which was followed by a bend in the distribution and a more gradual reduction in h. In some cases conditions were characterized by a secondary peak, which became more pronounced with increasing Re_{ri}. The bend and secondary peak were attributed to a transition to turbulence. In a radially spreading flow, the local coefficient will decrease as the mean film velocity decreases. The fact that this trend is exhibited by the data of this study suggests that portions of the individual jets comprising the array maintain their identities as "radially spreading flows" for some distance after impingement.

Contrasting values of $\bar{h}$ from Figs. 4(*a*) and 4(*b*), average coefficients for the planar jet exceed those for the row of circular jets and differences increase from approximately 5 to 26 percent with increasing velocity. In comparing their predictions for a single circular jet with results obtained for a planar jet, Liu and Lienhard (1989) found that average Nusselt numbers for a planar jet exceeded those for a single circular jet. Differences were attributed to development of the viscous boundary layer and the fact that it reached the free surface of the radial wall jet and did not do so for the planar jet.

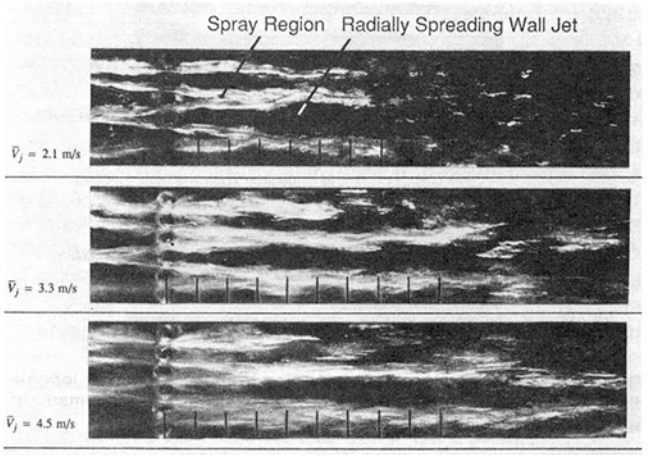

Fig. 5 Visualization of flows associated with a single row of circular jets

Flow visualization results are shown in Fig. 5 for a single row of circular jets. Immediately following impingement, flows from adjoining jets interacted, forming sprays that ascended from the impingement surface. The sprays were seen from below as bright areas issuing from regions between the jets. Ideally, sprays generated by colinear circular jets should be ejected in a direction normal to the row. In practice, such a condition was not achieved, since small differences in tube geometry or position altered colinearity of the jets within a row and produced the converging/diverging sprays exhibited in Fig. 5. Spray patterns were nozzle specific and independent of impingement velocity. The spray pattern strongly influenced the momentum flux distribution in the wall jet and, for dual row conditions, the dynamics of the interaction zone.

Water ejection from the plate was observed to occur at longitudinal stations up to 20 jet diameters (for large $\bar{V}_j$), suggesting that interactions between radially spreading flows continued to occur well downstream of the impingement zone. However, with increasing x, the decelerating radial flows collided at progressively smaller angles, and eventually velocities and angles were insufficient to eject water from the plate, as the merger of flows from adjoining jets became complete. Similar behavior was noted by Koopman and Sparrow (1976) in their study of a linear array of submerged circular jets. In their case, the individual flows were able to persist only up to five nozzle diameters. However, since free-surface jets do not lose appreciable momentum to the ambient, independent jet behavior should persist farther downstream, with merger delayed as $\bar{V}_j$ is increased. For the lowest impingement velocity, 2.1 m/s, sprays ascended up to 2 cm above the plate, and the elevation increased with increasing impingement velocity to values of up to 20 cm for $\bar{V}_j$ = 4.5 m/s. The increase in h observed for $\bar{V}_j$ = 2.1 m/s and $x \gtrsim 70$ mm, in Fig. 4(*b*), is attributed to cool fluid, which has been transported downstream as a spray, causing droplet impingement on the plate and heat transfer enhancement.

Heat transfer to a planar jet should vary only with longitudinal distance from the stagnation line. Although some edge effects may exist, flow along the longitudinal midline of the heater is representative of conditions over much of the spanwise direction. For the circular array, however, hydrodynamic conditions are nonuniform across the plate width. Figure 6(*a*) shows a photograph of flow conditions for which heat transfer measurements were made at different spanwise locations. Because the thermocouple array was fixed at the midline of the heater, the four cases were determined by translating the jet

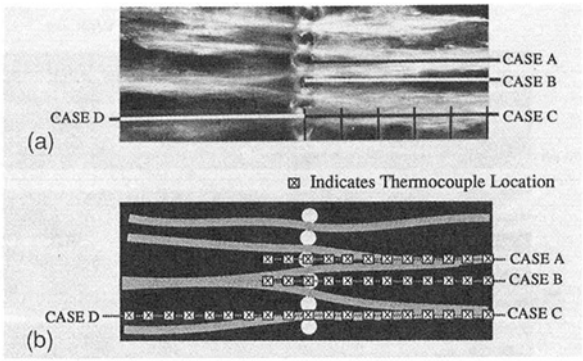

Fig. 6 Spanwise locations corresponding to measurement of longitudinal temperature distributions (*a*) flow visualization, (*b*) schematic of interaction zones and thermocouple locations

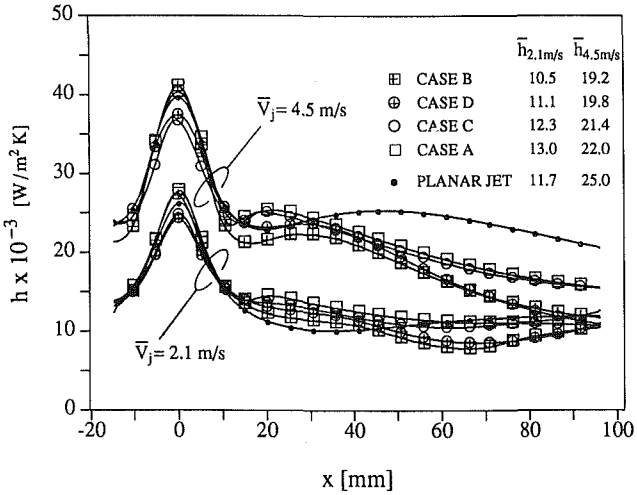

Fig. 7 Spanwise variation of longitudinal heat transfer coefficient distribution for the circular array of Fig. 6 and the corresponding distribution for equivalent planar jet conditions

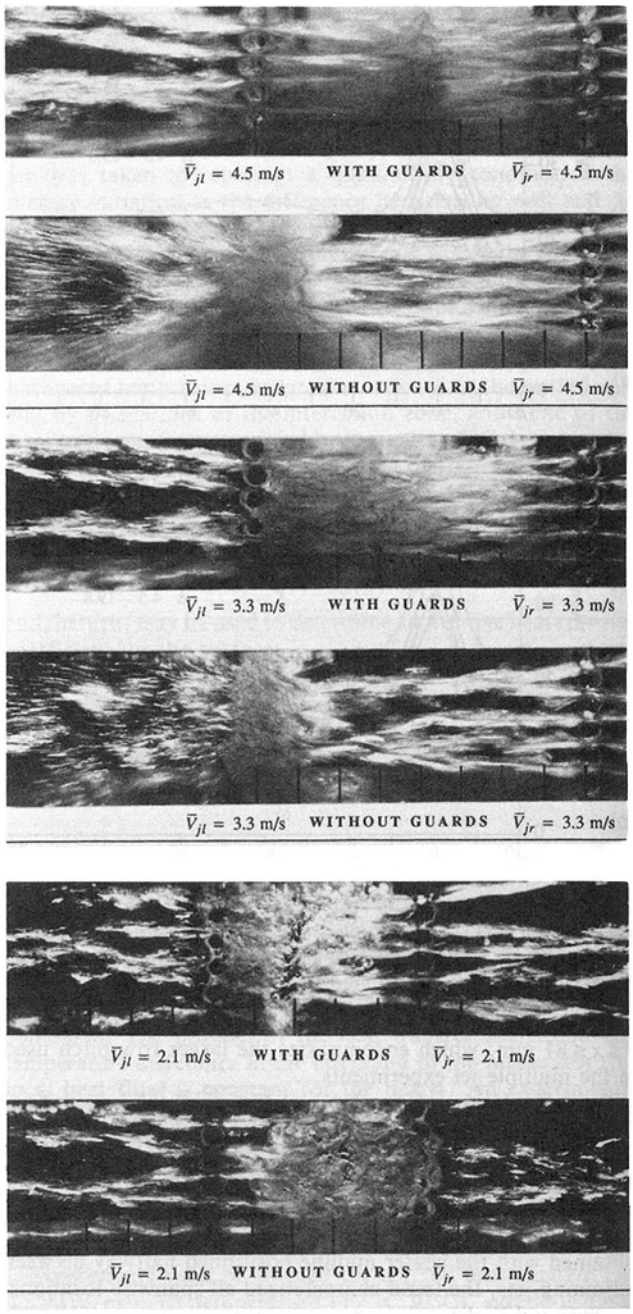

Fig. 8 Twin circular array jets viewed from below (P_r = 81 mm)

array in the spanwise direction. In the impingement region, measurements could be made directly beneath a jet or between adjacent jets. In the wall jet region, data could be taken in the region of radial spread or under a spray.

Figure 7 provides an indication of the spanwise variation of the local heat transfer coefficient corresponding to the array of circular jets depicted in Fig. 6. The largest coefficients exist in the stagnation zone directly beneath a jet (Cases A and B). Although there is a slight reduction in h (approximately 10 percent) between the jets (Case C and D), local coefficients remain high relative to downstream locations. Heat transfer at the impingement point directly beneath a circular jet closely matches that of a planar jet of equal impingement velocity. In the wall jet region, heat transfer is enhanced at spanwise locations occupied by the sprays (Cases A and C) and decays more rapidly in regions of radial spread (Cases B and D). The sprays enhance turbulent mixing in the liquid film, as indicated by the accelerated transition to turbulence.

With the longitudinal average heat transfer coefficients calculated over the region from impingement to 81 mm, the planar jet clearly provides superior performance at the larger velocity. For the lower velocity, however, impingement of the sprays counteracts the deterioration heat transfer in the wall jet region, and the thermal performance of the circular jets is comparable to that of the equivalent planar jet.

Dual Row Conditions. The sprays and radially spreading flows of guarded twin circular arrays created a jagged interaction zone that did not necessarily reside midway between the rows of jets (Fig. 8). Because of this nonuniformity and the fact that the impingement velocity is not preserved by the radially spreading flows, fountains in the interaction zones ascended to lower elevations (from approximately 20 to 200 mm for impingement velocities from 2.1 to 4.5 m/s) than the fountains associated with impinging planar jets (Slayzak et al., 1994). Because wall jets associated with the circular array continuously lose fluid due to the generation of sprays and become thinner and slower as they proceed from the line of impingement, the fluid layer thicknesses in the interaction zones are much smaller than the jet diameter. With decreasing impingement velocity, the weakening interaction fountain redirected more of the spent flow onto the wall jets, thereby increasing disruption of momentum exchange in the interaction zone. The interaction zone oscillated with increasing amplitude and decreasing physical cohesiveness, until, at $\bar{V}_j$ = 2.1 m/s, it could barely be discerned by visualization from below. An extremely unstable interaction zone appeared to be centered

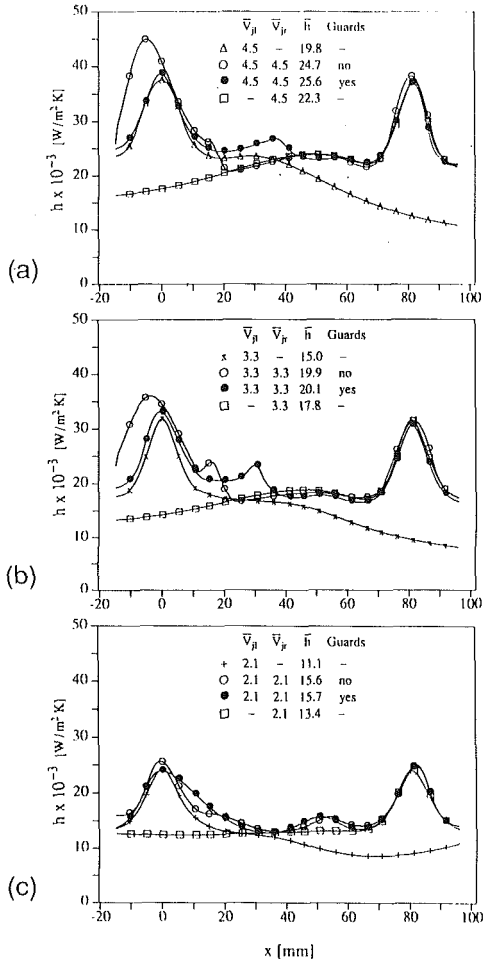

Fig. 9 Local heat transfer coefficients for twin arrays of circular jets (P_r = 81 mm): (*a*) $\overline{V}_j$ = 4.5 m/s, (*b*) $\overline{V}_j$ = 3.3 m/s, (*c*) $\overline{V}_j$ = 2.1 m/s

at $x \approx 50$ mm and to meander periodically toward the left jet (in apparent deference to the competing actions of opposing sprays) before returning to $x = 50$ mm.

Unguarded twin circular arrays exhibited different hydrodynamic conditions. In particular, when the sprays reached far enough to impact one of the rows of jets, the interaction zone moved to the affected row and remained there. This condition is clearly revealed by results obtained for impingement velocities of 3.3 and 4.5 m/s. This *dominant/subordinate* row behavior was not the result of systematic error in measurement of flow rate or positioning of the nozzles, but in fact resulted from the nozzle-specific spray patterns previously described. Because the spray pattern is affected by small variations in nozzle and row alignments, momentum exchange at the interaction zone and disruption of the jets are similarly affected. In addition to creating an irregular interaction zone for the guarded rows, the alignment and spray pattern of Fig. 8 increased hydrodynamic conditions for which the right and left rows were dominant and subordinate, respectively. Since the sprays generated by a row of nozzles only reached 65 mm for $\overline{V}_j$ = 2.1 m/s, dominant/subordinate behavior was not exhibited for $P = 81$ mm, and there was little difference between results for the guarded and unguarded conditions. In both cases the interaction zone oscillated about an equilibrium position at $x \approx 50$ mm.

Convection heat transfer coefficient distributions associated with adjoining rows of circular jets are shown in Fig. 9 for P_r = 81 mm, along with results for a single row positioned at x = 0 (left) or $x = 81$ mm (right). Relative to results obtained for dual planar jets (Slayzak et al., 1994), a prominent feature of the data for guarded rows of circular jets is the absence of significant heat transfer enhancement in the interaction zones. Although secondary peaks do exist, they are much less pronounced than those associated with interacting planar jets. At the highest velocity ($\overline{V}_j$ = 4.5 m/s), for which the fountains are most stable, heat transfer in the impingement and wall jet regions is largely unaffected by the jet interactions, Fig. 9(*a*), while slight enhancement is experienced in the left impingement and wall jet regions for the intermediate velocity, Fig. 9(*b*). These results are in sharp contrast to those obtained for planar jets, where convection coefficients in the impingement and wall jet regions were significantly degraded by the interaction fountain. At the lowest velocity, Fig. 9(*c*), the interaction zone spent a good deal of time centered at $x \approx 50$ mm, as indicated by the small local maximum, and periodic excursions to the left enhanced local coefficients for $0 \lesssim x \lesssim 30$ mm.

For the unguarded rows, the significant features are revealed by the heat transfer distributions for the larger velocities ($\overline{V}_j$ = 3.3, 4.5 m/s): (*i*) There is significant enhancement in the impingement region of the subordinate row, and (*ii*) for $x \gtrsim$ 20 mm, the subordinate row has no effect on conditions imposed by the dominant row. Although not evident from Fig. 8, impingement of the subordinate row did occur and an interaction zone existed at $10 \lesssim x \lesssim 15$ mm. However, sprays were not formed by the subordinate row, indicating that individual axisymmetric flows associated with each of the jets had totally lost their identities. Nevertheless, incidence of the spray generated by the dominant row and pronounced mixing in the interaction zone combined to enhance heat transfer in proximity to the subordinate jet. Since sprays generated by interactions between the jets of one row could not reach the other row for $\overline{V}_j$ = 2.1 m/s, the foregoing dominant/subordinate behavior did not characterize conditions for the smallest impingement velocity. In fact, there is little to differentiate distributions for the guarded and unguarded conditions.

Average convection coefficients over the region $0 \lesssim x \lesssim 81$ mm are virtually identical for the guarded and unguarded dual row conditions and exceed results for a single row by approximately 15 to 20 percent. For dual row conditions, average coefficients for the planar jets exceed those for circular jets by approximately 8 percent at the largest velocity (4.5 m/s), but the difference decreases with decreasing velocity and is negligible at the smallest velocity (2.1 m/s). Note that, for the circular nozzles, longitudinal averages vary only slightly in the spanwise direction and that, for equivalent impingement velocities, the circular nozzles use 43 percent less water than the planar nozzles.

With decreasing row pitch, circular array hydrodynamic conditions continued to be determined by the interaction of the sprays. Once again interaction zones were shifted to the left, with dominant /subordinate behavior occurring at the higher velocities when jet guards were not employed (Fig. 10). For the higher velocities, interaction zone behavior was unaffected by the decreased pitch. Moreover, although the spray generated by the interacting jets of one row could reach the other row for $\overline{V}_j$ = 2.1 m/s, dominant/subordinate behavior for the unguarded jets remained absent. Barely reaching the other row in the downward phase of their trajectories, the sprays did not carry sufficient horizontal momentum to disturb the associated jets significantly. As for the larger pitch, the resulting interaction zone was weak, meandering slowly from jet to jet. However, the reduction in pitch did create a thicker interaction zone for the guarded jets, which became more clearly defined with increased collision velocity. For equal impingement velocities, collision velocities for P_r = 51 mm exceeded those for P_r = 81 mm due to reduced spreading of the individual radial flows.

Contrasting Figs. 9 and 11, the most significant effect of the reduction in P_r is the establishment of a secondary maxi-

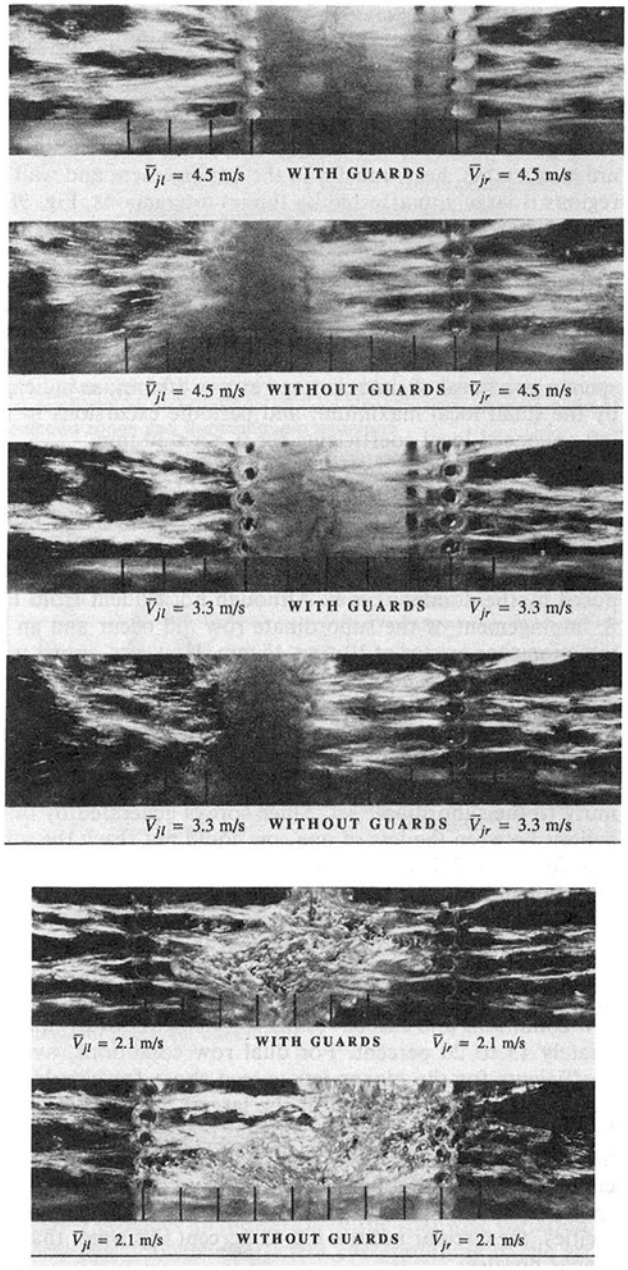

Fig. 10 Twin circular array jets viewed from below (P = 51 mm)

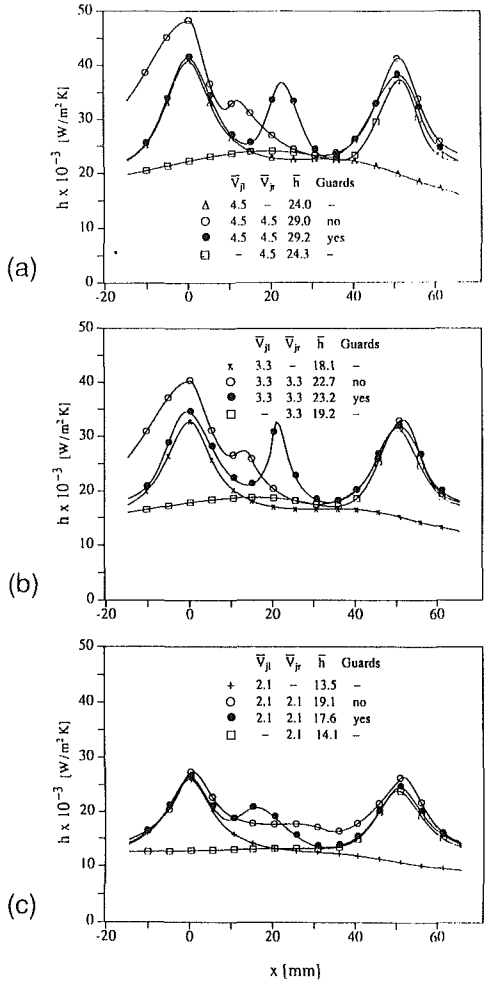

Fig. 11 Local heat transfer coefficients for twin arrays of circular jets (P_r = 51 mm): (*a*) $\bar{V}_j$ = 4.5 ms, (*b*) $\bar{V}_j$ = 3.3 m/s, (*c*) $\bar{V}_j$ = 2.1 m/s

Table 1 Average heat transfer coefficients for the dual circular jet array of this study and the comparable dual planar jets considered by Slayzak et al. (1994)

NOZZLE TYPE	$\bar{V}_j$ (m/s)	GUARDS		$\bar{h}$ (kW/m^{2}K)	
				P_r = 81 mm	P_r = 50 mm
Planar	4.5	Yes		26.8	28.6
			No	27.2	29.4
	3.3	Yes		20.4	23.4
			No	21.7	23.6
	2.1	Yes		14.9	17.8
			No	15.5	17.4
Circular Array	4.5	Yes		25.6	29.2
			No	24.7	29.0
	3.3	Yes		20.1	23.2
			No	19.9	22.7
	2.1	Yes		15.7	17.6
			No	15.6	19.1

mum in the interaction zone for the guarded condition. For this condition, the distributions more closely resemble those for guarded planar jets (Slayzak et al., 1994) and average convection coefficients for the planar and circular arrays differ by no more than 2 percent, irrespective of velocity. Also, as with planar jets, $\bar{h}$ increases with decreasing P_r (by approximately 15 percent for a reduction from P_r = 81 mm to P_r = 51 mm). This increase is due to a reduction in the extent of the wall jet region, over which local coefficients are much smaller than those in the impingement regions.

At the higher velocities, the unguarded system exhibited dominant/subordinate behavior just as it did for P_r = 81 mm. Heat transfer in the highly turbulated impingement region of the subordinate jet is again enhanced relative to single jet impingement. Moreover, as with the larger pitch, there is little difference in $\bar{h}$ for the unguarded and guarded cases. Average coefficients for the dual planar and circular jet arrays are summarized in Table 1.

Summary

For an equivalent impingement velocity, maximum convection coefficients beneath a planar and a linear array of circular jets are comparable. However, for an array of circular jets the secondary maximum produced by a downstream transition to turbulence is less pronounced and the ensuing monotonic decay is more rapid. This enhanced decay of local coefficients is attributed to deceleration and thinning of the liquid film due

to increasing circumferential flow area. If the thermal boundary layer thickness is less than the film thickness, the free-stream fluid temperature is unaffected by heat transfer from the plate. However, when the thermal boundary layer reaches the free surface of the liquid, the free-surface temperature begins to increase and degradation of the convection coefficient becomes more pronounced. Hence, over a region that transcends the impingement zone, local and average coefficients for a linear array of circular jets are less than those for an equivalent planar jet. However, for the conditions of this study, the circular array nozzles required a 43 percent smaller flow rate to produce impingement velocities equal to those of the planar jet.

Although portions of the axisymmetric jets produced by the array of circular nozzles persisted as distinct radially spreading wall jets for some distance from impingement, interactions between adjoining jets did occur and fluid was ejected from the plate in the form of sprays. Mixing associated with these interactions enhanced local heat transfer and accelerated the transition to turbulence. Eventual reimpingement of the sprays also increased heat transfer at downstream locations.

In contrast to conditions for interacting planar jets (a well-defined interaction zone midway between the impinging jets), interaction zones produced by two linear arrays of circular jets are irregular and take an equilibrium position, which differs from the midway point. Although convection coefficients in stable interaction zones between planar jets are characterized by pronounced secondary maxima, comparable to those at impingement, dual arrays of circular jets do not necessarily produce such strong peaks. Existence of such peaks for the smaller, but not the larger, of the two pitches considered is attributed to the availability of cool, free-stream fluid just prior to collision. If this hypothesis is correct, it would follow that planar jet systems for which W_n/P_r is less than some critical value would be without a pronounced maximum in the interaction zone, as thermal boundary layers in the wall jets become fully developed prior to collision. Local coefficients are largely unaffected outside the interaction zone.

When guards are not used to protect one row of jets from the spray generated by the other row, a dominant/subordinate behavior is exhibited, for which the equilibrium position of the interaction zone is located in close proximity to the subordinate row of jets. Under this scenario, the subordinate row is strongly influenced by sprays issuing from the dominant row and there is significant heat transfer enhancement in the impingement and wall jet regions of the subordinate row.

Row pitch plays a significant role in the behavior of twin circular array jet systems. The effect of sprays is greater at smaller pitch, where their impact on the subordinate jet is stronger. Moreover, with increasing pitch in circular array systems, mechanisms for heat transfer enhancement in the interaction zone are diminished by a reduction in the momentum and an increase in the free-stream temperature of the wall jets. Wall jets experience a reduction in velocity due to radial spread and in film thickness due to the generation of sprays, thereby accelerating merger of the thermal boundary layer with the free surface. At the larger spacing, interaction zone heat transfer coefficients between guarded circular array jets are much less than those generated by planar fountains. Hence, average coefficients for the larger pitch are lower for the circular arrays. When the pitch is reduced, however, interaction maxima increase and average heat transfer coefficients are comparable to those for the corresponding planar jets.

Acknowledgments

Funding for this research was provided by the National Science Foundation under Grant No. CTS-8912831.

References

Behbahani, A. I., and Goldstein, R. J., 1983, "Local Heat Transfer to Staggered Arrays of Impinging Circular Air Jets," ASME *Journal of Engineering for Power*, Vol. 105, pp. 354-360.

Filopovic, J., Viskanta, R., Incropera, F. P., and Veslocki, T. A., 1992, "Thermal Behavior of a Moving Steel Strip Cooled by an Array of Planar Water Jets," *Steel Research*, Vol. 63, pp.438-446.

Gardon, R., and Cobonpue, J., 1962, "Heat Transfer Between a Flat Plate and Jets of Air Impinging on It," in: *Proceedings of the Second International Heat Transfer Conference*, ASME, New York, pp. 454-460.

Gardon, R., and Akfirat, J. C., 1966, "Heat Transfer Characteristics of Impinging Two-Dimensional Air Jets," ASME JOURNAL OF HEAT TRANSFER, Vol. 88, pp. 101-108.

Incropera, F. P., 1989, "Liquid Immersion Cooling of Electronic Components," *Bulletin of the International Centre for Heat and Mass Transfer*, Vol. 3, pp. 29-64.

Ishigai, S., Nakanishi, S., Mizuno, M., and Imamura, T., 1977, "Heat Transfer of the Impinging Round Water Jet in the Interference Zone of the Film Flowing Along the Wall," *Bulletin of JSME*, Vol. 20, pp. 85-92.

Koopman, R. N., and Sparrow, E. M., 1976, "Local and Average Transfer Coefficients Due to an Impinging Row of Jets," *International Journal of Heat and Mass Transfer*, Vol. 19, pp. 673-683.

Korger, M., and Křížek, F., 1966, "Mass-Transfer Coefficient in Impingement Flow From Slotted Nozzles," *International Journal of Heat and Mass Transfer*, Vol. 9, pp. 337-344.

Lienhard, J. H., V, Liu, X., and Gabour, L. A., 1992, "Splattering and Heat Transfer During Impingement of a Turbulent Liquid Jet," ASME JOURNAL OF HEAT TRANSFER, Vol. 114, pp. 362-372.

Liu, X., and Lienhard, J. H., 1989, "Liquid Jet Impingement Heat Transfer on a Uniform Flux Surface," in: *Heat Transfer Phenomena in Radiation, Combustion and Fires*, R. H. Shah, ed., ASME HTD-Vol. 106, pp. 523-530.

Martin, J., 1977, "Heat and Mass Transfer Between Impinging Gas Jets and Solid Surfaces," in: *Advances in Heat Transfer*, J. P. Hartnett and T. F. Irvine, eds., Academic Press, New York, Vol. 13, pp. 1-60.

McMurray, D. C., Myers, P. S., Uyehara, O. A., 1966, "Influence of Impinging Jet Variables on Local Flat Surface With Constant Heat Flux," in: *Proceedings of the Third International Heat Transfer Conference*, AIChE, New York, Vol. II, pp. 292-299.

Mikhail, S., Morcos, S. M., Abou-Ellail, M. M. M., and Ghaly, W. S., 1982, "Numerical Prediction of Flow Field and Heat Transfer From a Row of Laminar Slot Jets Impinging on a Plate," in: *Proceedings of the Seventh International Heat Transfer Conference*, U. Grigull, E. Hahne, K. Stephan, and J. Straub, eds., Hemipshere, New York, Vol. 3, pp. 337-382.

Moffat, R. J., 1988, "Describing the Uncertainties in Experimental Results," *Experimental Thermal and Fluid Science*, Vol. 1, pp. 3-17.

Saad, N. R., Mujumdar, A. S., and Douglas, W. J. M., 1980, "Heat Transfer Under Multiple Turbulent Slot Jets Impinging on a Flat Plate," in: *Drying '80*, A. S. Mujumdar, ed., Hemisphere, New York, Vol. 1, pp. 422-430.

Slayzak, S. V., Viskanta, R., and Incropera, F. P., 1994, "Effects of Interaction Between Adjacent Free Surface Planar Jets on Local Heat Transfer From the Impingement Surface," *International Journal of Heat and Mass Transfer*, in press.

Stevens, J., and Webb, B. W., 1991, "Local Heat Transfer Coefficients Under an Axisymmetric, Single-Phase Liquid Jet," ASME JOURNAL OF HEAT TRANSFER, Vol. 113, pp. 71-78.

Tseng, A. A., Gunderia, A. S., and Sun, P., 1991, "Cooling of Roll and Strip in Steel Cooling," *Steel Research*, Vol. 62, No. 5, pp. 207-215.

Vader, D. T., Incropera, F. P., and Viskanta, R., 1991, "A Method for Measuring Steady, Local Heat Transfer to an Impinging Liquid Jet," *Experimental Thermal and Fluid Science*, Vol. 4, pp. 1-11.

Zumbrunnen, D. A., Incropera, F. P., and Viskanta, R., 1990, "A Method and Apparatus for Measuring Heat Transfer Distributions on Moving and Stationary Plates Cooled by a Planar Liquid Jet," *Experimental Thermal and Fluid Science*, Vol. 3, pp. 202-213.

Natural Convection Heat Transfer From Long Horizontal Isothermal Cylinders

S. B. Clemes

K. G. T. Hollands

A. P. Brunger

University of Waterloo,
Waterloo, Ontario,
Canada N2L 3G1

A new set of measurements is reported on natural convection heat transfer in air from isothermal long horizontal cylinders of noncircular cross section at various orientations, covering the Rayleigh number (Ra) range from about 10^3 to about 10^9. The data are correlated reasonably well by a conduction layer model with a constant value (i.e., the same for all body shapes and orientations) of 5.42 for the Churchill–Usagi coefficient blending the laminar and turbulent asymptotes. The resulting correlation equation normally requires only the geometric specification of the body height and perimeter. This model is also tested against data in the literature on the subject problem, and found to be generally predictive, to within about ±10 percent. A new set of data covering the same Ra range is also reported for the circular cross-section case, i.e., the long horizontal isothermal circular cylinder. Comparison of this data with the several existing correlations for this well-known problems shows that the Kuehn and Goldstein equation predicts the data best, although the Raithby and Hollands equation also predicts the data very well, but only after a revision to the blending coefficient.

1 Introduction

Natural convection heat transfer from very long horizontal cylinders of noncircular cross section has received only limited attention in the literature, even though there are a number of practical problems where such heat transfer needs to be predicted. Extensive experimental data are particularly lacking. Raithby and Hollands (1976) analyzed the elliptic cylinders from a conduction layer point of view, but except for the special cases of the circular cross section and the flat plate cross section, they had no experimental data with which to compare their analysis. Nakamura and Asako (1978) presented an analysis based on very thin laminar boundary layers, as well as some experimental results on cylinders of prismatic cross section with rounded corners in the Rayleigh number range from about 10^6 to about 10^9. Their predictions fell 10 to 30 percent below their measurements, perhaps because they did not account for turbulence and for curvature affects. Oosthuizen and Paul (1984) presented a set of experimental results detailing the effect of orientation and aspect ratio on the heat transfer, using two cross-sectional shapes: a rhombus-like prism and a finned circle. These results are, however, restricted to two Rayleigh numbers: 7.5×10^5 and 6×10^6, respectively.

Natural convection heat transfer from *three-dimensional* bodies, on the other hand, has received more attention. Much of the relevant literature for this problem was summarized by Hassani and Hollands (1989a, 1989b), who also provided a set of heat transfer measurements covering a Rayleigh number range 10^2 to 10^8 on a range of body shapes. They were able to correlate their Nusselt number versus Rayleigh number data, as well as those of other workers, by a single equation, which they derived by simplifying the conduction layer model discussed by Raithby and Hollands (1975, 1985). While one might surmise that the infinitely long cylinder may be treated as a special case of their multibody equation, in fact certain terms in their equation become indeterminate when the body area goes to infinity, as it does in the case of an infinite cylinder. The correlation equations for the two classes of body shape differ most in the low Rayleigh number range; taking, for example, the sphere and the infinite circular cylinder as representative of each class of body, we find that for small Ra, the form of the Nusselt number dependence for the sphere is $\mathrm{Nu} = 2 + c\mathrm{Ra}^{1/4}$, whereas for the cylinder, Nu shows a logarithmic dependence of Ra, with Nu going to zero when Ra approaches zero. It seems unlikely that a single equation will be found that can capture both types of asymptotic dependence.

Although Hassani and Hollands' exact formula cannot be used directly for infinite cylinders, the experimental method they used, as well as the conduction layer model that correlated their data, can be adapted to approach that extreme case, and it is the purpose of the present work to make this adaptation. Thus we present a set of wide-Rayleigh-number-range experimental results on long cylinders of various cross section (correcting for end effects), and then use the simplified conduction layer model to correlate the results. We then compare the correlation equation with the experimental data of previous workers.

Primarily as a check on the apparatus and method, a set of experiments was also performed on the cylinder of *circular* cross section. The results were compared to the several correlation equations available in the literature for this problem. The comparisons helped to evaluate these equations, which have been found to disagree somewhat with each other.

2 Experiment

The experimental method followed closely that of Hassani and Hollands (1989a), the same basic apparatus being used. Thus, for the sake of brevity, we describe below only how the method differed from that of the previous workers, full details being given by Clemes (1990). The main difference was in the construction of the models, which for the present study had to be very long and of cross-sectional shape invariant with axial distance.

Apparatus and Method. Each model (or body) was nominally 510 mm long, including the thickness of the end cap plates described later. Figure 1 shows a sketch of the square cross-sectional body. The other cross-sectional shapes (shown

Contributed by the Heat Transfer Division for publication in the JOURNAL OF HEAT TRANSFER. Manuscript received by the Heat Transfer Division July 1992; revision received March 1993. Keywords: Enclosure Flows, Measurement Techniques, Natural Convection. Associate Technical Editor: J. R. Lloyd.

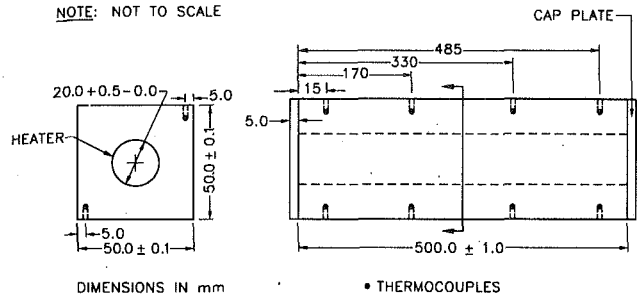

Fig. 1 Drawing of square cross-section model (not to scale) showing holes for heater and thermocouple placements

in the insets in Figs. 2–5) were as follows: the circle, the square, the semicircle, and finally, a circle having two symmetrically placed rectangular slots cut out of it on opposite faces. The (nominal) values of the key dimensions of the cross-sectional shapes were as follows: for the square, length of a side = 50 mm; for the semicircle, diameter = 60 mm; and for the circle (slotted or plain), diameter = 50 mm. Machined from aluminum, each body had a 20 mm diameter longitudinal hole drilled along its full length, in order to receive an electrical heater, a common electrical heater being used for all the bodies. To construct the heater, a 16 mm diameter aluminum rod, 500 mm long, was covered with electrically insulating aluminum putty, threaded at 8 threads per cm and wound around with 22 gage nickel-chrome electrical heating wire, so that the wire followed the thread grooves. Then three longitudinal strips of aluminum putty were added to hold the wire in place. Covered in vacuum grease, the heater fit snugly into the hole in the body. A 5-mm-thick plate, having the same cross-sectional shape as the body, was attached to each end of the body with machine screws; this "cap-plate" secured the heater in place and sealed in the vacuum grease. Eight copper-constantan thermocouples were coated in epoxy, and embedded in aluminum putty (4 mm below the surface) in each body at locations on opposite faces 20 mm, 175 mm, 335 mm, and 490 mm from one end. The thermocouple locations on the square cylinder, as a typical example, are shown in Fig. 1. For the circular cylinder, the four bottom thermocouple lead wires were passed through circumferential grooves to the top of the cylinder to avoid interference of the leads with the boundary layer growth. For the other bodies, the thermocouple leads extended out, away from the body. All holes and grooves for the lead wires were filled with aluminum putty to maintain smooth body surfaces. The circular body had an extra thermocouple at the 335 mm station, equidistant from the other two at that station.

To correct for radiant heat losses and to permit the data reduction of the transient test results, accurate values of the effective emissivity $\bar{\epsilon}$ and the heat capacity C^* of each body were needed. Using the technique of Hassani and Hollands (1989a), these were measured in a separate transient test at very low pressure (less than 10^{-5} mm Hg). The surfaces of each body were machined smooth and polished, and the effective thermal emissivities varied between 0.078 ± 0.004 and 0.091 ± 0.006.

In the data reduction, it was necessary to somehow correct for the finite length of the cylinder; any actual experimental model must have finite length, but it is the heat flow per unit length of an infinite cylinder that is the experiment's goal. In the present experiments, the cylinder ends represented only

Nomenclature

A = surface area of body
A_h = downward- (upward-) facing horizontal part of A for a heated (cooled) body
a = 0.0972
B = thickness of a uniform layer surrounding a two-dimensional body
b = $0.0815 - 0.06\mathrm{Pr}^*$
C^* = heat capacity of body
$\overline{C}_l$ = laminar coefficient = $0.671/[1 + (0.492/\mathrm{Pr})^{9/16}]^{4/9}$
$\overline{C}_t$ = turbulent coefficient, can be evaluated using Eq. (3)
$\hat{C}_t$ = $\overline{C}_t(P/4z_f)^{1/3}$
D = diameter of circular cylinder, or longest body cross-section dimension measured perpendicular to direction in which L is measured
e = $0.08\mathrm{Pr}^* - 0.0548 - 6 \times 10^{-6}$ Pr (note: b and e have been tabulated by Hassani and Hollands, 1989b)
G = body shape parameter (see Eq. (2) or (4))
g = acceleration of gravity
H = $(4z_fP^2)^{1/3}$
h = convective heat transfer coefficient = $Q'/(P\Delta T) = Q/(A\Delta T)$
k = thermal conductivity of fluid evaluated at T_f
L = characteristic length, normally taken as longest dimension of body cross section
m = Churchill–Usagi coefficient blending laminar and turbulent asymptotes of $\overline{\Delta}/L$ (Eq. (1))
Nu, Nu_L = Nusselt number = hL/k
Nu_D = hD/k
Nu_p = Nusselt number based on perimeter = $hP/k = Q'/k\Delta T$
Pr = Prandtl number of fluid, evaluated at T_f
Pr^* = $\mathrm{Pr}^{0.22}/(1 + 0.61\mathrm{Pr}^{0.81})^{0.42}$
P = perimeter of cylinder in vertical cross section
P_h = downward- (upward-) facing horizontal part of P for a heated (cooled) cylinder
Q, Q' = heat transfer from body and heat transfer from cylinder per unit of axial length, respectively
Ra, Ra_L = Rayleigh number = $g\beta\Delta TL^3/\nu\alpha$
Ra_D, Ra_H = $g\beta\Delta TD^3/\nu\alpha$ and $4g\beta\Delta Tz_fP^2/\nu\alpha$, respectively
S = conduction shape factor
T_a = temperature of ambient fluid
T_b = body temperature
T_f = film temperature = $(T_b + T_a)/2$
ΔT = $T_b - T_a$
W = length of cylinder in axial direction
z_f = height of cylinder; distance measured vertically from lowest point on cylinder to highest point on cylinder
α = thermal diffusivity of fluid evaluated at T_f
β = thermal expansion coefficient of fluid evaluated at T_a
$\bar{\epsilon}$ = effective emissivity of body surface
θ = angle of inclination of body from reference position
θ_r = a reference value of θ
ν = kinematic viscosity of fluid evaluated at T_f
$\bar{\rho}$ = height-averaged perimeter of a three-dimensional body, in plan (see Hassani and Hollands, 1989a)

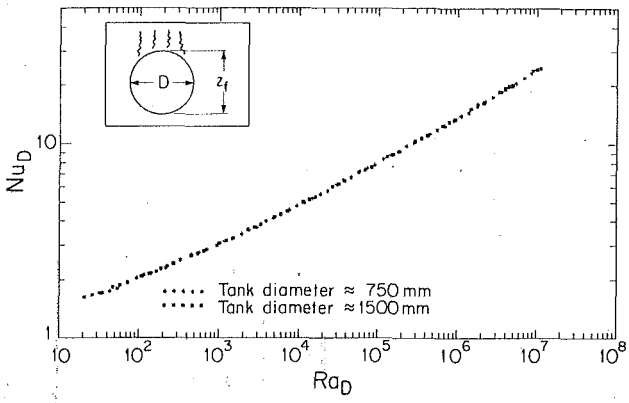

Fig. 2 Results for the circular cylinder. Results are shown for the cylinder mounted inside each of two tanks: one with diameter of about 750 mm; the other with diameter about 1500 mm. The close agreement between the two sets of measurement provides evidence that enclosure effects were not affecting the results.

about 5 percent of the total body area. Thus, provided one could estimate the heat transfer over this end area with a 10 percent or better accuracy, then, by straightforward calculations, one could calculate the heat transfer (per unit length) from the sides with an accuracy better than 0.5 percent of the total heat transfer. This is the strategy adopted here, the equations given by Raithby and Hollands (1985) being used to calculate the convective component of the end face heat transfer.

Like the experiments of Hassani and Hollands (1989a), the experiments were conducted with the body contained centrally in a cylindrical pressure vessel 750 mm in diameter by 1 m long. Before each experiment, the pressure vessel was evacuated and then filled with dry air, one step at a time. The temperature difference between the body and the air ambient to the body was measured with a resolution of 0.01°C and an accuracy of ±0.21°C by using a thermopile of 16 copper-constantan thermocouples. The eight thermocouples measuring the air temperature were located at the same height as the body, and along a horizontal line parallel to and 250 mm from the body's centerline. Calculations indicated that these thermocouples should be outside the largest boundary layer thickness expected to grow around the cylinder, over the Rayleigh number range covered.

Checks on the Experimental Method. Temperature measurements on the circular cylinder were carried out (at atmospheric pressure) to check that the body was indeed isothermal during the actual tests. Although significant temperature variations were observed while the body was being raised in temperature with the electrical heater, once the body had reached 35°C above ambient, the heater turned off, and the body temperature had cooled to 30°C above ambient, the temperature variation across the body, as sensed by the embedded thermocouples, was less than 0.2°C. This is less than 1 percent of the corresponding body-to-air temperature difference ΔT. Since in the actual experimental runs, the transient tests were not started until the body had cooled to a temperature difference of 30°C, it was concluded that the cylinders were sufficiently isothermal during the tests.

To check if the air inside the vessel was stratified, a test was carried out, over a range in pressures, in which the vertical temperature gradient was measured by means of five thermocouples, uniformly spaced at 6 cm intervals along a vertical line 250 mm away from the body's centerline, the central thermocouple being at the same height as the body's centerline. The maximum gradient of 0.09 ± 0.05°C per cm was found to occur at the highest pressure (6 atm) and the lowest cylinder-to-air temperature difference, ΔT = 15°C. Using Chan and Eichhorn's (1976) equation, we calculated that the effect of this gradient on the heat transfer would be to increase the Nusselt number by between 0.4 and 1.3 percent over that which would exist if there were zero gradient. Since this was a "worst-case" condition, it was concluded that temperature stratification was not appreciably influencing the Nusselt number values measured subsequently.

To verify that the finite extent of the tank was not appreciably altering the measured Nusselt number from that which it could be if the body were in infinite surrounds, a second series of tests was carried out (using the circular cylinder body), in which the body was contained in a second, larger, pressure vessel. This cylindrical vessel had linear dimensions roughly twice those of the smaller tank. Figure 2 shows the comparison of the two sets of results. The very close agreement between the two sets indicates that the finite size of the smaller tank was not appreciably influencing the Nusselt number.

Implicit in the transient cooling method adopted in this work is the assumption that the temperature decay process is slow enough that the measured results are near enough to steady state, so that what is being measured is the equivalent to steady-state data. This assumption was checked in the present experiments using the same method as Hassani and Hollands used; truly steady-state measurements were carried out, at each of several pressure settings, in which a measured steady DC power was applied to the electric heater inside the cylinder, and steady conditions were then allowed to prevail. The results agreed with the transient results, well within experimental error. (Since a steady-state condition takes many hours to establish, it was impractical to use this technique for all the measurements.) Full details are given by Clemes (1990).

Table 1 Uncertainty in Nusselt and Rayleigh numbers

Ra^*_L	$\frac{\delta Ra}{Ra}$	$\delta Nu / Nu$			
		circular	semi-circular	square	slotted
5×10^1	0.050	0.090	0.067	0.104	0.071
5×10^2	0.024	0.072	0.056	0.082	0.059
5×10^3	0.021	0.062	0.049	0.069	0.052
5×10^4	0.020	0.053	0.043	0.059	0.046
5×10^5	0.020	0.048	0.040	0.053	0.043
5×10^6	0.020	0.046	0.039	0.050	0.042

Error Analysis. An error analysis gave the uncertainties, δNu in Nu and δRa in Ra, shown in Table 1. The dominant error in the Rayleigh number was that in the pressure measurement, which decreased in relative terms, as the pressure increased. Many minor error sources contributed to δNu, including the uncertainties in C^* and $\bar{\epsilon}$. The values of δNu given in the Table include a 1 percent uncertainty in Nu associated with estimating the end losses.

3 Results for Circular Cylinder

We present first the results for the circular cylinder, which are columnized in the first two columns in Table 2, and plotted in Fig. 2. A comparison between the present results and those of previous workers on the same problem showed that the present data agree with previous results to the degree that the previous results agree with each other. (See Appendix A for details.) This general agreement provided confidence that the experimental method was basically sound, and so measurements could go ahead on other body shapes, the primary purpose of the measurements on the circular cylinder having been served.

These data can also be used, however, to evaluate and sort

out the various correlation equations for circular cylinders developed in the literature. Table 2 shows the comparison with four such correlation equations, columnizing the Nusselt numbers predicted, for air, at each measured Ra_D, by the equations of Kuehn and Goldstein (1976), Raithby and Hollands (1985), Churchill and Chu (1975), and Morgan (1975). (The final column will be explained shortly.) The Kuehn and Goldstein equation predicts the present results with a very high degree of fidelity; it departs from the data by an rms deviation of only 2.1 percent and a maximum deviation of 5.6 percent (reducing to only 3 percent if one ignores the first three data points). The other equations, however, show larger deviations; their respective rms and maximum deviations from the data are 6.1 and 15.1 percent for the Raithby and Hollands equation, 6.3 and 11.6 percent for the Morgan relations, and 13.4 and 28.8 percent for the Churchill and Chu equation.

There are two reasons that can explain the rather large deviations between Morgan's relations and the present data. First, Morgan based β on T_f rather than T_a. Second, Morgan included data on liquids in his correlation, yet he did not allow for any effect of Prandtl number on the Nu_D (Ra_D) relation. Since both of these effects would increase the Nusselt number, the Morgan relation overpredicts the present Nusselt number data.

Since, as it happens, the Raithby–Hollands equation had been fitted to the Morgan relations, it differs from the present data for the same reason the Morgan relations do. The Raithby and Hollands and the Kuehn and Goldstein equations are very similar; both are based on a conduction layer model and both use a Churchill–Usagi blending of purely laminar and purely turbulent asymptotes. They differ, however, in their choice of the Churchill–Usagi blending exponent m; m was made to equal 15 by Kuehn and Goldstein, and 3.3 by Raithby and Hollands. Making $m = 15$ in the Raithby–Hollands equation gives the values at the far right of Table 2, which agree closely with the experimental values; the rms deviation is 1.4 percent and the maximum deviation is 3.8 percent. In researching to find why the different authors differed in their choice of m, we have found that Raithby and Hollands were guided by the correlation of Morgan (1975), which they mistakenly took to be derived for air. Kuehn and Goldstein, on the other hand, accounted for the Prandtl (or Schmidt) number effect on the relation. They included mass transfer data in their data base, and they also were looking for a global value suitable for spheres, concentric spheres, and concentric cylinders, as well as single cylinders, both vertical and horizontal. Thus their data base was broader than that used by Raithby and Hollands.

Distinct differences can be seen between the Churchill and Chu correlation and the other correlations. The differences seem to be attributable to the form of the correlating equation chosen by Churchill and Chu. By not choosing a form that had the correct logarithmic dependence as Ra goes to zero, they were forced to accept fairly large differences between the experimental data they used and their equation; the scatter in their final correlating plot is relatively large.

In summary, the present data are consistent with previous data, and they support the correlation equation of Kuehn and Goldstein. The Kuehn and Goldstein equation fits the data very closely, and so does the Raithby and Hollands equation, once the blending coefficient has been changed to 15.

4 Results for Noncircular Cylinders and Their Correlation

Results. Figures 3–5 show the results for the noncircular cylinders. They plot the Nusselt number Nu_P, based on the perimeter of the body's cross-sectional shape, versus the Rayleigh number Ra_H based on the dimension H defined by $H = (4z_f P^2)^{1/3}$ where z_f is the vertical height of the body (see insets on Figs. 3–8) and P is its perimeter. For comparison, a line of slope 1/4 is drawn near the data in the high Rayleigh number

Table 2 Comparison of circular cylinder data with various correlations

Ra_L	Nu_L					
	Present Data	Kuehn-Goldstein 1976	Raithby-Hollands 1985	Churchill-Chu 1974	Morgan 1975	Raithby-Hollands modified
34.6	1.71	1.79	1.69	1.39	1.72	1.69
42.9	1.75	1.84	1.75	1.44	1.78	1.74
53.2	1.80	1.91	1.81	1.49	1.84	1.81
93.6	2.04	2.08	1.99	1.65	2.00	1.98
116	2.12	2.16	2.06	1.71	2.08	2.05
143	2.16	2.23	2.14	1.78	2.16	2.13
215	2.30	2.39	2.30	1.92	2.33	2.29
267	2.44	2.48	2.39	2.00	2.43	2.38
330	2.53	2.57	2.48	2.09	2.53	2.47
458	2.69	2.73	2.64	2.23	2.69	2.62
570	2.76	2.83	2.75	2.32	2.80	2.73
710	2.86	2.95	2.86	2.43	2.92	2.84
939	3.00	3.10	3.02	2.58	3.08	3.00
1170	3.16	3.23	3.15	2.70	3.21	3.12
1450	3.25	3.37	3.29	2.82	3.34	3.26
1900	3.43	3.54	3.47	2.99	3.51	3.43
2360	3.60	3.69	3.63	3.14	3.66	3.58
2930	3.71	3.85	3.79	3.29	3.81	3.74
3860	4.01	4.06	4.02	3.50	4.01	3.95
4770	4.15	4.24	4.20	3.68	4.18	4.13
5900	4.33	4.42	4.39	3.86	4.35	4.31
7670	4.57	4.66	4.65	4.10	4.57	4.55
9500	4.80	4.87	4.87	4.32	4.76	4.76
11800	4.98	5.09	5.10	4.55	5.00	4.98
15100	5.28	5.36	5.39	4.82	5.32	5.25
18700	5.52	5.61	5.65	5.08	5.61	5.49
23300	5.73	5.87	5.94	5.36	5.93	5.76

Ra_L $\times 10^{-3}$	Nu_L					
	Present Data	Kuehn-Goldstein 1976	Raithby-Hollands 1985	Churchill-Chu 1974	Morgan 1975	Raithby-Hollands modified
29.9	6.19	6.20	6.29	5.71	6.31	6.08
37.0	6.52	6.49	6.61	6.02	6.66	6.37
46.0	6.72	6.80	6.95	6.36	7.03	6.68
58.8	7.24	7.17	7.36	6.77	7.47	7.05
72.7	7.54	7.51	7.74	7.15	7.88	7.39
90.2	7.82	7.88	8.15	7.57	8.32	7.75
116	8.39	8.33	8.66	8.08	8.86	8.20
143	8.77	8.73	9.12	8.55	9.34	8.61
178	9.15	9.16	9.62	9.05	9.86	9.03
226	9.79	9.67	10.20	9.65	10.46	9.54
281	10.18	10.16	10.77	10.23	11.05	10.03
351	10.72	10.69	11.39	10.87	11.68	10.55
450	11.28	11.32	12.14	11.64	12.44	11.18
557	11.86	11.89	12.82	12.34	13.11	11.75
692	12.36	12.50	13.56	13.11	13.85	12.36
885	13.27	13.24	14.46	14.04	14.72	13.09
1100	13.92	13.93	15.30	14.92	15.53	13.77
1370	14.52	14.67	16.22	15.87	16.42	14.51
1780	16.05	15.63	17.41	17.12	17.54	15.46
2200	16.50	16.44	18.43	18.18	18.49	16.26
2730	17.38	17.32	19.53	19.33	19.51	17.13
3530	18.53	18.45	20.96	20.83	20.80	18.25
4350	19.68	19.44	22.20	22.14	21.92	19.23
5390	20.47	20.51	23.56	23.56	23.12	20.30
6910	21.80	21.87	25.27	25.36	24.61	21.65
8540	23.15	23.12	26.81	26.99	25.95	22.89
10600	24.19	24.49	28.51	28.77	27.32	24.26

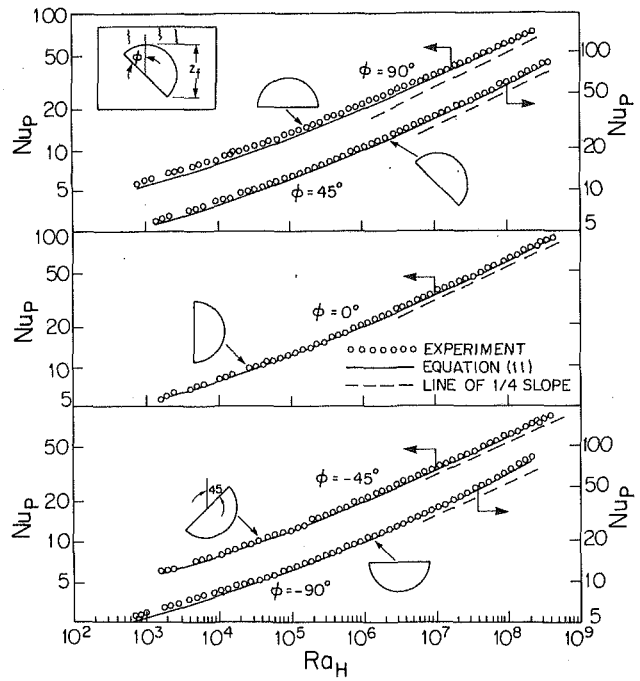

Fig. 3 Plots of measurements on square cylinder

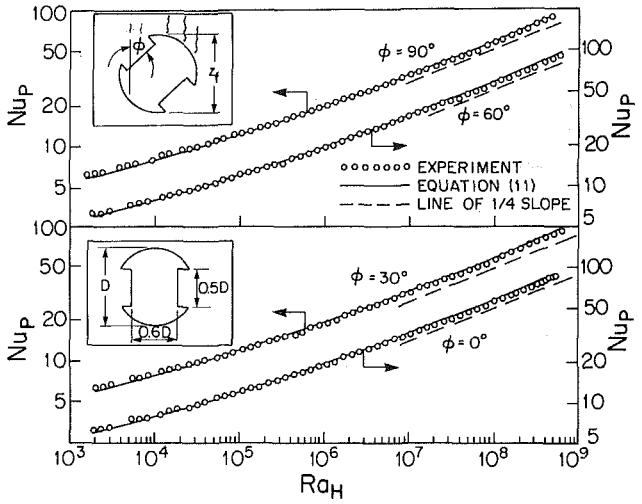

Fig. 4 Plots of measurements on semicircular cylinder

range. Most of the plots are asymptotic to the 1/4 slope, although a number of them, especially those with horizontal upward-facing surfaces like the semicircle, show a rise at high Rayleigh number indicative of a move toward the 1/3 slope expected in the turbulent regime.

Derivation of Correlation Equation. To correlate the data for different shapes and orientations, we used a conduction layer model (Raithby and Hollands, 1985), using the Hassani and Hollands multi-Prandtl number formula for the average conduction layer thickness $\overline{\Delta}$:

$$\overline{\Delta} = L\{(G\overline{C}_l \mathrm{Ra}_L^{1/4})^m + (\overline{C}_l \mathrm{Ra}_L^{1/3})^m\}^{-1/m} \tag{1}$$

where m is the Churchill–Usagi coefficient blending the laminar and turbulent asymptotes for $\overline{\Delta}$, L is any (finite) characteristic dimension, $\overline{C}_l$ is a specified function of the Prandtl number (see Nomenclature) and G and $\overline{C}_l$ are given by

$$G = \left(\frac{z_f L \bar{\rho}^2}{A^2}\right)^{1/4} \tag{2}$$

and

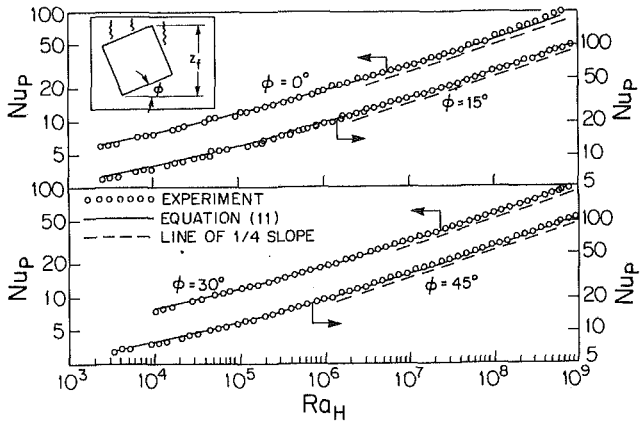

Fig. 5 Plots of measurements on slotted circular cylinder

$$\overline{C}_l = a - (a-b)A_h/A + e\frac{z_f\bar{\rho}}{A} \tag{3}$$

In these equations, z_f is the body's vertical height, A is its area; A_h (for a heated body) is the downward-facing horizontal part of A (for a cooled body it is the upward-facing horizontal part of A); a, b, and e are functions of Prandtl number (see Nomenclature); and $\bar{\rho}$ is the body's perimeter measured in a *horizontal* cross section and averaged over the whole vertical height of the body, as explained by Hassani and Hollands (1989a). Specializing the dimensions $\bar{\rho}$ and A to the case of a very long body of axial length W, we find that $\bar{\rho}$ approaches $2W$ and A approaches WP (where P is the perimeter of the body's *vertical* cross section), as W approaches infinity. Thus in the limit of infinite W, the parameter G is given by:

$$G = (4z_f L/P^2)^{1/4} \tag{4}$$

Also, since A_h approaches $P_h W$, where P_h is the downward-facing horizontal part of P for a heated body (or upward-facing horizontal part of P for a cooled body), it follows that in the limit of infinite W, $\overline{C}_l$ is given by

$$\overline{C}_l = a - (a-b)(P_h/P) - e(2z_f/P) \tag{5}$$

If we choose for L the quantity H defined by

$$H = (4z_f P^2)^{1/3} \tag{6}$$

then Eq. (1) can be written in the more compact form

$$\overline{\Delta} = P\{(\overline{C}_l \mathrm{Ra}_H^{1/4})^m + \hat{C}_l \mathrm{Ra}_H^{1/3})^m\}^{-1/m} \tag{7}$$

where

$$\hat{C}_l = (P/4z_f)^{1/3}[a - (a-b)(P_h/P) + e(2z_f/P)] \tag{8}$$

According to the conduction layer model, the heat transfer per unit axial length from the body is given by

$$Q' = kS\Delta T \tag{9}$$

where k is the fluid conductivity, ΔT is the temperature difference between the body and the fluid far away, and S is the conduction shape factor of a uniform layer of thickness $\overline{\Delta}$ surrounding the body. According to Hassani et al. (1992), an equation giving an approximation, good to within about 1 percent, to the shape factor of a uniform layer of thickness B surrounding a two-dimensional body of perimeter P is

$$S = \frac{2\pi}{\ln(1 + 2\pi B/P)} \tag{10}$$

Putting $B = \overline{\Delta}$, noting that the Nusselt number $\mathrm{Nu}_P = Q'/k\Delta T$, and combining these latter equations with Eqs. (6), (8) and (9), one obtains

$$\mathrm{Nu}_P = \frac{2\pi}{\ln[1 + 2\pi\{(\overline{C}_l \mathrm{Ra}_H^{1/4})^m + (\hat{C}_l \mathrm{Ra}_H^{1/3})^m\}^{-1/m}]} \tag{11}$$

Table 3 Optimal value of m and deviation of data from Eq. (11) according to differing values for m

Body		Optimal value for m	Deviation, %			
			using optimal m		using constant m = 5.42	
Shape	Inclination Angle, degrees		*rms*	maximum	*rms*	maximum
square	0	3.77	2.8	5.9	3.90	10.30
square	15	5.89	3.1	8.5	3.20	8.50
square	30	4.94	2.0	5.0	2.10	4.90
square	45	4.22	2.0	4.0	2.90	4.90
semi-circle	-90	3.44	4.3	8.7	5.90	9.50
semi-circle	-45	3.68	3.8	8.5	4.30	6.90
semi-circle	0	3.22	2.4	6.1	4.80	7.50
semi-circle	45	3.30	3.7	7.3	5.50	7.70
semi-circle	45	2.64	6.4	11.0	8.10	11.90
slotted-circle	0	9.77	2.0	6.6	3.50	6.50
slotted-circle	30	9.11	2.7	7.0	3.50	6.40
slotted-circle	60	9.66	1.7	7.0	3.30	7.00
slotted-circle	90	6.74	2.5	6.2	2.80	6.20
Average		5.42	3.27		4.42	

Correlation. Equation (11) (with $\hat{C}_f$ given by Eq. (8)) is the conduction layer model to which the experimental data were fitted, the only fitting parameter being the Churchill-Usagi coefficient m. The best value for m for each body at each inclination was determined by a least-square fitting routine. The resulting optimal values for m, summarized in Table 3, ranged from 2.64 to 9.66, the average value being 5.42. Table 3 also gives the rms and maximum deviation between the measured Nu_P and the Nu_P obtained using Eq. (11) with (*a*) the optimal value of m for each body/inclination, and (*b*) the average value of m = 5.42 the same for all bodies. The rms deviations averaged over all the body shape and orientations combinations is 3.27 percent when the optimal values of m are used, and it is 4.42 percent when the same (average) value of m is used for all body and inclination combinations. The maximum deviation, which was found to be 11 percent when the optimal values of m are used, changed by only 0.9 to 11.9 percent when the average value of m is used. Taken overall, in view of its simplicity and its apparent applicability to any body shape, we recommend the use of Eq. (11) with a constant value of m, namely m = 5.42. Equation (11) with m = 5.42 is plotted against the data in Figs. 3–5.

(While one can attempt to relate the value of m to some geometric property of the body and its orientation, the best such a procedure can do is to lower the rms error from 4.42 to 3.27 percent. Out of interest we may note here that the parameter m was indeed found to correlate to body shape, through the parameter $\hat{C}_f$. We found that using the values predicted by this correlation of m versus $\hat{C}_f$ reduced the rms derivation to 4.07 percent; see Clemes (1990) for details. Using the equation for m provided by Hassani and Hollands, which makes m to be a function of $\hat{C}_f Ra_H^{1/2}$, gave an rms deviation between Eq. (11) for Nu and the data of 5.2 percent and a maximum deviation of 12.3 percent.)

Comparisons. Equation (11) with m = 5.42 appears to be a suitable equation for two-dimensional cylinders of any irregular cross-sectional shapes, the expected errors associated with its use being of the order of a few percent. To further test its ability, we tested it against some data taken from the literature: that of Oosthuizen and Paul (1984) and Nakamura and Asako (1978). The comparisons, shown in Figs. 6, 7, and

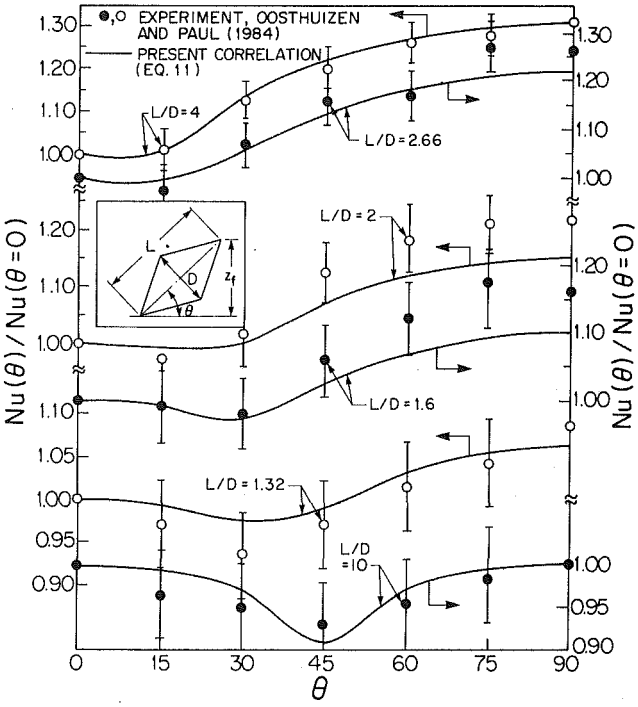

Fig. 6 Effect of angular position on the heat transfer from a rhombic cylinder in air at $Ra_L \approx 6 \times 10^6$, as measured by Oosthuizen and Paul (1984) and predicted by the present model (Eq. (11) with m = 5.42)

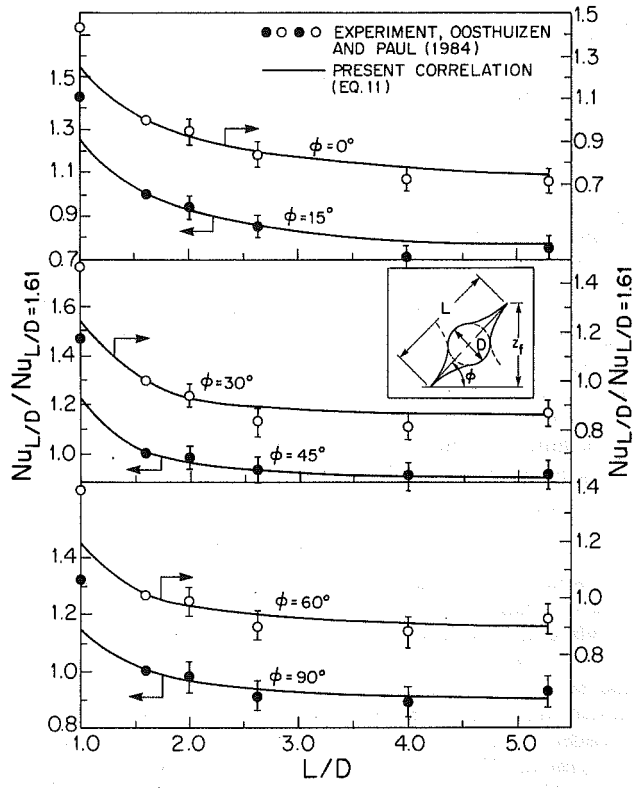

Fig. 7 Effect of shape factor L/D on the heat transfer from a circular cylinder with attached circular fins, in air at $Ra_L \approx 6 \times 10^6$, as measured by Oosthuisen and Paul (1984) and predicted by the present model (Eq. (11) with m = 5.42)

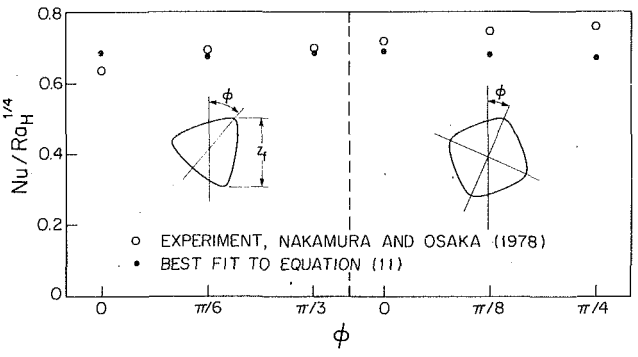

Fig. 8 Comparison between experimental data of Nakamura and Asako (1987) with the present model (Eq. (11) with $m = 5.42$)

8, suggest that Eq. (11) can predict other measurements (including those for liquids) with an accuracy better than about 10 percent. Details of the comparisons are given in Appendix B.

6 Conclusions

A new set of experimental data using air has been reported for the heat transfer from noncircular cylinders in the Ra range from about 2×10^3 to 2×10^8. The data are fitted well by a conduction layer model using a constant value of $m = 5.42$ for the Churchill-Usagi parameter that blends the laminar and turbulent asymptotes. The resulting model has been found to be predictive of other available experimental data for both air and liquids, involving a variety of body shapes. Users of the model can be reasonably confident of predicting the heat transfer over two-dimensional cylinders of arbitrary cross section to within 10 percent.

The model is relatively easy to implement, requiring only three geometric properties of the body. Thus to find the body's average convective heat transfer coefficient h, one proceeds as follows: Find the perimeter P of the cylinder's cross-sectional shape, and also the vertical height z_f from the cross section's lowest point to its highest point (see insets in Figs. 3-8). If (*a*) the body is being heated (i.e., if $T_b > T_a$) and if its cross section has some downward-facing horizontal parts, evaluate the total length P_h of these parts. On the other hand, if (*b*), the body is being cooled (i.e., if $T_b < T_a$) and its cross section has some upward-facing horizontal parts, evaluate the total length P_h of these parts. If neither (*a*) nor (*b*) applies, set $P_h = 0$. Find, for the Prandtl number of interest, Pr^* and $\overline{C}_t$, using equations in the Nomenclature. Calculate $\hat{C}_t$:

$$\hat{C}_t = (P/4z_f)^{1/3}\{0.0972 - (0.0157 + 0.06\mathrm{Pr}^*)P_h/P + (0.08\mathrm{Pr}^* - 0.0548 - 6\times 10^{-6}\mathrm{Pr})(2z_f/P)\} \quad (13)$$

and $\mathrm{Ra}_H = 4g\beta\Delta T z_f P^2/\nu\alpha$. Substitute into Eq. (11) with $m = 5.42$ to obtain Nu_p. Then $h = \mathrm{Nu}_p k/P$.

While this model has been validated only over $10^3 \le \mathrm{Ra} \le 10^8$ at $\mathrm{Pr} \approx 0.7$ and over $10^8 \le \mathrm{Ra}_H \le 5 \times 10^{10}$ at $\mathrm{Pr} \approx 6$, the equations (principally those for $\overline{C}_f$ and $\overline{C}_t$) on which its development has been based have been tested over a much broader range in Ra and Pr (for example, they were tested by Hassani and Hollands (1989a, b) for three-dimensional bodies over $10^3 \le \mathrm{Ra} \le 10^{13}$ and $0.7 \le \mathrm{Pr} \le 2000$). The broad model development has been aimed at producing equations valid for any Ra and for $\mathrm{Pr} \ge 0.7$, but the lack of available experimental data prevents model validation over this full range.

In addition to these results on noncircular cylinders, a new set of data has been presented for the circular cylinder. The data are predicted very closely (within about 5 percent and to an rms of only 2.1 percent) by the Kuehn and Goldstein (1976), and also are fitted very closely (within about 4 percent and an rms deviation of 1.4 percent) by the Raithby and Hollands (1985) equation provided the Churchill-Usagi coefficient is changed to 15. These equations are recommended for the circular shape, giving greater accuracy than that obtained by applying the general model (Eq. (11)) to the circle.

Acknowledgments

The authors are indebted to the Natural Sciences and Engineering Research Council Canada and Energy Mines and Resources Canada, CANMET Branch, for providing financial support for this study. We also acknowledge, with thanks, the technical assistance of Mr. Bert Habicher and the advice of Dr. A. V. Hassani and Professor G. D. Raithby.

References

Chan, C. C., and Eichhorn, R., 1976, "Natural Convection From a Vertical Surface to a Thermally Stratified Fluid," ASME JOURNAL OF HEAT TRANSFER, Vol. 98, pp. 446-451.

Churchill, S. W., and Usagi, R., 1972, "A General Expression for the Correlation of Rates of Transfer and Other Phenomena," *AIChE Journal*, Vol. 18, pp. 1121-1128.

Churchill, S. W., and Chu, H. H. S., 1975, "Correlating Equations for Laminar and Turbulent Free Convection From a Horizontal Cylinder," *Int. J. Heat Mass Transfer*, Vol. 18, pp. 1049-1053.

Clemes, S. B., 1990, "Free Convection Heat Transfer From Two-Dimensional Bodies," MASc Thesis, University of Waterloo, Waterloo, Canada.

Hassani, A. V., and Hollands, K. G. T., 1989a, "On Natural Convection Heat Transfer From Three-Dimensional Bodies of Arbitrary Shape," ASME JOURNAL OF HEAT TRANSFER, Vol. 111, pp. 363-371.

Hassani, A. V., and Hollands, K. G. T., 1989b, "Prandtl Number Effect on External Natural Convection Heat Transfer From Irregular Three-Dimensional Bodies," *Int. J. Heat Mass Transfer*, Vol. 32, No. 11, pp. 2075-2080.

Hassani, A. V., Hollands, K. G. T., and Raithby, G. D., 1992, "A Close Upper Bound for the Conduction Shape Factor of a Uniform Thickness, 2D Layer," submitted to *Int. J. of Heat and Mass Transfer*, May.

Kuehn, T. H., and Goldstein, R. J., 1976, "Correlating Equations for Natural Convection Heat Transfer Between Horizontal Circular Cylinders," *Int. J. Heat Mass Transfer*, Vol. 19, pp. 1127-1134.

Morgan, V. T., 1975, "The Overall Convective Heat Transfer From Smooth Circular Cylinders," *Advances in Heat Transfer*, Academic Press, Vol. 11, pp. 199-264.

Nakamura, H., and Asako, Y., 1978, "Laminar Free Convection From a Horizontal Cylinder With Uniform Cross Section of Arbitrary Shape," *Bulletin of the JSME*, Vol. 21, No. 153, pp. 471-478.

Oosthuizen, P. H., and Paul, J. T., 1984, "An Experimental Study of Free-Convective Heat Transfer From Horizontal Non-circular Cylinders," in: *Fundamentals of Natural Convection/Electronic Equipment Cooling*, L. C. Witte and L. S. Saxena, eds., ASME HTD-Vol. 32, pp. 91-97.

Raithby, G. D., and Hollands, K. G. T., 1975, "A General Method of Obtaining Approximate Solutions to Laminar and Turbulent Free Convection Problems," *Advances in Heat Transfer*, Academic Press, Vol. 11, pp. 265-315.

Raithby, G. D., and Hollands, K. G. T., 1976, "Laminar and Turbulent Convection From Elliptic Cylinders, With a Vertical Plate and Horizontal Cylinder as Special Cases," ASME JOURNAL OF HEAT TRANSFER, Vol. 98, pp. 72-80.

Raithby, G. D., and Hollands, K. G. T., 1985, *Handbook of Heat Transfer Fundamentals*, 2nd ed., Chap. 6, Rohsenow, Hartnett, and Ganić, eds., McGraw-Hill, New York.

APPENDIX A

Comparison of Circular Cylinder Results With Those of Other Works

To compare the circular cylinder results with those of previous experimental workers on the circular cylinder, Fig. 9 was prepared. It draws on all the experimental studies that used air as the fluid and had results in the Ra_D range from 10 to 10^7 that were reported by Morgan (1975), who made a comprehensive analysis of all relevant data reported up to 1974. Morgan listed the correlation equations—each covering a limited Ra range—found by each worker. Using these equations, we calculated values of Nusselt number at specific Ra values (10^2, 10^3, 10^4, 10^5, and 10^6) covered by at least two workers. This gave six values of Nu_D at $\mathrm{Ra}_D = 10^6$, ten at $\mathrm{Ra}_D = 10^5$, seven at $\mathrm{Ra}_D = 10^4$, four at $\mathrm{Ra}_D = 10^3$, and two at $\mathrm{Ra}_D = 10^2$. Next, each of these Nu_D values was corrected for the fact that the thermal expansion coefficient β in Morgan's analysis had been based on the film temperature T_f rather than at the

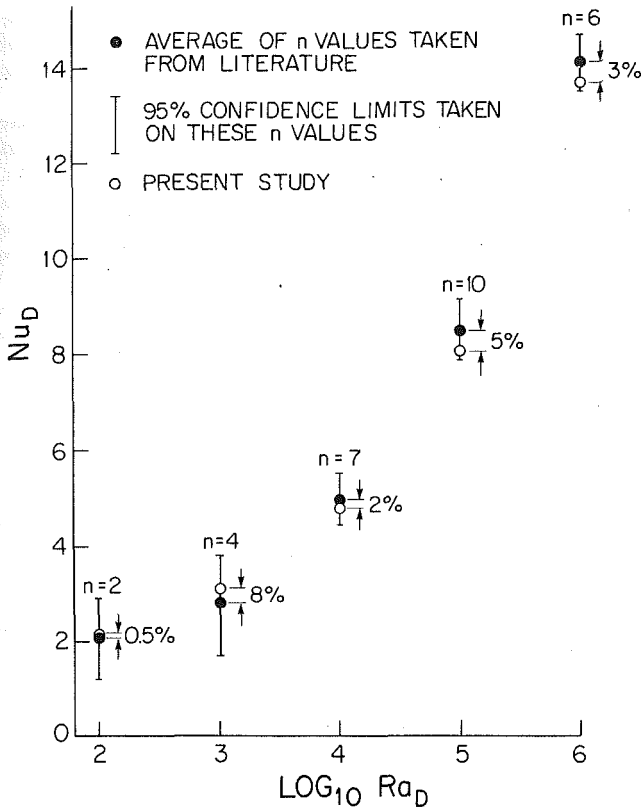

Fig. 9 Comparison between present results on the circular cylinder and those of 17 previous workers on the subject problem, as reported by Morgan (1975)

ambient air temperature T_a, the latter being the temperature used for the present data. (See Raithby and Hollands (1985), among others, for a rationalization for basing β on T_a rather than T_f.) The resulting correction factor on Nu_D (calculated by using the maximum T_f/T_a of each worker, as tabulated by Morgan), was about 0.95, on average. Following this correction, a statistical analysis was carried out on the Nu_D values at each Ra_D, to obtain the mean and the 95 percent confidence interval on the Nu_D at that Ra_D, and it is these results that are plotted in Fig. 9. In this statistical procedure, each worker's value was treated as constituting a single experiment, and each was given equal weight (even though there were one or two outliers). The values marked "present study" in Fig. 9 were obtained by interpolating across the first two columns in Table 2.

From Fig. 9 it was concluded that the present results are not significantly different from those of previous workers; that is, they agree with previous results to the degree that those results agree with each other. The maximum percent deviation between the mean of the previous workers' values and the present results was 8 percent, but, if the one outlier at this Ra_D were ignored, the deviation from the mean at this Ra_D would reduce to 1.2 percent. Morgan critiqued the literature values, noting that many workers did not use cylinders long enough to eliminate end effects and that this results in an apparent increase in the heat transfer. This could explain why, after correction for the outlier at $Ra_D = 10^3$, the present results are generally slightly lower than the average of other workers.

APPENDIX B

Comparison of Correlation Equation With Results of Other Workers for Noncircular Cylinders

Comparison With Data of Oosthuizen and Paul. Oosthuizen and Paul (1984) measured natural convection heat transfer, in air, from cylinders with prismatic (diamond) cross section and from cylinders with the cross section of a circle having circularly curved fins attached on opposing sides. Their measurements were all at fixed Rayleigh number Ra_L, with L, the longest dimension of the cross section, being kept constant in all their tests. They were mainly interested in examining the relative effect of body orientation and shape on the Nusselt number. Thus in comparing their results with Eq. (11), we will plot measured and computed values of the ratio $Nu(\theta)/Nu(\theta_r)$ versus θ where θ_r is a reference value of θ, or the ratio $Nu(L/D)/Nu((L/D)_r)$, where $(L/D)_r$ is a reference value of L/D. (Here the orientation has been represented by inclination angle θ, and the shape by aspect ratio L/D where D is the longest body dimension measured perpendicular to the direction along which L is measured.)

Representative comparisons are plotted in Figs. 6 and 7. Shown on the experimental point symbols are the error bounds, estimated as follows: Oosthuizen and Paul estimated the accuracy of their measured heat transfer coefficients as significantly better than ± 5 percent. The ratio of Nusselt numbers given on the ordinate on Figs. 6 and 7 will be proportional to the ratio of the heat transfer coefficients, and since maximum relative errors add on division, the maximum relative error in the ratio will be $\sqrt{2} \times 5$ percent or 10 percent, and the expected error equal to $\sqrt{2} \times 5$ percent or about 7 percent. There will also be errors in determining the Rayleigh number; it seems unlikely that all the measurements were made at exactly the same Rayleigh numbers. If the Rayleigh numbers ever matched to within 6 percent, the error associated with nonmatching Rayleigh numbers would be about 1.5 percent. Thus there is reason to believe that the experimental error is about 8.5 percent. The errors shown in Figs. 6 and 7 actually underestimate this estimate of the experimental error; they are set at 5 percent error.

Figure 6 shows the angular effect on the Nusselt number for the diamond-shaped body, with $\theta_r = 0$. All but four of the 36 experimental points agree with Eq. (11) to within 5 percent and all agree to within 7 percent. The rms deviation between the experimental data and Eq. (11), taken over all the data points (except that at $\theta = 0$, for which the error has to be zero) is 3.5 percent, which is well within experimental error. A similar set of plots was made to compare the angular effect for the finned circle, with L/D ratios running from 1 to 5.3; the same level of agreement was observed, with about the same rms deviations and the same maximum deviation. Thus it is concluded that, within experimental error, Eq. (11) predicts the observed angular effect on the heat transfer for diamond-shaped and finned-circle shaped two-dimensional bodies for L/D up to about 5.5.

Figure 7 shows the aspect ratio effect on the Nusselt number for the finned circular body, with the reference value of L/D, $(L/D)_r$, being 1.61. Equation (11) predicts all of the data points to a degree well within experimental error, *except* those for which $L/D = 1$. The data for the diamond shape show similar comparisons when plotted in this format; more specifically, Eq. (11) predicts the observed dependence of $Nu(L/D)/Nu(L/D = 1.32)$ to well within experimental error, except for the points at $L/D = 1.0$. For either body, the disagreement at $L/D = 1$ ranges up to 25 percent. We have no explanation for this discrepancy. We do note, however, that for both bodies, the experimental points at $L/D = 1$ lie well off the trend of the data at other values of L/D, that is, an extrapolation of the other data to $L/D = 1.0$ would not be expected to produce the observed value at $L/D = 1.0$.

Comparison With Data of Nakamura and Asako. Hassani and Hollands (1989b) showed that their three-dimensional body model (Hassani and Hollands, 1989a), (which, like the present one, had been fitted around data for *air*), was reasonably predictive of the available experimental data for *liquids*, once

the Prandtl number dependence of $\bar{C}_l$ and $\hat{C}_l$ (the latter through a, b, and e in Eq. (3)) had been taken into account. In this section, we compare the present model (Eq. (11) with the available literature data for two-dimensional bodies on liquids, being sure to account for the Prandtl number dependence of $\bar{C}_l$ and $\hat{C}_l$.

Nakamura and Asako (1978) carried out experiments using water as the fluid ($3 \leq \mathrm{Pr} \leq 8$) covering the Rayleigh number range $10^8 \leq \mathrm{Ra} \leq 3 \times 10^{10}$ on two-dimensional bodies having one of two cross-sectional shapes: a "modified" equilateral triangle and a modified square. The modifications to these basic shapes were to replace the sides with large-diameter circular arcs covering most of the sides and small-diameter circular arcs at the corners, giving the shapes sketched in the insets in Fig. 8. The workers fitted their data to a one-quarter power law equation, i.e., to

$$\mathrm{Nu} = c\mathrm{Ra}^n \tag{12}$$

with $n = 1/4$, and reported their results in terms of the value of c for each body in each of three orientations. Equation (11), while fitted very accurately by a power law function over the limited Ra range $10^8 \leq \mathrm{Ra} \leq 3 \times 10^{10}$, requires a value for n of 0.285 rather than 0.25 to give the most accurate fit. On the other hand, Eq. (11) can be fitted reasonably well over the range by Eq. (12) with $n = 1/4$, yielding in this case an rms deviation of about 4 percent. To make the comparison between the Nakamura and Asako data and Eq. (11), we have chosen to fit Eq. (11) to Eq. (12) with $n = 1/4$ over the relevant Ra range—thus following the same procedure as Nakamura and Asako applied to their data—and then compare the corresponding values of c. Of course we made sure both sets of results were put into a common representative-length scale format.

Figure 8 shows the comparison. Agreement is everywhere within 7.5 percent for the triangular body, but differences extend to 12 percent for the square body in one orientation. Nakamura and Asako did not provide error-bound estimates for their measurements, so it is difficult to state whether this degree of agreement is within experimental error. It may be noted, however, that the Prandtl number variations (from 3 to 8) over their experimental range would be expected to produce an extreme 2 1/2 percent variation in Nusselt, and the error associated with this variation would be expected to be about one half of this, or about 1.25 percent. In addition, plots of their water temperature distribution show that the fluid was stably stratified, to a degree that the Nusselt number may have been increased, by about 2 percent at the high temperature difference settings, above what would be expected for an isothermal fluid. Finally, the uncertainty in the temperature difference ΔT, caused by observed variations in the body surface temperature of up to $\pm 1.5°\mathrm{C}$ and in the fluid temperature of $\pm 1.5°\mathrm{C}$, would appear to produce an uncertainty in the Nusselt number of about ± 7 percent. Thus, while experimental error probably does not explain all the differences observed in Fig. 8, it could explain much of it, almost certainly enough to bring the margin of error to ± 10 percent in rms deviation, which is the margin observed by Hassani and Hollands (1989b) for three-dimensional bodies in liquids.

A. Karagiozis[1]

G. D. Raithby
Mem. ASME

K. G. T. Hollands
Mem. ASME

Department of Mechanical Engineering,
University of Waterloo,
Waterloo, Ontario, Canada, N2L 3G1

Natural Convection Heat Transfer From Arrays of Isothermal Triangular Fins in Air

Measurements of the heat transfer to air by natural convection from arrays of isothermal triangular fins on a vertical base plate are reported for several array geometries, for a large range of Rayleigh number, and for two orientations (vertical fins and horizontal fins). The data are believed to be the first available for this important geometry. A single equation is provided that correlates the measured Nusselt numbers for the vertical orientation with an rms error of 4.8 percent. The horizontal fin orientation was shown to have inferior heat transfer performance.

Introduction

Heat transfer from fins is a topic of continuing interest in heat transfer. Although in practice the rectangle has been the most common fin shape, the triangular fin (Fig. 1) is known to have a higher rate of heat transfer per unit of material volume; indeed, by this measure, its performance approaches quite closely that of the optimal shape (Eckert and Drake, 1972). The common practice of using rectangular fins would seem to stem from the difficulty of manufacturing other shapes, particularly when the fins are fabricated from sheet metal. When the fins are extruded, however, they are more often triangular (or trapezoidal). This is often the case even when rectangular fins were intended, because of limitations in the extrusion process.

To design a fin properly one needs to know the convective coefficient to the surrounding fluid. Interestingly, it appears that no measurements have been reported in the literature of the natural convective heat transfer coefficients from triangular fins mounted in a vertical surface, which is the most common orientation. Fins can be mounted on a vertical surface with their midplanes vertical, as illustrated in Fig. 1(A), or horizontal, as illustrated in Fig. 1(B). The horizontal orientation seems to have gained recent popularity in electronic cooling applications.

Many workers (Elenbaas, 1942; Starner and McManus, 1963; Welling and Wooldridge, 1965; Schult, 1966; Aihara, 1970a; Chaddock, 1970) have measured heat transfer coefficients for vertical *rectangular* fins, and correlated their data into recommended equations for calculating the heat transfer in that situation. It seems likely that designers of triangular fins have used these equations to calculate heat transfer from the triangular fins assuming, for example, that the triangular fin will convect the same as a rectangular fin of the same perimeter facing a passage of the same cross-sectional area. Of course there are no data on which to judge the accuracy of such a practice, and the practice would certainly seem to be questionable for cases in which the fins interfere thermally; for a given fin spacing and height, a triangular fin would have less interference near its tips and more interference near its base. Also, heat transfer from the fin ends is going to be different in the two cases. Even if the rectangular fins and triangular fins did dissipate heat at the same rate, there would still be a problem: For vertical rectangular fins there are substantial differences between the recommended equations of different workers, and for *horizontal* fins there seem to be no data available at all.

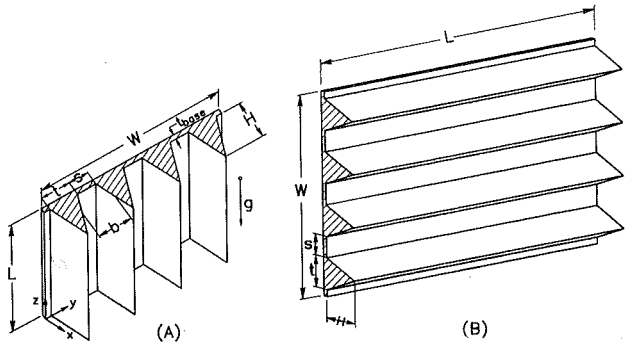

Fig. 1 Vertical fins on a vertical surface (A), and horizontal fins on a vertical surface (B)

Thus there would appear to be a real need for experimental measurements on natural convection heat transfer from both vertical and horizontal fins mounted in a vertical surface, and it is the purpose of this paper to address that need for triangular fins. In studying the literature reporting measurements on vertical rectangular fins, we have noted that the discrepancy between workers is most pronounced at low Rayleigh numbers. The reason is that the corrections for the radiant losses and for the back losses (i.e., the heat losses off the back or nonfinned side of the base plate) become relatively large at low Rayleigh number, and there is usually a large uncertainty in both of these corrections. Thus in the present measurements, every effort was made to minimize or eliminate these losses.

As will be clear from the dimensional analysis given in the next section, the dimensionless heat transfer, the Nusselt number, is a function of several dimensionless groups. These include the Rayleigh number, the Prandtl number, and other groups defining the fin geometry. Although it was clearly not possible experimentally to cover all combinations of values of all groups, a range fairly representative of common practice was covered. The Rayleigh number ranged over six decades (typically from 1 to 10^6) for any one fin geometry. The Prandtl number was constant at about 0.71. For the vertical fins, a single correlation equation, closely fitting the convective component of the Nusselt number's dependence on the Rayleigh, was developed, the equation being common to all fin geometries tested. Data for horizontal fins are also presented.

Dimensional Analysis

If Q_{CONV} is the convective heat transfer to the ambient fluid

[1] Current Address: Building Performance Lab., National Research Council of Canada, Ottawa, Ontario, K1A 0R6, Canada.

Contributed by the Heat Transfer Division for publication in the JOURNAL OF HEAT TRANSFER. Manuscript received by the Heat Transfer Division November 1992; revision received April 1993. Keywords: Finned Surfaces, Natural Convection. Associate Technical Editor: J. R. Lloyd.

from the surface area A_s, where A_s is the entire surface area of the array except the "back" (see Fig. 2), the average heat transfer coefficient is embodied in the Nusselt number as follows:

$$\mathrm{Nu} = \frac{\bar{h}\, b}{k} = \frac{Q_{\mathrm{CONV}}\, b}{A_s \Delta T k} \tag{1}$$

The parameters on which Nu depends are obtained by a dimensional analysis. By retaining only the terms in the governing equations that are important for natural convection (see Raithby and Hollands, 1985), and neglecting property value variations, the nondimensional equations of continuity, momentum, and energy, for the vertical fin array in Fig. 1(A), can be expressed by

$$\frac{\partial u^*}{\partial x^*} + \frac{\partial v^*}{\partial y^*} + \frac{\partial w^*}{\partial z^*} = 0 \tag{2}$$

$$u^* \frac{\partial u^*}{\partial x^*} + v^* \frac{\partial u^*}{\partial y^*} + w^* \frac{\partial u^*}{\partial z^*} = -\left(\frac{L}{b}\right)^2 \frac{\partial p^*}{\partial x^*} + \sqrt{\mathrm{Pr}\frac{(1+\mathrm{Pr})}{\mathrm{Ra}}}\left(\frac{\partial^2 u^*}{\partial x^{*2}} + \frac{\partial^2 u^*}{\partial y^{*2}} + \frac{b^2}{L^2}\frac{\partial^2 u^*}{\partial z^{*2}}\right) \tag{3}$$

$$u^* \frac{\partial w^*}{\partial x^*} + v^* \frac{\partial w^*}{\partial y^*} + w^* \frac{\partial w^*}{\partial z^*} = -\frac{\partial p^*}{\partial z^*} + \sqrt{\mathrm{Pr}\frac{(1+\mathrm{Pr})}{\mathrm{Ra}}}\left(\frac{\partial^2 w^*}{\partial x^{*2}} + \frac{\partial^2 w^*}{\partial y^{*2}} + \frac{b^2}{L^2}\frac{\partial^2 w^*}{\partial z^{*2}}\right) + (1+\mathrm{Pr})\theta \tag{4}$$

$$u^* \frac{\partial \theta}{\partial x^*} + v^* \frac{\partial \theta}{\partial y^*} + w^* \frac{\partial \theta}{\partial z^*} + \sqrt{\frac{(1+\mathrm{Pr})}{\mathrm{Ra\,Pr}}}\left(\frac{\partial^2 \theta}{\partial x^{*2}} + \frac{\partial^2 \theta}{\partial y^{*2}} + \frac{b^2}{L^2}\frac{\partial^2 \theta}{\partial z^{*2}}\right) \tag{5}$$

$$\mathrm{Ra} = \frac{g\beta\Delta T(b^4/L)}{\nu\alpha} \tag{6}$$

(The v^* momentum equation has not been written since it is exactly the same as Eq. (3) with the dependent variable u^* replaced by v^*). The coordinates are shown in Fig. 1(A), and the dimensionless variables are defined in the nomenclature. It should be noted that in deriving these equations the length and velocity scales used in the vertical direction are different from those in the horizontal direction. The Rayleigh number based on the length scale in Eq. (6) is often referred to as the Elenbaas Rayleigh number.

The boundary conditions must still be recorded, and examined for additional dimensionless groups. On the fin surface the boundary conditions are

$$u^* = v^* = w^* = 0 \quad \theta = 1 \tag{7}$$

When the fin surface is plotted in (x^*, y^*, z^*) coordinates, all fin arrays will be coincident if the ratios H/b, t/b, W/b and t_{base}/b are all identical; it is important to note that L/b does not appear in this list because, by the definition $z^* = z/L$, all fin surfaces lie in the range $0 \le z^* \le 1$.

The outer surface, far removed from the fin array, can be assumed to be a sphere, of radius R_o, centered at the origin. Hence for

$$\sqrt{x^{*2} + y^{*2} + z^{*2}} = R_o^* = R_o/b: \quad u^* = v^* = w^* = \theta = 0 \tag{8}$$

If R_o^* is not large, there will be hydrodynamic and thermal interference between the fin array and the outer surface (i.e., enclosure effects).

Equation (1) for Nusselt number can be rewritten as

$$\mathrm{Nu} = \int_{A_s^*} [\nabla^* \theta]_s \cdot \hat{n}\, dA_s^*; \quad \nabla^* \theta = \frac{\partial \theta}{\partial x^*} i + \frac{\partial \theta}{\partial y^*} \hat{j} + \frac{b}{L}\frac{\partial \theta}{\partial z^*} \hat{k} \tag{9}$$

where $[\nabla^* \theta]_s$ is the nondimensional gradient of θ evaluated on the fin surface, $\hat{n}$ is the unit surface normal, and A_s^* is the

Nomenclature

A_s = surface area of fin array, excluding the "back" (see Fig. 2), m^2
b = mean fin spacing, Fig. 1, mm
C = thermal capacitance of array, J/K
g = gravitational acceleration, m/s^2
$\bar{h}$ = convective heat transfer coefficient = $Q_{\mathrm{CONV}}/A_s\Delta T$, W/mK
$\hat{i}, \hat{j}, \hat{k}$ = unit vectors in the x, y, and z directions
H = fin height, Fig. 1, mm
k = thermal conductivity of air at T_f, W/mK
L = fin length, Fig. 1, mm
Nu = Nusselt number for convection = $\bar{h}\, b/k$
Nu_L = Nusselt number for convection = $\bar{h}\, L/k$
$\mathrm{Nu}_{\mathrm{COND}}$ = Nusselt in the conduction limit (Ra$\to$0)
$\mathrm{Nu}_{\mathrm{RAD}}$ = $Q_{\mathrm{RAD}}\, b/(A_s\, \Delta T\, k)$
p = pressure, relative to hydrostatic, Pa
p^* = $p/\rho w_o^2$
Pr = Prandtl number = ν/α
Q_{CONV} = total convective heat transfer from A_s, W
Q_L = heat loss from fin array via lead wires, W
Q_{RAD} = heat loss from A_s by radiation, W
Q_{TOT} = defined in Eq. (13), W
Ra = Rayleigh number = $g\beta_\infty \Delta T b^4/\nu\alpha L$
Ra_L = Rayleigh number = $g\beta_\infty \Delta T L^3/\nu\alpha$
s = spacing between fins at base plate, Fig. 1, m
t = width of fin at its base, Fig. 1, m
T_f = film temperature = $(T_s + T_\infty)/2$
T_l = temperature of tank liner, K
T_s = surface temperature of fin array, K
T_∞ = ambient fluid temperature, K
ΔT = $T_s - T_\infty$
u^*, v^* = nondimensional velocities = u/v_o, u/v_o
u, v, w = velocity components in x, y, z directions
v_o = $\sqrt{g\beta\Delta TL/(1+\mathrm{Pr})}$ (b/L)
w^* = nondimensional velocity = w/w_o
w_o = $\sqrt{g\beta\Delta TL/(1+\mathrm{Pr})}$
W = width of base plate, Fig. 1, m
x^*, y^*, z^* = nondimensional coordinates = x/b, y/b, z/L, respectively
x, y, z = Cartesian coordinates, see Fig. 1, m
α = thermal diffusivity at T_f, m^2/s
β = thermal expansion coefficient at T_∞, 1/K
ΔT = $T_s - T_\infty$, K
ϵ = surface emissivity of fin array
θ = $(T - T_\infty)(T_s - T_\infty)$
ν = kinematic viscosity at T_f, m^2/s
ρ = fluid density at T_f, kg/m^3
σ = 5.670×10^8 W/m^2 K^4

nondimensional surface area. Note that the L/b ratio appears in Eq. (9), but it has not affect on Nu on surfaces where $\hat{n} \cdot \hat{k}$ is zero (i.e., vertical surfaces).

From the differential equation, their boundary conditions, and the equation for Nu, it is therefore concluded that Nu depends on the following nondimensional groups:

$$\mathrm{Nu} = f\left(\mathrm{Ra},\ \mathrm{Pr},\ \frac{L}{b},\ \frac{H}{b},\ \frac{t}{b},\ \frac{W}{b},\ \frac{t_{\mathrm{base}}}{b},\ \frac{R_o}{b}\right) \tag{10}$$

By introducing approximations, the dependence of Nu on some of these parameters can be eliminated. In the problems of interest, $R_o^* \to \infty$ (i.e., no enclosure effects). The changes in Nu due to changes of the base-plate thickness t_{base} can reasonably be ignored since the surface area of the edge of the base plate is small. Furthermore, when L/b is large, the dependence on L/b can usually be ignored for several reasons: z diffusion in Eqs. (3)–(5) can be ignored, the lateral pressure gradient in the u^* and v^* momentum equations can be shown to be negligible by an order-of-magnitude analysis, and the L/b that enters through Eq. (9) affects the Nusselt number only through the contribution of the top and bottom ends of the array to the heat transfer (and this area is small for large L/b). Hence, to good approximation for a vertical fin array with $R_o/b \to \infty$, large L/b, and small edge area of the base

$$\mathrm{Nu} = f\left(\mathrm{Ra},\ \mathrm{Pr},\ \frac{H}{b},\ \frac{t}{b},\ \frac{W}{b}\right) \tag{11}$$

Note that the effect of the L/b ratio is still present since it appears in the Rayleigh number, as defined by Eq. (6). That this is its *only* means of effect, for large L/b, was shown by Martin et al. (1991), for a different geometry. For an array with many fins, W/b will be large so it could also be dropped as a parameter; this is because the heat transfer from an entire array of N fins will approach N times the heat transfer from one of the interior fins, independent of W/b. In the present experiments there were as few as four fins in the array, so the W/b group is retained.

When Ra is sufficiently high for the boundary layers to be much smaller than the fin spacing, each vertical strip of the fin array will transfer the same heat as any other strip. Hence the Nusselt number over the vertical surface should become independent of the fin shape. If the heat transfer from the top and bottom ends of the array is also ignored (so that geometric parameters are not required to calculate the fraction of the surface area covered by the ends), the dependence on all length ratios in Eq. (11) disappears. Hence for the conditions on Eq. (11), plus the conditions that the end areas of the array are small compared to the vertical surface area, and that Ra is large,

$$\mathrm{Nu} = f(\mathrm{Ra},\ \mathrm{Pr}) \tag{12}$$

Experiment

Measurements were obtained for the three fin arrays shown in Fig. 2. The dimensions and aspect ratios are summarized in Table 1. The objective was to measure the convective heat transfer Q_{CONV}, from which Nu in Eq. (1) can be found. From the dimensional analysis, these Nusselt numbers should be applicable to all geometrically similar arrays, for the same Ra and Pr.

To measure the total heat loss from the fin array, a transient technique, developed for natural convection by Raithby et al. (1976) and refined by Chamberlain et al. (1985) and Hassani and Hollands (1989), was used. The fin array was hung in air from fine nylon lines, and it was heated prior to the measurements by impressing 240 volts via very fine copper leads across a heater embedded in the array. When the array reached a specified temperature above ambient, the heater was switched off and the transient cooling curve of the array (array temperature versus time) was measured. From these measurements, and a knowledge of the total heat capacitance of the array, a curve fitting procedure, described by Chamberlain (1983) and Hassani (1987), was used to find the total rate of heat loss, Q_{TOT}, at three values of ΔT during the transient decay. This heat loss consists of three components:

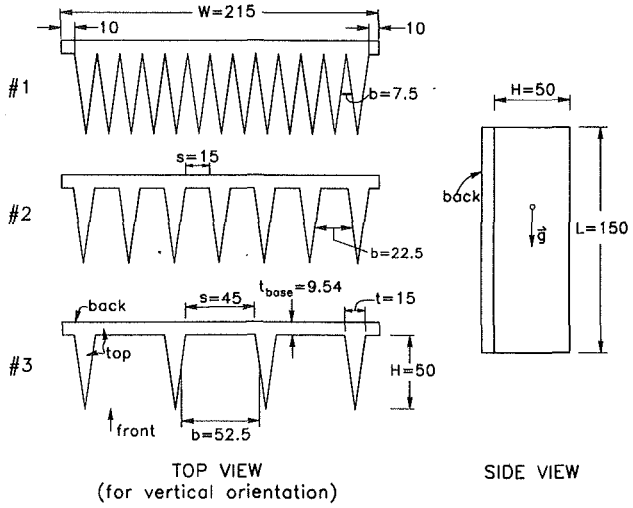

Fig. 2 Definition of the fin arrays used in the present study; all dimensions in mm

Table 1 Dimensions and aspect ratios of fin arrays (all dimensions in mm)

	L	H	W	s	b	L/b	H/b	W/b
Array #1	150	50	215	0	7.5	20	6.67	28.7
Array #2	150	50	215	15	22.5	6.67	2.22	9.56
Array #3	150	50	215	45	52.5	2.86	0.952	4.10
	t_{base} = 9.54, t = 15							

$$Q_{\mathrm{TOT}} = Q_{\mathrm{CONV}} + Q_{\mathrm{RAD}} + Q_L \tag{13}$$

where Q_{RAD} is the radiation loss, and Q_L is the loss via the leads to the array. From Eq. (13), Q_{CONV} can be found at the three ΔT values by subtracting Q_{RAD} and Q_L. The method used to find Q_{RAD} is described later; Q_L was found to be negligible.

For this method to be used, the body temperature must be uniform. This was ensured by constructing the base plate and fins from relatively good heat conductors, namely aluminum 2024-T35 and 6061-T6, respectively. The fins were bolted to the base plates, and good thermal contact was obtained by placing a strip of aluminum foil smeared with vacuum grease between the fin and base plate. Twenty 30 and 36 gage copper-constantan high precision thermocouples were imbedded throughout the model. These were used initially to check the isothermality of the model. These measurements showed that the maximum temperature variation within the array was 0.3 K, and this occurred at the largest ΔT. This high degree of isothermality was not surprising since the Biot number of the array was about 0.007. For the heat transfer measurements the thermocouples in the array were connected into a thermopile to measure the average temperature difference between the ambient air and the array.

To achieve the objective of the experiment, the heat loss from the back of the fin array had to be eliminated, as noted in the Introduction. In the present experiments, this heat loss was eliminated by creating a second identical fin array, and attaching it to the back of the first, so that the back surface was a symmetry surface. In the measurements, then, the heat transfer from the entire fin array was measured, and this was halved to get the heat transfer from the front part only.

Table 2 Measured values of C, $\mathcal{F}$, and Nu_{COND} for the three fin arrays

Array Number (see Table 1)	Heat Capacitance, C (J/K)	$\mathcal{F}$ (-)	Nu_{COND} (-)
1	5307	0.084	0.028
2	3630	0.132	0.160
3	2795	0.173	0.533

From the description so far, Nu values would be found at only three ΔT corresponding to three Ra values. To increase the range of Ra for a given array, measurements were carried out with the array hung near the center of a pressure vessel, and the transient cooling experiment was repeated at various pressure levels. Three data points were obtained at each pressure level, as already described. Varying the Rayleigh number by varying pressure was originally proposed by Saunders (1936) and recently discussed by Hollands (1988). The pressure tank (Shewen, 1986) was 1.5 m in diameter and 2.1 m long, with a working pressure range of 1 Pa to 1.04 MPa. The large dimensions of the vessel ensured that the outer wall was sufficiently far from the fin array to avoid interference (i.e., $R_o^* \to \infty$ in Eq. (8), so the enclosure effects were negligible). The inner wall of the pressure vessel was covered by a copper water-cooled liner to maintain isothermality. A heat exchanger at the same temperature as the liner was operated at the top of the tank to remove heat from the plume rising from the array. By these measures, the temperature variations within the ambient air around the array were held to within 1/30 of the temperature difference between the body and the air. The tank liner temperature, T_l, was measured for use in calculating the radiation loss.

For the horizontal orientation in Fig. 1(B), the array was simply rotated 90 deg, keeping the base plate vertical.

(The present measurement technique could not be used for a horizontal base plate, because heat loss can no longer be blocked from the back side of the base plate, because of the loss of symmetry.)

To determine accurately the total heat loss from the array from the transient cooling curve, the heat capacitance of the body, C, was needed. Furthermore, the radiant loss, Q_{RAD}, was needed to provide the convective heat transfer. Q_{RAD} was calculated from

$$Q_{RAD} = \sigma A_s \mathcal{F} (T_s^4 - T_l^4) \tag{14}$$

where the radiant exchange factor $\mathcal{F}$ (Kreith, 1968) accounts for both geometric and surface emissivity effects governing radiant exchange between the fins and the tank liner. Both C and $\mathcal{F}$ were measured using the method of Hassani and Hollands (1989). This involved measuring the transient temperature response of the array, for a constant power at the array heater, with the array in an evacuated bell jar ($p = 10^{-4}$ Pa) where convection and conduction are virtually eliminated so the heat transfer is by radiation alone. The values of C and $\mathcal{F}$ for the three arrays are given in Table 2. The measured capacitance includes the capacitance of embedded heaters, bolts holding the fins to the base plate, the aluminum base plate and fins, etc. It is assumed that the value of $\mathcal{F}$ is the same when the array is in the pressure vessel as it is when the array is in the bell jar, because in both cases the containing vessel emissivity was close to unity and its area was substantially greater than the fin array area.

A detailed error analysis for this experiment has been prepared by Karagiozis (1991). Following the procedure of Moffat (1988), precision errors and bias errors were combined to produce an overall measure of uncertainty based on 95 percent confidence values for the precision errors. This analysis showed that the uncertainty in the measured Ra values decreased from 3.5 percent at $Ra = 10^{-2}$ to 2.3 percent at $Ra = 10^8$; the major source of uncertainty in Ra was the measurement of the low values of pressure. The uncertainty in Nu decreased from 12 percent for $Nu = 0.08$ (at very low pressures) to 2.5 percent at $Nu = 7$. The large uncertainty for low Nu values was dominated by uncertainty in the radiation correction; heat loss via the lead wires contributed little to either the heat transfer or the uncertainty.

Validation of Experimental Method

The transient procedure was used because it permitted many data points to be obtained quickly. (In the more usual measurement procedure, power is supplied to the heater at a constant known rate, which equals the heat loss from the body when steady state is achieved; the time to reach steady state can be very large.) To ensure that the transient and steady-state procedures gave the same results, steady-state measurements were performed on one of the fin arrays, and results compared to the transient method results. Steady-state tests were repeated at seven pressure levels, the temperature difference between the array and the air varying by less than 0.07°C over each one-hour test. The tests yielded Nu values between 0.5 and 9.2, and the maximum difference in Nu measured by the two procedures was 2.0 percent.

Nusselt numbers were also measured with the fin array replaced by the base plate alone. The base plate itself constituted a $170 \times 150 \times 9.54$ mm vertical plate. For the same Ra, the results were compared with measurements of Hassani (1987) who used a plate ($81 \times 81 \times 8.1$ mm) that was close to being geometrically similar. The two sets of measurements were found to agree to within 5.5 percent, which was within the combined experimental uncertainty of 6 percent.

Measurements for a fin array were normally obtained over the portion of the transient decay curve from $\Delta T = 20$ to 5°C. For one array, these measurements were repeated for the $\Delta T = 40$ to 30°C portion of the decay curve. The Nusselt numbers from the two independent experiments agreed to within about 1 percent, showing that Nu was independent of the range of ΔT used. In making these comparisons, it is important to evaluate property values at the temperatures indicated in the nomenclature.

As a final validation test, heat transfer from Array #1 in Fig. 2 was measured at low Ra for both the vertical and horizontal orientations (Fig. 1). It would be expected that heat transfer would become independent of orientation for sufficiently low Ra, because heat conduction from the array would dominate. For $Ra < 1$, the Nu values from the two orientations were indeed found to be virtually identical.

Results

Measured values of Nu are shown in Fig. 3 for the three fin arrays in their vertical orientation. For high Ra the curves coalesce along a single curve, as anticipated in Eq. (12). Plotted on the same figure is the result of the classical solution to the laminar thin layer boundary layer equations for a single vertical, thin isothermal, flat plate for $Pr = 0.71$ (Incropera and De Witt, 1990), namely $Nu_L = 0.515\ Ra_L^{1/4}$, which can be recast into the form $Nu = 0.515\ Ra^{1/4}$ The data lie within 3.3 percent of this curve for $Ra > 4000$. At low Ra the curves appear to approach a constant value, suggesting that the convective motion contributes little to the heat transfer. This constant value is the conductive limit, denoted here by Nu_{COND}.

To determine Nu_{COND}, additional Nu measurements were taken at very low pressures. These data were fit well to an equation of the form:

$$Nu = Nu_{COND} + \xi\ Ra^{\eta} \tag{15}$$

where ξ and η are constants for a particular array. A nonlinear regression software package was used to find the three con-

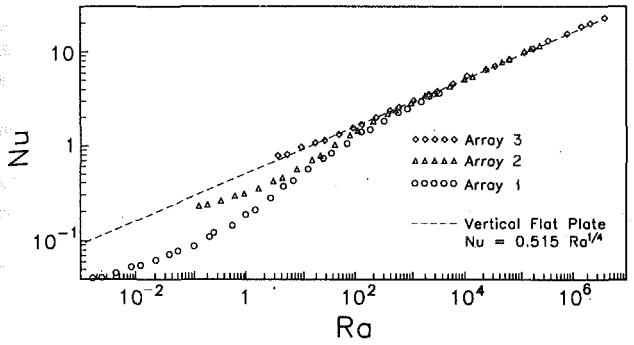

Fig. 3 Measured Nusselt numbers for the three fin arrays in Fig. 2 in the vertical orientation (Fig. 1A)

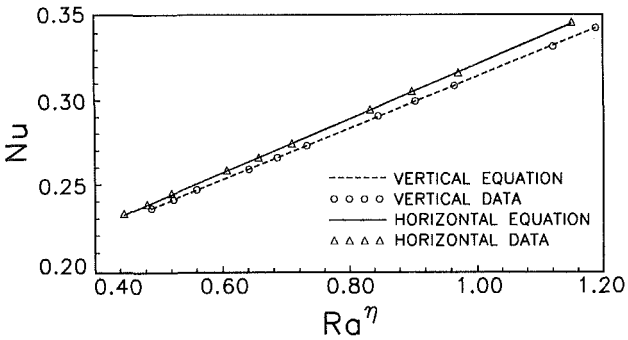

Fig. 4 Data fit at low Ra to determine the conductive limit, Nu_{COND}

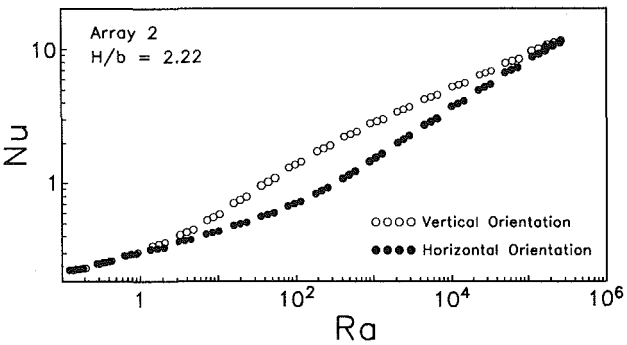

Fig. 5 Comparison of convective heat transfer from Array #2 in a vertical and horizontal orientation

stants, Nu_{COND}, ξ, and η for each body in each orientation. A plot of Eq. (15) and the data is shown in Fig. 4 for Array #2 in both the horizontal and vertical orientations. While ξ and η in Eq. (15) depend strongly on orientation, in the limit as $Ra \to 0$, $Nu \to Nu_{COND}$, independent of orientation. Nu_{COND} values obtained from the vertical and horizontal orientations were found to agree within 2.0 percent for all three arrays. The values of Nu_{COND} obtained are listed in Table 2.

The convective heat transfer from Array #2 is plotted in Fig. 5 for both the horizontal and vertical orientations. For $Ra \to 0$, the heat transfer becomes independent of Ra, as already discussed. At intermediate Ra, which is the usual range of interest to designers, the Nusselt number for the vertical orientation is up to 87 percent higher than for the horizontal orientation. Based on these results, it is difficult to justify the practice of choosing the horizontal orientation to cool electronic components. At high Ra, $Ra > 2 \times 10^5$, Nu becomes virtually the same for both orientations, and the trends suggest that the horizontal orientation might even give slightly higher Nu outside the experimental range of Ra.

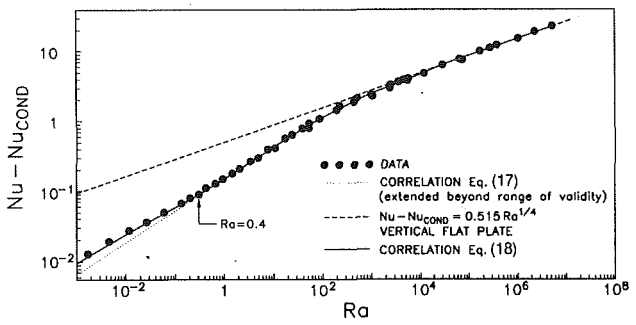

Fig. 6 Heat transfer ($Nu - Nu_{COND}$) from vertical fin arrays, together with correlation equations

Correlation of Data, Vertical Orientation

When replotted in the form $Nu - Nu_{COND}$ versus Ra, the data for all three arrays in the vertical orientation were found very nearly to collapse onto a single curve, as shown in Fig. 6. This was somewhat surprising for low Ra, since a dependence on geometric parameters was expected from Eq. (11). For fin geometries outside the range used in the present experiments, the expected dependence could still arise.

For $Ra > 4 \times 10^3$, the data fall near the classical equation for a vertical flat plate, discussed previously:

$$Nu - Nu_{COND} = 0.515\,Ra^{1/4}; \quad Ra > 4 \times 10^3 \qquad (16)$$

Equation (16) is plotted on Fig. 6. The rms deviation from this equation is 3.3 percent and the maximum deviation is 8.4 percent.

At lower Ra, thermal interference between the fins reduce the heat transfer. For $Ra \geq 0.4$ the following correlation equation has been derived using the Churchill–Usagi (1972) procedure

$$Nu - Nu_{COND} = 0.515\,Ra^{1/4}\left[1 + \left(\frac{3.26}{Ra^{0.21}}\right)^3\right]^{-1/3}; \quad Ra > 0.4 \qquad (17)$$

This equation is also plotted in Fig. 6. The measured Nu values are fit by this equation with an rms error of 4.8 percent and a maximum error of 11 percent.

For $Ra < 0.4$, Eq. (17) can normally be used with little overall error because conduction and radiation dominate the heat transfer. For completeness, however, the convection data in Fig. 6 can be fitted by adding a quantity denoted δNu to Eq. (17) as follows:

$$Nu - Nu_{COND} = 0.515\,Ra^{1/4}\left[1 + \left(\frac{3.26}{Ra^{0.21}}\right)^3\right]^{-1/3} + \delta Nu \qquad (18a)$$

where

$$\delta Nu = \{0.147\,Ra^{0.39} - 0.158\,Ra^{0.46}, 0\}_{MAX}; \quad Ra > 10^{-3} \qquad (18b)$$

In Eq. (18*b*) the maximum of the two quantities in brackets is used. Equation (18) fits all the data with an rms error of 4.8 percent and a maximum error of 11 percent.

Discussion

Since the paper provides information for design, it seems appropriate to stress that radiation and conduction can play significant roles. Figure 7 shows, in the bottom-most curve, a plot of $Nu - Nu_{COND}$. Adding Nu_{COND} from Table 1 to obtain the convective Nusselt number Nu (plotted in the next curve up) causes a very significant difference at low Ra. This Nu_{COND} value, in the present experiments, is based on heat transfer only to the surrounding air. If other cool surfaces were located in the vicinity of the fin array, Nu_{COND} will be higher due to direct conduction to those surfaces. On the other hand, if the

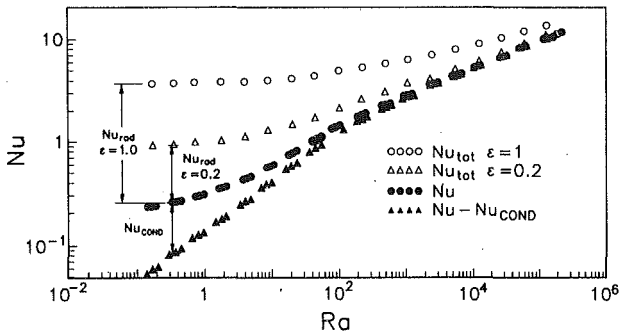

Fig. 7 The effect of conduction and radiation on the heat transfer from Array #2

fin array were mounted on a heated surface that extends beyond the array, Nu_{COND} could be decreased. Each application will have its own Nu_{COND}, and the determination of its value will often be important.

To show the magnitude of radiation on the heat loss from Array #2 in the present experiments, the radiative heat transfer, Q_{RAD}, is calculated for $T_s = 34.8°C$ and $T_l = 14.7°C$ using Eq. (14), and this is used in a "radiation Nusselt number" Nu_{RAD} where Q_{CONV} in Eq. (1) is replaced by Q_{RAD}. The total Nusselt number, $Nu_{TOT} = Nu + Nu_{RAD}$, is also plotted in Fig. 7 for every third data point. The emissivity of the present arrays was quite low ($\epsilon \approx 0.2$); this value was calculated from the measured $\mathcal{F}$ in Eq. (14), by roughly estimating the angle factor from the array to its environment. (This value of emissivity was confirmed using direct measurements using a Gier-Dunkle infrared reflectometer.) For a black surface, $\epsilon = 1.0$, the Nu_{RAD} value would be larger by five times; the Nu_{TOT} for a black surface is shown as the top curve in Fig. 7. It is clear from this figure that failure to account for radiation will result in a severe underestimation of the heat loss from the surface.

The results obtained in the present study strictly apply only to fin arrays that are geometrically similar to the tested ones. For Array #1, Fig. 2, the heat transfer is obtained for many fins so that application of the results to wider arrays (i.e., larger W/b) would seem to be valid, as discussed in relation to Eq. (11). For Array #3, however, there are only four fins of which the two outside fins "see" quite different conditions than the interior fins; applying Eqs. (17) or (18) to wider arrays of such fins therefore seems quite risky. This caution is somewhat balanced by two facts: The fins should behave as vertical flat plates in the high Ra limit, and the data for all Ra did collapse to a single curve for the three arrays that would not be expected if the edge fins in Array #3 had significantly different heat transfer than the interior fins.

No attempt has been made to correlate the results for the horizontal orientation because the heat transfer would depend on the number of fins. The air heated by the lower fins is swept up, and blankets the higher fins, and the effects of this will depend on the number of fins present. A correlation for the specific arrays in this study would therefore by of very limited interest. Besides, the present results show that the horizontal orientation should be avoided.

The present results also supply strictly to isothermal fins. The error in applying the correlation for the convective heat transfer should be quite small for fin efficiencies near unity. Dusinberre (1958) claims that the heat transfer coefficients can be adequately corrected to account for nonisothermally for fin efficiencies as low as 75 percent.

Summary

The present paper reports measurements of convective heat transfer from three triangular, isothermal, fin arrays to air. The main points related to heat transfer from a vertical fin array are summarized as follows:

1 The measured values of Nu approach very closely the theoretical equation for a vertical flat plate for $Ra \geq 4000$.
2 As $Ra \to 0$, $Nu \to Nu_{COND}$, where Nu_{COND} is the limiting value for heat loss by conduction to the ambient air.
3 For $Ra < 4000$, the appropriate Nu value depends on Nu_{COND}, which will change with geometry.
4 All results collapsed on a single curve when plotted as $Nu - Nu_{COND}$ versus Ra. A correlation equation was provided.
5 It was noted that radiation and Nu_{COND} will depend strongly on the application of interest.

For fins running horizontally on a vertical base plate, the Nusselt number was found to be significantly lower than when the fins were vertical.

Acknowledgments

This work was supported by Operating Grants to the second and third authors from the Natural Sciences and Engineering Research Council of Canada. The first author was also supported by a NATO Fellowship for a one-year study at the Von Karman Institute.

References

Aihara, T., 1970a, "Natural Convection Heat Transfer From Vertical Rectangular-Fin Arrays/Part 1," *Rep. Inst. High Sp. Mech., Japan*, Vol. 21, No. 213, pp. 105–134.

Aihara, T., 1970b, "Natural Convection Heat Transfer From Vertical Rectangular-Fin Arrays/Part 2," *Rep. Inst. High Sp. Mech., Japan*, Vol. 13, No. 641, pp. 1182–1191.

Chaddock, J. B., 1970, "Free Convection Heat Transfer From Vertical Rectangular-Fin Arrays," *ASHRAE Journal*, Vol. 12, Aug., pp. 53–60.

Chamberlain, M. J., 1983, "Free Convection Heat Transfer From a Sphere, Cube and Vertically Aligned Bi-Sphere," MASc Thesis, University of Waterloo, Canada.

Chamberlain, M. J., Hollands, K. G. T., and Raithby, G. D., 1985, "Experiments and Theory on Natural Convection Heat Transfer From Bodies of Complex Shape," ASME JOURNAL OF HEAT TRANSFER, Vol. 107, pp. 624–629.

Churchill, S. W., and Usagi, R., 1972, "A General Expression for the Correlation of Rates of Transfer and Other Phenomena," JOURNAL OF HEAT TRANSFER, Vol. 18, pp. 1121–1128.

Dusinberre, G. M., 1958, "Effective and Local Surface Coefficients in Fin Systems," *Transactions of the ASME*, Vol. 80, pp. 1596–1597.

Eckert, E. R. G., and Drake, R. M., 1972, *Analysis of Heat and Mass Transfer*, McGraw-Hill, NY, pp. 89–90.

Elenbaas, W., 1942, "Heat Dissipation of Parallel Plates by Free Convection," *Rep. Physica*, Vol. IX, pp. 1–28.

Hassani, A., 1987, "An Investigation of Free Convection Heat Transfer From Bodies of Arbitrary Shape," PhD Thesis, University of Waterloo, Canada.

Hassani, A. V., and Hollands, K. G. T., 1989, "On Natural Convection Heat Transfer From Three-Dimensional Bodies of Arbitrary Shape," ASME JOURNAL OF HEAT TRANSFER, Vol. 111, pp. 363–371.

Hollands, K. G. T., 1988, "Direct Measurement of Gaseous Natural Convective Heat Fluxes," *Proceedings from: First World Conference on Experimental Heat Transfer, Fluid Mechanics and Thermodynamics*, Dubrovnik, Yugoslavia.

Incropera, F. P., and De Witt, D. P., 1990, *Fundamentals of Heat and Mass Transfer*, Wiley, New York.

Karagiozis, A. N., 1991, "An Investigation of Laminar Free Convection Heat Transfer from Isothermal Finned Surfaces," PhD Thesis, Dept. Mech. Eng., University of Waterloo, Canada.

Kreith, F. C., 1968, *Heat Transfer*, International Textbook Company, Scranton, PA.

Martin, L., Raithby, G. D., and Yovanovich, M. M., 1991, "On the Low Rayleigh Number Asymptote for Natural Convection Through an Isothermal, Parallel-Plate Channel," ASME JOURNAL OF HEAT TRANSFER, Vol. 113, pp. 899–905.

Moffat, R. J., 1988, "Describing the Uncertanties in Experimental Results," *Experimental Thermal and Fluid Science*, Elsevier Science Publishing Co., Inc., pp. 3–17.

Raithby, G. D., Pollard, A., Hollands, K. G. T., and Yovanovich, M. M., 1976, "Free Convection Heat Transfer From Spheroids," ASME JOURNAL OF HEAT TRANSFER, Vol. 98, pp. 452–458.

Raithby, G. D., and Hollands, K. G. T., 1985, *Handbook of Heat Transfer Fundamentals*, 2nd ed., Chap. 6, A. B. Rohsenow, C. D. Hartnett, and E. F. Ganić, eds., McGraw-Hill, New York.

Saunders, O. A., 1936, "The Effect of Pressure on Natural Convection in Air," *Proc. Royal Society, Series A*, Vol. 157, pp. 278–291.

Schult, T. H., 1966, "Free Convection Heat Transfer From Rectangular Fin Arrays," M.S. Thesis, Mech. Eng. Dept., Purdue University, W. Lafayette, IN.

Shewen, E. C., 1986, "A Peltier-Effect Technique for Natural Convection Heat Flux Measurements Applied to the Rectangular Open Cavity," PhD Thesis, Mechanical Engineering Department, University of Waterloo, Canada.

Starner, K. E., and McManus, H. N., 1963, "An Experimental Investigation of Free Convection Heat Transfer From Rectangular Fin Arrays," ASME JOURNAL OF HEAT TRANSFER, Vol. 85, pp. 273–278.

Welling, J. R., and Wooldridge, C. B., 1965, "Free Convection Heat Transfer Coefficients From Rectangular Vertical Fins," ASME JOURNAL OF HEAT TRANSFER, Vol. 87, pp. 439–444.

Liquid Immersion Cooling of a Substrate-Mounted Protrusion in a Three-Dimensional Enclosure: The Effects of Geometry and Boundary Conditions

D. E. Wroblewski
Department of Aerospace and Mechanical Engineering,
Boston University,
Boston, MA 02215

Y. Joshi
Department of Mechanical Engineering and CALCE Electronics Packaging Center,
University of Maryland,
College Park, MD 20742

A three-dimensional computational study of steady natural convection cooling of a substrate-mounted protrusion (chip) in a rectangular enclosure filled with dielectric liquid is described. Energy is generated in the chip at a uniform rate Q. Conduction within the chip and substrate are accounted for in the model, as is the coupled natural convection in the surrounding liquid. The nondimensional governing equations with the appropriate boundary conditions have been solved in the primitive variable form for $Ra = 10^8$ using a fully implicit finite volume formulation. Baseline computations have been performed for a cubical enclosure with a centrally placed silicon chip on a vertical alumina substrate, which forms one enclosure wall. The cooling liquid was Fluorinert FC 75 resulting in $Pr = 25$. The effects of conductive spreading along the substrate were found to be quite pronounced due to the low thermal conductivity of the liquid. Effects of chip and enclsoure sizes on the maximum chip temperatures displayed a strong dependence on the substrate to fluid thermal conductivity ratio, R_S. Conditions for the validity of two-dimensional approximations were investigated for large and small R_S. Two other thermal boundary conditions on the enclosure walls were also considered, with the smallest chip temperatures found for the top and one vertical sidewall cooled condition. For the baseline boundary conditions a numerical correlation for the maximum chip temperature was obtained.

1 Introduction

Direct immersion in dielectric liquids is currently under active study as a means for thermal control of electronic components. The stringent limits on the maximum device operating temperatures are set by their long-term reliability characteristics, which show a reduction by half in the mean time between failures for every 10°C increase in junction temperature above 85°C. Candidate liquids for immersion cooling must have high dielectric strength, be chemically inert, environmentally safe, and nontoxic. A family of such coolants is now commercially available as Fluorinerts (1985) with a wide range of boiling points. Their availability has prompted a number of investigations of their heat transfer characteristics for both single phase and phase-change schemes. A number of these are reviewed by Bergles and Bar-Cohen (1990) and Bar-Cohen (1991).

The fluid circulation in immersion cooling is either forced or buoyancy induced. Since the passive liquid cooling systems employing buoyancy-induced flow typically provide significant heat transfer enhancement over forced convection air cooling, along with design simplicity and resulting high reliability, they are of considerable current interest. Both experimental and computational investigations have been undertaken to characterize the resulting transport in configurations of interest in electronic packaging. Typically, the electronic components in the available studies have been simulated as discrete heat sources flush mounted on, or protruding from a substrate.

Experimental studies of natural convection liquid cooling have investigated arrays of simulated electronic components arranged (*i*) on vertical surfaces (Park and Bergles, 1987; Joshi et al., 1989a), (*ii*) in vertical channels (Joshi et al., 1989b), and (*iii*) in rectangular enclosures (Kelleher et al., 1987; Keyhani et al., 1988, 1990; Joshi et al., 1990).

These studies have attempted to characterize the flow and heat transfer behavior over a range of operating conditions for the selected configuration. However, due to the multiplicity of length scales and the large variability in the thermophysical properties of the various electronic packaging materials, the reported correlations are only applicable for limited conditions. Their greatest utility perhaps is in providing a database against which numerical schemes can be validated.

Numerical computations have also been reported for the last category listed above. Two-dimensional computations of transport for a protruding heat source in an enclosure were carried out by Lee et al. (1987) and for three flush heat sources in a liquid-filled enclosure by Prasad et al. (1990). In both of these studies the heat sources were simulated as uniform flux regions and the substrate was considered adiabatic. The fluorocarbon coolants used in liquid immersion cooling are characterized by thermal conductivity values almost an order of magnitude smaller than conventional coolants such as water. This, in combination with the use of moderate thermal conductivity substrate materials such as ceramics, makes the conductive spreading within the substrate an important and sometimes dominant mode of heat removal from the electronic component. These effects were examined for a substrate mounted protruding heat source in the two-dimensional computations by Sathe and Joshi (1991).

Three-dimensional computations of transport from a three-

Contributed by the Heat Transfer Division and presented at the ASME National Heat Transfer Conference, San Diego, California, August 9–12, 1992. Manuscript received by the Heat Transfer Division October 1992; revision received June 1993. Keywords: Conjugatic Heat Transfer, Electronic Equipment, Natural Convection. Associate Technical Editor: J. R. Lloyd.

by-three array of rectangular protrusions in a liquid filled enclosure were performed by Liu et al. (1987a, b). The liquid exposed protrusion surfaces were considered to dissipate uniform heat fluxes, while the substrate was adiabatic. Substrate conduction effects were included by Wroblewski and Joshi (1993) in their study of natural convection from a centrally mounted heat generating protrusion (chip or electronic package) in a dielectric liquid-filled cubical enclosure. Comparisons of the computations with the experimental results of Joshi and Paje (1991) for the same configuration were also provided.

The present computations investigate a more general configuration than the one examined by Wroblewski and Joshi (1993). The effects of important geometric parameters associated with the protrusion and the enclosure on transport are specifically examined including the variation of these with the substrate thermal conductivity. Also investigated is the role of the enclosure boundary conditions. Based on the trends predicted by the computations, a correlation is proposed for the maximum chip temperature.

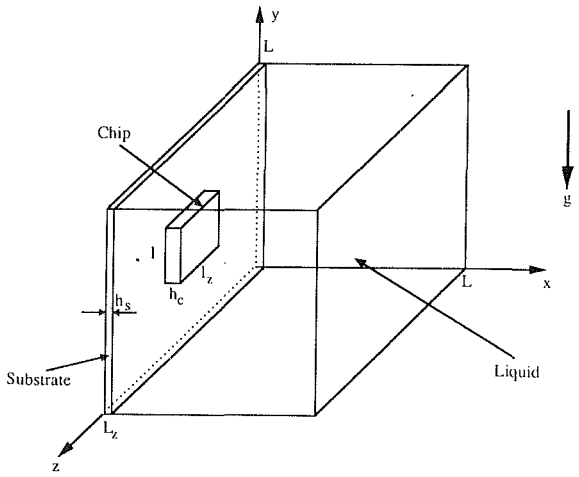

Fig. 1 Configuration examined in computational study

2 Analysis

The configuration examined in the present numerical study is seen in Fig. 1. The natural convection due to a single substrate mounted, uniform heat-generating chip of dimensions $h_c \times l \times l_z$ in a dielectric liquid filled rectangular enclosure of dimensions $L \times L \times L_z$ is considered. The chip is assumed to have uniform properties and an internal heat generation rate of Q. It is centrally mounted on a substrate of thickness h_s whose back forms one of the vertical walls of the enclosure. In the baseline computations the vertical enclosure wall facing the substrate is maintained at a constant temperature of T_c, while all other walls, including the back of the substrate, are insulated. Two other enclosure boundary conditions are also studied: (I) section of the top boundary in contact with the liquid is at temperature T_c, while all other walls are insulated, and (II) section of the top boundary in contact with the liquid and the vertical wall facing the substrate are at T_c, with all other walls insulated.

2.1 Governing Equations. The nondimensional governing equations for the three-dimensional steady transport, assuming constant properties in each region and the Boussinesq approximations in the liquid, are as follows:

Continuity

$$\frac{\partial U}{\partial X}+\frac{\partial V}{\partial Y}+\frac{\partial W}{\partial Z}=0 \tag{1}$$

x Momentum

$$\frac{\partial (UU)}{\partial X}+\frac{\partial (VU)}{\partial Y}+\frac{\partial (WU)}{\partial Z} = -\frac{\partial P}{\partial X}+(\mathrm{Pr}/\mathrm{Ra})^{1/2}\cdot\left(\frac{\partial^2 U}{\partial X^2}+\frac{\partial^2 U}{\partial Y^2}+\frac{\partial^2 U}{\partial Z^2}\right) \tag{2}$$

Nomenclature

c_p = specific heat at constant pressure, J/kg-K
g = gravitational acceleration, m/s^2
h_c = thickness of protrusion, m
h_s = thickness of substrate, m
H_c = (h_c/l) = nondimensional thickness of protrusion
H_s = (h_s/l) = nondimensional thickness of substrate
k = thermal conductivity, W/m-K
l = protrusion dimension in y direction, m
l_z = protrusion dimension in z direction, m
L = enclosure dimension in the x and y directions, m
L_z = enclosure dimension in the z direction, m
Nu = $(q_i'' L/k_f(T_i - T_c))$ = Nusselt number
p = pressure, N/m^2
P = $(p/\rho U_0^2)$ = nondimensional pressure
Pr = (ν/α) = Prandtl number of fluid
Q = heat generation rate, W
q_i'' = heat flux crossing a solid surface, W/m^2
Ra = $(g\beta Q l^2/\nu\alpha k_f)$ = Rayleigh number
R_c = (k_c/k_f) = ratio of protrusion thermal conductivity to fluid thermal conductivity
R_s = (k_s/k_f) = ratio of substrate thermal conductivity to fluid thermal conductivity
T = temperature, K
T_c = temperature at cold surface, K
u, v, w = velocity components, m/s
U, V, W = nondimensional velocity components
x, y, z = dimensional coordinates, m
X, Y, Z = nondimensional coordinates
X_L = (L/l) = nondimensional enclosure length
Z_c = (l_z/l) = nondimensional chip width
Z_L = (L_z/l) = nondimensional enclosure width
α = fluid thermal diffusivity, m^2/s
β = coefficient of thermal expansion, 1/K
θ = $((T - T_c)/Q/k_f l)$ = nondimensional temperature
ν = kinematic viscosity, m^2/s
ρ = fluid density, kg/m^3

Subscripts

c = protrusion (chip)
f = fluid
i = condition at a solid surface
s = substrate

y Momentum

$$\frac{\partial(UV)}{\partial X}+\frac{\partial(VV)}{\partial Y}+\frac{\partial(WV)}{\partial Z} = -\frac{\partial P}{\partial Y}+(\mathrm{Pr/Ra})^{1/2}\cdot\left(\frac{\partial^2 V}{\partial X^2}+\frac{\partial^2 V}{\partial Y^2}+\frac{\partial^2 V}{\partial Z^2}\right)+\theta \quad (3)$$

z Momentum

$$\frac{\partial(UW)}{\partial X}+\frac{\partial(VW)}{\partial Y}+\frac{\partial(WW)}{\partial Z} = -\frac{\partial P}{\partial Z}+(\mathrm{Pr/Ra})^{1/2}\cdot\left(\frac{\partial^2 W}{\partial X^2}+\frac{\partial^2 W}{\partial Y^2}+\frac{\partial^2 W}{\partial Z^2}\right) \quad (4)$$

Energy (fluid)

$$\frac{\partial(U\theta)}{\partial X}+\frac{\partial(V\theta)}{\partial Y}+\frac{\partial(W\theta)}{\partial Z} = (1/\mathrm{PrRa})^{1/2}\cdot\left(\frac{\partial^2\theta}{\partial X^2}+\frac{\partial^2\theta}{\partial Y^2}+\frac{\partial^2\theta}{\partial Z^2}\right) \quad (5)$$

Energy (chip)

$$\left(\frac{\partial^2\theta}{\partial X^2}+\frac{\partial^2\theta}{\partial Y^2}+\frac{\partial^2\theta}{\partial Z^2}\right)+1/R_cH_cZ_c=0 \quad (6)$$

Energy (substrate)

$$\left(\frac{\partial^2\theta}{\partial X^2}+\frac{\partial^2\theta}{\partial Y^2}+\frac{\partial^2\theta}{\partial Z^2}\right)=0 \quad (7)$$

where $\mathrm{Ra} = g\beta Ql^2/\alpha\nu k_f$, $\mathrm{Pr} = \nu/\alpha$, $U = u/U_o$, $V = v/U_o$, $W = w/U_o$, $U_o = (g\beta Q/k_f)^{1/2}$, $\theta = (T - T_c)/(Q/lk_f)$, $P = p/(\rho U_o^2)$, $X = x/l$, $Y = y/l$, $Z = z/l$, $H_c = h_c/l$, $Z_c = l_z/l$, $R_c = k_c/k_f$, and $H_s = h_s/l$.

The boundary conditions at the enclosure walls for the baseline case are as follows:

$$X=0; \quad \frac{\partial\theta}{\partial X}=0,\ U=0,\ V=0,\ W=0$$

$$X=X_L; \quad \theta=0,\ U=0,\ V=0,\ W=0$$

$$Y=0,\ X_L; \quad \frac{\partial\theta}{\partial Y}=0,\ U=0,\ V=0,\ W=0$$

$$Z=0,\ Z_L; \quad \frac{\partial\theta}{\partial Z}=0,\ U=0,\ V=0,\ W=0$$

where $X_L = L/l$ and $Z_L = L_z/l$.

For case (I) the thermal boundary condition at $X = X_L$ is $\partial\theta/\partial X = 0$ and at $Y = X_L$, $\theta = 0$ for $X > H_s$ with all other conditions unchanged. For case (II) at $X = X_L$, $\theta = 0$ and at $Y = X_L$, $\theta = 0$ for $X > H_s$ with the rest of the conditions unchanged. Also, the matching of temperatures and heat fluxes at the interfaces of dissimilar materials was implicitly carried out by the use of the harmonic mean procedure for numerically evaluating diffusion coefficients (Patankar, 1980).

2.2 Numerical Scheme. The governing equations are discretized using a control-volume approach as described by Patankar (1980). This approach uses control volumes for velocities that are staggered with respect to those for temperature and pressure; a power law scheme for the differencing of dependent variables; harmonic mean formulation for the interface diffusivities; and the SIMPLER algorithm for the velocity–pressure coupling. The solution is obtained from an initial guess through an iterative scheme using a line-by-line tridiagonal matrix algorithm. The conjugate conduction in the chip and substrate is handled numerically by solving the same full set of momentum and energy equations throughout the entire enclosure, but with a large value of viscosity specified for the solid regions. The results reported in the following were obtained with a 24 × 22 × 22 nonuniform grid, with a higher density of grid points near the hot and cold surfaces to capture the thermal boundary layers. Results for finer grids (31 × 26 × 16 and 31 × 30 × 20) obtained for the baseline case showed good agreement (Wroblewski and Joshi, 1993).

The numerical solution is assumed converged when the maximum temperature change during successive iterations is less than 0.00001 times the maximum temperature for that iteration, and when overall energy balances on the enclosure, the chip, and the fluid are obtained within 1 percent. The use of the maximum changes of the variables as convergence criteria has to be used with caution. As pointed out by Patankar (1980), monitoring the changes in dependent variables from iteration to iteration may not be sufficient if underrelaxation is being employed. In the present study, strong underrelaxation is required for the velocities, particularly on the V component because of the strong source term from the buoyancy. On the other hand, temperature required only minor underrelaxation. As a result, the velocity changes from iteration to iteration are somewhat artificial, while the temperature changes are a better reflection of the problem convergence. Maximum changes in the velocities from iteration to iteration were also monitored, along with the overall mass balances, and these were found to satisfy the convergence criteria well before the temperatures were converged.

With the conjugate conduction, the solution took much longer for convergence than for a comparable three-dimensional enclosure problem with simple temperature boundary conditions. Typically, 3000 to 20,000 iterations were needed for convergence, requiring from 200 to 1000 CPU minutes on an Amdahl 5990/500 mainframe. Use of previously converged solutions at different conditions reduced the run times somewhat.

The solution was obtained throughout the entire enclosure; no symmetry condition was imposed at $Z = X_L/2$. This prevented the forcing of a symmetric solution where one may not exist, as may be the case if the plume above the chip became unsteady. A separate transient version of the program was employed to check whether any unsteady behavior occurred, which might invalidate the steady-state assumptions. As it turned out, the solutions were indeed steady and symmetric for all conditions examined.

The numerical code was validated using a simple three-dimensional cubical enclosure without the substrate and protruding element, and with $\theta = 0$ at $X = 0$ and $\theta = 1$ at $X = 1$. The Rayleigh number was assumed to be 10^6 and the Prandtl number was 0.7, corresponding to one of the cases investigated by Lankhorst and Hoogendoorn (1988). Using a similar (but not identical) 30 × 30 × 15 nonuniform grid, and using the same symmetry assumption, the resulting Nusselt numbers at the hot wall were within 1.5 percent of Lankhorst and Hoogendoorn (1988). In addition, flow patterns and isotherms identical to those in the study by Lankhorst and Hoogendoorn (1988) were observed in both the X–Y and Z–X planes.

3 Results and Discussion

For this investigation, the Prandtl number was chosen as 25, with $R_c = 2360$ and $R_s = 575$. These values correspond to the use of fluorinert liquid FC-75 as the coolant with a silicon chip mounted on an alumina substrate. The Rayleigh number was kept fixed at 10^8, which corresponds to a one centimeter square chip operated with a power level of 0.15 W in FC-75. The nondimensional substrate and chip thicknesses were chosen as $H_s = 0.08$ and $H_c = 0.21$, respectively. For the baseline computations a cubic enclosure was investigated with $X_L = Z_L = 5.1$. These substrate, chip, and enclosure dimensions correspond to the experimental study of Joshi and Paje (1991). Comparison of the computations with these ex-

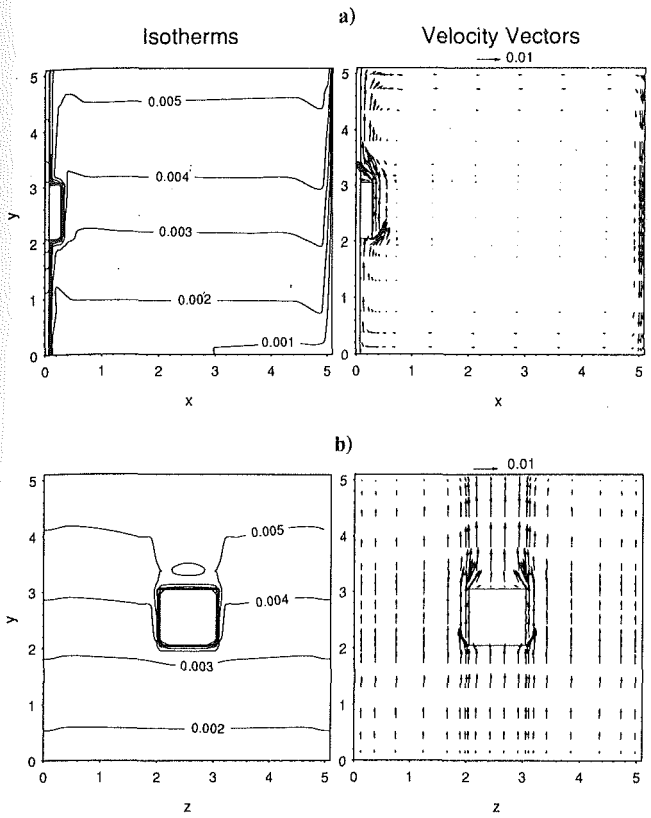

Fig. 2 Isotherms and velocity vectors for the baseline case: (*a*) in the *X-Y* plane at $Z = 2.55$, (*b*) in the *Z-Y* plane at $X = 0.185$

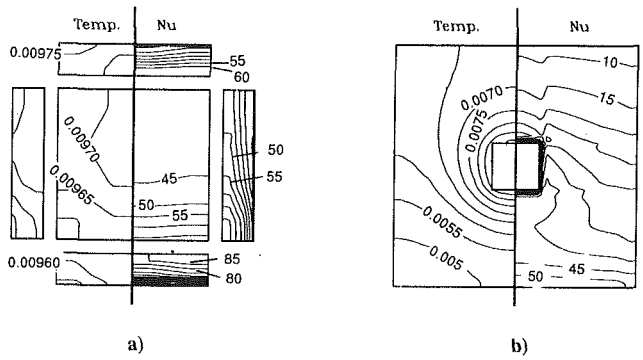

Fig. 3 Surface isotherms and Nusselt numbers contours for the baseline case: (*a*) chip surfaces and (*b*) substrate

periments is reported by Wroblewski and Joshi (1993). The parameters varied in the present study included H_c (0.05–0.4), Z_c (1.0–4.5), Z_L (2.55–7.65), and R_s (0.5–575).

The numerical computations for the baseline conditions are discussed first. The effects of increasing the chip and enclosure dimensions are then investigated. The role of the enclosure boundary conditions is next examined. Finally, a numerical correlation is proposed for the maximum chip temperature. The results are illustrated as isotherms and velocity vectors in selected planes. Also presented are the chip and substrate surface temperatures and heat transfer coefficients.

3.1 Baseline Computations. The isotherms within the various regions and the fluid velocity vectors are seen in Fig. 2 in two planes. Figure 2(*a*) displays the transport in the *X-Y* plane passing through the chip center, $Z = 2.55$. The large values of R_c and R_s ensure low resistance conduction paths within the chip and the substrate. The entire chip is almost isothermal. As expected, there is some temperature drop along the substrate.

The flow velocities along the substrate are seen to increase in the vertical direction starting from the bottom of the enclosure. The flow deflects around the two chip edges. A strong plumelike flow is shed above the chip. This upflow turns around the upper horizontal enclosure boundary and returns along the vertical heat sink wall. The flow velocities in the bulk of the enclosure are much smaller than near the boundaries, representing entrainment between the boundary layers. The isotherms show that indeed this region is thermally stratified. Due to the high substrate thermal conductivity, some of the general flow features resemble those for the well-studied opposite fully heated and cooled enclosure boundaries. However, the strong plume above the chip and the effect of the chip on the flow are unique to this configuration.

Flow vectors and isotherms in the *Y-Z* plane through $X = 0.185$, the midthickness of the chip, are seen in Fig. 2(*b*). The flow patterns clearly show the strong buoyant flow above the chip. The upflow extends in the spanwise direction almost throughout along the substrate, due to the buoyancy produced by the substrate, which is heated by conduction. The isotherms show thin thermal boundary layers in the liquid along the chip surfaces and a symmetry about the midspan. The bulk of the enclosure is thermally stratified.

The symmetry about the midspan of the chip was observed for all the cases examined in this study. Figure 3(*a*) takes advantage of this feature in displaying the isotherms and the Nusselt number contours in the form of a composite diagram. The surface temperatures were calculated by the harmonic mean interpolation of the nodal temperatures on the two sides of the interface. The Nusselt numbers were evaluated using the definition outlined in the nomenclature. It is noted that the surface temperatures and the Nusselt numbers are undefined along the edges.

There is only about a 2 percent variation in temperature along the chip surfaces due to its high thermal conductivity. The coolest temperature is on the bottom face and the warmest on the top due to the growing thermal layer along the chip. The Nusselt numbers are the highest on the bottom chip face due to the impingement type flow seen in Fig. 2(*b*). On the front face, the Nusselt number decreases downstream due to the thickening thermal layer. The lowest Nu values exist on the top and side faces near the substrate. The low fluid velocities in these regions contribute to this reduction.

The isotherms on the substrate surface exposed to the fluid and the corresponding Nu distributions are seen in Fig. 3(*b*). The buoyant plume above the chip results in an elongation of the isotherms in the vertical direction. This behavior is qualitatively in accordance with the observations of Joshi and Paje (1991) who used liquid crystals to visualize the surface temperature patterns on the substrate. The maximum temperature drop along the substrate is only about 50 percent of the chip level, confirming the strong role of substrate conduction, which accounts for 80 percent of the heat removal from the chip. The Nu values above the vertical chip edges show a drop, characterized as bends along the contours. These appear to be due to the warm buoyant flow shed above the vertical edges.

3.2 Responses Due to Changing Chip Size. Figure 4 shows the variation in maximum chip temperature, θ_{max}, with the chip aspect ratio for several different values of R_s. For fixed R_s, θ_{max} drops as Z_c is increased. In the present analysis, Ra is held constant, which implies that Q, the total heat input to the chip, is also constant (for the same fluid and length scale). With Q constant, increasing Z_c leads to a greater chip surface area over which the heat can be transferred to the fluid, leading to lower chip temperatures.

Figure 4 also shows that as the substrate thermal conductivity

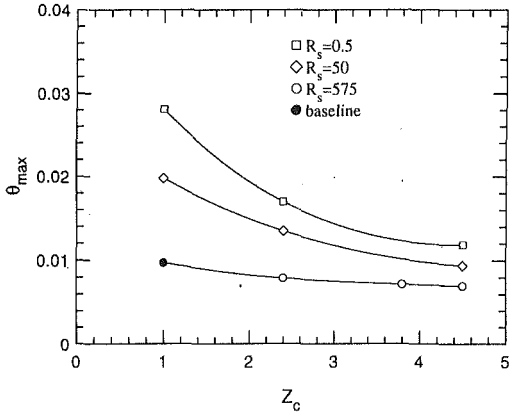

Fig. 4 Effect of chip aspect ratio on maximum chip temperature

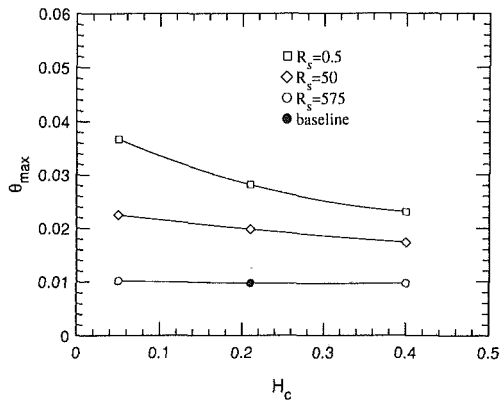

Fig. 5 Effect of chip thickness on maximum chip temperature

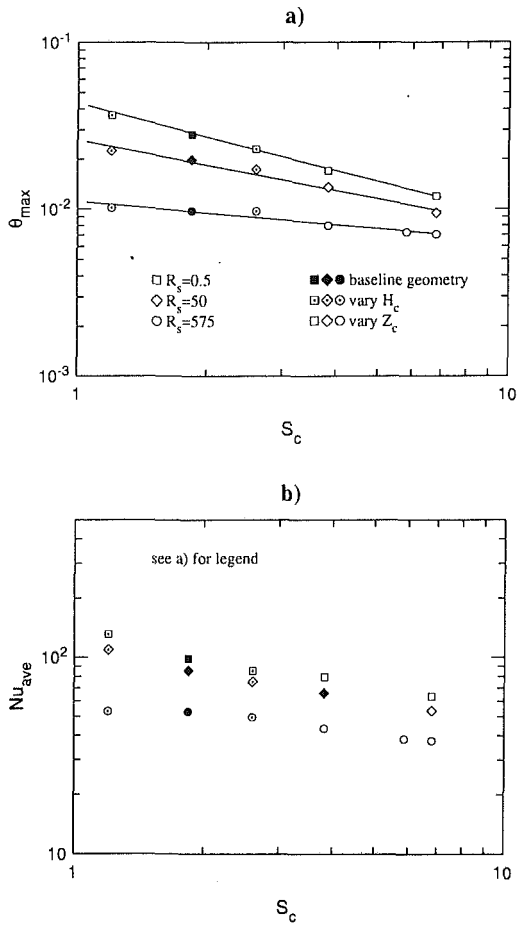

Fig. 6 Effect of exposed chip surface area: (*a*) effect on maximum chip temperature, (*b*) effect on chip-surface-average Nusselt number

is reduced, the effect of varying the chip aspect ratio on θ_{max} becomes more pronounced. For lower R_s, less heat is conducted through the substrate, and hence a greater proportion of the heat loss to the fluid occurs directly from the chip surfaces. For example, for $R_s = 0.5$, and $Z_c = 1$, 99 percent of the total heat generated within the chip is transferred directly to the fluid through the exposed chip surfaces compared to only 21 percent for $R_s = 575$. Therefore variations in the chip aspect ratio, and thus the exposed chip surface area, have a greater effect on the chip temperature when the substrate thermal conductivity is small.

The effect of variations in chip thickness relative to its width (H_c) on θ_{max} are displayed in Fig. 5 for several values of R_s. The results show that increases in H_c lead to reductions in θ_{max}, with greater variations occurring at lower values of R_s. This effect is similar to that observed for Z_c, discussed above; a larger chip thickness leads to increased surface area available for cooling the chip, which is more significant for poorly conductive substrates.

Based on the above results, the chip geometry affects the cooling of the chip mainly through surface area effects. Figure 6(*a*) shows the data of Figs. 4 and 5 recast with the nondimensional, total fluid exposed chip surface area, $S_c = Z_c + 2H_c(Z_c + 1)$, as the abscissa. The relatively good correlation between θ_{max} and the chip surface area confirms the fact that the surface area effects on θ_{max} are more significant than those due to the changes in flow patterns. This does not imply that the heat transfer coefficients on the chip faces are insensitive to chip geometry changes. In fact the Nu values along the chip surfaces decrease with an increase in surface area. This is a result of lower chip temperatures and the reduction in the flow vigor. This can be seen in Fig. 6(*b*), which shows the average Nu for the exposed chip surfaces, defined as

$$\mathrm{Nu}_{avg} = \sum_i \frac{q_i}{k_f A_i (T_{i,avg} - T_c)} L$$

where q_i is the total heat loss from one of the chip surfaces (top, bottom, front, or sides) and $T_{i,avg}$ the average temperature of that surface. As in Fig. 6(*a*), Nu_{avg} data for variations in H_c and Z_c follow nearly the same trend in Fig. 6(*b*), indicating that the average heat transfer coefficient changes in response to chip geometry changes mainly due to this surface area effect. Although it may be obvious that increasing surface area will result in lower chip temperatures, it is significant that the temperature correlates so well based solely on the total exposed surface area, rather than the individual length scales.

3.3 Responses Due to Changes in Enclosure Aspect Ratio. Figure 7 shows the effect of enclosure width, Z_L, on θ_{max} for several values of R_s. As Z_L is decreased, θ_{max} rises. This trend is due mainly to two surface area effects. First, changing the enclosure width changes the surface area of the substrate in contact with the fluid. This influences the chip cooling when substrate conduction is important, i.e., when R_s is large. Second, changing the enclosure width also changes the surface area of the heat sink wall. This effect is likely to be smaller than the substrate surface area influence for large R_s, but is significant at lower values of R_s for which substrate conduction is negligible.

3.4 Two-Dimensional Versus Three-Dimensional Computations. Because of the large CPU time required for the three-dimensional computations, the possibility of using a two-dimensional approximation in the X–Y plane to predict the maximum chip temperatures was investigated. Figure 8(*a*) shows the ratio of the maximum chip temperatures obtained from

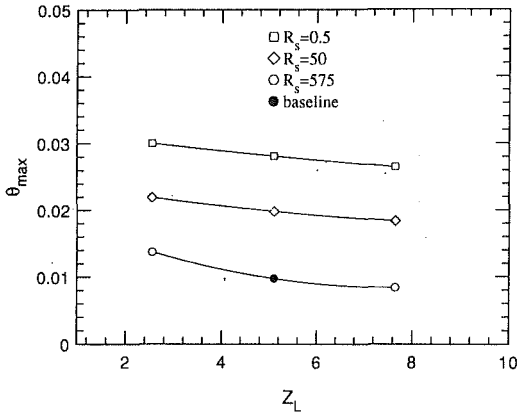

Fig. 7 Effect of enclosure width on maximum chip temperature

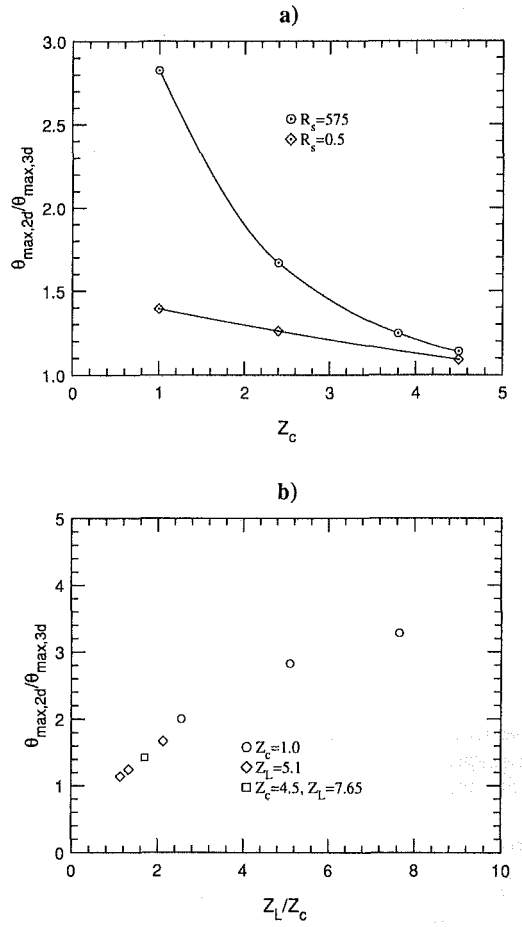

Fig. 8 Effect of chip aspect ratio on the ratio of maximum chip temperature obtained from two-dimensional computations to that obtained from three-dimensional analysis

such two-dimensional computations to those obtained from three-dimensional computations, for $R_s = 575$ and $R_s = 0.5$. When this ratio approaches unity, the two-dimensional approximation provides a good prediction. The two-dimensional values are calculated with a different value of Q, and hence Ra, for each value of Z_c in order to match the volumetric heat generation rate for the three-dimensional results.

For the baseline geometry, $Z_c = 1$, the chip temperature is over 2.8 times higher for the two-dimensional case for $R_s = 575$ and about 38 percent higher for $R_s = 0.5$. This is due to two effects—the neglect of the heat loss from the chip sides

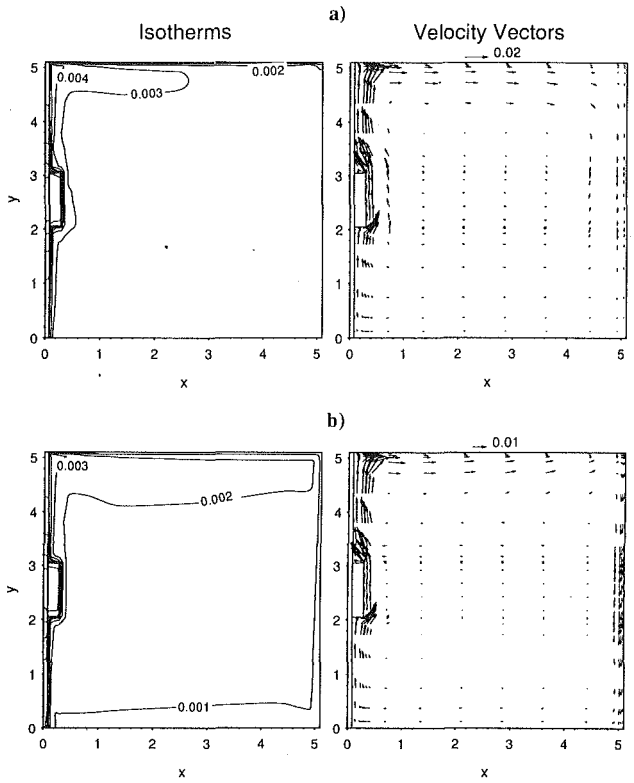

Fig. 9 Effect of enclosure boundary conditions on isotherms and velocity vectors in the X-Y plane at $Z = 2.55$: (*a*) top wall cooled, (*b*) top and opposite wall cooled

and the greatly reduced substrate surface area for the two-dimensional analysis. The former is important when R_s is small, when the side heat loss accounts for nearly 15 percent of the total, while the latter is significant when R_s is larger and substrate conduction is dominant.

For wider chips, the side heat loss effect is less critical, since it represents a smaller percentage of the total. For $R_s = 0.5$, the two-dimensional analysis predicts the maximum chip temperature to within 10 percent when $Z_c = 4.5$. The substrate surface area effect is also less important for wider chips, since the width of the chip approaches that of the enclosure, and thus the substrate area for the two and three-dimensional analyses are nearly equal. For $R_s = 575$ and $Z_c = 4.5$, the difference in θ_{max} is less than 15 percent. When R_s is large, the important parameter to consider is not the width of the chip, but the ratio of the chip width to enclosure width, since this ratio determines the relative size of the chip compared to the substrate. This is confirmed in Fig. 8(*b*), which presents the ratio of chip temperatures from the two and three-dimensional analyses as a function of the ratio of enclosure width to chip width, for both variations in Z_c at a fixed enclosure width and variations in Z_L at a fixed chip width for $R_s = 575$.

Based on the results in Fig. 8, the use of a two-dimensional analysis could be justified for chips with aspect ratios greater than about 4, for small values of R_s. For large value of R_s, the two-dimensional analysis should be valid when the enclosure width is less than 1.1 times the chip width.

3.5 Responses Due to Change in Enclosure Boundary Conditions. Isotherms and velocity vectors for the boundary conditions (I) and (II) are seen in Fig. 9. When the heat sink is the top enclosure wall instead of the side, case (I), the resulting isotherms in Fig. 9(*a*) are markedly different than for the baseline conditions, Fig. 2(*a*). The temperature gradients are confined near the left and the top enclosure boundaries and the remaining fluid is almost isothermal. The flow patterns

are generally the same as for the baseline conditions, with the exception of a weaker downflow along the right boundary and a stronger horizontal flow along the cold upper wall. The maximum chip temperature was about 5 percent less than the baseline value.

When both the upper and side boundaries are used as heat sinks, Fig. 9(*b*), the temperatures everywhere are reduced compared to both the baseline conditions, as well as case (I). This is expected due to the larger heat sink area available. The maximum chip temperature was 16 percent lower compared to the baseline conditions. A larger temperature gradient exists near the upper boundary, compared to the side. This indicates that a larger portion of the generated power within the chip is removed at the top boundary. Energy balance computations revealed that about 2/3 of the net power is removed at the upper boundary.

3.6 Correlation of Maximum Temperature Data. In cooling of electronic systems, the maximum chip temperature is a critical parameter, because of its effect on component reliability. To aid in the use of the data presented here and in a previous study (Wroblewski and Joshi, 1993), which included effects of Ra and R_s, a correlation between the maximum chip temperature and the important nondimensional parameters was developed.

As discussed in Sections 3.2 and 3.3, changing the geometric parameters affected the maximum chip temperature mainly through the surface area available for cooling. Increasing the chip or substrate surface area led to reduced chip temperatures and vice versa. This suggests correlating the data using nondimensional surface areas rather than the individual length parameters.

The final correlation for the maximum chip temperature is as follows:

$$\theta_{\max} = 102.5 \exp[0.0291 R_s^{0.45}(Z_L^{0.45} - 5.1^{0.45})] \quad \text{(I)}$$

$$\cdot[(0.0455 R_c^{-1.038}\mathrm{Ra}^{-0.003})^{3/4} + (0.518\mathrm{Ra}^{-0.25} + 0.0044)^{3/4}]^{4/3} \quad \text{(II)}$$

$$\cdot[(0.0062 + 0.242 S_c^{-0.546} R_s^{-0.589})^{-2.2} + (0.0433 S_c^{-0.674})^{-2.2}]^{-1/2.2} \quad \text{(III)} \qquad (8)$$

The first term in Eq. (8), (I), accounts for variations in the enclosure width (and hence the total substrate surface area). Note the dependence on R_s as observed in Fig. 7. The second term (II) is similar to one obtained by Sathe and Joshi (1991) for a two-dimensional study, the form of which accounts for the asymptotic behavior for large and small values of R_c (Churchill and Usagi, 1972). However, one key difference between this correlation and that of Sathe and Joshi is the slight Ra dependence for the solution at small R_c, which most likely arises here because of the larger range of Ra considered (10^3 to 10^9). The last term (III) accounts for variations in the chip surface area and substrate thermal conductivity, R_s. It has a form similar to the second term, exhibiting asymptotic behavior for small and large values of R_s.

Equation (8) predicts all of the numerical results (a total of 50 runs) to within ±9 percent, and 79 percent of the data to within ±5 percent. The correlation is applicable to the following ranges of parameters: $10^3 < \mathrm{Ra} < 10^9$, $0.5 < R_s < 575$, $0.1 < R_c < 2360$, $1 < Z_c < 4.5$, $2.55 < Z_L < 7.65$, $0.05 < H_c < 0.4$, $10 < \mathrm{Pr} < 1000$, and $X_L = Y_L = 5.1$. When applying Eq. (8), care must be taken to assure that $Z_L > Z_c$. This wide range of parameters covers a variation of almost two orders of magnitude in $\theta_{\max}$.

4 Conclusions

The present computations reveal the importance of substrate conduction during natural convection liquid cooling using low thermal conductivity dielectric liquids. For moderately conducting substrates such as ceramics, substrate conduction was found to account for 80 percent of the chip power generation for the baseline conditions at $\mathrm{Ra} = 10^8$. Some of the resulting flow features were similar to the fully heated and cooled opposite walls enclosure, such as the single large clockwise primary cell. However, the flow near the chip and above it was considerably modified. These flow patterns and the conductive spreading had a significant effect on the chip and substrate temperatures and the resulting Nu.

As expected, changing the chip or enclosure dimensions changed the flow and temperature patterns compared to the baseline conditions. However, the effects of these changes on the maximum chip temperature, $\theta_{\max}$, were well correlated using the available heat transfer area of the chip and substrate. The area effect was strongly dependent on the substrate thermal conductivity ratio, R_s. A greater influence on $\theta_{\max}$ of the chip area variations was observed for smaller R_s due to decreased importance of substrate conduction.

By varying the chip and enclosure sizes, conditions have also been identified when a two-dimensional approximation provides a reasonable prediction for $\theta_{\max}$ for the configuration considered. Again, a strong dependence on R_s exists. For R_s below 1, this is valid for $Z_c > 4$ and for large R_s the required condition is $Z_L < 1.1\ Z_c$.

The maximum chip temperatures decreased by 5 and 16 percent, respectively, for enclosure boundary conditions (I) and (II). There were minor changes in the observed flow patterns for both conditions compared to the baseline. Since the primary interest in packaging applications is in the maximum chip temperature, the present computations show that either the top or the vertical enclosure surface can be the heat sink. A relatively modest improvement is obtained by increasing the heat sink area to include both the top and side faces.

For the baseline boundary conditions, a numerical correlation for the maximum chip temperature is proposed. This correlation displays the expected asymptotic behavior. It is applicable over large ranges of variation in Ra, R_c, R_s, and the chip and enclosure size parameters.

Acknowledgments

The authors are grateful for the support of this study through a grant from the Naval Surface Warfare Center, Crane, Indiana, under the SHARP effort. The efforts of Dr. S. B. Sathe in developing the original version of the code are acknowledged. D. E. W. acknowledges support in the form of course release from Boston University during the preparation of the manuscript. This work was performed at the Naval Postgraduate School.

References

Bar-Cohen, A., 1991, "Thermal Management of Electronic Components With Dielectric Liquids," *Proc. ASME/JSME Thermal Engineering Joint Conference*, Vol. 2, pp. xv-xxxix.

Bergles, A. E., and Bar-Cohen, A., 1990, "Direct Liquid Cooling of Microelectronic Components," *Advances in Thermal Modeling of Electronic Components and Systems*, Vol. 2, A. Bar-Cohen and A. D. Kraus, eds., ASME Press, pp. 233-342.

Churchill, S. W., and Usagi, R., 1972, "A General Expression for the Correlation of Rates of Transfer and Other Phenomena," *AIChE J.*, Vol. 18, pp. 1121-1128.

Flourinert Liquids, 1985, Product Manual, 3M Corporation, Minneapolis, MN.

Joshi, Y., and Paje, R. A., 1991, "Natural Convection Cooling of a Ceramic Substrate Mounted Leadless Chip Carrier in Dielectric Liquids," *Int. Comm. Heat Mass Transfer*, Vol. 18, pp. 39-47.

Joshi, Y., Willson, T., and Hazard, S. J., III, 1989a, "An Experimental Study of Natural Convection From an Array of Heated Protrusions on a Vertical Surface in Water," ASME *Journal of Electronic Packaging*, Vol. 111, pp. 121-128.

Joshi, Y., Willson, T., and Hazard, S. J., III, 1989b, "An Experimental Study of Natural Convection Cooling of an Array of Heated Protrusions in a Vertical Channel in Water," ASME *Journal of Electronic Packaging*, Vol. 111, pp. 33-40.

Joshi, Y., Kelleher, M. D., and Benedict, T. J., 1990, "Natural Convection Immersion Cooling of an Array of Simulated Electronic Components in an Enclosure Filled With Dielectric Fluid," *Heat Transfer in Electronic and Microelectronic Equipment*, A. E. Bergles, ed., Hemisphere, Washington, DC, pp. 445-468.

Kelleher, M. D., Knock, R. H., and Yang, K. T., 1987, "Laminar Natural Convection in a Rectangular Enclosure Due to a Heated Protrusion on One Vertical Wall. Part I: Experimental Investigation," *Proc. 2nd ASME-JSME Joint Thermal Engineering Conf.*, Vol. II, Honolulu, HI, pp. 169-178.

Keyhani, M., Prasad, V., and Cox, R., 1988, "An Experimental Study of Natural Convection in a Vertical Cavity With Discrete Heat Sources," ASME JOURNAL OF HEAT TRANSFER, Vol. *110*, pp. 616-624.

Keyhani, M., Chen, L., and Pitts, D. R., 1990, "The Aspect Ratio Effect on Natural Convection in an Enclosure With Protruding Heat Sources," presented at the AIAA/ASME Thermophysics and Heat Transfer Conference, Seattle, WA.

Lankhorst, A. M., and Hoogendoorn, C. J., 1988, "Three-Dimensional Calculations of High Rayleigh Natural Convection Flows in Enclosed Cavities," *Proc. National Heat Transfer Conference*, Vol. 3, Houston, TX, pp. 463-470.

Lee, J. J., Liu, K. V., Yang, K. T., and Kelleher, M. D., 1987, "Laminar Natural Convection in a Rectangular Enclosure Due to a Heated Protrusion on One Vertical Wall—Part II: Numerical Simulations," *Proc. 2nd ASME-JSME Joint Thermal Engineering Conf.*, Vol. III, Honolulu, HI, pp. 179-185.

Liu, K. V., Yang, K. T., and Kelleher, M. D., 1987a, "Three-Dimensional Natural Convection Cooling of an Array of Heated Protrusions in an Enclosure Filled With a Dielectric Fluid," *Proc. Int. Symp. on Cooling Technology for Electronic Equipment*, Honolulu, HI, pp. 486-497.

Liu, K. V., Yang, K. T., Wu, Y. W., and Kelleher, M. D., 1987b, "Local Oscillatory Surface Temperature Responses in Immersion Cooling of a Chip Array by Natural Convection in an Enclosure," *Proc. Symp. on Heat and Mass Transfer in Honor of B. T. Chao*, University of Illinois, Urbana-Champaign, IL.

Park, K. A., and Bergles, A. E., 1987, "Natural Convection Heat Transfer Characteristics of Simulated Microelectronic Chips," ASME JOURNAL OF HEAT TRANSFER, Vol. *109*, pp. 90-96.

Patankar, S. V., 1980, *Numerical Heat Transfer and Fluid Flow*, Hemisphere/McGraw-Hill, New York.

Prasad, V., Keyhani, M., and Shen, R., 1990, "Free Convection in a Discretely Heated Vertical Enclosure: Effects of Prandtl Number and Cavity Size," ASME *Journal of Electronic Packaging*, Vol. 112, pp. 63-74.

Sathe, S., and Joshi, Y., 1991, "Natural Convection Arising From a Heat Generating Substrate-Mounted Protrusion in a Liquid-Filled Two-Dimensional Enclosure," *Int. J. Heat Mass Transfer*, Vol. 34, pp. 2149-2163.

Wroblewski, D. E., and Joshi, Y., 1993, "Computations of Liquid Immersion Cooling for a Protruding Heat Source in a Cubical Enclosure," *Int. J. Heat Mass Transfer*, Vol. 36, pp. 1201-1218.

Experiments on Convective Instability of Large Prandtl Number Fluids in a Vertical Slot

S. Wakitani
Department of Mechanical Engineering,
College of Industrial Technology,
Nishikoya 1-27-1, Amagasaki 661, Japan

The stability of thermal convection of large Prandtl number fluids in a vertical slot (aspect ratio = 10, 15, or 20) was studied experimentally. Secondary cells began to appear from the center of the slot and then prevailed. The critical Rayleigh number showed an increasing trend as the aspect ratio was increased, and became higher than that obtained from a linear stability analysis owing to a possible traveling wave mode of instability. As the Rayleigh number was increased, either the onset of the tertiary cells or the traveling waves occurred depending on the Prandtl number. In the transition process from laminar to turbulent flow, the secondary cells around the end regions split into smaller cells and an unsteady flow structure appeared with an original secondary cell in the center region and some smaller cells along the sidewalls.

Introduction

Two-dimensional natural convection in a vertical slot, or a tall cavity, with a fixed temperature difference between the sidewalls was first studied analytically by Batchelor (1954). Since that time a number of analytical, experimental, and numerical investigations on this type of convection have been continued because of the importance in engineering and geophysical applications. For these references the reader should refer to papers by Lee and Korpela (1983) and Le Quéré (1990), and to a book by Gebhart et al. (1988).

In a two-dimensional vertical slot, fluid rises along the hot wall, turns in the top end, sinks along the cold wall, and turns again in the bottom end to set up a unicellular convection. The independent parameters that describe the flow are the Rayleigh number Ra, the Prandtl number Pr, and the aspect ratio A (height/width). It is well known that the flow is classified into three types of regime: the conduction, the transition, and the boundary-layer regime according to a different range of Ra (Eckert and Carlson, 1961). In the conduction regime (small Rayleigh numbers), there is little variation of the fluid temperature with height and heat is transferred primarily by conduction from the hot to the cold wall. In the transition regime (intermediate Rayleigh numbers), a stable vertical temperature gradient develops in the core region of the flow. In the boundary-layer regime (high Rayleigh numbers), the flow is confined to boundary layers at the sidewalls and heat is transferred primarily by convection.

Elder (1965) conducted detailed experiments in a cavity of $A \approx 10$–20 using fluids with $\mathrm{Pr} \approx 1000$. When Ra exceeded a first critical value Ra_c ($= 3 \times 10^5 \pm 30$ percent), a unicellular convection broke down into a multicellular convection arranged in a series of secondary cells. At about 3 Ra_c, he observed tertiary cells that were counterrotating between the secondary cells. Vest and Arpaci (1969) obtained $\mathrm{Ra}_c = 3.7 \times 10^5 \pm 10$ percent from their experiments for $\mathrm{Pr} = 900$ and $A = 20$. The appearance of the tertiary cells in large Pr fluids has been confirmed numerically by de Vahl Davis and Mallinson (1975) and experimentally by Seki et al. (1978). For $\mathrm{Pr} = 1000$ and $A = 10$, de Vahl Davis and Mallinson (1975) obtained $\mathrm{Ra}_c = 5 \times 10^5$ as the onset of secondary flow, and they found the pattern of tertiary flow at 1.88 Ra_c.

Bergholz (1978) performed a linear stability analysis of convection in an infinitely tall cavity (infinite A) with a basic flow in which, for nonzero vertical temperature stratification, the wall temperatures increase linearly with height. Bergholz showed that, in fluids with $\mathrm{Pr} \geq 50$, as the stratification parameter γ exceeds a certain value, a transition occurs from the traveling wave to the stationary cell mode of initial instability. In a moderately tall cavity with a finite A, as Ra is increased, the flow enters the transition or boundary-layer regime with a temperature stratification before the instability from the conduction regime occurs (Elder, 1965). However, it is questionable whether the stability characteristics obtained by Bergholz are applicable to a cavity with a finite A and isothermal walls.

Lee and Korpela (1983) performed numerical calculations of multicellular convection in a vertical slot. They tried to compare their results with the stability characteristics obtained by Bergholz (1978). For $\mathrm{Pr} = 20$ and $A = 15$, they did not find any traveling wave in such a condition that, according to Bergholz's result, the flow is unstable for the traveling wave mode but stable for the stationary cell mode. For the disagreement, they stated two reasons that the basic flow used in the stability analysis is different from the actual flow for the isothermal wall and the small amplification rate does not allow sufficient growth for the disturbances to be observed. For $\mathrm{Pr} = 1000$ and $A = 15$, they showed that the number of secondary cells changed from three to seven and then to five as Ra was increased. For $\mathrm{Pr} = 20$ and 1000, they confirmed the appearance of secondary cells predicted by Bergholz (1978) and observed by Elder (1965), but they did not determine Ra_c explicitly.

Chen and Thangam (1985) conducted experiments on the stability of convection in fluids with highly temperature-dependent viscosity in a vertical slot of $A = 15$. As working fluids, they used glycerin–water solutions of 70, 80, and 90 percent glycerin, which correspond to the mean values of $\mathrm{Pr} = 160$, 405 and 720, respectively. They showed that Ra_c decreased slightly from 4.10×10^5 to 3.32×10^5 as the glycerin concentration was increased. For the mean Pr of 160, they observed the onset of tertiary cells at 2.5 Ra_c and traveling waves at 5.4 Ra_c. They concluded that at about 7 Ra_c boundary layers along the sidewalls became unstable and the cellular pattern was disrupted. Only for $\mathrm{Pr} = 160$ and $A = 15$, they conducted experiments on the various instabilities at the supercritical conditions. Therefore, an important problem has been left unsolved: whether

Contributed by the Heat Transfer Division for publication in the JOURNAL OF HEAT TRANSFER. Manuscript received by the Heat Transfer Division February 1993; revision received June 1993. Keywords: Flow Instability, Flow Visualization, Natural Convection. Associate Technical Editor: J. R. Lloyd.

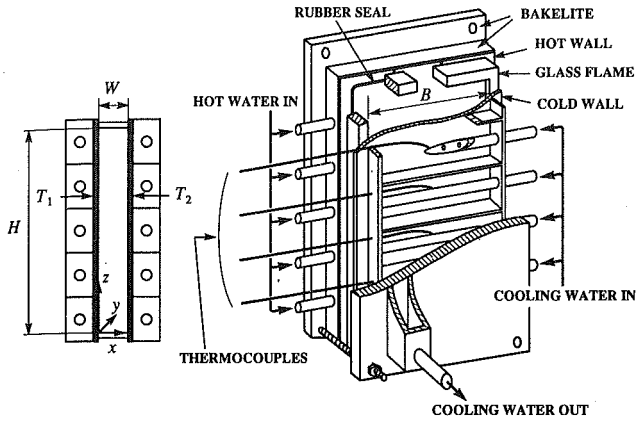

Fig. 1 Experimental apparatus and coordinate system

the disruption of the pattern as well as the onset of tertiary cells or traveling waves depends on Pr and A.

In this paper, we examine how the onsets of such instabilities as secondary cells, tertiary cells, and traveling waves depend on Pr and A, and clarify the transition process from laminar to turbulent flow for convection of large Pr fluids in a vertical slot. Experimental results are compared with predictions based on stability analyses, and with previous numerical and experimental results.

Experimental Apparatus and Procedure

The experimental apparatus and the coordinate system are shown in Fig. 1. Experiments were carried out in a vertical slot of dimensions 300 mm high (H) × 150 mm deep (B) × 15, 20, or 30 mm wide (W). Thus three aspect ratios ($A = 20$, 15, and 10) are available. Three kinds of silicone oils (Toshiba Silicone TSF451 series) with Pr ≈ 50, 125, and 900 at temperature of about 300 K were used as the working fluids. They show about a 2 percent decrease in viscosity as temperature increases by 1 K in the range 273 K ≤ T ≤ 323 K. We evaluated physical properties of the fluids at the mean value between the sidewall temperatures. The slot consists of two vertical sidewalls (340 mm × 190 mm) made of two 5-mm-thick copper plates and an 8-mm-thick Pyrex glass frame of variable width. The copper plates separate the slot from two water jackets, each with five separate water passages. The flow rate of each passage was controlled so that the sidewalls could be maintained at temperatures constant within 0.005 ΔT for $\Delta T \geq 10$ K and 0.05 K for $\Delta T < 10$ K. We could operate the apparatus at temperature differences up to 50 K. The water jackets were insulated with styrofoam boards. The water temperatures in the jackets could be controlled by means of two constant-temperature baths (Neslab RTE-9 and EX-210).

To measure sidewall temperatures, nine sheathed copper-constantan thermocouples 1 mm in diameter were embedded in each copper plate through the water jacket. Seven of these thermocouples were located at intervals of 40 mm on $y = B/2$ and others at midheight. Measurements of the fluid temperature were performed through a probe, on which several chromel-alumel thermocouples 50 μm in diameter are placed at intervals of 3 mm horizontally or 55 mm vertically. The probe was fed through the slit at the top of the frame and traversed the x, y, and z axes by using stepping-motor-drive mechanisms with a movement of 12.5 μm per pulse. The measurements were performed only in the x–z plane through $y = B/2$ except in cases measured for a special purpose. The thermocouple wires were connected to a digital data acquisition system (Scanner: Advantest R7210 and DVM: Advantest TR6851) controlled through a personal computer. With this system, voltage fluctuations could be measured to 0.1 μV.

Two methods were used to visualize the flow pattern. One is a tracer injection method for observation of the cellular pattern and other a shadowgraph method for detection of the onset of traveling waves. In the injection method, aluminum oxide powder mixed with the same as working fluid was carefully dropped into the fluid from the top of the slot. The aluminum oxide particles were illuminated by laser light from a 15 mW He–Ne laser through the top. The laser beam was expanded into a sheet in the x–z plane through $y = B/2$ using a cylindrical lens to obtain still photographs of cellular patterns. The photographs were taken with an exposure time of 15 s. In the shadowgraph method, on the other hand, a projection lamp was used as the light source to illuminate the whole flow. This method enabled us to detect the onset of the traveling wave mode of instability.

Uncertainty Assessment

Measurement using a pair of calipers showed that the width W of a slot was flat within ±0.1 mm over the whole height. A maximum uncertainty associated with the length scale in the data reduction was ±0.2 mm. The digital data acquisition system could detect temperature fluctuations of 0.0025 K (0.1 μV). In consideration of the errors induced by thermocouples, reference junction compensation, temperature difference among terminals, e.m.f. at scanner junction, DVM accuracy and output offset, the entire accuracy of the temperature measurements was within ±0.1 K. An uncertainty associated with physical properties of silicone oils in the data reduction was less than ±1 percent.

The critical temperature differences at which instability first appears were determined from visual or photographic observation by means of repeatedly small increment and decrement in ΔT around the critical condition. This procedure resulted in a maximum uncertainty of ±10 percent in determination of the critical value.

Experimental Results and Discussion

Experiments were performed using the working fluids with

Nomenclature

A = aspect ratio = H/W
B = depth of slot in the y direction, m
g = acceleration due to gravity, m/s^2
H = height of slot, m
Pr = Prandtl number = ν/κ
Ra = Rayleigh number = $g\beta W^3 \Delta T/\nu\kappa$
S = vertical temperature gradient, K/m
T = temperature, K
W = width of slot, m
x, y, z = Cartesian coordinates, m
β = volumetric expansion coefficient
ΔT = temperature difference between sidewalls = $T_1 - T_2$, K
γ = dimensionless stratification parameter = $(\tau \mathrm{Ra}/4)^{1/4}$
κ = thermal diffusivity, m^2/s
ν = kinematic viscosity, m^2/s
θ = dimensionless temperature = $(T - T_2)/\Delta T$
τ = dimensionless temperature gradient = $SW/\Delta T$

Subscripts

1 = hot wall
2 = cold wall
c = critical value
m = midplane ($x = W/2$)

Superscripts

t = tertiary cell mode
w = traveling wave mode

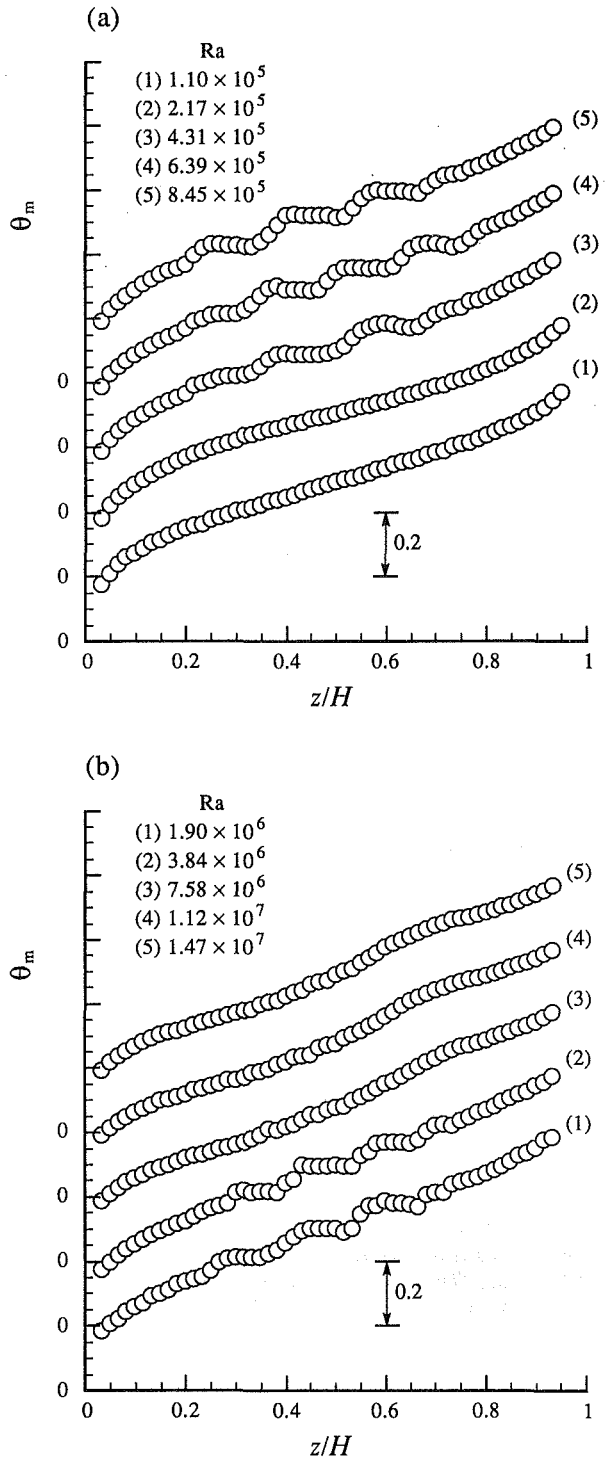

Fig. 2 Vertical variations of midplane temperature: (*a*) Pr = 900, *A* = 10; (*b*) Pr = 50, *A* = 15

Pr = 50, 125, and 900 for $A = 10$, 15, and 20. The results are given for Ra range of 1.26×10^4 to 4.90×10^7.

Temperature Distribution. Figure 2 shows vertical variations of the temperature on the midplane ($x/W = 0.5$). Each ordinate for the data plots that corresponds to (2)–(5) in the figure is shifted respectively by 0.2 in the vertical direction. Every temperature profile indicates a nearly uniform vertical gradient in the core region. Thus the flow lies in the transition or boundary-layer regime. Figure 2(*a*) reveals that as Ra is increased, a unicellular convection breaks down into a multicellular convection, where the temperature inside a secondary cell is seen to be nearly constant. As a preliminary experiment, we measured simultaneous temperatures in the unicellular and multicellular convection at five y positions ($y = 15$, 45, 75, 105, 145 mm) on the midplane, and confirmed their two dimensionality except near the top and bottom ends. On the other hand, the steplike profile for Ra ($\Delta T = 4.2$ K) corresponding to (1) in Fig. 2(*b*) shows that secondary cells have already appeared there. At this Ra, traveling waves and tertiary cells have also appeared, as becomes evident from visual observations in the subsequent subsection, but these appearances cannot be detected from Fig. 2(*b*). The steplike profile that characterizes the existence of the secondary flow disappears at $\mathrm{Ra} = 7.58 \times 10^6$. This seems to indicate that the cellular pattern was disrupted there by traveling waves.

Values of the vertical temperature gradient, $d\theta_m/d(z/H) = \tau A$, are given in Table 1 for various values of Pr and A, and plotted in Fig. 3 as a function of Ra. They were obtained from the temperatures measured in the height range from $z/H = 0.3$ to 0.7 for Pr = 900, and from 0.25 to 0.75 for others. For $\mathrm{Ra} \geq 10^5$, our results are slightly lower than Elder's result (1965) but show substantial deviation for $\mathrm{Ra} < 10^5$. This de-

Table 1 Vertical temperature gradients

Pr	A	Ra × 10^-5	τA	Pr	A	Ra × 10^-5	τA
900	20	0.126	0.330	125	20	2.09	0.635
		0.153	0.398			3.82	0.448
		0.207	0.525			5.72	0.412
		0.259	0.602			6.79	0.404
		0.508	0.736			7.54	0.401
		0.760	0.719			11.2	0.469
	15	0.331	0.721		15	4.99	0.418
		0.645	0.631			9.64	0.466
		1.27	0.491			19.0	0.516
		1.89	0.431			28.3	0.524
		2.51	0.405				
	10	1.10	0.447		10	15.7	0.478
		2.17	0.393			31.7	0.491
		4.31	0.452			61.7	0.495
		6.39	0.486			91.6	0.491
		8.45	0.489				
50	10	64.6	0.529				
		132	0.562				
		255	0.676				
		373	0.706				
		490	0.692				

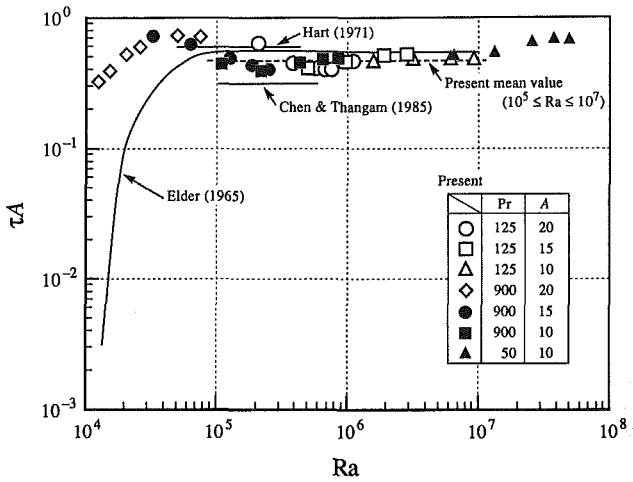

Fig. 3 Vertical temperature gradient as a function of Rayleigh number

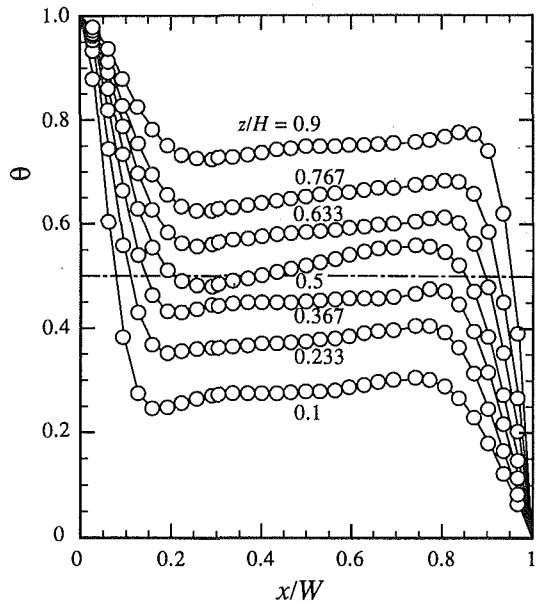

Fig. 4 Typical temperature profiles across the slot in the boundary-layer regime: Pr = 125, $A = 15$, Ra = 2.15×10^6

viation is probably due to the disagreement between the boundary conditions on the top end of the slot. The fluid in Elder's experiment had a free upper surface, in contrast to our experiments. The data plots exhibit a maximum around $\mathrm{Ra} = 5 \times 10^4$. In the range $10^5 \le \mathrm{Ra} \le 10^7$, τA remains constant at a mean value of 0.468, not depending on Pr and A. The broken line in Fig. 3 indicates this mean value. As an asymptotic value of τA for $\mathrm{Ra} \ge 10^5$, Elder obtained a value of 0.55 for 100 cSt silicone oil with $\mathrm{Pr} \approx 1000$, and Hart (1971) obtained 0.6 for water. Chen and Thangam (1985) obtained a smaller value of 0.315 as a mean value for τA in the range $10^5 \le \mathrm{Ra} \le 5 \times 10^5$, for glycerin solutions with variable viscosity ($160 \le \mathrm{Pr} \le 720$).

Figure 4 shows typical temperature profiles at various values of z in a multicellular convection in the boundary-layer regime. The reversal in the horizontal temperature gradient occurs at every z, as indicated by Elder (1965). The magnitude of the reverse gradient is largest at midheight. The boundary layer grows in thickness in an upward direction on the hot wall and in a downward direction on the cold wall. However, the profile at midheight does not show such clear asymmetry resulting from the temperature-dependent properties as indicated by MacGregor and Emerry 1969).This may be because the temperature dependence on viscosity of silicone oils in the present experiment is an order of magnitude smaller than that of the castor oil used by MacGregor and Emerry. As far as temperature is concerned, the profile on the midheight agrees well with that of the basic flow used by Bergholz (1978).

Fow Visualization. Figure 5 shows the typical flow patterns visualized near the critical Rayleigh numbers where secondary and tertiary cells first occur. The hot wall is on the left side in every photopgraph. No traveling wave could be observed at Ra corresponding to Figs. 5(*a–g*) for Pr = 125 and $A = 15$. A primary flow circulating in the slot (clockwise in the figure) is visualized in Fig. 5(*a*), and some secondary cells begin to appear near the center of the slot in Fig. 5(*b*). From visual inspection we could easily detect the weak flows induced by these secondary cells, and chose this condition as the criterion for determination of Ra_c. Three secondary cells with the same sense of circulation as the primary flow obviously appear in Fig. 5(*c*), where the velocities in the secondary cells increase. The onset of secondary cells from the center agrees with numerical results by de Vahl Davis and Mallinson (1975) and Lee and Korpela (1983) for large Pr. The wavelength of these secondary cells is about 1.5 W. As Ra is slightly increased, the secondary flow prevails in the slot and six cells appear in Fig. 5(*d*). However, the wavelength of the secondary cells does not appear to vary at this stage. As Ra is further increased, the

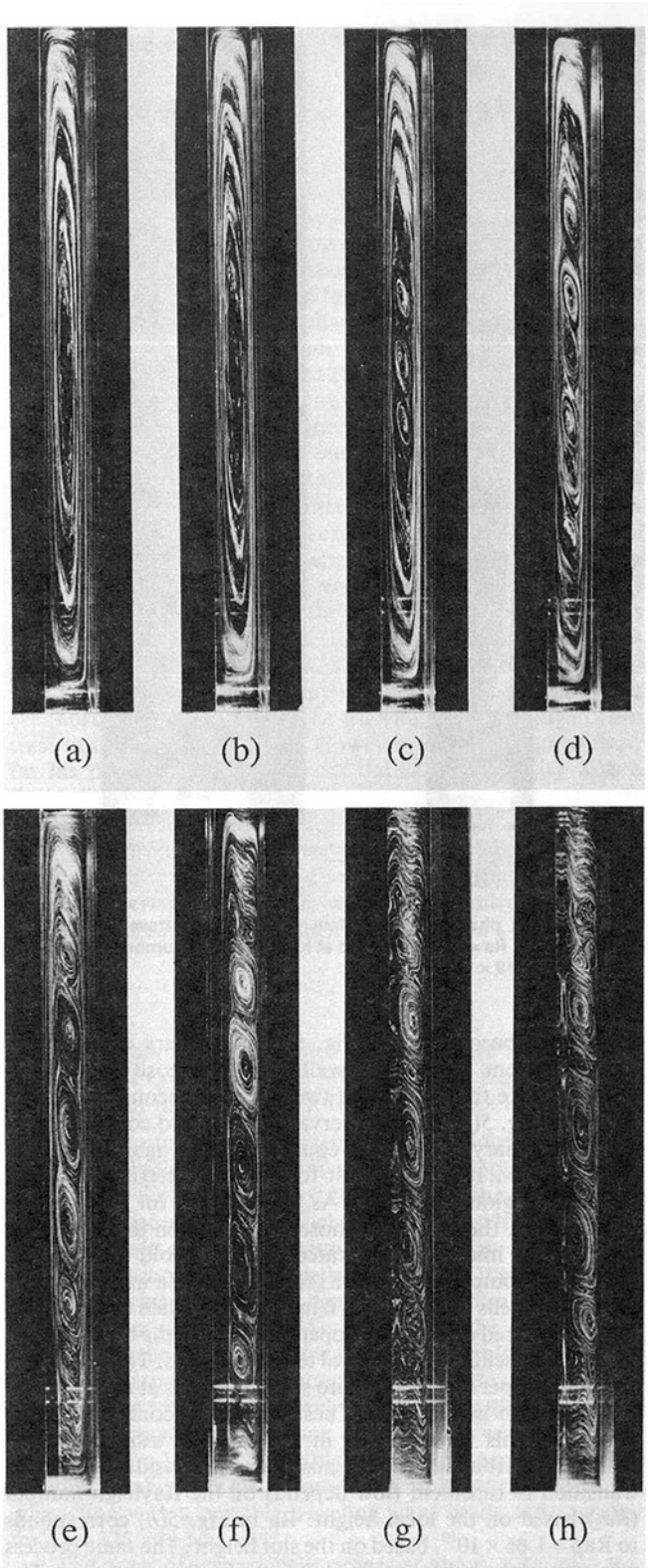

Fig. 5 Streak photographs of flow patterns near the onsets of secondary and tertiary cells for Pr = 125 and $A = 15$: (*a*) Ra = 4.41×10^5; (*b*) 5.54×10^5; (*c*) 6.62×10^5; (*d*) 7.49×10^5; (*e*) 9.40×10^5; (*f*) 1.80×10^6; (*g*) 2.68×10^6; (*h*) 4.91×10^6

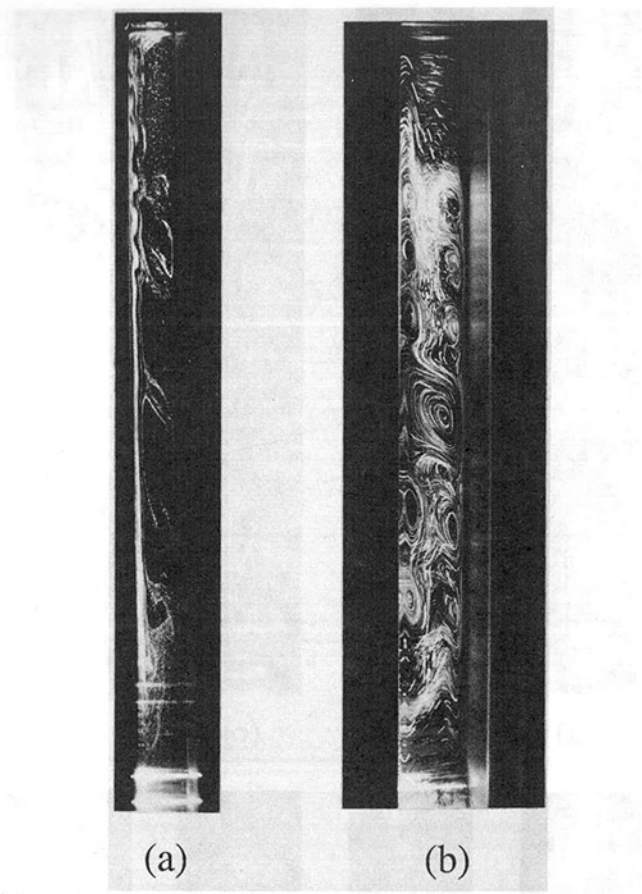

Fig. 6 Streak photographs of flow patterns with traveling wave: (*a*) Pr = 50, $A = 15$, Ra = 2.34×10^6; and at high Rayleigh number: (*b*) Pr = 125, $A = 10$, Ra = 9.19×10^6

wavelength becomes long (Fig. 5*e*) and tertiary cells are initiated adjacent to the cold wall (higher viscosity region) to accommodate the rotation of two adjacent secondary cells as shown in Fig. 5(*f*). From observation we could confirm easily that the tertiary flows were counterrotating against the secondary flows. It was difficult to detect the tertiary flows in the upper region of the slot. As the criterion for the onset of tertiary cells, therefore, we chose the condition that a tertiary cell near the midheight separated from the cold wall and established a complete loop for its rotation. As Ra was increased, the tertiary cells grew as shown in Fig. 5(*g*). Then the traveling waves appeared around the upper region near the hot wall with a period of oscillation of several tens of seconds. The secondary cell in the upper region split into small two cells at about Ra = 9 Ra_c as shown in Fig. 5(*h*). These cells were confirmed to be unsteady. This flow may be in the stage of transition from laminar to turbulent flow. A possibility is considered that the transition to turbulent flow depends on the Rayleigh number (Ra_z) based on the local height. Ra in Fig. 5(*h*) corresponds to $Ra_H = 1.66 \times 10^{10}$, based on the slot height. The same process was seen in the lower region as Ra was further increased. The flow pattern resembles that visualized by Keyhani et al. (1988) for ethylene glycol ($Pr \approx 150$) in a vertical slot with discrete heat sources, and analogous destruction of the cells was observed by Chen and Thangam (1985).

In the observation for $A = 20$ ($W = 15$ mm), tertiary flows could not be found for any Pr. Elder (1965) considered that the appearance of tertiary flows depends on a measure of the secondary-flow amplitude relative to that of the primary flow. He indicated that the tertiary flows appeared when the measure was sufficiently large. The measure increases with a lateral size of the secondary flow. This suggests that the appearance of

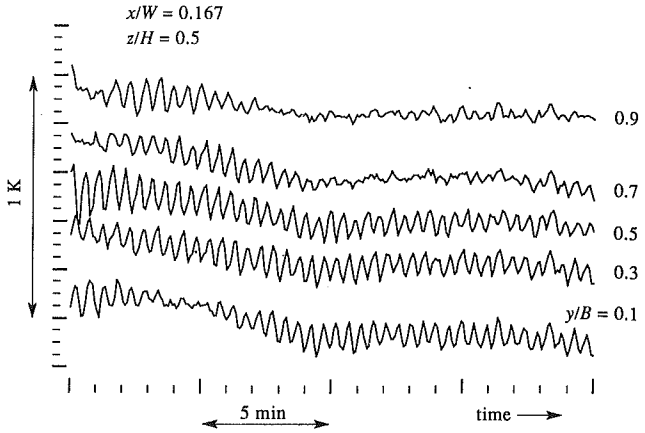

Fig. 7 Temperature fluctuations at midheight in transition region from laminar to turbulent flow: Pr = 125, $A = 10$, Ra = 1.17×10^7 ($Ra_z = 1.46 \times 10^9$)

tertiary flows in the boundary-layer regime depends on the slot width W.

Figure 6(*a*) shows the well-developed traveling wave observed near the hot wall together with the secondary and tertiary cells for Pr = 50 and $A = 15$. Visual inspection showed that such a traveling wave was nearly two dimensional. For this Pr, the traveling waves first appeared at relatively smaller Ra as shown later. The criterion for the onset of traveling waves was based on their first visible appearances in shadowgraphs around the upper region near the hot wall.

Figure 6(*b*) presents an example of unsteady flow patterns at high Ra($= 9.19 \times 10^6$) for Pr = 125 and $A = 10$. There can be seen an original secondary cell in the center region and some smaller cells along the sidewalls in the upper and lower regions. This flow pattern has been not reported by previous experiments. The cells near the top and bottom have been disrupted by traveling waves and the cellular patterns disappear there. The flow is turbulent among the cells but still laminar inside. Visual inspection showed that these cells were oscillating in a period of the order of a minute. It is obvious that the transition to turbulent flow has progressed more than the case Fig. 5(*h*). However, its Ra corresponds to $Ra_H = 9.19 \times 10^9$, which is lower than one in Fig. 5(*h*). Therefore, this suggests that the beginning and end of transition cannot be predicted by Ra_z or Ra_H alone as indicated by Gebhart et al. (1988) for natural convection boundary layer along a vertical wall. The beginning of transition seems to depend on A strongly. From this experiment, however, we cannot find out other parameters to correlate the beginning and end of transition. Such a remarkable flow pattern as this case could not be observed apparently for Pr = 50 owing to a rapid growth of the traveling waves.

Figure 7 shows temperature fluctuations near the hot wall at the midheight in the transition region ($Ra = 1.17 \times 10^7$, $Ra_z = 1.46 \times 10^9$). The fluctuations were measured simultaneously at five y positions. Traveling waves are seen with a period of oscillation of several tens of seconds and the waves lost their two dimensionality at this high Ra.

Onset of Instability. From the above criteria, we determined critical Rayleigh numbers. To distinguish from Ra_c for the onset of secondary cells, we denote the critical Rayleigh numbers Ra_c^t and Ra_c^w for tertiary cells and traveling waves, respectively. These critical values are summarized in Table 2 for several values of Pr and A, and plotted in Fig. 8 as a function of stratification parameter γ. Here, in evaluation of γ we used a mean value of vertical temperature gradient ($\tau A = 0.468$). In Table 2 maximum Ra in each run and Ra_H corresponding to each Ra_c^w are also given. Possible errors in the critical values were within ±10 percent and errors in γ within ±5 percent. The plotted data are compared with the

Table 2 Critical Rayleigh numbers determined from experiments

Pr	A	Ra_c	Ra_c^t	Ra_c^w (Ra_H)	max. Ra
50	15	6.0×10^5	1.7×10^6	7.3×10^5 (2.5×10^9)	1.47×10^7
125	10	5.1×10^5	1.0×10^6	4.1×10^6 (4.1×10^9)	1.68×10^7
125	15	5.5×10^5	1.8×10^6	4.2×10^6 (1.4×10^{10})	5.18×10^6
125	20	6.8×10^5	———	———	2.12×10^6
900	10	2.9×10^5	8.5×10^5	———	1.04×10^6

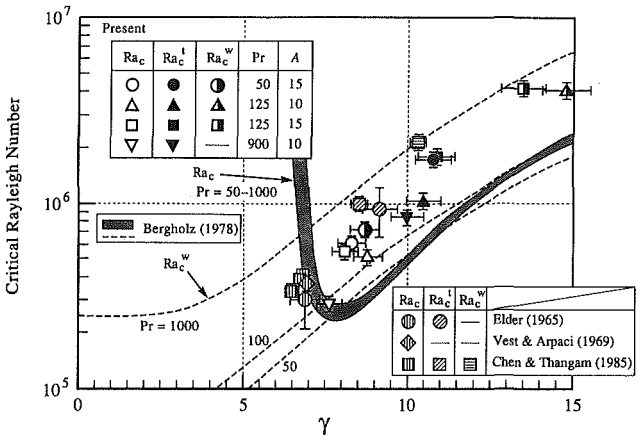

Fig. 8 Critical Rayleigh numbers for secondary cells, tertiary cells, and traveling waves as a function of stratification parameter γ

predictions of the linear stability analysis by Bergholz (1978) and with the other experimental results (Elder, 1965; Vest and Arpaci, 1969; Chen and Thangam, 1985). The values of γ in the other experiments were evaluated from the vertical temperature gradients that they obtained. Figure 8 reveals that, for Pr range of 50 to 1000, the critical conditions calculated by Bergholz for the stationary cell mode of first instability are confined to a narrow area in a γ–Ra_c plane.

In the present experiments except for $Pr = 900$, the values of Ra_c are higher than those predicted by Bergholz for the corresponding γ. This may be attributed to the interaction with a possible traveling wave mode of instability for $Pr = 125$ and 50. For $Pr = 900$, the onset of tertiary cells occurred at 2.9 Ra_c, which agrees with Elder's experimental result. According to Bergholz's result, the flows at such Ra_c and Ra_c^t are stable for the traveling wave mode as shown in Fig. 8. Due to the limits of the experimental condition ($\Delta T \le 50$ K), we could not continue experiments for this Pr up to Ra at which traveling waves could be observed.

In previous experimental studies it has been not revealed how the critical Rayleigh number depends on the aspect ratio. Obviously, Ra_c for $Pr = 125$ shows a slightly increasing trend as A is increased, i.e., the width W becomes small. For $A = 20$, we could not perform experiments at $Ra > 2.12\times10^6$ due to the limits of the experimental condition. The tertiary cells appeared at 2.0 Ra_c and 3.3 Ra_c for $A = 10$ and 15, respectively. It seems that Ra_c^t becomes higher as A is increased. In both cases, however, the traveling waves appeared at about 8 Ra_c. This value is higher than that of Chen and Thangam (1985) obtained with an analogous Pr. They obtained $Ra_c \approx 4\times10^5$, $Ra_c^t = 2.5\ Ra_c$ and $Ra_c^w = 5.4\ Ra_c$ for a mean value of $Pr \approx 160$. However, it should be noted that the value of Ra_c^w corresponds to about 10 Ra_c, based on viscosity corresponding to the temperature at the hot wall. Therefore, it is considered that the result of $Ra_c^w \approx 8\ Ra_c$ is valid. The result for $Pr = 125$ shows that the onset of traveling waves seems to be correlated by Ra rather than Ra_H.

According to Bergholz's s stability characteristics, the flow around Ra_c determined experimentally for $Pr = 125$ is considered unstable for both of the stationary cell and the traveling wave mode. However, the traveling waves did not appear to about 8 Ra_c, where the amplification rate of the wave mode may be large. As a possible reason, we consider nonlinear interactions between the stationary cell and the traveling wave mode of disturbances. The weakly nonlinear theory taking into account the nonlinear evolution of two modes of disturbances in a vertical slot was developed by Gotoh and Mizushima (1984). The theoretical result indicates that, for $Pr = 10$, the stationary cell mode approaches the equilibrium but the supercritical traveling wave mode decays out in some range of stratification parameter due to the mutual interaction. Therefore, the growth of traveling waves may be suppressed by the interaction. The problem in the nonlinear evolution for large Pr is the subject for a future study.

For $Pr = 50$, we obtained $Ra_c = 6.0\times10^5$, $Ra_c^t = 2.8\ Ra_c$ and $Ra_c^w = 1.2\ Ra_c$. For this Pr, since the critical temperature difference at which the onset of secondary cells occurs is as small as 1.3 K, the error in the determination of the critical values may be large. The traveling waves appeared at Ra slightly higher than Ra_c, preceding the onset of tertiary cells. This occurrence is quite an unexpected one from previous experimental and numerical studies. This result may support Bergholz's predictions that the flows around these critical values are thoroughly unstable for the traveling wave mode, in contrast to the case of $Pr = 125$. However, we do not know how far his predictions deviate from the case in a cavity with a finite A and isothermal walls.

We must refer to the critical wave number of secondary cells. The wavelengths observed from experiments were in the range of 1.5 W to 1.8 W. These correspond to the dimensionless wave numbers of 3.5 to 4.2, which are slightly larger than Bergholz's predictions and Chen and Thangam's results of 2.9 to 3.4.

Summary

Experiments were performed on convective instability of fluids with $Pr = 50$, 125, and 900 in vertical slots of $A = 10$, 15, and 20 in the range $1.26\times10^4 \le Ra \le 4.90\times10^7$.

- The data for the vertical temperature gradient in the core of the slot indicate agreement with those reported by Elder (1965) when $Ra \ge 10^5$. For $Ra < 10^5$, however, they do not show decrease in the gradient so much as Elder's result. The present data obviously exhibit a maximum around $Ra = 5\times10^4$.
- The onset of secondary cells occurs from the center of the slot, in contrast to Elder's observation. This result agrees with previous numerical results. As Ra exceeds the critical value Ra_c slightly, the secondary flow prevails in the slot. It is found that as the aspect ratio is increased, the value of Ra_c shows an increasing trend. The critical value for $Pr = 900$ agrees with Bergholz's result and previous experimental results, but the values for $Pr = 125$ and 50 are higher than those predicted from the linear stability. This is considered to be attributed to the interaction with a possible traveling wave mode of instability for $Pr = 125$ and 50.
- The onset of tertiary cells occurs at about 2 Ra_c to 3 Ra_c in the range $50 \le Pr \le 900$ for $A = 15$ and 10. These critical values agree with those obtained from previous experimental and numerical studies. However, it is found that the onset of tertiary cells occurs preceding the onset of traveling waves for $Pr = 125$ but following it for $Pr = 50$. The traveling waves first appear at high Ra of about 8 Ra_c for $Pr = 125$. This result is higher than that reported by Chen and Thangam (1985) for fluids with highly temperature-dependent viscosity. The present result seems to support the result from the weakly nonlinear theory. It is found that for $Pr = 50$ the traveling waves appear at Ra slightly higher than Ra_c owing to possibly large ampli-

fication rate there. For $A = 20$ ($W = 15$ mm), the tertiary cells were not observed for $50 \le Pr \le 900$ and $Ra \le 2.12 \times 10^6$.

- It is found that as Ra is increased, the secondary cells in the end regions of the slot split into smaller cells at about 9 Ra_c and the flow enters transition region from laminar to turbulent flow. For $Pr = 125$, an unsteady flow pattern is observed with an original secondary cell in the center region and some of smaller cells arranged along the sidewalls. This process and flow pattern have not been reported by previous experimental studies.

The problem in heat transfer for different cellular patterns and traveling waves as well as further examination on the transition to turbulence is the subject for a future study.

Acknowledgments

This work is partially supported by Grant-in-Aid for Scientific Research Nos. 61750044 and 62750048 from the Ministry of Education, Science, and Culture of Japan.

References

Batchelor, G. K., 1954, "Heat Transfer by Free Convection Across a Closed Cavity Between Vertical Boundaries at Different Temperatures," *Quarterly Journal of Applied Mathematics*, Vol. 12, pp. 209–233.

Bergholz, R. F., 1978, "Instability of Steady Natural Convection in a Vertical Fluid Layer," *Journal of fluid Mechanics*, Vol. 84, pp. 743–768.

Chen, C. F., and Thangam, S., 1985, "Convective Stability of a Variable-Viscosity Fluid in a Vertical Slot," *Journal of Fluid Mechanics*, Vol. 161, pp. 161–173.

de Vahl Davis, G., and Mallinson, G. D., 1975, "A Note on Natural Convection in a Vertical Slot," *Journal of Fluid Mechanics*, Vol. 72, pp. 87–93.

Eckert, E. R. G., and Carlson, W. O., 1961, "Natural Convection in an Air Layer Enclosed Between Two Vertical Plates With Different Temperatures," *International Journal of Heat and Mass Transfer*, Vol. 2, pp. 106–120.

Elder, J. W., 1965, "Laminar Free Convection in a Vertical Slot," *Journal of Fluid Mechanics*, Vol. 23, pp. 77–98.

Gebhart, B., Jaluria, Y., Mahajan, R. L., and Sammakia, B., 1988, *Buoyancy-Induced Flows and Transport*, Hemisphere, New York.

Gotoh, K., and Mizushima, J., 1984, "Nonlinear Evolution of Disturbances of Two Modes in the Natural Convection Induced in a Vertical Fluid Layer," *Proceedings of the International Symposium on Turbulence and Chaotic Phenomena in Fluids*, T. Tatsumi, ed., Elsevier, Amsterdam, pp. 47–52.

Hart, J. E., 1971, "Stability of the Flow in a Differentially Heated Inclined Box," *Journal of Fluid Mechanics*, Vol. 47, pp. 547–576.

Keyhani, M., Prasad, V., and Cox, R., 1988, "An Experimental Study of Natural Convection in a Vertical Cavity With Discrete Heat Sources," ASME JOURNAL OF HEAT TRANSFER, Vol. 110, pp. 616–624.

Le Quéré, P., 1990, "A Note on Multiple and Unsteady Solutions in Two-Dimensional Convection in a Tall Cavity," ASME JOURNAL OF HEAT TRANSFER, Vol. 112, pp. 965–974.

Lee, Y., and Korpela, S. A., 1983, "Multicellular Natural Convection in a Vertical Slot," *Journal of Fluid Mechanics*, Vol. 126, pp. 91–121.

MacGregor, R. K., and Emerry, A. F., 1969, "Free Convection Through Vertical Plane Layers—Moderate and High Prandtl Number Fluids," ASME JOURNAL OF HEAT TRANSFER, Vol. 91, pp. 391–403.

Seki, N., Fukusako, S., and Inaba, H., 1978, "Visual Observation of Natural Convective Flows in a Narrow Vertical Cavity," *Journal of Fluid Mechanics*, Vol. 84, pp. 695–704.

Vest, C. M., and Arpaci, V. S., 1969, "Stability of Natural Convection in a Vertical Slot," *Journal of Fluid Mechanics*, Vol. 36, pp. 1–15.

M. J. Tan

D. H. Cho

Reactor Engineering Division,
Argonne National Laboratory,
Argonne, IL 60439

F. B. Cheung

Department of Mechanical Engineering,
The Pennsylvania State University,
University Park, PA 16802

Thermal Analysis of Heat-Generating Pools Bounded From Below by Curved Surfaces

A computer code that features the use of a directional effective thermal conductivity in modeling natural convection in heat-generating pools has been developed to analyze heat transfer in such pools, which are bounded from below by curved surfaces. Illustrative calculations pertaining to two published experimental studies on convective heat transfer in water pools with uniformly distributed volumetric energy sources are carried out using the code. The water pools used in the two studies under consideration were cooled either from the top or from the bottom, but not from both. The utility as well as the limitations of the effective thermal conductivity approach in the context of addressing the issue of melt-pool coolability is demonstrated by comparisons of calculated results with the experimental data.

1 Introduction

Heat transfer in pools of heat-generating liquid bounded from below by curved surfaces has received considerable attention in the nuclear industry (Moore and Tolman, 1988; O'Brien and Hawkes, 1991). Under conditions of failure of the emergency core cooling system in a water-cooled nuclear reactor, core meltdown may occur and molten fuel may come into contact with the lower head of the reactor vessel. The assessment of the coolability of the core melt and the estimation of the bounds within which the melt may be retained in vessel entails the knowledge of the transient thermal behavior of the heat-generating melt pool.

A finite-difference code, ACCORD, has been developed that aims at tracking the thermal behavior of a melt pool formed on the lower head of a reactor vessel and analyzing the interactions between the melt pool and the lower head. One of the features of the ACCORD code is the use of a directional effective thermal conductivity to model natural convection in the melt pool. A number of studies have been reported in the literature that illustrate the use of an effective thermal conductivity: for example, the theoretical analysis of experimental data of free convection heat transfer in concentric cylindrical and concentric as well as eccentric spherical annuli by Raithby and Hollands (1975), the theoretical analysis of experimental data of direct contact condensation of steam on liquid jets by Celata et al. (1989), and the modeling of heat transfer in a horizontal heat-generating liquid layer by Cheung et al. (1992). These examples are mostly concerned with simple flow situations. This paper presents a first attempt to use the effective thermal conductivity approach to modeling heat transfer from internally heated liquid pools that are bounded from below by curved surfaces. The effective thermal conductivity approach as described in this paper allows the use of steady-state and overall heat transfer correlations to predict transient and local thermal behavior. The particular model of effective thermal conductivity depends on the geometry and the boundary conditions of the system under consideration. However, the formulation is conceptually simple. The convection and conduction effects are aggregrated in the form of an effective thermal conductivity and only heat conduction equations need to be solved as a boundary value problem in space and an initial value problem in time. In this respect, modeling natural convection in internally heated liquid pools using an effective thermal conductivity may be an approach considered to be similar to, say, that of modeling two-phase flow using a particular flow-regime map.

Another feature of the ACCORD code is that the discretization scheme for the melt pool is designed specifically for liquid pools bounded from below by curved surfaces. This feature eliminates the additional approximation error that would be introduced when, as is the approach used in conventional finite-difference codes, the shape of the bottom boundary is reshaped to that of stairsteps so as to conform to the rectangular grid.

The main objective of this paper is to demonstrate the utility as well as the limitations of the effective thermal conductivity approach to analyzing heat transfer in pools of heat-generating liquid bounded from below by curved surfaces. The paper is organized as follows: Sections 2 and 3 describe the basic equations and their solution method. Section 4 presents comparisons of predicted results with experimental data of Min and Kulacki (1978) and Gabor et al. (1980). Section 5 summarizes the present work.

2 Basic Equations

The liquid pool is considered to be bounded below and sideways by the inner surface of a vessel. The inner surface of the bottom of the vessel is prescribed in cylindrical coordinates as $z = \mathcal{Z}(r)$ with $0 \le r \le R^*$, where R^* denotes the radius of the vessel and $\mathcal{Z}(r)$ is a function satisfying $\mathcal{Z}(0) = 0$. The inner surface of the side of the vessel is prescribed as $r = R^*$ with $\mathcal{Z}(R^*) \le z \le L$, where L denotes the maximum depth of the liquid pool. An outline of the system under consideration is shown in Fig. 1, in which L^* denotes the maximum depth of the bottom of the vessel.

The temperature distribution $T(t, r, z)$ in the pool is considered to be axisymmetric, two dimensional, and governed by

$$\rho c \frac{\partial T}{\partial t} = -\frac{1}{r}\frac{\partial (rq_r)}{\partial r} - \frac{\partial q_z}{\partial z} + \dot{S} \tag{1a}$$

with

$$q_r = -k_{er}\frac{\partial T}{\partial r} \tag{1b}$$

$$q_z = -k_{ez}\frac{\partial T}{\partial z} \tag{1c}$$

Contributed by the Heat Transfer Division and presented at the ASME Winter Annual Meeting, Anaheim, California, November 8–13, 1992. Manuscript received by the Heat Transfer Division December 1992; revision received June 1993. Keywords: Computer Codes, Natural Convection, Transient and Unsteady Heat Transfer. Associate Technical Editor: J. H. Kim.

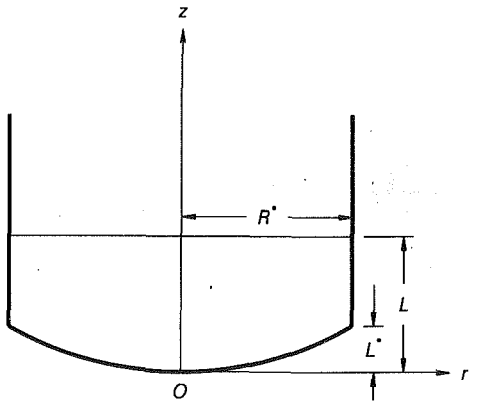

Fig. 1 An outline of the system under consideration

where q_r and q_z are, respectively, the r and z components of heat flux; S is the heat generation rate per unit volume; ρ and c are, respectively, the density and the specific heat of the liquid; and k_{er} and k_{ez} are, respectively, the r- and z-direction effective thermal conductivities in the pool. The effective thermal conductivity may be regarded as an anisotropic property of the *pool* that is defined by Eqs. (1*a*)–(1*c*). Thus, it would vary according to the direction in which it is measured; k_{er} would aggregate the effects of conduction and r-direction convection and k_{ez} would aggregate the effects of conduction and z-direction convection. As will be seen later in the illustrative calculations, the particular model of effective thermal conductivity depends on the geometry and the boundary conditions of the pool under consideration. For the time being, it is assumed that the ratios k_{er}/k and k_{ez}/k where k is the thermal conductivity of the liquid are specifiable as local Nusselt numbers of the following forms:

$$\frac{k_{er}}{k} = \mathfrak{N}_r(t, r, z, T) \tag{1d}$$

and

$$\frac{k_{ez}}{k} = \mathfrak{N}_z(t, r, z, T). \tag{1e}$$

Note that the system under consideration is axisymmetric and two dimensional, thereby precluding azimuthal variation of the effective thermal conductivity.

The boundary conditions are

$$q_z = q_l(T, T_a) \text{ on the top surface of the pool,} \tag{2a}$$

$$q_r = 0 \text{ on the centerline of the pool,} \tag{2b}$$

and

$$\mathbf{q}\cdot\mathbf{n} = q_l \text{ on the bottom and lateral surfaces of the pool,} \tag{2c}$$

where q_l denotes the outwardly directed heat flux over the top surface of the liquid pool, T_a denotes the ambient temperature, $\mathbf{n}$ denotes the outwardly directed unit normal to the bottom and lateral surfaces of the liquid pool, q_l denotes a prescribed heat flux distribution over the bottom and lateral surfaces of the liquid pool. Note that the heat flux over the top surface of the liquid pool is formulated as a function of local liquid temperature and ambient temperature.

All physical properties of the liquid are regarded as functions of temperature. The heat generation rate and the ambient temperature are considered as functions of time and position. Symbolically, ρ, c, S and T_a are given as

$$\rho = \mathfrak{R}(T) \tag{3a}$$

Nomenclature

A_{bot} = surface area of bottom surface of pool, m^2
A_{top} = surface area of top surface of pool, m^2
a = regression constant
b = regression constant
C = parameter used in Eq. (33)
c = specific heat of liquid, J/kg K
g = acceleration due to gravity, m/s^2
h_z = heat transfer coefficient used in Eq. (32), W/m^2 K
k = thermal conductivity of liquid, W/m K
k_{er} = r-direction effective thermal conductivity in pool, W/m K
k_{ez} = z-direction effective thermal conductivity in pool, W/m K
L = maximum depth of pool, m
L^* = maximum depth of bottom surface of pool, m
$\mathbf{q}$ = heat flux in pool, W/m^2
q_r = radial component of $\mathbf{q}$, W/m^2
q_z = axial component of $\mathbf{q}$, W/m^2
q_l = heat flux over top surface of pool, W/m^2
q_l = heat flux over bottom and lateral surfaces of pool, W/m^2
$\bar{q}_l$ = average heat flux over bottom surface of pool, defined by Eq. (37*b*), W/m^2
r = radial coordinate, m
R = radius or half-width of top surface of pool, m
R_l = radius of curvature of bottom surface of pool, m
R^* = radius of vessel, m
S = heat generation rate per unit volume, W/m_3
s = arc length, m
t = time, s
T = temperature in pool, K
T_a = ambient temperature, K
T_{bot} = prescribed constant temperature over bottom surface of pool, K
T_{top} = prescribed constant temperature over top surface of pool, K
V = volume of pool, m^3
z = axial coordinate, m
α = thermal diffusivity of liquid, m^2/s
β = coefficient of thermal expansion of liquid, K^{-1}
ζ = dimensionless axial coordinate
Θ = dimensionless temperature
Θ_0 = dimensionless temperature at bottom center of pool
θ = angle between plane tangent to bottom surface and vertical axis
Λ = dimensionless heat flux distribution over bottom surface of pool defined by Eq. (41)
Λ' = dimensionless heat flux distribution over bottom surface of pool given by Eq. (39)
μ = viscosity of liquid, N s/m^2
ν = kinematic viscosity of liquid, m^2/s
ρ = density of liquid, kg/m^3
τ = dimensionless time

Dimensionless Numbers

Gr_z = Grasholf number defined by Eq. (34)
Nu = Nusselt number defined by Eq. (26) or Eq. (38)
Nu′ = Nusselt number defined by Eq. (24)
Nu″ = Nusselt number defined by Eq. (37*a*)
Nu_r = Nusselt number defined by Eq. (18)
Nu_z = Nusselt number defined by Eq. (32)
Pr = Prandtl number
Ra = Rayleigh number defined by Eq. (25)
Ra_r = Rayleigh number defined by Eq. (20)

$$c = \mathcal{C}(T) \tag{3b}$$

$$k = \mathcal{K}(T) \tag{3c}$$

$$\dot{S} = \mathcal{S}(t, r, z) \tag{3d}$$

$$T_a = \mathcal{T}(t, r) \tag{3e}$$

3 Solution Procedure

The bottom surface of the pool is partitioned into M segments whose projections on the r and z axes are, respectively, Δr_i and Δz_i, $i = 1, \ldots, M$. The lateral surface of the pool is partitioned into $M' - M$ segments whose projections on the z axis are Δz_i, $i = M + 1, \ldots, M'$. Let

$$r_0 = 0,\ r_i = r_{i-1} + \Delta r_i \text{ for } i = 1, \ldots, M \tag{4}$$

$$z_0 = 0,\ z_j = z_{j-1} + \Delta z_j \text{ for } j = 1, \ldots, M' \tag{5}$$

and let

$$t_0 = 0,\ t_n = t_{n-1} + \Delta t_n \text{ for } n \geq 1. \tag{6}$$

Finite difference equations are developed applying integral energy balance to the computational cells instead of differencing the basic differential Eqs. (1*a*)–(1*c*). The finite difference equations thus developed are implicit in form and consistent with the basic differential equations. A successive overrelaxation (SOR) method is used to advance calculations sequentially from line $z = z_0$ to line $z = z_{M'}$. When the calculations proceed to a line, only the values of variables at nodes on the line are unknown, the values of variables at nodes on the two adjacent lines are treated as known, either from the preceding calculations at the current iteration or from the preceding iteration. The superscripts ν and $\nu + 1$ are used on a variable to denote its values at the preceding and the current SOR iterations, respectively.

Let χ_{ij} denote the value of a variable χ at node (i, j) and at the current time step. Let $j^* = \min(j, M)$. At each $z = z_j$, $j = 0, \ldots, M'$, the equations to be solved consist of $j^* + 1$ functions of the $j^* + 1$ variables $T_{0j}, T_{1j}, \ldots, T_{j^*j}$; they can be rewritten in matrix form as

$$\mathbf{f}_j(\mathbf{x}_j) \overset{\text{def}}{=} [\mathcal{F}_{j(1)}(\mathbf{x}_j), \mathcal{F}_{j(2)}(\mathbf{x}_j), \ldots, \mathcal{F}_{j(j^*+1)}(\mathbf{x}_j)]^T = 0, \tag{7}$$

where the solution vector $\mathbf{x}_j$ is defined as

$$\mathbf{x}_j \overset{\text{def}}{=} [T_{0j}, T_{1j}, \ldots, T_{j^*j}]^T. \tag{8}$$

Newton's method is used to solve the system of nonlinear Eqs. (7) for the unknown T_{ij}, $0 \leq i \leq j^*$. The solution procedure starts with the vector

$$\mathbf{x}_j^{(0)} = [T_{0j}^{\nu}, T_{1j}^{\nu}, \ldots, T_{j^*j}^{\nu}]^T \tag{9}$$

and ends when the convergence criterion

$$\sum_{i=0}^{j^*} \left| \frac{T_{ij}^{(\alpha+1)} - T_{ij}^{(\alpha)}}{T_{ij}^{(\alpha)}} \right| \leq \epsilon_3 \tag{10}$$

where ϵ_3 is a prescribed small positive number[1] is satisfied. The superscripts (α) and $(\alpha + 1)$ are used to denote values at the preceding and the current Newton iterations, respectively.

Once T_{ij}, $0 \leq i \leq j^*$, are solved for, $T_{ij}^{\nu+1}$, $k_{erij}^{\nu+1}$ and $k_{ezij}^{\nu+1}$ are calculated using, respectively,

$$T_{ij}^{\nu+1} = \omega T_{ij} + (1 - \omega) T_{ij}^{\nu} \tag{11}$$

where ω is a prescribed relaxation factor,[2]

$$k_{erij}^{\nu+1} = \mathcal{K}(T_{ij}^{\nu+1}) \cdot \mathcal{R}_r(t_{n+1}, r_i, z_j, T_{ij}^{\nu+1}) \tag{12a}$$

and

$$k_{ezij}^{\nu+1} = \mathcal{K}(T_{ij}^{\nu+1}) \cdot \mathcal{R}_z(t_{n+1}, r_i, z_j, T_{ij}^{\nu+1}). \tag{12b}$$

The values that start the SOR iterative procedure are those obtained at the preceding time step. The convergence criterion for the SOR method is

$$\sum_{i=0}^{j^*} \sum_{j=0}^{M'} \left| \frac{T_{ij}^{\nu+1} - T_{ij}^{\nu}}{T_{ij}^{\nu}} \right| \leq \epsilon_2 \tag{13}$$

where ϵ_2 is a prescribed small positive number[3].

4 Illustrative Calculations

Two sets of calculations that demonstrate the utility as well as the limitations of the effective thermal conductivity approach are described in this section. They pertain to the experimental studies by Min and Kulacki (1978) and Gabor et al. (1980) on convective heat transfer in liquid pools with uniformly distributed volumetric energy sources.

4.1 Pools Cooled From Top. Min and Kulacki (1978) reported measurements of transient temperature distribution along the centerline of an internally heated liquid pool and correlations between the Nusselt number and the Rayleigh number for steady convection in the pool. The pool was bounded from below by a segment of a spherical shell maintained at zero heat flux, from the side by a cylindrical wall also maintained at zero heat flux, and from above by a horizontal surface maintained at constant temperature. The heat was generated at constant rates. The working liquid was dilute aqueous copper sulfate solution.

The experiment under consideration, in which the pool was thermally insulated at the bottom and the heat generated was removed from the pool through top cooling, is modeled mathematically with the basic differential Eqs. (1*a*)–(1*c*), the condition (2*b*), and the following boundary conditions:

$$T = T_{\text{top}} \text{ on the top surface of the pool,} \tag{14}$$

where T_{top} denotes the prescribed constant temperature over the top surface of the liquid pool, and

$$\mathbf{q} \cdot \mathbf{n} = q_l = 0 \text{ on the bottom and lateral surfaces of the pool.} \tag{15}$$

Since the pool is thermally insulated at the bottom, the temperature distribution along a given radial position in the pool at any given times has its maximum at the bottom surface of the pool; i.e.,

$$\max_{\mathcal{Z}(r) \leq z \leq L} T(t, r, z) = T(t, r, \mathcal{Z}(r)). \tag{16}$$

Imagine the pool to be partitioned into a number of vertical annuli, the width of each being small compared to the radius of the pool and the height of each being equal to the distance between the top surface and the bottom surface of the pool, $L - \mathcal{Z}(r)$. In view of Eq. (16), heat transfer in each annulus would be vertically unstable. Consequently, the dominant heat transfer mechanism in each annulus would be fine-scale turbulent convection driven mainly by the difference between the temperature at the bottom surface and that at the top surface. Thus, the ratios k_{er}/k and k_{ez}/k are assumed to be approximated, respectively, as

$$\frac{k_{er}}{k} \approx 1 \tag{17}$$

and

$$\frac{k_{ez}}{k} \approx \text{Nu}_r \overset{\text{def}}{=} \frac{\dot{S}[L - \mathcal{Z}(r)]^2}{2k[T(t, r, \mathcal{Z}(r)) - T_{\text{top}}]}. \tag{18}$$

[1]The value 5×10^{-5} was specified for ϵ_3 for the calculations described in Section 4.

[2]The value 1.4 was specified for ω for the calculations described in Section 4.

[3]The value 5×10^{-5} was specified for ϵ_2 for the calculations described in Section 4.

Table 1 Values of pertinent geometric parameters used in the present calculation

No. of Runs	R^*, m	R^*/L	L^*, m	L^*/L
23	0.2286	4.646	0.02904	0.5902
47	0.4572	3.160–3.382	0.1225	0.8466–0.9061
20	0.4572	1.239–1.263	0.1225	0.3321–0.3385
16	0.4572	0.7108–0.7340	0.1225	0.1905–0.1967

Note that the Nusselt number Nu_r as defined in Eq. (18) is independent of the axial position at a given radial position in the pool. Its form corresponds to that of the Nusselt number for convection heat transfer in a horizontal internally heated liquid layer (Cheung et al., 1992).

Utilizing the correlation developed by Cheung (1980) between Nusselt number and Rayleigh number for turbulent convection heat transfer in horizontal heat-generating liquid layers that are subjected to the same type of boundary conditions as Eqs. (14) and (15), we obtain the following expression for k_{ez}:

$$k_{ez}=\frac{0.104\mathrm{Ra}_r^{1/4}\,k}{1-0.751\mathrm{Ra}_r^{-1/12}} \tag{19}$$

where Ra_r is a Rayleigh number defined as

$$\mathrm{Ra}_r \overset{\text{def}}{=} \frac{g\beta\dot{S}[L-\mathcal{Z}(r)]^5}{2k\alpha\nu}. \tag{20}$$

Here g is the acceleration due to gravity; β, α, and ν are the coefficient of thermal expansion, the thermal diffusivity, and the kinematic viscosity, respectively, of the liquid.

The bottom surface of the pool is taken to be exactly spherical in shape and the function $\mathcal{Z}(r)$ that describes it is expressed as

$$\mathcal{Z}(r)=R_1\left[1-\sqrt{1-\left(\frac{r}{R_1}\right)^2}\right], \quad 0\le r\le R^* \tag{21}$$

where R_1 is the radius of curvature of the spherical shell.

Calculations have been carried out using values of parameters pertaining to 106 experimental runs. Each calculation run was allowed to proceed to reach steady state. Those runs can be divided into four groups based on the aspect ratios R^*/L and L^*/L. Table 1 summarizes the values of the aspect ratios and other pertinent geometric parameters for the four groups. In addition, the value of R_1 used in the calculations is 0.9144 m.

Temperature-dependent equations for the physical properties of water at atmospheric pressure are obtained by fitting the respective data for water from 293.15 K to 373.15 K tabulated in the *CRC Handbook of Chemistry and Physics* and are used to evaluate the physical properties for the liquid.

The calculated temperature distributions along the centerline of the liquid pool at four different times along with the experimental ones for one of the ten transient runs reported by Min and Kulacki (1978) are summarized in Figs. 2 and 3, wherein the following dimensionless variables have been introduced:

$$\tau \overset{\text{def}}{=} \frac{\alpha t}{L^2}, \quad \zeta \overset{\text{def}}{=} \frac{z}{L}$$

$$\Theta(\tau,\zeta) \overset{\text{def}}{=} \frac{T(t,0,z)-T_{\text{top}}}{\dot{S}L^2/2k} \text{ and } \Theta_0(\tau) \overset{\text{def}}{=} \frac{T(t,0,0)-T_{\text{top}}}{\dot{S}L^2/2k}. \tag{22}$$

Figure 2 shows that the calculation overpredicts the temperature in the region near the bottom surface of the pool initially and underpredicts the temperature in the region near the top surface of the pool at all times. Figure 3 shows that the calculation slightly overpredicts the initial rate of temperature rise in the region near the bottom surface of the pool and underpredicts the time needed to reach steady state.

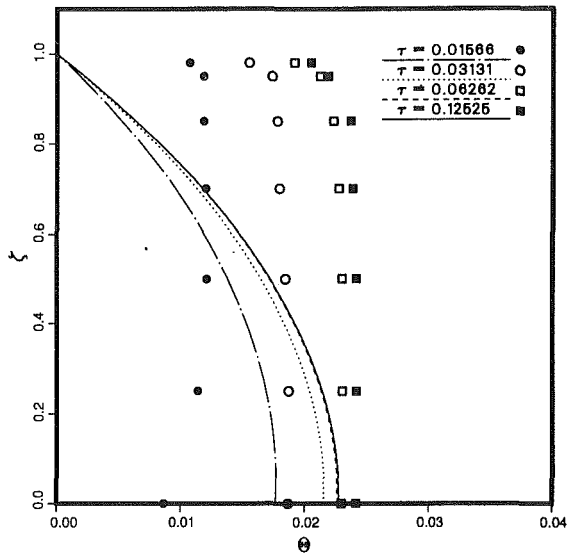

Fig. 2 Transient temperature profiles along the centerline of the pool for Run No. 148 of Min and Kulacki (1978): L^*/L = 0.3385; $\dot{S}$ = 12.744 kW/m^3

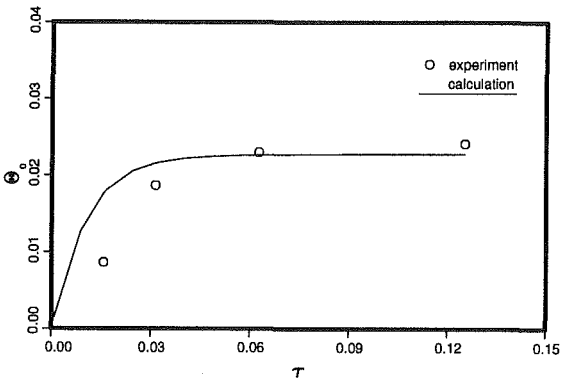

Fig. 3 Time history of temperature at the bottom center of the pool for Run No. 148 of Min and Kulacki (1978): L^*/L = 0.3385; $\dot{S}$ = 12.744 kW/m^3

That the calculation fails to predict the detailed temperature distribution within the pool is one of the limitations of the effective thermal conductivity approach. This finding should not be surprising inasmuch as a lumped-parameter correlation between Nusselt number and the Rayleigh number has been used to model the effective thermal conductivity in a distributed-parameter setting. Note that while the experimental data appear to indicate that the z-direction effective thermal conductivity k_{ez} was smaller in the region near the top than in the region near the bottom, the k_{ez} that is prescribed with Eq. (19) is not explicitly dependent on the axial coordinate z. Moreover, the r-direction effective thermal conductivity k_{er} may depend on the Rayleigh number when the Rayleigh number is very large. The results would probably be better if a correlation based on heat transfer from internally heated vertical circular cylinders or a correlation base on natural convection from vertical heated plates instead of Eq. (17) were used to model k_{er}.

On the other hand, Fig. 3 shows that the calculated steady-state temperature at the bottom center of the pool[4] is in better agreement with the experimental datum. Min and Kulacki

[4] $T(t, 0, 0)$ is the maximum temperature in the pool at time t.

Table 2 Regression constants a and b for steady-state heat transfer

L^*/L	a		b	
	experiment	calculation	experiment	calculation
0.5902	0.9514440	0.1282895	0.1539782	0.2494166
0.8466–0.9061	1.899417	0.1503148	0.1324623	0.2409220
0.3321–0.3385	0.4328663	0.1714430	0.1872779	0.2360734
0.1905–0.1967	0.1672048	0.1849405	0.2312950	0.2343647
overall	0.5112755	0.1511131	0.1874589	0.2409421

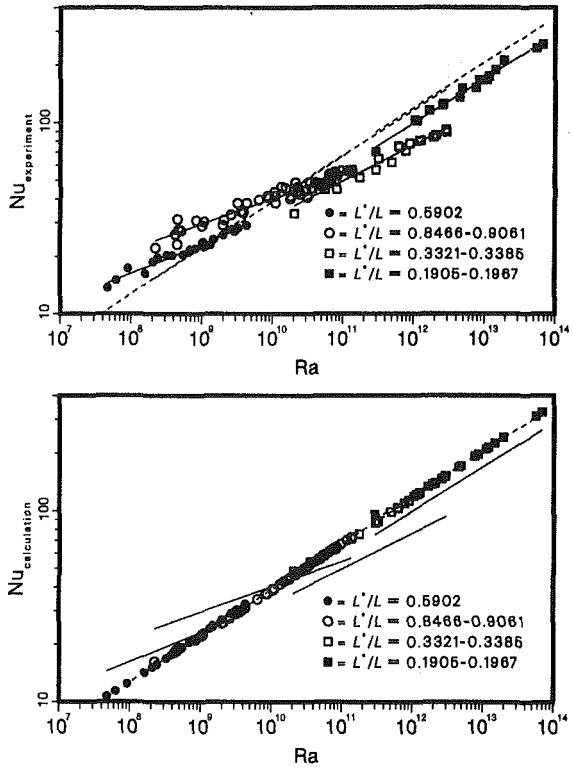

Fig. 4 Experimental and calculated Nusselt numbers versus Rayleigh number for the study of Min and Kulacki (1978)

(1978) discussed their experimental results for steady-state heat transfer in terms of correlations of the form

$$\mathrm{Nu}' = a\mathrm{Ra}^b \tag{23}$$

where a and b are regression constants and the Nusselt number Nu' and the Rayleigh number Ra are defined, respectively, by

$$\mathrm{Nu}' \overset{\text{def}}{=} \frac{\dot{S}VL}{kA_{\text{top}}[T(\infty, 0, 0) - T_{\text{top}}]} \tag{24}$$

and

$$\mathrm{Ra} \overset{\text{def}}{=} \frac{g\beta\dot{S}L^5}{2k\alpha\nu}. \tag{25}$$

In Eq. (24) V and A_{top} denote the volume and the area of the top surface of the pool. In order to be consistent with the use of the effective thermal conductivity introduced in Eq. (18) and the use of the dimensionless variable $\Theta(\tau, \zeta)$ in discussing the transient results, the steady-state experimental results are presented in the present paper along with the calculated results in terms of correlations between the Nusselt number defined by

$$\mathrm{Nu} \overset{\text{def}}{=} \frac{\dot{S}L^2}{2k[T(\infty, 0, 0) - T_{\text{top}}]} \tag{26}$$

and the Rayleigh number given by Eq. (25). All material properties in Eqs. (25) and (26) are evaluated at the upper surface temperature T_{top}. Note that $\mathrm{Nu} \equiv 1/\Theta_0(\infty)$. Thus, the Nusselt

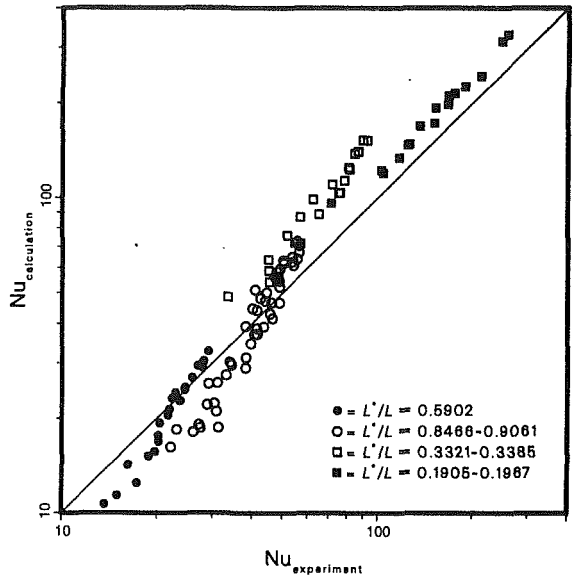

Fig. 5 Experimental Nusselt number versus calculated Nusselt number for the study of Min and Kulacki (1978)

Table 3 Key statistics of deviation of calculated results from experimental results

L^*/L	maximum	minimum	mean	standard deviation
0.5902	11.05%	-39.10%	11.90%	10.86%
0.8466–0.9061	23.75%	-67.22%	19.12%	13.46%
0.3321–0.3385	41.13%	16.26%	31.07%	6.71%
0.1905–0.1967	26.08%	12.01%	17.28%	4.02%
overall	41.13%	-67.22%	19.53%	12.39%

number as defined in Eq. (26) represents the inverse of the steady-state temperature at the bottom center of the pool.

The results of the regression analysis are summarized in Table 2 and presented graphically in Fig. 4. The solid lines and the dashed lines in Fig. 4 represent the regression lines obtained using the experimental and the calculated data, respectively.

It can be seen from Table 2 and Fig. 4 that the experimental correlations appear to depend upon the aspect ratios, but no trend of the dependency is apparent, whereas the calculated correlations are essentially independent of the aspect ratios. Figure 4 shows that the experimental data scatter around the regression lines, whereas the calculated data fall on the regression lines with negligibly small variances. That the calculated results are independent of the aspect ratios is consistent with the assumptions underlying Eqs. (18)–(20). Note that the values of the regression constant b obtained using the calculated results are all very close to 0.25, the exponent of Ra_r in the numerator of the term on the right-hand side of Eq. (19). Figure 5 shows a comparison between the predicted and the experimental steady-state temperatures at the bottom center of the pool. The maximum, minimum, and mean and standard deviation of the absolute value of the prediction errors are summarized in Table 3, where the prediction error is defined as $(\mathrm{Nu}_{\text{calc}} - \mathrm{Nu}_{\text{expt}})/\mathrm{Nu}_{\text{expt}}$. It can be seen that, on average, the predicted steady-state temperatures at the bottom center of the pool lie within a 40 percent band of the experimental results.

4.2 Pools Cooled From Bottom. Gabor et al. (1980) conducted an experimental investigation on steady-state heat transfer to curved surfaces from an internally heated liquid pool. The pool was bounded from below by an array of six plates that were configured into a shape resembling that of a segment of a cylindrical shell. The heat was generated at con-

stant rates. The working liquid was dilute aqueous zinc sulfate solution.

The experiments under consideration consisted of 25 runs for which the top of the pool was thermally insulated and the heat generated was removed from the pool through bottom cooling. It is modeled with the conduction equation

$$\rho c \frac{\partial T}{\partial t} = -\frac{\partial q_r}{\partial r} - \frac{\partial q_z}{\partial z} + \dot{S} \tag{27}$$

in conjunction with Eqs. (1*b*) and (1*c*), the condition (2*b*) and the following boundary conditions:

$$q_1(T, T_a) = 0 \text{ on the top surface of the pool,} \tag{28}$$

and

$$T = T_{\text{bot}} \text{ on the bottom surface of the pool} \tag{29}$$

where T_{bot} denotes the prescribed constant temperature over the bottom surface of the liquid pool. Note that the lateral surface of the vessel is absent in this case.

Since the pool is cooled from the bottom, heat transfer in the pool is vertically stable and the temperature distribution along a given axial position in the pool at any given time is expected to have its maximum at the centerline of the pool; i.e.,

$$\max_{0 \le r \le \mathcal{Z}^{-1}(z)} T(t, r, z) = T(t, 0, z), \tag{30}$$

where $\mathcal{Z}^{-1}(z)$ is the inverse function of $\mathcal{Z}(r)$. In such a situation, the liquid in the pool is expected to undergo large-scale circulating motion. As a result, the temperature variation in the pool would be primarily in the vertical direction except for the boundary layer near the wall where the temperature variation in the radial direction would become significant. Hence, the dominant heat transfer mechanism in the pool would be conduction in the vertical direction and gravity-driven natural convection in the radial direction. The ratios k_{ez}/k and k_{er}/k are assumed to be approximated, respectively, as

$$\frac{k_{ez}}{k} \approx 1 \tag{31}$$

and

$$\frac{k_{er}}{k} \approx \text{Nu}_z \overset{\text{def}}{=} \frac{h_z \mathcal{Z}^{-1}(z)}{k} \tag{32}$$

where h_z is a quasi-local heat transfer coefficient for heat transfer across the boundary layer developed over the bottom surface of the pool. It is assumed that the Nusselt number Nu_z as defined in Eq. (32) is independent of the radial position at a given axial position in the pool. Its form corresponds to that of the Nusselt number for convective heat transfer from an inclined surface.

Making use of the modified Eckert equation for laminar natural convective heat transfer from inclined surfaces (Rich, 1953), we obtain in this case the following expression for k_{er}:

$$k_{er} = \frac{C\text{Pr}^{1/2}}{(0.952 + \text{Pr})^{1/4}} \left[\text{Gr}_z \frac{\mathcal{Z}^{-1}(z)}{s(z)} \right]^{1/4} k \tag{33}$$

where C is a constant,[5] $\text{Pr} \overset{\text{def}}{=} \nu/\alpha$ is the Prandtl number, $s(z)$ is the arc length along the bottom boundary as measured from the edge of the pool, and Gr_z is a modified Grasholf number defined as

$$\text{Gr}_z \overset{\text{def}}{=} \frac{[g \cos \theta(z)]\beta[T(t, 0, z) - T(t, \mathcal{Z}^{-1}(z), z)][\mathcal{Z}^{-1}(z)]^3}{\nu^2}. \tag{34}$$

Here $\theta(z)$ is the angle between the plane tangent to the bottom surface and the vertical axis. Note that the model for effective thermal conductivity as embodied in Eqs. (31), (33), and (34) does not depend on the term $\dot{S}$ that represents heat generation rate.

[5]It is equal to 0.508 in the original Eckert equation.

Table 4 Values of pertinent parameters used in the present calculation

4 plates			6 plates		
Run No.	T_{bot}, K	$\dot{S}$, kW/m^3	Run No.	T_{bot}, K	$\dot{S}$, kW/m^3
44	312.05	85.542	37	305.85	23.470
45	314.45	88.441	48	307.75	23.470
46	318.95	94.241	51	304.85	23.930
35	320.75	120.338	49	324.35	46.479
36	320.05	120.338	38	320.65	49.700
37	320.25	120.338	50	338.65	71.789
38	319.95	120.338	39	330.45	73.170
40	332.85	146.436	31	318.15	88.356
41	333.25	147.886	40	338.65	99.401
42	334.45	147.886	30	334.55	150.482
43	335.45	149.335			
39	331.55	150.785			
34	330.05	162.384			
33	329.55	163.834			
32	328.35	168.184			

The bottom surface of the pool is assumed to be exactly cylindrical in shape so that it can be described by

$$\mathcal{Z}(r) = R_1 \left[1 - \sqrt{1 - \left(\frac{r}{R_1} \right)^2} \right], \quad 0 \le r \le R \tag{35}$$

where R_1 is the radius of the cylindrical shell and R denotes the half-width of the upper surface of the pool; i.e., $R = \mathcal{Z}^{-1}(L)$.

Calculations have been carried out using values of parameters pertaining to the 25 experimental runs. Each calculation run was allowed to proceed to reach steady state. Those runs can be divided into two groups based on whether four or six plates were covered by the pool. Gabor et al. (1980) reported that the bottom of the pool was an arc with a radius of 0.450 m and that the pool depth was 0.055 m when four plates were covered and 0.113 mm when six plates were covered. The value of R_1 used in the calculations is 0.450 m and the values of L are 0.055 m and 0.113 m for four-plate and six-plate runs, respectively. It should be pointed out that while Gabor et al. (1980) reported that four plates subtended an angle of 60 deg and six plates subtended an angle of 90 deg, calculations showed that if the bottom surface were exactly a segment of a cylindrical surface of radius 0.450 m, a pool depth of 0.055 m would subtend an angle of 57 deg and a pool depth of 0.113 m would subtend an angle of 83 deg. Table 4 summarizes the values of pertinent parameters used in the calculations (Gabor, 1992).

In addition to using the value 0.508 for the constant coefficient C in Eq. (33), another value, 0.254, is used for each of the 25 runs so as to study the sensitivity of the calculated results to the magnitude of k_{er}. The temperature-dependent equations developed for the physical properties of water at atmospheric pressure are used to evaluate the physical properties for the liquid.

The experimental results for overall heat transfer were presented in the form

$$\text{Nu}'' = a\text{Ra}^b \tag{36}$$

where the Nusselt number Nu'' is defined by

$$\text{Nu}'' \overset{\text{def}}{=} \frac{\bar{q}_1 L}{k[T(\infty, 0, L) - T_{\text{bot}}]} \tag{37a}$$

with

$$\bar{q}_1 \overset{\text{def}}{=} \frac{\Sigma_{i=1}^{4 \text{ or } 6} q_{1i} A_{\text{bot}i}}{\Sigma_{i=1}^{4 \text{ or } 6} A_{\text{bot}i}}, \tag{37b}$$

Table 5 Regression constants a and b for overall heat transfer

	4 plates		6 plates	
	a	b	a	b
experiment	0.1193442	0.2088528	2.222311	0.1022021
calu., $C = 0.508$	0.3170776	0.1839849	0.3490627	0.2023145
calu., $C = 0.254$	0.2155504	0.1783841	0.1857198	0.2060420

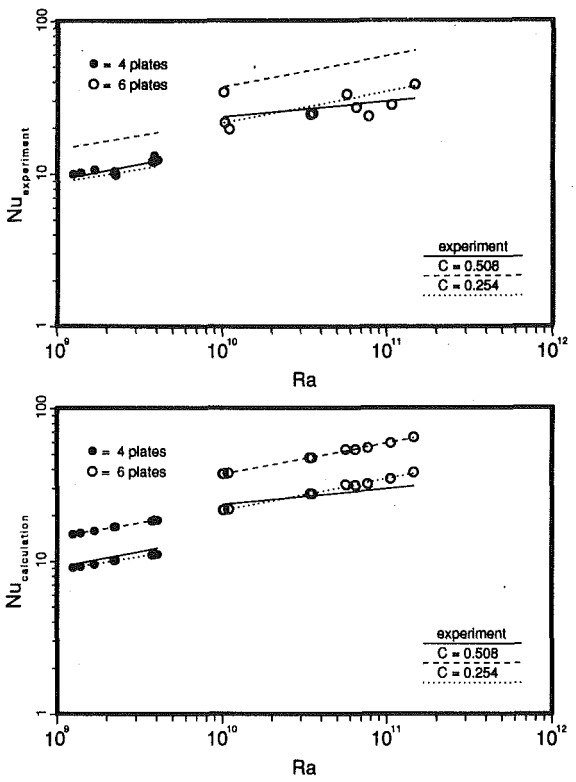

Fig. 6 Experimental and calculated Nusselt numbers versus Rayleigh number for the study of Gabor et al. (1980)

and the Rayleigh number Ra is given in Sec. 4.1 by Eq. (25). In Eq. (37*b*) $A_{\text{bot}i}$ denotes the surface area of the ith plate. In order to be consistent with the definition, Eq. (26), of the Nusselt number introduced in Sec. 4.1, the experimental results are presented in the present paper along with the calculated results in terms of correlations between the Nusselt number defined by

$$\text{Nu} \overset{\text{def}}{=} \frac{\dot{S}L^2}{2k[T(\infty, 0, L) - T_{\text{bot}}]} \tag{38}$$

and the Rayleigh number given by Eq. (25). All material properties in Eqs. (25) and (38) are evaluated at the lower surface temperature T_{bot}. Note that the Nusselt number as defined in Eq. (38) represents the inverse of the steady-state temperature at the top center of the pool.

The results of the regression analysis are summarized in Table 5 and presented graphically in Figs. 6 and 7. The solid lines, dashed lines, and dotted lines in Fig. 6 represent the regression lines obtained using the experimental data, the calculated data for $C = 0.508$, and the calculated data for $C = 0.254$, respectively.

It can be seen from Table 5 and Fig. 6 that both the experimental and the calculated correlations vary with the depths of the pool and that varying the magnitude of the coefficient C results in distinct values of the regression coefficient a but has little effect on the values of the regression exponent b. Figures 6 and 7 show that the calculations using $C = 0.254$ are better than the calculations using $C = 0.508$ in predicting the steady-state temperatures at the top center of the pool and

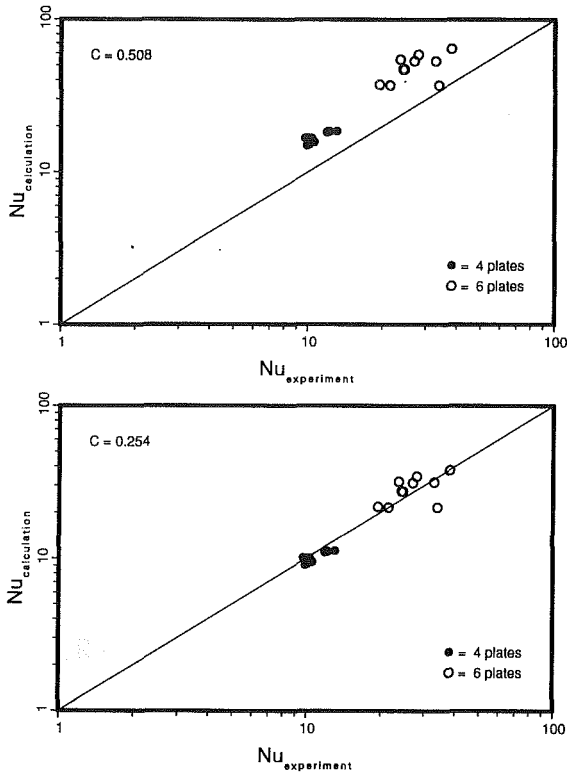

Fig. 7 Experimental Nusselt number versus calculated Nusselt number for the study of Gabor et al. (1980)

that the calculated steady-state temperatures at the top center of the pool for the four-plate experiment have better agreement with the experimental data than those for the six-plate experiment do. Figure 6 also shows that the calculated data fall on the regression lines with negligibly small variances, whereas the experimental data scatter around the regression lines with one datum in the six-plate experiment appearing to be an outlier. When the run corresponding to the probable outlier is excluded from the regression analysis, the regression constants a and b associated with the remaining data in the six-plate experiment are found to be 0.3083236 and 0.1811274, respectively. Contrasting these two values with those listed in Table 5 and considering the reported magnitudes of the experimental uncertainties, we conclude that for $C = 0.254$ the predicted steady-state temperatures at the top center of the pool are in good agreement with the experimental ones.

Gabor et al. (1980) also reported local heat transfer data in terms of a dimensionless heat flux at the center of each bottom plate. The reported data were averages over all 15 runs for the four-plate experiment and over all 10 runs for the six-plate experiment. The dimensionless heat flux, denoted herein as Λ', was calculated by Gabor et al. (1980) using

$$\Lambda' = \frac{q_l}{\bar{q}_l}. \tag{39}$$

Overall energy balance based on the experimental data of Gabor (1992) indicated that the heat removed from the bottom plates was less than the heat generated in the pool for each of the 25 runs—the shortfalls ranged from 5.27 to 25.72 percent with an average of 14.50 percent for the four-plate experiment and from 2.88 to 32.91 percent with an average of 19.49 percent for the six-plate experiment. This suggests that the top surface of the experimental apparatus was not truly adiabatic. Consequently, the dimensionless heat fluxes as calculated by Eq. (39) would contain additional uncertainties to those reported by Gabor et al. (1980). Moreover, the dimensionless heat fluxes

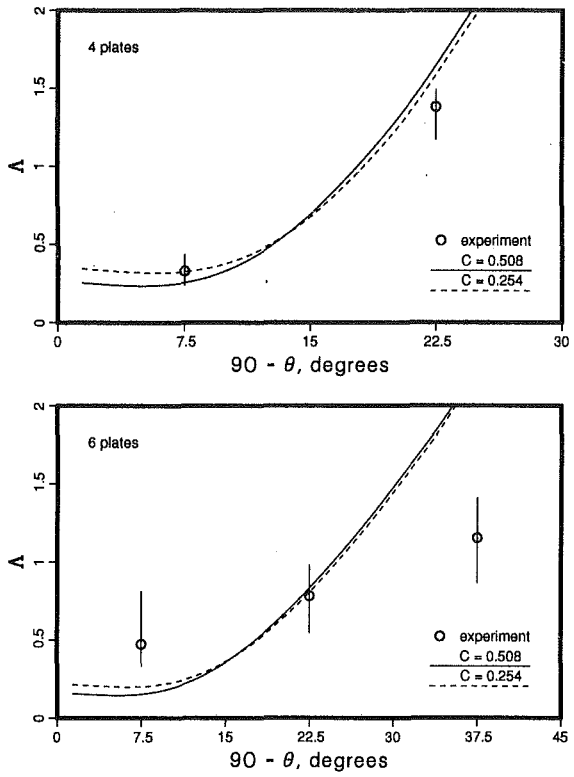

Fig. 8 Heat flux distribution over the bottom surface of the pool for the study of Gabor et al. (1980)

calculated using Eq. (39) should satisfy the following condition:

$$\frac{\Sigma_{i=1}^{4 \text{ or } 6} \Lambda_i' A_{\text{bot}i}}{\Sigma_{i=1}^{4 \text{ or } 6} A_{\text{bot}i}} = 1, \tag{40}$$

but did not with the reported data of the six-plate experiment. In view of the aforementioned uncertainties, the experimental local heat transfer data are presented in the present paper along with the calculated heat flux distributions in terms of a dimensionless heat flux defined by

$$\Lambda = \frac{q_1 A_{\text{bot}}}{SV}, \tag{41}$$

where V and A_{bot} are the volume and the bottom surface area, respectively, of the pool. Figure 8 shows the experimental results along with the calculated ones, where both results represent averages over all 15 runs for the four-plate experiment and over all 10 runs for the six-plate experiment. It can be seen from Fig. 8 that varying the magnitude of the coefficient C has little effect on the calculated dimensionless heat flux distribution over the bottom surface of the pool, that the calculations predict well the location of the maximum heat flux, which appeared to be at the edge of the pool, and that the calculated heat flux distributions over the bottom surface of the pool for the four-plate experiment have better agreement with the experimental data than those for the six-plate experiment do. As pointed out previously, the bottom of the experimental apparatus was made to model a segment of a circle, but was not truly a segment of a circle. The deviation of the bottom surface of the pool from being truly circular is larger for the six-plate runs than for the four-plate runs. The top surface of the experimental apparatus was intended to be adiabatic, but might not have been truly adiabatic, as suggested earlier in the discussion regarding the overall energy balance. Moreover, in view of the heating method used by Gabor et al. (1980), the volumetric heat generation in the experiment was not truly uniform and the nonuniformity would be more pronounced in the six-plate runs than in the four-plate runs. These reasons may help explain why the magnitude of the calculated maximum heat flux deviates considerably from the magnitude of the experimental maximum heat flux for the six-plate experiment. In the light of the preceding discussion, it appears that the calculated heat flux distributions over the bottom of the pool are in reasonable agreement with the experimental ones. That the calculated heat flux distribution over the bottom surface of the pool has its minimum at the bottom center and increases monotonically as the position moves up toward the edge of the pool is also in qualitative agreement with the experimental results of Jahn and Reineke (1974) and those of Frantz and Dhir (1992). It is worth noting that preliminary calculations carried out with $k_{er} = k$ showed the maximum heat flux to be at the bottom center of the pool.

5 Summary

A computer code has been developed to track the thermal behavior of a melt pool formed on the lower head of a reactor vessel and to analyze the interactions between the melt pool and the lower head. The code makes use of a directional effective thermal conductivity to model natural convection in the melt pool. The effective thermal conductivity approach allows the use of steady-state and overall heat transfer correlations to predict transient and local thermal behavior. The particular model of effective thermal conductivity depends on the geometry and the boundary conditions of the system under consideration. The simplicity of the effective thermal conductivity approach is illustrated in the analysis. Based on comparisons of calculated results with available experimental data on convective heat transfer in water pools with uniformly distributed volumetric energy sources, the following observations can be made:

1 For both top- and bottom-cooled pools, the effective thermal conductivity approach predicts reasonably well the overall heat transfer rate (in terms of correlations between the Nusselt number and the Rayleigh number) as well as the maximum steady-state temperature in the pools.

2 For bottom-cooled pools, the effective thermal conductivity approach provides a reasonable prediction of the steady-state heat flux distribution over the bottom surface of the pools.

3 For top-cooled pools, the effective thermal conductivity approach has a limited capability to predict either the transient or the steady-state temperature distributions *within* the pools, as has been noted by Cheung et al. (1992).

In the context of melt-pool coolability, the melt pool would be expected to be cooled from below and the temperature distribution of primary concern would be the one over the bottom surface of the melt pool. This paper demonstrates that with an appropriate heat transfer correlation between the Nusselt number and the Rayleigh number, the effective thermal conductivity approach to modeling natural convective in the melt pool can be utilized to provide useful information for analyzing the interactions between the melt pool and the lower head.

Acknowledgments

This work was supported by the U.S. Department of Energy, Office of New Production Reactors under Contract No. W-31-109-Eng-38.

References

Celata, G. P., Cumo, M., Farello, G. E., and Focardi, G., 1989, "A Comprehensive Analysis of Direct Contact Condensation of Saturated Steam on Subcooled Liquid Jets," *Int. J. Heat Mass Transfer*, Vol. 32, pp. 639–654.

Cheung, F. B., 1980, "Heat Source-Driven Thermal Convection at Arbitrary Prandtl Number," *J. Fluid Mech.*, Vol. 97, pp. 743–758.

Cheung, F. B., Shiah, S. W., Cho, D. H., and Tan, M. J., 1992, "Modeling of Heat Transfer in a Horizontal Heat-Generating Layer by an Effective Diffusivity Approach," *Thermal Hydraulics of Severe Accidents*, R. M. Singer and M. S. El-Genk, eds., ASME HTD-Vol. 192, pp. 55–62.

Frantz, B., and Dhir, V. K., 1992, "Experimental Investigation of Natural Convection in Spherical Segments of Volumetrically Heated Pools," *Thermal Hydraulics of Severe Accidents*, R. M. Singer and M. S. El-Genk, eds., ASME HTD-Vol. 192, pp. 69–76.

Gabor, J. D., Baker, L., Jr., Cassulo, J. C., Erskine, D. J., and Warner, J. G., 1980, "Heat Transfer to Curved Surfaces From Heat Generating Pools," ASME JOURNAL OF HEAT TRANSFER, Vol. 102, pp. 519–524.

Gabor, J. D., 1992, private communication.

Jahn, M., and Reineke, H. H., 1974, "Free Convection Heat Transfer With Internal Heat Sources, Calculations and Measurements," *Proc. 5th Int. Heat Transfer Conf.*, Tokyo, Japan, Paper NC 2.8.

Min, J. H., and Kulacki, F. A., 1978, "Steady and Transient Natural Convection With Volumetric Energy Sources in a Fluid Layer Bounded From Below by a Segment of a Sphere," NUREG/CR-0006.

Moore, R. L., and Tolman, E. L., 1988, "Estimated TMI-2 Vessel Thermal Response Bounds Based on the Lower Plenum Debris Configuration," presented at the ASME National Heat Transfer Conference, Houston, TX, July 24–27.

O'Brien, J. E., and Hawkes, G. L., 1991, "Thermal Analysis of a Reactor Lower Head With Core Relocation and External Boiling Heat Transfer," presented at the ASME National Heat Transfer Conference, Minneapolis, MN, July 28–31.

Raithby, G. D., and Hollands, K. G. T., 1975, "A General Method of Obtaining Approximate Solutions to Laminar and Turbulent Free Convection Problems," *Advances in Heat Transfer*, Vol. 11, pp. 265–315.

Rich, B. R., 1953, "An Investigation of Heat Transfer From an Inclined Flat Plate in Free Convection," *Trans. ASME*, Vol. 75, pp. 489–498.

F. J. Hamady

J. R. Lloyd

Heat Transfer Group,
Department of Mechanical Engineering,
Michigan State University,
E. Lansing, MI 48824

K. T. Yang

Department of Aerospace and
Mechanical Engineering,
University of Notre Dame,
Notre Dame, IN 46556

H. Q. Yang

CFD Research Corporation,
Huntsville, AL 35805

A Study of Natural Convection in a Rotating Enclosure

The local and mean natural convection heat transfer characteristics and flow fields were studied experimentally and numerically in an air-filled, differentially heated enclosure with a cross-sectional aspect ratio of one. The enclosure is rotated above its longitudinal horizontal axis. A Mach-Zehnder interferometer was employed to reveal the entire temperature field, which enable the measurement of the local and mean Nusselt numbers at the hot and cold surfaces. Laser sheet flow visualization was employed to observe the flow field. The result showed that the Coriolis and centrifugal buoyancy forces arising from rotation have a remarkable influence on the local heat transfer when compared with the nonrotating results. Local heat fluxes were obtained as a function of Taylor ($Ta \leq 4 \times 10^5$) and Rayleigh numbers ($10^4 < Ra \leq 3 \times 10^5$), at different angular positions of the enclosure. In addition, a series of interferograms, stream function and isotherm plots demonstrated the strong effect of rotation on the flow field and heat transfer. A correlation of Nusselt number as a function of Taylor and Rayleigh numbers is presented.

Introduction

The effects of multiple, interacting body forces found in rotating systems will be the subject of extensive research effort in the future as space-based manufacturing processes increase in importance. Most of the analytical and experimental works of the past have dealt mainly with high rotational speeds, and in these studies it typically has been assumed that the fluid is in a solid body rotation. A monograph on the theory of rotating fluids by Greenspan (1968) contained most of what is necessary for a basic understanding of the theory. Recently, a somewhat similar monograph on heat transfer and fluid flow in rotating coolant channels was prepared by Morris (1981). Interest in that presentation was centered on design requirements for cooling rotating equipment.

One of the early studies of heat transfer in a tube rotating about an axis perpendicular to that of the tube was made by Schmidt (1951). He suggested passing cooling fluid through narrow passages in a turbine blade, which then opened to a reservoir of circulating cool fluid in the hub. Mori and Nakayama (1968) studied the fully developed laminar flow and temperature fields in a pipe rapidly rotating around a perpendicular axis. Their analysis revealed that the flow resistance coefficient and the Nusselt number increased remarkably due to a secondary flow driven by the Coriolis force. In a second report, Mori et al. (1971) extended their work to include both experimental and theoretical analyses of the turbulent regime with fully developed velocity and temperature fields. In this study, it was found that the increases in Nusselt number and flow resistance are less than the corresponding increase for laminar flow. Hence, the influence of the secondary flow produced by the Coriolis force is not as significant in turbulent flow as in laminar flow.

The effect of rotating on the hydrodynamic and thermal characteristics was treated in detail according to its functional and practical importance in the design of cooling systems for electrical machines. Morris (1965) and Davis and Morris (1966) discussed the influence of rotating on laminar heat convection when the fluid flows through a vertical tube with a uniform heat flux boundary condition that rotates about a parallel axis. Their results clearly showed that rotation can induce a secondary natural convection flow in a plane perpendicular to the axis, which causes a distortion in both the velocity and temperature profiles and modifies the flow and heat transfer rate. Humphreys et al. (1967) experimentally studied the local and mean heat transfer rate for air in a turbulent flow through the entrance region of a tube rotating about a parallel axis. On the other hand, Neti et al. (1985) and Levy et al. (1986) carried out numerical studies of laminar heat transfer for air in a rectangular duct rotating about a parallel axis. Their results indicate a significant effect of the secondary flow induced by the Coriolis force and density gradient on the heat transfer and pressure drop.

Thermal convection in a vertical rotating cylinder heated from above has been studied by Homsy and Hudson (1971) and Abell and Hudson (1975). Differences between rotating and nonrotating convection were presented in terms of the centrifugal acceleration, which is a strong function of the radial position, and the Coriolis acceleration, which contributes significantly to the heat transfer as a consequence of the induced secondary flow.

Benard convection in a rotating fluid was studied by Veronis (1966, 1968) and Rossby (1969). Stability of the fluids was considered as a function of Rayleigh, Taylor, and Prandtl numbers. Measurements performed on fluids of different Prandtl numbers exhibit markedly different behaviors. Catton (1970) employed the Landau method to analyze the effect of rotation on natural convection in a horizontal liquid layer. His results compared quite well with Rossby's experimental results up to a Taylor number of 10^5. Buhler and Oertel (1982) conducted a theoretical and experimental study of thermal cellular convection in a rotating rectangular box. Their interest was centered on the effect of Prandtl number. Linear stability theory employing the Boussinesq approximation was used in the analysis. Their computations showed that the roll cells change their orientation with increasing Taylor number, and led to the conclusion that centrifugal forces dominate in high Prandtl number fluids, while Coriolis forces dominate in low Prandtl number fluids.

Natural convection in differentially heated enclosures has only been considered for gravitational forces oriented in the vertical direction (Bernard convection, or heated from above), or in enclosures rotated about a vertical axis passing through their center. No studies have considered the influence of Cor-

Contributed by the Heat Transfer Division and presented at the ASME National Heat Transfer Conference, San Diego, California, August 9–12, 1992. Manuscript received by the Heat Transfer Division November 1992; revision received April 1993. Keywords: Enclosure Flows, Natural Convection, Rotating Flows. Technical Editor: R. Viskanta.

iolis forces and its interaction between centrifugal and gravitational buoyancy on the flow and heat transfer in a differentially heated enclosure rotating about its own longitudinal horizontal axis. This particular geometry is important to study because it is possible to sort out the interactions of the multiple body forces due to rotation since the nonrotating case has also served as the basic geometry for the "standard" differentially heated enclosure. The purpose of this work is to study the effects of the additional body forces produced by rotation, namely the Coriolis and centrifugal forces, and to determine how they interact with the gravitational body force in influencing the flow patterns and heat transfer distributions in enclosures.

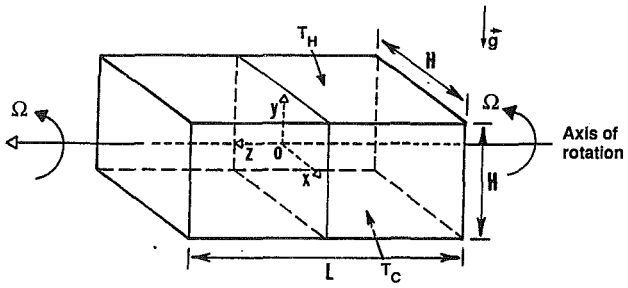

Fig. 1 Geometric configuration of the three-dimensional enclosure

Mathematical Formulation and Numerical Solution

The enclosure is constructed to rotate about its longitudinal, horizontal z axis with a uniform counterclockwise angular velocity, Ω, as illustrated in Fig. 1. The surfaces at $y=-H/2$ and $y=H/2$ are at uniform cold and hot temperatures, respectively. All the other surfaces are insulated. Aspect ratios that relate the dimensions of the enclosure are $A_x=D/H=1$ and $A_z=L/H=10$. The working fluid is air. Using H, α/H, H^2/α, $\alpha\nu\rho/H^2$ and T_H-T_C as scales for length, velocity, time, pressure, and temperature, respectively, the dimensionless governing equations for continuity, energy, and momentum based on the rotational frame of reference can be written in the form

$$\nabla\cdot\mathbf{V}_r=0 \tag{1}$$

$$\frac{D\theta}{D\tau}=\nabla^2\theta \tag{2}$$

$$\frac{1}{\mathrm{Pr}}\frac{D\mathbf{V}_r}{D\tau}-\nabla^2\mathbf{V}_r=-\nabla p-(\mathrm{Ta})^{1/2}(\mathbf{k}\times\mathbf{V}_r)+\mathrm{Ra}_r\theta\mathbf{R}+\mathrm{Ra}\theta\frac{\mathbf{g}}{|g|} \tag{3}$$

The analysis assumes that the Boussinesq approximation is valid as demonstrated by Zhong et al. (1985), and that viscous dissipation and pressure work are negligible. The important dimensionless parameters entering the equations of motion are: $\mathrm{Pr}=\nu/\alpha$, the Prandtl number; $\mathrm{Ra}=g\beta H^3(T_H-T_c)/\alpha\nu$, the gravitational Rayleigh number; $\mathrm{Ra}_r=\beta(T_H-T_C)\Omega^2H^4\alpha\nu/\nu\alpha$, the rotational Rayleigh number; $\mathrm{Ta}=4\Omega^2H^4/\nu^2=(2\mathrm{Re})^2$, the Taylor number; and $\mathrm{Re}=\Omega H^2/\nu$, the rotational Reynolds number. In Eq. (3) the second term on the right characterizes the effect of Coriolis forces, and the third and last terms account for the centrifugal and the gravitational buoyancy effects, respectively. It is also noted that in the present problem the direction of the Coriolis forces, given by $\mathbf{k}\times\mathbf{V}_r$ where $\mathbf{k}$ is the unit vector along the axis of rotation in the z direction, always lies in the x-y plane. Consequently, with negligible end wall effects, the flow and temperature fields in the enclosure can be approximated as two dimensional.

In the present study the control-volume finite-difference method as described by Yang et al. (1987) is utilized. Two issues, however, need to be addressed regarding boundary conditions and the usual assumption of two dimensionality. As discussed by Yang (1987), the specification of thermal boundary conditions in simulating experimental work has always been difficult. It is due in part to the fact that experimentally the lateral walls are neither perfectly insulated, nor perfectly conducting. Several studies have discussed this problem (Kim and Viskanta, 1985; Kaminski and Prakash, 1986), and it is clear that the thermal boundary conditions must be specified directly from the corresponding experiments if the numerical solution is to attempt to describe the physical experiment. In this work, the actual experimentally measured boundary conditions were employed in the numerical computations. For the isothermal hot and cold walls, the actual measured temperatures were used. For the lateral walls, we measured the surface temperature outside of the enclosure and then calculated the inside surface temperature utilizing a conduction analysis through the walls. Thus, the measured boundary conditions were employed.

A second important issue addresses the possibility of three-dimensional transitions. For tilted stationary enclosures, three-dimensional transition is known to be possible when the enclosure is heated from below (Yang et al., 1986; Hamady et al., 1989). Two-dimensional calculations are obviously not

Nomenclature

A_x = aspect ratio (height/width)
A_z = longitudinal aspect ratio (length/width)
g = gravitational acceleration, m/s^2
H = enclosure height ($H=D$), m
h = convective heat transfer coefficient, W/m^{2}K
k = thermal conductivity, W/mK
L = length of the enclosure, m
Nu = local Nusselt number, see Eq. (4)
$\overline{\mathrm{Nu}}$ = mean Nusselt number, see Eq. (5)
p = pressure
Pr = Prandtl number = ν/α
$\mathbf{r}$ = position vector, m
$\mathbf{R}$ = nondimensional position vector = $\mathbf{r}/H$
Ra = Rayleigh number = $g\beta H^3(T_H-T_C)/\alpha\nu$
Ra_r = rotational Rayleigh number = $\beta\Omega^2H^4(T_H-T_C)/\alpha\nu$
Re = rotational Reynolds number = $\Omega H^2/\nu$
t = time, s
T = temperature, °C
Ta = Taylor number = $4\Omega^2H^4/\nu^2$
x, y, z = coordinates in the x, y, and z directions
$\mathbf{v}$ = velocity vector, m/s
$\mathbf{V}$ = nondimensional velocity vector = $\mathbf{v}H/\alpha$
α = thermal diffusivity, m^2/s
β = volumetric thermal expansion coefficient, 1/K
ζ = nondimensional distance along the x direction = x/H
θ = nondimensional temperature = $(T-T_C)/(T_H-T_C)$
ν = kinematic viscosity, m^2/s
ρ = density, kg/m^3
τ = nondimensional time = $\alpha t/H^2$
ϕ = inclination angle between the cold surface and the horizontal direction, deg
ω = angular speed, s^{-1}
Ω = angular speed = $2\pi\omega$, rad/s

Subscripts

C = cold surface
H = hot surface
R = reference
r = rotation
s = surface

valid to predict such transitions. However, experimental observations have shown that such transitions do not occur in the range of parameters covered by the experiments in this study. Consequently, detailed numerical computations in this study have been carried out with the two-dimensional computer code. A uniform grid of 36×36 calculation cells for the square enclosure have been utilized, together with an additional grid of 18×38 to cover the thickness of the plexiglass plates for the lateral walls. A typical calculation to reach the periodic long-time solution takes approximately one hour CPU time on an IBM 3033 mainframe computer.

The validation studies of the present computer code have been given by Yang et al. (1988a) on three-dimensional vertical enclosures, and by Hamady et al. (1989) and Yang et al. (1988, 1986) on the tilted rectangular enclosure by comparing numerical results with the corresponding experimental data. In the present study, as will be seen later, good agreement between the numerical calculations and the experimental data has been achieved. This observation, coupled with validation studies as mentioned above, which utilized grids up to 120×120, clearly demonstrated that the 38×38 grid provided for a sufficient degree of grid independence of the results. It was not necessary to go to finer grids to capture the physics of the problem studied.

Experimental Apparatus and Procedure

The experimental apparatus employed in this study is shown in Fig. 2. The test section consists of two vertical aluminum plates and two horizontal plexiglass plates, which are contained inside the rotating frame. The internal dimensions of the enclosure are $5.08 \times 5.08 \times 50.80$ cm. Details of the apparatus and the experimental procedure were reported in previous studies by Hamady et al. (1989) and Hamady (1987) and hence will not be repeated here. It is worth mentioning the special problems of obtaining the thermocouple output and of accomplishing the connection of the hot and cold water to the rotating frame. A special slipring-brush assembly was used to transfer the thermocouple signals out of the rotating system. The slipring assembly is composed of four silver-plated copper rings, 28.575 cm in diameter and 0.635 cm square cross section. The brushes are made of silver graphalloy, and the brush holders are made of silver-plated brass spring stock to provide the required pressure for a good connection between the slipring assembly mounted on the rotating front wheel and the brushes, which are held by the moving frame. Thermocouple readings were taken with and without rotation to examine the frictional heat effect between the slipring and the brushes. However, in all the cases the thermocouple readings were found to vary by less than $\pm 0.05°C$, which is within the accuracy of the meter employed.

The differentially heated plates of the test section are maintained at isothermal temperature distributions by circulating hot and cold water insides the plates. Water entered the rotating system through a four-channel rotary union mounted on the back side wheel (see Fig. 2). The rotary union was designed specifically for this experiment in order to avoid any leakage. More details are given by Hamady (1987).

The rotating apparatus is driven by a 1/4 hp (1750 rpm) DC motor equipped with a variable speed control. The speed of the rotating unit is varied between 0 and 17.5 rpm.

Local Nusselt numbers were calculated from the nondimensional temperature gradients along the heated walls multiplied by the ratio of the fluid thermal conductivity at the hot and cold surface, respectively:

$$\mathrm{Nu}(\zeta) = \left[\frac{k_H}{k_C} \frac{\partial (T - T_C)/(T_H - T_C)}{\partial (x/H)} \right]_s \tag{4}$$

and the average Nusselt number was determined by integrating

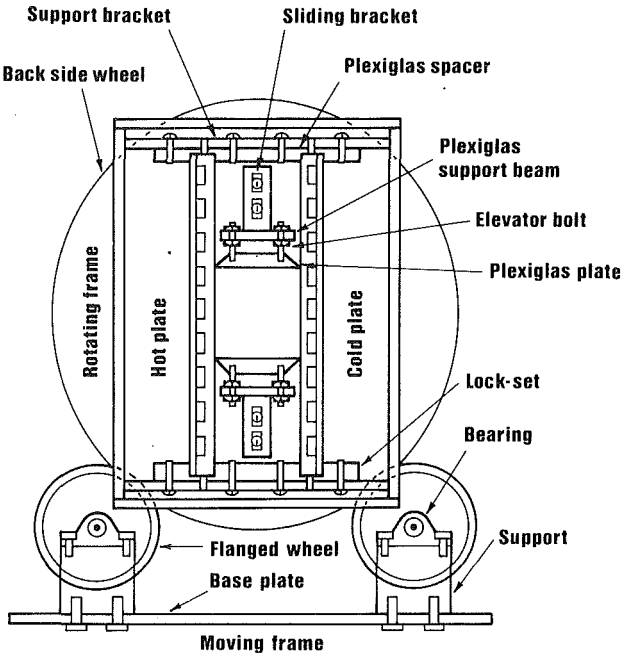

Fig. 2 Side view of test section inside the rotating frame

the local Nusselt number over the height of the enclosure surface:

$$\overline{\mathrm{Nu}} = \int_0^1 \mathrm{Nu}(\zeta) d\zeta \tag{5}$$

The errors in estimating the temperature gradient along the isothermal walls are within ± 3 percent, and the total error is on the order of ± 6 percent. Detailed error and interferogram analyses are given by Hamady (1987).

Finally, the requirement to obtain steady-state operating conditions was satisfied as follows. First, the experiment was operated for at least 4 hours. Then it was very essential to verify that: (*a*) thermocouple variations are no more than $\pm 0.1°C$ for at least a time span of 15 minutes and (*b*) the hot and cold walls temperature difference variations are not to exceed $\pm 0.05°C$ over a span of 15 min.

Results and Discussion

Rotation introduces two additional controlling body forces, which are expressed through the Taylor and rotational Rayleigh numbers. It is constructive to determine the relative importance of the various body forces. In the moderate and high Rayleigh number range, the dimensionless velocity along the isothermal walls can be scaled as (Yang, 1987),

$$V_r \propto \mathrm{Ra}^{1/2} \tag{6}$$

This suggests that the ratio of the Coriolis to the gravitational buoyancy force behaves as

$$\mathrm{Ta}^{1/2} V_r / \mathrm{Ra} \propto (\mathrm{Ta}/\mathrm{Ra})^{1/2} \tag{7}$$

Direct comparison of the Taylor and the Rayleigh numbers will give an indication of the dominance of either the Coriolis force (if $\mathrm{Ta}/\mathrm{Ra} > 1$), or the gravitational buoyancy force (if $\mathrm{Ta}/\mathrm{Ra} < 1$).

On the other hand, the ratio of the centrifugal force to the gravitational force is

$$1/2\, \mathrm{Ra}_r/\mathrm{Ra} = \Omega^2 H/(2g) \tag{8}$$

In the present experimental study, $H = 5.08$ cm and $\Omega = 2\pi\omega$ (ω is the rotational rate between 6.0–18 rev/min), so that

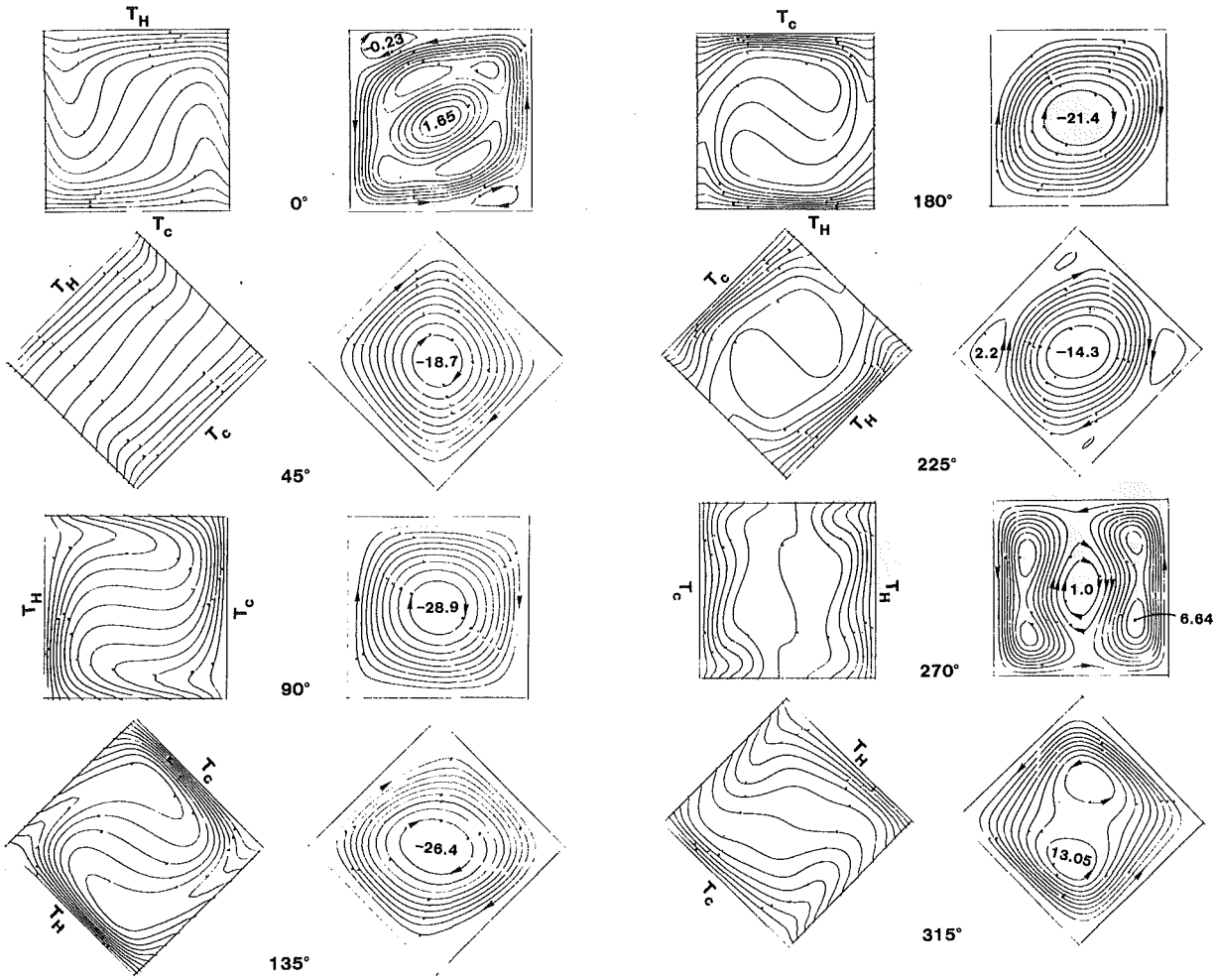

Fig. 3 Isotherms and streamlines at $Ra = 1.2 \times 10^5$ and $Ta = 8.9 \times 10^4$ ($\omega = 8.5$ rpm) at various angles

$$0.001 < \Omega^2 H/2g < 0.009 \quad (9)$$

which indicates that centrifugal forces are negligible. The real interaction is between the Coriolis and the gravitational buoyancy forces. The results from the computations will also demonstrate this point.

In what follows, the numerical results in terms of streamlines, isotherms, and heat transfer rates at various instantaneous angles are first shown and discussed in terms of the general physics in the rotational enclosure phenomena. The experimental data and direct comparison with the numerical results are then presented.

At the onset of this discussion it is important to gain an understanding of the overall behavior of the flow and thermal fields during rotation. To this end isotherms and streamlines at $Ra = 1.2 \times 10^5$ and $Ta = 8.9 \times 10^4$ ($\omega = 8.5$ rev/min) are shown in Fig. 3 for various angles during the rotation. Starting from 45 deg where the heated wall is above the cold wall, one observes a clockwise circulation induced by the buoyancy force. This motion persists up to 180 deg, after which the buoyancy force reverses the flow direction. In the range of angles up to 180 deg the physical behaviors are all essentially the same as for steady inclined enclosure (Zhong et al., 1985; Hamady et al., 1989). The Coriolis force, on the other hand, is directed into the core region according to $\mathbf{k} \times \mathbf{V}_r$, and tends to enhance the circulation. As a result, higher heat transfer is expected. The isotherms from 90 to 180 deg show properties similar to those in the inclined enclosure with boundary layers near the walls and stratification in the core. The streamlines show the unicellular motion. At a rotational angle of 225 deg, however, several mechanisms are acting. The effect of the gravitational buoyancy force now is to induce a counterclockwise circulation. However, the flow inertia from the clockwise circulation in the smaller angle region still persists. The Coriolis force, on the other hand, has an aiding effect on the clockwise motion. The resulting flow is thus a clockwise flow in the core and four counterclockwise cells in the corners where the effect of the Coriolis force is small. With increasing angle the gravitational force increases so that the size of the corner cells grows bigger. For an angle of 270 deg, the effect of the buoyancy force almost balances the effect of the inertial force of the clockwise circulation. The four corner cells combine into two, leaving a relatively weak motion of the original circulation in the center. At 315 deg, the transition from clockwise to counterclockwise motion is completed. It is interesting to note that the Coriolis force now is directed outward from the core and tends to stabilize the motion, thus reducing the heat transfer rate to the wall. This point can be well understood from the plots at 360 deg (0 deg) where the motion is so weak that the multicell structure is seen to exist in the core. At 45 deg, this motion rapidly changes to a clockwise circulation, which is comparable in character to the reverse transition found at 225 to 315 deg. Another interesting phenomenon to observe from the isotherms and the streamlines is their asymmetry with respect to the center of the enclosure, or the axis of rotation. This indicates the negligible effect of the rotational Rayleigh number here, which is the only term in the momentum Eqs. (3) that induces symmetry.

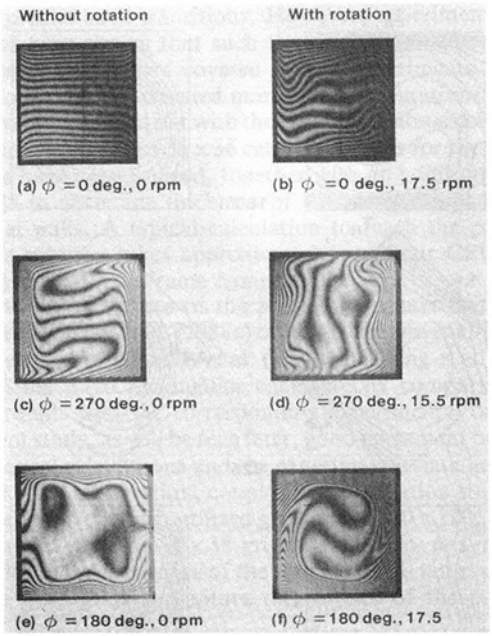

Fig. 4 Interference fringe patterns (isotherms) at Ra = 3.0 x 10^5: (*a*) $\phi = 0$ deg, 0 rpm; (*b*) $\phi = 0$ deg, 17.5 rpm; (*c*) $\phi = 270$ deg, 0 rpm; (*d*) $\phi = 270$ deg, 15.5 rpm; (*e*) $\phi = 180$ deg, 0 rpm; (*f*) $\phi = 180$ deg, 17.5 rpm

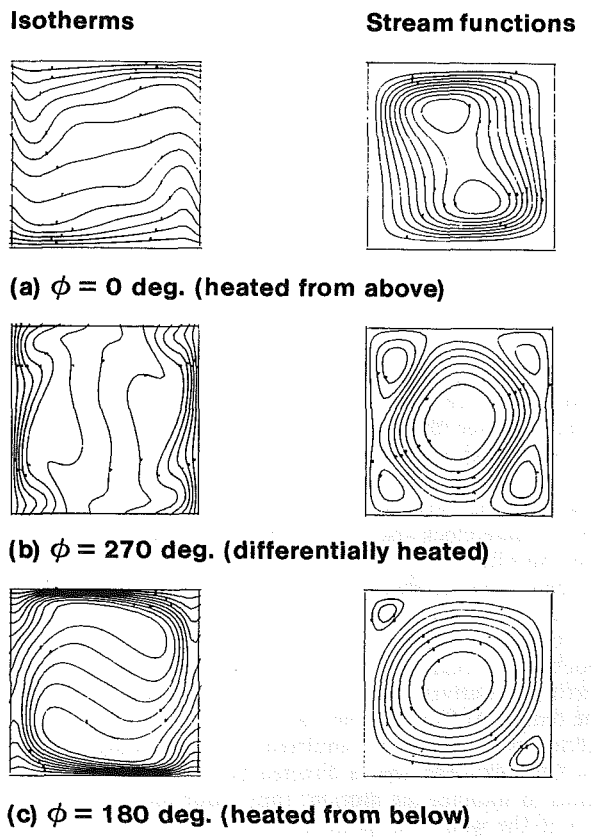

Fig. 5 Isotherms and stream functions at Ra = 3.0 x 10^5 and rotational rate $\omega = 15.5$ rpm: (*a*) $\phi = 0$ deg (heated above, cooled below); (*b*) $\phi = 270$ deg (heated and cooled on sides); (*c*) $\phi = 180$ deg (heated below, cooled above)

Figures 4 and 5 compare isotherms from numerical calculations and experiment for similar operating conditions. Measured boundary conditions were used in the calculations as was discussed previously. Also shown in Fig. 5 are the comparable streamlines. It is seen that the numerical and experimental isotherms compare very favorably. Also, the relation between the isotherms and the flow patterns can be observed. These comparisons of isotherm patterns gives a good qualitative observation on the validity of the numerical computations.

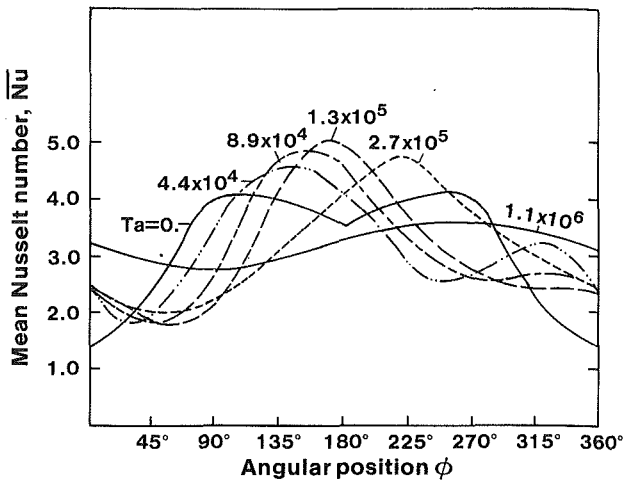

Fig. 6 Average Nusselt number as a function of angular position for various Taylor numbers

The average Nusselt number at $Ra = 1.2 \times 10^5$ over one cycle for several rotational speeds (Taylor numbers) is shown in Fig. 6. The curve for $Ta = 0$ is for the nonrotating inclined enclosure, which has been well documented from 0 to 180 deg, while the distribution from 180 to 360 deg is shown here as symmetric with respect to 180 deg (heated from below). It is to be pointed out that these curves are based on two-dimensional calculations, and so they can be meaningfully compared with the two-dimensional flows found experimentally in the rotating enclosure. For $Ta = 8.9 \times 10^4$, one sees that there is a shift of about 40 deg in the angular location of the peak Nusselt number, and that the local maximum heat transfer is higher due to the aiding effect of the Coriolis force in this range. The interaction of the gravitational, inertial, and Coriolis forces gives rise to a decrease in Nusselt number in the range from 180 to 270 deg, where the Coriolis buoyancy force starts to become important. The second local maximum in the Nusselt number, located now at almost 360 deg, is much lower than the one at $Ta = 0$, which indicates a relatively slow flow. For different rotational speeds the Nusselt number profiles show different characteristics. The basic trend is that with an increase of rotational speed (Taylor number), the angular phase shift becomes larger, and the local maxima increase up to about $Ta = 1.3 \times 10^5$ and then decrease, while the secondary local maxima finally disappear as a result of the incomplete transition from clockwise motion to counterclockwise motion. Obviously, the Coriolis force plays an essential role in maintaining the clockwise motion. Finally, at $Ta = 1.1 \times 10^6$ ($\omega = 30.0$ rev/min), the distribution of Nusselt number approaches a nearly uniform value of $\overline{Nu} = 3.2 \pm 10$ percent throughout the full range of angles. Here the Coriolis force is dominant, and the flow is in clockwise circulation at all angles.

Next we consider both numerically and experimentally the local heat transfer distributions with an emphasis on the angular positions of 180, 270, and 360 deg. These angles are selected because they represent the base cases: heated from below, the basic differentially heated enclosure, and heated from above for the stationary enclosure.

(i) Angular Position of 180 deg (Heated From Below). The onset of cellular convection in a nonrotating enclosure results from the unstable temperature stratification in the vertical direction (Hamady, 1987). Accordingly, the effect of rotation on the onset of thermal instability can be analyzed here.

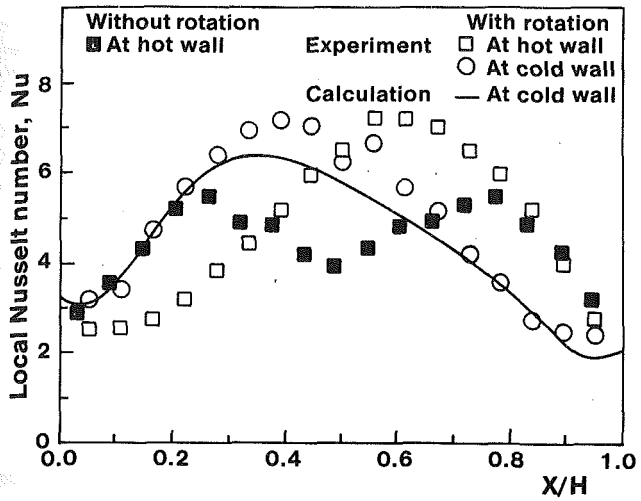

Fig. 7 Effect of rotation on the local Nusselt number distribution for air, at $Ra = 1.2 \times 10^5$, rotational rate = 8.5 rpm, and $\phi = 180$ deg (heated from below)

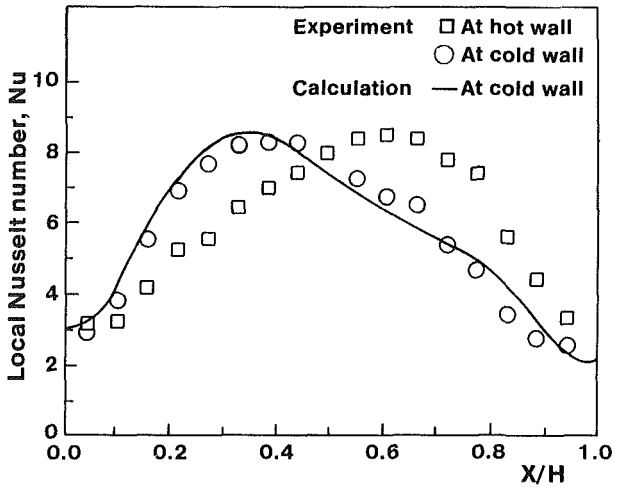

Fig. 8 Effect of rotation on the local Nusselt number distribution for air, at $Ra = 3.0 \times 10^5$, rotational rate = 8.5 rpm, and $\phi = 180$ deg (heated from below)

Local measurements of Nusselt number are used to interpret the developments that occur in the thermal boundary layer and the extent of inhibition of the onset of cellular motion.

The effects of rotation on the local distribution of Nusselt number are shown in Fig. 7 for $Ta = 8.9 \times 10^4$ ($\omega = 8.5$ rev/min), $Ra_r = 4.9 \times 10^2$ and $Ra = 1.2 \times 10^5$. It is evident from this figure that rotation produces a marked effect on the local heat transfer distribution as compared with the stationary experimental data. It is also apparent from the figure that the flow is unicellular, which has also been observed from the streamlines and the local Nusselt numbers from the numerical calculations. The increase in heat transfer is due to the Coriolis force, which has an additional effect on the thermal instability at this point as it is directed toward the core.

The local Nusselt number distributions for rotational rates of 8.5 and 11.2 rev/min, for a Rayleigh number of 3.0×10^5 are illustrated in Figs. 8 and 9. It is apparent that the distribution of heat transfer is almost the same as before, which means that the fluid motion is similar to that at the angular position of 90 deg (clockwise). An increase in heat transfer with increases in rotational speed and imposed temperature difference is detectable but not very marked. Also shown in Figs. 7, 8, and 9 are the corresponding numerical results at

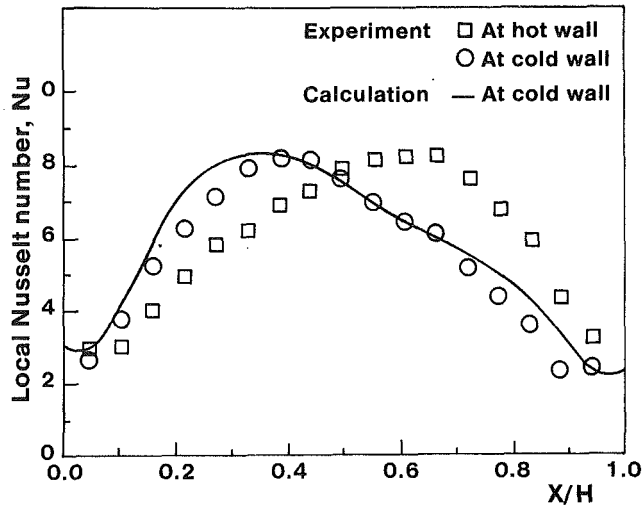

Fig. 9 Effect of rotation on the local Nusselt number distribution for air, at $Ra = 3.0 \times 10^5$, rotational rate = 12.2 rpm and $\phi = 180$ deg (heated from below)

the cold wall, again giving an indication of the validity of the numerical computations.

(ii) Angular Position of 270 deg (Vertical Enclosure). Figure 10 shows the variation of the local Nusselt number along the hot and cold surfaces under rotating and nonrotating conditions for a variety of rotation rates. Shown in the figure are the actual data plus the corresponding calculations of the cold wall. The calculated profiles are not presented for the hot walls for the sake of clarity, but it should be mentioned that the results show the same favorable comparisons between actual data and calculated profiles as is shown for the cold walls. The reduction in the local heat transfer at Taylor number of 4.4×10^4 ($\omega = 6.0$ rev/min) is evident when compared to the nonrotating results. The main flow in the core of the enclosure is counterclockwise. The decrease in heat transfer compared to that for the nonrotating enclosure is related to the stabilizing effects of the Coriolis force. The local heat transfer distribution along the cold wall from the numerical computations is also shown in the figure. Good agreement with the experimental data is found in this regard.

The complex interaction of the Coriolis and gravitational buoyancy forces commences to develop at Taylor numbers of 8.9×10^4 ($\omega = 8.5$ rev/min) and 1.3×10^5 ($\omega = 10.2$ rev/min) with a Rayleigh number of 1.2×10^5. This can be seen in Fig. 10 where two local maximum Nusselt numbers appear along the hot wall. The flow is now in the process of changing from a clockwise circulation to a counterclockwise one, which results from the interaction of the Coriolis and the gravitational buoyancy forces. This is characterized by the two cells each near the walls, as shown in Fig. 3 for the case of $Ta = 8.9 \times 10^4$. Again, the numerical results are found to match very well with the experimental measurements.

At a Taylor number of 1.8×10^5, which is higher than the gravitational Rayleigh number, one observes a totally different local heat transfer distribution in that the local maximum shifts from the lower region of the hot wall under the nonrotating condition to the upper region under the rotating effect. The flow circulation is now clockwise, which is the opposite direction of the buoyancy-driven flow. The clockwise circulation is indeed found in the calculation, and the corresponding heat transfer rates again compare well with the experimental data.

The local Nusselt number profiles are also shown at rotational speeds characterized by Taylor numbers of 2.7×10^5 ($\omega = 15.0$ rev/min) and 3.8×10^5 ($\omega = 17.5$ rev/min). The gen-

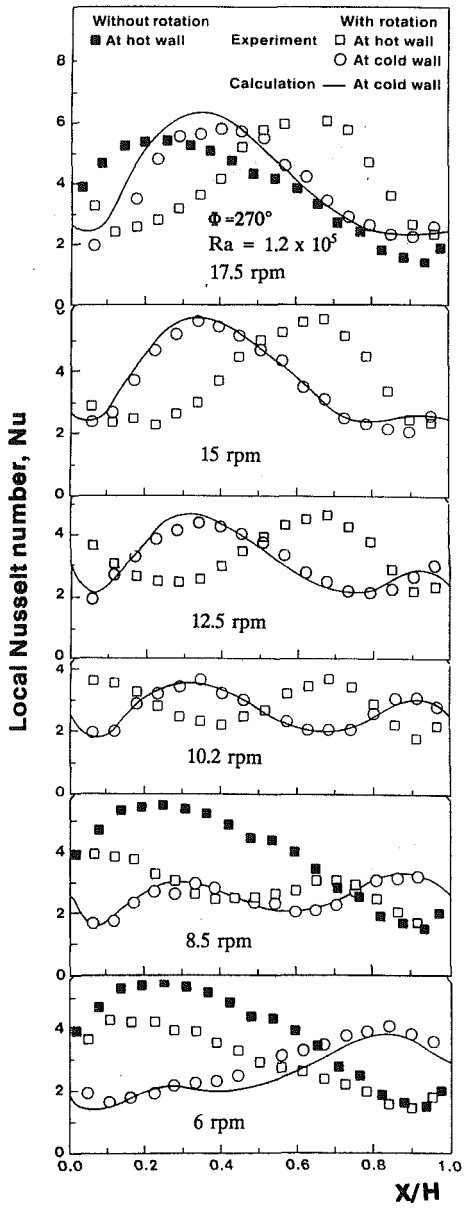

Fig. 10 Effect of rotation on the local Nusselt number distribution; $Ra = 1.2 \times 10^5$, $\phi = 270$ deg, $\omega = 6.0$, 8.5, 10.2, 12.5, 15, and 17.5 rpm

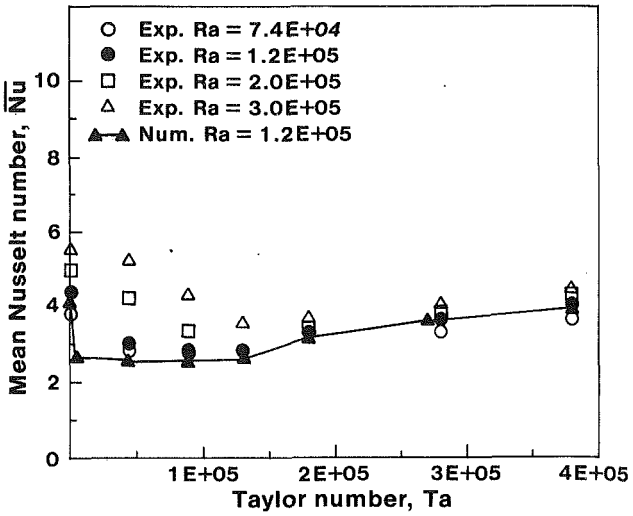

Fig. 11 Effect of rotation on mean Nusselt number for air, at $A_x = 1.0$ and $\phi = 270$ deg (vertical configuration)

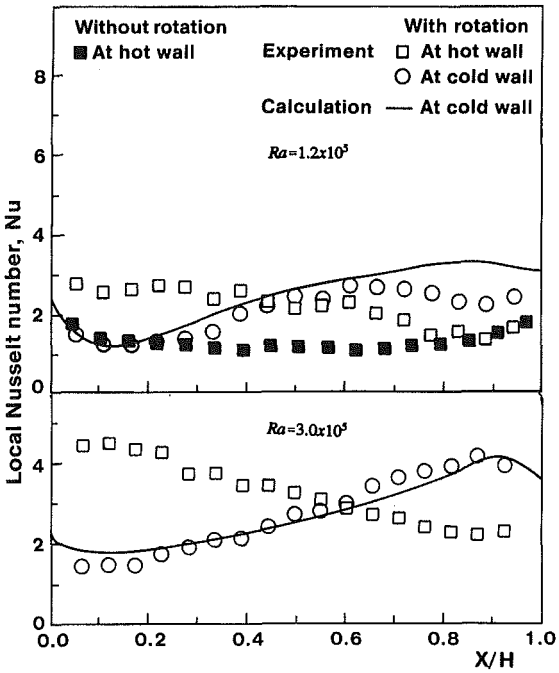

Fig. 12 Effect of rotation on the local Nusselt number distribution for air, rotational rate = 8.5 rpm and $\phi = 0$ deg (heated from above), $Ra = 1.2 \times 10^5$, 3.0×10^5

eral pattern of the local distribution of Nusselt number remains almost the same as that at $Ta = 1.8 \times 10^5$. It is readily observable, however, that the local heat transfer is enhanced with an increase of the rotational speed. This is because the Coriolis force tends to pull the flow toward the core and to accelerate the present clockwise circulation.

So far, the discussion has been focused on the influence of the controlling parameters arising from the rotation at a gravitational Rayleigh number of 1.2×10^5. An assessment of the effect of buoyancy interaction with Coriolis force on heat transfer will be presented in terms of the mean Nusselt number variations. Figure 11 illustrates the mean Nusselt number at 270 deg as a function of rotational speeds for various Rayleigh numbers. The general characteristics of the influence of Coriolis force are that the mean Nusselt number decreases first to a minimum and then starts to increase with rotational speed (Taylor number). The minimum varies with the Rayleigh number and corresponds to the balance of the effects of the interacting forces at the point of transition from clockwise motion to the counterclockwise motion. At a rotational speed below that for the minimum in the mean Nusselt number, the circulation is counterclockwise. The direction of Coriolis force is from the core region, so that both flow and heat transfer are reduced. When the Taylor number is larger than the Rayleigh number, the motion is clockwise, and the transition is prevented. The Coriolis force now tends to promote the flow circulation and therefore to increase the mean heat transfer. Nusselt numbers at the different Rayleigh numbers approach almost the same value with further increase in the rotational speed, due to the increasing dominance of the Coriolis force. The mean Nusselt numbers from the numerical calculations for $Ra = 1.2 \times 10^5$ are also shown in Fig. 11, and again the comparison is quite satisfactory.

(iii) Angular Position of 360 deg (0 deg Heated From Above). The flow and temperature fields in nonrotating enclosures heated from above are usually characterized by stable

stratification, which produces Nusselt number values that are approximately equal to one. Hence, as might be expected, any disturbance in the flow may cause an increase in the heat transfer. Since rotation is capable of disturbing the flow, it is not surprising to observe the significant effect on the heat transfer.

Figure 12 demonstrates the local variation in heat transfer from the experimental data and the numerical results, together with the experimental data in a nonrotating enclosure. The change in the heat transfer variations is quite evident. In Fig. 12 the fact that the Nusselt numbers are relatively uniform and lower than at other angles indicates relatively weak motion, which is confirmed from the calculations previously discussed in Fig. 3 for an angular position of 0 deg. Here the Coriolis force, which is comparable with the gravitational force, has a restricting influence on the flow motion, and the flow is in transition to the clockwise circulation. At a higher Rayleigh number ($Ra = 3.0 \times 10^5$), however, the restricting effects of Coriolis force are not important. The counterclockwise circulation of the flow is seen to persist, thus giving a higher local heat transfer rate on the lower portion of the hot wall.

Conclusions

The influence of rotation on the thermal and hydrodynamic boundary layers of a differentially heated enclosure is discussed as a function of Taylor and rotational and gravitational Rayleigh numbers as the controlling parameters. In view of the experimental and numerical results, the following features are noteworthy:

When the flow is driven primarily by gravitational buoyancy forces and is in the opposite direction of the rotation of the enclosure, the rotation increases the heat transfer and the stability of the flow. When the flow motion is in the same direction as rotation, a reversed effect of the Coriolis force occurs.

For an angular position of 270 deg (vertical enclosure), the Coriolis and buoyancy force interactions at first create a minimum heat transfer at a point where the Taylor number is comparable with the Rayleigh number. An increase in heat transfer was observed as the rotational speed increased. This was a result of the Coriolis force becoming stronger and therefore enhancing the circulation.

For an angular position of 180 deg (heated from below), it was found that rotation has a tendency to inhibit the onset of the longitudinal roll-cell convection, which is characteristically found in nonrotating enclosures. Also, a small increase in heat transfer was observed.

For an angular position of 360 deg (heated from above), an increase in heat transfer is detected with increases in the rotational speed. However, it is more markedly influenced by the imposed temperature difference.

Finally, progress has been made in describing quantitatively the heat transfer characteristics of rotating enclosures, but more study remains to be carried out. For instance, a study of the rotational effect on the flow and heat transfer at higher rotational speeds, where centrifugal Rayleigh number may become important, may give more physical insight of the interaction of the various controlling mechanisms.

Acknowledgments

The authors would like to express their gratitude for the support of the National Science Foundation under Grant No. CBT 82-19158, as well as to the Michigan State University and the University of Notre Dame for the use of their computing facilities.

References

Abell, S., and Hudson, J. L., 1975, "An Experimental Study of Centrifugally Driven Free Convection in a Rectangular Cavity," *Int. J. Heat Mass Transfer*, Vol. 18, pp. 1415–1423.

Buhler, K., and Oertel, H., 1982, "Thermal Cellular Convection in Rotating Rectangular Boxes," *J. Fluid Mech.*, Vol. 114, pp. 261–282.

Catton, I., 1970, "The Influence of Rotation on Natural Convection in Horizontal Liquid Layers," *Fourth International Heat Transfer Conference*, Paris–Versailles, Vol. IV, NC 4.1

Davis, T. H., and Morris, W. D., 1966, "Heat Transfer Characteristics of a Closed Loop Rotating Thermosyphon," *Third International Heat Transfer Conference*, Chicago, Paper 59, Vol. 2, pp. 172–181.

Greenspan, H. P., 1968, *The Theory of Rotating Fluids*, University Press, Cambridge, United Kingdom.

Hamady, F. J., 1987, "Experimental Study of Local Natural Convection Heat Transfer in Inclined and Rotating Enclosures," Ph.D. Dissertation, Michigan State University.

Hamady, F. J., LLoyd, J. R., Yang, H. Q., and Yang, K. T., 1989, "Study of Local Natural Convection Heat Transfer in an Inclined Enclosure," *Int. J. Heat Mass Transfer*, Vol. 32, No. 9, pp. 1697–1708.

Homsy, G. M., and Hudson, J. L., 1971, "Heat Transfer in a Rotating Cylinder of Fluid Heated From Above," *Int. J. Heat Mass Transfer*, Vol. 14, pp. 1149–1159.

Humphreys, J. F., Morris, W. D., and Barrow, H., 1967, "Convective Heat Transfer in the Entry Region of a Tube Which Revolves Above an Axis Parallel to Itself," *Int. J. Heat Mass Transfer*, Vol. 10, pp. 333–347.

Kaminski, D. A., and Prakash, C., 1986, "Conjugate Natural Convection in a Square Enclosure: Effect of Conduction in One Vertical Wall," *Int. J. Heat Mass Transfer*, Vol. 29, pp. 1979–1988.

Kim, D. M., and Viskanta, R., 1985, "Effect of Wall Conduction and Radiation on Natural Convection in a Rectangular Cavity," *Numerical Heat Transfer*, Vol. 7, pp. 449–470.

Levy, E., Neti, S., Brown, G., and Bayat, F., 1986, "Laminar Heat Transfer and Pressure Drop in a Rectangular Duct," ASME JOURNAL OF HEAT TRANSFER, Vol. 108, pp. 350–356.

Mori, Y., Fukada, T., and Nakayama, W., 1971, "Convective Heat Transfer in a Rotating Radial Circular Pipe, 2nd Report," *Int. J. Heat Mass Transfer*, Vol. 14, pp. 1807–1824.

Mori, Y., and Nakayama, W., 1968, "Convective Heat Transfer in Rotating Radial Circular Pipes, 1st Report," *Int. J. Heat Mass Transfer*, Vol. 11, pp. 1027–1040.

Morris, W. D., 1965, "Laminar Convection in a Heated Vertical Tube Rotating About a Parallel Axis," *J. Fluid Mech.*, 21, Part 3, pp. 453–464.

Morris, W. D., 1981, *Heat Transfer and Fluid Flow in Rotating Coolant Channels*, Research Studies Press, a division of John Wiley, New York.

Neti, S., Warnock, A. S., Levy, E. K., and Kannan, K. S., 1985, "Computation of Laminar Heat Transfer in Rotating Rectangular Ducts," ASME JOURNAL OF HEAT TRANSFER, Vol. 107, pp. 575–582.

Rossby, H. T., 1969, "A Study of Bernard Convection With and Without Rotation," *J. Fluid Mech.*, Vol. 36, Part 2, pp. 309–335.

Schmidt, E. H., 1951, "Heat Transmission by Natural Convection at High Centrifugal Acceleration in Water-Cooled Gas-Turbine Blades, General Discussion in Heat Transfer," Inst. Engr. London, p. 361.

Veronis, G., 1966, "Motions at Subcritical Values of the Rayleigh Number in a Rotating Fluid," *J. Fluid Mech.*, Vol. 24, Part 3, pp. 545–554.

Veronis, G., 1968, "Large-Amplitude Bénard Convection in a Rotating Fluid," *J. Fluid Mech.*, Vol. 31, Part 1, pp. 113–139.

Yang, H. Q., Yang, K. T., and Lloyd, J. R., 1986, "Flow Transition in Laminar Flow in a Three-Dimensional Tilted Rectangular Enclosure," *Proc. 8th Int. Heat Transfer Conf.*, Vol. 4, pp. 1495–1500.

Yang, H. Q., Yang, K. T., and Lloyd, J. R., 1987, "Laminar Natural Convection Flow Transition in Tilted Three-Dimensional Longitudinal Enclosures," *Int. J. Heat Mass Transfer*, Vol. 30, pp. 1637–1644.

Yang, H. Q., Yang, K. T., and Lloyd, J. R., 1988a, "Three-Dimensional Buoyant Flow Transition in Tilted Enclosures," *Int. J. Heat Fluid Flow*, Vol. 9, No. 2, pp. 145–161.

Yang, H. Q., Yang, K. T., and Lloyd, J. R., 1988b, "Buoyant Flow Calculations With Non-orthogonal Curvilinear Coordinates for Vertical and Horizontal Parallelepipeds," *Int. J. Numer. Math. Engr.*, in press.

Yang, K. T., 1987, "Natural Convection in Enclosures," *Handbook of Single Phase Convection Heat Transfer*, Chap. 13, K. Kakac, R. K. Shah, and W. Aung, eds., Wiley-Interscience, NY.

Zhong, Z. Y., Yang, K. T., and Lloyd, J. R., 1985, "Variable-Property Natural Convection in Tilted Enclosures With Thermal Radiation," *Numerical Methods in Heat Transfer*, R. W. Lewis and K. Morgan, III, eds., Wiley, pp. 195–214.

Scattering Tomography and Its Application to Sooting Diffusion Flames

M. P. Mengüç
Professor.

P. Dutta
Graduate Student.

Department of Mechanical Engineering,
University of Kentucky,
Lexington, KY 40506

A new analytical tomographic reconstruction technique was developed for the determination of the extinction and scattering coefficient distributions in axisymmetric media. This method, called "scattering tomography," was tested for several particle concentration profiles corresponding to those for diffusion flames. After that, a series of experiments were performed on sooting acetylene flames using an argon-ion laser nephelometer. The experimental results were reduced using both the transmission and scattering tomography techniques to obtain the extinction coefficient profiles. It was shown that in the center of the flame, the results from these two approaches were in good agreement. Scattering tomography can be used to determine both the absorption and scattering coefficient distributions in the medium. In addition to that, it is preferable over the transmission tomography if the medium is optically very thin and particles are predominantly scattering.

1 Introduction

In high-temperature combustion systems such as furnaces and pulverized coal fired flames, radiation is the predominant mode of heat transfer (Viskanta and Mengüç, 1987). In order to account for the contribution of radiative transfer to total heat transfer in such systems, the radiative properties of combustion products, such as particles and gases, should be known correctly.

Because of the large uncertainty in shape and material properties, it is not always possible to calculate the radiative properties of particles theoretically. However, these properties can be determined from experiments. Here, laser or other light diagnostic techniques are used to measure the transmission and scattering characteristics of a cloud of particles, such as a particle-laden flame. Then, an inverse radiation analysis can be followed and "effective" radiative property distributions within the cloud can be determined using the measured radiosity data.

Most inverse analyses can be considered as optimization schemes, where the forward problem is solved several times using different sets of "guessed" properties until a given set yields reasonable agreement with the measured quantities. There are only a few inverse schemes where a direct relation between the measurements and the medium properties can be written explicitly. For example, for a simple homogeneous, absorbing, nonscattering medium, the inverse analysis is based on the Beer's law (see Viskanta and Mengüç, 1987). If the medium is radially nonhomogeneous and nonscattering, the Abel transform technique can be used to recover the absorption coefficient profiles (Cremers and Birkebak, 1966; Deutsch and Beniaminy, 1983). In addition to this approach, an algebraic "onion-peeling" technique (Chen and Goulard, 1976) or analytical tomographic reconstruction method (Ramachandran and Lakshminarayanan, 1971; Emmermann et al., 1980) can be used for such media. In tomographic methods, line of sight measurements are made at spatial and angular locations to get path integrated data for the parameters investigated. The mathematical basis for tomography was first introduced by Radon in 1917 (Deans, 1983), and a general discussion of different tomographic applications, especially for medical applications, was given by Barrett and Swindell (1981). The reviews and evaluations of these three techniques for absorbing media are available in the literature (Hughey and Santavicca, 1982; Chakravarty et al., 1988); therefore, there is no need to discuss them here.

If the medium is scattering and radially nonhomogeneous, none of the classical techniques would yield the complete radiative property data. It is important to realize that in many practical combustion systems scattering particles are present. In order to determine the effect of radiation transfer in such systems, both absorption and scattering coefficients of the particles should be known. Scattering characteristics of particles are usually more useful in investigating the change in particle size or agglomeration rate in flames. For example, the morphology of soot agglomerates can be determined from their scattering characteristics rather than the extinction coefficients (Charalampopoulos and Chang, 1991; Mengüç et al., 1992). Given this, it is desirable to develop accurate inversion algorithms that can be used to reduce the experimental data to determine the scattering coefficients and phase functions of particles in axisymmetric systems.

In a scattering medium, the transmission data would not be exclusively related to absorption profiles, and therefore cannot be used to determine particle concentration distributions. The measured transmitted intensities would include forward scattered energy, which might vary as a function of off-axis measurement locations, as the size, size distribution, shape, and optical properties of the particles would be different along the radius in an axisymmetric system. In order to account for the effect of forward scattering, some modifications to the transmission measurements are needed (Deepak and Box, 1978), or additional scattering measurements should be performed. However, the measured scattered intensity distribution is dependent on the extinction coefficient profile in the medium. This means that to separate the scattering coefficient profile from the extinction coefficient distribution in the medium, a complicated iteration scheme has to be followed. Such an approach was given by Manickavasagam and Mengüç (1993) for interpretation of ex situ experiments on coal particles suspended in a KBr matrix. Even though the medium studied was homogeneous in nature, the required data reduction scheme was extensive. Also, the analysis showed that without having additional scattering information, it is not possible obtain effective radiative properties of particles deterministically.

For scattering media, there are only a few inverse analyses

Contributed by the Heat Transfer Division and presented at the ASME National Heat Transfer Conference, San Diego, California, August 9–12, 1992. Manuscript received by the Heat Transfer Division August 1992; revision received April 1993. Keywords: Radiation, Thermophysical Properties. Associate Technical Editor: W. L. Grosshandler.

available in the literature. Agarwal and Mengüç (1991) used an exact analytical approach for homogeneous media with one and two orders of scattering. Mengüç and Manickavasagam (1993) extended this approach to radially nonhomogeneous media. An inverse radiation analysis based on a Monte-Carlo scheme was applied to multiple-scattering nonhomogeneous planar media (Subramaniam and Mengüç, 1991), and later extended to nonhomogeneous scattering media (Mengüç and Sitaraman, 1993).

The objective of the present study is to introduce a new analytical approach applicable to single scattering media. It is called "angular" or "scattering tomography"; the theory behind it was first introduced by Mengüç (1989). Later, an experimental system based on an argon-ion laser nephelometer was designed and the measurements were carried out on acetylene flames, where the extinction coefficient profile varied radially (Dutta, 1991). Both transmission and scattering tomography were utilized to determine the extinction coefficient distributions in the medium.

2 Analytical Formulation

An inverse radiation analysis is based on the radiative transfer equation (RTE), which is a mathematical expression of the conservation of energy principle applied to a monochromatic beam of radiation propagating in an absorbing, emitting, and scattering medium. In this section, first, the forward problem will be discussed and the governing equations will be introduced. Then the formulation for the inverse problem will be given. After that, the outline of the scattering tomography will be summarized.

2.1 Forward Problem. Consider a cylindrical and axisymmetric medium, as shown in Fig. 1. Assume that the medium is absorbing and anisotropically scattering and its optical thickness is low ($\tau \leq 0.1$) so that the single scattering approximation can hold. Suppose a collimated light source is incident on the medium at C, which is off the center of the medium by a distance x_0. The transmitted component leaves the medium at C'' and the light scattered from a small volume on the centerline at A leaves the medium at C'. If the distributions of the radiative properties, i.e., the absorption coefficient distribution $\kappa(s)$, the scattering coefficient distribution $\sigma(s)$, and the scattering phase function $\Phi(s, \phi)$ of the axisymmetric medium are known, the scattered intensity distribution outside the medium can be calculated, which yields the angular radiosity distribution on the detector plane at C' for all values of ψ. Here, s is general spatial coordinate, and ψ is the scattering angle (for azimuthally symmetric medium).

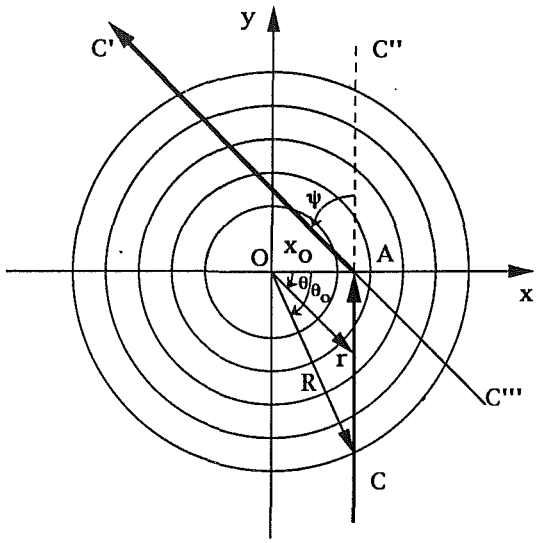

Fig. 1 Schematic for the physical system considered

Medium emission does not need to be considered if the incident beam is modulated using an optical chopper. The effects of second and other higher orders of scattering can also be neglected as the optical thickness is low. Thus only the radiation intensity along the line of sight of incident radiation contributes to the in-scattering term. Using the definition of the single scattering albedo as $\omega(s) = \sigma(s)/\beta(s)$ where $\beta(s)$ is the extinction coefficient, the governing radiative transfer equation can be written as

$$\frac{di}{ds}(s, \Omega) = -i(s, \Omega)\beta(s)\left[1 - \omega(s)\Phi(s, \psi = 0)\frac{\Delta\Omega}{4\pi}\right] \quad (1)$$

where $\Delta\Omega$ is the small solid angle in the forward direction. If an effective extinction coefficient is defined as:

$$\bar{\beta}(s) = \beta(s)\left[1 - \omega(s)\Phi(s, \psi = 0)\frac{\Delta\Omega}{4\pi}\right] \quad (2)$$

Equation (1) becomes:

$$\frac{di}{ds}(s, \Omega) = -\bar{\beta}(s)i(s, \Omega) \quad (3)$$

Nomenclature

A = area
a = spatial distance between successive increments; see Eq. (32)
F = optical system parameter used in Eq. (20)
I = angular radiosity, W/m^2
I_0 = power of the incident laser beam, W/m^2
i = intensity, W/m^2-sr
i_0 = incident laser intensity, W/m^2-sr
J = transmission functions, see Eq. (27)
K = number of angular orientations used, see Eq. (32)
K_s = system parameter $= \Delta\Omega_s\Delta\Omega_i\Delta A_l$
M = number of spatial increments used, see Eq. (32)
N = normalized transmission function, see Eq. (28)
N = number of Gaussian quadrature points, see Eq. (19)
P = projection intensity distribution, see Eq. (29)
R = radius of the cylindrical medium
S = stretch factor, see Eq. (9)
s = line-of-sight path
T = normalized angular radiosity, see Eq. (10)
ΔV = control volume $= \Delta A_l \Delta s$
x, y = coordinate axes
x_0 = radial location of the incident beam
β = extinction coefficient $= \sigma + \kappa$, m^{-1}
θ = general mapping angle, see Fig. 1
κ = absorption coefficient, m^{-1}
λ = wavelength
ξ = parameter defined in Eq. (30)
Σ = scattered energy, see Eq. (23)
σ = scattering coefficient, m^{-1}
τ = optical thickness
Φ = scattering phase function
ϕ = scattering angle measured from horizontal axis $= 90 - \psi$
φ = angle defined by Eq. (11); see Fig. 2
ψ = scattering angle; see Fig. 2
ω = single scattering albedo
$\Delta\Omega_i$ = solid angle of incident laser beam
$\Delta\Omega_s$ = detector solid angle

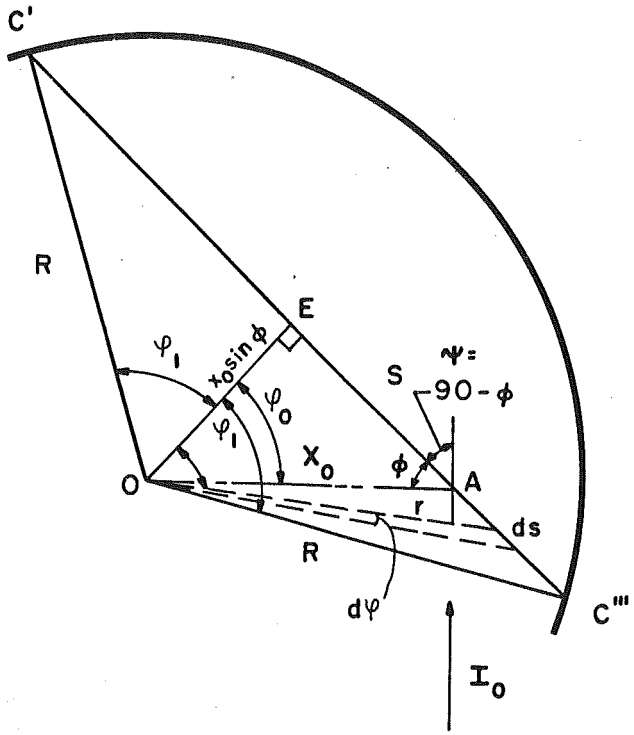

Fig. 2 Nomenclature for the analysis and mapping

Integration of Eq. (3) would yield the radiation intensity at any point along the direction Ω. The beam of light is attenuated along the path CA, scattered at A to all directions including the direction AC' and attenuated along the path AC'. The radiation intensity at point A is given by:

$$i_A = i_0 \exp\left[-\int_C^A \bar{\beta}(r)dy \right] \tag{4}$$

The relations between x_0 $(=OA)$, y, r, and R are given as:

$$R = \frac{x_0}{\cos\theta_0},\ y = r\sin\theta,\ dy = -\frac{x_0 d\theta}{\cos^2\theta} \tag{5}$$

where θ is measured in a clockwise direction starting from the horizontal axis. Using these definitions and normalizing Eq. (4), we obtain:

$$T_{CA} = \frac{i_A}{i_0} = \exp\left[-\int_0^{\theta_0} \bar{\beta}\left(\frac{x_0}{\cos\theta}\right)\frac{x_0}{\cos^2\theta}\,d\theta \right] \tag{6}$$

The angular radiosity at A toward the detector at C' (i.e., the integrated intensity within the small solid angle subtended by the detector) is given by:

$$I_A' = i_A \sigma(x_0)\frac{\Phi(x_0, \psi)}{4\pi} K_s \Delta s \tag{7}$$

where $K_s = \Delta\Omega_s \Delta\Omega_i \Delta A_l$. Here Δs is the length of the scattering volume, $\Delta\Omega_i$ is the solid angle for incident radiation, $\Delta\Omega_s$ is the solid angle for the scattered radiation and ΔA_l is the area of the cross section of the light source at A. The power of the incident laser beam per unit area is given by $I_0 = i_0 \Delta\Omega_i$, where i_0 is the laser beam intensity. The scattering volume ΔV is equal to $\Delta s \Delta A_l$, where Δs is a function of ψ. Note that the use of radiosity, which is energy per unit area, is consistent with what we measure from the experiments. The term "angular" radiosity is used to emphasize the fact that the integration is performed over a small solid angle subtended by the detector, which is located at a scattering angle of interest. Therefore, the angular radiosity is a function of x_0 and the scattering angle ψ.

The beam incident on to small volume element A in the medium is attenuated along the AC' path after scattering toward the detector. The angular radiosity at C' is expressed as:

$$I_{C'} = i_0 \sigma(x_0)\frac{\Phi(x_0, \psi)}{4\pi} \times K_s \Delta s \exp\left(-\int_A^{C'} \bar{\beta}(r)ds - \int_C^A \bar{\beta}(r)dy \right). \tag{8}$$

Two approaches may be adopted for calculating the radiation intensities at C'. The path AC' may be mapped on AC'' or the path CA may be mapped on $C'''A$ as shown in Fig. 1. For the application of tomographic reconstruction techniques, it is more convenient to adopt the latter approach, for which the detailed geometry is shown in Fig. 2.

For mapping CA onto $C'''A$, the stretch factor $\mathbf{S} = ds/dy$ must be evaluated. After a lengthy algebraic manipulation, it is found as:

$$\mathbf{S} = \frac{ds}{dy} = \frac{\sin\theta}{\sin\varphi} = \left(\frac{r^2 - x_0^2}{r^2 - x_0^2 \sin^2\phi} \right)^{1/2} \tag{9}$$

The stretch factor is a measure of how the properties along the CA path can be mapped onto the $C'''A$ path. As ϕ increases from 0 to 90°, $\mathbf{S}$ increases and achieves its maximum value of 1 at any x_0. Note that its value never exceeds 1.

The normalized angular radiosity is defined, starting from Eq. (8), as

$$T(x_0, \psi) = \frac{I_{C'}}{i_0 \sigma \dfrac{\Phi}{4\pi} K_s \Delta s} = \exp\left(-\int_A^{C'} \bar{\beta}(r)ds - \int_{C'''}^A \bar{\beta}(r)\frac{1}{\mathbf{S}}\,ds \right). \tag{10}$$

Gaussian quadrature schemes can be used to integrate the above equation. In order to do this, the parameter ds is to be replaced by $d\varphi$. Note that

$$\varphi = \arctan\left(\frac{s}{x_0 \sin\phi} \right) \tag{11}$$

The φ varies from $-\varphi_1$ to 0 to $+\varphi_1$ (i.e., positive in counterclockwise direction), where φ_1 is obtained from Fig. 2 for $\Delta OC''E$ as:

$$\cos\varphi_1 = \frac{x_0 \sin\phi}{R} \tag{12}$$

By differentiating Eq. (11) and rearranging, the relation between $d\varphi$ and ds is established:

$$ds = \frac{x_0 \sin\phi}{\cos^2\varphi}\,d\varphi \tag{13}$$

Now define

$$\bar{\varphi} = \varphi/\varphi_1, \tag{14}$$

and

$$\bar{\beta}'(r, \varphi_0) = \frac{\bar{\beta}(r)}{\mathbf{S}},\ \text{if}\ \bar{\varphi}\cdot\varphi_1 < \varphi_0 \tag{15}$$

$$\bar{\beta}'(r, \varphi_0) = \bar{\beta}(r),\ \text{if}\ \bar{\varphi}\cdot\varphi_1 > \varphi_0 \tag{16}$$

where $\varphi_0 = \arccos(\sin\phi)$. Using

$$r = x_0 \sin\phi/\cos\varphi \tag{17}$$

the modified stretch factor is given as

$$\mathbf{S} = \left(\frac{\sin^2\phi - \cos^2\varphi}{\sin^2\phi \sin^2\varphi} \right)^{1/2} \tag{18}$$

Equation (10) can be expressed in terms of an N point Gaussian quadrature scheme as:

$$T=\exp\left(-x_0 \sin\phi \arccos\left(\frac{x_0 \sin\phi}{R}\right)\sum_{i=-N}^{N}\frac{\overline{\beta_i'}\,w_i}{\cos^2(\overline{\varphi_i}\varphi_1)}\right) \quad (19)$$

where w_i are the weights of the quadrature scheme. This transformation is the backbone of the scattering tomography.

2.2 Inverse Problem. The inverse problem consists of determining the radiative property distributions within the medium from the experimentally measured light intensities outside the medium. In the classical tomographic reconstruction technique (i.e., transmission tomography), several line-of-sight measurements, called projection intensity data, obtained from experiments are used to determine the arbitrary absorption coefficient distribution in both symmetric and nonsymmetric media (Ramachandran and Lakshminarayanan, 1971). The change in radiation intensity as a light beam moves through the medium is recorded at M radial locations and at K angular orientations. For an absorbing medium, transmitted light incident on the detector can be calculated from the Beer law:

$$\frac{I_1}{i_0 F}=\exp\left(-\int_s\sum_j N_j C_{a,j}ds\right)=\exp\left(-\int_s \kappa(s)ds\right) \quad (20)$$

Here, N_j is the number density distribution of particles, $C_{a,j}$ is the absorption cross section corresponding to particle size j, $\kappa(s)$ is the absorption coefficient, s is the path length of radiation, and F is the parameter to take into account the effects of the solid angle of detectors, size of apertures, etc. In these relations, although not shown explicitly, all parameters are wavelength dependent. Note that the left-hand side of Eq. (20) is similar to the normalized angular radiosity given by Eq. (10). Therefore, the arguments of the exponential terms of Eqs. (10) (or (19)) and (20) are similar. This means that a classical tomographic reconstruction technique used to recover absorption coefficient profile can be employed to recover the argument of Eq. (19).

Equation (20) may be rewritten as

$$-\ln\frac{I_1}{i_0 F}=P(r,\theta)=\int_s \kappa(x,y)ds \quad (21)$$

where $\kappa(x,y)=\sum_j N_j(x,y)C_{a,\lambda,j}(x,y)$. Once the line-of-sight readings are obtained for M spatial and K angular locations, the absorption coefficient distribution can be determined. For an axisymmetric medium, one set of spatial and angular measurements may be used to calculate data for all other orientations (Emmermann et al., 1980).

2.3 Scattering Tomography. As can be seen from Fig. 2, when the path CA of scattered light is mapped onto path $C'''A$, the scattered intensity data recorded at C' can be reduced to line-of-sight data. Then this information can be used to determine both the extinction and scattering coefficient profiles in the medium. Following is the derivation of the governing equations for the scattering tomography.

Let two collimated light beams be incident on the medium at $+x_0$ and $-x_0$ as shown in Fig. 3. If the same scattering angles ψ are considered, the scattering terms will be the same for both beams. Let the initial intensity be I_0 and the detected intensities at D^+ and D^- be denoted by I^+ and I^-, respectively. These beams will be absorbed and scattered by the medium along their respective paths. Now assume that two separate detectors are located on an optical platform around the medium. They are arranged in such a way that each one is focused on a small control volume (A^+ or A^-) at the medium centerline to detect the scattered light at a scattering angle ψ. Each of them sees about the same size scattering volume, and by rotating the optical table, scattering at different angles can be obtained. If the medium is axisymmetric, each light beam is attenuated equally along the path from the medium boundary to the centerline:

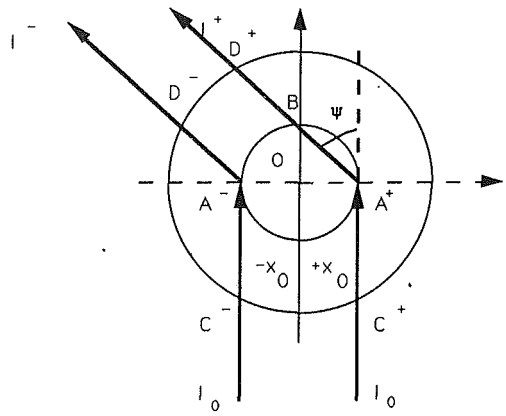

Fig. 3 Nomenclature for the scattering tomography

$$\int_{C^-A^-}\beta dy=\int_{C^+A^+}\beta dy \quad (22)$$

Also, the light scattered at a fixed angle ψ will be the same:

$$\Sigma(-x_0,\psi)=\Sigma(+x_0,\psi)=\sigma(x_0)\frac{\Phi(x_0,\psi)}{4\pi}K_s\Delta s \quad (23)$$

where $\Sigma(x_0,\psi)$ represents the amount of energy scattered toward the detector (see Eq. (7)). A careful examination of the symmetry reveals that the attenuation of the first beam along the A^-D^- path is equal to the attenuation of the second beam along the BD^+ path:

$$\int_{A^-D^-}\beta ds=\int_{BD^+}\beta ds \quad (24)$$

Now, we can write angular radiosity detected by each detector as:

$$I^-=i_0\Sigma(-x_0,\psi)\exp\left(-\int_{C^-A^-}\beta dy-\int_{A^-D^-}\beta ds\right) \quad (25)$$

$$I^+=i_0\Sigma(+x_0,\psi)\exp\left(-\int_{C^+A^+}\beta dy-\int_{A^+B}\beta ds-\int_{BD^+}\beta ds\right) \quad (26)$$

We define transmission functions as

$$J^+=\frac{I^+}{i_0\Sigma(+x_0,\psi)}\ \text{and}\ J^-=\frac{I^-}{i_0\Sigma(-x_0,\psi)} \quad (27)$$

which are obtained from Eq. (19) for scattering media. The ratio J^+/J^- becomes

$$N(x_0,\psi)=\frac{J^+}{J^-}=\frac{I^+/i_0}{I^-/i_0}=\exp\left(-\int_{A^+B}\beta ds\right) \quad (28)$$

The $N(x_0,\psi)$ function is equivalent to transmission function along the A^+B path of a secondary, axisymmetric cylindrical medium of diameter $2x_0$, shown by the inner circle in Fig. 2. If this procedure is repeated at several scattering angles, the $N(x_0,\psi)$ function along the paths shown on Fig. 4(a) can be obtained. For an axisymmetric medium, the paths shown on Fig. 4(a) are equivalent to Fig. 4(b). Therefore, the extinction coefficient distribution within this secondary medium can be obtained using the classical tomographic reconstruction technique. Note that the range studied by the scattering tomography is limited to $2x_0$, which is determined by the location of

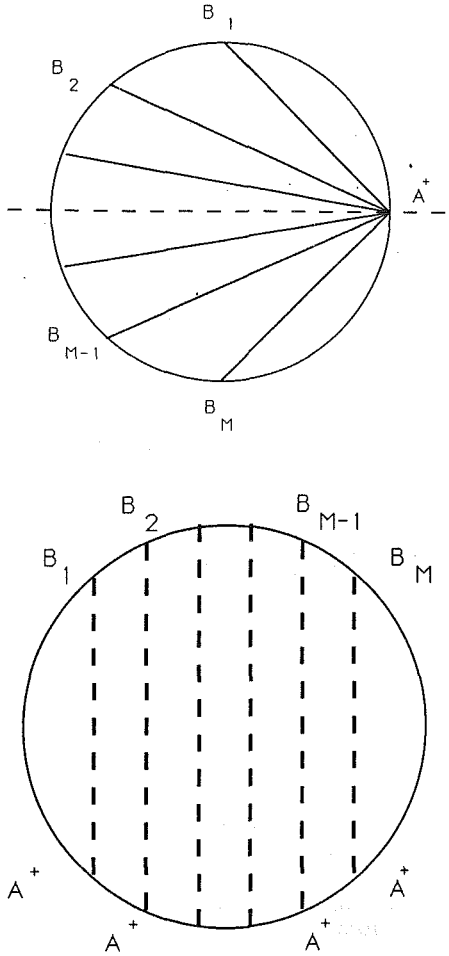

Fig. 4 Equivalence of scattered-beam paths to transmission paths

the laser beams incident on the flame. Although theoretically it is possible to claim that the maximum value of x_0 can be equal to the radius R of the medium, in experiments the maximum value is decreased dramatically because of factors such as beam diameter, refraction in the medium, etc. With increasing flame diameter, the x_0/R ratio increases (i.e., approaches 1), which makes the application of scattering tomography more feasible.

Now, another quantity $P(\xi, \psi)$ can be defined as:

$$P(\xi, \psi) = -\ln N(x_0, \psi) \tag{29}$$

where ξ is related to x_0 and the scattering angle ψ (see Figs. 1 and 2) and is given by

$$\xi = x_0 \cos \psi \tag{30}$$

$P(\xi, \psi)$ gives us one set of data at radial locations ξ and angle ψ (see Eq. (21)). For an axisymmetric system, this data can be extended to K angles and the projection intensities $P(r, \psi)$ can be obtained.

Following the convolution procedure of Ramachandran and Lakshminarayanan (1971), the following relations are written:

$$\bar{\beta}(r, \psi) = \frac{\pi}{M} \sum_{i=1}^{M} h(jr_0 \cos(\psi - i\phi_0), i\phi_0) \tag{31}$$

$$h(ma, \phi) = \frac{P(ma, \phi)}{4a} - \frac{1}{a\pi^2} \sum_{k,\text{odd}}^{K} \frac{1}{k^2} P((m+k)a, \phi) \tag{32}$$

where P is the projection intensity distribution (see Eq. (29)), a is the spatial distance between successive increments, m and k are the indices for the M spatial and K angular measurements, i is an integer, and r_0 and ϕ_0 are intervals of r and ϕ.

After recovering the β distribution, the $\sigma\Phi$ product can be obtained from Eqs. (23), (25), and (26). If the phase function is known, the scattering coefficient can readily be determined. Otherwise, the $\sigma\Phi$ product is to be integrated over the entire solid angle range (or, over 2π zenith angle for azimuthally symmetric phase functions) to obtain the local σ value. In order to obtain the scattering cross section, on additional experimental measurement is to be performed against a standard medium (for example, propane gas) to determine the system parameter $K\Delta s$ product. Also, any difference between the two incident beams has to be determined to reduce the measured data correctly. If only a single beam is used, there will be no need for this measurement. Here, we will concentrate only on the extinction coefficient profiles, as the rest of the calculations can be performed easily.

Preliminary calculations show that if x_0 is very close to the edge of the flame, the experimental data cannot be inverted accurately. For practical purposes, the scattering tomography is restricted to about 80 percent of the diameter of a medium if the absorption and scattering profiles are similar to those observed in diffusion flames.

3 Experimental Setup

The tomographic technique discussed in the previous section requires that two parallel collimated light sources be incident at two symmetrically off-center points in the medium. The intensity of light scattered from small control volumes on the centerline is to be recorded for both beams at different scattering angles.

Different approaches can be followed in order to achieve this objective. For example, a single laser beam can be used and the data can be recorded at different spatial locations one at a time. If the test medium is steady, this approach yields desired results with minimum cost. Instead of one beam, two beams can be used for simultaneous measurements at two spatial locations. For this purpose, a beam from a single laser may be split into two required beams. The simultaneity of the readings is achieved at the cost of using two choppers, two lock-in amplifiers, and also a different set of apertures for different scattering angles.

3.1 Optical Setup. The optical system designed for this study can be used with either one- or two-beam configurations (see Fig. 5). In the experiments, a single 5 W argon-ion laser at $\lambda = 514$ nm was used. Experiments carried out with two beams require two separate optical beam choppers (*CH*1 and *CH*2) to modulate each beam at a different frequency. Therefore, the two beams may later be separated from the same output using two lock-in amplifiers. The modulation of the beams also helps eliminate the medium emission contribution, undesired extraneous signals, and random noise from the recorded data. If one beam is used, only one chopper and one amplifier are needed.

The collection optics are mounted on an optical platform, which rests on a precision motorized rotary table (Newport, Model #496-A). The rotary table has a bi-directional, continuous 360 deg rotation, an accuracy of 0.01 deg, and a resolution of 0.001 deg. The optical platform is a circular aluminum piece mounted on the rotary table. It has a hole at the center through which the burner assembly may be moved up or down. The platform has four grooves cut on its upper surface for mounting optical rails. The first component of the collection system is the set of apertures mounted on the rail at a distance of 50 mm from the centerline of the flame (see Fig. 6). The separation between the two beams decreases as the scattering angle increases. As a result, different sets of apertures are required for different scattering angles. Apertures used are 0.0135″ (0.3375 mm) diameter holes drilled on thin aluminum pieces and separated by a distance of 1, 2, 3, 4, 5, 6, and 7 mm (Dutta, 1991). The scattering angles corresponding to these

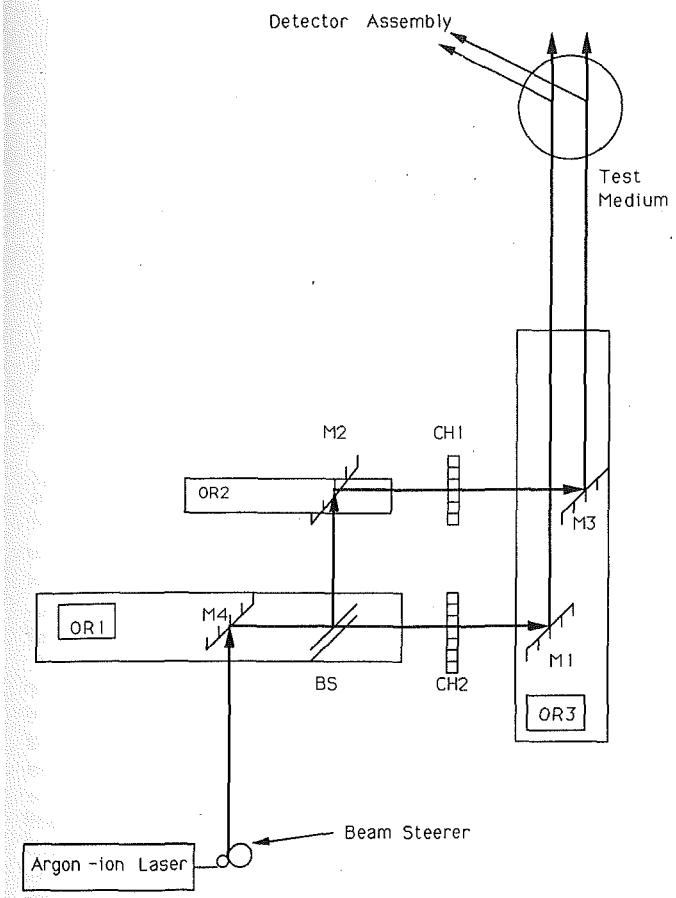

Fig. 5 Schematic for the optical system: *OR*: optical rail; *M*: mirror; *CH*: beam chopper; *BS*: beam splitter

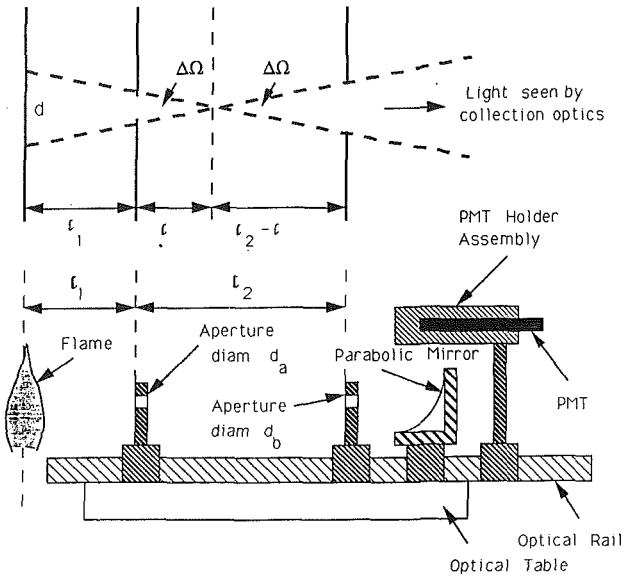

Fig. 6 Schematic for the light collection system

beam separations are predetermined to measure the scattered light intensities. For single-beam measurements, only one-hole apertures are employed. The solid angle seen by the collection system can be calculated using the aperture sizes and locations (see Fig. 6).

In the experimental setup, a parabolic mirror (Melles Griot, Model #02 POA 015) is used to focus both scattered beams onto the sensitive surface of a photomultiplier tube (PMT, RCA, Model #4840). The maximum angular deviation of the reflected ray from ideal path for this mirror is 6 arc-minutes. The voltage drop in PMT is amplified 10 times before it is fed to the lock-in amplifier. The output is directed to both lock-in amplifiers (Stanford Research Systems, Model #SR510), along with the reference signal from the choppers. The output of the lock-in amplifier is fed to a data acquisition system running on an IBM-PC/AT and recorded by the Labtech Notebook software.

3.2 Burner. A coflow diffusion flame burner is used; the details of the burner have been given by Mengüç et al. (1992). The burner consists of a central fuel tube surrounded by a co-annular oxidizer tube, having diameters of 1 cm and 5 cm, respectively. The overall height of the burner assembly is 35 cm. Diffusion flames produced on the burner would typically remain stable up to flame heights of 15 cm. The burner is mounted on a mechanism enabling vertical and horizontal translation. Acetylene (99.9 percent purity) and filtered shop air were used in the experiments.

4 Results and Discussion

Here, the theoretical comparisons for the scattering tomography will be presented only for the extinction coefficient profiles similar to those observed in sooting diffusion flames. After that, results from the experiments will be discussed.

4.1 Theoretical Results. The reconstruction process is a limited data problem and, therefore, it is sensitive to the sufficiency and accuracy of data. An increase in the spatial and angular resolution of data leads to more accurate results. The spatial resolution in the present technique is determined by the number of scattering angles considered. Two approaches can be followed in choosing the angles at which the measurements to be made. The angles may be selected to make the spatial distance between the "modified" projections (Eq. (29)) uniform or by using uniform angular increments. If the experiments are conducted using two beams, the former approach is preferable. This, however, requires the use of custom-made aperture pairs. If a single beam is used, uniform angular increments are easier to implement. The theoretical calculations were performed for both cases, and no drawbacks of one approach over the other were observed.

To simulate the absorption coefficient distribution in a flame, three different profiles were employed. A double bell shaped distribution was used with peaks near the edges and low values near the center, which is given by:

$$\beta(r) = r^2 - r^3 \tag{33}$$

Using this profile, first the projection intensities were generated by solving the forward problem. Then, this information was used for the retrieval of the medium properties. The exact and reconstructed profiles are shown in Fig. 7. The reconstructed curve follows the actual curve closely except near the centerline where the values of the extinction coefficient are low. The accuracy of the recovered values near the centerline is not important as the actual values are nearly zero.

Another extinction coefficient profile with a peak at the center, followed by a dip and an increase near the edge was also considered. The equation for this profile is given by:

$$\beta(r) = 1 - r^2 + r^3 \tag{34}$$

The comparison between the exact and recovered profiles is shown on Fig. 8. Except at the outer regions where there is a dip in the extinction coefficient, the reconstructed profile is good. If there is a rapid change in β profile near the periphery of the medium, the error in the recovered parameters increases. The reason for this is best explained using Fig. 1. If x_0 is large, the path of the laser beam within the outermost layers is large

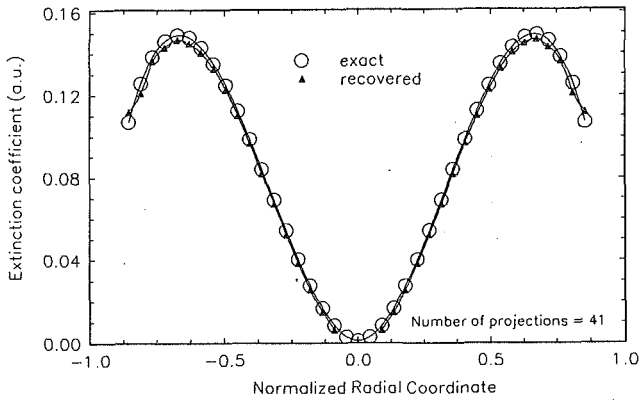

Fig. 7 Exact and recovered extinction coefficient profiles based on Eq. (33)

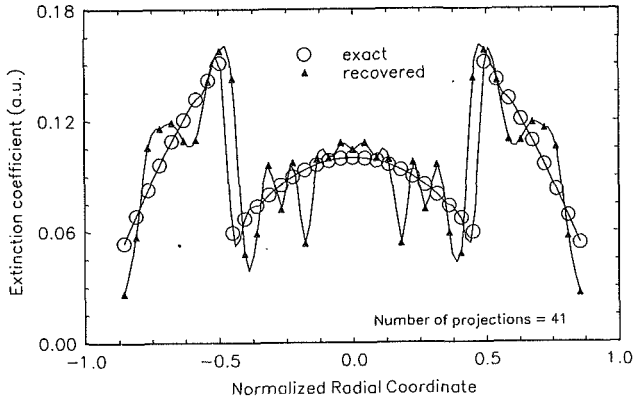

Fig. 9 Exact and recovered extinction coefficient profiles based on Eqs. (35)–(36)

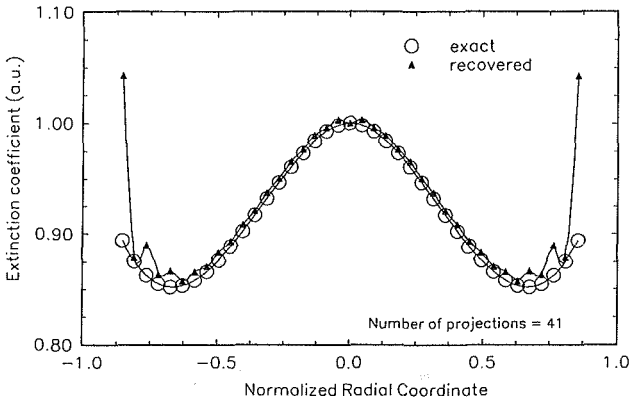

Fig. 8 Exact and recovered extinction coefficient profiles based on Eq. (34)

compared to that in the inner layers. In the model, the path in each layer is assumed homogeneous and based on a mean value. Therefore, the rapidly varying β is not accounted for correctly. The error in the transmission function propagates and affects the recovered β values. One can avoid this problem by dividing the medium in thinner circles as r increases. However, this is a tedious approach for both numerical studies and experiments.

Another extinction coefficient profile with very sharp changes was also considered:

$$\beta = 0.2(1 - r^2) \text{ for } r > 0.45 \quad (35)$$

$$\beta = 0.2(0.5 - r^2) \text{ for } r \leq 0.45 \quad (36)$$

The reconstructed profiles for this case are shown in Fig. 9. In this case, the recovered profile has sharp fluctuations. Again, the reason for this is the sudden change in the β profiles. Using a much finer spatial grid in the experiments (i.e., by making several measurements after moving light source horizontally infinitesimal amount), better results can be obtained. Also, use of filter functions to smooth the data will improve the accuracy (see, e.g., Hughey and Santavicca, 1982).

4.2 Experimental Results. The experiments were conducted on acetylene-air diffusion flames with a height of approximately 110 mm. The air flow rate was about 500 cc/s, which always yielded overventilated conditions to eliminate small fluctuations in the flame. The fuel flow rate was 4.4 cc/s.

At the burner base, the flame diameter was small and only about 10 mm. It decreased even further at the measurement plane. At the sooting heights, the flame was just 4–5 mm in diameter. Because of this, there were practical difficulties for the application of two-beam tomography. It appeared that for larger flames, the two-beam setup would work more reliably. Based on this, it was decided to perform experiments with only one beam, and sweep the flame by moving the burner to different locations. This horizontal movement was handled precisely by measuring displacements in the order of 0.2 mm. The beam splitter *BS* was taken off, and the beam was focused by a converging lens ($f = 750$ mm) to the flame. The beam diameter within the flame was about 0.8 mm.

Scattering data were collected between angles ranging from 40 deg in the forward direction to 140 deg in the backward direction, in intervals of 10 deg. The data beyond 150 deg could not be considered because at backward angles the collection optics comes in the way of the direct beam. Readings were not taken between 0 and 30 deg because there was a possibility of receiving some radiation from the forward-scattered light. The experimental data were smoothed using an available algorithm (subroutine E02BAF from NAG FORTRAN Library on the IBM 3090 main frame computer), which computes a weighted least-squares approximation to an arbitrary set of data points by a cubic spline. This smoothing eliminates the effects of a few "off" points on the accuracy of the retrieved results. In the inversion scheme, the smoothed J^+ and J^- profiles were employed.

One set of transmission and scattering measurements were performed at a height of 17 mm above the burner port. The width of the flame at that height was measured to be 8 mm. The off-center beam was at a distance of 2 mm from the centerline.

The extinction coefficient distributions obtained from transmission and scattering measurements are depicted in Fig. 10. Note that in reducing transmission data by classical tomography, ten angular orientations were assumed. This arbitrary number was chosen after comparing the results obtained from different numerical experiments performed earlier. In general, the agreement between data recovered from two different inversion techniques is very good. The profile recovered from experiments is similar to that depicted in Fig. 9. Extinction coefficient varies sharply in radial direction, which yields relatively more errors in the recovered profiles, especially toward the edges. However, in the center the error is smaller (see Fig. 9). Therefore, it is reasonable to claim that the profile recovered from experiments is more accurate near the center.

The range of the experimental data obtained from scattering tomography is small compared to that from transmission tomography. There were a few reasons for this. First of all, the physical size of the flame was quite small, which restricted the usable x_0/R range for a fixed laser size and optical parameters. Also, there were strong temperature and concentration gra-

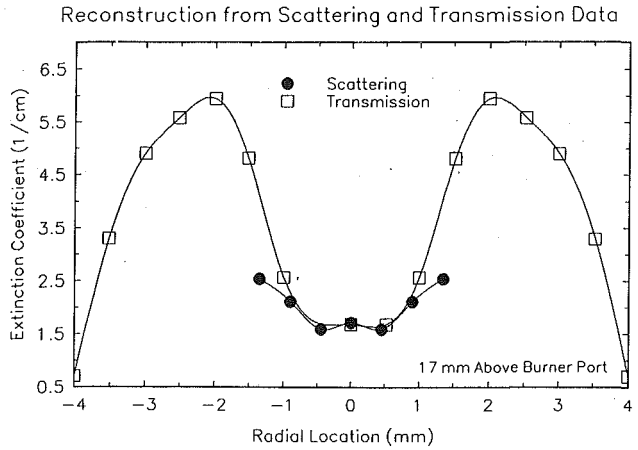

Fig. 10 Comparison of recovered extinction coefficient profiles from transmission and scattering tomography for the acetylene-air diffusion flame

dients, which caused beam refraction. Although the corrections for this problem could be made numerically, it required consideration of additional details unrelated to the idea tested here, and scattering tomography measurements were restricted to the inner zone of the flame where the optical thickness is not larger than 0.2 (see Fig. 10). Also note that the largest optical thickness in the flame is about 0.6, indicating the possibility of multiple scattering effects. However, given the fact that the scattering coefficient is smaller than the absorption coefficient of soot particles and agglomerates present in these flames, the error due to multiple scattering effects would not alter the result reported significantly.

5 Summary

In this study, a new inverse analysis, called scattering tomography, was applied to a scattering sooting diffusion flame. The experimental transmission and scattering signals obtained from an acetylene-air diffusion flame were employed to recover the extinction coefficient profiles using the transmission and scattering tomography, respectively. It was shown that the results from these experiments were in agreement with each other at the center of the flame. Additional theoretical calculations showed that unless there was a large increase or decrease in the extinction coefficient profiles, the scattering tomography yields accurate results.

The scattering tomography is the only analytical technique that can be used to obtain both scattering and extinction coefficient profiles in a radially nonhomogeneous media. As it is formulated, however, it cannot be used if the medium is multiple scattering. For such systems, a semi-analytical inversion scheme has been developed that accounts for two orders of scattering (Mengüç and Manickavasagam, 1993).

The advantage of scattering tomography over the classical transmission tomography can be realized for certain physical conditions. For example, if the particles are highly scattering but their concentration distributions are small, then the scattering tomography would be more reliable. Also, the scattering coefficient distribution can be obtained, which is not possible with the transmission tomography. This extra information can be used to characterize the morphology of particles in the medium.

Acknowledgments

This study is supported by the National Science Foundation Grant No. CBT-8708679 and the Department of Energy Grant No. DE-FG22-87PC79916. We would like to thank the anonymous reviewers, whose detailed and constructive comments and suggestions improved the paper significantly.

References

Agarwal, B. M., and Mengüç, M. P., 1991, "Forward and Inverse Analysis of Single and Multiple Scattering of Collimated Radiation in an Axisymmetric System," *International Journal of Heat and Mass Transfer*, Vol. 34, No. 3, pp. 633-647.

Barrett, H. H., and Swindell, W., 1981, *Radiological Imaging*, Academic Press, New York.

Chakravarty, S., Mengüç, M. P., Mackowski, D. W., and Altenkirch, R. A., 1988, "Application of Two Inversion Schemes to Determine the Absorption Coefficient Distribution in Flames," in: *1988 National Heat Transfer Conference Proceedings*, Vol. 1, H. R. Jacobs, ed., ASME HTD-Vol. 96, pp. 171-178.

Charalampopoulos, T. T., and Chang, R., 1991, "Agglomerate Parameters and Fractal Dimension of Soot Using Light Scattering: Effects on Surface Growth," *Combustion and Flame*, Vol. 87, pp. 89-99.

Chen, F. P., and Goulard, R., 1976, "Retrieval of Arbitrary Concentration and Temperature Fields by Multiangular Scanning Techniques," *J. Quant. Spectrosc. Radiat. Transfer*, Vol. 16, pp. 819-827.

Cremers, C. J., and Birkebak, R. C., 1966, "Application of the Abel Integral Equation to Spectroscopic Data," *Applied Optics*, Vol. 5, p. 1057.

Deans, S. R., 1983, *The Radon Transform and Some of Its Applications*, Wiley, New York.

Deepak, A., and Box, M. A., 1978, "Forwardscattering Corrections for Optical Extinction Measurements in Aerosol Media," *Applied Optics*, Vol. 17, pp. 2900-2908.

Deutsch, M., and Beniaminy, I., 1983, "Inversion of Abel's Integral Equation for Experimental Data," *Journal of Applied Physics*, Vol. 54, p. 137.

Dutta, P., 1991, "Application of Angular Tomography to Scattering Diffusion Flames," MSME Thesis, Department of Mechanical Engineering, University of Kentucky, Lexington, KY.

Emmermann, P. J., Goulard, R., Santoro, R. J., and Semerjian, H. G., 1980, "Multiangular Absorption Diagnostics of a Turbulent Argon-Methane Jet," *AIAA Proceedings*, Mar.-Apr., pp. 70-77.

Hughey, B. J., and Santavicca, D. A., 1982, "A Comparison of Techniques for Reconstructing Axisymmetric Reacting Flow Fields From Absorption Measurements," *Combustion Science and Technology*, Vol. 29, pp. 167-190.

Manickavasagam, S., and Mengüç, M. P., 1993, "Effective Optical Properties of Pulverized Coal/Char Particles Determined From FT-IR Spectrometer Experiments," *Energy and Fuels*, in press.

Mengüç, M. P., 1989, "Solution of the Inverse Radiation Problem to Determine Medium Radiative Properties In Situ," Final Report for Project No.: CBT-8708679, submitted to National Science Foundation, Washington, DC.

Mengüç, M. P., Mahadeviah, A., Saito, K., and Manickavasagam, S., 1992, "Application of the Discrete Dipole Approximation to Determine the Radiative Properties of Soot Agglomerates," Minisymposium in Fire and Combustion Systems, 1992 ASME/AIChE National Heat Transfer Conference, San Diego, CA.

Mengüç, M. P., and Manickavasagam, S., 1993, "Inverse Radiation Problem in Axisymmetric Cylindrical Scattering Media," *AIAA Journal of Thermophysics and Heat Transfer*, Vol. 7, No. 3, pp. 479-486; also in: *Fundamentals of Radiation Heat Transfer*, W. A. Fiveland, A. L. Crosbie, A. M. Smith, and T. F. Smith, eds., ASME National Heat Transfer Conference, Minneapolis, MN, HTD-Vol. 160, pp. 61-68, 1991.

Mengüç, M. P., and Sitaraman, S., 1993, "Inverse Monte-Carlo Technique for Cylindrical Media," in preparation.

Ramachandran, G. N., and Lakshminarayanan, A. V., 1971, "Three-Dimensional Reconstruction From Radiographs and Electron Micrographs: Application of Convolutions Instead of Fourier Transforms," *Proceedings of the National Academy of Sciences of USA*, Vol. 68, pp. 2236-2240.

Subramaniam, S., and Mengüç, M. P., 1991, "Solution of the Inverse Radiation Problem for Inhomogeneous and Anisotropically Scattering Media Using a Monte-Carlo Technique," *International Journal of Heat and Mass Transfer*, Vol. 34, No. 1, pp. 253-266.

Viskanta, R., and Mengüç, M. P., 1987, "Radiation Heat Transfer in Combustion Systems," *Progress in Energy and Combustion Sciences*, Vol. 13, pp. 97-160.

Optical Properties of Overfire Soot in Buoyant Turbulent Diffusion Flames at Long Residence Times

Ü. Ö. Köylü
Research Fellow.

G. M. Faeth
Professor.
Fellow ASME

Department of Aerospace Engineering,
The University of Michigan,
Ann Arbor, MI 48109-2140

The optical properties of soot were studied for the fuel-lean (overfire) region of buoyant turbulent diffusion flames in still air. Results were limited to the long residence time regime where soot structure is independent of position in the overfire region and residence time for a particular fuel. Measurements included scattering, absorption, and extinction cross sections at 514.5 nm and extinction cross sections at 632.8 and 1152 nm for flames fueled with acetylene, propylene, ethylene, and propane. The measurements were used to evaluate scattering predictions based on the Rayleigh–Debye–Gans (RDG) approximation for randomly oriented polydisperse fractal aggregates of spherical primary soot particles having constant diameters. The present soot aggregates exhibited significant departures from Rayleigh-scattering behavior at 514.5 nm, with forward scattering roughly 100 times larger than wide-angle scattering and ratios of scattering to absorption cross sections in the range 0.22–0.41, increasing with increasing propensity of the fuel to soot. The approximate RDG theory generally provided an acceptable basis to treat the optical properties of the present overfire soot aggregates, although additional measurements in the Guinier (small angle) regime are needed for a definitive evaluation of model performance.

Introduction

Soot optical properties must be understood in order to estimate continuum radiation from flames and to develop nonintrusive laser-based methods for measuring soot properties. Estimating soot optical properties is challenging, however, because soot structure is complex. In particular, although soot consists of small spherical primary particles that generally satisfy the Rayleigh scattering approximation, the primary particles collect into wispy aggregates that do not exhibit either simple Rayleigh or Mie scattering behavior (Erickson et al., 1964; Dalzell et al., 1970; Wersborg et al., 1973; Magnussen, 1974). In spite of the complexities, however, potentially effective theories of soot optical properties have been developed based on mass fractal concepts; see Jullien and Botet (1987), Martin and Hurd (1987), Dobbins and Megaridis (1991), and references cited therein. Nevertheless, these methods have not been directly evaluated at conditions where both soot structure and optical properties are known (Köylü and Faeth, 1993). Thus, the objective of the present investigation was to undertake such an evaluation by completing measurements of soot optical properties at conditions where Köylü and Faeth (1992) had recently completed measurements of soot structure. In addition, the existing theories were extended in order to resolve problems disclosed by the present evaluation.

The soot structure measurements of Köylü and Faeth (1992) were carried out in the fuel-lean (overfire) region of buoyant turbulent diffusion flames burning in still air within the long residence time regime, where characteristic flame residence times are roughly an order of magnitude longer than the laminar smoke point residence time. These conditions are of interest because overfire soot aggregates are large, providing a stringent test of theories of soot optical properties. Additionally, soot structure for a particular fuel in the long residence time regime is independent of position in the overfire region and residence time, which both simplifies measurements of optical properties and provides results of some general interest for studies of flame radiation. The structure measurements were carried out by thermophoretic sampling and analysis using transmission electron microscopy (TEM). The findings include fractal dimensions, and the probability density distributions of primary particle diameters and the number of primary particles in aggregates, for a variety of gaseous and liquid fuels. Present measurements included scattering, absorption, and extinction cross sections at 514.5 nm, and extinction cross sections at 632.8 and 1152 nm, for flames fueled with acetylene, propylene, ethylene, and propane.

The paper begins with descriptions of experimental and theoretical methods. This is followed by results, considering estimates of soot structure parameters from scattering measurements, angular scattering patterns, and extinction properties, in turn. The present discussion is brief, additional details, and a complete tabulation of data can be found in Köylü (1992).

Experimental Methods

Apparatus. A sketch of the test apparatus appears in Fig. 1. The arrangement was the same as for the soot structure measurements of Köylü and Faeth (1992) except for the presence of a soot collection system needed for the scattering measurements. Combustion was in still air with the burners located within a large enclosure (2.4 × 2.4 × 3.6 m high). The enclosure had a metal hood at the top and an adjustable exhaust system to collect and remove combustion products. The side walls of the enclosure were plastic strips to minimize effects of room disturbances. A water-cooled burner having an exit diameter of 50 mm, described by Sivathanu and Faeth (1990), was used to yield strongly buoyant, pool-like turbulent flames in the long residence time regime.

Soot optical properties were measured by collecting the combustion products in a heated sampling duct (to prevent thermophoretic deposition of soot on the duct surfaces). The duct had a 152-mm-dia exhaust at the top, which discharged into the main hood of the apparatus. Measurements showed that mixing within the heated duct was sufficient to yield uniform soot and gas species concentrations across the exit of the exhaust duct where the scattering and extinction measurements

Contributed by the Heat Transfer Division for publication in the JOURNAL OF HEAT TRANSFER. Manuscript received by the Heat Transfer Division August 1992; revision received May 1993. Keywords: Fire/Flames, Radiation, Radiation Interactions. Associate Technical Editor: W. L. Grosshandler.

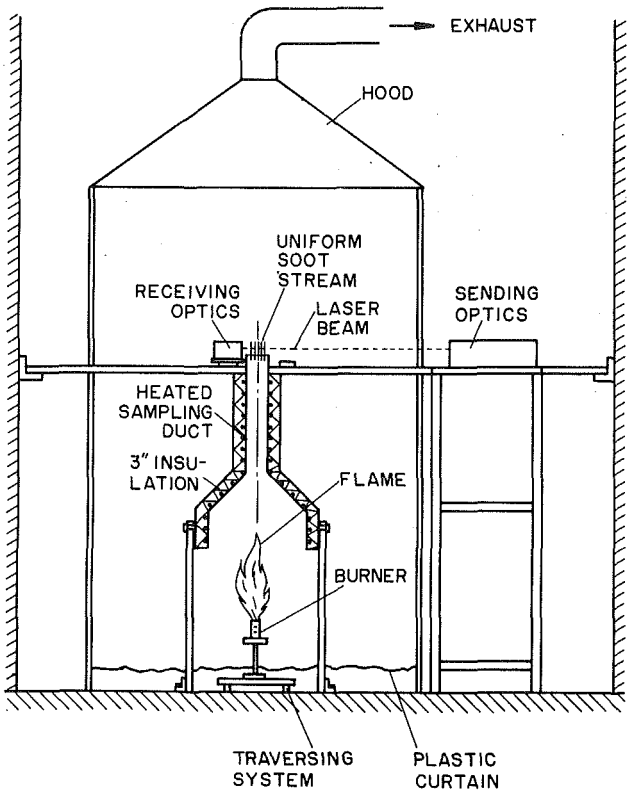

Fig. 1 Sketch of the experimental apparatus

were made. Note that since soot structure is independent of position in the overfire region at long residence time conditions, collection in this manner does not affect soot structure properties.

Scattering Measurements. An argon-ion laser having an optical power of 1.7 W at 514.5 nm was used for the scattering measurements. The incident laser beam was passed through a polarization rotator and a mechanical chopper (operating at 1250 Hz) before being focused at the center of the exhaust duct using a 1000 mm focal length lens. This yielded a waist diameter of 260 μm and a confocal length of roughly 400 mm. The collecting optics were mounted on a turntable surrounding the exhaust duct so that scattering angles, θ = 5–160 deg, could be considered. The collecting optics consisted of an 85 mm focal length lens, a dichroic sheet polarizer, a laser line filter (1 nm bandwidth), and a photomultiplier. The lens aperture defined a solid collection angle of 0.7 msr with a 1 mm long sampling volume at θ = 90 deg, which increased to roughly 11 mm at θ = 5 deg. Neutral-density filters were used in the optical path to control the dynamic range of detection. The experimental area as well as the receiving optics were covered with black cloth to reduce optical noise from the room lighting and the flame. The detector output passed through a lock-in amplifier and was stored on a computer, sampling at 500 Hz for 10 s and averaging five sampling intervals to achieve a repeatability within 10 percent.

The angular light scattering system was calibrated by measuring Rayleigh scattering from nitrogen gas. After correction for the reciprocal sin θ dependence of the scattering volume, the *vv* and *hh* differential cross sections were within 10 percent of Rayleigh scattering predictions for θ = 5–160 deg. Absolute volumetric differential scattering cross sections of soot were found from ratios of the detector signal for soot and nitrogen, after accounting for signal attenuation in the optical path for soot, based on the nitrogen optical properties of Rudder and Bach (1968). Total volumetric scattering cross sections were found by integrating the volumetric differential scattering cross sections over the whole spherical surface. This required extrapolation of the measurements to reach θ = 0 and 180 deg; however, uncertainties caused by the extrapolations were small due to the relatively small solid angle involved for forward scattering and the relatively slow variation of scattering with θ in the backward direction. The overall experimental uncertainties (95 percent confidence) of the angular and the total light scattering measurements were comparable and were estimated to be less than 20 percent, dominated by finite sampling

Nomenclature

C = optical cross section
d_p = primary particle diameter
D_f = mass fractal dimension
$E(m)$ = refractive index function = $Im((m^2 - 1)/(m^2 + 2))$
$f(q\,R_g)$ = aggregate form factor, Eq. (3)
f_{VA}, f_{VR} = soot volume fractions from aggregate and Rayleigh theories
$F(m)$ = refractive index function = $|(m^2 - 1)/(m^2 + 2)|^2$
$g(kR_g, D_f)$ = aggregate total scattering factor, Eq. (7)
i = $(-1)^{1/2}$
k = wave number = $2\pi/\lambda$
k_f = fractal prefactor, Eq. (1)
m = refractive index of soot = $n + i\kappa$
n = real part of refractive index of soot
n_a = mean number of aggregates per unit volume
n_p = mean number of primary particles per unit volume
N = number of primary particles per aggregate
N_c = aggregate size for onset of power-law regime, Eq. (16)
N_g = geometric mean number of primary particles per aggregate
$p(N)$ = probability density function of aggregate size
q = modulus of scattering vector = $2k \sin(\theta/2)$
Q = volumetric optical cross section
R_g = radius of gyration of an aggregate
x_p = primary particle size parameter = $\pi d_p/\lambda$
β = aggregate scattering parameter = $3D_f/(8k^2R_g^2)$
θ = angle of scattering from forward direction
κ = imaginary part of refractive index of soot
λ = wavelength of radiation
ρ_{sa} = ratio of scattering to absorption cross section
ρ_v = depolarization ratio
σ_g = geometric standard deviation of aggregate size distribution

Subscripts

a = absorption
d = differential
e = extinction
h = horizontal polarization
ij = incident (i) and scattered (j) polarization direction
s = total scattering
v = vertical polarization

Superscripts

a = aggregate property
p = primary particle property
$\bar{(\ )}$ = mean value over a polydisperse aggregate population

times, the finite aperture of the detector, and the angular uncertainty of the collecting optics.

Extinction Measurements. Volumetric extinction cross sections were measured at 514.5 nm using the argon-ion leaser, and at 632.8 and 1152 nm using 15 and 40 mW HeNe lasers, respectively. Laser power meters were used to measure the intensity of the beams before and after crossing the 152-mm-long path through the exhaust flow. The extinction ratio was found by sampling at 500 Hz for 20 s and averaging five sampling intervals to achieve a repeatability within 5 percent. Experimental uncertainties (95 percent confidence) of these measurements were generally less than 20 percent, largely controlled by the magnitude of the extinction ratio and finite sampling times. Volumetric absorption cross sections were found by subtracting the total scattering cross sections from the extinction cross sections, yielding uncertainties (95 percent confidence) generally less than 20 percent.

Theoretical Methods

General Description. Predictions of soot optical properties were based on methods described by Jullien and Botet (1987), Martin and Hurd (1987), and Dobbins and Megaridis (1991). These methods were extended, however, to improve the treatment of polydisperse aggregate populations in view of the large size and broad size distributions of the present overfire soot. Major assumptions with respect to aggregate structure are as follows: spherical primary particles having constant diameters, primary particles just touching one another, uniform refractive indices, log-normal aggregate size distributions, and the aggregates are mass fractal-like objects. The mass fractal approximation implies the following relationship between the number of particles in an aggregate and its radius of gyration (Jullien and Botet, 1987):

$$N = k_f (R_g/d_p)^{Df} \tag{1}$$

The assumptions of nearly constant diameter spherical primary particles, log-normal size distributions, and mass fractal-like behavior are justified by the soot structure measurements for present conditions (Köylü and Faeth, 1992). The remaining assumptions are typical of past treatments of soot optical properties; see Köylü and Faeth (1993) and references cited therein.

Scattering was found using the Raleigh–Debye–Gans (RDG) approximation where effects of multiple- and self-scattering are ignored so that the electric field of each primary particle is the same as the incident electric field, and differences of the phase shift of scattered light from various points within a particular primary particle are ignored. RDG scattering requires that both $|m-1| \ll 1$ and $2x_p|m-1| \ll 1$ (Kerker, 1969; van de Hulst, 1957; Bohren and Huffman, 1983), which is questionable for soot aggregates due to the relatively large refractive indices of soot. In addition, recent computational studies suggest significant effects of multiple scattering for aggregates typical of overfire soot; see Berry and Percival (1986), Chen et al. (1990), Ku and Shim (1992), and Nelson (1989). Thus, use of RDG theory can only be justified by its capabilities to treat measured soot optical properties effectively, which was the main motivation for the present investigation.

Single Aggregates. Under the present approximations, individual primary particles satisfy the Rayleigh scattering approximation, yielding the following expressions for their optical properties (Bohren and Hoffman, 1983; Kerker, 1969):

$$C_a^p = 4\pi x_p^3 E(m)/k^2,\ C_s^p = 8\pi x_p^6 F(m)/(3k^2),\ C_{vv}^p = x_p^6 F(m)/k^2 \tag{2}$$

where $C_{hv}^p = C_{vh}^p \approx 0$, $C_{hh}^p = C_{vv}^p \cos^2\theta$ and $C_e^p = C_a^p + C_s^p$. The cross sections in Eq. (2) will be used in the following to normalize aggregate optical cross sections. The treatment of aggregate optical properties will begin with the scattering cross sections found for fractal aggregates under the RDG approximation (Kerker, 1969):

$$C_{vv}^a(\theta) = C_{hh}^a(\theta)/\cos^2\theta = N^2 C_{vv}^p f(qR_g) \tag{3}$$

where the form factor, $f(qR_g)$, is expressed as follows in the Guinier (small-angle) and power law (large-angle) regimes, respectively (Jullien and Botet, 1987; Martin and Hurd, 1987; Dobbins and Megaridis, 1991):

$$f(qR_g) = \exp(-(qR_g)^2/3), \quad \text{Guinier regime} \tag{4}$$

$$f(qR_g) = (qR_g)^{-D_f}, \quad \text{power-law regime} \tag{5}$$

where the boundary between the Guinier and power-law regimes is taken to be $(qR_g)^2 = 3D_f/2$, following Dobbins and Megaridis (1991). Within the present approximations, $C_{hv}^a = C_{vh}^a = 0$ so that the differential scattering cross section for unpolarized light becomes:

$$C_d^a(\theta) = (C_{vv}^a(\theta) + C_{hh}^a(\theta))/2 = C_{vv}^a(\theta)(1+\cos^2\theta)/2 \tag{6}$$

The total scattering cross section can be found by integrating Eq. (6) over the whole spherical surface to yield:

$$C_s^a = N^2 C_s^p g(kR_g, D_f) \tag{7}$$

The aggregate total scattering factor, $g(kR_g, D_f)$, takes on different forms depending on whether the power-law regime is reached for $\theta \le 180$ deg, as follows:

$$g(kR_g, D_f) = 1 - 2(kR_g)^2/3,\ (kR_g)^2 \le 3D_f/8 \tag{8}$$

$$g(kR_g, D_f) = \frac{\beta}{2}(3 - 3\beta + 2\beta^2) - \frac{(kR_g\beta)^2}{3} \times (3 - 4\beta + 3\beta^2) + (2kR_g)^{-D_f} \left[\frac{3}{2-D_f} - \frac{12}{(6-D_f)(4-D_f)} - 3\beta^{1-D_f/2} \times \left(\frac{1}{2-D_f} - \frac{2\beta}{4-D_f} + \frac{2\beta^2}{6-D_f}\right)\right],\ (kR_g)^2 > 3D_f/8 \tag{9}$$

At this point, the present treatment departs from Dobbins and Megaridis (1991) for single aggregates, which was limited to the Guinier regime, i.e., Eq. (8).

Based on the simulations of Nelson (1989) and Chen et al. (1990), it is assumed that absorption is not affected by aggregation, yielding

$$C_a^a = N\, C_a^p \tag{10}$$

The extinction cross section is the sum of the absorption and scattering cross sections, i.e.,

$$C_e^a = C_a^a + C_s^a = NC_a^p(1+\rho_{sa}^a) \tag{11}$$

where

$$\rho_{sa}^a = \rho_{sa}^p\, Ng(kR_g, D_f) \tag{12}$$

The parameters ρ_{sa}^p and ρ_{sa}^a are the ratio of scattering to absorption cross sections for primary particles and aggregates, respectively. For aggregates, ρ_{sa}^a represents the error in soot volume fraction determinations when extinction measurements are processed using the Rayleigh scattering approximation (which implies $\rho_{sa}^a \approx 0$). At the limit of large aggregates, ρ_{sa}^a saturates to a value that is independent of N, where Eqs. (9) and (12) yield:

$$\rho_{sa}^a = \rho_{sa}^p k_f (4x_p)^{-D_f}(3/(2-D_f) - 12/((6-D_f)(4-D_f))) \tag{13}$$

This behavior is fundamentally different from Mie scattering for an equivalent spherical aggregate, where ρ_{sa}^a continues to increase as N increases, as discussed by Berry and Percival (1986), Nelson (1989), and Dobbins and Megaridis (1991).

Polydisperse Aggregate Populations. The mean optical cross sections of populations of randomly oriented polydis-

perse aggregates (polydisperse aggregates) are found by integrating over all aggregate sizes, as follows:

$$\overline{C}_j^a = \int_{N=1}^{\infty} C_j^a(N) p(N) dN; \quad j = pp, s, a \tag{14}$$

where $p(N)$ is the log-normal size distribution function from Köylü and Faeth (1992). Continuing the assumption that $C_{hv}^a = C_{vh}^a \approx 0$, the expression for the differential scattering cross sections of polydisperse aggregates becomes

$$\overline{C}_{vv}^a(\theta)/C_{vv}^p = \overline{C}_{hh}^a(\theta)/(C_{vv}^p \cos^2\theta) = \int_{N=1}^{N_c} N^2 \exp(-q^2 R_g^2/3) p(N) dN + \int_{N=N_c}^{\infty} N^2 (qR_g)^{-D_f} p(N) dN \tag{15}$$

where

$$N_c = k_f (3D_f/(2q^2 d_p^2))^{D_f/2} \tag{16}$$

is the aggregate size at the matching point between the Guinier and power-law regimes, and differs for each angle. Equation (15) must be integrated numerically for general variations of aggregate size and scattering angle; however, simple limits are obtained for the Guinier and large-angle regimes. In the Guinier regime, $p(N) \ll 1$ for $N \geq N_c$ and the contribution of the second integral in Eq. (15) is negligible, yielding (Guinier and Fournet, 1955):

$$\overline{C}_{vv}^a(\theta)/(\overline{N^2} C_{vv}^p) = 1 - q^2 \overline{R}_g^2/3 + \ldots \approx \exp(-q^2 \overline{R}_g^2/3), \quad \text{Guinier regime} \tag{17}$$

where

$$\overline{R}_g^2 = \int_{N=1}^{\infty} [R_g(N)]^2 N^2 p(N) dN / \int_{N=1}^{\infty} N^2 p(N) dN, \quad \text{Guinier regime} \tag{18}$$

In the power-law regime, $p(N) \ll 1$ for $N \leq N_c$ and the contribution of the first integral in Eq. (15) is negligible, yielding (Köylü, 1992):

$$\overline{C}_{vv}^a(\theta) \,/\, C_{vv}^p = \overline{N} k_f (qd_p)^{-D_f} = \overline{N^2} (q^2 \overline{R}_g^2)^{-D_f/2}, \quad \text{power-law regime} \tag{19}$$

where

$$\overline{R}_g^2 = \left[\int_{N=1}^{\infty} [R_g(N)]^{2D_f} p(N) dN / \int_{N=1}^{\infty} [R_g(N)]^{D_f} p(N) dN \right]^{2/D_f}, \quad \text{power-law regime} \tag{20}$$

The difference between the mean square radius of gyration in the Guinier and power-law regimes is expected because large aggregates dominate scattering at small angles while small aggregates contribute more to the scattering pattern at large angles. Thus, using one definition for $\overline{R}_g^2$ at all scattering angles is not correct. Furthermore, at any angle, some of the aggregates are in the Guinier regime while others are in the power-law regime; thus, the crossover between small- and power-law behavior is more gradual for polydisperse aggregate populations than for individual aggregates.

The total scattering cross section of polydisperse aggregates is found from Eqs. (7) and (14) as follows:

$$\overline{C}_s^a = C_s^p \int_{N=1}^{\infty} N^2 g(kR_g, D_f) p(N) dN \tag{21}$$

Equation (21) must be numerically integrated, using Eq. (1) to relate R_g and N, after substituting for $g(kR_g, D_f)$ from Eqs. (8) and (9) and introducing the log-normal function for $p(N)$.

The absorption cross section of polydisperse aggregates can be evaluated easily from Eqs. (10) and (14), as follows:

Table 1 Structure and optical cross section properties of overfire soot[a]

Fuel	Acetylene	Propylene	Ethylene	Propane
Primary Particles:				
d_p (nm)	47	41	32	30
x_p (-)	0.287	0.250	0.195	0.183
C_{vv}^p (nm^2/sr)	0.814	0.359	0.0811	0.0551
C_s^p (nm^2)	6.82	3.01	0.679	0.462
C_e^p (nm^2)	524	346	164	134
ρ_{sa}^p (-)	0.0132	0.0088	0.0042	0.0034
n_p (mm^{-3}) $\times 10^{-6}$	6.2	6.4	2.6	2.5
Aggregates:				
$\overline{N}$ (-)	417	400	467	364
$\overline{C}_{vv}^a(90°)$ (nm^2/sr)	3710	2370	1020	559
$\overline{C}_s^a$ (nm^2) $\times 10^{-3}$	92.9	55.0	21.8	10.4
$\overline{C}_e^a$ (nm^3) $\times 10^{-3}$	321	194	98.2	58.8
$\overline{\rho}_{sa}^a$ (-)	0.41	0.40	0.29	0.22
$\overline{\rho}_v^a$ (-)	0.041	0.033	0.028	0.022
n_a (mm^{-3}) $\times 10^{-3}$	14	16	5.5	6.8

[a]For buoyant turbulent diffusion flames in still air at long residence times with optical properties at 514.5 nm: structure properties from Köylü and Faeth, (1992); soot refractive indices used in the computations from Dalzell and Sarofim (1969).

$$\overline{C}_a^a = \overline{N} C_a^p \tag{22}$$

Similar to a single aggregate, the extinction cross section can be written in terms of the ratio of scattering to absorption cross sections, $\overline{\rho}_{sa}^a = \overline{C}_s^a/\overline{C}_a^a$, to yield:

$$\overline{C}_e^a = \overline{N} C_a^p (1 + \overline{\rho}_{sa}^a) \tag{23}$$

where $\overline{\rho}_{sa}^a$ reduces to ρ_{sa}^a from Eq. (13) at the limit of large monodisperse aggregates.

Results and Discussion

Optical Cross Sections. The measured volumetric optical cross sections were converted to optical cross sections using the approximation that absorption is not affected by aggregation. Then the number of primary particles per unit volume, n_p, can be computed from

$$n_p = \overline{Q}_a^a / C_a^p \tag{24}$$

C_a^p was found from Eq. (2), given d_p from the structure measurements, and adopting the refractive indices of Dalzell and Sarofim (1969), i.e., $m = 1.57 + 0.56i$ at 514.5 and 632.8 nm and $1.65 + 0.75i$ at 1152 nm. The Dalzell and Sarofim (1969) refractive indices were used to be consistent with Köylü and Faeth (1992); however, they also are preferred based on the present scattering measurements, as discussed later. Then, given $\overline{N}$ from the soot structure measurements, the mean number of aggregates per unit volume, n_a, can be found from

$$n_a = n_p/\overline{N} \tag{25}$$

yielding the optical cross sections as follows:

$$\overline{C}_j^a(\theta) = \overline{Q}_j^a(\theta)/n_a; \quad j = pp, s, a \tag{26}$$

Soot Structure Parameters. Reference soot structure and optical cross section properties at 514.5 nm are summarized in Table 1 for the four fuels. The table also includes the primary particle properties and the values of $\overline{N}$ that were used to find the optical cross sections of aggregates, as well as the resulting values of n_p and n_a. At 514.5 nm, x_p is in the range 0.183–0.287, which marginally places the primary particles in the Rayleigh scattering regime (Kerker, 1969). The values of $\overline{\rho}_{sa}^a$ are roughly two orders of magnitude larger than ρ_{sa}^p, highlight-

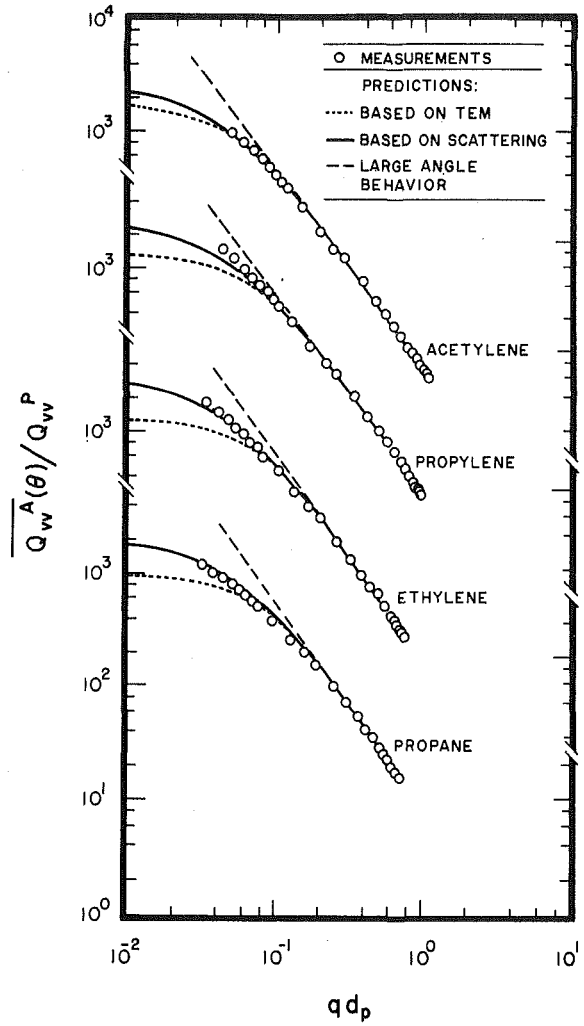

Fig. 2 Measured and predicted volumetric *vv* cross sections as a function of the modulus of the scattering vector

ing the much greater degree of scattering from aggregates than from individual primary particles. As discussed earlier, $\overline{\rho}_{sa}^{a}$ can be viewed as the error made when soot volume fractions are computed from laser extinction measurements using the small particle (Rayleigh) scattering limit. The results of Table 1 show that this practice causes errors of 22–41 percent for present conditions, increasing with increasing tendency of the fuel to soot. Nevertheless, it seems premature to correct earlier measurements of soot volume fractions at the same conditions (Sivathanu and Faeth, 1990) because current uncertainties of soot refractive indices can affect these results to a much larger extent, e.g., by roughly a factor of two (Dobbins and Megaridis, 1991).

Measured and predicted values of $\overline{Q}_{vv}^{a}(\theta)$ are plotted as a function of qd_p at 514.5 nm in Fig. 2 for the four fuels. Extrapolations of large-angle behavior also are shown on the plots for reference purposes. The substantial departure from Rayleigh scattering behavior (where $\overline{Q}_{vv}^{a}(\theta)$ would be independent of qd_p) is evident, with forward scattering roughly 100 times larger than large-angle scattering for all the fuels. The large size of the present soot aggregates, and the extended transition between the Guinier and power-law regimes due to polydisperse effects, prevented fully reaching the Guinier regime even though scattering angles as small as 5 deg were considered. However, the measurements provide an extended range within the power-law regime, e.g., roughly $qd_p > 0.1$.

The measurements in the power-law regime in Fig. 2 can be

Table 2 Soot aggregate fractal properties from thermophoretic sampling (*TS*) and light scattering (*LS*) measurements[a]

Fuel	D_f		k_f	
	TS	LS	TS[b]	LS[c]
Acetylene	1.79	1.85	9.2	7.0
Propylene	1.75	1.84	—	8.6
Ethylene	1.73	1.83	8.6	8.8
Propane	1.74	1.77	—	8.0

[a]For overfire soot from buoyant turbulent diffusion flames in still air at long residence times; light scattering measurements from the power-law regime at 514.5 nm.

[b]From Puri et al. (1993).

[c]Based on the soot refractive indices of Dalzell and Sarofim (1969).

interpreted to yield information about the fractal properties and refractive indices of the present overfire soot. At large angles, through Eqs. (19) and (26), the slope and magnitude of plots of $\overline{Q}_{vv}^{a}(\theta)$ as a function of qd_p yield D_f and k_f. These values are summarized Table 2 for the four fuels, along with values found from structure measurements using thermophoretic sampling and analysis with TEM. The values of D_f from the structure measurements of Köylü and Faeth (1992) and the present scattering measurements agree within experimental uncertainties and exhibit little variation with fuel type, yielding average values of 1.82 and 1.79 with standard deviations of 0.04 and 0.05, for the scattering measurements and over all the measurements. The fact that $D_f < 2$ implies fractal aggregate scattering behavior with scattering properties saturating when N is large, as suggested by Eq. (13), rather than Mie scattering for an equivalent sphere where ρ_{sa}^{a} continues to increase as N increases (Berry and Percival, 1986). Thus, aggregate sizes preclude Rayleigh scattering behavior while aggregate fractal dimensions preclude treating size effects by Mie scattering for an equivalent sphere. The variations of k_f with fuel type also are relatively small, yielding a mean value of 8.1 with a standard deviation of 0.8 over all the fuels (which is consistent with the estimated experimental uncertainty (95 percent confidence) of less than 23 percent for the k_f determinations). The present values of k_f are similar to the values found by Puri et al. (1993) of 9.2 and 8.6 for acetylene and ethylene flames from thermophoretic sampling measurements. Thus, both D_f and k_f appear to be relatively independent of fuel type for overfire soot aggregates.

Information about refractive indices can be obtained from the measurements in the power-law regime by finding $\overline{Q}_{vv}^{a}(\theta)/\overline{Q}_{a}^{a}$ from Eqs. (19), (22), and (26) and eliminating C_{vv}^{p} and C_{a}^{p} from this expression using Eq. (2). After rearranging, the following expression is obtained:

$$F(m)/E(m) = 4\pi(q\,d_p)^{D_f}\,\overline{Q}_{vv}^{a}(\theta)/(k_f x_p^3\,\overline{Q}_{a}^{a}), \quad \text{power-law regime} \quad (27)$$

All the quantities on the right-hand side of Eq. (27) are known from either the structure or power-law scattering measurements: d_p and x_p are summarized in Table 2, $D_f = 1.8$ and $k_f = 9.0$ are reasonable averages for present test conditions, based on the thermophoretic sampling results of Köylü and Faeth (1992) and Puri et al. (1993); while the values of $\overline{Q}_{a}^{a}$ are known from the present optical measurements. Then introducing $\overline{Q}_{vv}^{a}(\theta)$ at $\theta = 160$ deg, which is well within the power-law regime, yields $F(m)/E(m) = 0.74$ with a standard deviation of 0.09 over all the fuels. Available values of refractive indices at this wavelength include $m = 1.57 + 0.56i$ (Dalzell and Sarofim, 1969), $1.90 + 0.55i$ (Tien and Lee, 1982) and $1.63 + 0.48i$ (Chang and Charalampopoulos, 1990), yielding $F(m)/$

Table 3 Soot aggregate size distribution properties from thermophoretic sampling (*TS*) and light scattering (*LS*) measurements[a]

Fuel	N_g		σ_g		$\overline{N^2}/\overline{N}$	
	TS	LS	TS	LS	TS	LS
Acetylene	214	180	3.3	3.8	1330	1840
Propylene	227	162	3.0	3.9	1200	2860
Ethylene	290	189	2.7	3.9	1130	2390
Propane	224	162	2.9	3.6	930	2300

[a]For overfire soot from buoyant turbulent diffusion flames in still air at long residence times; light scattering measurements from near-Guinier regime at 514.5 nm. Light scattering measurements based on the soot refractive indices of Dalzell and Sarofim (1969); $\overline{N}$ for each fuel the same for both TS and LS measurements.

$E(m)$ = 0.84, 1.55, and 0.96, respectively. Thus, the measurements of Dalzell and Sarofim (1969) are most consistent with present soot aggregate scattering measurements when analyzed by the approximate theory developed in the previous section. These results also suggest that $F(m)/E(m)$ is relatively independent of fuel type for present conditions.

Two predictions based on the RDG polydisperse fractal aggregate theory are illustrated in Fig. 2, one entirely based on results from the structure (TEM) measurements, the other based on refitted aggregate size distributions (keeping $\overline{N}$ the same), which best match the scattering measurements. Both predictions use D_f = 1.8 and the individual k_f values deduced from the light scattering measurements for each fuel as summarized in Table 2. Since the predictions use the same $\overline{N}$, they yield identical results in the power-law regime through Eq. (19); they also are in good agreement with the measurements in this regime. However, predictions based on the structure measurements significantly underestimate scattering levels as the Guinier regime is approached. This is plausible due to the sampling limitations of the TEM measurements, where large aggregates that dominate forward scattering might not be found in sufficient quantities. In particular, the moment $\overline{N^2}$, which is crucial for scattering properties in the Guinier regime (see Eq. (17)), exhibited large uncertainties, 40–90 percent (see Table 3), suggesting potential sampling difficulties (Köylü and Faeth, 1992). Thus, the aggregate size distribution functions were refitted, keeping $\overline{N}$ constant as noted earlier, to achieve the reasonably good match of measured scattering properties in the transition regime illustrated in Fig. 2. The original (*TS*) and refitted (*LS*) aggregate size distribution parameters are summarized in Table 3 for all the fuels; changes of N_g and σ_g are within experimental uncertainties while the main difference between the thermophoretic sampling and scattering measurements is the higher order moment, $\overline{N^2}$, which easily is biased during TEM measurements due to sampling limitations, e.g., a small variation in the number of large aggregates in the sample will change this moment substantially. This suggests that the RDG polydisperse fractal aggregate theory provides a reasonable basis for treating overfire soot aggregates. However, additional study of the Guinier regime is needed to definitively evaluate the approach.

Angular Scattering Patterns. Predicted and measured angular scattering patterns at 514.5 nm are plotted in Figs. 3 and 4 for acetylene and ethylene as examples of strongly and weakly sooting fuels; results for propylene and propane were similar; see Köylü (1992). The predictions of $\overline{C}^a_{vv}(\theta)$ are based on the refitted soot structure properties from the light scattering measurements, and are in excellent agreement with the measurements as discussed in connection with Fig. 2. These results clearly show very strong scattering at small values of θ. The

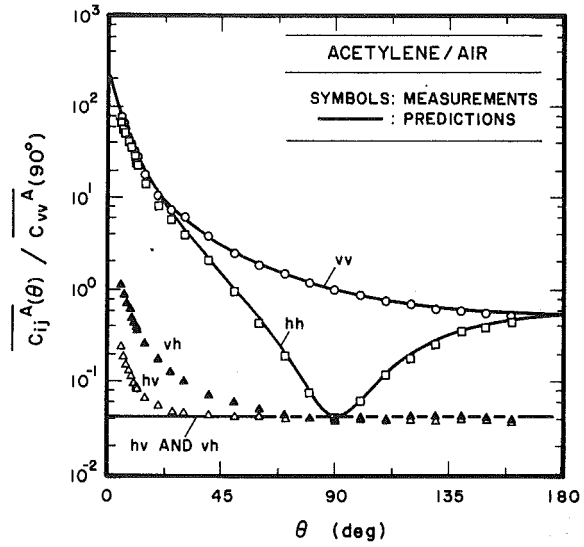

Fig. 3 Measured and predicted angular scattering patterns of overfire soot aggregates in turbulent acetylene/air diffusion flames

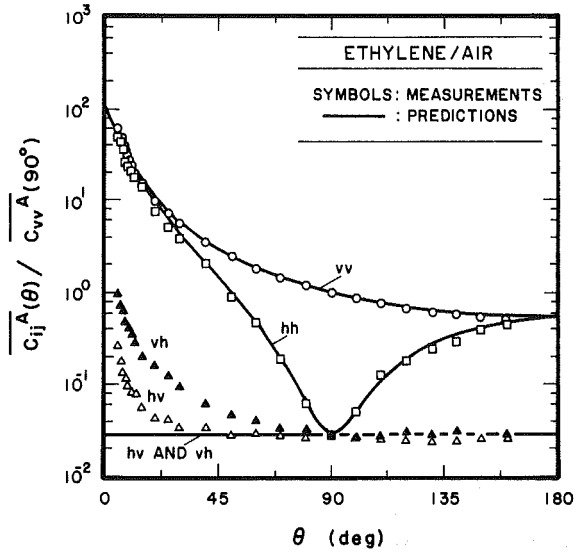

Fig. 4 Measured and predicted angular scattering patterns of overfire soot aggregates in turbulent ethylene/air diffusion flames

formulations for *hh*, *vh*, and *hv* scattering cross sections were modified slightly to account for observed depolarization effects. This was done by introducing depolarization ratios for soot aggregates, $\overline{\rho}^a_v$, analogous to Rayleigh scattering theory (Rudder and Bach, 1968), as follows:

$$\overline{C}^a_{hh}(\theta) = \overline{C}^a_{vv}(\theta)[(1-\overline{\rho}^a_v)\cos^2\theta + \overline{\rho}^a_v] \quad (28)$$

$$\overline{C}^a_{hv} = \overline{C}^a_{vh} = \overline{C}^a_{vv}(90 \text{ deg})\overline{\rho}^a_v \quad (29)$$

The measured values of $\overline{\rho}^a_v$ are summarized in Table 1; they increase with increasing propensity of the fuel to soot and generally are an order of magnitude larger than values found for Rayleigh scattering from molecules (Rudder and Bach, 1968). The resulting predictions of $\overline{C}^a_{hh}(\theta)$ are excellent, similar to $\overline{C}^a_{vv}(\theta)$. The predicted and measured scattering cross sections for the *vh* and *hv* components also are in good agreement with Rayleigh scattering ideas, except near the forward-scattering direction where the measured values increase and the *vh* and *hv* components no longer are equal. This behavior may be caused by experimental difficulties because uncertainties increase for both the *vh* and *hv* scattering components in the forward scattering direction due to effects of polarization vec-

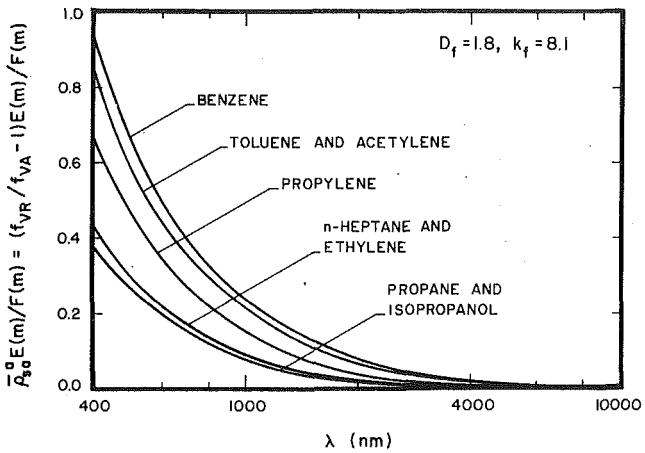

Fig. 5 Mean ratios of scattering to absorption cross sections as a function of wavelength for overfire soot aggregates in turbulent diffusion flames based on the predictions of the RDG polydisperse fractal aggregate theory

Table 4 Measured and predicted extinction cross sections, $\bar{C}^a_e$ (nm²) × 10^{-3}, for overfire soot aggregates[a]

Fuel	Acetylene	Propylene	Ethylene	Propane
514.5 nm:				
Measured	321	194	98.2	58.8
Predicted[b]	321	194	98.2	59.3
632.8 nm:				
Measured	290	172	73.1	43.7
Predicted[b]	248	143	74.7	46.5
1152 nm:				
Measured	176	86.8	45.5	26.9
Predicted[b]	144	84.4	45.3	28.4

[a]For buoyant turbulent diffusion flames in still air at long residence times.
[b]Based on the laser scattering properties of soot aggregates fitted at 514.5 nm and the soot refractive indices of Dalzell and Sarofim (1969).

tor misalignment when scattering is strong. In particular, experimental problems are suggested in this region because there is no fundamental reason for the *vh* and *hv* scattering components to differ for randomly oriented aggregates of small primary particles. However, the behavior also may reflect limitations of the RDG theory due to effects of multiple scattering in the forward direction. Thus, additional theoretical consideration of the depolarization ratios of soot aggregates would be interesting to help assess both the experimental and theoretical limitations of present methods. As a practical matter, however, the *vh* and *hv* components are small in comparison to *vv* and *hh* scattering and can be neglected for typical scattering calculations.

Extinction at Various Wavelengths. Extinction cross sections at 514.5, 632.8, and 1152 nm were measured in order to evaluate the capabilities of the RDG polydisperse fractal aggregate theory to estimate optical cross sections at various wavelengths. The results of these measurements and predictions are summarized in Table 4. The predictions are based on $D_f = 1.8$, $k_f = 8.1$ as reasonable averages of present estimates of fractal properties from Table 2, the aggregate size distribution properties from the scattering data summarized in Table 3, and the refractive indices of Dalzell and Sarofim (1969) listed earlier. Measured and predicted extinction cross sections at 514.5 nm are in close agreement, but this is not very significant because soot structure and optical properties were matched at this condition. Nevertheless, predicted extinction cross sections are within 18 percent of the measurements at both 632.8 and 1152 nm, with the largest errors exhibited for heavily sooting fuels like acetylene and propylene; this is good agreement in view of the uncertainties of soot refractive indices and the approximate nature of the scattering theory.

The present RDG polydisperse fractal aggregate theory was used to estimate the scattering contribution to extinction at other wavelengths since the predictions were reasonably good at the wavelengths where measurements were made. The predicted ratios of scattering to absorption cross sections are illustrated as a function of wavelength in Fig. 5. Results are shown for both the gaseous and liquid fuels studied by Köylü and Faeth (1992), using $D_f = 1.8$ and $k_f = 8.1$ as before. The soot aggregate size distribution parameters (N_g and σ_g) for these calculations were drawn from the thermophoretic sampling measurements of Köylü and Faeth (1992), even though present scattering measurements for gaseous fuels suggested the need for adjusting these parameters somewhat, see Table 3. This is justified because total scattering predictions using the thermophoretic sampling measurements agreed with present measurements within 15 percent, because the changes of the size distribution parameters only affected results at very small angles. The predictions are presented as $\bar{\rho}^a_{sa}\,E(m)/F(m)$ to avoid complications due to the considerable uncertainties of soot refractive indices discussed earlier. The plot of Fig. 5 updates results reported by Köylü and Faeth (1992), based on the RDG polydisperse fractal aggregate theory of Dobbins and Megaridis (1991), which is mainly designed to treat the Guinier regime as discussed earlier; there are quantitative differences between the two sets of results but the general trends are similar.

The plots of $\bar{\rho}^a_{sa}$ in Fig. 5 indicate departure of aggregate scattering properties from the small particle (Rayleigh) scattering limit. The results show that this departure is greatest for strongly sooting fuels like toluene, benzene, and acetylene in the visible portion of the spectrum. Noting that $F(m)/E(m)$ is of order unity, soot volume fractions would be overestimated by 20–50 percent for laser extinction measurements at 632.8 nm, analyzed using the Rayleigh scattering approximation. The value of $\bar{\rho}^a_{sa}$, however, decreases with increasing wavelength and becomes relatively small for wavelengths greater than 2000 nm. Thus, the effect of aggregate scattering appears to be relatively small for estimates of soot radiation properties in the infrared, when compared with other uncertainties of such calculations, even for the present rather large overfire soot aggregates.

Discussion. The reasonably good overall comparison between predictions using the RDG polydisperse fractal aggregate theory and the present measurements is promising. However, the evaluation was limited with respect to the general effectiveness of the RDG scattering approximation for treating soot optical properties. First of all, the large size of the present aggregates implied that the bulk of the measurements were in the power-law regime. In this regime, the computations of Nelson (1989) suggest that effects of multiple scattering are relatively small, and that the RDG approximation of Eq. (5) is satisfactory even for large aggregates. Thus, while it is encouraging that predictions based solely on structure measurements were satisfactory in this regime, this does not constitute a definitive evaluation of the RDG approximation for soot aggregates.

Effects of multiple scattering are most significant for forward scattering in the Guinier regime, which would provide a strong test of the RDG scattering approximation. Unfortunately, two difficulties were encountered during the present evaluation of predictions in this regime. First of all, the large size of the present aggregates precluded fully reaching the Guinier regime for experimentally accessible scattering angles so that the full effect of potential multiple scattering was not observed. Secondly, it was necessary to refit the aggregate size distribution function, to increase the higher moment $\overline{N^2}$, in

order to match the scattering data. While such refitting is plausible due to the sampling limitations of the structure measurements, as discussed earlier, the refitting also could mask fundamental deficiencies of the RDG scattering approximation. Thus, while it is encouraging that the RDG polydisperse fractal aggregate approach seems capable of correlating the present measurements of soot optical properties, and scattering measurements eventually may prove to be the best way to find the higher moments of the soot aggregate size distributions, additional evaluation of the RDG approximation is needed. This will require measurements of both structure and optical properties for soot populations having smaller aggregates and thus a more extensive Guinier regime.

Conclusions

The optical properties of overfire soot were measured for buoyant turbulent diffusion flames burning in still air. The fuels considered included acetylene, propylene, ethylene, and propane. Measurements were limited to the long residence time regime where soot structure was known from earlier thermophoretic sampling measurements (Köylü and Faeth, 1992), and is independent of position and residence time in the overfire region. The combined soot structure and optical property measurements were used to evaluate an approximate RDG polydisperse fractal aggregate theory of soot optical properties. The main conclusions of the study are as follows:

1 The optical properties of the present soot at 514.5 nm departed significantly from Rayleigh scattering behavior: Forward scattering was roughly 100 times larger than large-angle scattering, total scattering was 22–41 percent of absorption, and depolarization ratios were roughly an order of magnitude larger than values typical of Rayleigh scattering from molecules. This causes soot volume fractions to be overestimated up to 70 percent for heavily sooting fuels when laser extinction measurements in the visible are interpreted using the Raleigh scattering approximation; see Fig. 5.

2 The present scattering measurements in the power-law regime yield aggregate fractal properties that are relatively independent of fuel type, as follows: fractal dimension, D_f = 1.82 with a standard deviation of 0.04; and fractal prefactor, k_f = 8.1 with a standard deviation of 0.09. These values agree within experimental uncertainties with earlier structure measurements for overfire soot obtained by thermophoretic sampling (Köylü and Faeth, 1992; Puri et al., 1993), and appear to be relatively robust properties of overfire soot aggregates.

3 Present scattering measurements in the power-law regime at 514.5 nm yielded the soot refractive index ratio, $F(m)/E(m)$ = 0.74 with a standard deviation of 0.09, over all the fuels. The refractive index measurements of Dalzell and Sarofim (1969) yield $F(m)/E(m)$ = 0.84, which is in good agreement with present observations, while newer values from Tien and Lee (1982) and Chang and Charalampopoulos (1990) are somewhat higher, 1.55 and 0.96, respectively. The continued uncertainties of soot refractive indices are a substantial limitation to reliable nonintrusive laser-based measurements of soot properties and should be resolved.

4 The RDG polydisperse fractal aggregate theory provided reasonably good predictions of present soot optical property measurements. This was accomplished with predictions based solely on soot structure measurements in the power-law regime, and after refitting the aggregate size distribution in the Guinier regime in order to adjust $\overline{N^2}$ since it could not be determined very accurately from the structure measurements. While this is promising, present measurements only approached the Guinier regime where potential deficiencies of the RDG scattering approximation should be most apparent. Thus, additional work at conditions that extend farther into the Guinier regime is needed in order to establish reliably the effectiveness of the RDG approximation for soot optical properties.

Acknowledgments

This research was supported by the Building and Fire Research Laboratory of the National Institute of Standards and Technology, Grant No. 60NANB1D1175, with H. R. Baum serving as Scientific Officer.

References

Berry, M. V., and Percival, I. C., 1986, "Optics of Fractal Clusters Such as Smoke," *Optica Acta*, Vol. 33, pp. 577–591.

Bohren, C. F., and Huffman, D. R., 1983, *Absorption and Scattering of Light by Small Particles*, Wiley, New York, pp. 477–482.

Chang, H., and Charalampopoulos, T. T., 1990, "Determination of the Wavelength Dependence of Refractive Indices of Flame Soot," *Proc. R. Soc. London A*, Vol. 430, pp. 577–591.

Chen, H. Y., Iskander, M. F., and Penner, J. E., 1990, "Light Scattering and Absorption by Fractal Agglomerates and Coagulations of Smoke Aerosols," *J. Modern Optics*, Vol. 2, pp. 171–181.

Dalzell, W. H., and Sarofim, A. F., 1969, "Optical Constants of Soot and Their Application to Heat Flux Calculations," ASME JOURNAL OF HEAT TRANSFER, Vol. 91, pp. 100–104.

Dalzell, W. H., Williams, G. C., and Hottel, H. C., 1970, "A Light Scattering Method for Soot Concentration Measurements," *Combust. Flame*, Vol. 14, pp. 161–170.

Dobbins, R. A., and Megaridis, C. M., 1991, "Absorption and Scattering of Light by Polydisperse Aggregates," *Appl. Optics*, Vol. 30, pp. 4747–4754.

Erickson, W. D., Williams, G. C., and Hottel, H. C., 1964, "Light Scattering Measurements on Soot in a Benzene–Air Flame," *Combust. Flame*, Vol. 8, pp. 127–132.

Guinier, A., and Fournet, G., 1955, *Small-Angle Scattering of X-Rays*, Wiley, New York.

Jullien, R., and Botet, R., 1987, *Aggregation and Fractal Aggregates*, World Scientific Publishing Co., Singapore, pp. 46–50.

Kerker, M., 1969, *The Scattering of Light*, Academic Press, New York, pp. 414–486.

Köylü, Ü. Ö., 1992, "Emission, Structure and Optical Properties of Overfire Soot From Buoyant Turbulent Diffusion Flames," Ph.D. Thesis, The University of Michigan, Ann Arbor, MI.

Köylü, Ü. Ö., and Faeth, G. M., 1992, "Structure of Overfire Soot in Buoyant Turbulent Diffusion Flames at Long Residence Times," *Combust. Flame*, Vol. 89, pp. 140–156.

Köylü, Ü. Ö., and Faeth, G. M., 1993, "Radiation Properties of Flame-Generated Soot," ASME JOURNAL OF HEAT TRANSFER, Vol. 115, pp. 409–417.

Ku, J. C., and Shim, K.-H., 1992, "Optical Diagnostics and Radiative Properties of Simulated Soot Agglomerates," ASME JOURNAL OF HEAT TRANSFER, Vol. 113, pp. 953–958.

Magnussen, B. F., 1974, "An Investigation Into the Behavior of Soot in a Turbulent Free Jet C_2H_2-Flame," *Fifteenth Symposium (International) on Combustion*, The Combustion Institute, Pittsburgh, PA, pp. 1415–1425.

Martin, J. E., and Hurd, A. J., 1987, "Scattering From Fractals," *J. Appl. Cryst.*, Vol. 20, pp. 61–78.

Nelson, J., 1989, "Test of a Mean Field Theory for the Optics of Fractal Clusters," *J. Modern Optics*, Vol. 36, pp. 1031–1057.

Puri, R., Richardson, T. F., Santoro, R. J., and Dobbins, R. A., 1993, "Aerosol Dynamic Processes of Soot Aggregates in a Laminar Ethene Diffusion Flame," *Combust. Flame*, Vol. 92, pp. 320–333.

Rudder, R. R., and Bach, D. R., 1968, "Rayleigh Scattering of Ruby-Laser Light by Neutral Gases," *J. Opt. Soc. Amer.* Vol. 58, pp. 1260–1266.

Sivathanu, Y. R., and Faeth, G. M., 1990, "Soot Volume Fractions in the Overfire Region of Turbulent Diffusion Flames," *Combust. Flame*, Vol. 81, pp. 133–149.

Tien, C. L., and Lee, S. C., 1982, "Flame Radiation," *Prog. Energy Combust. Sci.*, Vol. 8, pp. 41–59.

van de Hulst, H. C., 1957, *Light Scattering by Small Particles*, Dover Publications, New York.

Wersborg, B. L., Howard, J. B., and Williams, G. C., 1972, "Physical Mechanisms in Carbon Formation in Flames," *Fourteenth Symposium (International) on Combustion*, The Combustion Institute, Pittsburgh, pp. 929–940.

Investigation of Radiative Transfer in Nongray Gases Using a Narrow Band Model and Monte Carlo Simulation

J. Liu
Graduate Research Assistant.
Student Mem. ASME

S. N. Tiwari
Eminent Professor.
Fellow ASME

Department of Mechanical Engineering
and Mechanics,
Old Dominion University,
Norfolk, VA 23529-0247

The Monte Carlo method (MCM) is applied to analyze radiative heat transfer in nongray gases. The nongray model employed is based on the statistical narrow band model with an exponential-tailed inverse intensity distribution. The amount and transfer of the emitted radiative energy in a finite volume element within a medium are considered in an exact manner. The spectral correlation between transmittances of two different segments of the same path in a medium makes the statistical relationship different from the conventional relationship that only provides the noncorrelated results for nongray analysis. Two features of the MCM that are different from other nongray numerical methods are discussed. The simplicity of the MCM is demonstrated by considering the case of radiative transfer between two reflecting walls. The results for the radiative dissipation distributions and the net radiative wall heat fluxes are obtained for uniform, parabolic, and boundary layer type temperature profiles, as well as for a parabolic concentration profile. They are compared with available results of other methods. Good agreements are found for all the cases considered.

Introduction

Radiative interactions become important in many engineering problems involving high-temperature gases. Recent interest lies in the areas of design of high-pressure combustion chambers and high enthalpy nozzles, entry and re-entry phenomena, hypersonic propulsion, and defence-oriented research. In order to analyze radiative heat transfer, many numerical methods have been developed. These include the P-N method, the discrete ordinate method, the zoning method, the finite element method, and MCM. A review of available solution techniques is given by Howell (1988).

The MCM is a probabilistic method that can exactly simulate all important physical processes. In this method, the numerical treatment of mathematical formulations is easy and the usual difficulties encountered in complex geometries can be circumvented easily. It is due to these advantages that the MCM has been applied to solve many radiative transfer problems. The earliest application of this method for radiative transfer problems was made by Howell and Perlmutter (1964a). Radiative problems of increasing complexity that have been investigated by this method have appeared in the literature (Perlmutter and Howell, 1964; Howell and Perlmutter, 1964b; Steward and Cannon, 1971; Dunn, 1983; Gupta et al., 1983; Taniguchi et al., 1991). Studies on reducing the computational time by using this method are also available (Kobiyama et al., 1979; Kobiyama, 1986). The gray gas assumption, however, is made in most of these analyses. In many practical applications, this approximation is too crude to provide reliable quantitative predictions.

Application of the MCM for analysis of radiative transfer in nongray gases has received little attention. Howell and Perlmutter (1964) were the first to take into account the effect of nongray radiation. The spectral absorption coefficient of hydrogen at very high pressure and temperature was obtained by experimental procedures and used for analysis of radiation by the MCM. Another technique that approximates a real gas by the weighted-sum-of-gray-gases approach was also modeled using the MCM (Steward and Cannon, 1971). Recently, Modest (1992) has applied the MCM to the radiative heat transfer with molecular gases. It is pointed out that the narrow band model may be applied successfully to the MCM after verification in an isothermal and homogeneous medium.

This work is motivated by our interest to apply a general and accurate nongray model to investigate radiative heat transfer using the MCM. This investigation includes derivation of the statistical relationships, discussion of the special features different from other methods, and demonstration of the capability of the MCM for nongray analysis. The nongray model used in this work is a statistical narrow band model with an exponential-tailed-inverse intensity distribution (Malkmus, 1967). To check the accuracy of the nongray Monte Carlo analysis, the results for radiative dissipation distributions and net radiative wall heat fluxes are obtained and compared with other available solutions for uniform, parabolic, and boundary layer type temperature profiles, as well as uniform and parabolic concentration profiles.

Analysis of Monte Carlo Simulation Using a Narrow Band Model

Consider an absorbing and emitting molecular gas between two infinite parallel plates with the slab thickness of L as shown in Fig. 1. Temperature, concentration, and pressure in the medium are supposed to be known. The walls are assumed to be diffuse but not necessarily gray. The wall temperature is also known. The quantities of interest in this study are the net radiative wall flux and the radiative dissipation inside the medium. The radiative dissipation is nothing but the divergence of radiative heat flux with an opposite sign. In order to calculate these quantities, the medium considered is divided into $(M-2)$ volume elements. The grid numbers on the lower and upper walls are 1 and M, respectively. Temperature, concen-

Contributed by the Heat Transfer Division for publication in the JOURNAL OF HEAT TRANSFER. Manuscript received by the Heat Transfer Division December 1992; revision received June 1993. Keywords: Numerical Methods, Radiation, Radiation Interactions. Associate Technical Editor: R. O. Buckius.

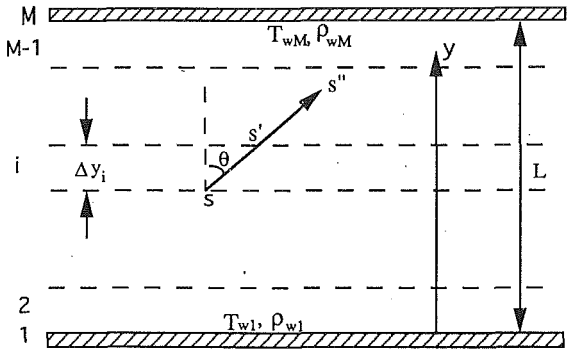

Fig. 1 Planar medium between two parallel walls

tration, and pressure are assumed to be constant in each volume element. The typical method for handling radiative exchange between surface and/or volume elements is to evaluate the multiple integral that describes the exchange by some type of numerical integration technique. This, usually, is a good approach for simple problems. An alternate method is used here. Radiative transfer in the computation domain is simulated using the MCM.

The MCM uses a large number of bundles of energy to simulate the actual physical processes of radiant emission and absorption of energy occurring in a medium. These energy bundles are similar to photons in their behavior. The histories of these energy bundles are traced from their point of emission to their point of absorption. What happens to each of these bundles depends on the emissive, scattering, and absorptive behavior within the medium, which is described by a set of statistical relationships. The net radiative wall flux or the radiative dissipation in an element is equal to the total radiative energy absorbed in the element minus its emitted radiative energy, divided by the area or the volume of the element.

Radiation Absorption Model. The study of radiative transmission in nonisothermal and inhomogeneous gaseous systems requires a detailed knowledge of the absorption, emission, and scattering characteristics of the specific gas. Several models are available in the literature to represent the absorption emission characteristics of molecular species. The gray gas model is the simplest model to employ in radiative transfer analyses. In many practical applications, the radiative transfer by hot molecular gases such as H_2O and CO_2 involves vibration-rotation bands that are difficult to model by a gray gas model due to the strong wavenumber dependent properties of the bands.

The nongray gas models include line-by-line models, narrow band models, and wide band models. The solution of line-by-line formulations requires considerably large computational resources. The wide band model and band absorptance correlations also present some disadvantages (Zhang et al., 1988). Various wide and narrow band models have been tested with line-by-line calculations (Tiwari, 1978; Soufiani et al., 1985; Soufiani and Taine, 1987). Accurate results for temperature and heat flux distribution are obtained with the narrow band model, which assumes the absorption lines to be randomly placed and the intensities to obey an exponential-tailed-inverse distribution. The transmittance of a homogeneous and isothermal column of length l due to gas species j, averaged over $[\omega-(\Delta\omega/2), \omega+(\Delta\omega/2)]$, is then given by (Malkmus, 1967)

$$\bar{\tau}_\omega^j = \exp\left[-\frac{\bar{\beta}}{\pi}\left(\sqrt{\left(1+\frac{2\pi x_j P l \bar{k}}{\bar{\beta}}\right)}-1\right)\right] \tag{1}$$

where x_j represents the mole fraction of the absorbing species j and P is total pressure; $\bar{k}$ and $\bar{\beta} = 2\pi\bar{\gamma}/\bar{\delta}$ are the band model parameters, which account for the spectral structure of the gas. The overbar symbol indicates that the quantity is averaged over a finite wavenumber interval $\Delta\omega$. The parameters $\bar{k}$ and $1/\bar{\delta}$, generated from a line-by-line calculation, have been published for H_2O and CO_2 (Ludwig et al., 1973; Hartmann et al., 1984; Soufiani et al., 1985). The mean half-width $\bar{\gamma}$ is obtained using the parameters suggested by Soufiani et al. (1985). The narrow bandwidth considered is usually 25 cm^{-1}.

For a nonisothermal and inhomogeneous column, the Curtis-Godson approximation (Godson, 1953) leads to accurate results if pressure gradients are not too large. Basically, this approach consists of transformation of such a column into an equivalent isothermal and homogeneous one. Effective band model parameters $\bar{k}_e$ and $\bar{\beta}_e$ are introduced by averaging $\bar{k}$ and $\bar{\beta}$ over the optical path U of the column as

$$U(l) = \int_0^l P(y)x_j(y)dy \tag{2}$$

$$\bar{k}_e = \frac{1}{U(l)}\int_0^l P(y)x_j(y)\bar{k}(y)dy \tag{3}$$

$$\bar{\beta}_e = \frac{1}{\bar{k}_e U(l)}\int_0^l P(y)x_j(y)\bar{k}(y)\beta(\bar{y})dy \tag{4}$$

The transmittance of this equivalent column is then calculated from Eq. (1).

Monte Carlo Formulation. Use of a narrow band model in the MCM presents new features in the analysis of radiative heat transfer. The statistical relationships currently in use need to be modified. The following Monte Carlo analyses are based on an arbitrarily chosen finite volume element. The statistical relationships for an energy bundle emitted from a surface element can be derived by following the same procedure.

Let us consider the Planck spectral blackbody intensity $I_{b\omega}$ that enters the ith volume element at point s on the lower side and intersects the upper side at point s' as shown in Fig. 1. A spherical coordinate system is established and centered at points s. Under the condition of local thermodynamic equilibrium, an amount of energy absorbed in a finite volume element is equal to that emitted by the volume element. Thus,

Nomenclature

I_ω = spectral radiative intensity, $kW/(m^2 \cdot sr \cdot cm^{-1})$
k = line intensity to spacing ratio, $cm^{-1} \cdot atm^{-1}$
L = slab thickness, m
M = number of elements
P = gas pressure, atm
$-dq_R/dy$ = radiative dissipation, kW/m^3
Q = emitted radiative energy per unit volume, kW/m^3
R = random number
s, s', s'' = position variables, m
T = absolute temperature, K
U = pressure path length parameter, atm•m
x = mole fraction
y = y coordinate, m
β = line width to spacing ratio
γ = halfwidth of an absorption line, cm^{-1}
δ = equivalent line spacing, cm^{-1}
θ = core angle
μ = y-direction cosine = $\cos\theta$
ρ = reflectivity
τ_ω = spectral transmittance
ψ = circumferential angle
ω = wavenumber, cm^{-1}
Ω = solid angle

the amount of energy emitted for a wavenumber range $d\omega$ and along a pencil of columns $s \rightarrow s'$ with a solid angle increment $d\Omega$ is

$$dQ_i = I_{b\omega}[1 - \tau_\omega(s \rightarrow s')] \cos\theta d\Omega d\omega \tag{5}$$

where $\tau_\omega(s \rightarrow s')$ is the spectral transmittance over the path $s \rightarrow s'$, θ is the cone angle between the y axis and the direction of the column $s \rightarrow s'$, and $d\Omega = \sin\theta d\theta d\psi$ where ψ is the circumferential angle. The total emitted energy per unit volume is obtained by integrating Eq. (5) over the wavenumber, cone, and circumferential angle as

$$\begin{aligned} Q_i &= \int_0^\infty \int_0^\pi \int_0^{2\pi} I_{b\omega}[1 - \tau_\omega(s \rightarrow s')] \cos\theta \sin\theta d\psi d\theta d\omega \\ &= 2\pi \int_0^\infty \int_0^\pi I_{b\omega}[1 - \tau_\omega(s \rightarrow s')] \cos\theta \sin\theta d\theta d\omega \\ &= 2\pi \int_0^\infty \int_{-1}^1 I_{b\omega}[1 - \tau_\omega(\Delta y_i/\mu)]\mu d\mu d\omega; \quad \mu = \cos\theta \end{aligned} \tag{6}$$

where Δy_i is the thickness of the ith volume element. It should be noted that the sign of Δy_i is different when μ varies from positive to negative.

The simulation of an energy bundle includes the determination of wavenumber and direction of emission of this energy bundle in the finite volume element. The statistical relationships for determining these parameters are readily obtained from Eq. (6) as (Howell, 1968; Siegel and Howell, 1981; Haji-Sheikh, 1988)

$$R_\omega = \frac{2\pi \int_0^\omega \int_{-1}^1 I_{b\omega}[1 - \tau_\omega(\Delta y_i/\mu)]\mu d\mu d\omega}{Q_i} \tag{7}$$

$$R_\mu = \frac{2\pi \int_\mu^1 \int_0^\infty I_{b\omega}[1 - \tau_\omega(\Delta y_i/\mu)]\mu d\omega d\mu}{Q_i} \tag{8}$$

where R_ω and R_μ are random numbers, which are uniformly distributed between zero and one. In Eqs. (6)–(8), τ_ω is a real spectral transmittance. Before solving these equations to obtain ω and μ from a set of given values of R_ω and R_μ, the narrow band model should be applied to approximate the real spectral transmittance.

For the narrow band model, the absorption bands of the gas are divided into spectral ranges $\Delta\omega$ wide; each is centered at ω^k and characterized by the superscript k; the band parameters obtained are the averaged quantities over a narrow band. So, the spectral quantities in Eqs. (6)–(8) should be transformed into the averaged quantities over a narrow band for practical applications. Taking the spectral average over all narrow bands, Eqs. (6)–(8) are expressed as

$$Q_i = 2\pi \sum_{k=1}^{m_\omega} \left\{ \int_{-1}^1 \overline{I_{b\omega^k}}[1 - \overline{\tau_{\omega^k}}(\Delta y_i/\mu)]\mu d\mu \right\} \Delta\omega^k \tag{9}$$

$$R_\omega = \frac{2\pi \sum_{k=1}^{n} \left\{ \int_{-1}^1 \overline{I_{b\omega^k}}[1 - \overline{\tau_{\omega^k}}(\Delta y_i/\mu)]\mu d\mu \right\} \Delta\omega^k}{Q_i}, \quad (\omega^{n-1} < \omega \le \omega^n) \tag{10}$$

$$R_\mu = \frac{2\pi \sum_{k=1}^{m_\omega} \left\{ \int_{\mu}^1 \overline{I_{b\omega^k}}[1 - \overline{\tau_{\omega^k}}(\Delta y_i/\mu)]\mu d\mu \right\} \Delta\omega^k}{Q_i} \tag{11}$$

where m_ω is the total number of narrow bands. The following narrow band approximation has been used in obtaining Eqs. (9)–(11)

$$\begin{aligned} \overline{I_{b\omega^k}\tau_{\omega^k}} &= \frac{1}{\Delta\omega^k} \int_{\Delta\omega^k} I_{b\omega}\tau_\omega d\omega \\ &\approx \overline{I_{b\omega^k}} \left(\frac{1}{\Delta\omega^k} \int_{\Delta\omega^k} \tau_\omega d\omega \right) \\ &= \overline{I_{b\omega^k}}\,\overline{\tau_{\omega^k}} \end{aligned} \tag{12}$$

This is because $I_{b\omega}$ is essentially constant over a narrow band and may be taken out of the spectral integral. Otherwise, the average product $\overline{I_{b\omega^k}\tau_{\omega^k}}$ is not equal to the product $\overline{I_{b\omega^k}}$ and $\overline{\tau_{\omega^k}}$.

Equations (10) and (11) are solved for ω and μ each time a set of values of R_ω and R_μ are chosen. The computing time becomes too large for practical calculations since the integrands in these equations are very complex functions of integration variables and the number of energy bundles usually is very large. To circumvent this problem, interpolation and approximation methods are employed. For example, to obtain the value of ω for a given value of R_ω, we first choose different values of ω and obtain the corresponding values of R_ω from Eq. (10). Then, a smooth curve is constructed to match these data points, and ω values are easily obtained from this curve for selected values of R_ω. The procedures for determining μ are similar to those for ω.

Following the determination of wavenumber and direction of an energy bundle, it is essential to find the location of absorption of the energy bundle in the participating medium. Let us still consider the emitted radiant energy along a pencil of column $s \rightarrow s'$ (Fig. 1). After this amount of energy is transmitted over a column $s' \rightarrow s''$, the remaining radiant energy is given by

$$dQ_i' = I_{b\omega}[1 - \tau_\omega(s \rightarrow s')]\tau_\omega(s' \rightarrow s'') \cos\theta d\Omega d\omega \tag{13}$$

where $\tau_\omega(s' \rightarrow s'')$ is the spectral transmittance over the path $s' \rightarrow s''$. Taking a narrow band average over Eqs. (5) and (13) and dividing the latter with the first one, the statistical relationship for determining the location of absorption can be expressed as

$$\begin{aligned} R_l &= \frac{\overline{[1 - \tau_\omega(s \rightarrow s')]\tau_\omega(s' \rightarrow s'')}}{1 - \overline{\tau_\omega}(s \rightarrow s')} \\ &= \frac{\overline{\tau_\omega}(s' \rightarrow s'') - \overline{\tau_\omega(s \rightarrow s')\tau_\omega(s' \rightarrow s'')}}{1 - \overline{\tau_\omega}(s \rightarrow s')} \end{aligned} \tag{14}$$

where R_l is a random number. The averaged product

$$\overline{\tau_\omega(s \rightarrow s')\tau_\omega(s' \rightarrow s'')}$$

is not equal to the product $\overline{\tau_\omega(s \rightarrow s')}$ and $\overline{\tau_\omega(s' \rightarrow s'')}$ because the $\tau_\omega(s \rightarrow s')$ and $\tau_\omega(s' \rightarrow s'')$ have a strong wavenumber dependence due to the high resolution structure in a very small range of an absorption band (hundreds of major absorption lines in a 25 cm^{-1} spectral interval), and must be treated in a spectrally correlated way. Equation (14) can be simplified as

$$R_l = \frac{\overline{\tau_\omega}(s' \rightarrow s'') - \overline{\tau_\omega}(s \rightarrow s'')}{1 - \overline{\tau_\omega}(s \rightarrow s')} \tag{15}$$

If the spectral correlation between $\tau_\omega(s \rightarrow s')$ and $\tau_\tau(s' \rightarrow s'')$ is not taken into account, then Eq. (14) becomes

$$R_l = \overline{\tau_\omega}(s' \rightarrow s'') \tag{16}$$

Equation (16) is the statistical relationship usually employed for determining the location of absorption in the Monte Carlo simulation and is quite different from Eq. (15). For an isothermal and homogeneous medium, the traveling distance of an energy bundle can be obtained directly by solving Eq. (15) for a given random number. But this procedure turns out to be somewhat complicated for a nonisothermal and inhomo-

geneous medium. It becomes necessary to try each volume element starting from the adjacent element of the location where an energy bundle emits until a finite volume element is found in which Eq. (15) can be satisfied.

Special Features of MCM for Nongray Analysis. The MCM is quite different from other numerical techniques for the analysis of radiative heat transfer. Its characteristics have been discussed in detail by Siegel and Howell (1981). Use of a nongray model in the radiative transfer analysis requires significant changes. Two special features of incorporating the nongray model in the MCM are discussed here.

Most of the existing analyses in radiative heat transfer start with the transfer equation of the type given by Siegel and Howell (1981). In order to apply a narrow band model, this equation has to be spectrally averaged over a narrow band. This averaging treatment results in two kinds of spectral correlations. One is the spectral correlation between the intensity and the transmittance within the medium. Another is the spectral correlation between the reflected component of the wall radiosity and the transmittance. In order to investigate the first kind of spectral correlation, all the intermediate transmittances in each finite volume element of medium along the path the radiative energy travels must be calculated and stored to make a correlated calculation. In order to investigate the second kind of spectral correlation, a series expansion of the wall radiosity is required. Essentially, this series expansion is utilized along with a technique for closure of the series.

The simulation of radiative heat transfer in the MCM is not directly based on the radiative transfer equation. This results in the MCM having features different from the other methods for nongray analysis. When the radiative energy is transmitted in the medium, the spectral correlation does occur in the MCM, but it occurs between the transmittances of two different segments of the same path which is different from other methods. This is the first feature with the MCM for nongray analysis.

The MCM procedures are based on the direct simulation of the path of an energy bundle. For the case with reflecting walls, the mechanism of the reflections simulation in the MCM is the same as a series expansion of the wall radiosity. However, this simulation process becomes much simpler because of a probabilistic treatment. Also, there are no spectrally correlated quantities involved. This is the second feature of the MCM for nongray analysis. Exact treatment of the reflections in the MCM in nongray gases is the same as that in gray gases and may be found in the literature (Howell, 1968; Siegel and Howell, 1981).

The second feature of the MCM allows one to obtain results for a reflecting wall with very little increase in the computation time compared to that for a nonreflecting wall. But in other methods, considering the history of a finite number of reflections and approximating the remaining reflections by a closure method in the radiative transfer equation complicates the mathematical formulation and increases the computer time considerably. As the geometry considered becomes complicated, exact simulation of radiative heat transfer in the case with reflecting wall will be very difficult for most existing methods, while it is not a big problem for the MCM. So, it seems that the MCM is able to retain the feature of simplicity in dealing with the complicated problems while a narrow band model is employed.

Results and Discussion

In order to validate the Monte Carlo simulation along with a narrow band model, results for radiative dissipation inside the medium and the net radiative wall heat flux have been obtained for different temperature and concentration profiles with nonreflecting and reflecting walls. In this work, the reflectivities of two parallel diffuse walls are assumed to be identical and are denoted by the symbol ρ. Three different

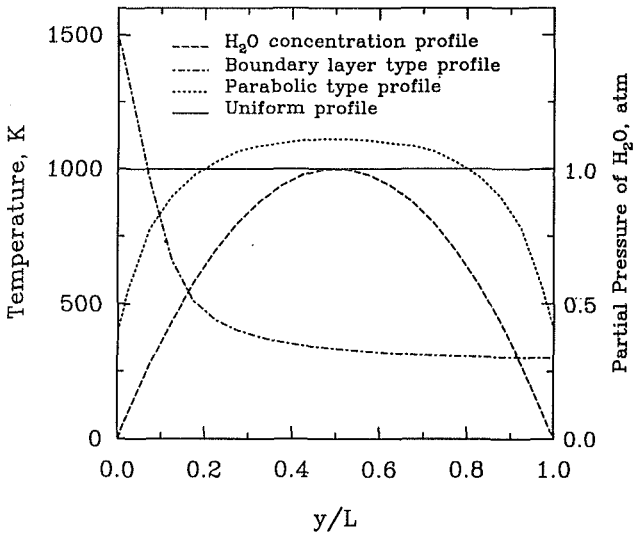

Fig. 2 Temperature and concentration profiles

temperature profiles are used here and these are uniform, boundary layer type, and parabolic profiles (Fig. 2). They are obtained from Kim et al. (1991a) and Menart et al. (1993). For the uniform temperature profile, the gas temperature is chosen to be 1000 K, while the walls are held at 0 K. Also shown in the figure is a parabolic H_2O concentration profile for a mixture of H_2O and N_2 at 1 atm, and it is also taken from the above-cited references. A uniform composition of pure H_2O vapor at 1 atm is another H_2O concentration profile used. Several cases with the selected temperature and H_2O concentration profiles have been considered previously using the S-N discrete ordinates method by including all important bands. The Monte Carlo solutions are compared with the available solutions for identical conditions.

In the Monte Carlo simulation, the entire slab of the physical problem is divided into 20 sublayers for all calculations. Further subdivision of the computation domain yields little change in the results. The computation were performed on a Sun Sparc workstation. The total number of energy bundles for each case was chosen to be 50,000. This choice represents a compromise between accuracy and saving of computation time. When the relative statistical errors of the results were chosen to be less than ± 3 percent, the probability of the results lying within these limits was greater than 95 percent. The computing times for the correlated and noncorrelated formulations were essentially the same. For an isothermal and homogeneous medium, the required CPU time was about 1–2 minutes for each case. For nonisothermal and inhomogeneous medium, the CPU time was increased to 5–7 minutes, and it was nearly 10 minutes for the case with strongly reflecting walls ($\rho = 0.9$) and large optical length ($L = 0.5$ m).

The situation with nonreflecting walls is considered first. Figures 3(*a–c*) show the comparisons between the Monte Carlo solutions and S-N discrete ordinates solutions. Four different S-N discrete ordinates solutions, employing different band models are available in the literature (Kim et al., 1991a). For our comparison, we selected the S-20 nongray narrow band solution because it employs the same narrow band model as used in this study.

Figure 3(*a*) shows the radiative dissipation results obtained for the uniform temperature and uniform pure H_2O vapor distribution with a slab thickness of 1.0 m. The Monte Carlo results essentially match the S-N discrete ordinates results. Figure 3(*b*) presents the results with the boundary layer type temperature profile and for the same concentration distribution as in Fig. 3(*a*). The Monte Carlo results predict the same change of gas behavior (from a net emitter near the hot wall

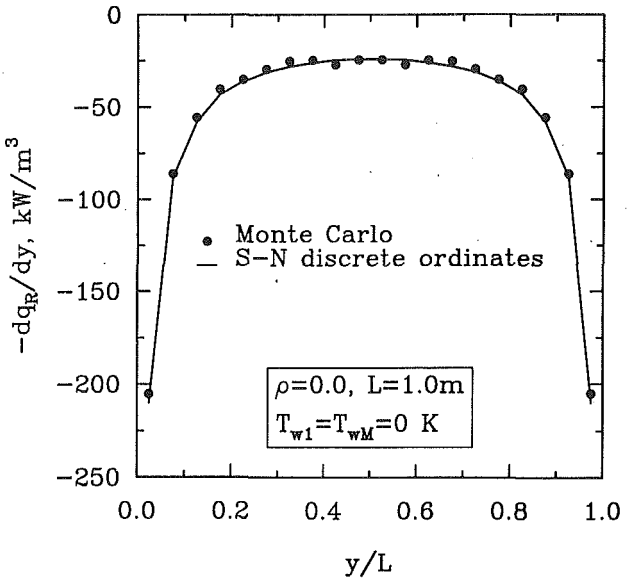

Fig. 3(*a*) Comparison of radiative dissipation for the uniform temperature profile

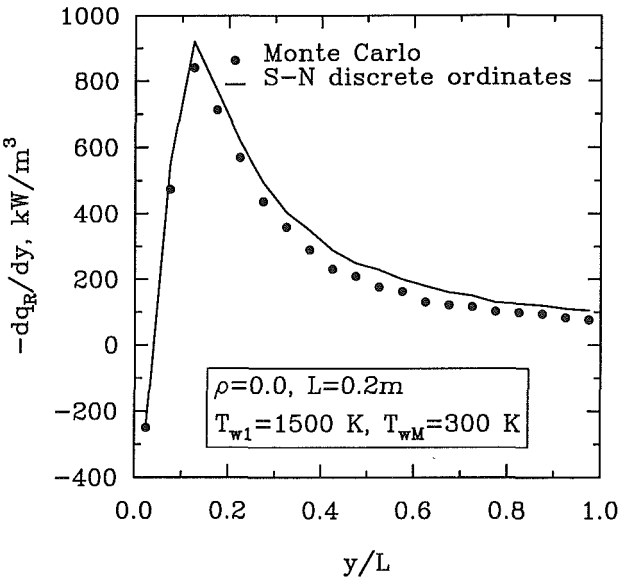

Fig. 3(*b*) Comparison of radiative dissipation for the boundary layer type temperature profile

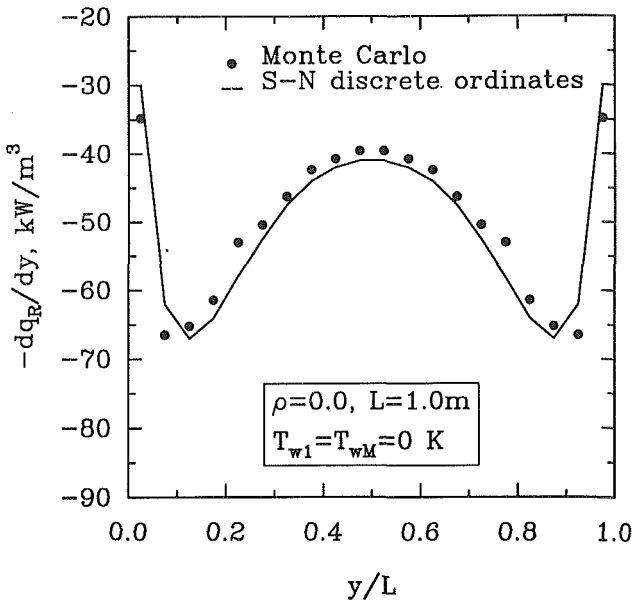

Fig. 3(*c*) Comparison of radiative dissipation for the parabolic H_2O concentration profile

to a net absorber away from the hot wall) as the S-N discrete ordinates results. The results for the parabolic H_2O concentration distribution (with a uniform temperature profile) are shown in Fig. 3(*c*). The Monte Carlo method also predicts the interesting **W** type shape distribution of $-\partial q_R/\partial y$ as in the S-N discrete ordinates method. Here the Monte Carlo solutions appear to be a little higher than the S-N discrete ordinates solutions, especially in the central region.

The results for the net radiative wall heat flux obtained for the cases presented in Figs. 3(*a–c*) are given in Table 1. The differences of results between different solutions for the three cases are not more than 3.5 percent. This shows agreement similar to that for the radiative dissipation results.

The situation with reflecting walls is considered next. Figures 4(*a*) and 4(*b*) show the comparisons between the Monte Carlo solutions and the S-N discrete ordinates solutions for different wall reflectivities. For these results, the parabolic type temperature profile and the uniform composition of pure H_2O vapor at 1 atm are assumed. The S-N discrete ordinates solutions are based on the second-degree closure results (Menart et al., 1993). The second-degree closure means that the history of two reflections is considered in the radiative flux equation and the remaining reflections are approximated by a closure method. Based on the study by Kim et al. (1991b), the second-degree discrete ordinates solutions for typical cases required about 160 minutes on the Cray-2 supercomputer. This is significantly higher than the CPU time required for the MCM, which is not more than 10 minutes on a Sun Sparc workstation.

Figure 4(*a*) presents the results of $-\partial q_R/\partial y$ for wall reflectivities of $\rho = 0.5$, with a slab thickness of $L = 0.5$ m. Excellent agreements between different solutions are seen in the figure. In the central region, the values of $-\partial q_R/\partial y$ are approaching a plateau. The Monte Carlo results appear to be slightly oscillating in this region. The reason is that the total number of energy bundles is a finite number and the Monte Carlo results are of a statistical nature. The oscillation decreases and the results of $-\partial q_R/\partial y$ become smoother as the total number of energy bundles is increased. This oscillation is also found in other figures. Figure 4(*b*) shows the results for the more strongly reflecting walls of $\rho = 0.9$ with the same slab thickness. Again, the Monte Carlo solutions appear very close to the S-N discrete ordinates solutions.

Table 1 also shows the net radiative wall heat fluxes for the cases presented in Figs. 4(*a*) and 4(*b*). The Monte Carlo results are slightly lower than the S-N discrete ordinates results. But the differences are within 6 percent. There are physical justifications for such discrepancies. In the S-N discrete ordinates method, the history of two reflections is taken into account and the remaining reflections are approximated as traveling in a medium without any attenuation. This approximation overpredicts the radiative energy absorbed on the walls. In the MCM, the history of the reflections is simulated in an exact manner. In addition, the Monte Carlo solutions are also subject to small statistical errors.

The spectrally correlated results are compared with the noncorrelated results in Figs. 5(*a*) and 5(*b*). A spectral correlation has been considered in all the results presented in previous figures. In a spectrally noncorrelated formulation, the correlation between spectrally dependent quantities is neglected. By using Eq. (16), the Monte Carlo noncorrelated results can be obtained. The temperature and H_2O concentration distributions considered here are the same as those in Figs. 4(*a*) and

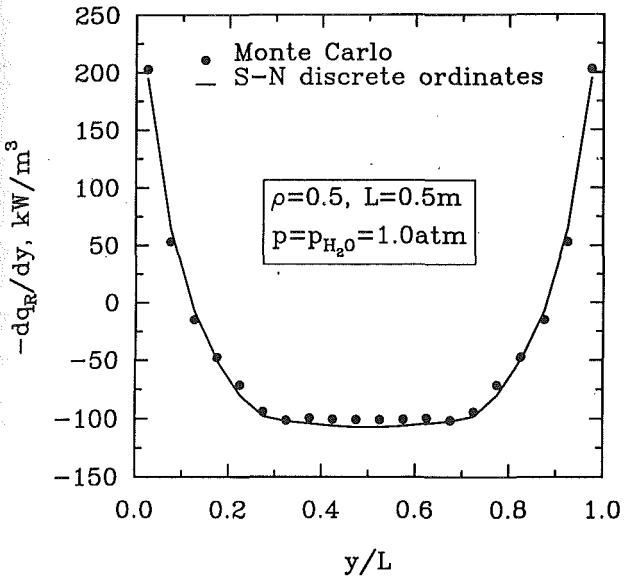

Fig. 4(*a*) Comparison of radiative dissipation in pure H_2O for $\rho = 0.5$, $L = 0.5$ m

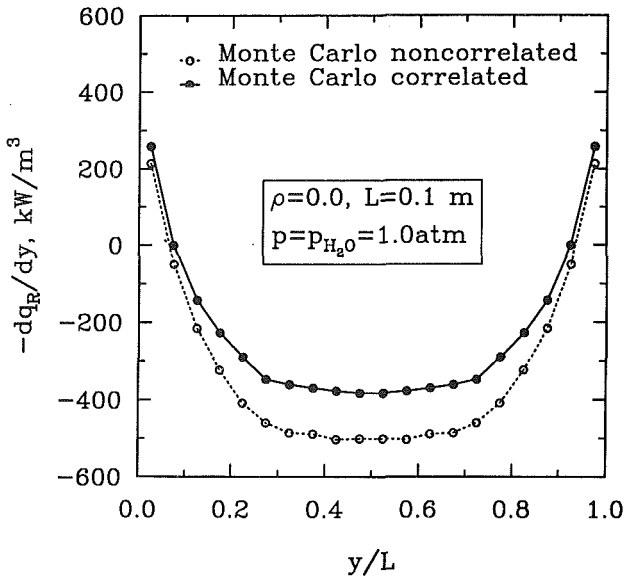

Fig. 5(*a*) Comparison of correlated and noncorrelated results in pure H_2O for $\rho = 0.0$, $L = 0.1$ m

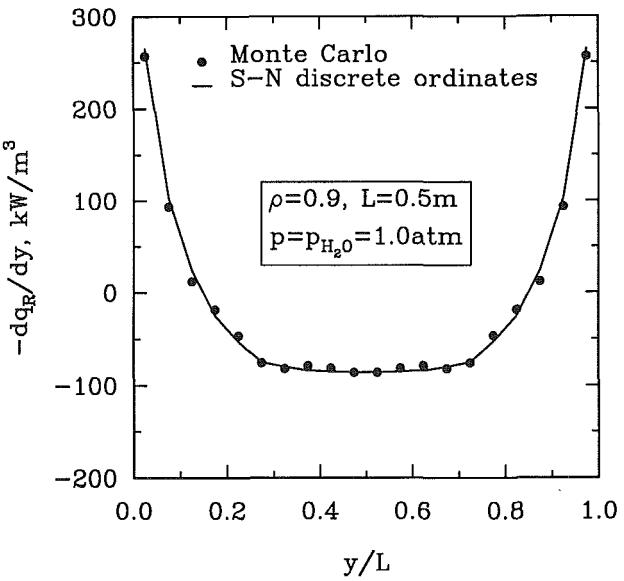

Fig. 4(*b*) Comparison of radiative dissipation in pure H_2O for $\rho = 0.9$, $L = 0.5$ m

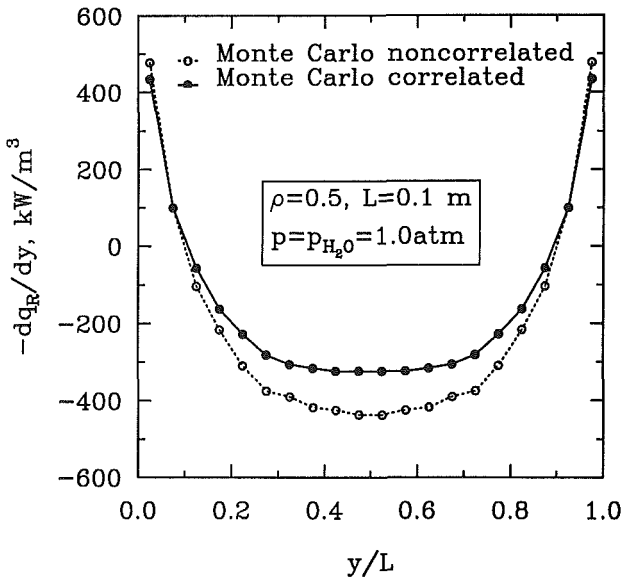

Fig. 5(*b*) Comparison of correlated and noncorrelated results in pure H_2O for $\rho = 0.5$, $L = 0.1$ m

Table 1 Comparison of the net radiative wall heat fluxes (kW/m^2)

	L (m)	ρ	Monte Carlo	S-N Discrete Ordinates
Uniform T	1.0	0.0	-27.6	-28.2
Boundary layer T	0.2	0.0	280.4	277.4
Uniform T with concentration profile	1.0	0.0	-24.5	-25.4
Parabolic T	0.5	0.5	9.47	9.66
Parabolic T	0.5	0.9	2.55	2.70

4(*b*). The wall reflectivities are $\rho = 0.0$ for Fig. 5(*a*) and $\rho = 0.5$ for Fig. 5(*b*), and the slab thickness L is 0.1 m for the two cases. The figures clearly show that the noncorrelated results overestimate the gas emission in the central region, and differ by about 30–35 percent from the correlated results. The reason for this discrepancies is in the derivation of the statistical relationship for determining the location of absorption of an energy bundle. The term

$$\overline{\tau_\omega(s \to s')\tau_\omega(s' \to s'')}$$

in Eq. (14) can be treated in two different ways, that is,

$$\overline{\tau_\omega(s \to s')\tau_\omega(s' \to s'')} = \overline{\tau_\omega(s \to s'')}$$

and

$$\overline{\tau_\omega(s \to s')} \cdot \overline{\tau_\omega(s' \to s'')},$$

respectively. The first choice results in the correlated formulation given by Eq. (15) and the second choice results in the noncorrelated formulation given by Eq. (16). Since the value of

$$\overline{\tau_\omega(s \to s')\tau_\omega(s' \to s'')}$$

is greater than the value of

$$\overline{\tau_\omega(s \to s')} \cdot \overline{\tau_\omega(s' \to s'')},$$

the R_1 calculated from Eq. (15) is smaller than that calculated from Eq. (16) for the same conditions. This means that an energy bundle travels a shorter distance by using the correlated

formulation in comparison to that by using the noncorrelated formulation. So, it is concluded that an energy bundle is more likely to be absorbed near the point of emission for the correlated case and near or on the walls for the noncorrelated case. Because correlated results and noncorrelated results differ significantly, the spectral correlation must be taken into account in order to predict the radiative heat transfer accurately.

Conclusions

The MCM has been applied to investigate the radiative heat transfer in a nongray participating medium. When a narrow band model is employed in the MCM, the spectral correlation between the transmittances of two different segments of the same path must be taken into account in the statistical relationship for determining the absorption location in order to get accurate results. For the nongray case with reflecting walls, the advantages of the MCM are very clear in comparison to other methods. Based on the cases considered in this study, the MCM is found to be a very reliable and efficient method to analyze nongray radiative heat transfer. The analysis can be extended to multidimensional problems easily, and the MCM can become a viable procedure for evaluation of radiation in many complicated practical problems.

Acknowledgments

This work, in part, was supported by the NASA Langley Research Center through grant No. NAG-1-363 entitled "Institute for Computational and Applied Mechanics (CAM)." The authors extend their thanks to Dr. R. Krishnamurthy for many useful discussions.

References

Dunn, W. L., 1983,"Inverse Monte Carlo Solutions for Radiative Transfer in Inhomogeneous Media," *Journal of Quantitative Spectroscopy and Radiative Transfer*, Vol. 29, No. 1, pp. 19–26.

Godson, W. L., 1953, "The Evaluation of Infrared Radiation Fluxes Due to Atmospheric Water Vapor," *Quarterly Journal of the Royal Meteorological Society*, Vol. 79, pp. 367–379.

Gupta, R. P., Wall, T. F., and Truelove, J. S., 1983, "Radiative Scatter by Fly Ash in Pulverized-Coal-Fired Furnaces: Application of the Monte Carlo Method to Anisotropic Scatter," *International Journal of Heat and Mass Transfer*, Vol. 26, No. 11, pp. 1649–1660.

Haji-Sheikh, A., 1988, "Monte Carlo Methods," in: *Handbook of Numerical Heat Transfer*, W. J. Minkowycz, E. M. Sparrow, G. E. Schneider, and R. H. Pletcher, eds., Wiley, New York, Chap. 16.

Hartmann, J. M., Levi Di Leon, R., and Taine, J., 1984, "Line-by-Line and Narrow-Band Statistical Model Calculations for H_2O," *Journal of Quantitative Spectroscopy and Radiative Transfer*, Vol. 32, No. 2, pp. 119–127.

Howell, J. R., and Perlmutter, M., 1964a, "Monte Carlo Solution of Thermal Transfer Through Radiant Media Between Gray Walls," ASME JOURNAL OF HEAT TRANSFER, Vol. 86, pp. 116–122.

Howell, J. R., and Perlmutter, M., 1964b, "Monte Carlo Solution of Radiant Heat Transfer in a Nongray Nonisothermal Gas With Temperature Dependent Properties," *American Institute of Chemical Engineers Journal.*, Vol.10, No. 4, pp. 562–567.

Howell, J. R., 1968, "Application of Monte Carlo to Heat Transfer Problems," *Advances in Heat Transfer*, Vol. 5, Academic Press, New York.

Howell, J. R., 1988, "Thermal Radiation in Participating Media: The Past, the Present, and Some Possible Futures," ASME JOURNAL OF HEAT TRANSFER, Vol. 110, pp. 1220–1229.

Kim, T. K., Menart, J. A., and Lee, H. S., 1991a, "Nongray Radiative Gas Analyses Using the S-N Discrete Ordinates Method," ASME JOURNAL OF HEAT TRANSFER, Vol. 113, pp. 946–952.

Kim, T. K., Menart, J. A., and Lee, H. S., 1991b, "S-N Discrete Ordinates Solutions of Nongray Radiative Transfer With Diffusely Reflecting Walls," *Proceedings of the 28th National Heat Transfer Conference*, ASME HTD-Vol. 160, pp. 79–87.

Kobiyama, M., Taniguchi, H., and Saito,T., 1979, "The Numerical Analysis of Heat Transfer Combined With Radiation and Convection," *Bulletin of the Japan Society of Mechanical Engineers*, Vol. 22, No. 167, May 1979, pp 707–714.

Kobiyama, M., 1986, "A Study on the Reduction of Computing Time of the Monte Carlo Method Applied to the Radiative Heat Transfer," *Bulletin of the Japan Society of Mechanical Engineers*, Vol. 29, No. 255, pp. 3000–3006.

Ludwig, C. B., Malkmus, W., Reardon, J. E., and Thompson, J. A. L., 1973, "Handbook of Infrared Radiation From Combustion Gases," NASA SP-3080.

Malkmus, W., 1967, "Random Lorentz Band Model With Exponential-Tailed S^{-1} Line-Intensity Distribution Function," *Journal of the Optical Society of America*, Vol. 57, No. 3, pp. 323–329.

Menart, J. A., Lee, H. S., and Kim, T. K., 1993,"Discrete Ordinates Solutions of Nongray Radiative Transfer With Diffusely Reflecting Walls," ASME JOURNAL OF HEAT TRANSFER, Vol. 115, pp. 184–193.

Modest, M., 1992, "The Monte Carlo Method Applied to Gases With Spectral Line Structure," *Proceedings of the 28th National Heat Transfer Conference*, ASME HTD-Vol. 203, pp.79–84.

Perlmutter, M., and Howell, J. R., 1964, "Radiative Transfer Through a Gray Gas Between Concentric Cylinders Using Monte Carlo," ASME JOURNAL OF HEAT TRANSFER, Vol. 86, pp. 169–179.

Siegel, R., and Howell, J. R., 1981, *Thermal Radiation Heat Transfer*, McGraw-Hill, New York, 1971; 2nd ed., 1981.

Soufiani, A., Hartmann, J. M., and Taine, J., 1985, "Validity of Band-Model Calculation for CO_2 and H_2O Applied to Radiative Properties and Conductive-Radiative Transfer," *Journal of Quantitative Spectroscopy and Radiative Transfer*, Vol. 33, No. 3, pp. 243–257.

Soufiani, A., and Taine, J., 1987, "Application of Statistical Narrow-Band Model to Coupled Radiation and Convection at High Temperature," *International Journal of Heat and Mass Transfer*, Vol. 30, No. 3, pp. 437–447.

Steward, F. R., and Cannon, P., 1971, "The Calculation of Radiative Heat Flux in a Cylindrical Furnace Using the Monte Carlo Method," *International Journal of Heat and Mass Transfer*, Vol. 14, No. 2, pp. 245–262.

Taniguchi, H., Kudo, K., Otaka, M., Sumarsono, M., and Obata, M., 1991, "Non-gray Analysis on Radiative Energy Transfer Through Real Gas Layer by Monte Carlo Method," *Proceedings of the 7th International Conference on Numerical Methods of Thermal Problems*.

Tiwari, S. N., 1978, "Models for Infrared Atmospheric Radiation," *Advances in Geophysics*, Vol. 20, Academic Press, New York.

Zhang, L., Soufiani, A., and Taine, J., 1988, "Spectral Correlated and Noncorrelated Radiative Transfer in a Finite Axisymmetric System Containing an Absorbing and Emitting Real Gas-Particle Mixture," *International Journal of Heat and Mass Transfer*, Vol. 31, No. 11, pp. 2261–2272.

Cooling of a Heated Surface by Mist Flow

S. L. Lee
Professor,
Department of Mechanical Engineering,
State University of New York
at Stony Brook,
Stony Brook, NY 11794-2300

Z. H. Yang
Senior Research Engineer,
Heat Transfer Research, Inc.,
College Station, TX 77842

Y. Hsyua[1]
Graduate Assistant,
Department of Mechanical Engineering,
State University of New York
at Stony Brook,
Stony Brook, NY 11794-2300

Cooling requirements in modern industrial applications, such as the removal of heat from electronic equipments, often demand the simultaneous attainment of a high heat flux and a low and relatively uniform and steady temperature of the heated surface to be cooled. The conventional single-phase convection cooling obviously cannot be expected to function adequately, since the heat flux there is directly proportional to the temperature difference between the heated surface and the surrounding medium. To maintain a high heat flux, the temperature of the heated surface usually must be kept at a high level. An attractive alternative is cooling by a spray, which takes advantage of the significant latent heat of evaporation of the liquid. However, in conventional industrial spray coolings, such as in the case of the cooling tower of a power plant, the temperature of the heated surface usually remains relatively high and is nonuniform and unsteady containing numerous flashy hot spots. In order to optimize the performance of the spray cooling of a heated surface by a mist flow, a clear understanding is required of (1) the dynamic interaction between the droplets and the carrier fluid and (2) the thermal reception of the droplets at the heated surface. It is the dynamic interaction between the phases that is causing the droplets to deposit onto the heated surface. The thermal reception at the heated wall develops mass and heat transfer leading to the mode of cooling of the heated surface. In the present study, an experimental investigation was made of the combination of the dynamic depositional behavior of droplets in a water droplet–air mist flow with the use of a specially designed particle-sizing two-dimensional laser-Doppler anemometer. Also, the heat transfer characteristics at the heated surface were investigated in relation to droplet deposition on the heated surface for wide ranges of droplet size, droplet concentration, mist flow velocity, and heat flux. It was discovered that over a certain suitable range of combination of these parameters, a superbly effective cooling scheme could be established by the evaporation on the outside surface of an ultrathin liquid film. Such a film was formed on the heated surface by the continuous deposition of fine droplets from the mist flow. Under these conditions, the heat flux is primarily related to the evaporation of the ultrathin liquid film on the heated surface and thus depends less on the temperature difference between the heated surface and the ambient mist flow. The heated surface is quenched to a low, relatively uniform and steady temperature at a very high level of heat flux. Heat transfer enhancement as high as seven times has been found so far. This effective heat transfer scheme is here termed mist cooling.

Introduction

Augmentation of heat transfer from a heated surface is a problem of importance in a variety of industrial and technical problems, such as nuclear power plant emergency cooling, design of compact heat exchangers, cooling of electrical and electronic devices, etc. It has been well known for some time that introducing water droplets into an air stream increases heat transfer (Acrivos et al., 1964; Hodgson et al., 1968; Thomas and Sunderland, 1970). The evaporation of a single droplet in a gas stream without deposition was analyzed (Bhatti and Savery, 1975). An analytical study was made of the evaporation cooling of a single droplet deposited on a heated plate in which the heat conduction through the flattened droplet was taken as the main heat transfer mechanism (Bonacina et al., 1979; Grissom and Wierum, 1981). Heat transfer enhancement due to evaporation of water droplets within the thermal boundary layer was investigated (Hishida et al., 1980) and it was found that the heat transfer coefficient varied linearly with the water flux. The evaporation of a liquid film was investigated and the heat transfer enhancement in terms of the mist quality was semi-empirically estimated for a very low heat flux heated plate exposed to a very low velocity mist flow (Trela, 1981). Substantial studies have been reported on the impaction of liquid droplets of a stationary hot surface (Kendall and Rohsenow, 1978; Pederson, 1970; Yao and Choi, 1987). Experimental studies on droplet dynamics and heat transfer characteristics of the impaction of liquid droplets on a moving hot surface have been carried out (Shalnev et al., 1975; Yao and Cai, 1985; Choi and Hong, 1990). Typically, the droplet size was in the range of 600–1200 μm and the wall temperature was in the range of 120–320°C. It should be noted that the droplets were of relatively large size and the wall temperature was maintained above the boiling point for water (100°C). Consequently, the heat transfer characteristics could be divided into three regions similar to a conventional boiling curve, i.e., film, transition, and nucleate boiling regions (Choi and Hong, 1990).

In general, the effect of a single depositing droplet on the cooling of a heated surface depends strongly on the size-dependent Weber number of the droplet. The very small droplet (say, ~10 μm) may have completely evaporated before reaching the surface. Thus its effect would be a slight lowering of the flow temperature and the consequent slight improvement in the cooling of the surface. On the other hand, when a very

[1] Partially contributed to discussion on results of measurement of droplet deposition characteristics.

Contributed by the Heat Transfer Division for publication in the JOURNAL OF HEAT TRANSFER. Manuscript received by the Heat Transfer Division January 1992; revision received April 1993. Keywords: Evaporation, Multiphase Flows, Thin Film Flow. Associate Technical Editor: T. W. Simon.

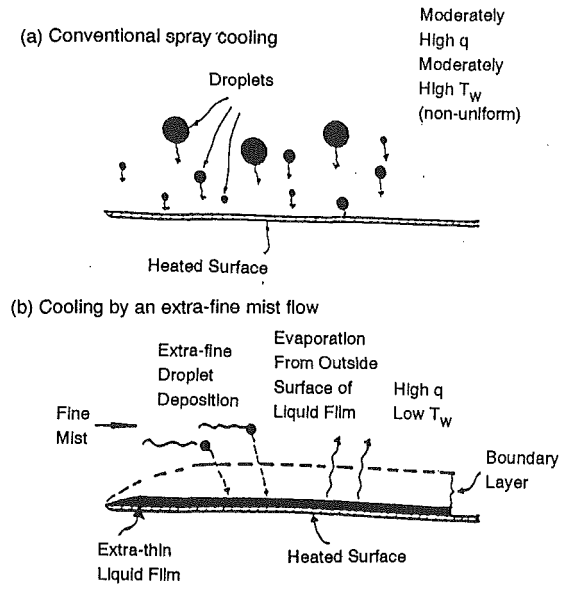

Fig. 1 Spray cooling

large droplet (say, >500 μm) approaches a high heat flux surface, rapid evaporation from the surface that faces the heated surface would generate a vapor barrier between the droplet and the heated surface. Thus the heat transfer in this case would be retarded. Under certain circumstances, a droplet of an intermediate suitable size, which is large enough so as not to become totally evaporated before reaching the surface yet small enough so as not to generate a vapor barrier on approach to the surface, can reach the heated surface and flatten out into a small piece of thin liquid film. If this flattened droplet is thin enough, the evaporation will take place on the outside surface of the flattened droplet during the short time before its complete evaporation. Under such circumstances, that portion of the heated surface would acquire a low temperature at a high heat flux. Providing the steady cooling of the entire heated surface would require the continuous deposition of droplets of the proper size and amount such that a continuous ultrathin evaporating surface liquid film is formed. A sketch of the conventional spray cooling and the mist cooling is shown in Fig. 1.

Accordingly, a key to the understanding of the complicated problem of mist cooling of a heated surface lies in the ability to take dynamic measurement of the size-associated transverse migratory behavior of droplets in the mist flow, in particular, in the region adjacent to the heated surface. Of particular interest in this regard is the development of a particle-sizing two-dimensional reference-mode laser-Doppler anemometry technique specially designed for the measurement of the dynamics of a two-phase suspension in a turbulent shear flow such as those in the region adjacent to a boundary wall (Lee and Srinivasan, 1982). Its output consists of the local instantaneous measurements of the size and two velocity-component distributions of the particulate phase together with the two velocity-component distributions of the continuous carrier phase together with the two velocity-component distributions of the continuous carrier phase in between the droplets in a very small nonintrusive optical measuring volume. Measurements are taken as close as 0.5 mm from the wall. Typically, signals from 20,000 to 100,000 droplets would be taken at any measuring point to arrive at the statistics for the analysis. The results include, at each measuring position, the number density distribution according to droplet size, the time-mean and turbulent fluctuating velocities in both the longitudinal and transverse directions for each of droplet size ranges, and the time-mean and turbulent fluctuating velocities in both the longitudinal and transverse directions of the continuous carrier phase.

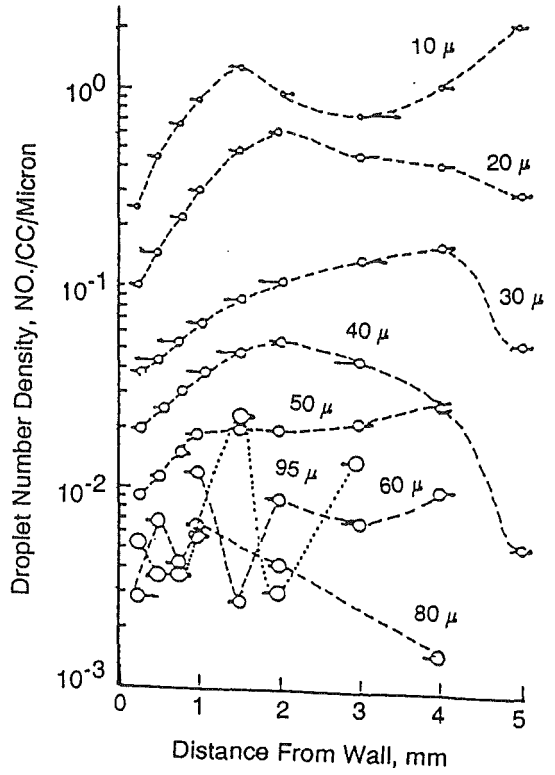

Fig. 2 Droplet concentration distribution in most flow in vertical channel (Lee and Srinivasan, 1982)

By the use of this experimental technique, a study of the depositional behavior of water droplets of a size range of up to 100 μm of a fine mist flow inside an unheated vertical rectangular channel (Lee and Srinivasan, 1982) reveals that in the region close to the wall the smaller droplets (<60 μm) all have the tendency of moving transversely toward the wall with the droplets of an optimum intermediate size in the range of ~ 30 μm for this case taking the most vigorous lead as shown in Fig. 2. This finding can be readily explained by a unified particle transport theory, which is based on the dynamic interaction between the phases in a turbulent two-phase suspension flow (Lee, 1987).

Experimental Arrangement

The experimental setup consists mainly of a vertical flow channel as shown in the sketch of Fig. 3. The channel is made of plexiglass with a square cross section of 41 mm $\times$ 41 mm. The total height of the channel is 1850 mm and a test section 250 mm long is mounted in the channel 860 mm from the lower entrance of the channel. The two symmetrically opposing inside walls of the test section are covered by a thin rectangular stainless steel sheet 250 mm $\times$ 41 mm and 0.25 mm thick, which is heated electrically by low-voltage, high-current AC power. The stainless steel sheet is made of four parallel strips 9.5 mm wide and 250 mm long, with a gap of 1 mm between every two adjacent strips. They are connected in series to insure uniform heating across the width of the sheet. Two of a total of fourteen Omega 36 gage copper-constantan thermocouples are installed in the flow and the others are at the various points on one of the two heated surfaces, which are instrumented for heat transfer measurements. A liquid atomizing nozzle (Spraco hydraulic atomizing nozzle) is placed at the center of a lower chamber below the flow channel. Tap water, being inexpensive, readily available, and environmentally harmless, is used as the

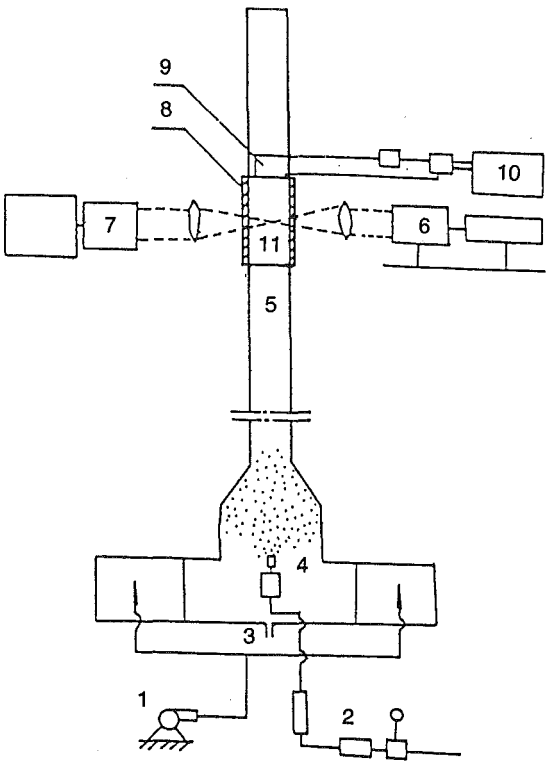

1. Blower 2. Droplet supplies 3. Drain
4. Nozzle 5. Flow channel 6. LDA system
7. Data process system 8. Measuring window
9. Thermocouples 10. Heating system
11. Heated wall

Fig. 3 Schematic diagram of flow system

working liquid for the mist flow. The size and concentration of the atomized droplets are controlled by using different nozzle sizes and different flow rates of liquid supplied to the nozzle. Liquid droplets are carried upward to form a mist flow in the flow channel by air flow supplied to the lower chamber from a blower. The specially designed laser-Doppler anemometer system is mounted on a precision three-dimensional traverse of 25 μm accuracy aligned with the two opposing clear movable optical windows one on each side of the flow channel at the test section. Small holes have been drilled through these windows to let the laser beams through without the obstruction of the deposited droplets on these windows.

Experimental Procedure

The temperature and heat flux measurements were conducted simultaneously with the measurements of the time-mean and turbulent fluctuating droplet and carrier velocities, and the droplet size-number density distribution. The experimental measurements were done at two selected levels in the flow channel. The distances from the leading edge of the heated section to the selected measuring levels were 20 mm and 240 mm. In order to understand the phenomenon of mist quench cooling and compare its effectiveness, single-phase air convective heat transfer experiments, without the introduction of droplets, were performed first. The wall heat flux was varied from 0.15 W/cm^2 to 5.3 W/cm^2. The air velocity was varied from 4 m/s to 32 m/s. Measurements were made of the temperatures at the center of the heated plate as well as in the channel. At the same time, measurements were also made of the distribution of velocity of air at the various transverse locations in the channel by using the very small droplets (a few microns) as tracers.

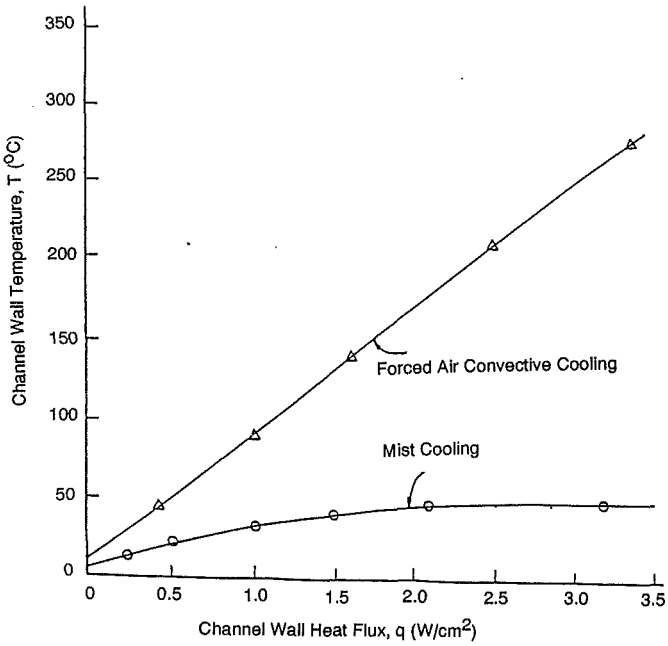

Fig. 4 Sample plots of channel wall temperature distribution versus wall heat flux by forced air convective cooling and mist cooling

The mist flow experiments were started by setting the water flow rate to the atomizating nozzle as desired, and then turning the blower and transformer power on. Depending on the values of the wall heat flux and air velocity chosen, the droplet concentration could be adjusted by changing the water supply rate to attain the establishment of an ultrathin (50–100 μm) evaporating liquid film on the heated wall surface. Once the flow and heat transfer became steady, measurements were made of the temperatures at the center of the heated plate as well as in the channel. At the same time, measurements were also made of the distributions of the two velocities of the two phases and the size of the droplets at the various transverse locations ranging from the centerline to 0.5 mm away from the heated wall by the use of the specially designed particle-sizing laser Doppler anemometer (Lee and Srinivasan, 1982). The mean droplet diameter d_p was varied from a few microns to 200 μm and the standard deviation of the droplet size distribution was found to cluster around 20 percent of the mean droplet size in all cases. The mean droplet concentration C_o was varied from 0.05 kg/m^3 to 0.09 kg/m^3. The measurement errors for air and water flow rates were respectively less than 1 and 3 percent. The measurement errors for temperature and velocity were respectively less than 0.1 and 1 percent. The measurement error for heat flux was less than 1 percent and the measurement error for droplet size was less than 3 percent.

Results and Discussion

(A) Mist Cooling Heat Transfer Measurements. Figure 4 shows sample plots of the channel wall temperature T versus wall heat flux, $\dot{q}$, for forced air convective cooling and for water droplet–air mist cooling respectively. Mist cooling brings down the channel wall temperature drastically for the same heat flux.

Figure 5 shows sample plots of the channel wall temperature T versus the droplet Sauter mean diameter d_p for the two values of the wall heat flux, $\dot{q}$ (5.05 and 2.797 W/cm^2, respectively), at the same channel centerline velocity ($U_o = 26.45$ m/s) and the ambient mean droplet mass concentration ($C_o = 0.089$ kg/m^3). The droplet size can be divided into three ranges. For this case, the mist quench cooling is established in the droplet size range of about 30 ~ 80 μm in which an ultrathin evaporating

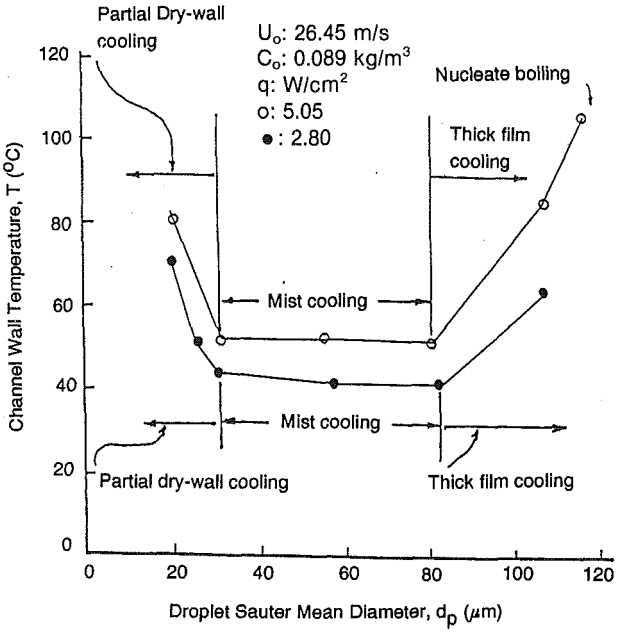

Fig. 5 Sample plots of wall temperature versus droplet Sauter mean diameter by mist flow

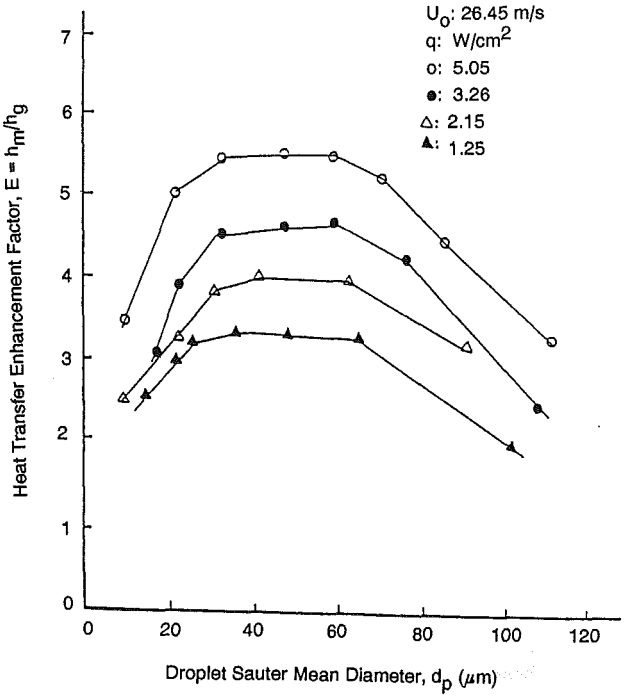

Fig. 6 Sample plots of heat transfer enhancement factor versus droplet Sauter mean diameter by mist cooling

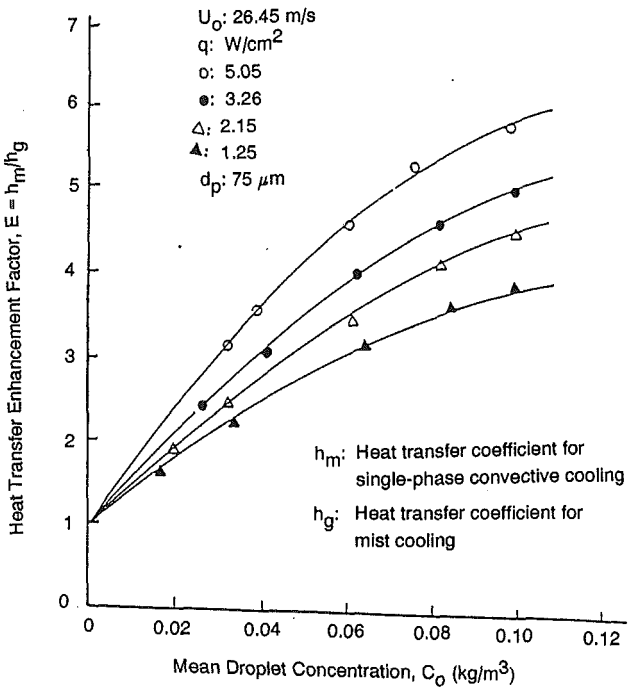

Fig. 7 Sample plots of heat transfer enhancement factor versus mean droplet concentration

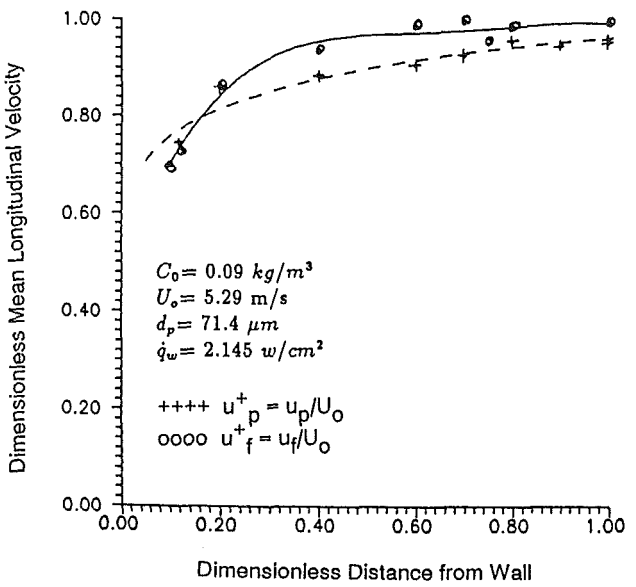

Fig. 8 Sample plots of mean longitudinal velocity distribution

liquid film is found to be attached to the heated surface, which is quenched to a very low temperature. The thickness of this liquid film has been estimated to be about 50 ~ 100 μm by measuring the relocation of the reflection of one of the optical beams of the laser-Doppler anemometer system. For smaller droplets ($d_p < 30$ μm), the heated wall becomes partially or totally drop and its temperature shoots up to a very high value. On the other hand, for larger droplets ($d_p > 80$ μm), the liquid film becomes so thick and consequently the temperature of the heated surface also shoots up to a higher value. For the case of $d_p = 115$ μm, $C_o = 0.089$ kg/m^3, and $\dot{q} = 5.05$ W/cm^2, the wall temperature was raised to 104°C and nucleate boiling appeared to take place at the heated surface.

Figure 6 shows sample plots of the heat transfer enhancement factor $E = h_m/h_g$, where h_m and h_g are the heat transfer coefficients for the mist flow and single-phase air flow, respectively, versus the droplet Sauter mean diameter d_p for four different values of the wall heat flux $\dot{q}$ at the same channel centerline velocity ($U_o = 26.45$ m/s). The heat transfer enhancement shows a peak plateau for $d_p = 30 \sim 80$ μm.

Figure 7 shows sample plots of the heat transfer enhancement factor $E = h_m/h_g$ versus the mean droplet mass concentration C_o for four different values of the wall heat flux $\dot{q}$ for the same channel centerline velocity ($U_o = 26.45$ m/s) and the same droplet size ($d_p = 75$ μm). It is seen that the heat transfer enhancement improves with the increase with the droplet concentration, with $E = 6$ for $\dot{q} = 5.05$ W/cm^2 and $C_o = 0.10$ kg/m^3.

(B) Measurement of Mist Flow in the Channel in Conjunction With Mist Cooling of Its Heated Walls by an Ultrathin Evaporating Liquid-Film. Figure 8 shows sample plots of

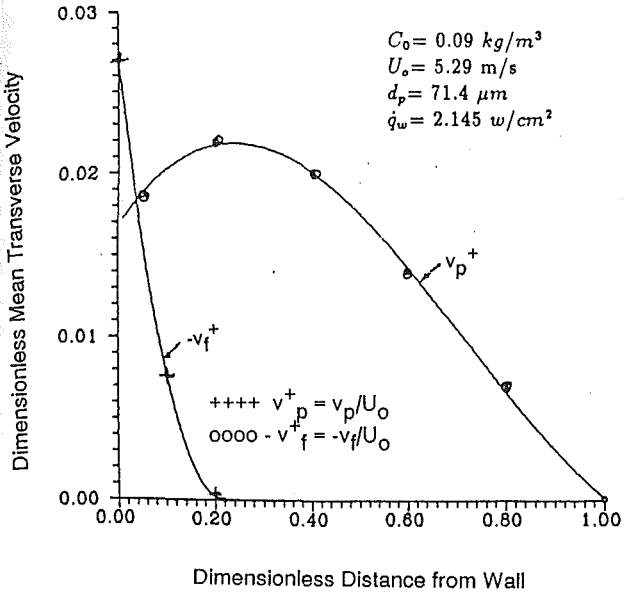

Fig. 9 Sample plots of mean transverse droplet and fluid velocity distributions (toward wall)

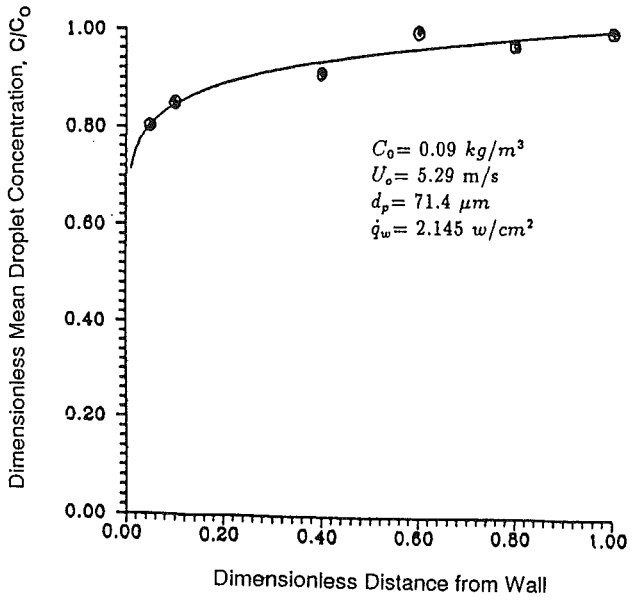

Fig. 10 Sample plot of droplet concentration distribution

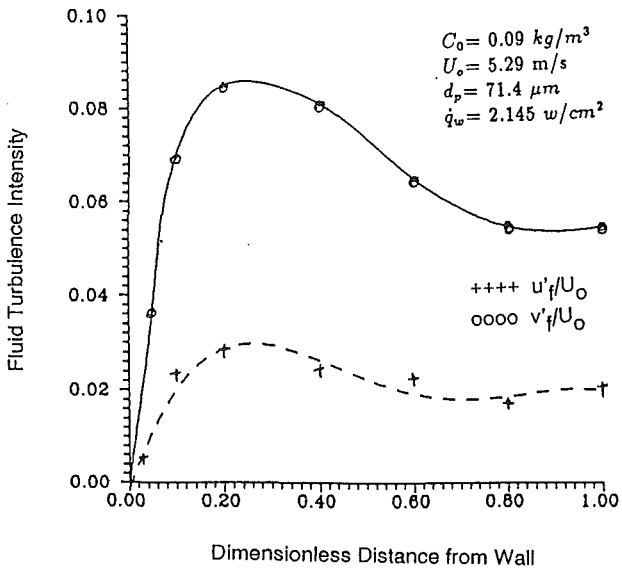

Fig. 11 Sample plots of fluid turbulence intensity distribution

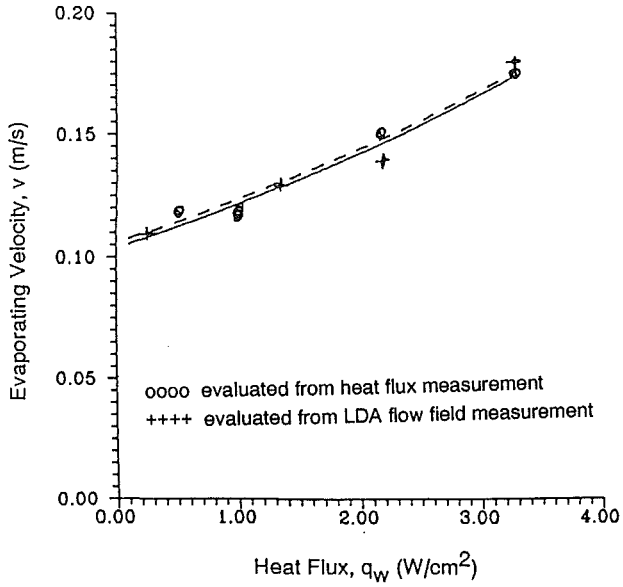

Fig. 12 Sample plots of comparison of vapor evaporation velocity from evaporating liquid film evaluated from heat flux measurement to evaluated from LAD flow field measurement

profiles of longitudinal (vertical) velocities in the channel for both the carrier air and droplet phases for the case of $U_o = 5.29$ m/s, $d_p = 71.4$ μm, and $\dot{q} = 2.145$ W/cm^2. It is seen that for small droplets the two phases follow each other closely in the longitudinal direction.

Figure 9 shows sample plots of the profiles of the droplet and fluid transverse (horizontal) velocities, $\bar{v}_p$ and $\bar{v}_f$, in the channel for the same case. It is seen that the droplets are pushed toward the heated wall with the transverse velocity peaking for this case at a distance of about 25 percent of the channel half-width and being reduced beyond this point possibly due to the onrushing of the evaporating vapor from the ultrathin liquid film on the heated wall. It is indeed shown that there is a sizable transverse velocity $\bar{v}_f$ (pointing away from the wall) in the carrier phase (air/vapor) in the near-wall region apparently due to the evaporation from the ultrathin liquid film on the heated wall.

Figure 10 shows a sample plot of the profile of the mean droplet mass concentration for the same case in the channel.

Figure 11 shows sample plots of the profiles of the turbulence intensities of the carrier phase u'_f and v'_f in the longitudinal and transverse directions, respectively, for the same case.

Figure 12 shows a sample comparison of the mean carrier phase transverse velocity v_f at the outer surface of the ultrathin liquid film on the heated wall from heat transfer measurement with that from mist flow LDA measurement. From the heat transfer measurement, it is obtained by a mass balance directly connected with a heat balance at the outer surface of the evaporating ultrathin liquid film. From the mist flow LDA measurement, it is obtained by measuring the transverse velocity of the smallest droplets, which serve as tracers, at the closest measuring location to the heated wall.

Figure 13 shows a sample comparison between the mass flux obtained from the measurement of the heat flux to the evaporating liquid film and the mass flux obtained from the measurement of the deposition of droplets from the mist flow. The mass flux from liquid film evaporation $\dot{m}_e$ is related to the heat flux $\dot{q}$ through the following relationship:

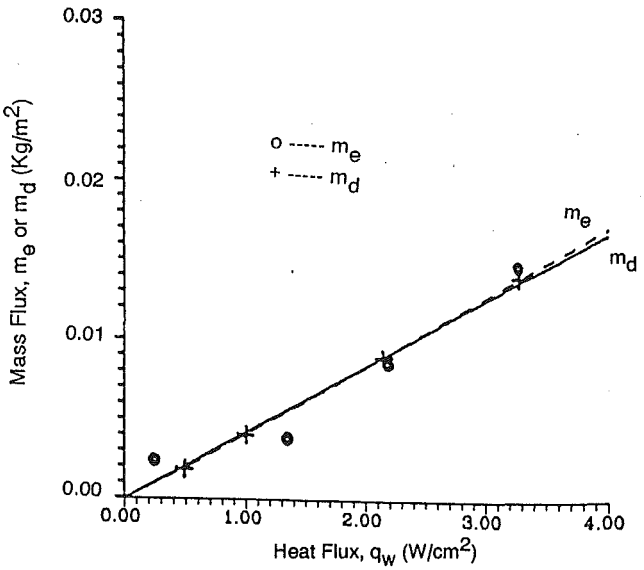

Fig. 13 Sample plots of comparison between mass flux based on heat flux to evaporating liquid film and mass flux based on droplet deposition from mist flow

$$\dot{m}_e = \dot{w}/h_{fg}$$

where h_{fg} is the latent heat of evaporation of the liquid. The mass flux due to deposition of droplets from the mist flow onto the liquid film $\dot{m}_d$ can be computed from:

$$\dot{m}_d = [\overline{v}_p \overline{C}]_{\text{near wall}}$$

where $\overline{C}$ is the droplet mass concentration. In this case, both the values of v_p and $\overline{C}$ are taken to be those measured at the measuring location closest to the heated wall. It is seen that close agreement has been established.

Conclusion

An effective heat transfer scheme of mist cooling has been established for the cooling of a heated surface. In this scheme, for certain ranges of droplet size and concentration , mist flow velocity and heat flux, an ultrathin evaporating liquid film, with evaporation taking place from its outer surface, can be maintained by the continuous deposition of extra-fine droplets from the mist flow. The heated surface is quenched to a very low level of relatively uniform and steady temperature at a very high level of heat flux. A heat transfer enhancement over a comparable single-phase convective cooling of as high as seven times has so far been established.

References

Acrivos, A., Ahern, J. E., and Navy, A. R., Jr., 1964, "Research Investigation of Two-Component Heat Transfer," Marquardt Aerospace Research Laboratories, Wright-Patterson Air Force Base, Report ARL, pp. 61-116.

Bhatti, M. S., and Savery, C. W., 1975, "Augmentation of Heat Transfer in a Laminar External Gas Boundary Layer by the Vaporization of Suspended Droplets," ASME JOURNAL OF HEAT TRANSFER, Vol. 97, pp. 179-184.

Bonacina, C., Del Giudice, S., and Comini, G., 1979, "Dropwise Evaporation," ASME JOURNAL OF HEAT TRANSFER, Vol. 101, pp. 441-446.

Choi, K. J., and Hong, J. S., 1990, "Heat Transfer Characteristics of Water Droplets Interacting With a Rotating Hot Surface," *Int. Comm. Heat Mass Transfer*, Vol. 17, pp. 419-429.

Grissom, W., and Wierum, F., 1981, "Liquid Spray Cooling of a Heated Surface," *Int. J. Heat Mass Transfer*, Vol. 24, pp. 261-271.

Hishida, K., Maeda, M, and Ikai, S., 1980, "Heat Transfer From a Flat Plate in Two-Component Mist Flow," ASME JOURNAL OF HEAT TRANSFER, Vol. 102, pp. 513-518.

Hodgson, J. W., Saterbac, R. T., and Sunderland, J. E., 1968, "An Experimental Investigation of Heat Transfer From a Spray Cooled Isothermal Cylinder," ASME JOURNAL OF HEAT TRANSFER, Vol. 90, pp. 457-463.

Kendall, G. E., and Rohsenow, W. M., 1978, "Heat Transfer to Impacting Drops and Post Critical Heat Flux Dispersed Flow," Heat Transfer Lab. Report No. 85694-100, MIT.

Lee, S. L., and Srinivasan, J., 1982, "A Laser-Doppler Velocimetry Technique for In-Situ Local Measurement of Dilute Two-Phase Suspension Flow," *Eng. Application of Laser Velocimetry*, ASME, New York, pp. 117-125.

Lee, S. L., 1987, "A Unified Theory on Particle Transport in a Turbulent Dilute Two-Phase Suspension Flow," *Int. J. Multiphase Flow*, Vol. 13, pp. 137-144.

Pederson, C. O., 1970, "An Experimental Study of the Dynamic Behavior and Heat Transfer Characteristics of Water Impinging Upon a Heated Surface," *Int. J. Heat Mass Transfer*, Vol. 13, pp. 369-381.

Shalnev, F. K., Povarov, O. A., Nazarov, O. I., and Shalobosov, I. A., 1975, *Proc. 5th Conf. Fluid Machinery*, Vol. 2, p. 1011.

Thomas, W. C., and Sunderland, J. E., 1970, "Heat Transfer Between a Plane Surface and Air Containing Suspended Water Droplets," *Ind. Eng. Chem. Fundamental*, Vol. 9, No. 3, pp. 368-374.

Trela, M., 1981, "An Approximate Calculation of Heat Transfer During Flow of an Air-Water Mist Along a Heated Flat Plate," *Int. J. Heat Mass Transfer*, Vol. 24, No. 4, pp. 749-755.

Yao, S. C., and Cai, K. Y., 1985, "The Dynamics and Leidenfrost Temperature of Drops Impacting on a Hot Surface at Small Angles," ASME 85-WA/HT-39.

Yao, S. C., and Choi, K. J., 1987, "Heat Transfer Experiments of Mono-Dispersed Vertically Impacting Spray," *Int. J. Multiphase Flow*, Vol. 13, No. 5, pp. 639-648.

Rewetting Theory and the Dryout Heat Flux of Smooth and Grooved Plates With a Uniform Heating

S. H. Chan

W. Zhang

Department of Mechanical Engineering,
University of Wisconsin—Milwaukee,
P.O. Box 784,
Milwaukee, WI 53201

The evaporation and condensation of thin liquid films are of significant importance in a wide variety of problems ranging from specific applications in the heat pipe field to more general ones in the chemical, nuclear, and petrochemical industries. Although several investigations have been conducted to determine the rewetting characteristics of liquid films on heated rods, tubes, and flat plates, no solutions are yet available to describe the rewetting process of a hot plate subjected to a uniform heating. A model is presented to analyze the rewetting process of such plates with and without grooves. Approximate analytical solutions are presented for the prediction of the rewetting velocity and the transient temperature profiles of the plates. It is shown that the present rewetting velocity solution reduces correctly to the existing solution for the rewetting of an initially hot isothermal plate without heating from beneath the plate. Numerical solutions have also been obtained to validate the analytical solutions. Finally, a simple method is presented to predict the dryout heat flux of a liquid film flowing over a heated smooth or grooved plate. The results of the prediction are found to be in reasonable agreement with the existing experimental data.

Introduction

The rewetting process is a conjugated heat transfer problem involving interactions between a solid wall and flowing fluids. The process for rewetting of a grooved plate with a uniform heating is complicated, as the rewetting velocity varies with time, physical geometry of the grooves, plate properties, fluid properties, and the applied heat flux. Although several investigations (Yamanouchi, 1968; Thompson, 1972; Duffey and Porthouse, 1973; Sun et al., 1974; Alario et al., 1983; Grimley et al., 1988; Stroes et al., 1990; Ferng et al., 1991; Peng and Peterson, 1991) have been made to determine the rewetting characteristics of liquid films on heated rods, tubes, and flat plates, none has yet presented the solution for the rewetting process of a heated plate with a smooth or grooved surface subjected to a uniform heat flux. Is is noted that the surface with small grooves has received increasing attention as it has many practical applications. For instance, the microgrooved surface is employed most often to enhance heat transfer (Grimley et al., 1988). Microgrooves are also useful for replacing the wicking material in heat pipes. In fact, they are used in the innovative monogroove heat pipe design for the thermal radiators of the space station (Alario et al., 1983). When the thermal radiator is overloaded with a heat flux discharged from the condenser of the thermal bus system in the space station, the circumferential section of the monogrooved heat pipe directly underneath the heat flux is the location where dryout occurs first. In a recent space shuttle flight test, dryout of the heat pipe did occur. Therefore, it is of interest here to investigate the rate of rewetting speed and the condition that leads to the dryout of a plate subjected to uniform heating.

There are fundamental differences between the rewetting of a hot plate with a uniform heating and that without heating. As shown later (Eq. (1) and Appendix A), unlike the case without heating, the heat conduction equation is a transient equation even after the equation is transformed to the Lagrangian coordinate moving with the liquid rewetting front. Secondly, the plate temperature in the dry, insulated region far ahead of the rewetting front is not only invariant in the axial direction, but also a linear function of time due to a uniform heating (see Eq. (8)). A recent attempt (Peng and Peterson, 1991, 1992) to solve for the rewetting process of a plate subjected to a uniform flux has not accounted for these differences. They apparently encountered a compatibility difficulty in matching the solution of the temperature profile of the heated plate with a proper boundary condition because of the use of the steady-state transformed heat conduction equation, which is basically valid only for the case without internal or external heating (Yamanouchi, 1968; Thompson, 1972; Duffy and Porthouse, 1973; Sun et al., 1974; Tien and Yao, 1975).

One of the objectives here is to present a physical model suitable for the rewetting analysis of a plate heated by a constant heat flux from below. Solutions for the transient temperature profile and the rewetting velocity are presented. The incompatibility problem is also resolved. Another objective is to analyze the dryout limit of a grooved surface initially wetted by a liquid film. A means is provided for the prediction of the maximum heat input that results in the dryout of the liquid on the plate. The result of the prediction is compared with the experimental data of Grimley et al. (1988).

Rewetting Model and Solutions

We consider the rewetting process of a hot plate initially at a uniform temperature T_i with no liquid on the plate as shown in Fig. 1. The plate is heated from below by a uniform heat flux and is quenched by a liquid advancing along the direction of the grooves on the top surface of the plate. In order to simplify the complexity of the physical phenomena of the rewetting process, we consider first a heated smooth surface plate with no parallel grooves.

1 Smooth Surface Plate. The rewetting process of a hot dry plate is sketched in Fig. 1. A liquid film from a liquid reservoir, driven by its surface tension, is to advance along the hot plate. Similar to prior studies by Yamanouchi (1968), Duffey and Porthouse (1973), and Sun et al. (1974), the initial

Contributed by the Heat Transfer Division and based on a paper presented at ASME Winter Annual Meeting, Anaheim, CA, November 8–13, 1992. Manuscript received by the Heat Transfer Division October 1992; revision received June 1993. Keywords: Augmentation and Enhancement, Heat Pipes and Thermosyphons, Space Power Systems. Associate Technical Editor: L. C. Witte.

temperature of the plate is assumed to be higher than the Leidenfrost temperature T_0 such that the rewetting process is assumed to be conduction controlled. For a liquid film on a plate, there exist three heat transfer regimes: boiling, convective evaporation, and single-phase convection. However, similar to these prior studies, the following assumptions are made: a constant averaged heat transfer coefficient, for simplicity, in the wet region to remove the heat from the thin plate to the liquid film, no heat loss to the environment in the dry region, the plate at the rewet front remains at a constant Leidenfrost temperature, the liquid film remains at the saturation temperature T_s, and the plate is thin enough that the one-dimensional rewetting model can be invoked. It is therefore proposed to solve the following governing equation (see Appendix A) on a Lagrangian coordinate moving with the rewetting front:

$$\frac{\partial\theta}{\partial\tau}=\frac{\partial^2\theta}{\partial\eta^2}+P\frac{\partial\theta}{\partial\eta}-B\theta+A \tag{1}$$

where

$$P=\frac{U_r s_1\rho C_p}{K};\qquad B=\frac{hs_1}{K}$$

$$A=\frac{qs_1}{K(T_0-T_s)};\quad \theta(\eta,\tau)=\frac{T-T_s}{T_0-T_s} \tag{2}$$

$$\eta=\frac{x}{s_1};\qquad \tau=\frac{t}{s_1^2\rho C_p/K)}$$

where B is the Biot number; A, P, $\theta(\eta, \tau)$, η, and τ are the dimensionless heat source, rewetting velocity, temperature, length, and time respectively. In the wet region ($-L_1 \le x \le 0$), $h=\text{const}\neq 0$ while in the dry region ($0\le x\le L_2$), $h=B=0$.

The above governing equation is different from the equation in all prior rewetting models (Yamanouchi, 1968; Duffey and Porthouse, 1973; Sun et al., 1974; Peng and Peterson, 1991, 1992) in that an extra term, namely, the transient term on the left-hand side of the equation, is added. The addition of this transient term is essential in analyzing the rewetting process of the heated plate subjected to a heat flux conduction as shown in Fig. 1. This is because the temperature profile of the plate in the Lagrangian coordinate (x, y) is no longer invariant with time as in the case of rewetting an initially hot isothermal plate without heating from beneath the plate. Without it, the incompatibility difficulty as noted above will arise and the final solution cannot be expected to satisfy the transient boundary condition at $x=\infty$. The addition of the transient term is therefore essential. It, however, renders some mathematical complications in the solution of the rewetting velocity.

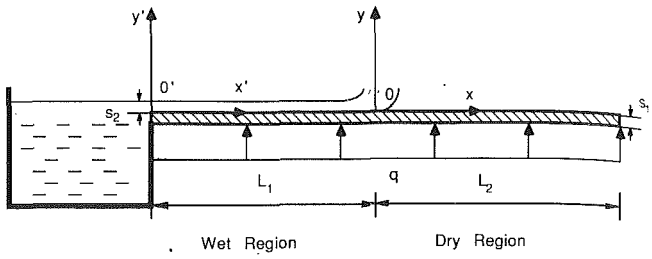

Fig. 1 Schematic of the rewetting film on the heated plate

The initial condition is

$$\theta(\eta, 0)=\frac{T_1-T_s}{T_0-T_s}=\theta_1 \tag{3}$$

while the boundary conditions are

$$\theta(-\eta_{L_1}, \tau)=0 \tag{4}$$

$$\theta(0, \tau)=1 \tag{5}$$

$$\theta(\eta_{L_2}, \tau)=\frac{T_L-T_s}{T_0-T_s}=\theta_1+A\tau \tag{6}$$

where η_{L1} and η_{L2} are defined as

$$\eta_{L_1}=\frac{L_1}{s_1},\qquad \eta_{L_2}=\frac{L_2}{s_1} \tag{7}$$

Nomenclature

A = dimensionless heat source
a_1 = coefficient defined in Eq. (65)
B = Biot number with respect to the convective heat transfer coefficient
C_p = thermal capacitance, J/kg-°C
h = surface convective heat transfer coefficient, W/m^2-°C
$\bar{h}$ = average boiling heat transfer coefficient, W/m^2-°C
h_a = convective coefficient between plate and environmental gas, W/m^2-°C
K = thermal conductivity, W/m-°C
L = length of the plate, m
L_1 = length of wet region, m
L_2 = length of dry region, m
N = grooved geometric coefficient
n = exponent defined in Eq. (65)
P = dimensionless rewetting velocity
q = uniform heat flux, W/m^2
q_{CHF} = critical heat flux (CHF), W/m^2
q_i = incipient boiling heat flux, W/m^2
q_{max} = maximum heat flux, W/m^2
s = plate thickness for smooth (s_1) or grooved ($s_1-\ell_1$) plate, m
s_1 = plate thickness, m
s_2 = liquid film thickness, m
T = temperature, °C
T_a = environmental temperature, °C
T_f = inlet liquid temperature, °C
T_i = incipient boiling temperature, °C
T_0 = Leidenfrost temperature, °C
T_s = saturation temperature, °C
T_1 = initial hot surface temperature, °C
t = time, s
U_r = rewetting front velocity, m/s
x = length of liquid film in moving front coordinate, m
x' = length of liquid film in stationary system, m
α_1 = constant defined in Eq. (23)
α_2 = constant defined in Eq. (45)
β_1 = constant defined in Eq. (23)
β_2 = constant defined in Eq. (45)
η = dimensionless length coordinate with respect to x
η' = dimensionless length coordinate with respect to x'
θ = dimensionless temperature
θ_h = dimensionless temperature of the transient part
θ_s = dimensionless temperature of the steady-state part
ρ = density, kg/m^3
τ = dimensionless time

Subscripts

d = dry region
g = grooved plate
L = total length of the plate
L_1 = length of wet region
L_2 = length of dry region
s = smooth plate
w = wet region

and T_L is the dry plate temperature at η_{L2}. The condition given in Eq. (6) implies that the plate is long enough that, within the time period of interest, the plate temperature at η_{L2} is not thermally affected by the rewetting process. Consequently, it can be expressed as

$$T_L = T_1 + \frac{qt}{\rho C_p s_1} \tag{8}$$

which is used in Eq. (6).

In the wet region ($-\eta_{L1} \le \eta \le 0$), the mathematical model of this problem is given as

$$\frac{\partial\theta}{\partial\tau} = \frac{\partial^2\theta}{\partial\eta^2} + P\frac{\partial\theta}{\partial\eta} - B\theta + A \tag{9}$$

$$\theta(\eta, 0) = \theta_1 \tag{10}$$

$$\theta(-\eta_{L_1}, \tau) = 0 \tag{11}$$

$$\theta(0, \tau) = 1 \tag{12}$$

Solving for the exact, analytical solution of the above equations appears to be difficult, if not impossible. Therefore an approximate, analytical solution is sought. This is made possible by treating the Peclet number, P, as a constant value in the mathematical deliberation in order to achieve a closed-form solution. This approximation appears to be reasonable as the rewetting velocity tends to reach a quasi-steady state after an initial period when the liquid film is brought into contact with the hot plate. The numerically exact solution will be presented later to check the accuracy of the closed form solution. Accordingly, the solution is split into two parts,

$$\theta(\eta, \tau) = \theta_{s,w}(\eta) + \theta_{h,w}(\eta, \tau) \tag{13}$$

where $\theta_{s,w}$ is the solution for the steady-state part of the problem,

$$\frac{d^2\theta_{s,w}}{d\eta^2} + P\frac{d\theta_{s,w}}{d\eta} - B\theta_{s,w} + A = 0 \tag{14}$$

$$\theta_{s,w}(0) = 1 \tag{15}$$

$$\theta_{s,w}(-\eta_{L_1}) = 0 \tag{16}$$

while $\theta_{h,w}$ is the solution to the transient part of the problem

$$\frac{\partial\eta_{h,w}}{\partial\tau} = \frac{\partial^2\theta_{h,w}}{\partial\eta^2} + P\frac{\partial\theta_{h,w}}{\partial\eta} - B\theta_{h,w} \tag{17}$$

$$\theta_{h,w}(\eta, 0) = \theta_1 - \theta_{s,w}(\eta) \tag{18}$$

$$\theta_{h,w}(0, \tau) = 0 \tag{19}$$

$$\theta_{h,w}(-\eta_{L_1}, \tau) = 0 \tag{20}$$

The solution of the steady-state problem is given as

$$\theta_{s,w}(\eta) = \left[1 - \frac{A}{B} - \frac{\left(1-\frac{A}{B}\right)e^{-r_1\eta_{L_1}} + \frac{A}{B}}{e^{-r_1\eta_{L_1}} - e^{-r_2\eta_{L_1}}}\right]e^{r_1\eta} + \left[\frac{\left(1+\frac{A}{B}\right)e^{-r_1\eta_{L_1}} + \frac{A}{B}}{e^{-r_1\eta_{L_1}} - e^{-r_2\eta_{L_1}}}\right]e^{r_2\eta} + \frac{A}{B} \tag{21}$$

$$r_1 = \frac{-P + \sqrt{P^2 + 4B}}{2}$$

$$r_2 = \frac{-P - \sqrt{P^2 + 4B}}{2}$$

To solve the transient solution, the following transformation is introduced:

$$\theta_{h,w}(\eta, \tau) = e^{\alpha_1\eta + \beta_1\tau}v(\eta, \tau) \tag{22}$$

where

$$\alpha_1 = -P/2, \ \beta_1 = -B - P^2/4 \tag{23}$$

Then Eqs. (17) to (20) become

$$\frac{\partial v}{\partial\tau} = \frac{\partial^2 v}{\partial\eta^2} \tag{24}$$

$$v(\eta, 0) = e^{-\alpha_1\eta}(\theta - \theta_{s,w}(\eta)) \equiv f_1(\eta) \tag{25}$$

$$v(0, \tau) = 0 \tag{26}$$

$$v(-\eta_{L_1}, \tau) = 0 \tag{27}$$

The solution of the above can be readily obtained from Carslaw and Jaeger (1959) as follows:

$$v(\eta, \tau) = \sum_{n=1}^{\infty} a_{n_1} \sin\left[-\frac{n\pi\eta}{\eta_{L_1}}\right]e^{-n^2\pi^2\tau/\eta_{L_1}^2} \tag{28}$$

where

$$a_{n_1} = -\frac{2}{\eta_{L_1}} f_1 \int_{-\eta_{L_1}}^{0} f_1(V) \sin\left[\frac{-n\pi V}{\eta_{L_1}}\right]dV \tag{29}$$

$$f_1(V) = e^{-\alpha_1 V}\left\{\theta_1 - \left[1 - \frac{A}{B} - \frac{\left(1-\frac{A}{B}\right)e^{-r_1\eta_{L_1}} + \frac{A}{B}}{e^{-r_1\eta_{L_1}} - e^{-r_2\eta_{L_1}}}\right]e^{r_1 V} - \left[\frac{\left(1+\frac{A}{B}\right)e^{-r_1\eta_{L_1}} + \frac{A}{B}}{e^{-r_1\eta_{L_1}} - e^{-r_2\eta_{L_1}}}\right]e^{r_2 V} - \frac{A}{B}\right\} \tag{30}$$

Therefore, the combined solution is

$$\theta(\eta, \tau) = \theta_{s,w}(\eta) + \theta_{h,w}(\eta, \tau)$$

$$= \left[1 - \frac{A}{B} - \frac{\left(1-\frac{A}{B}\right)e^{-r_1\eta_{L_1}} + \frac{A}{B}}{e^{-r_1\eta_{L_1}} - e^{-r_2\eta_{L_1}}}\right]e^{r_1\eta} + \left[\frac{\left(1+\frac{A}{B}\right)e^{-r_1\eta_{L_1}} + \frac{A}{B}}{e^{-r_1\eta_{L_1}} - e^{-r_2\eta_{L_1}}}\right]e^{r_2\eta} + \frac{A}{B} + e^{\alpha_1\eta + \beta_1\tau}\sum_{n=1}^{\infty} a_{n_1} \sin\left(-\frac{n\pi\eta}{\eta_{L_1}}\right)e^{-n^2\pi^2\tau/\eta_{L_1}^2} \tag{31}$$

where a_{n1} and $f_1(V)$ are given by Eqs. (29) and (30), respectively; α_1 and β_1 are given by Eq. (23).

Before proceeding to the solution for the dry region, it is noted that the steady-state solution given above is identical to the solution presented by previous workers (Sun et al., 1974) when $A = 0$ (or $q = 0$).

Similarly, the problem in the dry region ($0 \le \eta \le \eta_{L2}$) is described by

$$\frac{\partial\theta}{\partial\tau} = \frac{\partial^2\theta}{\partial\eta^2} + P\frac{\partial\theta}{\partial\eta} + A \tag{32}$$

$$\theta(\eta, 0) = \theta_1 \tag{33}$$

$$\theta(0, \tau) = 1 \tag{34}$$

$$\theta(\eta_{L_2}, \tau) = \theta_1 + A\tau \tag{35}$$

which is likewise split up into the steady-state and transient solutions,

$$\frac{d^2\theta_{s,d}}{d\eta^2}+P\frac{d\theta_{s,d}}{d\eta}+A=0 \tag{36}$$

$$\theta_{s,d}(0)=1 \tag{37}$$

$$\theta_{s,d}(\eta_{L_2})=\theta_1 \tag{38}$$

and

$$\frac{\partial\theta_{h,d}}{\partial\tau}=\frac{\partial^2\theta_{h,d}}{\partial\eta^2}+P\frac{\partial\theta_{h,d}}{\partial\eta} \tag{39}$$

$$\theta_{h,d}(\eta,0)=\theta_1-\theta_{s,d}(\eta) \tag{40}$$

$$\theta_{h,d}(0,\tau)=0 \tag{41}$$

$$\theta_{h,d}(\eta_{L_2},\tau)=A\tau \tag{42}$$

The solution of the steady-state problem is

$$\theta_{s,d}(\eta)=\left[1-\frac{\theta_1+\frac{A}{P}\eta_{L_2}-1}{e^{-p\eta_{L_2}}-1}\right]-\frac{A}{P}\eta+\left[\frac{\theta_1+\frac{A}{P}\eta_{L_2}-1}{e^{-p\eta_{L_2}}-1}\right]e^{-p\eta} \tag{43}$$

A similar transformation is introduced

$$\theta_{h,d}(\eta,\tau)=e^{\alpha_2\eta+\beta_2\tau}u(\eta,\tau) \tag{44}$$

where

$$\alpha_2=-p/2,\qquad \beta_2=-p^2/4 \tag{45}$$

to reduce Eqs. (39) to (42) to the form

$$\frac{\partial u}{\partial\tau}=\frac{\partial^2 u}{\partial\eta^2} \tag{46}$$

$$u(\eta,0)=(\theta_1-\theta_{s,d}(\eta))e^{-\alpha_2\eta}\equiv f_2(\eta) \tag{47}$$

$$u(0,\tau)=0 \tag{48}$$

$$u(\eta_{L_2},\tau)=A\tau\cdot e^{-(\alpha_2\eta_{L_2}+\beta_2\tau)}\equiv\phi_2(\tau) \tag{49}$$

which can be solved by the method of linear superposition. Thus, the transient temperature profile in the dry region can be readily found as

$$\theta(\eta,\tau)=e^{\alpha_2\eta+\beta_2\tau}\left[\sum_{n=1}^{\infty}a_{n2}\sin\left(\frac{n\pi\eta}{\eta_{L_2}}\right)e^{-n^2\pi^2\tau/\eta_{L_2}^2}+\frac{\eta}{\eta_{L_2}}(A\tau)\,e^{-(\alpha_2\eta_{L_2}+\beta_2\tau)}+\frac{2}{\eta_{L_2}}\sum_{n=1}^{\infty}(-1)^n\frac{\sin\beta_n\eta}{\beta_n}\int_0^{\tau}-\beta_n^2(\tau-\lambda)d\phi_2(\lambda)\right]+1-\left(\frac{\theta_1+\frac{A}{P}\eta_{L_2}-1}{e^{-p\eta_{L_2}}-1}\right)+\left(\frac{\theta_1+\frac{A}{P}\eta_{L_2}-1}{e^{-p\eta_{L_2}}-1}\right)e^{-p\eta}-\frac{A}{P}\eta \tag{50}$$

where $\beta_n=n\pi/\eta_{L2}$ and

$$a_{n2}=\frac{2}{\eta_{L_2}}\int_0^{\eta_{L_2}}f_2(w)\sin\frac{n\pi w}{\eta_{L_2}}\,dw$$

At the rewetting front, the conductive heat flux is continuous (Yamanouchi, 1968; Thompson, 1972; Duffey and Porthouse, 1973; Sun et al., 1974), i.e.,

$$\left.\frac{\partial\theta}{\partial\eta}\right|_{\eta=0^-}=\left.\frac{\partial\theta}{\partial\eta}\right|_{\eta=0^+} \tag{51}$$

Upon the substitution of Eqs. (31) and (50) into Eq. (51), the dimensionless rewetting velocity P can be determined by the expression

$$-\frac{P}{2}\left(1+\frac{A}{B}\right)+\frac{\sqrt{P^2+4B}}{2}\left(1-\frac{A}{B}\right)-\sqrt{P^2+4B}\left[\frac{(1-\frac{A}{B})e^{-r_1\eta_{L_1}}+\frac{A}{B}}{e^{-r_1\eta_{L_1}}-e^{-r_2\eta_{L_1}}}\right]+e^{\beta_1\tau}\sum_{n=1}^{\infty}\left(-\frac{n\pi}{\eta_{L_1}}\right)a_{n1}e^{e^{-n^2\pi^2\tau/\eta_{L_1}^2}}=e^{\beta_2\tau}\sum_{n=1}^{\infty}a_{n2}\left(\frac{n\pi}{\eta_{L2}}\right)e^{-n^2\pi^2\tau/\eta_{L_2}^2}+\frac{1}{\eta_{L_2}}(A\tau)e^{-\alpha_2\eta_{L_2}}+\frac{2e^{\beta_2\tau}}{\eta_{L_2}}\sum_{n=1}^{\infty}(-1)^n\left\{\frac{Ae^{-\alpha_2\eta_{L_2}-\beta_n^2}}{(\beta_n^2-\beta_2)}[e^{(\beta_n^2-\beta_2)\tau}-1-\tau\beta_2e^{(\beta_n^2-\beta_2)\tau}+\frac{\beta_2}{(\beta_n^2-\beta_2)}(e^{(\beta_n^2-\beta_2)\tau}-1)]\right\}-P\left(\frac{\theta_1+\frac{A}{P}\eta_{L_2}-1}{e^{-P\eta_{L_2-1}}}\right)-\frac{A}{P} \tag{52}$$

It is of interest to examine the limiting solution of the above for the case that has been investigated by Yamanouchi (1968), namely, the rewetting of an infinitely long, hot, and isothermal plate without any heating. In this case, $A=0$ (i.e., $q=0$) and then by setting $\eta_{L1}=\eta_{L2}\to\infty$, $r\to\infty$, the above solution reduces to

$$U_r=\left\{\frac{\rho C_p}{2}\sqrt{\frac{s_1}{kh}}\sqrt{\left[\frac{2(T_1-T_0)}{T_0-T_s}+1\right]^2-1}\right\}^{-1} \tag{53}$$

which is exactly the same as the well-known Yamanouchi's solution (1968).

Due to the absence of data on rewetting velocity on a hot plate heated by a uniform heat flux beneath the plate, the solution given by Eq. (52) cannot be compared with experimental data. However, experimental data are available on a hot plate without heating from below.

Yamanouchi (1968), for example, has confirmed reasonable agreement between the limiting solution given by Eq. (53) and his data. The general solution presented above for a smooth plate will be used in the following section to yield the solution for the plate with axial grooves.

2 Grooved Plate. The rewetting model of the grooved plate is based on that of the smooth surface plate. The coolant is driven by the wicking (surface tension) effect of microfins and is assumed, without loss of generality, to fill up the grooves as shown in Fig. 2.

At the level of $y=0$, for a thin plate and thin grooves,

$$-K\left.\frac{\partial T}{\partial y}\right|_{y=0}\cdot(2\ell_2+\ell_3)\simeq h(T-T_s)\times(2\ell_1+\ell_3)+h_a(T-T_a)\cdot 2\ell_2 \tag{54}$$

where h is the convective coefficient of a smooth surface, T_a is the environmental temperature, h_a is the convective coefficient between the plate surface and the environmental gas above ($h_a=0$). At the level of $y=-(s_1-\ell_1)$,

$$\left.\frac{\partial T}{\partial y}\right|_{y=-(s_1-\ell_1)}=-\frac{q}{K} \tag{55}$$

Since the plate is thin,

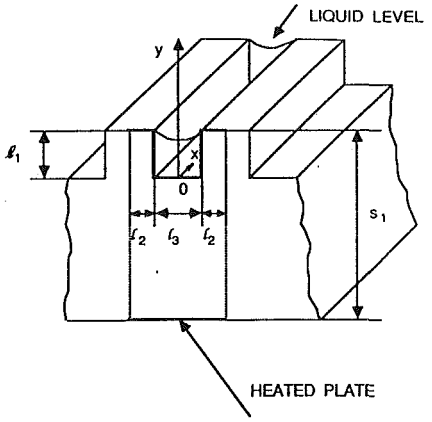

Fig. 2 Microfin structure and cross-sectional shape of grooved plate

$$\frac{\partial^2 T}{\partial y^2} = \lim_{\delta y \to 0} \left[\frac{\frac{\partial T}{\partial y}\Big|_{y+\delta y} - \frac{\partial T}{\partial y}\Big|_{y}}{\delta y} \right]$$

$$\approx \left[\frac{\frac{\partial T}{\partial y}\Big|_{y=0} - \frac{\partial T}{\partial y}\Big|_{y=-(s_1-\ell_1)}}{s_1 - \ell_1} \right] \tag{56}$$

Combining Eqs. (54), (55), and (56) yields

$$\frac{\partial^2 T}{\partial y^2} = -\left[\frac{Nh}{K} (T - T_s) - \frac{q}{K} \right] / (s_1 - \ell_1) \tag{57}$$

where the grooved geometric coefficient is defined as

$$N = (2\ell_1 + \ell_3)/(2\ell_2 + \ell_3)$$

The result given by Eq. (57) suggests two useful simplifications. First, the factor (Nh) is the equivalent convective heat transfer coefficient of the grooved plate and can be approximated by that of a thin liquid film on a smooth plate multiplied by a factor of N, namely,

$$\left(\frac{\text{heat transfer coefficient}}{\text{of a grooved plate}} \right) = N \left(\frac{\text{heat transer coefficient}}{\text{of a smooth plate}} \right)$$

where N is more generally defined as

$$N = \frac{\text{the wetted perimeter}}{\text{width of the cross section}} \tag{58}$$

Second, the governing equation for the grooved plate with a uniform heating remains unchanged provided h is replaced by (Nh) and the dimensionless variables are properly scaled as follows:

$$P = U_r \rho C_p (s_1 - \ell_1)/K; \qquad B = Nh(s_1 - \ell_1)/K$$

$$A = q(s_1 - \ell_1)/[K(T_0 - T_s)]; \qquad \eta = x/(s_1 - \ell_1)$$

$$\eta_{L1} = L_1/(s_1 - \ell_1); \qquad \eta_{L2} = L_2/(s_1 - \ell_1)$$

$$\tau = t/[(s_1 - \ell_1)^2 \rho\, C_p/K] \tag{59}$$

where h is the convective coefficient of the smooth plate with a uniform heating. Therefore, the solution of the grooved plate with a uniform heating in the wet region is the same as Eq. (31) with the modification above and the solution for the dry region is identical to Eq. (50).

Numerical solutions have also been obtained by solving for the original governing equation (see Appendix A, Eq. (A7)) fixed to the nonmoving coordinates (x', t),

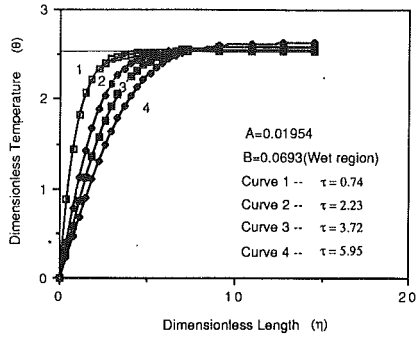

Fig. 3 Numerical solution for grooved plate

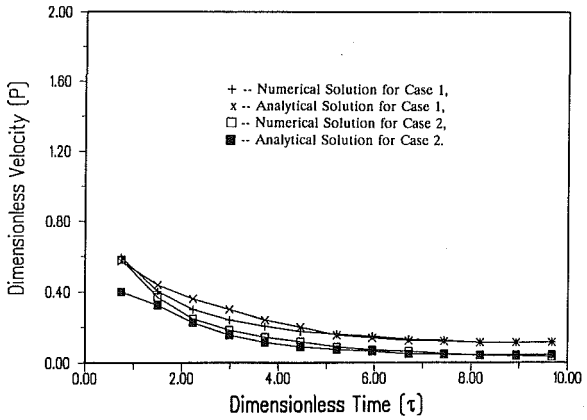

Fig. 4 Rewetting velocity comparison, $\theta_1 = 2.5143$, $\eta_L = 14.5445$, $B = 0.0693$ (wet region), $A = 0.01954$ (Case 1), $A = 0.08142$ (Case 2)

$$\frac{\partial \theta}{\partial \tau} = \frac{\partial^2 \theta}{\partial \eta'^2} - B\theta + A \tag{60}$$

subject to

$$\theta(\eta', 0) = \theta_1 \tag{61}$$

$$\theta(0, \tau) = 0 \tag{62}$$

$$\theta(\eta_L', \tau) = \theta_1 + A\tau \tag{63}$$

where $\eta' \equiv x'/s$, $\eta_L' \equiv L/s$, and $s = s_1$ and $(s_1 - \ell_1)$ for the smooth and grooved plates, respectively. The rewetting front location, η_{L1}', is determined from $\theta(\eta_{L1}', \tau) = 1$. The differential equation is discretized by a standard finite-difference approach. Figure 3 illustrates the computed wall temperature of the grooved (or smooth) plate versus the plate length, the so-called rewetting temperature curve, at various times when the liquid film is FC-72, which is Case 1 of Fig. 4. These numerical values are selected from the experimental condition of Fig. 5 of Grimley et al. (1988), namely, for FC-72 fluid on the smooth surface, $T_i - T_s = 11°C$, $T_0 - T_s = 17.5$ °C, $T_s = 56°C$, $T_1 = 100°C$ from which θ_1 is calculated. Other dimensionless parameters A, B, and η_L are estimated from the following values. The needed heat transfer coefficient $\bar{h} = 2779.49$ W/m^2 C is calculated from their boiling curve by Eq. (65). For the grooved copper plate, $C_p = 383.1$ J/kg°C, $\rho = 8954$ kg/m^3, K = 386 W/m°C. When the liquid fills up the grooves as shown in Fig. 2, the grooved geometric coefficient is $N = 1.75$, which is based on their geometric dimension of $\ell_1 = 0.5$ mm, $\ell_2 = 0.2$ mm, $\ell_3 = 0.4$ mm, $s_1 = 6$ mm, and $q = 24{,}000$ and $100{,}000$ W/m^2 for cases 1 and 2, respectively. They also reported dryout heat flux data, which will be used in comparison later. From Fig. 3, it is clearly shown that the rewetting temperature profiles are transient in nature, even in the coordinate frame moving with the rewetting front.

The successful prediction of the rewetting curve by the approximate analytical solution, Eq. (52), for the grooved (or smooth) plate with uniform heating is illustrated in Fig. 4. It is shown that the approximate closed-form solution is in reasonably good agreement with the numerical solution. This may appear to be somewhat of a surpise in view of the seemingly inconsistent approximation of treating P (or U_f) as constant. As mentioned above, such an approximation was necessarily made in the mathematical manipulation to achieve an approximate closed-form solution. It is equivalent to neglecting higher order terms attributed to the transient components of P. Figure 4 shows that such an approximation does yield good results as is expected because all rewetting velocities tend to level off quickly. In fact, beyond $\tau = 5.208$ (or $t = 1.4$ s), the difference between the closed-form and the numerical solutions is also indiscernible.

Figure 4 shows that the predicted rewetting velocity decreases with time. This is physically explainable because the plate temperature and, therefore, the thermal capacity to be removed ahead of the wet front increase with time due to heating beneath the plate. Consequently, the rewetting velocity slows down as it proceeds forward. In the case of quenching a hot plate without subjecting to a heating condition, as studied by previous investigators, the rewetting velocity is constant. Thus, the present study reveals a fundamental difference between the quenching of a hot plate with heating and that without heating. In the former, the wetting speed is time dependent, while in the latter, it is simply time invariant.

In a recent study, Grimley et al. (1988) conducted experiments to investigate the enhancement of convective boiling heat transfer by grooves on a plate heated from beneath. Unfortunately no rewetting velocity data were reported that could otherwise be useful to check the validity of the solutions discussed above. However, they did report interesting data on the maximum heat flux (the critical heat flux, CHF) that the heater could supply to the plate without causing dryout of the flowing liquid film. Since the dryout and the subsequent rewet of a heated surface are an integrated problem in heat pipe applications, it is desirable to be able to explain or predict the heat flux condition that leads to dryout of the plate. To achieve this objective, a simple method is presented next and comparisons will be made with the reported data.

Prediction of the Maximum Dryout Heat Flux

Under consideration is a smooth or a grooved plate initially covered by a thin flowing liquid film at a temperature T_s. The plate is subjected to a uniform heating. It is of interest to predict the maximum heat flux that triggers the dryout of the film.

A simple method based on the above rewetting concept is now extended to provide a means of estimating this maximum dryout heat flux. For a flowing liquid film over a plate heated by a heat flux that exceeds the maximum heat removal capability by convection and boiling, the liquid will cease to advance and begin to recede. Thus dryout will occur. On this physical premise, the maximum rate of the heat removal is given by

$$q_{\max,\, s} = \bar{h}\,(T_{0,\, s} - T_s) \tag{64}$$

Following the work of Howard et al. (1975), the average convective boiling heat transfer coefficient of the liquid film is estimated from

$$\bar{h} = \frac{1}{T_{0,\, s} - T_i} \int_{T_i}^{T_{0,\, s}} \frac{Q_b}{T - T_f}\, dT \tag{65}$$

in which T_i is the plate temperature at the onset of boiling, and $T_{0,\, s}$ is the smooth plate Leidenfrost temperature of the rewetting front and is approximated by the plate temperature at the CHF location. Q_b is the boiling curve of the liquid film over the plate. As an approximation, a form $Q_b = a_1 (T - T_s)^n$, which fits the boiling curve, can be used. In the event that the boiling curve of the flowing film is unavailable, the pool boiling curve could be used as the first-order approximation (Howard et al., 1975).

Table 1 Comparison between predicted and measured (Grimley et al.,1988, Figs. 8 and 9) maximum dryout heat flux

Geometry	Mean Inlet Velocity [m/s]	$T_i - T_s$ [°C]	$T_0 - T_s$ [°C]	a_1	n	$\bar{h}$ [W/m²·°C]	q_i [W/m²]	q_{CHF} [W/m²] (data)	q_{max} [W/m²] (pred.)
Smooth Surface	0.5	12	18	15.39256	2.84286	2286.43	18000	57000	41155.74
Grooved Surface	0.5		15			$N \cdot \bar{h}$ = 5144.468		80000	77167.01

Table 2 Comparison between predicted and measured (Grimley et al., 1988, Fig. 5) maximum dryout heat flux

Geometry	Mean Inlet Velocity [m/s]	$T_i - T_s$ [°C]	$T_0 - T_s$ [°C]	a_1	n	$\bar{h}$ [W/m²·°C]	q_i [W/m²]	q_{CHF} [W/m²] (data)	q_{max} [W/m²] (pred.)
Smooth Surface	1.0	11	17.5	230.5495	1.93726	2779.49	24000	59000	48641.08
Grooved Surface	1.0		14.3			$N \cdot \bar{h}$ = 6253.85		90000	89430.10

In the case of the grooved plate, the same analogy developed above is adopted here. The maximum dryout heat flux is estimated from

$$q_{\max,\, g} = N \cdot \bar{h} \cdot (T_{0,\, g} - T_s) \tag{66}$$

where $T_{0,\, g}$ is the Leidenfrost temperature of the grooved plate, also approximated by its CHF temperature. Based on the experimental data of Grimley et al. (1988) for a fluorocarbon (FC-72) liquid film falling over heated smooth and grooved plates, $T_{0,\, g}$ was found to be slightly lower than $T_{0,\, s}$. Thus, if $T_{0,\, g}$ of the grooved plate is unavailable due to the lack of boiling curve for the grooved plate, one may attempt to approximate $T_{0,\, g}$ from the smooth surface data $T_{0,\, s}$. Then the predicted maximum heat flux may be slightly overestimated, namely,

$$q_{\max,\, g} < N \cdot \bar{h} \cdot (T_{0,\, s} - T_s)$$

As an application to show the feasibility of the above method, the experimental conditions and geometries of Grimley et al. (1988) are used. In their experiments, the liquid film completely covered the smooth and grooved plates, $\ell_1 = 0.5$ mm, $\ell_2 = 0.2$ mm, and $\ell_3 = 0.4$ mm, such that $N = 2.25$ (from Eq. (58)). $(T_i - t_s)$ and $(T_0 - T_s)$ are taken from their boiling curves. The average boiling heat transfer coefficient is calculated from their smooth surface boiling curve and Eq. (65). The two correlation constants a_1 and n are determined by arbitrarily collocating the boiling curve of the smooth surface plate at two locations, T_i and T_0, where the boiling heat fluxes are designated by q_i and q_{CHF}, respectively. Table 1 shows the comparison between the predicted maximum dryout heat flux, q_{max}, using Eqs (64) and (65), and the reported dryout data q_{CHF} for both types of plates. The agreement is satisfactory particularly in view of the simplicity of the method proposed for the grooved plate. The same agreement is shown in Table 2 when the mean inlet velocity of the falling film is increased from 0.5 m/s to 1.0 m/s.

Conclusions

The rewetting process of a smooth surface plate subject to a uniform heating has been investigated. A proper governing transient heat conduction with a convective boiling condition has been presented and solved to yield an approximate closed-form solution for the plate temperature profiles in the wet and dry regions of the plate. From the temperature profiles, an

approximate closed-form solution for the rewetting velocity over the heated plate has been obtained. Numerical solutions have also been presented to check the validity of the closed-form solution. The closed-form rewetting velocity was found to be in good agreement with that of the numerical solution. It is shown that in a limiting condition the present rewetting velocity solution reduces correctly to the existing solution for the rewetting of a hot, isothermal plate without heating. However, contrary to the case without heating, the rewetting process on the plate with uniform heating is found to be transient (time variant) even on the coordinate frame moving with the rewetting front. The rewetting velocity is found to be much faster initially and then levels off later.

A method to address the rewetting process of the grooved plate based on the smooth plate rewetting model has been developed. It is shown that, by properly defined scalings, the solution for the smooth plate can be made to be applicable for the grooved plate.

Finally, the dryout of a liquid film over a heat plate has been investigated. A simple method has been proposed to predict the dryout critical heat flux of the smooth and grooved plates. The results of the prediction were compared and found to be in reasonable agreement with the existing experimental data.

Acknowledgments

This work is supported by NASA L.B. Johnson Space Center, Contract No. NAG9-525, under the technical management of Eugene K. Unger.

References

Alario, J., Brown, R., and Kosson, R., 1983, "Monogroove Heat Pipe Development of the Space Constructible Radiator System," Paper No. AIAA-83-1431.

Carslaw, H. S., and Jaeger, J. C., 1959, *Conduction of Heat in Solids*, Clarendon Press, Oxford, United Kingdom.

Duffey, R. B., and Porthouse, D. T. C., 1973, "The Physics of Rewetting in Water Reactor Emergency Core Cooling," *Nuclear Engineering and Design*, Vol. 25, pp. 379–394.

Ferng, Y. J., Chieng, C. C., and Pan, C., 1991, "Predictions of Rewetting Process for a Nuclear Fuel Rod Using First-Principles Equations," *Nuclear Engineering and Design*, Vol. 126, pp. 189–205.

Grimley, T. A., Mudawwar, I., and Incropera, F. P., 1988, "CHF Enhancement in Flowing Fluorocarbon Liquid Films Using Structured Surfaces and Flow Deflectors," *Int. J. Heat Mass Transfer*, Vol. 31, No. 1, pp. 55–65.

Howard, P. A., Linehan, J. H., and Grolmes, M. A. 1975, "Experimental Study of the Stationary Boiling Front in Liquid Film Cooling of a Vertical Heated Rod," presented at the 15th National Heat Transfer Conference, Paper No. CSChE/CSME-75-HT-14, San Francisco.

Kosson, R., Brown, R., and Ungar, E., 1990, "Space Station Heat Pipe Advanced Radiator Element (SHARE) Flight Test Results and Analysis," AIAA Paper No. 90-0059.

Peng, X., and Peterson, G., 1991, "Analytical Investigation of the Rewetting Characteristics of Heated Plates With Grooved Surfaces," presented at the 1991 National Heat Transfer Conference, Paper No. AIAA-91-4004, Minneapolis, MN.

Peng, X. F., and Peterson, G. P., 1992, "Analysis of Rewetting for Surface Tension Induced Flow," ASME JOURNAL OF HEAT TRANSFER, Vol. 114, pp. 703–707.

Sun, K.H., Dix, G. E., and Tien, C. L., 1974, "Cooling of a Very Hot Vertical Surface by a Falling Liquid Film," ASME JOURNAL OF HEAT TRANSFER, Vol. 96, pp. 126–131.

Stroes, G., Fricker, D., Issacci, F., and Catton, I., 1990, "Heat Flux Induced Dryout and Rewet in Thin Films," *Proc. 9th Int. Heat Trans. Conf.*, Vol. 6, pp. 359–364.

Thompson, T. S., 1972, "An Analysis of the Wet-Side Heat-Transfer Coefficient During Rewetting of a Hot Dry Patch," *Nuclear Engineering and Design*, Vol. 22, pp. 212–224.

Tien, C. L., and Yao, L. S., 1975, "Analysis of Conduction-Controlled Rewetting of a Vertical Surface," ASME JOURNAL OF HEAT TRANSFER, Vol. 97, pp. 161–165.

Yamanouchi, A., 1968, "Effect of Core Spray Cooling in Transient State After Loss of Coolant Accident," *Journal of Nuclear Science and Technology*, Vol. 5, pp. 547–558.

APPENDIX A

Coordinate Transformation

The heat conduction equation within a smooth plate as shown in Fig. 1 is

$$\rho C_p \left(\frac{\partial T}{\partial t}\right)_{x'} = K \left(\frac{\partial^2 T}{\partial x'^2} + \frac{\partial^2 T}{\partial y'^2}\right) \tag{A1}$$

For a coordinate system x-o-y moving with the rewetting front,

$$x' = x + \int_0^t U_r(t)\, dt \tag{A2}$$

$$T(x', t) = T(x(x', t), t) \tag{A3}$$

Then, noting that

$$\left(\frac{\partial T}{\partial t}\right)_{x'} = \left(\frac{\partial T}{\partial t}\right)_x + \left(\frac{\partial T}{\partial x}\right)_t \left(\frac{\partial x}{\partial t}\right)_{x'} = \left(\frac{\partial T}{\partial t}\right)_x - U_r \left(\frac{\partial T}{\partial x}\right)_t \tag{A4}$$

Eq. (A1) can be written as

$$\rho C_p \left[\left(\frac{\partial T}{\partial t}\right)_x - U_r \left(\frac{\partial T}{\partial x}\right)_t\right] = K \left(\frac{\partial^2 T}{\partial x^2} + \frac{\partial^2 T}{\partial^2 y}\right) \tag{A5}$$

For a thin plate subjected to heating from below, it further reduces to

$$\left(\frac{\partial T}{\partial t}\right)_x = \frac{K}{\rho C_p}\frac{\partial^2 T}{\partial x^2} + U_r \frac{\partial T}{\partial x} - \frac{h}{\rho C_p s_1}(T - T_s) + \frac{q}{\rho C_p s_1}$$

or in dimensionless form

$$\frac{\partial \theta}{\partial \tau} = \frac{\partial^2 \theta}{\partial \eta^2} + P\frac{\partial \theta}{\partial \eta} - \beta\theta + A \tag{A6}$$

where the dimensionless variables are parameters are given by Eq. (2).

For the purposes of comparison and numerical computation, the above is written in untransformed coordinates (x', t) as

$$\frac{\partial \theta}{\partial \tau} = \frac{\partial^2 \theta}{\partial \eta'^2} - \beta\theta + A \tag{A7}$$

where

$$\eta' \equiv x'/s_1 \tag{A8}$$

Numerical Modeling Using a Quasi-Three-Dimensional Procedure for Large Power Plant Condensers

C. Zhang
Department of Mechanical Engineering,
University of Windsor,
Windsor, Ontario, Canada N9B 3P4

A quasi-three-dimensional numerical model is proposed to predict the performance of large power plant condensers. The proposed model is applied to a 350 MW power plant condenser under two different loading and operational conditions to demonstrate its predictive capability. The predictions are compared with the experimental data. The comparison is favorable. The equations governing the conservation of mass, momentum, and air mass fraction are solved in primitive variable form using a semi-implicit consistent control-volume formulation in which a segregated pressure correction linked algorithm is employed. The modeling of the condenser geometry, including the tube bundle and baffle plates, is carried out based on a porous media concept using applicable flow, heat, and mass transfer resistances.

I Introduction

Condenser-related problems cause substantial losses of availability and performance in large power plants. EPRI (Diaz-Tous, 1983) estimated that one percent loss of availability by units could cost the utility industry US $2.2 billion during the period 1979–1984 in the U.S.A. To correct this situation the design tools should be improved even further. Accurate and detailed predictions of the flow distribution and heat transfer are of primary importance in performing the hydraulic design analysis of condensers. Eventually, the reliability and performance of condensers could therefore be improved with such information.

The advent of high-speed and large storage digital computers has made it possible to solve complex condenser problems. Modeling a condenser, however, in most cases, is conducted under the assumption that the flow is two dimensional. The two dimensionality condition may impose undue restrictions upon the analysis, as explained by Brickell (1981). The shell-side flow within large power plant condensers, in general, is three dimensional. The flow in different bays along the tube length will differ due to the temperature rise of the cooling water. Thus, a practical approach is needed in which three-dimensional effects are considered in order to predict the flow field more realistically. The present study is a step forward to fulfill this need.

The purpose of the present study is to develop an algorithm that can be used to predict the nature of three-dimensional fluid flow and heat transfer in large power plant condensers. The three-dimensional effects due to the difference of cooling water temperature and the existence of noncondensable pockets along the tube length have been included in the proposed procedure. The present study is a further extension of the recent work by Zhang et al. (1991a, 1993). In the work by Zhang et al. (1991a), a two-dimensional numerical procedure was proposed and the numerical predictions were critically assessed by comparison to available experimental data for an experimental condenser. In the work by Zhang et al. (1993), the two-dimensional approach was extended to a quasi-three-dimensional numerical procedure by a series of step-by-step two-dimensional calculations and the proposed model was applied to a complex industrial condenser. The capability of quasi-three-dimensional models raises a problem of specifying the inlet mass flow rate for each bay. The previous model (Zhang et al., 1993) was developed based on the assumption that the steam flow rate that enters each bay is equal to the condensing capability of that bay, which implies that all the heat transfer surface is active and the same exit stream–air ratio exists for all bays. The model cannot predict the existence of noncondensable pockets along the tube length. In the present work, the pressure drop balancing concept, first used by Barsness (1963), and recently used by Rabas and Kassem (1985) and Mochida and Miura (1990), is employed to adjust the inlet mass flow rate for each bay. The advantage of the model proposed in this paper is its ability to predict air blanketing.

In order to demonstrate the applicability and predictive capability of the proposed algorithm for complex power plant condensers, the algorithm is applied to simulate the three-dimensional velocity, pressure, temperature, and air mass fraction distributions in a 350 MW unit power plant condenser under two different loading and operational conditions as reported by Zhang et al. (1991b). The predicted results are compared with measurements (Zhang et al., 1991b) to benchmark the procedure and validate the computer program.

II Numerical Method

In the simulation, the following assumptions are made:

1. The working fluid is a mixture of noncondensable gases (air) and steam, behaving as an ideal gas.
2. The steam is saturated.
3. The air is of sufficiently small volume that the air momentum differences can be neglected and it can be treated solely by diffusion theory.
4. The pressures at the inlet boundary of all the bays are the same.
5. The shell-side pressure drops from the inlet to the noncondensable gas offtake are identical for all the bays.

The porous medium concept is used in the simulation. An isotropic porosity, β, which is defined as the ratio of the volume occupied by the fluid to the total volume, is employed to describe the flow volume reduction due to the tube bundle and baffles.

2.1 Conservation Equations. The governing equations are the equations of conservation of mass, momentum, and non-

Contributed by the Heat Transfer Division for publication in the JOURNAL OF HEAT TRANSFER. Manuscript received by the Heat Transfer Division September 1992; revision received April 1993. Keywords: Condensation, Heat Exchangers, Numerical Methods. Associate Technical Editor: J. H. Kim.

condensable gas mass fraction. The two-dimensional steady-state porous medium volume-averaged conservation equations of mass, momentum, and air mass fraction, with flow, heat and mass transfer resistances, are written in the Cartesian coordinate system as:

Mass Conservation Equation for the Mixture:

$$\frac{\partial}{\partial x}(\beta\rho u)+\frac{\partial}{\partial y}(\beta\rho v)=-\beta\dot{m} \tag{1}$$

Momentum Conservation Equations for the Mixture:

$$\frac{\partial}{\partial x}(\beta\rho uu)+\frac{\partial}{\partial y}(\beta\rho vu)=\frac{\partial}{\partial x}\left(\beta\mu_e\frac{\partial u}{\partial x}\right)+\frac{\partial}{\partial y}\left(\beta\mu_e\frac{\partial u}{\partial y}\right)-\beta\frac{\partial p}{\partial x}-\beta\dot{m}u-\beta F_u \tag{2}$$

$$\frac{\partial}{\partial x}(\beta\rho uv)+\frac{\partial}{\partial y}(\beta\rho vv)=\frac{\partial}{\partial x}\left(\beta\mu_e\frac{\partial v}{\partial x}\right)+\frac{\partial}{\partial y}\left(\beta\mu_e\frac{\partial v}{\partial y}\right)-\beta\frac{\partial p}{\partial y}-\beta\dot{m}v-\beta F_v \tag{3}$$

Conservation of Air Mass Fraction:

$$\frac{\partial}{\partial x}(\beta\rho\phi u)+\frac{\partial}{\partial y}(\beta\rho\phi v)=\frac{\partial}{\partial x}\left(\beta\rho D\frac{\partial\phi}{\partial x}\right)+\frac{\partial}{\partial y}\left(\beta\rho D\frac{\partial\phi}{\partial y}\right) \tag{4}$$

2.2 Auxiliary Relationships

(*i*) *Momentum Source Term.* The local hydraulic flow resistances, F_u and F_v, in the momentum equations caused by the tube bundle and/or baffles, are related to the pressure loss coefficients, ξ_u and ξ_v, by

$$F_u=\xi_u\rho uU_p, \tag{5}$$

$$F_v=\xi_v\rho vU_p, \tag{6}$$

The expressions proposed by Rhodes and Carlucci (1983) for the loss coefficients, ξ_u and ξ_v, are used, namely:

$$\xi_u=2\left(\frac{f_u}{P}\right)\left(\frac{P\beta}{P-D_o}\right)^2\left(\frac{1-\beta}{1-\beta_t}\right)+\xi_b, \tag{7}$$

$$\xi_v=2\left(\frac{f_v}{P}\right)\left(\frac{P\beta}{P-D_o}\right)^2\left(\frac{1-\beta}{1-\beta_t}\right)+\xi_b. \tag{8}$$

where

$$f_u=\begin{cases}0.619\,\mathrm{Re}_u^{-0.198}; & \mathrm{Re}_u<8000\\ 1.156\,\mathrm{Re}_u^{-0.2647}; & 8000\le\mathrm{Re}_u\le 2\times10^5,\end{cases}$$

$$f_v=\begin{cases}0.619\,\mathrm{Re}_v^{-0.198}; & \mathrm{Re}_v<8000\\ 1.156\,\mathrm{Re}_v^{-0.2647}; & 8000\le\mathrm{Re}_v\le 2\times10^5,\end{cases}$$

$$\xi_b=\begin{cases}\infty; & \text{baffle-filled region,}\\ 0; & \text{baffle-free region.}\end{cases}$$

In the present work, the tube bundle is laid out in an equilateral triangular pattern, and the porosity within the entirely tube-filled region, β_t, is defined as

$$\beta_t=1-\frac{\pi}{2\sqrt{3}}\left(\frac{D_o}{P}\right)^2. \tag{9}$$

The local porosity, β, is determined by

$$\beta=1+F(\beta_t-1), \tag{10}$$

where F, the fraction of a control volume filled with tubes, is defined as the ratio of actual number of tubes in the control volume to the number of tubes if the control volume was fully tube-filled. For partially tube-filled control volume, $0<F<1$ and $\beta_t<\beta<1$.

(*ii*) *Mass Source Term.* The steam condensation rate per unit volume, $\dot{m}$, can be obtained by equating the phase change enthalpy with the heat transfer rate, namely:

$$\dot{m}LV=\frac{T-T_w}{R}A. \tag{11}$$

Nomenclature

A = heat transfer area, m^2
C = gas constant, J/kg K
c_p = specific heat at constant pressure, J/kg K
D = diffusivity of air in vapor, m^2/s
D_i = inner diameter of tube, m
D_o = outer diameter of tube, m
F = fraction of a given control volume filled with tubes
Fr = Froude number = $M^2/\rho_s^2gD_o$
F_u, F_v = flow resistance forces in momentum equations, N/m^3
f_u, f_v = friction factors
g = gravitational acceleration, m/s^2
L = latent heat of condensation, J/kg
M = mass velocity of steam through maximum flow area, kg/m^{2}s
$\dot{M}$ = total steam condensation rate, kg/s
$\dot{M}_n$ = steam condensation rate on the nth tube row, kg/s
$\Sigma\dot{M}_n$ = total water flow rate over the nth tube row, kg/s
$\dot{m}$ = steam condensation rate per unit volume, kg/m^{2}s
N = number of bays in a condenser
P = tube pitch, m
Pr = Prandtl number = $c_p\mu/\lambda$
p = pressure, Pa
R = thermal resistance, m^{2}K/W
Re_m = Reynolds number for maximum flow area = $\rho_cMD_o/\rho_s\mu_c$
Re_u = x-direction Reynolds number = $\rho uD_o/\mu$
Re_v = y-direction Reynolds number = $\rho vD_o/\mu$
T = temperature, K
U_p = velocity vector magnitude = $(u^2+v^2)^{1/2}$, m/s
u = velocity component in the x direction, m/s
V = volume, m^3
v = velocity component in the y direction, m/s
x = main flow direction coordinate, m
y = cross-stream coordinate, m
α = heat transfer coefficient of shell side = $1/(R_c+R_a)$, W/m^2 K
β = local volume porosity
β_t = porosity in tube bundle region
λ = thermal conductivity, W/m K
μ = dynamic viscosity, kg/m s
μ_e = effective dynamic viscosity, kg/m s
μ_t = turbulent dynamic viscosity, kg/m s
ξ_u, ξ_v = pressure loss coefficients, 1/m
ρ = density, kg/m^3
ϕ = air mass fraction = ρ_a/ρ

Subscripts

a = air
c = condensate
cs = steam/condensate interface
s = steam
t = tube wall or tube bundle
tot = total
u = parameter in x-momentum equation
v = parameter in y-momentum equation
w = cooling water

Unsubscripted properties are properties of the mixture.

The cooling water temperature for each control volume, T_w, is obtained by a heat balance between the steam and the cooling water. The overall thermal resistance for each control volume, R, is calculated from various empirical heat transfer correlations.

For the water side thermal resistance, the McAdams relation (ASHRAE, 1989) is employed:

$$\frac{1}{R_w} = 0.023 \frac{\lambda_w}{D_i} \mathrm{Re}_w^{0.8} \mathrm{Pr}_w^{0.4}. \tag{12}$$

The fouling resistance, R_f, is taken as 3.5×10^{-5} m^{2}K/W as suggested by Naviglio et al. (1988). The wall resistance for each tube is obtained with the assumption of one-dimensional, steady-state conduction, and it is given by:

$$R_t = \frac{D_o \ln\left(\frac{D_o}{D_i}\right)}{2\lambda_t}. \tag{13}$$

The existing data for heat transfer coefficients when condensation occurs do not lead to easy generalization, and, in general, information from different sources is required in order that a wide range of flow conditions can be studied. In this paper, since its purpose is to demonstrate the numerical calculation method rather than to conduct a detailed analysis of the process, filmwise condensation is assumed and its resistance is calculated based on the work of Fujii et al. (1972):

$$\frac{1}{R_{Fu}} = K_X \left(1 + \frac{0.276}{X^4 \mathrm{Fr} H}\right)^{1/4} \mathrm{Re}_m^{1/2} \frac{\lambda}{D_o}, \tag{14}$$

where

$$\begin{aligned} K &= \begin{cases} 0.8 \text{ for in-line arrangement;} \\ 1.0 \text{ for staggered arrangement;} \end{cases} \\ X &= 0.9[1 + 1/(r H)]^{1/3}; \\ \mathrm{Fr} &= M^2/\rho_s^2 g D_o; \\ H &= c_{pc}(T - T_t)/\mathrm{Pr}_c L; \\ \mathrm{Re}_m &= \rho_c M D_o/\rho_s \mu_c; \\ r &= (\rho_c \mu_c/\rho_s \mu_s)^{1/2}. \end{aligned}$$

Equation (14) does not consider the condensate from the tubes above the nth tube where the condensate can reduce the effective heat transfer between the steam and the cooling water. The effect of inundation on condensation heat transfer is accounted for by using the correction term proposed by Grant and Osment (1968) and Wilson (1972). The condensate resistance, R_c, is evaluated by

$$\frac{1}{R_c} = \frac{1}{R_{Fu}} \left[\frac{\Sigma \dot{M}_n}{\dot{M}_n}\right]^{-0.16}. \tag{15}$$

The resistance, to account for condensing steam having to diffuse through an air film close to tube surface, is evaluated by the Berman and Fuks relation (1958):

$$\frac{1}{R_a} = \frac{aD}{D_o} \mathrm{Re}_s^{1/2} \left(\frac{p}{p - p_s}\right)^b p^{1/3} \left(\frac{\rho_s L}{T}\right)^{2/3} \frac{1}{(T - T_{cs})^{1/3}}, \tag{16}$$

where

$$a = 0.52 \text{ and } b = 0.7 \quad \text{for } \mathrm{Re}_s < 350;$$

$$a = 0.82 \text{ and } b = 0.6 \quad \text{for } \mathrm{Re}_s > 350.$$

The overall resistance to heat transfer for each control volume, R, is the sum of all individual resistances, thus, R, when related to the outer surface of the tube, can be written as

$$R = R_w \left(\frac{D_o}{D_i}\right) + R_f + R_t + R_c + R_a. \tag{17}$$

(*iii*) *Equation of State.* The air and steam mixture is assumed to behave as a perfect gas. The perfect gas state equation is used to calculate the local mixture density,

$$\rho = \frac{p}{CT}, \tag{18}$$

where p is the local mixture pressure obtained from momentum and continuity equations, C is the gas constant for the mixture, and T is the saturation temperature determined by the partial steam pressure.

(*iv*) *Effective Viscosity.* The concept of an effective viscosity is used, which is defined as the sum of the laminar and turbulent viscosities, namely:

$$\mu_e = \mu + \mu_t. \tag{19}$$

For all simulations, the turbulent viscosity, μ_t, is assumed to be constant, which is equal to 100 times the value of the dynamic viscosity, μ; however, studies indicate that severalfold variations in μ_t have no significant effect on the results (Zhang et al., 1991a). This to some extent is not surprising, since the effect of turbulent wall shear stresses is introduced via the local hydraulic flow resistances.

2.3 Boundary Conditions. The boundary conditions for the inlet, vent, solid walls, and plane of symmetry are:

Inlet: The mass flow rate and air mass fraction are specified at the inlet boundary of each bay. The inlet velocity profile of each bay is assumed to be uniform, and the magnitude of the inlet velocity in each bay is determined by the mass flow rate at this bay.

Vent: A mass imbalance correction scheme is used to update the velocity and air mass fraction at the vent.

Walls: The shell walls of the condenser are assumed to be nonslip, impervious to flow, and adiabatic. Thus, the normal and tangential velocity components are equal to zero and air mass fraction gradients normal to the walls are set to zero.

Plane of symmetry: Along the centerline, the derivatives with respect to the cross stream direction of all field variables are set to zero.

2.4 Three-Dimensional Effects. Three-dimensional effects occur in large power plant condensers primarily due to cooling water temperature gradients, which lead to a space-variable sink potential. For power plant condensers with partition plates and large entrance area, however, a valid assumption is to consider that the shell-side flow has negligible velocity components parallel to the tube bundle since the partition plates restrict flow in the third direction. Thus, the condenser shell-side may be subdivided into a number of two-dimensional bays normal to the cooling water flow direction. In each bay, the flow is therefore assumed to be two dimensional, with the bays interacting with each other through the "thermal memory" of the cooling water on the tube-side. Calculations for each plane are made sequentially starting from the cooling water inlet end. The outlet cooling water temperature of the preceding bay is used as the inlet cooling water temperature for the successive bay. A similar marching procedure is used for the successive bays of the condensers. Thus, the three-dimensional mapping of the variables of interest is constructed by a series of step-by-step two-dimensional calculations, each being for one bay.

2.5 Solution Procedure. The discretization of the differential equations, Eqs. (1), (2), (3), and (4), is carried out by integrating over small control volumes in a staggered grid. The resulting discretized equations are solved in primitive variables using the SIMPLEC algorithm (Van Doormaal and Raithby, 1984). These equations are coupled together and are highly nonlinear, thus an iterative approach is used for their solution.

The iteration employed comprises the following sequence of operations:

(*i*) The momentum equations, Eqs. (2) and (3) after discretization, are solved based on a pressure field taken from the previous iteration.

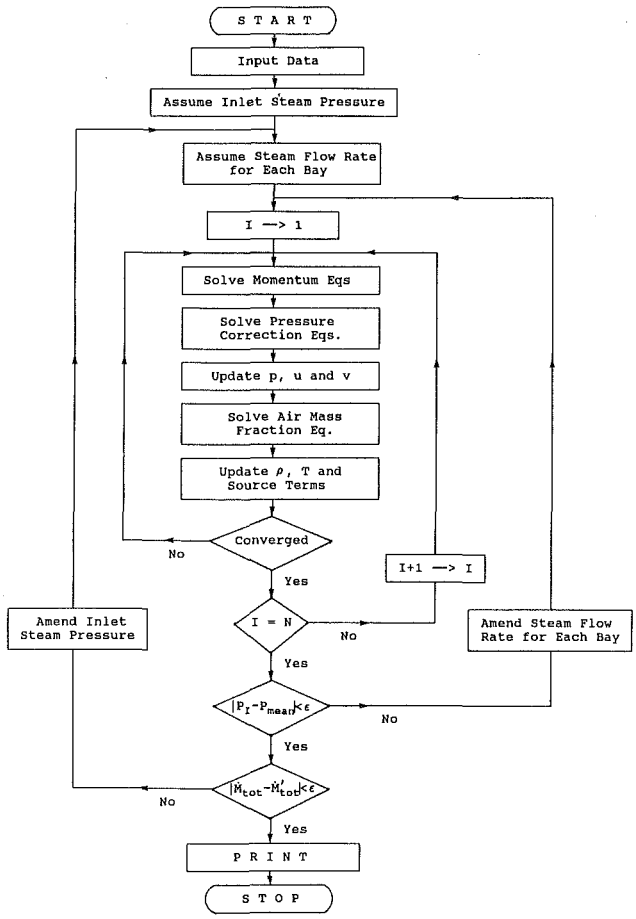

Fig. 1 Flow chart

(*ii*) A Poisson equation for the pressure correction, derived from the continuity equation, Eq. (1), is solved, and at the end of each outer iteration loop, pressures and velocities are corrected.

(*iii*) The air mass fraction ϕ is obtained from the discretized form of its transport equation, Eq. (4).

(*iv*) The temperatures of mixture and cooling water, density, mass source term, and momentum source term are then updated.

(*v*) A new cycle is started unless the prescribed accuracy has been reached.

The above iterative procedure is repeated for each of every bay. Figure 1 shows the flow chart of the overall solution procedure. The total inlet mass flow rate into the condenser is given. However, the mass flow rate at the inlet of each transverse bay of the condenser to be given as a boundary condition was unknown when carrying the simulation. Repeated calculation is conducted as shown in the flow chart (Fig. 1). The inlet mass flow rate at each bay of the condenser is determined by the pressure difference from the condenser inlet to the vent channel. The constraint that the pressure drops from inlet to the vent for all the bays must be the same is used

Table 1 Geometric and operating parameters

Geometrical Parameters	
Number of Tube Bundles	2
Number of Tubes Per Bundle	3360
Condenser Length (m)	17
Tube Outer Diameter (mm)	25.4
Tube Inner Diameter (mm)	22.9
Tube Pitch (mm)	33.3
Operating Parameters at 245 MW	
Inlet Temperature of Cooling Water (°C)	11.58
Inlet Velocity of Cooling Water (m/s)	2.42
Total Steam Condensation Rate (kg/s)	91.01
Operating Parameters at 350 MW	
Inlet Temperature of Cooling Water (°C)	10.53
Inlet Velocity of Cooling Water (m/s)	2.42
Total Steam Condensation Rate (kg/s)	135.9

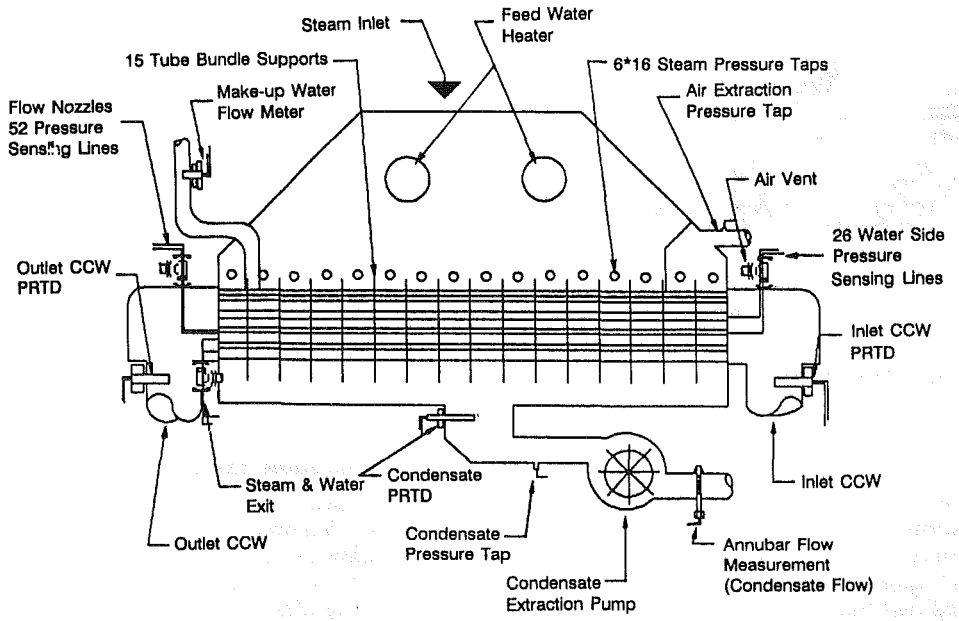

Fig. 2 Longitudinal section of unit #1 condenser at NBEPC Coleson Cove

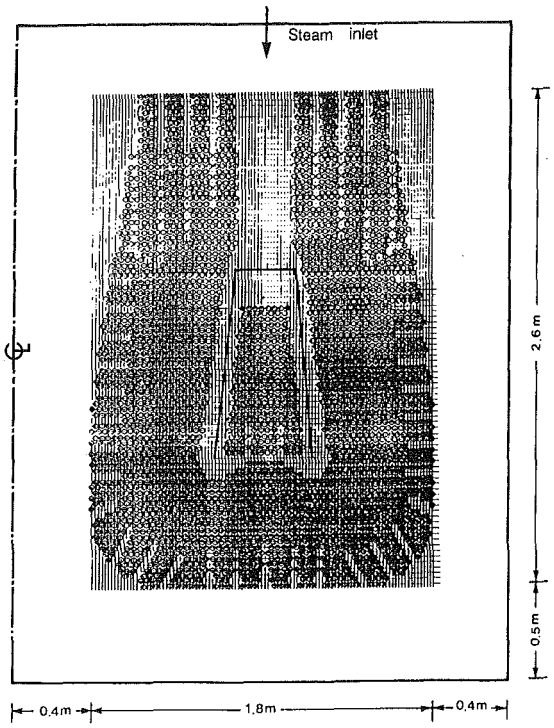

Fig. 3 Tubing arrangement of condenser

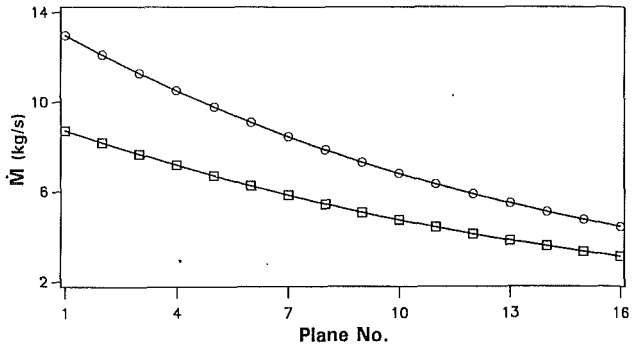

Fig. 5 Distribution of condensation rate: (□: 245 MW; ○: 350 MW)

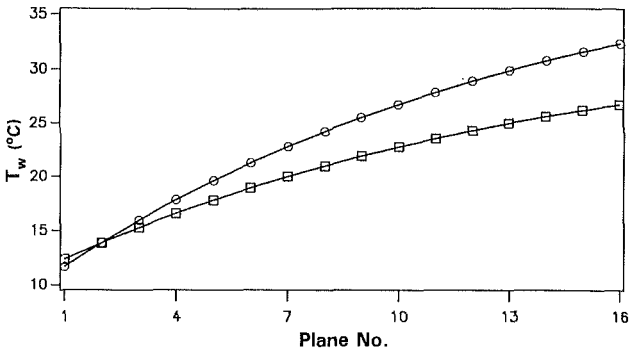

Fig. 6 Distribution of averaged cooling water temperature: (□: 245 MW; ○: 350 MW)

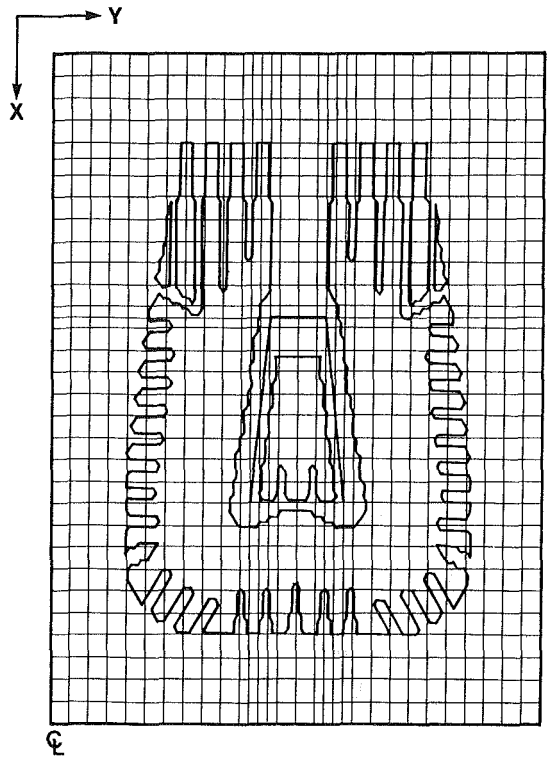

Fig. 4 Grid used for the simulation

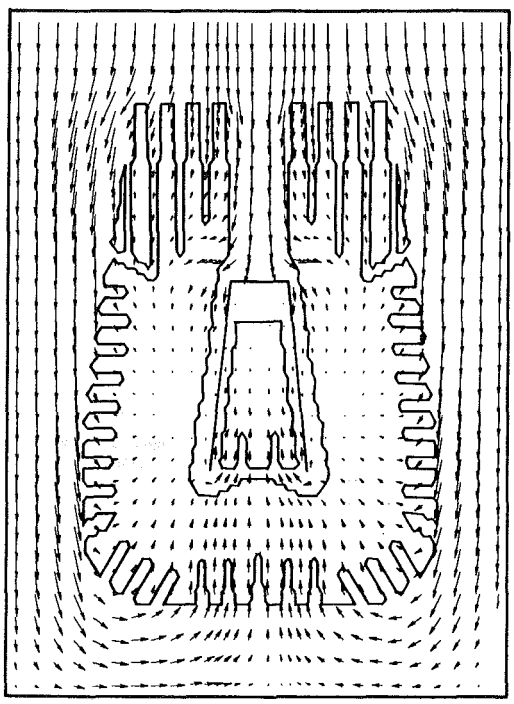

Fig. 7 Velocity vector plot (plane No. 1) for full load

to adjust the mass flow rate into each bay. This is the pressure-drop balancing concept first used by Barsness (1962). By knowing the total condensation rate, the steam inlet pressure can be determined. Since the steam inlet pressure was unknown, the procedure was repeated while varying the steam inlet pressure until the predicted total condensation rate was equal to the given value (within specified tolerance).

III Application Example

The condenser selected here is a typical power plant condenser which is operating at Coleson Cove Generating Station, New Brunswick, Canada. The experimental data in terms of the pressure and temperature distributions for this condenser are available (Zhang et al., 1991b), so the predictions can be compared with the experimental data to validate the proposed

numerical procedure. Since there are no other experimental data for power plant condensers available in the open literature, the numerical procedure is applied to one condenser only. The geometric and operating parameters of the condenser are given in Table 1. Figure 2 depicts a side view of this dual bundle in-line underslung condenser. The dimension of the condenser is $5.2 \times 3.5 \times 17$ m^3 and consists of 6720 tubes in two bundles. There are 15 full partition plates (tube bundle supports), which divide the condenser into 16 bays in the direction of the cooling water flow. The system shown in Fig. 2 is considered to be symmetric with respect to the vertical center plane. The tube layout of the tube bundle for one half of the condenser placed in the shell is shown in Fig. 3. The steam from the turbine enters from the top of the condenser. The right-hand side and the bottom are solid walls and the left-hand side is a presumed symmetric centerline. The air extraction vent is located in the middle of the tube bundle and is surrounded by a "skirt" baffle to prevent steam from going to the vent directly.

The predictions are carried out in all 16 bays of the condenser. The flow is assumed to be two-dimensional in each bay, since partition plates restrict the fluid flow in the third direction. The calculations are thus made for 16 planes, which are located half way between two successive partition plates. It is expected that fluid flow and heat transfer conditions should differ in each bay due to the increase of cooling water temperature. The calculation domain is limited to only one half of the condenser due to symmetry as shown in Fig. 3. The calculations were carried out by a nonuniform mesh of 32 by 30 in the main and crossflow directions, respectively, as shown in Fig. 4. Previous studies conducted by Zhang et al. (1991a) have indicated that a grid of this size can adequately reflect the geometry, flow, and heat transfer. Since the inlet air mass fraction is not available at this stage, a tentative value of 0.15 percent of inlet air mass fraction was made based upon the capacity of the air extraction system. The sensitivity studies on the effects of the inlet air mass fraction were made by Zhang et al. (1993).

IV Results and Discussion

4.1 Typical Results. Figures 5 and 6 depict, for two power loads considered, the distribution of the condensation rate and the averaged cooling water temperature, respectively, for each bay. The results can be explained by considering the three dimensionality of the steam flow in the condenser. Due to the increase of cooling water temperature along the condenser, the potential for condensation is greatest at the cooling water inlet end. Thus, the condensation rate is greater at the cooling water inlet end than that at the outlet end.

The velocity vector plot of Plane No. 1 for full load is shown in Fig.7. It can be seen from this figure that the velocity distribution in the vicinity of the tube bundle is nearly "parallel" to the tube bundle edge except for the "hot well" region. This particular flow pattern can be inferred from experimental observations and since a large proportion of the steam flow goes through steam lanes, the result is not unexpected. Figure 8 provides contour maps of velocity magnitude in the first and last planes of the condenser under full load. The inlet flow rate at the first bay is greater than that at the last bay since the condensation rate at the first bay is greater than that at the last bay.

The air mass fraction contour maps are given in Fig. 9. The air mass fraction is much less than 1 percent in the vicinity of the tube bundle and increases as condensation takes place. The figure shows a sharp increase of air mass fraction in the vent region of the first plane. The values of air mass fraction are about 70 percent at the vent in the first plane under full load. The air mass fraction at the vent in the last plane is much lower than that in the first plane. This is the result of the nonuniform condensing capability along the cooling water flow direction and has been confirmed from experimental observations. Since the condensing potential is highest at the first bay, the air mass fraction reaches higher values than elsewhere.

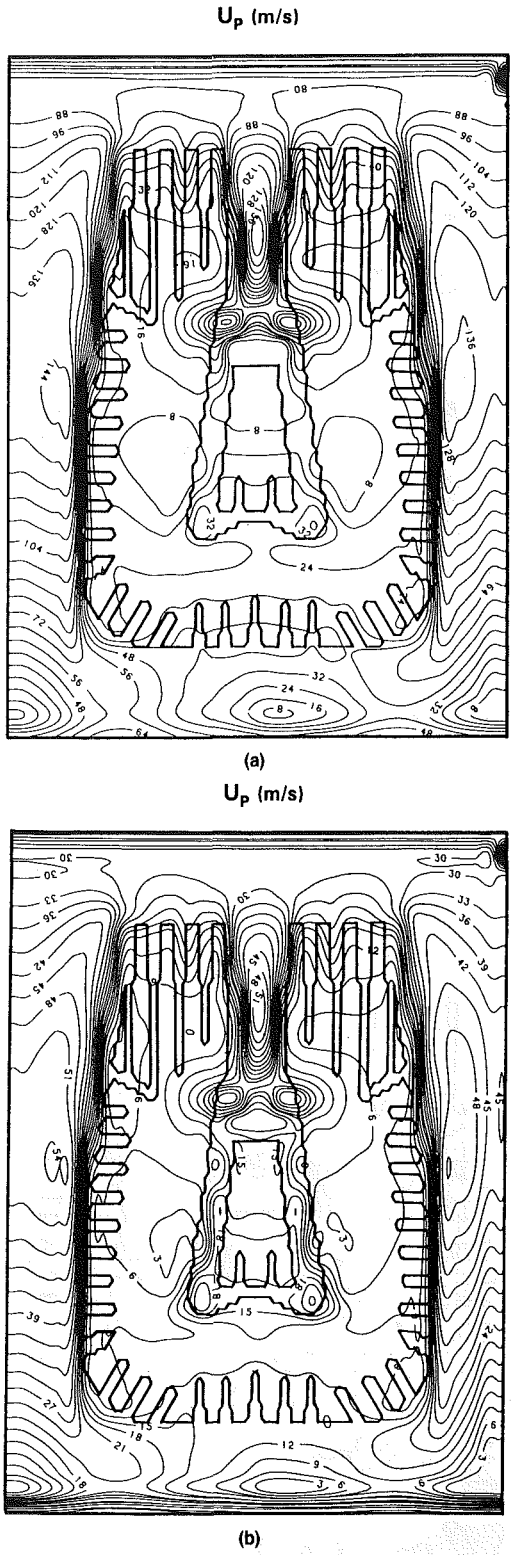

Fig. 8 Velocity magnitude distribution for full load (*a*) Plane No. 1; (*b*) Plane No. 16.

4.2 Comparison With Experimental Data. The experimental data in terms of pressure and temperature distributions are taken from Zhang et al. (1991b). The estimated precision of the pressure and temperature measurements is ±15 Pa and

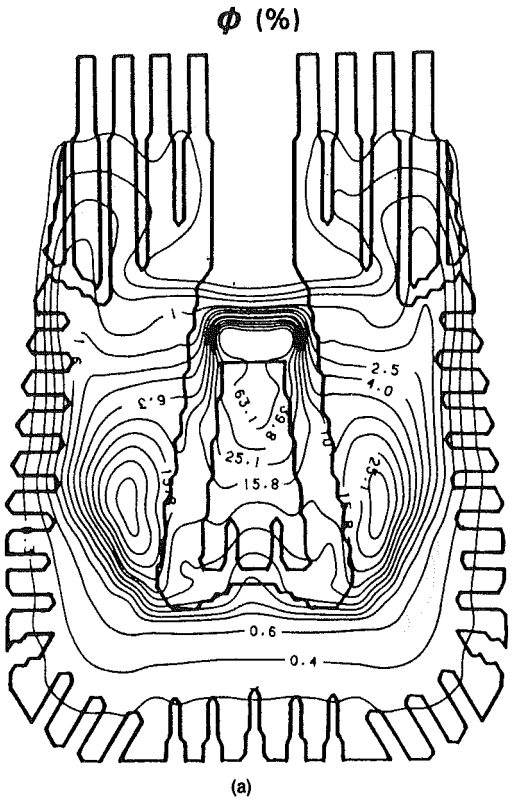

Fig. 9 Air concentration distribution for full load: (*a*) Plane No. 1; (*b*) Plane No. 16.

± 0.2°C, respectively. Comparisons for the steam pressures and steam temperatures at the locations shown in Fig. 10 for each of the 16 planes are listed in Tables 2(*a*)–3(*b*) under two loads. The overall agreement is good considering the complicity of inlet conditions and the simplifying assumptions made. The

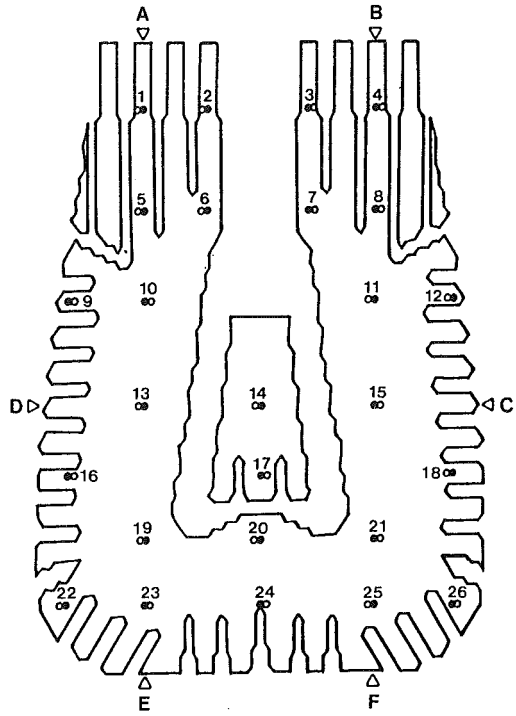

Fig. 10 Locations of steam pressure, steam temperature, and cooling water temperature measurement: A–F: steam pressures on 16 planes; 5, 8, 13, 14, 15, 23, 25: steam temperatures on 16 planes; 1–26: outlet cooling water temperatures.

average deviations of the predictions from the measurements are about 2.3 and 4.3 percent for the pressures and the temperatures under 245 MW load, and 1.8 and 2.6 percent for the pressures and the temperatures under 350 MW load. The most noticeable differences between the predicted and the experimental pressures occur at locations *A* and *B* for the first plane under both loads. The experimental pressures at *A* and *B* for the first plane are much lower than those for the other planes. The predicted pressures at *A* and *B*, however, are close to those for the other planes. After the first plane, the predicted pressures at *B* agree well with the experimental data. Tables 2(*b*) and 3(*b*) show that the differences between the predicted and experimental temperatures at location 8 for the first plane are 0.3 and 1.6 percent under 245 MW and 350 MW, respectively, although the pressures at *B* for the first plane are overpredicted by 9.8 and 7.5 percent, respectively. For the first three planes, the difference of experimental pressures at *A* and *B* is large and pressure at *A* is much lower than that at *B*, while the difference of the predicted pressures at *A* and *B* is small. After the third plane, the experimental pressure difference between *A* and *B* is small, and the predicted pressures at *A* agree well with the experimental data. A possible explanation for the large pressure difference between *A* and *B* may be attributed to the inlet velocity distribution. This is a prime source of uncertainty between the predictions and the experiments. The assumption of flow symmetry between bundles for this type of condensers may also be questionable.

VII Concluding Remarks

The proposed quasi-three-dimensional numerical procedure has been applied to simulate the shell-side flow and heat transfer for a industrial steam surface condenser under two different loading and operational conditions. The method proposed in the present study has shown the capability of predicting the performance of condensers including the three-dimensional effects due to the increase of cooling water temperature. It can predict the existence of noncondensable pockets along the tube length, which are the result of nonuniform condensing

Table 2(*a*) Comparison of predicted and experimental steam pressures, 245 MW

Steam pressure (Pa)

Location		A	B	C	D	E	F
Plane #1	Pred.	5460.9	5479.6	5178.0	5098.4	5234.1	5290.4
	Exp.	4614.4	4990.0	4892.2	4668.0	4926.9	4958.4
Plane #2	Pred.	5452.9	5470.4	5202.7	5129.8	5252.1	5300.0
	Exp.	5027.9	5409.8	5150.9	4876.4	5116.2	5141.5
Plane #3	Pred.	5445.6	5462.0	5224.9	5158.2	5267.7	5309.0
	Exp.	5160.4	5375.1	5223.5	4917.4	5119.4	5242.5
Plane #4	Pred.	5439.1	5454.3	5244.8	5183.8	5281.4	5317.3
	Exp.	5267.7	5302.5	5283.5	4677.5	5196.0	5302.5
Plane #5	Pred.	5433.4	5447.5	5262.5	5206.4	5293.3	5324.9
	Exp.	5207.7	5258.3	5311.9	5176.2	5296.1	5315.1
Plane #6	Pred.	5428.3	5441.3	5278.2	5226.8	5303.9	5331.8
	Exp.	5482.4	5495.0	5302.5	5062.6	5270.9	5337.2
Plane #7	Pred.	5423.8	5435.9	5292.2	5245.0	5313.3	5338.1
	Exp.	5311.9	5479.2	5337.2	5106.7	5337.2	5406.6
Plane #8	Pred.	5419.9	5431.0	5304.5	5261.2	5321.7	5343.7
	Exp.	5321.4	5457.1	5324.5	5289.9	5384.5	5400.3
Plane #9	Pred.	5416.4	5426.7	5315.2	5275.5	5329.1	5348.8
	Exp.	5040.5	5226.7	5106.7	5037.3	5169.9	5311.9
Plane #10	Pred.	5413.5	5423.0	5324.7	5288.2	5335.8	5353.3
	Exp.	5356.1	5419.2	5220.4	4914.2	5210.9	5340.3
Plane #11	Pred.	5410.9	5419.6	5333.0	5299.5	5341.6	5357.3
	Exp.	5311.9	5381.3	5261.5	5207.7	5324.5	5343.5
Plane #12	Pred.	5408.6	5416.7	5340.2	5309.4	5346.9	5360.9
	Exp.	5400.3	5346.7	5330.9	5318.3	5308.7	5330.9
Plane #13	Pred.	5406.7	5414.1	5346.6	5318.3	5351.5	5364.1
	Exp.	5428.7	5293.0	5334.0	5097.3	5239.3	5346.7
Plane #14	Pred.	5405.0	5411.9	5352.1	5326.2	5355.7	5367.0
	Exp.	5334.0	5375.1	5293.0	5160.4	5324.5	5362.4
Plane #15	Pred.	5403.5	5409.9	5357.0	5333.2	5359.5	5369.6
	Exp.	5375.1	5444.5	5346.7	5201.5	5318.3	5274.1
Plane #16	Pred.	5402.2	5408.1	5361.3	5339.4	5362.8	5371.9
	Exp.	5394.0	5444.5	5233.0	5223.5	5270.9	5270.9

Table 2(*b*) Comparison of predicted and experimental steam temperatures, 245 MW

Steam temperature (°C)

Location		5	8	13	14	15	23	25
Plane #1	Pred.	32.70	32.82	25.44	28.29	30.66	32.78	32.99
	Exp.	31.22	32.72	31.76	32.04	31.52	35.05	33.75
Plane #2	Pred.	32.86	32.97	28.16	29.50	31.27	32.93	33.11
	Exp.	31.41	33.08	32.03	*	32.12	35.05	34.07
Plane #3	Pred.	33.01	33.11	29.74	30.21	31.72	33.06	33.22
	Exp.	*	33.30	32.37	*	31.93	35.13	34.02
Plane #4	Pred.	33.14	33.23	30.74	30.72	32.08	33.18	33.32
	Exp.	32.06	33.54	32.61	33.79	32.07	35.25	*
Plane #5	Pred.	33.25	33.33	31.39	31.08	32.36	33.29	33.41
	Exp.	32.37	34.14	*	33.12	32.89	35.37	34.35
Plane #6	Pred.	33.35	33.43	31.82	31.37	32.58	33.38	33.49
	Exp.	32.71	34.31	33.23	33.46	32.86	35.32	34.31
Plane #7	Pred.	33.44	33.51	32.13	31.60	32.76	33.46	33.56
	Exp.	33.07	34.62	*	33.00	33.18	35.44	34.64
Plane #8	Pred.	33.52	33.58	32.36	31.81	32.90	33.54	33.63
	Exp.	33.43	34.93	33.88	33.10	33.85	36.11	34.88
Plane #9	Pred.	33.59	33.64	32.56	32.00	33.03	33.60	33.68
	Exp.	33.65	34.93	34.05	33.07	33.87	36.80	34.90
Plane #10	Pred.	33.65	33.70	32.72	32.16	33.14	33.66	33.73
	Exp.	34.06	*	34.05	33.00	33.90	37.37	34.64
Plane #11	Pred.	33.70	33.74	32.85	32.32	33.23	33.71	33.77
	Exp.	33.86	35.26	34.31	33.07	34.42	37.75	35.10
Plane #12	Pred.	33.75	33.79	32.97	32.45	33.32	33.75	33.81
	Exp.	34.32	35.53	34.50	33.14	34.95	38.80	35.29
Plane #13	Pred.	33.79	33.82	33.07	32.58	33.39	33.79	33.85
	Exp.	34.42	35.55	34.60	33.00	34.88	38.01	34.59
Plane #14	Pred.	33.83	33.85	33.16	32.70	33.46	33.83	33.88
	Exp.	34.46	35.29	36.34	33.10	35.31	37.75	35.07
Plane #15	Pred.	33.86	33.88	33.24	32.81	33.51	33.86	33.91
	Exp.	34.66	35.01	36.19	33.07	35.76	37.78	35.36
Plane #16	Pred.	33.89	33.91	33.31	32.91	33.56	33.89	33.93
	Exp.	34.70	34.86	36.24	33.61	36.41	37.25	35.50

* - Experimental data are not available.

Table 3(*a*) Comparison of predicted and experimental steam pressures, 350 MW

Steam pressure (Pa)

Location		A	B	C	D	E	F
Plane #1	Pred.	8751.3	8770.1	8344.9	8265.2	8454.0	8513.5
	Exp.	7615.8	8155.7	7959.9	7628.2	8007.5	8013.7
Plane #2	Pred.	8738.8	8756.4	8381.2	8308.3	8476.9	8527.6
	Exp.	8130.2	8641.8	8303.9	7890.2	8253.6	8288.1
Plane #3	Pred.	8727.3	8743.7	8414.1	8347.4	8496.6	8540.6
	Exp.	8338.4	8600.4	8398.4	7966.1	8266.0	8408.0
Plane #4	Pred.	8717.1	8732.2	8443.3	8382.3	8513.7	8552.4
	Exp.	8487.3	8534.2	8512.1	7641.3	8361.1	8537.6
Plane #5	Pred.	8708.2	8722.2	8469.3	8413.3	8528.8	8563.1
	Exp.	8386.0	8439.7	8515.6	8351.5	8509.4	8515.6
Plane #6	Pred.	8700.3	8713.3	8491.9	8440.5	8542.1	8572.7
	Exp.	8771.4	8755.5	8525.2	8124.0	8490.1	8581.8
Plane #7	Pred.	8693.6	8705.5	8511.6	8464.4	8553.8	8581.1
	Exp.	8543.9	8733.5	8565.9	8301.2	8581.8	8670.0
Plane #8	Pred.	8687.7	8698.7	8529.0	8485.6	8564.2	8588.6
	Exp.	8572.1	8720.4	8550.1	8525.2	8632.1	8651.4
Plane #9	Pred.	8682.6	8692.7	8544.2	8504.3	8573.4	8595.4
	Exp.	8297.7	8540.4	8329.4	8209.5	8452.2	8607.3
Plane #10	Pred.	8678.1	8687.5	8557.4	8520.7	8581.6	8601.2
	Exp.	8641.8	8758.3	8461.8	8045.4	8505.9	8645.2
Plane #11	Pred.	8674.3	8683.0	8568.9	8535.0	8588.7	8606.4
	Exp.	8585.2	8685.9	8565.9	8398.4	8622.5	8654.2
Plane #12	Pred.	8671.0	8679.1	8578.9	8547.7	8595.1	8611.0
	Exp.	8739.7	8645.2	8641.8	8648.0	8638.3	8648.0
Plane #13	Pred.	8668.2	8675.6	8587.6	8559.0	8600.8	8615.2
	Exp.	8739.7	8657.6	8597.6	8316.3	8537.6	8654.2
Plane #14	Pred.	8665.7	8672.6	8595.2	8568.9	8605.9	8618.8
	Exp.	8585.2	8670.0	8559.7	8389.4	8625.9	8657.6
Plane #15	Pred.	8663.6	8669.9	8601.9	8577.7	8610.4	8622.0
	Exp.	8619.7	8711.4	8603.8	8477.7	8588.0	8547.3
Plane #16	Pred.	8661.8	8667.6	8607.8	8585.5	8614.5	8624.9
	Exp.	8670.0	8714.2	8483.9	8480.4	8550.1	8528.0

Table 3(*b*) Comparison of predicted and experimental steam temperatures, 350 MW

Steam temperature (°C)

Location		5	8	13	14	15	23	25
Plane #1	Pred.	41.64	41.72	35.45	37.97	39.40	41.75	41.89
	Exp.	38.70	42.38	36.53	35.91	*	43.25	40.13
Plane #2	Pred.	41.79	41.86	38.25	39.00	40.17	41.88	42.01
	Exp.	38.96	42.19	36.89	*	*	43.13	40.58
Plane #3	Pred.	41.93	41.99	39.48	39.56	40.64	42.00	42.11
	Exp.	*	42.59	37.27	*	*	43.11	40.61
Plane #4	Pred.	42.05	42.10	40.16	39.95	40.98	42.11	42.21
	Exp.	39.62	43.80	37.44	37.89	*	42.99	*
Plane #5	Pred.	42.15	42.20	40.58	40.24	41.23	42.20	42.29
	Exp.	40.07	43.23	*	38.48	*	42.82	41.15
Plane #6	Pred.	42.24	42.29	40.89	40.48	41.43	42.28	42.36
	Exp.	40.38	42.95	38.77	37.58	*	42.59	41.18
Plane #7	Pred.	42.32	42.36	41.13	40.69	41.59	42.36	42.43
	Exp.	40.83	43.70	*	38.63	*	42.35	41.70
Plane #8	Pred.	42.39	42.42	41.32	40.87	41.73	42.42	42.48
	Exp.	41.16	43.61	40.03	39.03	*	42.35	42.07
Plane #9	Pred.	42.45	42.48	41.48	41.05	41.85	42.47	42.53
	Exp.	41.52	43.75	40.53	39.88	*	42.28	42.17
Plane #10	Pred.	42.50	42.53	41.61	41.21	41.95	42.52	42.58
	Exp.	42.09	*	40.96	40.07	*	42.16	42.19
Plane #11	Pred.	42.55	42.57	41.72	41.35	42.04	42.57	42.61
	Exp.	41.90	44.10	41.57	40.41	*	41.93	42.62
Plane #12	Pred.	42.59	42.61	41.82	41.48	42.11	42.60	42.65
	Exp.	42.44	44.06	42.16	40.52	*	41.83	43.00
Plane #13	Pred.	42.62	42.64	41.91	41.60	42.18	42.64	42.68
	Exp.	42.56	43.96	42.73	40.86	*	41.29	42.69
Plane #14	Pred.	42.65	42.66	41.98	41.71	42.24	42.67	42.70
	Exp.	42.68	43.80	*	41.31	*	41.24	43.14
Plane #15	Pred.	42.68	42.69	42.05	41.81	42.29	42.69	42.73
	Exp.	42.96	43.06	*	41.12	*	41.34	43.61
Plane #16	Pred.	42.70	42.71	42.10	41.90	42.34	42.72	42.75
	Exp.	43.03	43.01	*	41.29	*	40.86	43.87

* - Experimental data are not available.

capability along the tube length. The comparisons of the predictions against experimental data indicate that the predicted local pressures and temperatures are in good agreement with the measured values in most locations of the tube bundle. When consideration is given to the uncertainties of the experimental data, the assumptions undertaken, and the limitations of the

computational procedure, the predictive capability of the model is very encouraging.

Full benchmarking of the procedure for the condenser simulation is still required and for this purpose extensive experimental data, including fluid and temperature fields, and flow visualization data will be needed.

References

ASHRAE, 1989, *Handbook, Fundamentals*, SI Edition, American Society of Heating, Refrigerating and Air Conditioning Engineers Inc., Atlanta, GA, p. 3.14.

Barsness, E. J., 1963, "Calculation of the Performance of Surface Condensers by Digital Computer," *National Power Conference*, Cincinnati, OH, ASME Paper No. 63-PWR-2.

Berman, L. D, and Fuks, S. N., 1958, "Mass Transfer in Condensers With Horizontal Tubes When the Steam Contains Air," *Teploenergetica*, Vol. 5, No. 8, pp. 66–74.

Brickell, G. M., 1981, "Potential Problem Areas in Simulating Condenser Performance," in: P. J. Marto and R. H. Nunn, eds., *Power Condenser Heat Transfer Technology*, Hemisphere, Washington, DC, pp. 51–61.

Diaz-Tous, I. A., 1983, Keynote Address, *Proc. Symposium on State-of-the-Art Condenser Technology*, Orlando, FL, pp. 1:1–1:22.

Fujii, T., Uehara, H., Hirata, K., and Oda, K., 1972, "Heat Transfer and Flow Resistance in Condensation of Low Pressure Steam Flowing Through Tube Banks," *Int. J. Heat Mass Transfer*, Vol. 15, pp. 247–260.

Grant, I. D. R., and Osment, B. D. J., 1968, "The Effect of Condensate Drainage on Condenser Performance," NEL Report No. 350.

Mochida, Y., and Miura, Y., 1990, "Performance Analysis of Condenser for Large Power Stations," *Proc. 2nd Int. Symposium on Condensers and Condensation*, Bath, United Kingdom, pp. 213–222.

Naviglio, A., Sala, M., Socrate, S., Stefani, A., and Vigevano, L., 1988, "Distribution of Non-condensable Gases Within the Tube Bundle of Surface Condensers," *TEC 88—Conference, Recent Advances in Heat Exchangers*, Grenoble, France, Dec. 10–13.

Rabas, T. J., and Kassem, A. E., 1985, "The Effect of Equal Shellside Pressure Drops on the Thermal Performance of Single-Pass, 'X'-Shell, Steam Condensers," *23rd National Heat Transfer Conference*, ASME HTD-Vol. 44, pp. 35–44.

Rhodes, D. B., and Carlucci, L. N., 1983, "Predicted and Measured Velocity Distributions in a Model Heat Exchanger," *International Conference on Numerical Methods in Nuclear Engineering*, Canadian Nuclear Society/American Nuclear Society, Montreal.

Van Doormaal, J. P., and Raithby, G. D., 1984, "Enhancements of the SIMPLE Method for Predicting Incompressible Fluid Flow," *Numerical Heat Transfer*, Vol. 7, pp. 147–163.

Wilson, J. L., 1972, "The Design of Condensers by Digital Computers," Institute of Chemical Engineers Symposium Series No. 35.

Zhang, C., Sousa, A. C. M., and Venart, J. E. S., 1991a, "Numerical Simulation of Different Types of Steam Surface Condensers," ASME *Journal of Energy Resources Technology*, Vol. 113, No. 2, pp. 63–70.

Zhang, C., Dutcher, C., Cooper, W., Daib, K., Sousa, A. C. M., and Venart, J. E. S., 1991b, "Measurement and Modelling: A 350 MW_e Plant Power Condenser," *Design and Operation of Heat Exchangers*, W. Roetzel, P. J. Heggs, and D. Butterworth, eds., Springer-Verlag, Berlin, Germany, pp. 340–361.

Zhang, C., Sousa, A. C. M., and Venart, J. E. S., 1993, "The Numerical and Experimental Study of a Power Plant Condenser," ASME JOURNAL OF HEAT TRANSFER, Vol. 115, pp. 435–445.

Thermal Analysis of a Micro Heat Pipe

D. Khrustalev

A. Faghri

Department of Mechanical and Materials Engineering, Wright State University, Dayton, OH 45435

A detailed mathematical model is developed in which the heat and mass transfer processes in a micro heat pipe (MHP) are examined. The model describes the distribution of the liquid in a MHP and its thermal characteristics depending upon the liquid charge and the applied heat load. The liquid flow in the triangular-shaped corners of a MHP with polygonal cross section is considered by accounting for the variation of the curvature of the free liquid surface and the interfacial shear stresses due to a liquid–vapor frictional interaction. The predicted results obtained are compared to existing experimental data. The importance of the liquid fill, minimum wetting contact angle, and the shear stresses at the liquid–vapor interface in predicting the maximum heat transfer capacity and thermal resistance of the MHP is demonstrated.

Introduction

Due to miniaturization in the field of electronics, problems associated with overheating of electronic components have increased significantly. To address these difficulties, it has been proposed to cool electronic components with micro heat pipes, which are either surface-mounted or are an integral part of the component in question. The micro heat pipe (MHP) was originally defined by Cotter (1984) as one in which the mean curvature of the vapor–liquid interface is of the same magnitude as the reciprocal of the hydraulic radius of the total flow channel. In a MHP, condensate return is accomplished by the flow of liquid in the corners of the polygonal heat pipe container; the condensate being held in the corners by surface tension. A detailed literature review related to miniature and micro heat pipes has recently been given by Cao and Faghri (1993). The objective of the present study is to develop a mathematical model that can determine the maximum heat transfer capacity and thermal resistance of MHPs. The present model incorporates the following new features:

- The influence of the liquid charge on the length of the liquid blocking zone and on the liquid distribution is studied.
- The heat transfer through a liquid film in the evaporator is described with respect to the disjoining pressure.
- The heat transfer through a film of condensate in the condenser is considered and the closed-form solutions are obtained using an approach similar to that developed for axially grooved heat pipes.
- The influence of shear stresses at the free liquid surface in a corner due to the frictional vapor–liquid interaction on the liquid flow is taken into consideration.
- The possibility of the variation of the meniscus contact angle in the condenser is treated by considering the condensate film formation.
- The model describes MHP operation in the case of convective heat transfer outside the evaporator and condenser as well as that for a prescribed heat flux distribution.

Mathematical Model

The present model deals with a polygonal MHP having N triangular corners, which can easily be extended for cross sections having different corner configurations. Figure 1 presents cross sections of the triangular micro heat pipe used to illustrate

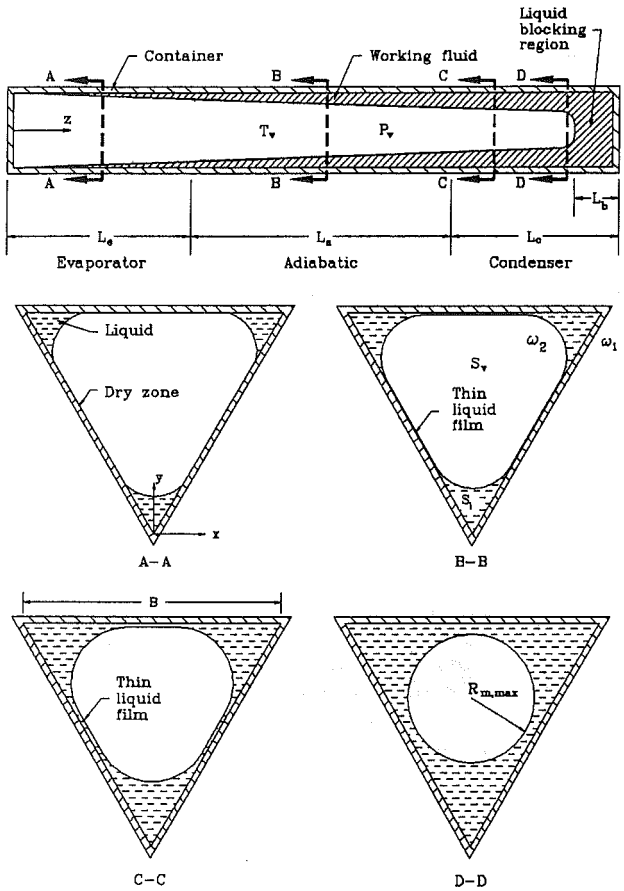

Fig. 1 Schematic of the micro heat pipe and coordinate systems for analysis

the methodology of the present study. The heat load is uniformly distributed between all of the corners. Near the evaporator end cap, if the heat load is sufficient, the liquid meniscus is depressed in the corner, and its cross-sectional area and radius of curvature of the free surface are extremely small. Most of the wall is dry or is covered by a nonevaporating liquid film. In the adiabatic section, the liquid cross-sectional area is comparatively larger. The inner wall surface may be covered with a thin liquid film due to the disjoining pressure. At the beginning of the condenser, a film of condensate is present on the wall, and liquid flows through this film toward the meniscus region under the influence of surface tension. For normal

Contributed by the Heat Transfer Division for publication in the JOURNAL OF HEAT TRANSFER. Manuscript received by the Heat Transfer Division February 1993; revision received April 1993. Keywords: Heat Pipes and Thermosyphons, Thermocapillary Flows, Thin Film Flow. Technical Editor: R. Viskanta.

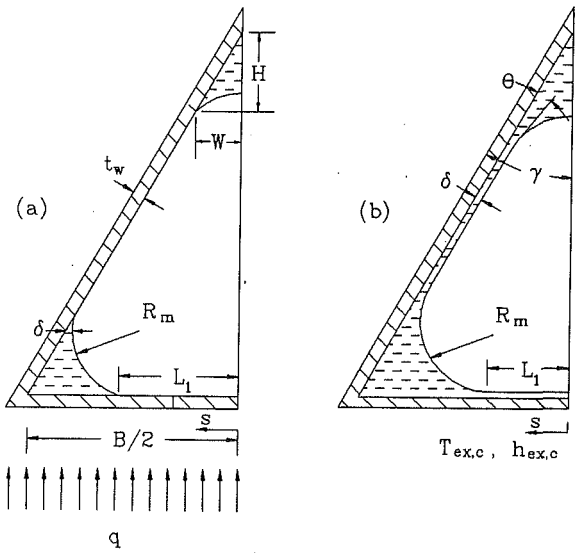

Fig. 2 Details of the micro heat pipe cross section in: (*a*) the evaporator: (*b*) the condenser

operation, the contact angle of the meniscus θ is constant and equal to the minimum wetting contact angle θ_0 in the evaporator and adiabatic sections and the beginning of the condenser zone, which is fixed for a specific working-fluid/container combination. In Fig. 1, the possibility of liquid blocking the end of the condenser is shown. The details of the evaporator and condenser sections are shown in Fig. 2.

The fluid flow and heat transfer within a micro heat pipe operating under steady-state conditions are modeled, neglecting axial heat conduction in the wall and liquid. The conservation equations for the steady-state operation of a MHP are the continuity, momentum, and energy equations for the liquid, vapor, and wall, and the Laplace–Young equation for the radius of curvature at the liquid–vapor interface. At any axial location, the following mass conservation equation must hold over the cross section of the MHP:

$$\overline{w}_v \rho_v S_v = N \overline{w}_l \rho_l S_l \equiv N G_l \tag{1}$$

where G_l is the mass flow rate through a corner. The average liquid and vapor velocities in the axial direction in Eq. (1) are:

$$\overline{w}_l = \frac{1}{S_l} \int \int_{S_l} w_l(x, y)\, dx\, dy, \tag{2}$$

$$\overline{w}_v = \frac{1}{S_v} \int \int_{S_v} w_v(x, y)\, dx\, dy$$

A MHP contains a definite amount of a working fluid M_t, which is distributed in accordance with the following relation:

$$M_t = N \int_0^{L_t - L_b} \rho_l S_l\, dz + \int_0^{L_t - L_b} \rho_v S_v\, dz + M_b + M_\delta \tag{3}$$

where M_b and L_b are the mass and length of the liquid that blocks the condenser, and M_δ is the mass of the thin liquid films in the condenser and adiabatic sections in the interval $0 \le s \le L_1$ (see Fig. 2(*b*)) for all of the MHP walls, while S_l doesn't include the thin film existing in this interval. It is anticipated that the excessive liquid, the amount of which depends upon the operating conditions, is contained at the end of the condenser because of the MHP small inner diameter and the effect of the vapor flow on the liquid (Fig. 1).

The axial conservation of momentum equation for an in-

Nomenclature

A = dispersion constant, J
B = width of inner wall, m
a, b, C = constants
c_p = specific heat at constant pressure, J/(kg-K)
c_v = specific heat at constant volume, J/(kg-K)
D_h = hydraulic diameter, m
F = dimensionless shear stress
f_v = friction coefficient
g = gravity constant, m/s^2
G = mass flow rate, kg/s
H = meniscus height, m
h_{fg} = latent heat of vaporization, J/kg
h = heat transfer coefficient, W/(m^2-K)
k = thermal conductivity, W/(m-K)
L = length, m
L_1 = half-length of thin film or dry zone (Fig. 2), m
M = mass, kg
Ma = $\overline{w}_{v,a}/\sqrt{\gamma_0 R_g T_v}$ = Mach number
N = number of corners
P = pressure, Pa
P_d = disjoining pressure, Pa
Q = axial heat rate, W
Q_a = total heat input to MHP, W
q = heat flux, W/m^2
R_m = radius of curvature of the meniscus, m
R_g = individual gas constant, J/(kg-K)
Re = $\overline{w}_v D_{h,v}/\nu_v$ = axial Reynolds number
Re$_r$ = $\overline{v}_{v,w} D_{h,v}/\nu_v$ = radial Reynolds number
r = thermal resistance, K/W
S = cross-sectional area, m^2
s = coordinate, m
T = temperature, K
t_w = wall thickness, m
v = radial velocity, m/s
V = dimensionless volume flux
w = axial velocity, m/s
$\overline{w}$ = mean axial velocity, m/s
W = half-width of meniscus, m
x, y = coordinates, m
$\dot{x}, \dot{y}$ = coordinates (Fig. 3), m
Y = curvature of meniscus, 1/m
z = axial coordinate, m
α = accommodation coefficient
β = momentum flux coefficient
γ = half-angle of the corner
γ_0 = c_p/c_v = ratio of specific heats
δ = film thickness, m
ΔP = $P - P_{v0} + \sigma/R_{m0}$ = pressure variation, N/m^2
ΔQ = heat flow per unit groove length, W/m
ϵ = emissivity
θ = meniscus contact angle
θ_0 = minimum wetting contact angle
μ = dynamic viscosity, Pa-s
ν = kinematic viscosity, m^2/s
ρ = density, kg/m^3
σ = surface tension, N/m
σ_0 = Stefan–Boltzmann constant, W/(m^2-K^4)
ϕ = inclination angle
ω_1 = liquid–wall interface
ω_2 = liquid–vapor interface

Subscripts

a = adiabatic
b = blocking
c = condenser
e = evaporator
ex = external
f = thin film
l = liquid
max = maximum
men = meniscus
min = minimum
pc = phase change
sat = saturation
t = total
v = vapor
w = wall
δ = liquid film free surface

compressible vapor flow using the one-dimensional boundary-layer approximation is:

$$\frac{d}{dz}\left(P_v+\rho_v g z\sin\phi+\rho_v\beta_v\overline{w}_v^2\right)=-f_v\frac{2\rho_v\overline{w}_v^2}{D_{h,v}} \tag{4}$$

where β_v is the momentum flux coefficient, f_v is the friction coefficient, and $D_{h,v}$ is the hydraulic diameter of the vapor channel. The values of these coefficients can be determined using the results of previous investigators for the two-dimensional, laminar boundary-layer equations with suction and injection. For example, for the small radial Reynolds numbers usually seen in MHPs ($0\le \mathrm{Re}_r<2$), in the evaporator and adiabatic sections, the results given by Bankston and Smith (1971) can be approximated as follows:

$$f_v=\left(\frac{16+0.25\mathrm{Re}_r^2}{\mathrm{Re}}\right),\quad \beta_v=1.33-0.0075\mathrm{Re}_r^2$$

In the condenser section (Bowman and Hitchcock, 1988; Jang et al., 1991):

$$f_v=16[1.2337$$
$$-0.2337\exp(-0.0363\mathrm{Re}_r)][\exp(1.2\mathrm{Ma})]/\mathrm{Re},\quad \beta_v=1.33$$

The velocity of the liquid phase is very small in comparison to that of the vapor flow, so the interfacial shear for the vapor is computed by assuming the liquid to be stationary (Longtin et al., 1992).

The axial transport of condensate in a MHP takes place in the corners, where most of the liquid resides. The thickness of the liquid films in the condenser and adiabatic sections in the interval $0\le s\le L_1$ (see Fig. 2(*b*)) is assumed to be too small to contribute to the axial mass transport. Since the axial Reynolds number for liquid flow in a MHP is usually less than 1, it can be considered to be viscous and quasi-one-dimensional. Thus, the conservation of momentum equation for the liquid flow in a corner with cross-sectional area S_l is:

$$\frac{dP_l}{dz}+\frac{\rho_l}{2S_l}\frac{d}{dz}\left(\overline{w}_l^2S_l\right)+\rho_l g\sin\phi=\mu_l\left(\frac{\partial^2 w_l}{\partial x^2}+\frac{\partial^2 w_l}{\partial y^2}\right) \tag{5}$$

The second term in Eq. (5) gives the contributions of the dynamic component of the flow rate and the axial variation of the cross-sectional area on the liquid pressure gradient. The present numerical results have shown that this term changes the liquid pressure gradient by less than 0.1 percent.

The conservation of energy equation is cast into a form that reflects the change in the axial mass flow rate of liquid due to evaporation and condensation:

$$\frac{d}{dz}\left(\rho_l\overline{w}_lS_l\right)=\begin{cases}\dfrac{B}{h_{fg}}h_{ex,e}(T_{ex,e}-T_v)\left(1+\dfrac{h_{ex,e}}{\overline{h}_e}\right)^{-1}, & 0\le z\le L_e\\ 0\quad\text{(adiabatic section)}, & L_e<z<L_e+L_a\\ \dfrac{B}{h_{fg}}h_{ex,c}(T_{ex,c}-T_v)\left(1+\dfrac{h_{ex,c}}{\overline{h}_c}\right)^{-1}, & L_e+L_a\le z\le L_t-L_b\end{cases} \tag{6}$$

where $\overline{h}_e$ and $\overline{h}_c$ are the mean internal heat transfer coefficients between the wall and vapor, and $h_{ex,e}$ and $h_{ex,c}$ are the heat transfer coefficients between the wall and the ambient. The mean coefficients $\overline{h}_e$ and $\overline{h}_c$ for evaporation and condensation, respectively, include the resistances of the wall and liquid film, which are given by the heat transfer analysis for each of the heat loaded sections at every point on z. The vapor temperature is denoted by T_v. For a given axial heat load function $Q(z)$, Eq. (6) can be rewritten as:

$$\frac{d}{dz}\left(\rho_l\overline{w}_lS_l\right)=\frac{1}{h_{fg}N}\frac{dQ(z)}{dz} \tag{7}$$

For the case of radiative heat transfer in the condenser region, the heat transfer coefficient in Eq. (6) is:

$$h_{ex,c}=\sigma_0\epsilon(T_v+T_{ex,c})\left(T_v^2+T_{ex,c}^2\right) \tag{8}$$

An iterative procedure can be used to determine $h_{ex,c}$ from Eq. (8), since it is a strong function of T_v in the case of a radiative boundary condition.

The interfacial meniscus radius of curvature is related to the pressure difference between the liquid and vapor by the Laplace–Young equation, which, in differential form, is:

$$\frac{dP_l}{dz}=\frac{dP_v}{dz}-\frac{d}{dz}\left(\frac{\sigma}{R_m}\right) \tag{9}$$

The vapor temperature and pressure are related by the perfect gas equation:

$$P_v=\rho_vR_gT_v \tag{10}$$

Equation (10) is accurate enough for comparatively low pressure values for the conditions considered in the present study (the maximum error value was 0.73 percent). However, in the general case, one should use an empirical equation based on saturation conditions and the Clausius–Clapeyron equation instead of Eq. (10).

The mean axial liquid and vapor velocities at the evaporator and condenser end caps are:

$$\overline{w}_l|_{z=0}=\overline{w}_v|_{z=0}=0 \tag{11}$$

$$\overline{w}_l|_{z=L_t-L_b}=\overline{w}_v|_{z=L_t-L_b}=0 \tag{12}$$

Referring to Fig. 1, the liquid in the corner is attached to two walls, ω_1, and interacts with the vapor flow at the liquid–vapor interface, ω_2. Therefore, the no-slip condition and relation for the equality of tangential shear stress on these surfaces are:

$$w_l|_{\omega_1}=0;\quad \left.\frac{\partial w_l}{\partial n}\right|_{\omega_2}=-\frac{f_v}{2\mu_l}\rho_v\overline{w}_v^2 \tag{13}$$

The second boundary condition in Eq. (13) is an essential feature of the present model. Here n is the normal vector on the free surface of the liquid meniscus. The cross section of the vapor channel has a complicated shape and the assumption of a circular cross section is not completely exact for $N\le 3$, but it is very close for $N>3$, where the vapor channel is nearly circular.

The vapor and liquid pressures at the evaporator end cap are:

$$P_v|_{z=0}=P_{v0},\quad P_l|_{z=0}=P_{vo}-\frac{\sigma}{R_{m0}} \tag{14}$$

The values of P_{v0} and R_{m0} are to be determined using additional conditions. When solving Eq. (6), where $T_v(z)$ is also unknown and depends on P_v, the value of P_{v0} must be chosen such as to satisfy Eq. (12). When $Q(z)$ and T_{v0} are known, $P_{v0}=P_v(T_{v0})$, which can be obtained using the perfect gas law, Eq. (10). The radius of curvature of the meniscus at the evaporator end cap, R_{m0}, is found using Eq. (3), since the value of B_{m0} influences the axial distribution of liquid. In general, the radius of curvature of the meniscus is bounded by $R_{m,\min}\le R_{m0}\le R_{m,\max}$. When liquid blocks part of the condenser section, R_{m0} is specified such that $R_m\simeq R_{m,\max}$ at the location where the liquid blocking begins, where $R_{m,\max}$ is approximately the radius of the largest circle that can be inserted in the inner MHP cross section (Fig. 1). For the case in which no liquid

blocks the condenser, the value of R_{m0} is given by Eq. (3) where $M_b=0$ and $L_b=0$, or $R_{m0}=R_{m,\min}$ when $Q_a=Q_{\max}$.

To determine the heat transfer coefficients $\bar{h}_e$ and $\bar{h}_c$ in Eq. (6), the heat transfer during evaporation and condensation in a triangular capillary groove is examined.

Heat Transfer in the Condenser Section

The equation for the condensate film thickness distribution, $\delta(s)$, shown in Figs. 1 and 2, is given by Kamotani (1976a) for a low-temperature heat pipe with axial grooves:

$$\frac{\rho_l \sigma \delta^3}{3\mu_l}\frac{d^3\delta}{ds^3}=\frac{k_l(T_v-T_w)}{h_{fg}}\int_0^s \frac{ds}{\delta} \tag{15}$$

For the case of a polygonal MHP, the boundary conditions are:

$$\left.\frac{d\delta}{ds}\right|_{s=0}=0;\quad \left.\frac{d^3\delta}{ds^3}\right|_{s=0}=0;\quad \left.\frac{d^2\delta}{ds^2}\right|_{s=L_1}=\frac{1}{R_m};\quad \left.\frac{d\delta}{ds}\right|_{s=L_1}=\tan\theta \tag{16}$$

Equation (15) has been derived from the conservation of mass, momentum, and energy equations for the flow of a thin film and the relation between the thickness and the curvature. The interfacial thermal resistance is usually neglected in comparison to the resistance of the liquid film, but it can be accounted for in the expressions for the condenser heat resistance. Equation (15) can be solved for the film thickness by numerical methods. In the present paper, however, an approximate closed-form solution is obtained using the assumption that the liquid film thickness variation along the s direction is small in comparison to its thickness; i.e., the film is assumed to be nearly planar. The film thickness in the middle region of the wall (see Fig. 2(b)) can be approximated by:

$$\frac{\delta}{B}=C_0+C_1\frac{s}{B}+C_2\frac{s^2}{B^2}+C_3\frac{s^3}{B^3}+C_4\frac{s^4}{B^4} \tag{17}$$

From the boundary conditions in Eq. (16), the coefficients are:

$$C_1=C_3=0;\quad C_4=\frac{L_1/R_m-\tan\theta}{8(L_1/B)^3},\quad C_2=\frac{B}{2R_m}-6\left[\frac{L_1}{B}\right]^2 C_4 \tag{18}$$

The value of C_0 is obtained by differentiating Eq. (15), inserting Eq. (17), and neglecting the term that contains the first derivative of δ. The mean heat transfer coefficient of the thin film region, $\bar{h}_{c,f}=k_l/\bar{\delta}$, is approximated as:

$$\bar{h}_{c,f}=\frac{k_l}{BC_0}=\left[\frac{h_{fg}\rho_l\sigma k_l^3(L_1/R_m-\tan\theta)}{\mu_l L_1^3(T_v-T_w)}\right]^{0.25} \tag{19}$$

From Fig. 2 (b), the value of $L_1$is defined as:

$$L_1=\frac{B}{2}-R_m\frac{\cos(\gamma+\theta)}{\sin\gamma}-\frac{C_0}{\tan\gamma}B \tag{20}$$

Equations (19) and (20) are solved for C_0 and L_1 using an iterative procedure. The increase of the liquid film thickness along the s coordinate in the interval $s=0$ to $s=L_1$ in the numerical experiments is less than 8.0 percent, so Eq. (19), where it is assumed that $\bar{\delta}=BC_0$, gives $\bar{h}_{c,f}$ to within 4.0 percent.

The heat transfer coefficient in the meniscus region can be estimated as follows. For $s>L_1$, the film thickness increases sharply (see Fig. 2 (b)):

$$\delta=\delta|_{s=L_1}-R_m+[R_m^2+(s-L_1)^2+2(s-L_1)R_m\sin\theta]^{0.5} \tag{21}$$

Then, for the mean heat transfer coefficient in the meniscus region, $\bar{h}_{c,\text{men}}$, we have:

$$\bar{h}_{c,\text{men}}=\int_{L_1}^{B/2}\frac{k_l\,ds}{(B/2-L_1)\delta} \tag{22}$$

For $\theta>20$ deg there is a simple analytical approximation for $\bar{h}_{c,\text{men}}$:

$$\bar{h}_{c,\text{men}}=\frac{k_l}{B/2-L_1}\frac{1}{\sin\theta}\ln\left[1+\left(\frac{B}{2}-L_1\right)\frac{\sin\theta}{\delta|_{s=L_1}}\right] \tag{23}$$

Equation (23) is obtained from Eqs. (21) and (22) by approximating the film thickness as

$$\delta=\delta|_{s=L_1}+s\left.\frac{d\delta}{ds}\right|_{s=L_1} \tag{24}$$

The mean heat transfer coefficient in the condenser section for a given z can be obtained by combining $\bar{h}_{c,f}$ and $\bar{h}_{c,\text{men}}$ with their respective areas, and including the thermal resistance of the wall:

$$\bar{h}_c=\left(\left[\frac{2L_1}{B}\bar{h}_{c,f}+\left(1-\frac{2L_1}{B}\right)\bar{h}_{c,\text{men}}\right]^{-1}+\frac{t_w}{k_w}\right)^{-1} \tag{25}$$

The wall temperature in Eq. (19) is determined by the thermal resistance between the vapor temperature and the ambient temperature:

$$T_w=T_{ex,c}+(T_v-T_{ex,c})\frac{1}{h_{ex,c}}\left(\frac{1}{h_{ex,c}}+\frac{1}{\bar{h}_c}\right)^{-1} \tag{26}$$

Therefore, Eqs. (19)–(26) are solved for $\bar{h}_c$ and T_w using an iterative procedure.

Depending on the amount of working fluid within the MHP, part of the condenser may be blocked with liquid. In this case, the effective condenser length is L_c-L_b, where L_b is the length blocked by liquid.

$$L_b=\frac{M_b}{(S_v+NS_l)\rho_l}\equiv\frac{M_b}{S_t\rho_l} \tag{27}$$

The overall thermal resistance of the condenser can then be determined as follows:

$$r_c=\frac{1}{Q_a(L_c-L_b)}\int_{(L_e+L_a)}^{(L_t-L_b)}\frac{dQ}{dz}\frac{1}{BN}\frac{1}{\bar{h}_c}\,dz \tag{28}$$

In the numerical procedure, for the case of convective heat transfer outside the MHP, dQ/dz is defined using Eq. (7).

Now the variation of the contact angle of the meniscus along the condenser is to be considered. At the inlet of the condenser, the contact angle is $\theta=\theta_0$. In the region near the liquid blocking zone, $\theta=0$. Therefore, variation of the contact angle within the condenser takes place. At the beginning of the condenser, usually $L_1/R_m>\tan\theta$ and the liquid film is very thin. Along the condenser, while L_1/R_m is decreasing, there is a z location where $L_1/R_m\approx\tan\theta$. In the vicinity of this location, Eq. (15) cannot be solved; that is, the conservation of mass and energy in the film cannot be satisfied. This causes the contact angle θ to begin changing, starting from this particular z location in the condenser. In the present model, it is assumed that the θ variation after this location along the z axis in the condenser is described by the relation:

$$\frac{L_1}{R_m}-\tan\theta=0.01 \tag{29}$$

The value 0.01 is taken from both physical and numerical considerations. The choice of this value is made since it is very close to zero in comparison to that given by the right-hand side of Eq. (29) at the beginning of the condenser, which can be greater than unity. This value, unlike zero, still provides a physically reasonable solution for Eqs. (15) and (16). This method allows for the approximate equality of the contact angles of the liquid flow in the corner and at the beginning of the liquid blocking zone.

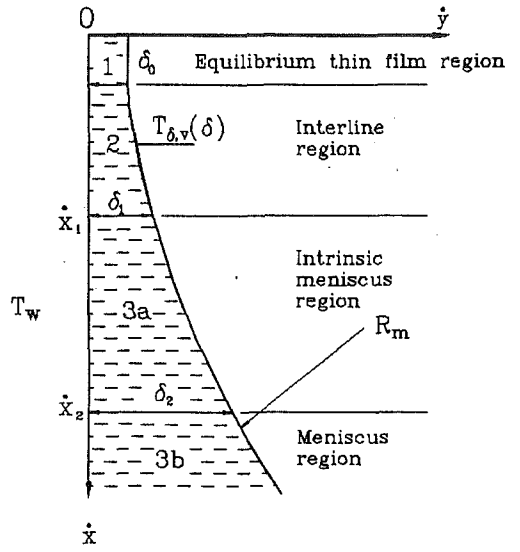

Fig. 3 Cross section of the end of the extended meniscus region near a heated wall

Heat Transfer in the Evaporator Section

Following the approaches of Stephan and Busse (1992), Solov'yev and Kovalev (1984), and Holm and Goplen (1979) for the description of the heat transfer in the meniscus/thin-film transition region, an approximate thermal analysis of evaporative heat transfer in a MHP can be provided. The liquid flow in a thin evaporating liquid film toward the point $\dot{x}=0$, as shown in Fig. 3, takes place under the influence of surface tension and the solid-liquid-vapor interfacial force field (disjoining pressure). The heat flux due to conduction through the liquid in the microlayer region of the meniscus is approximated as (Stephan and Busse, 1992):

$$q=\left[\frac{\delta}{k_l}+\frac{T_v(2\pi R_g T_v)^{0.5}}{h_{fg}^2\rho_v}\frac{(2-\alpha)}{2\alpha}\right]^{-1}(T_w-T_{\delta,v}) \tag{30}$$

where the interfacial thermal resistance is included. The disjoining pressure is (Derjaguin, 1955):

$$P_d=\frac{A}{\delta^3} \tag{31}$$

It is more convenient, however, to describe the disjoining pressure for extremely thin films by the following relation (Solov'yev and Kovalev, 1984; Holm and Goplen, 1979):

$$P_d=\rho_l R_g T_{\delta,v}\ln\left[a\left(\frac{\delta}{3.3}\right)^b\right] \tag{32}$$

where a and b are constants. Equation (32) was initially obtained by Potash and Wayner (1972). For pure water on quartz glass, $a=1.534$ and $b=0.0243$ (Holm and Goplen, 1979). In the adiabatic section, the thickness of the liquid film, which is extremely small, can be obtained from the relation $P_d=-\sigma/R_m$ by combining with Eq. (32).

It is essential to describe the difference between the temperature $T_{\delta,v}$ at the vapor side of the liquid-vapor interface and the saturation temperature T_v due to the disjoining pressure of the film. The following expression for the pressure drop at the surface of the film in the interline region is used by Solov'yev and Kovalev (1984), which is consistent with that by Carey (1992).

$$\ln\left[\frac{P_{\delta,v}}{P_{\text{sat}}(T_{\delta,v})}\right]=\frac{P_d}{\rho_l R_g T_{\delta,v}} \tag{33}$$

Solov'yev and Kovalev (1984) obtained closed-form solutions for q for three regions of an evaporating film, as shown in Fig. 3 (see also Carey, 1992), which are used in the present analysis. Region 1 represents the equilibrium (nonevaporating) thin film, and Region 2 (interline) is dominated by the disjoining pressure. In Region 3a (intrinsic meniscus), the curvature of the film varies under the influence of surface tension. In Region 3b (meniscus), the curvature is constant. The solutions by Solov'yev and Kovalev were obtained using the boundary-layer approximation for a liquid flow, and the relation between the thickness and the curvature of the film. The heat fluxes per unit groove length can then be estimated as:

$$\Delta Q_2=1.6\rho_v h_{fg}(T_w-T_v)\left[\frac{h_{fg}\rho_l R_g^2 b(\delta_1^4-\delta_0^4)}{\nu_l k_l(T_w-T_v)}\right]^{0.5} \tag{34}$$

δ_0 is the equilibrium (nonevaporating) thin film thickness, which can be obtained from Eqs. (32) and (33) at $P_{\delta,v}=P_v$ and $T_{\delta,v}=T_w$, where the subscript v denotes the bulk conditions of the saturated vapor. For pure water on quartz glass, $\delta_0=1.8\times10^{-9}$ m. δ_1 is defined from the relation $a\delta_1^b=1$; for water, $\delta_1=9.28\times10^{-9}$ m.

$$\Delta Q_{3a}=\int_{\dot{x}_1}^{\dot{x}_2}\frac{(T_w-T_v)}{1/h_{pc}+\delta(\dot{x})/k_l}\,d\dot{x}$$
$$=1.5\rho_v h_{fg}(T_w-T_v)\left(\frac{R_g}{T_v}\right)^{0.5}\left(\frac{h_{fg}\sigma\delta_2^5}{\nu_l k_l(T_w-T_v)}\right)^{0.25} \tag{35}$$

$$\Delta Q_{3b}=\int_{\dot{x}_2}^{W/\sin\gamma}\frac{(T_w-T_v)}{1/h_{pc}+\dot{x}^2/2R_m k_l}\,d\dot{x}$$
$$=1.4(T_w-T_v)(h_{pc}k_l R_m)^{0.5}\left[\frac{\pi}{2}-\arctan\left(\frac{h_{pc}\delta_2}{k_l}\right)^{0.5}\right] \tag{36}$$

where h_{pc} is the phase-change heat transfer coefficient at the liquid-vapor interface for the intensive evaporation process:

$$h_{pc}=3.2\rho_v h_{fg}\sqrt{\frac{R_g}{T_v}} \tag{37}$$

where it has been assumed $\alpha=1$.

In Eqs. (35) and (36), δ_2 is the radius of the effective influence of surface tension forces. For water, $\delta_2\approx10^{-7}$ m (Solov'yev and Kovalev, 1984). The heat transfer coefficient of the wetted zone for a given cross section is:

$$h_{e,\text{men}}=\frac{\Delta Q_2+\Delta Q_{3a}+\Delta Q_{3b}}{T_w-T_v}\cdot\frac{\sin\gamma}{R_m\cos(\gamma+\theta)} \tag{38}$$

It should be mentioned that the third term in Eq. (38) is dominant. Then, for heat input from a hot fluid, taking the dry zone into account, it is possible to estimate the mean heat transfer coefficient in the evaporator as follows:

$$\bar{h}_e=\left(\left[\frac{2R_m}{B}\frac{\cos(\gamma+\theta)}{\sin\gamma}h_{e,\text{men}}\right]^{-1}+\frac{t_w}{k_w}\right)^{-1} \tag{39}$$

The effective wall temperature in the evaporator in Eqs. (34)–(38) is obtained in a manner similar to that in the condenser (Eq. (26)):

$$T_w=T_{ex,e}+(T_v-T_{ex,e})\frac{1}{h_{ex,e}}\left(\frac{1}{h_{ex,e}}+\frac{1}{\bar{h}_e}\right)^{-1} \tag{40}$$

When a heat input in the evaporator is given by $Q(z)$, the dry zone of the wall can be overheated (see Figs. 1 and 2(a)). To estimate the overheating, the thermal conductance equation is considered:

$$-k_w t_w\frac{d^2T}{ds^2}=\frac{1}{2N(B/2+t_w)}\frac{dQ}{dz} \tag{41}$$

where T is the mean cross-sectional wall temperature at each point on s. In deriving Eq. (41), it is assumed that the heat

flux on the wall at each point on z is constant. The boundary conditions are:

$$T|_{s=L_1} = T_w; \quad \left.\frac{dT}{ds}\right|_{s=0} = 0 \tag{42}$$

Solving Eq. (41), the overheat can be expressed as

$$\Delta T_{e,w} = T|_{s=0} - T|_{s=L_1} = \frac{L_1^2}{2N(B/2+t_w)k_w t_w}\frac{dQ}{dz} \tag{43}$$

Therefore, the maximum thermal resistance of the evaporator is:

$$r_e = \frac{T_{w,\max} - T_v}{Q_a} = \frac{1}{Q_a L_e N}\int_0^{L_e}\frac{dQ}{dz}\left[\frac{L_1^2}{2(B/2+t_w)k_w t_w} + \frac{1}{B\bar{h}_e}\right]dz \tag{44}$$

Liquid Flow in a Capillary Groove

The problem of liquid flow in triangular grooves (Eqs. (5) and (13)) was solved in dimensionless form by Ayyaswamy et al. (1974) and Khrustalev (1981). Ayyaswamy et al. (1974) neglected the effects of shear stresses at the liquid-vapor interface. Since the effects of shear stresses at a free liquid surface may be important for MHPs, the results of Khrustalev (1981) are used, where this two-dimensional boundary-value problem was solved by the Ritz method in terms of R functions. The solution gives the values of the dimensionless volume flux through a triangular groove, which is defined similar to that given by Kamotani (1976b):

$$V(\gamma, \theta, F) = \int\int_{S_l}\frac{w_l(x,y)\mu_l}{HW^3\left(\frac{dP_l}{dz} + \frac{\rho_l}{2S_l}\frac{d}{dz}(\overline{w}_l^2 S_l) + \rho_l g\sin\phi\right)}dx\,dy \tag{45}$$

where

$$F = -\frac{f_v\rho_v\overline{w}_v^2}{2W\left(\frac{dP_l}{dz} + \frac{\rho_l}{2S_l}\frac{d}{dz}(\overline{w}_l^2 S_l) + \rho_l g\sin\phi\right)} \tag{46}$$

The variable $1/V$ represents the hydraulic resistance of the groove. Then, using Eqs. (2) and (45), the pressure gradient can be defined as:

$$\frac{dP_l}{dz} + \frac{\rho_l}{2S_l}\frac{d}{dz}(\overline{w}_l^2 S_l) + \rho_l g\sin\phi = \frac{\mu_l\overline{w}_l S_l}{W^3 HV} \tag{47}$$

where

$$W = R_m\cos(\gamma+\theta), \quad H = W/\tan\gamma \tag{48}$$

and

$$S_l = R_m^2\left[\cos(\gamma+\theta)\left(\sin(\gamma+\theta) + \frac{\cos(\gamma+\theta)}{\tan\gamma}\right) - \left(\frac{\pi}{2} - \gamma - \theta\right)\right] \tag{49}$$

For $\gamma = 30$ deg and relatively small values of F, the results given by Khrustalev (1981) can be approximated as follows:

$$V(\theta, F) = (a_0 + a_1\theta + a_2\theta^2)e^F \tag{50}$$

where $a_0 = 0.0241$, $a_1 = 0.000905$, $a_2 = 8.75\times10^{-6}$, and θ is in arc degress. This approximation is in agreement with the results of Ayyaswamy et al. (1974) for $F = 0$.

Numerical Treatment

The four main variables dependent on z to be found are as follows:

$Y = R_m^{-1}$: curvature of the free surface of the meniscus,

$G = \overline{w}_l\rho_l S_l$: mass flow rate of liquid in one corner,

P_l: liquid pressure,

P_v: vapor pressure.

The following system of four ordinary differential equations were solved numerically using the fourth-order Runge-Kutta procedure:

$$\frac{dY}{dz} = \frac{1}{\sigma}\left(\frac{dP_v}{dz} - \frac{dP_l}{dz}\right) \tag{51}$$

$$\frac{dG}{dz} = \frac{B}{h_{fg}}h_{ex,i}(T_{ex,i} - T_v)\left(1 + \frac{h_{ex,i}}{\bar{h}_i}\right)^{-1}, \quad i = e, c, a \tag{52}$$

or for a given heat-load function $Q(z)$

$$\frac{dG}{dz} = \frac{1}{h_{fg}N}\frac{dQ(z)}{dz} \tag{53}$$

$$\frac{dP_l}{dz} = \frac{\mu_l G}{W^3 HV\rho_l} - \rho_l g\sin\phi - \frac{1}{2S_l\rho_l}\frac{d}{dz}\left(\frac{G^2}{S_l}\right) \tag{54}$$

$$\frac{dP_v}{dz} = -\frac{d}{dz}\left(\beta_v\frac{N^2G^2}{S_v^2\rho_v}\right) - f_v\frac{2}{D_{h,v}}\frac{N^2G^2}{S_v^2\rho_v} - \rho_v g\sin\phi \tag{55}$$

The boundary conditions at $z = 0$ are:

$$Y = R_{m0}^{-1}, \quad G = 0, \quad P_v = P_{v0}, \quad P_l = P_{v0} - \frac{\sigma}{R_{m0}} \tag{56}$$

The following expressions were also used: Eqs. (3), (10), (18)-(27), (34)-(40), (44), (46), (48), (49), and (50).

For the case of a known heat load, it is convenient to use the approximation for the vapor pressure distribution given by Faghri (1989), instead of numerically solving Eq. (55):

$$P = P_{v,0} + \rho_v\left[-8\left|\frac{\mathrm{Re}_r}{2}\right| - \frac{16}{3}\left|\frac{\mathrm{Re}_r}{2}\right|^2\right]\left(\frac{4z\nu_v}{D_{h,v}^2}\right)^2, \quad 0 \le z \le L_e \tag{57}$$

$$P = P_{0,a} + \rho_v\overline{w}_{v,a}\left(-\frac{32(z-L_e)\nu_v}{D_{h,v}^2}\right), \quad L_e \le z \le L_e + L_a \tag{58}$$

$$P = P_{0,c} + 8\rho_v\overline{w}_{v,a}^2 \times\left(1 - \frac{2}{3}\left|\frac{\mathrm{Re}_r}{2}\right|\right)\left(\left|\frac{\mathrm{Re}_r}{2}\right|\right)\left[\frac{4(z-L_e-L_a)\nu_v}{\overline{w}_{v,a}D_{h,v}^2}\right]^2 - 8\rho_v\overline{w}_{v,a}^2\left(1 - \frac{2}{3}\left|\frac{\mathrm{Re}_r}{2}\right|\right)\left[\frac{4(z-L_e-L_a)\nu_v}{\overline{w}_{v,a}D_{h,v}^2}\right], \quad L_e + L_a \le z \le L_t - L_b \tag{59}$$

where $P_{0,a}$ and $P_{0,c}$ are the values of the pressure at the inlets of the adiabatic and condenser zones, respectively. The agreement of the results of the numerical solution of Eq. (55) and Eqs. (57)-(59) is within several percent of the total vapor pressure drop for the given MHP parameters.

An iterative procedure was used to obtain the maximum heat transfer capacity, $Q_{\max}$, and the overall thermal resistance, r_t, of a MHP. The overall thermal resistance is:

$$r_t = r_e + r_c + r_v \tag{60}$$

where r_v is the thermal resistance of the vapor flow, which is defined as

$$r_v = \frac{1}{Q_a}\left[\frac{1}{L_e}\int_0^{L_e}T_v dz - \frac{1}{L_c - L_b}\int_{L_e+L_a}^{L_t-L_b}T_v dz\right] \tag{61}$$

The mass of circulating fluid, $M_l = M_t - M_b$, which represents the right-hand side of Eq. (3) minus M_b, and the meniscus radius $R_m = Y^{-1}$ are obtained as functions of several parameters:

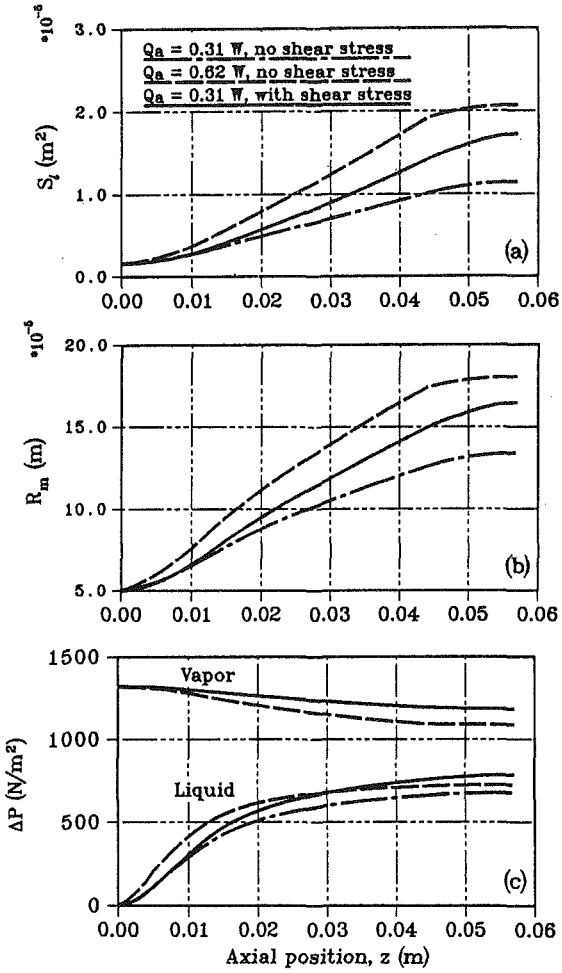

Fig. 4 Comparison of the performance of the micro heat pipe with and without shear stress at the vapor-liquid interface for the case of no excess liquid in the MHP ($\theta_0 = 10$ deg): (*a*) liquid cross-sectional area; (*b*) radius of curvature of the meniscus; (c) pressure variation

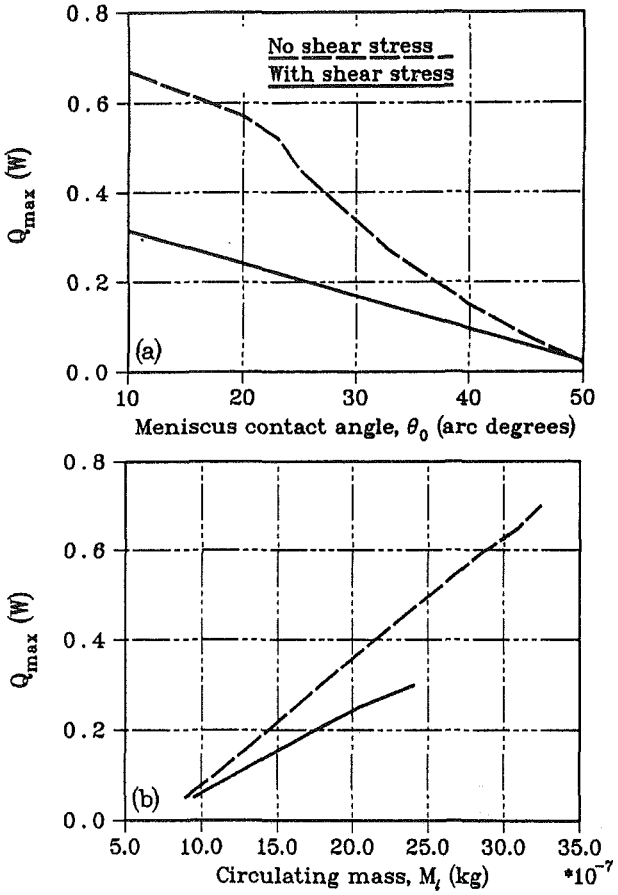

Fig. 5 Dependence of the maximum heat transfer on: (*a*) meniscus contact angle at the evaporator end cap; (*b*) mass of circulating liquid in the case of insufficient liquid fill ($\theta_0 = 10$ deg, $R_{m0} \simeq 50$ μm)

$$M_l = M_l(R_{m0},\ Q_a,\ \theta,\ T_v,\ \phi,\ \ldots) \tag{62}$$

$$R_m = R_m(z,\ R_{m0},\ Q_a,\ \theta,\ T_v,\ \phi,\ \ldots) \tag{63}$$

Analyzing these functions and taking into account Eq. (3), some conclusions concerning r_l, L_b, and Q_{max} can be made. For the distribution of the liquid in an MHP, it is logical to assume that, at the maximum heat load ($Q_a = Q_{max}$), R_{m0} has the smallest value possible, provided that Eqs. (51)-(55) can still be solved successfully and Eq. (3) is satisfied. It should be noted that the variation of the maximum heat transport due to decreasing R_{m0} is very small when $R_{m0} < 0.1 D_{h,v}$. The exact value of $R_{m,min}$, which is different for each MHP design, can be obtained by comparison of the predicted and experimental results for Q_{max} for MHP operation against gravity. To obtain the value for L_b and r, an iterative procedure is used, varying the effective condenser length and R_{m0}.

The numerical results for the maximum heat transfer capacity Q_{max} are obtained with the following procedure:

1 For a definite small R_{m0} and Q_a', the system of Eqs. (51)-(55) is solved, and the obtained values of M_l and $R_m(L_t)$ are analyzed. If $M_l \ll M_t$ and $R_m(L_t) < R_{m,max}$, liquid may be blocking part of the condenser. Therefore, the length of the liquid blocking zone L_b is estimated and the new effective condenser length $L_c' = L_c - L_b$ is set.

2 The value of the total heat load is increased, $Q_a'' = Q_a' + \Delta Q_a$, and step 1 is repeated unitl $R_m(L_t) \simeq R_{m,max}$, and the variation of the meniscus contact angle θ occurs near the beginning of the blocking zone. This total heat load is Q_{max}.

3 The validity of Q_{max} is checked by decreasing R_{m0}'. If no change occurs, go to step 4. Otherwise, repeat steps 1 and 2.

4 If there is a lack of liquid in the MHP and $M_l = M_t$ is obtained in the first two steps for $R_m(L_t) < R_{m,max}$, the corresponding maximum value of Q_a is considered to be Q_{max}, provided that decreasing R_{m0} has no effect on the results.

Results and Discussion

To verify the numerical results obtained, the experimental data provided by Wu and Peterson (1991) were used. Therefore, the presented results refer to an MHP with the following characteristics: $L_e = 0.013$ m, $L_a = 0.031$ m, $L_c = 0.013$ m, $B = 0.0007$ m, $\gamma = 30$ deg, $\phi = 0$, $M_t = 0.0032$ g, $N = 4$, $t_w = 0.00019$ m, $\alpha = 1$. The working fluid was water, and two containers, made of copper and silver, were examined. The axial heat distribution, $Q(z)$, was specified as:

$$Q = \begin{cases} Q_a z/L_e, & 0 \le z \le L_e \\ Q_a, & L_e < z < L_e + L_a \\ Q_a\left(1 + \dfrac{L_e + L_a - z}{L_c - L_b}\right), & L_e + L_a \le z \le L_t - L_b \end{cases} \tag{64}$$

and Eq. (53), instead of Eq. (52), was used in the numerical procedure.

Most of the results of the present analysis are for heat loads close to the performance limitations. The data in Figs. 4, 5, and 7-9 were obtained for a vapor temperature at the evaporator end cap of $T_{v0} = 60°C$. The hydrodynamic performance

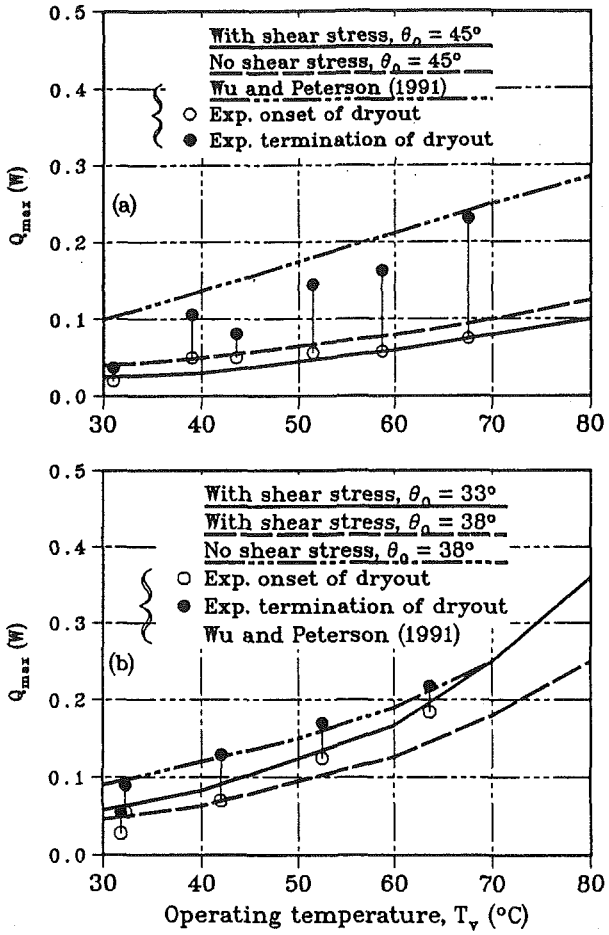

Fig. 6 Maximum heat transfer versus operating temperature: (*a*) copper-water MHP; (*b*) silver-water MHP

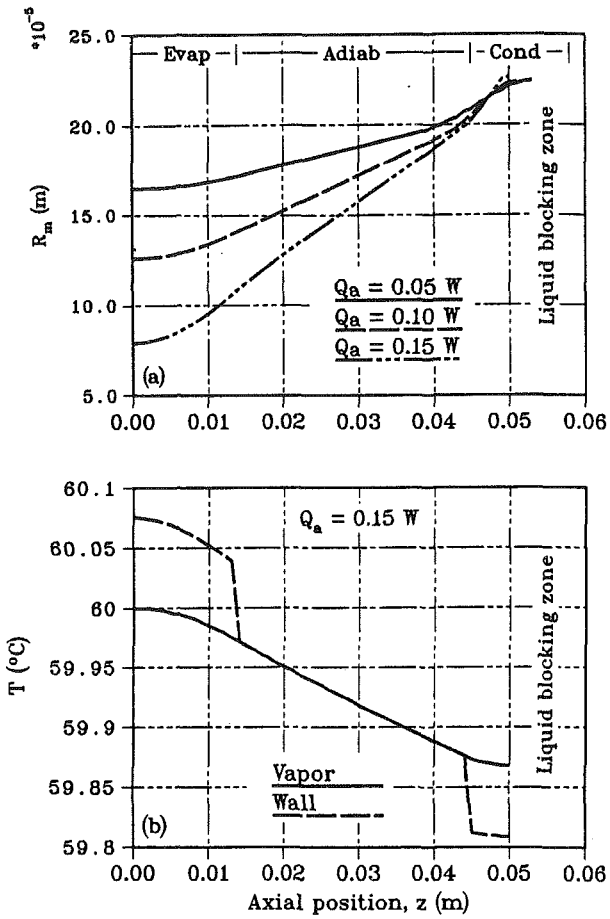

Fig. 7 Performance characteristics of the copper-water MHP: (*a*) radius of the liquid surface curvature; (*b*) temperature distribution

characteristics of the MHP with no excess liquid is shown in Fig. 4. Dashed lines correspond to the case of neglecting shear stresses in the liquid at the liquid–vapor interface, and solid lines refer to the case of including the effects of shear stresses (in both cases the vapor pressure is the same). One of the distinguishing features of a MHP is the variable liquid cross-sectional area along the axis. As seen in Fig. 4(*a*) for $\theta_0 = 10$ deg, S_l increased by more than ten times along the length of the MHP, while the radius of the meniscus, R_m, changed by only four times, as shown in Fig. 4(*b*). For an inclination angle of $\phi = 0$, the meniscus curvature decreased monotonically along the z direction. The pressure drop in the liquid was several times higher than that of the vapor, which is illustrated in Fig. 4(*c*). The liquid pressure increased drastically in the evaporator, where the cross-sectional area of the liquid was small. Thus, extending the cross-sectional area of the liquid, due to the decrease of that of the vapor, may increase the maximum heat transfer capacity of the MHP. The results in Fig. 4 are given to show some basic information concerning the hydrodynamic characteristics of the MHP when the radius of curvature R_{m0} is held constant at 50 μm. It should be noted that, in this example, the mass of liquid within the heat pipe is not fixed, but the value of R_{m0} was the same for all curves, which gave the opportunity to show the influence of the vapor-liquid interaction on the hydraulic MHP characteristics more clearly.

The influence of the liquid charge on Q_{max} in the case when there is a lack of liquid in the MHP is illustrated in Fig. 5 ($\theta_0 = 10$ deg). For the MHP considered, this situation only occurs in the absence of shear stress at the free liquid surface and for small θ_0. The minimum contact angle, θ_0, has a significant influence on the performance of the MHP, especially

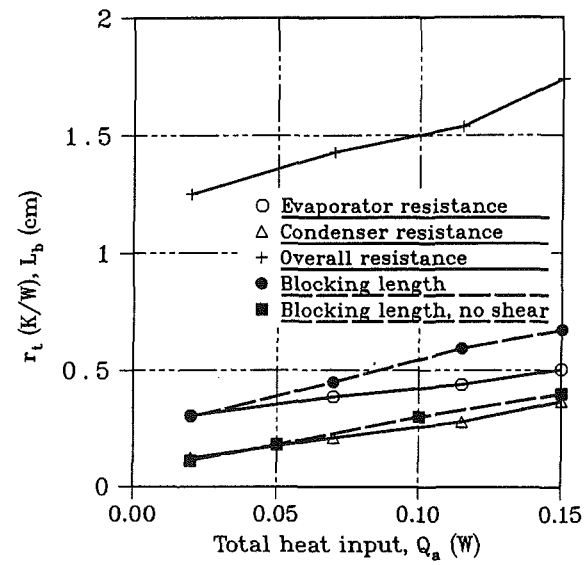

Fig. 8 Influence of total heat input on the thermal resistance and liquid blocking length (copper-water MHP)

on the maximum heat transfer capacity, as shown in Fig. 5 for small liquid charges. According to Stepanov et al. (1977), $\theta_0 = 33$ deg for copper-water and 38 deg for silver-water pairs, and Wu and Peterson (1991) gave these values to be 55 and 45 deg, respectively.

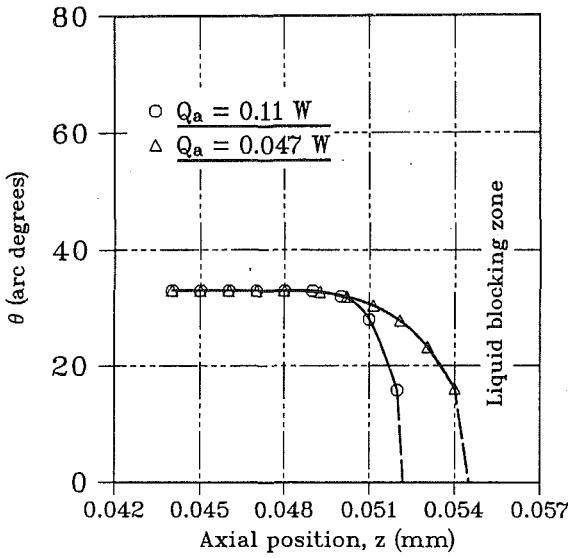

Fig. 9 Variation of the contact angle in the condenser

The comparison of the numerical results and the experimental data reported by Wu and Peterson (1991) for the maximum heat transfer capacity are shown in Fig. 6 for MHPs with copper and silver casings. While the data for the minimum contact angles are contradictory and can be influenced by many physical factors, the numerical results are presented for $\theta_0 = 33$, 38 and 45 deg. The agreement between the experimental results of the onset of dryout and the present numerical prediction is good. Neglecting the shear stress at the free surface of the liquid due to vapor/liquid frictional interaction ("no shear stress" in Figs. 6 and 8) can lead to an overestimation of the maximum heat transfer capacity. The shear stress at the free liquid surface influences the liquid distribution along the heat pipe, which can result in an increase of the liquid blocking of the condenser end in comparison with the case of neglecting this shear stress. The liquid distribution in an MHP is affected by the heat load, as shown in Fig. 7(*a*) ($\theta_0 = 33$ deg). The liquid distribution and the heat load determine the temperature variation along a heat pipe (Fig. 7(*b*)).

As seen in Fig. 8 ($\theta_0 = 33$ deg), the overall thermal resistance of the MHP is summarized by three terms: r_e, r_c, r_v, which must be taken into consideration, although the resistance of the vapor flow is the greatest for the conditions studied. It should be noted that according to experimental data by Wu and Peterson (1991), the thermal resistance of the MHP that was not charged with working fluid (empty tube) was approximately 150 K/W.

The variation of the meniscus contact angle in the condenser is shown in Fig. 9. In this region, where progressive variation of the contact angle occurred, the liquid cross-sectional height H increased sharply. Therefore, the second radius of curvature of the liquid surface, R_2, becomes significant in this region. In the present paper, its influence on the distribution of liquid along the MHP was neglected for all zones. However, to complete the physical model, it can be assumed that the free surface of the liquid blocking zone has a curvature with a main radius of R_b, which should be estimated as:

$$\frac{2}{R_b} = \left(\frac{1}{R_2} + \frac{1}{R_m}\right)_{z=L_t-L_b} \tag{65}$$

From the results of the MHP mathematical model, a new flat MHP configuration with an increased liquid cross-sectional area for electronic cooling applications is proposed, as shown in Fig. 10. Due to surface tension forces, liquid is contained in the narrow passages separating the vapor spaces,

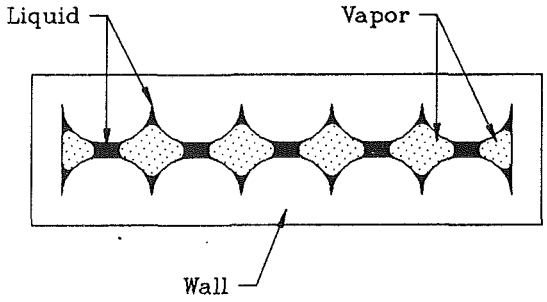

Fig. 10 New configuration cross section of a flat MHP

and is also distributed along the flat heat-loaded walls. The advantages of this configuration are an increase in the maximum heat transfer capacity and a lower manufacturing price in compared to several MHPs investigated by Wu and Peterson (1991).

Conclusions

The numerical results of the mathematical model describing the fluid flow and heat transfer within a micro heat pipe are summarized as follows:

1 Shear stresses in the liquid at the liquid–vapor interface due to frictional interaction significantly influenced the maximum heat transfer capacity.

2 Accounting for shear stresses at the liquid free surface increased the length of the liquid blocking zone in the condenser.

3 The dynamic component of the pressure gradient in the liquid had no pronounced effect on the performance characteristics of the MHP.

4 For nearly maximum heat loads, the largest portion of the liquid pressure drop occurred in the evaporator and the beginning of the adiabatic section, where the liquid cross-sectional area was several times smaller than that in the condenser.

5 The dominant thermal resistances within the MHP were those of the vapor flow and the liquid film in the evaporator and condenser.

6 The amount of working fluid and the minimum wetting contact angle strongly influenced the performance characteristics of the MHP.

7 The variation of the meniscus contact angle in the condenser occurred near the liquid blocking zone.

References

Ayyaswamy, P. S., Catton, I., and Edwards, D. K., 1974, "Capillary Flow in Triangular Grooves," ASME *Journal of Applied Mechanics*, Vol. 41, No. 2, pp. 332–336.

Bankston, C. A., and Smith, H. I., 1971, "Incompressible Laminar Flow in Cylindrical Heat Pipes," ASME Paper No. 71-WA/HT-15.

Bowman, W. J., and Hitchcock, J. E., 1988, "Transient, Compressible Heat-Pipe Vapor Dynamics," *Proc. ASME National Heat Transfer Conf.*, Houston, TX, Vol. 1, pp. 329–338.

Cao, Y., and Faghri, A., 1993, "Micro/Miniature Heat Pipes and Operating Limitations," *Proc. ASME National Heat Transfer Conf.*, Atlanta, GA, Vol. 236, pp. 55–62.

Carey, V. P., 1992, *Liquid-Vapor Phase-Change Phenomena: An Introduction to the Thermophysics of Vaporization and Condensation Processes in Heat Transfer Equipment*, Hemisphere, New York, p. 645.

Cotter, T. P., 1984, "Principles and Prospects for Micro Heat Pipes," *Proc. 5th Int. Heat Pipe Conf.*, Tsukuba, Japan, pp. 328–335.

Derjaguin, B. V., 1955, "Definition of the Concept of and Magnitude of the Disjoining Pressure and Its Role in the Statics and Kinetics of Thin Layers of Liquid," *Kolloidny Zhurnal*, Vol. 17, pp. 191–197.

Faghri, A., 1989, "Performance Characteristics of a Concentric Annular Heat Pipe: Part II—Vapor Flow Analysis," ASME JOURNAL OF HEAT TRANSFER, Vol. 111, pp. 851–857.

Holm, F. W., and Goplen, S. P., 1979, "Heat Transfer in the Meniscus Thin-Film Transition Region," ASME JOURNAL OF HEAT TRANSFER, Vol. 101, No. 3, pp. 543–547.

Jang, J. H., Faghri, A., and Chang, W. S., 1991, "Analysis of the Transient Compressible Vapor Flow in Heat Pipes," *Int. J. Heat Mass Transfer*, Vol. 34, pp. 2029–2037.

Kamotani, Y., 1976a, "Analysis of Axially Grooved Heat Pipe Condensers," AIAA Paper No. 76–147.

Kamotani, Y., 1976b, "Thermal Analysis of Axially Grooved Heat Pipes," *Proc. 2nd Int. Heat Pipe Conf.*, Bologna, Italy, pp. 83–91.

Khrustalev, D. K., 1981, "Liquid Flow Through Capillary Grooves With Shear Stresses on a Free Surface," in: *Heat and Mass Transfer in Porous-Element Systems*, HMTI, Minsk, pp. 51–56.

Longtin, J. P., Badran, B., and Gerner, F. M., 1992, "A One-Dimensional Model of a Micro Heat Pipe During Steady-State Operation," *Proc. 8th Int. Heat Pipe Conf.*, Beijing, China, Preprints, pp. C-5-1 to C-5-7.

Potash, M., Jr., and Wayner, P. C., Jr., 1972, "Evaporation From a Two-Dimensional Extended Meniscus," *Int. J. Heat Mass Transfer*, Vol. 15, pp. 1851–1863.

Solov'yev, S. L., and Kovalev, S. A., 1984, "Mechanism of Evaporation of a Liquid From a Porous Surface," *Proc. 5th Int. Heat Pipe Conf.*, Tsukuba, Japan, Preprints Vol. II, pp. 77–82.

Stephan, P. C., and Busse, C. A., 1992, "Analysis of the Heat Transfer Coefficient of Grooved Heat Pipe Evaporator Walls," *Int. J. Heat Mass Transfer*, Vol. 35, No. 2, pp. 383–391.

Stepanov, V. G., Volyak, L. D., and Tarlakov, Yu, V., 1977, "Wetting Contact Angles for Some Systems," *J. Engineering Physics*, Vol. 32, No. 6, pp. 1000–1003.

Wu, D., and Peterson, G. P., 1991, "Investigation of the Transient Characteristics of a Micro Heat Pipe," *J. Thermophysics*, Vol. 5, No. 2, pp. 129–134.

Experimental Study of the Convective Cooling of a Heated Continuously Moving Material

B. H. Kang[1]

J. Yoo[2]

Y. Jaluria

Department of Mechanical and Aerospace Engineering, Rutgers University, New Brunswick, NJ 08903

An experimental investigation of the heat transfer associated with a continuously moving material has been carried out. This thermal transport circumstance is encountered in many manufacturing processes, such as hot rolling, fiber drawing, plastic extrusion, crystal growing, and continuous casting. The transport associated with a heated plate or a cylindrical rod being cooled due to its own movement at uniform velocity in a stationary extensive fluid is considered. Very little experimental work has been done on this problem and this study focuses on the resulting thermal fields. Time-dependent temperature distributions in the solid, as well as in the flow, are measured for the material moving vertically downward in water and moving vertically upward or downward in air. The effects of thermal buoyancy, material speed, and properties of the material and the fluid on the thermal field are studied. The results indicate that the temperature profiles obtained are similar to those obtained in earlier numerical and analytical studies. At low material speeds, the upstream penetration of the conductive transport due to temperature variation in the material was seen to be substantial. This effect decreased with an increase in the material speed. The thermal boundary layer is found to be thicker in air than in water, as expected. The effect of thermal buoyancy on the temperature distributions in air was found to be very significant. High-thermal-conductivity materials, such as aluminum, are cooled down more rapidly than low-conductivity materials, such as teflon. The experimental results obtained lead to a better understanding of the underlying transport mechanisms and add to the data base needed for the design and optimization of the relevant systems.

Introduction

A problem of considerable practical and fundamental interest is that of the thermal transport associated with continuously moving materials, which lose energy by convection and radiation at the surface to the ambient medium. This circumstance is of importance in a wide variety of manufacturing processes such as hot rolling, plastic extrusion, metal forming, glass fiber drawing, and wire drawing processes; see, for instance, Tadmor and Klein (1970), Fisher (1976), and Altan et al. (1979). In many cases, the ambient fluid, far from the moving material, is stationary, with the fluid flow being induced by thermal buoyancy and by the motion of the solid material undergoing thermal processing. Therefore, the resulting flow and thermal fields are determined by these two mechanisms, buoyancy and surface motion.

The essential features of the flow induced by a long, continuously moving flat plate or a cylindrical rod are shown schematically in Fig. 1. The material moves out of the slot in an extrusion die or between a set of rollers, and proceeds at constant speed U_s through an otherwise quiescent ambient medium. Due to the viscous drag exerted on the ambient fluid by the surface of the material, a flow is induced in the fluid. The material, if it is warmer than the fluid, also loses heat to the fluid. The flow may often be considered as two dimensional for a wide plate and as axisymmetric for the cylindrical case. There are several important considerations in this process that need a detailed investigation. These include the effects of the conjugate conditions at the surface, of thermal buoyancy, of the initial transient variation toward a steady-state circumstance, and of the geometry on the resulting thermal field and on the heat transfer rate. The dependence of the thermal field on the physical variables of the process, such as speed of the material and the fluid used, is important in determining, for instance, if the transport rate is adequate for cooling to a given temperature level over the available distance, or if an additional heat transfer mechanism, such as spray cooling, is necessary.

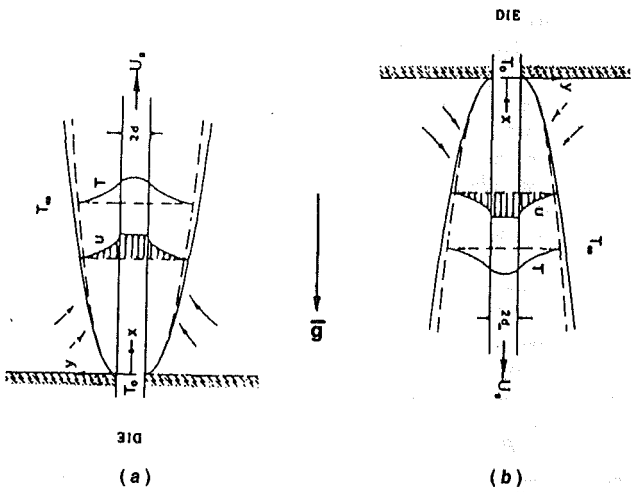

Fig. 1 Schematic of the velocity and temperature profiles in the conjugate problem for a continuously moving plate in a quiescent ambient medium, along with the coordinate system

[1]Present address: Air Conditioning and Environmental Control Laboratory, Korea Institute of Science and Technology, Cheongryang, Seoul, Korea.

[2]Present address: Department of Mechanical Engineering, Ajou University, Suwon, Korea.

Contributed by the Heat Transfer Division for publication in the JOURNAL OF HEAT TRANSFER. Manuscript received by the Heat Transfer Division June 1992; revision received May 1993. Keywords: Conjugate Heat Transfer, Materials Processing and Manufacturing Processes, Mixed Convection. Associate Technical Editor: T. W. Simon.

Buoyancy forces could also substantially affect the flow field and, thus, the local surface heat transfer rate. This could, in turn, result in a substantial effect on the local thermal field. The transient effects are particularly important at the start of the process and, thus, determine the amount of material that may undergo unsatisfactory thermal processing.

The resulting flow was approximated as a boundary layer by Sakiadis (1961) who obtained a numerical solution for the flow field, using a similarity transformation. The velocity boundary layer was found to grow in the direction of the motion of the flat plate or of the cylindrical rod. Tsou et al. (1967) showed experimentally that such a flow indeed arises and studied its basic characteristics. There are a few other studies that have considered the cooling of glass or polymer fibers by convection; see, for instance, Glicksman (1968), Chen and Strobel (1980), and Moutsoglou and Chen (1980). They have considered the effects of thermal buoyancy in the case of a continuously moving flat sheet. The sheet was assumed to be isothermal or a uniform heat flux condition was applied at the surface. However, in actual practice, the thickness of the moving plate is finite. The temperature distribution within the material can be important from the viewpoint of microstructure within the solid as well as of thermal stresses that are introduced in the material.

The conjugate convection and conduction problem with a moving plate of finite thickness has also been considered. Chida and Katto (1976) computed the flow and temperature fields for a plate of finite thickness, employing boundary layer approximations. Ignoring the effects of buoyancy, they obtained the downstream temperature variation at high values of the Peclet number, Pe. In this work, heat transfer within the solid was included. However, axial conduction, in the direction of material motion, was neglected. Recently, Karwe and Jularia (1988, 1991) and Kang and Jaluria (1990, 1992) have numerically studied the heat transfer from a plate of finite thickness moving in a quiescent, isothermal, ambient medium or in a uniform forced flow.

From the above review of the literature, it is seen that mixed convection heat transfer from a continuous moving surface has been studied only for the steady-state conditions and little attention has been given to the transient process in such problems. Jaluria and Singh (1983), in a numerical study, obtained the transient temperature distribution in a moving plate and a circular rod with an assumed convective heat transfer coefficient h at the surface. They also presented some results on the length required to bring the temperature of the moving material to a desired level. Khader (1981) solved the transient momentum and energy boundary layer equations for a moving vertical plate,using an explicit finite difference scheme. In his study, the plate was assumed to be isothermal and conduction effects in the plate were neglected. Poulos and Chung (1983) analytically investigated the transient conjugate heat transfer problem for a stationary plate of finite thickness in an incoming, incompressible flow. In this case, the flow distribution in the fluid is quite different from that for a plate moving in a stationary medium. Thus, the resulting transport mechanisms are affected by this difference in the flow circumstance. Kang et al. (1991) studied, numerically, the transient transport from a heated plate of finite thickness moving in a quiescent fluid. In this study, a long plate was assumed, neglecting the leading edge effects.

Not much attention has been given to the experimental study of this problem because of the complications involved with a moving surface. Tsou et al. (1967) studied the boundary layer on a continuous moving surface, using a rotating drum. Heated flat belts moving in water were employed by Chida and Katto (1976). Velocity and temperature data were obtained. Karwe and Jaluria (1992) carried out an experimental study on the thermal transport from a heated moving aluminum plate, using air and water as the quiescent ambient fluids. This study focused on the temporal behavior and obtained data for a highly conducting material, for which the temperature may be taken as uniform across the thickness. The temperature profiles in the fluid and across the solid were not investigated in any detail. Also, only a flat plate, which simulates a two-dimensional circumstance, was considered. Thus, this was a preliminary study on which the present work is based.

Clearly, there is a strong need to obtain experimental data on this problem for a variety of materials, fluids, operating conditions, and configurations. The present study is directed at the thermal transport processes associated with a continuously moving flat plate or cylindrical rod, considering different materials. The material was heated to a uniform temperature and then moved at a uniform speed into the ambient fluid, which was either water or air. The experiments investigated vertical, upward and downward, motion in air and vertical downward motion in water. The vertical upward movement results in thermal buoyancy effects aiding the flow and the

Nomenclature

B = physical properties parameter $= (\rho Ck)_f/(\rho Ck)_s$
C = specific heat of solid or fluid at constant pressure
d = half thickness of the moving flat plate
g = magnitude of gravitational acceleration
Gr = Grashof number $= g\beta(T_o - T_\infty)d^3/\nu^2$ or $g\beta(T_o - T_\infty)R_o^3/\nu^2$
h = surface convective heat transfer coefficient
$\bar{h}$ = average convective heat transfer coefficient
k = thermal conductivity
Nu = local Nusselt number $= hd/k_f$ or hR_o/k_f
$\overline{\text{Nu}}$ = average Nusselt number $= hd/k_f$ or hR_o/k_f
Pe = Peclet number $= U_s d/\alpha_s$ or $U_s R_o/\alpha_s$
Pr = Prandtl number $= \nu/\alpha_f$
r = radial coordinate distance in cylindrical configuration
R = dimensionless coordinate in radial direction in cylindrical configuration $= r/R_o$
R_o = radius of the cylindrical rod
Re = Reynolds number $= U_s d/\nu$ or $U_s R_o/\nu$
t = physical time
T = local physical temperature
T_o = initial temperature of the heated material
U_s = speed of the moving material
x = coordinate distance along the length of the plate
X = dimensionless coordinate distance along the length of the plate or cylinder x/d or x/R_o
y = coordinate distance, normal to the plate surface
Y = dimensionless coordinate distance, normal to the plate surface $= y/d$
α = thermal diffusivity
β = coefficient of thermal expansion of the fluid
θ = dimensionless local temperature $= (T - T_\infty)/(T_o - T_\infty)$
ν = kinematic viscosity of the fluid
ξ = dimensionless coordinate distance in the direction of material motion $= x(\rho Ck)_f/(U_s d^2 \rho_s^2 C_s^2)$
ρ = density
τ = dimensionless time

Subscripts

∞ = ambient medium
f = fluid
s = solid material, i.e., plate or cylindrical rod

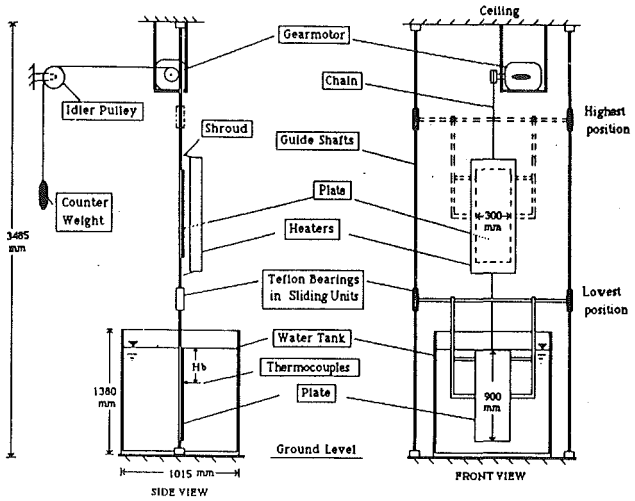

Fig. 2 Schematic diagram of the experimental arrangement

downward movement opposing it. The axial and transverse temperature variations within the plate and the transverse temperature variation within the fluid were measured. The effects of thermal buoyancy, material speed, and properties of the material and fluid on the thermal fields were studied. The results obtained add to the understanding of the underlying physical processes and also provide inputs that may be used for validation of existing mathematical and numerical models and for the design and optimization of the relevant system.

Experimental System

Experiments are carried out to investigate the temperature field in the solid and in the flow when a plate or a cylindrical rod moves through an otherwise quiescent fluid medium. The material chosen is aluminum or teflon and the fluid medium is taken as water or air. The schematic diagram of the experimental arrangement is shown in Fig. 2, with a flat plate as the moving material. For experiments on a moving cylindrical rod, the moving plate and the flat heating unit in the experimental arrangement of Fig. 2 are replaced by the cylindrical rod and a hollow cylindrical-shaped heating unit. The system consists of the solid material under study, the material traversing mechanism, fluid tank, heating unit, thermocouple rake, and the data acquisition system. A wide flat plate is used for approximating a two-dimensional circumstance and a cylindrical rod for an axisymmetric one. The flat plate was 0.9 m long, 0.3 m wide,and 5 mm thick. Cylindrical rods, of diameter 25.4 mm and 6 mm and 1 m length, were used. In both cases, a sharp leading edge is employed to minimize the disturbance as the material enters the water. No splashing or separation bubble was found to arise because of the geometry of the leading edge and the low speeds employed here.

The temperature distribution inside the material and at the surface were measured by means of 11 thermocouples (copper-constantan, 0.025 mm wire diameter) located along the centerline of the material, 11 thermocouples positioned at the surface of the material, and 4 thermocouples located midway between the centerline and the surface of the material. Special surface thermocouples supplied by Omega were attached to the surface for temperature measurements there and embedded thermocouples were used for other locations. To avoid disturbance due to the embedded thermocouples, these were inserted from the back of the flow region where measurements are taken. Several holes, 1 mm in diameter and 3 mm deep, were made at chosen intervals along the plate length. For the cylindrical rod (25.4 mm diameter), holes were made with 6.35 mm depth for the midway location and 12.7 mm depth for the centerline. Each cavity was filled with Omegabond 200 high-temperature, high-thermal-conductivity epoxy. A thermocouple was then inserted in each hole, along with a small ceramic tube just behind the thermocouple bead. This allowed local temperature measurements within the solid material. A simple analysis for the thermocouple junction energy balance indicated an accuracy of better than about 0.25°C with a spatial resolution of around 0.5 mm. For further details on the temperature measurements, see Karwe (1987) and Kang (1990).

The moving plate or the cylindrical rod was mounted on an aluminum frame, as shown in Fig. 2. Aluminum channels of dimensions 18.75 × 18.75 × 3.125 mm were used for the vertical portions of the frame, in order to increase its rigidity. Sliding units, which could be traversed up and down two guide shafts, were then attached to the frame. Each sliding unit contained two Teflon bushings, one at the top and the other at the bottom. The guide shafts were mounted parallel, at a distance 1.5 m apart, on the top and the bottom steel plates, which were then bolted to the ceiling and the ground, respectively. The sliding unit had to be made long enough to prevent caulking between the bearings and the shafts when the entire assembly is moved upward or downward. The entire material and frame assembly could be moved upward and downward with the help of the gear-motor, chain, and counterweight arrangement shown in Fig. 2. The motor could be adjusted to desired values of speed and torque with a controller. The downward motion of the material was driven by gravity. To prevent acceleration under gravity, the motor was set to a fixed speed and the counterweight was adjusted to almost equal the weight of the moving assembly. In the absence of the counterweight, the weight of the material assembly was enough to cause the downward motion of the material even when the motor was turned off. At a fixed rpm of the gear-motor,the time required to establish a constant speed of the material was of the order of a second, starting from the position of rest.

The heating unit consisted of 4 flat or hollow, cylindrical-shaped, Nichrome coil heaters embedded in ceramic. These heaters were mounted on a frame suspended from the ceiling. The vertical location of the heaters could be adjusted by raising or lowering the frame. Usually, the location was adjusted so as to heat the material when it was at its topmost position. The gap between the material surface and the heaters was about 60 mm for the plate and about 40 mm for the cylinder rod. Therefore, the plate or rod was heated by radiation and convection from the heaters. The output of each heater was controlled through a variable transformer. In addition, one of the heaters was controlled by a thermostat, which could be set to a desired temperature level. When the plate or the cylinder was being heated, both the material and the heaters were enclosed in a shroud of aluminum foil. This reduced the radiation losses and formed an enclosure. The setting of the controllers and the variable transformers had to be adjusted by trial and error to achieve the required final material temperature. During heating, the temperature distribution in the material was monitored through a data acquisition system, which is described later. The final temperature distribution within the material was fairly uniform, with a maximum deviation of about ±1°C.

The fluid tank was made of 9.5-mm-thick plexiglass. The tank cross section was 1 m × 1 m and the height was 1.3 m. It could hold up to 1365 liters (360 gallons) of water. The tank was also suitable for experiments in air since ambient disturbances were reduced in the tank. For air, $x = 0$ is taken at the exit from the heating unit, where x is the vertical coordinate distance. For water, $x = 0$ represents the location of the water surface. For this latter circumstance, the cooling in air was found to be negligible as compared to that in water. The dimensions of the tank were chosen so as to simulate the conditions of a quiescent ambient medium. The width of the tank was large enough to neglect any boundary effects. The plexiglass walls of the tank were supported by a strong steel frame

made of angle irons. A polyurethane adhesive sealant was used to seal the tank at the corners. The temperature distribution within the flow induced in the fluid by the motion of the moving material was measured by means of a thermocouple arrangement. The arrangement was designed to measure the temperature distribution across the flow without significantly disturbing the flow. This was achieved by avoiding placement of the thermocouple functions across the flow at the same transverse or circumferential location. The underlying assumption in using such an arrangement is, of course, that the induced flow field is two dimensional or axisymmetric. This was confirmed to be the case in the present system by measurements along the third direction.

The major task of the data acquisition system was to measure the output from the 26 thermocouples inside the material and at its surface and from the 5 thermocouples in the thermocouple rake for the temperature measurement in the fluid. All 31 output values had to be read within a very short period of time to get an almost instantaneous variation of temperature within the material and in the flow field. This required small sampling times, which were of the order of 10^{-4} s. In order to reduce the noise level in the signal obtained from the thermocouples, a grounding cable was immersed in the water and connected to the moving material. This reduced the noise level substantially for experiments with water as the fluid. The thermocouple signals were measured by means of an Apple microcomputer-based data acquisition system (Keithley Series 500 measurement and control system). Additional quantities that were measured were the time elapsed between the instant at which the material starts moving and the instant when the tip of the material enters the water at the surface. The depth of thermocouples below the water surface and the instantaneous location of the moving material were also measured. The material speed, U_s, can, thus, be obtained. The data processing and graphics were done on a Sun computer system; see Karwe and Jaluria (1992).

Therefore, it is seen that considerable care had to be taken to ensure accurate and repeatable measurements. Repeatability of the temperature data was found to be very high, being within 5–6 percent for different experimental runs with chosen operating conditions. Similarly, the errors in the temperature measurements were estimated to be less than 7.5 percent of the values reported here, usually being only a few percent in error for most of the data. The inaccuracies in °C were given earlier. Errors in other measurements such as speed U_s and location (x, y) were also considered and estimated to be within 5–10 percent, indicating the overall accuracy of the results presented in this paper. The next section presents the typical results and trends obtained in this investigation.

Experimental Results and Discussion

Plate Moving in a Quiescent Ambient Medium. The experiments are conducted with teflon or aluminum as the plate material and with either water or air as the ambient fluid. With water, only the opposing flow situation, in which the heated plate moves vertically downward into water, could be studied experimentally, because of the constraints imposed by the experimental arrangement. With air as the ambient fluid, experiments are carried out for the opposing flow situation as well as the aiding flow situation, in which the heated plate moves vertically upward. In the aiding flow circumstances, the buoyancy force is in the same direction as the flow induced by the plate. The results based upon the experimental data were plotted in terms of dimensionless quantities, defined as $\theta = (T - T_\infty)/(T_o - T_\infty)$, $X = x/d$, $Y = y/d$, $\tau = tU_s/d$,

$$\mathrm{Pe} = U_s d/\alpha_s, \quad \mathrm{Re} = U_s d/\nu, \quad \mathrm{Gr} = g\beta(T_o - T_\infty)d^3/\nu^2 \quad (1)$$

where d is the half thickness of the plate and U_s the speed of the moving plate. These are the dimensionless variables employed for moving materials, with conjugate transport, in earlier studies (Karwe and Jaluria, 1988, 1991; Kang et al., 1991).

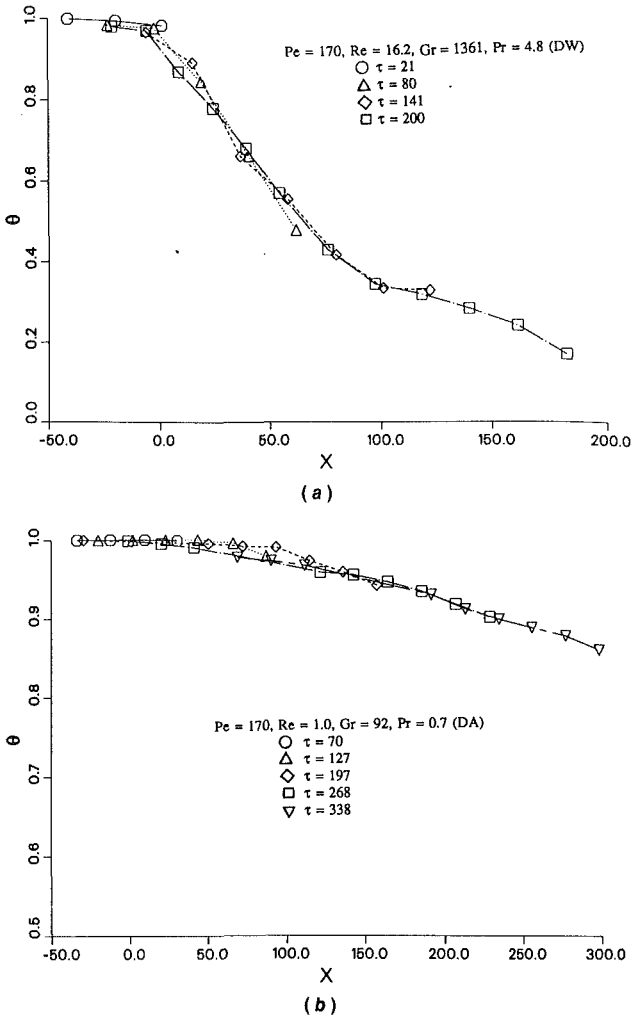

Fig. 3 Variation of the measured temperature at the midplane with the downstream distance X for a teflon plate moving downward in (*a*) water (DW), and (*b*) air (DA) at Pe = 170 and different time intervals

Typical results for a teflon plate moving downward into water and air are shown in Figs. 3 and 4 at Pe = 170. The temperature of the plate is kept below 100°C in order to prevent any boiling when the plate is immersed in water. In the presence of boiling, the heat transfer characteristics would be substantially different. Time-dependent temperature distributions at the midplane ($Y = 0$) of the plate are shown in Fig. 3. Here, $X = 0$ indicates the location of the water surface or the exit from the furnace for air and X is the downward vertical distance from this location. As time elapses, the plate moves farther into the water and cools down rapidly; see Fig. 3(*a*). At high speeds it may not be possible to achieve steady-state conditions away from the leading edge due to the finite length of the plate. The approach to steady state may similarly be observed on temperature versus time plots. The heat transfer in the region near the leading edge is time dependent because of the changing location of the edge (Jaluria and Singh, 1983). However, the temperature profiles obtained at locations far from the leading edge at various times indicated little change when the dimensionless time τ is larger than about 140, suggesting that the temperature distribution approaches a steady-state situation as time increases to this value. The main effect of time is seen to be the moving location of the leading edge. The temperatures close to $X = 0$ attain steady state in a very short time.

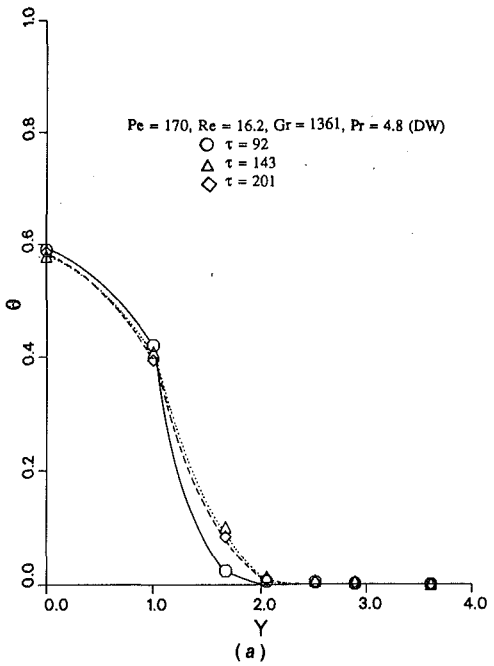

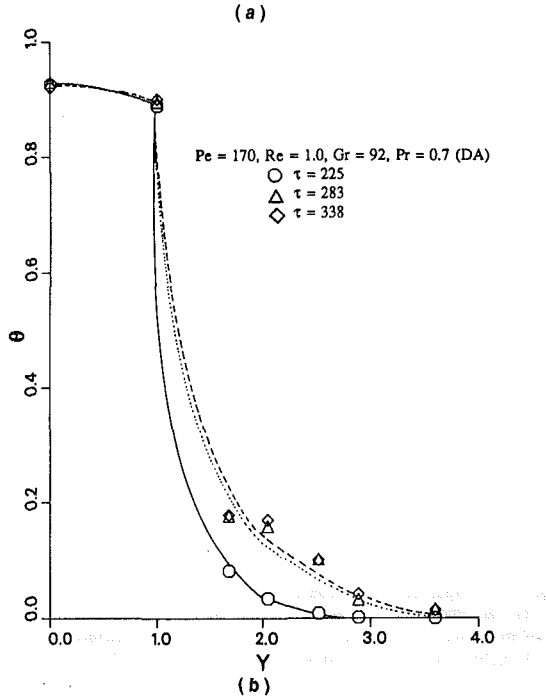

Fig. 4 Transient temperature distributions in the material and in the fluid for a teflon plate moving downward at Pe = 170: (*a*) water (DW), X = 50.0; (*b*) air (DA), X = 179.0

In the case of air as the ambient fluid, the experiments were carried out for both aiding and opposing flow situations. Figure 3(*b*) shows the results when a teflon plate moves vertically downward into air at Pe = 170 and Gr = 92. This gives rise to flow with opposing buoyancy effects. The temperature drop is small as compared to that in water, shown earlier in Fig. 3(*a*). This is obviously due to the smaller heat transfer rate in air, as compared to that in water. When time τ is larger than 268, the steady-state temperature distribution is obtained over the distance shown. It is found that more time is needed to reach the steady-state situation in air than in water, as expected from the smaller heat transfer rate for the former.

Figure 4 shows the transient variation of the measured temperature distribution at X = 50 in water and X = 179.0 in air. Since Y is measured outward from the midplane of the plate, Y= 1 indicates the surface of the plate. The plate tip

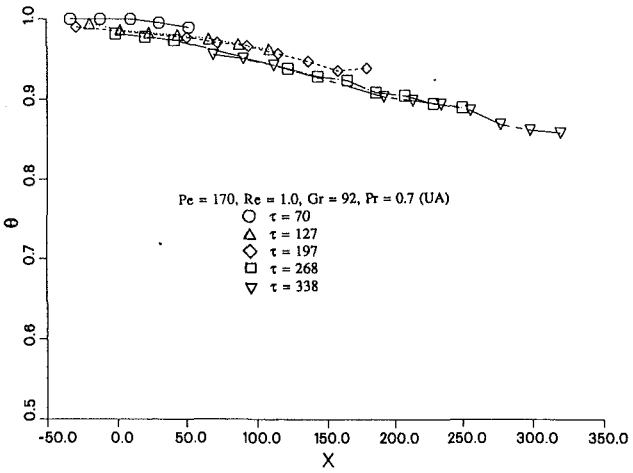

Fig. 5 Measured temperature distributions, at the midplane, for a teflon plate moving upward in air (UA) at Pe = 170 and Gr = 92

reaches the downstream distance X = 50, where the thermocouple rake is installed to measure the water temperature, at τ = 50. Thus, water adjacent to the plate starts heating up at this time. It is found that temperature oscillations arise in the water when the plate moves at high speed, such as U_s = 25 mm/s. However, the temporal oscillations were not observed at lower values of the plate speed, such as U_s = 10.8 mm/s taken for this figure. A detailed discussion on separation at high speeds is given by Karwe and Jaluria (1992). Instability arises, leading to separation and large disturbances downstream. The temperature level within the plate decreases as time increases, while that in water adjacent to the plate rises. It is also noted here that the temperature difference between the surface and the midplane of the teflon plate is substantial due to the low thermal conductivity of the material, whereas it was found to be very small for the aluminum plate due to the high thermal conductivity of aluminum. Similar trends were obtained in the numerical results (Kang et al., 1991). Quantitative comparisons between the experimental and numerical results are given later.

The measured temperature variation with Y in air, at X = 179, is shown in Fig. 4(*b*) at different time intervals. The trends are similar to those obtained for water. However, the thermal boundary layer is found to be thicker in air than in water, as seen in the numerical results (Kang et al.,1991) and as expected for the lower Prandtl number for air.

Figures 5 and 6 show the typical results for a teflon plate moving vertically upward in air. This represents a buoyancy-aided flow situation. In this case, the heating unit was located at the bottom, near the floor. When the plate was moved vertically downward, the heating units were positioned at the top. Therefore, in this case, any plume of hot air rising upward did not affect the flow near the plate surface. However, in the case when the plate was moved vertically upward, the plume of hot air from the heating units could affect the flow near the plate. To reduce this effect, a horizontal blocker plate was placed just above the heaters to divert the plume of hot air away from the moving plate. It is seen that the general trends indicated in these figures are similar to those for the opposing buoyancy case in air.

The effect of the direction of motion on the steady-state temperature distributions is shown in Fig. 7. The aiding flow situation, in which the plate moves upward in air (UA), cools the plate somewhat faster than that for the opposing flow situation (DA), as seen from the lower temperatures for the former case in Fig. 7(*a*). Similar tends were observed for other parameter values. However, the effect on the heat transfer rate is small, as also discussed later. The thermal boundary layer

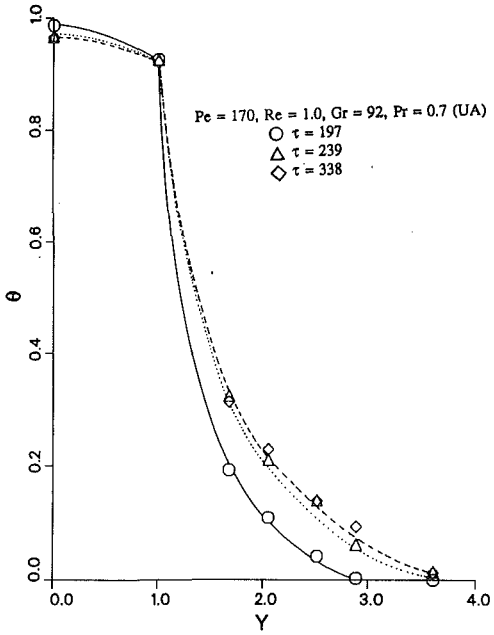

Fig. 6 Measured temperature distributions in the material and in the fluid at X = 93.0 for a teflon plate moving upward in air (UA) at Pe = 170 and Gr = 92

thickness increases downstream. Also, the boundary layer may be turbulent and thermal effects may become small far downstream. The temperature distribution at the downstream distance $X = 93$ for the aided flow situation (UA) is compared with that at $X = 179$ for the opposed flow situation (DA), in Fig. 7(b). Even though the downstream distance in the DA case is almost double that in the UA case, the thermal boundary layer is found to be thinner in DA than in UA. This indicates that the buoyancy effect on the temperature distribution is very significant in air. But the resulting effect on the heat transfer rate from the solid was small, as seen here. A comparison between the present experimental data and the numerical results is also made in these figures. The numerical calculations were performed for only the aided flow situations, due to the numerical instability encountered with the opposed flow circumstances. Consequently, a comparison is made even though the numerical predictions are for upward movement of the plate and the experimental data for the downward movement. Despite this difference, as seen in these figures, a good agreement is obtained between the numerical and experimental results. This lends strong support to the numerical model and to the experimental procedure used.

The effect of the plate material on the surface temperature distributions is shown in Fig. 8. The comparison is made for a teflon and an aluminum plate moving downward into water. Here, ξ is a dimensionless coordinate distance in the direction of the material motion, with $\xi = x(\rho Ck)_f/(U_s d^2 \rho_s^2 C_s^2)$, and B is the physical properties parameter, where $B = (\rho Ck)_f/(\rho Ck)_s$. These dimensionless variables were employed by Chida and Katto (1976). The dimensionless value ξ has an advantage over X because it includes the speed of the material. However, ξ has a shortcoming because log ξ cannot be defined at $x = 0$. Thus, the upstream penetration of conduction effects in the material cannot be investigated with these dimensionless variables. As seen in the figure, the aluminum plate is cooled down more rapidly than the teflon plate, as also seen in the numerical results presented in earlier papers. The corresponding values of B for these two cases are 0.005 and 4.02, respectively. As found by Chida and Katto (1976), with decreasing B the surface temperature level rises at small values of ξ. However, it decreases sharply, below the values for large B, as ξ increases.

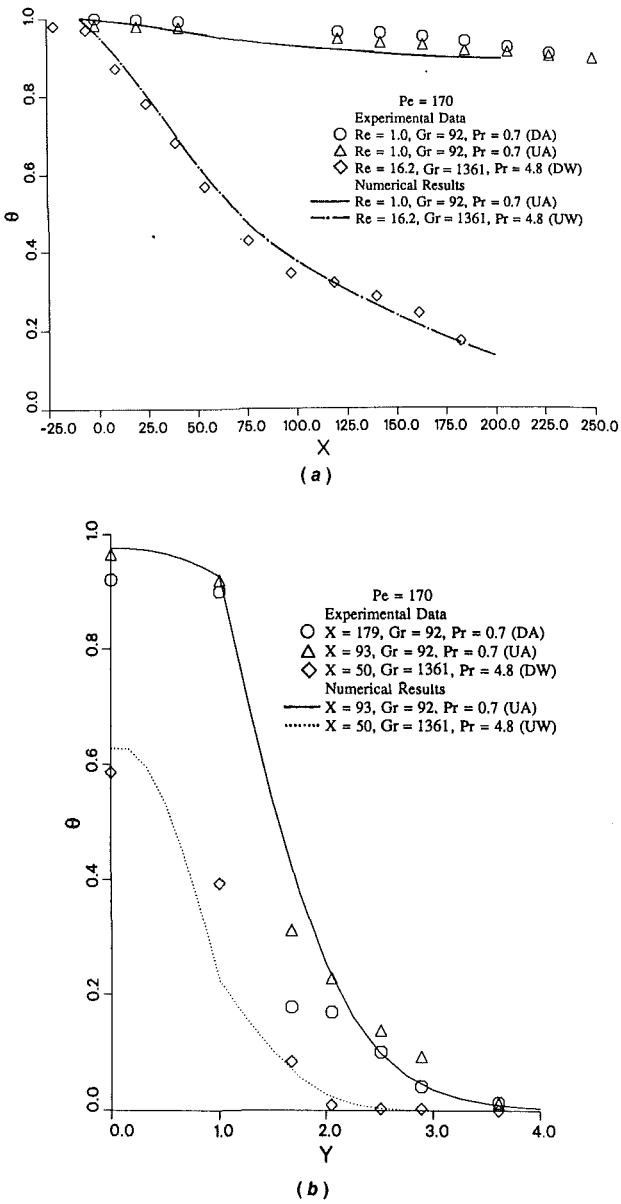

Fig. 7 Comparisons between numerical (Kang et al.,1991) and experimental results under steady-state conditions for a teflon plate moving in air or water; (*a*) temperature variation at the midplane of the plate (Y = 0);(*b*) temperature variation with Y at different X

Thus, the observed trends agree with those obtained in the earlier study.

Experimental results on the temperature distributions in the fluid and in the moving plate have been presented so far. The implications with respect to the heat transfer rates were also indicated at several places. However, the local and average heat transfer data may also be derived from these. Results are presented in terms of the Nusselt number Nu where $\mathrm{Nu} = hd/k_f$ and $\overline{\mathrm{Nu}} = \bar{h}d/k_f$, $\bar{h}$ and $\overline{\mathrm{Nu}}$ being the average values. The local Nusselt number Nu is obtained from the temperature gradient in the fluid at the plate surface and is given by $\mathrm{Nu} = -[(\partial\theta/\partial Y)/\theta]_{Y=0}$. The temperature gradient is determined by curve fitting the temperature data in the fluid. The average value $\overline{\mathrm{Nu}}$ is obtained from an energy balance for the plate over the distance where measurements are taken to yield the average convective heat transfer coefficient $\bar{h}$.

Several interesting features are obtained from the heat transfer data. The local Nusselt numbers from the temperature measurements in Fig. 4 are 1.43 for water and 0.91 for air.

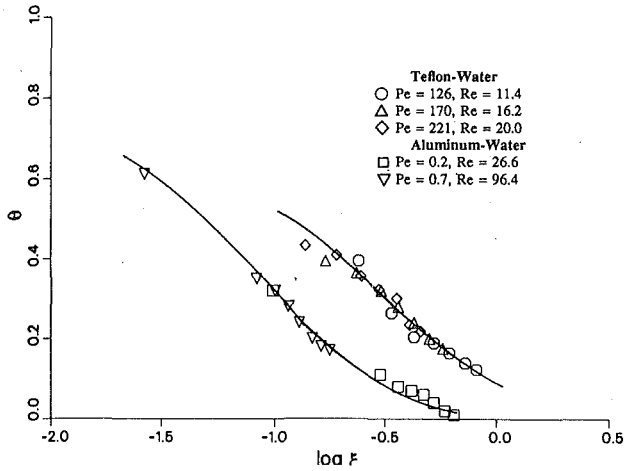

Fig. 8 Effect of the properties of the moving material on the surface temperature distributions, for a plate moving downward in water

Given the much larger thermal conductivity of water, the local convective heat transfer coefficient is much larger for water, as expected. Similar values were obtained from other measurements. The average Nusselt numbers $\overline{Nu}$ derived from Figs. 3 and 5 yielded 0.59 and 0.57 for water and air, respectively. In fact, the value for air is somewhat of an overestimate since thermal radiation effects are significant, particularly at small X. An estimate of radiative transport indicated that it contributes about 10 percent of the total energy loss in air.

The average Nusselt number $\overline{Nu}$ was obtained for varying Peclet number Pe at a constant value of Gr, Gr = 1330, and may be listed as:

Pe	126	170	221	320
$\overline{Nu}$	0.535	0.593	0.599	0.602

for a heated plate moving downward in water. Therefore, as the speed of the plate increases, reflected in terms of an increase in Pe, the average Nusselt number increases. These trends agree with the theoretical findings of Kang et al. (1991). The average values, as well as local values, of the Nusselt number are also in good agreement with the theoretical results for this material. The local Nusselt number was found, numerically, to decrease with X, as expected, varying from about 4.0 to 0.2 as X increases from close to zero to about 200 for water. For air, the values ranged from about 2.0 to 0.2, being almost equal to water at large X. Therefore, for a poor conductor like teflon, the distance over which cooling occurs is very large and the average Nusselt numbers are small.

With varying Gr, Nu was found to remain essentially unchanged. Thus, even through the thermal field is affected substantially by buoyancy, the effect on the Nusselt number is small, as also observed by Karwe and Jaluria (1988, 1991) and by Kang et al. (1991). In fact, an increase in Gr is obtained with an increase in the temperature level, which affects the fluid properties significantly. This effect is of the same order as the effect of buoyancy. Consequently, the heat transfer rate is largely affected by the material speed, fluid employed, and plate material properties.

Cylinder Moving in a Quiescent Ambient Medium. The experiments are carried out for an aluminum rod moving downward into water or air. Only the opposing flow situation, in which the cylindrical rod moves vertically downward in either water or air, is considered. In this case, the buoyancy effects are upward, whereas the flow due to the motion of the material is downward. The characteristic length is the radius

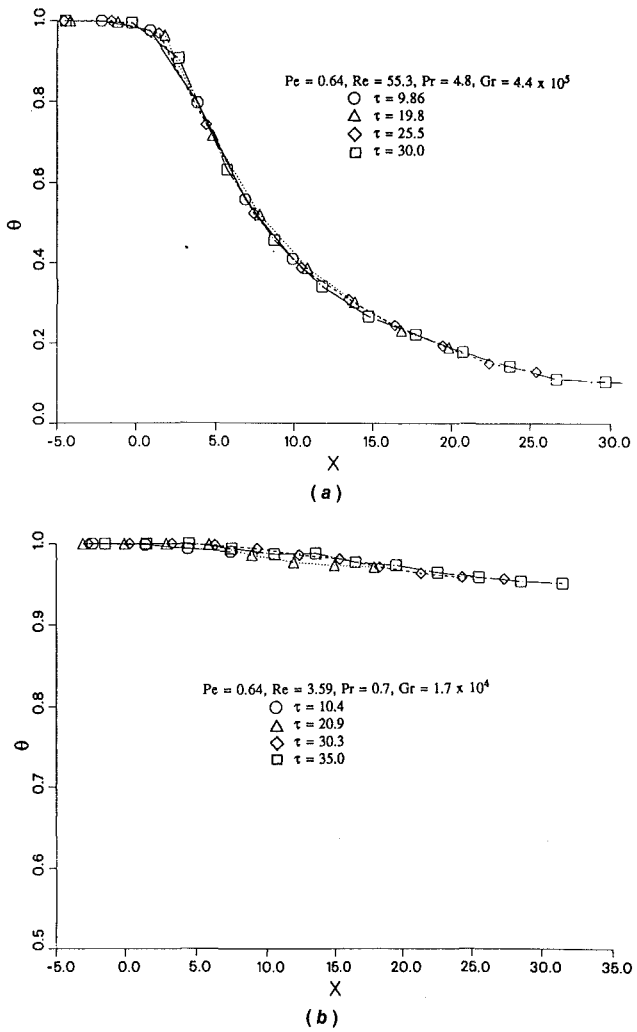

Fig. 9 Time-dependent temperature distributions at the centerline for *an aluminum cylinder moving downward in (a) water and (b) air*

of the cylindrical rod and the dimensionless variables that are used to present the experimental data are defined as follows:

$$X = x/R_o, \quad R = r/R_o, \quad \tau = tU_s/R_o, \quad \theta = (T - T_\infty)/(T_o - T_\infty)$$

$$\mathrm{Pe} = U_s R_o/\alpha_s, \quad \mathrm{Re} = U_s R_o/\nu, \quad \mathrm{Gr} = g\beta(T_o - T_\infty)R_o^3/\nu^2 \quad (2)$$

where R_o is the radius and U_s is the speed of the moving cylinder.

Typical results for an aluminum cylinder (25.4 mm diameter) moving downward into water and air are shown in Figs. 9 and 10 at Pe = 0.64. The time-dependent temperature variation at the centerline (R = 0) of the cylinder with the downstream distance X is shown in Fig. 9. Again, X = 0 indicates the water surface or the exit from the furnace for air and X is the vertical downward distance from the water level. As time elapses, the cylinder moves deeper into the water and the cylinder cools down rapidly. The temperature profiles obtained at locations away from the leading edge at various times show little change, indicating that the temperature distribution attains a steady-state situation very rapidly. However, the leading edge continues to move with time and transient effects are apparent ner the edge until the temperature there attains the ambient value. Figure 10(*a*) shows the transient variation of the measured temperature distributions at X = 5.9. Since R is measured from the center of the cylinder, R = 0 indicates the centerline of the cylinder and R = 1 the surface of the cylinder. The leading edge of the cylinder reaches the downstream distance X = 5.9, where the thermocouple rake is

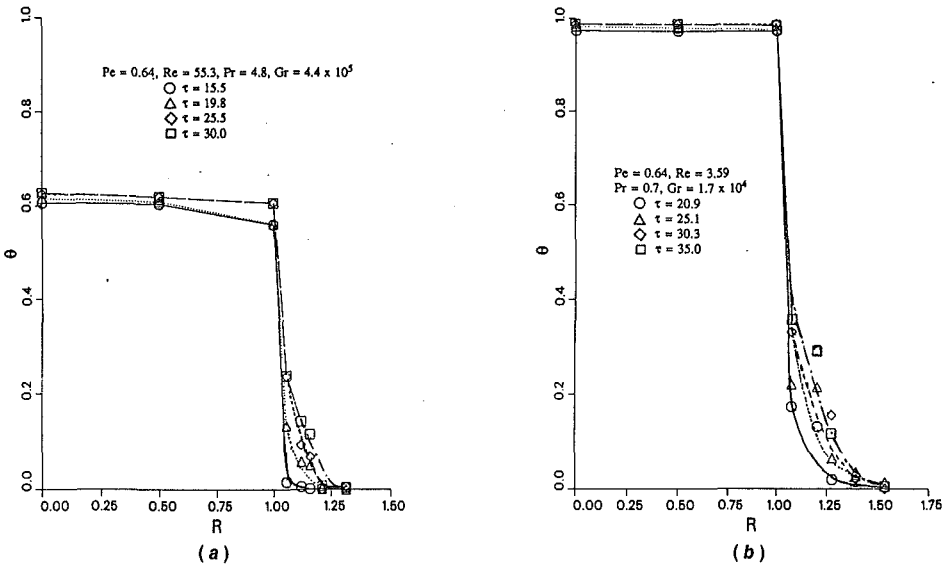

(a) (b)

Fig. 10 Time-dependent temperature distributions for an aluminum cylinder moving downward in (a) water, $X = 5.9$; (b) air, $X = 14.0$

installed to measure the water temperature, at $\tau = 5.9$. Thus, the water adjacent to the moving surface starts getting heated up by the cylinder at this time. The temperature level within the cylinder decreases as time increases, while that in the water increases. The trends obtained for the cylindrical case are qualitatively similar to those for the flat plate.

The experiments, in the case of air as an ambient fluid, were also carried out for these cases. Figures 9(b) and 10(b) show the results when an aluminum cylinder moves vertically downward in air at Pe = 0.64 and Gr = 1.7×10^4. The temperature drop is smaller than that in water, as expected from the smaller heat transfer coefficient for air. When τ becomes larger than about 30, the temperature distribution over the distance considered is seen to remain unchanged with increasing time, indicating that steady state has been obtained. The transient variation of the measured temperature distributions at $X = 14.0$ is shown in Fig. 10(b). The trends are similar to those seen for water. However, the thermal boundary layer is found to be thicker in air than in water, due to the smaller Prandtl number for air. It was also found that the temperature in air was fluctuating substantially while that in water was steady for a cylinder speed $U_s = 4.4$ mm/s. An explanation for these fluctuating temperatures in air may be given in terms of the shear flow and flow separation. When a strong shear layer is generated in the flow, near the cylinder, in the presence of buoyancy, the velocity distribution undergoes a sign change, the velocity being downward near the cylinder and upward away from the cylinder. This gives rise to an unstable flow situation and to flow separation (Karwe and Jaluria, 1992). Because of the observed larger temperature levels in air, resulting from smaller heat transfer rates, the opposing buoyancy effects are larger as compared to the corresponding values in water. Thus, it is seen that the experimental data in air are more scattered than those for water.

In order to study the effect of speed on the steady-state temperature distributions in the cylinder, the cylinder was initially taken at a uniform temperature of T_o and was moved at various speeds U_s. Figure 11 shows the temperature variation with the downstream distance X at steady state, obtained at large time as discussed earlier, for increasing cylinder speed in water. It is found that the temperature starts dropping earlier at lower cylinder speeds. At higher cylinder speeds, the temperature drops more gradually. This is expected because the time taken by the cylindrical material to pass through a given distance is smaller at a faster speed. Thus, a smaller amount

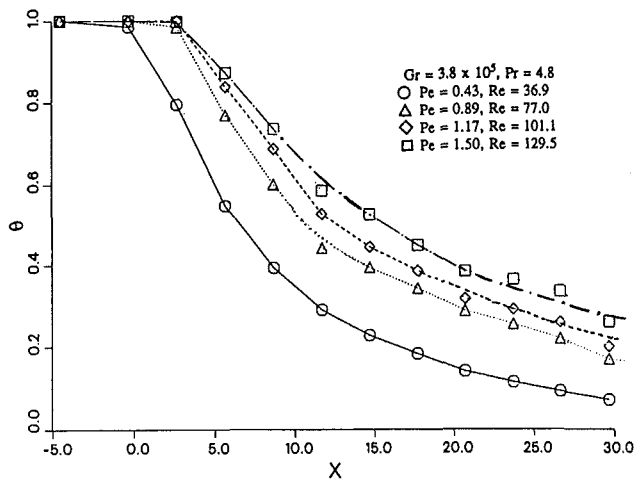

Fig. 11 Steady-state variation of the surface temperature of the cylinder for various values of the Peclet number Pe at Gr = 3.8×10^5 for an aluminum cylinder moving downward in water

of thermal energy is transferred from the cylinder to the fluid up to a given downstream distance. This results in higher temperature levels as the cylinder speed increases. Therefore, at a higher speed, the temperature gradients in the downstream distance X become more gradual, especially near the entry point into the fluid.

The effect of the thermal buoyancy on the temperature field is also studied. The initial temperature T_o of the cylinder is varied at a fixed cylinder speed $U_s = 4.5$ mm/s, for an aluminum cylinder moving downward into water, and the results are shown in Fig. 12. The corresponding Grashof number varies from Gr = 2.0×10^5 to Gr = 5.7×10^5. Since the dimensionless temperature is based on the difference between the initial plate temperature T_o and that of the ambient water, the physical temperature is different when the Grashof number is varied, even though the dimensionless temperature values may be the same. As Gr increases, the temperature of the cylinder drops rapidly, due to the larger temperature difference between the moving material and the water. However, it is seen that the variation in the temperature distributions is small for a further change in Gr, at higher values of the Grashof number.

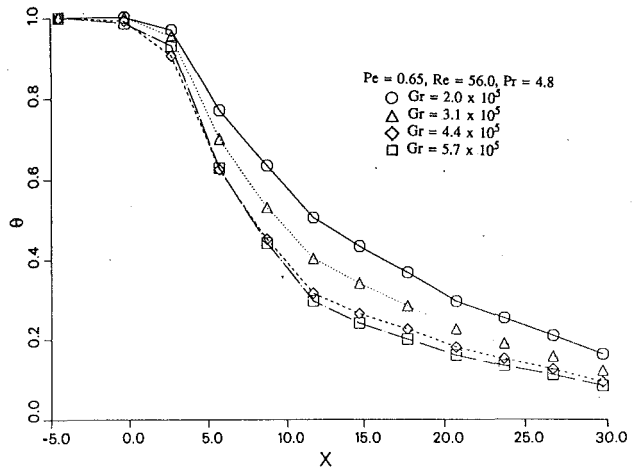

Fig. 12 Steady-state variation of the surface temperature of the cylinder for various values of the Grashof number Gr for an aluminum cylinder moving downward in water at Pe = 0.65

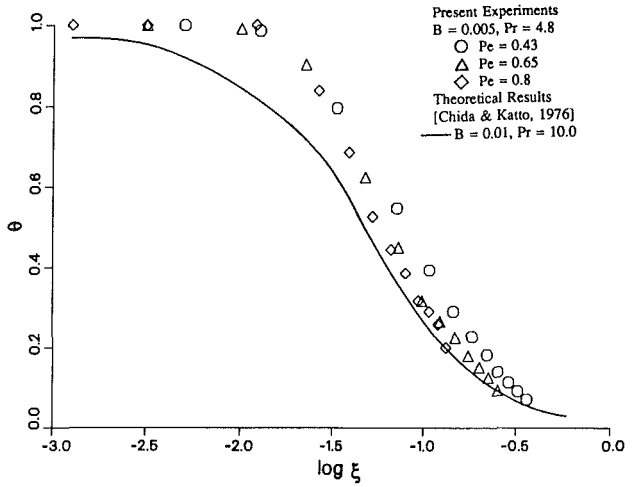

Fig. 13 Comparison between experimental and numerical results on the surface temperature distributions for a cylinder moving vertically downward in water

A comparison of the surface temperature distributions between the present experimental data and the theoretical results of Chida and Katto (1976) is shown in Figs. 13 and 14. Here, ξ is a dimensionless coordinate distance in the direction of material motion, with $\xi = x(\rho Ck)_f / (U_s R_o^2 \rho_s^2 C_s^2)$ This variable is, therefore, similar to that defined earlier for the moving plate case. Figure 13 shows the surface temperature distribution when an aluminum cylinder moves vertically downward into water. The experimental data are taken at $B = 0.005$ and Pr = 4.8, while the theoretical curve is given for $B = 0.01$ and Pr = 10.0. A comparison is made between these two results even though the parametric values are not the same since no other theoretical results are available in the literature for this circumstance. As either Pr or B is decreased, the temperature levels are predicted to be higher by the theoretical investigation of Chida and Katto (1976). Considering the effect of Pr and B on the results, the present experimental results agree fairly well with the theoretical results.

Figure 14 shows the surface temperature distribution when an aluminum cylinder moves vertically downward in air. Two different diameters, 25.4 mm and 6 mm, of the aluminum cylinder are employed for the present data. Also shown are other experimental data (Alderson et al., 1968; Arridge and Prior, 1964), which are obtained for a very thin glass fiber moving downward in air. Comparisons are made between the

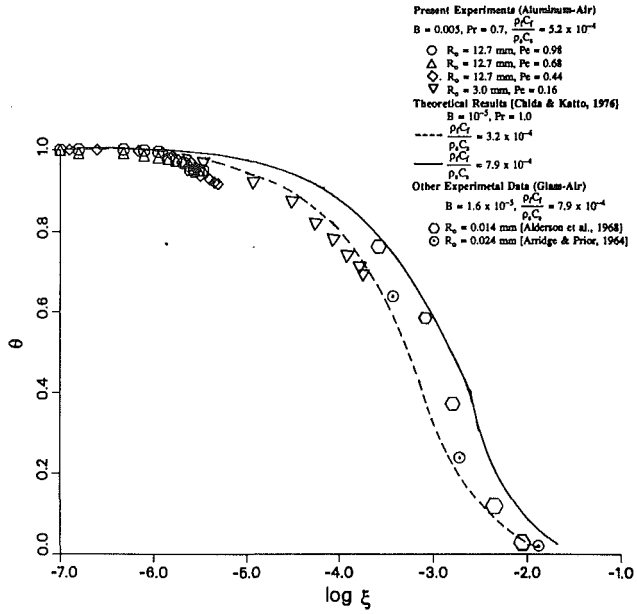

Fig. 14 Comparison between experimental and numerical results on the surface temperature distributions for a cylinder moving vertically downward in air

experimental data and the theoretical results of Chida and Katto (1976). The present experimental data are plotted in the region of the small values of ξ, since the diameter of the cylinder employed is much larger than that in the earlier experiments. The temperature variation in the present experimental data is seen to be lower than that from the theoretical results and the earlier experimental data. This difference may be attributed to the material property effects because the present experiments are carried out with an aluminum cylinder while the others were conducted with glass fiber.

Heat transfer rates were also obtained from the temperature measurements, as done earlier for a plate. The local Nusselt numbers were obtained from Fig. 10 as 8.0 and 4.0 for water and air, respectively, again indicating the much larger convective heat transfer coefficient in water. The average Nusselt numbers were derived from the data in Fig. 9 to yield values of 7.9 and 4.3 for water and air, respectively. For air, thermal radiation loss leads to about a 10 percent overestimate in the convective heat transfer rate, as mentioned earlier.

The variation of $\overline{Nu}$ with Pe, from Fig. 11, at Gr = 3.8×10^5 is obtained as:

Pe	0.43	0.89	1.17	1.5
$\overline{Nu}$	6.39	8.49	9.41	10.22

for an aluminum cylinder moving downward in water. Thus, the heat transfer rate increases with the cylinder speed, given in terms of increasing Pe.

With increasing Gr, the average Nusselt number $\overline{Nu}$ is obtained as 8.05, 8.28, 7.92, and 7.64 for Gr $\times 10^{-5}$ values of 2.0, 3.1, 4.4, and 5.7, respectively. Therefore, the effect of thermal buoyancy on the heat transfer rate is small, even though the effect on the temperature distribution is more substantial. Also, a larger Gr is obtained at a larger value of T_o, which gives rise to larger property variation effects. It is interesting to note that a highly conductive material like aluminum helps in the transport process due to thermal diffusion in the material. Consequently, most of the energy is lost in a very short distance, as compared to that for teflon. This also affects the average Nusselt number since the average is obtained over a much shorter region, being up to $X = 30.0$ for an aluminum rod as compared to $X = 200.0$ for a teflon plate in water. Since h decreases with x, this results in a larger average Nusselt

number for aluminum. This effect is clearly a result of the conjugate nature of the problem, since the Nusselt numbers will be independent of the solid material properties if an isothermal moving surface were considered. Therefore, it is again seen that the heat transfer is largely affected by rod speed, fluid employed, and solid material properties.

Conclusions

An experimental study has been carried out on the thermal transport from a heated plate or cylinder moving in an otherwise quiescent fluid medium. The material is taken as aluminum or teflon and air and water are the ambient fluids considered. The experiments investigated vertical upward and downward motion in air, and vertical downward motion in water. Thus, the experiments with water gave rise to a buoyancy force opposing the flow due to the material motion. Experiments in air simulate opposed, as well as aided, mixed convection flow situations.

In the experiments with water, the results indicated a fairly close attainment of steady-state conditions. However, with air, a quasi-steady-state circumstance was achieved, which approaches steady state at large times. In water, the temperature of the plate or cylindrical rod dropped to the ambient temperature level very rapidly. With air, much larger distances are required to obtain a comparable drop in temperature and to obtain a steady-state condition, because of the much lower heat transfer coefficients in air. The temperature profiles obtained with water, as well as with air, agreed with the results from the earlier numerical studies. At low material speeds, implying small Peclet number Pe, the upstream penetration of the conduction effects was substantial. This effect decreased with an increase in the material speed. The experimental results obtained were in fair agreement with the analytically and numerically predicted results. The deviation between the two was largest near the tip of the material, since the numerical models assumed an infinite moving material.

The problem considered here is an important one, though very little experimental information is available in the literature on the thermal transport processes. This paper presents the work done on moving flat plates and cylinders in a quiescent isothermal environment, with the speeds small enough to give rise to laminar flow in the fluid. The results obtained indicate the important basic features of this transport circumstance and also present data that may be used for validation of analytical and numerical models, as well as for the design of practical systems concerned with such processes.

Acknowledgments

This work was supported by the National Science Foundation, under Grant Nos. CBT-88-03049 and DDM-92-13458. J. Yoo acknowledges the support from the Korea Science and Engineering Foundation for a post-doctoral fellowship during his stay at Rutgers University.

References

Alderson, J. V., Caress, J. B., and Sager, R. L., 1968, "The Cooling Rate of a Glass Fiber in a Continuous Filament Process," Lab. Report No. LR235, Pilkingston Bros. Ltd., Latham, Lancashire, United Kingdom.

Altan, T., Oh, S., and Gegel, H., 1979, *Metal Forming Fundamentals and Applications*, American Society of Metals, Metals Park, OH.

Arridge, R. G. C., and Prior, K., 1964, "Cooling Time of Silica Fibers," *Nature*, Vol. 203, pp. 386–387.

Chen, T. S., and Strobel, F. A., 1980, "Buoyancy Effects in Boundary Layer Flow Adjacent to a Continuous Moving Horizontal Flat Plate," ASME JOURNAL OF HEAT TRANSFER, Vol. 102, pp. 170–172.

Chida, K., and Katto, Y., 1976, "Conjugate Heat Transfer of Continuously Moving Surfaces," *Int. J. Heat Mass Transfer*, Vol. 19, pp. 461–470.

Fisher, E. G., 1976, *Extrusion of Plastics*, Wiley, New York.

Glicksman, L. R., 1968, "Cooling of Glass Fibres," *Glass Technology*, Vol. 9, No. 5, pp. 131–138.

Jaluria, Y., and Singh, A. P., 1983, "Temperature Distribution in a Moving Material Subjected to Surface Energy Transfer," *Comp. Meth. Appl. Mech. Eng.*, Vol. 41, pp. 145–157.

Kang, B. H., 1990, "Conjugate Heat Transfer From a Continuously Moving Material and From an Isolated Heat Source," Ph.D. thesis, Rutgers University, New Brunswick, NJ.

Kang, B. H., and Jaluria, Y., 1990, "Conjugate Heat Transfer From a Continuously Moving Material in a Parallel Channel Flow for Cooling in Forming Manufacturing Processes," in: *Transport Pheno. Materials Proc.—1990*, ASME HTD, Vol. 144, pp. 25–35.

Kang, B. H., Jaluria, Y., and Karwe, M. V., 1991, "Numerical Simulation of Conjugate Transport From a Continuous Moving Plate in Materials Processing," *Numerical Heat Transfer*, Vol.19, pp. 151–176.

Kang, B. H., and Jaluria, Y., 1992, "A Numerical Study of the Fluid Flow and Heat Transfer Due to a Heated Plate Moving in a Uniform Forced Flow," *Numerical Heat Transfer*, Vol. 22, pp. 143–165.

Karwe, M. V., 1987, "Thermal Transport Between a Continuously Moving Heated Plate and a Quiescent Ambient Medium," Ph.D. thesis, Rutgers University, New Brunswick, NJ.

Karwe, M. V., and Jaluria, Y., 1988, "Fluid Flow and Mixed Convection Transport From a Plate in Rolling and Extrusion Processes," ASME JOURNAL OF HEAT TRANSFER, Vol. 110, pp. 655–661.

Karwe, M. V., and Jaluria, Y., 1991, "Numerical Simulation of Thermal Transport Associated With a Continuously Moving Flat Sheet in Materials Processing," ASME JOURNAL OF HEAT TRANSFER, Vol. 113, pp. 612–619.

Karwe, M. V., and Jaluria, Y., 1992, "Experimental Investigation of Thermal Transport From a Heated Moving Plate," *Int. J. Heat Mass Transfer*, Vol. 35, pp. 493–511.

Khader, M. S., 1981, "Transient Laminar Mixed Convection From a Moving Vertical Plate," ASME Paper No. 81-HT-40.

Moutsoglou, A., and Chen, T. S., 1980, "Buoyancy Effects in Boundary Layers on Inclined, Continuous, Moving Sheets," ASME JOURNAL OF HEAT TRANSFER, Vol. 102, pp. 371–372.

Poulos, E. N., and Chung, T. F., 1983, "Transient Conjugated Heat Transfer Between a Thick Plate and a Nonsteady Laminar Incompressible Flow," ASME Paper No. 83-HT-101.

Sakiadis, B. C., 1961, "Boundary Layer Behavior on Continuous Solid Surfaces: I. Boundary Layer Equations for Two-Dimensional and Axisymmetric Flow," *AIChE Journal*, Vol. 7, No. 1, pp. 26–28.

Tadmor, Z., and Klein, I., 1970, *Engineering Principles of Plasticating Extrusion*, Polymer Science and Engineering Series, Van Nostrand Reinhold Company, New York.

Tsou, F. K., Sparrow, E. M., and Goldstein, R. J., 1967, "Flow and Heat Transfer in the Boundary Layer on a Continuous Moving Surface," *Int. J. Heat Mass Transfer*, Vol. 10, pp. 219–235.

Charn-Jung Kim

Sangken Kauh

Sung Tack Ro

Joon Sik Lee

Department of Mechanical Engineering,
Seoul National University,
Seoul 151-742, Korea

Parametric Study of the Two-Dimensional Keyhole Model for High Power Density Welding Processes

This study presents a parametric study of the two-dimensional steady-state keyhole model for high power density welding processes. Keyhole formation is common to electron beam welding, laser welding, and plasma arc welding, all of which are important techniques for high-quality, high-precision welding. Computation was performed by adopting a recently developed concept of the position correction and modifying it suitably for the problem of interest. The dimensionless parameters pertaining to the model were identified and the influence of each parameter was investigated separately. Although the mathematical model employed here has been used in previous studies, a thorough investigation successfully revealed new features that have not been previously recognized in the literature.

Introduction

When a metal surface is exposed to a beam of concentrated energy over 10^9 W/m^2, vaporization of metal takes place and the coupling effect of the beam pressure and the vaporizing pressure creates a long, cylindrical hole, which is usually called a keyhole. Within the keyhole, the vaporized metal is ionized and absorbs energy carried by the beam. The absorbed energy is then conveyed to the material, thus producing molten metal around the keyhole. This phenomenon has been applied to welding processes such as laser welding, plasma arc welding, electron beam welding, etc., depending on the mode of energy generation. These welding processes may be categorized as the keyhole welding owing to a common feature of the keyhole formation. They are able to minimize several undesirable properties such as internal stress, crack, and distortion, because the weld width as well as the heat affected zone is relatively small and the impurities are rarely present in the welded part. The use of high power density welding has increasingly attracted the attention of engineers for welding with high precision and quality (Lancaster, 1983).

As an example of high power density welding, Fig. 1 illustrates an electron beam welding process in which the beam impinges on the metal surface perpendicularly to the plane and creates a keyhole. With respect to a frame of reference moving with the keyhole, molten metal in the upstream flows around the keyhole and solidifies downstream. In addition, the fluid flow and heat transfer phenomena rapidly reach steady states when the weld speed u_w is kept constant. Experimental evidence indicates that the depth of the keyhole is an order of magnitude larger than the keyhole diameter. From this observation and considering that the molten metal flows mostly around the keyhole, a two-dimensional model in the xy plane has been considered in the literature. Earlier studies on thermal characteristics of keyhole-mode welding considered heat diffusion only (Swift-Hook and Gick, 1973; Mazumder and Steen, 1980; Miyazaki and Giedt, 1982). Later, the effect of fluid flow was included in a number of studies (Dowden et al., 1983; Davis et al., 1985; Hsu and Rubinsky, 1988). A survey of literature is well documented in the work of Hsu and Rubinsky (1988)

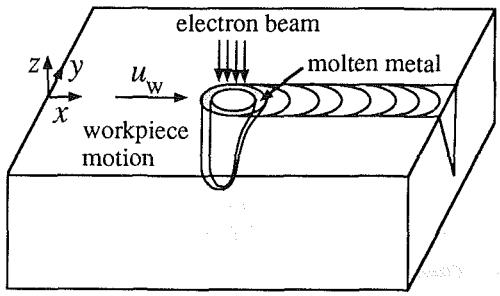

Fig. 1 Schematic diagram to illustrate electron beam welding

and, therefore, an extensive discussion of the current state of the art of this topic is omitted here. The primary objective of this work is to provide a thorough parametric analysis of an existing keyhole model with associated simplifications and assumptions taken for granted. In this matter, this study successfully revealed several new features that previous investigations had failed to recognize. It is our hope that the present work provides a deeper insight into the keyhole mode of the welding process and thus enhances our understanding of it.

Analysis

A physical model to analyze the keyhole welding process is shown in Fig. 2. The material properties are assumed constant in the solid and liquid phases but are not necessarily the same between phases; however, the densities of solid and liquid phases are taken to be identical. The region $y \geq 0$ only is considered by assuming symmetry with respect to the x axis. Further approximations to simplify the analysis can be found elsewhere (e.g., Davis et al., 1985) and are not repeated here.

A question of special interest is how to identify the position of the solid/liquid interface, which is unknown a priori. Since the method of solution selected here is based on a multidomain approach, the interface-identifying procedure is of major difficulty. Nevertheless, it can be resolved with ease by applying the concept of the position correction (Kim and Kaviany, 1992a), as will be shown later.

For the systematic presentation of our numerical results, mathematical formulation of the problem is made in terms of the dimensionless quantities listed below:

Contributed by the Heat Transfer Division for publication in the JOURNAL OF HEAT TRANSFER. Manuscript received by the Heat Transfer Division October 1992; revision received June 1993. Keywords: Laser Processing, Numerical Methods, Phase-Change Phenomena. Associate Technical Editor: Y. Bayazitoglu.

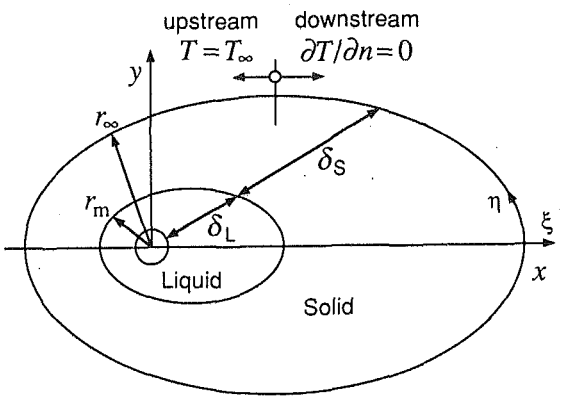

Fig. 2 Two-dimensional steady-state keyhole model; the frame of reference is moving with the center of the keyhole

$$x^+=\frac{x}{a},\quad y^+=\frac{y}{a},\quad u^+=\frac{u}{u_w},\quad v^+=\frac{v}{u_w},\quad h^+=\frac{h}{h_{\text{ref}}}$$

$$p^+=\frac{p}{\rho u_w^2},\quad \text{Pr}=\frac{\nu}{\alpha_L},\quad \text{Pe}=\frac{u_w a}{\alpha_L}$$

$$\text{Ste}=\frac{h_{sf}}{h_{\text{ref}}},\quad \Theta=\frac{c_S(T_m-T_\infty)}{h_{\text{ref}}} \tag{1}$$

where the specific enthalpies are defined such that

$$h_S=c_S(T_S-T_\infty),\quad h_L=c_L(T_L-T_m)+h_{sf}+c_S(T_m-T_\infty). \tag{2}$$

Note that Ste defined as above is the reciprocal of the Stefan number conventionally used and simply represents the dimensionless latent heat. The dimensionless governing equations in the solid and liquid phases are given below.

Liquid Phase

Continuity Equation:

$$\frac{\partial u^+}{\partial x^+}+\frac{\partial v^+}{\partial y^+}=0 \tag{3}$$

Momentum Equations:

$$\frac{\text{Pe}}{\text{Pr}}\left\{\frac{\partial}{\partial x^+}(u^+u^+)+\frac{\partial}{\partial y^+}(v^+u^+)\right\}=\frac{\partial^2 u^+}{\partial x^{+2}}+\frac{\partial^2 u^+}{\partial y^{+2}}-\frac{\text{Pe}}{\text{Pr}}\frac{\partial p^+}{\partial x^+} \tag{4}$$

$$\frac{\text{Pe}}{\text{Pr}}\left\{\frac{\partial}{\partial x^+}(u^+v^+)+\frac{\partial}{\partial y^+}(v^+v^+)\right\}=\frac{\partial^2 v^+}{\partial x^{+2}}+\frac{\partial^2 v^+}{\partial y^{+2}}-\frac{\text{Pe}}{\text{Pr}}\frac{\partial p^+}{\partial y^+} \tag{5}$$

Energy Equation:

$$\text{Pe}\left\{\frac{\partial}{\partial x^+}(u^+h_L^+)+\frac{\partial}{\partial y^+}(v^+h_L^+)\right\}=\frac{\partial^2 h_L^+}{\partial x^{+2}}+\frac{\partial^2 h_L^+}{\partial y^{+2}} \tag{6}$$

Solid Phase

$$\frac{\text{Pe}}{(\alpha_S/\alpha_L)}\frac{\partial h_S^+}{\partial x^+}=\frac{\partial^2 h_S^+}{\partial x^{+2}}+\frac{\partial^2 h_S^+}{\partial y^{+2}} \tag{7}$$

$$u^+=1,\quad v^+=0. \tag{8}$$

Omitting the details (e.g., see Davis et al., 1985), the boundary conditions are

$$\text{at } y=0\text{: } \frac{\partial u^+}{\partial x^+}=0,\ v^+=0,\ \frac{\partial h_L^+}{\partial y^+}=\frac{\partial h_S^+}{\partial y^+}=0 \tag{9}$$

$$\text{at } r\to\infty\text{: } h_S^+=0 \tag{10}$$

$$\text{at } r=a\text{: } u_r^+=0,\ \frac{\partial}{\partial r^+}\left(\frac{u_\theta^+}{r^+}\right)=0,\ h_L^+=\Theta+\text{Ste}+1 \tag{11}$$

$$\text{at } r=r_m\text{: } u^+=1,\ v^+=0,\ h_S^+=\Theta,\ h_L^+=\Theta+\text{Ste} \tag{12}$$

$$\Theta-\frac{\alpha_S/\alpha_L}{\text{Pe}}\frac{\partial h_S^+}{\partial x^+}=(\Theta+\text{Ste})-\frac{1}{\text{Pe}}\frac{\partial h_L^+}{\partial x^+}. \tag{13}$$

In the above, Eq. (13) represents a special feature of Stefan problems in which the release/absorption of the latent heat occurs. The infinity is represented by a distance 200 to 500 times farther away than the interface, i.e., $r_\infty=(200\sim500)r_m$, depending on the magnitude of parameters. In addition, the thermal boundary condition at infinity is modified downstream into the condition of zero temperature-gradient (see Fig. 2). From Eqs. (1)–(13), it can be easily recognized that the dimensionless numbers characterizing the mathematical model are

$$\text{Pe, Pr, } \alpha_S/\alpha_L\text{, Ste, } \Theta. \tag{14}$$

This implies that u_w and a are not independent variables by themselves but are correlated through the combination Pe. Interestingly, use of u_w and a, although not suitable for a parametric study, has been more popular in most previous works. One thing worthy of further remark is that for a given material all the dimensionless parameters other than Pe are prescribed once and for all. Although the above-listed dimensionless numbers do not fully characterize the process because of the simplified assumptions introduced earlier, the use of them is preferred here owing to the merits of succinctness and clarity. Table 1 summarizes the values of dimensionless parameters pertaining to a number of metals considered in the analysis.

Solution Procedure

The present solution procedure is mainly composed of two parts. The first is that, with a tentatively prescribed position

Nomenclature

a = keyhole radius
h_{ref} = $c_L(T_V-T_m)$ = reference enthalpy
h_{sf} = latent heat
Pe = Péclet number
Pr = Prandtl number
r = radial coordinate
r_m = interface radius
r_∞ = radius of outermost boundary at infinity
Ste = dimensionless latent heat
T_m = melting temperature
T_V = vaporizing temperature
T_∞ = 20°C = ambient temperature
u_w = weld speed
δ = radial thickness of phase
θ = angular coordinate
Θ = dimensionless parameter, Eq. (1)
ξ, η = dimensionless transformed coordinates

Superscripts

$+$ = dimensionless
$\hat{}$ = interface

Subscripts

L = liquid
S = solid

Table 1 Dimensionless parameters for four different metals [see Davis et al. (1985) for dimensional properties]

	Pe†	Pr	α_s/α_L	Ste	Θ
Titanium	0.3571	0.1806	3.0679	0.3236	0.6693
Iron	0.1815	0.0567	3.8657	0.2388	0.5474
Lead	0.2457	0.0368	5.7740	0.1181	0.2047
Aluminium	0.0285	0.0111	2.7778	0.2024	0.2926

† evaluated with $u_w = 1$ mm/s and $a = 1$ mm

of the interface, field variables are sought separately in the solid and liquid domains such that all the given boundary conditions other than Eq. (13) are satisfied. The next is to identify the exact location of the solid/liquid interface that satisfies both the governing equations and all the boundary conditions including the interfacial energy balance Eq. (13). The primary difficulty associated with the former part lies in handling an irregularity of solution domains, and one way to circumvent it is to use coordinate transformations. For this matter the methodology developed by Karki and Patankar (1988) seems to be well suited to treat this kind of problem. The latter part requires successive iterations, which is intrinsic to the nature of multidomain approaches. In order to facilitate the interface-identifying procedure, the concept of the position correction recently proposed by Kim and Kaviany (1992a) is utilized for the treatment of the two-dimensional shape of the interface. Since the details can be found in the above-mentioned papers, only a brief discussion is presented below.

Transformed Equations. By introducing a curvilinear coordinate system

$$x = x(\xi, \eta), \quad y = y(\xi, \eta), \tag{15}$$

the general conservation equation is transformed such that (Vinokur, 1974)

$$\frac{\partial}{\partial \xi}\left(\rho U\phi - \frac{\alpha_\xi \Gamma}{h_\xi}\frac{\partial \phi}{\partial \xi}\right) + \frac{\partial}{\partial \eta}\left(\rho V\phi - \frac{\alpha_\eta \Gamma}{h_\eta}\frac{\partial \phi}{\partial \eta}\right)$$

$$= JS(\xi, \eta) - \frac{\partial}{\partial \xi}\left(\frac{\beta_\xi \Gamma}{h_\eta}\frac{\partial \phi}{\partial \eta}\right) - \frac{\partial}{\partial \eta}\left(\frac{\beta_\eta \Gamma}{h_\xi}\frac{\partial \phi}{\partial \xi}\right) \tag{16}$$

and

$$\begin{aligned} U &= y_\eta u - x_\eta v, & V &= x_\xi v - y_\xi u \\ \alpha_\xi &= h_\xi h_\eta^2 / J, & \alpha_\eta &= h_\eta h_\xi^2 / J \\ \beta_\xi &= \lambda h_\eta / J, & \beta_\eta &= \lambda h_\xi / J \\ h_\xi &= (x_\xi^2 + y_\xi^2)^{1/2}, & h_\eta &= (x_\eta^2 + y_\eta^2)^{1/2} \\ \lambda &= x_\xi x_\eta + y_\xi y_\eta, & J &= x_\xi y_\eta - y_\xi x_\eta. \end{aligned} \tag{17}$$

Once the domain boundaries of each phase are appropriately prescribed, the above set of transformed equations can be immediately discretized and solved as in Karki and Patankar (1988). The momentum equation is solved in a staggered-grid system in terms of the covariant velocity components.

To exploit the interface shape shown in Fig. 2, polar coordinates are selected as a subsidiary system to deploy the corner points of the node cells in the physical space [rectangular coordinates serve as a primary system, as can be seen from Eqs. (15)–(17)]. As such, the following transformation relation

$$\begin{aligned} r &= \begin{cases} a + \delta_L \xi, & 0 \le \xi \le 1 \\ a + \delta_L + \delta_S(\xi - 1), & 1 \le \xi \le 2 \end{cases} \\ \theta &= \eta, \quad 0 \le \eta \le \pi \end{aligned} \tag{18}$$

is chosen where δ_L and δ_S are functions of η only. In the transformed coordinates, the interface is located at $\xi = 1$ and the keyhole at $\xi = 0$. If the flux quantities

$$F = \rho U, \quad J = Fh - \frac{\alpha_\xi \Gamma}{h_\xi}\frac{\partial h}{\partial \xi} \tag{19}$$

across the interface are introduced, the conditions of the interfacial mass and energy conservations can be expressed as

$$\hat{F}_L = \hat{F}_S \tag{20}$$

$$\hat{J}_L = \hat{J}_S \tag{21}$$

which are of natural-boundary-condition type and thus have several remarkable advantages over the conventional expressions (Kim and Kaviany, 1992a, b; Kim et al., 1993). Note that the condition $\partial h/\partial \eta = 0$ at the interface has been employed in Eq. (19).

Identification of the Interface Location. The exact location of the interface is determined iteratively starting from an arbitrarily prescribed interface shape. For economy of computation, an intermediate interface position for each iteration should remain as close to the final solution as possible, especially at the end of the iteration procedure. To achieve this objective, the position-correction equation (Kim and Kaviany, 1992a) is employed in such a way that it is applied individually to each circumferential node by assuming locally one-dimensional behavior. First, the interface and the boundary at infinity are expressed as

$$r_m = a + \delta_L, \quad r_\infty = a + \delta_L + \delta_S \equiv C r_m \tag{22}$$

where C is a predetermined constant ($200 \sim 500$) and its value is selected so as not to affect the solution. Unless the interface is correctly located, the temperature field thereby obtained will not in general satisfy Eq. (21) along the interface. Therefore, the tentative interface position is corrected at each point by

$$r_m = r_m^*(1 + \omega_m) \tag{23}$$

where an asterisk denotes the value at the previous iteration [note that $\omega_m = \omega_\infty$ from Eq. (22)]. With the details omitted, a concise expression for ω_m becomes (Kim and Kaviany, 1992a)

$$p_m \omega_m = \hat{J}_L - \hat{J}_S, \quad p_m = \frac{a}{\delta_L}(\hat{J} - \hat{F}\bar{h})_L. \tag{24}$$

Iteration continues until $\hat{J}_L$ agrees with $\hat{J}_s$ to within 99.95 percent all over the peripheral nodes. The above correction equation allows for an assessment to be made of the validity of convergence in the light of physical reality. This is because the interfacial energy conservation is itself chosen to be the convergence criterion.

Results and Discussion

After a number of test runs, a 45×31 grid system was deployed nonuniformly in the liquid region and a 95×31 grid system in the solid region for computation. Such an arrangement was selected because the results were consistent with those using denser grid systems.

Figure 3 illustrates, in a panoramic view, the way the final interface position is progressively determined. As shown in the figure, iteration begins with a tentative interface that lies inside the exact one; otherwise numerical solutions become unstable in some cases. The question of why such a directional behavior exists in the iteration procedure remains unsolved. In recognition of this trend, we prescribed the initial interface position to be slightly larger than the keyhole and found the desired solutions very easily for all the cases presented below. A tip for enhancing computation efficiency further is to use a large value for the convergence criterion (for the solution of linear algebraic equations) at an early stage of iteration and reduce it as iteration continues. Figure 4 displays a comparison between the present results and those of Davis et al. (1985). It can be seen that the interface size from the work of Davis et al. is notably smaller than ours; the reason for this is probably the relatively coarse grid system used in their work.

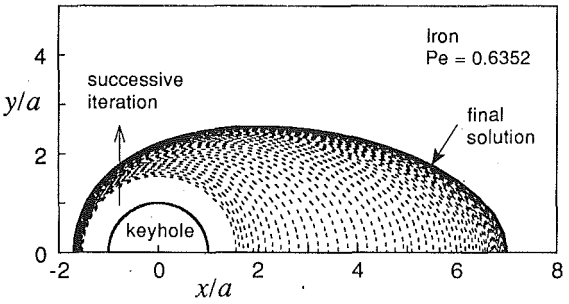

Fig. 3 A panoramic view of the typical procedure to identify the solid/liquid interface location; each curve in the figure corresponds to one iteration step

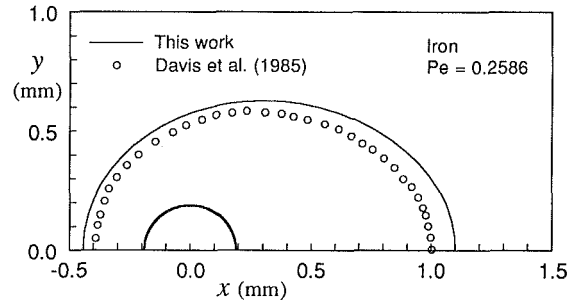

Fig. 4 Comparison of the interface position with an existing solution for the case of iron and Pe = 0.2586 (e.g., $a = 0.19$ mm, $u_w = 7.5$ mm/s)

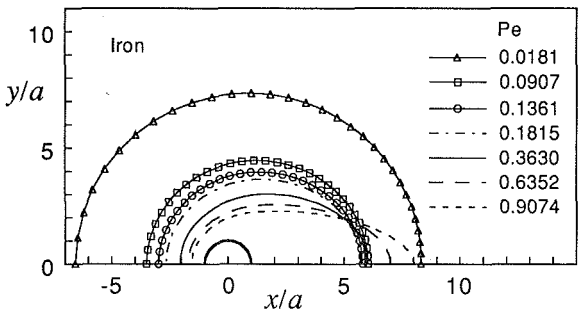

Fig. 5 Interface migration pattern in response to variation of Pe for the case of iron

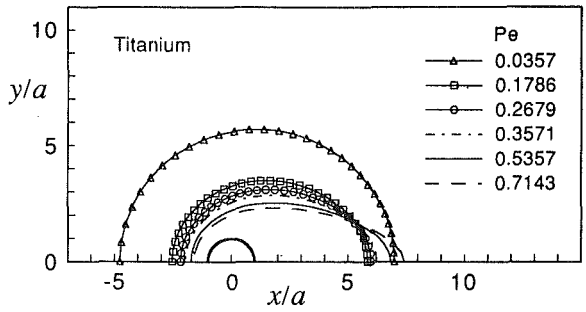

Fig. 6 The influence of Pe on the molten-titanium morphology

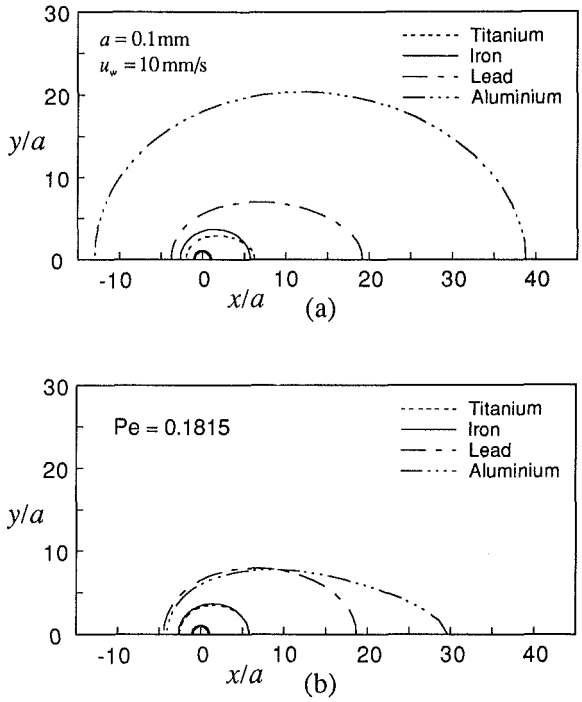

Fig. 7 Melt-zone morphology for various materials: (*a*) fixed values of u_w and a, (*b*) fixed Pe

Figure 5 shows how the interface migrates in response to variation of the Péclet number. In order to facilitate discussion, the keyhole radius is regarded as fixed and, therefore, Fig. 5 represents the changes in the interface positions subject to increasing u_w. From the known fact that the case of $Pe = 0$ gives rise to no steady-state solution due to a singularity (Davis et al., 1985), it might be inferred that the smaller Pe, the farther away the interface is from the keyhole at all angles. But this hasty conclusion is valid only up to $Pe \sim 0.18$, as is apparent from Fig. 5. In fact there exists a transition Péclet number above which the melt zone is more streamlined and elongated downstream. However, in a previous numerical study by Hsu and Rubinsky (1988) on keyhole welding with stainless-steel 304, this fact has apparently not been recognized, probably due to the restricted range of weld speed considered in their work. Meanwhile, a feature that is in good agreement with their work is that the width of the melt zone narrows down continuously with increasing Pe. In order to see if the observed transition behavior is of a universal character, we repeated the same kind of analysis but, this time, for the case of titanium; the results so obtained are presented in Fig. 6. An interface migration pattern similar to Fig. 5 can be readily recognized there but with a slightly different transition Pe. Therefore, we conclude that the melt zone has a large and nearly circular shape at lower Pe, its size (normalized by the keyhole area) diminishes with increasing Pe up to a certain point, and then starts to elongate downstream with further increase in Pe. We also conclude that such a migration pattern takes place irrespective of the materials used.

So far we have discussed the influence of Pe on the melt-zone morphology for given material properties. We now turn our attention to the effects of material properties. For this, the role of weld speed is fixed by specifying either the values of u_w and a or the Péclet number. Both cases are plotted in Fig. 7 where four different metals (titanium, iron, lead, and aluminum) are considered. The case in Fig. 7(*a*) is in reality the same as the one considered by Davis et al. (1985). However, comparison (cf. Fig. 9 in their work) shows some discrepancies. First, the melt zone from the present study is generally of a larger size, which might be due to different grid arrangements employed. Second, the interfaces both for iron and for titanium intersect downstream in our study. Third, Davis et al. claimed that the melt-zone size is the largest for the case of lead, which is in direct contrast with our results.

These discrepancies led us to investigate them further, especially the last one. Figure 7(*b*) informs us that even for a fixed Pe, aluminum has the largest size of molten zone. Therefore, with the remaining dimensionless parameters (Pr, α_s/α_L,

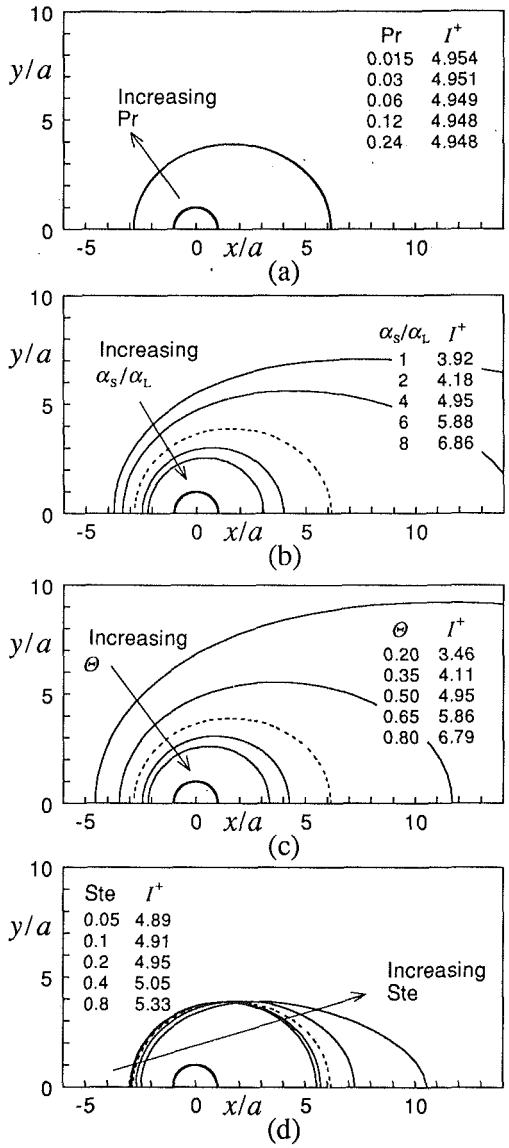

Fig. 8 Interface migration pattern subject to variation of each dimensionless property. The results are for a hypothetical material whose properties are Pr = 0.06, $\alpha_S/\alpha_L = 4$, Ste = 0.2 and $\Theta = 0.5$ and obtained by varying only (*a*) Pr, (*b*) α_S/α_L, (*c*) Θ, and (*d*) Ste. The Péclet number is fixed as Pe = 0.18 for all cases.

Ste, and Θ), a parametric study is undertaken to identify the influence of each dimensionless number. Accordingly, an imaginary material is taken into consideration purely for a parametric study such that Pr = 0.06, $\alpha_S/\alpha_L = 4$, Ste = 0.2, and $\Theta = 0.5$. For the case of this material and a fixed Pe (Pe = 0.18), Fig. 8 exhibits the migration patterns of the interface morphology in response to variation of each dimensionless property alone. Also shown is the dimensionless power absorbed by the material that is evaluated as

$$I^+ = \frac{I}{k_L(T_V - T_m)D}, \quad I = \int_0^{2\pi} -k_L Dr \frac{\partial T_L}{\partial r}\bigg|_{r=a} d\theta \qquad (25)$$

where D is the plate thickness. Generally speaking, the melt zone shrinks as α_S/α_L and Θ increase, while it expands and shifts downstream with increasing Ste (Fig. 8). In particular, variation of Pr brings forth negligible changes in the interface location and in the dimensionless power input I^+. Here, Ste acts as thermal inertia so that solidification takes place quickly downstream at lower Ste, thus creating a melt zone of small size. Furthermore, the width of the melt zone is hardly affected

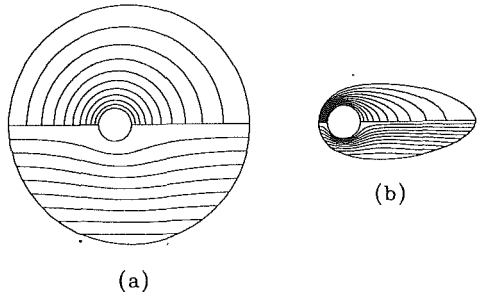

Fig. 9 Contour plots for velocity and temperature fields in the molten iron: (*a*) Pe = 0.0181 and (*b*) Pe = 0.9074; isolines are drawn by equal increments

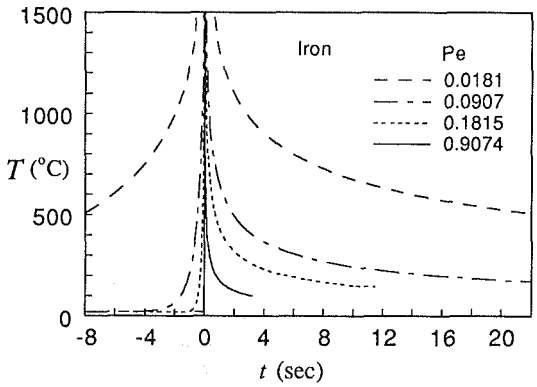

Fig. 10 Timewise variation of temperature at a fixed position ($x = 0$, $y = 0$) in the weld path for the case of iron

by changes in Ste. This is caused by the fact that melting and resolidification occur mostly in a direction parallel to the weld path and do not propagate far away in the vertical direction. Variation of I^+ has a tendency to increase with α_S/α_L, Θ, and Ste. It should be kept in mind that, even though material properties actually do not change in the above manner, the main purpose of working with Fig. 8 was to enhance our understanding of the influence of each parameter.

Now we go back to address the discrepancy discussed with Fig. 7. When dimensionless properties between lead and aluminum are examined (see Table 1), α_S/α_L and Ste vary in such a way as to make the melt zone of aluminum larger than is the case with lead, while Θ varies in the opposite direction. As was noted from Fig. 8(*a*), Pr alone has a negligible effect on the interface location. It is highly likely from Table 1 that the combined effect caused by changes in α_S/α_L and Ste is predominant thus causing aluminum to have the largest size of melt zone; this reasoning is confirmed by the results shown in Fig. 7.

The flow and temperature distributions in the molten iron are plotted in Fig. 9 for Pe = 0.0181 and 0.9074. It is evident that isotherms are of elliptic shape and shift downstream as Pe increases. The flow pattern shows streamlined behavior well and no wake is evident at the rear of the keyhole; the latter is because a frame of reference moving with the keyhole has been used in the model formulation. These results agree qualitatively with previous studies (Davis et al., 1985; Hsu and Rubinsky, 1988). The temperature distribution in the solid iron along the x axis only is depicted Fig. 10, where the abscissa is adjusted by a time scale a/u_w. Since $x/a \sim t(a/u_w)^{-1}$, the curves in Fig. 10 are interpreted as timewise variation of the temperature at a fixed point in the weld path. As expected, heating and cooling of the material proceeds more rapidly with increasing Pe; this fact has also been observed in other works (Dowden et al., 1983; Hsu and Rubinsky, 1988). Because a rapid rate of change

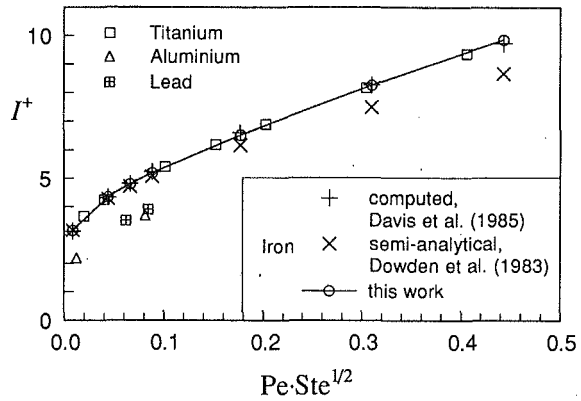

Fig. 11 The dimensionless minimum power supply to maintain keyhole-welding

in temperature may cause fracture of the weld, the results are of importance in understanding the welding process (Hsu and Rubinsky, 1988). Therefore, an optimum value of the weld speed should be determined by two conflicting considerations—the increasing possibility of fracture of the weld on the one hand and the diminishing size of the heat affected zone on the other, at higher weld speeds.

Figure 11 displays the dimensionless minimal power input, I^+, to maintain keyhole welding versus $Pe \cdot Ste^{1/2}$. The results are consistent with the accepted fact that the input power increases almost linearly with weld speed for a given material and keyhole size. Figure 11 shows that variation of I^+ for both iron and titanium correlates well with $Pe \cdot Ste^{1/2}$; this might be due to moderate changes of α_S/α_L and Θ between iron and titanium. For the case of lead and aluminum, deviation from the curve is expected to be mostly due to lower Θ values (see Table 1). Comparison with the results of Davis et al. (1985) shows good agreement in spite of a significant discrepancy between the interface locations (see Fig. 4); this is because the minimal input power is evaluated by integration of the temperature gradient at the keyhole surface and thus is insensitive to the exact location of the solid/liquid interface.

Conclusion

An existing two-dimensional steady-state keyhole model for high power density welding processes was studied, focusing on the interface morphology, the fluid flow, and heat transfer characteristics as well as other relevant features. The concept of the position correction via successive iterations was employed to identify the location of the solid/liquid interface which is unknown a priori. From the nondimensionalization procedure, the dimensionless numbers associated with the keyhole model were considered. It is found that the effect of keyhole radius and the weld speed can be solely represented by Pe. A parametric study reveals a new pattern of the interface migration in response to variation of Pe. It is also found that the material properties can be effectively described by four dimensionless numbers: Pr, α_S/α_L, Θ, and Ste. The influence of each of these numbers is for the first time investigated by varying each parameters and fixing others. The results reveal that the size of the molten region, and thereby the heat affected zone, diminishes as α_S/α_L and Θ increase, is hardly affected by Pr, and increases with an increase in Ste. Together with these new findings, features already observed in previous studies are reaffirmed in this study.

Acknowledgments

This research was carried out under the financial support of the Korea Science and Engineering Foundation (KOSEF) through the Seoul National University for which support the authors are grateful.

References

Davis, M., Kapadia, P., and Dowden, J., 1985, "Solution of a Stefan Problem in the Theory of Laser Welding by Method of Lines," *Journal of Computational Physics*, Vol. 60, pp. 534–548.

Dowden, J., Davis, M., and Kapadia, P., 1983, "Some Aspects of the Fluid Dynamics of Laser Welding," *Journal of Fluid Mechanics*, Vol. 126, pp. 123–146.

Hsu, Y. F., and Rubinsky, B., 1988, "Two-Dimensional Heat Transfer Study on the Keyhole Plasma Arc Welding Process," *International Journal of Heat and Mass Transfer*, Vol. 31, pp. 1409–1421.

Karki, K. C., and Patankar, S. V., 1988, "Calculation Procedure for Viscous Incompressible Flows in Complex Geometries," *Numerical Heat Transfer*, Vol. 14, pp. 295–307.

Kim, C.-J., and Kaviany, M., 1992a, "A Fully Implicit Method for Diffusion-Controlled Solidification of Binary Alloys," *International Journal of Heat and Mass Transfer*, Vol. 35, pp. 1143–1154.

Kim, C.-J., and Kaviany, M., 1992b, "A Numerical Method for Phase-Change Problems With Convection and Diffusion," *International Journal of Heat and Mass Transfer*, Vol. 35, pp. 457–467.

Kim, C.-J., Ro, S. T., and Lee, J. S., 1993, "An Efficient Computational Technique to Solve the Moving Boundary Problems in the Axisymmetric Geometries," *International Journal of Heat and Mass Transfer*, Vol. 36, pp. 3759–3764.

Lancaster, J. F., 1983, *The Physics of Welding*, Pergamon Press, NY.

Mazumder, J., and Steen, W. M., 1980, "Heat Transfer Model for CW Laser Material Processing," *Journal of Applied Physics*, Vol. 51, pp. 941–947.

Miyazaki, T., and Giedt, W. H., 1982, "Heat Transfer From an Elliptic Cylinder Moving Through an Infinite Plate Applied to Electron Beam Welding," *International Journal of Heat and Mass Transfer*, Vol. 25, pp. 807–814.

Swift-Hook, D. T., and Gick, A. E., 1973, "Penetration Welding With Lasers," *Welding Journal*, Vol. 52, pp. 492–499.

Vinokur, M., 1974, "Conservative Equations of Gas Dynamics in Curvilinear Coordinate Systems," *Journal of Computational Physics*, Vol. 14, pp. 105–125.

Coupled Heat and Mass Transfer With One Discrete Sublimation Moving Interface and One Desorption Mushy Zone

Shi-Wen Peng[1]
Department of Power Engineering,
Huazhong University of
Science & Technology,
Wuhan, Hubei, 430074,
People's Republic of China

Guo-Qian Chen
Department of Mechanics,
Peking University,
Beijing, 100871,
People's Republic of China

The present work discusses coupled heat and mass transfer during freeze-drying of a rigid product, as well as accelerated freeze-drying where sublimation and desorption occur concurrently. A desorption mushy zone model was developed to describe the desorption drying. An exact solution was obtained for coupled heat and mass transfer with one discrete sublimation moving interface and one desorption mushy zone where mass transfer is controlled by both Fick and Darcy laws. The effects of several parameters on the sublimation and desorption are analyzed and discussed.

Introduction and Concept of Desorption Mushy Zone

Freeze-drying of moisture in a porous medium has wide applications in separation processes, food technology, etc. Systematic freeze-drying requires two successive steps, i.e., sublimation drying and desorption drying. Sublimation drying has received considerable attention over the past thirty years. Lin (1981, 1982a, 1982b) analyzed the sublimation and desublimation processes in a semi-infinite porous medium by assuming the mass transfer is controlled by Fick Law due to the extremely low vacuum pressure. Fey and Boles (1987a, 1987b, 1988) presented a complete description of the vacuum sublimation process for which exact analytical solutions were obtained to analyze the effect of convection, Fick and Darcy Laws, and recondensation on the rate of sublimation. Their formulation was based on the Luikov (1975) system, and the vapor flow in the dried region was considered as the result of both moisture concentration and pressure gradients in the porous medium. Peng and Cheng (1990, 1991) developed some approximate solutions of the sublimation dehydration. However, in the strict sense, since only sublimation was considered, these results may only apply where the surface heating temperature is lower than when desorption takes place.

Peng et al. (1992a, 1992b) discussed accelerated freeze-drying where sublimation and desorption occur simultaneously (Mellor, 1978, p. 73). By assuming the desorption drying as the second discrete moving interface, they derived the exact solutions of coupled heat and mass transfer with double moving interfaces in a porous half-space for two cases where mass transfer is controlled by Fick law, and both Fick and Darcy laws, respectively.

In what follows, further attention is paid to desorption process. The desorption of moisture depends on the temperature and pressure (Kumagai et al., 1978). However, the pressure gradient in the medium may be much less than that of temperature for low vacuum pressure case, so that the desorption may be approximately viewed as an isobaric process (Lin, 1981). Figure 1 shows a typical adsorption isobar where adsorption amount is plotted as the function of temperature. The vapor or moisture is adsorbed on the porous wall by physisorption and chemisorption. Since chemisorption moisture is very difficult to desorb due to the strong combination of chemical key and ion, only physisorption moisture can be desorbed in the freeze-drying process (Mellor, 1978), which occurs over an extended temperature range (desorption mushy zone). The present work addresses the analysis of coupled heat and mass transfer with one discrete sublimation moving interface and one desorption mushy zone.

Statement of the Problem

The physical model is shown in Fig. 2. A semi-infinite frozen porous medium is exposed to an environment where the pressure and the vapor concentration are maintained below the triple point of the bounded substance, and the temperature is higher than the desorption temperature of the residual moisture in the sublimated region. The porous medium is assumed to be composed of very small solid particles of equal size. Also, the medium is isotropic, homogeneous, and rigid. The temperature and mass content are initially constant throughout the medium.

Although a practical freeze-drying process is subject to radiation boundary condition, the temperature, concentration, and pressure at the surface change with time. As the first step,

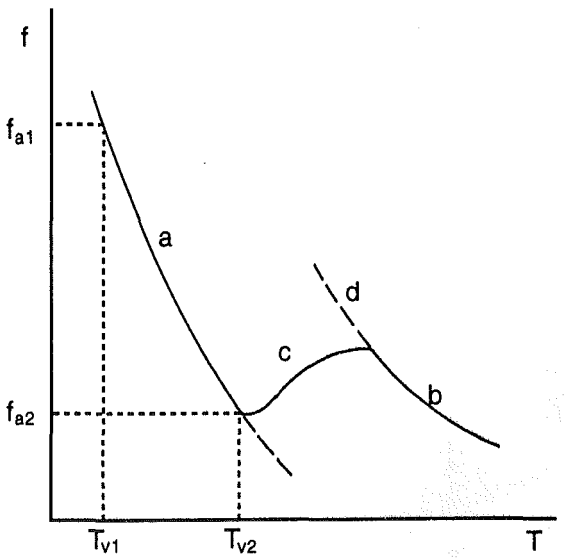

Fig. 1 A typical adsorption isobar: (*a*) physical adsorption equilibrium; (*b*) chemical adsorption equilibrium; (*c*) unstable transition region

[1]Present address: Department of Mechanical Engineering, Ehime University, Matsuyama 790, Japan.

Contributed by the Heat Transfer Division for publication in the JOURNAL OF HEAT TRANSFER. Manuscript received by the Heat Transfer Division October 1992; revision received June 1993. Keywords: Moving Boundaries, Phase-Change Phenomena, Porous Media. Associate Technical Editor: R. Viskanta.

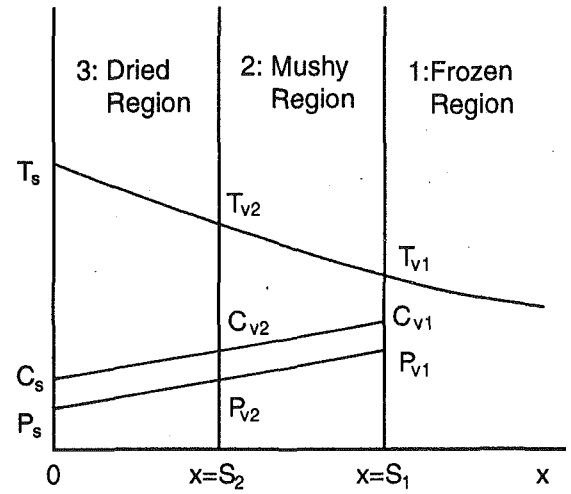

Fig. 2 Physical model

we consider the case where the temperature, vapor concentration, and surface pressure at $x = 0$ are maintained at constant values at times greater than zero (Fey and Boles, 1988), and the sublimation and desorption processes begin.

The assumption is made that the desorption takes place just after the sublimation interface. Since the vapor is transferred outwardly and heat is supplied from the dried region, the frozen region, the desorption mushy region, and the dried region are formed and separated by two constant temperature moving interfaces (Hill and Sunderland, 1971) defined by $x_1 = S_1(t)$ and $x_2 = S_2(t)$, respectively. $S_1(t)$ refers to the sublimation front, and the first desorption front also. $S_2(t)$ refers to the second desorption front. The concentration and pressure at the sublimation and second desorption fronts are assumed as unknown constants, which will be determined in the process of solution. The sublimation and second desorption temperatures are assumed as known constants.

To formulate the theoretical model of the coupled heat and mass transfer with one discrete sublimation moving interface and one desorption mushy zone in a porous body, additional assumptions are made as follows:

(*i*) One-dimensional heat and mass transfer is considered. Both the Darcy and Fick laws for vapor transfer are valid through the mushy and dried regions (Fey and Boles, 1987b).

(*ii*) The solid phase density of moisture in the porous medium is far larger than its vapor phase density so that the effect of convection may be neglected (Fey and Boles, 1987a). Similarly, the heat radiation and thermal expansion of the medium, condensation, and Soret and Dufour effects are assumed to be small and negligible.

(*iii*) The mushy and dried regions contain the vapor resulting from the sublimation and desorption processes and a small amount of residual air in relation to the vapor mass. Furthermore, the effect of desorption on the diffusion of pressure is neglected due to a small amount of residual moisture for desorption.

(*iv*) The thermophysical properties remain constant, but they may be different for different regions.

Nomenclature

C = molar concentration of moisture, mol/m^3
C_i = molar concentration of frozen bounded substance, mol/m^3
$\overline{C}$ = C/C_3 = nondimensional molar concentration of vapor
$\overline{C}_i$ = C_i/C_3 = nondimensional molar concentration of frozen bounded substance
E = $C_3 M_m \alpha_2^* L(\epsilon - f_{a1})/(T_3 k_2)$ = nondimensional free water fraction
f_{a1} = adsorption water volume fraction just after sublimation ends
f_{a2} = adsorption water volume fraction due to chemical adsorption, etc., which cannot be desorbed
H_p = desorption heat, J/kg
k = effective thermal conductivity, W/mK
k_{21} = k_2/k_1
k_{23} = k_2/k_3
kT_1 = $k_1(\vartheta_{v1} - \vartheta_0)/[k_2(\vartheta_{v2} - \vartheta_{v1})]$
kT_3 = $k_3(\vartheta_s - \vartheta_{v2})/[k_2(\vartheta_{v2} - \vartheta_{v1})]$
L = latent heat of sublimation, J/kg
Lu_2 = α_{m2}/α_2^* = Luikov number in the mushy zone
Lu_{p2} = α_{p2}/α_2^* = Luikov filtration diffusivity in the mushy zone
M_m = molecular weight of water
P = pressure, Pa
$\overline{P}$ = P/P_3 = nondimensional pressure
R = $C_3 R_0 T_3/P_3$ = nondimensional gas constant
R_0 = universal gas constant
$S_1(t)$ = position of sublimation front, m
$S_2(t)$ = position of desorption front, m
t = time, s
T = temperature, K
T_0 = initial temperature, K
x = space coordinate, m
$Z_2(\eta)$ = $C_2(\eta) + \beta_1 P_2(\eta) + \beta_2 T_2(\eta)$
$Z_3(\eta)$ = $C_3(\eta) + \beta_3 P_3(\eta)$
α = thermal diffusivity, m^2/s
α_m = effective diffusivity of moisture, m^2/s
α_p = filtration motion diffusion coefficient of vapor, m^2/s
α_{21} = α_2^*/α_1
α_{23} = α_2^*/α_3
α_{m23} = α_{m2}/α_{m3}
α_{p23} = α_{p2}/α_{p3}
α_2^* = effective thermal diffusivity defined by Eq. (11)
φ_2 = desorption parameter defined by Eq. (12)
ϵ = porosity
κ = permeability in Luikov (1975) system, s
ϑ = T/T_3 = nondimensional temperature
ϑ_0 = T_0/T_3 = nondimensional initial temperature
ρ = molar density of absorbed water, mol/m^3
λ_1, λ_2 = nondimensional position of sublimation and desorption fronts
η = $x/2\sqrt{\alpha_2^* t}$
β_1 = $\dfrac{\kappa_2}{\alpha_{m2} - \alpha_{p2}}$
β_2 = $\dfrac{\varphi_2}{\alpha_{m2} - \alpha_2^*}$
β_3 = $\dfrac{\kappa_3}{\alpha_{m3} - \alpha_{p3}}$
Δ_1 = $-\dfrac{\beta_1 P_3}{C_3}$
Δ_2 = $-\dfrac{\beta_2 T_3}{C_3}$
Δ_3 = $-\dfrac{\beta_3 P_3}{C_3}$

Subscripts

1 = frozen region
2 = desorption mushy region
3 = dried region; triple point
s = surface
$v1$ = sublimation front
$v2$ = second desorption front

(v) The ideal gas law is assumed to be valid at the sublimation and second desorption interfaces.

From the above assumptions, the temperature distribution in the frozen region ($S_1(t) < x < \infty$) is expressed by Eq. (1), and the temperature, concentration, and pressure distributions in the dried region ($0 < x < S_2(t)$) are represented by Eqs. (5), (6), and (7) in our recent work (Peng et al., 1992b), while heat and mass transfer in the desorption mushy zone ($S_2(t) < x < S_1(t)$) may be formulated by the following equations:

$$\partial T_2(x, t)/\partial t = \alpha_2 \partial^2 T_2(x, t)/\partial x^2 - \alpha_2(\rho M_m H_p/k_2)\partial f_a(x, t)/\partial t \quad (1)$$

$$\partial C_2(x, t)/\partial t = \alpha_{m2}\partial^2 C_2(x, t)/\partial x^2 + \kappa_2 \partial^2 P_2(x, t)/\partial x^2 + \rho \partial f_a(x, t)/\partial t \quad (2)$$

$$\partial P_2(x, t)/\partial t = \alpha_{p_2}\partial^2 P_2(x, t)/\partial x^2 \quad (3)$$

where Eq. (1) describes the temperature distribution. Equations (2) and (3), based on the theories described above and the Luikov system (Luikov, 1975), describe the concentration and pressure fields, respectively. It should be noted that the first and second terms on the right-hand side of Eq. (2) represent the Fick and Darcy Laws, respectively. The second term on the right of Eq. (1) and third term on the right of Eq. (2) represent the desorption heat and mass generation terms, respectively.

The initial and boundary conditions are described by Eqs. (8), (9), and (10); the matching conditions of temperature, concentration, and pressure on the sublimation front can be expressed by Eqs. (11), (12), and (13) in our recent work (Peng et al., 1992b), respectively.

The energy and moisture balances at the sublimation interface yield

$$-k_2 \frac{\partial T_2(S_1, t)}{\partial x} + k_1 \frac{\partial T_1(S_1, t)}{\partial x} = (\epsilon - f_{a1}) C_i M_m L \frac{dS_1(t)}{dt} \quad (4)$$

$$\alpha_{m2} \frac{\partial C_2(S_1, t)}{\partial x} + \kappa_2 \frac{\partial P_2(S_1, t)}{\partial x} = (\epsilon - f_{a1})(C_i - C_{v1}) \frac{dS_1(t)}{dt} \quad (5)$$

By applying the ideal gas law on the sublimation interface, we have

$$P_{v1} = C_{v1} R_0 T_{v1} \quad (6)$$

The matching conditions of temperature, concentration, and pressure on the second desorption front are expressed by Eqs. (17), (18), and (19) in our recent work (Peng et al., 1992b), respectively.

The energy and moisture balances at the desorption interface yield

$$-k_3 \frac{\partial T_3(S_2, t)}{\partial x} + k_2 \frac{\partial T_2(S_2, t)}{\partial x} = 0 \quad (7)$$

$$\alpha_{m3} \frac{\partial C_3(S_2, t)}{\partial x} + \kappa_3 \frac{\partial P_3(S_2, t)}{\partial x} - \alpha_{m2} \frac{\partial C_2(S_2, t)}{\partial x} - \kappa_2 \frac{\partial P_2(S_2, t)}{\partial x} = 0 \quad (8)$$

By applying the ideal gas law at the second desorption interface, we have

$$P_{v2} = C_{v2} R_0 T_{v2} \quad (9)$$

Here we consider the special case in which the adsorption amount $f_a(x, t)$ is a linear function of the temperature of desorption mushy zone, $T_2(x, t)$. As indicated by Glasstone and Lewis (1960), this assumption is a good approximation of desorption process:

$$f_a(x, t) = f_{a1} + \frac{f_{a1} - f_{a2}}{T_{v1} - T_{v2}} (T_2(x, t) - T_{v1}) \quad (10)$$

where f_{a1} represents the adsorption water fraction just after sublimation ends. f_{a2} represents the adsorption water fraction due to chemical adsorption, etc., which cannot be desorbed by desorption drying.

By substituting Eq. (10) into Eqs. (2) and (3) we obtain

$$\partial T_2(x, t)/\partial t = \alpha_2^* \partial^2 T_2(x, t)/\partial x^2 \quad (2')$$

$$\partial C_2(x, t)/\partial t = \alpha_2 \partial^2 C_2(x, t)/\partial x^2 + \kappa_2 \partial^2 P_2(x, t)/\partial x^2 + \varphi_2 \partial^2 T_2(x, t)/\partial x^2 \quad (3')$$

where

$$\frac{1}{\alpha_2^*} = -\frac{\rho M_m H_p}{k_2} \frac{f_{a1} - f_{a2}}{T_{v2} - T_{v1}} + \frac{1}{\alpha_2} \quad (11)$$

$$\varphi_2 = -\rho \alpha_2^* \frac{f_{a1} - f_{a2}}{T_{v2} - T_{v1}} \quad (12)$$

Solution

We introduce the nondimensional similarity variable as given by Özişik (1980):

$$\eta = x/2\sqrt{\alpha_2^* t} \quad (13)$$

into the equations described as above, and define two new variables $Z_2(\eta)$ and $Z_3(\eta)$ as follows:

$$Z_2(\eta) = C_2(\eta) + \beta_1 P_2(\eta) + \beta_2 T_2(\eta) \quad (14)$$

$$Z_3(\eta) = C_3(\eta) + \beta_3 P_3(\eta) \quad (15)$$

where

$$\beta_1 = \frac{\kappa_2}{\alpha_{m2} - \alpha_{p2}}, \quad \beta_2 = \frac{\varphi_2}{\alpha_{m2} - \alpha_2^*}, \quad \beta_3 = \frac{\kappa_3}{\alpha_{m3} - \alpha_{p3}} \quad (16)$$

The locations of the sublimation and the second desorption interfaces are assumed to be given by

$$S_1(t) = 2\lambda_1\sqrt{\alpha_2^* t}, \quad S_2(t) = 2\lambda_2\sqrt{\alpha_2^* t} \quad (17)$$

respectively, where λ_1 and λ_2 are two unknown constants to be determined during the solution. With the introduction of the two variables, η and λ, we note that the dried region corresponds to $0 < \eta < \lambda_2$, the desorption mushy region corresponds to $\lambda_2 < \eta < \lambda_1$, and the frozen region corresponds to $\lambda_1 < \eta < \infty$. The problem is transformed to a system of ordinary differential equations for T_1, T_2, T_3, P_2, P_3, Z_2, and Z_3 with variable coefficients subject to the transformed boundary and interface conditions. This system can be solved exactly, and the solutions of $C_2(\eta)$ and $C_3(\eta)$ are obtained from Eqs. (14) and (15), respectively. After substituting the solutions above into the interface equations and performing the necessary manipulations, we obtain the six transcendental interface equations. By using the nondimensional parameters defined in the nomenclature, the solutions are presented as follows:

$$\vartheta_1(\eta) = \vartheta_0 + (\vartheta_{v1} - \vartheta_0) \frac{\operatorname{erfc}(\eta\sqrt{\alpha_{21}})}{\operatorname{erfc}(\lambda_1\sqrt{\alpha_{21}})} \quad (18)$$

$$\vartheta_2(\eta) = \vartheta_{v1} + (\vartheta_{v2} - \vartheta_{v1}) \frac{\operatorname{erf}(\eta) - \operatorname{erf}(\lambda_1)}{\operatorname{erf}(\lambda_2) - \operatorname{erf}(\lambda_1)} \quad (19)$$

$$\vartheta_3(\eta) = \vartheta_s + (\vartheta_{v2} - \vartheta_s) \frac{\operatorname{erf}(\eta\sqrt{\alpha_{23}})}{\operatorname{erf}(\lambda_2\sqrt{\alpha_{23}})} \quad (20)$$

$$\overline{P}_2(\eta) = \overline{P}_{v2} + (\overline{P}_{v1} - \overline{P}_{v2}) \frac{\operatorname{erf}(\eta/\sqrt{\mathrm{Lu}_{p2}}) - \operatorname{erf}(\lambda_2/\sqrt{\mathrm{Lu}_{p2}})}{\operatorname{erf}(\lambda_1/\sqrt{\mathrm{Lu}_{p2}}) - \operatorname{erf}(\lambda_2/\sqrt{\mathrm{Lu}_{p2}})} \quad (21)$$

$$\overline{P}_3(\eta) = \overline{P}_s + (\overline{P}_{v2} - \overline{P}_s) \frac{\operatorname{erf}(\eta\sqrt{\alpha_{p23}/\mathrm{Lu}_{p2}})}{\operatorname{erf}(\lambda_2\sqrt{\alpha_{p23}/\mathrm{Lu}_{p2}})} \quad (22)$$

$$\overline{C}_2(\eta) = (\overline{C}_{v2} - \Delta_2\vartheta_{v2}) + \Delta_1(\overline{P}_{v1} - \overline{P}_{v2}) \times \frac{\mathrm{erf}(\eta/\sqrt{\mathrm{Lu}_{p2}}) - \mathrm{erf}(\lambda_2/\sqrt{\mathrm{Lu}_{p2}})}{\mathrm{erf}(\lambda_1/\sqrt{\mathrm{Lu}_{p2}}) - \mathrm{erf}(\lambda_2/\sqrt{\mathrm{Lu}_{p2}})} + [(\overline{C}_{v1} - \overline{C}_{v2}) - \Delta_1(\overline{P}_{v1} - \overline{P}_{v2}) + \Delta_2(\vartheta_{v2} - \vartheta_{v1})] \frac{\mathrm{erf}(\eta/\sqrt{\mathrm{Lu}_2}) - \mathrm{erf}(\lambda_2/\sqrt{\mathrm{Lu}_2})}{\mathrm{erf}(\lambda_1/\sqrt{\mathrm{Lu}_2}) - \mathrm{erf}(\lambda_2/\sqrt{\mathrm{Lu}_2})} + \Delta_2\vartheta_{v1} + \Delta_2(\vartheta_{v2} - \vartheta_{v1}) \frac{\mathrm{erf}(\eta) - \mathrm{erf}(\lambda_1)}{\mathrm{erf}(\lambda_2) - \mathrm{erf}(\lambda_1)} \quad (23)$$

$$\overline{C}_3(\eta) = \overline{C}_s + \Delta_3(\overline{P}_{v2} - \overline{P}_s) \frac{\mathrm{erf}(\eta\sqrt{\alpha_{p23}/\mathrm{Lu}_{p2}})}{\mathrm{erf}(\lambda_2\sqrt{\alpha_{p23}/\mathrm{Lu}_{p2}})} + [\Delta_3(\overline{P}_s - \overline{P}_{v2}) + (\overline{C}_{v2} - \overline{C}_s)] \frac{\mathrm{erf}(\eta\sqrt{\alpha_{m23}/\mathrm{Lu}_2})}{\mathrm{erf}(\lambda_2\sqrt{\alpha_{m23}/\mathrm{Lu}_2})} \quad (24)$$

The sublimation interface conditions of energy and moisture become

$$\frac{e^{-\lambda_1^2}}{\mathrm{erf}(\lambda_1) - \mathrm{erf}(\lambda_2)} - \sqrt{\alpha_{21}}kT_1 \frac{e^{-\lambda_1^2\alpha_{21}}}{\mathrm{erfc}(\lambda_1\sqrt{\alpha_{21}})} = \frac{\sqrt{\pi}\overline{C}_i E\lambda_1}{\vartheta_{v2} - \vartheta_{v1}} \quad (25)$$

$$\sqrt{\mathrm{Lu}_{p2}}\Delta_1(\overline{P}_{v1} - \overline{P}_{v2}) \frac{e^{-\lambda_1^2/\mathrm{Lu}_{p2}}}{\mathrm{erf}(\lambda_1/\sqrt{\mathrm{Lu}_{p2}}) - \mathrm{erf}(\lambda_2/\sqrt{\mathrm{Lu}_{p2}})} + \sqrt{\mathrm{Lu}_2}[(\overline{C}_{v1} - \overline{C}_{v2}) - \Delta_1(\overline{P}_{v1} - \overline{P}_{v2}) + \Delta_2(\vartheta_{v2} - \vartheta_{v1})] \times \frac{e^{-\lambda_1^2/\mathrm{Lu}_2}}{\mathrm{erf}(\lambda_1/\sqrt{\mathrm{Lu}_2}) - \mathrm{erf}(\lambda_2/\sqrt{\mathrm{Lu}_2})} - \mathrm{Lu}_2\Delta_2(\vartheta_{v2} - \vartheta_{v1}) \times \frac{e^{-\lambda_1^2}}{\mathrm{erf}(\lambda_1) - \mathrm{erf}(\lambda_2)} = \sqrt{\pi}(\epsilon - f_{a1})(C_i - C_{v1})\lambda_1 \quad (26)$$

The ideal gas law on the sublimation front becomes

$$\overline{P}_{v1} = \overline{C}_{v1}R\vartheta_{v1} \quad (27)$$

The second desorption interface conditions of energy and moisture become

$$-\frac{e^{-\lambda_2^2}}{\mathrm{erf}(\lambda_1) - \mathrm{erf}(\lambda_2)} + \sqrt{\alpha_{23}}kT_3 \frac{e^{-\lambda_2^2\alpha_{23}}}{\mathrm{erf}(\lambda_2\sqrt{\alpha_{23}})} = 0 \quad (28)$$

$$\sqrt{\frac{\mathrm{Lu}_{p2}}{\alpha_{p23}}} \frac{\alpha_{m23}}{\mathrm{Lu}_2} \Delta_3(\overline{P}_{v2} - \overline{P}_s) \frac{e^{-\lambda_2^2\alpha_{p23}/\mathrm{Lu}_{p2}}}{\mathrm{erf}(\lambda_2\sqrt{\alpha_{p23}/\mathrm{Lu}_{p2}})} + \sqrt{\frac{\alpha_{m23}}{\mathrm{Lu}_2}} [\Delta_3(\overline{P}_s - \overline{P}_{v2}) + (\overline{C}_{v2} - \overline{C}_s)] \frac{e^{-\lambda_2^2\alpha_{m23}/\mathrm{Lu}_2}}{\mathrm{erf}(\lambda_2\sqrt{\alpha_{m23}/\mathrm{Lu}_2})} - \sqrt{\mathrm{Lu}_{p2}} \frac{\alpha_{m23}}{\mathrm{Lu}_2} \Delta_1(\overline{P}_{v1} - \overline{P}_{v2}) \frac{e^{-\lambda_2^2/\mathrm{Lu}_{p2}}}{\mathrm{erf}(\lambda_1/\sqrt{\mathrm{Lu}_{p2}}) - \mathrm{erf}(\lambda_2/\sqrt{\mathrm{Lu}_{p2}})} - \frac{\alpha_{m23}}{\sqrt{\mathrm{Lu}_2}} [(\overline{C}_{v1} - \overline{C}_{v2}) - \Delta_1(\overline{P}_{v1} - \overline{P}_{v2}) + \Delta_2(\vartheta_{v2} - \vartheta_{v1})] \times \frac{e^{-\lambda_2^2/\mathrm{Lu}_2}}{\mathrm{erf}(\lambda_1/\sqrt{\mathrm{Lu}_2}) - \mathrm{erf}(\lambda_2/\sqrt{\mathrm{Lu}_2})} + \alpha_{m23}\Delta_2(\vartheta_{v2} - \vartheta_{v1}) \frac{e^{-\lambda_2^2}}{\mathrm{erf}(\lambda_1) - \mathrm{erf}(\lambda_2)} = 0 \quad (29)$$

The ideal gas law on the second desorption front becomes

$$\overline{P}_{v2} = \overline{C}_{v2}R\vartheta_{v2} \quad (30)$$

The nondimensional constants λ_1 and λ_2, nondimensional pressure $\overline{P}_{v1}$, molar concentration $\overline{C}_{v1}$ at the sublimation interface, and pressure $\overline{P}_{v2}$, molar concentration $\overline{C}_{v2}$ at the second desorption interface are then obtained by numerically solving the simultaneous Eqs. (25)–(30). Once the interface constants are known, Eqs. (18)–(24) readily yield the exact solution to the coupled heat and mass transfer problem.

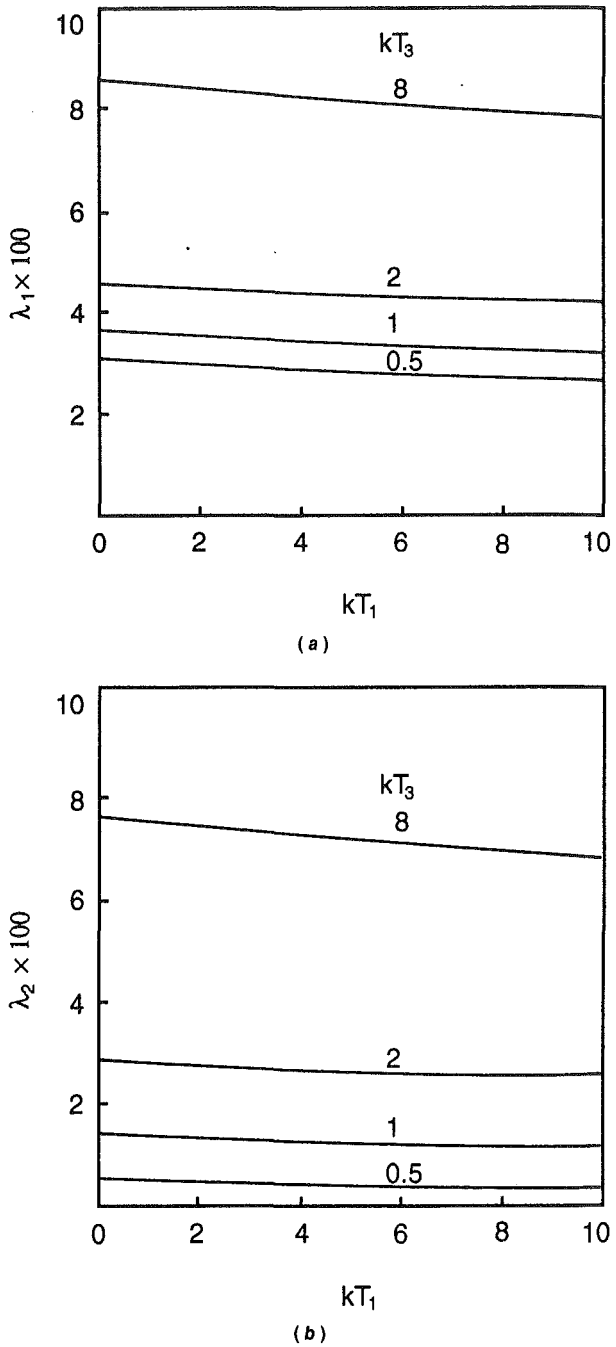

Fig. 3 Effect of dimensionless heat flux kT_1 on dimensionless positions of sublimation and second desorption interfaces λ_1 and λ_2 with dimensionless heat flux kT_3 as parameters

Results and Discussion

For the exact solution of coupled heat and mass transfer with one discrete sublimation moving interface and one desorption mushy zone, the effects of several parameters on the sublimation and desorption processes are analyzed with the help of a computer. On the figures presented in this study, only the parameters whose values are different from the reference values are indicated. The selected reference values include: $k_{21} = 0.037$, $\alpha_{21} = 1$, $\alpha_{23} = k_{23} = \alpha_{m23} = \alpha_{p23} = 1$, $\mathrm{Lu}_2 = 0.1$, $\mathrm{Lu}_{p2} = 300$, $kT_3 = 1$, $\overline{C}_i = 1.9 \times 10^{+5}$, $E = 9.73 \times 10^{-5}$, $\vartheta_s = 1.01$, $\vartheta_{v2} = 0.98$, $\vartheta_{v1} = 0.95$, $\vartheta_0 = 0.7835$, $\epsilon = 0.38$, $f_{a1} = 0.08$, $\Delta_1 = \Delta_2 = \Delta_3 = 0.1$, $\overline{C}_s = \overline{P}_s = 0.2$, $R = 0.987$. The reference values of λ_1 and λ_2 are obtained from Eqs. (25) and (28) based on the above-mentioned reference

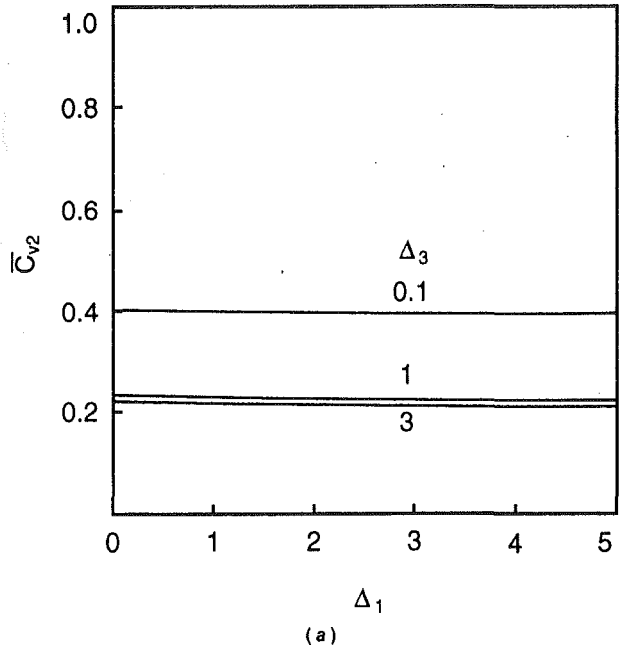

(a)

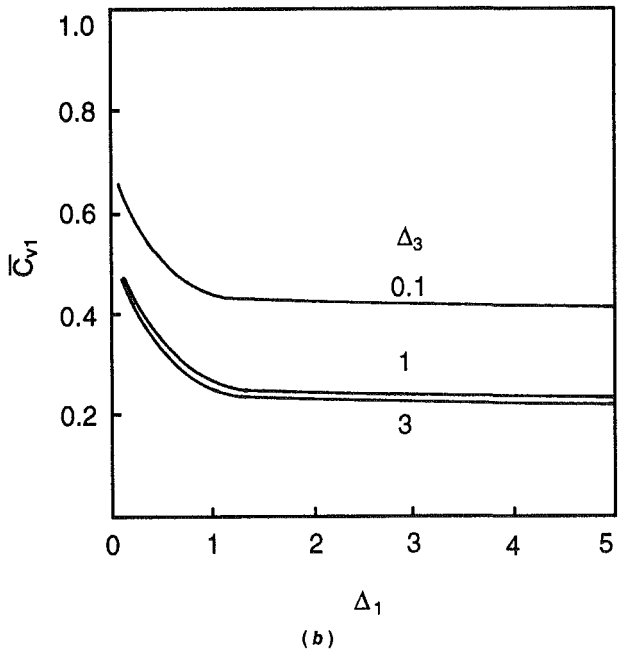

(b)

Fig. 4 Effect of dimensionless permeability Δ_1 on dimensionless vapor concentrations at sublimation and second desorption interfaces $\overline{C}_{v1}$ and $\overline{C}_{v2}$ with dimensionless permeability Δ_3 as parameters

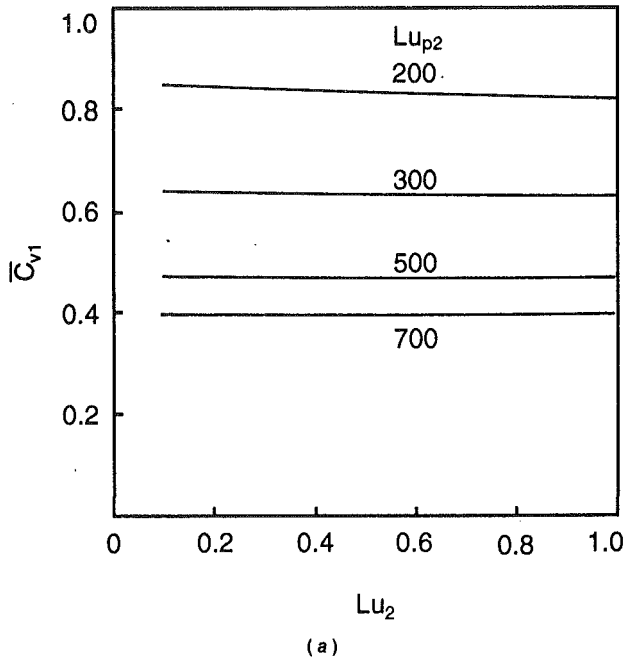

(a)

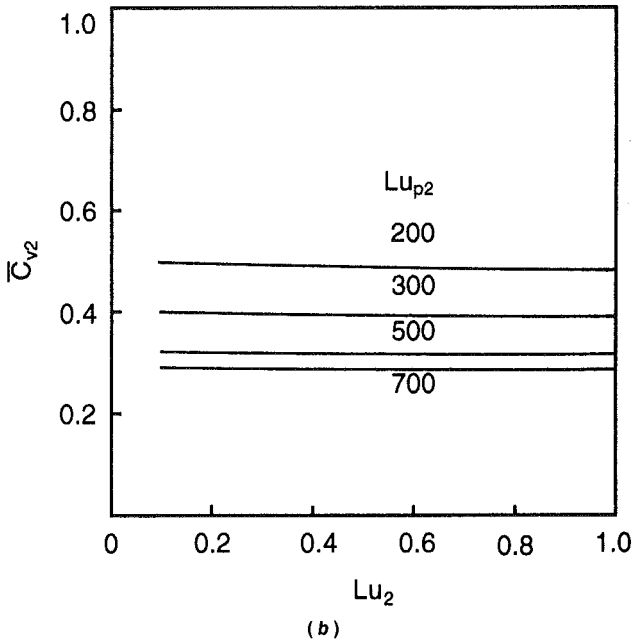

(b)

Fig. 5 Effect of Luikov number Lu_2 on dimensionless vapor concentrations at sublimation and second desorption interfaces $\overline{C}_{v1}$ and $\overline{C}_{v2}$ with Luikov filtration diffusivity Lu_{p2} as parameters

values: $\lambda_1 = 0.0102$, $\lambda_2 = 0.0048$. The reference values can be obtained in the references cited, which apply to the porous medium of sand and ice. It is noted from Luikov (1966) that the values of Lu_{p2} range from 100 to 1000; a value of $Lu_{p2} = 300$ is used here for illustration only.

Figure 3 illustrates the variation of the dimensionless sublimation interface position, λ_1, and the second desorption interface position, λ_2, with the dimensionless heat flux kT_1 for several values of the dimensionless heat flux kT_3. kT_1 represents the ratio of the steady heat flux in the frozen region to that in the mushy region with the same heat conduction distance, while kT_3 represents the ratio of the steady heat flux in the dried region to that in the mushy region with the same heat conduction distance. It is shown that the higher the value of kT_1 (which means that heat can be conducted into the frozen region more easily), the slower is the sublimation and desorption; the higher the value of kT_3 (which means that heat can be conducted into the mushy zone and the sublimation interface more easily), the faster is the sublimation and desorption.

Figure 4 illustrates the variation of the dimensionless concentrations at the sublimation and second desorption interfaces, $\overline{C}_{v1}$ and $\overline{C}_{v2}$, with the nondimensional permeability in the mushy region, Δ_1, for several values of nondimensional permeability in the dried region, Δ_3. A porous medium with high permeability allows the vapor to move easily through the medium and the concentrations become smaller. The effect of Δ_2 on the mass transfer is found to be negligible for a wide range of values of Δ_2.

Figure 5 illustrates the variation of $\overline{C}_{v1}$ and $\overline{C}_{v2}$ with the

Luikov moisture diffusivity in the mushy region, Lu_2, for several values of the Luikov filtration diffusivity in the mushy region, Lu_{p2}. Since Lu_2 is a measure of mass diffusion, and Lu_{p2} is a measure of the speed of propagation of pressure waves through the material, one would expect decreased vapor concentration in the mushy and dried regions as Lu_2 and Lu_{p2} increase.

Conclusion

As in our previous work, the present paper studies the accelerated freeze-drying where sublimation and desorption take place simultaneously. Special attention is paid to the desorption process, and a desorption mushy zone model was developed to describe the process. The assumption is made that the desorption occurs just after the sublimation interface, thus the whole porous body is divided into three regions, i.e., frozen region, desorption mushy region, and dried region by two interfaces, i.e., the sublimation moving interface and the second desorption interface.

An exact solution was obtained for coupled heat and mass transfer with one discrete sublimation moving interface and one desorption mushy zone in the porous half-space. Moisture transfer in the desorption mushy region and the dried region is the result of both vapor concentration and pressure gradients, with effects on the rates of sublimation, desorption, and vapor transfer analyzed.

The results indicate that the rates of sublimation and desorption are lowered with the increase of kT_1, but are raised with the increase of kT_3; the vapor concentrations in the mushy and dried regions diminish with the increase of Δ_1, Δ_3, Lu_2, and Lu_{p2}.

References

Fey, Y. C., and Boles, M. A., 1987a, "An Analytical Study of the Effect of Convection Heat Transfer on the Sublimation of a Frozen Semi-infinite Porous Medium," *International Journal of Heat and Mass Transfer*, Vol. 30, pp. 771–779.

Fey, Y. C., and Boles, M. A., 1987b, "An Analytical Study of the Effect of the Darcy and Fick Laws on the Sublimation of a Frozen Semi-infinite Porous Medium," ASME JOURNAL OF HEAT TRANSFER, Vol. 109, pp. 1045–1048.

Fey, Y. C., and Boles, M. A., 1988, "Analytical Study of Vacuum Sublimation in an Ideally Partially Filled Frozen Porous Medium With Recondensation," *International Journal of Heat and Mass Transfer*, Vol. 31, pp. 1645–1653.

Glasstone, S., and Lewis, D., 1960, *Elements of Physical Chemistry*, D. Van Nostrand Co., Inc., and Maruzen Co. Ltd., Tokyo.

Hill, J. E., and Sunderland, J. E., 1971, "Sublimation-Dehydration in the Continuum Transition and Free-Molecule Flow Regions," *International Journal of Heat and Mass Transfer*, Vol. 14, pp. 625–638.

Kumagai, H., Tominaga, G., Tuzi, Y., and Horikoshi, G., 1978, *Vacuum Science & Engineering* [in Japanese], Syokabo, Tokyo.

Lin, S., 1981, "An Exact Solution of the Sublimation Problem in a Porous Medium," ASME JOURNAL OF HEAT TRANSFER, Vol. 103, pp. 165–168.

Lin, S., 1982a, "An Exact Solution of the Sublimation Problem in a Porous Medium. Part II—With an Unknown Temperature and Vapor Concentration at the Moving Sublimation Front," ASME JOURNAL OF HEAT TRANSFER, Vol. 104, pp. 808–811.

Lin, S., 1982b, "An Exact Solution of the Desublimation Problem in a Porous Medium," *International Journal of Heat and Mass Transfer*, Vol. 25, pp. 625–630.

Luikov, A. V., 1966, *Heat and Mass Transfer in Capillary-Porous Bodies*, Pergamon Press, Oxford.

Luikov, A. V., 1975, "Systems of Differential Equations of Heat and Mass Transfer in Capillary-Porous Bodies (Review)," *International Journal of Heat and Mass Transfer*, Vol. 18, pp. 1–4.

Mellor, J. D., 1978, *Fundamentals of Freeze-Drying*, Academic Press, London.

Özişik, M. N., 1980, *Heat Conduction*, Wiley, New York.

Peng, S. W., and Cheng, S. M., 1990, "Perturbation Solution of Freeze-Drying Heated by Convection," *Advances in Energy Conversion Engineering, Proceedings, 1st International Conference of Energy Conversion and Energy Resources Engineering*, Huazhong Univ. Sci. Tech. Press, Wuhan, pp. 212–217.

Peng, S. W., and Cheng, S. M., 1991, "Perturbation Solution of Sublimation Problem of a Porous Slab Under the First Kind of Boundary Conditions" [in Chinese], *Journal of Chemical Industry and Engineering (China)*, Vol. 42, pp. 231–235.

Peng, S. W., Qin, Q. H., Cheng, S. M., and Chen, G. Q., 1992a, "Exact Solution of Coupled Heat and Mass Transfer With Double Moving Interfaces in a Porous Half-Space. Part 1. Mass Transfer Controlled by Fick's Law," *International Journal of Energy Research*, Vol. 16, pp. 387–400.

Peng, S. W., Qin, Q. H., Cheng, S. M., and Chen, G. Q., 1992b, "Exact Solution of Coupled Heat and Mass Transfer With Double Moving Interfaces in a Porous Half-Space. Part 2. Mass Transfer Controlled by the Fick and Darcy Laws," *International Journal of Energy Research*, Vol. 16, pp. 401–411.

Journal of Heat Transfer

Technical Notes

This section contains shorter technical papers. These shorter papers will be subjected to the same review process as that for full papers.

Significance of Non-Fourier Heat Waves in Conduction

Ali Vedavarz,[1] Sunil Kumar,[1] and M. Karim Moallemi[1]

Nomenclature

c = propagation speed of thermal wave = $\sqrt{\alpha/\tau}$
C = specific heat
E = kinetic energy of electrons = $mv^2/2$
k = Boltzmann constant
l = mean free path
L = thickness of medium
m = electron effective mass
n = number of electrons per unit volume
q = heat flux
Q = nondimensional heat flux
t = time
T = absolute temperature
v = phonon or electron velocity
x = Cartesian coordinate
α = thermal diffusivity = $\kappa/\rho C$
β = ratio of characteristic thermal length to physical length = $\sqrt{\alpha\tau}/L = l/L\sqrt{3}$
ϵ = dimensionless radiative absorption coefficient
ζ = nondimensional time = t/τ
θ = nondimensional temperature
κ = thermal conductivity
ρ = density
τ = thermal relaxation time
χ = nondimensional coordinate = x/L

Subscripts

f = Fourier
i = initial
nf = non-Fourier
ref = reference

[1]Department of Mechanical Engineering, Polytechnic University, 333 Jay Street, Brooklyn, NY 11201.

Contributed by the Heat Transfer Division and presented at the National Heat Transfer Conference, Minneapolis, Minnesota, July 28–31, 1991, and the ASME Winter Annual Meeting, Atlanta, Georgia, December 1–6, 1991. Manuscript received by the Heat Transfer Division June 1992; revision received June 1993. Keywords: Conduction, Materials Processing and Manufacturing Process, Transient and Unsteady Heat Transfer. Associate Technical Editor: L. S. Fletcher.

Introduction

In this study heat conduction problems are examined to ascertain the range of applications where hyperbolic non-Fourier effects are significant and the traditional Fourier heat conduction equation leads to inaccurate temperature and heat flux profiles. The traditional heat conduction equation implies an infinite speed of propagation of the thermal signal, indicating that a local change of temperature causes an instantaneous perturbation in the temperature at each point of the medium, even if the intervening distances are very large. To consider a finite speed of propagation, damped wave models were proposed in the literature by using a variety of reasonings and derivations. The development of these models is presented in detail in the review articles by Joseph and Preziosi (1989).

In the past, hyperbolic non-Fourier conduction has strictly been studied from a mathematical viewpoint (Joseph and Preziosi, 1989; Wiggert, 1977) with insufficient attention to its practical importance. The thrust of the studies was to obtain solutions to the wave equation for different conditions and to develop mathematical and numerical techniques that would accurately predict the non-Fourier temperature profiles for a wide range of physical geometries and boundary conditions. Two important issues were largely overlooked, namely, the thermodynamic validity of the hyperbolic formulation and the range of parameters over which this hyperbolic non-Fourier formulation is important. This information is of significance to thermal engineering applications since Fourier conduction, which leads to parabolic equations, is relatively easier to analyze than the non-Fourier wave formulation represented by hyperbolic equations. This is especially of interest to modern technological applications that are subjected to rapid thermal fluctuations. It is shown in the present paper that the parameters of importance are the ratio of the thermal length scale (mean free path) to the characteristic physical length scale and the ratio of the thermal relaxation time to the physical time scale of the imposed thermal conditions. A regime map is presented and some applications indicated on the map where Fourier results may be in error.

Analysis

To consider finite speed of propagation the following non-Fourier damped wave model (in nondimensionalized one-dimensional form) for heat conduction in solids is formulated (Joseph and Preziosi, 1989):

$$\frac{\partial^2\theta}{\partial\zeta^2}+\frac{\partial\theta}{\partial\zeta}=\beta^2\frac{\partial^2\theta}{\partial\chi^2},\quad \frac{\partial^2 Q}{\partial\zeta^2}+\frac{\partial Q}{\partial\zeta}=\beta^2\frac{\partial^2 Q}{\partial\chi^2}, \tag{1}$$

where, assuming constant properties,

$$\theta(\chi, \zeta)=\frac{T(x, t)-T_i}{T_{\text{ref}}-T_i}, \quad \chi=\frac{x}{L}, \quad \zeta=\frac{t}{\tau}, \quad Q=\frac{q}{q_{\text{ref}}},$$

$$q_{\text{ref}}=\frac{\kappa}{L}(T_{\text{ref}}-T_i), \quad \beta^2=\frac{\alpha\tau}{L^2}=\frac{1}{3}\frac{l^2}{L^2}. \quad (2)$$

The reference temperature and heat flux are obtained from the boundary conditions of either constant flux or constant temperature. The finite speed of propagation of the thermal wave is c, which is equal to $\sqrt{\alpha/\tau}$. The relationship $\alpha\tau = l^2/3$ in the above equation follows from the expressions for relaxation time (Chester, 1963; Maurer, 1969)

$$\tau_{\text{phonon}}=\frac{3\alpha}{v^2}, \quad \tau_{\text{electron}}=\frac{3m\kappa}{\pi^2 nk^2 T}, \quad (3)$$

and from the electron heat capacity per unit volume, which is $0.5\pi^2 nk^2 T/E$ where E is the kinetic energy. The mean free path is given by $l = v\tau$. It is assumed that the equations above, which tacitly assume a continuum formulation, are valid for scales of the conduction regimes being considered. This implies $L > O(l/10)$, i.e., β^2 should remain less than ≈ 30. This automatically precludes very thin films. The electron relaxation time of Eq. (3) presumes that the interactions between free electrons and phonons are independent to the first order (Maurer, 1969) which may not be valid for high-intensity laser pulses. However, this effect will not be explored in the present paper.

In order for the equations in the hyperbolic form above to satisfy the laws of thermodynamics, the following conditions must hold, else the equations will have additional terms that have to be included (Kaliski, 1965; Coleman et al., 1982):

$$\left|\frac{1}{2}\frac{d}{dT}\left(T^2\frac{d}{dT}\left(\frac{\tau}{T^2\kappa}\right)\right)q^2\right| \ll \rho C. \quad (4a)$$

An order of magnitude analysis shows that this condition is satisfied if

$$q^2 \ll \frac{\rho C\kappa}{\tau}T^2. \quad (4b)$$

Equation (4b) is satisfied by most short-pulse engineering and technical applications. For example, if the material considered is aluminum at 4 K, the conditions are satisfied if the heat flux q is much less than 6×10^6 W/m^2. At 50 K the condition is satisfied for fluxes less than 10^{10} W/m^2, and at room temperature by at least a few orders of magnitude greater due to the direct proportionality to T^2 in Eq. (4b) and the inverse proportionality to τ, where τ decreases rapidly with increasing temperature. Since heat fluxes higher than these are not encountered in engineering applications of interest (including high-temperature laser processing or low-temperature infrared flux detection), Eqs. (1) are adequate.

Three different one-dimensional cases are considered in this study. They are chosen because they represent widely different boundary conditions and can approximate many different types of applications.

Case I. The first case considered is a one-dimensional medium subjected to a heat flux of magnitude q_0 on the $x = 0$ face and the other face at $x = L$ is insulated. The reference heat flux is defined as $q_{\text{ref}} = q_0$ and the corresponding reference temperature T_{ref} is obtained from Eq. (2). The boundary and initial conditions are

$$Q(0, \zeta>0)=1, \quad Q(1, \zeta>0)=0, \quad \theta(\chi, 0)=0, \quad \partial\theta(\chi, 0)/\partial\zeta=0. \quad (5)$$

Closed-form solutions are obtained by using an integral transformation technique. They are not presented here for brevity and can be found elsewhere (Vedavarz, 1994).

Case II. The second case is a one-dimensional medium subjected to heat flux q_0 at the left face, but the right face has an infinite heat transfer coefficient, which effectively maintains the right surface at $\theta = 0$. This case is the other extreme of Case I where the right face had a zero heat transfer coefficient. The boundary and initial conditions are

$$Q(0, \zeta>0)=1, \quad \theta(1, \zeta>0)=0, \quad \theta(\chi, 0)=0, \quad \partial\theta(\chi, 0)/\partial\zeta=0. \quad (6)$$

The integral transform technique yields the solution for this case also (Vedavarz, 1994).

Case III. The third case considers a one-dimensional medium that is subjected to a radiative flux at the left surface, where q_0 is the radiative flux that penetrates into the medium at the left boundary. The radiative flux at any location in the medium, as well as the resulting volumetric heat source due to absorption, are assumed to decay exponentially with the distance from the left face. Defining the reference temperature as $T_{\text{ref}} - T_i = q_0 L\beta^2\epsilon/\kappa$, the non-Fourier wave equation becomes

$$Q+\frac{\partial Q}{\partial\zeta}=\frac{\partial\theta}{\partial\chi}, \quad \frac{\partial\theta}{\partial\zeta}=-\beta^2\frac{\partial Q}{\partial\chi} + \exp(-\epsilon\chi)(1-u(\zeta-\Delta\zeta_p))u(\zeta). \quad (7)$$

As indicated by the unit step function u, the source term in the above equation exists only between time $\zeta = 0$ to $\zeta = \Delta\zeta_p$ (i.e., between $t = 0$ and $t = \Delta t_p$). It is assumed that there is no heat loss from either face. The boundary and initial conditions are

$$Q(0, \zeta>0)=0, \quad Q(1, \zeta>0)=0, \quad \theta(\chi, 0)=0, \quad \partial\theta(\chi, 0)/\partial\zeta=0. \quad (8)$$

The results of this case have been obtained numerically via the method of characteristics (Vedavarz, 1994).

Results

Relaxation Time. By examining thermophysical property data for various materials (Touloukian et al., 1970) and using Eq. (3), a wide range of values of τ are obtained; see Table 1. The relaxation time τ_{phonon} is for cases where conduction is due to phonons and τ_{electron} is for metals where conduction is due to electronic transport only. Even though τ_{electron} for metals is derived for temperatures greater than the Debye temperature (Maurer, 1969), it can also be used for low temperatures (but not intermediate temperatures) for pure metals. With the exception of biological tissue and porous materials, the values of τ for engineering materials is of the order of nano- to picoseconds. This small value of relaxation time indicates that if the physical time scales are of the order of microsecond or larger, then non-Fourier effects will not be significant. While most traditional thermal engineering applications have time scales in excess of milliseconds, few modern technological processes such as laser melting deliver large values of heat fluxes in very short pulses, sometimes as short as femtoseconds

Table 1 Values of relaxation time τ

Material	τ (in seconds) as function of T cryogenic	room	high
Metals (Electron τ)			
Aluminum	10^{-11}–10^{-6}	10^{-14}–10^{-11}	$<10^{-14}$
Tantalium	10^{-8}–10^{-6}	10^{-13}–10^{-8}	$<10^{-13}$
Superconductors (Phonon τ)			
Tantalium	$\approx 10^{-8}$		
Niobium	$\approx 10^{-8}$		
YBaCuO	$\approx 10^{-10}$	$\approx 10^{-12}$	
Semiconductors (Phonon τ)			
Gallium Arsenide	10^{-10}–10^{-7}	10^{-13}–10^{-10}	$<10^{-13}$
Organic Materials†			
Tissue	10–1000	1–100	
Porous Materials†			
Sand (187μm, 42% porosity)		≈20	
Glass (206μm, 36% porosity)		≈10	

† see Kaminski (1990), Vedavarz *et al.* (1992).

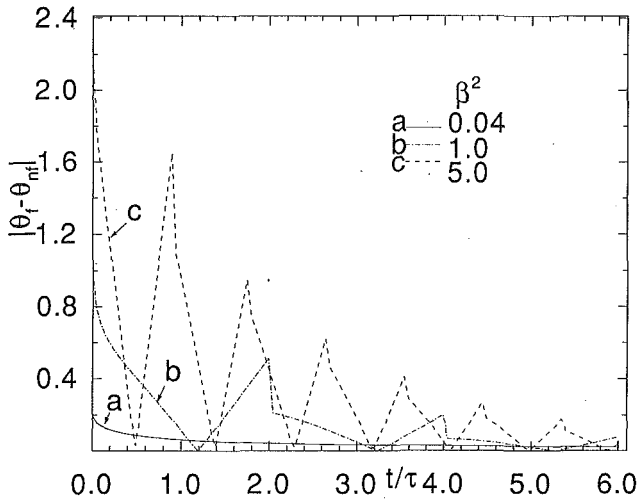

Fig. 1 The absolute difference in the surface temperature as function of time: Case I

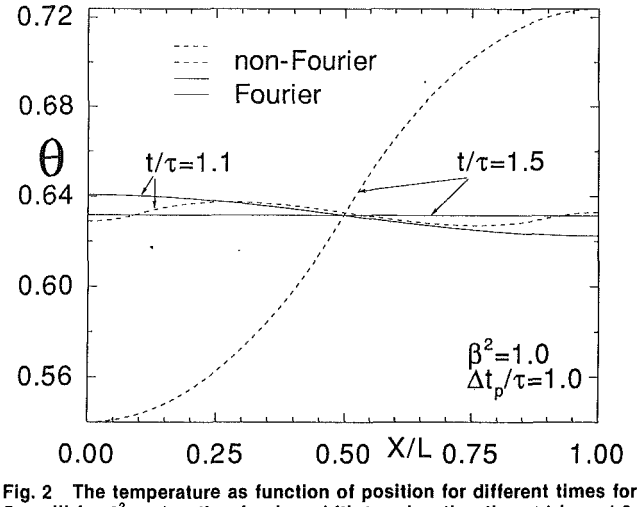

Fig. 2 The temperature as function of position for different times for Case III for $\beta^2 = 1$, ratio of pulse width to relaxation time $\Delta t_p/\tau = 1.0$, and nondimensional radiative absorption coefficient $\epsilon = 1$: comparison with Fourier

(Reitze et al., 1989). For such processes the non-Fourier conduction would certainly be very important and the Fourier formulation could conceivably be in great error.

Temperature Profiles. The temperature solutions give an insight to other variables, in addition to τ, that are of importance. Even though a series solution based on the integral transformation is developed and used for Case I and II, a separate numerical program based on the method of characteristics was also developed. Results from the literature (e.g., Wiggert, 1977, and others) were duplicated by using the numerical program to establish confidence in its accuracy. The numerical program was then used to check the accuracy of the series solution. It was found that the agreement was excellent, indicating that the exact solutions are error free. Case III is solved by modifying the numerical implementation of the method of characteristics to account for the exponentially decaying source term.

In order to judge the difference between Fourier and non-Fourier temperatures the absolute value of the difference between Fourier and non-Fourier surface temperatures of the left face is plotted in Fig. 1 for Case I. From the definition of β, it is noted that as $L \to \infty$ (semi-infinite case), or for the limiting case of $\tau \to 0$ (Fourier case), β^2 approaches zero. Physically, there is no wave traveling back to the surface at $x = 0$ for either of these cases and the temperature difference between Fourier and non-Fourier is monotonic. With increasing β^2 there is more reflection of the waves from both boundaries and therefore the surface temperature becomes increasingly oscillatory for the hyperbolic conduction solution. The non-Fourier temperature values may be less in magnitude than Fourier for some periods and greater in others. This is indicated in the graph where the *absolute value* of the difference is plotted. Thus the temperature difference $|\theta_f - \theta_{nf}|$ has larger values for higher values of β^2 in Fig. 1. The non-Fourier results in the figure match the numerical results obtained via method of characteristics (Wiggert, 1977). Similar results for Case II and the detailed temperature profiles for Cases I and II are not presented here for brevity and can be found elsewhere (Vedavarz et al., 1991; Vedavarz, 1994).

The non-Fourier solution predicts an instantaneous jump in surface temperature at the instant the heat flux is applied on the left face. This is in contrast with the Fourier solution where the surface temperature is zero. This jump is independent of the value of the thickness L since at the initial time $t = 0^+$ the wave cannot feel the presence of the other boundary. In nondimensional and dimensional forms this non-Fourier jump is given by

$$\theta(0, 0^+) = \beta, \quad T(0, 0^+) - T_i = \sqrt{\alpha\tau}\, q_0/\kappa. \tag{9}$$

Thus even if the value of τ may be small, the significance of non-Fourier formulation must not be summarily dismissed without evaluating the initial jump in surface temperature, which is proportional to the incident flux and may be important in temperature sensitive applications.

The temperature profiles for Case III, Fig. 2, are considered for $\epsilon = 1$ and $\beta = 1$. A pulse of duration Δt_p equal to the relaxation time τ is arbitrarily selected. The heat source term due to the absorbed radiative energy is assumed to be set up instantaneously at time $t = 0^+$ and disappears at $t = \Delta t_p$. Due to this volumetric heat source, the temperature variations in the medium are almost identical for both Fourier and non-Fourier cases during the "on" time of the pulse. However, when the pulse and its associated exponentially decaying heat source are removed, the new problem that is to be considered starts from temperatures that already possess spatial and temporal gradients. This leads to very interesting oscillating wave behavior where the initial conditions drive the temperatures at first to the back of the medium, which are then reflected as damped oscillations that finally collapse to a constant temperature. In contrast, the Fourier results are quite straightforward. The non-Fourier temperature wave achieves a higher absolute maximum as compared to the Fourier temperature solution and takes longer to reach steady state. The higher temperature may be very important for applications such as high-speed superconductor radiation detectors where the highest temperature may be correlated to the incident radiation. A previous model using a decaying source term based on thin film electromagnetic theory (Flik et al., 1990) used a Fourier conduction model, which could not predict the large values of temperatures required to match experimental data. Non-Fourier conduction was introduced by Bai and Lavine (1991) who used a constant volumetric heat source and obtained higher temperatures than that for Fourier cases.

Based on the numerical results of the first two cases, a regime map delineating the regions where non-Fourier effects are important is presented in Fig. 3. The lines separating the Fourier and non-Fourier regions correspond to the locus of points such that the maximum difference between the Fourier and non-Fourier temperatures at any location in the medium is greater than $0.05 \times (T_{\text{ref}} - T_i)$. The representative values of β on

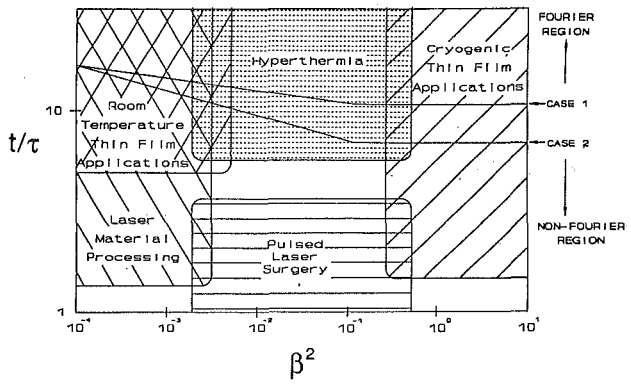

Fig. 3 Regime map for Fourier and non-Fourier regions for Cases I and II

the horizontal axis for the particular applications considered are evaluated by examining the range of τ and α values and estimating the range of L for practical engineering applications. Similarly, the characteristic process to relaxation time ratio on the vertical axis is considered by examining the values of characteristic process time, t_c, and τ in the range of applications.

In conclusion, the range of parameters over which non-Fourier effects are important for conduction is examined in this study and a regime map is presented that indicates such regions. Values of relaxation time for some common materials are evaluated, as are solutions for a few representative cases. As intuitively expected, it is found that non-Fourier effects are important during the initial stages of the transient thermal process or when the imposed thermal conditions are characterized by small time scales that are less than 10 times the order of magnitude of the relaxation time. The length of the medium has a lesser effect where smaller lengths approach Fourier results faster due to the reflection of the waves from the boundaries. Whereas the majority of engineering applications fall in the Fourier regime, non-Fourier effects are important for a few technologically important applications. Examples of practical applications where non-Fourier conduction effects could be quite significant are pulsed-laser processing of metals and semiconductors, thin film applications, and laser surgery.

References

Bai, C., and Lavine, A. S., 1991, "Hyperbolic Heat Conduction in a Superconducting Film," *ASME/JSME Thermal Engineering Conference (Reno)*, Vol. 4, pp. 87–92.

Chester, M., 1963, "Second Sound in Solids," *Physical Review*, Vol. 131, pp. 2013–2016.

Coleman, B. D., Fabrizio, M., and Owen, D. R., 1982, "On the Thermodynamics of Second Sound in Dielectric Crystals," *Archives of Rational Mechanical Analysis*, Vol. 80, pp. 135–158.

Flik, M. I., Phelan, P. E., and Tien, C. L., 1990, "Thermal Model for the Bolometric Response of High T_c Superconducting Films to Optical Pulses," *Cryogenics*, Vol. 30, pp. 1118–1128.

Joseph, D. D., and Preziosi, L., 1989, "Heat Waves," *Reviews of Modern Physics*, Vol. 61, pp. 41–73, Vol. 62, pp. 375–391.

Kaliski, S., 1965, "Wave Equation of Heat Conduction," *Bulletin of Polish Academy of Science*, Vol. 13, pp. 211–219.

Kaminski, W., 1990, "Hyperbolic Heat Conduction Equation for Materials With a Nonhomogeneous Inner Structure," ASME JOURNAL OF HEAT TRANSFER, Vol. 112, pp. 555–560.

Maurer, M. J., 1969, "Relaxation Model for Heat Conduction in Metals," *Journal of Applied Physics*, Vol. 40, pp. 5123–5127.

Reitze, D. H., Wang, X., Ahn, H., and Downer, M. C., 1989, "Femtosecond Laser Melting of Graphite," *Physical Review B*, Vol. 40, pp. 11986–11989.

Touloukian, Y. S., Powell, R. W., Ho, C. Y., and Klemens, P. G., 1970, *Thermophysical Properties of Matter* (13 volumes), IFI/Plenum, New York.

Vedavarz, A., Kumar, S., and Moallemi, M. K., 1991, "Significance of Non-Fourier Heat Waves in Conduction," ASME DSC-Vol. 32, pp. 109–122.

Vedavarz, A., Mitra, K., Kumar, S., and Moallemi, M. K., 1992, "Effect of Hyperbolic Conduction on Temperature Distribution in Laser Irradiated Tissue With Blood Perfusion," ASME HTD-Vol. 231, pp. 7–16.

Vedavarz, A., 1994, "Heat Waves in Thermal Conduction," PhD Dissertation, Polytechnic University, New York.

Wiggert, D. C., 1977, "Analysis of Early-Time Transient Heat Conduction by Method of Characteristics," ASME JOURNAL OF HEAT TRANSFER, Vol. 99, pp. 35–40.

Analytical Solution for Transient Heat Conduction in Two Semi-infinite Bodies in Contact

R. C. Xin[1] and W. Q. Tao[1]

Nomenclature

a = thermal diffusivity
b = contacting coefficient, Eq. (3)
G = dimensionless temperature gradient in TRC
h = convective heat transfer coefficient
h_s = contacting thermal conductance
k = thermal conductivity
q = interfacial heat source or heat flux
R = dimensionless heating rate in TRC
T = temperature
TB, $\overline{TB}$ = dimensionless time
x = coordinate
XB, $\overline{XB}$ = dimensionless coordinate
Θ, $\overline{\Theta}$ = dimensionless temperature
Θ^* = dimensionless temperature in TRC
τ = time
Φ = dimensionless variable
Ψ = dimensionless variable in TRC

Subscripts

c = cold
h = hot
i = initial value
n = 1, 2, representing bodies 1 and 2, respectively
s = boundary or interface
∞ = fluid

1 Introduction

Transient heat conduction in semi-infinite bodies is often encountered in many scientific and technological fields, such as geothermal physics, civil engineering, metal casting, etc. The analytical solutions for heat conduction in a single semi-infinite body with three typical boundary conditions have been obtained by the use of integral transformation techniques (Carslaw and Jaeger, 1959; Schneider, 1955; Özişik, 1980), and the corresponding temperature response charts have also been obtained (Schneider, 1963). However, a related problem, i.e., the transient heat conduction in two semi-infinite bodies in contact with identical or different materials has not been systematically investigated. A search of the literature only revealed a limited number of works that deal with this problem. When two semi-infinite bodies at uniform but different temperatures are placed together in perfect contact, the analytical solution of the tem-

[1]Department of Power Machinery Engineering, Xi'an Jiaotong University, Xi'an, Shaanxi 710049, The People's Republic of China.

Contributed by the Heat Transfer Division of THE AMERICAN SOCIETY OF MECHANICAL ENGINEERS. Manuscript received by the Heat Transfer Division December 1992; revision received July 1993. Keywords: Conduction, Direct-Contact Heat Transfer. Associate Technical Editor: Y. Bayazitoglu.

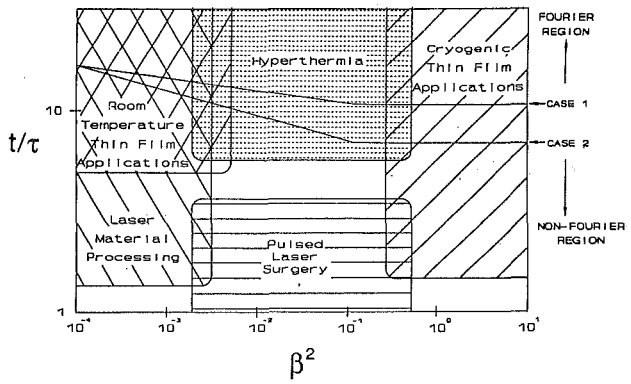

Fig. 3 Regime map for Fourier and non-Fourier regions for Cases I and II

the horizontal axis for the particular applications considered are evaluated by examining the range of τ and α values and estimating the range of L for practical engineering applications. Similarly, the characteristic process to relaxation time ratio on the vertical axis is considered by examining the values of characteristic process time, t_c, and τ in the range of applications.

In conclusion, the range of parameters over which non-Fourier effects are important for conduction is examined in this study and a regime map is presented that indicates such regions. Values of relaxation time for some common materials are evaluated, as are solutions for a few representative cases. As intuitively expected, it is found that non-Fourier effects are important during the initial stages of the transient thermal process or when the imposed thermal conditions are characterized by small time scales that are less than 10 times the order of magnitude of the relaxation time. The length of the medium has a lesser effect where smaller lengths approach Fourier results faster due to the reflection of the waves from the boundaries. Whereas the majority of engineering applications fall in the Fourier regime, non-Fourier effects are important for a few technologically important applications. Examples of practical applications where non-Fourier conduction effects could be quite significant are pulsed-laser processing of metals and semiconductors, thin film applications, and laser surgery.

References

Bai, C., and Lavine, A. S., 1991, "Hyperbolic Heat Conduction in a Superconducting Film," *ASME/JSME Thermal Engineering Conference (Reno)*, Vol. 4, pp. 87–92.

Chester, M., 1963, "Second Sound in Solids," *Physical Review*, Vol. 131, pp. 2013–2016.

Coleman, B. D., Fabrizio, M., and Owen, D. R., 1982, "On the Thermodynamics of Second Sound in Dielectric Crystals," *Archives of Rational Mechanical Analysis*, Vol. 80, pp. 135–158.

Flik, M. I., Phelan, P. E., and Tien, C. L., 1990, "Thermal Model for the Bolometric Response of High T_c Superconducting Films to Optical Pulses," *Cryogenics*, Vol. 30, pp. 1118–1128.

Joseph, D. D., and Preziosi, L., 1989, "Heat Waves," *Reviews of Modern Physics*, Vol. 61, pp. 41–73, Vol. 62, pp. 375–391.

Kaliski, S., 1965, "Wave Equation of Heat Conduction," *Bulletin of Polish Academy of Science*, Vol. 13, pp. 211–219.

Kaminski, W., 1990, "Hyperbolic Heat Conduction Equation for Materials With a Nonhomogeneous Inner Structure," ASME JOURNAL OF HEAT TRANSFER, Vol. 112, pp. 555–560.

Maurer, M. J., 1969, "Relaxation Model for Heat Conduction in Metals," *Journal of Applied Physics*, Vol. 40, pp. 5123–5127.

Reitze, D. H., Wang, X., Ahn, H., and Downer, M. C., 1989, "Femtosecond Laser Melting of Graphite," *Physical Review B*, Vol. 40, pp. 11986–11989.

Touloukian, Y. S., Powell, R. W., Ho, C. Y., and Klemens, P. G., 1970, *Thermophysical Properties of Matter* (13 volumes), IFI/Plenum, New York.

Vedavarz, A., Kumar, S., and Moallemi, M. K., 1991, "Significance of Non-Fourier Heat Waves in Conduction," ASME DSC-Vol. 32, pp. 109–122.

Vedavarz, A., Mitra, K., Kumar, S., and Moallemi, M. K., 1992, "Effect of Hyperbolic Conduction on Temperature Distribution in Laser Irradiated Tissue With Blood Perfusion," ASME HTD-Vol. 231, pp. 7–16.

Vedavarz, A., 1994, "Heat Waves in Thermal Conduction," PhD Dissertation, Polytechnic University, New York.

Wiggert, D. C., 1977, "Analysis of Early-Time Transient Heat Conduction by Method of Characteristics," ASME JOURNAL OF HEAT TRANSFER, Vol. 99, pp. 35–40.

Analytical Solution for Transient Heat Conduction in Two Semi-infinite Bodies in Contact

R. C. Xin[1] and W. Q. Tao[1]

Nomenclature

a = thermal diffusivity
b = contacting coefficient, Eq. (3)
G = dimensionless temperature gradient in TRC
h = convective heat transfer coefficient
h_s = contacting thermal conductance
k = thermal conductivity
q = interfacial heat source or heat flux
R = dimensionless heating rate in TRC
T = temperature
TB, $\overline{TB}$ = dimensionless time
x = coordinate
XB, $\overline{XB}$ = dimensionless coordinate
Θ, $\overline{\Theta}$ = dimensionless temperature
Θ^* = dimensionless temperature in TRC
τ = time
Φ = dimensionless variable
Ψ = dimensionless variable in TRC

Subscripts

c = cold
h = hot
i = initial value
n = 1, 2, representing bodies 1 and 2, respectively
s = boundary or interface
∞ = fluid

1 Introduction

Transient heat conduction in semi-infinite bodies is often encountered in many scientific and technological fields, such as geothermal physics, civil engineering, metal casting, etc. The analytical solutions for heat conduction in a single semi-infinite body with three typical boundary conditions have been obtained by the use of integral transformation techniques (Carslaw and Jaeger, 1959; Schneider, 1955; Özişik, 1980), and the corresponding temperature response charts have also been obtained (Schneider, 1963). However, a related problem, i.e., the transient heat conduction in two semi-infinite bodies in contact with identical or different materials has not been systematically investigated. A search of the literature only revealed a limited number of works that deal with this problem. When two semi-infinite bodies at uniform but different temperatures are placed together in perfect contact, the analytical solution of the tem-

[1]Department of Power Machinery Engineering, Xi'an Jiaotong University, Xi'an, Shaanxi 710049, The People's Republic of China.

Contributed by the Heat Transfer Division of THE AMERICAN SOCIETY OF MECHANICAL ENGINEERS. Manuscript received by the Heat Transfer Division December 1992; revision received July 1993. Keywords: Conduction, Direct-Contact Heat Transfer. Associate Technical Editor: Y. Bayazitoglu.

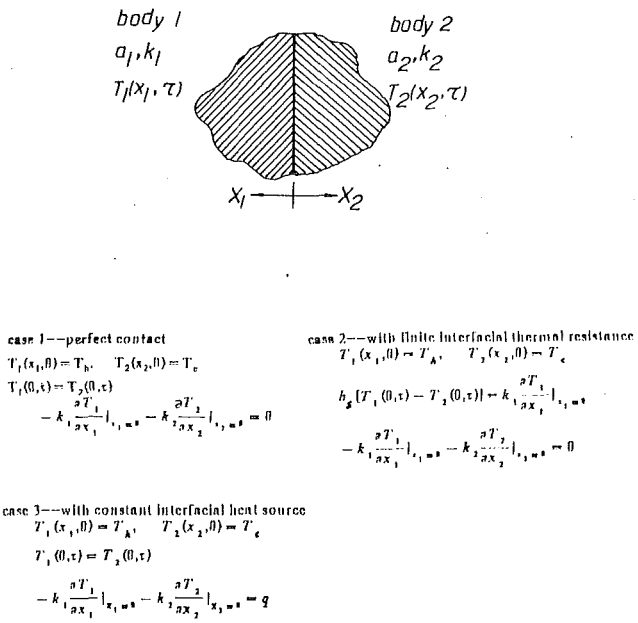

Fig. 1 Transient heat conduction of two semi-infinite bodies in contact

perature response in the two bodies can be found in Eckert and Drake (1972), Rohsenow et al. (1985), and Incropera and Dewitt (1990). This analytical solution has been used to measure thermal physical properties of material (Osipova, 1979). For most practical situations, however, the contact between two bodies is likely to be nonperfect. The contacting interface often provides a certain amount of thermal resistance, i.e., the contact conductance is of finite value. An investigation on the transient heat conduction in two contacting bodies with finite contact conductance is of great importance for modern material engineering, cooling of electronic equipment, biomedical engineering, and the development of measurement techniques (Fletcher, 1988), but the solution for this problem has not been found in published works. Moreover, engineering practices often provide more complicated ingredients. For instance, in butt welding and large-scale bearing, a heat source is induced at the contacting interface by technology process. A reasonably simplified model for this practical problem is the transient heat conduction in two semi-infinite bodies with a given heat source on the contacting interface. For a related problem, i.e., transient heat conduction of a sliding contact system, Barber (1967, 1970) has found an approximate solution.

Based on the fundamental solutions for transient heat conduction in single semi-infinite body with three boundary conditions, this work attempts to obtain analytical solutions of transient heat conduction in two contacting semi-infinite bodies initially at uniform but different temperatures with finite contact conductance or given heat source. The present work differs from that of Barber in several ways. These include: (1) The contact between the two semi-infinite bodies is assumed to occur at a single area in this work. (2) The temperatures at infinity in the semi-infinite solids are kept constant in our study. (3) Hence, analytical rather than approximate solutions are derived in this paper.

The assumption of constant thermal physical properties is adopted in the analysis.

2 Analysis

Consider the case of two semi-infinite bodies each with constant but different physical properties. The two bodies are held initially at two uniform temperatures, T_h and T_c, respectively. At time zero, the bodies are placed together, then heat exchange occurs between the two bodies, and each one experiences a

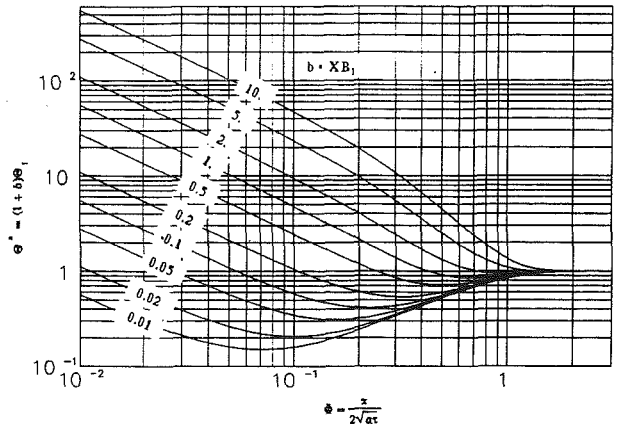

Fig. 2(*a*) Temperature response in two semi-infinite bodies with different initial temperatures after sudden contact and heating by a constant interfacial heat source (body 1)

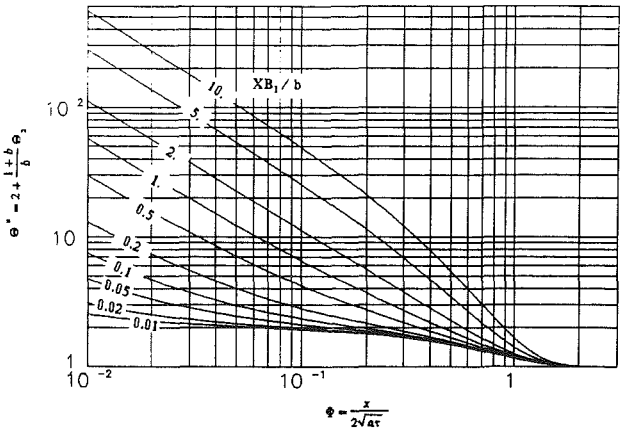

Fig. 2(*b*) Temperature response in two semi-infinite bodies with different initial temperatures after sudden contact and heating by a constant interfacial heat source (body 2)

transient heat conduction process. The problem is schematically shown in Fig. 1, where x_1 and x_2 are the two coordinates, which start from the contacting interface and extend to infinity in the positive directions of the two coordinates.

The governing equations for the temperatures of the two bodies may be expressed as

$$\frac{\partial T_n}{\partial \tau} = a_n \frac{\partial^2 T_n}{\partial X_n^2} \quad (n = 1, 2) \tag{1}$$

where the subscript n refers to one of the two bodies. Our analysis will consider the following three interface conditions: (1) perfect contact; (2) finite contacting thermal resistance, and (3) constant interfacial heat source.

2.1 Perfect Contact. For the perfect contact case, it can be shown (Eckert and Drake, 1972; Incropera and Dewitt, 1990) that the contacting interface temperature (T_s) remains constant, which can be determined by the equation below:

$$T_s = \frac{T_h \cdot b + T_c}{1 + b} \tag{2}$$

where

$$b = \frac{k_1}{k_2}\sqrt{\frac{a_2}{a_1}} = \sqrt{\frac{k_1 \rho_1 c_1}{k_2 \rho_2 c_2}} \tag{3}$$

and will be called the contacting coefficient. Thus, the temperature variation at any inner point of each body may be determined by the use of the analytical solution for semi-

infinite body with constant surface temperature (Carslaw and Jaeger, 1959; Schneider, 1955).

Introducing the following dimensionless quantities into the analytical solutions for each body:

$$\Theta_n=\frac{T_n(x_n,\tau)-T_s}{T_h-T_c},\quad \Phi_n=\frac{x_n}{2\sqrt{a_n\tau}},\quad (n=1,2)$$

we have

$$\Theta_1=\frac{1}{1+b}\,\mathrm{erf}(\Phi_1),\quad \Theta_2=-\frac{b}{1+b}\,\mathrm{erf}(\Phi_2) \tag{4}$$

2.2 Finite Contacting Thermal Resistance. For most practical situations, the contact between two bodies is often not perfect, and there is a finite value of interfacial thermal resistance between the two contacting surfaces. Let the contacting conductance by h_s, which is the reciprocal of the contacting thermal resistance. Then, the interface conditions can be formulated as follows:

$$h_s[T_1(0,\tau)-T_2(0,\tau)]=k_1\left.\frac{\partial T_1}{\partial x_1}\right|_{x_1=0} \tag{5a}$$

$$k_1\left.\frac{\partial T_1}{\partial x_1}\right|_{x_1=0}=-k_2\left.\frac{\partial T_2}{\partial x_2}\right|_{x_2=0} \tag{5b}$$

For this case, the contacting surface temperatures will be different and no longer remain constant; rather, they change with time. Now consider the limiting case: τ approaches infinity. The heat transfer rate between the two contacting bodies will approach zero, and the surface temperatures of the two bodies will approach some equilibrium temperature T_s. That is

$$\lim_{\tau\to\infty}T_1(0,\tau)=\lim_{\tau\to\infty}T_2(0,\tau)=T_s$$

At this point we shall boldly suppose that the conduction process in the two bodies is equivalent to that in single semi-infinite body with the third kind of boundary condition in which the fluid temperature T_∞ equals the equilibrium surface temperature T_s mentioned above. When time approaches infinity, the surface temperature of each single semi-infinite body will take the value of the fluid temperature T_∞ ($=T_s$). If this idea works, the analytical solution to this case could be readily obtained.

To verify this idea, we shall first investigate two related problems. Consider two separate semi-infinite bodies with uniform initial temperatures T_h and T_c, respectively. At the time $\tau=0$, they are cooled by fluid at the surfaces. The fluid temperature is T_s and the heat transfer coefficients are h_1 and h_2, respectively. The temperature distributions in the two bodies may be determined by following equations (Carslaw and Jaeger, 1959; Schneider, 1955):

$$\frac{T_1(x_1,\tau)-T_h}{T_s-T_h}=\mathrm{erfc}\left(\frac{x_1}{2\sqrt{a_1\tau}}\right)-\left[\exp\left(\frac{h_1x_1}{k_1}+\frac{h_1^2a_1\tau}{k_1^2}\right)\right]\cdot\left[\mathrm{erfc}\left(\frac{x_1}{2\sqrt{a_1\tau}}+\frac{h_1\sqrt{a_1\tau}}{k_1}\right)\right] \tag{6a}$$

$$\frac{T_2(x_2,\tau)-T_c}{T_s-T_c}=\mathrm{erfc}\left(\frac{x_2}{2\sqrt{a_2\tau}}\right)-\left[\exp\left(\frac{h_2x_2}{k_2}+\frac{h_2^2a_2\tau}{k_2^2}\right)\right]\cdot\left[\mathrm{erfc}\left(\frac{x_2}{2\sqrt{a_2\tau}}+\frac{h_2\sqrt{a_2\tau}}{k_2}\right)\right] \tag{6b}$$

From Eq. (6*a*), the surface heat flux of body 1 is

$$q_1=h_1[T_1(0,\tau)-T_s]=h_1(T_h-T_s)\exp\left(\frac{h_1^2a_1\tau}{k_1^2}\right)\cdot\mathrm{erfc}\left(\frac{h_1\sqrt{a_1\tau}}{k_1}\right) \tag{7a}$$

and that of body 2 is

$$q_2=h_2(T_c-T_s)\exp\left(\frac{h_2^2a_2\tau}{k_2^2}\right)\cdot\mathrm{erfc}\left(\frac{h_2\sqrt{a_2\tau}}{k_2}\right) \tag{7b}$$

The governing equations of the above-stated transient heat conduction problems of two separate semi-infinite bodies are the same as those of the two contacting semi-infinite bodies. Therefore, if Eqs. (7*a*) and (7*b*) can satisfy the contacting interface conditions, Eqs. (5*a*) and (5*b*), and the corresponding values of h_1, h_2, and T_s can be determined, Eqs. (6*a*) and (6*b*) could be used to describe the solution of the problem formulated by Eq. (1) and Eqs. (5*a*) and (5*b*).

From Eqs. (7*a*) and (7*b*), it can be seen that the flux continuity condition Eq. (5*b*) will be satisfied if the following two expressions are valid:

$$\frac{h_1\sqrt{a_1}}{k_1}=\frac{h_2\sqrt{a_2}}{k_2} \tag{8a}$$

$$h_1(T_h-T_s)=h_2(T_s-T_c) \tag{8b}$$

To satisfy simultaneously the interface condition (5*a*), the superposition principle of thermal resistance in series will be applied, and we have

$$\frac{1}{h_1}+\frac{1}{h_2}=\frac{1}{h_s} \tag{8c}$$

From Eqs. (8*a*,*b*,*c*), h_1 h_2, and T_s can be obtained as

$$h_1=(1+b)h_s,\quad h_2=\frac{1+b}{b}\,h_s \tag{9}$$

$$T_s=\frac{T_h\cdot b+T_c}{1+b} \tag{2}$$

where b, the contacting coefficient, is defined by Eq. (3).

It thus has been demonstrated that Eq. (6) is the solution of the problem considered, where h_1, h_2, and T_s are defined by Eqs. (9) and Eq. (2), respectively. Substituting Eqs. (2) and (9) into Eq. (6), and introducing dimensionless variables:

$$XB_n=\frac{h_sx_n}{k_n},\quad TB_n=\frac{h_s\sqrt{a_n\tau}}{k_n},\quad (n=1,2)$$

the analytical solution in nondimensional form is

$$\Theta_1=\frac{1}{1+b}\left\{\mathrm{erf}\left(\frac{XB_1}{2TB_1}\right)+\exp\left[(1+b)XB_1+(1+b)^2TB_1^2\right]\cdot\mathrm{erfc}\left[\frac{XB_1}{2TB_1}+(1+b)TB_1\right]\right\} \tag{10a}$$

$$\Theta_2=-\frac{b}{1+b}\left\{\mathrm{erf}\left(\frac{XB_2}{2TB_2}\right)+\exp\left[\frac{1+b}{b}XB_2+\frac{(1+b)^2}{b^2}TB_2^2\right]\cdot\mathrm{erfc}\left(\frac{XB_2}{2TB_2}+\frac{1+b}{b}TB_2\right)\right\} \tag{10b}$$

If h_s approaches infinity, the contact between the two bodies becomes perfect, and the second terms in the right-hand side of Eqs. (10*a*) and (10*b*) approach zero. Equation (10) thus reduces to the analytical solution of the case of perfect contact.

2.3 Constant Interfacial Heat Source

2.3.1 $T_h=T_c=T_i$. Consider the case of $T_h=T_c=T_i$. At the time $\tau=0$, the two contacting bodies are taken into contact and heated by a constant heat source (q) at the interface. The contact is supposed to be perfect, i.e., no thermal resistance exists at the interface. For this case, the governing equation and interfacial and initial conditions are:

$$\frac{\partial T_n}{\partial\tau}=a_n\frac{\partial^2T_n}{\partial x_n^2}\quad (n=1,2) \tag{1}$$

$$T_1(x_1,0)=T_i,\quad T_2(x_2,0)=T_i \tag{11}$$

$$-k\frac{\partial T_1}{\partial x_1}\bigg|_{x_1=0}-k_2\frac{\partial T_2}{\partial x_2}\bigg|_{x_2=0}=q \tag{12a}$$

$$T_1(0,\tau)=T_2(0,\tau) \tag{12b}$$

To solve this problem, consider two separate semi-infinite bodies with uniform initial temperature (T_i) to be heated at the boundaries by constant heat fluxes, q_1 and q_2, respectively. The corresponding solutions can be obtained (Carslaw and Jaeger, 1959; Schneider, 1955):

$$T_n(x_n,\tau)-T_i=\frac{2q_n(a_n\tau/\pi)^{1/2}}{k_n}\exp\left(-\frac{x_n^2}{4a_n\tau}\right)-\frac{q_nx_n}{k_n}\operatorname{erfc}\left(\frac{x_n}{2\sqrt{a_n\tau}}\right)\quad(n=1,2) \tag{13}$$

The boundary temperatures take the following equations:

$$T_n(0,\tau)=\frac{2q_n(a_n\tau/\pi)^{1/2}}{k_n}+t_i \tag{14}$$

By examining Eq. (14), it can be seen that Eq. (14) would satisfy the interfacial condition, Eq. (12), if:

$$\frac{q_1a_1^{1/2}}{k_1}=\frac{q_2a_2^{1/2}}{k_2},\quad q_1+q_2=q$$

that is

$$q_1=\frac{b}{1+b}q,\quad q_2=\frac{1}{1+b}q \tag{15}$$

In other words, if q_1 and q_2 take the values of Eq. (15), Eq. (13) would be the solution of the discussed problem. Substituting Eq. (15) into Eq. (13) and introducing the following dimensionless variables:

$$\overline{\Theta}_n=\frac{k_n}{2q\sqrt{a_n\tau}}(T_n(x_n,\tau)-T_2)\quad\Phi_n=\frac{x_n}{2\sqrt{a_n\tau}}$$

we obtain the dimensionless solution of the problem:

$$\overline{\Theta}_1=\frac{h}{(1+b)\sqrt{\pi}}\exp(-\Phi_1^2)-\frac{b\Phi_1}{1+b}\operatorname{erfc}(\Phi_1) \tag{16a}$$

$$\overline{\Theta}_2=\frac{1}{(1+b)\sqrt{\pi}}\exp(-\Phi_2^2)-\frac{\Phi_2}{1+b}\operatorname{erfc}(\Phi_2) \tag{16b}$$

2.3.2 $T_h\neq T_c$. Generally, the initial temperatures of the two bodies are different ($T_h\neq T_c$). According to the superposition principle, the solution for this case is equal to the sum of the solution of the problem in section 2.1 and that of the problem described in section 2.3.1. The final solution can be presented in following dimensionless form:

$$\Theta_1=\frac{1}{1+b}\operatorname{erf}\left(\frac{\overline{XB}_1}{2\sqrt{\overline{TB}_1}}\right)+\frac{2b}{1+b}\frac{\overline{TB}_1}{\sqrt{\pi}}\exp\left(-\frac{\overline{XB}_1^2}{4\overline{TB}_1^2}\right)-\frac{b}{1+b}\overline{XB}_1\operatorname{erfc}\left(\frac{\overline{XB}_1}{2\sqrt{\overline{TB}_1}}\right) \tag{17a}$$

$$\Theta_2=-\frac{b}{1+b}\operatorname{erf}\left(\frac{\overline{XB}_2}{2\sqrt{\overline{TB}_2}}\right)+\frac{2}{1+b}\frac{\overline{TB}_2}{\sqrt{\pi}}\exp\left(-\frac{\overline{XB}_2^2}{4\overline{TB}_2^2}\right)-\frac{1}{1+b}\overline{XB}_2\operatorname{erfc}\left(\frac{\overline{XB}_2}{2\sqrt{\overline{TB}_2}}\right) \tag{17b}$$

where

$$\overline{XB}_n=\frac{q}{T_h-T_c}\cdot\frac{x_n}{k_n},\quad\overline{TB}_n=\frac{q}{T_h-T_c}\frac{\sqrt{a_n\tau}}{k_n}\quad(n=1,2)$$

It is interesting to note that the assumption of constant heat source at the interfacial surface in section 2.3 seems not very realistic. However, the solution of constant heat flux case lays the foundation for solving the problem with variable heat source. If the variation pattern of interfacial source is known, it may be approximated by a stepwise profile, and in each step the solution for constant heat source will work. By use of Duhamel's theorem, the solution for the variable heat source may be obtained.

3 Temperature Response Charts (TRC)

In the case of perfect contact of two semi-infinite bodies with uniform but different initial temperatures, the temperature responses, temperature gradients, and heating rates in the two bodies can be represented by the curves of single semi-infinite body with sudden change in surface temperature (Chart 1, Schneider, 1963) with some modifications in dimensional variable definitions. Space limitations do not allow for their reproduction in this note; only the definitions of the dimensionless variables for the present case are shown below:

For body 1:

$$\Theta^*=1-(1+b)\Theta_1,\quad G=\frac{x_1}{\Theta_h}\cdot\frac{\partial\Theta_1}{\partial x_1},\quad R=-\frac{\sqrt{\pi\tau}}{\Theta_h}\cdot\frac{\partial\Theta_1}{\partial\tau}$$

For body 2:

$$\Theta^*=1+\frac{1+b}{b}\Theta_2,\quad G=\frac{x_2}{\Theta_c}\cdot\frac{\partial\Theta_2}{\partial x_2},\quad R=-\frac{\sqrt{\pi\tau}}{\Theta_c}\cdot\frac{\partial\Theta_2}{\partial\tau}$$

$$\Phi=\frac{x_n}{2\sqrt{a_n\tau}}\quad(n=1,2)$$

where

$$\Theta_h=\frac{T_h-T_s}{T_h-T_c},\quad\text{and}\quad\Theta_c=\frac{T_c-T_s}{T_h-T_c}.$$

When there is a finite contacting thermal resistance at the interface, and the initial temperatures in two semi-infinite contacting bodies are different, the temperature responses in the two bodies can be represented by the curves of single semi-infinite body with convective boundary condition (Chart 22, Schneider, 1963). However, the parameters must be redefined as below:

$$\Theta^*=1-(1+b)\Theta_1,\quad\Psi=(1+b)TB_1\quad\text{(body 1)}$$

$$\Theta^*=1+\frac{1+b}{b}\Theta_2,\quad\Psi=\frac{1+b}{b}TB_2\quad\text{(body 2)}$$

$$\Phi=\frac{x_n}{2\sqrt{a_n\tau}}\quad(n=1,2)$$

When the initial temperatures of the two contacting semi-infinite bodies are the same, the temperature response chart for two contacting bodies heated by a constant interfacial heat source can be presented by the curves of single semi-infinite body with boundary condition of constant heat input (chart 41, Schneider, 1963). In this case, the dimensionless variables are defined as follows:

For body 1:

$$\Theta^*=\frac{1+b}{b}\overline{\Theta}_1,\quad G=-\frac{(1+b)k_1}{bq}\cdot\frac{\partial T_1}{\partial x_1},\quad R=\frac{(1+b)k_1}{bq}\sqrt{\frac{\pi\tau}{a_1}}\frac{\partial T_1}{\partial\tau}$$

For body 2:

$$\Theta^*=(1+b)\overline{\Theta}_2,\quad G=-\frac{(1+b)k_2}{q}\cdot\frac{\partial T_2}{\partial x_2},\quad R=\frac{(1+b)k_2}{q}\sqrt{\frac{\pi\tau}{q_2}}\frac{\partial T_2}{\partial\tau}$$

$$\Phi=\frac{x_n}{2\sqrt{a_n\tau}}\quad(n=1,2)$$

For the case of constant interfacial heat source and uniform but different initial temperatures in the two contacting bodies, the temperature response charts are presented in Figs. 2(*a*) and 2(*b*).

Acknowledgments

This work was partly supported by the National Natural Science Foundation of China. The authors would also like to acknowledge the helpful discussion with Professor M. A. Ebadian of Florida International University.

References

Barber, J. R., 1967, "The Distribution of Heat Between Sliding Surfaces," *J. Mech. Eng. Sci.*, Vol. 9, pp. 351–354.

Barber, J. R., 1970, "The Conduction of Heat From Sliding Solids," *Int. J. Heat Mass Transfer*, Vol. 13, pp. 857–869.

Carslaw, H. S., and Jaeger, J. C., 1959, *Conduction of Heat in Solids*, 2nd ed., Oxford University Press, London, United Kingdom.

Eckert, E. R. G., and Drake, R. M., Jr., 1972, *Analysis of Heat and Mass Transfer*, McGraw-Hill, New York.

Fletcher, L. S., 1988, "Recent Developments in Contact Conductance Heat Transfer," ASME JOURNAL OF HEAT TRANSFER, Vol. 110, pp. 1059–1070.

Incropera, F. P., and Dewitt, D. P., 1990, *Fundamentals of Heat and Mass Transfer*, 3rd ed., Wiley, New York.

Osipova, B. A., 1979, "Experimental Investigation of Heat Exchange Process," *Power*, Moscow [in Russian].

Özişik, M. N., 1980, *Heat Conduction*, Wiley, New York.

Rohsenow, W. M., Hartnett, J. P., and Ganic, E. N., 1985, *Handbook of Heat Transfer, Fundamentals*, 2nd ed., McGraw-Hill, New York.

Schneider, P. J., 1955, *Conduction Heat Transfer*, Addison-Wesley, Reading, MA.

Schneider, P. J., 1963, *Temperature Response Charts*, Wiley, New York.

A Control Theory Method for Solutions of Inverse Transient Heat Conduction Problems

Li Zongrui[1,2] and Lu Zhongwu[1]

1 Introduction

Over the last thirty years, various numerical methods have been proposed to deal with the inverse heat conduction problem (IHCP), which involves the calculation of surface heat fluxes and other boundary conditions from transient, measured temperatures inside solids. In this paper, the concepts and analytic approach of modern control theory are introduced in order to establish a new numerical method including both one and two-dimensional algorithms, which is characterized by feedback.

To illustrate the method, numerical tests are performed to estimate the deterministic bias and standard deviation for a one-dimensional problem, and the criteria presented by Raynaud and Beck (1988) are used as a means of comparison of the present method with the methods considered by the same authors.

[1]Thermal Engineering Department, Northeastern University, Shenyang, People's Republic of China.

[2]Present address: Department of Mechanical Engineering, Ecole Polytechnique, University of Montreal, Montreal, Quebec, H3C 3A7, Canada.

Contributed by the Heat Transfer Division of THE AMERICAN SOCIETY OF MECHANICAL ENGINEERS. Manuscript received by the Heat Transfer Division July 1992; revision received August 1993. Keywords: Conduction, Numerical Methods, Transient and Unsteady Heat Transfer. Associate Technical Editor: L. S. Fletcher.

2 Formulation

2.1 One-Dimensional Problem. The boundaries at $x=L$ and $x=0$ are considered as insulated and with an imposed heat flux q, respectively. With a forward difference approximation for the time derivative and a central difference approximation for the space derivative, the one-dimensional heat conduction equation with temperature-variable thermal properties and internal heat generation may be written as follows:

$$T(k+1)=A(k)T(k)+B(k)q(k)+f(k) \tag{1}$$

where

$$A=\begin{bmatrix} a_{1,1} & a_{1,2} & & & & \\ a_{2,1} & a_{2,2} & a_{2,3} & & & \\ & \cdot & \cdot & \cdot & & \\ & & \cdot & \cdot & \cdot & \\ & & & a_{N-1,N-2} & a_{N-1,N-1} & a_{N-1,N} \\ & & & & a_{N,N-1} & a_{N,N} \end{bmatrix}$$

$$B^T=[b_1\ b_2\ b_3\ \ldots\ b_N]$$

$$=[b_1\ 0\ 0\ \ldots\ 0]$$

Equation (1) is also referred to as the system equation in modern control theory. Note that the noisy vector $f(k)$ is the internal heat generation term and Eq. (1) may be readily extended to multi-dimensions by rewriting matrices A and B.

For the inverse heat conduction problem, only one temperature in the solid is measured if only one temperature sensor is being used. To recover the surface heat flux, a simulated temperature at the same location needs to be determined in the vector $T(k+1)$ in Eq. (1). Introducing an expression from control theory for the output, one may obtain the simulated temperature as follows:

$$z(k+1)=CT(k+1) \tag{2}$$

where

$$C=[c_1\ c_2\ c_3\ \ldots\ c_N]$$

$$=[0\ 0\ \ldots\ c_n\ 0\ \ldots\ 0]$$

and N is the total number of spatial nodes. The element $c_{j,j=n}$, is equal to one at the temperature sensor, and the elements $c_{j,j=1,2,3,\ldots,N;j\neq n}$ are all equal to zero.

Based on the expression above, one may take the square of the measurement-simulation temperature difference to find the unknown surface heat flux components, i.e.,

$$J=[y(k+1)-z(k+1)]^2 \tag{3}$$

If we substitute Eqs. (2) and (1) into Eq. (3), and differentiate the result with respect to $q(k)$, we might not obtain a unique solution to the IHCP. This means that output $z(k+1)$ is not fully controllable through $q(k)$ according to the concept of control ability. However, other cases may exist where the output $z(k+1)$ may be controllable through $q(k-1)$, or $q(k-2)$, etc., depending on where the temperature sensor is located. In a general context, we differentiate Eq. (3) with respect to $q(k-r+1)$ where r is an arbitrary integer, taking for the sake of convenience the thermal properties as constant, which yields

$$q(k-r+1)=[CA^{r-1}B]^{-1}\left[y(k+1)-CA^rT(k-r+1)-\sum_{s=1}^{r}CA^{s-1}f(k-s+1)-\sum_{s=1}^{r-1}CA^{s-1}Bq(k-s+1)\right] \tag{4}$$

If we choose a specific value for the integer r, such as n, Eq. (4) would become simpler. For this purpose, we introduce

$$D^{(1)}=CA$$

$$=[d_1^{(1)}\ d_2^{(1)}\ \ldots\ d_N^{(1)}] \tag{5a}$$

For the case of constant interfacial heat source and uniform but different initial temperatures in the two contacting bodies, the temperature response charts are presented in Figs. 2(*a*) and 2(*b*).

Acknowledgments

This work was partly supported by the National Natural Science Foundation of China. The authors would also like to acknowledge the helpful discussion with Professor M. A. Ebadian of Florida International University.

References

Barber, J. R., 1967, "The Distribution of Heat Between Sliding Surfaces," *J. Mech. Eng. Sci.*, Vol. 9, pp. 351–354.

Barber, J. R., 1970, "The Conduction of Heat From Sliding Solids," *Int. J. Heat Mass Transfer*, Vol. 13, pp. 857–869.

Carslaw, H. S., and Jaeger, J. C., 1959, *Conduction of Heat in Solids*, 2nd ed., Oxford University Press, London, United Kingdom.

Eckert, E. R. G., and Drake, R. M., Jr., 1972, *Analysis of Heat and Mass Transfer*, McGraw-Hill, New York.

Fletcher, L. S., 1988, "Recent Developments in Contact Conductance Heat Transfer," ASME JOURNAL OF HEAT TRANSFER, Vol. 110, pp. 1059–1070.

Incropera, F. P., and Dewitt, D. P., 1990, *Fundamentals of Heat and Mass Transfer*, 3rd ed., Wiley, New York.

Osipova, B. A., 1979, "Experimental Investigation of Heat Exchange Process," *Power*, Moscow [in Russian].

Özişik, M. N., 1980, *Heat Conduction*, Wiley, New York.

Rohsenow, W. M., Hartnett, J. P., and Ganic, E. N., 1985, *Handbook of Heat Transfer, Fundamentals*, 2nd ed., McGraw-Hill, New York.

Schneider, P. J., 1955, *Conduction Heat Transfer*, Addison-Wesley, Reading, MA.

Schneider, P. J., 1963, *Temperature Response Charts*, Wiley, New York.

A Control Theory Method for Solutions of Inverse Transient Heat Conduction Problems

Li Zongrui[1,2] and Lu Zhongwu[1]

1 Introduction

Over the last thirty years, various numerical methods have been proposed to deal with the inverse heat conduction problem (IHCP), which involves the calculation of surface heat fluxes and other boundary conditions from transient, measured temperatures inside solids. In this paper, the concepts and analytic approach of modern control theory are introduced in order to establish a new numerical method including both one and two-dimensional algorithms, which is characterized by feedback.

To illustrate the method, numerical tests are performed to estimate the deterministic bias and standard deviation for a one-dimensional problem, and the criteria presented by Raynaud and Beck (1988) are used as a means of comparison of the present method with the methods considered by the same authors.

[1]Thermal Engineering Department, Northeastern University, Shenyang, People's Republic of China.

[2]Present address: Department of Mechanical Engineering, Ecole Polytechnique, University of Montreal, Montreal, Quebec, H3C 3A7, Canada.

Contributed by the Heat Transfer Division of THE AMERICAN SOCIETY OF MECHANICAL ENGINEERS. Manuscript received by the Heat Transfer Division July 1992; revision received August 1993. Keywords: Conduction, Numerical Methods, Transient and Unsteady Heat Transfer. Associate Technical Editor: L. S. Fletcher.

2 Formulation

2.1 One-Dimensional Problem. The boundaries at $x=L$ and $x=0$ are considered as insulated and with an imposed heat flux q, respectively. With a forward difference approximation for the time derivative and a central difference approximation for the space derivative, the one-dimensional heat conduction equation with temperature-variable thermal properties and internal heat generation may be written as follows:

$$T(k+1)=A(k)T(k)+B(k)q(k)+f(k) \tag{1}$$

where

$$A=\begin{bmatrix} a_{1,1} & a_{1,2} & & & & \\ a_{2,1} & a_{2,2} & a_{2,3} & & & \\ & \cdot & \cdot & \cdot & & \\ & & \cdot & \cdot & \cdot & \\ & & & a_{N-1,N-2} & a_{N-1,N-1} & a_{N-1,N} \\ & & & & a_{N,N-1} & a_{N,N} \end{bmatrix}$$

$$B^T=[b_1\ b_2\ b_3\ \ldots\ b_N]$$

$$=[b_1\ 0\ 0\ \ldots\ 0]$$

Equation (1) is also referred to as the system equation in modern control theory. Note that the noisy vector $f(k)$ is the internal heat generation term and Eq. (1) may be readily extended to multi-dimensions by rewriting matrices A and B.

For the inverse heat conduction problem, only one temperature in the solid is measured if only one temperature sensor is being used. To recover the surface heat flux, a simulated temperature at the same location needs to be determined in the vector $T(k+1)$ in Eq. (1). Introducing an expression from control theory for the output, one may obtain the simulated temperature as follows:

$$z(k+1)=CT(k+1) \tag{2}$$

where

$$C=[c_1\ c_2\ c_3\ \ldots\ c_N]$$

$$=[0\ 0\ \ldots\ c_n\ 0\ \ldots\ 0]$$

and N is the total number of spatial nodes. The element $c_{j,j=n}$, is equal to one at the temperature sensor, and the elements $c_{j,j=1,2,3,\ldots,N;j\neq n}$ are all equal to zero.

Based on the expression above, one may take the square of the measurement-simulation temperature difference to find the unknown surface heat flux components, i.e.,

$$J=[y(k+1)-z(k+1)]^2 \tag{3}$$

If we substitute Eqs. (2) and (1) into Eq. (3), and differentiate the result with respect to $q(k)$, we might not obtain a unique solution to the IHCP. This means that output $z(k+1)$ is not fully controllable through $q(k)$ according to the concept of control ability. However, other cases may exist where the output $z(k+1)$ may be controllable through $q(k-1)$, or $q(k-2)$, etc., depending on where the temperature sensor is located. In a general context, we differentiate Eq. (3) with respect to $q(k-r+1)$ where r is an arbitrary integer, taking for the sake of convenience the thermal properties as constant, which yields

$$q(k-r+1)=[CA^{r-1}B]^{-1}\left[y(k+1)-CA^rT(k-r+1)-\sum_{s=1}^{r}CA^{s-1}f(k-s+1)-\sum_{s=1}^{r-1}CA^{s-1}Bq(k-s+1)\right] \tag{4}$$

If we choose a specific value for the integer r, such as n, Eq. (4) would become simpler. For this purpose, we introduce

$$D^{(1)}=CA$$

$$=[d_1^{(1)}\ d_2^{(1)}\ \ldots\ d_N^{(1)}] \tag{5a}$$

By calculating Eq. (5*a*), we can obtain

$$D^{(1)} = [0 \ \ldots \ 0 \ d_{n-1}^{(1)} \ d_n^{(1)} \ d_{n+1}^{(1)} \ 0 \ \ldots \ 0] \tag{5b}$$

For $1 < n \leq N$, this gives a general expression

$$D^{(n-1)} = CA^{n-1} = D^{(n-2)}A \tag{5c}$$

where

$$D^{(n-1)} = [d_1^{(n-1)} \ d_2^{(n-1)} \ \ldots \ d_{2n-1}^{(n-1)} \ 0 \ \ldots \ 0] \tag{5d}$$

In this case, $d_1^{(n-1)} \neq 0$, and $CA^{n-1}B$ is not equal to zero in Eq. (4) with $r = n$. For $r < n$, $CA^{r-1}B = 0$. Thus a solution of the IHCP can be obtained from Eq. (4) and is given as

$$q(k-n+1) = [CA^{n-1}B]^{-1}\left[y(k+1) - CA^nT(k-n+1) - \sum_{s=1}^{n} CA^{s-1}f(k-s+1)\right] \tag{6}$$

If one chooses the integer $r > n$, additional assumptions, in which all $q(k-s+1)$, n, $n+1$, . . ., s, are temporarily set equal to zero with $s = r-1$ or a constant flux with $s = r$, should be made to obtain approximate solutions. As the integer r increases, the estimated heat flux components would be shifted in time $(r-n)$ time steps ahead because of the assumptions. It should be noted that both this method and the sequential function specification method use a least-squares minimization procedure for the measurement-simulation temperature difference. The difference between the two is that, if $r = n$, the term in summation with $CA^{s-1}B$, $s = 1, 2, \ldots, n-1$, is equal to zero in Eq. (4), whether a constant flux or adiabatic condition is imposed, whereas the heat flux is assumed constant within future time steps in the sequential specification method.

In Eq. (6), the effect of feedback on the surface heat flux is shown through a difference between a future measurement temperature and a pseudo-future temperature simulated from the current temperature and heat generation terms. This behavior would make one obtain slightly higher resolution from the zero-flux assumption, and that may also increase the sensitivity to measurement errors (standard deviation) for inverse problems.

2.2 Two-Dimensional Problem. Consider the boundaries at $x = L$ and $y = H$ as insulated, and those at $x = 0$ and $y = 0$ with imposed heat fluxes q_2, q_1, respectively. The objective function for a multidimensional problem is given as

$$J = [Y(k+1) - Z(k+1)]^T[Y(k+1) - Z(k+1)] \tag{7}$$

where Y and Z are vectors of the measured and simulated temperatures, respectively. By differentiating Eq. (7) with respect to $\mathbf{q}(k-r+1)$, one obtains a formula similar to Eq. (4), i.e.,

$$\mathbf{q}(k-r+1) = [CA^{r-1}B]^{-1}\left[Y(k+1) - CA^rT(k-r+1) - \sum_{s=1}^{r} CA^{s-1}f(k-s+1) - \sum_{s=1}^{r-1} CA^{s-1}B\mathbf{q}(k-s+1)\right] \tag{8}$$

where

$$A = \begin{bmatrix} a_{1,1} & a_{1,2} & & a_{1,1+m} & & & & & & & \\ a_{2,1} & a_{2,2} & a_{2,3} & & a_{2,2+m} & & & & & & \\ & \ddots & \ddots & \ddots & & \ddots & & & & & \\ & & \ddots & \ddots & \ddots & & \ddots & & & & \\ & a_{i,i-m} & & a_{i,i-1} & a_{i,i} & a_{i,i+1} & & & a_{i,i+m} & & \\ & & \ddots & & \ddots & \ddots & \ddots & & & \ddots & \\ & & & \ddots & & \ddots & \ddots & \ddots & & & \\ & & & & a_{N-1,N-m-1} & & & a_{N-1,N-2} & a_{N-1,N-1} & a_{N-1,N} & \\ & & & & & a_{N,N-m} & & & a_{N,N-1} & a_{N,N} & \end{bmatrix}$$

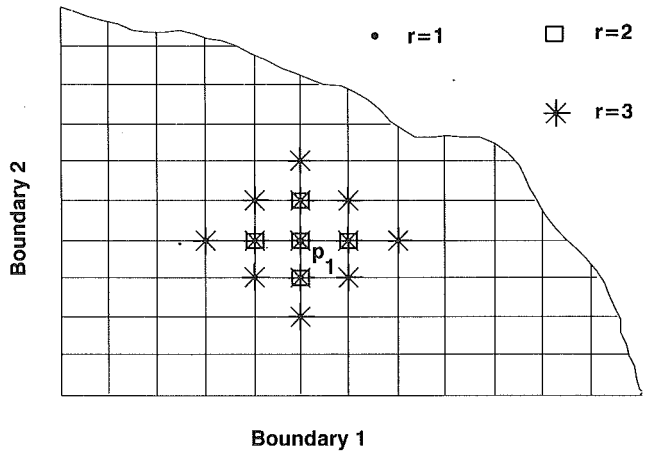

Fig. 1 Expansion of the element $d_{1,j}^{(r-1)}$ in matrix $D^{(r-1)}$ with a temperature sensor at node p_1

$$C = \begin{bmatrix} 0 \ 0 \ \ldots \ c_{1,p_1} \ 0 \ \ldots \ 0 \\ 0 \ 0 \ \ldots \ c_{2,p_2} \ 0 \ \ldots \ 0 \end{bmatrix}_{2\times N}$$

$$B^T = \begin{bmatrix} b_{1,1} \ b_{2,1} \ b_{3,1} \ \ldots \ b_{m,1} \ 0 \ \ldots \ 0 \ 0 \ \ldots \ 0 \\ b_{1,2} \ 0 \ \ldots \ b_{(i'-1)m+1,2} \ 0 \ \ldots \ 0 \ b_{N-m+1,2} \ 0 \ \ldots \ 0 \end{bmatrix}$$

$$Y^T = [y_1(k+1) \ y_2(k+1)]$$

$$\mathbf{q}^T(k+1) = [q_1(k+1) \ q_2(k+1)]$$

$$i = (i'-1)m + j'; \ i' = 1,2,3 \ \ldots, n; \ j' = 1,2,3, \ \ldots, m$$

$$i = 1,2,3, \ \ldots, N$$

in which p_i is a node number referring to the location of temperature sensor for recovering the heat flux on the boundary i; while n and m are node numbers of the domain in the x and y directions, respectively.

A unique solution of Eq. (8) exists only for a nonsingular matrix $CA^{r-1}B$, with the proper determination of the integer r. For convenience, we let

$$D^{(r-1)} = CA^{r-1}, \ G = D^{(r-1)}B \tag{9}$$

where

$$G = \begin{bmatrix} g_{11} & g_{12} \\ g_{21} & g_{22} \end{bmatrix}$$

Introducing the same approach as that discussed in the one-dimensional problem, the expansion of the nonzero elements of $d_{1,j}^{(r-1)}$ in the matrix $D^{(r-1)}$ with a temperature sensor located at node p_1 is shown in Fig. 1. Note that the nonzero elements in matrix B are all related to the nodes located on the boundaries. So, when a nonzero element of the $d_{1,j}^{(r-1)}$ appears at a boundary node with the increase of the integer r, one of the elements in G will become nonzero. For example, if a nonzero element of the $d_{1,j}^{(r-1)}$ corresponding to the node p_1 with a temperature sensor appears at a node on the boundary 1, $g_{11} \neq 0$; and $g_{12} \neq 0$ if one of those appears at a node on the

boundary 2, etc. From Fig. 1, the following relations are apparent:

$$g_{ij} \neq 0; \quad r \geq n_{i-j}; \quad i=1,2; \quad j=1,2 \tag{10}$$

where n_{i-j} is the number of nodes in the vertical segment from p_i to the node on boundary j. Equation (10) implies that the higher the n_{i-j} is, the larger is r with a nonzero value of g_{ij}.

For the two-dimensional problem, if the embedded temperature sensor is satisfied with

$$\begin{aligned} n_{1-1} &< n_{1-2} \\ n_{2-2} &< n_{2-1} \end{aligned} \tag{11}$$

the integer r for nonvanishing g_{11} and g_{22} will be smaller than that for g_{12} and g_{21}, respectively. The necessity for the matrix G to be nonsingular, so that the matrix $CA^{r-1}B$ can be inversed, requires that $g_{11}g_{12} \neq 0$, and that could be satisfied by defining a proper r in Eq. (8) with

$$r = \max\{n_{1-1}, n_{2-2}\} \tag{12}$$

and temporarily assuming that

$$q_i(k-s+1)=0; \quad \min\{n_{1-1}, n_{2-2}\} \leq s < \max\{n_{1-1}, n_{2-2}\} \quad i=1, 2 \tag{13}$$

where i is a boundary number related to heat flux. In this case, if $n_{1-1}=n_{2-2}$, the g_{11} and g_{22} will have nonzero values simultaneously with the same r, and Eq. (13) is not required. Also, the summation of $CA^{s-1}B\mathbf{q}(k-s+1)$, $s=1, 2, \ldots, r-1$, will be eliminated in Eq. (8) by the assumption shown in Eq. (13).

From the above, one could obtain the solution of a three-dimensional inverse problem in transient heat conduction by applying the same approach.

3 Application

To illustrate the method, a semi-infinite slab is considered. For convenience, the linear and dimensionless forms of the heat conduction equation are used with constant thermal properties and the heat generation per volume $f_i(k)=0$.

The tests of the method, for examining both the accuracy (or deterministic bias instead) of the flux recovery and sensitivity to measurement errors (standard deviation), are consistent with the study by Raynaud and Beck (1988). We select the location of the temperature sensor at $x=0.5$ and that of a pulse heat flux at $t_0=10\Delta t$. In order to make the comparisons, the number of spatial node points N and Fourier modulus f_o should be chosen carefully because of the stability of solutions. It seems that the stability of the method only depends on the eigenvalues of matrix A in Eq. (1) and is independent of the time steps. The largest modulus of the eigenvalues of matrix A should also be less than or equal to unity according to Smith (1975). From the tests of the one-dimensional algorithm, stable results are usually obtained by using one future temperature under $f_o<0.8$. Considering the limitation of f_o, $N=5$ is a suitable value for the time steps $\Delta t=0.005$, 0.01, and 0.05. Comparisons are shown in Tables 1 and 2 for the results with this method with those reported by Raynaud and Beck (1988), where methods A, B, C, D, E correspond to the D'Souza, Raynaud and Bransier, Weber, Beck, and control theory methods, with $N=11$ for the first two methods and $\gamma=0.5f_o\Delta t$, $R=5$, and $N=5$ for the remaining methods, respectively. Moreover, γ is a parameter in the Weber method and R is the number of future temperatures.

4 Conclusion

A new numerical method has been described for one and two-dimensional inverse problems in transient heat conduction. As an example, a one-dimensional problem was solved in order to illustrate the method's applicability. The comparisons for the deterministic bias in Table 1 show that the control theory method is better than the D'Souza method and not as good as the others at the present time. From Table 2, the standard deviation obtained by the control theory method is less sensitive to the time steps; this makes the method more convenient than the others for the engineering applications. In the study, it has been found that the disturbances caused by a single error for a smaller or larger time step are always symmetric about the abscissa and dampen quickly within less than five time steps. This shows two advantages over the existing methods, i.e., a measurement error is easily identified and can be filtered out from the symmetry; and a measurement error would have a much smaller effect on the subsequent estimations of the heat flux.

The control theory method is the only other that can directly solve the multidimensional problems besides Beck's method.

Table 1 Comparisons for the two measures of deterministic bias B_1 and B_2

Δt	0.005		0.01		0.05	
	B_1	B_2	B_1	B_2	B_1	B_2
Method A	1.00	1.85	0.94	1.65	0.77	1.43
Method B	0.70	0.79	0.73	0.81	0.73	0.80
Method C	0.76	0.76	0.75	0.84	0.92	1.03
Method D	0.71	0.82	0.77	0.84	0.85	0.91
Method E	0.96	1.00	0.79	0.85	0.86	1.09

Table 2 Comparisons for the standard deviation of the estimates δ_q

Δt	0.005	0.01	0.05
Method A	35832	3302	78.2
Method B	573	63	5.4
Method C	883	103	10.8
Method D	442	53	3.1
Method E	291	136	27.7

References

Raynaud, M., and Beck, J. V., 1988, "Methodology for Comparison of Inverse Heat Conduction Methods," ASME JOURNAL OF HEAT TRANSFER, Vol. 110, pp. 30-36.

Smith, G. D., 1975, *Numerical Solution of Partial Differential Equations*, Oxford University Press, London, United Kingdom.

On Multiple Moving Sources of Heat and Implications for Flash Temperatures

G. B. Sinclair[1]

Introduction

When two surfaces come into sliding contact (Fig. 1), the friction heat generated at their interface can lead to a sudden rise in the common temperature there. The general determination of the partitioning of the friction heat between the two solids and the companion flash temperature has attracted a number of investigators; Kennedy (1984) furnishes a comprehensive review. Typically, initially the heat is split in proportion to thermal properties, but subsequently the solid that sees a

[1]Department of Mechanical Engineering, Carnegie Mellon University, Pittsburgh, PA 15213.

Contributed by the Heat Transfer Division of THE AMERICAN SOCIETY OF MECHANICAL ENGINEERS. Manuscript received by the Heat Transfer Division January 1993 revision received June 1993. Keywords: Conduction, Moving Boundaries. Associate Technical Editor: L. S. Fletcher.

boundary 2, etc. From Fig. 1, the following relations are apparent:

$$g_{ij} \neq 0; \quad r \geq n_{i-j}; \quad i=1,2; \quad j=1,2 \tag{10}$$

where n_{i-j} is the number of nodes in the vertical segment from p_i to the node on boundary j. Equation (10) implies that the higher the n_{i-j} is, the larger is r with a nonzero value of g_{ij}.

For the two-dimensional problem, if the embedded temperature sensor is satisfied with

$$\begin{aligned} n_{1-1} &< n_{1-2} \\ n_{2-2} &< n_{2-1} \end{aligned} \tag{11}$$

the integer r for nonvanishing g_{11} and g_{22} will be smaller than that for g_{12} and g_{21}, respectively. The necessity for the matrix G to be nonsingular, so that the matrix $CA^{r-1}B$ can be inversed, requires that $g_{11}g_{12} \neq 0$, and that could be satisfied by defining a proper r in Eq. (8) with

$$r = \max\{n_{1-1}, n_{2-2}\} \tag{12}$$

and temporarily assuming that

$$q_i(k-s+1)=0; \quad \min\{n_{1-1}, n_{2-2}\} \leq s < \max\{n_{1-1}, n_{2-2}\} \quad i=1, 2 \tag{13}$$

where i is a boundary number related to heat flux. In this case, if $n_{1-1}=n_{2-2}$, the g_{11} and g_{22} will have nonzero values simultaneously with the same r, and Eq. (13) is not required. Also, the summation of $CA^{s-1}B\mathbf{q}(k-s+1)$, $s=1, 2, \ldots, r-1$, will be eliminated in Eq. (8) by the assumption shown in Eq. (13).

From the above, one could obtain the solution of a three-dimensional inverse problem in transient heat conduction by applying the same approach.

3 Application

To illustrate the method, a semi-infinite slab is considered. For convenience, the linear and dimensionless forms of the heat conduction equation are used with constant thermal properties and the heat generation per volume $f_i(k)=0$.

The tests of the method, for examining both the accuracy (or deterministic bias instead) of the flux recovery and sensitivity to measurement errors (standard deviation), are consistent with the study by Raynaud and Beck (1988). We select the location of the temperature sensor at $x=0.5$ and that of a pulse heat flux at $t_0=10\Delta t$. In order to make the comparisons, the number of spatial node points N and Fourier modulus f_o should be chosen carefully because of the stability of solutions. It seems that the stability of the method only depends on the eigenvalues of matrix A in Eq. (1) and is independent of the time steps. The largest modulus of the eigenvalues of matrix A should also be less than or equal to unity according to Smith (1975). From the tests of the one-dimensional algorithm, stable results are usually obtained by using one future temperature under $f_o<0.8$. Considering the limitation of f_o, $N=5$ is a suitable value for the time steps $\Delta t=0.005$, 0.01, and 0.05. Comparisons are shown in Tables 1 and 2 for the results with this method with those reported by Raynaud and Beck (1988), where methods A, B, C, D, E correspond to the D'Souza, Raynaud and Bransier, Weber, Beck, and control theory methods, with $N=11$ for the first two methods and $\gamma=0.5f_o\Delta t$, $R=5$, and $N=5$ for the remaining methods, respectively. Moreover, γ is a parameter in the Weber method and R is the number of future temperatures.

4 Conclusion

A new numerical method has been described for one and two-dimensional inverse problems in transient heat conduction. As an example, a one-dimensional problem was solved in order to illustrate the method's applicability. The comparisons for the deterministic bias in Table 1 show that the control theory method is better than the D'Souza method and not as good as the others at the present time. From Table 2, the standard deviation obtained by the control theory method is less sensitive to the time steps; this makes the method more convenient than the others for the engineering applications. In the study, it has been found that the disturbances caused by a single error for a smaller or larger time step are always symmetric about the abscissa and dampen quickly within less than five time steps. This shows two advantages over the existing methods, i.e., a measurement error is easily identified and can be filtered out from the symmetry; and a measurement error would have a much smaller effect on the subsequent estimations of the heat flux.

The control theory method is the only other that can directly solve the multidimensional problems besides Beck's method.

Table 1 Comparisons for the two measures of deterministic bias B_1 and B_2

Δt	0.005		0.01		0.05	
	B_1	B_2	B_1	B_2	B_1	B_2
Method A	1.00	1.85	0.94	1.65	0.77	1.43
Method B	0.70	0.79	0.73	0.81	0.73	0.80
Method C	0.76	0.76	0.75	0.84	0.92	1.03
Method D	0.71	0.82	0.77	0.84	0.85	0.91
Method E	0.96	1.00	0.79	0.85	0.86	1.09

Table 2 Comparisons for the standard deviation of the estimates δ_q

Δt	0.005	0.01	0.05
Method A	35832	3302	78.2
Method B	573	63	5.4
Method C	883	103	10.8
Method D	442	53	3.1
Method E	291	136	27.7

References

Raynaud, M., and Beck, J. V., 1988, "Methodology for Comparison of Inverse Heat Conduction Methods," ASME JOURNAL OF HEAT TRANSFER, Vol. 110, pp. 30-36.

Smith, G. D., 1975, *Numerical Solution of Partial Differential Equations*, Oxford University Press, London, United Kingdom.

On Multiple Moving Sources of Heat and Implications for Flash Temperatures

G. B. Sinclair[1]

Introduction

When two surfaces come into sliding contact (Fig. 1), the friction heat generated at their interface can lead to a sudden rise in the common temperature there. The general determination of the partitioning of the friction heat between the two solids and the companion flash temperature has attracted a number of investigators; Kennedy (1984) furnishes a comprehensive review. Typically, initially the heat is split in proportion to thermal properties, but subsequently the solid that sees a

[1]Department of Mechanical Engineering, Carnegie Mellon University, Pittsburgh, PA 15213.

Contributed by the Heat Transfer Division of THE AMERICAN SOCIETY OF MECHANICAL ENGINEERS. Manuscript received by the Heat Transfer Division January 1993 revision received June 1993. Keywords: Conduction, Moving Boundaries. Associate Technical Editor: L. S. Fletcher.

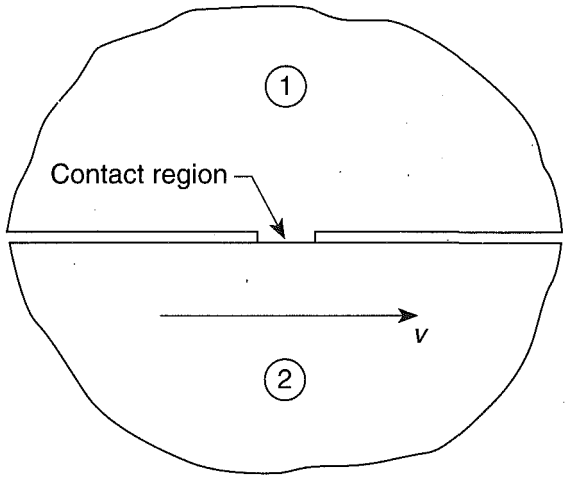

Fig. 1 Local sliding contact between two solids

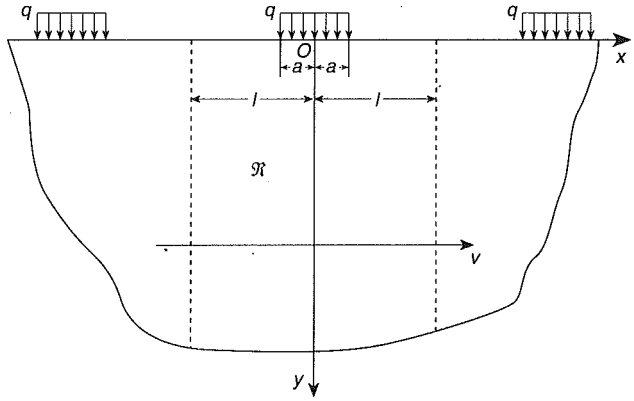

Fig. 2 Geometry and coordinates

moving source gets more of the heat because it keeps providing new unheated material (solid 2 in Fig. 1).

The particular instance of interest here is when contact occurs simultaneously at a number of points. In practice, this is the case when the loading is not sufficient so as to completely flatten surface roughness. Then touching may only really occur at asperity peaks and the true area of contact can be at least an order of magnitude less than the apparent. Such is the situation, for example, in magnetic recording when read/write heads have intermittent collisions with the disks they fly over. These impacts are virtually inevitable because of the low-flying heights sought, and the temperatures during such incidences are of some concern to the data storage industry.

Compared to isolated contact, there are relatively few contributions in the literature on flash temperatures in the presence of multiple contact. Ling (1969) develops a method for studying two comparably rough surfaces and generating the statistics of their interaction. He takes contact between two half spaces as occurring on square subregions whose locations vary randomly. The three-dimensional geometry involved requires numerical analysis, and results are presented for up to 20 contacting subregions. He finds that, with time, the interaction between contacts mitigates the effects of velocity somewhat. This is in line with expectations because, as a result of possibly touching earlier, the solid that sees moving sources has been preheated to some extent.

Here we seek to investigate what is the greatest effect on flash temperatures that interaction between contacting asperities can produce. We do this by viewing one solid as being relatively rough; in this way the contact locations for this solid remain fixed and promote interaction. We also use a periodic model problem that in effect has an infinite number of asperities touching. In addition, we successively reduce the spacing between contact regions. Further, by following the approach adopted in the seminal work of Jaeger (1943) and treating strip contact regions with their finite dimension in the direction of motion, we arrive at a transient two-dimensional problem that is tractable to analytical analysis rather than numerical. In what follows, we first formulate our model problem for a single solid, then outline its solution. Thereafter we compare response for different velocities and spacings, and combine two such models to infer the possible influence of multiple contact on flash temperatures.

Periodically Spaced Strip Sources on a Moving Half Space—Formulation and Analysis

The configuration of concern consists of a homogeneous half space moving horizontally with velocity v while being heated by a periodic array of surface sources that supply a uniform heat flux q over strips of width $2a$, with the strips having a center-to-center separation of $2l$ (Fig. 2). The strips are infinite in the out-of-plane direction in Fig. 2. To describe this two-dimensional geometry, we use rectangular Cartesian coordinates x, y with origin O fixed at the center of a strip source, x being horizontal, y vertical. The temperature field T for the problem thus must be periodic in x with period $2l$, i.e.,

$$T(@x) = T(@x + 2l). \tag{1}$$

Accordingly, we can focus attention on the representative region $\Re$ given by

$$\Re = \{(x, y) \mid -l < x < l,\ 0 < y < \infty\}. \tag{2}$$

We seek then, the transient temperature $T = T(x, y, t)$, throughout $\Re$ and for all time $t > 0$, satisfying the following requirements. The *equation of heat conduction* in the presence of convection in the x-direction,

$$\frac{\partial^2 T}{\partial x^2} + \frac{\partial^2 T}{\partial y^2} = \frac{1}{\alpha}\frac{\partial T}{\partial t} + \frac{v}{\alpha}\frac{\partial T}{\partial x}, \tag{3}$$

on $\Re$ for $t > 0$, where α is the diffusivity. The *initial condition*,

$$T = 0 \ @\ t = 0, \tag{4}$$

on $\Re$. The *surface heat flux condition*, which inputs q on the strip $-a < x < a$ and otherwise takes the surface as insulated, viz.,

$$-k\frac{\partial T}{\partial y} = q[U(x + a) - U(x - a)]U(t)\,@y = 0, \tag{5}$$

for $-l < x < l$, $t > 0$, wherein k is the thermal conductivity and U the unit step function. The *periodicity requirement* (1): for continuous internal response on $\Re$, this reduces to

$$T(@-l) = T(@l),\ \frac{\partial T}{\partial x}(@-l) = \frac{\partial T}{\partial x}(@-l), \tag{6}$$

for $0 < y < \infty$, $t > 0$. Finally, the *infinity condition*,

$$T = 0 \text{ as } y \to \infty, \tag{7}$$

on $\Re$ for $t > 0$.

Some comments on the foregoing problem statement are in order. The problem has fixed sources atop a moving half space; it can alternatively be formulated with moving sources on a stationary half space; the present formulation is simply convenient in ensuing analysis. These sources are taken as uniform over their "contact" strips; while this in not likely to be locally correct in a true asperity contact situation, it is probably sufficiently accurate for the average temperature matching between *two* half spaces used later to study flash response, and it does enable comparison with the solution to the *isolated* strip source. The insulating of the remainder of the surface can also be expected to have little effect on subsequent tem-

Table 1 Values of $\bar{T}_o$

$\bar{l}$	$\bar{v}=0$	$\bar{v}=\pi/10$	$\bar{v}=\pi$	$\bar{v}=10\pi$
2	0.271	0.268	0.159	0.046
4	0.678	0.649	0.300	0.088
10	1.253	1.084	0.424	0.126

perature matching, because typical heat losses there are small relative to other heat transport. It follows, too, that in studying flash temperatures between two half spaces, we are going to be most interested in the surface values of the temperature fields complying with Eqs. (3)–(7).

To analyze the preceding problem, we take a Laplace transform on time, invoking the initial condition, then form separable solutions that are periodic in x. Summing such solutions enables satisfaction of the surface heat flux condition via Fourier series and leads to a formal solution for our problem. For subsequent temperature matching, we take the average of this formal solution over the surface strip, $-a<x<a$, $y=0$. For this surface average formal solution, the inverse in the short and long times can readily be obtained via the usual asymptotics on the transform variable, while the inversion for all time follows from a rearrangement of tabulated inverses (see Sinclair, 1993, for details).

Results and Comparisons

In presenting results for the surface strip average temperature, T_a, we employ dimensionless variables, distinguished by a bar and defined as follows:

$$\bar{T}_a = T_a k/qa,\ \bar{t} = t\alpha/a^2,\ \bar{l} = l/a,\ \bar{v} = a/\alpha. \tag{8}$$

The last of Eq. (8) is a Peclet number for a single strip source and hence facilitates an assessment of the effects of varying velocity independent of changing spacing, and vice versa. In terms of these variables, our *short-time* and *long-time*, average surface temperatures, respectively, are:

$$\bar{T}_a = 2\sqrt{\frac{\bar{t}}{\pi}}\ (0 \le \bar{t} < \bar{t}_o), \tag{9}$$

$$\bar{T}_a = \frac{2}{\bar{l}}\sqrt{\frac{\bar{t}}{\pi}} + \bar{T}_o (\bar{t}_o < \bar{t} < \infty), \tag{10}$$

where

$$\bar{T}_o = \sum_{n=1}^{\infty} \frac{2}{n\pi}\left(\frac{\sin a_n}{a_n}\right)^2 \left[\frac{1+\sqrt{(1+(\bar{v}/a_n)^2)}}{2(1+(\bar{v}/a_n)^2)}\right]^{1/2},\quad \bar{t}_o = \frac{\pi}{4}\left(\frac{\bar{l}\bar{T}_o}{\bar{l}-1}\right)^2. \tag{11}$$

Herein $\bar{t}_o$ is the time at which the short-time and long-time solutions are equal. Equation (9) shows that, in the short time, the surface temperature is unaware that the half space is moving as well as being insensitive to the presence of the other sources. In the long time, the dominant term in Eq. (10) is also independent of velocity. Basically, this term controls the response when interaction has occurred to such an extent that the effect of movement is confined to simply an averaging of the heat influx over the entire surface of $\mathcal{R}$, viz., $-l<x<l$. This long-time response is more rapidly felt with increasing velocity and closer spacing, since $\bar{T}_o$, and hence also $\bar{t}_o$, decreases with $\bar{v}$, $1/\bar{l}$. More specifically in this regard, Table 1 presents values

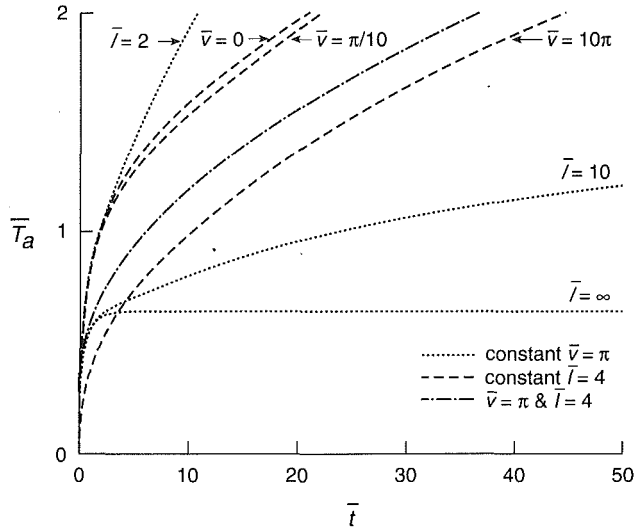

Fig. 3 Average surface temperatures for varying velocities and spacings

of $\bar{T}_o$ for almost separated strip sources ($\bar{l}=10$), closely spaced sources ($\bar{l}=4$), and very closely spaced sources ($\bar{l}=2$), and for high velocity ($\bar{v}=10\pi$), medium velocity ($\bar{v}=\pi$), and low velocity ($\bar{v}=\pi/10$), as well as the stationary case ($\bar{v}=0$).

Our *complete solution* then provides the transition between short and long time, the period during which the greatest interplay between motion and interaction takes place. After nondimensionalizing, this is:

$$\bar{T}_a = \bar{T}_o + \frac{2}{\bar{l}}\left[\sqrt{\frac{\bar{t}}{\pi}} + \sum_{n=1}^{\infty}\left(\frac{\sin a_n}{a_n}\right)^2 \frac{\bar{t}_n}{\bar{v}_n}\right], \tag{12}$$

where

$$\bar{t}_n = \mathrm{Re}\ z_n(\mathrm{Re\ erf}\ (z_n\sqrt{\bar{t}}) - 1) + \mathrm{Im}\ z_n\ \mathrm{Im\ erf}\ (z_n\sqrt{\bar{t}}), \tag{13}$$

$$\begin{Bmatrix}\mathrm{Re}\\ \mathrm{Im}\end{Bmatrix} z_n = \sqrt{(\bar{v}_n \{^{+}_{-}\} a_n^2)/2},\quad \bar{v}_n = a_n\sqrt{\bar{v}^2 + a_n^2}. \tag{14}$$

Real and imaginary parts of the error function, erf, are tabulated in Ch. 7 of Abramowitz and Stegun (1968).

Aside from the short time during which Eq. (9) captures $\bar{T}_a$ reasonably accurately, convergence is sufficiently rapid in Eq. (12) that only one term of the series is needed to give results within 10 percent of the complete series for the range of $\bar{v}$, $\bar{l}$ considered (i.e., as in Table 1). A comparison of the *effects of varying velocity* for fairly closely spaced sources ($\bar{l}=4$), and a comparison of the *effects of changing spacing* for a medium velocity ($\bar{v}=\pi$), are given in Fig. 3 (the forms used to compute the isolated case in this figure are provided in the appendix).

Implications for Flash Temperatures

To obtain flash temperature estimates, we follow Jaeger (1943) and match the average temperature in a contacting strip (Symm, 1967, provides a justification of this approach). Using the solutions developed for our model problem and referring to Fig. 1, we set $\nu=0$ for solid 1 and subscript its thermal properties (α, k) with one, let $\nu=\nu$ for solid 2 and distinguish its thermal properties by the subscript two. Further, q is now the total frictional heat flux generated at the interface and must be partitioned. We let λ be the fraction of heat entering solid 2, whence $1-\lambda$ is the fraction entering solid 1. With these preliminaries in place, we can distinguish three time intervals in which T_a is to be matched: (*i*) short time, (*ii*) a transition time, and (*iii*) the long time. Treating each of these in turn we find as follows.

For the *short time*, equating T_a of Eqs. (8), (9) for solids 1 and 2 directly yields:

$$\lambda=\frac{k_2\sqrt{\alpha_1}}{k_2\sqrt{\alpha_1}+k_1\sqrt{\alpha_2}},\quad T_a=\frac{2q\sqrt{\alpha_1\alpha_1 t/\pi}}{k_2\sqrt{\alpha_1}+k_1\sqrt{\alpha_2}}. \tag{15}$$

For the *transition time*, the solids behave as if the strip sources were isolated. This is established by comparing the full solution of Eq. (12) with that for a single strip source (Eq. (21) of the appendix); during the transition time these agree to within 5 percent for the range of velocities and spacings entertained in Table 1. Herein, the matching is not so straightforward since, while the moving strip source has a bounded steady-state solution, the stationary strip does not (see appendix). Consequently, for high speed we match a moving strip source with a stationary square source, while for low speeds we match a moving square source with a stationary one (see Jaeger, 1943, for further explanation). Thus for va/α_2 large we obtain

$$\lambda=\frac{k_2\sqrt{va/\alpha_2}}{k_2\sqrt{va/\alpha_2}+1.124\ k_1},T_a=\frac{1.064\ qa}{k_2\sqrt{va/\alpha_2}+1.124\ k_1}, \tag{16}$$

while for va/α_2 small, we have

$$\lambda=\frac{k_2}{k_1+k_2},\ T_a=\frac{0.946\ qa}{k_1+k_2}. \tag{17}$$

For the *long time*, matching the dominant term in $\bar{T}_a$ of Eq. (10) for solids 1 and 2 recovers Eq. (15) again, except that now T_a is multiplied by a/l reflecting the averaging of the heat supplied over the entire surface of a representative region. Accordingly, interaction effects have virtually removed convective influences in this time domain.

What are not so easily obtained for the foregoing description are the demarcation times that separate responses. We cannot do this precisely here since, in an actual contact situation, the heat flux into the different solids generally varies with time whereas the underlying solution we are matching assumes a constant heat flux. However, we can obtain estimates by observing, for (*i*) to (*ii*), when a single strip source effectively reaches its steady state, and, for (*ii*) to (*iii*), when the full solution for multiple sources starts to diverge from that of an isolated source. Hence, for the short-time to transition response and for the transition to long-time behavior, respectively,

$$t_{st-t}=6\sqrt{\alpha_2 a/v^3},\ t_{t-lt}=l/v, \tag{18}$$

provided $\pi/10\le v\alpha_2/a\le 10\pi$ for t_{st-t}. In the event that $t_{t-lt}\le t_{st-t}$, we have no transition time interval. What t_{t-lt} indicates is that once a large number of sliding contact sources have traveled half of their center-to-center separation, interaction effects *start* to be felt. Ultimately, such interaction can essentially negate convective effects. As an estimate of when this takes place, we determine the time when the first term in the long-time solution of Eq. (10) is an order of magnitude greater than the second: thus

$$t_{lt}=25\pi(\bar{T}_o l)^2/\alpha_2. \tag{19}$$

For very closely spaced sources ($\bar{l}=2$), this time occurs after the contact areas have covered about 10 times their center-to-center separation; for closely spaced sources ($\bar{l}=4$), about 100 times; and for almost separated sources ($\bar{l}=10$), about 1000 times.

Acknowledgments

The financial assistance of the Data Storage Systems Center at Carnegie Mellon University is gratefully acknowledged. This material is based upon work supported by the National Science Foundation under Grant No. ECD-8907068. The government has certain rights in this material.

References

Abramowitz, M., and Stegun, I. A., eds., 1968, *Handbook of Mathematical Functions*, Dover, New York.

Jaeger, J. C., 1943, "Moving Sources of Heat and the Temperature at Sliding Contacts," *Proceedings of the Royal Society of New South Wales*, Vol. 76, pp. 203–224.

Kennedy, F. E., Jr., 1984, "Thermal and Thermomechanical Effects in Dry Sliding," *Wear*, Vol. 100, pp. 453–476.

Ling, F. F., 1969, "On Temperature Transients at Sliding Interface," ASME *Journal of Lubrication Technology*, Vol. 91, pp. 397–405.

Sinclair, G. B., 1993, "Derivation of the Transient Temperature Fields in a Moving Half Space Subject to Surface Strip Sources," Report SM 93-4, Carnegie Mellon University, Pittsburgh, PA.

Symm, G. T., 1967, "Surface Temperatures of Two Rubbing Bodies," *Quarterly Journal of Mechanics and Applied Mathematics*, Vol. 20, pp. 381–391.

APPENDIX

Here we furnish series solution forms for the average surface temperature under an isolated strip heat source atop a moving half space, i.e., for T_a as $l\to\infty$ in the preceding. A description of the derivation of these series may be found in Sinclair (1993). The end results are as follows:

$$\bar{T}_a=\sqrt{\frac{\bar{t}}{\pi}}\,\bar{T}_1+\bar{T}_2-\frac{2\bar{v}^{-2}}{3\pi}\left[2+\sum_{n=1}^{\infty}b_n\bar{t}^{n-1}E_n\left(\frac{1}{\bar{t}}\right)\right], \tag{20}$$

or

$$\bar{T}_a=\bar{T}_{ss}+\sqrt{\frac{\bar{t}}{\pi}}\,\bar{T}_1+\bar{T}_2(1-\mathrm{ch}\bar{v})+\sum_{n=0}^{\infty}c_n\bar{t}^{1-n}E_n\left(\frac{\bar{v}^2\bar{t}}{4}\right), \tag{21}$$

where

$$\bar{T}_1=\left(1+\frac{\bar{v}\bar{t}}{6}\right)\mathrm{erf}\left(\frac{2+\bar{v}\bar{t}}{2\sqrt{\bar{t}}}\right)+\left(1-\frac{\bar{v}\bar{t}}{6}\right)\mathrm{erf}\left(\frac{2-\bar{v}\bar{t}}{2\sqrt{\bar{t}}}\right)-\frac{\bar{v}\bar{t}}{3}\,\mathrm{erf}\left(\frac{\bar{v}\sqrt{\bar{t}}}{2}\right), \tag{22}$$

$$\bar{T}_2=\frac{2\bar{v}^{-2}}{3\pi}(2-\bar{v}^2\bar{t})e^{-\bar{v}^2\bar{t}/4}, \tag{23}$$

$$\bar{T}_{ss}=\frac{8}{3\pi}\left[\mathrm{ch}\bar{v}K_o(\bar{v})+\left(\mathrm{sh}\bar{v}+\frac{\mathrm{ch}\bar{v}}{2\bar{v}}\right)K_1(\bar{v})-\frac{1}{2\bar{v}^2}\right], \tag{24}$$

$$b_n=[2(n-1)((2n-1)\mathrm{ch}\bar{v}+2\bar{v}\mathrm{sh}\bar{v})-3\bar{v}^2\mathrm{ch}\bar{v}]\,\frac{(-\bar{v}^2/4)^{n-1}}{(n-1)!}, \tag{25}$$

$$c_n=\left[\left(2n+1-2U(n)-\frac{\bar{v}^2}{6(n+1)}\right)\mathrm{ch}\bar{v}-\frac{2\bar{v}}{3}\,\mathrm{sh}\bar{v}\right]\frac{(-)^n}{\pi n!}. \tag{26}$$

Herein E_n are exponential integrals (defined in Ch. 5, Abramowitz and Stegun, 1968), K_o, K_1 are modified Bessel functions of order 0, 1 (defined in Ch. 9, *ibid.*), and we have retained the same normalization as earlier. While the series in Eqs. (20) and (21) have infinite radii of convergence, the first converges better for $\bar{v}\bar{t}$ small, the second for $\bar{t}$ large. In fact, $\bar{T}_a$ to within 10 percent can be obtained on taking, from Eq. (20),

$$\bar{T}_a=2\sqrt{\frac{\bar{t}}{\pi}}-\frac{\bar{t}}{\pi}\left[1+\frac{\bar{v}^2\bar{t}}{8}+\frac{\bar{v}^4\bar{t}^2}{288}\right] \tag{27}$$

for $\bar{t}$ small, and $\bar{T}_a$ of Eq. (21) with n just equal to 0 and 1 for $\bar{t}$ large. Further, $\bar{T}_a$ is within 5 percent of its steady-state value, $\bar{T}_{ss}$, for $\bar{t}\ge 6\bar{v}^{-3/2}$ ($\pi/10\le\bar{v}\le 10\pi$), and $\bar{T}_{ss}$ of Eq. (24) can be approximated for $\bar{v}\to 0$, ∞, respectively, by:

$$\bar{T}_{ss}=\frac{2}{\pi}\,[-\ln\bar{v}+1.616],\ \bar{T}_{ss}=\frac{4}{3}\sqrt{\frac{2}{\pi\bar{v}}}\left[1+\frac{1}{8\bar{v}}\right]. \tag{28}$$

These last are in agreement with Jaeger (1943).

Transient Conjugated Heat Transfer in Developing Laminar Pipe Flow

M. A. AL-Nimr[1] and M. A. Hader[1]

Nomenclature

c = specific heat capacity
k = thermal conductivity
K_R = thermal conductivity ratio $= k_s/k_f$
p = pressure
p_o = pressure of the fluid at tube entrance
P = dimensionless pressure $= (p-p_o)/\rho_f \bar{u}^2$
Pr = Prandtl number $= \nu_f/\alpha_f$
Q_w = dimensionless interfacial heat flux $= q_w r_i/k_f(T_i - T_w)$
r = radial coordinate
r_i = inner radius of the tube
r_o = outer radius of the tube
R = dimensionless radial coordinate $= r/r_i$
Re = Reynolds number $= 2r_i\bar{u}/\nu_f$
t = time
T = temperature
T_m = mixing cup temperature
T_i = inlet and initial temperature
T_w = outer surface temperature of the wall
u = axial velocity
$\bar{u}$ = average axial velocity
U = dimensionless axial velocity $= u/\bar{u}$
v = radial velocity
V = dimensionless radial velocity $= vr_i/\nu_f$
z = axial coordinate
Z = dimensionless axial coordinate $= 2z/r_i\text{Re}$
α = thermal diffusivity
α_R = thermal diffusivity ratio $= \alpha_s/\alpha_f$
β = radius ratio $= r_o/r_i$
θ = dimensionless temperature $= (T-T_w)/(T_i-T_w)$
μ = dynamic viscosity
ν = kinematic viscosity
ρ = density
τ = dimensionless time $= \nu_f t/r_i^2$

Subscripts

i = inlet or initial conditions
f = fluid properties
m = mixing cup temperature
R = ratio
s = solid properties
w = wall conditions

Introduction

Investigation in the field of transient conjugated heat transfer has been developing since a need appeared for unsteady conjugated heat transfer calculations in many engineering applications. One of these applications is the increasing need to procure the precise thermal control of various heat exchange devices encountered in chemical process, nuclear energy systems, and aerospace equipment.

The conjugated heat transfer problem has been widely analyzed in the past. Extensive reviews on this subject (Barozzi and Pagliarini, 1985; Olek et al., 1991; Scutt et al., 1992) show that the transient conjugated heat transfer problem for simultaneous, hydrodynamically and thermally developing laminar pipe flow has not been extensively investigated. Therefore, the objective of this paper is to present a numerical solution in the developing region of a pipe. Special attention has been devoted to showing the wall effects on the thermal characteristics of the tube. Examples of these characteristic are the wall heat flux, solid-fluid interface temperature, and thermal entrance length of the tube.

Problem Formulation

Under the assumptions of steady incompressible axisymmetric flow with constant physical properties, negligible viscous dissipation, and unsteady thermal behavior and using the usual Prandtl boundary layer approximation (Schlichting, 1991), the dimensionless governing equations of the problem are:

Continuity Equation:

$$\frac{\partial U}{\partial Z} + \frac{1}{R}\frac{\partial (RV)}{\partial R} = 0 \tag{1}$$

Axial Momentum Equation:

$$U\frac{\partial U}{\partial Z} + V\frac{\partial U}{\partial R} = -\frac{\partial P}{\partial Z} + \frac{1}{R}\frac{\partial}{\partial R}\left(R\frac{\partial U}{\partial R}\right) \tag{2}$$

Energy Equation in the Fluid:

$$\frac{\partial \theta_f}{\partial \tau} + U\frac{\partial \theta_f}{\partial Z} + V\frac{\partial \theta_f}{\partial R} = \frac{1}{\text{Pr}}\left[\frac{1}{R}\frac{\partial}{\partial R}\left(R\frac{\partial \theta_f}{\partial R}\right)\right] \tag{3}$$

Energy Equation in the Solid Wall:

$$\frac{\partial \theta_s}{\partial \tau} = \frac{\alpha_R}{\text{Pr}}\frac{1}{R}\frac{\partial}{\partial R}\left(R\frac{\partial \theta_s}{\partial R}\right) \tag{4}$$

The Integral Form of Continuity:

$$\int_0^1 URdR = \frac{1}{2} \tag{5}$$

The initial and boundary conditions in dimensionless form are:

$$\text{At } \tau = 0,\ Z \geq 0 \text{ and } 0 \leq R \leq \beta;\quad \theta_s = \theta_f = 1 \tag{6}$$

$$\text{At } \tau \geq 0,\ Z = 0 \text{ and } 0 \leq R \leq 1;\quad U = 1 \text{ and } V = 0 \tag{7}$$

$$\text{At } \tau \geq 0,\ Z > 0 \text{ and } R = 1;\quad U = V = 0;$$

$$\theta_s = \theta_f;\quad K_R\frac{\partial \theta_s}{\partial R} = \frac{\partial \theta_f}{\partial R} \tag{8}$$

$$\text{At } \tau \geq 0,\ Z > 0 \text{ and } R = 0;\quad \frac{\partial U}{\partial R} = \frac{\partial V}{\partial R} = 0;\quad \frac{\partial \theta_f}{\partial R} = 0 \tag{9}$$

$$\text{At } \tau > 0,\ Z = 0 \text{ and } 0 \leq R \leq \beta;\quad \theta_s = \theta_f = 1 \tag{10}$$

$$\text{At } \tau > 0,\ Z > 0 \text{ and } R = \beta;\quad \theta_s = 0 \tag{11}$$

Solution Methodology

To solve the problem under consideration by the finite difference technique, the governing partial differential equations are converted into the corresponding finite difference equations, which form a set of algebraic equations applied to the nodes of the grid.

A rectangular grid is superimposed on the half of the tube flow field in the R-Z plane. This grid is used once to get the velocity field. To solve the energy equation, the nondimensional time τ is simulated as a third coordinate normal to the R-Z plane. The dimensions of the three-dimensional grid that ensure accurate results are found to be: $\Delta Z = 0.0001$, $\Delta R = 0.005$ and $\Delta\tau = 1 \times 10^{-5}$. The number of steps in the axial direction

[1]Mechanical Engineering Department, Jordan University of Science and Technology, Irbid, Jordan.

Contributed by the Heat Transfer Division of The American Society of Mechanical Engineers. Manuscript received by the Heat Transfer Division September 1992; revision received June 1993. Keywords: Conjugate Heat Transfer, Forced Convection, Transient and Unsteady Heat Transfer. Associate Technical Editor: J. H. Kim.

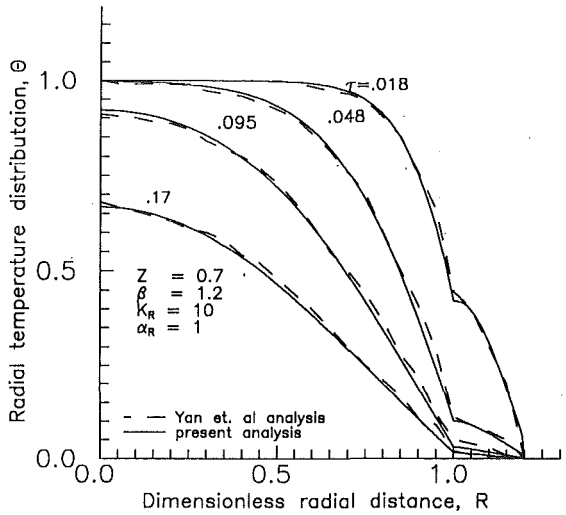

Fig. 1 Transient temperature distribution in the radial direction

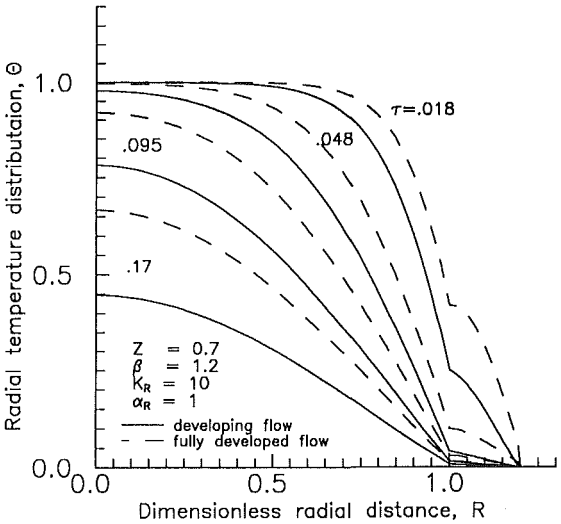

Fig. 2 Transient temperature distribution in the radial direction

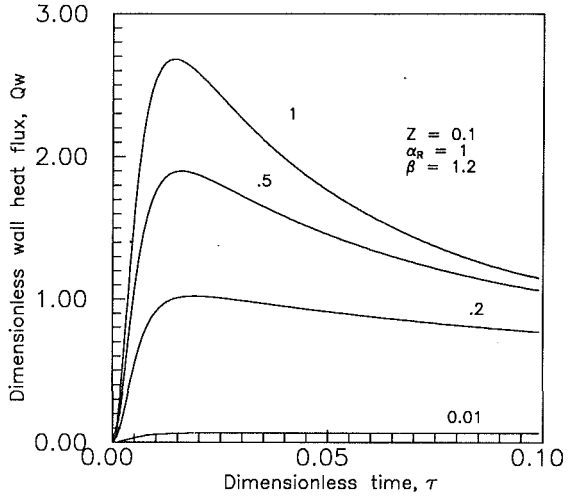

Fig. 3 Effect of the conductivity ratio on the transient wall heat flux

is chosen such that the hydrodynamic fully developed conditions are ensured and the number of steps in the imagined time direction is chosen such that the steady state conditions are achieved. The details of the used numerical scheme may be found in the work of Hader (1992).

In the present work, the hydrodynamics of the flow is independent of both temperature and time. In other words, due to the assumption of constant physical properties, the energy equation is not coupled with the equations of mass and momentum. Thus, the velocity field has to be obtained once from the finite difference form of Eqs. (1), (2), and (5) irrespective of the time, then the obtained velocity values are inserted in the finite difference form of Eq. (3), which with Eq. (4) are used to obtain the temperature field.

Results

The problem under consideration will be solved using $\mathrm{Pr} = 0.7$ and different values of K_R, α_R, and β. To verify the adequacy of the numerical scheme for the present problem, a special case of the problem is considered where the flow is assumed to be hydrodynamically fully developed. The obtained results for the temperature distribution, in the region far from the entrance and for different times, are compared with the results of Yan et al. (1989). As shown in Fig. 1, the agreement is good over wide ranges of the solid-fluid parameters β, K_R, and α_R. In our work, numerical errors resulted from different sources are estimated by repeating the calculations using coarser grids by doubling the grid size. It is found that the results are in error by as much as 4 percent. This maximum error occurs near the boundaries of the tube and in early stages of time.

Due to space limitations, only a sample of the results will be presented here; detailed results may be found in the work of Hader (1992). To show the hydrodynamic effects of the flow on the thermal behavior, the transient temperature distribution in the radial direction is obtained for the two cases of hydrodynamically developing and fully developed flow. As is clear from Fig. 2, the response of the hydrodynamically developing flow to the variation in the thermal condition of the outer surface of the wall is faster than that in the case of hydrodynamically fully developed flow. This is due to the fact that the heat transfer coefficient in the hydrodynamically fully developed case is lower than that in the developing case. The amount of the flow in the thermal boundary layer for the hydrodynamic fully developed case is less than that for the hydrodynamic developing case. As a result the temperature distribution in the fully developed case is broader and heat transfer coefficient is lower. Also, the fully developed case is broader and heat transfer coefficient is lower. Also, as is clear from Fig. 2, the deviation between the cases of hydrodynamically developing and hydrodynamically fully developed profiles increases with the time progress. The effect of the thermal conductivity ratio K_R on the transient behavior of the wall heat flux is shown in Fig. 3 where increasing K_R (i.e., increasing the thermal conductivity of the wall or reducing the thermal conductivity of the fluid) will enhance the wall heat flux. This is due to the fact that increasing the solid-wall conductivity will intensify the fluid response to any variation in the thermal boundary condition. The effects of different solid-fluid parameters, i.e., α_R, K_R, and β, on the thermal entrance length of the tube, which is defined as the required length for the temperature profile to be fully developed ($1/\theta_m(\tau, Z)\ \partial\theta(\tau, Z, 1)/\partial R = \text{const}$), are shown in Figs. 4-6. As is clear from these figures, increasing α_R and K_R will increase the thermal entrance length. On the other hand, increasing β will reduce the thermal entrance length.

Concluding Remarks

This study numerically investigates the transient conjugated heat transfer in laminar pipe flow where the flow is both hydrodynamically and thermally developing. The transient effects result from a sudden change in the thermal conditions

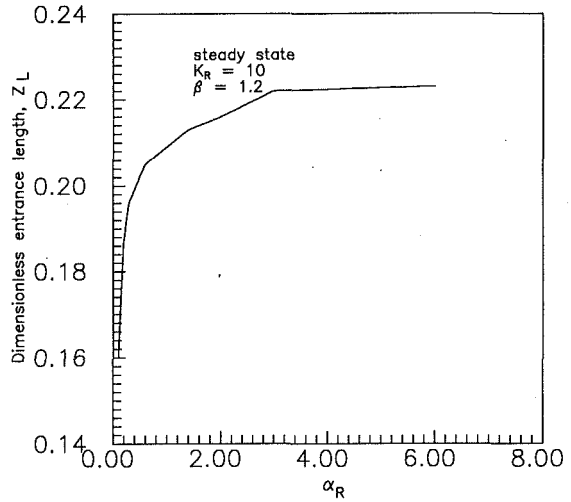

Fig. 4 Effect of the thermal diffusivity ratio on the thermal entrance length

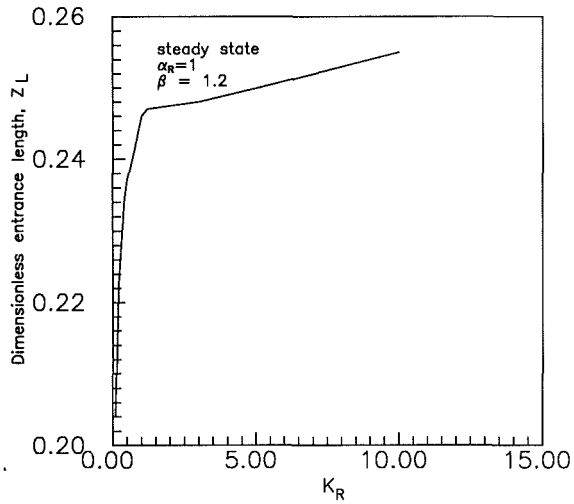

Fig. 5 Effect of the thermal conductivity ratio on the thermal entrance length

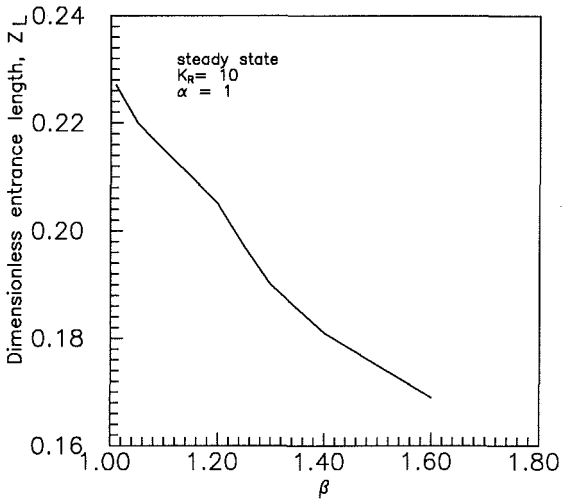

Fig. 6 Effect of the radius ratio on the thermal entrance length

of the outer surface of the pipe wall. To verify the adequacy of the numerical scheme used in this work, the hydrodynamic fully developed case is solved and the results are compared with previous work. It is found that the hydrodynamic history of the flow in the entrance length of the pipe has important effects on its thermal behavior. The solid-fluid parameters that affect the thermal behavior of the pipe flow are found to be conductivity ratio, diffusivity ratio, and radius ratio. The effect of these parameters on the temperature distribution, in both fluid and solid domains and on the wall heat flux, is studied. It is found that increasing the thermal conductivity ratio will increase the wall heat flux. Also, the effect of K_R, α_R, and β on the thermal entrance length of the tube is studied. It is concluded that increasing the conductivity and the diffusivity ratios will increase the thermal entrance length of the tube. On the other hand, increasing the radius ratio will reduce the thermal entrance length.

References

Barozzi, G. S., and Pagliarini, G., 1985, "A Method to Solve Conjugate Heat Transfer Problems: The Case of Fully Developed Laminar Flow in a Pipe," ASME JOURNAL OF HEAT TRANSFER, Vol. 107, pp. 77–83.

Hader, M. A., 1992, "Unsteady Conjugated Heat Transfer in Cocentric Annuli," M.Sc. Thesis, Department of Mechanical Engineering, Jordan University of Science and Technology, Irbid, Jordan.

Olek, S., Elias, E., Wacholder, E., and Kaizerman, S., 1991, "Unsteady Conjugated Heat Transfer in Laminar Pipe Flow," *Int. J. Heat Mass Transfer*, Vol. 34, pp. 1443–1450.

Schlichting, H., 1991, *Boundary-Layer Theory*, 6th ed., McGraw-Hill, New York.

Scutt, D. J., Rahman, M. M., and Faghri, A., 1992, "Transient Conjugated Heat Transfer in a Thick-Walled Pipe With Developing Laminar Flow," *Numerical Heat Transfer*, Part A, Vol. 21 pp. 163–186.

Yan, W. M., Tsay, Y. L., and Lin, T. F., 1989, "Transient Conjugated Heat Transfer in Laminar Pipe Flows," *Int. J. Heat Mass Transfer*, Vol. 32, No. 4, pp. 775–777.

Effects of Particulate Diffusion on the Thermal Flat Plate Boundary Layer of a Two-Phase Suspension

A. J. Chamkha[1]

Nomenclature

c = fluid-phase specific heat at constant pressure
d = particle diameter
D = diffusion coefficient
E_c = fluid-phase Eckert number
$\mathbf{e}_x$, $\mathbf{e}_y$ = unit vectors in x and y directions, respectively
F = nondimensionalized fluid-phase tangential velocity
G = nondimensionalized fluid-phase normal velocity
H = nondimensionalized fluid-phase temperature
H_0 = nondimensionalized fluid-phase wall temperature
$\underline{\underline{I}}$ = unit tensor
k = fluid-phase thermal conductivity
P = fluid-phase pressure
Pr = fluid-phase Prandtl number
Q_p = particle-phase density
$\hat{q}_w$ = wall heat transfer
S_e = interphase heat transfer rate per unit volume to the particle phase
S_I = interphase force per unit volume acting on the particle phase

[1]Department of Mechanical Engineering, Kuwait University, P. O. Box 5969, Safat, 13060 Kuwait.

Contributed by the Heat Transfer Division of THE AMERICAN SOCIETY OF MECHANICAL ENGINEERS. Manuscript received by the Heat Transfer Division February 1993; revision received May 1993. Keywords: Forced Convection, Multiphase Flows, Numerical Flows. Associate Technical Editor: J. H. Kim.

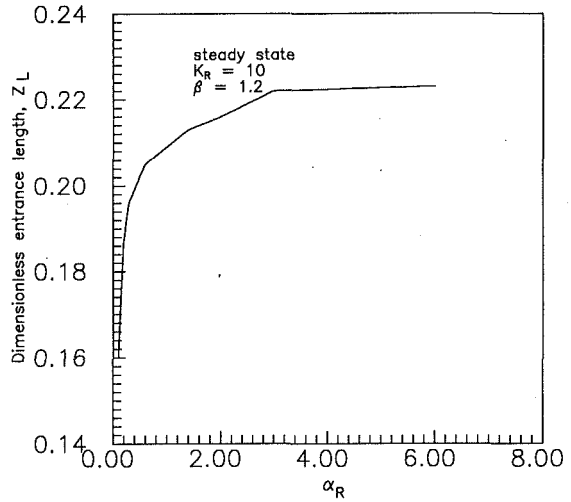

Fig. 4 Effect of the thermal diffusivity ratio on the thermal entrance length

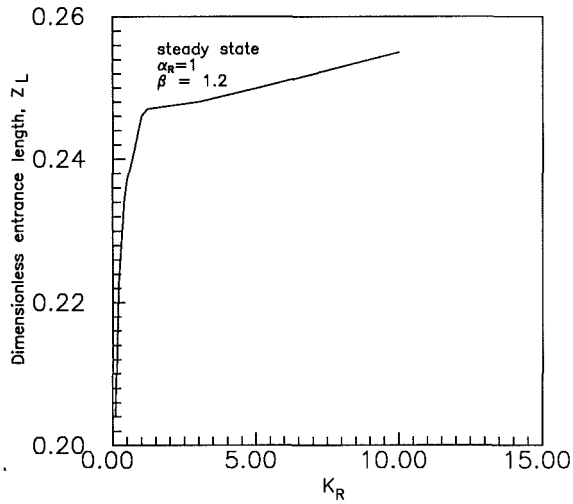

Fig. 5 Effect of the thermal conductivity ratio on the thermal entrance length

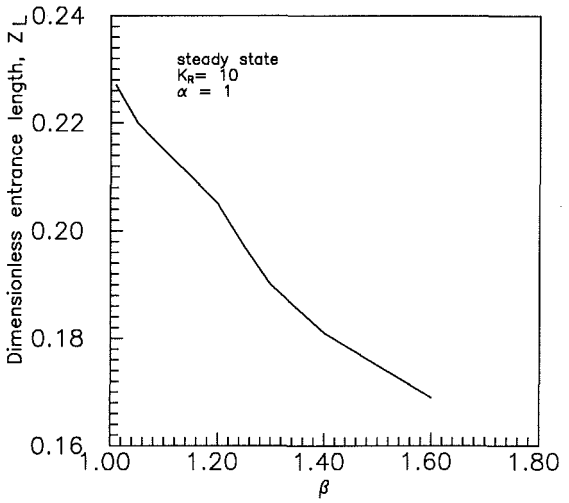

Fig. 6 Effect of the radius ratio on the thermal entrance length

of the outer surface of the pipe wall. To verify the adequacy of the numerical scheme used in this work, the hydrodynamic fully developed case is solved and the results are compared with previous work. It is found that the hydrodynamic history of the flow in the entrance length of the pipe has important effects on its thermal behavior. The solid-fluid parameters that affect the thermal behavior of the pipe flow are found to be conductivity ratio, diffusivity ratio, and radius ratio. The effect of these parameters on the temperature distribution, in both fluid and solid domains and on the wall heat flux, is studied. It is found that increasing the thermal conductivity ratio will increase the wall heat flux. Also, the effect of K_R, α_R, and β on the thermal entrance length of the tube is studied. It is concluded that increasing the conductivity and the diffusivity ratios will increase the thermal entrance length of the tube. On the other hand, increasing the radius ratio will reduce the thermal entrance length.

References

Barozzi, G. S., and Pagliarini, G., 1985, "A Method to Solve Conjugate Heat Transfer Problems: The Case of Fully Developed Laminar Flow in a Pipe," ASME JOURNAL OF HEAT TRANSFER, Vol. 107, pp. 77–83.

Hader, M. A., 1992, "Unsteady Conjugated Heat Transfer in Cocentric Annuli," M.Sc. Thesis, Department of Mechanical Engineering, Jordan University of Science and Technology, Irbid, Jordan.

Olek, S., Elias, E., Wacholder, E., and Kaizerman, S., 1991, "Unsteady Conjugated Heat Transfer in Laminar Pipe Flow," *Int. J. Heat Mass Transfer*, Vol. 34, pp. 1443–1450.

Schlichting, H., 1991, *Boundary-Layer Theory*, 6th ed., McGraw-Hill, New York.

Scutt, D. J., Rahman, M. M., and Faghri, A., 1992, "Transient Conjugated Heat Transfer in a Thick-Walled Pipe With Developing Laminar Flow," *Numerical Heat Transfer*, Part A, Vol. 21 pp. 163–186.

Yan, W. M., Tsay, Y. L., and Lin, T. F., 1989, "Transient Conjugated Heat Transfer in Laminar Pipe Flows," *Int. J. Heat Mass Transfer*, Vol. 32, No. 4, pp. 775–777.

Effects of Particulate Diffusion on the Thermal Flat Plate Boundary Layer of a Two-Phase Suspension

A. J. Chamkha[1]

Nomenclature

c = fluid-phase specific heat at constant pressure
d = particle diameter
D = diffusion coefficient
E_c = fluid-phase Eckert number
$\mathbf{e}_x$, $\mathbf{e}_y$ = unit vectors in x and y directions, respectively
F = nondimensionalized fluid-phase tangential velocity
G = nondimensionalized fluid-phase normal velocity
H = nondimensionalized fluid-phase temperature
H_0 = nondimensionalized fluid-phase wall temperature
$\underline{\underline{I}}$ = unit tensor
k = fluid-phase thermal conductivity
P = fluid-phase pressure
Pr = fluid-phase Prandtl number
Q_p = particle-phase density
$\hat{q}_w$ = wall heat transfer
S_e = interphase heat transfer rate per unit volume to the particle phase
S_I = interphase force per unit volume acting on the particle phase

[1]Department of Mechanical Engineering, Kuwait University, P. O. Box 5969, Safat, 13060 Kuwait.

Contributed by the Heat Transfer Division of THE AMERICAN SOCIETY OF MECHANICAL ENGINEERS. Manuscript received by the Heat Transfer Division February 1993; revision received May 1993. Keywords: Forced Convection, Multiphase Flows, Numerical Flows. Associate Technical Editor: J. H. Kim.

S_m = source term
T = fluid-phase temperature
V = fluid-phase velocity
x, y = Cartesian coordinate variables
γ = specific heat ratio
δ = inverse Schmidt number
ϵ = temperature inverse Schmidt number
κ = particle loading
μ = fluid-phase dynamic viscosity
ν = fluid-phase kinematic viscosity $=\mu/\rho$
ξ, η = transformed coordinates
ρ = fluid-phase density
$\underline{\underline{\sigma}}$ = fluid-phase stress tensor
τ_T = temperature relaxation time $=\rho_s d^2 c_p/(12k)$
τ_v = momentum relaxation time $=\rho_s d^2/(18\mu)$
∇ = gradient operator
∇^2 = Laplacian operator

Subscripts

∞ = free stream
p = particle phase
s = particulate material

Superscripts

T = transpose of a second-order tensor

Introduction

The Eulerian description of particulate suspensions has been employed extensively in modeling processes involving such suspensions. This approach treats the two phases (fluid and particle) as interacting continua (see, for instance, Marble, 1970). Because the solid phase consists of discrete particles of different sizes and shapes, a representation of the particles variables by averaged continuous functions leads to excess source terms in the governing equations of motion (see Drew and Segal, 1971). The source term resulting from the particle-phase continuity equation is modeled herein as diffusive in nature. It is of interest in the present paper to study the effects of particulate diffusivity on the thermal boundary layer of a two-phase particulate suspension past a semi-infinite impermeable plate. This is a classical problem in fluid mechanics and heat transfer, which has not been fully investigated.

Related work on this problem can be found in the papers by Soo (1968), Osiptsov (1980), Prabha and Jain (1980), and Chamkha (1992). It has been reported in all these papers that if the original dusty-gas equations, which do not account for particulate diffusivity, are used in solving this problem, a singularity in the particle-phase density is predicted. However, when the model is modified to include particulate diffusion, a singularity-free solution is possible (see Chamkha and Peddieson, 1989, who considered the hydrodynamic aspects of this problem). This work considers the thermal aspects of the problem. The fluid phase is assumed incompressible and has constant properties. The particle phase is assumed to consist of small solid spherical particles of uniform size with no mutual collision and radiative heat transfer and the particle-phase volume fraction is assumed to be small.

Governing Equations

Let the plate occupy the half of the x, z plane corresponding to $x>0$ with the y axis being normal to the plate, and let the flow far from the plate be a uniform stream in the x direction parallel to the plate with both phases in equilibrium. The governing equations for this problem are based on the balance laws of mass, linear momentum, and energy for both the fluid and particulate phases (see, for instance Marble, 1970). These can be written as

$$\nabla\cdot(\rho\mathbf{V})=S_m,\quad \nabla\cdot(\rho_p\mathbf{V}_p)=S_{pm},\quad \rho\mathbf{V}\cdot\nabla\mathbf{V}=\nabla\cdot\underline{\underline{\sigma}}+\mathbf{S}_l,$$
$$\rho_p\mathbf{V}_p\cdot\nabla\mathbf{V}_p=\nabla\cdot\underline{\underline{\sigma}}_p+\mathbf{S}_{pl},$$
$$\rho c\mathbf{V}\cdot\nabla T=k\nabla^2 T+\underline{\underline{\sigma}}:\nabla\mathbf{V}+(\mathbf{V}-\mathbf{V}_p)\cdot\mathbf{S}_l+S_e,$$
$$\rho_p c_p\mathbf{V}_p\cdot\nabla T_p=\underline{\underline{\sigma}}_p:\nabla\mathbf{V}_p+S_{pe} \tag{1}$$

where

$$S_m=0,\quad S_{pm}=D_p\nabla^2\rho_p,\quad \underline{\underline{\sigma}}=-p\underline{\underline{I}}+\mu(\nabla\mathbf{V}+\nabla\mathbf{V}^T),\quad \underline{\underline{\sigma}}_p=0$$
$$\mathbf{S}_{pl}=-\mathbf{S}_l=\rho_p(\mathbf{V}-\mathbf{V}_p)/\tau_v,\quad S_e=-S_{pe}=\rho_p c_p(T_p-T)/\tau_T \tag{2}$$

It is useful to nondimensionalize Eqs. (1), and transform the computational domain from semi-infinite ($0\le x<\infty$) to finite ($0\le\xi\le 1$). This is achieved by substituting the modified Blasius transformations

$$x=V_\infty\tau_v\xi/(1-\xi),\quad y=(2\nu\tau_v\xi/(1-\xi))^{1/2}\eta$$
$$\mathbf{V}=\mathbf{e}_x V_\infty F(\xi,\eta)+\mathbf{e}_y(\nu(1-\xi)/(2\tau_v\xi))^{1/2}(G(\xi,\eta)+\eta F(\xi,\eta))$$
$$\mathbf{V}_p=\mathbf{e}_x V_\infty F_p(\xi,\eta)+\mathbf{e}_y(\nu(1-\xi)/(2\tau_v\xi))^{1/2}(G_p(\xi,\eta)+\eta F_p(\xi,\eta))$$
$$\rho_p=\rho_{p\infty}Q_p(\xi,\eta),\quad T=T_\infty H(\xi,\eta),\quad T_p=T_\infty H_p(\xi,\eta) \tag{3}$$

into the boundary-layer form of the governing equations to give

$$\partial_\eta G+F+2\xi(1-\xi)\partial_\xi F=0,$$
$$\delta\partial_{\eta\eta}Q_p-(\partial_\eta(Q_pG_p)+Q_pF_p+2\xi(1-\xi)\partial_\xi(Q_pF_p))=0,$$
$$\partial_{\eta\eta}F-G\partial_\eta F-2\xi(1-\xi)F\partial_\xi F+2\xi\kappa Q_p(F_p-F)/(1-\xi)=0$$
$$G_p\partial_\eta F_p+2\xi(1-\xi)F_p\partial_\xi F_p+2\xi(F_p-F)/(1-\xi)=0$$
$$G_p\partial_\eta G_p+\eta(G_p\partial_\eta F_p-F_p^2)+2\xi(1-\xi)F_p(\partial_\xi G_p+\eta\partial_\xi F_p)$$
$$+2\xi(G_p-G+\eta(F_p-F))/(1-\xi)=0$$
$$\partial_{\eta\eta}H-\mathrm{Pr}G\partial_\eta H+\mathrm{Pr}E_c(\partial_\eta F)^2-2\xi(1-\xi)\mathrm{Pr}F\partial_\xi H$$
$$+2\xi\kappa\mathrm{Pr}Q_p(\gamma\epsilon(H_p-H)+E_c(F_p-F)^2)/(1-\xi)=0$$
$$G_p\partial_\eta H_p+2\xi(1-\xi)F_p\partial_\xi H_p-2\xi\epsilon(H-H_p)/(1-\xi)=0 \tag{4}$$

where

$$\delta=D_p/\nu,\quad \kappa=\rho_{p\infty}/\rho,\quad \mathrm{Pr}=(\mu c)/k,\quad E_c=V_\infty^2/(cT_\infty),$$
$$\gamma=c_p/c,\quad \epsilon=\tau_v/\tau_T. \tag{5}$$

are the inverse Schmidt number, particle loading, fluid-phase Prandtl number, Eckert number, specific heat ratio, and the ratio of momentum relaxation time to the temperature relaxation time, respectively. It should be pointed out that the use of the modified Blasius transformations eliminates the singularities associated with the sharp leading edge of the plate.

The boundary and matching conditions used in obtaining the solution of this problem are

$$F(\xi,0)=0,\quad G(\xi,0)=0,\quad H(\xi,0)=H_0,\quad \partial_\eta Q_p(\xi,0)=0,$$
$$F(\xi,\infty)\to 1,\quad F_p(\xi,\infty)\to 1,\quad G_p(\xi,\infty)\to G(\xi,\infty),$$
$$Q_p(\xi,\infty)\to 1,\quad H(\xi,\infty)\to 1,\quad H_p(\xi,\infty)\to 1 \tag{6}$$

where H_0 is a dimensionless wall temperature. It should be noted that the fourth equation in Eqs. (6) allows the particle-phase diffusivity effects to vanish at the wall.

The wall heat transfer coefficient is an important physical thermal property, which can be used as a measure of the wall heat gain or loss that can be brought about by physical changes in the flow field. It can be defined in dimensionless form as

$$\hat{q}_w(\xi)=-\partial_\eta H(\xi,0)/(\mathrm{Pr}E_c). \tag{7}$$

Results

The boundary-layer equations, Eqs. (4), are solved subject to the boundary and matching conditions, Eqs. (6), using a fully implicit finite-difference scheme similar to that described by Blottner (1970). It is a well-known fact that the flow and temperature fields experience large velocity and temperature gradients near the plate surface and the leading edge. For this reason, a variable mesh (with initial step size $\Delta\eta_1=0.001$ and

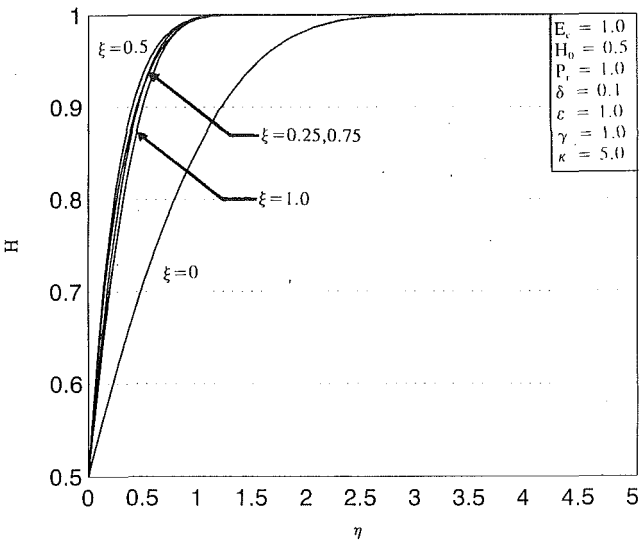

Fig. 1 Fluid-phase temperature profiles

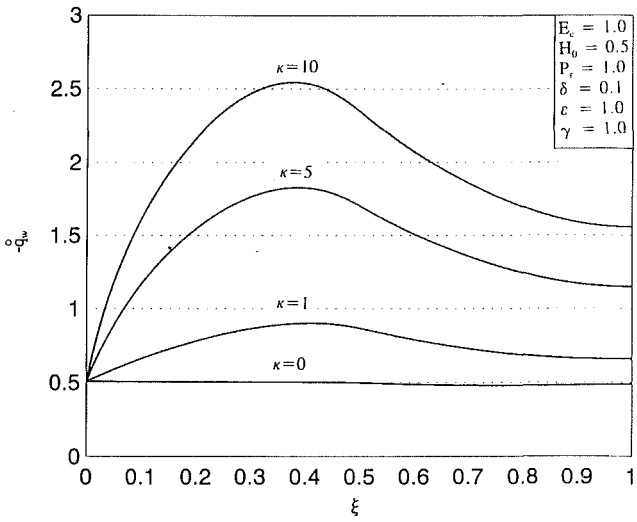

Fig. 3 Wall heat transfer coefficient versus position

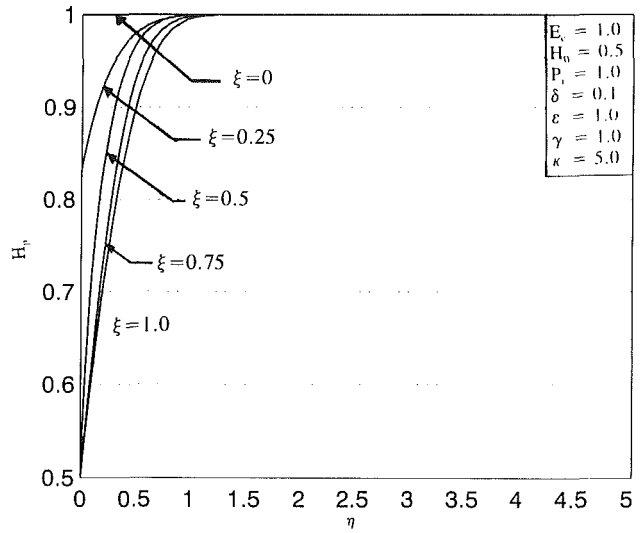

Fig. 2 Particle-phase temperature profiles

a growth factor of 1.03) is placed in the direction normal to the flow (η direction) to minimize the number of nodes and yet provide a sufficient number of nodes in the immediate vicinity of the wall where viscous effects are dominant. Fine meshes are used near the surface, while coarser ones are employed far from the plate as the free stream conditions are approached. Uniform fine meshes (with step size $\Delta\xi = 0.001$) are used in the flow direction parallel to the plate (ξ direction) in order to capture any discontinuities or singularities that may occur along the plate.

The first-order derivatives with respect to ξ are approximated by two-point backward difference quotients, whereas equations with second-order derivatives with respect to η are approximated by three-point central difference quotients. Differencing of first-order equations in η is accomplished by the trapezoidal rule. The solution is started at $\xi = 0$ and marched forward toward $\xi = 1$. At each line of constant ξ, a tridiagonal matrix of algebraic equations representing the partial differential equations is solved. Because of the nonlinear nature of the governing equations, iteration is used until convergence of the desired solution is reached. Since the solution of the hydrodynamic problem is independent from the thermal problem, the balance laws of mass and linear momentum for both phases are solved first. Once the hydrodynamic solution is obtained, it is used to solve the energy equations of both phases. At each line of constant ξ, iteration is continued until the desired convergence criterion between the current and the previous iteration (10^{-5} in this case) is satisfied.

Many numerical results were obtained through the course of this work. For brevity, a few are shown graphically in Figs. 1–5 to illustrate the influence of the particle loading κ and the inverse Schmidt number δ on the solutions.

Figures 1 and 2 present the fluid-phase temperature H and the particle-phase temperature H_p at various ξ locations along the plate, respectively. It is apparent that unlike the dusty-gas results (without diffusion), continuous solutions exhibiting the proper transition from thermally frozen conditions to thermally equal conditions exist. Figure 3 shows the development of the wall heat transfer coefficient $\mathring{q}_w$ along the plate for various particle loading conditions. It can be seen from this figure that the wall heat transfer increases as the particle loading increases. This is due to the increase in the interaction between the two phases in which the fluid gains kinetic and thermal energy from the particles. Figures 4 and 5 depict the effect of the inverse Schmidt number δ on the particle-phase density at the wall $Q_p(\xi, 0)$ and the wall heat transfer coefficient $\mathring{q}_w$, respectively. It can be seen that while δ appears to have a significant effect on the behavior of the particle-phase wall density, it seems to have little effect on the wall heat transfer. Figure 4 shows a situation in which a limiting process by a gradual reduction in the value of δ produces a closer and closer approach to the original dusty-gas solution. This is an indication that the singularity in the particle-phase density observed in the original dusty-gas model is real and not an artifact of the numerical procedure. It should be noted that the peaks in $\mathring{q}_w$ are expected and they are well-known features of relaxation type problems. Since the value of ϵ used to produce the numerical results is taken to be unity, the approach of the velocity and temperature profiles from frozen to equilibrium conditions occurs at the same rate.

Conclusion

Equations governing boundary-layer flow of a particulate suspension exhibiting small volume fraction with particulate diffusivity past a semi-infinite flat plate were developed. A fully implicit finite difference scheme was employed to solve the governing equations, and graphic results for the temperature profiles of both the fluid and particle phases, the particle-phase wall density, and the rate of heat transfer to the plate surface were presented and discussed. These results were used

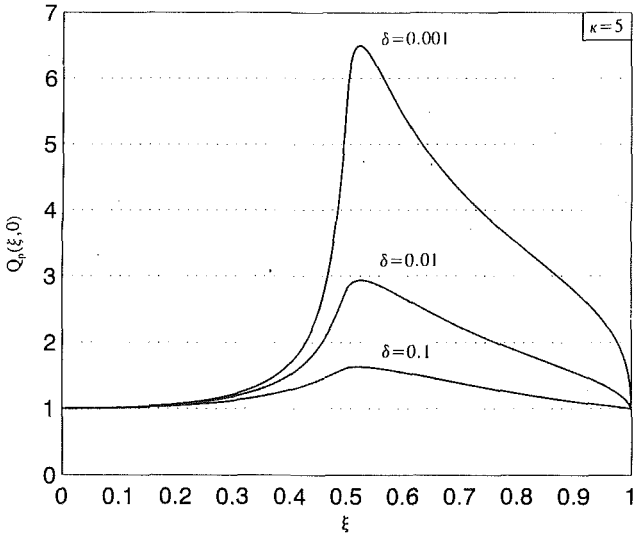

Fig. 4 Particle-phase wall density versus position

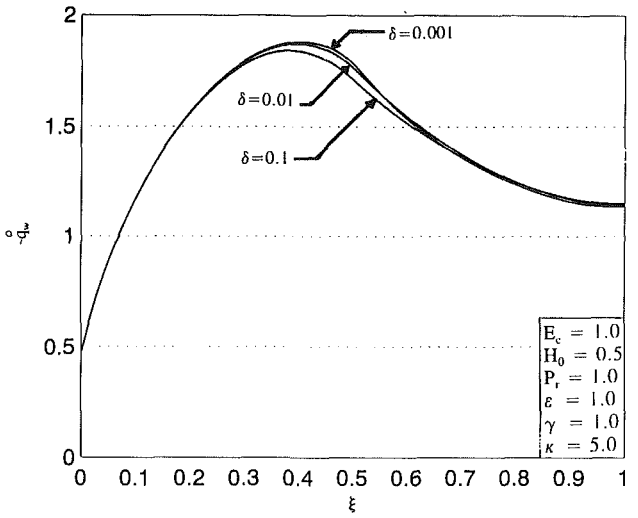

Fig. 5 Wall heat transfer coefficient versus position

to show the influence of the particle loading and the inverse Schmidt number on the thermal aspects of this problem. It was found that when the dusty-gas model is modified to include such effects as diffusion of particles, a singularity-free solution exists. The presence of the particle-phase diffusivity in the model provides enough smoothing to prevent a singularity from forming in the particle-phase density as predicted by the diffusionless dusty-gas equations. This is an example where a small change in the physical model causes significant changes in predictions. It was also found that while particle-phase diffusion affects the particle-phase density greatly, it has slight effect on the wall heat transfer. It should be pointed out that comparison of the numerical results with experimental data is not possible at present due to the absence of such data.

References

Blottner, F. G., 1970, "Finite Difference Methods of Solution of the Boundary Layer Equations," *AIAA Journal*, Vol. 8, pp. 193–205.

Chamkha, A. J., and Peddieson, J., 1989, "Boundary Layer Flow of a Particle-Fluid Suspension Past a Flat Plate," *Developments in Mechanics*, Vol. 15, pp. 315–316.

Chamkha, A. J., 1992, "Thermal Boundary Layer for Flow of a Particulate Suspension Over a Flat Plate," *Developments in Theoretical and Applied Mechanics*, Vol. 16, pp. II-4.24–II-4.30.

Drew, D. A., and Segal, L. A., 1971, "Analysis of Fluidized Beds and Foams Using Averaged Equations," *Studies in Applied Mathematics*, Vol. 50, pp. 233–252.

Marble, F. E., 1970, "Dynamics of Dusty Gases," *Annual Review of Fluid Mechanics*, Vol. 2, pp. 397–446.

Osiptsov, A. N., 1980, "Structure of the Laminar Boundary Layer of a Disperse Medium on a Flat Plate," *Fluid Dynamics*, Vol. 15, pp. 512–517.

Prabha, S., and Jain, A. C., 1980, "On the Use of Compatibility Conditions in the Solution of Gas Particulate Boundary Layer Equations," *Applied Scientific Research*, Vol. 36, pp. 81–91.

Soo, S. L., 1968, "Non-equilibrium Fluid Dynamics—Laminar Flow Over a Flat Plate," *Z. angew. Math. Phys.*, Vol. 19, pp. 545–563.

Transport Phenomena at Entrance Regions of Rotating Heated Channels With Laminar Throughflow

Shin Fann,[1] Wen-Jei Yang,[1] and S. Mochizuki[2]

Nomenclature

a = channel height in the y direction, m
b = channel width in the z direction, m
f = friction factor
H = distance from rotational axis to inlet, m
h = convective heat transfer coefficient, W/m^2-°C
k = conductivity of fluid
Nu_x = locally averaged Nusselt number over a wall $= ha/k$
Nu = circumferentially averaged Nusselt number
$\overline{\mathrm{Nu}}$ = the integrated mean value of the circumferentially averaged Nu over the flow channel from inlet $x=0$ to be designated distance $x=1.0$ $(X=20a)$
Pr = Prandtl number
q_w = local wall heat flux, W/m^2
Re = Reynolds number $= U_o a/\nu$
Ro = Rossby number $= \Omega a/U_o$
Ta = Taylor number $= \Omega a^2/\nu =$ ReRo
T_o = inlet mean temperature, °C
T = fluid temperature, °C
T_w = wall temperature, °C
U, V, W = velocity components in the x, y, z directions, respectively, m/s
U_o = inlet mean velocity, m/s
u, v, w = dimensionless velocity components in (x, y, z) directions, respectively
X = distance in the axial direction measured from flow inlet, m
Y = coordinate in the direction of rotation, m
Z = distance along rotational axis, m
x, y, z = dimensionless coordinate system with origin at center of channel cross section
x', y', z' = dimensionless coordinate system with origin at intersection of left side wall and trailing wall
ζ = aspect ratio $= b/a$
ν = kinematic viscosity, m^2/s
Ω = angular velocity of rotation, s^{-1}

[1] Department of Mechanical Engineering and Applied Mechanics, University of Michigan, Ann Arbor, MI 48109.

[2] Department of Mechanical Systems Engineering, Tokyo University of Agriculture and Technology, Koganei, Tokyo, Japan.

Contributed by the Heat Transfer Division for publication in the JOURNAL OF HEAT TRANSFER. Manuscript received by the Heat Transfer Division September 1991; revision received August 1993. Keywords: Numerical Methods, Rotating Flows. Associate Technical Editor: R. J. Simoneau.

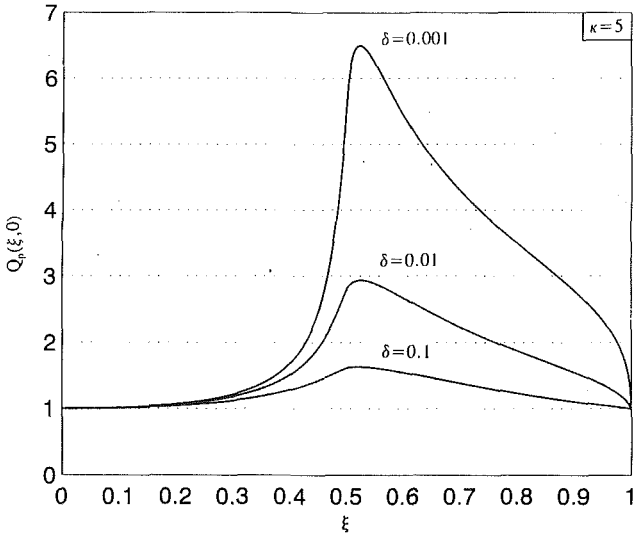

Fig. 4 Particle-phase wall density versus position

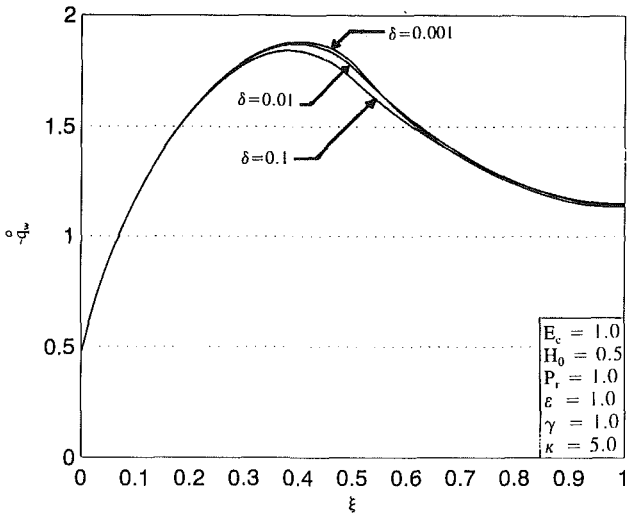

Fig. 5 Wall heat transfer coefficient versus position

to show the influence of the particle loading and the inverse Schmidt number on the thermal aspects of this problem. It was found that when the dusty-gas model is modified to include such effects as diffusion of particles, a singularity-free solution exists. The presence of the particle-phase diffusivity in the model provides enough smoothing to prevent a singularity from forming in the particle-phase density as predicted by the diffusionless dusty-gas equations. This is an example where a small change in the physical model causes significant changes in predictions. It was also found that while particle-phase diffusion affects the particle-phase density greatly, it has slight effect on the wall heat transfer. It should be pointed out that comparison of the numerical results with experimental data is not possible at present due to the absence of such data.

References

Blottner, F. G., 1970, "Finite Difference Methods of Solution of the Boundary Layer Equations," *AIAA Journal*, Vol. 8, pp. 193–205.

Chamkha, A. J., and Peddieson, J., 1989, "Boundary Layer Flow of a Particle-Fluid Suspension Past a Flat Plate," *Developments in Mechanics*, Vol. 15, pp. 315–316.

Chamkha, A. J., 1992, "Thermal Boundary Layer for Flow of a Particulate Suspension Over a Flat Plate," *Developments in Theoretical and Applied Mechanics*, Vol. 16, pp. II-4.24–II-4.30.

Drew, D. A., and Segal, L. A., 1971, "Analysis of Fluidized Beds and Foams Using Averaged Equations," *Studies in Applied Mathematics*, Vol. 50, pp. 233–252.

Marble, F. E., 1970, "Dynamics of Dusty Gases," *Annual Review of Fluid Mechanics*, Vol. 2, pp. 397–446.

Osiptsov, A. N., 1980, "Structure of the Laminar Boundary Layer of a Disperse Medium on a Flat Plate," *Fluid Dynamics*, Vol. 15, pp. 512–517.

Prabha, S., and Jain, A. C., 1980, "On the Use of Compatibility Conditions in the Solution of Gas Particulate Boundary Layer Equations," *Applied Scientific Research*, Vol. 36, pp. 81–91.

Soo, S. L., 1968, "Non-equilibrium Fluid Dynamics—Laminar Flow Over a Flat Plate," *Z. angew. Math. Phys.*, Vol. 19, pp. 545–563.

Transport Phenomena at Entrance Regions of Rotating Heated Channels With Laminar Throughflow

Shin Fann,[1] Wen-Jei Yang,[1] and S. Mochizuki[2]

Nomenclature

a = channel height in the y direction, m
b = channel width in the z direction, m
f = friction factor
H = distance from rotational axis to inlet, m
h = convective heat transfer coefficient, W/m^2-°C
Nu_x = locally averaged Nusselt number over a wall $= ha/k$
Nu = circumferentially averaged Nusselt number
$\overline{\mathrm{Nu}}$ = the integrated mean value of the circumferentially averaged Nu over the flow channel from inlet $x=0$ to be designated distance $x=1.0$ $(X=20a)$
Pr = Prandtl number
q_w = local wall heat flux, W/m^2
Re = Reynolds number $= U_o a/\nu$
Ro = Rossby number $= \Omega a/U_o$
Ta = Taylor number $= \Omega a^2/\nu =$ ReRo
T_o = inlet mean temperature, °C
T = fluid temperature, °C
T_w = wall temperature, °C
U, V, W = velocity components in the x, y, z directions, respectively, m/s
U_o = inlet mean velocity, m/s
u, v, w = dimensionless velocity components in (x, y, z) directions, respectively
X = distance in the axial direction measured from flow inlet, m
Y = coordinate in the direction of rotation, m
Z = distance along rotational axis, m
x, y, z = dimensionless coordinate system with origin at center of channel cross section
x', y', z' = dimensionless coordinate system with origin at intersection of left side wall and trailing wall
ζ = aspect ratio $= b/a$
ν = kinematic viscosity, m^2/s
Ω = angular velocity of rotation, s^{-1}

[1] Department of Mechanical Engineering and Applied Mechanics, University of Michigan, Ann Arbor, MI 48109.

[2] Department of Mechanical Systems Engineering, Tokyo University of Agriculture and Technology, Koganei, Tokyo, Japan.

Contributed by the Heat Transfer Division for publication in the JOURNAL OF HEAT TRANSFER. Manuscript received by the Heat Transfer Division September 1991; revision received August 1993. Keywords: Numerical Methods, Rotating Flows. Associate Technical Editor: R. J. Simoneau.

Subscripts

o = value at inlet
w = value on wall
x = local value at x

Superscripts

— = averaged value

Introduction

Heat transfer in rotating systems is encountered in many engineering applications. One of these widely used systems is a heated rectangular channel subjected to a radial rotation, where the rotating axis is perpendicular to the channel axis as described in Fig. 1. One typical example of the application of radial rotation is the internal cooling in turbine blade.

Both Mori and Nakayama (1968) and Ito and Nanbu (1971) studied theoretically a fully developed, laminar flow assuming that the flow consists of a central core with a relatively thin boundary layer in the immediate vicinity of the wall. The former concluded that the Coriolis force caused a significant increase in both friction coefficient and Nusselt number under two limiting thermal boundary conditions, i.e., constant wall heat flux and wall temperature. In an experimental study on the effect of radial rotation on heat transfer, Mori et al. (1971) disclosed that the heat transfer data for the uniform wall heat flux case were closed to those of the uniform wall temperature case but were higher than theoretical predictions (Mori and Nakayama, 1968). The study was extended to the theoretical study of turbulent flow. The results for friction coefficient agreed well with experimental data. An experimental study was performed on laminar heat transfer in the entrance region with rotation by Metzger and Stan (1977). Heat transfer enhancement was found to be significantly lower than that predicted by Mori and Nakayama (1968).

In the experimental investigation on heat transfer inside tubes in either radial- or parallel-mode rotation, Morris (1981) disclosed that irrespective of throughflow rate, an increase in the heat flux resulted in a retardation of both the local and mean Nusselt numbers in the radial outflow case but an enhancement in the inward flow case. Harasgama and Morris (1988) revealed that an increase in the centripetal buoyancy caused a decrease in the average heat transfer performance in the radial outflow case. The opposite was true in the inward flow case, where heat transfer was enhanced on the leading (suction) side but diminished on the trailing (pressure) side.

In a theoretical investigation on a hydrodynamically and thermally fully developed flow inside a rotating isothermal duct, Hwang and Jen (1990) employed a temperature distribution equation for a forced or combined convection flow through a nonrotating passage (Shah and London, 1978) to estimate the temperature field in the rotating duct. In an experimental study, Soong et al. (1991) disclosed that (*i*) the growth and strength of the secondary flow depends on the rotational Reynolds number, (*ii*) the effect of buoyancy flow is characterized by the rotational Rayleigh number, and (*iii*) the aspect ratio of the duct is a critical parameter in the heat transfer mechanism, affecting the secondary flow and buoyancy flow. However, the averaged Nusselt numbers appeared to be much higher than the previous results (Mori and Nakayama, 1968; Mori et al., 1971; Metzger and Stan, 1977). Jen et al. (1992) investigated the entrance region of a rotating isothermal square channel, ranging from the entrance to about 0.2–0.25 $X/(a\,\mathrm{Re})$. A secondary vortex breakdown was disclosed at certain Reynolds and Rossby numbers. In an independent study taking into account the centripetal buoyancy effects, Fann and Yang (1992) and Fann et al. (1992) studied the transport phenomena numerically in the entrance region of rotating channels, taking into account the effects of the aspect ratio. Principal vortices are found in the entrance region

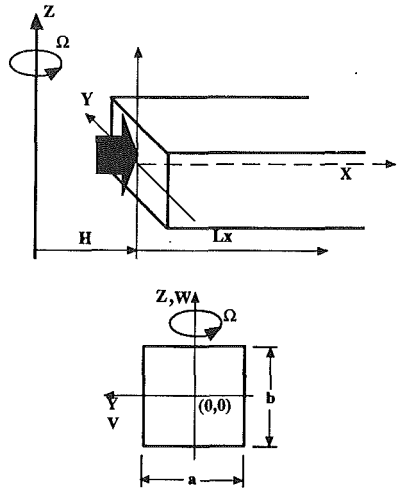

Fig. 1 Coordinate system on rotating channel

at a very short distance from the entrance. Vortex numbers are varied with the geometry, Reynolds number, Rossby number, and location along the channel.

The present study treats the transport phenomena in a radially outward laminar, incompressible flow through rotating channels with either uniform wall temperature or uniform wall heat flux. The flow is hydrodynamically and thermally developing in the region from the inlet up to 20 times channel height taking into account the effect of aspect ratios. The velocity-vorticity method (Ramakrishna et al., 1982; Chou, 1986) is employed in formulation. The transverse velocities are determined directly from two Poisson equations, which are derived from the axial vorticity and the continuity equation. The resulting equations in the form of parabolic flow (Patankar, 1982) are numerically calculated for the axial velocity, axial vorticity, and temperature. The heat transfer performance for the two limiting thermal conditions is determined and results are compared with those available in the existing literature.

Results and Discussion

The formulation and numerical scheme used by Fann and Yang (1992) are adopted here and thus are not repeated. The ranges of parameters used in the present study are: (1) $\mathrm{Re}=500$, 1000, 1500, 2000, and 2300; (2) $\mathrm{Ro}=0.0$, 0.001, 0.01, 0.1, 0.25, and 0.4; (3) $\mathrm{Pr}=0.70$ (air); (4) characteristic temperature $T_w-T_o=10.0$ for the isothermal case and $q_w\,a/k=10.0$ for the iso-flux case; (5) aspect ratio $\zeta=0.50$, 1.0, and 2.0; (6) eccentricity distance $h^*=10a$. The trailing wall refers to the wall at $y'=0.0$, leading wall at $y'=1.0$, and side walls at $z'=0.0$ and 1.0. The trailing half represents the area beyond $y'=0.50$ in the channel cross section, while the leading half preceding $y'=0.50$.

It should be noted that although Jen et al. (1992) disclosed that the vortices become asymmetric at long distance from the entrance at certain Reynolds and Rossby numbers, the flows are fairly symmetric (with respect to the channel centerline $z'=0.5$) within the distance discussed in the present study. Figure 2 plots the product of the circumferentially averaged friction factor f and Reynolds number, $f\mathrm{Re}$, against the axial location X/a at $R_0=0.25$ for various aspect ratios. The entrance effect is manifested by a drastic fall in $f\mathrm{Re}$ at downstream from the inlet. At a low value of Re; e.g., $\mathrm{Re}=500$, the variation of $f\mathrm{Re}$ with X/a is monatomic, similar to that in the entrance region of a nonrotating channel flow. However, as the Reynolds number is increased, the variation of friction factor along the channel is intensified. It is caused by the emergence and enhancement of the principal vortices (primary vortices) and, in some cases, by the generation of secondary

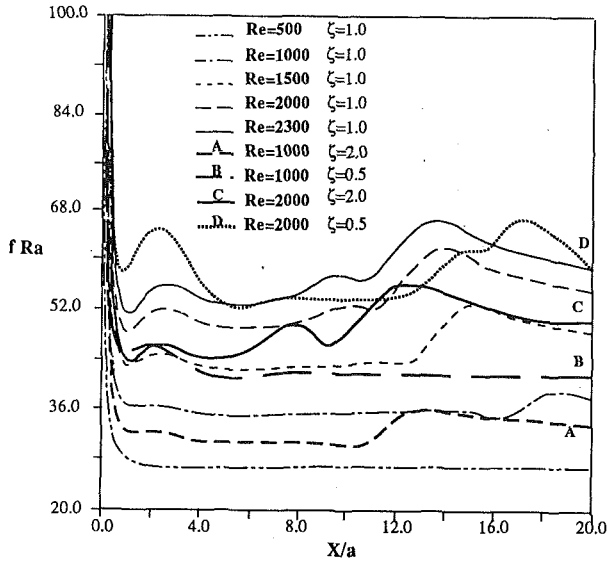

Fig. 2 Effects of Re and ζ on variation of circumferentially averaged friction performance along channel axis at Ro = 0.25, $q_w a/k = 10$ (or $T_w - T_o = 10$), and Pr = 0.7

vortices (small vortices near the trailing walls). The inception of the secondary vortices triggers an increase in the flow resistance. Once the secondary vortices are developed, the friction factor tends to stabilize, as evidenced in the curves for Re = 1500, 2000, and 2300. Figure 2 also depicts the effects of the aspect ratio ζ on fRe, which takes a higher value in the narrow rectangular channel ($\zeta = 0.5$) and a lower one in the flat rectangular channel ($\zeta = 2.0$) than the one in the square channel ($\zeta = 1.0$). The curve D for Re = 2000 and $\zeta = 0.5$ exhibits a rebound followed by a flat valley until X approaches $12a$ in the absence of secondary vortices.

Figure 3 compares the circumferentially averaged heat transfer coefficients, Nu, between the uniform wall temperature and uniform wall heat flux cases. It is observed that in the entrance region the former is lower in magnitude than the latter and diminishes more rapidly. This is in agreement with the stationary tubes or ducts in which the uniform wall heat flux case has higher heat transfer performance than the uniform wall temperature case, as seen in Fig. 3(b) for Ro = 0.0. Also observed is that the effect of the Coriolis force on convective heat transfer is negligible in the entrance region. As the flow proceeds downstream, however, the circumferentially averaged Nusselt number for the uniform wall temperature case surpasses that for the uniform wall heat flux case, exhibiting distinct bumps. It suggests a complexity of the Coriolis effect on the heat transfer performance in a rotating, uniform temperature flow passage. In contrast, Figs. 3(a-c) demonstrate a stronger effect of rotation on the uniform wall temperature case than on the uniform wall heat flux one. Figure 3(a) reveals that the bump moves upstream with an increase in Re, because an increase in flow promotes the incipience of the secondary vortices. Although an increase in rotational speed enhances the heat transfer performance, an augmentation of Nu from Ro = 0.25 to 0.40 is less than that between Ro = 0.10 and 0.25. Heat transfer enhancement is practically null at a very slow rotational speed; e.g., from Ro = 0.0 to 0.001 in Fig. 3(b). Figure 3(c) depicts that the heat transfer performance in a narrow channel is better than that in square and flat channels in both the uniform wall temperature and wall heat flux cases.

$\overline{\text{Nu}}$ is defined as the integrated mean value of the circumferentially averaged heat transfer coefficients Nu over the square channel from the entrance to designated distance $X/a = 20$. It is plotted against PrReTa in Figs. 4(a,b) for the uniform wall temperature and wall heat flux cases, respectively.

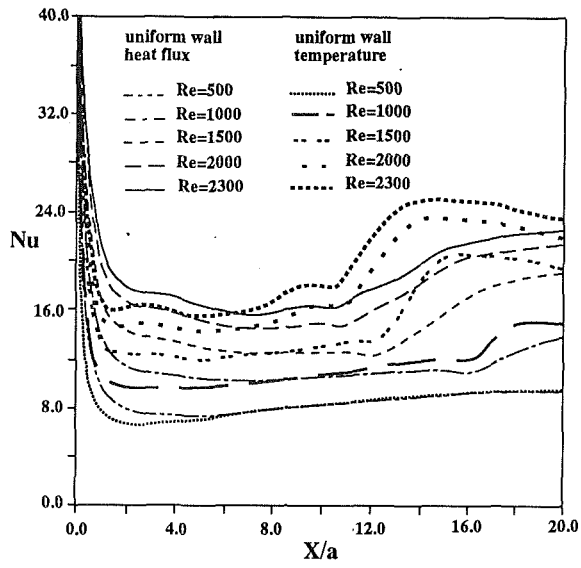

(a)

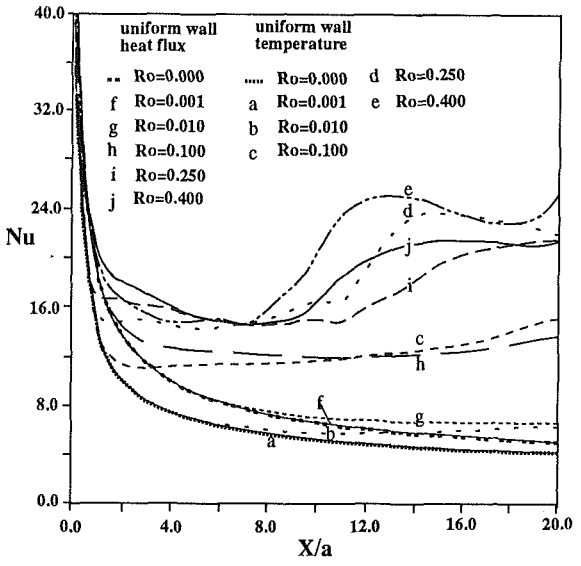

(b)

Fig. 3 Comparison of the circumferentially averaged Nusselt number for the uniform wall temperature ($T_w - T_o = 10$) and uniform wall heat flux ($q_w a/k = 10$) cases, (a) Ro = 0.25, Pr = 0.7, and $\zeta = 1.0$, (b) Re = 2000, Pr = 0.7, and $\zeta = 1.0$, and (c) Re = 2000, Ro = 0.25, and Pr = 0.7

Superimposed on the figures for comparison are results of the existing literature, including: (1) empirical correlation for isothermal circular tubes by Mori et al. (1971), (2) experimental data for isothermal square channels with $L/D = 30$ from Hwang and Jen (1990), (3) numerical results for fully developed flow in isothermal square channels by Hwang and Jen (1990) and Soong et al. (1991), (4) numerical results for fully developed flow in circular tubes with isothermal or iso-flux wall by Mori and Nakayama (1968), and (5) experimental results of isothermal circular tubes with various L/D by Metzger and Stan (1977). It is seen in both Figs. 4(a) and (b) that in comparison with the empirical correlation (Mori et al., 1971) and test data (Metzger and Stan, 1977), the present theory overpredicts in the range of lower PrReTa but agrees satisfactorily in the higher PrReTa range. The overprediction is expected since the present study deals with a developing velocity and temperature case where the entrance effects result in a higher heat transfer performance. The theoretical prediction for the uniform wall tem-

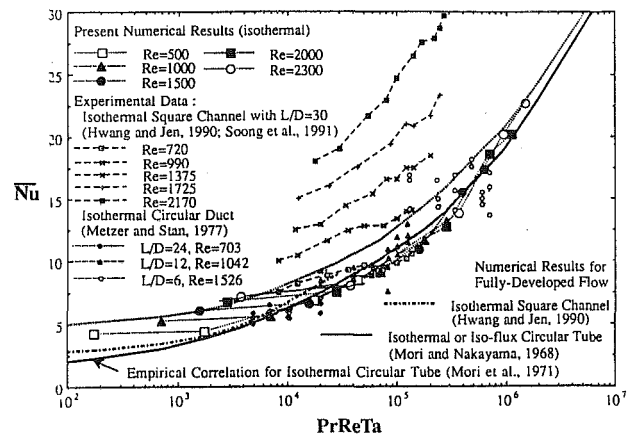

(a)

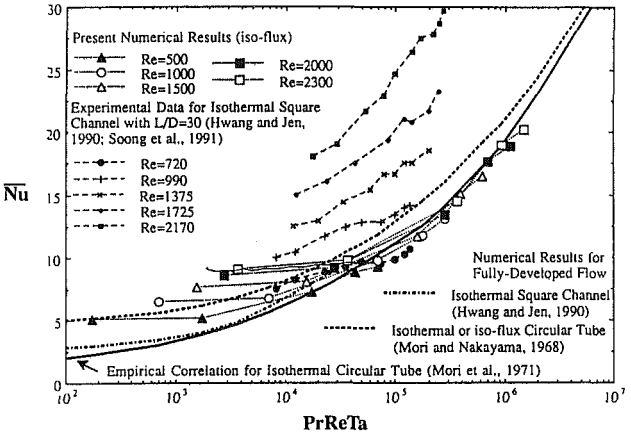

(b)

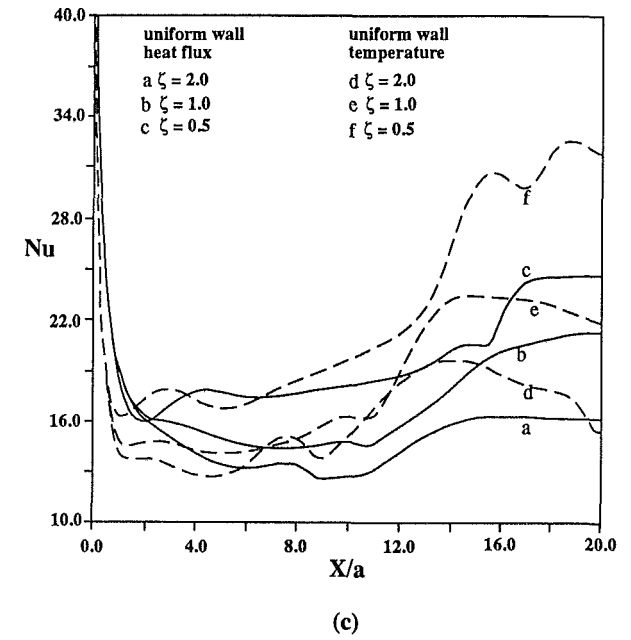

(c)

Fig. 4 Comparison of the present theory with existing literature on $\overline{Nu}$ versus PrReTa: (*a*) uniform wall temperature case, and (*b*) uniform wall heat flux case

perature case falls within the region between the empirical correlation (Mori et al., 1971) and analytical result (Mori and Nakayama, 1968) in the lower PrReTa range. The high data of Hwang and Jen (1990) and Soong et al. (1991) may be caused by the end effect of short ducts.

Conclusions

The Coriolis force induces the generation or decay of vortex pairs on the trailing wall, which undergo complex interactions. This results in an enhancement in both the circumferentially averaged friction factor f and Nusselt number Nu, and fluctuations of f and Nu along the flow. In general, both f and Nu are augmented with an increase in the rotational speed Ro and the throughflow rate Re. At stationary and low rotational speed cases ($Ro \leq 0.01$), the circumferentially averaged Nu for the uniform wall temperature case is lower than that for the uniform wall heat flux case. As the rotational speed is increased, the Nu for the uniform wall temperature case is lower than that for the uniform wall heat flux case near the inlet but surpasses it downstream. Generally, heat transfer in a narrow channel is better than that in square and flat channels in both the uniform wall temperature and wall heat flux cases. In summary, the mean heat transfer coefficient for the uniform wall temperature case is lower than that for the uniform wall heat flux case in the low PrReTa range and the opposite is true in the high PrReTa range.

Acknowledgments

This study was supported by the Electric Power Research Institute under EPRI Agreement RP 8006-11.

References

Chou, F. C., 1986, "Combined Free and Forced Laminar Convection in Horizontal Rectangular Channels," Ph.D. Thesis, National Tsing Hua University, Taiwan.

Fann, S., and Yang, W. J., 1992, "Hydrodynamically-Thermally Developing Laminar Flow Through Rotating Channels Having Isothermal Walls," *Numerical Heat Transfer*, Vol. 22, No. 3, pp. 257-288.

Fann, S., Yang, W. J., and Mochizuki, S., 1992, "Heat and Fluid Flow at Entrance Regions of Rotating Iso-heat Flux Channels With Laminar Throughflow," *Int. J. Numerical Methods for Heat and Fluid Flow*, Vol. 2, pp. 335-358.

Harasgama, S. P., and Morris, W. D., 1988, "The Influence of Rotation on the Heat Transfer Characteristics of Circular, Triangular, and Square-Section Coolant Passages of Gas Turbine Rotor Blade," ASME *Journal of Turbomachinery*, Vol. 110, pp. 44-50.

Hwang, G. J., and Jen, T. C., 1990, "Convective Heat Transfer in Rotating Isothermal Ducts," *International Journal of Heat and Mass Transfer*, Vol. 33, No. 9, pp. 1817-1828.

Ito, H., and Nanbu, K., 1971, "Flow in Rotating Straight Pipes of Circular Cross Section," ASME *Journal of Basic Engineering*, Vol. 93, pp. 383-394.

Jen, T. C., Lavine, A. S., and Hwang, G. J., 1992, "Simultaneously Developing Laminar Convection in Rotating Isothermal Square Channels," *International Journal of Heat Mass Transfer*, Vol. 35, No. 1, pp. 239-254.

Metzger, D. E., and Stan, R. L., 1977, "Entry Region Heat Transfer in Rotating Radial Tubes," *AIAA 15th Aerospace Science Meeting*, pp. 77-189.

Mori, Y., and Nakayama, W., 1968, "Convective Heat Transfer in Rotating Radial Circular Pipe (1st Report, Laminar Region)," *International Journal of Heat and Mass Transfer*, Vol. 11, pp. 1027-1040.

Mori, Y., Fukada, T., and Nakayama, W., 1971, "Convective Heat Transfer in Rotating Circular Pipe (2nd Report)," *International Journal of Heat and Mass Transfer*, Vol. 14, pp. 1807-1824.

Morris, W. D., 1981, *Heat Transfer and Fluid Flow in Rotating Coolant Channels*, Wiley, New York.

Patankar, S. V., 1982, *Numerical Heat Transfer and Fluid Flow*, Hemisphere, New York.

Ramakrishna, K., Rubin, S. G., and Khosla, P. K., 1982, "Laminar Natural Convection Along Vertical Square Ducts," *Numerical Heat Transfer*, Vol. 5, pp. 59-79.

Shah, R. K., and London, A. L., 1978, *Laminar Flow Forced Convection in Ducts*, Academic Press, New York.

Soong, C. Y., Lin, S. T., and Hwang, G. J., 1991, "An Experimental Study of Convective Heat Transfer in Radially Rotating Rectangular Ducts," ASME JOURNAL OF HEAT TRANSFER, Vol. 113, pp. 604-611.

A Study of Natural Convection Between Inclined Isothermal Plates

A. G. Straatman,[1] D. Naylor,[2] J. M. Floryan,[3] and J. D. Tarasuk[3]

Nomenclature

b = channel half-width
g = acceleration due to gravity
Gr = Grashof number $= g\beta(T_w - T_o)b^3/\nu^2$
k = thermal conductivity of fluid
L = height of heated channel
Nu_m = average channel Nusselt number
Nu_y = local Nusselt number
Pr = Prandtl number
Q^* = dimensionless induced flow rate
r = radial coordinate in semicircular region
R = inlet radius
Ra^* = modified Rayleigh number $= \mathrm{GrPr}(b/L)$
T_o = ambient fluid temperature
T_w = wall temperature
u, v = velocity components in x and y directions
x, y = Cartesian coordinates
β = volumetric expansion coefficient
θ = angle of inclination with respect to gravity
ν = kinematic viscosity
ψ = dimensionless stream function

Subscripts

m = average
o = ambient
w = wall
y = local

Introdution

Natural or free convection between flat parallel surfaces is one of many fundamental engineering problems. Continued studies in this area are motivated by the increasing importance of accurately estimating heat dissipation and fluid flow in different situations. Heated channel configurations are found in computers and modern electronics where waste heat is still commonly extracted by natural convection. The case where the surfaces are parallel and vertical has received much attention in the past (see Elenbaas, 1942; Bodoia and Osterle, 1962; Aung, 1972; Sparrow and Bahrami, 1980; Wirtz and Stutzman, 1982; Naylor et al., 1991). In comparison, the inclined channel has received relatively little attention since the pioneering work by Elenbaas (1942) until recently.

Azevedo and Sparrow (1985) performed experiments on an inclined, isothermal channel using water as the convecting fluid. Three modes of heating were investigated; both walls heated, top wall only heated, and bottom wall only heated. Heat transfer was calculated using an energy balance technique and only overall quantities were discussed. No detailed information showing local heat transfer along each wall was presented. The recent numerical study by Naylor et al. (1991) was an investigation of free convection from an isothermal, vertical channel, which disclosed some previously undocumented flow behavior. Nontrivial inlet boundary conditions derived from Jeffrey-Hamel flow were imposed on a semicircular boundary located near the channel inlet. New information regarding flow separation above the channel inlet was discussed in terms of its effect on local heat transfer. The existence of flow separation above the channel inlet raises questions as to whether the symmetry of the flow, and more importantly, the local heat transfer will be affected when the channel is inclined with respect to gravity.

The present study was undertaken to examine the effects of inclining an isothermal, parallel-walled channel with respect to gravity. The main objective was to provide the local heat flux distributions along the walls emphasizing the behavior near the inlet where flow separation was expected to occur (in the upper portion of the heating range). The channel was investigated for a single aspect ratio, $L/b = 24$, over the range: $2.917 \le \mathrm{Ra}^* \le 291.7$, $0 \text{ deg} \le \theta \le 30$ deg. The full elliptic form of the governing equations was solved using FIDAP (Fluid Dynamics International, Version 4.2, 1989) which is based on the finite element discretization technique. Experimental validation was done for one set of heating conditions using a Mach-Zehnder interferometer.

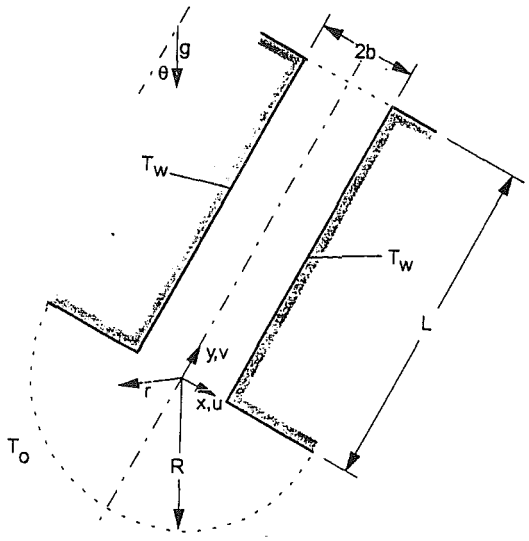

Fig. 1 Geometry under investigation, showing dimensions and coordinate system

Theoretical Formulation

The geometry to be analyzed is shown in Fig. 1. Two plates of length L, and width w are set a distance $2b$ apart and inclined by an angle θ with respect to gravity. The plates are maintained at a constant temperature T_w above the ambient T_o. Assuming that the width of the plates is very large compared to the other dimensions, the edge effects (three-dimensional effects) are ignored and the geometry of the problem is reduced to a two-dimensional section of the channel formed by the two plates. The formulation of the dimensionless governing equations and the boundary conditions used in the present study are described in the elliptic solution given by Naylor et al. (1991) and are omitted here for brevity. The important difference in the present treatment is that symmetry about the channel centerline is not assumed a priori; thus, the solution domain and boundary conditions were extended to include both walls of the heated

[1]Graduate Student, The University of Waterloo, Waterloo, Ontario, Canada.
[2]Postdoctoral Fellow, Queen's University, Kingston, Ontario, Canada.
[3]Professor of Mechanical Engineering, The University of Western Ontario, London, Ontario, Canada.

Contributed by the Heat Transfer Division of The American Society of Mechanical Engineers. Manuscript received by the Heat Transfer Division February 1, 1993; revision received August 12, 1993. Keywords: Electronic Equipment, Flow Separation, Natural Convection. Associate Technical Editor: J. R. Lloyd.

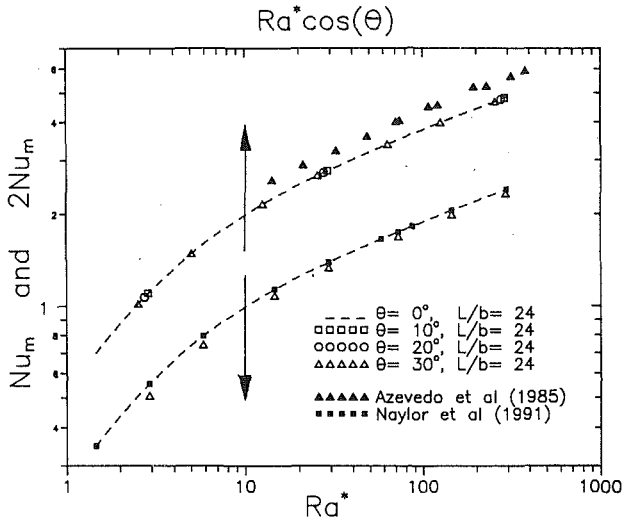

Fig. 2 Present numerical results of overall channel Nusselt number for 0 deg $\leq \theta \leq$ 30 deg shown with existing numerical data for $\theta = 0$ deg and existing experimental data for $\theta = 30$ deg

channel and the entire inlet and outlet regions (as shown in Fig. 1).

Numerical Solution

The numerical solution was computed using the commercial software FIDAP (Fluid Dynamics International, Version 4.51, 1989), which utilizes finite element discretization. As mentioned in the *Theoretical Formulation*, the possibility of asymmetry about the channel center line was a consideration in the present work. For this reason, the finite element grid was designed to model the entire channel and inlet regions. A final mesh, which consisted of 5136 nine-node quadrilateral elements (19,793 nodes), was established by performing a sequence of calculations at an increasing grid density. In addition, the radius of the inlet, $R = 5$, was established through a sequence of calculations with increasing R. The results for flow rate, Q^*, and overall Nusselt number, Nu_m, were numerically accurate to better than 1 percent with these parameters. Local Nusselt numbers, Nu_y, were unchanged to within 3 percent near the bottom corners of the channel tapering off to better than 1 percent for the remainder of the walls. Computations were carried out for air ($\mathrm{Pr} = 0.7$) over the range $2.917 \leq \mathrm{Ra}^* \leq 291.7$, 0 deg $\leq \theta \leq$ 30 deg for $L/b = 24$.

Experimental Solution

Experiments were performed in ambient air using a Mach-Zehnder interferometer. The reader is directed to Naylor (1991) for a detailed description of the experimental model used. The experiment was carried out to validate the results for the largest inclination angle studied numerically ($\theta = 30$ deg) and the highest heating that could be achieved with the experimental model ($\mathrm{Ra}^* = 7.788$).

The experiment was initiated by obtaining an infinite fringe setting on the interferometer across the aligned, unheated model using the procedure outlined by Tarasuk (1968). After a scale photograph was taken, direct current was applied to the heaters and the walls were brought up to the required temperature. When the model reached steady state (usually 30–40 min), an infinite fringe photograph was taken for observation of the temperature field. The interferometer setting was then changed to observe finite fringes and a photograph was obtained for analysis purposes. Local fringe shift gradients were extracted from the fringe photographs using a digital imaging system. Local and overall Nusselt numbers were calculated from the experimental fringe shift gradients for comparison with the numerical results. The estimated experimental error in the local heat transfer coefficients was ± 8 percent and for the overall channel heat transfer, about ± 4 percent. For a detailed treatment of the experimental error for this model, refer to Straatman (1992).

Discussion of Results

The present numerical results for the overall channel Nusselt number, Nu_m, over the entire heating range, Ra^*, and all inclination angles, θ, is shown in Fig. 2. The dashed curve on Fig. 2 represents the reference case where $\theta = 0$ (i.e., vertical channel) computed as part of the present study. The reference case is compared to similar results obtained in the numerical study by Naylor et al. (1991) (solid symbols). Close observation of the results in Fig. 2 indicates that the overall heat transfer from the channel is reduced as the inclination angle is increased ($\theta > 0$ deg), over the entire heating range studied. Results for the overall channel flow rate, Q^* (not shown), were also seen to decrease with increased channel inclination.

The amount by which these quantities are reduced by channel inclination can be quantified by replotting them as a function of the product $\mathrm{Ra}^* \cos(\theta)$. This modification to the independent variable, Ra^*, is widely used in correlations describing free convection from inclined plates. Azevedo and Sparrow (1985) successfully adopted this modification for the presentation of their experimental results from inclined channels. The upper portion of Fig. 2 shows the overall Nusselt number, Nu_m, as a function of the new independent variable, $\mathrm{Ra}^* \cos(\theta)$. The heat transfer results for all angles (0 deg $< \theta <$ 30 deg) collapse to a single curve with no observable scatter indicating the effectiveness of this parameter.

Figure 2 includes a comparison of the present numerical results for Nu_m with experimental results obtained by Azevedo and Sparrow (1985) for $\theta = 30$ deg and various aspect ratios close to $2b/L = 1/12$. Their experimental results, obtained using water ($\mathrm{Pr} = 5$), are an average of about 9 percent higher than the present numerical results for air. Although this difference is within reasonable experimental error, it can be partially attributed to the effect of Prandtl number. Sparrow et al. (1984) made some numerical comparisons of heat transfer in a vertical channel using fluids with Prandtl numbers ranging from 0.7 to 10.0. Their results showed that increasing the Prandtl number enhanced the heat transfer from the channel; thus, the deviation shown above is artificially large because of the different convecting fluids considered. The overall results obtained for $\mathrm{Ra}^* = 7.788$, $\theta = 30$ deg in the present experiments were in excellent agreement with the numerical results.

Figure 3 shows the present numerical results for the heat flux distribution given in terms of the local Nusselt number, Nu_y, along the height of each wall for an inclination angle of $\theta = 30$ deg. Distributions for the upper and lower walls are shown on the same plot to highlight their similarities and differences. The distributions are shown only to $y/L = 0.3$, beyond which they are indistinguishable. Close examination of the graph indicates that the only region where local Nusselt numbers differ slightly is above the channel entrance where flow separation exists. The onset of asymmetry approximately parallels the onset of flow separation, which occurred at $\mathrm{Ra}^* \approx 70$. It is also apparent from the graph that the asymmetry grows with increasing Rayleigh number, Ra^*. This could be associated with the relative growth of the recirculating regions as Ra^* is increased. Figure 4 gives a closeup of identical streamline plots generated for each of the recirculating regions near the inlet of the channel for $\theta = 30$ deg and $\mathrm{Ra} = 291.7$ (most extreme

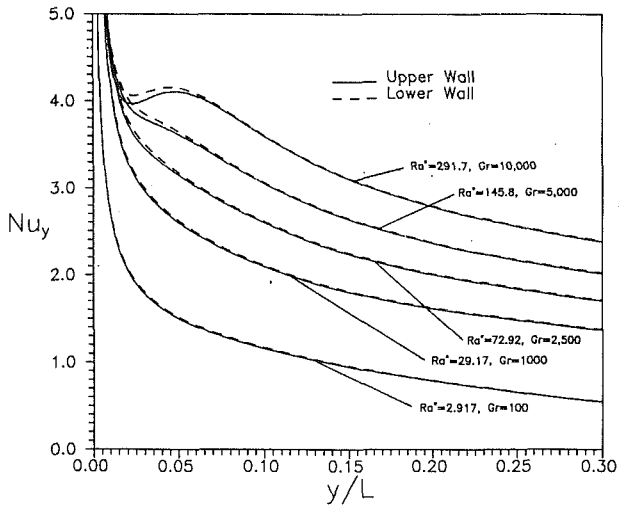

Fig. 3 Comparison of local Nusselt numbers, Nu_y, from the upper and lower walls for $\theta = 30$ deg at selected Rayleigh numbers, Ra^*

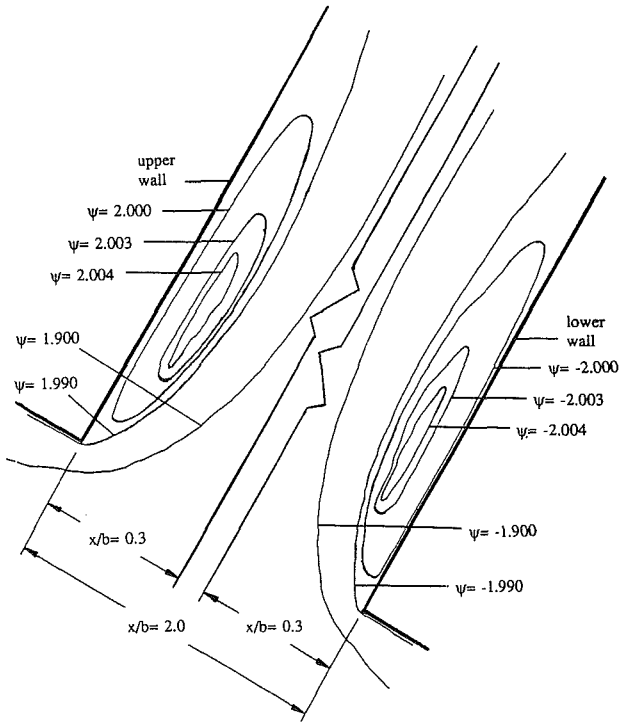

Fig. 4 Streamline plots of the separation regions adjacent to upper and lower walls

case considered). At these conditions, no significant difference exists between the separation regions adjacent to the upper and lower walls. A comparison of the heat transfer results at the same conditions showed that local Nusselt numbers on the lower wall were a maximum of 2.5 percent higher than those on the upper wall (at $y/L \approx 0.02$). This is within the numerical accuracy of the local Nusselt numbers (~3 percent); thus, the asymmetry must be considered insignificant. The present experimental results were obtained at a Rayleigh number ($Ra^* = 7.788$) well below that required to produce flow separation ($Ra^* \approx 70$) due to physical restrictions of the model used. At these conditions, the local Nusselt numbers extracted from the upper and lower walls were identical within the experimental accuracy.

The lack of significant asymmetry agrees qualitatively with the experimental results for single inclined plates obtained by Fujii and Imura (1972). Their experiments concluded that the heat transfer is the same for an upward or downward-facing plate at moderate inclination angles ($0 < 45$ deg) when the flow is laminar. It is important, however, to realize that different physical effects (caused by geometry) take place at the leading edge of a single plate and the inlet corner of a channel (i.e., flow separation). The existence of flow separation at the channel inlet may result in significant asymmetries of heat transfer between the upper and lower walls at higher Rayleigh numbers, Ra^*, and higher inclination angles.

Conclusions

The present study was undertaken to investigate the effect that angle of inclination had on the natural convection heat transfer from an isothermal channel. The overall heat transfer was found to decrease as the inclination angle increased. The amount of the decrease was in good agreement with previous experimental results and is related to the cosine of the inclination angle. Distributions of heat flux along each wall were presented. No significant asymmetric heat transfer was observed in the range of parameters studied. Experimental results obtained using a Mach-Zehnder interferometer were in excellent agreement with the numerical results.

Acknowledgments

The authors gratefully acknowledge the computer funding and resources received from The University of Western Ontario.

References

Aung, W., 1972, "Fully Developed Laminar Free Convection Between Vertical Plates Heated Asymmetrically," *Int. J. Heat Mass Transfer*, Vol. 15, pp. 1577–1580.

Azevedo, L. F. A., and Sparrow, E. M., 1985, "Natural Convection in Open-Ended Inclined Channels," *Int. J. Heat Mass Transfer*, Vol. 107, pp. 893–901.

Batchelor, G. K., 1967, *An Introduction to Fluid Dynamics*, University Press, Cambridge, United Kingdom.

Bodoia, J. R., and Osterle, J. F., 1962, "The Development of Free Convection Between Heated Vertical Plates," ASME JOURNAL OF HEAT TRANSFER, Vol. 84, pp. 40–44.

Elenbaas, W., 1942, "Heat Dissipation of Parallel Plates by Free Convection," *Physica*, Vol. 9, No. 1, pp. 1–28.

Fluid Dynamics International Inc., 1989, Evanston, IL, USA, FIDAP Version 4.51.

Fujii, T., and Imura, H., 1972, "Natural Convection Heat Transfer From a Plate With Arbitrary Inclination," *Int. J. Heat Mass Transfer*, Vol. 15, pp. 755–767.

Naylor, D., 1991, "A Numerical and Interferometric Study of Natural Convective Heat Transfer From Divided and Undivided Vertical Channels," PhD Theses, The University of Western Ontario, Nov.

Naylor, D., Floryan, J. M., and Tarasuk, J. D., 1991, "A Numerical Study of Developing Free Convection Between Isothermal Vertical Plates," ASME JOURNAL OF HEAT TRANSFER, Vol. 113, pp. 620–626.

Sparrow, E. M., and Bahrami, P. A., 1980, "Experiments on Natural Convection From Vertical Parallel Plates With Either Open or Closed Edges," ASME JOURNAL OF HEAT TRANSFER, Vol. 102, pp. 221–227.

Sparrow, E. M., Chrysler, G. M., and Azevedo, L. F., 1984, "Observed Flow Reversals and Measured-Predicted Nusselt Numbers for Natural Convection in a One-Sided Heated Vertical Channel," *Int. J. Heat Mass Transfer*, Vol. 106, pp. 325–330.

Straatman, A. G., 1992, "Heat Transfer Enhancement From a Vertical, Isothermal Channel Generated by the Chimney Effect," Master's Thesis, The University of Western Ontario, Aug.

Tarasuk, J., D., 1968, "The Theory, Design and Operation of the University of Saskatchewan 8-inch Mirror Mach-Zehnder Interferometer," Technical Report C-3, Mechanical Engineering Department, The University of Saskatchewan, June.

Wirtz, R. A., and Stutzman, R. J., 1982, "Experiments on Free Convection Between Vertical Plates With Symmetric Heating," ASME JOURNAL OF HEAT TRANSFER, Vol. 104, pp. 501–507.

Turbulent Natural Convection Heat Transfer to Gases at High Wall Temperatures

K. O. Pasamehmetoglu[1]

Introduction

Turbulent natural convection heat transfer data are typically correlated by

$$\mathrm{Nu} = C \times \mathrm{Ra}^{1/3} \tag{1}$$

where C is the correlation constant. The Nusselt (Nu) and Rayleigh (Ra) numbers are defined as

$$\mathrm{Nu} \equiv \frac{hx}{k} \text{ and } \mathrm{Ra} \equiv \mathrm{Gr} \times \mathrm{Pr} \equiv \frac{g\beta(T_w - T_a)x^3}{\nu^2} \times \mathrm{Pr},$$

where h is the heat transfer coefficient (HTC), x is the characteristic length, k is the fluid thermal conductivity, Gr is the Grashof number, Pr is the Prandtl number, g is the gravitational acceleration, β is the coefficient of thermal expansion for the fluid, T_w is the wall temperature, T_a is the ambient temperature, and ν is the fluid kinematic viscosity. The correlation given by Eq. (1) has been tested successfully against many data points with low wall-to-ambient temperature ratios ($T_w/T_a < 1.25$). In general, most of the more recent turbulent natural convection correlations converge around the Bayley correlation (Bayley, 1955), where $C = 0.1$. However, the Bayley correlation deviates from the data when $T_w/T_a > 1.25$.

Unfortunately, there are very few studies in the literature where turbulent natural convection data from high-temperature walls to ambient gas are collected. Pirovano et al. (1970) obtained data using ambient air and a vertical heating plate (maximum $T_w/T_a \sim 1.5$). They correlated their turbulent data by the correlation

$$\mathrm{Nu}_r = 0.092 \times \mathrm{Gr}_r^{1/3}, \tag{2}$$

where the subscript r indicates that the properties are evaluated at a reference temperature defined as $T_r = T_a + \omega(T_w - T_a)$, using a weighting factor ω. The coefficient of thermal expansion is evaluated at T_a ($\omega = 0$). The thermal conductivity and the kinematic viscosity are evaluated using $\omega = 0.2$.

Clausing and Kempka (1981) obtained natural-convection data from a vertical cylinder to gaseous nitrogen at cryogenic temperature. In these experiments, the ratio T_w/T_a was increased to 2.6. Clausing and Kempka suggested that in addition to Nu, Gr, and Pr, a fourth dimensionless number T_w/T_a is needed to correlate the data. However, the data reported and correlated by Clausing and Kempka do not reflect the local HTC. They correlated the HTC averaged over the heater surface. As a result, the correlation proposed by Clausing and Kempka is in major disagreement with the data previously discussed by Pirovano et al. and with the data of Siebers et al. (1985), which are discussed next.

More recently, Siebers et al. obtained high-temperature, natural convection data from a vertical flat plate exposed to ambient air (maximum $T_w/T_a = 2.7$). They correlated the turbulent data as

$$\mathrm{Nu}_a = 0.098 \times \mathrm{Gr}_a^{1/3} \times \left(\frac{T_w}{T_a}\right)^{-0.14}, \tag{3}$$

where the subscript a denotes that all the properties are evaluated at T_a ($\omega = 0$).

Proposed Model

If evaluated at the film temperature (T_f), Ra or Gr shows a decreasing trend with increasing temperature difference ($T_w - T_a$) beyond a certain value of $T_w - T_a$. As a result, the correlation reaches a point where further increase in T_w causes a decrease in the HTC. To circumvent this problem, one approach is to use T_r, which is weighted toward T_a. Another approach is to add a temperature-dependent correction term, as done by Siebers et al.

In reviewing the high wall temperature data, we observed that the turbulent natural convection from vertical plates may be predicted by Eq. (1). Existing data may successfully be predicted by Eq. (1) if (*a*) k in the Nusselt number is evaluated at T_w, and (*b*) the properties within the Rayleigh number are evaluated at T_f.

Comparison of the Proposed Model With Other Correlations

To compare the different models, we ran a conceptual experiment where T_a is set to 20°C and T_w is increased to $T_w/T_a = 4.5$ ($T_w = 1050$°C). This conceptual experiment encompasses the experimental range of the studies by Pirovano et al. and Siebers et al. In Fig. 1, the proposed model is compared with Eqs. (2) and (3). In this figure, we plot C' versus T_w/T_a, where C' is defined as

$$C' = C\mathrm{Pr}^{1/3} = \frac{h}{k_w\left(\dfrac{g\beta_f(T_w - T_a)}{\nu_f^2}\right)^{1/3}}. \tag{4}$$

In Eq. (4) h is obtained from either Eq. (2) or Eq. (3). In this comparison, we did not account for the temperature dependence of Pr. Within the temperature range of the conceptual experiment, the minimum and maximum air Prandtl numbers are 0.68 and 0.7. We used a constant value of 0.69, which introduces less than 0.5 percent error in the predicted HTC. The primary motivation for using a constant Pr was that the Prandtl number effects were not considered in Eqs. (2) and (3).

As shown in Fig. 1, the correlation of Siebers et al. is in good agreement with the proposed correlation if $C' = 0.095$ for $T_w < 550$°C. The maximum deviation between the two correlations within this range of temperatures is less than 3 percent. The correlation of Siebers et al. provides a ±6 percent fit to the data. When extrapolated outside its data range for T_w/T_a, the correlation of Siebers et al. overpredicts the present correlation. At $T_w/T_a = 4.34$ ($T_w = 1000$°C), the difference between the two correlations is 11.5 percent. Also, the current model predicts the correlation of Pirovano et al. very accurately using $C' = 0.091$. Although the data base of Pirovano et al. is restricted to $T_w/T_a < 1.5$, their correlation and the current model are in very good agreement (within ±2 percent) up to $T_w/T_a = 2.6$. Note that the uncertainty reported by Pirovano et al. for their correlation is ±5 percent.

We would have liked to compare the present model to the actual data. Unfortunately, the raw data are not readily available. The original publications indicate that the data almost randomly scatter around the correlation line, indicating that the scatter may be the result of experimental uncertainties. With the proper choice of the correlation constants, this study shows that all data by Siebers et al. and Pirovano et al. can be bounded within a ±9 percent band of the present model.

[1]Nuclear Technology and Engineering Division, Los Alamos National Laboratory, Los Alamos, NM 87545.

Contributed by the Heat Transfer Division of The American Society of Mechanical Engineers. Manuscript received by the Heat Transfer Division November 1992; revision received June 1993. Keywords: High-Temperature Phenomena, Modeling and Scaling, Natural Convection. Associate Technical Editor: J. R. Lloyd.

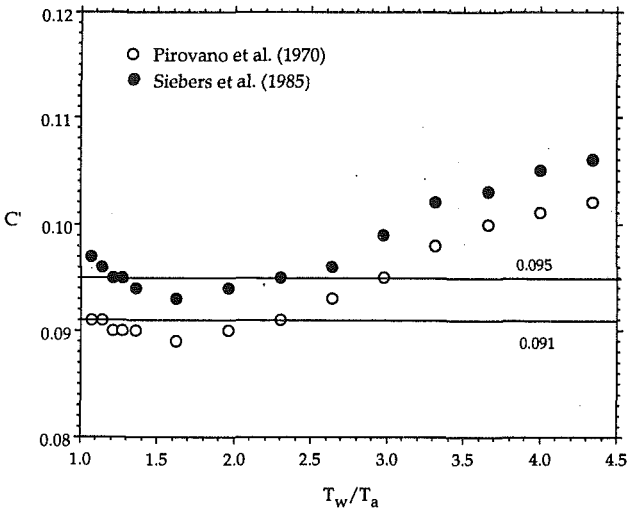

Fig. 1 Comparison of the present model with other correlations for air at atmospheric pressure ($T_a = 10°C$)

Having different values of C' for different experiments is not a major concern. The constant C' is strongly affected by the test-section and test-chamber geometry. Siebers et al. used a plate placed in a wind tunnel; this plate was wider than the one used by Pirovano et al. The hot air from the top of the plate was sucked out to prevent stratification. This suction effect might have enhanced the heat transfer. Such small differences in the test section geometry and the experimental conditions may easily account for the 4 percent difference in C' obtained for these experiments. Also, it is important to note that C' for the Bayley correlation is equal to 0.089. Thus, the proposed model, along with the obtained constants, also merges well with the Bayley correlation at the limit when T_w approaches T_a.

Concluding Remarks

As shown in this paper, the present model provides good agreement when compared with the correlations of Pirovano et al. and Siebers et al. within the parametric range of the existing data. In general, however, it can be stated that the current model disagrees with models suggesting an explicit temperature correction term, such as the model of Siebers et al., outside the parametric range of the data. The major disagreement in the two types of models arises when they are applied to the conditions when hot gases are cooled by natural convection while in contact with a cold wall ($T_w/T_a < 1$). However, there are no pertinent data to verify the applicability of either model to such conditions.

References

Bayley, F. J., 1955, "An Analysis of the Turbulent Free Convection Heat Transfer," *Institute of Mechanical Engineering Proceedings*, Vol. 169, pp. 361–368.

Clausiong, A. M., and Kempka, S. N., 1981, "The Influence of Property Variations on Natural Convection From Vertical Surfaces," ASME JOURNAL OF HEAT TRANSFER, Vol. 103, pp. 609–612.

Clausing, A. M., 1983, "Natural Convection Correlations for Vertical Surfaces Including Influences of Variable Properties," ASME JOURNAL OF HEAT TRANSFER, Vol. 105, pp. 138–143.

Pirovano, A., Viannay, S., and Jannot, M., 1970, "Convection Naturelle en Regime Turbulent le Long d'Une Plaque Verticale," *Proceedings of the 4th International Heat Transfer Conference*, Paris-Versailles, France, Vol. 4, Paper No., NC1.8.

Siebers, D. L., Moffatt, R. F., and Schwind, R. G., 1985, "Experimental, Variable Properties Natural Convection From a Large Vertical, Flat Surface," ASME JOURNAL OF HEAT TRANSFER, Vol. 107, pp. 124–132.

Measurements in Buoyancy-Opposing Laminar Flow Over a Vertical Backward-Facing Step

H. I. Abu-Mulaweh,[1] B. F. Armaly,[1] and T. S. Chen[1]

Introduction

Flow separation occurs in many heat transfer devices (such as high-performance heat exchangers, combustion chambers, and cooling systems for electronic equipment) and affects their heat transfer performance. The phenomenon of flow separation due to a sudden expansion in a flow passage (such as a backward-facing step) has been examined extensively for both forced and mixed convection flows (see, for example, Abu-Mulaweh et al., 1993, and Baek et al., 1993, and the references cited therein). To the best knowledge of the present authors, all of the previously reported studies of mixed convection in the backward-facing step have dealt with the case of a buoyancy-assisting flow condition. The buoyancy-opposing case seems not to have been investigated and this has motivated the present study.

Experimental Apparatus and Analysis

The experimental study was performed in an existing low-turbulence, open-circuit air tunnel, as described by Ramachandran et al. (1985). In this experiment, the backward-facing step geometry in the test section of the tunnel was identical to that used by Baek et al. (1993), except that the orientation of the air tunnel was changed by 180 deg to create buoyancy-opposing flow conditions as shown in a schematic diagram of the calculation domain, Fig. 1. The backward-facing step was formed by an adiabatic upstream section (30.48 cm in length) and a heated constant-temperature downstream section (79 cm in length). The heated test surface and the step geometry spanned the entire width of the tunnel (30.48 cm) and the expansion ratio, the ratio of the downstream to upstream heights above the test surface in the air tunnel, was less than 1.04. The heated test surface was instrumented with thermocouples and with heaters that are controlled to maintain the surface at a uniform temperature. The air flow velocities were measured by a laser-Doppler velocimeter (LDV) and the air temperatures were measured by a cold-wire anemometer. These measurements, along with the uncertainties and magnitude of errors, are described in detail by Baek et al. (1993). Flow visualization was also performed by using a 15-W collimated white light beam, 2.5 cm in diameter, with glycerin particles seeding the flow. This flow visualization method provided the capabilities of locally probing the flow domain for determining turbulent transition and the reattachment length. This experimental geometry was also modeled, as shown in Fig. 1, for numerical simulation, in a manner similar to that described by Baek et al. (1993), where the solution procedure, convergence criterion, grid distributions, and numerical uncertainties are presented and discussed. In Fig. 1, u and v denote the

[1]Department of Mechanical and Aerospace Engineering and Engineering Mechanics, University of Missouri—Rolla, Rolla, MO 65401.

Contributed by the Heat Transfer Division of THE AMERICAN SOCIETY OF MECHANICAL ENGINEERS. Manuscript received by the Heat Transfer Division November 1992; revision received April 1993. Keywords: Flow Separation, Measurement Techniques, Mixed Convection. Associate Technical Editor: T. W. Simon.

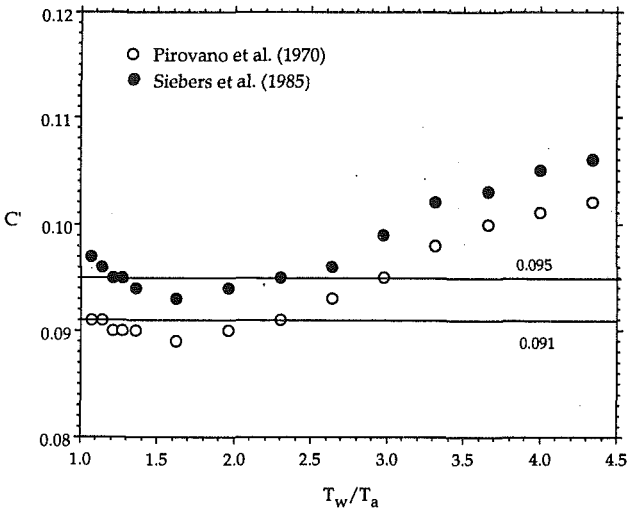

Fig. 1 Comparison of the present model with other correlations for air at atmospheric pressure ($T_a = 10°C$)

Having different values of C' for different experiments is not a major concern. The constant C' is strongly affected by the test-section and test-chamber geometry. Siebers et al. used a plate placed in a wind tunnel; this plate was wider than the one used by Pirovano et al. The hot air from the top of the plate was sucked out to prevent stratification. This suction effect might have enhanced the heat transfer. Such small differences in the test section geometry and the experimental conditions may easily account for the 4 percent difference in C' obtained for these experiments. Also, it is important to note that C' for the Bayley correlation is equal to 0.089. Thus, the proposed model, along with the obtained constants, also merges well with the Bayley correlation at the limit when T_w approaches T_a.

Concluding Remarks

As shown in this paper, the present model provides good agreement when compared with the correlations of Pirovano et al. and Siebers et al. within the parametric range of the existing data. In general, however, it can be stated that the current model disagrees with models suggesting an explicit temperature correction term, such as the model of Siebers et al., outside the parametric range of the data. The major disagreement in the two types of models arises when they are applied to the conditions when hot gases are cooled by natural convection while in contact with a cold wall ($T_w/T_a < 1$). However, there are no pertinent data to verify the applicability of either model to such conditions.

References

Bayley, F. J., 1955, "An Analysis of the Turbulent Free Convection Heat Transfer," *Institute of Mechanical Engineering Proceedings*, Vol. 169, pp. 361–368.

Clausiong, A. M., and Kempka, S. N., 1981, "The Influence of Property Variations on Natural Convection From Vertical Surfaces," ASME JOURNAL OF HEAT TRANSFER, Vol. 103, pp. 609–612.

Clausing, A. M., 1983, "Natural Convection Correlations for Vertical Surfaces Including Influences of Variable Properties," ASME JOURNAL OF HEAT TRANSFER, Vol. 105, pp. 138–143.

Pirovano, A., Viannay, S., and Jannot, M., 1970, "Convection Naturelle en Regime Turbulent le Long d'Une Plaque Verticale," *Proceedings of the 4th International Heat Transfer Conference*, Paris-Versailles, France, Vol. 4, Paper No., NC1.8.

Siebers, D. L., Moffatt, R. F., and Schwind, R. G., 1985, "Experimental, Variable Properties Natural Convection From a Large Vertical, Flat Surface," ASME JOURNAL OF HEAT TRANSFER, Vol. 107, pp. 124–132.

Measurements in Buoyancy-Opposing Laminar Flow Over a Vertical Backward-Facing Step

H. I. Abu-Mulaweh,[1] B. F. Armaly,[1] and T. S. Chen[1]

Introduction

Flow separation occurs in many heat transfer devices (such as high-performance heat exchangers, combustion chambers, and cooling systems for electronic equipment) and affects their heat transfer performance. The phenomenon of flow separation due to a sudden expansion in a flow passage (such as a backward-facing step) has been examined extensively for both forced and mixed convection flows (see, for example, Abu-Mulaweh et al., 1993, and Baek et al., 1993, and the references cited therein). To the best knowledge of the present authors, all of the previously reported studies of mixed convection in the backward-facing step have dealt with the case of a buoyancy-assisting flow condition. The buoyancy-opposing case seems not to have been investigated and this has motivated the present study.

Experimental Apparatus and Analysis

The experimental study was performed in an existing low-turbulence, open-circuit air tunnel, as described by Ramachandran et al. (1985). In this experiment, the backward-facing step geometry in the test section of the tunnel was identical to that used by Baek et al. (1993), except that the orientation of the air tunnel was changed by 180 deg to create buoyancy-opposing flow conditions as shown in a schematic diagram of the calculation domain, Fig. 1. The backward-facing step was formed by an adiabatic upstream section (30.48 cm in length) and a heated constant-temperature downstream section (79 cm in length). The heated test surface and the step geometry spanned the entire width of the tunnel (30.48 cm) and the expansion ratio, the ratio of the downstream to upstream heights above the test surface in the air tunnel, was less than 1.04. The heated test surface was instrumented with thermocouples and with heaters that are controlled to maintain the surface at a uniform temperature. The air flow velocities were measured by a laser-Doppler velocimeter (LDV) and the air temperatures were measured by a cold-wire anemometer. These measurements, along with the uncertainties and magnitude of errors, are described in detail by Baek et al. (1993). Flow visualization was also performed by using a 15-W collimated white light beam, 2.5 cm in diameter, with glycerin particles seeding the flow. This flow visualization method provided the capabilities of locally probing the flow domain for determining turbulent transition and the reattachment length. This experimental geometry was also modeled, as shown in Fig. 1, for numerical simulation, in a manner similar to that described by Baek et al. (1993), where the solution procedure, convergence criterion, grid distributions, and numerical uncertainties are presented and discussed. In Fig. 1, u and v denote the

[1]Department of Mechanical and Aerospace Engineering and Engineering Mechanics, University of Missouri—Rolla, Rolla, MO 65401.

Contributed by the Heat Transfer Division of THE AMERICAN SOCIETY OF MECHANICAL ENGINEERS. Manuscript received by the Heat Transfer Division November 1992; revision received April 1993. Keywords: Flow Separation, Measurement Techniques, Mixed Convection. Associate Technical Editor: T. W. Simon.

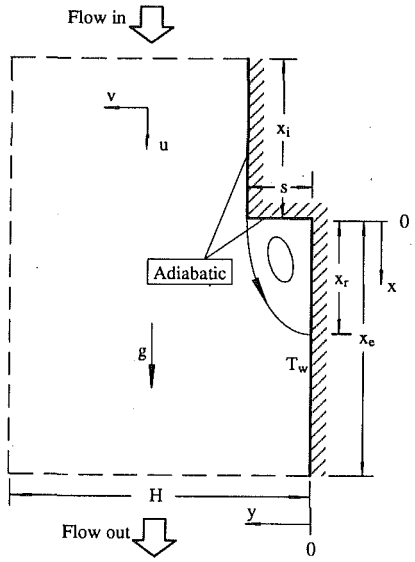

Fig. 1 Schematic diagram of the calculation domain

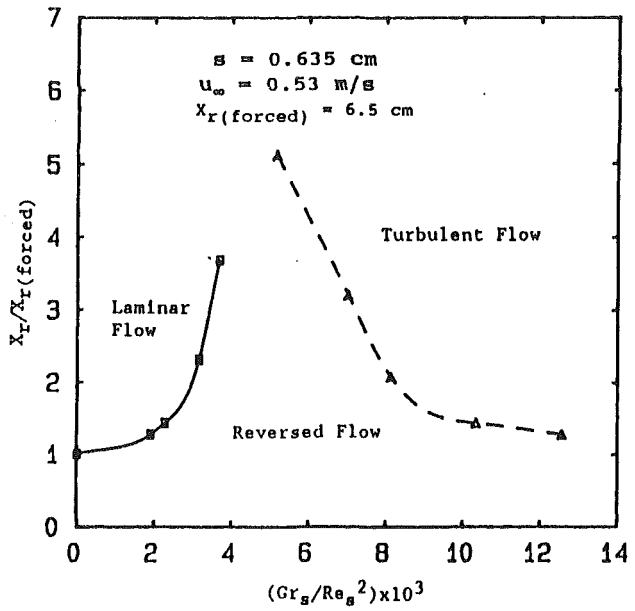

Fig. 2 Effects of buoyancy force on the reattachment length (uncertainty in X_r is ± 0.25 and in ξ is $\pm 4 \times 10^{-5}$)

streamwise and the transverse velocity components in the x and y directions, respectively, g is the gravitational acceleration, T_w is the heated wall temperature, x_i, x_e, and H are, respectively, the upstream length, the downstream length, and the height of the calculation domain (with $x_i = 30.48$ cm, $x_e = 40$ cm, and $H = 15$ cm), s is the step height, and x_r is the reattachment length as measured from the step.

Results and Discussion

The uniformity and the two-dimensional nature of the flow were verified through flow visualization and through measurements of velocity and temperature across the width of the air tunnel, at various y locations above the heated test surface. These measurements displayed a wide region (about 80 percent of the width of the heated test surface) around the center of the tunnel's width where the flow velocity is almost constant (to within 5 percent) at a fixed height above the heated test surface, thus justifying the two-dimensional flow approximation. Results presented in this note are limited to a backward-facing step height, s, of 0.635 cm and a free-stream velocity, u_∞, of 0.53 m/s. Measurements were performed with other step heights 0.4 cm $\le s \le$ 0.8 cm and with other free-stream velocities 0.41 m/s $\le u_\infty \le$ 0.66 m/s for a range of wall heating of 0°C $\le \Delta T \le$ 30°C, where $\Delta T = (T_w - T_\infty)$ is the temperature difference between the heated wall and the free stream. These results are not presented here due to space limitations, but their trends are similar to the results reported here.

Figure 2 describes, from flow visualization results, the influence of the buoyancy force on the length of the laminar recirculation region, x_r. It is noted that in this figure, $x_{r(\text{forced})}$ is the reattachment length under pure forced convection conditions, i.e., without heating the test surface, which was measured as $x_{r(\text{forced})} = 6.5$ cm for the experimental conditions of $u_\infty = 0.53$ m/s and $s = 0.635$ cm. The buoyancy-induced flow adjacent to the heated wall is in a direction opposite to the main forced flow. The main flow and the buoyancy-induced flow interact with each other, and for low buoyancy levels, $\xi < 4.4 \times 10^{-3}$ (where $\xi = \text{Gr}_s/\text{Re}_s^2$ is the buoyancy parameter, $\text{Gr}_s = g\beta(T_w - T_\infty)s^3/\nu^2$ is the Grashof number, and $\text{Re}_s = u_\infty s/\nu$ is the Reynolds number, with β denoting the coefficient of thermal expansion and ν the kinematic viscosity), the flow remains laminar throughout the test section. In this laminar regime, the length of the recirculation region downstream of the backward-facing step increases rapidly as the buoyancy level increases (i.e., with an increase in wall temperature or step height and/or a decrease in free-stream velocity) due to the buoyancy-induced velocity, which is opposing the forced flow direction adjacent to the heated wall. The interaction between the main forced flow and the buoyancy-induced flow, however, causes the flow to become turbulent downstream of the recirculation region as the buoyancy level increases. In this flow regime, the flow inside the recirculation region remains laminar, but the length of the recirculation region decreases rapidly with increasing buoyancy level as a result of the transition from laminar to turbulent flow, as shown in Fig. 2. It should be noted that, in order to reduce visualization errors, the measured reattachment lengths reported are the average of several readings. The uncertainty in these measurements is ± 1 mm, which is less than 5 percent of the smallest measured reattachment length. The solid line in Fig. 2 represents the conditions where the flow remains laminar throughout the test section, while the dashed line represents the conditions where the flow is laminar in the recirculation region but turbulent outside and downstream of the recirculation region.

The LDV-measured and the predicted velocity distributions in the laminar recirculating region behind the step are presented in Fig. 3. The figure shows clearly that the numerical predictions that utilize a laminar elliptic flow model agree favorably well with the measured results (within 5 percent) for the cases of $\Delta T = 0$ and 3.1°C. For these cases the flow is laminar throughout the test section. Since the numerical scheme does not include turbulence modeling, it fails to predict the measured results in the laminar recirculation region when the flow becomes turbulent anywhere in the calculation domain. The developed turbulent flow downstream of the recirculation region makes this numerical model (see Baek et al., 1993, and Lin et al., 1990) unsuitable for predicting this flow. It can also be seen from the figure that, inside the recirculation region, the velocity gradient at the wall increases in the negative sense as the streamwise distance from the step increases where the flow becomes turbulent downstream of the recirculation region, i.e., for the cases of $\Delta T = 7.0$ and 11.5°C, whereas it decreases in the negative sense and eventually becomes positive where the flow is laminar throughout the test section, i.e., for the cases of $\Delta T = 0$ and 3.1°C. The corresponding reattachment lengths and the size of the recirculation regions for this flow at $\Delta T = 0$, 3.1, 7.0, and 11.5°C are 6.5, 9, 32, and 11 cm,

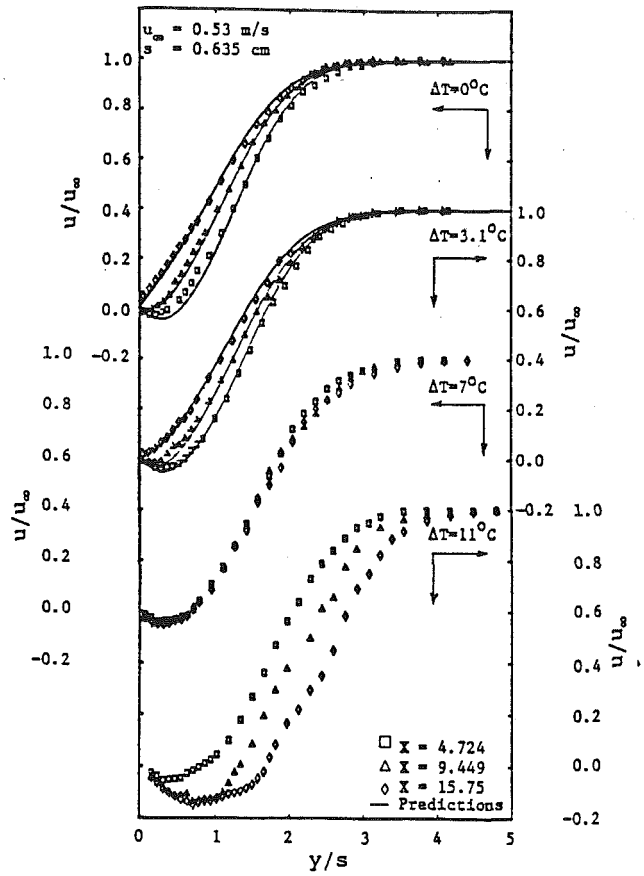

Fig. 3 Effects of wall temperature on the velocity distribution (uncertainty in u/u_∞ is ± 0.014 and in y/s it is ± 0.022)

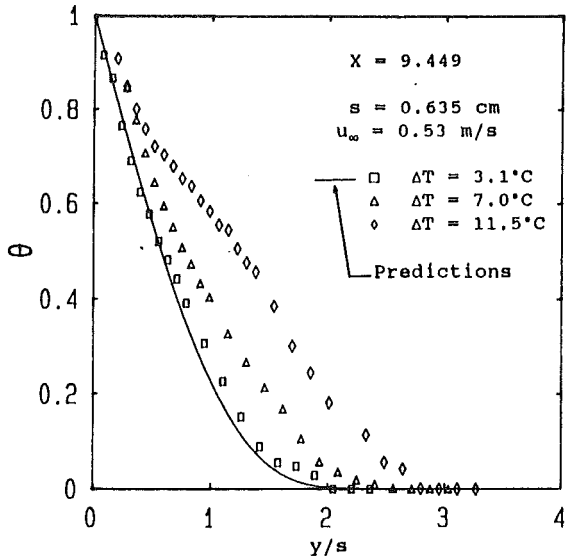

Fig. 4 Effects of wall temperature on the temperature distribution (uncertainty in y/s is ± 0.022 and in θ is ± 0.025)

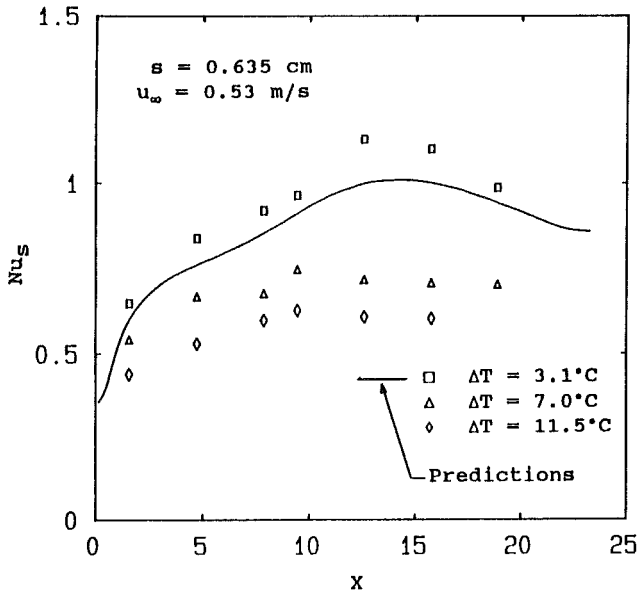

Fig. 5 Effects of wall temperature on the axial variation of the Nusselt number (uncertainty in Nu_s is ± 0.05 and in X it is ± 0.05)

respectively. Measurements also reveal that the velocity gradient at the wall increases in the negative sense and that the thickness of the recirculation region increases as the buoyancy level increases (i.e., by decreasing the free-stream velocity for a fixed wall temperature).

The effects of buoyancy (due to changes in wall temperature) on the dimensionless temperature distribution, $\theta = (T - T_\infty)/(T_w - T_\infty)$, are shown in Fig. 4, where T is the local fluid temperature. In contrast to the buoyancy-assisting flow case, the temperature gradient at the wall decreases (i.e., the heat transfer rate decreases) as the temperature difference (and hence the buoyancy force) increases. Measurements also reveal that for a fixed wall temperature the temperature gradient at the wall increases as the free-stream velocity increases.

The effects of buoyancy forces on the local Nusselt number downstream of the backward-facing step are illustrated in Fig. 5. The Nusselt number is defined as $Nu_s = hs/k$, where the local heat transfer coefficient h is defined as $h = -k(\partial T/\partial y)y = 0/(T_w - T_\infty)$, with k denoting the thermal conductivity. Again, in contrast to the buoyancy-assisting flow case, the local Nusselt number decreases as the buoyancy force increases (i.e., with increasing wall heating). The figure also shows that reasonable agreement exists (within 10 percent) between predictions (solid line) and measured results for the case of $\Delta T = 3.1°C$ in which the flow is laminar throughout the test section.

Conclusion

Measurements of velocity and temperature distributions are reported for buoyancy-opposing, laminar, mixed convection flow over a vertical backward-facing step. It has been found that the length of the recirculation region increases as the buoyancy force increases when the flow is laminar throughout the test section. The reverse trend occurs when turbulent flow develops downstream of the recirculation region. In contrast to the buoyancy-assisting flow, the local Nusselt number in buoyancy-opposing flow decreases as the buoyancy force increases.

Acknowledgments

The present study was supported by a grant from the National Science Foundation (NSF CTS-8923010). Mr. Bin Hong assisted in the numerical computations.

References

Abu-Mulaweh, H. I., Armaly, B. F., and Chen, T. S., 1993, "Measurements of Laminar Mixed Convection in Boundary-Layer Flow Over Horizontal and Inclined Backward-Facing Steps," *International Journal of Heat and Mass Transfer*, Vol. 36, No. 7, pp. 1883–1895.

Baek, B. J., Armaly, B. F., and Chen, T. S., 1993, "Measurements in Buoyancy-Assisting Separated Flow Behind a Vertical Backward-Facing Step," ASME JOURNAL OF HEAT TRANSFER, Vol. 115, pp. 403-408.

Lin, J. T., Armaly, B. F., and Chen, T. S., 1990, "Mixed Convection in Buoyancy-Assisting Vertical Backward-Facing Step Flows," *International Journal of Heat and Mass Transfer*, Vol. 33, pp. 2121-2132.

Ramachandran, N., Armaly, B. F., and Chen, T. S., 1985, "Measurements and Predictions of Laminar Mixed Convection Flows Adjacent to a Vertical Surface," ASME JOURNAL OF HEAT TRANSFER, Vol. 107, pp. 636-641.

Mixed Convection in the Cusped Duct

Z. F. Dong[1] and M. A. Ebadian[1,2]

Introduction

In the unlikely event of a loss of coolant accident (LOCA) in a pressurized water reactor, the fuel rod cladding may swell due to a combination of pressure difference across the cladding and increase of the temperature level in the core. In this case, adjacent fuel rods may balloon until they make contact with their neighbors, leading to a reduction in the subchannel flow area and a worsening of the core heat transfer in the region of the blockage. This blockage can be visualized as a cusped duct with four corners formed by assembling four rods of equivalent diameters, as seen in Fig. 1. Therefore, for better design of the emergency core cooling system (ECCS), it is imperative that the behavior of fluid flow and heat transfer in such a duct is fully understood. Generally, except for the forced convection in the cusped duct, natural convection due to the high temperature of the cladding is a significant factor affecting heat transfer behavior.

An extensive survey of literature dealing with the cusped duct reveals that there has been a limited number of investigations in this area of research. Gunn and Darling (1963) measured the friction factor for a range of laminar, transition, and turbulent flow in the cusped duct. Gerard and Baines (1977) experimentally investigated the velocity and boundary shear stress distributions for turbulent flow in a cusped duct. Turner and Hague (1983) performed an experimental study of fluid flow and heat transfer in the core of a pressurized water reactor, and at the same time they compared the results with a computational study for flow and heat transfer within the cusped duct. Hague et al. (1982) employed the damped mixed length turbulent model of Barrow et al. (1978) to predict the fully developed flow conditions in the cusped channel. Hassan and Barrow (1984) also numerically studied turbulent flow in a four-cusped channel. Furthermore, they also considered the thickness of the cladding, and the K–ϵ two-equation turbulence model was used in their computation. Maliska and Silva (1986) applied a boundary-fitted coordinate system (BFCS) to simulate laminar flow and heat transfer. They illustrated the effects of nonorthogonal and orthogonal grids on the solution. Recently, Duck and Turner (1987) imposed a uniform heat flux condition at the fuel-cladding interface and included the thickness of the cladding in their analysis. Dong et al. (1991) conducted a numerical investigation of thermal developing flow in the various cusped ducts. In addition, numerical research on fully developed flow and an experimental study on turbulent flow with the aid of the naphthalene sublimation technique was performed by Dutra et al. (1991). The foregoing papers deal with either fully developed laminar flow or turbulent flow, considering forced convection only. However, due to the higher temperature of the cladding in the actual flow and heat transfer in the channel formed by the swelling of the cladding, a secondary flow will occur as a result of the change in density of the fluid. This will have a significant impact on the friction factor and the heat transfer coefficient. Therefore, analysis of combined forced and natural convection is essential for better design of the ECCS. However, based on the authors' knowledge, this information is absent in the open literature. Consequently, the motivation behind the present investigation is to study the effects of natural convection, in addition to forced convection, in the cusped duct.

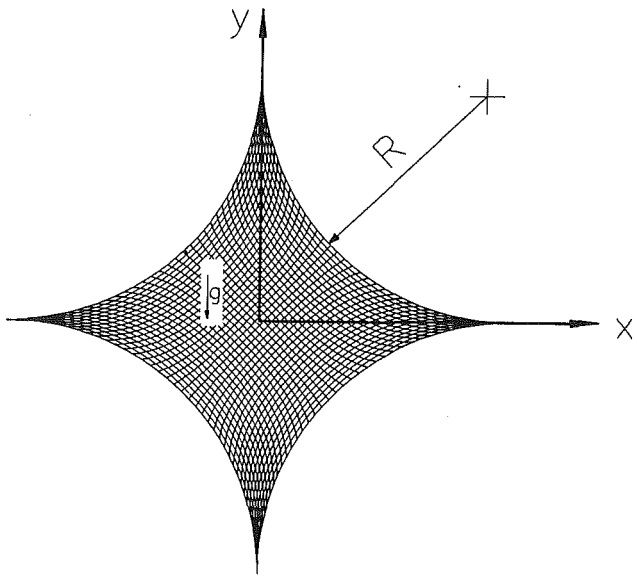

Fig. 1 Schematic of the problem and grid configuration

Problem Formulation

The analysis in this technical note is conducted for steady, combined, natural and forced convection in a horizontal cusped duct. The flow is assumed to be both hydrodynamically and thermally fully developed laminar flow. The Newtonian fluid, with constant thermal properties, is considered, except for the density in the buoyancy term, which is approximated by Boussinesq assumption. The viscous dissipation and compression work terms are also neglected in the energy equation. The thermal boundary condition imposed is that of a uniform wall temperature circumferentially, but uniform heat flux axially. A nonslip hydraulic condition is employed on all solid boundaries. On the other hand, a numerically generated boundary-fitted coordinate system (BFCS) is applied because of the complex geometry and the curved boundary of the cusped duct. The entire cross section of the cusped duct has been used as a solution domain. The resulting grid configurations are the coordinate system shown in Fig. 1. Based on the above assumptions, the governing equations for fully developed mixed convection in the boundary-fitted coordinate system are:

$$\frac{\partial}{\partial \xi}(\overline{U}\Omega)+\frac{\partial}{\partial \eta}(\overline{V}\Omega)=\frac{\partial}{\partial \xi}\left[\frac{\Gamma_\Omega}{J}\left(\alpha\frac{\partial \Omega}{\partial \xi}-\beta\frac{\partial \Omega}{\partial \eta}\right)\right]+\frac{\partial}{\partial \eta}\left[\frac{\Gamma_\Omega}{J}\left(\gamma\frac{\partial \Omega}{\partial \eta}-\beta\frac{\partial \Omega}{\partial \xi}\right)\right]+JS_\Omega(\xi,\eta), \quad (1)$$

[1]Department of Mechanical Engineering, Florida International University, Miami, FL 33199.

[2]Fellow ASME.

Contributed by the Heat Transfer Division of THE AMERICAN SOCIETY OF MECHANICAL ENGINEERS. Manuscript received by the Heat Transfer Division December 1992; revision received June 1993. Keywords: Heat Exchangers, Mixed Convection, Numerical Methods. Associate Technical Editor: J. H. Kim.

Baek, B. J., Armaly, B. F., and Chen, T. S., 1993, "Measurements in Buoyancy-Assisting Separated Flow Behind a Vertical Backward-Facing Step," ASME JOURNAL OF HEAT TRANSFER, Vol. 115, pp. 403-408.

Lin, J. T., Armaly, B. F., and Chen, T. S., 1990, "Mixed Convection in Buoyancy-Assisting Vertical Backward-Facing Step Flows," *International Journal of Heat and Mass Transfer*, Vol. 33, pp. 2121-2132.

Ramachandran, N., Armaly, B. F., and Chen, T. S., 1985, "Measurements and Predictions of Laminar Mixed Convection Flows Adjacent to a Vertical Surface," ASME JOURNAL OF HEAT TRANSFER, Vol. 107, pp. 636-641.

Mixed Convection in the Cusped Duct

Z. F. Dong[1] and M. A. Ebadian[1,2]

Introduction

In the unlikely event of a loss of coolant accident (LOCA) in a pressurized water reactor, the fuel rod cladding may swell due to a combination of pressure difference across the cladding and increase of the temperature level in the core. In this case, adjacent fuel rods may balloon until they make contact with their neighbors, leading to a reduction in the subchannel flow area and a worsening of the core heat transfer in the region of the blockage. This blockage can be visualized as a cusped duct with four corners formed by assembling four rods of equivalent diameters, as seen in Fig. 1. Therefore, for better design of the emergency core cooling system (ECCS), it is imperative that the behavior of fluid flow and heat transfer in such a duct is fully understood. Generally, except for the forced convection in the cusped duct, natural convection due to the high temperature of the cladding is a significant factor affecting heat transfer behavior.

An extensive survey of literature dealing with the cusped duct reveals that there has been a limited number of investigations in this area of research. Gunn and Darling (1963) measured the friction factor for a range of laminar, transition, and turbulent flow in the cusped duct. Gerard and Baines (1977) experimentally investigated the velocity and boundary shear stress distributions for turbulent flow in a cusped duct. Turner and Hague (1983) performed an experimental study of fluid flow and heat transfer in the core of a pressurized water reactor, and at the same time they compared the results with a computational study for flow and heat transfer within the cusped duct. Hague et al. (1982) employed the damped mixed length turbulent model of Barrow et al. (1978) to predict the fully developed flow conditions in the cusped channel. Hassan and Barrow (1984) also numerically studied turbulent flow in a four-cusped channel. Furthermore, they also considered the thickness of the cladding, and the K–ϵ two-equation turbulence model was used in their computation. Maliska and Silva (1986) applied a boundary-fitted coordinate system (BFCS) to simulate laminar flow and heat transfer. They illustrated the effects of nonorthogonal and orthogonal grids on the solution. Recently, Duck and Turner (1987) imposed a uniform heat flux condition at the fuel-cladding interface and included the thickness of the cladding in their analysis. Dong et al. (1991) conducted a numerical investigation of thermal developing flow in the various cusped ducts. In addition, numerical research on fully developed flow and an experimental study on turbulent flow with the aid of the naphthalene sublimation technique was performed by Dutra et al. (1991). The foregoing papers deal with either fully developed laminar flow or turbulent flow, considering forced convection only. However, due to the higher temperature of the cladding in the actual flow and heat transfer in the channel formed by the swelling of the cladding, a secondary flow will occur as a result of the change in density of the fluid. This will have a significant impact on the friction factor and the heat transfer coefficient. Therefore, analysis of combined forced and natural convection is essential for better design of the ECCS. However, based on the authors' knowledge, this information is absent in the open literature. Consequently, the motivation behind the present investigation is to study the effects of natural convection, in addition to forced convection, in the cusped duct.

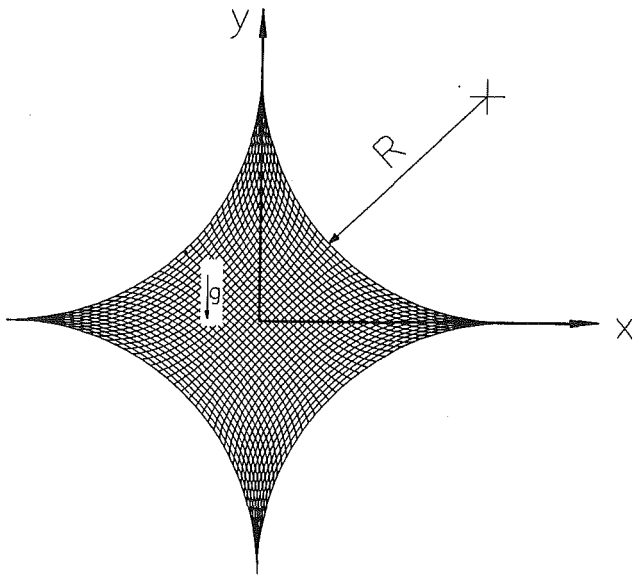

Fig. 1 Schematic of the problem and grid configuration

Problem Formulation

The analysis in this technical note is conducted for steady, combined, natural and forced convection in a horizontal cusped duct. The flow is assumed to be both hydrodynamically and thermally fully developed laminar flow. The Newtonian fluid, with constant thermal properties, is considered, except for the density in the buoyancy term, which is approximated by Boussinesq assumption. The viscous dissipation and compression work terms are also neglected in the energy equation. The thermal boundary condition imposed is that of a uniform wall temperature circumferentially, but uniform heat flux axially. A nonslip hydraulic condition is employed on all solid boundaries. On the other hand, a numerically generated boundary-fitted coordinate system (BFCS) is applied because of the complex geometry and the curved boundary of the cusped duct. The entire cross section of the cusped duct has been used as a solution domain. The resulting grid configurations are the coordinate system shown in Fig. 1. Based on the above assumptions, the governing equations for fully developed mixed convection in the boundary-fitted coordinate system are:

$$\frac{\partial}{\partial \xi}(\overline{U}\Omega)+\frac{\partial}{\partial \eta}(\overline{V}\Omega)=\frac{\partial}{\partial \xi}\left[\frac{\Gamma_\Omega}{J}\left(\alpha\frac{\partial \Omega}{\partial \xi}-\beta\frac{\partial \Omega}{\partial \eta}\right)\right]+\frac{\partial}{\partial \eta}\left[\frac{\Gamma_\Omega}{J}\left(\gamma\frac{\partial \Omega}{\partial \eta}-\beta\frac{\partial \Omega}{\partial \xi}\right)\right]+JS_\Omega(\xi,\eta), \quad (1)$$

[1]Department of Mechanical Engineering, Florida International University, Miami, FL 33199.

[2]Fellow ASME.

Contributed by the Heat Transfer Division of THE AMERICAN SOCIETY OF MECHANICAL ENGINEERS. Manuscript received by the Heat Transfer Division December 1992; revision received June 1993. Keywords: Heat Exchangers, Mixed Convection, Numerical Methods. Associate Technical Editor: J. H. Kim.

Table 1 Variables in the conservation equation

Equation	Ω	Γ_Ω	S_Ω
Continuity	1	0	0
U-momentum	U	Pr	$-\frac{\Pr}{J}\left[\frac{\partial P}{\partial \xi}\frac{\partial Y}{\partial \eta}-\frac{\partial P}{\partial \eta}\frac{\partial Y}{\partial \xi}\right]$
V-momentum	V	Pr	$-\frac{\Pr}{J}\left[-\frac{\partial P}{\partial \xi}\frac{\partial X}{\partial \eta}+\frac{\partial P}{\partial \eta}\frac{\partial X}{\partial \xi}\right]$
W-momentum	W	Pr	J Pr
Energy	θ	1	$-4J\frac{W}{\overline{W}}$

where

$$\alpha=\left(\frac{\partial X}{\partial \eta}\right)^2+\left(\frac{\partial Y}{\partial \eta}\right)^2 \qquad \beta=\frac{\partial X}{\partial \xi}\frac{\partial X}{\partial \eta}+\frac{\partial Y}{\partial \xi}\frac{\partial Y}{\partial \eta}$$

$$\gamma=\left(\frac{\partial X}{\partial \xi}\right)^2+\left(\frac{\partial Y}{\partial \xi}\right)^2 \qquad J=\frac{\partial X}{\partial \xi}\frac{\partial Y}{\partial \eta}-\frac{\partial X}{\partial \eta}\frac{\partial Y}{\partial \xi}$$

$$\overline{U}=U\frac{\partial Y}{\partial \eta}-V\frac{\partial X}{\partial \eta} \qquad \overline{V}=V\frac{\partial Y}{\partial \xi}-U\frac{\partial Y}{\partial \xi}. \tag{2}$$

The general dependent variable, Ω, the diffusivity coefficient, Γ_Ω, and the source term, S_Ω, are given in Table 1. In Eqs. (1) and (2), the following dimensionless variables have been used:

$$X=\frac{x}{D_h}, \qquad Y=\frac{y}{D_h}, \qquad U=\frac{uD_h}{\alpha_T},$$

$$V=\frac{vD_h}{\alpha_T}, \qquad W=\frac{w}{-\frac{d\overline{p}}{dz}\frac{D_h^2}{\mu}}, \qquad P=\frac{p}{\rho_w\left(\frac{\nu\alpha_T}{D_h^2}\right)},$$

$$\theta=\frac{T-T_w}{\overline{q}D_h/k}, \qquad \mathrm{Ra}=\frac{g\beta_T\overline{q}D_h^4}{\nu\alpha_T k}, \qquad \Pr=\frac{\nu}{\alpha_T}, \tag{3}$$

where u, v, w, are dimensional velocities in the x, y, z directions, respectively; k, α_T, ρ_w, ν are thermal conductivity, thermal diffusivity, density in the wall temperature, and kinematic viscosity, respectively. T, T_w, $\overline{q}$, g, β_T, $\overline{w}$, $d\overline{p}/dz$, and D_h are temperature, wall temperature, average wall heat flux, gravitational acceleration, volumetric thermal expansion coefficient, mean axial velocity, axial pressure gradient, and hydraulic diameter, respectively.

In addition, the boundary condition for Eq. (1) is expressed as:

$$\Omega=0 \quad \text{on the wall.} \tag{4}$$

Numerical Method

The governing equations with the boundary conditions are solved by using the control volume-based finite difference method in the boundary-fitted coordinate system. A staggered grid is employed for the velocity components U and V, as well as $\overline{U}$ and $\overline{V}$. The convection terms are discretized by a power-law scheme (Patankar, 1980), which is an approximation of the exponential scheme, and a second-order central difference formula is used to approximate the diffusion terms. In the momentum equation, the Cartesian velocity components are treated as the primary variables and contravariant velocity components are used in the continuity equation to derive the pressure correction equation. The cross derivative term, $\partial^2/\partial\xi\partial\eta$, is noted as an additional source term and the standard, second-order central difference approximation is applied to calculate the value of α, β, γ, and J on each node. The solution is obtained by an iterative scheme of modified SIMPLE algorithm. The criterion for a solution convergence is set for all nodes as:

$$\frac{\|\Omega_{ij}^{k+1}-\Omega_{ij}^{k}\|_\infty}{\|\Omega_{ij}^{k+1}\|_\infty}\le 10^{-5}, \tag{5}$$

where Ω represents U, V, W, and θ. The subscripts i and j represent the ξ and η coordinates, and the superscript k represents the kth iteration. $\|\cdot\|_\infty$ is the infinite norm.

Numerical experiments have been conducted to explore grid sensitivity on the results. Three grids of 20 × 20, 40 × 40, and 60 × 60 are chosen for different Rayleigh numbers. The results show that the deviations for the fRe and Nu values between the coarse grid of 40 × 40 and the finer grid of 60 × 60 are less than 2 percent. Therefore, a grid of 40 × 40 is used in the entire calculation. Underrelaxation parameters ranging from 0.15 to 0.5 for velocity and temperature have been applied to obtain a converged solution because of the strong nonlinear characteristics of the governing equations.

The present numerical method has been verified by applying it to analyze pure forced convection in the cusped duct and laminar mixed convection in a concentric annulus. The friction factor times the Reynolds number (fRe) for the pure forced convection is 26.422, and the corresponding value from the literature (Shah and London, 1978) is 26.424, indicating an insignificant difference between these results. Also, discrepancies of less than 2 and 5 percent for the fRe and Nu values, respectively, between the present prediction and Choudhury and Karki (1992) have been achieved in the case of mixed convection in a concentric annulus.

Table 2 The calculated results

Ra	Pr = 0.01		Pr = 0.7		Pr = 8	
	fRe	$\overline{\mathrm{Nu}}$	fRe	$\overline{\mathrm{Nu}}$	fRe	$\overline{\mathrm{Nu}}$
0	26.422	1.352	26.422	1.352	26.422	1.352
10	28.044	1.542	26.427	1.353	26.422	1.352
10^2	34.228	2.274	26.538	1.365	26.426	1.353
10^3	46.304	3.684	28.701	1.620	26.518	1.363
10^4	68.001	6.227	35.622	2.439	28.441	1.589
10^5	105.070	10.688	48.930	3.989	35.083	2.372
10^6	167.144	18.360	72.538	6.766	47.920	3.872
10^7	--	--	112.750	11.626	70.796	6.559

Results and Discussion

Solutions have been obtained for different Rayleigh numbers ranging from 0 (pure forced convection) to 10^7, and for three values of Prandtl numbers, Pr = 0.01, 0.7, and 8. The most interesting parameters are the product of the overall friction factor times the Reynolds number, fRe, the local Nusselt number, Nu, and the average Nusselt number, $\overline{\mathrm{Nu}}$. They are defined respectively as:

$$f\mathrm{Re}=2/\overline{W}, \qquad \mathrm{Nu}=-\frac{\partial\theta}{\partial n}/\theta_b, \qquad \overline{\mathrm{Nu}}=-\frac{1}{\theta_b}, \tag{6}$$

where n refers to the normal direction on the boundary and θ_b is the bulk dimensionless temperature.

The predictions of fRe and $\overline{\mathrm{Nu}}$ have been tabulated in Table 2. For the forced convection (Ra = 0), it was found that the average Nusselt number subject to a uniform boundary temperature in the cusped duct is 1.08 (Dong et al., 1991). How-

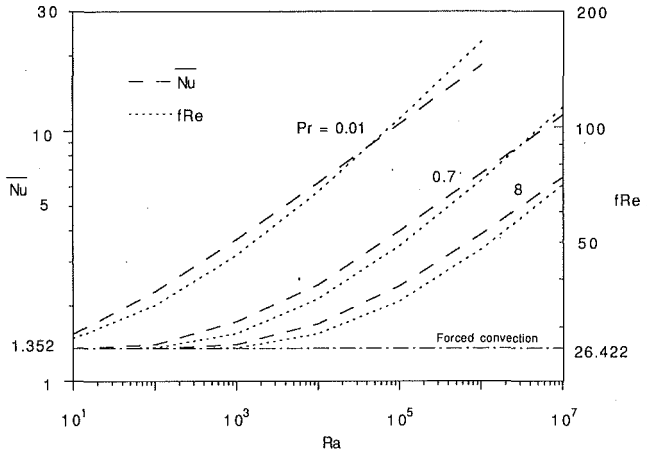

Fig. 2 Effect of the Rayleigh number on fRe and $\overline{Nu}$

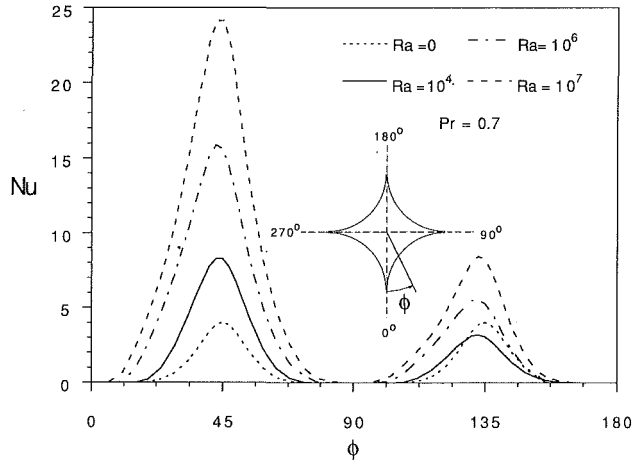

Fig. 3 Effect of the Rayleigh number on the local Nusselt number distribution

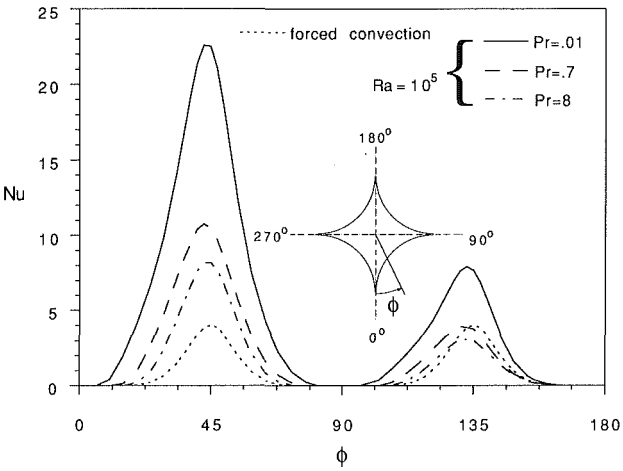

Fig. 4 Effect of the Prandtl number on the local Nusselt number distribution

ever, the average Nusselt number for the cusped duct subject to uniform axial heat flux and a circumferential uniform temperature is 1.352. When natural convection is taken into account, fRe and $\overline{Nu}$ increase. In order to obtain a clearer insight of the effects of the Rayleigh number and the Prandtl number, the data listed in Table 2 are used to draw Fig. 2, and an explanation is documented.

The effects of Rayleigh number, Ra, on the fRe and $\overline{Nu}$ values are displayed for Pr = 0.01, 0.7, 8 in Fig. 2. The fRe and $\overline{Nu}$ values for pure forced convection (Ra = 0 or Pr = ∞) are also drawn in this figure as a reference. It can be seen from the figure that both fRe and $\overline{Nu}$ increase as the Rayleigh number increases for all Prandtl numbers considered. This enhancement is caused by the secondary flow due to thermal buoyancy. When the Rayleigh number is small, the secondary flow is weak. The effects of natural convection on forced convection can be neglected. However, when the Rayleigh number is greater than 10^4, natural convection due to buoyancy is no loner negligible, regardless of the Prandtl number value. It is apparent that the Nusselt number is dramatically intensified simultaneously with an increase in the fRe. On the other hand, the fRe and Nusselt number decrease as the Prandtl number increases. This means that the secondary flow of the natural convection diminishes with a larger Pr fluid and the flow seems more stable. Based on the data given in Table 2, the correlations for fRe and $\overline{Nu}$ variations with Ra and Pr have been found as follows:

$$f\mathrm{Re} = 7.073\ \mathrm{Ra}^{0.167}\ \mathrm{Pr}^{-0.178} \tag{7}$$

$$\overline{\mathrm{Nu}} = 0.337\ \mathrm{Ra}^{0.212}\ \mathrm{Pr}^{-0.251}. \tag{8}$$

The discrepancies between the predictions from Eqs. (7) and (8) and the data in Table 2 are less than 5.5 percent when the Rayleigh number is greater than 10^4.

The distribution of the local Nusselt number on the boundary for angle ϕ, is shown in Fig. 3 with a fixed Prandtl number, Pr = 0.7. When only the forced convection (Ra = 0) occurs, an expected symmetric distribution of the local Nusselt number can be seen in this figure. The maximum value of the Nusselt number is located on the boundary at angles 45 or 135 deg. However, the zero value of the Nusselt number in the corner region of the duct indicates that the surface of the duct in the corner region does not participate in the heat transfer. This finding was also reported by Dutra et al. (1991). In the case of mixed convection, the fluid near the hot boundary will flow upward and downward in the middle to create a secondary circulation in the cross section. As a result, the velocity and temperature distributions are very different from the one for pure forced convection. Shown in Fig. 3 are the effects of the Rayleigh number on the local Nusselt number distribution. First, a similar distribution of the local Nusselt number can be seen for different Rayleigh numbers. The local Nusselt number value increases as Rayleigh number increases in most areas, except at the angles of 120 ~ 160 deg for Ra = 10^4, where the Nusselt number value is lower than the value of the forced convection. Probably the reason for this is that the fluid with a more uniform temperature is collected there, leading to the decreasing temperature gradient on the boundary. On the other hand, the location of the local maximum Nusselt number shifts toward a small angle direction. By evaluating the Nusselt number magnitude shown in this figure, it follows that in the boundary from 0 ~ 90 deg, the heat transfer is greater than the heat transfer from 90 ~ 180 deg, which means that the flow and heat transfer are more improved in the bottom part than in the top part of the duct. Also, the area with a zero value Nusselt number is very much reduced in the corner regions. However, heat transfer in the top corner (near 180 deg) is not much improved by natural convection.

The influence of the Prandtl number on the local Nusselt number distribution is displayed in Fig. 4, where Ra = 10^5.

For a small Prandtl number fluid, the Nusselt number at any location has a larger value, and at the boundary, 0 ~ 90 deg, the overall heat transfer is much higher than in the 90 ~ 180 deg region. It is also found that the local maximum Nusselt number location shifts toward the direction of the smaller angle; the smaller the Prandtl number, the more the location shifts. Furthermore, the local heat transfer in the 90 ~ 180 deg region can be enhanced by natural convection only when the smaller Prandtl number fluid is used.

Conclusion

Fully developed laminar mixed convection in the cusped duct has been investigated in this technical note. The results from this investigation provide an important contribution to the understanding of the characteristics of flow and heat transfer in a cusped duct. It has been revealed that natural convection due to buoyancy will enhance heat transfer, as well as the friction factor. Intensification of heat transfer and increase of the friction factor appear at a higher Rayleigh number, Ra $> 10^4$. The effect of natural convection at lower Rayleigh numbers can be neglected. The fluid having a smaller Prandtl number will result in a higher Nusselt number and greater friction. In addition, the flow and heat transfer in the corner region of the duct are much improved by the secondary flow of natural convection. It is believed that results from the present research will be helpful in the design of the ECCS, and the data base for mixed convection in complicated shape ducts.

Acknowledgments

The results presented in this paper were obtained in the course of research sponsored by the National Science Foundation (NSF) under Grant No. CTS-9017732.

References

Barrow, H., Hornby, R. P., and Mistry, J., 1978, "The Calculation of Fully Developed Turbulent Flow Using a New Mixing Length Model," *Proc. 6th Int. Heat Mass Conf.*, Toronto, Vol. 2, pp. 549–554.

Choudhury, D., and Karki, K., 1992, "Laminar Mixed Convection in an Eccentric Annulus," *Numerical Heat Transfer*, Part A, Vol. 22, pp. 87–108.

Dong, Z. F., Ebadian, M. A., and Campo, A., 1991, "Numerical Analysis of Convective Heat Transfer in the Entrance Region of Cusped Ducts," *Numer. Heat Transfer*, Part A, Vol. 20, pp. 459–472.

Duck, P. W., and Turner, J. T., 1987, "Pressurized Water Reactor Blockage Prediction of Laminar Flow and Temperature Distribution Following a Loss of Coolant Accident," *J. Heat Flow*, Vol. 8(2), pp. 149–155.

Dutra, A. S., Souza-Mendes, P. R., and Parise, J. A. R., 1991, "Transport Coefficients for Laminar and Turbulent Flow Through a Four-Cusp Channel," *Int. J. Heat Fluid Flow*, Vol. 12, No. 2, pp. 99–105.

Gerard, R., and Baines, W. D., 1977, "Turbulent Flow in a Very Nonlinear Conduit," ASCE *J. Hyd. Div.*, Vol. 103 (HY8), pp. 829–841.

Gunn, D. J., and Darling, C. W., 1963, "Fluid Flow and Energy Losses in Noncircular Conduits," *Trans. Inst. Chem. Engineers*, Vol. 41, pp. 163–173.

Hague, M. A., Hassan, A. K. A., Turner, J. T., and Barrow, H., 1982, "The Prediction of Forced Convection in a Cusped Shaped Channel," *Proc. 7th Int. Heat Transfer Conf.*, Munich, Vol. 5, pp. 459–465.

Hassan, A. K. A., and Barrow, H., 1984, "A Numerical Investigation of Turbulent Flow and Conjugate Heat Transfer in a Four-Cusp Channel," *UK Nat'l Conf. on Heat Transfer*, Leeds, Vol. 1, pp. 337–346.

Maliska, C. R., and Silva, A. F. C., 1986, "Local Effects of Highly Non-orthogonal Grids in the Solution of Heat Transfer Problems in Cusped Corners," *Proc. 1st Int. Conf. on Numerical Grid Generation in Comp. Fluid Mechanics*, Germany, pp. 679–690.

Patankar, S. V., 1980, *Numerical Heat Transfer and Fluid Flow*, Hemisphere, Washington, DC.

Shah, R. K., and London, A. L., 1978, *Laminar Flow Forced Convection in Ducts*, Academic Press, New York.

Turner, J. T., and Hague, M. A., 1983, "Pressurized Water Reactor Blockage: An Experimental Study of Fluid Flow and Heat Transfer in a Model Core," *Proc. Inst. Mech. Engineers*, Vol. C106, pp. 163–173.

Infrared Optical Constants of the High-T_c Superconductor $YBa_2Cu_3O_7$

Z. M. Zhang,[1, 2] T. A. Le,[1, 3] M. I. Flik,[1] and E. G. Cravalho[1]

Introduction

High-T_c superconductors possess a near-unity reflectivity at low temperatures in the far-infrared spectral region for incident radiation polarized parallel to their crystalline *a–b* plane. Two promising applications that exploit this property are thermal-radiation shields and Fabry–Perot resonators. An accurate assessment of the potential of the $YBa_2Cu_3O_7$ superconductor for these applications requires a precise prediction of its infrared reflectivity. By comparing the two-fluid model to the relations of Mattis and Bardeen (1958), Phelan et al. (1991) recommended the use of the latter to calculate the radiative properties of $YBa_2Cu_3O_7$ in the superconducting state. This prediction yields a deviation from the reflectivity data of as large as 12 percent. The Mattis–Bardeen relations are applicable only to superconductors at the impure limit, while $YBa_2Cu_3O_7$ is a pure superconductor. Zhang et al. (1992) showed that the infrared reflectance of $YBa_2Cu_3O_7$ superconducting film–substrate composites can be predicted using the optical constants obtained from the Zimmermann theory (Zimmermann et al., 1991), applicable to superconductors with arbitrary purity. The predicted reflectance agrees well with that measured in the midinfrared region at $2.5\ \mu m < \lambda < 25\ \mu m$.

The objective of this work is to develop a dielectric function for the *a–b* plane of superconducting $YBa_2Cu_3O_7$ in both the midinfrared and far-infrared regions. Latest theoretical and experimental results are incorporated with rational assumptions. Besides considering a finite electron scattering rate and a midinfrared absorption band, this study employs a model for the free-carrier conductivity that accounts for the contribution of residual normal electrons. Comparisons with an extensive set of reflectivity data for epitaxial films and single crystals yield a set of recommended parameters for the dielectric function of the *a–b* plane of $YBa_2Cu_3O_7$. The absorptivity determined from this dielectric function is compared with existing infrared and microwave absorptivity measurements.

Dielectric Function Model

The frequency-dependent dielectric function of $YBa_2Cu_3O_7$ can be expressed by a linear superposition (Timusk and Tanner, 1989):

$$\epsilon(\omega) = \epsilon_\infty + \epsilon_{\text{phonon}} + \frac{\omega_{pe}^2}{\omega_e^2 - \omega^2 - i\omega\gamma_e} + \frac{i\sigma(\omega)}{\omega\epsilon_0} \quad (1)$$

The first term on the right, ϵ_∞, is the high-frequency dielectric constant, which is approximately 4. The second term is the phonon contribution, which is negligible for the *a–b* plane of $YBa_2Cu_3O_7$ single crystals and epitaxial films. The third term

[1]Department of Mechanical Engineering, Massachusetts Institute of Technology, Cambridge, MA 02139.

[2]Current Address: Radiometric Physics Division, National Institute of Standards and Technology, Gaithersburg, MD 20899.

[3]Current Address: Devices R & D, Ethicon Inc., Somerville, NJ 08876.

Contributed by the Heat Transfer Division and presented at the ASME Winter Annual Meeting, Anaheim, California, November 8–13, 1992. Manuscript received by the Heat Transfer Division August 1992; revision received July 1993. Keywords: Cryogenics, Radiation, Thermophysical Properties. Associate Technical Editor: R. O. Buckius.

For a small Prandtl number fluid, the Nusselt number at any location has a larger value, and at the boundary, 0 ~ 90 deg, the overall heat transfer is much higher than in the 90 ~ 180 deg region. It is also found that the local maximum Nusselt number location shifts toward the direction of the smaller angle; the smaller the Prandtl number, the more the location shifts. Furthermore, the local heat transfer in the 90 ~ 180 deg region can be enhanced by natural convection only when the smaller Prandtl number fluid is used.

Conclusion

Fully developed laminar mixed convection in the cusped duct has been investigated in this technical note. The results from this investigation provide an important contribution to the understanding of the characteristics of flow and heat transfer in a cusped duct. It has been revealed that natural convection due to buoyancy will enhance heat transfer, as well as the friction factor. Intensification of heat transfer and increase of the friction factor appear at a higher Rayleigh number, Ra $> 10^4$. The effect of natural convection at lower Rayleigh numbers can be neglected. The fluid having a smaller Prandtl number will result in a higher Nusselt number and greater friction. In addition, the flow and heat transfer in the corner region of the duct are much improved by the secondary flow of natural convection. It is believed that results from the present research will be helpful in the design of the ECCS, and the data base for mixed convection in complicated shape ducts.

Acknowledgments

The results presented in this paper were obtained in the course of research sponsored by the National Science Foundation (NSF) under Grant No. CTS-9017732.

References

Barrow, H., Hornby, R. P., and Mistry, J., 1978, "The Calculation of Fully Developed Turbulent Flow Using a New Mixing Length Model," *Proc. 6th Int. Heat Mass Conf.*, Toronto, Vol. 2, pp. 549–554.

Choudhury, D., and Karki, K., 1992, "Laminar Mixed Convection in an Eccentric Annulus," *Numerical Heat Transfer*, Part A, Vol. 22, pp. 87–108.

Dong, Z. F., Ebadian, M. A., and Campo, A., 1991, "Numerical Analysis of Convective Heat Transfer in the Entrance Region of Cusped Ducts," *Numer. Heat Transfer*, Part A, Vol. 20, pp. 459–472.

Duck, P. W., and Turner, J. T., 1987, "Pressurized Water Reactor Blockage Prediction of Laminar Flow and Temperature Distribution Following a Loss of Coolant Accident," *J. Heat Flow*, Vol. 8(2), pp. 149–155.

Dutra, A. S., Souza-Mendes, P. R., and Parise, J. A. R., 1991, "Transport Coefficients for Laminar and Turbulent Flow Through a Four-Cusp Channel," *Int. J. Heat Fluid Flow*, Vol. 12, No. 2, pp. 99–105.

Gerard, R., and Baines, W. D., 1977, "Turbulent Flow in a Very Nonlinear Conduit," ASCE *J. Hyd. Div.*, Vol. 103 (HY8), pp. 829–841.

Gunn, D. J., and Darling, C. W., 1963, "Fluid Flow and Energy Losses in Noncircular Conduits," *Trans. Inst. Chem. Engineers*, Vol. 41, pp. 163–173.

Hague, M. A., Hassan, A. K. A., Turner, J. T., and Barrow, H., 1982, "The Prediction of Forced Convection in a Cusped Shaped Channel," *Proc. 7th Int. Heat Transfer Conf.*, Munich, Vol. 5, pp. 459–465.

Hassan, A. K. A., and Barrow, H., 1984, "A Numerical Investigation of Turbulent Flow and Conjugate Heat Transfer in a Four-Cusp Channel," *UK Nat'l Conf. on Heat Transfer*, Leeds, Vol. 1, pp. 337–346.

Maliska, C. R., and Silva, A. F. C., 1986, "Local Effects of Highly Non-orthogonal Grids in the Solution of Heat Transfer Problems in Cusped Corners," *Proc. 1st Int. Conf. on Numerical Grid Generation in Comp. Fluid Mechanics*, Germany, pp. 679–690.

Patankar, S. V., 1980, *Numerical Heat Transfer and Fluid Flow*, Hemisphere, Washington, DC.

Shah, R. K., and London, A. L., 1978, *Laminar Flow Forced Convection in Ducts*, Academic Press, New York.

Turner, J. T., and Hague, M. A., 1983, "Pressurized Water Reactor Blockage: An Experimental Study of Fluid Flow and Heat Transfer in a Model Core," *Proc. Inst. Mech. Engineers*, Vol. C106, pp. 163–173.

Infrared Optical Constants of the High-T_c Superconductor $YBa_2Cu_3O_7$

Z. M. Zhang,[1, 2] T. A. Le,[1, 3] M. I. Flik,[1] and E. G. Cravalho[1]

Introduction

High-T_c superconductors possess a near-unity reflectivity at low temperatures in the far-infrared spectral region for incident radiation polarized parallel to their crystalline *a–b* plane. Two promising applications that exploit this property are thermal-radiation shields and Fabry–Perot resonators. An accurate assessment of the potential of the $YBa_2Cu_3O_7$ superconductor for these applications requires a precise prediction of its infrared reflectivity. By comparing the two-fluid model to the relations of Mattis and Bardeen (1958), Phelan et al. (1991) recommended the use of the latter to calculate the radiative properties of $YBa_2Cu_3O_7$ in the superconducting state. This prediction yields a deviation from the reflectivity data of as large as 12 percent. The Mattis–Bardeen relations are applicable only to superconductors at the impure limit, while $YBa_2Cu_3O_7$ is a pure superconductor. Zhang et al. (1992) showed that the infrared reflectance of $YBa_2Cu_3O_7$ superconducting film–substrate composites can be predicted using the optical constants obtained from the Zimmermann theory (Zimmermann et al., 1991), applicable to superconductors with arbitrary purity. The predicted reflectance agrees well with that measured in the midinfrared region at $2.5\ \mu m < \lambda < 25\ \mu m$.

The objective of this work is to develop a dielectric function for the *a–b* plane of superconducting $YBa_2Cu_3O_7$ in both the midinfrared and far-infrared regions. Latest theoretical and experimental results are incorporated with rational assumptions. Besides considering a finite electron scattering rate and a midinfrared absorption band, this study employs a model for the free-carrier conductivity that accounts for the contribution of residual normal electrons. Comparisons with an extensive set of reflectivity data for epitaxial films and single crystals yield a set of recommended parameters for the dielectric function of the *a–b* plane of $YBa_2Cu_3O_7$. The absorptivity determined from this dielectric function is compared with existing infrared and microwave absorptivity measurements.

Dielectric Function Model

The frequency-dependent dielectric function of $YBa_2Cu_3O_7$ can be expressed by a linear superposition (Timusk and Tanner, 1989):

$$\epsilon(\omega) = \epsilon_\infty + \epsilon_{\text{phonon}} + \frac{\omega_{pe}^2}{\omega_e^2 - \omega^2 - i\omega\gamma_e} + \frac{i\sigma(\omega)}{\omega\epsilon_0} \quad (1)$$

The first term on the right, ϵ_∞, is the high-frequency dielectric constant, which is approximately 4. The second term is the phonon contribution, which is negligible for the *a–b* plane of $YBa_2Cu_3O_7$ single crystals and epitaxial films. The third term

[1]Department of Mechanical Engineering, Massachusetts Institute of Technology, Cambridge, MA 02139.

[2]Current Address: Radiometric Physics Division, National Institute of Standards and Technology, Gaithersburg, MD 20899.

[3]Current Address: Devices R & D, Ethicon Inc., Somerville, NJ 08876.

Contributed by the Heat Transfer Division and presented at the ASME Winter Annual Meeting, Anaheim, California, November 8–13, 1992. Manuscript received by the Heat Transfer Division August 1992; revision received July 1993. Keywords: Cryogenics, Radiation, Thermophysical Properties. Associate Technical Editor: R. O. Buckius.

is a midinfrared absorption band, accounting for interband electronic transitions, which is temperature-independent and has a center frequency ω_e, a plasma frequency ω_{pe}, and a damping coefficient γ_e. The last term is the free-carrier contribution, where ϵ_0 is the electrical permittivity of free space and $\sigma(\omega)$ is the free-carrier conductivity. The free-carrier conductivity dominates the dielectric function in the infrared region.

In the present study, the free-carrier conductivity is modeled using two components. One is the contribution of the electrons whose behavior can be modeled by the BCS theory (Bardeen et al., 1957), viz., BCS electrons. The BCS electrons include both superconducting electrons, the Cooper pairs, and quasiparticles that will condense to Cooper pairs at very low temperatures. The other is the contribution of the residual normal electrons that remain in the normal state even when temperature approaches zero.

The expression for the complex conductivity for a BCS superconductor, $\sigma_{ss}(\omega)$, derived by Zimmermann et al. (1991) and Scharnberg (1978) can be written as

$$\frac{\sigma_{ss}(\omega)}{\sigma_0} = F\left(\frac{\omega}{\omega_g}, \frac{T}{T_c}, \frac{\bar{h}}{2\tau\Delta}\right) \tag{2}$$

where $\sigma_0 = n_e e^2 \tau / m_e$ is the DC conductivity, where n_e, e, and m_e are the number density, charge, and effective mass of electrons, $\omega_g = \Delta/\bar{h}$ is the gap frequency, where Δ is the energy gap and $\bar{h}$ is Planck's constant, and $1/\tau$ is the electron scattering rate. The explicit expression of the function F and a computer program for calculating σ_{ss} were provided by Zimmermann et al. (1991). The input parameters are σ_0, Δ, $1/\tau$, and T/T_c. The conditions for Eq. (2) to be valid were discussed by Zimmermann et al. (1991) and Zhang et al. (1992).

In the dirty limit, when $\tau = 0$, Eq. (2) reduces to the Mattis–Bardeen relations (Mattis and Bardeen, 1958). When $T = 0$, the real part of σ_{ss} from Eq. (2) is identical to that given by Leplae (1983) who evaluated the imaginary conductivity from the real part using the Kramer–Kronig relation. The optical conductivity for high-T_c superconducting materials was also calculated from strong-coupling theory by several groups. The electron-phonon coupling strength and the Fermi-surface data must be known in order to evaluate the conductivity from the strong-coupling theory (Lee et al., 1989).

The frequency derivative of the conductivity is discontinuous at $\omega = 2\omega_g$. At temperature equals zero, all BCS electrons condense to Cooper pairs; therefore, incident photons with energy, $\bar{h}\omega < 2\Delta$, can not be absorbed by the superconductor. Hence, a BCS superconductor is a perfect reflector at $T = 0$ for $\omega < 2\omega_g$, when the real part of the conductivity is zero.

The energy gap parameter, $A = 2\Delta_0/k_B T_c$, where k_B is the Boltzmann constant and Δ_0 is the energy gap at zero temperature, for BCS weak-coupling superconductors is approximately 3.53. There exist controversial viewpoints regarding the value, and even the existence, of the energy gap for high-T_c materials. In the present study, the energy gap at zero temperature is taken as an adjustable parameter. The temperature-dependent energy gap is calculated from the BCS theory using an approximate formula as in the work of Flik et al. (1992).

Far-infrared and microwave measurements (Renk et al., 1991; Miller et al., 1992) indicated a residual absorption at $T \ll T_c$ due to the existence of nonpairing charge carriers. As suggested by Kobayashi and Imai (1991), a temperature-independent fraction of normal electrons is considered, which obeys the Drude model, $\sigma_{nr} = \sigma_0/(1 - i\omega\tau)$. If f_{nr} denotes the fraction of residual normal electrons, the number density of residual normal electrons is $f_{nr} n_e$ and that of BCS electrons is $(1 - f_{nr}) n_e$. The DC conductivity is proportional to the electron number density. If the same scattering rate, charge, and effective mass are applied to both the BCS electrons and residual normal electrons, the free-carrier conductivity is

$$\sigma(\omega) = (1 - f_{nr})\sigma_{ss}(\omega) + f_{nr}\sigma_{nr}(\omega) \tag{3}$$

Equation (3) is distinguished from the conventional two-fluid model (Timusk and Tanner, 1989) in two ways. First, the conductivity of the BCS electrons, σ_{ss}, comprises contributions of both the Cooper pairs and quasi-particles. Second, the fraction of normal electrons includes only the nonpairing electrons and, therefore, is temperature independent. An explanation of the origin of residual normal electrons was given by Flik et al. (1992), considering the layered crystalline structures of $YBa_2Cu_3O_7$. The CuO_2 planes contribute to the BCS component, while the CuO chains contain the nonpairing electrons. Other possible mechanisms of the residual normal electrons are weak links or planar defects (Halbritter, 1992), impurities (Renk et al., 1991), and surface contamination (Pham et al., 1991).

Frequency-independent scattering rate was successfully applied to the normal state of high-T_c superconductors by several groups (Kamaras et al., 1990; Zhang et al., 1992). On the other hand, frequency-dependent scattering rate and electron mass were also employed to model the complex conductivity (Schlesinger et al., 1990; Schützmann et al., 1989). In these studies, the scattering rate decreases linearly with frequency in the infrared region. A frequency-independent scattering rate is employed for both the residual normal electrons and the BCS electrons in the present study since no conclusion can be drawn at this moment regarding the frequency dependence of the electron scattering rate.

As in the work of Flik et al. (1992), a hypothetical DC conductivity, σ_0, is obtained for $T < T_c$ by extrapolating the normal-state electrical resistivity. The temperature dependence of the electrical resistivity due to electron-phonon scattering is determined using the Bloch formula. The DC conductivity obtained at $T \ll T_c$ is 4 to 6 times that of the room-temperature values.

Kobayashi and Imai (1991) determined $\sigma_{ss}(\omega)$ in Eq. (3) with a two-fluid model. By adding a temperature-independent fraction of residual normal electrons, they suggested a three-fluid model and obtained good agreement with microwave surface resistance measurements. This model, however, yields a large deviation between the predicted and the measured reflectivity for $5\ \mu\text{m} < \lambda < 30\ \mu\text{m}$.

Van der Marel et al. (1991) proposed an ad hoc two-fluid model. In their model, $\sigma_{ss}(\omega)$ is calculated from the Zimmermann theory with a temperature-independent energy gap distribution, $(1 - f_{nr})$ is assumed to be proportional to $[1 - (T/T_c)^4]$ for $T < T_c$, and $\sigma_{nr}(\omega)$ is calculated from a temperature- and frequency-dependent scattering rate. This makes their model complicated and difficult to use practically.

Comparison Between the Predicted and Measured Optical Properties

The real part, $n(\omega)$, and the imaginary part, $\kappa(\omega)$, of the refractive index are related to the dielectric function by $[n(\omega) + i\kappa(\omega)]^2 = \epsilon(\omega)$. For semi-infinite media, the reflectivity for normal incidence is

$$\rho(\omega) = \frac{[n(\omega) - 1]^2 + \kappa(\omega)^2}{[n(\omega) + 1]^2 + \kappa(\omega)^2} \tag{4}$$

The absorptivity is obtained by subtracting the reflectivity from unity: $\alpha(\omega) = 1 - \rho(\omega)$.

The adjustable parameters are the energy gap parameter, A, the normalized scattering rate, $1/\tau$, and the fraction of residual normal electrons, f_{nr}. The center frequency, ω_e, of the midinfrared band is fixed at 1800 cm^{-1} (Zhang et al., 1992). The plasma frequency and damping coefficient of the midinfrared band, ω_{pe} and γ_e, are allowed to vary within the values reported in the literature (Timusk and Tanner, 1989) from 18,000 to 24,000 cm^{-1} and from 4200 to 7500 cm^{-1}, respec-

Table 1 Parameters that fit to five sets of reflectivity data and the recommended values for the 5 to 200 μm wavelength region, where $\omega_e = 1800\ \text{cm}^{-1}$ and the scattering rate in cm^{-1} is calculated by $(2\pi c_0 \tau)^{-1}$, where c_0 is the speed of light in vacuum. The uncertainties are 0.5 for A, 20 cm^{-1} for $1/\tau$, and 0.1 for f_{nr}.

AUTHORS, YEAR, AND SAMPLE TYPE	T_c (K)	T (K)	σ_0 $(\Omega\,\text{m})^{-1}$	A	$1/\tau$ (cm^{-1})	$\left(\frac{\omega_{pe}}{\omega_e}\right)^2$	$\frac{\gamma_e}{\omega_e}$	f_{nr}
COLLINS ET AL., 1989 CRYSTAL	92	45	2.5×10^6	6	95	178	2.8	0.30
COOPER ET AL., 1989 CRYSTAL	90	20	2.6×10^6	8	100	150	4.0	0.20
RENK ET AL., 1991 FILM ON $SrTiO_3$	91	10	2.5×10^6	8	100	150	4.0	0.20
SCHÜTZMANN ET AL., 1989, FILM ON $SrTiO_3$	91	20	2.5×10^6	6	95	178	2.8	0.15
VAN DER MAREL ET AL., 1991, FILM ON $SrTiO_3$	90	30	2.0×10^6	8	125	100	2.3	0.30
RECOMMENDED	91		2.5×10^6	7	100	100	2.8	0.20

tively. In the fitting procedure, the gap parameter A is chosen between 6 and 8 by observing the sharp transition between 20 and 25 μm in the reflectivity, and the fraction of normal electrons f_{nr} is fitted by comparing the calculated and measured reflectivity at $\lambda > 25$ μm, where the influence of the other parameters is small. The electron scattering rate is obtained based on the comparison of the calculated and measured reflectivity at 5 $\mu\text{m} < \lambda < 25$ μm. The sensitivity to the fitting parameters is examined by varying individual parameters and comparing the calculated with the measured reflectivity.

The samples of Kamaras et al. (1990), Renk et al. (1991), Schützmann et al. (1989), and van der Marel et al. (1991) are epitaxial c-axis $YBa_2Cu_3O_7$ films deposited by laser ablation on $SrTiO_3$ substrates. The typical film thickness of 400 nm is much larger than the radiation penetration depths in the infrared region and the films can be treated as semi-infinite media. The room-temperature resistivity is approximately 200 $\mu\Omega$ cm. Collins et al. (1989) and Cooper et al. (1989) measured the a–b plane reflectivity of single crystals. Fourier-transform infrared spectrometers were used to measure the reflectivity with an estimated uncertainty of 1 percent.

The foregoing reflectivity data are fitted using the procedure described above, except that of Kamaras et al. (1990) due to the lack of normal-state electrical resistivity data. Table 1 lists the fitting parameters for individual data set and the recommended values that fit the five sets of data. The root-mean-square deviation between the reflectivity calculated using the fitting parameters and the data is less than 0.004. Figure 1 compares the measured reflectivity to that calculated from the recommended parameters at $T = 10$ K. The reflectivity obtained by Kamaras et al. (1990) is shown only for comparison.

A multiparameter least-squares fitting program (Press et al., 1986) is employed to check the fitting quality. The variation of the plasma frequency and damping coefficient in the ranges given above does not cause large difference in the calculated dielectric function. If the midinfrared-band parameters are fixed, the optimized A, $1/\tau$, and f_{nr} obtained by multiparameter least-squares fitting agree with those listed in Table 1. The sensitivity of the reflectivity to the fitting parameters determines the fitting uncertainties, which are 0.5 for A, 20 cm^{-1} for $1/\tau$, and 0.1 for f_{nr}.

The energy gap obtained in Table 1 agrees with that reported by Collins et al. (1989) and Renk et al. (1991). The values of DC conductivity are within the range between 1.2 and 3.6×10^6 $(\Omega\text{m})^{-1}$ obtained by Miller et al. (1992) by fitting the absorptivity data to a two-fluid model. The electron scattering rate at low temperatures of 100 cm^{-1} is comparable with the value of 90 cm^{-1} obtained by Flik et al. (1992) for a set of epitaxial

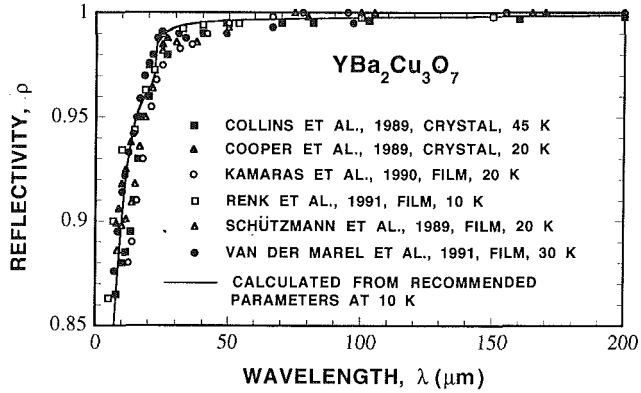

Fig. 1 Comparison of the reflectivity of $YBa_2Cu_3O_7$ calculated from the recommended parameters to six sets of data

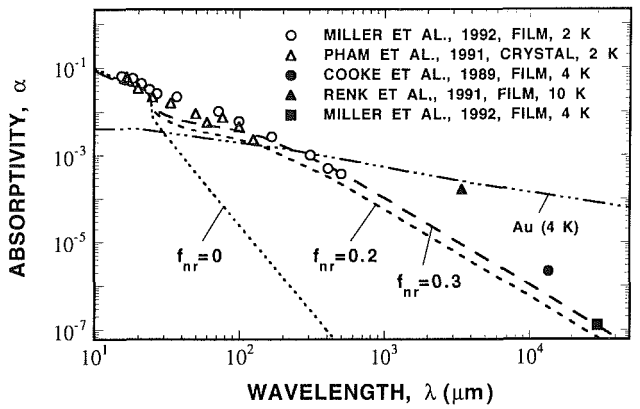

Fig. 2 Comparison of the calculated to the measured absorptivity in the infrared and microwave regions of $YBa_2Cu_3O_7$ films, where the absorptivity of gold at 4 K is also shown

thin $YBa_2Cu_3O_7$ films from both infrared spectroscopy and transport measurements. Bonn et al. (1992) studied the microwave properties of a high-quality $YBa_2Cu_3O_7$ crystal at ~3 GHz. They measured a sharp drop of the surface resistance below T_c, a peak at approximately 35 K, and a finite value of 15 $\mu\Omega$ at $T = 1.7$ K. Using a two-fluid model, they obtained that, at 80 K and 60 K, $1/\tau$ drops to 1/6 and 1/20 of the normal-state value at 95 K, respectively. The rapid decrease of the electron scattering rate was attributed to the inelastic electron–electron scattering. The ratios of the mean free path at 70 K and 50 K to that at 90 K obtained by Halbritter (1992) from the surface-impedance consideration were ~2 and ≥ 4, respectively. Miller et al. (1992) obtained the electron scattering rates of $YBa_2Cu_3O_7$ films at $T \ll T_c$ from far-infrared and microwave measurements using a two-fluid model. The values were between 300 and 600 cm^{-1}. The electron–electron and electron–phonon interaction mechanisms in the high-T_c superconducting materials need to be further investigated.

Figure 2 compares the far-infrared and microwave absorptivity of $YBa_2Cu_3O_7$ measured by different groups with that calculated using the proposed dielectric function for $f_{nr} = 0$, 0.2, and 0.3 and at $T = 10$ K. The microwave absorptivity is calculated from the measured surface resistance, R_s, using $\alpha = 4R_s/\sqrt{\mu_0/\epsilon_0}$, where μ_0 is the magnetic permeability of free space. This relation is a good approximation when the imaginary part of the conductivity is much larger than its real part and the surface resistance is much less than the impedance of free space, $\sqrt{\mu_0/\epsilon_0}$. The absorptivity of gold at 4 K calculated from the theory of the anomalous skin effect (Toscano and

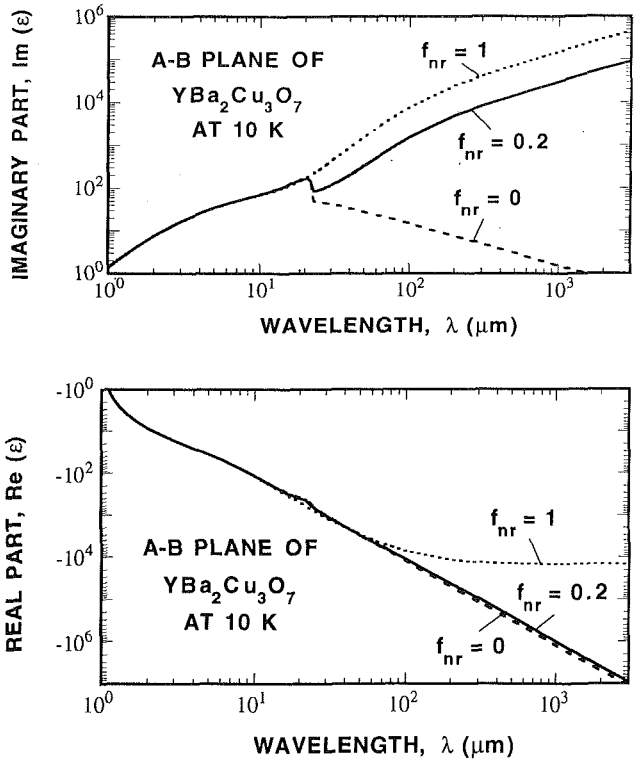

Fig. 3 Real and imaginary parts of the recommended dielectric function of $YBa_2Cu_3O_7$

Cravalho, 1976) is also shown in Fig. 2. At long wavelengths, the absorptivity of the $YBa_2Cu_3O_7$ superconductor is less than that of gold. This is why high-T_c materials are potentially better than gold as radiation shields at low temperatures, when most of the radiation energy is emitted at long wavelengths.

Miller et al. (1992) measured the infrared absorptivity of $YBa_2Cu_3O_7$ superconducting films. In their apparatus, the beam from the interferometer of a Fourier-transform spectrometer was split symmetrically by a wedge-shaped mirror into two paths, one to the superconducting film and the other to a reference bolometer with known absorptivity. The absorptivity data of sample A from Miller et al. (1992) is used in the present study because it possesses the lowest microwave surface resistance. The $YBa_2Cu_3O_7$ film was deposited on a MgO substrate by an off-axis sputtering method. A microwave surface resistance of 12 $\mu\Omega$ at 10 GHz and 4 K was measured for this sample with a parallel-plate-resonator technique (Miller et al., 1992). Figure 2 also shows the average absorptivity for the *a*- and *b*-axis polarization measured by Pham et al. (1991) for an untwinned single crystal. Cooke et al. (1989) measured a surface resistance of 0.2 mΩ at 22 GHz and 4 K for an *ex situ* grown $YBa_2Cu_3O_7$ film on a $LaGaO_3$ substrate. The microwave absorptivity data at 10 and 22 GHz shown in Fig. 2 are the lowest values reported for epitaxial $YBa_2Cu_3O_7$ films at these frequencies (Piel and Müller, 1991). Figure 2 suggests that, even for the best samples currently available, the fraction of residual normal electrons is still of the order of 20 to 30 percent.

At temperatures below $T_c/2$, the free-carrier conductivity, and thus the dielectric function, is only a weak function of temperature. Figure 3 shows the real and imaginary parts of the dielectric function at 10 K calculated from Eq. (1) using the recommended parameters from Table 1 with $f_{nr}=0$, 0.2, and 1. For wavelengths larger than 1 μm, the real part of the dielectric function is negative due to the large imaginary part of the free-carrier conductivity. A sharp change in the imaginary part of the dielectric function occurs at the gap wavelength of approximately 23 μm due to the sharp change in real part of the conductivity of the BCS electrons. For $f_{nr}=1$, the conductivity is obtained from the Drude model. Since $\mathrm{Re}(\sigma)\to\sigma_0$ and $\mathrm{Im}(\sigma)\to\omega\tau\sigma_0$ as $\lambda\to\infty$, $\mathrm{Re}(\epsilon)$ approaches a negative constant, $-\tau\sigma_0/\epsilon_0$, and $\mathrm{Im}(\epsilon)$ approaches $\sigma_0/(\omega\epsilon_0)$, which is proportional to λ. For the BCS electrons at $T\ll T_c$, $\mathrm{Re}(\sigma)=0$ at $\omega<2\omega_g$ and $\mathrm{Im}(\sigma)\propto\lambda$ as $\lambda\to\infty$. Hence, for $f_{nr}=0$ when $\lambda\gg 1$, $|\mathrm{Re}(\epsilon)|$ is proportional to λ^2 and the imaginary part of the dielectric function is determined from the midinfrared band, viz., $\mathrm{Im}(\epsilon)\to\omega\gamma_e\omega_{pe}^2/\omega_e^4\propto\lambda^{-1}$. The reflectance always approaches unity as $\lambda\to\infty$ since either κ or both n and κ go to infinity.

Concluding Remarks

A dielectric function is proposed for the *a*–*b* plane of the superconductor $YBa_2Cu_3O_7$, which accounts for residual normal electrons, a finite electron scattering rate, and a midinfrared absorption band. Although there is no conclusive solution regarding the energy gap, the electron scattering rate below T_c, and the origin of the residual normal electrons in the high-T_c superconductors, the calculated infrared reflectivity, absorptivity, and microwave absorptivity are in good agreement with those measured by different groups. This work suggests a set of parameters for the dielectric function of $YBa_2Cu_3O_7$ in the superconducting state for engineering applications in the wavelengths from 5 μm to the far-infrared. There exists a fraction of normal electrons of about 20 to 30 percent even at $T\ll T_c$ in the best available $YBa_2Cu_3O_7$ samples. Hence, the success of high-T_c superconducting films for high-reflectivity applications will be enhanced by a reduction of the fraction of residual normal electrons.

Acknowledgments

The authors wish to thank Professor T. P. Orlando, Professor H. D. Drew, J. P. Hebb, and C. G. Malone for valuable discussions. The critical comments from the official reviewers are appreciated. This work was supported by the C. S. Draper Laboratory, Cambridge, MA, contract No. DL-H-418480, and by the National Science Foundation, contract No. CTS-9007765.

References

Bardeen, J., Cooper, L. N., and Schrieffer, J. R., 1957, "Theory of Superconductivity," *Phys. Rev.*, Vol. 108, pp. 1175–1204.

Bonn, D. A., Dosanjh, P., Liang, R., and Hardy, W. N., 1992, "Evidence of Rapid Suppression of Quasiparticle Scattering Below T_c in $YBa_2Cu_3O_{7-\delta}$," *Phys. Rev. Lett.*, Vol. 68, pp. 2390–2393.

Collins, R. T., Schlesinger, Z., Holtzberg, F., and Feild, C., 1989, "Infrared Evidence for Gap Anisotropy in $YBa_2Cu_3O_7$," *Phys. Rev. Lett.*, Vol. 63, pp. 422–425.

Cooke, D. W., Gray, E. R., Houlton, R. J., Rusnak, B., Meyer, E. A., Beery, J. G., Brown, D. R., Garzon, F. H., Raistrick, I. D., Rollet, A. D., and Bolmaro, R., 1989, "Surface Resistance of $YBa_2Cu_3O_7$ Films on $SrTiO_3$ and $LaGaO_3$ Substrates," *Appl. Phys. Lett.*, Vol. 55, pp. 914–916.

Cooper, S. L., Thomas, G. A., Orenstein, J., Rapkine, D. H., Capizzi, M., Timusk, T., Millis, A. J., Schneemeyer, L. F., and Waszczak, J. V., 1989, "Properties of Optical Features in $YBa_2Cu_3O_{7-\delta}$," *Phys. Rev. B*, Vol. 40, pp. 11358–11361.

Flik, M. I., Zhang, Z. M., Goodson, K. E., Siegal, M. P., and Phillips, J. M., 1992, "Electron Scattering Rate in Epitaxial $YBa_2Cu_3O_7$ Superconducting Films," *Phys. Rev. B*, Vol. 46, pp. 5606–5614.

Halbritter, J., 1992, "On Intrinsic and Extrinsic Effects in the Surface Impedance of Cuprate Superconductors," *J. Supercond.*, Vol. 5, pp. 331–337.

Kamaras, K., Herr, S. L., Porter, C. D., Tache, N., Tanner, D. B., Etemad, S., Venkatesan, T., Chase, E., Inam, A., Wu, X. D., Hegde, M. S., and Dutta, B., 1990, "In a Clean High-T_c Superconductor You Do Not See the Gap," *Phys. Rev. Lett.*, Vol. 64, pp. 84–87.

Kobayashi, Y., and Imai, T., 1991, "Phenomenological Description of Conduction Mechanism of High-T_c Superconductors by Three-Fluid Model," *IEICE Trans.*, Vol. E74, pp. 1986–1992.

Leplae, L., 1983, "Derivation of an Expression for the Conductivity of Superconductors in Terms of the Normal-State Conductivity," *Phys. Rev. B*, Vol. 27, pp. 1911–1912.

Lee, W., Rainer, D., and Zimmermann, W., 1989, "Holstein Effect in the Far-Infrared Conductivity of High-T_c Superconductors," *Physica C*, Vol. 159, pp. 535–544.

Mattis, D. C., and Bardeen, J., 1958, "Theory of the Anomalous Skin Effect in Normal and Superconducting Metals," *Phys. Rev.*, Vol. 111, pp. 412-417.

Miller, D., Richards, P. L., Etemad, S., Inam, A., Venkatesan, T., Dutta, B., Wu, X. D., Eom, C. B., Geballe, T. H., Newman, N., and Cole, B. F., 1992, "Correspondence Between Microwave and Submillimeter Absorptivity in Epitaxial Thin Films of $YBa_2Cu_3O_7$," *Phys. Rev. B*, Vol. 47, pp. 8076-8088.

Pham, T., Lee, M. W., Drew, H. D., Welp, U., and Fang, Y., 1991, "Far-Infrared Absorptivity of Single-Domain $YBa_2Cu_3O_7$," *Phys. Rev. B*, Vol. 44, pp. 5377-5381.

Phelan, P. E., Flik, M. I., and Tien, C. L., 1991, "Radiative Properties of Superconducting Y-Ba-Cu-O Thin Films," ASME JOURNAL OF HEAT TRANSFER, Vol. 113, pp. 487-493.

Piel, H., and Müller, G., 1991, "The Microwave Surface Impedance of High-T_c Superconductors," *IEEE Trans. Magn.*, Vol. 27, pp. 854-862.

Press, W. H., Flannery, B. P., Teukolsky, S. A., and Vetterling, W. T., 1986, *Numerical Recipes*, Cambridge University Press, Cambridge, UK, Chap. 14.

Renk, K. F., Gorshunov, B., Schützmann, J., Prückl, A., Brunner, B., Betz, J., Orbach, S., Klein, N., Müller, G., and Piel, H., 1991, "Far-Infrared and Microwave Intragap Absorption in a $YBa_2Cu_3O_{7-\delta}$ Thin Film at Low Temperature," *Europhys. Lett.*, Vol. 15, pp. 661-666.

Scharnberg, K., 1978, "Effect of Finite Electron Mean Free Path on the Attenuation, Electromagnetic Generation, and Detection of Ultrasonic Shear Waves in Superconductors," *J. Low Temp. Phys.*, Vol. 30, pp. 229-263.

Schlesinger, Z., Collins, R. T., Holtzberg, F., Feild, C., Blanton, S. H., Welp. U., Crabtree, G. W., Fang, Y., and Liu, J. Z., 1990, "Superconducting Energy Gap and Normal-State Conductivity of a Single-Domain $YBa_2Cu_3O_7$ Crystal," *Phys. Rev. Lett.*, Vol. 65, pp. 801-804.

Schützmann, J., Ose, W., Keller, J., Renk, K. F., Roas, B., Schultz, L., and Saemann-Ischenko, G., 1989, "Far-Infrared Reflectivity and Dynamical Conductivity of an Epitaxial $YBa_2Cu_3O_{7-\delta}$ Thin Film," *Europhys. Lett.*, Vol. 8, pp. 679-684.

Timusk, T., and Tanner, D. B., 1989, "Infrared Properties of High-T_c Superconductors," in: *Physical Properties of High-Temperature Superconductors*, D. M. Ginsberg, ed., World Scientific Publishing Co., Singapore, Vol. 1, pp. 339-407.

Toscano, W. M., and Cravalho, E. G., 1976, "Thermal Radiation Properties of the Noble Metals at Cryogenic Temperatures," ASME JOURNAL OF HEAT TRANSFER, Vol. 98, pp. 438-445.

Van der Marel, D., Habermeier, H.-U., Heitmann, D., König, W., and Wittlin, A., 1991, "Infrared Study of the Superconducting Phase Transition in $YBa_2Cu_3O_{7-x}$," *Physica C*, Vol. 176, pp. 1-18.

Zhang, Z. M., Choi, B. I., Le, T. A., Flik, M. I., Siegal, M. P., and Phillips, J. M., 1992, "Infrared Refractive Index of Thin $YBa_2Cu_3O_7$ Superconducting Films," ASME JOURNAL OF HEAT TRANSFER, Vol. 114, pp. 644-652.

Zimmermann, W., Brandt, E. H., Bauer, M., Seider, E., and Genzel, L., 1991, "Optical Conductivity of BCS Superconductors With Arbitrary Purity," *Physica C*, Vol. 183, pp. 99-104.

Dimensionality Issues in Modeling With the Discrete-Ordinates Method

A. Sánchez A.,[1] T. F. Smith,[2] and W. F. Krajewski[3]

Nomenclature

a = absorption coefficient, m^{-1}
I = radiation intensity, W/m^2-sr-μm
L = length, m
s = scattering coefficient, m^{-1}
S = source term, W/m^3-sr-μm
x, y, z = coordinates, m
$\Delta x, \Delta y, \Delta z$ = differential lengths in x, y, and z directions, m
α = finite-difference weighting factor
β = extinction coefficient $= (a+s)$, m^{-1}
θ = polar angle, rad
μ, δ, γ = cosine of angles between I and x, y, and z axes
τ = optical thickness $= \beta L$
ϕ = azimuthal angle, rad

Subscripts

c = parallel beam
d = sensor
i = discrete direction i
x, y, z = coordinates

Superscripts

P = control volume label
xr, yr, zr = reference faces in x, y, and z directions

Introduction

The discrete-ordinates method has been successfully applied to the solution of one-, two-, and three-dimensional radiative transfer problems in Cartesian coordinates (Carlson and Lathrop, 1968; Gerstl and Zardecki, 1985; Stamnes et al., 1988; Kim and Lee, 1990; Fiveland and Jamaluddin, 1991; Sánchez et al., 1991). Models of the discrete-ordinates method have been developed to take advantage of the symmetry and invariance related to each level of dimensionality. These models fail to retain, in one- and two-dimensional applications, the three-dimensional effects implied by the presence of incident collimated sources and/or detecting sensors at locations that are outside the planes of symmetry. As a consequence, most applications found in the literature limit parallel beam radiation and intensity output to a sensor to zero azimuthal angles (Kim and Lee, 1989) or a further treatment of the intensity field is required (Stamnes et al., 1988).

In a few occasions, a higher dimensionality (three-dimensional) discrete-ordinates model has been used to solve lower dimensionality (one- or two-dimensional) problems by (1) modifying the aspect ratio of the numerical domain to imply infinite length(s), (2) modeling the boundaries in the infinite direction(s) as specular boundaries, or (3) assuming the boundary conditions in the infinite direction(s) periodic. This classical approach is not practical in optically thick problems where a very large number of control volumes, and, therefore, computer resources, would be required. Because of this and other disadvantages of the classical methodology (ray and end effects), the mirror technique (periodic or symmetric boundaries) was introduced by Sánchez et al. (1991).

After each iteration for the control volume intensity, the discrete-ordinates method gives the intensity field. A mirror technique can be applied to the direction (two-dimensional) or directions (one-dimensional) of infinite length making the boundaries in these directions behave as periodic boundaries. Thus, the intensities leaving a surface on the boundary are placed as intensities arriving at the opposite boundary for the next iteration for the infinite direction(s). In the mirror technique, the aspect ratio is irrelevant and no special consideration about the side walls is needed. Although the mirror approach is a step in the right direction, its slow rate of convergence reduces its practical applicability.

The two approaches (classical and mirror) to the lesser dimensionality problem fail to recognize the simple solution offered by the discrete-ordinates formulation. The verification of a simple procedure (shortcut approach) that uses the same

[1]Professor, Escuela de Ingeniería Mecánica, Universidad de los Andes, Mérida, Venezuela.

[2]Professor, Department of Mechanical Engineering, The University of Iowa, Iowa City, IA 52242; Mem ASME.

[3]Associate Professor, Department of Civil and Environmental Engineering, Iowa Institute of Hydraulic Research, The University of Iowa, Iowa City, IA 52242.

Contributed by the Heat Transfer Division and based on a paper presented at the National Heat Transfer Conference, San Diego, California, August 9-12, 1992. Manuscript received by the Heat Transfer Division May 1992; revision received March 1993. Keywords: Numerical Methods, Radiation. Associate Technical Editor: W. A. Fiveland.

Mattis, D. C., and Bardeen, J., 1958, "Theory of the Anomalous Skin Effect in Normal and Superconducting Metals," *Phys. Rev.*, Vol. 111, pp. 412–417.

Miller, D., Richards, P. L., Etemad, S., Inam, A., Venkatesan, T., Dutta, B., Wu, X. D., Eom, C. B., Geballe, T. H., Newman, N., and Cole, B. F., 1992, "Correspondence Between Microwave and Submillimeter Absorptivity in Epitaxial Thin Films of $YBa_2Cu_3O_7$," *Phys. Rev. B*, Vol. 47, pp. 8076–8088.

Pham, T., Lee, M. W., Drew, H. D., Welp, U., and Fang, Y., 1991, "Far-Infrared Absorptivity of Single-Domain $YBa_2Cu_3O_7$," *Phys. Rev. B*, Vol. 44, pp. 5377–5381.

Phelan, P. E., Flik, M. I., and Tien, C. L., 1991, "Radiative Properties of Superconducting Y–Ba–Cu–O Thin Films," ASME JOURNAL OF HEAT TRANSFER, Vol. 113, pp. 487–493.

Piel, H., and Müller, G., 1991, "The Microwave Surface Impedance of High-T_c Superconductors," *IEEE Trans. Magn.*, Vol. 27, pp. 854–862.

Press, W. H., Flannery, B. P., Teukolsky, S. A., and Vetterling, W. T., 1986, *Numerical Recipes*, Cambridge University Press, Cambridge, UK, Chap. 14.

Renk, K. F., Gorshunov, B., Schützmann, J., Prückl, A., Brunner, B., Betz, J., Orbach, S., Klein, N., Müller, G., and Piel, H., 1991, "Far-Infrared and Microwave Intragap Absorption in a $YBa_2Cu_3O_{7-\delta}$ Thin Film at Low Temperature," *Europhys. Lett.*, Vol. 15, pp. 661–666.

Scharnberg, K., 1978, "Effect of Finite Electron Mean Free Path on the Attenuation, Electromagnetic Generation, and Detection of Ultrasonic Shear Waves in Superconductors," *J. Low Temp. Phys.*, Vol. 30, pp. 229–263.

Schlesinger, Z., Collins, R. T., Holtzberg, F., Feild, C., Blanton, S. H., Welp. U., Crabtree, G. W., Fang, Y., and Liu, J. Z., 1990, "Superconducting Energy Gap and Normal-State Conductivity of a Single-Domain $YBa_2Cu_3O_7$ Crystal," *Phys. Rev. Lett.*, Vol. 65, pp. 801–804.

Schützmann, J., Ose, W., Keller, J., Renk, K. F., Roas, B., Schultz, L., and Saemann-Ischenko, G., 1989, "Far-Infrared Reflectivity and Dynamical Conductivity of an Epitaxial $YBa_2Cu_3O_{7-\delta}$ Thin Film," *Europhys. Lett.*, Vol. 8, pp. 679–684.

Timusk, T., and Tanner, D. B., 1989, "Infrared Properties of High-T_c Superconductors," in: *Physical Properties of High-Temperature Superconductors*, D. M. Ginsberg, ed., World Scientific Publishing Co., Singapore, Vol. 1, pp. 339–407.

Toscano, W. M., and Cravalho, E. G., 1976, "Thermal Radiation Properties of the Noble Metals at Cryogenic Temperatures," ASME JOURNAL OF HEAT TRANSFER, Vol. 98, pp. 438–445.

Van der Marel, D., Habermeier, H.-U., Heitmann, D., König, W., and Wittlin, A., 1991, "Infrared Study of the Superconducting Phase Transition in $YBa_2Cu_3O_{7-x}$," *Physica C*, Vol. 176, pp. 1–18.

Zhang, Z. M., Choi, B. I., Le, T. A., Flik, M. I., Siegal, M. P., and Phillips, J. M., 1992, "Infrared Refractive Index of Thin $YBa_2Cu_3O_7$ Superconducting Films," ASME JOURNAL OF HEAT TRANSFER, Vol. 114, pp. 644–652.

Zimmermann, W., Brandt, E. H., Bauer, M., Seider, E., and Genzel, L., 1991, "Optical Conductivity of BCS Superconductors With Arbitrary Purity," *Physica C*, Vol. 183, pp. 99–104.

Dimensionality Issues in Modeling With the Discrete-Ordinates Method

A. Sánchez A.,[1] T. F. Smith,[2] and W. F. Krajewski[3]

Nomenclature

a = absorption coefficient, m^{-1}
I = radiation intensity, W/m^2-sr-μm
L = length, m
s = scattering coefficient, m^{-1}
S = source term, W/m^3-sr-μm
x, y, z = coordinates, m
$\Delta x, \Delta y, \Delta z$ = differential lengths in x, y, and z directions, m
α = finite-difference weighting factor
β = extinction coefficient $= (a+s)$, m^{-1}
θ = polar angle, rad
μ, δ, γ = cosine of angles between I and x, y, and z axes
τ = optical thickness $= \beta L$
ϕ = azimuthal angle, rad

Subscripts

c = parallel beam
d = sensor
i = discrete direction i
x, y, z = coordinates

Superscripts

P = control volume label
xr, yr, zr = reference faces in x, y, and z directions

Introduction

The discrete-ordinates method has been successfully applied to the solution of one-, two-, and three-dimensional radiative transfer problems in Cartesian coordinates (Carlson and Lathrop, 1968; Gerstl and Zardecki, 1985; Stamnes et al., 1988; Kim and Lee, 1990; Fiveland and Jamaluddin, 1991; Sánchez et al., 1991). Models of the discrete-ordinates method have been developed to take advantage of the symmetry and invariance related to each level of dimensionality. These models fail to retain, in one- and two-dimensional applications, the three-dimensional effects implied by the presence of incident collimated sources and/or detecting sensors at locations that are outside the planes of symmetry. As a consequence, most applications found in the literature limit parallel beam radiation and intensity output to a sensor to zero azimuthal angles (Kim and Lee, 1989) or a further treatment of the intensity field is required (Stamnes et al., 1988).

In a few occasions, a higher dimensionality (three-dimensional) discrete-ordinates model has been used to solve lower dimensionality (one- or two-dimensional) problems by (1) modifying the aspect ratio of the numerical domain to imply infinite length(s), (2) modeling the boundaries in the infinite direction(s) as specular boundaries, or (3) assuming the boundary conditions in the infinite direction(s) periodic. This classical approach is not practical in optically thick problems where a very large number of control volumes, and, therefore, computer resources, would be required. Because of this and other disadvantages of the classical methodology (ray and end effects), the mirror technique (periodic or symmetric boundaries) was introduced by Sánchez et al. (1991).

After each iteration for the control volume intensity, the discrete-ordinates method gives the intensity field. A mirror technique can be applied to the direction (two-dimensional) or directions (one-dimensional) of infinite length making the boundaries in these directions behave as periodic boundaries. Thus, the intensities leaving a surface on the boundary are placed as intensities arriving at the opposite boundary for the next iteration for the infinite direction(s). In the mirror technique, the aspect ratio is irrelevant and no special consideration about the side walls is needed. Although the mirror approach is a step in the right direction, its slow rate of convergence reduces its practical applicability.

The two approaches (classical and mirror) to the lesser dimensionality problem fail to recognize the simple solution offered by the discrete-ordinates formulation. The verification of a simple procedure (shortcut approach) that uses the same

[1]Professor, Escuela de Ingeniería Mecánica, Universidad de los Andes, Mérida, Venezuela.

[2]Professor, Department of Mechanical Engineering, The University of Iowa, Iowa City, IA 52242; Mem ASME.

[3]Associate Professor, Department of Civil and Environmental Engineering, Iowa Institute of Hydraulic Research, The University of Iowa, Iowa City, IA 52242.

Contributed by the Heat Transfer Division and based on a paper presented at the National Heat Transfer Conference, San Diego, California, August 9–12, 1992. Manuscript received by the Heat Transfer Division May 1992; revision received March 1993. Keywords: Numerical Methods, Radiation. Associate Technical Editor: W. A. Fiveland.

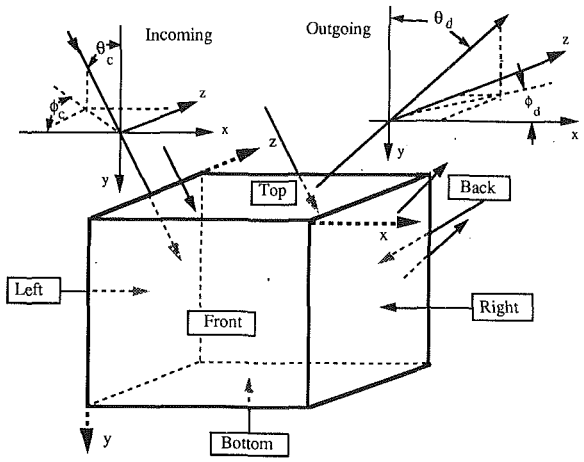

Fig. 1 General three-dimensional geometry

three-dimensional code, with the same quadrature set and without modifications, for the solution of one- and two-dimensional problems is the objective of this study. This approach allows the comparisons and parameterizations of predictions obtained using different dimensionalities in the solution of a given problem to be free from the influences of different quadratures or solution procedures.

Analysis

The three-dimensional system is shown in Fig. 1. The media, which can absorb, emit, and scatter radiation, is contained in a parallelepiped whose walls can be, in any combination, opaque or transparent. The direction of incidence of the parallel beam as well as the direction of the sensed intensity are arbitrary for both polar an azimuthal angles. The present formulation for the discrete-ordinates method is based on that of Sánchez et al. (1992) and Haferman et al. (1993). The three-dimensional geometry is discretized spatially into a number of control volumes, each with uniform properties. Of particular interest in this study is the expression for the radiant intensity for a control volume. In terms of the reference intensities, the intensity for control volume P in discrete direction i is given by

$$I_i^P = \frac{\frac{\mu_i}{\Delta x} I_i^{xr} + \frac{\delta_i}{\Delta y} I_i^{yr} + \frac{\gamma_1}{\Delta z} I_i^{zr} + \alpha S}{\frac{\mu_i}{\Delta x} + \frac{\delta_i}{\Delta y} + \frac{\gamma_1}{\Delta z} + \alpha\beta} \tag{1}$$

Note that the dimensionality of the problem is controlled by the presence of the direction cosines. For example, if $\mu = \delta = 0$, then a one-dimensional problem in the z direction is under study. Expressions for the reference intensities, the radiant source term, and the radiative flux are available (Sánchez et al., 1992; Haferman et al., 1993). The finite-difference weighting factor α is taken as unity.

The shortcut approach to simulate lower dimensionalities is implemented as follows:

1 A quadrature set is selected (three-dimensional). For the results that follow, the level sequential-odd quadrature (Fiveland, 1991) is used.

2 The scattering phase function is calculated for all pairs of directions (including, if present, beam and sensor). Using the quadrature set, the cosine of the angle between all pairs of discrete directions is found. The phase function is calculated from the scattering for a single sphere, and the integrated phase function for polydispersions is evaluated from standard formulas. The phase function is expressed in terms of Legendre polynomials and is renormalized. The phase function values preserve the implicit three-dimensional information due to beam and/or sensor.

3 The direction cosines in the direction (two-dimensional) or directions (one-dimensional) of infinite length are set to zero.

4 The resulting system of governing equations is solved as usual.

The shortcut approach is incorporated into a three-dimensional discrete-ordinates code, called ANDISORD4 (Sánchez et al., 1992) and allows solution of one-, two-, or three-dimensional geometries independently of the boundary conditions and presence or not of collimated sources and/or sensors.

Table 1 Heat flux for receiving wall

a. Average values		
Siegel and Howell (1981)	30417.00	W/m^2
Fiveland and Jamaluddin (1991)	29991.00	W/m^2
ANDISORD4 (Classical approach)	29991.75	W/m^2
b. Center values		
Fiveland and Jamaluddin (1991)	>31000.00	W/m^2
ANDISORD4 (Classical approach)	30483.38	W/m^2
ANDISORD4 (Mirror approach))	30576.84	W/m^2
ANDISORD4 (Shortcut approach)	30572.24	W/m^2

Results and Discussion

Test 1. Siegel and Howel (1981) and Fiveland and Jamaluddin (1991) predicted radiative transfer between two parallel, nongray plates spaced 2.54 cm apart in the y direction of Fig. 1. The hot and cold plates are maintained at 1111 K and 556 K. Pure CO_2 at a pressure of 1.013 MPa and a temperature of 556 K is between the plates. Spectral wall emittances and gas absorption coefficients are taken from Fiveland and Jamaluddin (1991). Three different approaches to the numerical solution of this one-dimensional problem using ANDISORD4 are presented.

Classical Approach. Siegel and Howell (1981) used analytical approaches to solve the one-dimensional problem and reported the heat flux on the receiving (cold) wall given in Table 1(*a*). Fiveland and Jamaluddin (1991) used a three-dimensional enclosure with $4 \times 4 \times 4$ control volumes and with an aspect ratio of 24:1:24 ($L_x/L_y = 24$, and $L_z/L_y = 24$). The end walls are cold, diffusely reflecting surfaces (with an emittance of 0.0001). Fiveland and Jamaluddin (1991) suggested, based on the average heat fluxes presented in Table 1(*a*), that their modeling of the one-dimensional geometry by means of the three-dimensional code was correct and that the nonuniform profiles shown in Fig. 2 are a consequence of end effects, which could be improved by increasing L_x/L_y and L_z/L_y. Using the same approach, ANDISORD4 is applied to $5 \times 5 \times 5$ control volumes with average and local heat fluxes reported in Table 1(*a*) and Fig. 2. Note that the results for these coarse grids may not be grid independent.

Modeling the side walls as diffusely reflecting walls (producing the results shown in Fig. 2 and Table 1*a*) should produce averaged heat fluxes on the receiving wall that are smaller than those for the parallel plate geometry. The reason is that part of the energy from the hot wall reaching the side walls (which in the one-dimensional geometry would arrive at the cold wall) is redirected back to the hot wall, resulting in a net decrease in the total energy arriving at the receiving wall. The average heat fluxes, therefore, do not provide enough information about the accuracy of the modeling.

When a one-dimensional geometry is modeled by a three-dimensional model with a large aspect ratio (classical approach), the local heat flux at the center should be the closest

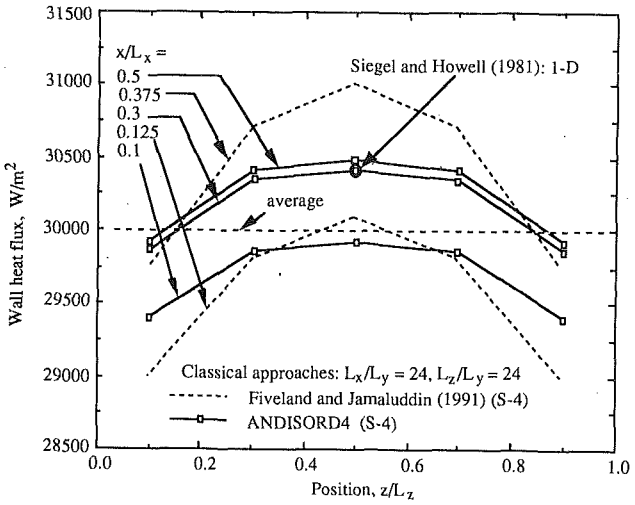

Fig. 2 Local wall heat fluxes to receiving wall

indication of the heat flux for the one-dimensional geometry. At this central location, end effects are minimized. Table 1(*b*) presents the heat flux at the central location of the receiving surface as predicted by Fiveland and Jamaluddin (1991) and ANDISORD4. Fiveland and Jamaluddin (1991) overestimate the heat flux reported by Siegel and Howell (1981). Good agreement between the result from ANDISORD4 and that of Siegel and Howell (1981) is shown.

Mirror Approach. When the mirror technique is used, ANDISORD4 produces a uniform heat flux of value shown in Table 1(*b*). The heat flux does not change when the aspect ratio is varied from 1:1:1 to 24:1:24. The heat flux indicates that ANDISORD4 overpredicts the heat flux of Siegel and Howell (1981) by less than 1 percent.

Shortcut Approach. For one-dimensional modeling using the shortcut approach, the results presented in Table 1(*b*) are obtained. The error (compared to that of Siegel and Howell, 1981) in the heat flux is less than 1 percent and the heat flux profiles are uniform.

Remarks. From the preceding discussion, it can be concluded that:

1 When the one-dimensional geometry is modeled with the classical approach, the local heat flux at the center of the receiving plate evaluated with ANDISORD4 correctly estimates the averaged heat flux.

2 Most of the energy transfer takes place in the transparent bands. Siegel and Howell (1981) report 97.46 percent of the total heat exchange as taking place in these bands. Computations using ANDISORD4 yielded a value of 97.59 percent. Discrete-ordinate codes are known to have difficulties in situations involving transparent media. These difficulties, known as ray effects, are mainly due to numerical diffusion as a consequence of coarse directional discretization for the problem and become important in two-dimensional and three-dimensional geometries (Gerstl and Zardecki, 1985; Sánchez and Smith, 1992). The applicability of the classical approach in situations involving large optical thickness is thus questionable.

3 The shortcut approach is numerically more efficient than the mirror method. On a personal computer, the shortcut approach needed 125 s while the mirror technique needed 916 s to solve the same problem. This numerical efficiency and accuracy and the fact that no modification of the original code is required make the shortcut approach superior to the classical and mirror approaches.

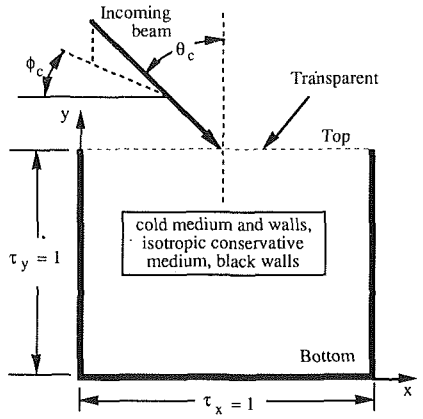

Fig. 3 Geometry for Test 2

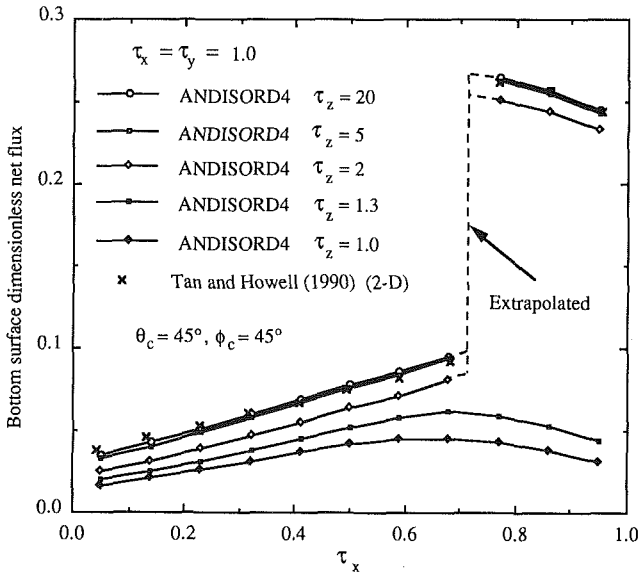

Fig. 4 Classical approach: bottom heat fluxes at $z = L_z/2$

Test 2. The geometry for Test 2 is shown in Fig. 3. The medium is cold, gray, and contained in a parallelepiped with a transparent top wall; the other enclosure walls are cold, opaque, and black. The length of the domain in the z direction is infinite. Scattering is isotropic and conservative.

Classical Approach. Starting with a cubical enclosure of unit optical thickness ($\tau_x = \tau_y = \tau_z = 1$), the optical thickness in the z direction is increased in ANDISORD4 to approach at $\tau_z/2$ the two-dimensional of Tan and Howell (1990). Results for five different values of τ_z are presented in Fig. 4, where the dimensionless heat fluxes are defined as the net fluxes divided by the heat flux at the top wall due to the parallel beam. For $\tau_z = 1.0$ and 1.3, the entire bottom surface is in a shadow. The two-dimensional results, including shadowing effects, are essentially represented by those for $\tau_z = 5$.

Mirror and Shortcut Approaches. Figure 5 shows results obtained when either the mirror or the shortcut approaches are applied. The results obtained for both approaches show excellent agreement with those from Tan and Howell (1990). The shadowing effects are also represented.

Remarks. The classical approach, applied to $11 \times 11 \times 11$ control volumes and with $\tau_z = 20$, required a wall clock time of 780 s to solve the problem. The mirror and shortcut ap-

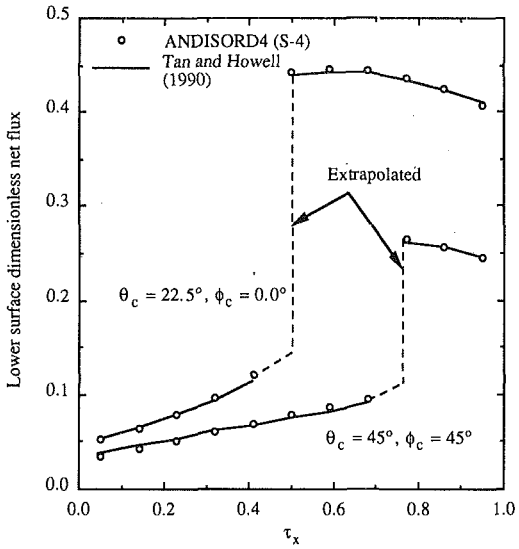

Fig. 5 Mirror or shortcut approach for Test 2

proaches used $11 \times 11 \times 1$ control volumes and 308 and 70 s, respectively, to achieve the same results.

Conclusions

The capability of a three-dimensional radiative transfer model based on the discrete-ordinates method to accommodate lower order dimensionality by setting to zero, after the evaluation of the scattering phase function, the direction cosine(s) corresponding to the infinite length(s) of the domain is verified. The shortcut approach to the lesser dimensionality issue is tested and compared to the classical and mirror approaches. From the examples presented, the shortcut approach allows for the solution of one-dimensional, two-dimensional, and three-dimensional problems by means of a single computer algorithm. Of particular importance is the fact that in all three dimensionalities, parallel beam and detectors can be included without any alteration of the code.

When compared with the classical and mirror approaches, the shortcut approach is noticeably faster and less memory demanding. In optically thick applications, if a three-dimensional procedure is employed, the shorcut approach is the only viable alternative to the lesser dimensionality problem. End effects, which can be important in the classical approach, are not a concern in either the mirror or the shortcut approaches.

Acknowledgments

This study was partially supported by grant No. NA89AA-D-AC195 from the National Oceanic and Atmospheric Administration: Global Change Program. The first author would also like to acknowledge the financial support received from Universidad de los Andes and Fundación Gran Mariscal de Ayacucho, both from the Republic of Venezuela.

References

Carlson, B. G., and Lathrop, K. D., 1968, "Transport Theory, The Method of Discrete-Ordinates," *Computing Methods in Reactor Physics*, H. Greenspan, C. N. Kelber, and D. Okrent, eds., Gordon and Breach, New York, pp. 171–266.

Fiveland, W. A., 1991, "The Selection of Discrete Ordinate Quadrature Sets for Anisotropic Scattering," *Fundamentals of Radiation Heat Transfer*, W. A. Fiveland, A. L. Crosbie, A. M. Smith, and T. F. Smith, eds., ASME HTD-Vol. 160, pp. 89–96.

Fiveland, W. A., and Jamaluddin, A. S., 1991, "Three Dimensional Spectral Radiative Heat Transfer Solutions by the Discrete-Ordinates Method," *J. Thermophysics and Heat Transfer*, Vol. 5, No. 3, pp. 335–339.

Gerstl, S. A. W., and Zardecki, A., 1985, "Discrete-Ordinates Finite-Element Method for Atmospheric Radiative Transfer and Remote Sensing," *Applied Optics*, Vol. 24, No. 1, pp. 81–93.

Haferman, J. L., Krajewski, W. F., Smith, T. F., and Sánchez, A., 1993, "Radiative Transfer for a Three-Dimensional Raining Cloud," *Applied Optics*, Vol. 32, No. 15, pp. 2795–2802.

Kim, T. K., and Lee, H. S., 1989, "Radiative Transfer in Two-Dimensional Anisotropic Scattering Media With Collimated Incidence," *J. Quant. Spectrosc. Radiat. Transfer*, Vol. 42, No. 3, pp. 225–238.

Kim, T. K., and Lee, H. S., 1990, "Modified δ-M Scalling Results for Mie-Anisotropic Scattering Media," ASME JOURNAL OF HEAT TRANSFER, Vol. 112, pp. 988–994.

Sánchez, A., Smith, T. F., and Krajewski, W. F., 1991, "Three-Dimensional Radiative Heat Transfer in a Polydispersion With Collimated Incident Source," *Fundamentals of Radiation Heat Transfer*, W. A. Fiveland, A. L. Crosbie, A. M. Smith, and T. F. Smith, eds., ASME HTD-Vol. 160, pp. 27–36.

Sánchez, A., and Smith, T. F., 1992, "Surface Radiant Exchange for Two-Dimensional Rectangular Enclosures Using the Discrete-Ordinates Method," ASME JOURNAL OF HEAT TRANSFER, Vol. 114, pp. 465–472.

Sánchez, A., Krajewski, W. F., and Smith, T. F., 1992, "A General Purpose Radiative Transfer Model for Application to Remote Sensing in Multi-dimensional Systems," IIHR Report No. 355, Iowa Institute of Hydraulic Research, The University of Iowa, Iowa City, IA.

Siegel, R., and Howell, J. R., 1981, *Thermal Radiation Heat Transfer*, Hemisphere Publishing Corporation, Washington, DC.

Stamnes, K., Tsay, S.-C., Wiscombe, W., and Jayaweera, K., 1988, "Numerically Stable Algorithm for the Discrete-Ordinate-Method Radiative Transfer in Multiple Scattering and Emitting Layered Media," *Applied Optics*, Vol. 27, No. 12, pp. 2502–2509.

Tan, Z., and Howell, J. R., 1990, "Two-Dimensional Radiative Heat Transfer in an Absorbing, Emitting, and Linearly Anisotropic Scattering Medium Exposed to a Collimated Source," *Radiation Heat Transfer: Fundamentals and Applications*, T. F. Smith, M. F., Modest, A. M. Smith, and S. T. Thynell, eds., ASME HTD-Vol. 137, pp. 101–116.

Improved Treatment of Scattering Using the Discrete Ordinates Method

J. C. Chai,[1] H. S. Lee,[2] and S. V. Patankar[1]

Introduction

The purposes of this study are to present an improved treatment for the equation of radiative transfer and to propose a modified-exponential scheme for the discrete ordinates method.

Presently available literature on the solution of radiation heat transfer problems using the discrete ordinates method treats the source function as a *constant* within each control volume (Fiveland, 1984, 1987, 1988; Truelove, 1987; Tsai and Özişik, 1990; Jamaluddin and Smith, 1988a, 1988b, 1992; Kim and Lee, 1988). It is well known that this constant source function treatment requires excessive source term iterations (Lewis and Miller, 1984). This is particularly noticeable in situations with large scattering albedos, large optical depths, and highly forward scattering phase functions and is one of the major shortcomings of the discrete ordinates method.

In this study, the source-term linearization treatment of Patankar (1980) is used. Unlike currently available acceleration schemes, this treatment reduces the number of iterations needed to obtain a converged solution without solving an additional set of equations. This source-term linearization treatment also results in the proposal of a modified-exponential scheme. This scheme is superior to the exponential scheme of Carlson and

[1]Department of Mechanical Engineering, University of Minnesota, Minneapolis, MN 55455.

[2]NASA Lewis Research Center, Cleveland, OH 44135.

Contributed by the Heat Transfer Division and presented at the ASME Winter Annual Meeting, Anaheim, California, November 8–13, 1992. Manuscript received by the Heat Transfer Division July 1992; revision received May 1993. Keywords: Radiation. Associate Technical Editor: W. A. Fiveland.

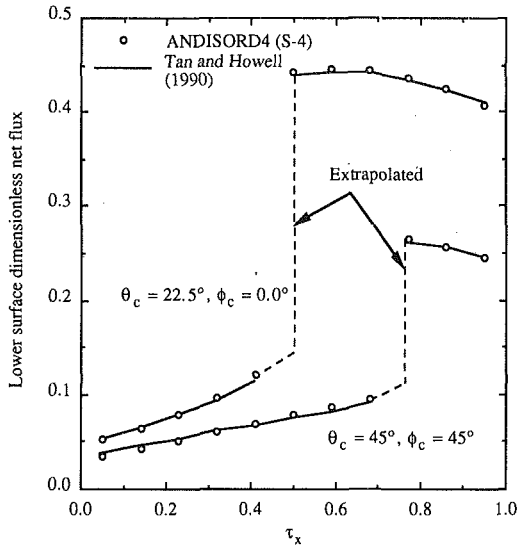

Fig. 5 Mirror or shortcut approach for Test 2

proaches used $11 \times 11 \times 1$ control volumes and 308 and 70 s, respectively, to achieve the same results.

Conclusions

The capability of a three-dimensional radiative transfer model based on the discrete-ordinates method to accommodate lower order dimensionality by setting to zero, after the evaluation of the scattering phase function, the direction cosine(s) corresponding to the infinite length(s) of the domain is verified. The shortcut approach to the lesser dimensionality issue is tested and compared to the classical and mirror approaches. From the examples presented, the shortcut approach allows for the solution of one-dimensional, two-dimensional, and three-dimensional problems by means of a single computer algorithm. Of particular importance is the fact that in all three dimensionalities, parallel beam and detectors can be included without any alteration of the code.

When compared with the classical and mirror approaches, the shortcut approach is noticeably faster and less memory demanding. In optically thick applications, if a three-dimensional procedure is employed, the shorcut approach is the only viable alternative to the lesser dimensionality problem. End effects, which can be important in the classical approach, are not a concern in either the mirror or the shortcut approaches.

Acknowledgments

This study was partially supported by grant No. NA89AA-D-AC195 from the National Oceanic and Atmospheric Administration: Global Change Program. The first author would also like to acknowledge the financial support received from Universidad de los Andes and Fundación Gran Mariscal de Ayacucho, both from the Republic of Venezuela.

References

Carlson, B. G., and Lathrop, K. D., 1968, "Transport Theory, The Method of Discrete-Ordinates," *Computing Methods in Reactor Physics*, H. Greenspan, C. N. Kelber, and D. Okrent, eds., Gordon and Breach, New York, pp. 171–266.

Fiveland, W. A., 1991, "The Selection of Discrete Ordinate Quadrature Sets for Anisotropic Scattering," *Fundamentals of Radiation Heat Transfer*, W. A. Fiveland, A. L. Crosbie, A. M. Smith, and T. F. Smith, eds., ASME HTD-Vol. 160, pp. 89–96.

Fiveland, W. A., and Jamaluddin, A. S., 1991, "Three Dimensional Spectral Radiative Heat Transfer Solutions by the Discrete-Ordinates Method," *J. Thermophysics and Heat Transfer*, Vol. 5, No. 3, pp. 335–339.

Gerstl, S. A. W., and Zardecki, A., 1985, "Discrete-Ordinates Finite-Element Method for Atmospheric Radiative Transfer and Remote Sensing," *Applied Optics*, Vol. 24, No. 1, pp. 81–93.

Haferman, J. L., Krajewski, W. F., Smith, T. F., and Sánchez, A., 1993, "Radiative Transfer for a Three-Dimensional Raining Cloud," *Applied Optics*, Vol. 32, No. 15, pp. 2795–2802.

Kim, T. K., and Lee, H. S., 1989, "Radiative Transfer in Two-Dimensional Anisotropic Scattering Media With Collimated Incidence," *J. Quant. Spectrosc. Radiat. Transfer*, Vol. 42, No. 3, pp. 225–238.

Kim, T. K., and Lee, H. S., 1990, "Modified δ-M Scalling Results for Mie-Anisotropic Scattering Media," ASME JOURNAL OF HEAT TRANSFER, Vol. 112, pp. 988–994.

Sánchez, A., Smith, T. F., and Krajewski, W. F., 1991, "Three-Dimensional Radiative Heat Transfer in a Polydispersion With Collimated Incident Source," *Fundamentals of Radiation Heat Transfer*, W. A. Fiveland, A. L. Crosbie, A. M. Smith, and T. F. Smith, eds., ASME HTD-Vol. 160, pp. 27–36.

Sánchez, A., and Smith, T. F., 1992, "Surface Radiant Exchange for Two-Dimensional Rectangular Enclosures Using the Discrete-Ordinates Method," ASME JOURNAL OF HEAT TRANSFER, Vol. 114, pp. 465–472.

Sánchez, A., Krajewski, W. F., and Smith, T. F., 1992, "A General Purpose Radiative Transfer Model for Application to Remote Sensing in Multi-dimensional Systems," IIHR Report No. 355, Iowa Institute of Hydraulic Research, The University of Iowa, Iowa City, IA.

Siegel, R., and Howell, J. R., 1981, *Thermal Radiation Heat Transfer*, Hemisphere Publishing Corporation, Washington, DC.

Stamnes, K., Tsay, S.-C., Wiscombe, W., and Jayaweera, K., 1988, "Numerically Stable Algorithm for the Discrete-Ordinate-Method Radiative Transfer in Multiple Scattering and Emitting Layered Media," *Applied Optics*, Vol. 27, No. 12, pp. 2502–2509.

Tan, Z., and Howell, J. R., 1990, "Two-Dimensional Radiative Heat Transfer in an Absorbing, Emitting, and Linearly Anisotropic Scattering Medium Exposed to a Collimated Source," *Radiation Heat Transfer: Fundamentals and Applications*, T. F. Smith, M. F., Modest, A. M. Smith, and S. T. Thynell, eds., ASME HTD-Vol. 137, pp. 101–116.

Improved Treatment of Scattering Using the Discrete Ordinates Method

J. C. Chai,[1] H. S. Lee,[2] and S. V. Patankar[1]

Introduction

The purposes of this study are to present an improved treatment for the equation of radiative transfer and to propose a modified-exponential scheme for the discrete ordinates method.

Presently available literature on the solution of radiation heat transfer problems using the discrete ordinates method treats the source function as a *constant* within each control volume (Fiveland, 1984, 1987, 1988; Truelove, 1987; Tsai and Özişik, 1990; Jamaluddin and Smith, 1988a, 1988b, 1992; Kim and Lee, 1988). It is well known that this constant source function treatment requires excessive source term iterations (Lewis and Miller, 1984). This is particularly noticeable in situations with large scattering albedos, large optical depths, and highly forward scattering phase functions and is one of the major shortcomings of the discrete ordinates method.

In this study, the source-term linearization treatment of Patankar (1980) is used. Unlike currently available acceleration schemes, this treatment reduces the number of iterations needed to obtain a converged solution without solving an additional set of equations. This source-term linearization treatment also results in the proposal of a modified-exponential scheme. This scheme is superior to the exponential scheme of Carlson and

[1]Department of Mechanical Engineering, University of Minnesota, Minneapolis, MN 55455.

[2]NASA Lewis Research Center, Cleveland, OH 44135.

Contributed by the Heat Transfer Division and presented at the ASME Winter Annual Meeting, Anaheim, California, November 8–13, 1992. Manuscript received by the Heat Transfer Division July 1992; revision received May 1993. Keywords: Radiation. Associate Technical Editor: W. A. Fiveland.

Lathrop (1968) for scattering media problems. The modified-exponential scheme reduces to the exponential scheme in non-scattering media.

Mathematical Formulation

Source-Term Linearization Treatment. The radiative transfer equation for an absorbing, emitting, and scattering gray medium can be discretized angularly, using the discrete ordinates method described in Chandrasekhar (1960), as

$$\frac{dI^l}{ds^l} = -\beta I^l + S^l \tag{1}$$

where I^l is the intensity in any direction l and position s, and β is the extinction coefficient. The source function S^l is

$$S^l \equiv \kappa I_b + \frac{\sigma}{4\pi} \sum_{l'=1}^{L} \Phi^{l'l} I^{l'} w^{l'} \tag{2}$$

where κ is the absorption coefficient, I_b is the blackbody intensity, σ is the scattering coefficient, and Φ is the scattering phase function. The superscript l represents the direction of interest, while l' represents the in-scattering from all possible directions including the direction of interest, l. The summation is performed over all chosen ordinates, L, using the angular weights, w.

Using the source-term linearization treatment of Patankar (1980), a *linearized* equation of transfer for the discrete ordinates method is obtained as

$$\frac{dI^l}{ds^l} = -\beta^l_m I^l + S^l_m \tag{3}$$

where the modified extinction coefficient, β^l_m, and the modified source function, S^l_m, are

$$\beta^l_m \equiv \beta - \frac{\sigma}{4\pi} \Phi^{ll} w^l \tag{4}$$

$$S^l_m \equiv \kappa I_b + \frac{\sigma}{4\pi} \sum_{l'=1, l' \neq l}^{L} \Phi^{l'l} I^{l'} w^{l'} \tag{5}$$

In scattering media, two immediate observations can be drawn from Eqs. (3)–(5). First, the modified source function, S^l_m, no longer contains the intensity of interest, I^l. This reduces the magnitude of the source function. Since the source function is obtained using values from the previous iteration, this treatment reduces the dependence of the present iteration on the previous iteration. Second, the modification of the extinction coefficient also scales the optical thickness of a problem and results in a reduced effective optical thickness.

Carlson and Lathrop (1968) presented a similar treatment for a solution of one-dimensional diffusion-approximation equations to the final discretized form of the equation of neutron transport. They subtracted the in-group flux terms in order to avoid in-group iterations. Unfortunately, they cannot easily subtract the forward scattering component as is done here, since the traditional discrete ordinates formulation expands the scattering source term into a series sum of Legendre-moments of intensity. In order to apply the current treatment, the primary form of the discretized phase function must be used as shown in Eq. (2).

Equation (3) is discretized according to the discrete ordinates procedure, and the resulting final discretization equations for a typical two-dimensional Cartesian control volume is presented below. To facilitate further discussion, the final discretization equations for the conventional treatment of the source function is also reproduced. For the $\mu^l > 0$ and $\xi^l > 0$ directions, the discretized equations are

Linearized Equation

$$I^l_P = \frac{\mu^l f^l_y \Delta y_P I^l_w + \xi^l f^l_x \Delta x_P I^l_s + (S^l_m)_P f^l_x f^l_y \Delta x_P \Delta y_P}{\mu^l f^l_y \Delta y_P + \xi^l f^l_x \Delta x_P + (\beta^l_m)_P f^l_x f^l_y \Delta x_P \Delta y_P} \tag{6}$$

Conventional Equation

$$I^l_P = \frac{\mu^l f^l_y \Delta y_P I^l_w + \xi^l f^l_x \Delta x_P I^l_s + S^l_P f^l_x f^l_y \Delta x_P \Delta y_P}{\mu^l f^l_y \Delta y_P + \xi^l f^l_x \Delta x_P + \beta_P f^l_x f^l_y \Delta x_P \Delta y_P} \tag{7}$$

In the above discretization equations, the subscript P refers to the control volume P, while n, s, e and w stand for the north, south, east, and west boundaries of the control volume P, respectively. In the formulation of the final discretization equations, the downstream intensities, I^l_n, and I^l_e were related to the upstream intensities I^l_P, I^l_w and I^l_s through the following *definitions*:

$$I^l_P \equiv f^l_y I^l_n + (1 - f^l_y) I^l_s \equiv f^l_x I^l_e + (1 - f^l_x) I^l_w \tag{8}$$

where f^l_x and f^l_y are the spatial weighting factors appropriate for a chosen differencing scheme.

Before proceeding further, a demonstration of what has been achieved with Eq. (6) is given. Consider the radiative heat transfer in a pure scattering medium with constant scattering coefficient, bounded by black walls. The phase function is assumed to be zero everywhere, except for the in-scattering in the direction of interest:

$$\Phi^{l'l} = \begin{cases} \Phi^{ll} & l' = l \\ 0 & l' \neq l. \end{cases} \tag{9}$$

For this sample problem with $f^l_x = f^l_y$ and $\Delta y_P = \Delta x_P$, Eq. (7) (conventional method) becomes

$$I^l_P = \frac{\mu^l I^l_w + \xi^l I^l_s + \frac{\sigma}{4\pi} \Phi^{ll} w^l f^l_y \Delta y_P I^{l*}_P}{\mu^l + \xi^l + \sigma f^l_y \Delta y_P} \tag{10}$$

while Eq. (6) (improved method) becomes

$$I^l_P = \frac{\mu^l I^l_w + \xi^l I^l_s}{\mu^l + \xi^l + \left(\sigma - \frac{\sigma}{4\pi} \Phi^{ll} w^l\right) f^l_y \Delta y_P} \tag{11}$$

Clearly, the improved method given by Eq. (11) will converge in *one* cycle. The conventional method will require a few cycles before a converged solution can be obtained, because it contains I^{l*}_P (the I^l_P from the previous iteration) on the right-hand side of Eq. (10). The improved method is also expected to converge faster than the conventional method, even for situations with nonblack walls and general phase functions. The improved method reduces to the conventional method for non-scattering media.

Modified-Exponential Scheme. Carlson and Lathrop (1968) presented an exponential scheme for assigning the spatial weights in Eq. (8). Their original scheme is based on the assumption of a *constant* source function S^l in Eq. (1) despite its dependence on I^l.

An improved spatial differencing scheme called the *modified-exponential scheme* is proposed. This scheme uses the *linearized* equation of transfer (Eq. 3). Since Eqs. (1) and (3) have the same form, the resulting weighting factors also have the same form. The *argument*, for the *modified*-exponential scheme, however, is based on a *modified* cell optical thickness, τ^l_m. The weighting factor for this scheme is

$$f^l = [1 - \exp(-\tau^l_m)]^{-1} - (\tau^l_m)^{-1} \tag{12}$$

where

$$\tau^l_m = \beta^l_m \Delta x / \mu^l \tag{13}$$

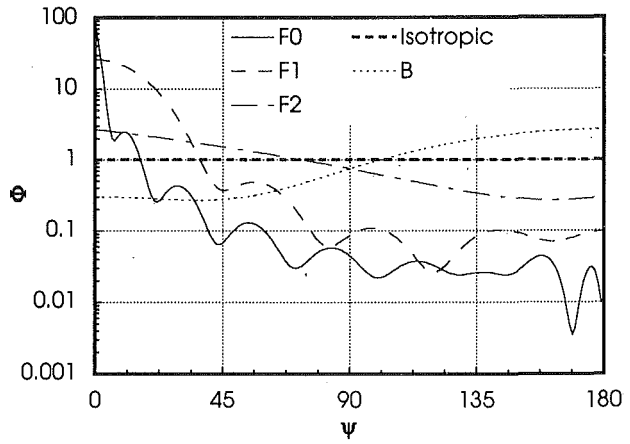

Fig. 1 Scattering phase functions

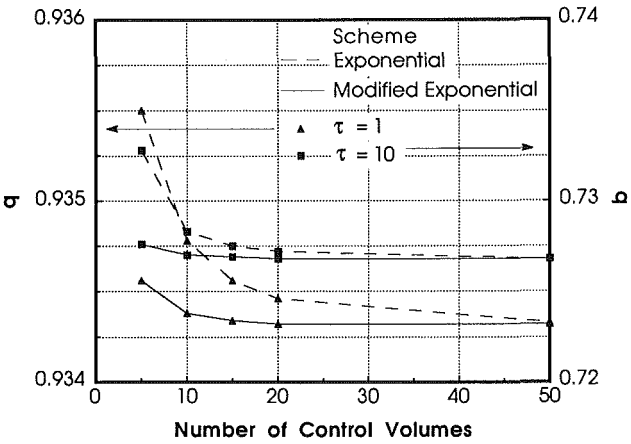

Fig. 2 Comparison of the spatial differencing schemes

The modified-exponential scheme reduces to the exponential scheme for nonscattering media. The present scheme is not much more expensive to compute than the exponential scheme. This is because all the in-scattering terms have to be computed for the final solution even when the exponential scheme is used.

Results

Three forward, one backward, and the isotropic scattering phase function are used to present the results. Figure 1 shows the variation of Φ with the scattering angle, ψ (Kim and Lee, 1988). Magnitude of the forward-scattering ($\psi = 0$ deg) for a given phase function corresponds to Φ'' and is part of the subtracted term in the *linearized* equation of transfer (Eqs. (3)–(5)).

Comparison of the Modified-Exponential and Exponential Spatial Differencing Schemes. Although it is possible to apply the modified-exponential scheme to Eqs. (6), (7), and (8), Chai et al. (1993) have shown that any scheme with $f \neq 1$ might produce physically unrealistic solutions in a *multi-dimensional* problem. A one-dimensional problem is therefore chosen to evaluate the modified-exponential scheme. This test problem consists of a pure-scattering ($\omega = \sigma/\beta = 1.0$), one-dimensional planar medium bounded by two black walls. For this chosen condition, the net flux is a constant at all locations and is evaluated from

$$q = \int_{\mu>0} I\mu d\mu + \int_{\mu<0} I\mu d\mu \qquad (14)$$

Figure 2 shows the net heat flux obtained using a S_6 level-symmetric quadrature set for $\tau = \beta D = 1$ and 10 with the phase function $F0$ (D = distance between the plates). The results obtained using 50 control volumes are the grid-independent results for the specified conditions.

Table 1 Number of iterations for four phase functions

$\tau =$	B	Isotropic	F2	F1
βD	Conv./Imp.	Conv./Imp.	Conv./Imp.	Conv./Imp.
1	13 / 12	13 / 12	14 / 12	17 / 7
2	19 / 18	19 / 18	20 / 16	24 / 9
3	25 / 24	26 / 23	26 / 19	30 / 10
4	31 / 29	32 / 29	31 / 23	35 / 10
5	37 / 34	37 / 33	36 / 26	40 / 11
6	41 / 39	42 / 38	41 / 29	45 / 12
7	46 / 43	47 / 42	46 / 32	49 / 12
8	50 / 46	51 / 46	51 / 35	53 / 13
9	53 / 50	55 / 49	55 / 38	57 / 13
10	57 / 53	59 / 52	59 / 40	61 / 14

Table 2 Number of iterations for three quadrature sets

$\tau =$	S_4	S_6	S_{12}
βD	Conv./Imp.	Conv./Imp.	Conv./Imp.
1	17 / 7	17 / 9	18 / 12
2	24 / 9	24 / 12	24 / 16
3	30 / 10	29 / 13	29 / 20
4	35 / 10	34 / 15	34 / 23
5	40 / 11	39 / 17	39 / 26
6	45 / 12	44 / 18	44 / 29
7	49 / 12	48 / 19	48 / 32
8	53 / 13	52 / 21	53 / 35
9	57 / 13	56 / 22	57 / 37
10	61 / 14	59 / 23	61 / 40

Both spatial differencing schemes converge to the same results, but the modified-exponential scheme reaches the grid-independent solutions with fewer control volumes. The exponential scheme requires anywhere between three and four times the number of control volumes to attain the accuracy of the improved scheme. For example, the solution obtained using the present scheme with five control volumes is as accurate as the solution using the exponential scheme with 15 control volumes when $\tau = 10$.

Effects of the Improved Source-Term Treatment. A two-dimensional, black, square enclosure filled with a scattering medium of $\omega = 0.9$ is considered for illustration. Three walls and the medium are cold, while the remaining wall is hot. Computations were carried out using 20 uniform control volumes in the x and y directions. Level-symmetric quadrature sets of order S_4, S_6, and S_{12} are used for the results that follow. The step scheme ($f = 1.0$) is used in this test problem. Solutions are considered converged when

$$|I_P^l - I_P^*|/I_P^l \leq 10^{-6} \qquad (15)$$

Table 1 shows the number of iterations needed to obtain converged solutions for four phase functions (*B*, *Isotropic*, *F2*, and *F1*) using a level-symmetric S_4 quadrature set. The conventional treatment is indicated as *Conv* in the table, and the improved treatment is *Imp*. As expected, more iterations are needed as the optical thickness increases. The number of iterations needed by the conventional treatment also increases as the phase function becomes more forward biased (see Fig. 1). On the contrary, when the improved treatment is used, the number of iterations is *reduced* as the phase function becomes more forward-peaked. In the limit of a completely forward-peaked phase function of Eq. (9), Eq. (11) shows that only *one* iteration would be needed. The savings with the improved treatment increase as the phase function becomes more forward biased.

Table 2 presents the number of iterations needed for convergence for phase function $F1$ and three quadrature sets. It can be seen that there is considerable savings with the improved (*Imp*) treatment over the conventional (*Conv*) treatment. For $\tau = 10$, the savings are 77, 61, and 34 percent for the S_4, S_6, and S_{12} approximations, respectively. Although the forward scattering component of the phase function in a given direction, Φ^{ll}, has the same magnitude for all orders, the weight, w^l, decreases as the order increases. This leads to a decrease in the product $\Phi^{ll} w^l$ and accounts for the decreases in percentage savings with increase in S_n order.

Concluding Remarks

The following conclusions are drawn from this study.

1 The modified-exponential spatial differencing scheme reduces to the exponential scheme in nonscattering media. In scattering media, it converges to the grid-independent solution with fewer grid points than the exponential scheme.

2 The improved source-term linearization treatment gives the *same* exact solution as the conventional iteration treatment.

3 The improved iteration treatment reduces to the conventional treatment in nonscattering media. In scattering media, the improved iteration method reduces the required number of iterations to obtain a converged solution. It is very effective in strongly scattering media and for large optical thicknesses.

Acknowledgments

This work was supported in part by NASA Lewis Research Center under Cooperative Agreement No. NCC3-238. The first author wishes to thank Mr. Slah Jendoubi for his discussions on the discrete ordinates method. A grant from the Minnesota Supercomputer Institute is also gratefully acknowledged.

References

Carlson, B. G., and Lathrop, K. D., 1968, "Transport Theory—The Method of Discrete-Ordinates," in: *Computing Methods in Reactor Physics*, H. Greenspan, C. N. Kelber, and D. Okrent, eds., Gorden and Breach, New York.

Chai, J. C., Lee, H. S., and Patankar, S. V., 1993, "An Evaluation of Three Spatial Differencing Schemes for the Discrete Ordinates Method in Participating Media," presented at the 31st Aerospace Sciences Meeting & Exhibits, AIAA 93-0140; also accepted in the *Journal of Thermophysics and Heat Transfer* as "An Evaluation of Spatial Differencing Practices for the Discrete-Ordinates Method."

Chandrasekhar, S., 1960, *Radiative Transfer*, Dover Publications, Inc., New York.

Fiveland, W. A., 1984, "Discrete-Ordinates Solutions of the Radiative Transport Equation for Rectangular Enclosures," ASME JOURNAL OF HEAT TRANSFER, Vol. 106, pp. 699–706.

Fiveland, W. A., 1987, "Discrete-Ordinates Methods for Radiative Heat Transfer in Isotropically and Anisotropically Scattering Media," ASME JOURNAL OF HEAT TRANSFER, Vol. 109, pp. 809–812.

Fiveland, W. A., 1988, "Three Dimensional Radiative Heat Transfer Solutions by the Discrete Ordinates Method," *Journal of Thermophysics and Heat Transfer*, Vol. 2, pp. 309–316.

Jamaluddin, A. S., and Smith, P. J., 1988a, "Predicting Radiative Transfer in Rectangular Enclosures Using the Discrete Ordinates Method," *Combustion and Technology*, Vol. 59, pp. 321–340.

Jamaluddin, A. S., and Smith, P. J., 1988b, "Predicting Radiative Transfer in Axisymmetric Cylindrical Enclosures Using the Discrete Ordinates Method," *Combustion and Technology*, Vol. 62, pp. 173–186.

Jamaluddin, A. S., and Smith, P. J., 1992, "Discrete-Ordinates Solution of Radiative Transfer Equation in Nonaxisymmetric Cylindrical Enclosures," *Journal of Thermophysics and Heat Transfer*, Vol. 6, pp. 242–245.

Kim, T.-K., and Lee, H. S., 1988, "Effects of Anisotropic Scattering on Radiative Heat Transfer in Two-Dimensional Rectangular Enclosures," *International Journal of Heat and Mass Transfer*, Vol. 31, pp. 1711–1721.

Lewis, E. E., and Miller, W. F., Jr., 1984, *Computational Methods of Neutron Transport*, Wiley International Publication, New York.

Patankar, S. V., 1980, *Numerical Heat Transfer and Fluid Flow*, Hemisphere Publishing, New York.

Truelove, J. S., 1987, "Discrete-Ordinate Solutions of the Radiation Transport Equation," ASME JOURNAL OF HEAT TRANSFER, Vol. 109, pp. 1048–1051.

Tsai, J. R., and Özişik, M. N., 1990, "Radiation in Cylindrical Symmetry With Anisotropic Scattering and Variable Properties," *International Journal of Heat and Mass Transfer*, Vol. 33, pp. 2651–2658.

Surface Temperature Measurement Using a Laser-Induced Fluorescence Thermal Imaging System

M. K. Chyu[1] and D. J. Bizzak[1]

Introduction

Laser-induced fluorescence (LIF) was first employed as an advanced optical diagnostic technique in combustion research for species measurements (Dyer and Crosley, 1982) and later for flame temperature measurements (Cattolica and Stephenson, 1984). In one of the first efforts to use such a technique for surface temperature measurement, the fluorescence lifetime of an emission line of a rare-earth ion-doped phosphor (i.e., thermographic phosphor) was correlated to temperature (Cates et al., 1985). While this technique has been successfully employed to provide point temperature measurements in an operating turbine engine (Noel et al., 1991), it is not an amenable approach for two-dimensional imaging because the decay time of most phosphors is so rapid that it is not possible to obtain the images necessary to compute decay times. The feasibility of two-dimensional thermal imaging, however, was recognized using the technique of ratioing the fluorescence intensity of two distinct emission lines of a rare-earth ion-doped phosphor and correlating it to temperature. Using such an approach, Goss et al. (1989) measured the surface temperature of a combusting rocket propellant seeded with dysprosium-doped lanthanum fluoride ($LaF_3:Dy^{+3}$) phosphor. Temperatures over the range of 300 to 1500 K were measured with an accuracy of approximately $\pm 10 \sim 50$ K.

In the present study, an LIF thermal imaging system, capable of accurate (± 0.5°C), two-dimensional surface temperature measurement, has been developed and demonstrated for use in general heat transfer studies. This system exploits the temperature sensitivity of both the fluorescence intensity and lifetime of certain europium-doped lanthanum oxysulfide ($La_2O_2S:Eu^{+3}$) emission lines. From the room temperature emission spectrum (Chyu and Bizzak, 1993), the temperature-sensitive emissions that may be employed are the 512 nm triplet, active from approximately -70°C to 60°C, and the 538 nm doublet, which is useful for temperature measurements in the range of 100°C to 230°C (Fonger and Struck, 1969). In this study fluorescent images of the 512 nm triplet, along with that of the relatively temperature-independent 620 nm emission line, are acquired. The ratio of the intensities of the 512 and 620 nm emissions is then correlated with temperature. A more detailed description of LIF operating principles is given by Chyu and Bizzak (1993).

Experimental Apparatus and Procedure

The primary components of the LIF thermal imaging, shown schematically in Fig. 1, are the neodymium-doped ytrrium aluminum garnet (Nd:YAG) pulsed laser and the image-intensified charge coupled device (ICCD) camera. To permit measurement of the integrated fluorescent emission over a narrow wavelength range during fluorescence decay, it is necessary to

[1]Department of Mechanical Engineering, Carnegie Mellon University, Pittsburgh, PA 15213.

Contributed by the Heat Transfer Division of THE AMERICAN SOCIETY OF MECHANICAL ENGINEERS. Manuscript received by the Heat Transfer Division January 1993; revision received July 1993. Keywords: Instrumentation, Measurement Techniques. Associate Technical Editor: M. F. Modest.

Table 2 presents the number of iterations needed for convergence for phase function $F1$ and three quadrature sets. It can be seen that there is considerable savings with the improved (*Imp*) treatment over the conventional (*Conv*) treatment. For $\tau = 10$, the savings are 77, 61, and 34 percent for the S_4, S_6, and S_{12} approximations, respectively. Although the forward scattering component of the phase function in a given direction, Φ^{ll}, has the same magnitude for all orders, the weight, w^l, decreases as the order increases. This leads to a decrease in the product $\Phi^{ll} w^l$ and accounts for the decreases in percentage savings with increase in S_n order.

Concluding Remarks

The following conclusions are drawn from this study.

1 The modified-exponential spatial differencing scheme reduces to the exponential scheme in nonscattering media. In scattering media, it converges to the grid-independent solution with fewer grid points than the exponential scheme.

2 The improved source-term linearization treatment gives the *same* exact solution as the conventional iteration treatment.

3 The improved iteration treatment reduces to the conventional treatment in nonscattering media. In scattering media, the improved iteration method reduces the required number of iterations to obtain a converged solution. It is very effective in strongly scattering media and for large optical thicknesses.

Acknowledgments

This work was supported in part by NASA Lewis Research Center under Cooperative Agreement No. NCC3-238. The first author wishes to thank Mr. Slah Jendoubi for his discussions on the discrete ordinates method. A grant from the Minnesota Supercomputer Institute is also gratefully acknowledged.

References

Carlson, B. G., and Lathrop, K. D., 1968, "Transport Theory—The Method of Discrete-Ordinates," in: *Computing Methods in Reactor Physics*, H. Greenspan, C. N. Kelber, and D. Okrent, eds., Gorden and Breach, New York.

Chai, J. C., Lee, H. S., and Patankar, S. V., 1993, "An Evaluation of Three Spatial Differencing Schemes for the Discrete Ordinates Method in Participating Media," presented at the 31st Aerospace Sciences Meeting & Exhibits, AIAA 93-0140; also accepted in the *Journal of Thermophysics and Heat Transfer* as "An Evaluation of Spatial Differencing Practices for the Discrete-Ordinates Method."

Chandrasekhar, S., 1960, *Radiative Transfer*, Dover Publications, Inc., New York.

Fiveland, W. A., 1984, "Discrete-Ordinates Solutions of the Radiative Transport Equation for Rectangular Enclosures," ASME JOURNAL OF HEAT TRANSFER, Vol. 106, pp. 699–706.

Fiveland, W. A., 1987, "Discrete-Ordinates Methods for Radiative Heat Transfer in Isotropically and Anisotropically Scattering Media," ASME JOURNAL OF HEAT TRANSFER, Vol. 109, pp. 809–812.

Fiveland, W. A., 1988, "Three Dimensional Radiative Heat Transfer Solutions by the Discrete Ordinates Method," *Journal of Thermophysics and Heat Transfer*, Vol. 2, pp. 309–316.

Jamaluddin, A. S., and Smith, P. J., 1988a, "Predicting Radiative Transfer in Rectangular Enclosures Using the Discrete Ordinates Method," *Combustion and Technology*, Vol. 59, pp. 321–340.

Jamaluddin, A. S., and Smith, P. J., 1988b, "Predicting Radiative Transfer in Axisymmetric Cylindrical Enclosures Using the Discrete Ordinates Method," *Combustion and Technology*, Vol. 62, pp. 173–186.

Jamaluddin, A. S., and Smith, P. J., 1992, "Discrete-Ordinates Solution of Radiative Transfer Equation in Nonaxisymmetric Cylindrical Enclosures," *Journal of Thermophysics and Heat Transfer*, Vol. 6, pp. 242–245.

Kim, T.-K., and Lee, H. S., 1988, "Effects of Anisotropic Scattering on Radiative Heat Transfer in Two-Dimensional Rectangular Enclosures," *International Journal of Heat and Mass Transfer*, Vol. 31, pp. 1711–1721.

Lewis, E. E., and Miller, W. F., Jr., 1984, *Computational Methods of Neutron Transport*, Wiley International Publication, New York.

Patankar, S. V., 1980, *Numerical Heat Transfer and Fluid Flow*, Hemisphere Publishing, New York.

Truelove, J. S., 1987, "Discrete-Ordinate Solutions of the Radiation Transport Equation," ASME JOURNAL OF HEAT TRANSFER, Vol. 109, pp. 1048–1051.

Tsai, J. R., and Özişik, M. N., 1990, "Radiation in Cylindrical Symmetry With Anisotropic Scattering and Variable Properties," *International Journal of Heat and Mass Transfer*, Vol. 33, pp. 2651–2658.

Surface Temperature Measurement Using a Laser-Induced Fluorescence Thermal Imaging System

M. K. Chyu[1] and D. J. Bizzak[1]

Introduction

Laser-induced fluorescence (LIF) was first employed as an advanced optical diagnostic technique in combustion research for species measurements (Dyer and Crosley, 1982) and later for flame temperature measurements (Cattolica and Stephenson, 1984). In one of the first efforts to use such a technique for surface temperature measurement, the fluorescence lifetime of an emission line of a rare-earth ion-doped phosphor (i.e., thermographic phosphor) was correlated to temperature (Cates et al., 1985). While this technique has been successfully employed to provide point temperature measurements in an operating turbine engine (Noel et al., 1991), it is not an amenable approach for two-dimensional imaging because the decay time of most phosphors is so rapid that it is not possible to obtain the images necessary to compute decay times. The feasibility of two-dimensional thermal imaging, however, was recognized using the technique of ratioing the fluorescence intensity of two distinct emission lines of a rare-earth ion-doped phosphor and correlating it to temperature. Using such an approach, Goss et al. (1989) measured the surface temperature of a combusting rocket propellant seeded with dysprosium-doped lanthanum fluoride ($LaF_3:Dy^{+3}$) phosphor. Temperatures over the range of 300 to 1500 K were measured with an accuracy of approximately $\pm 10 \sim 50$ K.

In the present study, an LIF thermal imaging system, capable of accurate (± 0.5°C), two-dimensional surface temperature measurement, has been developed and demonstrated for use in general heat transfer studies. This system exploits the temperature sensitivity of both the fluorescence intensity and lifetime of certain europium-doped lanthanum oxysulfide ($La_2O_2S:Eu^{+3}$) emission lines. From the room temperature emission spectrum (Chyu and Bizzak, 1993), the temperature-sensitive emissions that may be employed are the 512 nm triplet, active from approximately -70°C to 60°C, and the 538 nm doublet, which is useful for temperature measurements in the range of 100°C to 230°C (Fonger and Struck, 1969). In this study fluorescent images of the 512 nm triplet, along with that of the relatively temperature-independent 620 nm emission line, are acquired. The ratio of the intensities of the 512 and 620 nm emissions is then correlated with temperature. A more detailed description of LIF operating principles is given by Chyu and Bizzak (1993).

Experimental Apparatus and Procedure

The primary components of the LIF thermal imaging, shown schematically in Fig. 1, are the neodymium-doped ytrrium aluminum garnet (Nd:YAG) pulsed laser and the image-intensified charge coupled device (ICCD) camera. To permit measurement of the integrated fluorescent emission over a narrow wavelength range during fluorescence decay, it is necessary to

[1]Department of Mechanical Engineering, Carnegie Mellon University, Pittsburgh, PA 15213.

Contributed by the Heat Transfer Division of THE AMERICAN SOCIETY OF MECHANICAL ENGINEERS. Manuscript received by the Heat Transfer Division January 1993; revision received July 1993. Keywords: Instrumentation, Measurement Techniques. Associate Technical Editor: M. F. Modest.

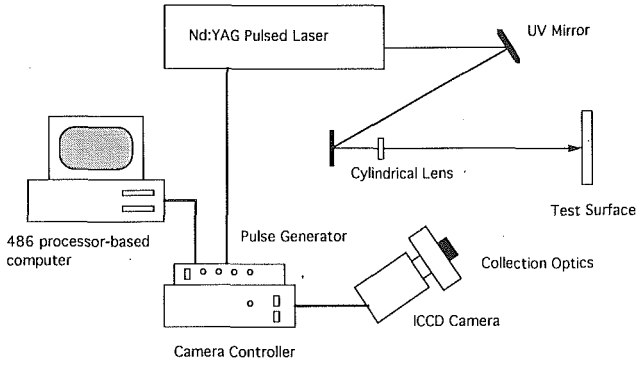

Fig. 1 Laser-induced fluorescence thermal imaging system

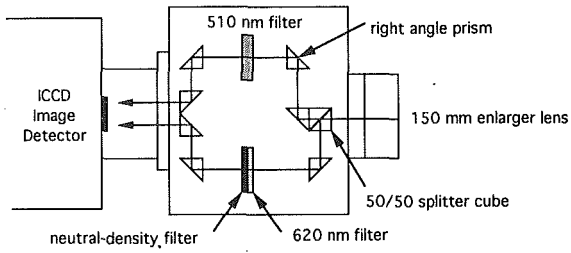

Fig. 2 Image collection optics

use a pulsed excitation source and an image detector capable of low-light level operation at gating speeds as rapid as a few microseconds. The timing and duration of the image-intensifier gate, or electronic shutter, on the ICCD camera is precisely coordinated with the laser pulse by a pulse generator. A 486 processor-based personal computer provides overall system control and image data storage, as well as image post-processing necessary to calculate surface temperatures.

To employ the LIF technique for temperature measurement, a phosphor coating must be applied to the test surface. This coating must be dense enough to provide a strong, uniform fluorescence signal, but it should not be so thick as to appreciably affect local surface profile. Furthermore, if the phosphor is applied using a binder such as an epoxy or silicon resin, the binder must be chosen to ensure that it does not fluoresce at the wavelengths of interest. For this experiment, europium-doped lanthanum oxysulfide crystals with a nominal grain size of 8 μm were applied using a settling technique commonly employed in the construction of cathode ray tubes. In this technique phosphor is suspended in a fluid and allowed to settle onto the test surface. It was determined that a phosphor coating density of 10 mg/cm^2, which is equivalent to a coating thickness of 100 μm, was necessary to obtain a fluorescence uniformity of ± 5 percent. Since the resulting phosphor coating using this technique is extremely fragile, a thin silicone overcoat was applied to protect the surface. Although the silicone overcoat provides sufficient protection of the phosphor surface in low-temperature applications, LIF thermal imaging in an inhospitable environment, e.g., an operating turbine engine, may require the phosphor to be applied using a molecular bonding technique such as sputtering or electron vapor deposition.

During temperature measurement, the phosphor coating on the test surface is excited by the 355 nm tripled output of the Nd:YAG laser. According to the room temperature excitation spectrum of $La_2O_2S:Eu^{+3}$ (Chyu and Bizzak, 1993), energy input at this particular frequency is quite efficient. Although individual laser pulses can be coordinated with ICCD image acquisition, the laser is allowed to operate at its optimum frequency of 10 Hz in order to minimize pulse-to-pulse energy deviations. Approximately 80 mJ of excitation energy over a beam diameter of 6.4 mm (0.25 in.) are provided during each 8 ns laser pulse. To permit temperature measurement over a more substantial target area, the laser output beam is passed through a -100 mm focal length plano-cylindrical lens, providing a 6.4 mm (0.25 in.) by 76 mm (3.0 in.) beam for illumination of the test surface.

Coordination of image acquisition with the laser pulse is accomplished via the laser Q-switch advance synchronization signal. This signal, which is adjusted to occur 500 ns before the laser pulse, serves as the input trigger for the pulse generator. Upon receipt of the trigger, the pulse generator provides a gate pulse that activates the ICCD image-intensifier. The width of this pulse determines the gating or "shutter" speed of the camera, and for the bulk of tests was adjusted to provide either a 35 or 40 μs gate. This gating ensures intensity integration over a period of time greater than the fluorescence lifetime of the 512 nm emission, which varies from approximately 10 μs at 20°C to 1 μms at 60°C (Cates et al., 1985).

As illustrated in Fig. 2 the fluorescence signal from the test surface is collected by a 150 mm enlarger lens and split into two equal length optical paths that are focused side-by-side onto the image detector. One optical path passes through a 510 nm narrow bandpass interference filter, while the other is directed through a 620 nm bandpass filter and a neutral density filter. The neutral density filter is required to reduce the intensity of the 620 nm fluorescence signal to a level comparable to that of the 512 nm signal, because the intensity and lifetime of the 620 nm emission are considerably greater than those of the 512 nm triplet. Due mainly to the weak emission intensity of the 512 nm triplet, integrated fluorescent emissions are accumulated over several laser pulses to increase the system signal-to-noise ratio. When the specified number of laser pulses comprising a single exposure have occurred, the camera controller disables image intensifier gating and stores the raw digital image data to a disk file for later analysis.

The simultaneous acquisition of fluorescent images at two distinct emission wavelengths is performed because intensity differences over the test surface occur as a result of spatial variations in the density of the phosphor coating and laser excitation energy. For three-dimensional surfaces variations in viewing angle caused by surface curvature may also affect spatial emission intensities. As previously noted, fluorescence intensity spatial deviations due to variations in the phosphor coating density on the test surfaces employed in this study are approximately ± 5 percent. Intensity differences due to energy level variations of the expanded laser beam output can be discerned by visual observation; therefore, these variations are more pronounced than those associated with the uniformity of the phosphor coating. Although differences in viewing angle in this study are negligible because all test surfaces are flat, this effect would be important for high-curvature surfaces such as turbine blades. The influence of these factors when correlating measured emission intensity values to temperature, however, can be eliminated by ratioing the intensity of two distinct emission lines. While the absolute value of the intensity of each emission line at any given location on the surface is affected by the density of the phosphor, the excitation energy level, and the viewing angle, the effect on the intensity ratio is minimal and can be corrected.

Prior to collecting fluorescent images for analysis, the proper pixel-to-pixel correspondence between the two images projected onto the CCD and the spatial intensity response of the camera must be established. To ensure proper alignment of the two images when performing individual pixel intensity ratio calculations, a thin black cross on a white background was imaged. The pixel location of the center of the cross for each of the images projected onto the CCD was calculated by identifying the edges of each arm of the cross. The criterion for identifying an edge was the pronounced increase in intensity between a pixel on the cross edge and its neighbor in the white

Table 1 $La_2O_2S:Eu^{+3}$ intensity ratio calibration with 40 μs intensifier gate

Temperature, °C (°F)	Average ratio	Standard deviation of ratio	Greatest deviation from average ratio
18.9 (66.0)	1.332	0.015 (0.21°C)	0.018 (0.26°C)
25.3 (77.5)	0.928	0.013 (0.23°C)	0.020 (0.37°C)
30.1 (86.2)	0.692	0.006 (0.14°C)	0.009 (0.21°C)
35.4 (95.7)	0.505	0.004 (0.12°C)	0.007 (0.24°C)
40.1 (104.2)	0.384	0.003 (0.14°C)	0.005 (0.24°C)
45.0 (113.0)	0.295	0.005 (0.33°C)	0.008 (0.52°C)
50.1 (122.2)	0.232	0.002 (0.23°C)	0.004 (0.39°C)
60.0 (140.0)	0.149	0.003 (0.47°C)	0.003 (0.53°C)

Table 2 $La_2O_2S:Eu^{+3}$ intensity ratio calibration comparison with 35 μs intensifier gate

Temperature, °C (°F)	Average ratio 1	Average ratio 2	Ratio difference
19.0 (66.2)	1.6914	1.6884	0.0030 (0.03°C)
25.1 (77.2)	1.1884	1.1863	0.0019 (0.03°C)
30.0 (86.0)	0.8714	0.8736	0.0022 (0.04°C)
35.0 (95.0)	0.6416	0.6459	0.0043 (0.11°C)
40.0 (104.0)	0.4804	0.4836	0.0032 (0.12°C)
45.0 (113.0)	0.3648	0.3658	0.0010 (0.05°C)
50.0 (122.0)	0.2827	0.2848	0.0021 (0.14°C)
60.0 (140.0)	0.1759	0.1776	0.0027 (0.66°C)

region surrounding the cross. Once the image centers are established, flat field image correction data can be collected. Variations in the phosphor coating of the ICCD camera photocathode, which converts photons into electrons that are in turn multiplied by the image intensifier, cause differences in pixel-to-pixel intensity values. To correct for these intensity response variations of the camera, a uniformly illuminated white surface is imaged. For each of the images focused on the detector, a correction array is obtained by dividing individual pixel intensity values by the average intensity of the image.

Post-acquisition analysis of fluorescent images is performed using computer software that allows the user to specify discrete points on the target surface at which local temperatures are to be calculated. The number of pixels to be used to calculate the intensity ratio at these points is also specified in terms of the size of the calculation area (e.g., a 10 by 10 pixel area). After these data are input, the flat field correction is applied to the raw image data and the first frame of the image is used to calculate a surface correction array to account for ratio variations caused by differences in phosphor density and laser excitation energy. These corrections are then applied to all succeeding frames of data. Intensity ratio values are calculated for each pixel within the calculation area and then averaged. The intensity ratio at each point can then be converted to a temperature using a calibration curve established by data obtained using an isothermal bath to heat a phosphor-coated copper test specimen.

Results and Discussion

A calibration curve for europium-doped lanthanum oxysulfide was established against the temperature on the surface of a copper block, 25 mm (1 in.) by 25 mm (1 in.), and 12.7 mm (0.5 in.) thick. The front surface of the copper block is coated with the phosphor, and its back surface is immersed in water. The water temperature can be adjusted and is controlled to within 0.1°C (0.18°F) by a circulating isothermal bath. Fluorescent image data are gathered at eight temperatures in the range of 18.9°C (66°F) to 60°C (140°F). At each temperature ten image frames, each recording the integrated fluorescence intensity over 20 laser pulses, are collected. The intensifier gate, or signal integration period, for each pulse is 40 μs. Calculated average values of the 510 nm to 620 nm intensity ratios for the ten image frames collected at each

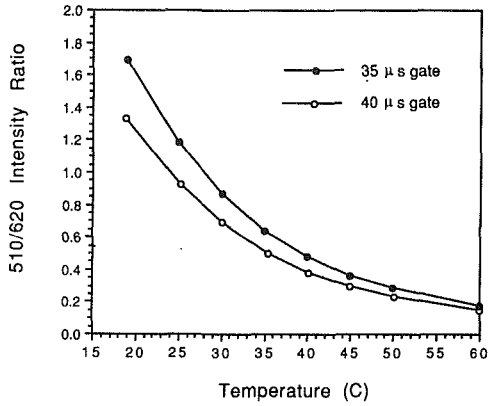

Fig. 3 Phosphor calibration

temperature examined are presented in Table 1, along with pertinent statistical data.

An 11×11 pixel array, equivalent to a 1.6 mm (0.0625 in.) square area on the copper block surface, was used to calculate the ratio data presented in Table 1. For an individual frame of data, the calculated ratio is accurate within 0.53°C (0.95°F) across the entire temperature range examined. Individual frame intensity ratio data become less accurate as temperature is increased because the integrated intensity of the 510 nm emission drops substantially, resulting in a decrease in the signal-to-noise ratio.

At lower temperatures within the useful temperature measurement range, measurement precision can be improved by decreasing the intensifier gate. As illustrated in Fig. 3, a reduction of the intensifier gate from 40 μs to 35 μs results in a considerable increase in the differential change in the intensity ratio with respect to temperature. Although the intensity ratio gradient is increased at lower temperatures, the tradeoff is less measurement accuracy at higher temperatures due to the reduced integrated intensity of the 512 nm emission.

The greatest portion of the frame-to-frame deviation in the calculated intensity ratio is related to electron shot noise. Since the image intensifier multiplies each incoming photon to produce as many as 100,000 electrons, small variations due to shot noise are multiplied. The most effective means of reducing the effects of shot noise is to average data over a greater number of frames. To illustrate the benefit of frame averaging, two independent calibrations using a 35 μs calibration were performed on different days. Comparing the results of these calibrations reveals that the individual frame-to-frame uncertainty for the frames from both calibrations is similar to that obtained for the 40 μs gate calibration, but the deviation between the intensity ratios averaged over 10 frames (i.e., the equivalent of 200 laser pulses) is much smaller. As presented in Table 2, repeatability over the greatest portion of the temperature range is better than 0.15°C (0.27°F).

Concluding Remarks

The calibration data presented here indicate that LIF thermal imaging may be used to obtain two-dimensional temperature measurements with exceptional accuracy. This technique also possesses many practical advantages over conventional as well as more modern temperature measurement methods. Although it is necessary to apply a thin phosphor coating to the surface on which temperature measurements are to be obtained, the thermal resistance of the coating in most applications is negligible, so the technique is relatively nonintrusive. The intrinsic accuracy of the technique can be attributed to the temperature-related properties of certain electronic transitions associated with the phosphor crystal. The fluorescence intensity of these

transitions provides a direct measure of temperature rather than an indirect measure such as radiant energy. Although the uniformity of the emission intensity varies with respect to the excitation energy, this effect is negated by ratioing the fluorescence intensity of a temperature-sensitive emission line to that of a relatively temperature independent line. Consequently, the technique is independent of excitation energy and optical viewing angle. With other optical temperature measurement techniques, however, these factors are important and must be closely monitored to ensure the accuracy of the results. Finally, with the choice of an appropriate thermographic phosphor, the approach can be employed in temperature ranges that encompass the cryogenic conditions encountered in superconductor research as well as the high-temperature environment associated with combustion research. The present system is also conceptually expandable for simultaneous measurement of surface temperature and rate of heat transfer.

Acknowledgments

This work, in part, is supported by NASA Marshall Space Flight Center, IBM Corp., and an NSF research equipment grant (CTS-9112284).

References

Cates, M. R., Allison, S. W., Marshall, B. R., Franks, L. A., Davies, T. J., Nelson, M. A., and Noel, B. W., 1985, "Applications of Pulsed-Laser Techniques and Thermographic Phosphors to Dynamic Thermometry of Rotating Surfaces," Martin Marietta Report K/TS-11, 504.

Cattolica, R. J., and Stephenson, D. A., 1984, "Two-Dimensional Imaging of Flame Temperature Using Laser-Induced Fluorescence," *Dynamics of Flames and Reactive Systems*, Progress in Astronautics and Aeronautics Series, Vol. 95, pp. 714–721.

Chyu, M. K., and Bizzak, D. J., 1993, "Two-Dimensional Laser-Induced Fluorescence Temperature Measurement on a Rotating Surface," presented at the 1993 National Heat Transfer Conference, Session: Visualization of Heat Transfer Processes, Atlanta, GA, Aug. 8–11.

Dyer, M. J., and Crosley, D. R., 1982, "Two-Dimensional Imaging of OH Laser-Induced Fluorescence in a Flame," *Opt. Lett.*, Vol. 7, pp. 382–384.

Fonger, W. H., and Struck, C. W., 1969, "$Eu^{+3.5}D$ Resonance Quenching to the Charge-Transfer States in Y_2O_2S, La_2O_2S, and LaOCL," *J. Chem. Physics*, Vol. 52, pp. 6364–6372.

Goss, L. P., Smith, A. A., and Post, M. E., 1989, "Surface Thermometry by Laser-Induced Fluorescence," *Rev. Sci. Instrum.*, Vol. 60, pp. 3702–3706.

Noel, B. W., Borella, H. M., Lewis, W., Turley, W. D., Beshears, D. L., Capps, G. J., Cates, M. R., Muhs, J. D., and Tobin, K. W., 1991, "Evaluating Thermographic Phosphors in an Operating Turbine Engine," ASME *Journal of Engineering for Gas Turbines and Power*, Vol. 113, pp. 242–245.

Experimental Study of R-152a Film Condensation on Single Horizontal Smooth Tube and Enhanced Tubes

B. Cheng[1, 2] and W. Q. Tao[1]

Nomenclature

A_o, A_t = outside surface area of smooth tube, total outside surface area of enhanced tube
c_i = correction factor in Gnielinski equation
D_i, D_o = inner and outside diameter
D_r = fin root diameter
e, e_t = fin height from base to tip, from valley to tip
g = gravitational acceleration
G = dimensionless argument $= gh_{fg}\rho^2 D_o^2/(\mu q)$
h_i, h_o = heat transfer coefficient of inner surface and outside surface
h_{fg} = latent heat
h_{ig} = heat transfer coefficient determined from Gnielinski equation
k = thermal conductivity
L = length of test tube
Nu_o = Nusselt number of condensation outside horizontal tube
Nu_q, Nu_t = Nusselt number calculated via q and via ΔT_{vs}
P_f, P_t = axial and circumferential fin pitch
Pr = Prandtl number
q = heat flux
Q_f, Q_w = heat transfer rate from refrigerant side and from water side
Q_m = mean heat transfer rate
Re = Reynolds number
R_{tb} = thermal resistance of tube wall
t_b, t_t = fin thickness at base and at tip
T_s = saturation temperature
$\Delta T_{\log}$ = log-mean temperature difference
ΔT_{vs} = vapor-to-wall temperature difference
U_o = overall heat transfer coefficient
μ = liquid dynamic viscosity
ξ = friction factor
ρ = density

Introduction

At present, extensive research is being conducted to replace CFCs. Among alternatives, R-152a is very promising (McLinden, 1990). However, current research on CFC alternatives is lagging behind industry's needs, especially as it relates to reliable heat transfer data. To the authors' knowledge, the only published work for phase change heat transfer of R-152a was conducted by Rose et al. (1987). They measured flow boiling heat transfer coefficients in a horizontal tube for pure R-152a and its mixture with R-13b1. No experimental values of condensation heat transfer coefficients of R-152a have been published.

In this work, experimental studies of film condensation heat transfer of R-152a vapor condensing on a single horizontal smooth tube and three enhanced tubes were conducted. Comparisons between experimental results of R-152a and R-12 were also performed.

Experimental Apparatus and Procedure

Figure 1 is a schematic of the apparatus, which consisted of a boiler, a condenser, an after-condenser, a water-cooling system, and a measurement system. The condenser and the boiler were stainless steel, while the vapor piping was copper. The boiler had an inner diameter of 257 mm and a length of 360 mm. It was fitted with two immersion heaters of 2.5 kW each. A copper tube 2.2 cm in diameter connected the boiler to the condenser shell. Saturated vapor was generated in the boiler and passed through a superheater to the condenser. The inner diameter of the condenser shell was 257 mm and its length was 800 mm. Five condensing tubes were mounted along the axis of the shell. The saturated or slightly superheated vapor was admitted to the top of the condenser shell. A specially fabricated metal sheet with a large number of small holes was mounted in the upper part of the shell to distribute the vapor uniformly along the test tube. The condensate was returned to the boiler by gravity. In the condensate return line, a box

[1]Department of Power Machinery Engineering, Xi'an Jiaotong University, Xi'an, Shaanxi 710049, The People's Republic of China.

[2]Now with Shangling Refrigerator Factory, Shanghai 200135, The People's Republic of China.

Contributed by the Heat Transfer Division of THE AMERICAN SOCIETY OF MECHANICAL ENGINEERS. Manuscript received by the Heat Transfer Division September 1992; revision received June 1993. Keywords: Augmentation and Enhancement, Condensation. Associate Technical Editor: L. C. Witte.

transitions provides a direct measure of temperature rather than an indirect measure such as radiant energy. Although the uniformity of the emission intensity varies with respect to the excitation energy, this effect is negated by ratioing the fluorescence intensity of a temperature-sensitive emission line to that of a relatively temperature independent line. Consequently, the technique is independent of excitation energy and optical viewing angle. With other optical temperature measurement techniques, however, these factors are important and must be closely monitored to ensure the accuracy of the results. Finally, with the choice of an appropriate thermographic phosphor, the approach can be employed in temperature ranges that encompass the cryogenic conditions encountered in superconductor research as well as the high-temperature environment associated with combustion research. The present system is also conceptually expandable for simultaneous measurement of surface temperature and rate of heat transfer.

Acknowledgments

This work, in part, is supported by NASA Marshall Space Flight Center, IBM Corp., and an NSF research equipment grant (CTS-9112284).

References

Cates, M. R., Allison, S. W., Marshall, B. R., Franks, L. A., Davies, T. J., Nelson, M. A., and Noel, B. W., 1985, "Applications of Pulsed-Laser Techniques and Thermographic Phosphors to Dynamic Thermometry of Rotating Surfaces," Martin Marietta Report K/TS-11, 504.

Cattolica, R. J., and Stephenson, D. A., 1984, "Two-Dimensional Imaging of Flame Temperature Using Laser-Induced Fluorescence," *Dynamics of Flames and Reactive Systems*, Progress in Astronautics and Aeronautics Series, Vol. 95, pp. 714–721.

Chyu, M. K., and Bizzak, D. J., 1993, "Two-Dimensional Laser-Induced Fluorescence Temperature Measurement on a Rotating Surface," presented at the 1993 National Heat Transfer Conference, Session: Visualization of Heat Transfer Processes, Atlanta, GA, Aug. 8–11.

Dyer, M. J., and Crosley, D. R., 1982, "Two-Dimensional Imaging of OH Laser-Induced Fluorescence in a Flame," *Opt. Lett.*, Vol. 7, pp. 382–384.

Fonger, W. H., and Struck, C. W., 1969, "$Eu^{+3.5}D$ Resonance Quenching to the Charge-Transfer States in Y_2O_2S, La_2O_2S, and LaOCL," *J. Chem. Physics*, Vol. 52, pp. 6364–6372.

Goss, L. P., Smith, A. A., and Post, M. E., 1989, "Surface Thermometry by Laser-Induced Fluorescence," *Rev. Sci. Instrum.*, Vol. 60, pp. 3702–3706.

Noel, B. W., Borella, H. M., Lewis, W., Turley, W. D., Beshears, D. L., Capps, G. J., Cates, M. R., Muhs, J. D., and Tobin, K. W., 1991, "Evaluating Thermographic Phosphors in an Operating Turbine Engine," ASME *Journal of Engineering for Gas Turbines and Power*, Vol. 113, pp. 242–245.

Experimental Study of R-152a Film Condensation on Single Horizontal Smooth Tube and Enhanced Tubes

B. Cheng[1, 2] and W. Q. Tao[1]

Nomenclature

A_o, A_t = outside surface area of smooth tube, total outside surface area of enhanced tube
c_i = correction factor in Gnielinski equation
D_i, D_o = inner and outside diameter
D_r = fin root diameter
e, e_t = fin height from base to tip, from valley to tip
g = gravitational acceleration
G = dimensionless argument $= gh_{fg}\rho^2 D_o^2/(\mu q)$
h_i, h_o = heat transfer coefficient of inner surface and outside surface
h_{fg} = latent heat
h_{ig} = heat transfer coefficient determined from Gnielinski equation
k = thermal conductivity
L = length of test tube
Nu_o = Nusselt number of condensation outside horizontal tube
Nu_q, Nu_t = Nusselt number calculated via q and via ΔT_{vs}
P_f, P_l = axial and circumferential fin pitch
Pr = Prandtl number
q = heat flux
Q_f, Q_w = heat transfer rate from refrigerant side and from water side
Q_m = mean heat transfer rate
Re = Reynolds number
R_{tb} = thermal resistance of tube wall
t_b, t_t = fin thickness at base and at tip
T_s = saturation temperature
$\Delta T_{\log}$ = log-mean temperature difference
ΔT_{vs} = vapor-to-wall temperature difference
U_o = overall heat transfer coefficient
μ = liquid dynamic viscosity
ξ = friction factor
ρ = density

Introduction

At present, extensive research is being conducted to replace CFCs. Among alternatives, R-152a is very promising (McLinden, 1990). However, current research on CFC alternatives is lagging behind industry's needs, especially as it relates to reliable heat transfer data. To the authors' knowledge, the only published work for phase change heat transfer of R-152a was conducted by Rose et al. (1987). They measured flow boiling heat transfer coefficients in a horizontal tube for pure R-152a and its mixture with R-13b1. No experimental values of condensation heat transfer coefficients of R-152a have been published.

In this work, experimental studies of film condensation heat transfer of R-152a vapor condensing on a single horizontal smooth tube and three enhanced tubes were conducted. Comparisons between experimental results of R-152a and R-12 were also performed.

Experimental Apparatus and Procedure

Figure 1 is a schematic of the apparatus, which consisted of a boiler, a condenser, an after-condenser, a water-cooling system, and a measurement system. The condenser and the boiler were stainless steel, while the vapor piping was copper. The boiler had an inner diameter of 257 mm and a length of 360 mm. It was fitted with two immersion heaters of 2.5 kW each. A copper tube 2.2 cm in diameter connected the boiler to the condenser shell. Saturated vapor was generated in the boiler and passed through a superheater to the condenser. The inner diameter of the condenser shell was 257 mm and its length was 800 mm. Five condensing tubes were mounted along the axis of the shell. The saturated or slightly superheated vapor was admitted to the top of the condenser shell. A specially fabricated metal sheet with a large number of small holes was mounted in the upper part of the shell to distribute the vapor uniformly along the test tube. The condensate was returned to the boiler by gravity. In the condensate return line, a box

[1]Department of Power Machinery Engineering, Xi'an Jiaotong University, Xi'an, Shaanxi 710049, The People's Republic of China.

[2]Now with Shangling Refrigerator Factory, Shanghai 200135, The People's Republic of China.

Contributed by the Heat Transfer Division of The American Society of Mechanical Engineers. Manuscript received by the Heat Transfer Division September 1992; revision received June 1993. Keywords: Augmentation and Enhancement, Condensation. Associate Technical Editor: L. C. Witte.

Table 1 Parameters of test tubes (length unit: mm)

Tube No.	D_o	D_r	D_i	P_f	P_l	e	e_l	t	t_t	t_b	A_t/A_o
1	15.77		12.60								1
2	15.85	14.30	12.60	1.270		0.775			0.540	0.770	2.13
3	17.44	15.16	12.90	0.671		1.138			0.288	0.255	4.46
4	16.43	15.83	12.90	0.675	0.700	0.300	0.238	0.150			3.68
5	19.65	17.60	15.50	0.825	0.750	1.025	0.525	0.400			4.55

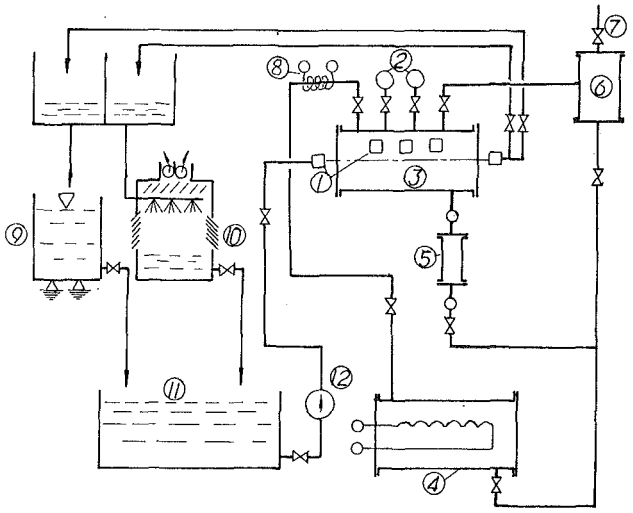

Fig. 1 Schematic diagram of experimental apparatus: (1) thermocouple; (2) pressure gage; (3) condenser; (4) boiler; (5) condensate measuring container; (6) after-condenser; (7) flushing vent; (8) superheater; (9) water rate measuring tank; (10) water cooling tank; (11) water storage tank; (12) pump

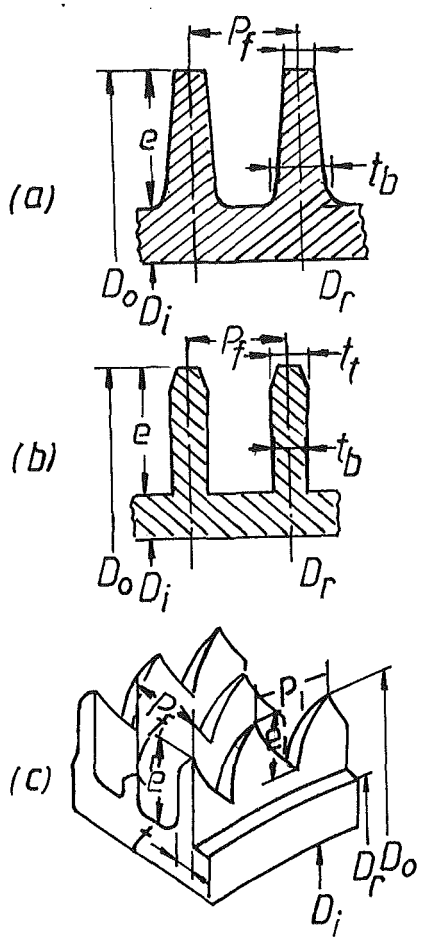

Fig. 2 Geometry of enhanced tubes: (*a*) integral fin No. 1; (*b*) integral fin No. 2; (*c*) sawtooth type

of fixed volume was mounted for measuring condensate flow rate. In order to remove noncondensable gas from the test section, an after-condenser was placed downstream from the test section.

The cooling water loop consisted of a storage tank, a centrifugal pump, a flow rate measuring tank, and lines from the storage tank to the condenser tubes. The condensing tubes mounted in the condenser shell were connected to the main circulating line in a parallel manner. Along the water flow direction, each tube was preceded by a valve, so that any four of the five tubes might be switched off from the circulating line when the experiment for the fifth tube was conducted. The apparatus was well insulated with 4-cm-thick foam plastic.

Copper-constantan thermocouples were used to measure the temperatures of vapor in boiler and condenser, and the inlet water temperature. Since the coolant temperature rise (which was from 1°C to 10°C) was a very important measurement in this study, a five-junction, series-connected copper-constantan thermocouple was used for its measurement. A digital voltmeter having a resolution of 0.1 μV was used to measure the thermocouple emfs. The vapor pressures in the boiler and the condenser were measured by pressure gages with an accuracy of 0.4 percent. The coolant flow rate was determined by a weight-time method, and the condensate flow rate was measured by a volume-time method.

During the experiments, noncondensable gases in the test loop were reduced to a negligible value by repeatedly opening a flushing vent at the top of the after-condenser. As a check of whether the noncondensable gases were reduced to a negligible value, the vapor temperature in the condenser shell measured by the thermocouples was compared with the saturation temperature corresponding to the measured pressure. The allowed difference was limited to 0.2–0.3°C (Webb et al., 1985; Sukhatme et al., 1990).

At a given water flow rate and vapor pressure, the following steady-state data were recorded: cooling flow rate, inlet water temperature and temperature rise, vapor pressure and temperatures, and refrigerant condensate flow rate. If the imbalance in heat transfer rate was larger than 5.5 percent, the reasons responsible for the large imbalance were analyzed and the run was repeated.

The tube specifications are listed in Table 1. The geometries are shown in Fig. 2. It should be noted that for integral fin tube No. 2 the inner surface was also roughened during the fin-making process. A spiral groove was formed on the inner surface. All the three types of enhanced tube are currently used in commercial freon condensers in China.

Data Reduction

A modified Wilson plot technique was used to obtain the vapor side heat transfer coefficients, h_o. The principles and advantages of the Wilson plot technique are well documented in the literature (Masuda and Rose, 1988). A brief description of its implementation is given as follows.

The overall heat transfer coefficient was calculated by

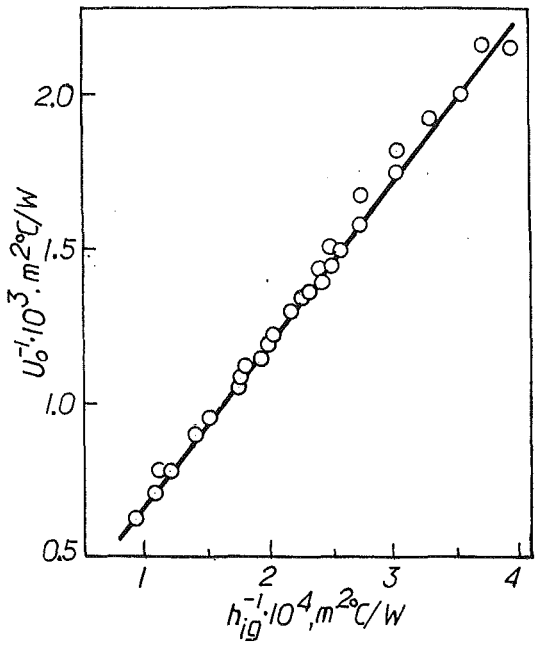

Fig. 3 Modified Wilson plot of tube No. 5 (inner surface smooth)

$$U_o = \frac{Q_m}{A_o \Delta T_{\log}} = \frac{(Q_f + Q_w)/2}{A_o \Delta T_{\log}} \tag{1}$$

For enhanced tubes, the outside area of the bare tube from which the enhanced tubes were made was used as the reference area, A_o. In the calculation of $\Delta T_{\log}$ the saturated temperature of the condensing vapor and the inlet and outlet temperatures of the cooling water were used.

The total thermal resistance $1/(A_o U_o)$ is related to the separate thermal resistances by the following equation:

$$\frac{1}{A_o U_o} = \frac{1}{h_i A_i} + R_{tb} + \frac{1}{h_o A_o} \tag{2}$$

To obtain h_o from Eq. (2) with good accuracy, the water side heat transfer coefficient h_i must be determined as accurately as possible.

According to the Nusselt theory for vapor condensation outside a single horizontal tube,

$$\mathrm{Nu}_t = 0.725 \left(\frac{g h_{fg} \rho^2 D_o^3}{k \mu \Delta T_{vs}}\right)^{1/4}, \tag{3a}$$

$$\mathrm{Nu}_q = 0.651 \left(\frac{g h_{fg} \rho^2 D_o^2}{\mu q}\right)^{1/3} \tag{3b}$$

Clearly, if the heat flux and vapor pressure are kept constant, the condensation heat transfer coefficient will not change. Then, Eq. (2) may be rewritten as

$$\frac{1}{U_o} = b + \frac{A_o}{A_i h_i} \tag{4}$$

where the term b indicates the tube wall resistance and the vapor side thermal resistance, which is kept constant for purposes of the Wilson plot.

Different correlations are available to calculate the water side heat transfer coefficients. In the present study, the Gnielinski equation was adopted (Gnielinski, 1976)

$$h_{ig} = \frac{k}{D_i} \frac{(\xi/8)(\mathrm{Re} - 1000)\mathrm{Pr}}{1 + 12.7(\xi/8)^{1/2}(\mathrm{Pr}^{2/3} - 1)} \left[1 + \left(\frac{D_i}{L}\right)^{2/3}\right] \left(\frac{\mathrm{Pr}}{\mathrm{Pr}_w}\right)^{0.11} \begin{pmatrix} \mathrm{Re} = 2300 - 10^6 \\ \mathrm{Pr} = 0.6 - 10^5 \end{pmatrix} \tag{5}$$

Equation (5) has two advantages over the other equations. First, the lower application limit of Reynolds number is 2300, which is much less than that of the Dittus-Boelter equation (10^4). Second, Eq. (5) may be used in the entrance region, which provides some convenience in designing the apparatus. To accommodate Eq. (5) with the individual tube tested, it is modified by an unknown coefficient c_i. Then Eq. (4) becomes

$$\frac{1}{U_o} = b + \frac{A_o}{A_i h_{ig}} \frac{1}{c_i} \tag{6}$$

Experiments were performed for two tubes with R-152a condensing outside the tubes: tube No. 2 (inner surface roughened) and tube No. 5 (inner surface smooth). The results for tube No. 5 are presented in Fig. 3. In the experiments, the Reynolds number varied from 6×10^3 to 3×10^4. For tube No. 5 the value of c_i obtained by a least-square method was 1.01, indicating very good agreement of experimental data with Eq. (5). For tube No. 2 c_i was 1.11. Equation (5) was used directly to reduce the data for tubes No. 1, 3, 4, and 5, while for tube No. 2, $c_i = 1.11$ was used.

An uncertainty analysis along the lines suggested by Kline and McClintock (1953) showed that the uncertainty in U_o was about ±3.5 percent. Since h_o was not directly measured, it was impossible to assign error estimates to it. However, the errors involved in determination of h_o were estimated as follows. First the error involved in determination of h_i was estimated. The Gnielinski equation fitted the data of this study very well. Figure 3 shows that the maximum deviation between the predicted values (solid line) and the experimental data is about 5 percent. This value was taken as the uncertainty in the calculation of h_i. The tube wall thermal resistance never exceeded 1 percent, and hence was neglected. In all experiments, the minimum percentage of water side thermal resistance was about 15 percent, and the maximum percentage was around 75 percent (when the Reynolds number was about 6×10^3). The worst situation occurred when the error in the total thermal resistance and that in water side resistance were in opposite directions (i.e., one was positive and the other negative), especially when the water flow rate was the lowest. This consideration yielded a maximum error in h_o of around ±5 percent at the highest water flow rate, and around ±19 percent at the lowest water flow rate.

Results and Discussion

Check of the Reliability of Experimental Data. Nu_o can be calculated either by heat flux (Eq. (3*b*)), or by temperature difference (Eq. (3*a*)). In the experiments, heat fluxes were measured directly. Therefore, the corresponding Nu_q was calculated from the measured heat flux. The value of ΔT_{vs} was obtained from the subtraction of thermal resistances. If this was correctly conducted, the resulting value of ΔT_{vs} should give an identical value of Nu_t. This comparison was performed for all data of R-152a and R-12 condensing outside a smooth tube. The ratios of $\mathrm{Nu}_t/\mathrm{Nu}_q$ were within the range of 0.95 to 1.05, indicating the reliability of the experimental data. The thermophysical properties were taken from ASHRAE (1985) and Jung and Radermacher (1991).

Condensation of R-152a Outside Smooth Tube. Two sets of experiments for R-152a were performed: one set at a fixed vapor pressure, and the other with variable vapor pressure and heat flux. For the first, the physical properties of condensate film were kept constant, thus the results may be presented in terms of h_o versus ΔT_{vs}; see Fig. 4. The second set of data should be presented in dimensionless form, so that the effects of variable physical properties may be taken into account, as shown in Fig. 5. In these two figures, the solid lines represent the Nusselt theory. The Nusselt equation agrees within 0–15 percent of the experimental data.

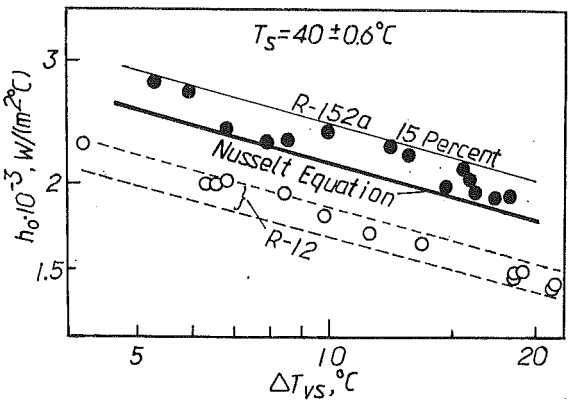

Fig. 4 Variation of h_o with ΔT_{vs} of R-152a and R-12 condensing outside a single smooth tube

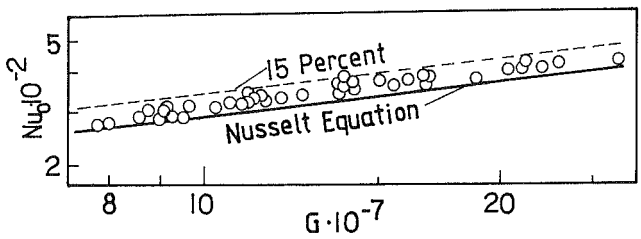

Fig. 5 Dimensionless presentation of R-152a condensing outside a single smooth tube

It is interesting to compare the condensation behavior of R-152a and R-12. To make an objective comparison, the experimental results should be compared directly without involving any physical property data. This was done by carrying out condensation of R-12 at a fixed pressure for which the saturation temperature was the same as that of R-152a (40°C). The results for R-12 are also presented in Fig. 4. The h_o for R-152a is about 20–25 percent higher than that for R-12.

Results of Enhanced Tubes

Figure 6 shows the variation of Nu_o with G for tubes No. 2, 3, and 4. For each Nu_o stays nearly constant with increasing values of G. The dashed line shown in Fig. 6 represents the smooth tube. For the same value of G, Nu_o for the enhanced tubes is 4 to 10 times that of the smooth tube. For the enhanced tubes the reference dimension in Nusselt number was the outside diameter of the bare tube from which the enhanced tube was made. The percentage enhancement in heat transfer is larger than that in surface area provided by the surface enhancement.

Similar experiments were conducted for R-12, and the results are provided in Fig. 7. Again, for each enhanced tube, the heat transfer intensity of R-152a is large than R-12, with 0 to 30 percent increase in Nusselt number. For R-152a the values of h_o were not obtained for tube No. 5. When R-152a condensed on tube No. 5, the water side thermal resistance became an overwhelming part of the total thermal resistance (as large as 90 percent) for most data runs. This caused the error involved in determining h_o to be as large as 80–100 percent. A direct method for measuring the mean temperature of the tube wall via the electrical resistance of the tube is now under way.

Conclusions

1 The predicted condensation heat transfer coefficients from Nusselt theory for R-152a agree within 15 percent of the experimental data.

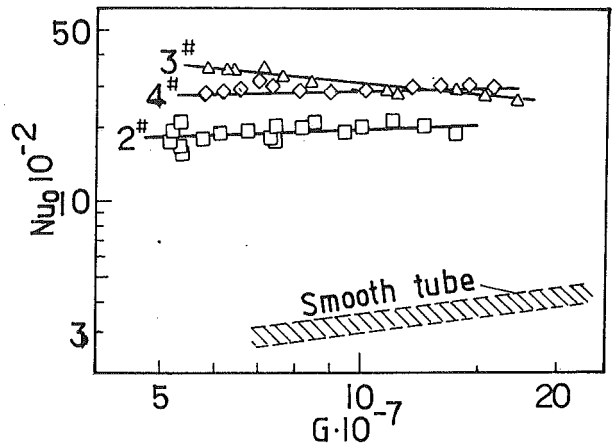

Fig. 6 Nusselt number variation for R-152a for three enhanced tubes

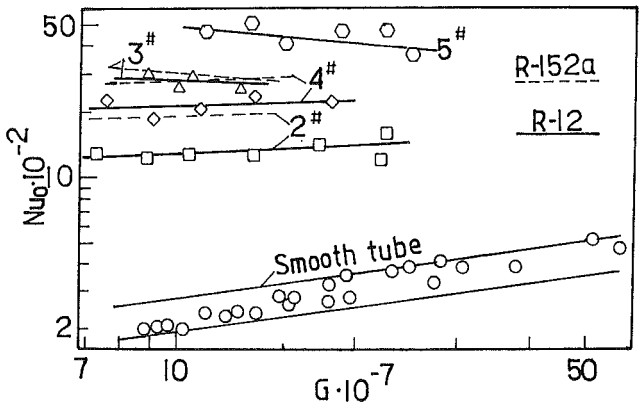

Fig. 7 Nusselt number variation for R-12 for four enhanced tubes

2 At a saturation temperature of 40°C and for the same values of ΔT_{us}, h_o of R-152a outside a single horizontal tube is about 20–25 percent higher than that of R-12. The higher heat transfer performance of R-152a can be explained by its higher values of latent heat and heat conductivity and lower value of liquid viscosity (ASHRAE, 1985; Jung and Radermacher, 1991).

3 The heat transfer coefficient of R-152a can be greatly enhanced by using such enhanced tubes as the integral fin and the sawtooth-type tube, and comparatively, the condensation heat transfer coefficients of R-152a on these tubes are higher than those of R-12, with a percentage of increase up to 30.

Acknowledgments

This work was supported by the Chinese State Key Laboratory of Multiphase Flow in Power Engineering and Natural Science Foundation of Shaanxi Province.

References

ASHRAE, 1985, *Fundamentals*, American Society of Heating, Refrigeration, and Air-Conditioning Engineers Inc., Atlanta, GA 30329.

Gnielinski, V., 1976, "New Equation for Heat and Mass Transfer in Turbulent Pipe and Channel Flow," *Int. Chem. Engng.*, Vol. 16, No. 2, pp. 359–367.

Jung, D., and Radermacher, R., 1991, "Transport Properties and Surface Tension of Pure and Mixed Refrigerants," *ASHRAE Trans.*, Vol. 97, Part 1, pp. 90–99.

Kline, S. J., and McClintock, F. A., 1953, "Description of Uncertainties in Single Sample Experiments," *Mechanical Engineering*, Vol. 75, Jan., pp. 3–9.

Masuda, H., and Rose, J. W., 1988, "Condensation of Ethylene Glycol on Horizontal Integral Fin Tubes," ASME JOURNAL OF HEAT TRANSFER, Vol. 110, pp. 149–162.

McLinden, M. O., 1990, "Thermodynamic Properties of CFC Alternatives: A Survey of the Available Data," *Int. J. Refrig.*, Vol. 13, pp. 149–162.

Rose, H., Radermacher, R., and Marzo, M. D., 1987, "Horizontal Flow Boiling of Pure and Mixed Refrigerants," *Int. J. Heat Mass Transfer*, Vol. 30, pp. 979–992.

Sukhatme, S. P., Jagadish, B. S., and Prabhakaran, P., 1990, "Film Condensation of R-11 Vapor on Single Horizontal Enhanced Condenser Tubes," ASME JOURNAL OF HEAT TRANSFER, Vol. 112, pp. 229–234.

Webb, R. L., Rudy, T. M., and Kedzierski, M. A., 1985, "Prediction of the Condensation Coefficient on Horizontal Integral-Fin Tubes," ASME JOURNAL OF HEAT TRANSFER, Vol. 107, pp. 369–376.

Two-Phase Thermal Asymptotic Suction Profile

A. J. Chamkha[1]

Nomenclature

c = fluid-phase specific heat at constant pressure
Ec = fluid-phase Eckert number
$\mathbf{e}_x$, $\mathbf{e}_y$ = unit vectors in x and y directions, respectively
F = nondimensionalized fluid-phase tangential velocity
$\mathbf{f}$ = interphase force per unit volume acting on the particle phase
H = nondimensionalized fluid-phase temperature
H_0 = nondimensionalized fluid-phase wall temperature
$\underline{I}$ = unit tensor
k = fluid-phase thermal conductivity
P = fluid-phase pressure
Pr = fluid-phase Prandtl number
Q_p = interphase heat transfer rate per unit volume to the particle phase
$\mathring{q}_w$ = wall heat transfer
T = fluid-phase temperature
$\mathbf{V}$ = fluid-phase velocity vector
x, y = Cartesian coordinate variables
α = velocity inverse Stokes number
β = viscosity ratio
γ = specific heat ratio
δ_t = thermal boundary layer
ϵ = temperature inverse Stokes number
η = transformed normal coordinate
κ = particle loading
μ = fluid-phase viscosity coefficient
ρ = fluid-phase density
$\underline{\sigma}$ = fluid-phase stress tensor
τ_T = temperature relaxation time
τ_v = momentum relaxation time
ϕ = volume fraction of particles
ω = slip coefficient
∇ = gradient operator

Subscripts

∞ = free stream
p = particle phase
s = surface

Superscripts

T = transpose of a second-order tensor

Introduction

Many industrial processes employ particle-fluid suspensions. Understanding such processes through analysis is essential for their optimization. The problem considered in this paper is steady two-phase flow past an infinite porous flat plate. This is one of the few two-phase flow problems for which the governing equations can be exactly reduced to ordinary differential equations for a variety of physical models and solved in closed form. Soo (1967) and Marble (1970), among others, have reported continuum equations governing two-phase particulate suspensions. Chamkha and Peddieson (1989) employed these equations with some modifications and reported exact solutions for the flow fields of the problem described above without considering the thermal aspects of it.

The purpose of this paper is to report exact solutions for the convective heat flux and the temperature distributions for both phases. The fluid phase is assumed incompressible. The particle phase is assumed viscous, incompressible, and pressureless. The particle volume fraction is assumed finite and uniform.

Governing Equations

Consider the two-dimensional steady laminar flow in a half-space bounded by an infinite porous flat plate. The half-space occupies the region $y>0$ with the plate being fixed and coincident with the plane $y=0$. The flow is a parallel stream with velocity V_∞ and at a temperature T_∞ in the x direction. The fluid phase exhibits a uniform suction with velocity V_s at the plate surface and the plate is maintained at a constant temperature T_s (see Fig. 1). The particles are assumed spherical in shape and uniformly distributed in the carrier fluid. Radiative heat transfer from one particle to another is neglected.

The governing equations, which are based on the balance laws of mass, linear momentum, and energy, generalize the dusty-gas equations given by Marble (1970) through the inclusion of particle-phase viscous stresses, and are applicable to any size particles. These are given by

$$\nabla\cdot((1-\phi)\mathbf{V})=0,\quad \nabla\cdot(\phi\mathbf{V}_p)=0$$
$$\rho(1-\phi)(\mathbf{V}\cdot\nabla V)=\nabla\cdot\underline{\sigma}-f,\quad \rho_p\phi\mathbf{V}_p\cdot\nabla\mathbf{V}_p=\nabla\cdot\underline{\sigma}_p+\mathbf{f}$$
$$\rho c(1-\phi)\mathbf{V}\cdot\nabla T=(1-\phi)k\nabla^2T+\underline{\sigma}:\nabla\mathbf{V}+Q_p+(\mathbf{V}-\mathbf{V}_p)\cdot\mathbf{f}$$
$$\rho_p c_p\phi\mathbf{V}_p\cdot\nabla T_p=\underline{\sigma}_p:\nabla\mathbf{V}_p-Q_p \qquad (1)$$

where

$$\underline{\sigma}=(1-\phi)(-P\underline{I}+\mu(\nabla\mathbf{V}+\nabla\mathbf{V}^T)),\quad \underline{\sigma}_p=\mu_p\phi\,(\nabla\mathbf{V}_p+\nabla\mathbf{V}_p^T)$$
$$\mathbf{f}=\rho_p\phi(\mathbf{V}-\mathbf{V}_p)/\tau_v,\quad Q_p=\rho_pc_p\phi(T_p-T)/\tau_T \qquad (2)$$

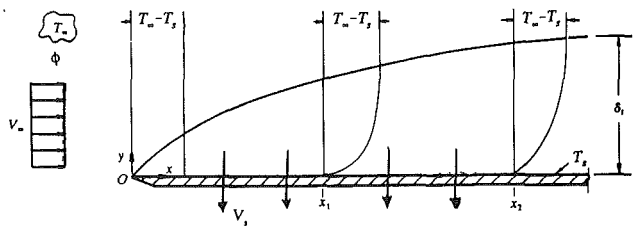

Fig. 1 Flat plate schematic

[1]Assistant Professor, Department of Mechanical Engineering, Kuwait University, P. O. Box 5969, Safat, 13060 Kuwait; Mem. ASME.

Contributed by the Heat Transfer Division of THE AMERICAN SOCIETY OF MECHANICAL ENGINEERS. Manuscript received by the Heat Transfer Division August 1992; revision received February 1993. Keywords: Forced Convection, Multiphase Flows. Associate Technical Editor: J. H. Kim.

Masuda, H., and Rose, J. W., 1988, "Condensation of Ethylene Glycol on Horizontal Integral Fin Tubes," ASME JOURNAL OF HEAT TRANSFER, Vol. 110, pp. 149–162.

McLinden, M. O., 1990, "Thermodynamic Properties of CFC Alternatives: A Survey of the Available Data," *Int. J. Refrig.*, Vol. 13, pp. 149–162.

Rose, H., Radermacher, R., and Marzo, M. D., 1987, "Horizontal Flow Boiling of Pure and Mixed Refrigerants," *Int. J. Heat Mass Transfer*, Vol. 30, pp. 979–992.

Sukhatme, S. P., Jagadish, B. S., and Prabhakaran, P., 1990, "Film Condensation of R-11 Vapor on Single Horizontal Enhanced Condenser Tubes," ASME JOURNAL OF HEAT TRANSFER, Vol. 112, pp. 229–234.

Webb, R. L., Rudy, T. M., and Kedzierski, M. A., 1985, "Prediction of the Condensation Coefficient on Horizontal Integral-Fin Tubes," ASME JOURNAL OF HEAT TRANSFER, Vol. 107, pp. 369–376.

Two-Phase Thermal Asymptotic Suction Profile

A. J. Chamkha[1]

Nomenclature

c = fluid-phase specific heat at constant pressure
Ec = fluid-phase Eckert number
$\mathbf{e}_x$, $\mathbf{e}_y$ = unit vectors in x and y directions, respectively
F = nondimensionalized fluid-phase tangential velocity
$\mathbf{f}$ = interphase force per unit volume acting on the particle phase
H = nondimensionalized fluid-phase temperature
H_0 = nondimensionalized fluid-phase wall temperature
$\underline{\underline{I}}$ = unit tensor
k = fluid-phase thermal conductivity
P = fluid-phase pressure
Pr = fluid-phase Prandtl number
Q_p = interphase heat transfer rate per unit volume to the particle phase
$\mathring{q}_w$ = wall heat transfer
T = fluid-phase temperature
$\mathbf{V}$ = fluid-phase velocity vector
x, y = Cartesian coordinate variables
α = velocity inverse Stokes number
β = viscosity ratio
γ = specific heat ratio
δ_t = thermal boundary layer
ϵ = temperature inverse Stokes number
η = transformed normal coordinate
κ = particle loading
μ = fluid-phase viscosity coefficient
ρ = fluid-phase density
$\underline{\underline{\sigma}}$ = fluid-phase stress tensor
τ_T = temperature relaxation time
τ_v = momentum relaxation time
ϕ = volume fraction of particles
ω = slip coefficient
∇ = gradient operator

Subscripts

∞ = free stream
p = particle phase
s = surface

Superscripts

T = transpose of a second-order tensor

Introduction

Many industrial processes employ particle-fluid suspensions. Understanding such processes through analysis is essential for their optimization. The problem considered in this paper is steady two-phase flow past an infinite porous flat plate. This is one of the few two-phase flow problems for which the governing equations can be exactly reduced to ordinary differential equations for a variety of physical models and solved in closed form. Soo (1967) and Marble (1970), among others, have reported continuum equations governing two-phase particulate suspensions. Chamkha and Peddieson (1989) employed these equations with some modifications and reported exact solutions for the flow fields of the problem described above without considering the thermal aspects of it.

The purpose of this paper is to report exact solutions for the convective heat flux and the temperature distributions for both phases. The fluid phase is assumed incompressible. The particle phase is assumed viscous, incompressible, and pressureless. The particle volume fraction is assumed finite and uniform.

Governing Equations

Consider the two-dimensional steady laminar flow in a half-space bounded by an infinite porous flat plate. The half-space occupies the region $y>0$ with the plate being fixed and coincident with the plane $y=0$. The flow is a parallel stream with velocity V_∞ and at a temperature T_∞ in the x direction. The fluid phase exhibits a uniform suction with velocity V_s at the plate surface and the plate is maintained at a constant temperature T_s (see Fig. 1). The particles are assumed spherical in shape and uniformly distributed in the carrier fluid. Radiative heat transfer from one particle to another is neglected.

The governing equations, which are based on the balance laws of mass, linear momentum, and energy, generalize the dusty-gas equations given by Marble (1970) through the inclusion of particle-phase viscous stresses, and are applicable to any size particles. These are given by

$$\nabla\cdot((1-\phi)\mathbf{V})=0,\quad \nabla\cdot(\phi\mathbf{V}_p)=0$$

$$\rho(1-\phi)(\mathbf{V}\cdot\nabla V)=\nabla\cdot\underline{\underline{\sigma}}-f,\quad \rho_p\phi\mathbf{V}_p\cdot\nabla\mathbf{V}_p=\nabla\cdot\underline{\underline{\sigma}}_p+\mathbf{f}$$

$$\rho c(1-\phi)\mathbf{V}\cdot\nabla T=(1-\phi)k\nabla^2T+\underline{\underline{\sigma}}:\nabla\mathbf{V}+Q_p+(\mathbf{V}-\mathbf{V}_p)\cdot\mathbf{f}$$

$$\rho_p c_p\phi\mathbf{V}_p\cdot\nabla T_p=\underline{\underline{\sigma}}_p:\nabla\mathbf{V}_p-Q_p \qquad (1)$$

where

$$\underline{\underline{\sigma}}=(1-\phi)(-P\underline{\underline{I}}+\mu(\nabla\mathbf{V}+\nabla\mathbf{V}^T)),\quad \underline{\underline{\sigma}}_p=\mu_p\phi\,(\nabla\mathbf{V}_p+\nabla\mathbf{V}_p^T)$$

$$\mathbf{f}=\rho_p\phi(\mathbf{V}-\mathbf{V}_p)/\tau_v,\quad Q_p=\rho_pc_p\phi(T_p-T)/\tau_T \qquad (2)$$

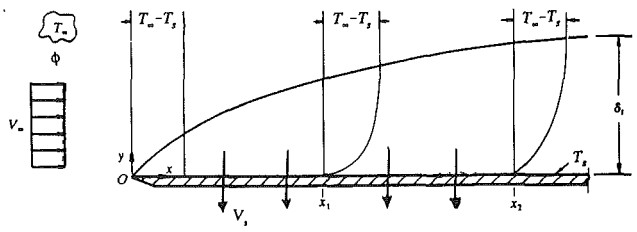

Fig. 1 Flat plate schematic

[1]Assistant Professor, Department of Mechanical Engineering, Kuwait University, P. O. Box 5969, Safat, 13060 Kuwait; Mem. ASME.

Contributed by the Heat Transfer Division of THE AMERICAN SOCIETY OF MECHANICAL ENGINEERS. Manuscript received by the Heat Transfer Division August 1992; revision received February 1993. Keywords: Forced Convection, Multiphase Flows. Associate Technical Editor: J. H. Kim.

It is evident from Eqs. (1) and (2) that both the fluid phase and the particulate phase are coupled through drag and heat transfer between them.

Equations (1) and (2) can be nondimensionalized by using

$$y=\mu\eta/(\rho V_\infty),\quad \mathbf{V}=\mathbf{V}_\infty F(\eta)\mathbf{e}_x - V_s\mathbf{e}_y$$

$$\mathbf{V}_p=V_\infty F_p(\eta)\mathbf{e}_x - V_s\mathbf{e}_y,\quad T=T_\infty H(\eta),\ T_p=T_\infty H_p(\eta) \tag{3}$$

and rearranging to give

$$F''+r_v F'+\kappa\alpha(F_p-F)=0,\quad \beta F_p''+r_v F_p'+\alpha(F-F_p)=0$$

$$H''+r_v\,\mathrm{Pr}H'+\kappa\mathrm{Pr}\gamma\epsilon(H_p-H)+\mathrm{Ec}\ \mathrm{Pr}(F')^2+\mathrm{Ec}\ \mathrm{Pr}\kappa\alpha(F_p-F)^2=0$$

$$r_v H_p'+\epsilon(H-H_p)+\mathrm{Ec}\beta/\gamma(F_p')^2=0 \tag{4}$$

where a prime denotes ordinary differentiation with respect to η and

$$r_v=V_s/V_\infty,\ \kappa=\rho_p\phi/(\rho(1-\phi)),\ \alpha=\mu/(\rho\tau_v V_\infty^2),\ \mathrm{Pr}=\mu c/k,$$

$$\gamma=c_p/c,\ \epsilon=\mu/(\rho\tau_T V_\infty^2),\ \mathrm{Ec}=V_\infty^2/(cT_\infty),\ \beta=\mu_p/\mu \tag{5}$$

are the suction parameter, the particle loading, the velocity inverse Stokes number, the fluid-phase Prandtl number, the specific heat ratio, the temperature inverse Stokes number, the Eckert number, and the viscosity ratio, respectively.

Equations (4) are solved subject to the following boundary conditions:

$$F(0)=0,\ F(\infty)=1,\quad F_p'(0)=\omega F_p(0),\quad F_p(\infty)=1,$$

$$H(0)=H_0,\ H(\infty)=1,\ H_p(\infty)=1 \tag{6}$$

Equation (6*c*) is borrowed from rarefied gas dynamics and used herein because the exact forms of boundary conditions for a particulate phase at a surface are not understood at present.

The wall heat flux coefficient is an important physical property of the thermal characteristics of this type of flow. It can be defined as

$$\mathring{q}_w=-H'(0)/(\mathrm{PrEc}) \tag{7}$$

where the minus sign indicates the direction of the heat transfer.

Results and Discussion

Chamkha and Peddieson (1989) reported among other things the solutions for the velocity profiles for both the fluid and particle phases for this problem. Attention will be focused herein on the solutions for the temperature fields for both phases and the wall heat flux.

The solutions for the fluid-phase velocity in the x direction F and the particle-phase velocity in the x direction F_p can, respectively, be shown to be

$$F=1-AC_3\exp(-\lambda_1\eta)-BC_4\exp(-\lambda_2\eta)$$

$$F_p=1-C_3\exp(-\lambda_1\eta)-C_4\exp(-\lambda_2\eta)$$

$$A=1+(r_v\lambda_1-\beta\lambda_1^2)/\alpha,\ B=1+(r_v\lambda_2-\beta\lambda_2^2)/\alpha$$

$$C_4=\lambda_1(1+\omega(\beta\lambda_1-r_v)/\alpha)/((\omega+\lambda_1)B-(\omega+\lambda_2)A)$$

$$C_3=(\omega+C_4(\omega+\lambda_2))/(\omega+\lambda_1) \tag{8}$$

λ_1 and λ_2 are the absolute values of the two negatives roots of the quartic equation

$$\beta\lambda^4+r_v(1+\beta)\lambda^3+(r_v^2-\alpha(1+\kappa\beta))\lambda^2-r_v\alpha(1+\kappa)\lambda=0 \tag{9}$$

Equations (4*c*) and (4*d*) governing the fluid-phase temperature and the particle-phase temperature fields, respectively, can be combined into a third-order differential equation in H. This can be shown to be (using the solutions for F and F_p in Eq. (8))

$$H'''+CH''+DH'=X\exp(-2\lambda_1\eta)+Y\exp(-2\lambda_2\eta)+Z\exp(-(\lambda_1+\lambda_2)\eta) \tag{10}$$

where

$$C=(r_v^2\mathrm{Pr}-\epsilon)/r_v,\quad D=-\mathrm{Pr}\epsilon(1+\kappa\gamma)$$

$$X=\mathrm{EcPr}C_3^2(2\lambda_1^3A^2+2\kappa\alpha\lambda_1(A-1)^2+\epsilon\lambda_1^2A^2/r_v+\kappa\alpha\epsilon(A-1)^2/r_v+\beta\kappa\epsilon\lambda_1^2/r_v)$$

$$Y=\mathrm{EcPr}C_4^2(2\lambda_2^3B^2+2\kappa\alpha\lambda_2(B-1)^2+\epsilon\lambda_2^2B^2/r_v+\kappa\alpha\epsilon(B-1)^2/r_v+\beta\kappa\epsilon\lambda_2^2/r_v)$$

$$Z=2\mathrm{EcPr}C_3C_4(\lambda_1\lambda_2AB(\lambda_1+\lambda_2)+\kappa\alpha(A-1)(B-1)(\lambda_1+\lambda_2)+\lambda_1\lambda_2\epsilon AB/r_v+\kappa\alpha\epsilon(A-1)(B-1)/r_v+\beta\kappa\epsilon\lambda_1\lambda_2/r_v) \tag{11}$$

Without going into the details (for brevity), Eq. (10) can be solved subject to the appropriate boundary conditions given in Eqs. (6) to yield

$$H=1+C_2\exp(-m_2\eta)+N\exp(-2\lambda_1\eta)+O\exp(-2\lambda_2\eta)+P_1\exp(-(\lambda_1+\lambda_2)\eta)$$

$$m_2=(C+(C^2-4D)^{1/2})/2,\ C_2=H_0-(1+N+O+P_1)$$

$$N=-X/(2\lambda_1(4\lambda_1^2-2\lambda_1C+D)),$$

$$O=-Y(2\lambda_2(4\lambda_2^2-2\lambda_2C+D))$$

$$P_1=-Z((\lambda_1+\lambda_2)((\lambda_1+\lambda_2)^2-(\lambda_1-\lambda_2)C+D)) \tag{12}$$

Knowing H, the solution for H_p from Eq. (4*d*) can then be determined and shown to be

$$H_p=1+Q\exp(-m_2\eta)+R\exp(-2\lambda_1\eta)+S\exp(-2\lambda_2\eta)+U\exp(-(\lambda_1+\lambda_2)\eta)$$

$$Q=\epsilon C_2/(r_v m_2+\epsilon),\quad R=\epsilon N/(2\lambda_1 r_v+\epsilon)$$

$$S=\epsilon O/(2\lambda_2 r_v+\epsilon),\quad U=\epsilon P_1/((\lambda_1+\lambda_2)r_v+\epsilon) \tag{13}$$

The wall heat transfer coefficient $\mathring{q}_w$ can be determined by differentiating Eq. (12*a*) once, evaluating it at $\eta=0$, and then substituting the result into Eq. (7). This can be shown to give

$$\mathring{q}_w=(m_2C_2+2\lambda_1N+2\lambda_2O+(\lambda_1+\lambda_2)P_1)/(\mathrm{Pr\ Ec}) \tag{14}$$

It should be mentioned that in the absence of particle-phase viscous effects ($\beta=0$), the solutions for H, H_p, and $\mathring{q}_w$ reported earlier reduce to those given by Chamkha (1992). It is difficult to gain insight into the thermal behavior of this problem from the form of the results given herein. For this reason, numerical evaluations of the results are performed and graphic solutions are presented and discussed below.

Figures 2 and 3 present the temperature profiles for the fluid and particle phases, respectively, for various values of the temperature inverse Stokes number ϵ. Increases in the values of ϵ cause the thermal interaction between the two phases to increase. This, in turn, increases the interphase energy transfer between the two phases, and, therefore increases the fluid-phase temperature at any position above the plate. This is evident from Fig. 2. For large values of ϵ, thermal equilibrium between the two phases occurs. This is apparent from both Figs. 2 and 3 since the temperature profiles associated with $\epsilon=100$ for both phases are essentially the same.

Figure 4 illustrates the behavior of the wall heat flux for different values of the particle loading κ and the temperature inverse Stokes number ϵ. Increases in the values of κ have a tendency to increase the fluid-phase temperature H and cause it to approach the free-stream temperature faster. This decreases the thermal boundary layer and increases the slope of the temperature profile at the wall, which, in turn, increases the wall heat transfer. This is reflected in the increases in $\mathring{q}_w$

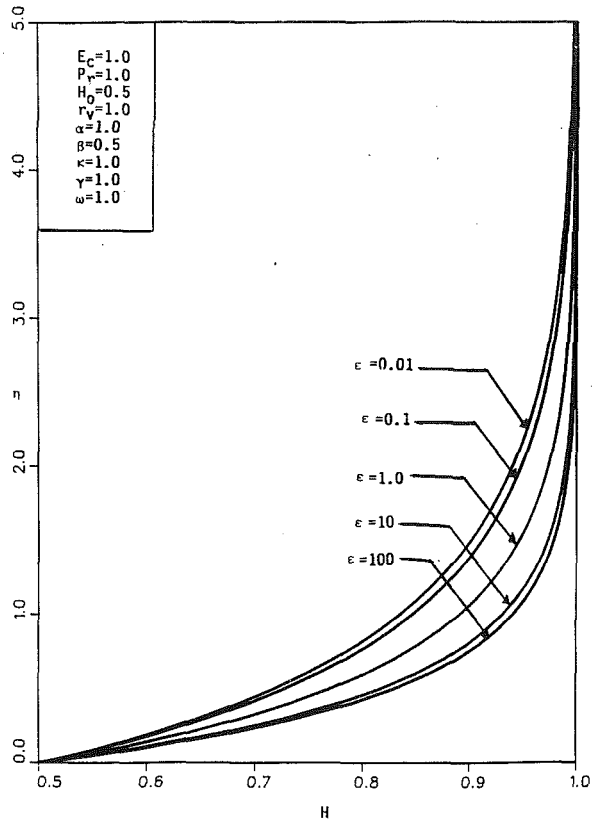

Fig. 2 Fluid-phase temperature profiles

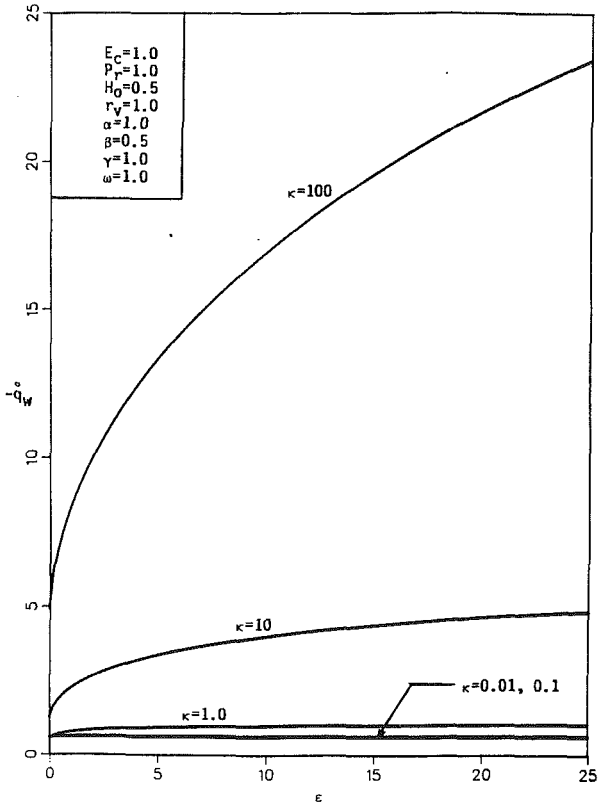

Fig. 4 Wall heat flux coefficient versus ϵ

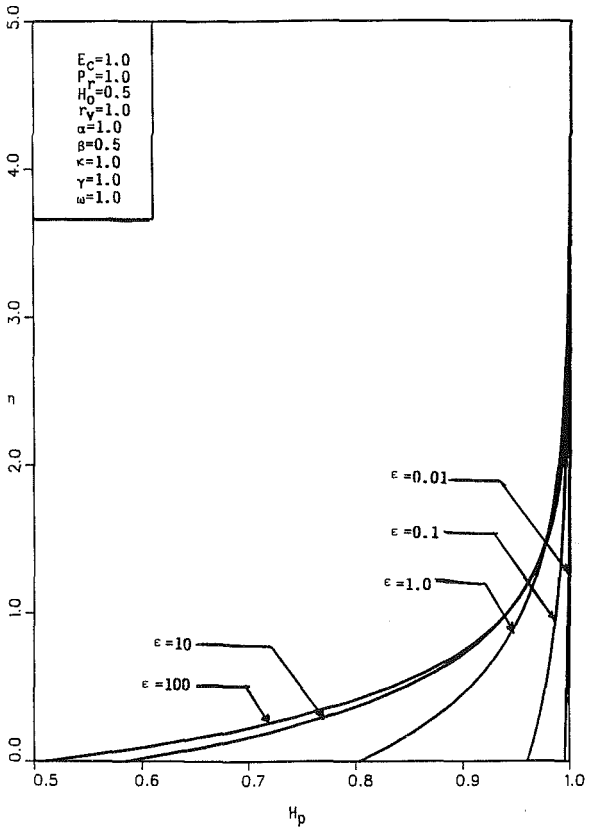

Fig. 3 Particle-phase temperature profiles

as κ increases, shown in Fig. 4. As mentioned before, the fluid-phase temperature above the plate increases by increasing the value of ϵ. This causes the same effect mentioned above, namely an increase in the wall heat flux.

In comparison with the inviscid results ($\beta = 0$) reported by Chamkha (1992), it is observed that the addition of particle-phase viscous effects causes the wall heat transfer to decrease.

Conclusion

The thermal aspects of flow of a dusty gas past an infinite porous flat plate are considered and the solutions are reported in closed form. Numerical evaluations of the exact solutions are performed and presented graphically to illustrate the influence of the various physical parameters on the solutions. It is concluded that, owing the presence of particles, the wall heat transfer coefficient is enhanced. In addition, the inclusion of particle-phase viscosity to the dusty gas model causes a decrease in the heat transfer toward the wall. It is not possible to evaluate these results in the absence of experimental data at present. It is hoped that these results can be utilized as a vehicle for understanding more complex problems.

References

Chamkha, A. J., and Peddieson, J., 1989, "Exact Solutions for the Two-Phase Asymptotic Suction Profile," *Developments in Theoretical and Applied Mechanics*, Vol. 14, pp. 215–222.

Chamkha, A. J., 1992, "Convective Heat Transfer of a Particle Suspension," *AIAA Journal of Thermophysics and Heat Transfer*, Vol. 6, No. 3, pp. 551–553.

Marble, F. E., 1970, "Dynamics of Dusty Gases," *Annual Review of Fluid Mechanics*, Vol. 2, pp. 397–446.

Soo, S. L., 1967, *Fluid Dynamics of Multiphase Systems*, Blaisdell Publishing Company, Waltham, MA.

A Note on Axial-Flow Sensible-Heat Solar-Dynamic Receivers

K. O. Lund[1]

Nomenclature

AF = fluid outlet temperature oscillation amplitude factor $= |\tilde{\psi}(1, p)|$
A_f = heat transfer convection film area $= L\Gamma_f$, m^2
c = specific heat of storage material, kJ/kgK
C_f = fluid heat capacity rate $= (\dot{m}C_p)_f$, W/K
D = flow-tube (hydraulic) diameter, mm
D_R = receiver diameter, m
f = normalized axial source flux
g = normalized temporal source flux
G = FFT transform of $g(p)$
L = length of receiver rods, m
m = linear mass of rod, kg/m
M = mass, kg
N = number of transfer units $= h_f A_f/C_f$
p = scaled time $= t/P$
P = period of orbit = 1.56 h
q_s = solar heat source, W/m
$\tilde{q}_s$ = oscillating part of heat source, W/m
$\bar{q}_s$ = time- and space-averaged heat source, W/m
s = transform variable $= i\omega$
t = time, s, h
t_c = time constant $= mc/h_f\Gamma_f = Mc/h_f A_f$, s, h
T_f = working fluid temperature, K
T_s = storage material temperature, K
x = nondimensional axial coordinate $= X/L$
X = axial coordinate, m
Γ = flow-tube perimeter, m
η = thermal efficiency
λ_m = decay constant for axial flux distribution
ψ = scaled fluid temperature $= h_f\Gamma_f(T_f - T_{fi})/\bar{q}_s$
$\bar{\psi}$ = time-averaged scaled fluid temperature
$\tilde{\psi}$ = oscillating scaled fluid temperature
Ψ = transform of $\tilde{\psi}(x, p)$
σ = argument $= \tau s$
τ = scaled time constant $= t_c/P$
θ = scaled solid temperature $= h_f\Gamma_f(T_s - T_{fi})/\bar{q}_s$
ω = nondimensional frequency

Subscripts

f = fluid
i = inlet
m = maximum
o = outlet
r = rod assembly
R = receiver assembly
s = solid, storage-material

Introduction

The receiver of space-based solar-thermal power systems (solar dynamics) is a critical component that must absorb incoming concentrated solar energy, store part of it for release during eclipse, and deliver a near-constant thermal power for both the solar insolation and eclipse parts of low earth orbit. These requirements have led to latent energy storage using phase-change materials (PCMs), which, however, involve comparatively massive containment canisters (Kerslake and Ibrahim, 1990; Strumpf and Coombs, 1990; Calogeras et al., 1991). Advanced PCM concepts strive to reduce the canister weights (Strumpf and Coombs, 1987; Brege and Heidenreich, 1991), whereas advanced sensible-heat concepts have utilized heat pipes and control logic (Bennett and Lacy, 1988), and carbon-fiber/carbon composites (Perez-Davis et al., 1991). This note uses the Fast Fourier Transform method (FFT) to analyze an axial-flow sensible-heat receiver, and compares its performance to PCM receivers.

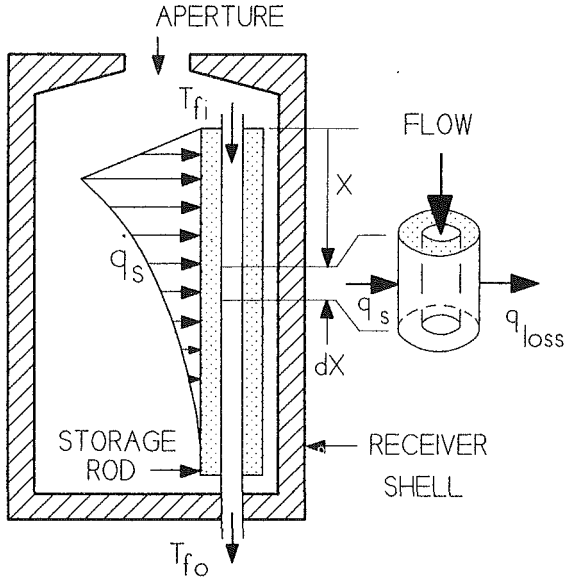

Fig. 1 Schematic cross section of solar dynamic receiver with typical axial distribution of source flux

Formulation of Problem

The basic, axial-flow receiver design in Fig. 1 is considered where n_r rods of sensible heat-storage material (SHM) surrounds n_r flow tubes. The storage-material temperature is radially "lumped" and axial conduction is neglected in the slender rod assembly; thus, an energy balance on the differential solid and fluid elements in Fig. 1 yields

$$mc\frac{\partial T_s}{\partial t} + h_f\Gamma_f(T_s - T_f) = q_s(X, t) - q_{\text{loss}}$$

$$\equiv \bar{q}_s([1 + g(p)]f(x) - [1 - \eta_R]) \quad (1)$$

$$C_f\frac{\partial T_f}{\partial X} = h_f\Gamma_f(T_s - T_f) \quad (2)$$

where the (gas) fluid inlet condition is $T_f(0, t) = T_{fi}$, where $f(x)$ is the axial variation of the source flux shown in Fig. 1, and $g(p)$ represents the "rectangular-wave" periodic time variation (Bennett and Lacy, 1988), shown overlaid in Fig. 2. $f(x)$ is approximated by:

$$f(x) = \begin{cases} f_m x/x_m, & 0 \le x \le x_m \\ f_m e^{-(x - x_m)/\lambda_m}, & x_m < x \le 1 \end{cases} \quad (3)$$

where

$$F(x) = \int_0^x f(z)dz, \quad F(1) = 1,$$

[1]Center for Energy and Combustion Research, University of California—0310, La Jolla, CA 92093-0310.

Contributed by the Heat Transfer Division and presented at the 27th Intersociety Energy Conversion Engineering Conference, San Diego, California, August 3-7, 1992. Manuscript received by the Heat Transfer Division September 1992; revision received August 1993. Keywords: Solar Energy, Space Power Systems, Transient and Unsteady Heat Transfer. Associate Technical Editor: W. A. Fiveland.

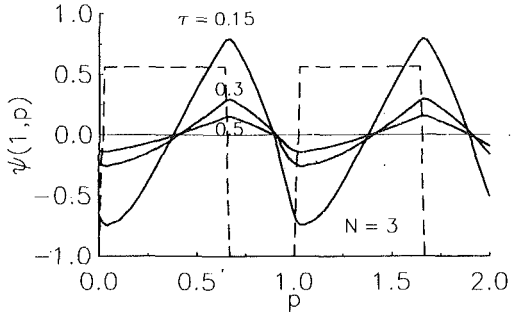

Fig. 2 Oscillating outlet fluid temperatures

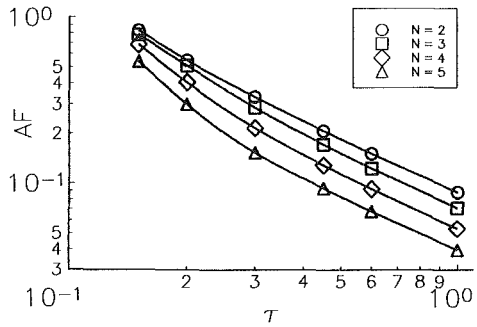

Fig. 3 Oscillation amplitude factor for fluid outlet temperature

and

$$\frac{1}{f_m}=\frac{x_m}{2}+\lambda_m(1-e^{-(1-x_m)/\lambda_m}).$$

For numerical calculations, the following parameter values are used: $f_m=3.88$ at $x_m=0.156$, with $\lambda_m=0.181$, which are typical of distributions obtained from ray tracing (Strumpf and Coombs, 1987). The integrated loss flux is typically less than 15 percent of the captured solar flux, and therefore q_{loss} is taken as constant so that $\eta_R=1-q_{\text{loss}}/\bar{q}_s=\text{const}$ is an input quantity based on other analyses. (Fundamentally, q_{loss} varies nonlinearly in space and time; however, its exact treatment requires receiver shell analysis, adds but little to the overall performance, and is beyond the scope of the present note.)

In nondimensional terms the above equations are:

$$\tau\frac{\partial\theta}{\partial p}+\theta-\psi=[1+g(p)]f(x)-(1-\eta_R) \tag{4}$$

$$\frac{\partial\psi}{\partial x}+N(\psi-\theta)=0 \tag{5}$$

$$\psi(0,p)=0 \tag{6}$$

or, eliminating θ between Eqs. (4) and (5) results in

$$\tau\frac{\partial}{\partial p}\left(\frac{\partial\psi}{\partial x}+N\psi\right)+\frac{\partial\psi}{\partial x}=N\{[1+g]f-(1-\eta_R)\} \tag{7}$$

Here $\tau=t_c/P$, where the usual lumped-mass time constant is $t_c=mc/h_f\Gamma_f=(Mc)_r/h_fA_f$, and $N=h_fA_f/C_f$ is the number of transfer units.

Solution of Equations

For the solution Eqs. (6) and (7) we consider the fluid temperature as the sum of time-averaged and periodic components, $\psi(x,p)=\bar{\psi}(x)+\tilde{\psi}(x,p)$. This yields the periodic equation and the steady-state solutions:

$$\tau\frac{\partial}{\partial p}\left(\frac{\partial\tilde{\psi}}{\partial x}+N\tilde{\psi}\right)+\frac{\partial\tilde{\psi}}{\partial x}=Ng(p)f(x) \tag{8}$$

$$\bar{\psi}(x)=N[F(x)-x(1-\eta_R)] \tag{9}$$

$$\bar{\theta}(x)=f(x)+NF(x)-(1-\eta_R)(1+Nx) \tag{10}$$

In particular, at the outlet, $\bar{\psi}(1)=\eta_RN$, which in dimensional terms is the overall rod energy balance: $Q_n=\eta_RL\bar{q}_s=C_f(\bar{T}_{fo}-T_{fi})$. The solid temperature peaks around $x=x_m$.

A compact solution of the periodic component is obtained by the Laplace transform of Eq. (8):

$$(1+\tau s)\frac{d\Psi}{dx}+\tau sN\Psi=NG(s)f(x) \tag{11}$$

which has the solution

$$\Psi(x,s)=\frac{G(s)}{1+\tau s}I(x,\tau s) \tag{12}$$

where

$$I(x,\sigma)=\int_0^x Ne^{-\frac{N\sigma}{1+\sigma}(x-z)}f(z)dz \tag{13}$$

Now, with $s=i\omega$, the complex valued $G(s)$ may be interpreted as the Fast Fourier Transform of $g(p)$ and, hence, $\Psi(x,s)$ as the FFT of $\tilde{\psi}(x,p)$; thus, the outlet temperature oscillations are given by the inverse $\tilde{\psi}(1,p)=FFT^{-1}\{\Psi(1,s)\}$.

Results

The solution, Eq. (12) and its inverse, is primarily a first-order lag, modified by the integral, Eq. (13). Using 32 data points with a standard FFT algorithm (e.g., Jacquot and Long, 1988), oscillating outlet temperatures were calculated as shown in Fig. 2, in comparison with the original input forcing function, $g(p)$; the maximum amplitude is quickly attenuated with increasing time constant, τ.

The maximum amplitude factor in Fig. 2, $AF\equiv|\tilde{\psi}(1,p)|$, depends on τ and N, and is plotted in Fig. 3; AF is reduced uniformly with τ and N. This is really a design chart for the axial-flow sensible-heat receiver: by knowing τ and N, the AF of the outlet gas temperature is predicted; conversely, if N and the allowable amplitude are specified, the chart determines τ and the required mass of the energy storage rod.

Application

The above is applied to the Space Station conditions with a net average receiver gain of 96.47 kW and inlet and average outlet temperatures of 797 K and 1012 K, for an electrical output of 32 kW (SSF Specifications, 1990). This results in a receiver overall fluid heat capacity rate of $C_{fR}=0.45$ kW/K (851 Btu/hr°F), such that for n_r rods,

$C_f=C_{fR}/n_r=0.45/n_r$ [kW/K]; thus, $N=n_rh_fA_f/0.45$.

Now, h_f and A_f depend on D and L, as does the pressure drop, here specified as 1 percent of inlet pressure, $0.01*356$ kPa = 3.56 kPa (0.51 psi), so that L may be solved in terms of D, n_r, and properties. With the Dittus-Boelter turbulent flow correlations (Incropera and DeWitt, 1985), and He/Xe gas properties (Kerslake and Ibrahim, 1990), the results of such calculations are shown in Table 1, where steady-state Eq. (9) determined the nondimensional amplitude,

$$AF=|\tilde{\psi}(1,p)|=\eta_RN\frac{|\tilde{T}_{fo}|}{\Delta\bar{T}_f}=0.11N \tag{14}$$

and where the allowable physical amplitude was taken as ±28 K (±50°F) and η_R as 85 percent. The time constant, τ, was estimated from Fig. 2 using the calculated values of N and AF, and the energy storage per degree was determined as

Table 1 Summary of calculations

Rod-Structure Receiver								
n_r	D, mm	L, m	h_f, W/m^{2}K	N	AF	τ	$(Mc)_r$, kJ/K	$(Mc)_R$, MJ/K
20	20	0.64	448	0.80	0.088	1.30	132	2.64
	25	1.87	300	1.97	0.216	0.41	102	2.03
	30	4.49	216	4.07	0.448	0.19	97.6	1.95
30	20	1.33	324	1.81	0.199	0.49	74.6	2.24
	25	3.88	217	4.42	0.486	0.17	65.0	1.95
	28	6.67	177	6.96	0.764	0.12	70.2	2.10
40	15	0.56	432	1.02	0.112	1.00	64.2	2.57
	20	2.23	257	3.22	0.354	0.20	48.7	1.95
	25	6.52	172	7.86	0.864	0.10	49.5	1.98
50	15	0.84	750	1.59	0.175	0.66	53.0	2.65
	18	2.01	260	3.30	0.363	0.24	40.0	2.00
	20	3.34	215	5.03	0.553	0.16	38.0	2.03
Slab-Structure Receiver								
D_R, m	D, mm	L, m	h_f, W/m^{2}K	N	AF	τ		$(Mc)_R$, MJ/K
1.7	5	0.47	323	1.82	0.200	0.48		2.20
	8	1.94	202	4.66	0.512	0.16		1.88
	10	3.78	162	7.28	0.800	0.11		2.02

Table 2 Required receiver mass for several materials

Material	c, kJ/kgK	M_R, kg (rods)	M_R, kg (slabs)
Beryllium	3.02	646	622
Boron	2.34	833	803
C/C (41 percent void)	0.70	2786	2686
304 SS	0.61	3197	3082
90 percent Be + 10 percent SS	2.78	701	676
SSF (PCM + Canisters)		1040	

$(Mc)_R = n_r(Mc)_r = n_r h_f A_f \tau P$. Several combinations were obtained, which in each case required at least $(Mc)_R = 1.95$ MJ/K, with $N = 3$ to 4. It is noted that flow rate, pressure drop, average fluid temperature rise, and allowable outlet temperature oscillation were specified for direct comparison to PCM performance. Solid temperatures were also calculated and found not to be excessive.

The rodded structure with flow tubes may not be best for sensible-heat receivers, but a circular "slab" or plate-fin of diameter D_R could be used, with results as shown in Table 1.

For the constraints of this analysis, the required receiver mass is now determined from $M_R = (Mc)_R/c$, as shown in Table 2 using $(Mc)_R = 1.95$ MJ/K for rods and 1.88 MJ/K for slabs; properties are for 1000 K. Beryllium and boron can save weight over the SSF design, but not the 41 percent void carbon/carbon composite (Perez-Davis et al., 1991), nor the stainless steel. The effect of cladding the beryllium with 10 percent 304 stainless steel is, in this analysis, just the weighted average shown.

References

Bennett, T. J., and Lacy, D. E., 1988, "Advanced Sensible Heat Solar Receiver for Space Power," *Proc. 23rd IECEC*, Denver, CO.

Brege, M. A., and Heidenreich, G. R., 1991, "Critical Technology Experiment Results for Light Weight Space Heat Receiver," *Proc. 26th IECEC*, Boston, MA.

Calogeras, J. E., Dustin, M. O., and Secunde, R. R., 1991, "Solar Dynamic Power for Earth Orbit and Lunar Applications," *Proc. 26th IECEC*, Boston, MA, Aug. 4-9, pp. 274-278.

Incropera, F. P., and DeWitt, D. P., 1985, *Introduction to Heat Transfer*, Wiley, New York, p. 360.

Jacquot, R. G., and Long, M., 1988, *Engineering Systems*, Allyn & Bacon.

Kerslake, T. W., and Ibrahim, M. B., 1990, "Analysis of Thermal Energy Storage Material With Change-of-Phase Volumetric Effects," *Proc. ASME Int'l. Solar Energy Conf.*, Miami, FL, Apr. 1-4, pp. 315-325.

Lund, K. O., 1992, "FFT Analysis of Sensible-Heat Solar-Dynamic Receivers," *Proc. 27th IECEC*, San Diego, CA, Vol. 2, pp. 2.359-2.367.

Perez-Davis, M. E., Gaier, J. R., and Petrefski, C., 1991, "Sensible Heat Receiver for Solar Dynamic Space Power System," *Proc. 26th IECEC*, Boston, MA, pp. 297-300.

Space Station Freedom Specification Document, 1990, RI/RD88-633, Chap. 3, "Solar Dynamic Definition," NASA Lewis Research Center, Cleveland, OH, Feb. 13.

Strumpf, H. J., and Coombs, M. G., 1990, "Solar Receiver Experiment for the Space Station Freedom Brayton Engine," ASME *Journal of Solar Energy Engineering*, Vol. 112, pp. 12-18.

Thermal Analysis of the Performance of a High-T_c Superconducting Microbolometer

K. Fushinobu,[1] P. E. Phelan,[2] K. Hijikata,[1] T. Nagasaki,[1] and M. I. Flik[3]

Nomenclature

A = contact area between film and substrate = $2d_1d_3$, m^2
c = specific heat capacity, J kg^{-1} K^{-1}
C = heat capacity, J K^{-1}
d^* = characteristic length, m
d_1, d_2, d_3 = heating element length, thickness, and half-width, m
f = heating modulation frequency, Hz
Fo = Fourier number
G = thermal conductance $\equiv Q/\Delta T$, W K^{-1}
I = bias current, A
k_B = Boltzmann constant = 1.380658×10^{-23} J K^{-1}
L_x, L_y, L_z = substrate length, thickness, and half-width, m
NEP = noise equivalent power, W Hz$^{-1/2}$
Q = film heating rate, W
R = resistance, Ω
S = responsivity, V W^{-1}
T = temperature, K
ΔT = average film temperature increase, K
T_o = environmental temperature, K
α = thermal diffusivity, m^2 s^{-1}
θ = nondimensional temperature increase
λ = thermal conductivity, W m^{-1} K^{-1}
ρ = density, kg m^{-3}
τ, ξ, η, ζ = nondimensional time and spatial coordinates

Subscripts

f = film
in = in-plane
out = out-of-plane
s = substrate

[1]Department of Mechanical Engineering Science, Tokyo Institute of Technology, 2-12-1 Ohokayama, Meguro-ku, Tokyo 152 Japan.

[2]Department of Mechanical Engineering, 2540 Dole St., Holmes 302, University of Hawaii, Honolulu, HI 96822.

[3]Department of Mechanical Engineering, Room 41-206, Massachusetts Institute of Technology, Cambridge, MA 02139.

Contributed by the Heat Transfer Division and presented at the National Heat Transfer Conference San Diego, California, August 9-12, 1992. Manuscript received by the Heat Transfer Division June 1992; revision received July 1993. Keywords: Conduction, Cryogenics. Associate Technical Editor: L. S. Fletcher.

Table 1 Summary of calculations

Rod-Structure Receiver								
n_r	D, mm	L, m	h_f, W/m^{2}K	N	AF	τ	$(Mc)_r$, kJ/K	$(Mc)_R$, MJ/K
20	20	0.64	448	0.80	0.088	1.30	132	2.64
	25	1.87	300	1.97	0.216	0.41	102	2.03
	30	4.49	216	4.07	0.448	0.19	97.6	1.95
30	20	1.33	324	1.81	0.199	0.49	74.6	2.24
	25	3.88	217	4.42	0.486	0.17	65.0	1.95
	28	6.67	177	6.96	0.764	0.12	70.2	2.10
40	15	0.56	432	1.02	0.112	1.00	64.2	2.57
	20	2.23	257	3.22	0.354	0.20	48.7	1.95
	25	6.52	172	7.86	0.864	0.10	49.5	1.98
50	15	0.84	750	1.59	0.175	0.66	53.0	2.65
	18	2.01	260	3.30	0.363	0.24	40.0	2.00
	20	3.34	215	5.03	0.553	0.16	38.0	2.03
Slab-Structure Receiver								
D_R, m	D, mm	L, m	h_f, W/m^{2}K	N	AF	τ		$(Mc)_R$, MJ/K
1.7	5	0.47	323	1.82	0.200	0.48		2.20
	8	1.94	202	4.66	0.512	0.16		1.88
	10	3.78	162	7.28	0.800	0.11		2.02

Table 2 Required receiver mass for several materials

Material	c, kJ/kgK	M_R, kg (rods)	M_R, kg (slabs)
Beryllium	3.02	646	622
Boron	2.34	833	803
C/C (41 percent void)	0.70	2786	2686
304 SS	0.61	3197	3082
90 percent Be + 10 percent SS	2.78	701	676
SSF (PCM + Canisters)		1040	

$(Mc)_R = n_r(Mc)_r = n_r h_f A_f \tau P$. Several combinations were obtained, which in each case required at least $(Mc)_R = 1.95$ MJ/K, with $N = 3$ to 4. It is noted that flow rate, pressure drop, average fluid temperature rise, and allowable outlet temperature oscillation were specified for direct comparison to PCM performance. Solid temperatures were also calculated and found not to be excessive.

The rodded structure with flow tubes may not be best for sensible-heat receivers, but a circular "slab" or plate-fin of diameter D_R could be used, with results as shown in Table 1.

For the constraints of this analysis, the required receiver mass is now determined from $M_R = (Mc)_R/c$, as shown in Table 2 using $(Mc)_R = 1.95$ MJ/K for rods and 1.88 MJ/K for slabs; properties are for 1000 K. Beryllium and boron can save weight over the SSF design, but not the 41 percent void carbon/carbon composite (Perez-Davis et al., 1991), nor the stainless steel. The effect of cladding the beryllium with 10 percent 304 stainless steel is, in this analysis, just the weighted average shown.

References

Bennett, T. J., and Lacy, D. E., 1988, "Advanced Sensible Heat Solar Receiver for Space Power," *Proc. 23rd IECEC*, Denver, CO.

Brege, M. A., and Heidenreich, G. R., 1991, "Critical Technology Experiment Results for Light Weight Space Heat Receiver," *Proc. 26th IECEC*, Boston, MA.

Calogeras, J. E., Dustin, M. O., and Secunde, R. R., 1991, "Solar Dynamic Power for Earth Orbit and Lunar Applications," *Proc. 26th IECEC*, Boston, MA, Aug. 4-9, pp. 274-278.

Incropera, F. P., and DeWitt, D. P., 1985, *Introduction to Heat Transfer*, Wiley, New York, p. 360.

Jacquot, R. G., and Long, M., 1988, *Engineering Systems*, Allyn & Bacon.

Kerslake, T. W., and Ibrahim, M. B., 1990, "Analysis of Thermal Energy Storage Material With Change-of-Phase Volumetric Effects," *Proc. ASME Int'l. Solar Energy Conf.*, Miami, FL, Apr. 1-4, pp. 315-325.

Lund, K. O., 1992, "FFT Analysis of Sensible-Heat Solar-Dynamic Receivers," *Proc. 27th IECEC*, San Diego, CA, Vol. 2, pp. 2.359-2.367.

Perez-Davis, M. E., Gaier, J. R., and Petrefski, C., 1991, "Sensible Heat Receiver for Solar Dynamic Space Power System," *Proc. 26th IECEC*, Boston, MA, pp. 297-300.

Space Station Freedom Specification Document, 1990, RI/RD88-633, Chap. 3, "Solar Dynamic Definition," NASA Lewis Research Center, Cleveland, OH, Feb. 13.

Strumpf, H. J., and Coombs, M. G., 1990, "Solar Receiver Experiment for the Space Station Freedom Brayton Engine," ASME *Journal of Solar Energy Engineering*, Vol. 112, pp. 12-18.

Thermal Analysis of the Performance of a High-T_c Superconducting Microbolometer

K. Fushinobu,[1] P. E. Phelan,[2] K. Hijikata,[1] T. Nagasaki,[1] and M. I. Flik[3]

Nomenclature

A = contact area between film and substrate = $2d_1d_3$, m^2
c = specific heat capacity, J kg^{-1} K^{-1}
C = heat capacity, J K^{-1}
d^* = characteristic length, m
d_1, d_2, d_3 = heating element length, thickness, and half-width, m
f = heating modulation frequency, Hz
Fo = Fourier number
G = thermal conductance $\equiv Q/\Delta T$, W K^{-1}
I = bias current, A
k_B = Boltzmann constant = 1.380658×10^{-23} J K^{-1}
L_x, L_y, L_z = substrate length, thickness, and half-width, m
NEP = noise equivalent power, W Hz$^{-1/2}$
Q = film heating rate, W
R = resistance, Ω
S = responsivity, V W^{-1}
T = temperature, K
ΔT = average film temperature increase, K
T_o = environmental temperature, K
α = thermal diffusivity, m^2 s^{-1}
θ = nondimensional temperature increase
λ = thermal conductivity, W m^{-1} K^{-1}
ρ = density, kg m^{-3}
τ, ξ, η, ζ = nondimensional time and spatial coordinates

Subscripts

f = film
in = in-plane
out = out-of-plane
s = substrate

[1]Department of Mechanical Engineering Science, Tokyo Institute of Technology, 2-12-1 Ohokayama, Meguro-ku, Tokyo 152 Japan.

[2]Department of Mechanical Engineering, 2540 Dole St., Holmes 302, University of Hawaii, Honolulu, HI 96822.

[3]Department of Mechanical Engineering, Room 41-206, Massachusetts Institute of Technology, Cambridge, MA 02139.

Contributed by the Heat Transfer Division and presented at the National Heat Transfer Conference San Diego, California, August 9-12, 1992. Manuscript received by the Heat Transfer Division June 1992; revision received July 1993. Keywords: Conduction, Cryogenics. Associate Technical Editor: L. S. Fletcher.

Introduction

One of the most promising applications of thin-film high-temperature superconductors (HTSC) is a bolometer operating above liquid-nitrogen (LN) temperature. A bolometer functions as a radiation detector by absorbing incident radiation, which causes its temperature to increase and thus changes its temperature-dependent electrical resistivity. By passing a bias current through the bolometer, the change in output voltage corresponding to the incident radiation can be detected. In order to optimize the bolometer design, it is crucial to understand the system thermal response, which can only be done through careful thermal analysis.

There are two important considerations when calculating the thermal response of a HTSC bolometer. First, it can be classified as a periodic steady-state heat conduction problem, since the radiation incident on the bolometer, which consists of a thin-film sensing element deposited on a relatively massive substrate, is chopped (at a frequency f) for noise reduction, resulting in periodic steady-state heating of the element and heat conduction to the substrate. Secondly, we have to deal with widely differing length scales. The sensing element is fabricated as small as possible—on the scale of microns or less—to allow for a fast, large thermal response. The substrate, on the other hand, has dimensions on the order of 1000 times larger than those of the sensing element. These two features make a numerical simulation of the thermal response difficult, because of the long computational time required for a transient numerical calculation to reach a periodic steady-state solution, and the large number of grid points required to resolve the temperature over the different length scales. To our knowledge, no numerical analysis has been reported that simultaneously incorporates these two features.

The performance of HTSC microbolometers is greatly impacted by both the sensing element temperature (T), and the volume-averaged temperature rise of the sensing element (ΔT) over the environmental temperature (T_o). Following Newhouse (1975), the noise equivalent power (NEP), which is a parameter used to characterize the performance of radiation detectors and will be discussed later, is a sensitive function of both T and ΔT. Therefore, accurate thermal modeling is essential to optimize the microbolometer design.

For these reasons, some studies have been presented that predict the temperature increase of microbolometers. Most previous analytical investigations of the performance of HTSC bolometers employed a rough approximation of the temperature field. Hu and Richards (1989) simplified the problem by modeling the film as a hemisphere, having a surface area equal to that of the film, that generated heat in a semi-infinite substrate. Flik et al. (1990) performed a detailed numerical calculation of the bolometric response of HTSC films to optical pulses. Their model considered only a single pulse and was one dimensional, while the actual temperature field in a microbolometer is three dimensional.

The authors earlier presented a three-dimensional numerical calculation (Fushinobu et al., 1992), which modeled the HTSC microbolometer fabricated by Nahum et al. (1991). In that study, we employed both a complex temperature (Arpaci, 1966), and the domain decomposition technique (Nagasaki et al., 1992) for accurate computation of the periodic steady-state heat conduction from the small sensing element to the much larger substrate. In the present study, we present a thermal noise analysis of the microbolometer to demonstrate the importance of a rigorous thermal analysis for bolometer design.

Numerical Model

Figure 1 shows a schematic of the computational model. The dimensions are $L_x = 5$ mm, $L_y = 0.5$ mm, $L_z = 2.5$ mm, $d_1 = 13$ μm, $d_2 = 0.1$ μm, and $d_3 = 3$ μm. We adopt the domain decomposition technique in order to resolve accurately the microscopic details of the macroscopic temperature field. Spatially uniform heat generation caused by radiation is assumed to occur in the film, but substrate radiation absorption is neglected. Joule heating in the sensing element, which is due to the bias current, is neglected, although a rough calculation shows that it is important at higher bias currents.

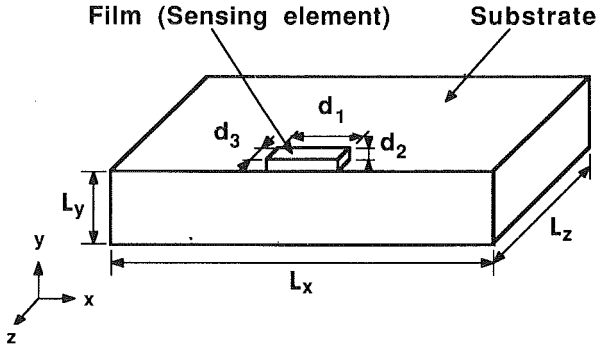

Fig. 1 Schematic diagram of the computational model, which is only half of the physical domain due to symmetry

The previously derived governing equations (Fushinobu et al., 1992) are given below in nondimensional form:

Film:

$$\frac{\partial\theta}{\partial\tau} = \mathrm{Fo}_{f,\,in}\left(\frac{\partial^2\theta}{\partial\xi^2}+\frac{\partial^2\theta}{\partial\zeta^2}\right) + \mathrm{Fo}_{f,\,\mathrm{out}}\left(\frac{\partial^2\theta}{\partial\eta^2}\right) + \frac{\sigma_{\mathrm{vol}}}{2}\left[1+e^{i\tau}\right] \quad (1)$$

Substrate:

$$\frac{\partial\theta}{\partial\tau} = \mathrm{Fo}_s\left(\frac{\partial^2\theta}{\partial\xi^2}+\frac{\partial^2\theta}{\partial\eta^2}+\frac{\partial^2\theta}{\partial\zeta^2}\right) \quad (2)$$

where the nondimensional variables are defined based on the characteristic length, $d^* \equiv \sqrt{2d_1d_3} = \sqrt{A}$, the characteristic time, $t^* = 1/(2\pi f)$, and the characteristic temperature rise, $\Delta T^* = Q/(\lambda_s d^*)$: $\xi = x/d^*$, $\eta = y/d^*$, $\zeta = z/d^*$, $\tau = t/t^*$, and $\theta = (T - T_o)/\Delta T^*$. The nondimensional source term σ_{vol} and Fourier numbers are given by

$$\sigma_{\mathrm{vol}} = \frac{q_{\mathrm{vol}}}{(\rho_f c_f \Delta T^*)/t^*},\quad \mathrm{Fo}_s = \frac{\alpha_s}{(d^*)^2 2\pi f},$$

$$\mathrm{Fo}_{f,\,in} = \frac{\alpha_{f,\,in}}{(d^*)^2 2\pi f},\quad \mathrm{Fo}_{f,\,\mathrm{out}} = \frac{\alpha_{f,\,\mathrm{out}}}{(d^*)^2 2\pi f} \quad (3)$$

in which the thermal diffusivities are given by $\alpha_s = \lambda_s/(\rho_s c_s)$, $\alpha_{f,\,in} = \lambda_{f,\,in}/(\rho_f c_f)$, and $\alpha_{f,\,\mathrm{out}} = \lambda_{f,\,\mathrm{out}}/(\rho_f c_f)$, where λ, ρ, and c are the thermal conductivity, the density, and the specific heat, respectively, while the subscript s refers to the substrate, and the subscript f refers to the film. The quantity Q is the film heating rate, and q_{vol} is the volumetric film heating rate. The thermophysical properties are assumed to be independent of the temperature, but the anisotropy of the superconducting film is taken into account by taking different values of λ for the direction parallel to the film/substrate interface (in-plane) and for the direction perpendicular to that interface (out-of-plane). The nondimensional temperature increase θ is separated into a steady component θ_t, and a periodic component, θ_p. The periodic component of θ is caused by the sinusoidal radiative heat input. A complex temperature (Arpaci, 1966) is introduced to calculate θ_p, which equals the real part of the complex temperature θ_p^{ξ}. The boundary conditions are as follows: The entire surface of the film/substrate system is assumed to be adiabatic except for the substrate lower surface, which is maintained at a constant temperature, T_o. The continuity of heat

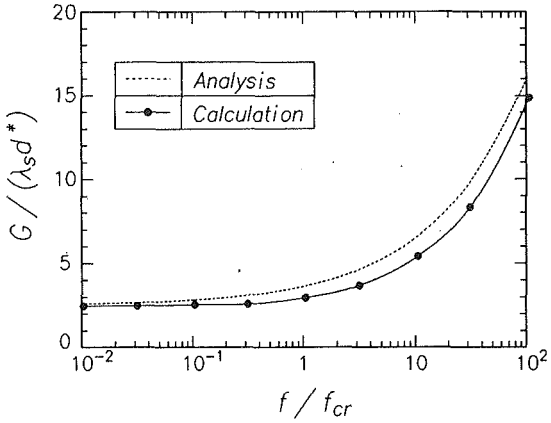

Fig. 2 Numerical ('Calculation') and approximate analytical thermal conductance between the microbolometer and the substrate as a function of modulation frequency

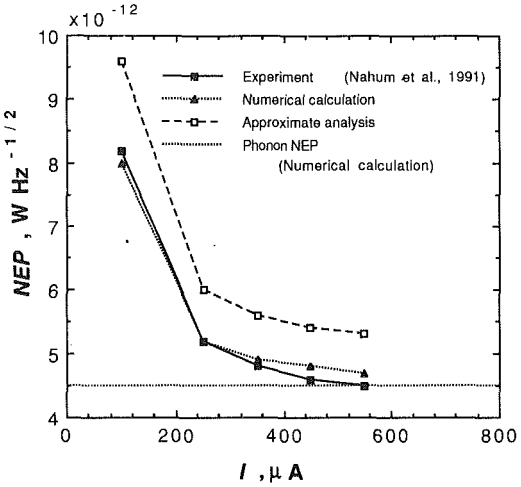

Fig. 3 Comparison of the noise equivalent power (NEP) between the experimental data and the approximate analysis (Nahum et al., 1991), and our numerical results. The chopping frequency is 10 kHz.

flux is imposed at the interface between the substrate and the film, but the film/substate boundary resistance is neglected. The finite difference method is used to discretize the three-dimensional governing equations, which are solved in the entire film and substrate with the SOR (Successive Over-Relaxation) method iteratively until the convergence criterion is fulfilled in all subdivided domains. A detailed discussion of the model and the solution procedure is given in the previous report (Fushinobu et al., 1992).

Results and Discussions

Thermal Conductance. Figure 2 provides a comparison between the present three-dimensional calculation and the earlier approximate analysis presented by Hu and Richards (1989), by showing the dependence of the nondimensionalized conductance $G/(\lambda_s d^*)$ on the nondimensionalized frequency f/f_{cr}. The thermal conductance G is defined as $G \equiv Q/\Delta T$. The critical frequency f_{cr}, which is the inverse of the time scale required for heat to diffuse a distance d^* from the film, is given by $f_{cr} = \alpha_s/(\pi A)$. For the conditions considered here, $f_{cr} = 9.5 \times 10^3$ Hz. The approximate analysis by Hu and Richards (1989) modeled the film as a hemisphere, embedded in the substrate, having an area equal to A, or $2\pi a^2 = A$, where a is the radius of the hemisphere. Although these two results demonstrate the same trend in terms of variation with frequency, the approximate analysis tends to predict consistently higher values, by as much as about 25 percent at $f/f_{cr} = 3.2$.

Noise Equivalent Power. Although the responsivity, which is the output bolometer voltage divided by the incident radiative power, is a basic characteristic parameter of an infrared detector, the ultimate performance of the detector is determined by the minimum power it can detect and limited by the noise generated in the detector. The performance of infrared detectors is therefore better characterized by the noise equivalent power (NEP), which is defined as the output noise voltage divided by the responsivity per square root of the bandwidth (Newhouse, 1975). According to Nahum et al. (1991), the optical NEP, in which the responsivity is defined as the output voltage divided by the power absorbed in the film, is written as follows:

$$\mathrm{NEP} = \frac{1}{\eta}\left[4k_B T^2 G(f) + \frac{4k_B TR}{|S|^2} + (\mathrm{NEP})_{1/f}^2 + \frac{4k_B T_n R}{|S|^2}\right]^{1/2} \quad (4)$$

where η is the optical efficiency (the ratio of the power absorbed in the film to the incident power), k_B the Boltzmann constant, R the film electrical resistance at the midpoint of its transition, S the responsivity, and T_n is the amplifier noise temperature. The first term is the phonon noise, the second term is the Johnson noise, the third term is the $1/f$ noise in the film, and the fourth term is the amplifier noise. The responsivity, S, is given by

$$S = \frac{I(dR/dT)}{G(f) + 2\pi i f C} \quad (5)$$

where I is the bias current, and C is the film heat capacity.

The NEP is profoundly influenced by the film temperature, i.e., the temperature of the sensing element. This is due to the fact that the phonon noise and the Johnson noise, which are the predominant noise sources in the HTSC microbolometer, result from fluctuations, both in the film temperature and in the electromagnetic field in the film, respectively (Newhouse, 1975). This can be seen in Eq. (4) where T is included not only explicitly, but also implicitly through G, R, and S. The film temperature rise ΔT also impacts the NEP, since $G = Q/\Delta T$. Therefore, an accurate noise analysis of a microbolometer, that is the calculation of the NEP, requires a rigorous thermal analysis of the device.

Using the values of G in Fig. 2, we can calculate the electrical NEP by considering only the first two terms of Eq. (1), and taking $\eta = 1$ (Nahum et al., 1991). Figure 3 shows a comparison between the electrical NEP measured in the experiment (Nahum et al., 1991) and our numerical results. The chopping frequency f is 10 kHz. Note that in our calculations, the values of R and dR/dT are taken from Fig. 2 of Nahum et al. (1991), which is rigorously valid only for $I = 100\ \mu A$. The actual values of R and dR/dT may be slightly different at other bias currents. In spite of this assumption, good agreement is obtained between the calculated and experimental results. In Fig. 3, the calculated NEP based on the approximate analysis is also shown. Since the approximate analysis gives a higher value of G than does the numerical calculation, the value of the NEP is also higher.

Figure 3 also shows that, at higher bias currents, the performance of a microbolometer is effectively limited by the phonon NEP,

$$\mathrm{NEP}_{\mathrm{phonon}} = \{4k_B T^2 G(f)\}^{1/2}. \quad (6)$$

Since we neglected the Joule heating term in our computation, as mentioned earlier, G is independent of I, and so is $\mathrm{NEP}_{\mathrm{phonon}}$. However, in a real microbolometer, the effect of the Joule heating term, which would tend to decrease G, cannot be neglected at high bias currents.

Conclusions

A numerical calculation has been carried out to predict the themal response of a microbolometer constructed from a Y-Ba-Cu-O thin film. The model is three dimensional, and it uses a domain decomposition technique in order to resolve the microscopic thermal phenomena over the macroscopic domain. Because the film is heated periodically, a complex temperature is employed that permits calculation of the periodic steady-state temperature.

The noise equivalent power (NEP) based on our numerical analysis shows good agreement with experimental results. A comparison of the present numerical results with the approximate analysis of Hu and Richards (1989), who modeled the film as a hemispherical heat source embedded in the substrate, indicates their analysis predicts relatively higher values of the NEP due to their prediction of G. The importance of an accurate prediction of the temperature increase is therefore clear for the purpose of designing HTSC microbolometers.

Acknowledgments

We would like to thank M. Nahum and Q. Hu for their kind help. Two of the authors (K.F. and P.E.P.) acknowledge the support of the Japan Society for the Promotion of Science.

References

Arpaci, V. S., 1966, *Conduction Heat Transfer*, Addison-Wesley, Boston, MA, pp. 324-327.

Flik, M. I., Phelan, P. E., and Tien, C. L., 1990, "Thermal Model for the Bolometric Response of High-T_c Superconducting Films to Optical Pulses," *Cryogenics*, Vol. 30, pp. 1118-1128.

Fushinobu, K., Phelan, P. E., Hijikata, K., Nagasaki, T., and Flik, M. I., 1992, "Periodic Steady-State Thermal Analysis of a High-T_c Superconducting Microbolometer," *Heat Transfer on the Microscale*, K. S. Udell, R. O. Buckius, and F. M. Gerner, eds., ASME HTD-Vol. 200, pp. 89-95.

Hu, Q., and Richards, P. L., 1989, "Design Analysis of a High-T_c Superconducting Microbolometer," *Applied Physics Letters*, Vol. 55, pp. 2444-2446.

Nagasaki, T., Hijikata, K., Fushinobu, K., and Phelan, P. E., 1992, "Numerical Simulation of the Conjugate Direct Cooling of a Micro Heat Generating Element," *Proc. Joint ASME/JSME Conference on Electronic Packaging*, pp. 217-223.

Nahum, M., Hu, Q., Richards, P. L., Sachtjen, S. A., Newman, N., and Cole, B. F., 1991, "Fabrication and Measurement of High-T_c Superconducting Microbolometers," *IEEE Transactions on Magnetics*, Vol. 27, pp. 3081-3084.

Newhouse, V. L., 1975, *Applied Superconductivity*, Academic Press, New York, pp. 284-294.

Experimental Study of Axial Temperature Profile Characteristics in a Purex Process Pulsed Column

T. Tsukada[1] and K. Takahashi[1]

Nomenclature

A = specific area of dispersion drop, cm^{-1}
C = specific heat, J/g°C
C_M = specific heat of column components, J/g
d = column diameter, cm
d_{32} = Sauter diameter, cm
E = effective longitudinal thermal diffusivity, cm^2/s
H = column height, cm
H_V = volumetric heat transfer coefficient, $J/cm^3s°C$
h = heat transfer coefficient between aqueous and organic phases, $J/cm^2s°C$
h_g = heat transfer coefficient for column wall, $J/cm^2s°C$
L = length of heat source section, cm
Q = hot water heat supply rate, J/s
q = volumetric heat generation rate, J/cm^3s
R = heat source existing rate; $R_a + R_o = 1$
S = specific area of column wall per 1 cm^3 of continuous phase, cm^{-1}
T = temperature, °C
T_g = air temperature, °C
T_P = peak temperature, °C
t = time, s
U = volumetric flux, cm/s
V_h = hot water volumetric flow rate, cm^3/s
X = aqueous equivalent uranium concentration, g/l
z = height, cm
ΔH_R = uranium extraction heat, J/g
Λ = heat capacity ratio
ρ = density, g/cm^3
ϕ = holdup

Subscripts

a = aqueous phase
f = feed
h = injected hot water
o = organic phase

Introduction

The uranium and plutonium found in spent nuclear fuel are conventionally recovered in commercial reprocessing plants using the Purex process, which employs a pulsed column extractor. These two elements are completely extracted within a small-length zone located near the top of the column, termed here the "uranium extraction zone." However, when the process disturbances occur such as a decrease in the solvent flow rate, an increase in feed solution flow rate, or an increase in the uranium concentration of the feed solution, the solvent's uranium concentration at the top of the column exceeds its saturation level, thereby resulting in the uranium extraction zone migrating to the bottom of the column. Since the plutonium distribution coefficient becomes very small in this condition, plutonium initially extracted by the solvent phase in the lower part of the column is stripped in the uranium extraction zone by the aqueous phase and eventually accumulates in the column. To prevent this plutonium accumulation, thus ensuring criticality safety is maintained, the position and movement behavior of the extraction zone must be detected.

It was reported that axial temperature profiles observed in a pulsed column originated from the reaction heat produced by uranium extraction, and also that these temperature data could be utilized to determine the uranium extraction zone.

Previously, temperature profiles in a pulsed column were estimated using the simulation code we developed, which showed that the flow rate of both the aqueous and organic phases and the position of the heat source were the dominant factors affecting temperature profile characteristics. This led to the present study, in which the model accuracy was estimated experimentally and heat transfer coefficient was evaluated.

Liquid/liquid direct contactors, e.g., spray and pulsed columns, have been extensively developed and studied for use as mass transfer contactors. In addition, this type of direct contactor has been used as a heat exchanger for geothermal applications (Jacobs, 1985) and also in sea water distillation

[1]Nuclear Fuel Section, Nuclear Engineering Department, Komae Research Laboratory, Central Research Institute of Electric Power Industry (CRIEPI), 11-1, Iwato Kita 2-chome, Komae-shi, Tokyo 201, Japan.

Contributed by the Heat Transfer Division of THE AMERICAN SOCIETY OF MECHANICAL ENGINEERS. Manuscript received by the Heat Transfer Division July 1992; revision received May 1993. Keywords: Direct-Contact Heat Transfer, Heat Exchangers, Mass Transfer. Associate Technical Editor: J. H. Kim.

Conclusions

A numerical calculation has been carried out to predict the themal response of a microbolometer constructed from a Y-Ba-Cu-O thin film. The model is three dimensional, and it uses a domain decomposition technique in order to resolve the microscopic thermal phenomena over the macroscopic domain. Because the film is heated periodically, a complex temperature is employed that permits calculation of the periodic steady-state temperature.

The noise equivalent power (NEP) based on our numerical analysis shows good agreement with experimental results. A comparison of the present numerical results with the approximate analysis of Hu and Richards (1989), who modeled the film as a hemispherical heat source embedded in the substrate, indicates their analysis predicts relatively higher values of the NEP due to their prediction of G. The importance of an accurate prediction of the temperature increase is therefore clear for the purpose of designing HTSC microbolometers.

Acknowledgments

We would like to thank M. Nahum and Q. Hu for their kind help. Two of the authors (K.F. and P.E.P.) acknowledge the support of the Japan Society for the Promotion of Science.

References

Arpaci, V. S., 1966, *Conduction Heat Transfer*, Addison-Wesley, Boston, MA, pp. 324-327.

Flik, M. I., Phelan, P. E., and Tien, C. L., 1990, "Thermal Model for the Bolometric Response of High-T_c Superconducting Films to Optical Pulses," *Cryogenics*, Vol. 30, pp. 1118-1128.

Fushinobu, K., Phelan, P. E., Hijikata, K., Nagasaki, T., and Flik, M. I., 1992, "Periodic Steady-State Thermal Analysis of a High-T_c Superconducting Microbolometer," *Heat Transfer on the Microscale*, K. S. Udell, R. O. Buckius, and F. M. Gerner, eds., ASME HTD-Vol. 200, pp. 89-95.

Hu, Q., and Richards, P. L., 1989, "Design Analysis of a High-T_c Superconducting Microbolometer," *Applied Physics Letters*, Vol. 55, pp. 2444-2446.

Nagasaki, T., Hijikata, K., Fushinobu, K., and Phelan, P. E., 1992, "Numerical Simulation of the Conjugate Direct Cooling of a Micro Heat Generating Element," *Proc. Joint ASME/JSME Conference on Electronic Packaging*, pp. 217-223.

Nahum, M., Hu, Q., Richards, P. L., Sachtjen, S. A., Newman, N., and Cole, B. F., 1991, "Fabrication and Measurement of High-T_c Superconducting Microbolometers," *IEEE Transactions on Magnetics*, Vol. 27, pp. 3081-3084.

Newhouse, V. L., 1975, *Applied Superconductivity*, Academic Press, New York, pp. 284-294.

Experimental Study of Axial Temperature Profile Characteristics in a Purex Process Pulsed Column

T. Tsukada[1] and K. Takahashi[1]

Nomenclature

A = specific area of dispersion drop, cm^{-1}
C = specific heat, J/g°C
C_M = specific heat of column components, J/g
d = column diameter, cm
d_{32} = Sauter diameter, cm
E = effective longitudinal thermal diffusivity, cm^2/s
H = column height, cm
H_V = volumetric heat transfer coefficient, $J/cm^3s°C$
h = heat transfer coefficient between aqueous and organic phases, $J/cm^2s°C$
h_g = heat transfer coefficient for column wall, $J/cm^2s°C$
L = length of heat source section, cm
Q = hot water heat supply rate, J/s
q = volumetric heat generation rate, J/cm^3s
R = heat source existing rate; $R_a + R_o = 1$
S = specific area of column wall per 1 cm^3 of continuous phase, cm^{-1}
T = temperature, °C
T_g = air temperature, °C
T_P = peak temperature, °C
t = time, s
U = volumetric flux, cm/s
V_h = hot water volumetric flow rate, cm^3/s
X = aqueous equivalent uranium concentration, g/l
z = height, cm
ΔH_R = uranium extraction heat, J/g
Λ = heat capacity ratio
ρ = density, g/cm^3
ϕ = holdup

Subscripts

a = aqueous phase
f = feed
h = injected hot water
o = organic phase

Introduction

The uranium and plutonium found in spent nuclear fuel are conventionally recovered in commercial reprocessing plants using the Purex process, which employs a pulsed column extractor. These two elements are completely extracted within a small-length zone located near the top of the column, termed here the "uranium extraction zone." However, when the process disturbances occur such as a decrease in the solvent flow rate, an increase in feed solution flow rate, or an increase in the uranium concentration of the feed solution, the solvent's uranium concentration at the top of the column exceeds its saturation level, thereby resulting in the uranium extraction zone migrating to the bottom of the column. Since the plutonium distribution coefficient becomes very small in this condition, plutonium initially extracted by the solvent phase in the lower part of the column is stripped in the uranium extraction zone by the aqueous phase and eventually accumulates in the column. To prevent this plutonium accumulation, thus ensuring criticality safety is maintained, the position and movement behavior of the extraction zone must be detected.

It was reported that axial temperature profiles observed in a pulsed column originated from the reaction heat produced by uranium extraction, and also that these temperature data could be utilized to determine the uranium extraction zone.

Previously, temperature profiles in a pulsed column were estimated using the simulation code we developed, which showed that the flow rate of both the aqueous and organic phases and the position of the heat source were the dominant factors affecting temperature profile characteristics. This led to the present study, in which the model accuracy was estimated experimentally and heat transfer coefficient was evaluated.

Liquid/liquid direct contactors, e.g., spray and pulsed columns, have been extensively developed and studied for use as mass transfer contactors. In addition, this type of direct contactor has been used as a heat exchanger for geothermal applications (Jacobs, 1985) and also in sea water distillation

[1]Nuclear Fuel Section, Nuclear Engineering Department, Komae Research Laboratory, Central Research Institute of Electric Power Industry (CRIEPI), 11-1, Iwato Kita 2-chome, Komae-shi, Tokyo 201, Japan.

Contributed by the Heat Transfer Division of THE AMERICAN SOCIETY OF MECHANICAL ENGINEERS. Manuscript received by the Heat Transfer Division July 1992; revision received May 1993. Keywords: Direct-Contact Heat Transfer, Heat Exchangers, Mass Transfer. Associate Technical Editor: J. H. Kim.

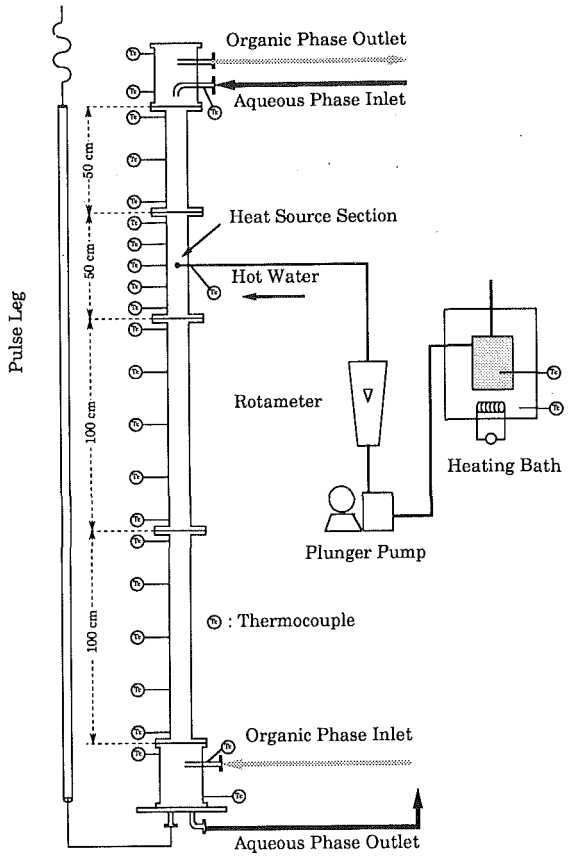

Fig. 1 Schematic diagram of the experimental pulsed column

equipment (Woodward, 1961) since it does not suffer from the scale/corrosion problems normally associated with heat transfer walls.

Direct-contact heat exchangers have had their heat transfer characteristics analyzed in detail (e.g., Jacobs, 1988), yet no previously reported investigations have been directed at clarifying the heat transfer phenomena in a pulsed column having an inner heat source, nor have they especially focused on variations occurring in the column's temperature profiles under different operating conditions.

To elucidate these phenomena, a small pulsed column utilizing deionized water and 30 percent tri-*n*-butyl-phosphate(TBP)/*n*-dodecane was fabricated. The experimental setup incorporated a heat source section, which was able to provide the same quantity of heat assumed to be generated during the uranium extraction process, and thus it enabled the temperature profiles for various heating and operating conditions to be measured.

Experiment and Calculation Model

Pulsed Column. A cylindrical type pulsed column (height: 3 m, diameter: 10 cm) was constructed having sieve plates installed for flow distribution (Fig. 1). The organic phase (30 percent TBP/*n*-dodecane) is fed into the column bottom as a continuous phase, whereas the aqueous phase (deionized water) is fed into the top as a dispersion phase.

Twenty thermocouples with an accuracy of ±0.1°C were placed along the column to measure vertical temperature distribution. A further five thermocouples were placed at the inlets and outlets of each phase.

Heat Source Section. Hot water was used to simulate the uranium extraction reaction heat, being injected by the heat source section at a specified column height where the uranium extraction heat source is assumed to exist (Fig. 2). Water was

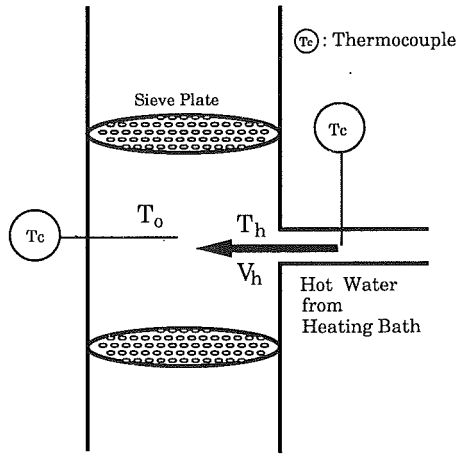

Fig. 2 Pulsed column heat source location

warmed to ~90°C in a heating bath and then transported by a plunger pump through a rotameter to the column injection point (~60°C).

The hot water temperature at the injection point (T_h) and the temperature of continuous phase near this point (T_o) were measured continuously during the experiments (Fig. 2). The input of heat in the hot water stream gives an effective local heat supply rate, which can be calculated by

$$Q = (T_h - T_0)(\rho C)_h V_h \quad \text{(J/s)} \tag{1}$$

This heat supply rate is equivalent to that given by uranium extraction from an aqueous feed stream, and converted by

$$X = \frac{Q \times 1000}{(-\Delta H_R)\pi\left(\frac{d}{2}\right)^2 U_a} \quad \text{(g/l)}, \tag{2}$$

where X represents the aqueous uranium concentration whose transfer into the organic phase would generate heat at the same rate as the heat input due to the hot water feed in the present work.

The column is comprised of four sections: two 50-cm-long upper sections and two 100-cm-long lower ones (Fig. 1). The hot water injection point is located at the center of one of the 50-cm-long sections. This design allowed the heat source location to be varied by changing the positions of the sections.

Calculation Model. In order to analyze temperature profile characteristics in a pulsed column, the one-dimensional dispersion model (Miyauchi and Vermeulen, 1963) was employed, which includes (1) effective longitudinal thermal diffusivities, E; (2) volumetric flux, U; (3) heat transfer between the aqueous and organic phases, h; (4) heat generation by uranium extraction, q; and (5) heat loss from the column wall, h_g.

Under the assumption that the injected hot water is almost instantaneously and uniformly dispersed within a short, narrow mixing area, the volumetric heat generation rate can be expressed.

$$q = \frac{Q}{\pi\left(\frac{d}{2}\right)^2 \cdot L} \quad \text{(J/cm}^3\text{s)} \tag{3}$$

where L is the length of the heat source section.

Since T_h and T_o do not remain constant during column operation, time-dependent measured values of these temperatures were input into the calculation code to model temperature profiles during transient conditions.

Aqueous and organic phase feed temperatures (T_{of}, T_{af}), used as boundary conditions, were input into the code similarly to T_h and T_o.

The aqueous phase volumetric flux below the heat source

location increases due to the injection of hot water at the heat source location; thus this volumetric flux was modified as

$$U_a = U_{af} + \frac{V_h}{\pi\left(\frac{d}{2}\right)^2} \quad \text{(cm/s)} \tag{4}$$

Furthermore, the heat capacity of the column wall and the sieve plates (C_M) must be taken into account to analyze a proper heat balance.

The resultant basic heat transfer equations used to analyze the experimental data are as follows:

For the aqueous phase (dispersion phase)

$$\phi_a\{(\rho C)_a + C_M\}\frac{\partial T_a}{\partial t} = (\rho C)_a E_a \frac{\partial^2 T_a}{\partial z^2} + (\rho CU)_a \frac{\partial T_a}{\partial z} + hA(T_o - T_a) + \phi_a R_a q \tag{5}$$

and for the organic phase (continuous phase)

$$\phi_o\{(\rho C)_o + C_M\}\frac{\partial T_o}{\partial t} = (\rho C)_o E_o \frac{\partial^2 T_o}{\partial z^2} - (\rho CU)_o \frac{\partial T_o}{\partial z} + hA(T_a - T_o) + \phi_o R_o q - h_g S(T_o - T_g) \tag{6}$$

where $R_a + R_o = 1$.

The boundary conditions are:

for the aqueous phase (dispersion phase)

$z = 0$:

$$\frac{\partial T_a}{\partial z} = 0 \tag{7}$$

$z = H$:

$$E_a \frac{\partial T_a}{\partial z} + U_a(T_a - T_{af}(t)) = 0 \tag{8}$$

and for the organic phase (continuous phase)

$z = 0$:

$$E_o \frac{\partial T_o}{\partial z} - U_o(T_o - T_{of}(t)) = 0 \tag{9}$$

$z = H$:

$$\frac{\partial T_o}{\partial z} = 0 \tag{10}$$

These equations were subsequently solved numerically using the finite-element method.

Results and Discussion

Effects of the Heat Capacity Ratio. The previously conducted numerical analysis showed that the heat capacity ratio between the two flows

$$\Lambda = \frac{(\rho CU)_o}{(\rho CU)_a}$$

affects the temperature profiles the most; hence the effects of this parameter were experimentally verified. The temperature dependence empirical formulas for the density and specific heat of the aqueous and organic phases used to analyze the experimental results were made by referring reported data of the Hanford report (1956) and Leroy (1970).

The ranges of T_o and T_h in Eq. (1) were respectively 25 ~ 37°C and 65 ~ 68°C and V_h was 5 cm^3/s. From Eq. (3), the heat supply rate per 1 cm^2 of the column cross section is then ~10.0 J/s, corresponding to a uranium concentration of 500 g/l in the feed aqueous solution (Eq. (2)). Although this value is three times greater than the normal uranium concentration in an extraction column, it is advantageous because it enhances the effects of varying the operating parameters.

Since it is difficult to vary the density and specific heat of the aqueous and organic phases experimentally without altering other aspects of the column behavior, the volumetric flux was changed, i.e., the aqueous volumetric flux (U_a) was fixed at 0.21 cm/s and the organic volumetric flux (U_o) was changed from 0.21 to 0.84 cm/s. The heat capacity ratio was therefore varied from 0.39 to 1.59.

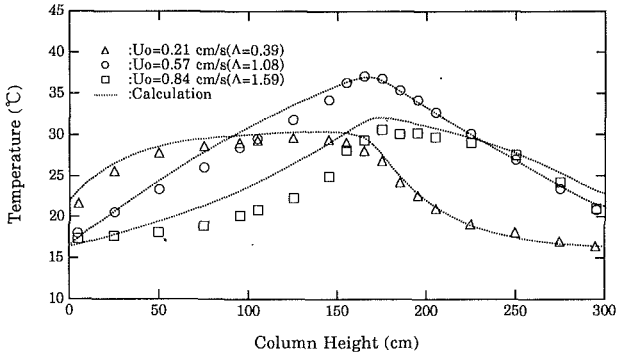

Fig. 3 Effect of the heat capacity ratio on the column temperature profiles; Exp.: U_a = 0.21cm/s, heat source location = 175 cm; Cal.: E_a = 1.0 cm^2/s, E_o = 4.0 cm^2/s, h = 0.027 J/cm^2°C

Figure 3 shows both the calculation and experimental temperature profiles with respect to various organic volumetric fluxes at a heat source location of 175 cm from the bottom settler, where good agreement is shown.

When U_o is 0.21 cm/s, then $(\rho CU)_a > (\rho CU)_o$, and Λ is 0.39. In this case, almost all the heat generated is carried by the aqueous phase, with the temperature below the heat source location (< 175 cm) being higher than above it.

As the organic volumetric flux is increased, $(\rho CU)_o$ increases and more heat is carried by the organic phase. At Λ = 1.08 (U_o = 0.57 cm/s), the highest peak temperature occurs and the temperature decreases linearly on each side of the peak.

When the organic volumetric flux is increased further (U_o = 0.84 cm/s; Λ = 1.59), most of the heat generated is carried by the organic phase, and this results in a higher temperature above the heat source than below it.

Using as a basis the axial temperature profiles shown in Fig. 3, where the effects of varying the heat capacity ratio are observed to be consistent with numerical results that indicated that this dominantly influences the column's temperature distribution, it is concluded that the calculation model adopted here is sufficient for estimating the axial temperature profiles in a pulsed column.

Heat Transfer Coefficient Between the Aqueous and Organic Phases. The heat transfer coefficient (h) between the aqueous and organic phases (Eqs. (5) and (6)) was estimated using experimental data.

If the respective effective longitudinal thermal diffusivities are given (E_a and E_o in Eqs. (5) and (6)), the heat transfer coefficient between the aqueous and organic phases can be determined.

In pulsed columns, axial dispersion coefficients of uranium have already been measured, although the effective longitudinal thermal diffusivities have not been investigated. The disturbances in the bulk flow seem to be the dominant factor to determine the axial dispersion of uranium in a pulsed column. Considering that the diffusivity of uranium in the water is 4.0 $\times$ 10^{-3} cm^2/s, which is much smaller than the reported axial dispersion coefficient of 0.1 ~ 1.0 cm^2/s (Gonda and Matsuda, 1982), the diffusion of uranium induced by the concentration gradient is less effective than the uranium dispersion. This leads to the hypothesis that the effective longitudinal thermal diffusion in pulsed columns is also affected more by disturbances in the bulk flow conditions rather than by the temperature gradient, because the thermal diffusivity in water is about 1.5 $\times$ 10^{-3} cm^2/s at 30°C. Thus, it is believed that similar

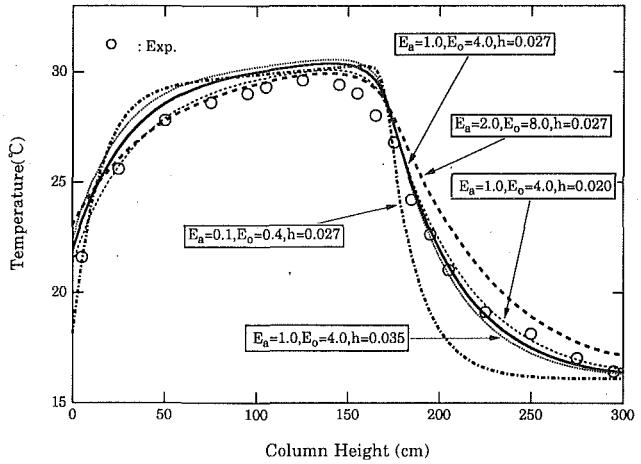

Fig. 4 Effect of the heat transfer coefficient on the column temperature profiles; Λ = 0.39, U_a = 0.21 cm/s, U_o = 0.21 cm/s, heat source location = 175 cm

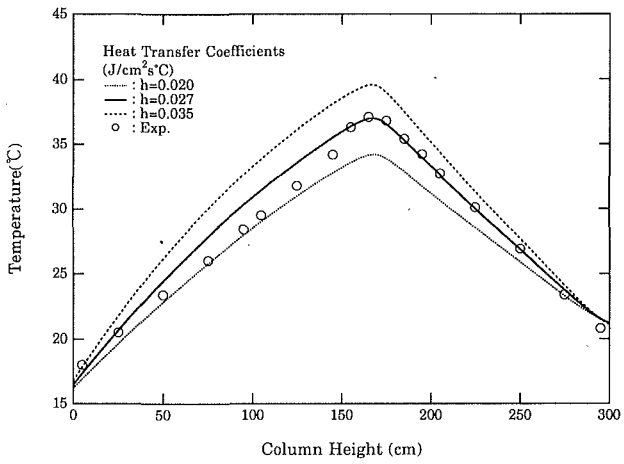

Fig. 5 Effect of the heat transfer coefficient on the column temperature profiles; Λ = 1.08, U_a = 0.21 cm/s, U_o = 0.57 cm/s, heat source location = 175 cm

values of the axial dispersion coefficients of uranium measured in a pulsed column can be substituted for effective longitudinal thermal diffusivities.

Using Gonda's empirical formulas, the axial dispersion coefficient in our pulsed column is estimated to be 0.1 cm^2/s for the aqueous phase (E_a) and 0.4 cm^2/s for the organic phase (E_o), respectively.

To estimate the heat transfer coefficient, three sets of values for effective longitudinal thermal diffusivities (E_a, E_o) are assumed, which are E_a = 0.1 and E_o = 0.4, E_a = 1.0 and E_o = 4.0, and E_a = 2.0 and E_o = 8.0 in cm^2/s.

Figure 4 compares the experimental data of U_o = 0.21 cm/s (Λ = 0.39) with calculated temperature profiles (thick lines) for E_a = 0.1 and E_o = 0.4, E_a = 1.0 and E_o = 4.0, and E_a = 2.0 and E_o = 8.0 cm^2/s when h = 0.027 $J/cm^2s°C$. When E_a = 1.0 and E_o = 4.0 cm^2/s, the calculation result agrees with the experimental results. For the same values of E_a and E_o, calculated temperature profiles when h is 0.020 and 0.035 $J/cm^2s°C$ are also shown in the same figure (thin lines).

When Λ = 0.39 and the heat transfer coefficient is changed from 0.020 to 0.035 $J/cm^2s°C$, the peak temperature varies only slightly, although the temperatures in the lower part of the column (< 50 cm) are somewhat increased. As a result, the heat transfer coefficient cannot be determined at this Λ.

On the other hand, when Λ = 1.08 (Fig. 5), the effect of the heat transfer coefficient is considerably enhanced and its value can be determined to be 0.027 $J/cm^2s°C$ for E_a = 1.0 and E_o = 4.0. Using the same method, the heat transfer coefficient was obtained to be 0.020 $J/cm^2s°C$ for E_a = 0.1 and E_o = 0.4, 0.035 $J/cm^2s°C$ for E_a = 2.0 and E_o = 8.0, respectively.

Because the heat transfer coefficient is such an important parameter for modeling of spray/pulsed column direct-contact type heat exchangers, the volumetric heat transfer coefficient (H_V) has been studied extensively. For example, the relationship between H_V and the operating conditions such as holdup and flow rate was obtained (Plass et al., 1979).

H_V is expressed by the heat transfer coefficient (h), holdup (ϕ), and Sauter mean diameter of droplet (d_{32}) as follows:

$$H_V = 6\frac{\phi}{d_{32}}h \tag{11}$$

For the estimated values of the holdup and Sauter diameter using an empirical formula by Gonda and Matsuda (1982), i.e., 0.096 and 0.25 cm, respectively, H_V was calculated from Eq. (11) as 0.062 $J/cm^3s°C$ using h = 0.027 $J/cm^2s°C$.

Of related interest, Kehat and Sideman (1970) performed a comprehensive literature review and summarized the volumetric heat transfer coefficients for many types of heat exchangers. In a pulsed column having a benzene-water system, H_V ranges from 0.020 to 0.11 $J/cm^3s°C$, whereas in a spray column it is much smaller because there is no pulsation. The experimentally determined value of h = 0.020 ~ 0.035 $J/cm^2s°C$ is fairly close to these reported values.

Conclusions

Axial temperature profiles were measured in an experimental pulsed column of the type conventionally used in nuclear spent fuel commercial reprocessing plants by injecting hot water at various column heights to simulate the uranium extraction heat. The effects of the flow and heating conditions were estimated and the obtained data were analyzed by a developed calculation code.

The effects of the heat capacity ratio on the temperature profiles, which were predicted earlier from the calculation analysis, were confirmed. This experiment demonstrates that the adopted model is sufficient for estimating the axial temperature profiles in the pulsed column.

The heat transfer coefficient between aqueous and organic phases was estimated from the temperature profiles, with this value being considered to be reasonable when compared to other reported results, which measured it in spray/pulsed columns using various liquid systems.

References

Gonda, K., and Matsuda, T., 1982, "Calculation Code PULCO for Purex Process in Pulsed Column," PNCT841-82-19.

Hanford Atomic Products Operation, 1955, "Purex Technical Manual," HW-31000.

Jacobs, H. R., 1985, "Direct Contact Heat Transfer Studies on Sieve Tray Columns for Geothermal Applications," Final Report U.S. DOE, Contract DE-AS07-84ID1252.

Jacobs, H. R., 1988, "Direct-Contact Heat Transfer for Process Technologies," ASME JOURNAL OF HEAT TRANSFER, Vol. 110, pp. 1259-1270.

Kehat, E., and Sideman, S., 1970, "Heat Transfer by Direct Liquid-Liquid Contact,"*Recent Advances in Liquid-Liquid Extraction*, Chap. 13, pp. 455-494.

Leroy, F., 1970, "Study of the Solvent 30% Tributyl Phosphate in Dodecane," ORNL-tr-4344.

Miyauchi, T., and Vermeulen, T., 1963, "Longitudinal Dispersion in Two-Phase-Flow Operations," *I&EC Fundamentals*, Vol. 2, No. 2, pp. 113-126.

Plass, S. B., Jacobs, H. R., and Boehm, R. F., 1979, "Operational Characteristics of a Spray Column Type Direct Contact Preheater," *AIChE Symposium Series, Heat Transfer*, San Diego, pp. 227-234.

Woodward, T., 1961, "Heat Transfer in a Spray Column," *Chemical Engineering Process*, Vol. 57, No. 1, pp. 52-57.